Proceedings of the

FOURTH PACIFIC CONGRESS
ON
MARINE SCIENCE AND TECHNOLOGY

VOLUME I

PACON 90

TOKYO, JAPAN   JULY 16-20, 1990

Proceedings of the

FOURTH PACIFIC CONGRESS
ON MARINE SCIENCE
AND TECHNOLOGY
—1990—

NIHON DAIGAKU KAIKAN
(NIHON UNIVERSITY CONFERENCE HALL)
TOKYO, JAPAN

July 16-20, 1990

ORGANIZERS

PACON International
Japan Marine Science and Technology Association
Foundation for Research and Development of Ocean City
College of Science and Technology, Nihon University

SPONSORS

MAJOR SPONSORS

Department of Business and Economic Development, State of Hawaii
Hawaii Natural Energy Institute/CORT, United States
Institute for Naval Oceanography, United States
The Motorcycle Racing Organization, Japan
National Ocean Service, United States
National Oceanic and Atmospheric Administration, United States
National Science Foundation, United States
Pacific International Center for High Technology Research, United States
River Environment Foundation, Japan
Sea Grant College Pragram, University of Hawaii, United States
SEACO, Division of Science Applications, United States
International Corporation, United States
The Japan Shipbuilding Industry Foundation
U.S. Geological Survey, United States

ORGANIZATION SPONSORS

Ministry of Agriculture, Forestry and Fisheries, Japan
Ministry of Construction, Japan
Ministry of International Trade and Industry, Japan
Ministry of Transport, Japan
Pacific Basin Development Council, United States
Science and Technology Agency, Japan
University of Hawaii, United States

SOCIETY SPONSORS

American Congress on Surveying, United States
American Geophysical Union, United States
American Society for Photogrammetry and Remote Sensing, United States

Architectural Institute of Japan
Coastal Development Institute of Technology, Japan
Engineering Advancement Association of Japan
International Society of Photogrammetry and Remote Sensing
IUGG Tsunami Commission, United States
Japanese Association for Petroleum Technology
Japan Association of Underwater Exploration
Japan Concrete Institure
Japan Deep Sea Technology Association
Japan Marine Science and Technology Center
Japan Society of Civil Engineers
Marine Acoustics Society, Japan
Marine Technology Society, United States
Marine Forum 21, Japan
Oceanographical Society of Japan
Research Institute for Ocean Economics, Japan
Societe France Japonese du Oceanografi, Japan
The Institute of Electrical Engineers of Japan
The Institute of Electronics, Information and Communication Engineers, Japan
The Iron and Steel Institute of Japan
The Japan Federation of Engineering Societies
The Japan Society of Mechanical Engineers
The Japan Society of Soil Mechanics and Foundation Engineering
The Japanese Institute of Technology on Fishing Ports & Communities
The Japanese Society of Scientific Fisheries
The Kozai Club, Japan
The Mining and Material Processing Institute of Japan
The Marine Acoustics Society of Japan
The Marine Meteorological Society
The Ocean Association of Japan
The Oceanography Society, United States
The Society of Fisheries Engineering
The Society of Naval Architects of Japan
The Telecommunications Association, Japan
The Tsunami Society, United States

VOLUME I

General Lectures
Ocean Science and Technology
Marine Resource Development

DEDICATED TO THE MEMORY OF

OUR FRIEND AND FOUNDER OF
PACON INTERNATIONAL, AUSTRALIA CHAPTER

PROFESSOR KELVIN P. STARK

MEMBER OF BOARD OF DIRECTORS
PACON INTERNATIONAL

PREFACE

The biennial Pacific Congresses on Marine Science and Technology (PACON), initiated in 1982, became truly Pacific-wide during the third Pacific Congress (PACON 88). At every level of the Congress, the Honorary Chairman, sponsors, society sponsors, session chairmen and, most importantly, the authors, representatives froms several Pacific nations joined in the effort to make PACON 88 an international forum.

This Fourth Congress (PACON 90), the first held outside Hawaii, has expanded further in its broad interdisciplinary scope, largely due to the important roles played by the technical program team members from Japan and Australia. A new technical session category "Ocean Space Utilization and Management (OSUM)" has been added to the two existing technical session groups "Ocean Sciences and Technology (OST)" and "Marine Resources Development (MRD)". The addition of the OSUM technical session group reflects the pioneering work done by Dr. Wataru Kato, Nihon University, Japan, and of Dr. Kevin P. Stark, James Cook University, Australia. This broadened scope is also evident in the increased number of workshops.

Although one hundred and eighty nine papers were submitted under thirty six technical sessions and workshops, only one hundred and sixty two papers were submitted in time to be included in this conference's Proceedings.

We thank the technical program coordinators, session and workshop chairmen who played a key role in designing their sessions/workshops by selecting the papers based upon the submitted abstracts.

We wish to express our thanks to all sponsors, which include professional/technical societies, federal/state agencies, academic organizations, ocean and space industries, and individuals for providing funds, support services, and announcements in technical publications. We thank the Scientific Advisory Committee and owe special thanks to the authors for submitting their manuscripts in time without which these Proceedings would not be possible.

Finally, our sincere thanks to the PACON 90 (Japan) Organizing Committee and Staff for the untiring support they have given us to make this Congress successful.

Wataru Kato and Narendra Saxena
Co-Chairmen
PACON 90

ORGANIZING COMMITTEE
(JAPAN AND HAWAII)

Honorary Chairman	Hajime Sako	John Carey
Co-chairmen	Wataru Kato Shigenori Kinoshita Kiyohide Terai	Jack Harmon Narendra Saxena
Technical Program Co-chairmen	Kenji Hotta	Narendre Saxena
Applications (Pre-registration)	Riichi Kobayashi	
Exhibits	Hiroo Oda	Richard Porter
Local Arrangements	Osamu Saijo	
Registration Host Audio-Visual Equipment	Koichi Masuda	
Promotion	Mitsuhiro Abe Eiichi Isobe	John Wiltshire
Treasurer	Riichi Kobayashi Shigeo Ozono	
Fiscal Planning	Riichi Kobayashi Hajime Sato	Narendra Saxena Sherwood Maynard
Technical Tours	Tamaki Ura	

BOARD OF DIRECTORS

United States

Representative Peter Apo
    State House of Representatives
Representative Robert Bunda
    State House of Representatives
Dr. John Craven
    University of Hawaii
Dr. Jack Davidson
    University of Hawaii
Dr. Sylvia Earle
    Deep Ocean Engineering Inc.
ADM Ronald Hays, USN (Ret)
    Pacific International Center for High Technology Research
Senator Ann Kobayashi
    State Senate
Dr. Fujio Matsuda
    Research Corporation of the University of Hawaii
Senator Richard Matsuura
    State Senate
Mr. Frank McHale
    Dillingham Hawaii Dredging and Construction Company
Mr. Jerry Norris
    Pacific Basin Development Council

Representative David Stegmaier
    State House of Representatives
Dr. Patrick Takahashi
    University of Hawaii
Mr. Paul Wolff
    Consultant
Dr. Paul Yuen
    University of Hawaii

JAPAN

Professor Wataru kato
    Nihon University
Professor Hisaaki Maeda
    University of Tokyo
Professor Seizo Motora
    Foundation for Shipbuilding Advancement
Professor Noriyuki Nasu
    University of the Air
Professor Masaaki Sakuta
    Nihon University
Professor Kiyohide Terai
    Foundation for Research and Development of Ocean City
Professor Koichiro Yoshida
    University of Tokyo

Foreign Countries

Dr. Ju-Chin Chen
    National Taiwan University, China
Dr. David Hopley
    Jemes Cook University of North Queensland, Australia
Professor Guo-Ben Hou
    Qingdao Ocean University, China
Dr. Hyung Tack Huh
    Korea Ocean Research and Development Institute, Korea
Dr. Sen-Shyong Jeng
    National Taiwan Ocean University, China
Dr. Donald Kinsey
    Great Barrier Reef Marine Park Authority, Australia
Dr. C. Y. Li
    The Executive Yuan, China
Dr. S. Z. Qasim
    Jamia Millia Islamia Central University, India
Dr. Aprilani Soegiarto
    Indonesian Institute of Sciences, Indonesia
Professor S. L. Soloviev
    Academy of Sciences, USSR
Dr. Kevin Stark *
    James Cook University of North Queensland, Australia
Dr. Suraphol Sudara
    Chulalongkorn University, Thailand

* deceased

SCIENTIFIC ADVISORY COMMITTEE

Dr. Jagdish Bhatt
    Community College of Rhode Island, United States
Dr. Su-Yen Chain
    Chinese Petroleum Corporation-Taiwan, United States
Dr. Sylvia Earle
    Deep Qcean Engineering, Inc., United States
Dr. David Hopley
    James Cook University of North Queensland, Australia
Dr. Kenji Hotta
    Nihon University, Japan

Dr. Hyung Tack Huh
    Korea Ocean Research and Development Institute, Korea
Dr. Sen-Shyong Jeng
    National Taiwan Ocean University, China
Dr. Wataru Kato
    Nihon University, Japan
Dr. Takeshi Kinoshita
    University of Tokyo, Japan
Dr. Riichi Kobayashi
    Taisei Construction Company, Japan
Dr. Koichi Masuda
    Nihon University, Japan
Dr. Christopher Mooers
    University of New Hampshire, United States
Dr. Seizo Motora
    Foundation for Shipbuilding Advancement, Japan
Dr. Hiroyoshi Nagai
    Foundation for Research and Development of Ocean City,
    Japan
Dr. Osamu Saijo
    Nihon University, Japan
Dr. Gunter Seeber
    University of Hannover, West Germany
Dr. Kevin Stark *
    James Cook University of North Queensland, Australia
Mr. Howard Talkington
    Naval Ocean Systems Center, United States

* deceased

ORGANIZING COMMITTEE

Host Country-Japan

Organizing Committee

Chairman: Seizo Motora
               Foundation for Shipbuilding Advancement
Vice-Chairman: Koichiro Yoshida
               University of Tokyo
Members: Noriyuki Nasu
               University of the Air
               Toshisugu Sakou
               Toukai University
               Shotaro Hattori
               Chuo University
               Toshiro Suhara
               University of Toua
               Kiyohide Terai
               Foundation for Research & Development of Ocean
               City
               Hiroyoshi Nagai
               Foundation for Research & Development of Ocean
               City
               Hisaaki Maeda
               University of Tokyo
               Hajime Sato
               Japan Marine Science and Technology Association
               Riichi Kobayashi
               Japan Marine Science and Technology Association
               Masaaki Sakuta
               Nihon University
               Toshiro Nishimura
               Nihon University

Academic Committee

Chairman: Masaaki Sakuta
               Nihon University
Vice-Chairman: Koichiro Yoshida
               University of Tokyo
Members: Kenji Hotta
               Nihon University
               Hisaaki Maeda
               University of Tokyo
               Osamu Saijo
               Nihon University
               Koichi Masuda
               Nihon University
               Kei Muneyama
               Japan Marine Science and Technology Center
               Hiromi Fujimoto
               University of Tokyo
               Tomoyoshi Takeuchi
               The University of Electro-Communications
               Takeshi Usami
               National Research Institute for Pollution and Re-
               sources
               Yoshinobu Tsuji
               University of Tokyo
               Hideaki Miyata
               University of Tokyo
               Hiroshi Kobayashi
               Shimizu Corporation
               Nobuo Suginohara
               University of Tokyo
               Toshifumi Noma
               National Research Inst. of Fisheries Engineering
               Yasuhiko Okano
               University of Tokyo
               Hideo Kondo
               Muroran Institute of Fisheries
               Fumio Takashima
               Tokyo University of Fisheries
               Hiroshi Tokuda
               University of Tokyo
               Norio Tanaka
               Nippon Tetrapod Company, Ltd.
               Norimoto Kashino
               Building Research Institute, Ministry of Construc-
               tion
               Yoshiharu kon
               New Land Development Laboratory Inc.
               Shigeo Tsujikawa
               University of Tokyo
               Mamoru Shinozuki
               Takenaka Cooperation Plannets, Architects, Engi-
               neers and Contractors
               Takeo Kondo
               Nihon University
               Souichi Ito
               NKK Corporation
               Takeshi Kinoshita
               University of Tokyo
               Shunji Fujii
               Taisei Corporation
               Takeshi Murai
               National Research Institute of Fishery Science
               Tomoyuki Moritani
               Geological Survey of Japan

Executive Committee

Chairman: Hisaaki Maeda
               University of Tokyo

CONTENTS

VOLUME I

GENERAL LECTURE

OCEAN SCIENCE AND TECHNOLOGY

MARINE RESOURCE DEVELOPMENT

VOLUME II

OCEAN SPACE UTILIZATION AND MANAGEMENT

GENERAL LECTURE

HISTORICAL CHANGES IN NATURAL WATER HAZARDS IN JAPAN

Yoshito Tsuchiya

Disaster Prevention Research Institute, Kyoto University, Japan

Abstract

In this paper, as one of the key indexes of social environment, the growth and decay of the total Japanese population is investigated for a period of about 10,000 years. Five major changes in total population are detected and then compared with the duration and magnitude of historical records of natural water hazards. Secondly this comparison is made in order to determine the natural hazard influence on total population trends.

The longer time scale of natural hazards (a period of about 10,000 years) is considered in relation to changes in natural forces and social environment. The natural water hazards and their changes in periods of past 2,000 and 300 years are considered in more detail in relation to natural forces such as climate change, typhoons, drought and plagues, and social environment such as reclamation, construction, internal disturbances, social activities and politics.

1. Introduction

Being located in the circum-Pacific diastrophic zone, Japan is a country that experiences disasters caused by such natural forces as typhoons, monsoons, volcano eruption, and earthquakes. Recently, Japan has shown remarkable technological development which should continue well into the next century. New problems have come into being that are related to this development which necessitate the advancement of marine science & technology in order to avert disasters.

Many years ago, Dr Torahiko Terada who was Japan's most famous scientist said: "Natural hazards are progressive in relation to civilization, they occur only once they have been forgotten". In relation to human activities natural hazards have changed and recently due to human activities the natural forces which induce disasters have been gradually changed. In other words, the global situation has been gradually changed due to current human activities throughout the world. Dr Terada also said: "Nature is faithful to her custom and experience". Once our societies have developed, natural hazards will occur again. As science and technology of natural hazard prevention and mitigation has progresed the occurrence probabilities of natural hazards have decreased. Nevertheless, the occurrence of a natural hazard may result in a major catastrophy.

In this general lecture, by use of historical data of natural water hazards including the so-called climate hazard, changes in natural water hazards are presented in relation to changes in natural forces and human activities. The changes in natural water hazards are considered in terms of defined time scales, such as longer and shorter ones. Consequently, three time scales are employed(10,000, 2,000 and 300 years) to consider the historical changes in natural water hazards due to long term climate change and human activities.

2. The Time & Spatial Scales in Hazards

2.1 Five stages in total population growth

By use of population data of Kito(1983) and Koyama(1984) the total population growth is shown in Figure 1 for a period of about 10,000 years. Obviously there exists five stages in the change of total population in the figure. These stages may be due to changes in natural forces and social environment resulting from human activities. This is to be considered in detail in terms of specified time scales.

2.2 Time & spatial scales in hazards

The main causes of the five stages in the population growth shown in Figure 1 are considered in terms of specified time scales. In the period specified, the causes to be considered are due to the time scale. In the period, of course, abnormal phenomena such as long term climate change occur following catastrophes such as storm surges and floods in a shorter time scale within the period.
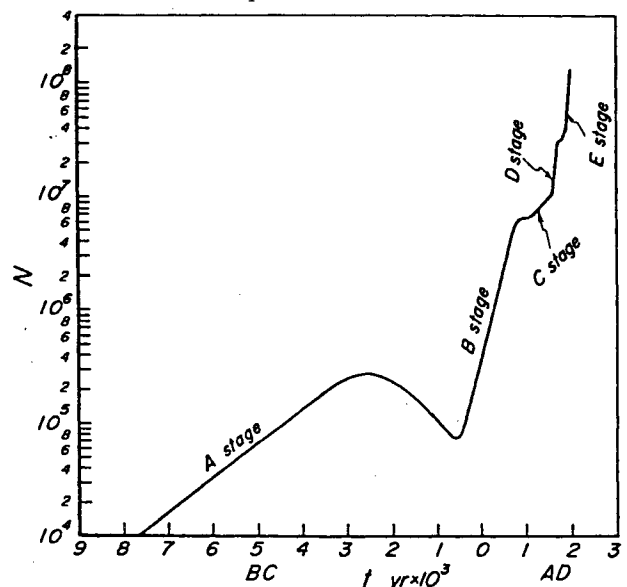
Figure 1 The five historical stages of Japan's total population growth

In the shorter time scale, the catastrophes are specified and these disasters are predominant. The former phenomena in the longer time scale are shown schematically in Fig-

ure 2(a). In a stable social and natural environment, popu-laltion may increase in terms of logistic equation. In the case shown in the figure, therefore, the population decreases as human activities decrease due to abnormal change in natu-ral forces such as climate change. This includes catastrophic population change due to abnormal forces. In a shorter time scale as shown in Figure 2(b), the population decreases sud-denly due to abnormal natural forces and then recovers to the stable population growth trend . This can be considered in the shorter time scale, but may be buried in the longer time scale.

Special scales are considered in relation to the time scales in Figures 3 and 4. In the longer time scale Figure 3 shows areas where the population decreased over the period be-tween 1721 and 1750 AD due to climate change. The area covers almost all northern areas of the Japanese islands, the time scale of this climate change is about 30 years. On the contrary, in the shorter time scale areas flooded by Ise Bay Typhoon in 1959 in which about 5,000 persons were killed only surround the Ise Bay to which the time scale is only one day.

(a) Longer timescale

(b) Shorter timescale
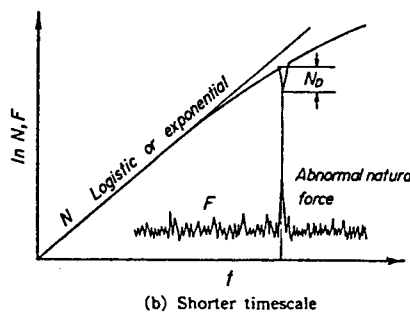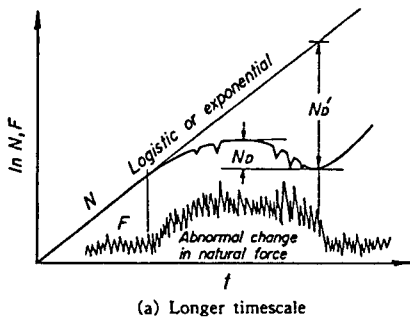
Figure 2 Definitions of time scales in natural disasters

3. Historical Change in Natural Water Hazards in Time Scale of 10,000 Years

In the period of past about 10,000 years changes in natural water hazards are considered in relation to civilization. The reasons for the five stages are considered.

3.1 Natural forces as natural environment

The change in solar activity is shown in Figure 4 for a period of past about 8,000 years. And changes in annual mean temperature (Yasuda, 1980), mean sea level at the southern Kanto district, Tokyo and Osaka bays, and temperature indexes modified by Sakaguchi(1984) data are shown in Figures 4, 5 and 6, respectively.

	1.000 - 0.991
	0.990 - 0.971
	0.970 - 0.951
	0.950 - 0.901
	0.900 -
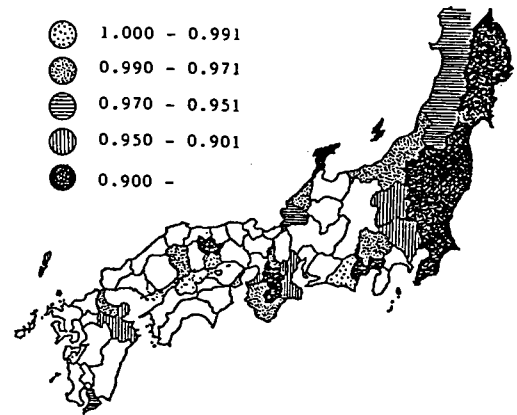
1750 to 1786 yg AD

(a) Areas where population decreased in the periods mentioned.
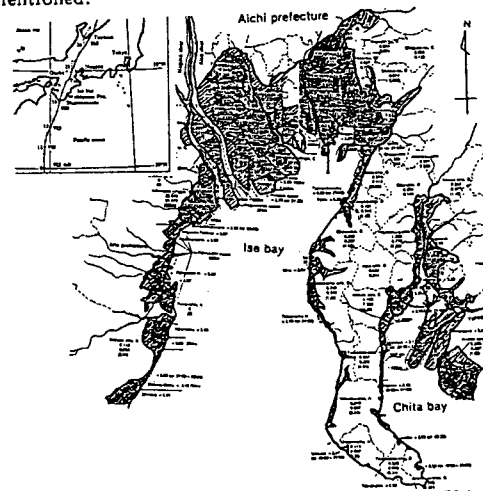
(b) Flooded areas surrounding Ise Bay at Ise Bay Typhoon.

Figure 3 Areas where population decreased
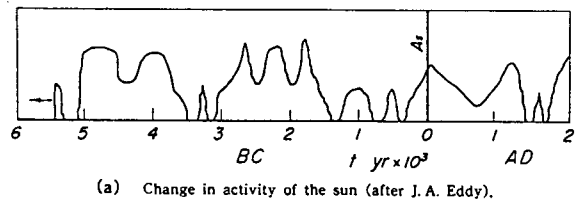
(a) Change in activity of the sun (after J. A. Eddy).
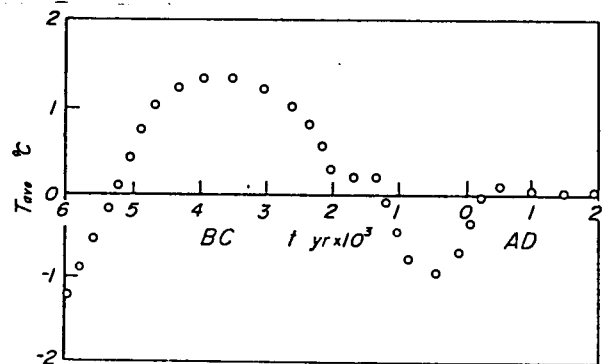
(b) Change in annual mean temperature[19].

Figure 4 Changes in solar activity and annual mean temperature

From these figures climate change and its effect on the an-nual mean temperature and sea level changes are considered as: 1) In the Jomon period especially around BC 4000 years

the annual mean temperature was high which resulted in high sea level which is called Jomon sea advancement. Due to the climate change land cultivation was changed to grow nut trees. 2) In the latter period around BC 1000 years, the annual mean temperature was low and consequently vegitable and sea level changes occurred. In this period vegitation changed from nut trees to cedar trees. 3) In the C, D and E stages no remarkable long term climate change was observed, but several changes in climate were of course observed as will be shown in the next chapter.
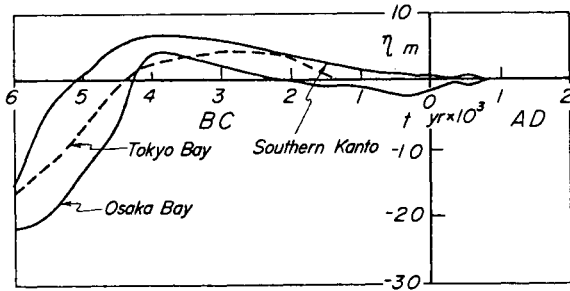
Figure 5   Change in mean sea level at southern Kanto district, Tokyo and Osaka bays
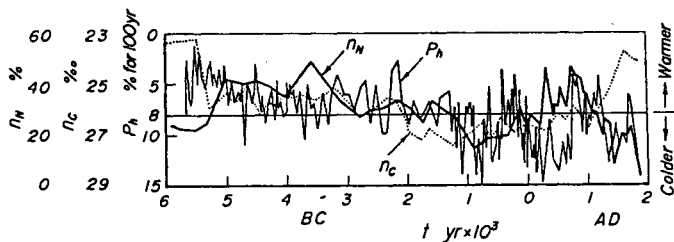
Figure 6   Changes in temperature indexes

3.2 Social environment and its change

In relation to the climate change described in 3.1, the main causes for the five stages in population are briefly considered by taking into account the changes in social environment.

1) The A stage social environment and its breakdown

In the Jomon period which covers the A stage, it is well known by the climate that most all areas of Japan were covered by beech trees. Nuts gathered in the forests were used for food together with the hunting of animals and birds. The societies were formed as hunting and nut-gathering ones. Koyama(1984) estimated that the potential population density in the Jomon period was one to two persons per square kilometer. The vegetation changes due to climate change were investigated by Yasuda(1986). The vegetation changed clearly in and around the period between BC 4,000 years and BC 1,000 years due to climate change. By use of Koyama population data, changes in population densities in the several districts are shown in Figure 7, where the Kyushu, Shikoku, Chugoku, Kinki, Tokai, Chubu, Hokuriku, Kanto and Tohoku districts are located from southern to northern parts of the Japanese islands, respectively. It is clearly understood that the potential population densities are nearly two persons per square kilometer, and that the more rapidly the population density increases, the more rapid decrease when reaching a certain potential population density. As described the main causes for the population shifts of Jomon period are long-term climate change, as well as plagues. Yasuda(1984) also suggested an additional cause which is the

increase in flood disasters due to forest destruction by the people.
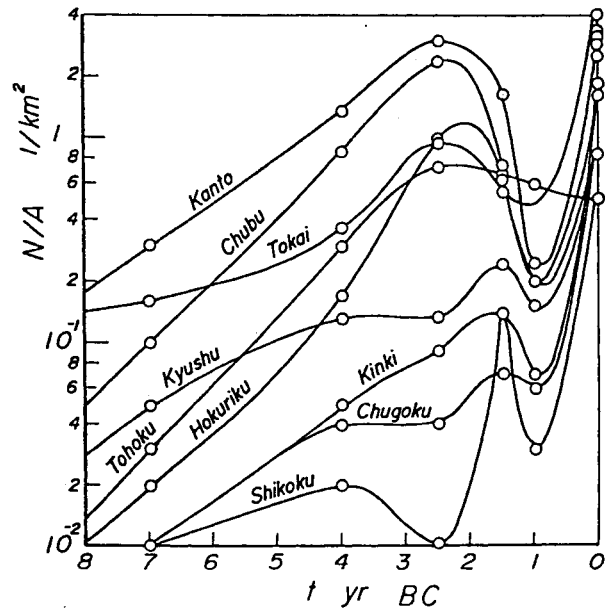
Figure 7   Changes population dencity in several districts in the Jomon period

2) The B stage social environment and its breakdown

This stage covers the Yayoi period from the late Jomon period to 1000 to 1200 AD, which is the Heian period. As stated in the introduction, Terada said: "Natural hazards are progressive in relation to civilization". What is the breakdown cause for this period? Since rice production technique was imported and transfered quickly from western areas to eastern and northern areas, the hunting and gathering societies were changed to agricultual ones.

As shown in Figure 4, cold weather was experienced in the periods from the late Jomon to the first Yayoi period and reexperienced in the old mound period (200 to 700 AD) through warm weather in the middle Yoyoi period. In this period, residents lived on natural banks and hills in alluvial fans on which they farmed. Owing to poor technique of flood control they probably suffered from flooding. A little progress in rice production and irrigation works was made and then farmers societies were gradually changed to a proprietary society in which larger irrigation works were constructed for more effective rice production. Many constructions were then made and many internal disturbances were experienced. Around 350 AD the Yamato court was born to control such large farming societies (Koyama, 1984).

In relation to development of rice production, population had increased rapidly as shown in Figure 1. It might be said that the large scale rice production was the first case of altering the natural environment for mans usage. We can now recognize nice examples of this developing culture, such as Toro and Uryudo relics which were developed in the waterbasins of the Abe and Yamato rivers. Around 900 AD which covers the late Yayoi, natural banks were formed and developed by frequent flooding. Disasters might have frequently taken place by changing of river courses and meandering. Yasuda(1980) described that a big flood disaster was experienced by the residents in the Uryudo relics. The old mound civilization began around 200 AD and was well developed around 400 AD extending around the whole areas of the Japanese islands, but was broken down around 600 AD. It is

said that the old mounds were surrounded by canals which were constructed to prevent natural disasters caused by fire and floods.

In the B stage where rice production techniques were developed and expanded to the whole areas of the Japanese islands, the breakdown of the Yayoi civilization resulted due to frequent flood disasters. A more detail explanation for this breakdown will be made in terms of more shorter time scale.

3) The C and D stage social environment and their breakdown

The C stage covers the so-called turbulent age and the D stage covers the Azuchi-Momoyama and Edo periods after the national unification in 1590 AD. In the former period little cultual exchange was made between the middle of 1200 AD and nearly the end of 1300 AD, but afterwards it recovered and developed. In the middle of 1400 AD which covers the Muromachi age, the age of turbulent age had come into being as the age of rival chiefs. The residents suffered from these disturbances and riots and monk disturbances frequently took place (Sugiyama, 1987). In the C stage the population growth stagnated showing a smaller population increase than the B stage. In this period colder weather was experienced, but such disturbances resulted in more effective influence on human activities than natural disasters caused by cold weather. In 1590 AD at which time national unification was sucessfully made, the social environment at last recovered after the century long internal disturbances. The population rapidly increased in the D stage thereafter.

In the period of D stage, many constructions for irrigation and reclamation had been promoted to expand farm land for rice production. Rapid development was strongly promoted. This resulted in considerable inharmionious situation with nature, as well as human activities (Wakita, 1987). Strong climate change occurred and then this situation reflected to accelerate natural disasters such as famines and droughts. We have to remember that natural hazards are progressive with civilization. More rapid increases in population results in more severe new natural hazards such as famines. During the Tenmei and Tenpo famines many people died, especially in the northern districts. The total population decreased suddenly, which is really the first experience in population decrease even though no internal wars were taken place. It should be recognized that in the biggest famines the wrong politics in the period accelerated the damage to human losses. A sorrowful sacrifice was experienced in this period. The next new age has come, the E stage.

4) The E stage social environment

As explained in 3), many riots and famines were taken place due to severe climate change and wrong politics. In 1868 the Meiji restoration was carried out by the strong resident wish, and then democratic societies came in the Meiji period. In this period many public works such as reclamation and short cutting of rivers for flood disasters were actively performed. Consequently, the population has increased rapidly, as shown in Figure 1. Due to such rapid development in alluvial areas, however, flood disasters have frequently taken place and these are really reaction from nature against the rapid development to nature. Since the Meiji period had gone the Showa period has come through the Taisho period of only about 15 years. In this period Japanese people first experienced wars with foreign countries. Through the period extending from World War I, World War II and the Japan-China War, the social environment have changed significantly and many of victims were bought into these wars. Especially severe was World War II environment by which

310 thousand persons lost their lives. In the Japanese history Japanese were the first to experience such a sudden decrease in population during this period, and never forget this fact for the human welfare of the world. The Japanese society had quickly changed and developed, so the population has increased.

4. Historical Change in Natural Hazards in Time Scale of 2,000 Years

In the shorter time scale of 2,000 years covering the period from the middle Yayoi to the present, in relation to the change of natural environment, historical changes in natural hazards are considered in more detail.

4.1 Natural forces as natural environment

Changes in the deposition rate of radioactive oxygen in the Yakusugi tree and the climate change index by Sakaguchi(1984) are shown in Figure 8 for a period of about 2,000 years.
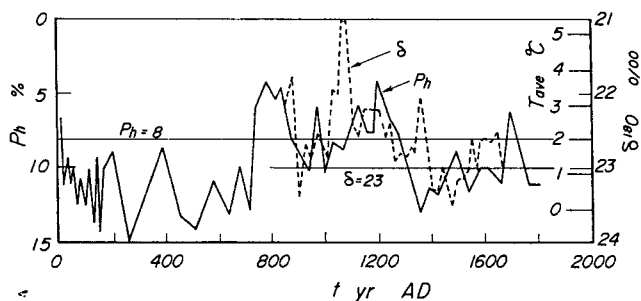
Figure 8   Changes in radioactive oxygen deposition rate in the Yakusugi tree and the climate change index by Sakaguchi(1984)
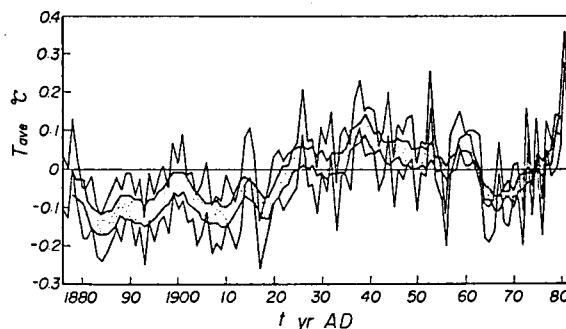
Figure 9   Changes in average temperature on the northern hemisphere since 1880 AD

As shown in Figure 4, the solar activities changed and resulted in the so-called Wolf, Schwabe and Mounder minimums. It is noticed from Figure 8 that colder weather was experienced in the middle Yayoi followed by warmer weather in the period between 700 and 1,200 AD and then again cold weather occurred corresponding to the Mounder minimum. Furthermore, the more recent change in average temperature is shown in Figure 9 revealing that it was cold in the period between 1800 and the first 1900 AD, and since then it has become warm due to the so-called green house effect and so on.

As shown in Figure 10, many typhoons had landed on the Japanese islands. This figure was constructed from natural disaster data. It is clearly noted that the frequency of typhoon landings are very high in the periods between 800 and

1000 AD, 1100 and 1300 AD, and 1600 and 1900 AD.

4.2 Social environment and natural hazards

In this period, by use of the historical disaster data by Arakawa & Usami(1985), changes in occurrences of natural disasters N_{ND}, plagues N_p, and droughts N_d, and in the number of typhoon landings N_T in relation to population N are shown in Figure 10 where all values shown were counted for every 25 year period, and no data were reported for the period between 0 and 410 AD. Furthermore, the natural disasters shown in the figure are classified into three categories which are caused by floods, storm surges and the others. Changes in the number of temples N_T, palaces N_P transfered and temples burned N_b, and occurrences of smallpox and plague are also shown in Figure 11 in relation to population change. Since Buddnism was transfered, many temples were built and palaces were also built and transfered.

As shown in Figure 9, the so-called old mound cold weather period lasted until 700 AD. This cold weather period was followed by a warming which lasted around until 1300 AD and then by another cold period(usually called as a little ice age) which ended around 1900 AD (Sakaguchi,1984). In the figure no data were reported in the first period where flood disaster might have occurred. In the next warm period many disasters caused by drought and famine were experienced. The frequency of disaster occurrence decreased following this period. Following the import of rice production technique, the population increased rapidly due to the changing social environment where large residents were formed. By the poor technique for rice production and storage, however, a new disaster, famine took place due to frequent occurrence of droughts. As seen in Figure 11, Buddism was transfered in 538 or 552 AD when many plagues prevailed due to the famines. It can therefore be supposed that such disasters and the altered social environment resulted in a stagnant or decreasing population, as shown in Figure 10. In this period, flood disasters caused by typhoons frequently took place, possibly due to increasing storm surge disasters.

In the Tenpyo(Nara) period from 710 to 783 AD, much timber was needed in constructing many temples and palaces as shown in Figure 11. The timber was harvested from forests in Koga, Shigaragi and Tanokami areas in Shiga Prefecture, the amount of timber was roughly estimated to be 75,000 m³. Such social evils, where timber used for construction was over harvested, had been continued for about three hundred years, which resulted in the ruin of the forests and the possible occurrence of many flood disasters in the period between 800 and 1000 AD. As shown in Figure 10, many people then died of smallpox and other plagues. In the period after 1300 AD which was called a little cold weather period, many typhoons landed on the Japanese islands and they were at their peak frequency of occurrence around 1700 AD. They resulted in many flood disasters by typhoons. Droughts and famines also had taken place and soon after plagues were in fashion. It is also noted that population growth increases the chances of storm surge disaster. After the long period of internal disturbances, in 1590 AD national unification was carried out. The population had increased rapidly. Many disasters as previously described resulted in severe famines by which many people died, consequently the population stagnated and decreased.

In this period, a great number of construction works were carried out to cultivate and extend farm lands. By use of a list of the construction works by the Japan Society of Civil

Engineers(1938), their historical changes are shown in Figure 11, where they are classified into four categories; they are irrigation ponds, weirs and dikes, reclamation and others. In the figure the population growth and the increase in farm lands are also shown. Until 800 AD, irrigation ponds were constructed only in the Nara district, then extending over all areas of Japan. Then population had increased in the period. After that time a few constructions of ponds were made.
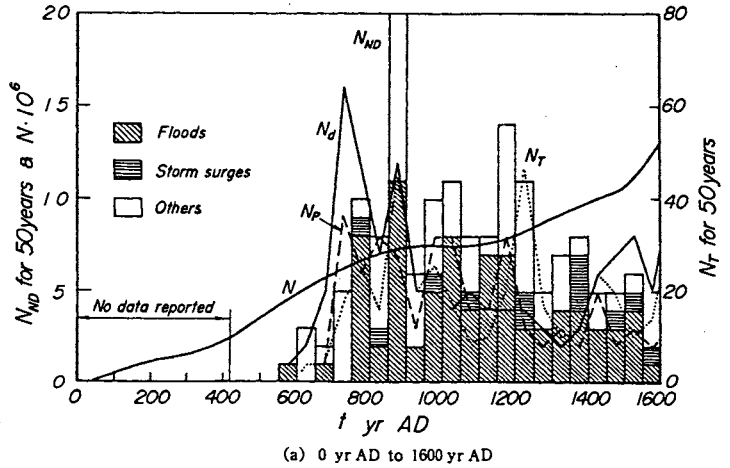
(a) 0 yr AD to 1600 yr AD
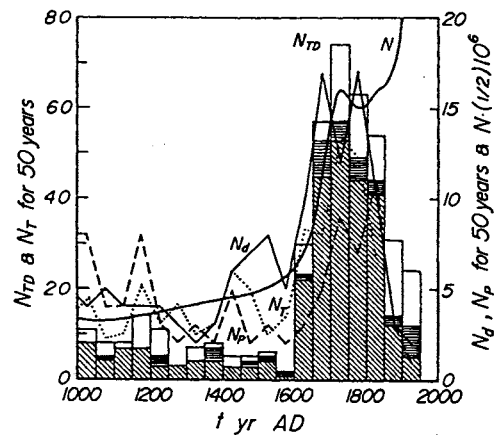
(b) 1000 yr AD to 1950 yr AD

Figure 10 Changes in occurrences of natural disasters, plagues, and droughts, and in number of typhoon landings in relation to population growth

Ohishi(1977) showed that the total areas of farm lands were not increasing, but in nearly constant until 1400 AD. After the national unification in 1590 AD, many kinds of construction works had rapidly been carried out. He called the period of many construction works as the new reclamation age which can be divided into the first and second stages. The first stage is a period of about one hundred years initiating with the national unification, and the second is around 1800 AD. In the first stage, as previously described, many construction works were made such as irrigation ponds, weirs and dikes for reclamation, and replacement or short-cutting of rivers for flood disaster prevention. Such typical constructions are the river branching works of the Kitakami river which was carried out in a period between 1623 and 1626 AD by Masamune Date, Lord of the Sendai clan, and the replacement works of the Tone river which was performed in the same period by Tadatsugu Inanokami and his son, Chief of the Kanto district of Japanese Feudal Government, and so on. In the second stage, the Feudal Government had also

promoted the development of reclamation and cultivation procedures. Large scale reclamation projects were carried out by the so-called tradesmen in the middle Edo period. The construction was financed by the tradesman, and the development was made by the farmers. A typical example is the Kanda new reclamation in the alluvial areas of the Kiso river which was developed in 1707 AD.

(a) 0 yr AD to 1600 yr AD

(b) 1000 yr AD to 1900 yr AD
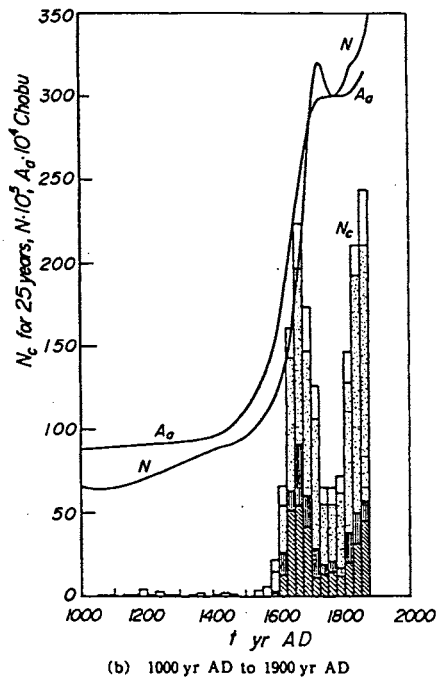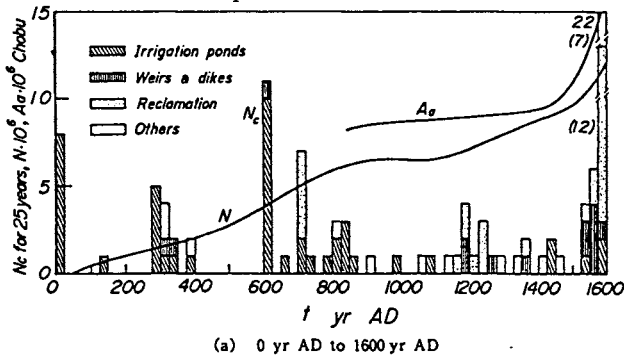
Figure 11 Histrical change in number of construction works in relation to population growth

In the first stage, as previously explained, a number of typhoons had landed resulting in flood and storm surge disasters. Ohishi(1977) pointed out that due to the poor techniques for flood disaster prevention in alluvial areas flood disasters frequently occurred. The ruin of the river basins may foster the disasters. Possibly the ruin is the direct influence of the rapid development. In 1666 AD, the government enforced a law for the controlling of the river basins for the flood disaster prevention.

Due to the cold weather (usually called as a little ice age) in the second stage, droughts were increased in frequence as shown in Figure 10. Consequently severe famines and plagues took place, especially in the periods between 1783 and 1787 AD and between 1833 and 1837 AD, respectively. The severe famines brought plagues and killed a great number of people. The population then decreased suddenly as shown in the figure. Furthermore, government policy accelerated the famines and the people sacrifice.

5. Historical Change in Natural Hazards in Time Scale of 300 Years

For the more shortest time scale of 300 years covering the Edo period, for example, historical changes in natural hazards are considered.

5.1 Natural forces as natural environment

By use of daily weather data listed in the Nikko-sosho(daily report of Nikko-Toshogu Temple located in the northern Kanto district), changes in weather for a period of 185 years from 1722 AD are shown in Figure 12, where the daily weather data listed were averaged for every five year period. In the figure, D_r, D_f and D_c indicate the ratios of rainy, fine and cloudy days to the total, respectively, and the change in the number of typhoon landings is also shown where the data were also averaged for every five year period. It is pointed out that fifty to sixty year periods exist in the changes in weather and number of typhoons, and that three cold weather terms exist in the period mentioned.
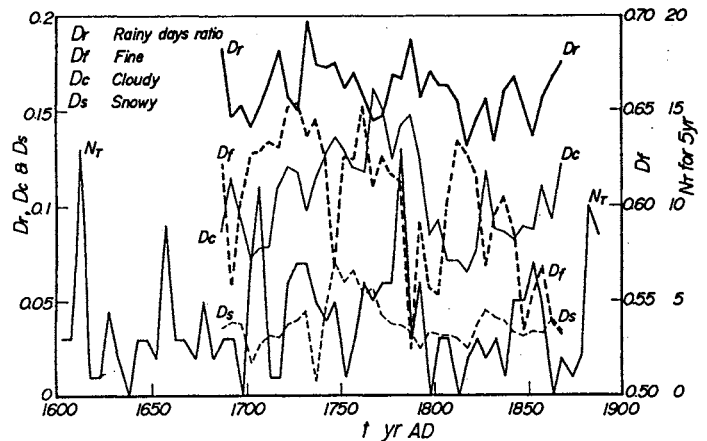
Figure 12   Changes in weather at Nikko and number of typhoon landings

5.2 Social environment and population growth

The population growth in this period is shown in Figure 13. In the figure the population growth in the several districts are also shown. It can be concluded as previously described in the Jomon period that the more rapidly the population increases, the more rapid decrease, as specially shown in the Kanto and Tohoku districts.

After the Meiji restoration in 1868 AD the population again increased rapidly. The Edo period has been called the "rice society". The Feudal Government tried to control the rice production rate, but its change occurred in relation to the social environment such as occurrence of droughts and famines. The change in the rice production rate in Kyoto (Yamashiro district) is shown in Figure 14, where the population change is also shown. As will be discussed, disasters such as drought, flooding and famine occurred in the period. Consequently, the rice production rate changed suddenly when severe disasters occurred. The figure therefore shows such social environment change in the rice society.

In Figure 15 historical changes in the number of construction works are shown in this period. It can be clearly noted that as described in Figure 10 two stages of the rapid construction and development exist, and that around 1666 AD where the rapid reclamation and cultivation were politically prohibited, the number of the constructions decreased, and after about twenty years it recovered again. In the middle

Edo period, a few constructions were only carried out due to severe social environment where many disasters and famines took place and a great number of people died. And in the late period, constructions were again carried out frequently, but little population growth occurred due to the social environment where many disasters were caused by flood, storm surge and drought which resulted in severe famines.
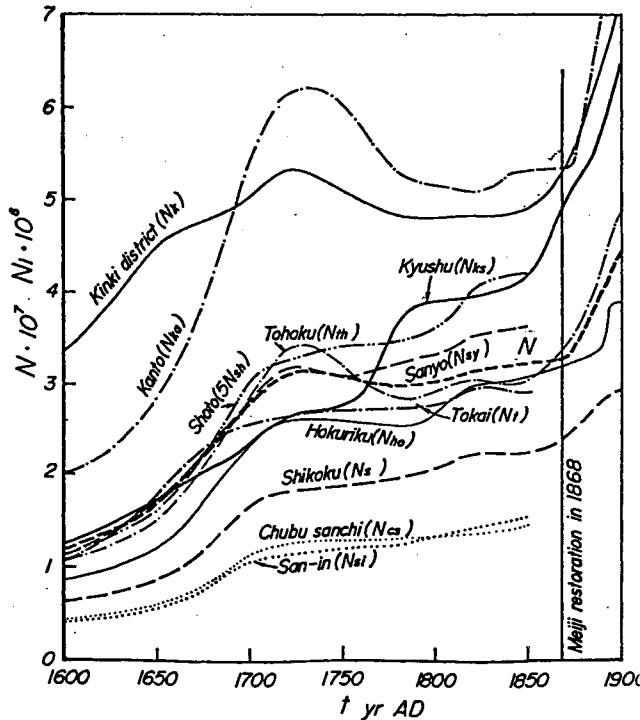
Figure 13 Population growth in several disrticts and total one (N) in the Edo period
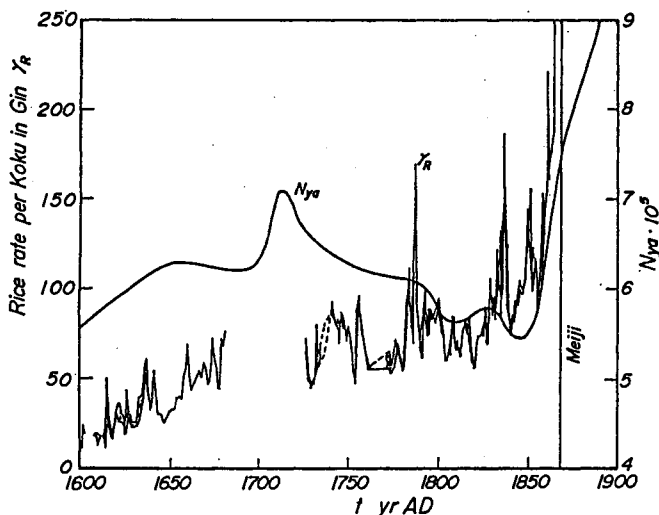
Figure 14 Changes in rice production rate and population in Kyoto

5.3 Changes in natural water hazards

As previously described, natural hazards are progressive in relation to civilization. In this period many disasters occurred by flood, storm surge and drought, the amount of rice production decreased resulting in severe famines by which many people died. They brought social disturbances such

as riots and farmer disorders. Figure 16 shows the historical changes in the number of riots and disorders N_r and their relative number to population N_r/N in relation to the population growth. It can be recognized that the riots and disorders occurred periodically at 50 to 60 year interval, and that the most frequent occurrences exist three times in the period from 1750 AD to the Meiji restoration in 1868 AD.

In Figure 17, change in the number of fires in Edo(presently Tokyo) is shown, where the thin line indicates the number of fires in every year and the thick line the occurrence number for every ten year period. It is clearly recognized that periodic occurrence of fires exists and its period is nearly 50 to 60 years, and that the number of fires was increasing in relation to the population growth. As the population began to concentrate in cities such as Kyoto and Edo, another new hazard, fire become remarkable. Fire as one of natural weather hazards is of course not only due to the weather such as strong wind but the social environment such as housing and living conditions. The periodicity in fire occurrence is due to the weather condition, and its seasonal change clearly exists. In Edo, therefore, clansmen who are on duty in the Edo Feudal Government did not like to accompany their families in winter seasons where fires occurred frequently.
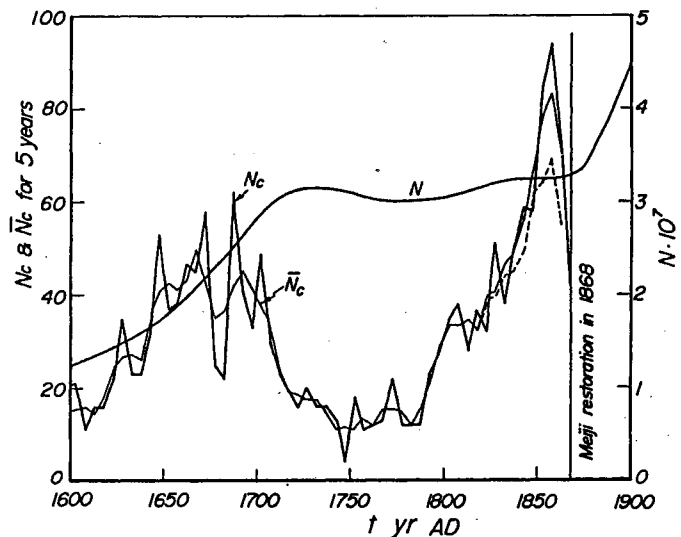
Figure 15 Historical changes in the number of construction works in the Edo period in relation to population growth

6. Conclusions

In this general lecture, historical changes in natural water hazards in a broad sense are described briefly in relation to changes in natural and social environment. In the consideration three time scales were employed for specifying disasters and their spatial scales; they are 10,000 years, 2,000 years and 300 years, respectively. Of course more shorter time scales are needed in studying catastrophic disasters occurred in a very short period, say one day. A typical example is the storm surge disaster in 1959, many other disasters can be selected. Further considerations for more shortest time scales will be discussed in the future. Conclusively, natural water hazards are truly in progress in relation to civilization. This has been examined by the historical changes in natural water hazards in Japan.

Figure 16　Changes in the number of riots and disorders
and their relative number to population in relation to
population growth
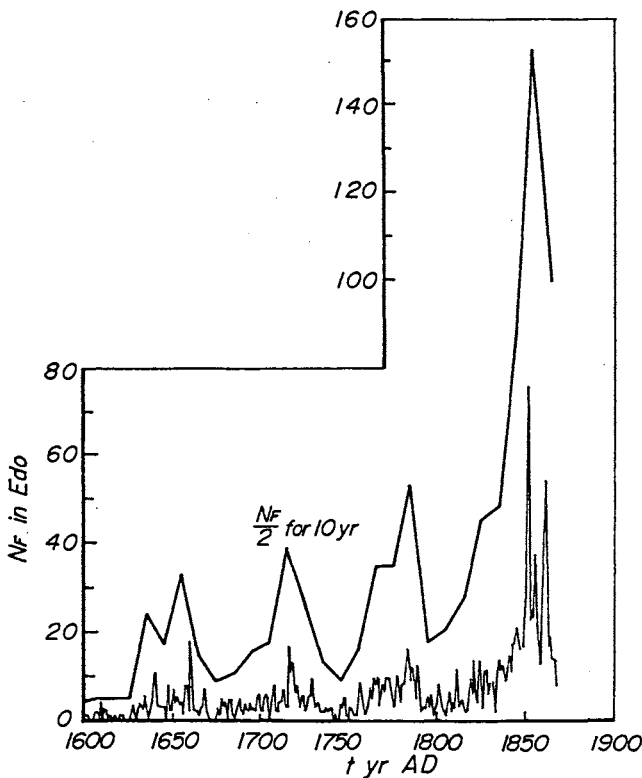
Figure 17　Changes in fire occurrence in Edo

References

Arakawa, H. and T. Usami(1985):Little Encyclopedia
of Japanese History, Disasters, Kondo-shuppan, 350p.(in
Japanese).

Kito, H.(1983):Japanese Population History of 2,000
Years, PHP, 210p.(in Japanese).

Koyama, S.(1984):The Jomom Period, Chuko-shinsho,
206p.(in Japanese).

Ohishi, S.(1977):The Edo Period, Chuko-shinsho, 266p.(in
Japanese).

Sakaguchi, Y.(1984):Climate change in Japanese prehis-
torical and historical periods, Nature, pp.18-36(in Japanese).

Sugiyama, H.(1987):Japanese History, 11, Chko-bunko,
502p. (in Japanese).

Terada, T.(1979):Terada Torahiko Series, Vol.　7,
Iwanami, pp. 145-151(in Japanese).

Tsuchiya, Y.(1988):Natural water hazards in urban areas
(1)-Time & spatial scales and historical changes in natural
water hazards-, Annuals, DPRI, Kyoto Univ., No. 31 B-2,
pp. 677-703(in Japanese).

　　　　(1989):Natural water hazards in urban areas
(2)-Changes in natural water hazardsin a time scale of 2,000
years(continued)-, Annuals, DPRI, Kyoto Univ., No. 32 B-
2, pp.909-934(in Japanese).

　　　　(1990):Natural water hazards in urban areas
(3)-Disasters in the Edo period-, Annuals, DPRI, Kyoto
Univ., No. 33 B-2(in printing).

Tsuchiya, Y. and Y. Kawata(1988): Historical changes of
storm surge disasters in Osaka, Natural & Man-Made Haz-
ards, D. Reidel Pub. Com., pp. 279-303.

OCEAN CITY

Dr. Kiyohide Terai

Foundation for Research and Development of Ocean City, Japan

Abstract

This is the generation we will begin to be able to selectively manage the many problems that present day Japan is now being faced with. These problems include the severe lack of the necessary land space for our cities and the outstandingly high land prices. Moreover, these trends are becoming more and more serious as the years progress.

Japan faces other types of problems which are becoming international dilemmas, problems it will not be able to resolve on it's own. The construction of a new 24 hour international airport for the HST aircraft so called "New Orient Express" which is capable of transpacific flights in just a few hours. Trade frictions between Japan and the United States and between Japan and Europe are now becoming serious problems.

Construction of the Ocean Community City will play a significant role in resolving the following such problems by "killing many birds with one stone".

1. The concept behind Ocean Community City or Ocean Communications City (OCC)

At the time construction of this Ocean Community City is completed, our future post-industrial society will be influenced by a number of factors. The study group for the Ocean Community City is especially interested in the following four points.

● Expensive land prices

The price of land in central Tokyo is becoming more expensive year after year. In a few years it will cost close to one "oku" (¥100 million or about half a million US dollars) for one "tsubo" (3.3 square meters) . It will thus be increasingly difficult to find a place to live which is both comfortable and convenient in Tokyo or the surrounding area. An attractive combination of comfort, convenience, and charm will become more elusive as time passes. If we want comfort, we must sacrifice convenience and/or charm, and vice-versa. Living in a city close to the working place, shopping, and entertainment centers also means having to put up with noise and pollution. This stems from the fact that today's cities are built on one plane and it takes time to transfer from one spot to

another. Suffice it to say that the current city is not functional.

● Airport for HST aircraft

Ultra-high speed planes, including the SST (MACH: 1-5) and HST (MACH: larger than 5), will be able to enter service through the 24 hour International Airport, located in the Pacific Ocean to minimize noise pollution.

In February 1985, NASA announced the development of high speed aircraft including a 500-passenger plane of MACH 2 (14,400km per hour), to be completed in 15 years. This plane will fly between Los Angeles and Tokyo.

In his State of the Union address of 1986 Mr. Reagan announced that NASA will undertake major R&D for a super-high speed plane of MACH 25 in the next ten years. This plane is scheduled to shuttle passengers between Washington's Dulles International and Tokyo. Therefore, speaking from the side of Japan, an actual concrete project will be needed as soon as possible to build an international airport operating 24 hours a day near Tokyo.
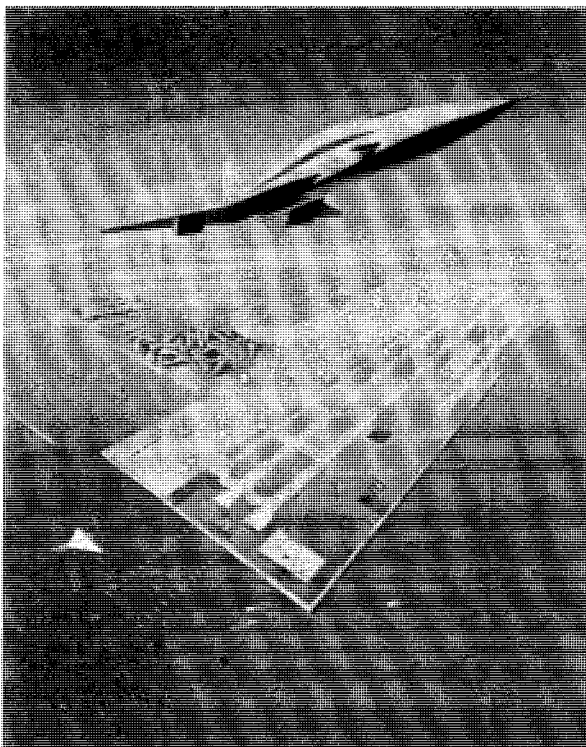
In the 21st century, high-speed travel will make the one-day business trip between the U.S.A. and Japan a reality.

● Internationalization into a 24 hour society

Three major cities are emerging as the centers of the new world economy. Longitudinally, these are London at zero degrees, New York at 74 degrees west and Tokyo at 140 degrees east. Overseas financial markets and foreign exchanges have already been internationalized and are to an increasing degree operating on a 24 hour basis.

For round -the- clock business cities 120 degrees to west and east of London would be ideal, making Los Angeles and Taipei the logical choices. However, by virtue of their economic prominence, New York and Tokyo have come to occupy these positions. Geographically, New York deviates from the ideal location by 46 degrees.

To make financial transactions flow continuously, New York must relay information to Tokyo very early in the morning Tokyo time, though the information sent to London can be received during regular business hours. The OCC environment can help to relieve the extreme physical burden from the long working day of those engaged in these transactions.

Fig. 1 (left) An artist's conception of the deck of the OCC. In the foreground, the world's two longest commercial runways, each 6,000 meters in length. To the left, there are eight eighteen-hole golf courses split in two areas, 400 tennis courts, two baseball stadiums, and numerous other sports facilities.

● Establishment of a society for longevity

One objective of the OCC is the promotion of longevity by creating an ideal environment. The maximum utilization of space in a city composed of four decks together with the clean ocean air and proper physical activity, can lead to a long life. This lesson has been learned from three areas noted for their exceptionally long average life span : Vilcabamba of Ecuador, the Kingdom of Hunza in Pakistan and Abkhaja, Gruziya in the USSR.

The optimal use of space in the OCC can minimize the time required to get from one place to another. In the ordinary city, community to work takes a sizable chunk of time. In Japan, it takes a full day to play a round of golf when the transportation time is included. In the OCC, however, offices are located on the second deck, and housing on the third. It would take 15 minutes at most to move from one point in the OCC to another, up to 5 minutes by elevator and then a maximum of 10 minutes moving horizontally.

2. The basic plan for the OCC

The basic plan for the OCC consists of four storeys, or decks each measuring five by five kilometers. Each storey has a height of twenty meters. The lowest deck is twenty meters from the surface of the sea, making the top deck eighty meters above sea level. The area of each deck is twenty-five square kilometers, for a total surface area of one hundred square kilometers.

These decks are a new type of offshore urban design. Each deck will have a particular function. Developed properly, this will make a highly efficient living
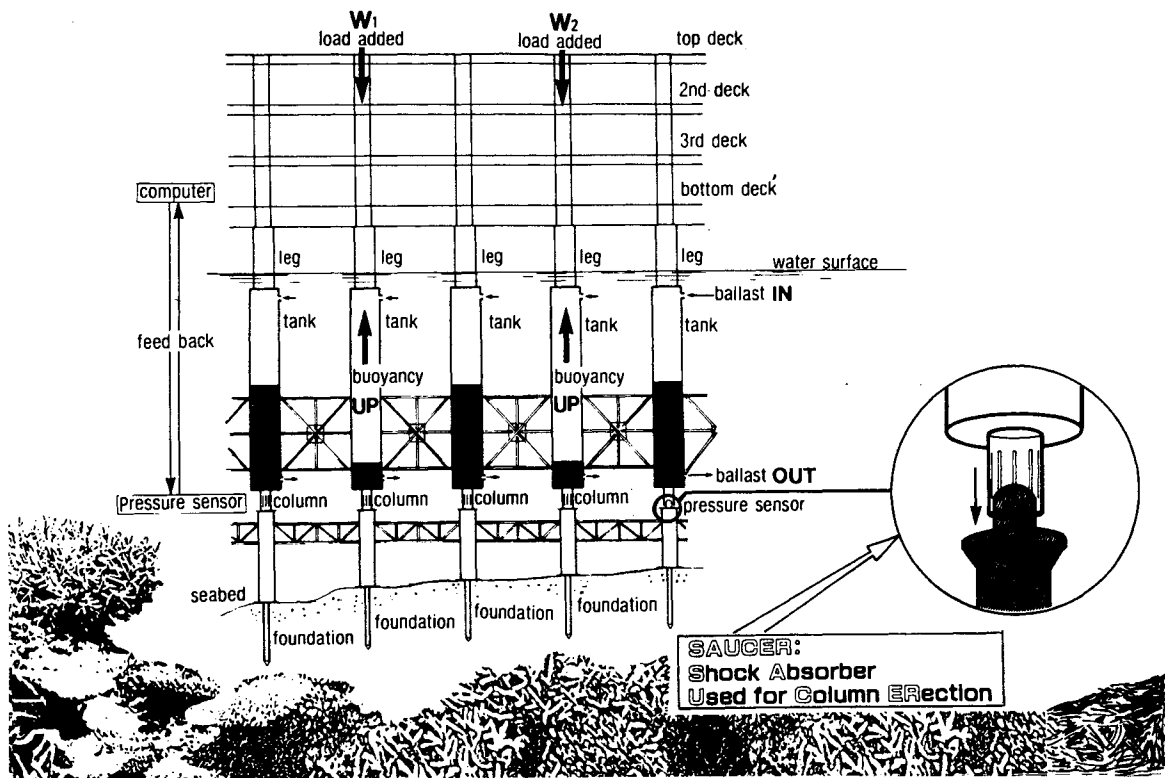
Fig. 2 Each of the OCC's legs consists of a pillar, tank and column. These legs rest on a SAUCER, or extention of the foundation. The columns have numerous thin slits and act as giant shock absorbers. Everything, including the legs and foundation will be designed to be finally constructed under the sea with bolts and pins and will require no welding.

environment. On the top level, for example, there will be an international airport and a sports center with eight golf courses with a total of 144 holes, 400 tennis courts, two weatherproof air - conditioned baseball stadiums, swimming pools and so on. International scientific research centers will also be established, including an International Research Center for Ocean Development, named "Jacques Yves Cousteau" Center, for which the OCC will donate an area of 10,000 tsubo on the deck.

The top deck will supports an international airport with two parallel 6 km runways. This adds two square kilometers to each level, raising the total surface area to 108 square kilometers, or approximately 1.8 times the area enclosed by Tokyo's Yamanote line, the railway that encircles central Tokyo. The steel required for this project is roughly 100 million metric tons, making it by far the largest steel structure in the world. The
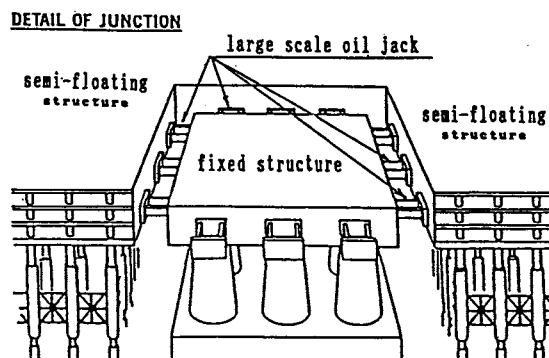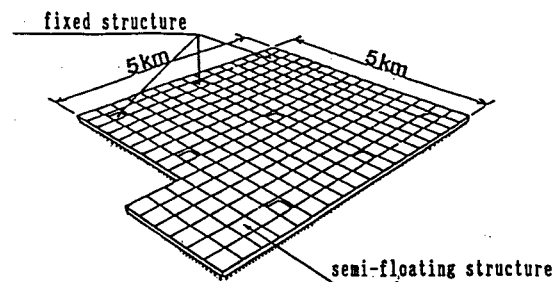
Fig. 3 A diagram of the OCC's semi-floating and partially fixed hybrid structure. Large scale oil jacks will act to affix the soft landing, that is, semi-floating infrastructure to the fixed structures in place.
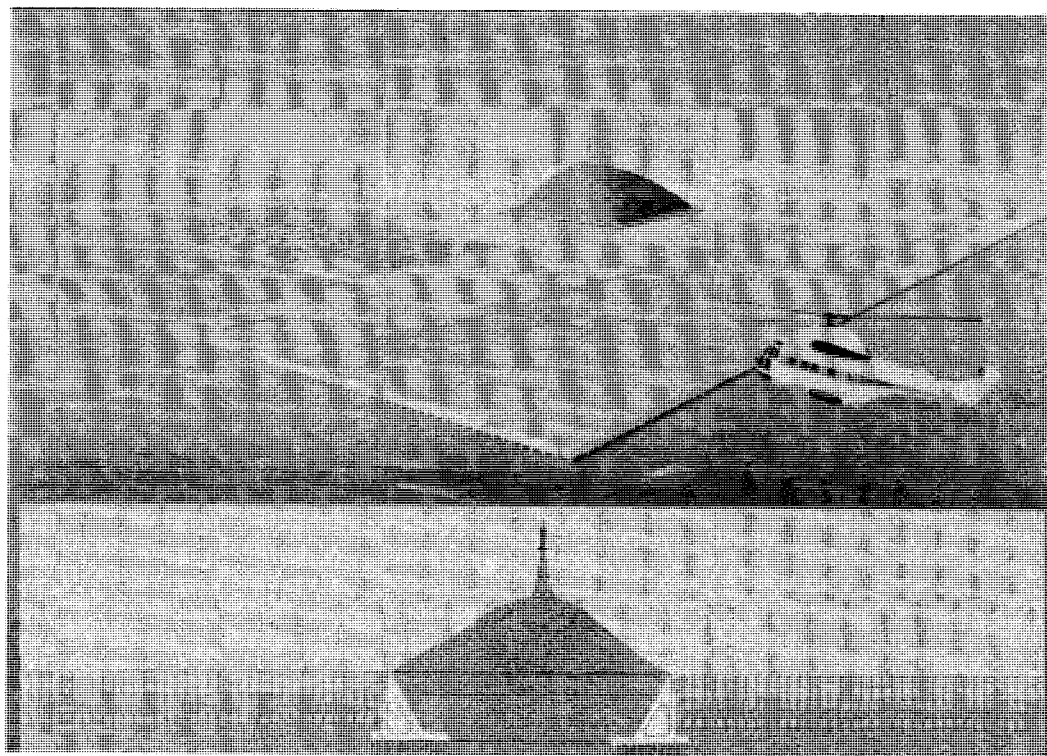
Fig. 4 While being utilized by the OCC as a fixed structure, the island will also offer a significant landmark.

total cost is estimated to be $200 billion dollars, or 30 trillion yen. On the second deck, there will be a large international business center including an international financial market. On the third deck are the living areas. Within this 25 sq.km. area, 40% is devoted to roads and parking lots, 20% to hotels, restaurants, shopping areas and the remaining 40% to five-storey buildings for private dwellings. Thus, the total living area is 50 sq.km. (= 25 sq.km. x 40% x 5 storeys). Allowing for an average living space of 200 sq.m., for a family of four, a permanent population of up to one million could be supported. The lowest deck will be devoted to utilities and services for the city, including garbage collection, recycling, water-works, energy supplies, fiber-opticals, a depot, and storage warehouses and an automated control system for cargo transportation. If these facilities are properly positioned, they will be more efficient, and thus, timesaving. Facilities such as the airport will operate twenty-four hours a day.

Looking towards the 21st Century, the developer has sought to incorporate the Integrated Service for Digital Network (ISDN) to establish this large scale information-oriented community. The city itself is a giant building, enclosed and air-conditioned.

Sophisticated electronics must be employed to control and monitor the wide range of technological innovaations incorporated in the city's design. One fashionable term in Japan nowadays is 'the intelligent building'. This project is nothing less than the embodiment of THE INTELLIGENT CITY.

3. Mechatronic structure

Each leg of the OCC comprises, from the top down, a pillar, a ballast tank, and a column. Because the legs are identical, they can be mass-produced. Each leg structure rests on a specially-designed foundation. Whereas the pillar and tank must be strong enough to withstand the dead weight pressure, the column and foundation will be under comparatively little stress because the entire stucture will be half floating. As a result, the design of the columns and foundations is relatively simple. Sensors in the legs monitor changes in pressure arising from local differences between the weight and the buoyancy. Information from the sensors is fedback to a central computer that controls separate adjustments in individual legs to compensate for any pressure change, when the pressure between the legs is uneven. The relevant ballast tanks are accordingly re-adjusted by increasing or decreasing the water level in the tanks. This idea integrating the functions of three elements, namely sensor, computer and actuator, can be referred to as an active control technology or simply ACT. It could signify a revolutionary new advance in design methods of various high technology products including ultra-large metallic structures such as the OCC and high performance vehicles such as motor cars or jet aircraft.

The OCC's structure can be thought of as being generally the same as that of a ship in that both are affected by external pressure from waves of varying height and length. Naturally, the larger the wave length and height, the greater the external pressure. The dimensions of the structure and the thickness of the plates would normally have to be increased to compensate, resulting in a large increase in the total weight of the structure. However, this ACT design system for the adjustment of both weight and height buoyancy solves the problem without an immense increase in the amount of the weight of steel or other structural materials.
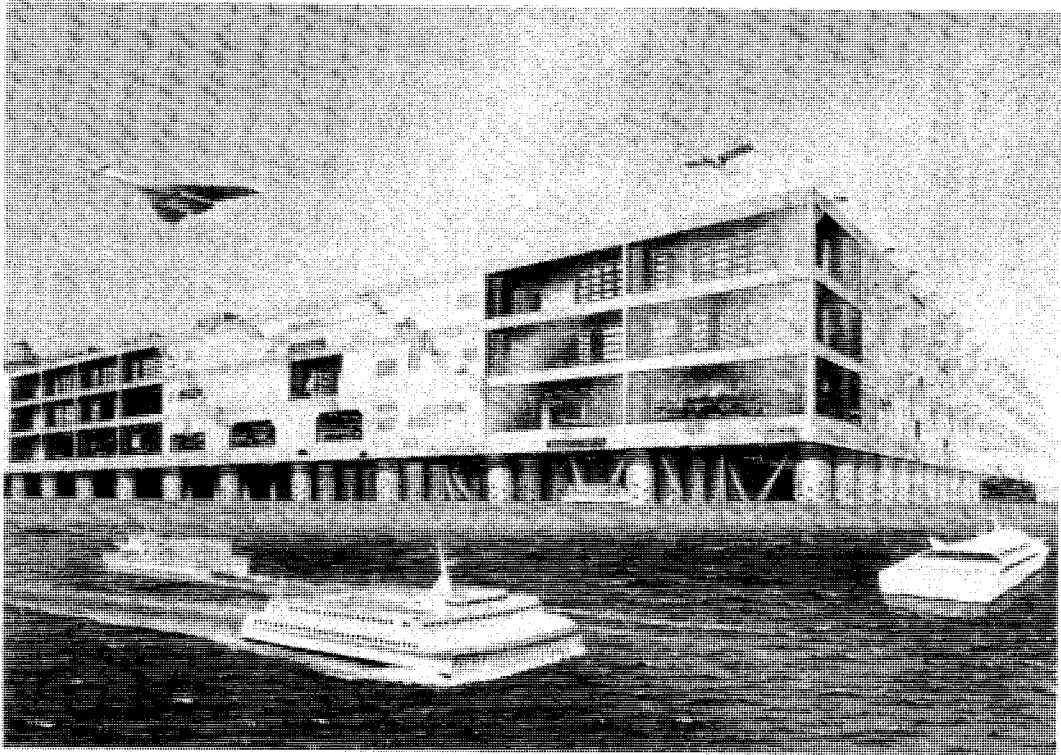
Fig. 5 A typical OCC multilayer structure. The outside wall has a sunflower-like
        lighting apparatus to activate marine life.
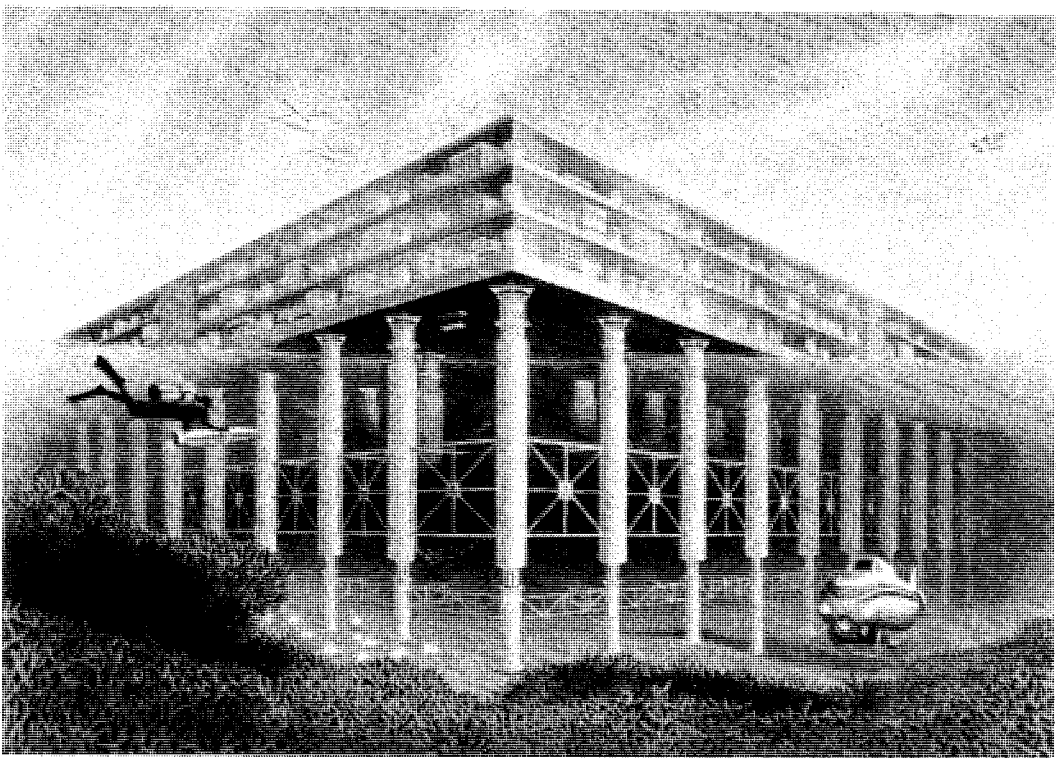
Fig. 6 The OCC's sub-marine structure. Mass production is facilitated by the fact
        that the sub-mmarine structure will be built in the same form as the main
        structure components.

Therefore, a lower budget and a shorter completion period can be attained.

4. Earthquake protection using the 'SAUCER'

The OCC must be made safe from disasters such as earthquakes, accompanying tidal waves and fires. Because the city will be surrounded by water, conventional fire fighting methods should suffice to ensure fire safety. By the 21st Century there should be some highly accurate method of forecasting earth tremors. However, as such a method is not yet available, a provisional protectionary measure will consist simply of discharging ballast water to make the whole city rise slightly from the quaking sea bed. This measure would alleviate the damage from a prolonged earthquake, but the problem of protection from the initial tremor would remain. To cope with this problem, the 'SAUCER' (Shock Absorber Used for Column Erection) system, has been devised (Fig. 1).

Simply put the column acts as a shock absorber. As shown in Fig.1, many vertical slits are cut all around the surface of the column to reduce the vertical rigidity. This is an efficient way to reduce the transmitted shocks of earthquake from foundations to the upper structure even if the lower end of the column touches the upper flange of the foundation.

There is no need for an elaborate foundation since the weight of the structure is counteracted by the positive buoyancy. Each column settles inside the SAUCER, and it is free to move only vertically. Horizontally it is absolutely stationary.

5. The half-floating (soft landing) and partially fixed hybrid structure

Exclusive reliance on the SAUCER system mentioned above would leave the OCC vulnerable to horizontal pressure from a tidal wave or typhoon. For this reason the OCC has been designed as a hybrid structure of semi-floating and partially fixed structures.

Each of the fixed structures will be a prestressed concrete block with an upper surface measuring 300 sq.m. and filled with water to make it weigh millions of metric tons. Between every fixed structure and the floating city's structure there is a surrounding space with many enormous hydraulic or oil jacks attached with bumpers and friction plates to lessen any impact on the floating structure (Fig.2).

The fixed structure attached to the sea floor will stabilize the OCC horizontally. During any earhquake the fixed structure will feel the full effect of the tremor, so there can be only aesthetic development such as scenic green parks on top of these blocks.

6. Creation of amenity

Generally speaking, the choice of one's residence is based on three factors. These are the size, the social environment and the location (the distance from a community center or a railway station, for example). The size and the environment help to create a comfortable dwelling, and a favorable location provides the convenience. A good combination of these factors makes for a pleasant place to live.

Thus, the OCC will encompass a wide range of high technology to create a highly organized, safe environment. Yet this city will also function as a transportation and communication center, which will pave the way to solving many of the problems facing future societies.

GLOBAL CHANGE AND THE COASTLINE : ENVIRONMENTAL, SOCIAL AND ECONOMIC IMPLICATIONS

David Hopley

Sir George Fisher Center for Tropical Marine Studies, James Cook University of North Queensland, Townsville, Queensland 4811, Australia

Abstract

Only a small proportion of funding for global change research programs has been directed at planning for sea level rise through mitigation projects. Although recent estimates of the rise by 2050 (25-40cm) are reduced compared to previous predictions and are now within the ranges achieved in the geological past, considerable changes will still take place in the coastal zone, especially when greater and more surge storm incidence and rainfall intensity factors are considered. Adjustments available include: no action; coastal defence based on present rates of sea level rise; retreat with planning and social engineering; protection; and abatement of global change processes. Actual decisions for specific reactions will vary according to risk and impact assessment. Production of Coastal Vulnerability Indeces (CVI) using Geographical Information Systems (GIS) is advocated at several scales for the identification of regional response planning strategies.

1. Introduction

In spite of a clear indication of increasing levels of CO_2 in the atmosphere (316 to 350 ppm, 1959-1989) only a combination of circumstances in the late 1980's led to acute concern about global environmental change. Government response has been a massive injection of funding into global change issues (eg $7.8 million for Greenhouse related projects in Australia in 1989 and a US Presidential proposal for a 1991 global change research budget of $1,034 million). Examination of these and other budgets announced elsewhere suggest that most expenditure is directed in two areas:

i) refinement of global change predictions
ii) curtailment of Greenhouse gas emissions

Whilst both are valid, what may be termed the middle ground, the planning, design and engineering programs for the next decades have been given low priority. Even the most conservative forecasts indicate that change is inevitable as the result of past pollution whatever abatement methods are employed in the next few years. Contingency planning for the considerable period of time until there is a change in direction of present trends is necessary.

This is particularly true of the coastal zone where social and economic changes may be felt first. Fifty percent of the world's population are coastal dwellers and it is potential total loss of land which places the problems of the coast in a special class. This review examines why mitigation planning is so backward, assesses what the critical problems are likely to be and the range of planning and design options available. It finally advocates a hierarchical regional approach to coastal planning incorporating environmental, social and economic variables.

2. The Uncertainty Factor and Analogues with the Past

Two factors work against any immediate response to the present predictions of global change: i) the period for significant change to take place by even the worst extreme predictions lies beyond the term of any elected government or equivalent body and ii) any response will be expensive and/or socially disruptive. For this reason the uncertainties associated with prediction are frequently grasped eagerly by those who wish to do nothing.

Unfortunately the uncertainties are likely to remain, though may become more refined. Global change becomes an issue to which response must come only when it affects budgets and societies. An increase in atmospheric CO_2 alone does not do this, nor do generally warmer temperatures. Changes to rainfall patterns or significant rises in sea level, on the other hand, do affect economies and people and both of these parameters are subject to a multitude of buffers and feedback mechanisms in which the world's oceans form an integral part. This problem was illustrated to this author recently in a joint paper which examined the significance of changes to coral reefs in response to a global rise in sea level to the global CO_2 budget (1). The paper concluded that calcium carbonate deposition in coral reefs at present acts as a sink for 111 million tonnes C y^{-1}, the equivalent of 2% of the present output of anthropogenic CO_2. In the short term this could increase to the equivalent of .4% of the present CO_2 output and in the much longer term (several centuries) this could increase to the equivalent of as much as .9% as unproductive reef flats become recolonised with corals. This all appears to be a good negative feed back response which will help the fight against global change. Further examination however, indicated that this was not so. Unfortunately this negative sink for C will most likely be of *negative* value in alleviating Greenhouse because the immediate effect of $CaCo_3$ precipitation is to raise pCO_2 of the surface oceans ie to encourage CO_2 efflux to the atmosphere and compounding the problem.

This example illustrates how complex the problems of prediction are. Nonetheless the efforts put into research over the last five years are paying off. Sea level predictions for the mid 21st century in 1983 ranged from 23.8 to 116.7cm (2). Today the envelope is narrower and more conservative at 25 to 40cm (3). This is most important as greater consensus and greater precision allow scientific assessment to be incorporated into project design. To date, lack of consensus (5) has done little to promote decision makers to make decisions. Whilst the priviledges of scientific and academic freedom and the requirement for caution remain, the trend towards definitive

Table 1 Examples of the Impact of Global Change on the Coastal Zone

	Type of Change	Impact	Other Implications
PRIMARY	Sea Level Rise	Inundation of wetlands and lowlands Erosion of Shorelines Salinity incursion in groundwater	Changes to Tidal prisms Changes to sedimentation patterns
SECONDARY	Increased frequency and intensity of hurricanes	Exacerbating sea level rise problems	Extension of hurricans into areas where design has probably not incorporated wind loading and surge factors
	Higher rainfall totals and intensity in lower latitudes	Exacerbating sea level rise problems Changing natural stream networks, leading to increased sedimentation	Changing salinities in nearshore zone
	Increased temperatures	Extension polewards of nuisance or dangerous species, eg malaria carrying mosquitoes	Changing tourism patterns
TERTIARY	Changes to economies of coastal hinterlands as result of climatic change	Changing crop patterns, leading to changes in past requirements Decline in coal ports	Changing location of specialised port bulk handling facilities
	Changes to trade as result of anti-Greenhouse measures	Decline in demand for wool in warmer world	

statements from specially constituted national and international committees is absolutely necessary for forward planning.

The more conservative figures for sea level rise are also important from another aspect. In making adjustments to perceived changes it has been common to examine the past for analogues which will aid the forecasting process (5). Climates have changed in the geological past (eg glacial/interglacial episodes) and sea levels have been as much as 150m different to present. However, emphasis has been put on the fact that the rates of changes in the past are far slower than those envisaged in the future. For example:

".. changes which have only ever previously occured in tens of thousands of years will have been compressed into half a human lifetime" (6).

This is certainly true of temperature changes. A 2 to 4°C change in global atmospheric temperature over fifty years compares to a 8°C warming over 100,000 years and >10,000 years since the height of the last glaciation (7). The predicted 1.5° to 4.5°C increase in sea surface temperatures (which will lag behind atmospheric T° change), compares to an average global figure of 2°C since the glacial period (8).

However, the rate of sea level change for the next 50 years which is now more conservatively predicted at 4 to 6mm y^{-1} is far less than that of the post-glacial transgression when rates averaged 12 to 15mm y^{-1} and at times may have been double. Unfortunately, beyond the year 2050 the steam roller effect of global change once underway may see the rate of sea level rise increase exponentially.

As all modern species and ecosystems were obviously able to survive the post glacial transgression, though for many it was a time of stress and forced adaptation, superficially the immediate outlook for natural systems would not appear to be too gloomy. However, this is far too great an oversimplification. In post-glacial times

migration of plants and animals was unhindered by human developments. Migration inland took place as sea level rose and zonal migration (northwards and southwards along coastlines) as temperature changed. Rivers changed their courses and estuaries their morphology. Few of these natural migrations or alterations will be as easy in the future. The inertia effect of human settlement and development will produces a stress additional to that produced by environmental change. Mangroves will not be allowed easy access onto sugar cane lands and sandy beaches rapidly disappear in front of rock walls. Estuaries included in protection works are likely to disappear completely on purely economic grounds as regional protection works costing upwards from $2000 per metre will follow straight lines, enclosing the lengthy indentations which provide unique habitats (for example see the effects of enclosure of the Eastern Scheldt in the Netherlands).

The major difference between the time of the post-glacial transgression (largely between 17000 and 7000 years BP) and the present is the comparative size and distribution of human populations. About 10,000 years BP total world populations stood at ca 10 million. Nonetheless the stress of rising sea level on coastal societies of hunters and gatherers was sufficient in wide coastal plains such as those bordering the Sunda Shelf to initiate widespread migrations as local land shortage caused demographic pressure. It has also been hypothesised that this pressure also initiated the first moves towards systematic agricultural cultivation (9). World population today is ca 5.1 billion, more than 50% of it located in coastal zones with an estimated 300 million susceptible to a 1m rise in sea level (10). Migration is not feasible in all but a few regions as there are no longer empty fertile areas to which peoples may move. In addition political boundaries further compound problems of migration. One has only to evaluate world reaction to the Vietnamese boat people to see how difficult accommodation of populations from Bangladesh or low lying Indonesia would be outside the country of origin. Problems from sea level rise will

require international political as well as engineering solutions, particularly as there is the potential for some of the worlds lowest and smallest nations such as the Maldives, Kiribati, the Marshall Islands, Tokelau and Tuvalu to be left completely landless (11).

3. The Impact on the Coastal Zone

Numerous assessments have been made of the effects of changing sea levels and other parameters, ranging from direct and physical (and generally most predictable) to indirect and largely economic or social (and least predictable). Examples are given in Table 1.

Primary impacts are directly related to sea level rise and are holistic in both time and space. Secondary impacts are those which result from changes in the environment which compound sea level rise. Most obvious are those related to increased frequency and intensity of tropical hurricanes or cyclones, exacerbating the problems of the coastal zone, not only in the areas in which such storms are currently experienced but also to polewards as higher sea surface temperatures allow an extension of the hurricane belt (12). Storm surges and extreme wave activity will extend the influence of the sea even further inland though only intermittently.

Changing temperatures will also affect the coastal zone, most obviously to distributional boundaries of temperature sensitive species of plants and animals. Such changes have economic and social implications. For example mosquito borne diseases, such as malaria may extend further polewards. Another example is provided from Australia by the box jellyfish, *Chironex fleckeri*. This marine stinger, which can cause human fatalities is currently found on the Queensland mainland coast between November and April (in wetter years as late as June) and as far south as Gladstone (24°S). A 3°C increase in sea surface temperatures could see extension of the box jellyfish in summer into waters of southern Queensland and northern New South Wales.

The impact on tourism of a polewards extension of box jellyfish is an excellent example of a tertiary impact. The box jellyfish curtails or modifies mainland beach activities in northern Australia during the summer season and is at least partially responsible for the tourist season being a winter one. If this animal were to extend into New South Wales it would include Australia's largest coastal tourist developments on the Gold and Sunshine Coasts within its biogeographic range.

The range of tertiary impacts are almost unlimited and require identification at the local level (see below). However, it is worthwhile pointing out the vulnerability of ports not only to the physical results of global change but also economically. Changing climate will modify the agricultural systems and productivity of port hinterlands. For example, in Australia wheatlands may shrink drastically in Western Australia and South Australia, but expand in Queensland. Other crops would have changing distributions and impacts on pastoral activity and forestry could be severe (13). Wool production and exports could be reduced not only by changing climate but also by a reduced demand in a warmer world. Trade in coal may decline drastically in an attempt to curb Greenhouse emissions. Most of these products form an important part of Australia's exports and are handled in bulk by specialised port facilities. Indeed, major changes to world trade may be expected as the result of global change and port handling facilities may alter dramatically as a result.

4. The Range of Adjustments

The range of options open to combat the effects of global change in the coastal zone range from no action, through protection of the worlds coastlines at their present position, to the ultimate solution of abatement of global warming by reducing emissions of Greenhouse gasses. Cost-benefit analysis of each option is required.

4.1 Do Nothing

This obviously costs least to implement but could result in major losses of coastal lands, amenities and structures. However, it is the acceptable option for many cliffed coastlines or coastal zones with no development such as much of northern Australia. Indeed presuming that there is no impediment to migration of littoral, intertidal and nearshore zones landward, and that the rate of migration required is within the capacity of the participating species (particularly plants) then this option also allows for the maintenance of coastal ecologies for sea level rises up to the rates obtained during the post-glacial transgression ie 12 to 15mm y⁻¹.

4.2 Coastal Defence Based on Present Rates of Sea Level Rise

Coastal defence works including sea walls, groynes, tetrapods, dune stabilisation programs and artificial beach replenishment are already in place along many coastlines to counter natural erosion of 70% of the worlds sandy coastlines resulting from the rise in sea level of the last 100 years and/or reduction in coastal sediment yield (14). Such measures can be successful only in the short term but are probably delaying the inevitable and even aggravating the ultimate losses during a major storm. As Titus (15) has pointed out, whilst the horizontal location of the beach may be maintained or its retreat slowed, deepening offshore will result in massive erosion in a culminating storm (16).

Protection at the present position also includes biophysical methods, largely involving planting or encouragement of vegetation. However it has been noted (17) that the results can be similar to those of hard engineering particularly in an era of rapidly rising sea level. Longshore movement of sediment or dune washovers may be hindered. For example, on barrier islands sand is accumulated in high dunes rather than on the beach or back barrier thus removing the washover back barrier area vital to the maintenance of the system.

In summary, coastal protection measures are costly, may aggravate erosion problems and can be ecologically damaging (eg loss of beaches in front of sea walls). At best this is a temporary adjustment suitable only for high value sites.

4.3 Retreat with Planning and Social Engineering

Where economics do not allow defence or protection then retreat may be greatly facilitated and impacts alleviated by forward planning. In reaching this decision it is important to consider not only the present value of land and property but what it may be in 50 years time given other reactive measures. For example it is futile protecting a coastal resort which is centred around its beach and natural environment if the end result is a far from aesthetically pleasing rock wall and no remaining beach. Defence or protection of such locations is meaningless and their present high values can do nothing but erode as quickly as their beaches into the next 100 years.

Whilst accepting that there are many developments currently within the susceptible coastal zone, future problems can be minimised by planning. Planning includes the strict enforcement of buffer zones in which development is banned or limited to structures which are expendable or can be moved (eg surf life saving facilities which must be close to the beach). Legislation which actually encourages coastal development such as the US National Flood

Insurance Plan of 1968 (17) requires reassessment on environmental grounds, not just for economic reasons as occured with the cutting of the NFIP in the late 1980's. Many coastal nations experiencing storm surges or tsunamis already have coastal zone management plans and these need extending.

If it is accepted that coastal retreat is inevitable and it is considered necessary to develop in the coastal zone, then design criteria become critical eg foundations suitable to withstand surges and high tides, buildings raised on platforms or public buildings such as hotels having ground floors utilised for purposes which will experience least damage if flooded eg car parks (18). In this way the design life of such buildings may be extended into the decades when sea level rise and storm activity increase the frequency of intermittent flooding but before sea level rise finally produces total inundation.

What Carter (17) terms "Social Engineering" include both legal and fiscal measures eg outlawing coast damaging activities, taxing provisions to enforce coastal zoning practices and incentive education programs. Such social engineering programs are most needed in developing nations but are most difficult to instigate. As Carter indicates, tradition and religion are entrenched in the way of life and loss of crops, property and even life is accepted as "Gods will". In addition provision of international relief aid has developed paradoxes in attitude in which many people will suffer the hurricane, surge or flood in anticipation of the relief aid to come. As such events become more severe and more frequent, improving technology is insufficient. For example, in Bangladesh only major land reform, better communications and other measures such as rephasing of crops so that harvests do not coincide with periods of maximum risk can alleviate even present problems without sea level rise (19).

Planning for retreat can also include help for natural systems. This ranges from measures to ensure that particularly susceptible species of plants and animals are given sanctuary, to sand pumping schemes which aid in the migration of shorelines without total loss of environment. Titus (20) for example suggests that sand pumping schemes on barrier islands of the US east coast should not concentrate on the eroding seaward beaches, but should be directed towards the inner prograding beach, thus aiding natural barrier island migration.

4.4   Protection

Complete protection *in situ* is warranted for some sites because of the amount of investment, the historical and/or heritage value, or because of the lack of alternatives. Some schemes are already in place or are under construction where local subsidence, both natural and man induced, or changes to tidal prisms (again man induced) have aggravated problems of sea level rise. The $1.7 billion Thames barrage protects land where a single major flood could cause $8 billion damage. The Japanese City of Osaka is similarly protected, Leningrad has a 25km barrier under construction and Venice's protective works have been planned for over 20 years. The Netherlands for centuries, has invested a considerable proportion of its national income on land reclamation and protection, of necessity for such a low lying country. The Dutch polders are often quoted as an example of how successful protective works can be, but the success is not just the result of the ingenuity of Dutch engineers which can be easily exported. The protection works were initiated from an economy bolstered by colonial trade and currently ʻmaintained by high value intensive industry and agriculture.

In all these examples the benefits greatly outweigh the costs and it is probable that many more such schemes will be developed in the near future. In Hamburg for example, sea level rise will result in a further 40 - 50cm alteration to the tidal prism, potentially flooding 20km² and threatening 320,000 people. The works proposed will cost DM 4 billion, protecting assets estimated at DM 16 billion (10).

Preliminary assessments in the USA indicate that it would cost approximately $100 billion to protect the most densely developed 15% of land threatened by sea level rise (3).

These are examples where the solutions are unambiguous. Decisions become difficult for nations which cannot afford billions of dollars and/or where the benefits are marginal. A 1.5m rise in sea level in Guyana is estimated to result in an annual loss of $800 million, $245 million from loss of agricultural products but more than twice that in "loss of rent" (21). Even the simplest sea walls cost ca $2000 per metre. However, in Guyana, and many other developing nations the lowest lying areas are underlain by muds and mangrove peats the foundational properties of which are dubious. Up to 3m of subsidence could take place so costs are far higher than the minimal figure. Some solutions are forthcoming: in Guyana it has been suggested that far less robust (and costly) sea walls could be planned further inland and mangroves be allowed to grow in front of them, adding to coastal protection, particularly as a wave barrier. However, this response is only partial, resembling coastal defence rather than protection and automatically leading to an acceptance of loss of a certain percentage of land.

Such marginal schemes also need to assess associated costs, both economic and environmental. For example impounding an area below sea level requires continuous pumping of surface water, and may have drastic effects on the groundwater table of adjacent areas. These need to be costed into such schemes. A further example of added costs is provided by the atoll nation of the Maldives. These low lying islands would require protective works of $8000 per metre but desalinisation plants which would be required to provide fresh water would cost $48 million per year to run (10). The Maldives has a population of 202,000!

Bangladesh is even more precariously situated. 40 to 80 million people are vulnerable to sea level rise and with storm surges already a major hazard. The estimate of protective works is minimally 5 to 10 times the perceived economic benefits (22). It is interesting to note that building of villages on mounds is suggested as an alternative solution. Although this has occured for centuries in parts of coastal north-west Europe, here population densities are low and an economic livelihood can be maintained from grazing and associated activities on the surrounding marshes when water levels recede. Populations of mound dwellers are not possible without access to subsistence maintaining land. Clinical economics cannot always direct the suitable response.

4.5   Abatement

The only final solution is a reversal of the global change processes. Reduction in Greenhouse gas emissions would reduce the rate of global warming and consequently slow sea level rise and its consequences. Delaying sea level rise will permit a slower deployment of mitigation measures. A number of agencies have suggested that a reasonable target would be to limit additional man induced sea level rise to an amount comparable to present rate of about 12cm/century. This could be attained by reducing emissions of CO_2 by 2% a year coupled with reductions in emissions of other trace gasses. However, this is a reversal of present trends (increase of .2% a year). It is unlikely to be agreed upon quickly by the world's nations and unlikely to result in sea level responses within the next century.

5.   An Approach to Mitigation Planning

Pier Vellinga of the Netherlands Climate Program has suggested that the global cost of 1m rise in sea level is $13.3 billion *annually*, and that half the world cannot afford this cost. In 1987 the various adoptions were costed at a conference in Bellagio, Italy (23). Using present costs of coastal management as a 1990 baseline the following

combinations were costed (abatement = reduction of emissions by 2% per year; mitigation = engineering, planning measures; minimal mitigation = *ad hoc* increases in response to disasters):

i)   no abatement, no mitigation: the most expensive option, almost 14 times present management costs even by the year 2040

ii)   no abatement, mitigation: about 6 times 1990 by 2040, but 13½ times by 2100

iii)   abatement, minimal mitigation: about 8 times 1990 by 2040, but less than 11 times by 2100

iv)   abatement, mitigation: the cheapest alternative beyond 2025, costing 5 times present levels by 2040 and only 6½ times by 2100.

The cost curves tended to remain close to each other until about 2020-2030 and it has been suggested that we can wait until then, when predictions may be far more refined than today, before decisions are taken. However, the costing presumes a 20 to 40 year planning lead time, obviously necessary for abatement but equally applicable to many major engineering works of the scale of the Netherlands Delta Plan.

Decisions on mitigation methods are thus required immediately. Adoptive strategies and decision pathways have been discussed at various levels (eg 2,3). The majortiy have aimed at a global or national level. Few (eg 24,25) have been at the local authority level of decision making. Planning decisions should be required for all new projects but few attempts have been made to determine the optimum scale of regional planning. Gornitz and Kanciruk (26) assessed the physical factors involved in sea level rise hazards, and these are included in the present assessment. However, final decisions will be based not only on the physical environment but also on economic, social and political grounds. All these influences have individual regional variations which need defining and then superimposition to provide the final scale for decision making.

Assessment factors include:

5.1   Physical Factors of the Land

i)   Relief: elevation of the coastal zone with respect to sea level rise and storm surge hazard

ii)   Lithology: the relative resistance of rock type to erosion

iii)   Landform: this needs to be assessed in combination with lithology and relief. Obviously unconsolidated landforms such as dunes, coastal barriers or glacial deposits have greater risk of erosion though height of dunes may affect the rate of recession and the amount of inundation.

iv)   Shoreline displacement at the present rates of erosion or accretion will give an indication of the sensitivity of the coastline to sea level rise. A coastline receiving a high sediment yield and accreting rapidly may be able to maintain the shoreline close to its present position even after 0.5m or more of sea level rise.

5.2   Physical Factors of the Sea

i)   Wave climate: maximum wave heights and 50% exceedence levels are important parameters when superimposed on sea level rise.

ii)   Tidal range: this is one of the most important factors in assessing risk. At the present time it can be assumed that no development is tuned to Highest Astronomical Tide (HAT).

In a micro tidal area (‹1m) the difference between even neap high tides and HAT is less than 0.5m and any sea level rise will cause water levels to exceed normally experienced levels. In contrast in macrotidal areas there may be several metres difference between even mean High Water Springs, and HAT. An 0.5m rise in sea level will cause total water levels to exceed previously experienced levels on only a handful of high tides each year. The risk is greatly minimised in macrotidal areas, as it is for storm surges (27). However, where possible, assessment needs to be made of the possible changes to the tidal prism caused by greater volumes of water entering for example estuarine systems with a higher sea level.

iii)   Storm surge risk: short term rises in sea level of up to 4m can be experienced with tropical and high latitude low pressure systems. Risk analysis is available for most developed countries and is related to frequency and intensity of storms, tidal range and local physiographic factors. However, future risk requires consideration of changes to distribution, frequency and intensity, superimposed on sea level rise (eg 12,28).

5.3   Land Movement

i)   Long term movements: it is important to differentiate between two types of movement. Steady continuous movements, (either uplift, as takes place in glacio-isostatic rebound areas, or subsidence, as in the adjacent collapsing forebulge zone (29)) can either alleviate or aggravate sea level rise. However, in tectonically active areas, even where *average* rates of land elevation may approach 1m/1000 years, it is not possible to discount the rise, as movements take place intermittently with long periods of stability possible.

ii)   Present relative sea level trends: because of the characteristics of the earth's crust, which responds differentially to various loading and unloading factors, great variations occur in sea level behaviour. This is reflected in Holocene sea level changes over the last 7000 years (30) and also in the records of the last 100 years as recorded on tide gauges (31,32). This is a very important variable in assessing risk during the early stages of sea level rise.

5.4   Economic Factors, including Infrastructure

i)   Value of the natural coastal zone: in its natural state the coastal zone may have a value which is sufficiently high to make preservation a viable option. For example mangroves have been valued at $5,000 ha y⁻¹ as fisheries breeding grounds (33). Tourism is also based on natural features of the coast and the value of the resulting income may surpass the cost of maintaining the natural landscape during sea level rise, eg by massive artificial sand replenishment schemes.

ii)   Value of structures within the risk zone: assessment is required of present value and also the possibly discounted value after defensive or protective works if these are deemed necessary. For example, an international airport may have little change to its value behind a massive sea wall, whilst a tourist resort would be drastically discounted. The architectural and engineering aspects of the infrastructure in the risk zone requires evaluation. Some may be able to withstand a small rise in sea level with minimum modification. Some may be able to be cost effectively moved. Finally, the cultural and heritage value of buildings, monuments etc may be a major factor in the final decision making.

iii)   Value of production in risk zone: although infrastructure value may have prime consideration the value of production

from risk zones also needs assessing against the cost of protection. This could be critical for industries or services which require access to the sea, particularly as alternate sites along an adjusted coastline may have many demands put upon them. Agricultural production should also be assessed, though costing of ancillary operations such as pumping, and indirect effects of sea level rise such as salinity problems should be considered.

iv)   Status of the economy: this applies to economic evaluation at all levels of Government. In developed countries, local government may be forced to take on at least part of the financial burden of required works. Although there will be a close correlation between the ability of a local government to pay and the benefits accruing there will be a regional variation which will affect decision making. At the national level it is already clear that half the nations of the world will be unable to afford the measures needed even where the benefits are clearly in favour of the required action. Political decisions at national and international levels will be necessary.

5.5   Social and Political Factors

i)   Population: security of human life must be paramount in any assessment process and population density in zones at risk need to be balanced against availability of sites to which migration may take place and the social impacts both on the population being moved and on any existing population in the migration target areas.

ii)   Religious, ethnic and traditional beliefs: these may tie people to particular areas, or give some areas special significance. It is doubtful whether such factors will be strong enough to result in costly protective works, but costs of education and social adjustment need to be incorporated in cost-benefit analyses.

iii)   Politics: decisions on the final actions to be taken will be made by politicians and much will depend on the political level at which planning responsibilities will lie. The higher the level, then the more rational the decisions made. For example, the solutions to the problems of nations which may disappear completely, such as the Maldvies, require action at an international level, as do the measures needed to resolve the global change problems of many of the poorer developing nations. At national levels, larger schemes at least will require input of major funds which can only be allocated by a central government. Defence and planned retreat may be more appropriate at state or even local government levels, but only after national strategies and priorities have been decided.

6. Conclusion

The majority of the factors discussed can be quantified, categorised for risk or impact and geographically located. However, the data will be in a variety of formats and spatial resolutions including:

i)   point data eg tide gauge information
ii)   line data eg shoreline characteristics, tides
iii) cell data eg relief of backshore, value of structures, population density.

As Gornitz and Kanciruk have suggested for the physical factors, all data can be integrated into a Geographic Information System (GIS). The value to planning will increase with larger scales of resolution. For example Gornitz and Kanciruk used 1:250,000 mapsheets and 15

minute coastal cells (ca 770km²) and smoothed or interpolated some line data by using 3 to 5 point running means. They suggest that sensitivity tests can be made to establish optimum values. In Australia a computerised data bank on coastal landforms has already been compiled based on 10km long strips of coastline and 1:250,000 mapsheets but containing information on population and land-use (34). This is an enormous and valuable data bank but even the authors note that: "about 300km of coast (30 coastal sections) is the practical lower limits of utility for the data". Obviously for detailed planning of moderately to densely settled areas the scale of resolution needs to be much smaller.

Nonetheless these approaches provide the basis for the identification of the most critical areas where higher resolution methods may be applied. Developing the model of Gornitz and Kanciruk the national level process may be:

1.   Development of a coarse scale Coastal Vulnerability Index (CV1) based on the physical factors of land and sea, and earth movements.

2.   Superimpose economic and social factors to produce coastal zone value indeces. This will almost certainly require several stages of compilation.

3.   Identify high risk, high value areas for fine scale resolution assessment.

4.   Decision making for regional strategies of no action, retreat with planning, defence or protection and for allocation of the financial burden of such measures at the most appropriate level of government. Processes such as this are particularly needed in preparation for global change but even without sea level rise, the data collected is essential for much needed coastal management planning over most of the world's shorelines.

Because the most recent estimates of sea level rise are more conservative than those of five years ago, there is some indication of relaxation in the level of government response at the present time. However, even a 25cm sea level rise in the next 50 years will produce major problems, particularly when accompanied by such regional factors as high and more frequent storm surges and higher rainfall intensities. Funding for coastal risk assessment and planning of mitigation works requires higher priority than it receives presently by most governments.

References

1.   Kinsey, D.W. and Hopley, D., "The response of coral reefs to Greenhouse - significance to global CO₂ budget", J. Global and Planetry Change, (in press).

2.   Hoffman, J.S. et al., "Projecting Future Sea Level Rise" 2nd ed. U.S. Environmental Protection Agency Washington D.C., 121 pp. (1983).

3.   Intergovernmental Panel on Climate Change, "Adoptive Options and Policy Implications of Sea Level Rise and Other Coastal Impacts of Global Climate Change". Workshop Report Coastal Zone Management Subgroup, (1989).

4.   Kerr, R.A., "Hansen vs the world on the Greenhouse threat", Science, Vol.244, p.1041-1043 (1989).

5.   Thom, B.G. and Roy, P.S., "Sea level rise and climate: lessons for the Holocene". In Pearman, G.I. (ed) Greenhouse: Planning for Climate Change, CSIRO, p.177-188, (1988).

6.   Lowe, I., "Living in the Greenhouse", Scribe, Newham, 179 pp. (1989).

7.   Shackleton, N.J. and Opdyke, N.D., "Oxygen isotope and paleo-magnetic stratigraphy of Equatorial Pacific core", V28-238: oxygen isotope temperatures and ice volumes, Quat. Res., Vol 3, p.39-55, (1973).

8.   CLIMAP, "The Surface of the ice age earth", Science, p.1131-1137, (1976).

9.   Bellwood, P. "Mans Conquest of the Pacific: The Prehistory of South-east Asia and Oceania", O.U.P. New York, p.422, (1979).

10.   O'Neill, B., "Cities against the seas", New Scientist, 3 Feb.1990, p.26-29, (1990).

11.   Roy, P., and Connell, J., "Greenhouse: the Impact of Sea Level Rise on Low Coral Islands in the South Pacific", Res. Inst. Asia and Pacif., Sydney University, occ.Pap.6, 55pp, (1989).

12.   Love, G., "Cyclone storm surges: post Greenhouse", In Pearman, G.I. (ed) Greenhouse: Planning for Climate Change, CSIRO, p.202-215, (1988).

13.   Russell, J.S., "The Effect of climate change on the productivity of Australian agro ecosystems". In Pearman, G.I. (ed) Greenhouse: Planning for Climate Change, CSIRO, p.491-505 (1988).

14.   Bird, E.C.F., "Coastline Changes", Wiley Interscience, Chichester, 219pp, (1985).

15.   Titus, J.G., "Planning for sea level rise before and after a coastal disaster", In Barth, M.C., and Titus, J.G. (eds), Greenhouse Effect and Sea Level Rise, Von Nostrand Reinhold, p.253-269, (1984).

16.   Thom, B.G., "Coastal erosion in eastern Australia". Search, Vol. 5, p.198-209, (1978).

17.   Carter, R.W.G., "Man's response to sea level change", In Devoy, R.J.N. (ed) Sea Surface Studies: A Global View, Croom Helm, p.464-498 (1987).

18.   Federal Emergency Management Agency (FEMA) "Design and Construction Manual for Residential Buildings in Coastal High Hazard Areas", US Dept. Housing and Urban Devel., Washington D.C., (1984).

19.   Islam, M.A., "Tropical cyclones: coastal Bangladesh", In White, G.F. (ed) Natural Hazards: Local National and Global, O.U.P., N.Y., p.19-25, (1974).

20.   Titus, J.G., "The Greenhouse effect, rising sea level and society's response:, In Devoy, R.J.N. (ed) Sea Surface Studies: A Global View, Croom Helm, p.499-528 (1987). See also Titus, J.G. ref (15).

21.   Sattaur, O., "Guyana's test at high tide", New Scientist, 31 March, 1990, p.28-31, (1990).

22.   Sinclair, J. "Rising sea levels could affect 300 million", New Scientist, 20 January 1990, p.9, (1990).

23.   Bellagio, "Priorities for future management - a new policy issues agenda". Policy Issues Workshop in Developing Policies for Responding to Climatic Changes, Bellagio, Italy, 9-13 Nov 1987, p.24-26, (1987).

24.   Childs, I.R.W., et al "Socio-economic impacts of climate change: potential for decision-making in Redcliffe, Queensland:. In Pearman, G.I. (ed), Greenhouse: Planning for Climate Change CSIRO, p.648-664, (1988).

25.   Gibb, J.G., "A coastal hazard management plan for Hokitika", N.Z. Water and Soil Tech. Publ., 29, Wellington, (1987).

26.   Gornitz, V., and Kanciruk, P., "Assessment of global coastal hazards from sea level rise", Proc. 6th Symp. Coastal and Ocean Management/ASCE, Charleston, S.C., (1989).

27.   Hopley, D., and Harvey, N., "Regional variations in storm surge characteristics around the Australian coast: a preliminary investigation", In Heathcote, R.L. and Thom, B.G., (eds), Natural Hazards in Australia, Aust. Acad. Sci., p.164-185, (1979).

28.   Stark, K.P., "Designing for coastal structures in a Greenhouse age", In Pearman, G.I. (ed), Greenhouse: Planning for Climate Change, CSIRO, p.161-176, (1988).

29.   Walcott, R.I., "Past sea levels, eustasy and deformation of the earth", Quat. Res., Vol.2, p.1-14, (1972).

30.   Clark, J.A. et al "Global changes in post glacial sea level: a numerical calculation:, Quat. Res., Vol.9, p.265-87, (1978).

31.   Gornitz, J, and Lebedeff, S., "Global sea level changes during the past century", In, Sea Level Fluctuation and Coastal Evolution, S.E.P.M. Spec. Publ. 41, p3-16, (1987).

32.   Pirazzoli, P.A., "Present and near-future global sea level changes:, Palaeogeog. Palaeoclim, Palaeoecol., Vol.75, p.241-258, (1989).

33.   Chapman, V.J., (ed) "Wet Coastal Ecosystems", Ecosystems of the World, 1, Elsevier, p.26, (1977).

34.   Galloway, R.W., et al "Coastal Lands of Australia", CSIRO Div. Land Use Res. Tech Mem, 80/24, 59pp, (1980).

OCEAN SCIENCE AND TECHNOLOGY

APPLICATION OF REMOTE SENSING TECHNIQUES TO WATER QUALITY MEASUREMENT IN COASTAL SEA

F. Suganuma*, K. Murakami*, Y. Miyahara**

* Port and Harbour Res. Inst., Ministry of Transport, Japan
** Ministry of Transport, Japan

Abstract

The remote sensing observations by LANDSAT satellite and aircraft with MSS(multispectral scanner), together with sea truth observation, were carried out simultaneously at the mouth of Tokyo Bay. The author applied the statistical analyses to the data obtained from remote sensings and sea truth observation. It has been found that turbidity and temperature in upper layer are highly correlated with remote sensing data. From these results, the estimated features of temperature and turbidity distributions were obtained. An attempt was made to estimate the concentration of chlorophyll-a, which led to a conclusion that it was very difficult to measure chlorophyll-a from the remote sensing data so far as the present study was concerned. It was found, however, that the satellite visible imagery showed the spectral characteristics similar to the airborne image and they were somewhat in good agreement with the ocean color obtained by the sea truth.

1.Introduction

The development of observation techniques of water quality distribution, in particular, the contamination phenomena with large spatial scale, such as red-tide phenomenon, is very important from the viewpoint of clarifying the contamination mechanism in coastal sea. The spatial observation of turbidity dispersion caused by huge marine works is also required for estimating their impacts on marine environment and ecology.

However, it is often very difficult to identify the horizontal distribution of water quality by the site observation at only a few points because of its complicated aspects due to current variation in coastal sea.

Remote sensing technique by satellite or airplane can provide much useful spatial information in that case.

In the present study, the simultaneous observation by airborne MSS(Multispectral scanner) and LANDSAT-5 TM, together with sea truth, were carried out near the mouth of Tokyo Bay. Based on the correlation and multivariate analyses with those data, the present paper describes the applicability of remote sensing technique to water quality monitoring in coastal and inland seas.

2. Observation Procedure

2.1 Remote Sensing Observations

The observation data on August 6 in 1986 by Thematic Mapper (TM) on LANDSAT-5, were utilized in the present

LANDSAT-5 Coverage Map
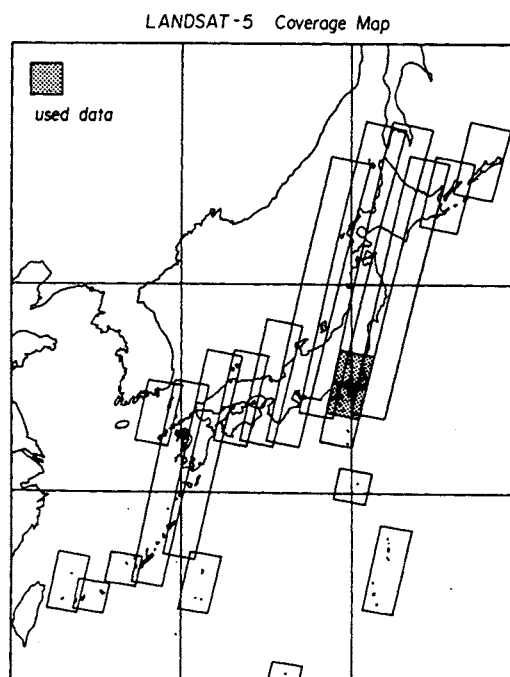
Figure 1 Observation area by LANDSAT-5 near Japan Islands

Table 1 Spectral properties of Thematic Mapper on LANDSAT-5

TM Spectral bands		LANDSAT-5 Thematic Mapper	
Band	wavelength (μm)		comments
1	0.45 - 0.52	↑	
2	0.52 - 0.60	visible	
3	0.63 - 0.69	↓	← strong absorption
4	0.76 - 0.90	↑	by chlorophyll-a pigment
5	1.55 - 1.75	infrared	
6	10.40-12.50		← thermal infrared band
7	2.08 - 2.35	↓	

Table 2 Spectral properties of MSS used in the present study

MSS Spectral bands		JSCAN-AT-18M		
Band	wavelength (μm)	color		comments
2	0.425 - 0.439	bluish purple	↑	← strong absorption
3	0.462 - 0.481	blue		by chlorophyll-a pigment
4	0.499 - 0.519	green		
5	0.535 - 0.557	yellowish green	visible	
6	0.570 - 0.592	yellow		
7	0.608 - 0.635	orange		
8	0.654 - 0.669	red		← strong absorption
9	0.688 - 0.708	red	↓	by chlorophyll-a pigment
10	0.723 - 0.740	dark red	↑	
11	0.762 - 0.782	–		
16	2.060 - 2.450	–	infrared	
17	8.000 - 12.00	–	↓	← thermal infrared band

study. The observation area is shown in figure 1, including the whole of Tokyo Bay. The properties of 7 spectral bands of TM are also shown in table 1.

The airborne MSS observation by Multispectral Scanner (MSS) was also carried out at the same time with LANDSAT observation. The airborne observation area is limited near the mouth of Tokyo Bay, shown in figure 2. The property of spectral bands of MSS is shown in table 2. The airborne MSS used in the present study is equipped with 12 spectral bands suitable for detecting the visible ocean color and the infrared emission.

2.2 Sea Truth Observation

Field measurements of water quality were carried out 0.5 m below sea surface at 9 points near the mouth of Tokyo Bay, of which each three points are located at the inside, the mouth and the outside of the bay, respectively, as shown in figure 3. The measured
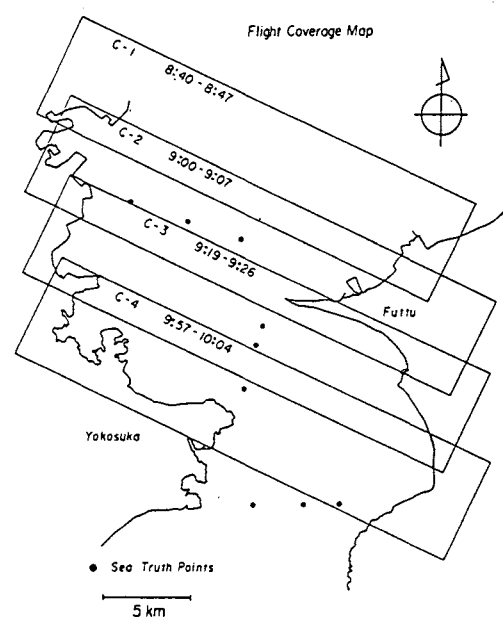
Figure 2 Observation area by airborne remote sensing
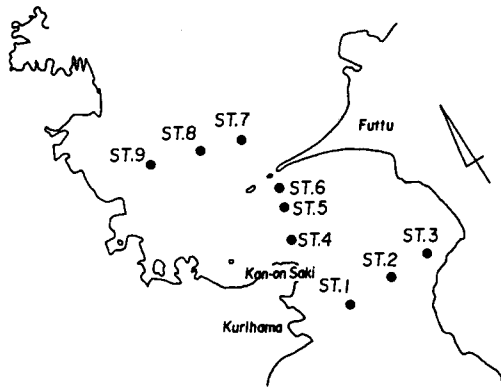
Figure 3   Observation points in the sea
truth

Table 3   Water quality items observed in the sea
truth

Symbol(*	Sea truth items
CHL	Concentration of chlorophyll-a
ATT	Attenuation rate of submerging light
TMP	Water temperature
TRB	Turbidity
SS	Suspended solids
DO	Concentration of dissolved oxygen
COD	Chemical oxygen demand
SAL	Salinity

(* referenced in the following figures and tables)

items are shown in table 3.

3. Data Analysis

3.1 Water Quality Items and Remote Sensing

In the present study, the relations of three water quality items; temperature, turbidity and chlorophyll-a to the remote sensing data were primarily investigated.

This section describes briefly the relations between these items and remote sensing.

1)WATER TEMPERATURE
Because, in general, the intensity of thermal infrared emission with the wave length of 12-14 micrometer is closely related to the temperature of objects, it is expected that the water temperature of sea surface could be estimated from remote sensing data.

2)TURBIDITY
The remotely-sensed light intensity seems to be highly correlated with the turbidity of water which is defined as the transmittance of light, though the optical process in waters is not so clear. The sunlight downwelling from sea surface is optically affected by the absorption and the scattering by dissolved and suspended materials. Through this optical process in waters, the upward component of radiance is produced and the upwelling radiance from sea surface reaches the remote sensor.

3)CHLOROPHYLL-A
The amount of phytoplankton, large mass of which often causes the red-tide phenomenon, can be estimated from the pigment concentration of chlorophyll-a contained in that. Pigment concentration of chlorophyll-a can be measured by the intensity of fluorescence in

Figure 4   Absorption spectrum by chlorophyll-a

water.
On the other hand, another method to detect the chlorophyll-a is to measure the optical properties of waters, such as light absorption and scattering. Figure 4 shows the light absorption properties of chlorophyll-a, which indicates the strong light absorption at the wavelengths of 400-450nm and 650-700nm. These unique optical properties imply the possibility of estimating the chlorophyll-a concentration by the visible imagery of remote sensing.

3.2 Estimated Features of Horizontal Distributions of Temperature and Turbidity in Tokyo Bay

Tables 4(a) and 4(b) show the correlation coefficients of water quality data with MSS data and TM data, respectively. In these tables, each of spectral bands has positive correlation with most of water quality items, except salinity. In particular, the very high correlation of 17th band of MSS with water temperature gives a verification of the physical relation between thermal infrared emission and temperature.

Turbidity is highly correlated with

Table 4 (a) Correlation coefficients (by MSS data and water quality data)

Band	C H L	A T T	T M P	T R B	S S	D O	C O D	S A L
2	0.419	0.585	0.873	0.775	0.608	0.668	0.814	0.260
3	0.509	0.689	0.893	0.676	0.578	0.733	0.910	0.025
4	0.446	0.643	0.870	0.735	0.631	0.680	0.846	0.119
5	0.380	0.635	0.822	0.772	0.617	0.655	0.827	0.170
6	0.495	0.674	0.867	0.736	0.682	0.721	0.873	0.028
7	0.561	0.687	0.899	0.677	0.677	0.750	0.897	-0.068
8	0.543	0.641	0.905	0.611	0.619	0.708	0.860	-0.078
9	0.667	0.663	0.920	0.581	0.686	0.781	0.889	-0.200
10	0.646	0.574	0.919	0.499	0.587	0.734	0.832	-0.172
16	0.219	0.331	0.658	0.841	0.449	0.546	0.598	0.661
17	0.682	0.299	0.924	0.536	0.681	0.781	0.711	-0.205

Table 4 (b) Correlation coefficients (by TM data and water quality data)

Band	C H L	A T T	T M P	T R B	S S	D O	C O D	S A L
1	0.454	0.532	0.830	0.904	0.678	0.693	0.758	0.552
2	0.354	0.426	0.776	0.763	0.636	0.539	0.618	0.414
3	0.554	0.496	0.858	0.773	0.750	0.659	0.692	0.370
5	0.520	0.403	0.814	0.616	0.555	0.577	0.612	0.413
7	0.661	0.471	0.895	0.626	0.654	0.694	0.707	0.264
6	0.731	0.336	0.852	0.352	0.544	0.701	0.654	-0.187
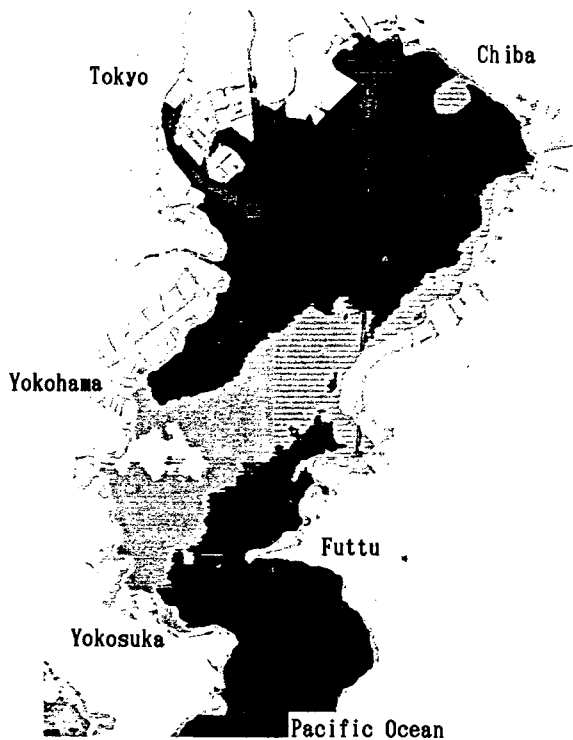
Figure 5 Temperature distribution in Tokyo Bay
estimated from LANDSAT TM data
(high temperature in brighten region)
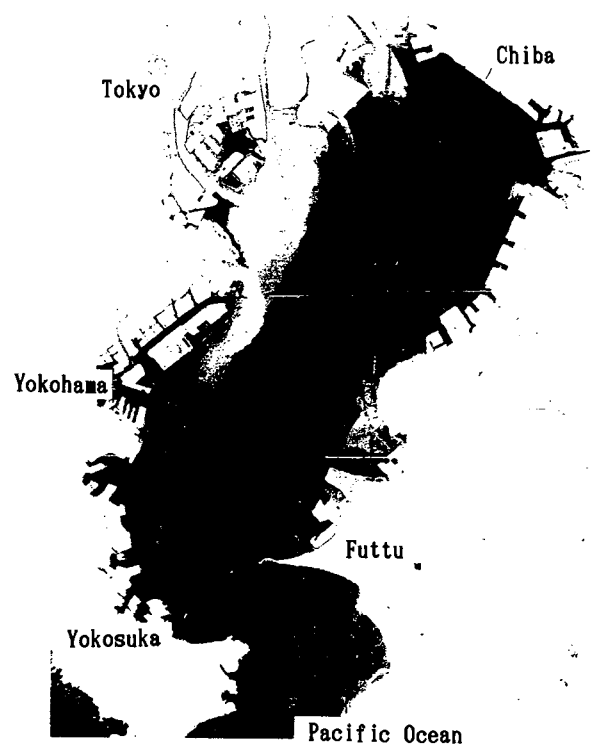
Figure 6 Turbidity distribution in Tokyo Bay
estimated from LANDSAT TM data
(high turbidity in brighten region)

spectral bands with relative short wave length in MSS and TM, except 16th of spectral bands in MSS. It is said that the 16th of MSS bands does not necessarily provide any information on water quality because the light absorption by water itself is very strong for this band.

Figures 5 and 6 show the estimated features of temperature and turbidity distributions, respectively, from 6th and 1st of spectral bands in LANDSAT TM. The dispersion pattern of river water with high turbidity from several river outlets and the cold water body in inner bay are shown in these images.

3.3 Possibility of Chlorophyll-a Detection in coastal waters

Compared with the above mentioned temperature and turbidity, it is not so obvious how the chlorophyll-a concentration could be related to any particular band of MSS in tables 4(a) and (b).

In order to clarify the relation between MSS data and water quality

data, the principal component analysis, which is a sort of multivariate analyses, is applied to those data.

Table 5 shows the eigenvalues and the contribution factors of three principal components for MSS data and water quality data. The cumulative contribution factor by the second principal component exceeds 85%. From this result, it is suggested that the property of MSS data and water quality data should be attributed to two components. Figure 7(a) shows the factor loadings of each of MSS data and water quality data to the first and the second principal components. Most of water quality items except salinity and MSS data are highly correlated with the first principal component, and only the salinity has high correlation with the second principal component. Since the used items in the present study, except temperature and salinity, are the water quality indices for water contamination, the first principal component, which is positive correlated with them, can be considered as the general indices for water contamination.

Thus, it is suggested that MSS data as a whole have the meaning of contamination parameter. However, it is obscure how each of spectral bands can characterize the water quality because the difference among the correlation coefficients of each spectral bands with water quality items is not so large.

Figure 7(b) show the factor loadings of Thematic Mapper (TM) data on LANDSAT and all of water quality data. From them, it is shown that the correlative properties of TM data is similar to that of MSS data in the above mention.

As shown in figures 8(a) and 8(b) for MSS and TM, respectively, the averaged radiation energy over a visible

Table 5 Eigenvalues and contribution factors of 1st to 3rd principal component

Principal component	1st	2nd	3rd
Eigenvalue	14.0	2.1	1.6
Contribution factor (%)	73.9	10.8	8.2
Cumulative contri.factor(%)	73.9	84.7	92.8
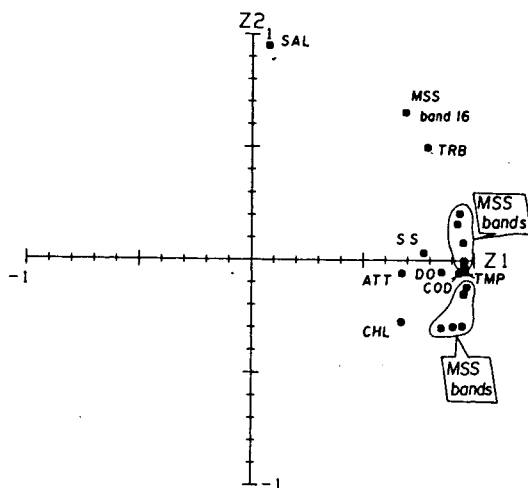
Figure 7(a) Factor loadings for the 1st(Z1)
and the 2nd(Z2) principal components
(by raw MSS data and water quality data)
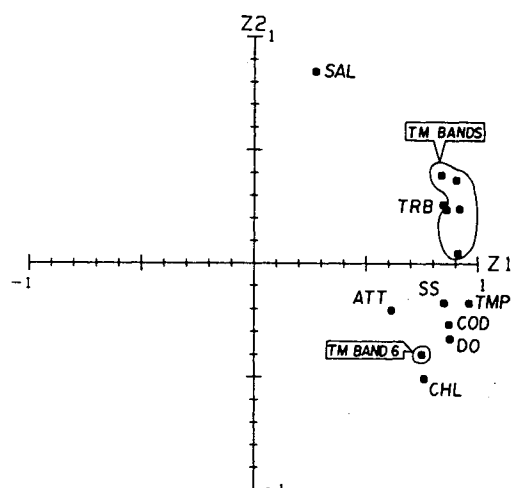
Figure 7(b) Factor loadings for the 1st(Z1)
and the 2nd(Z2) principal components
(by raw TM data and water quality data)
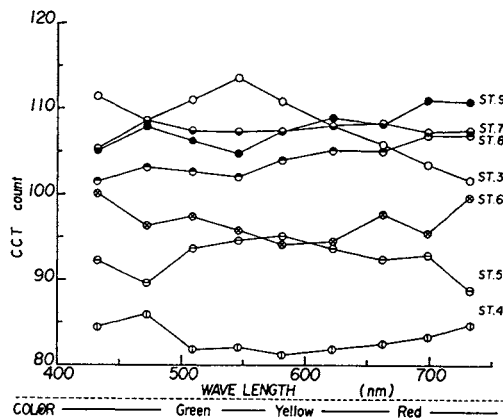
Figure 8(a) Intensity of radiance obtained by airborne MSS
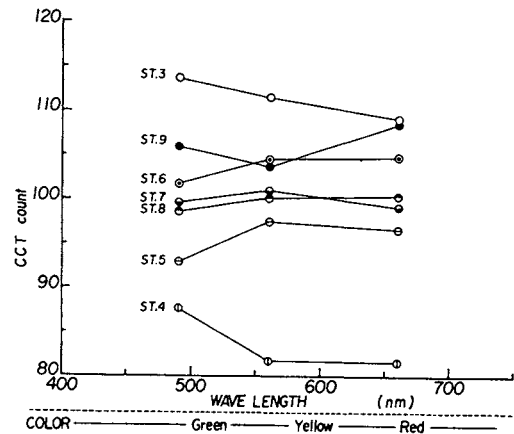
Figure 8(b) Intensity of radiance obtained by LANDSAT TM

Table 6 (a) Correlation coefficients (by normalized MSS data and water quality data)

Band	C H L	A T T	T M P	T R B	S S	D O	C O D	S A L
3 *	-0.161	-0.081	-0.205	-0.233	-0.471	-0.122	-0.075	0.108
4	-0.446	-0.126	-0.069	0.323	-0.065	-0.267	-0.182	0.792
5	-0.477	-0.029	-0.150	0.413	-0.025	-0.185	-0.089	0.668
6	0.048	0.292	0.170	0.520	0.470	0.230	0.269	0.136
7	0.623	0.462	0.447	0.151	0.568	0.540	0.525	-0.672
8	0.083	-0.276	-0.005	-0.585	-0.271	-0.201	-0.244	-0.460
9	0.510	-0.040	0.080	-0.408	0.113	0.184	0.013	-0.713

* The visible bands only are used in this analysis.

Table 6(b) Correlation coefficients (by normalized TM data and water quality data)

Band	C H L	A T T	T M P	T R B	S S	D O	C O D	S A L
1 *)	-0.136	0.003	-0.228	0.053	-0.262	0.021	0.018	0.245
2	-0.467	-0.217	-0.101	-0.132	-0.154	-0.387	-0.261	-0.113
3	0.622	0.193	0.422	0.044	0.520	0.324	0.212	-0.251

*) The visible bands only are used in this analysis.

range of wavelength at each observation point is much different from that at any other point. This is the primary reason why the difference among the correlation coefficients of each spectral bands with water quality items is not so large.

The above means the amount of radiation energy emerging from sea water changes over a considerable spatial range. Therefore, in the aim of investigating the ocean color variation in relation with chlorophyll-a, the following radiation energy of each band normalized by the amount of radiation energy is useful.

$$Bs_i = B_i / B, \quad B = \sum_i B_i$$

where Bs_i is a normalized digital count for i-th spectral band, B_i is a raw

digital count.

Tables 6(a) and 6(b) show the correlation coefficients of water quality data with airborne MSS data and LANDSAT TM data, respectively, which are normalized by the above method.

As is already stated in figure 4, it is said that the pigment concentration of chlorophyll-a is one of water quality items which can be detected by a visible imagery of remote sensing.

According to the absorption spectra of chlorophyll-a shown in figure 4, the correlation coefficients of the intensity of radiance with chlorophyll-a concentration should be nearby zero or negative at wavelengths of 400-450nm and 650-700nm which are the light absorption bands by chlorophyll-a, and positive at wavelength of 500-550nm. However, tables 6(a) and 6(b) show the
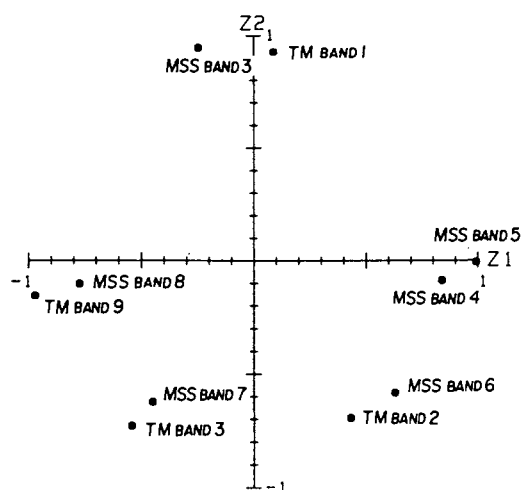
Figure 9   Factor loadings for the 1st(Z1)
            and the 2nd(Z2) principal components
            (by normalized MSS and TM data)
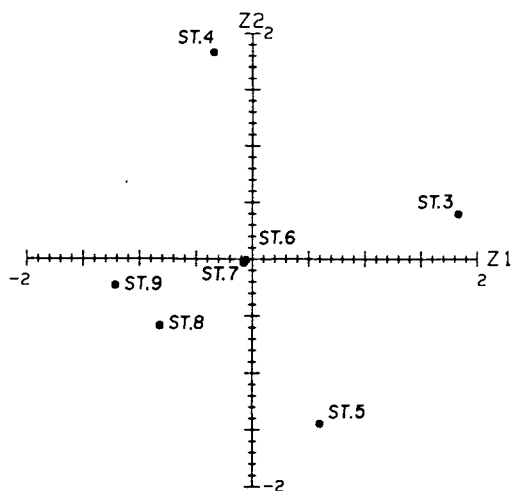
Figure 10   Score for each observation point
             derived from figure 9

contrary to that.

In general, it is not so difficult to detect the chlorophyll-a in the ocean water which does not contain any other material affecting optically the reflectance by chlorophyll-a, and the practical algorithm to predict the phytoplankton concentration has also been suggested.

On the other hand, as in the present study, in case of inner bay or coastal waters, many problems remains yet to be solved on the remote sensing of chlorophyll-a concentration. Because the water in an enclosed bay or coastal waters contains various sorts of organic matter and suspended load originating from the river effluent and the urban waste, and the light absorption or scattering by them often disturbs the detection of chlorophyll-a.

So far as the present study is concerned, an attempt to find out any relation between chlorophyll-a concentration and remote sensing data led to a conclusion that it was much difficult to detect the chlorophyll-a in inner bay water. However, it seems to be of importance that the ocean color information contained in the visible imagery of remote sensing is investigated in comparison with the apparent ocean color observed by the sea truth.

Figure 9 shows the factor loadings of each spectral bands for the first and the second principal components obtained from the normalized data of airborne MSS and LANDSAT TM. In addition, figure 10 shows the score derived from figure 9 for each observation point. According to the spectral properties shown in tables 1 and 2, it is suggested that the first and the second principal components in figure 9 are relatively related to the color of green and blue, respectively. In figure 10, therefore, it is suggested that the

Table 7 Apparent ocean color obtained
         by the sea truth

Station	ocean color
1	dark yellowish green
2	dark brown
3	dark brown
4	yellowish brown
5	brown
6	olive
7	dark yellowish green
8	dark yellowish brown
9	dark red

greenish color component is strong at station 3 in outer bay and the redish component is dominant at station 9 in inner bay.

On the other hand, the apparent ocean color obtained by the sea truth is shown in table 7. The apparent ocean color in table 7 cannot be directly compared with the color information obtained from figure 10 because figure 10 does not contain all of color informations, such as hue, value and chroma. However, "dark red" at station 9 seems to be in good agreement with the dominant color at the same station in figure 10.

Thus, since the ocean color obtained by not only airborne MSS but LANDSAT TM are somewhat in good agreement with that obtained by the sea truth , the validity of ocean color observation by remote sensing may be confirmed in the present study. Therefore, for further application of remote sensing technique to water quality measurement in coastal

waters, it is of great importance to develop the evaluation method for the relation of water quality, in particular, chlorophyll-a concentration, with the ocean color spectrum under the spectral disturbance by other contamination materials.

4. Concluding Remarks

The conclusions are summarized by the following.

i) From the correlation analysis for remotely-sensed data and sea truth data, the estimated features of surface water temperature and turbidity in Tokyo Bay were obtained. This technique also makes it possible to manage the turbidity dispersion caused by huge marine works and to make an optimum planning for them.

ii) So far as the present study is concerned, an attempt to find out any relation between chlorophyll-a concentration and remote sensing data led to a conclusion that it was very difficult to detect the chlorophyll-a in inner bay water. The bay water or coastal water, in general, contains various sorts of organic matter and suspended load, and the light absorption or scattering by them often disturbs the detection of chlorophyll-a. Therefore, for further application of remote sensing technique to water quality measurement, such as chlorophyll-a concentration in coastal waters, it is of great importance to investigate the effects of light absorption or scattering by various sorts of contaminants on the upwelling spectra of radiance through water surface.

Acknowledgement

References

1. Murakami,K.,Suganuma,F. and Miyahara,Y.,"Application of remote sensing technique to water quality measurement", Tech. Note of P.H.R.I., Ministry of Transport, No.626 (1988) (in Japanese)

ON-LINE DATA SERVICES OF NOAA SEA SURFACE TEMPERATURE IMAGES THROUGH VALUE ADDED NETWORKS

Seiich Saitoh*, Ichiro Saito** and Junko Abe***

* Japan Weather Association 4-5, Koujimachi, Chiyoda-ku, Tokyo 102, Japan
** Secomnet Co., Ltd. 3-1-8, Shiba-kouen, Minato-ku, Tokyo 105, Japan
*** IBM Japan, Ltd. 19-21, Hakozaki-cho, Nihonbashi, Chuo-ku, Tokyo 103, Japan

Abstract

We attempt to develop on-line data service system of NOAA AVHRR(Advanced Very High Resolution Radiometer) images throuth Network Management System(NMS) of IBM Value Added Network (VAN). NOAA High Resolution Picture Transmission(HRPT) data has been received through digital high-speed network on real-time basis. In image processing, firstly HRPT data is generated with in-flight calibration and secondly processed with geometric correction. Geometric correction is carried out for six areas and one mozaic area around Japan Island using mercator projection.

Single AVHRR image with data compressing has only from 20k to 32k bytes and it is possible to send this image about 1.0 - 1.7 minutes through 2400 bps line. In pre-processing, land, cloud and sea area are separated by using mask images. In this on-line data service system, It is possible to receive temperature enhanced color coded images. We are developed on-line and near-realtime data service within 2 hours through NMS network. The AVHRR images is storing in the each user electric mail in the Information Exchange(IE/EX) service of NMS for three days in free of charge.

The characteristics of this services are pointed out as (1)Timely and Fast, (2)Low cost, (3)Accessible for Various & Vast users. As a results, user will be free from receiving tasks and vast image data processing, then can monitor sea surface temperature on daily basis cost effectively.

1. Intoduction

Japan Weather Association (JWA) have been promoting satellite data service of NOAA Advanced Very High Resolution Radiometer (AVHRR) images on daily basis since November 1984. Recently, personal computer technology and telecommunication technology are well developed and it is easy to distribute information through several networks and to receive it by personal computer. We attempt to develop on-line data service system of NOAA AVHRR images throuth Network Management System(NMS) of IBM Value Added Network (VAN). In this system, Users can also utilize meteorological observation data, weather forecasting information and GMS LR-FAX cloud images as well as NOAA AVHRR SST images.

2. Data system

2.1 Network System

NOAA's operational polar orbiting satellite TIROS/NOAA series High Resolution Picture Transmission(HRPT) data has been received at Meteorological Satellite Center, Japan Meteorological Agency (JMA). HRPT data has been stored in cassette magnetic tapes of 32,000 bpi at the center and Japan Weather Association (JWA) has been receiving HRPT data through 768K bps digital high-speed network on real-time basis since 1986.

After receiving HRPT data, image processing and data compressing are carried out by host computer. Then on-line datasets is sent to IBM NMS network through 9600 bps private telephone networks of NTT with SNA telecommunication procedure. NMS has Information Exchange(IE/EX) services which anyone can send data to anyone and can store data in own erectric mail through the network. IE/EX services is a kind of electric mail services. JWA can send NOAA AVHRR images to each users at the same time. Users can access NMS network and can receive the data in any time by useing either IBM PC or host

computer. Data system configuration is shown in Fig. 1. IBM Japan, Ltd. has called this kind services as Provider's Products Marketing (PPM). JWA named this, services as "MERITS"; Meteorological, Environmental, & Resourceful Information Transfer Services. At present time, NMS holds 69 access points all over the Japan.

```
         ===========
            NOAA
         ===========
             |
             |HRPT
             |
             v
      +-------------+
      |  DPC/MSC    |
      |             |
      +-------------+
             |    (JMA)
             | NOAA HRPT
             |(768Kbps)
             v
      +---------------+
      |  MICOS/MIC    |
      |               |
      +---------------+
             |    (JWA)
             | NOAA AVHRR
      SNA    |(9600bps)
             v
   +-----------------------------+
   |         MERITS              |
   |          /NMS               |
   |                             |
   |         IE/EX               |
   |                             |
   |                             |
   +-----------------------------+
       |      |      |  (IBM Japan)
       |      |      |
       |      |      |(1200-9600bps)
       v      v      v
      /  \   /  \   +------+
     < PC >< PC >   | HOST |
      \  /   \  /   +------+
        U  S  E  R  S
```
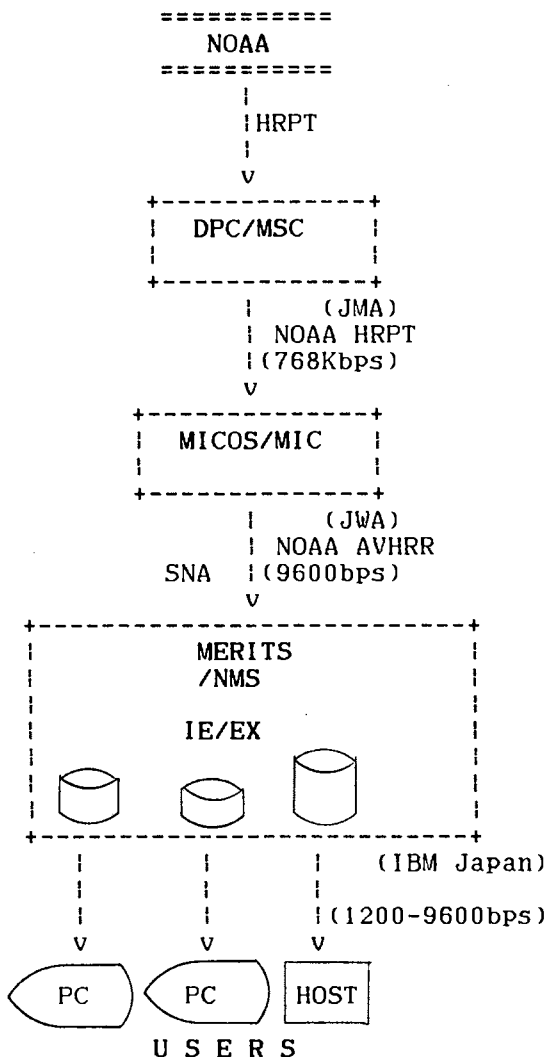
DPC   : Data Processing Center
MSC : Meteorological Satellite Center(JMA)
MICOS   : Meteorological Information
           Comprehensive Online Service
MIC : Meteorological Information Center(JWA)
MERITS : Meteorological, Environmental
           & Resourceful Information
           Transfer Services of JWA
NMS   : Network Management System

Fig. 1   Data system configuretion for
          distributing NOAA AVHRR SST data

2.2 Data Processing

In image processing, firstly HRPT data is generated with in-flight calibration[1] and secondly processed with geometric correction[2]. Geometric correction is carried out for six areas and one mozaic image(J) is generated Japan Island using mercator projection (Fig. 2). Six geometric corrected images is covering 1200 Km by 1200 Km with about 2.5 Km spatial resolution. Mozaic image is covering 2000 Km by 2000 Km with about 5.0 Km spatial resolution.

Single AVHRR image is 8 bits image of 512 columns by 480 lines which contains about 256k bytes. For the data compressing, We employ run length method, then data value becomes from 20k to 32k bytes and it is possible to send this image about 1.0 - 1.7 minutes through 2400 bps public telephone line. This run length method can represent 16 level values. In pre-processing, land, cloud and sea area are separated by using mask images and cloud classification. In this case, land has value 0 and cloud has value 16, so that sea surface temperature(SST) has value from 2 to 15 as 14 levels. It is important to enhance SST level for each time periods. We apply ten days mean SST data for controling of thermal enhancement. The enhance tables have been generated for each area and each ten days period. In this on-line data service system, It is possible to receive temperature enhanced color coded images. The processing procedure is shown in Fig. 3.

We are developed on-line and near-realtime data service within 2 hours after receiving HRPT data through NMS network. The AVHRR images is storing in the each user electric mail in the IE/EX service of NMS for three days in free of charge.

3. PC package

It is easy for users to receive and display images using PC package which was developed by SECOMNET Co., Ltd. The package has running only using PF keys and ten keys with menu driven system. The menu structure is generated by tree formation, escape key always works for the order of quit. This package is constructed with three modules : receiving module, archiving module and display module. The receiving module is prepared by IBM as the software package called "IBM IEEX-PS/55". The archiving module has management table for each datasets.

In the display module has following functions:
    1) display
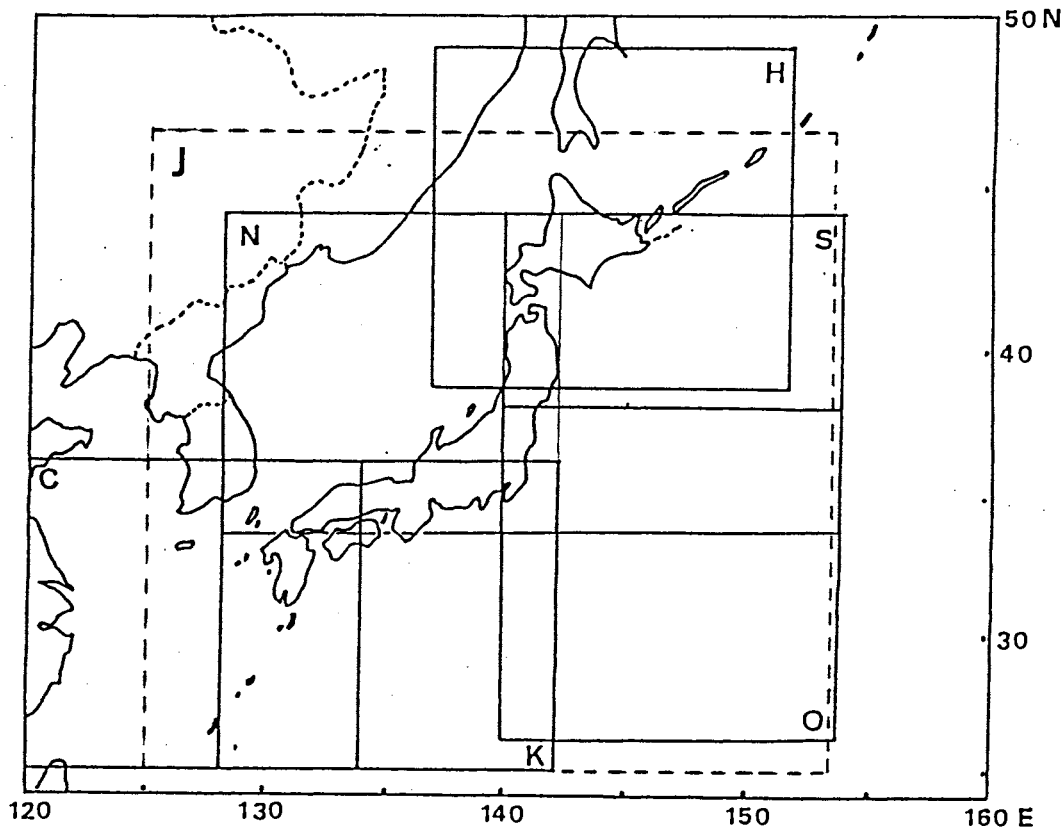
Fig. 2   Image processing area. Area J is
mozaic image.

2) image magnification
3) overlay of long. and lat. lines
4) animation

Appling such functions, it is easy for users to undersatnd dynamics of time-series SST. Fig. 4 is a sample image of NOAA AVHRR SST(Area H: see Fig. 2) on CRT of IBM PC. Land area is masked with mask image which generated by geographical information system(GIS) datasets(Fig. 3), so it is clear to identify ocean area. Color code located bottom in CRT represents enhanced thermal values. Information of location is overlayed on the image with the function 3). We can find that the cold water is distributing in the Sea of Okhotsk and the Tsushima warm current is running along the west cast of Hokkaido Island.

4. Conclusion Remarks

The characteristics of this services are pointed out as (1)Timely and Fast, (2)Low cost, (3)Accessible for Various & Vast users. As a results, user will be free from both receiving tasks and vast image data processing, then can monitor sea surface temperature on daily basis cost effectively. Monitoring SST using this system will be applied to fisheries research and fisheries operations with detecting distribution of oceanic fronts and rings[3].

References

1. Lauritson, L., Nelson, G.J., and Porto, F.W. "Data extraction and calibration of TIROS/NOAA radiometer" NOAA Technical Memorandum NESS 107, 83pp. (1979)

2. Tozawa, Y., Iisaka, J., Saitoh, S. Muneyama, K., and Sasaki, Y. "SST estimation by NOAA AVHRR and its application to oceanic front extraction" Tokyo Scientific Center Report G318-1556, IBM Japan, Ltd., 14pp. (1981)

3. Saitoh, S., Kosaka, S. and Iisaka, J. "Satellite infrared observation of Kuroshio warm-core rings and their application to study of Pacific saury migration", Deep-Sea Res., Vol.33, Nos 11/12, p.1601 (1986)

Fig. 4 Sample image of NOAA SST on CRT of IBM PC. Area: H, Date: March 9,1900, Satellite: NOAA-11, Orbit No.: 07485.

Fig. 3 Data processing procedure

SATELLITE ALTIMETRY DATA ANALYSIS FOR THE WESTERN NORTH PACIFIC

S. Imawaki, K. Ichikawa

Kyoto University, Japan

Abstract

Procedure is developed to estimate the sea-surface dynamic topography (the departure of sea surface from the geoid; hereafter abbreviated SSDT) from the satellite altimetry data by using optimal interpolation. The method is applied to the GEOSAT ERM altimetry data obtained southeast of Japan for one year in 1986-87. The estimated mean elevation field can not be used to give the temporal mean SSDT because even the best available geoid model is not precise enough. The temporal fluctuation SSDT is estimated successfully and combined with conversion of climatological mean geopotential anomalies at sea surface in order to give the approximated total SSDT, or the pseudo-SSDT. The time series of the pseudo-SSDT field shows meandering of the Kuroshio Extension, pinching-off of the meander to form a cyclonic eddy, westward movement of the eddy and coalescence of the eddy to the Kuroshio.

1. Introduction

Satellite radar altimetry is a very promising technique; it can provide the sea-surface height data repeatedly in a fairly short time interval (several to ten days) almost all over the world oceans. The primary information from satellite altimetry is for the shape of the geoid (an imaginary equi-geopotential surface near the earth's surface), since the actual distribution of the sea-surface height is mostly due to the undulation of the geoid; rms for the global geoid is about 25 m while rms for the rest is 0.5-1 m. The geoid is the surface of the ocean at rest, and only the departure of sea surface from the geoid is important in physical oceanography; the departure is proportional to the oceanic surface pressure and related with ocean currents. This small departure is called here the sea-surface dynamic topography, and hereafter abbreviated SSDT. For low-frequency motions, the geostrophic balance holds approximately, and velocities at sea surface can be estimated directly from the horizontal gradient of the SSDT. When the temporal mean of the SSDT is concerned, you need a precise geoid model which is obtained by a method other than the satellite altimetry. However, we have no global geoid model which is accurate enough. When the temporal fluctuation of the SSDT is concerned, you do not need a precise geoid model, as shown later.

GEOdetic SATellite (abbreviated GEOSAT) provided a unique set of satellite altimetry data for global oceans with a 17-day repeat period for about three years. GEOSAT was launched in March 1985 by U.S. Navy to obtain very precise global geoid data. It is the first satellite since SEASAT launched in 1978. The data during the first 20 months have been classified, but the data during the Exact Repeat Mission (abbreviated ERM) starting on November 8, 1986 are unclassified [1]. During the ERM, the satellite took repeat subsatellite tracks every 17 days; fluctuations of the tracks are said to be less than ± 1 km. GEOSAT carried out measurements successfully until the tape-recorder on board for collecting the global data stopped in October 1989. Finally, GEOSAT ended its measurements because of the drop of the power supply in January 1990. Therefore, GEOSAT carried out 62 times of the 17-day global measurements; it is for 1054 days, or about three years. They are epoch-making measurements which no other satellites have been able to perform. The accuracy of the altimeter itself on board the satellite is better than that on SEASAT. However, the GEOSAT data have some disadvantages. There were no direct measurements of the water vapor in the atmosphere, which are necessary for correction of the light speed. And the accuracy of the estimated satellite orbit height is poor; its rms for GEOSAT is said to be 3-4 m, while rms for SEASAT is about 1 m.

In this paper, we use the altimetry data taken for the first one year during the ERM of GEOSAT, and estimate the temporal fluctuation of the SSDT southeast of Japan. The estimated fluctuation SSDT is combined with conversion of climatological mean geopotential anomalies at sea surface in order to give an approximation to the total SSDT. The results are supported by fragmental results from conventional oceanographic

observations. The time series of the SSDT map shows meandering of the Kuroshio Extension, pinching-off of the meander to form a cyclonic eddy, westward movement of the eddy and coalescence of the eddy to the Kuroshio. We conclude that the altimetry data are very powerful and useful in physical oceanography.

2. Processing Altimetry Data

Satellite radar altimetry provides the sea-surface height data in a straightforward way. The distance from a satellite to the subsatellite point on sea surface is measured with microwaves and recorded by an altimeter on board the satellite. The height (relative to the reference ellipsoid of the earth) of the satellite is estimated by a numerical model for orbit calculation, using satellite position data obtained at satellite-tracking stations and the best available global gravity data. A continuous record of sea-surface height (relative to the reference ellipsoid of the earth) along the subsatellite ground track is obtained from these two sets of measurements. This record is subject to both distance measurement error and orbital height calculation error.

The measured sea-surface height $S(\mathbf{r}, t)$ is related to the sum of the geoid height $\hat{N}(\mathbf{r})$ (relative to the reference ellipsoid of the earth) and the SSDT $\zeta(\mathbf{r}, t)$ as well as to radial orbit error $\epsilon_s(\mathbf{r}) + \epsilon_r(t)$ and random measurement error $\epsilon_m(t)$ of the altimeter:

$$S(\mathbf{r}, t) = \hat{N}(\mathbf{r}) + \zeta(\mathbf{r}, t) + \epsilon_s(\mathbf{r}) + \epsilon_r(t) + \epsilon_m(t), \quad (1)$$

where $\mathbf{r}$ is the horizontal position vector on sea surface, and t the time. Here it is understood that the sea-surface height $S(\mathbf{r}, t)$ has been corrected for distance measurement error (several path length corrections) and that high frequency fluctuations of the sea-surface height have been eliminated (tide corrections). The random measurement error $\epsilon_m(t)$ includes the errors of all these corrections as well as altimeter sensor error.

Radial orbit error is comprised of systematic orbit error $\epsilon_s(\mathbf{r})$ and random orbit error $\epsilon_r(t)$. Systematic radial orbit error, or geographically dependent orbit error, is difficult to estimate and can not be reduced without improving the gravity data used in the orbit calculation model. As shown later, this systematic orbit error could contaminate estimates of the SSDT. Random radial orbit error, or geographically independent orbit error, is the largest error so far in known errors in satellite altimetry data; its rms amplitude is said to be 3-4 m for GEOSAT (here we use orbit heights newly recalculated [3], so the rms amplitude of the error is about 1 m). Fortunately, random radial orbit error is dominated by error component which has a frequency of one cycle per satellite revolution around the earth, or a wavelength of circumference of the earth, and can be separated relatively easily from the signal when only small or meso-scale phenomena are concerned.

We use optimal interpolation to pick up the altimetric elevation signal from noisy altimetry data. The so-called crossover difference technique has been used widely to reduce random radial orbit error. It is handy and efficient for removing random orbit error at long wavelengths, but it has several demerits: it can not be applied to global oceans; it does not utilize knowledge of features of random orbit error efficiently; it does not provide error maps about estimates; and it does not give estimates at grid points. Optimal interpolation (or objective analysis) has been proposed for altimetry data analysis [7,8]. It is based on the Gauss-Markov theorem, and produces an optimal (or statistically least square error) linear estimate of the signal from data which include measurement noise, provided that statistics of the signal and noise are known in advance. Although this method requires a fairly big computer to process the data, it overcomes the above-mentioned demerits of the cross-over technique. Optimal interpolation has been successfully applied to the actual satellite altimetry data for the same study area recently [4,5].

3. Estimating The SSDT

The time invariant elevation field during each repeat period is estimated from the altimetric sea-surface height data and the latest geoid data by use of optimal interpolation. Because the coverage of altimetry measurements is repeated at a given interval (a 17-day interval in the present case), the average sea-surface elevation $H_p(\mathbf{r})$ during a given repeat period p is estimated as follows. Provided that the best available data on geoid undulation $N(\mathbf{r})$ include unknown measurement error $\epsilon_N(\mathbf{r})$, the true geoid $\hat{N}(\mathbf{r})$ is written $N(\mathbf{r}) + \epsilon_N(\mathbf{r})$. Therefore, Equation (1) can be rewritten

$$R(\mathbf{r}, t) = H_p(\mathbf{r}) + E(\mathbf{r}, t), \quad (2)$$

where

$$
\begin{aligned}
R(\mathbf{r}, t) &= S(\mathbf{r}, t) - N(\mathbf{r}) \\
H_p(\mathbf{r}) &= \zeta_p(\mathbf{r}) + \epsilon_N(\mathbf{r}) + \epsilon_s(\mathbf{r}) \\
E(\mathbf{r}, t) &= \zeta'(\mathbf{r}, t) + \epsilon_r(t) + \epsilon_m(t).
\end{aligned}
$$

Namely, the data $R(\mathbf{r}, t)$ are related with the sum of the time invariant term $H_p(\mathbf{r})$ during the repeat period p and the time variant term $E(\mathbf{r}, t)$ during that. Here the sea-surface height $S(\mathbf{r}, t)$ is understood as all the altimetry data taken during that repeat period. We can now estimate the time invariant elevation field $H_p(\mathbf{r})$ by optimal interpolation regarding $R(\mathbf{r}, t)$ during the repeat period as the input data and $E(\mathbf{r}, t)$ as the noise. Note that the deviation $\zeta'(\mathbf{r}, t)$ of the SSDT from the time invariant SSDT $\zeta_p(\mathbf{r})$ during this period is included in $E(\mathbf{r}, t)$ because it is considered noise when estimating the average field during each repeat period. Note also that estimates of the time invariant elevation field $H_p(\mathbf{r})$ are related with the error of the best available geoid data and the systematic radial orbit error

as well as the time invariant SSDT $\zeta_p(\mathbf{r})$ during the repeat period p. Therefore, you need a precise geoid model and smaller systematic radial orbit error in order to obtain the time invariant SSDT $\zeta_p(\mathbf{r})$ from the time invariant elevation field $H_p(\mathbf{r})$.

The temporal fluctuation SSDT is estimated as follows. The above-mentioned time invariant SSDT $\zeta_p(\mathbf{r})$ during each repeat period (hereafter called the total SSDT) can be divided into two parts; the temporal mean SSDT $\bar{\zeta}(\mathbf{r})$ during the *entire* satellite measurement period and the temporal fluctuation SSDT $\zeta_p'(\mathbf{r})$, or the departure of the SSDT from that mean, for the repeat period p. That is, $\zeta_p(\mathbf{r}) = \bar{\zeta}(\mathbf{r}) + \zeta_p'(\mathbf{r})$. From all the estimates of the time invariant elevation field $H_p(\mathbf{r})$ during all the repeat periods, you can estimate the overall mean elevation field $\bar{H}(\mathbf{r})$; $\bar{H}(\mathbf{r}) = \bar{\zeta}(\mathbf{r}) + \epsilon_N(\mathbf{r}) + \epsilon_s(\mathbf{r})$. Therefore, Equation (2) is rewritten

$$R(\mathbf{r},t) - \bar{H}(\mathbf{r}) = \zeta_p'(\mathbf{r}) + E(\mathbf{r},t). \qquad (3)$$

Now we can estimate the fluctuation SSDT $\zeta_p'(\mathbf{r})$ for the repeat period p by optimal interpolation regarding $[R(\mathbf{r},t) - \bar{H}(\mathbf{r})]$ during the repeat period as the input data and $E(\mathbf{r},t)$ as the noise. Note that the estimated fluctuation SSDT $\zeta_p'(\mathbf{r})$ is free from both the error of the best available geoid data and the systematic radial orbit error, which could contaminate estimates of the total SSDT $\zeta_p(\mathbf{r})$ as noted in the previous paragraph.

The pseudo-SSDT, or an approximation to the total SSDT, is estimated as follows. For areas where pronounced temporal mean fields exist like the Kuroshio and Kuroshio Extension region in the North Pacific, it may not be suitable to look at the fluctuation SSDT; sometimes, it it appropriate to look at the total SSDT. However, you can not use the estimated time invariant elevation field $H_p(\mathbf{r})$ during the repeat period p to give an approximation to the total SSDT field $\zeta_p(\mathbf{r})$, because the geoid data available to us present are not accurate enough as noted above. Here we assume that conversion of climatological mean geopotential anomalies $\Delta D(\mathbf{r})$ at sea surface is close to the mean SSDT $\bar{\zeta}(\mathbf{r})$ during the entire satellite measurement period. We call the term $\tilde{\zeta}_p(\mathbf{r}) = \Delta D(\mathbf{r}) + \zeta_p'(\mathbf{r})$ the pseudo-SSDT, which is an approximation to the total SSDT for the repeat period p. A similar treatment is also done elsewhere [4].

4. An Example For The Western North Pacific

Here is an example of the present method applied to the GEOSAT ERM altimetry data obtained for a study area (20-50 °N, 120-150 °E) in the western North Pacific from November 8, 1986 through November 17, 1987. We choose this area because a very pronounced western boundary current system, the Kuroshio and Kuroshio Extension, is present and because fairly precise geoid data are available for that area only; we use the geoid data obtained from marine gravity data [2]

and improved recently by the Seasat altimetry data [5]. We excluded marginal seas such as the Japan Sea, the Yellow Sea, the Okhotsk Sea and part of the East China Sea because the tide model used for tide correction can not estimate the ocean tide precisely in those areas.

Details of optimal interpolation used are as follows. GEOSAT altimetry data were averaged over 10 datapoints (about 67 km) along subsatellite tracks to reduce the total data as well as to reduce measurement errors and small scale oceanic fluctuation. The signal covariance is prescribed by the negative squared exponential, or the Gaussian shape function, with a decorrelation spatial scale of 150 km. Therefore, fluctuations having scales smaller than this scale are smoothed out. The error covariance for the satellite random radial orbit error is prescribed by cosine function with the satellite revolution period and the amplitude of 1 m decaying in accordance with the Gaussian shape function with a decorrelation temporal scale of 20 times the satellite revolution period. The error covariance for the random measurement error is given by white noise with magnitude of 0.2 m.

The estimated temporal fluctuation SSDT in the Kuroshio Extension region shows westward movement of a cyclonic eddy. We estimate temporal fluctuation SSDT $\zeta_p'(\mathbf{r})$ for the 30 ° × 30 ° study region, and show here a part of it for the Kuroshio and Kuroshio Extension region as an example. Figure 1 shows the fluctuation SSDT for the region in repeat periods 12 through 16. Provided that ocean currents are in geostrophic balance, flow is parallel to the contour and stronger where spacing of contours is narrower. One of the most pronounced features during this period is the existence of a relatively low sea-surface height area, or a cyclonic eddy, centered around 35 °N, 145 °E. The previous and following maps (not shown here) of fluctuation SSDT show that the cyclonic eddy had its center at around 33-35 °N, appeared in this region in repeat period 8 (March 7-24, 1987), moved westward slowly (at a speed of about 4 cm/s), and coalesced with the Kuroshio around in repeat period 19 (September 12-28).

On the other hand, the pseudo-SSDT in the same region shows meandering of the Kuroshio Extension, pinching-off of the meander to form a cyclonic eddy, westward movement of the eddy, and coalescence of the eddy to the Kuroshio. Figure 2 shows the pseudo-SSDT $\tilde{\zeta}_p(\mathbf{r})$ for the same region and for the same repeat periods. Generally, the pseudo-SSDT in this region is high in the south and low in the north (no meaning in its absolute values). Features appearing in this pseudo-SSDT, which includes both the *mean* and fluctuation fields of the SSDT, are meandering of the Kuroshio Extension until repeat period 13, pinching-off of the meander to form a cyclonic eddy (probably a cold eddy) in repeat period 14, westward movement of the eddy, and absorption of the eddy by the Kuroshio in repeat period 19 (not shown here). After absorption, the Kuroshio

seems to have advected the cyclonic eddy eastward, and large fluctuation of the Kuroshio Extension continued until repeat period 22 (November 1-17; the last repeat period in the present analysis).

The pseudo-SSDT is compared well with fragmental results from conventional oceanographic observations obtained during this period. The sources used are the Prompt Report of the Oceanographic Conditions (*Kaiyo Sokuho*) published bimonthly by the Hydrographic Department, Maritime Safety Agency. They include locations of the 15 °C isotherm at 200 m depth (an indicator widely used for location of the axis of the Kuroshio and Kuroshio Extension) and surface velocities measured by GEK (Geomagnetic Electro-Kinematograph). Usually, observations were not extended to the Kuroshio Extension region, and we do not have a complete data set for comparison. However, all the observational results obtained for that region including those during repeat periods 2, 10, 16 (Fig. 2e), 18, 20 and 21 show good agreement with the pseudo-SSDT estimated in this paper.

A few scenes of the NOAA AVHRR (Advanced Very High Resolution Radiometer) available for this region during this period show existence of cold sea-surface waters corresponding to the cyclonic eddy detected in the pseudo-SSDT field. This region was covered by clouds almost always during that summer, and few AVHRR sea-surface temperature images are useful for comparison. However, images obtained in repeat periods 12 (Fig. 2a) and 21 show cold sea-surface waters centered around 35 °N, 145 °, which correspond to the meandering of the Kuroshio Extension and the cyclonic eddy absorbed and advected by the Kuroshio.

5. Concluding Remarks

In the present paper, we analyzed the GEOSAT altimetry data and showed in some details the temporal change of the SSDT southeast of Japan, especially for the Kuroshio Extension region. The results are supported by fragmental results obtained from usual oceanographic observations and also by a few sea-surface temperature images obtained from a satellite. The temporal resolution of 17 days is not satisfactorily fine (you may set the temporal resolution at 3 days, if you sacrifice the spatial resolution). But there are no data loss due to the presence of clouds, and the altimeter provides continuously the global data with certainty. We conclude that the altimetry data are very useful in physical oceanography.

Phenomenologically, the observed process is meandering of the strong current and detaching of the eddy, but it is understood simply as the westward movement of the cyclonic eddy in the fluctuation field. According to sketches of the fluctuation field over a wider area obtained from the GEOSAT altimetry data [6], the cyclonic eddy (or the cold water) observed in the Kuroshio Extension region is identical to the negative sea-surface height anomaly which had been located east

to the study region (centered at around 33 °N, 154 °E) in repeat period 1 (November 8-24, 1986) and moved westward to enter this region in repeat period 8. The cyclonic eddy continued to move westward until repeat period 19. On the other hand, in the pseudo-SSDT field (or the approximated total SSDT field), it is understood as the meander of the Kuroshio Extension moved westward, the cyclonic eddy pinched off from the meander and the detached cyclonic eddy moved westward. Which is the better description of the process to understand its mechanism ?

References

1. Cheney, R.E., Douglas, B.C., Agreen, R.W., Miller, L., Porter, D.L., and Doyle, N.S., "Geosat Altimeter Geophysical Data Record", *NOAA Technical Memorandum NOS NGS-46*, 29pp. (1987)

2. Ganeko, Y., "A 10' × 10' detailed gravimetric geoid around Japan", *Marine Geodesy*, *7*, 291-314 (1983)

3. Haines, B.J., Born, G.H., Marsh, J.G., and Williamson, R., "Precise Geosat orbits for the Exact Repeat Mission using the GEM-T1 gravity solution", (manuscript, 1989)

4. Ichikawa, K., and Imawaki, S., "Fluctuation of sea-surface dynamic topography southeast of Japan estimated from Seasat altimetry data", (submitted for publication, 1990)

5. Imawaki, S., Ichikawa, K., and Nishigaki, H., "Estimating mean sea-surface elevation field from satellite altimetry data by optimal interpolation", (submitted for publication, 1990)

6. Shibata, A., "Variations of relative sea level around Japan observed by the GEOSAT altimeter", *Umi to Sora*, *65*, 1-15 (in Japanese with English abstract) (1989)

7. Wunsch, C., "Calibrating an altimeter: How many tide gauges is enough?", *J. Atmos. and Oceanic Tech.*, *3*, 746-754 (1986)

8. Wunsch, C., and Zlotnicki, V., "The accuracy of altimetric surfaces", *Geophys. J. Roy. Astron. Soc.*, *78*, 795-808 (1984)
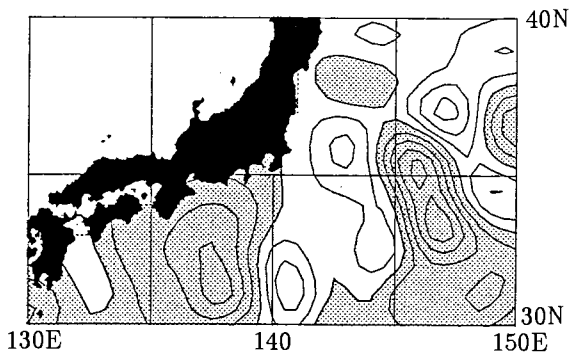
a. Repeat Period 12
(May 15-31)
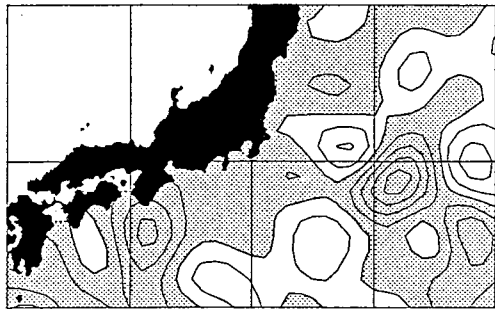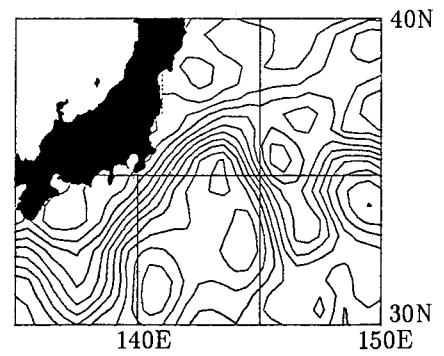
b. Repeat Period 13
(Jun. 1-17)
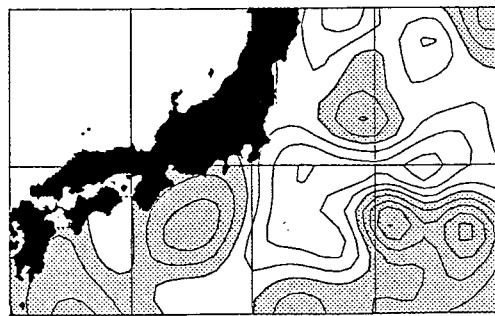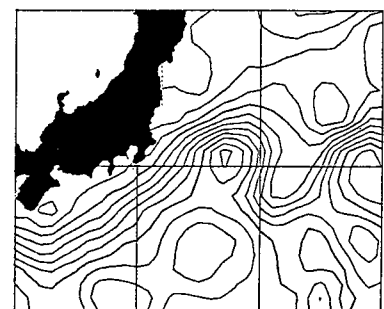
c. Repeat Period 14
(Jun. 18 - Jul. 4)
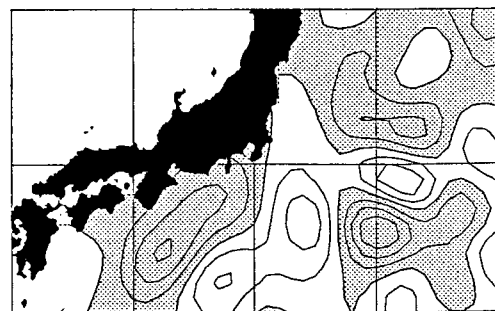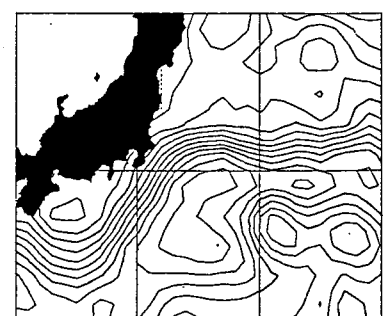
d. Repeat Period 15
(Jul. 5-21)
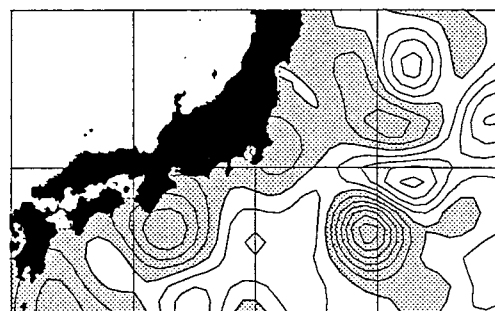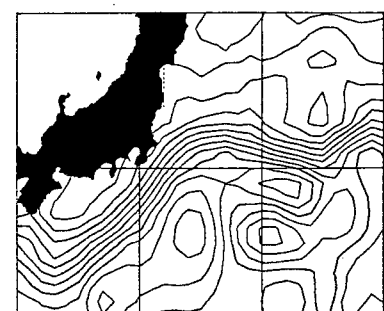
e. Repeat Period 16
(Jul. 22 - Aug. 7)
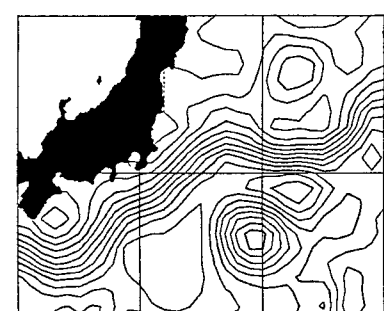
Fig. 1. Fluctuation SSDT fields for GEOSAT ERM repeat periods 12 (a) through 16 (e) in 1987. The contour interval is 0.1 m. Shading indicates negative values.

Fig. 2. Pseudo-SSDT fields for GEOSAT ERM repeat periods 12 (a) through 16 (e) in 1987. The contour interval is 0.1 m. Dotted line in (e) is the observed 15 °C isotherm at 200 m depth.

PLANS FOR THE KUROSHIO EXTENSION REGIONAL EXPERIMENT (KERE)

Jim L. Mitchell

Naval Oceanographic & Atmospheric Research Laboratory Sensing Space Center, MS 39529 U.S.A.

Abstract

During the mid-1990's, the Kuroshio Extension Regional Experiment (KERE) will examine the critical issues governing the dynamics and energetics of the Kuroshio Extension Current System. Specific scientific issues to be addressed are:

(a) the presence (?) and impact of a Deep Western Boundary Current (DWBC) on the Kuroshio Extension,

(b) the ratio of internal (gravest baroclinic) mode to barotropic mode and its effect on Kuroshio Extension mesoscale dynamics (particularly in the Oyashio Intrusion area),

(c) the relationship between surface wind stress forcing and gyre circulation of the NW Pacific.

Additionally, the impact on Kuroshio separation and eastward penetration by geometric forcing from coastlines and bathymetry will be studied.

Focussed on these issues will be several major new technologies (as most recently demonstrated during the NW Atlantic Regional Energetics Experiment (REX)). These will include:

(a) satellite altimetry (from TOPEX/Poseidon, ESA's ERS-1, and the U.S. Navy's SALT satellite),

(b) satellite scatterometry (from ESA's ERS-1),

(c) satellite infrared imagery (IR),

(d) numerical model experiments,

(e) a complimentary field program.

Introduction

The KERE represents a coordinated project involving the major techniques of remote sensing, field experiment, and ocean numerical modeling as depicted in Figure 1.
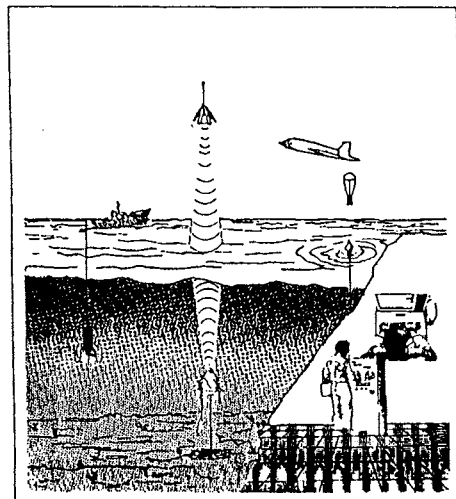
Figure 1-- Artist's concept of major components of the Kuroshio Extension Regional Experiment.

Key data types supporting the KERE are satellite altimetry and scatterometry from SALT, TOPEX/Poseidon, and the European ERS-1. In situ data will come from Inverted Echo Sounders with bottom Pressure Gauges (IES/PGs), current meters, and AXBT/XBT surveys. Data synthesis and analysis will proceed through the use of regional, eddy-resolving numerical models of the ocean circulation.Field experiment design will be largely motivated by (and its strategy planned) using numerical model simulations. Efficient and complementary field measurements will be emphasized. The vast quantities of altimeter-measured sea surface topography available from the altimetric satellites will allow

improved analyses using model-data assimilation schemes. Scatterometer-derived winds from ERS-1 will allow a detailed examination of the role of surface wind forcing in modulating a western boundary current, particularly over the larger North Pacific Basin (where the wind stress curl may play an even more dominant role than in the smaller North Atlantic). Analysis of these satellite data will proceed in both the Kuroshio Extension and Gulf Stream systems, while the collection of in situ data during the KERE will take place in the Kuroshio Extension only.

NW Atlantic Regional Energetics Experiment (REX)

The KERE is designed as a follow-on experiment to the presently concluding NW Atlantic Regional Energetics Experiment (REX). Some of the most notable preliminary REX results include:

(1) Consistent sea level variability amplitudes are observed from GEOSAT altimetry (see Figure 2), IES/PG arrays, and model simulations incorporating a Deep Western Boundary Current;
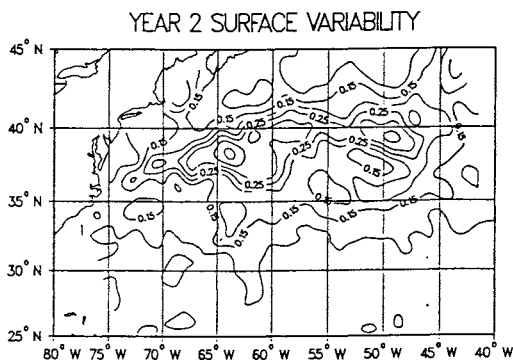
Figure 2-- Sea level variability (RMS in cm) of the NW Atlantic Gulf Stream region as observed during 1988 with GEOSAT-ERM altimetry.

(2) GEOSAT-ERM analysis indicates two-gyre structure in the recirculation south of the Gulf Stream (see Figure 3);
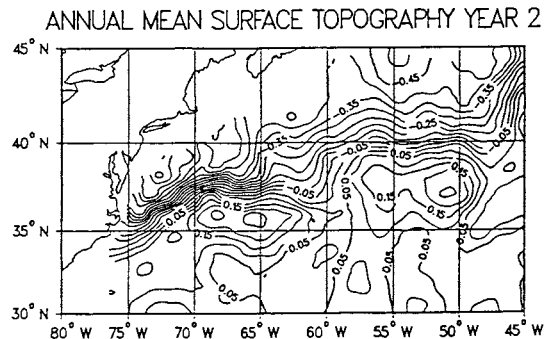
Figure 3-- Annual mean sea surface topography (cm) as observed during 1988 with GEOSAT-ERM altimetry. Note the prominence of two local recirculation gyres south of the Gulf Stream.

(3) Barotropic mode accounts for 1/3 of mesoscale RMS variability in sea level of the Gulf Stream;

(4) Precise alongtrack geoid profiles (computed from collinear altimetry and complementary AXBT sections) and/or IR images allow for the first detailed maps of both the mean and variable topography over the NW Atlantic (see Figures 2 and 3);

(5) Climatology-based regressions can be used to generate highly realistic "synthetic" thermal, salinity, and sound speed sections from collinear altimetry over the NW Atlantic.

Through the comparative effort mounted in KERE, some general conclusions regarding the basic nature of western boundary currents will be possible. KERE, in combination with REX, will represent a thorough study in the comparative anatomy of western boundary currents.

Satellite Analysis Plans for KERE

As already noted, a major component of the KERE will be the analysis of satellite altimetry, IR, and scatterometry in both the NW Pacific and NW Atlantic. Analyses of both the mean and variable surface topography (such as those depicted for the NW Atlantic in Figures 2 and 3) from satellite altimetry will play a major role in the KERE. Such analyses are useful for:

(a) Examining the impact of bathymetry on the western boundary current (for example, the two gyre recirculation structure seen in Figure 3 is clearly associated with the presence of the New England Seamount Chain (NESC) in the NW Atlantic),

(b) Tuning and adjusting numerical model simulations to obtain results in agreement with the altimetry (e.g., this is the way in which the importance of a DWBC in the NW Atlantic was first recognized during the REX; see Thompson and Schmitz, 1989),

(c) Studying the regional distributions of both eddy and mean kinetic and available potential energies (for example, see Figures 4 and 5).

**Eddy Available Potential Energy
from GEOSAT-ERM (1988)**

EAPE YEAR 2
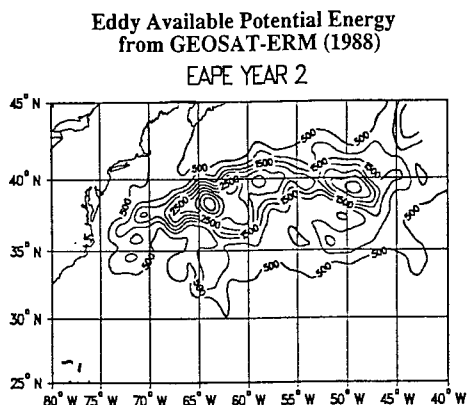
Figure 4-- Eddy Available Potential Energy (EAPE in cm²/sec²) of the Gulf Stream computed from surface topographic RMS observed with GEOSAT-ERM altimetry. Distribution and magnitudes depicted are in excellent agreement with other estimates of EAPE based upon in situ hydrography.

**Eddy Kinetic Energy
from GEOSAT-ERM (1988)**

EKE YEAR 2
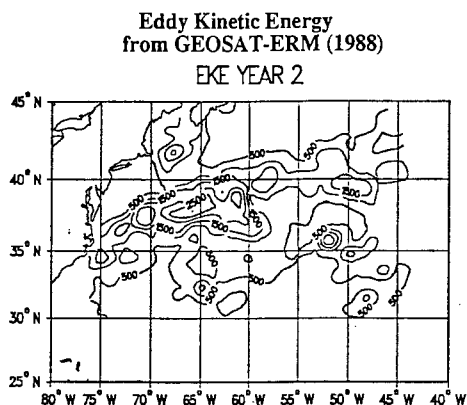
Figure 5-- Eddy Kinetic Energy (EKE in cm²/sec²) of the Gulf Stream computed from surface topographic RMS observed with GEOSAT-ERM altimetry. Distribution and magnitudes depicted agree well with other estimates of EKE based upon drifter data.

We will continue altimetric analyses of the NW Atlantic and extend these analyses to the NW Pacific during the KERE. Additionally, the statistics of mesoscale variability derived from satellite IR will play an important role in the KERE. Finally, surface wind stress fields observed by ESA's ERS-1 will provide important (and, long-awaited) input for the ocean circulation models.

Numerical Model Experiments in KERE

Work is already underway at the U.S. Naval Oceanographic & Atmospheric Research Laboratory (NOARL) on the development of realistic primitive equation (PE), layered models of the North Pacific Basin (including the Kuroshio and Kuroshio Extension). Use of these layered PE models has been demonstrated to have remarkable success in simulating and in providing meaningful forecasts of Gulf Stream evolution (see paper by Fox, Carnes, and Mitchell in this session). Using realistic bathymetry and coastline geometry, our 1/4°-resolution PE models are now able to successfully simulate many salient features of the North Pacific, including the Subartic Front and the Kuroshio Extension (see Figure 6). Comparison between model simulations (such as surface topographic variability shown in Figure 7), satellite analyses, and field data will serve as the basis for model improvements.
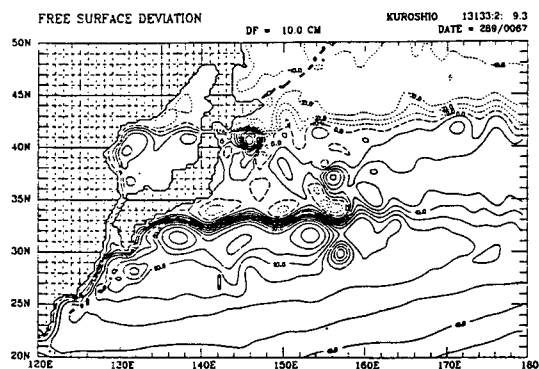
Figure 6-- A synoptic view of the Kuroshio Extension region from numerical model simulation. Contours represent sea surface topography (courtesy of Dr. H. Hurlburt, NOARL).
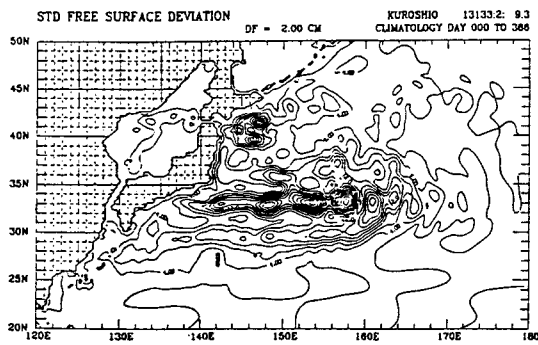
Figure 7-- Standard deviation in sea surface topography for the Kuroshio Extension region as simulated by numerical model experiment (courtesy of Dr. H. Hurlburt, NOARL).

Field Experiments in KERE

During 1992-94, field experiment components of the KERE will be underway, including:

(a) The deployment and subsequent recovery of a line of acoustic current meters (ACMs) and Inverted EchoSounders with Bottom Pressure Gauges (IES/PGs) arrayed along the section depicted in Figures 8 and 9. A major objective of these measurements will be the monitoring of any NW Pacific DWBC. As this line will coincide with a TOPEX/Poseidon altimeter groundtrack, comparison between the altimeter and in situ data will provide for analyses of both the timeseries and spectral nature of the mesoscale variability in this region as well as for an assessment of the relative importance of the barotropic and gravest baroclinic modes of this variability (see Hallock, Mitchell, and Thompson, 1989).
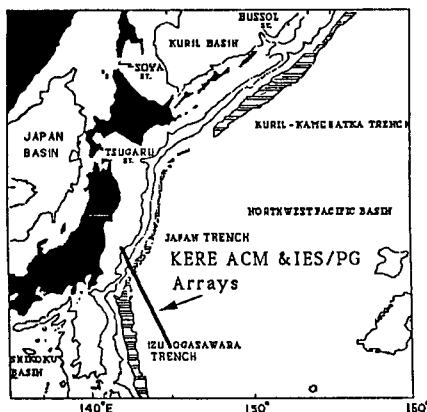
Figure 8-- Location of planned NOARL arrays of acoustic current meters and inverted echo sounders with pressure gauges. Line of arrays coincides with a groundtrack of the TOPEX/Poseidon altimeter (courtesy of Dr. Z. Hallock, NOARL).

Distance from coast of Honshu (km)
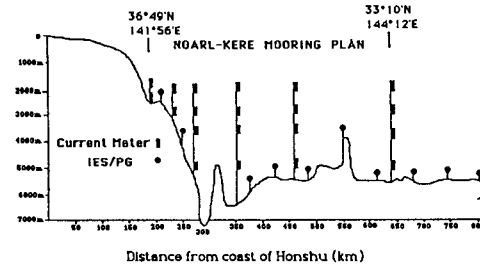
Figure 9-- Vertical cross section of NOARL ACM-IES/PG line across the Japan Trench and underneath a TOPEX/Poseidon groundtrack (courtesy of Dr. Z. Hallock, NOARL).

(b) Drops of Airborne Expendable Bathythermographs (AXBTs) along TOPEX/Poseidon groundtracks over the Kuroshio Extension region. These data will be used in conjunction with the satellite altimetry to provide for precise estimates of the alongtrack geoid profile (see Mitchell et al., 1990) which are necessary for subsequently inferring the temporal mean surface topography from the altimetry (see for example, Figure 3) and to provide for an error analysis of climatology-based inferences of deeper density structure from the altimeter alone (see Carnes et al., 1990).

(c) Other field work in the KERE will most likely focus on the use of deep floats for defining the current structure of the Kuroshio Extension, particularly near its separation from the Honshu coastline.

(d) Additionally, the feasibility of carrying out a regional, mesoscale-resolving acoustic tomography experiment is presently being examined as part of the planning for the KERE.

Summary

The KERE will culminate in a comparison of the dynamics and energetics of the Northern Hemisphere's two major western boundary currents. Following the NW Atlantic REX, the KERE will extend results and hypotheses derived from Gulf Stream studies to the Kuroshio Extension. Additionally, the collection and analyses of common data types in both the NW Atlantic and the NW Pacific, made possible by REX and KERE (i.e., satellite altimetry, model simulations, IES/PG data, etc.), will serve to enhance our understanding of the fundamental dynamics and energetics of western boundary currents in general.

An approximate time table for the KERE is given by:

*Detailed Planning for the KERE
   ---Through 1991

*Model Development (Pacific) and
   Simulations---1990-95

*ERS-1 altimeter/scatterometer data
   aquisition/analysis---1991-94

*TOPEX/Poseidon altimeter data
   aquisition/analysis---1992-95

*KERE Field Activities in the NW
   Pacific---1992-94

*Analysis of NW Pacific field data
   ---1993-95

*Model/Data Intercomparisons
   ---1992-95

*Kuroshio Extension/Gulf Stream
   Comparisons---1993-95.

References

Carnes, M.R., J.L. Mitchell, P.W. de Witt, Synthetic temperature profiles derived from GEOSAT altimetry: comparison with AXBT profiles. *J. Geophys. Res.*, In Press.

Hallock, Z.R., J.L. Mitchell, J.D. Thompson, Sea surface topographic variability near the New England Seamounts: an intercomparison among in situ observations, numerical simulations, and GEOSAT altimetry from the Regional Energetics Experiment. *J. Geophys. Res., 94 (C6)*, 8021-8028, 1989.

Mitchell, J.L., J.M. Dastugue, W.J. Teague, Z.R. Hallock. The estimation of geoid profiles in the NW Atlantic from simultaneous satellite altimetry and AXBT sections. *J. Geophys. Res.*, In Press.

Thompson, J.D. and W.J. Schmitz. A limited-area model of the Gulf Stream: design, initial experiments, and model-data intercomparison. J. Phys. Oceanogr., 19 (6), 791-814, 1989.

OBJECTIVE USE OF SATELLITE ALTIMETRY AND IR IN SIMULATIONS OF WESTERN BOUNDARY CURRENT DYNAMICS

Dantel N. Fox, Michael R. Cauocs, Jim L. Mitchell

Naval Oceanographic and Atmospheric Research Laboratory
Ocean Sensing and Production Division
Stennis Space Center, Mississippi, U.S.A. 39529-5004

Abstract

A series of numerical experiments to predict the evolution of the Gulf Stream have been performed. The forecast system uses a primitive equation model of the north western Atlantic Ocean and assimilation schemes which employ both a feature model and statistical correlations derived from the regional climatology of in situ data and long time-base numerical simulations. The evaluation criterion is the mean absolute distance between forecast locations of the Gulf Stream front and actual locations as verified from extensive satellite and in situ data. Eight one-week and five two-week evaluation intervals during 1986-1988 were selected to represent a variety of both active and inactive Gulf Stream regimes. To insure objectivity, hindcasting was disallowed. The resulting forecasts were significantly better than persistence at both one- and two-week intervals. This study indicates the feasibility of Gulf Stream forecasting using assimilation schemes which provide adequate deep information and numerical models which are designed to be consistent with available data.

1 Introduction

The western boundary current regions of the oceans represent domains of high variability and considerable eddy activity. They are not adequately sampled by in situ measurements or by satellite altimetry [10,13] to permit accurate, instantaneous estimates of sea surface topography. They are also regions of significant strategic importance. The development of numerical models of the North Atlantic [15] capable of reproducing the measured variabilities, large scale circulations, and eddy activity has given us the confidence to proceed with the construction of a system which will use such models to dynamically interpolate the asynoptic measurements available and thereby provide both improved nowcast and forecast capabilities.

A system for constructing initial state estimates and performing forecasts was constructed for the region of the North Atlantic by the Data Assimilation Research and Transition (DART) team at the U. S. Navy's Naval Oceanographic and Atmospheric Research Laboratory.

In order to provide a 'level playing field' in the arena of ocean forecasting, a set of reference data (i.e., Gulf Stream frontal locations) was created for a subset of the Gulf Stream region. Before any forecasts had been done, data over the preceding three years was examined to attempt to define several periods for which accurate positions of the Gulf Stream axis and eddies could be constructed for at least two weeks. Clear satellite IR imagery was required, and in most cases XBTs and GEOSAT altimetry [3] was used to refine the locations of the features. Four time periods were chosen in 1986 through 1988 which permitted eight 1-week forecast and verification experiments and five 2-week experiments.

The primary evolution criterion was the mean absolute distance between forecast locations of the Gulf Stream front and the actual (or verification) locations. Forecast error was computed as the *average absolute offset* between the forecasted position of the axis with the position given in the verification state. *Persistence*, the assumption of no motion over the forecast interval, was used as a comparison in judging forecast skill. For a model to have any significant skill in forecasting, the error in its forecast (the *forecast error*) must be less than the error computed by simply using the initial state as the forecast (the *persistence error*).

To examine the degree to which this small number of states was representative of the Gulf Stream as a whole, persistence errors were computed both from these states and from a year of the operationally produced front locations. The distributions were compared to verify that the cases chosen were representative.

The domain was divided into three subregions: a Western Region, extending from 73°W to 66°W longitude, a Central Region, extending from 66°W to 59°W longitude, and an Eastern Region, extending from 59°W to 53°W longitude. The average absolute offset error of each of these subregions was computed, as well as the overall region, extending from 73°W to 53°W longitude.

2 Forecast Experiment Results

Figure 2 presents the results from one of the 2-week forecast experiments. Measuring the errors in the overall region from 73°W to 53°W longitude, persistence represents an error of 50 km at 1-week and 65 km at 2-weeks. By comparison, the forecast provided errors of only 26 km and 39 km at 1- and 2-weeks respectively. When all eight 1-week and five 2-week cases are examined, it was found that the system provided forecasts which were better than persistence by approximately 6 km at 1-week and 10 km at 2-weeks. Standard statistical techniques were used to verify the significance of these results.

3 DART End-to-End Nowcast/Forecast System

In this section, we provide a detailed description of the DART Gulf Stream run stream. The procedure used to initialize and run the DART forecasts begins with the subjective preparation of an initial Gulf Stream frontal location map. This manually prepared map blends frontal location information contained in satellite IR imagery, satellite altimetry, and any available BTs into a continuous depiction of the surface frontal location. The resulting continuous depiction of North Wall location is then run through a feature model algorithm in the OTIS computer program which provides an initial state estimate of the dynamic height, which is then converted to an upper layer pressure anomaly (p1) in the NOARL primitive equation circulation model. Scaling between OTIS dynamic height and model p1 is necessary to correctly represent the transport in the model's thick upper layer. This initial p1 field is instantaneously converted in an accompanying lower layer pressure field (p2) using a statistical inference technique based upon the circulation model's climatology. Together, p1 and p2 are then used to provide for geostrophic initialization of the circulation model. For a brief interval immediately following these "cold start" initializations, a filter is applied in the circulation model run to nearly eliminate gravity waves. Finally, the $p1=0$ contour in the model's forecast state is used to define the forecast frontal location for direct comparison with independent verification frontal location maps.

Much of the success in these "cold start" DART forecasts is a result of the several techniques used to directly (and instantaneously) transfer upper layer information into the lower layer of the circulation model. These techniques are described chronologically in the following sections.

3.1 OTIS Feature Model

Maps of surface topography used to initialized the circulation model and to verify the forecasts were prepared using the regional OTIS, devel-

oped primarily at the Fleet Numerical Oceanography Center (FNOC) [5] with contributions from the Naval Oceanographic Office (NOO) and the Naval Oceanographic and Atmospheric Research Laboratory [1,2] OTIS is a data quality control and interpolation system which combines climatology, maps of front and eddy boundaries, MCSSTs (satellite IR multichannel sea surface temperatures), and measured temperature profiles to form gridded three-dimensional synoptic thermal analyses for selected ocean regions. A reduced set of the OTIS system capabilities was used in this study: the surface topography maps were produced using maps of front and eddy positions as the only data source. The OTIS software interprets these maps and applies models for the Gulf Stream front and eddies to form a gridded three dimensional field of temperature. Relative dynamic height at the surface is then computed directly from the grid of temperature profiles using relationships derived from analysis of regional historical temperature and salinity data sets.

All data for each analysis date were combined onto a single map consisting of frontal path segments from IR, locations of front and ring crossings from altimetry, and AXBT locations coded according to water type. An unbroken frontal path, from the western to the eastern boundaries of the model domain, was drawn by hand through the composite data set and then digitized, and ring radii and center locations were extracted.

OTIS uses parametric models of the Gulf Stream front, eddies, and the ambient background which have been developed from a combination of historical observations, simple dynamical models, and information obtained from published studies.

The OTIS system assimilates synthetic observations, true observations taken at irregular times and positions, and climatology to form synoptic maps using optimum interpolation [7,4] The synthetic observations provide a high-spatial resolution data set within and near fronts and eddies where observational data is often too sparse to resolve these features. Also, the synthetic profiles provide subsurface information, whereas most measurements are made only at the surface from satellites. This study uses only synthetic profiles to construct the final field of temperature.

The optimum interpolation results in a three-dimensional grid of temperature covering the domain of the grid of the circulation model. Since salinity is not available from this analysis, dynamic heights at the surface are computed from the same relationships between dynamic height and temperature used in modeling the structure of rings. The root-mean-square error in dynamic height computed by this method is about 0.065 dynamic meters.

3.2 Circulation Model

The circulation model used in this study is documented in Thompson and Hurlburt [14], Hurlburt and Thompson [9] and Thompson and Schmitz [15]. It is an n-layer, primitive equation model covering the region from 78°W to 45°W longitude and 30°N to 45°N latitude. It includes large-amplitude bottom topography. The model domain was chosen so that the variability in the location of the Gulf Stream entrance into the domain would be small. Figure 1 shows a plot of weekly axis locations taken from a year of NEOC boguses. The outlined box in the plot represents the circulation model domain. The relatively small variability in the position of the Gulf Stream axis where it enters the model domain permits the inflow to be specified at a fixed location south of Cape Hatteras. The version of the model used in this evaluation included two layers, with a deep western boundary current [15] supplied by an inflow port in the north eastern part of the lower layer. The model used in these experiments is on a spherical grid with a resolution of 1/6 degree in longitude and 1/8 degree in latitude, which represents a spatial sampling of approximately 14 km in each direction at the center of the grid.

Since layer thickness is included among the model variables, fluctuations of the pycnocline can be modelled by changes in the depth of the interface between the upper and lower layers. This permits a more efficient representation of the dominant dynamical modes in the domain than is possible with a model which uses fixed thickness *levels*. This was deemed of particular importance in these experiments, due both to the manner in which we initialize the lower layer (described in detail in the next section) and the number of experiments contemplated.

3.3 Statistical Inference of Subthermocline Information

Information on the subthermocline has been shown to be extremely valuable in forecasts based on numerical simulations of the Gulf of Mexico [8,11] and the Gulf Stream [6,12].

Long model simulations are used to derive statistical relationships between the subthermocline pressure (p2) at any given grid point in the model and the surface pressure (p1) at an array of grid points. Parameters which control this derivation are chosen to maximize the skill in estimating the lower layer pressure in an *independent dataset*. That is, coefficients are derived from one run of the model and are used to estimate the lower layer in an independent run.

Figure 3 shows an example of using these coefficients to estimate the lower layer pressure for the Gulf Stream. Note that while the pat-

tern correlation between p1 and p2 on this model day is only .26, the correlation exceeds .9 between p2 and the estimate of p2 computed from p1 by the statistical inference technique. The coefficients derived from these lengthy model simulations are applied to the surface height fields produced by the thermal analysis to provide an estimate of the lower layer pressure field, and thus the pycnocline depth anomaly for each of the forecast dates. The absolute accuracy of this estimate of the depth of the pycnocline has not been quantified, but for the purposes of initializing the circulation model, it represents lower layer information which is *dynamically consistent* with the upper layer information provided by OTIS.

To calculate the contribution to the forecast skill of including this deep pressure information, forecasts were made using the present reference datasets and using three alternatives for defining the lower layer pressure field in the initial states. Forecasts made using either a reduced gravity initialization or using the model's climatological lower layer pressure field resulted in a larger error than those made with the statistical inference initialization, generally by about 5 km.

3.4 Geostrophic Velocity Initialization

The remaining model variables, the u and v components of velocity for each of the two layers are computed geostrophically. For example, in the upper layer:

$$\hat{k} \times f\vec{v}_g = -g\nabla\eta$$

where f is the Coriolis parameter ($f = 2\omega \sin \theta$, where ω is the angular velocity of the earth's rotation and θ is the latitude), $\hat{k}$ is a unit vertical vector, $\vec{v}_g$ is the geostrophic component of the current and η is the free surface anomaly.

3.5 Gravity Wave Filter

Despite the statistical inference of the lower layer and the geostrophic velocity initialization, there will inevitably still be some dynamic imbalances in the initial state. One advantage of the primitive equation model approach is that such imbalances will be converted to short-period gravity waves, which can easily be removed by selective filtering. For the particular domain of this model, the dominant gravity wave period is approximately 8 to 9 hours. These waves are attacked in the NOARL circulation model by a time-domain running average with a length of 8.5 hours which is applied once at +12 hours into the forecast and again at +24 hours, after which no further filter is done during the remaining two weeks.

4 Summary

A series of numerical experiments to predict the evolution of the Gulf Stream have been performed. The nowcast/forecast system developed by the DART team at NOARL is the first such system to show significant skill in forecasting the evolution of the Gulf Stream frontal axis, providing estimates of the front that are (on average) 6 km better than persistence at 1-week and 10 km better at 2-weeks.

References

[1] Bennett, T. J., and P. May (1988), "An Optimal Thermal Analysis System for the Naval Oceanography Program." Naval Ocean Research and Development Activity Technical Report TR 206.

[2] Bennett T. J., M. R. Carnes, P. A. Phoebus, L. M. Reidlinger (1988), "Feature Modeling: The Incorporation of a Front and Eddy Map into Optimal Interpolation-based Thermal Analyses." Naval Ocean Research and Development Activity Technical Report TR 242.

[3] Born, G. H., J. L. Mitchell, G. A. Heyler (1987), "GEOSAT ERM - Mission Design." *J. Astronautical Sci.*, 35, 119-134.

[4] Bretherton, F. P., R. E. Davis, C. B. Fandry (1976), "A technique for objective analysis and design of oceanographic experiments applied to MODE-73."*Deep Sea Research*, 23, 559-582.

[5] Clancy, R. M., K. D. Pollack, J. D. Cummings, and P. A. Phoebus (1988), "Technical Description of the Optimum Thermal Interpolation System (OTIS) version 1: A model for oceanic data assimilation." FNOC Technical Note 422-86-02, 76 pp.

[6] Fox D.N., H. E. Hurlburt, J. D. Thompson, Z. R. Hallock, G. A. Ransford (1988), "Oceanic Data Assimilation and Prediction Using Remotely Sensed Data." In *Proceedings of the Pacific Congress on Marine Science and Technology (PACON 88)*, pp OST2/17-23.

[7] Gandin, L. S. (1963), *Objective Analysis of Meteorological Fields*, Leningrad: Gedrometeorizdat, 266 pp.

[8] Grant, D. P. and H. E. Hurlburt (1985), "Statistical inference of deep pressure fields from simulated altimeter data." *EOS*, 66, p. 1324.

[9] Hurlburt, H. E. and J. D. Thompson (1984),"Preliminary Results from a numerical study of the New England Seamount chain influence on the Gulf Stream." In *Predictability of Fluid Motions* (eds. G. Holloway and B. J. West) (American Institute of Physics, New York), pp. 489-504.

[10] Hurlburt, H. E. (1986), "Dynamic Transfer of Simulated Altimeter Data into Subsurface Information by a Numerical Ocean Model". *Journal of Geophysical Research*, vol. 91, no. C2, pp. 2372-2400.

[11] Hurlburt, H. E. (1987), "The ocean prediction problem and its diversity: some issues and possible solutions." In *Ocean Prediction Workshop 1986*. C. N. K. Mooers, A. R. Robinson and J. D. Thompson, editors, W. Simmons, technical editor, Sponsored by the Oceanographer of the Navy and the U.S. Office of Naval Research, pp. 192-226.

[12] Hurlburt H. E., D. N. Fox, J. J. Metzger (1990), "Statistical Inference of Weakly Correlated Sub-thermocline Fields from Satellite Altimeter Data.", *Journal of Geophysical Research*, in press.

[13] Kindle, J. C. (1986), "Sampling strategies and model assimilation of altimetric data for ocean monitoring and prediction." *J. Geophys. Res.*, 91, pp. 2418-2432.

[14] Thompson, J. D. and H. E. Hurlburt (1982), "A numerical study of the influence of the New England Seamount Chain on the Gulf Stream: Preliminary Results". In *Proc. Workshop on the Gulf Stream Structure and Variability*, Univ. of N. C., Chapel Hill, J. M. Bane, Jr., Ed., Office of Naval Research, pp. 346-362.

[15] Thompson, J. D. and W. J. Schmitz (1989), "A Limited-Area Model of the Gulf Stream: Design, Initial Experiments, and Model-Data Intercomparison". *Journal of Physical Oceanography*, vol. 19, no. 6, pp. 791-814.
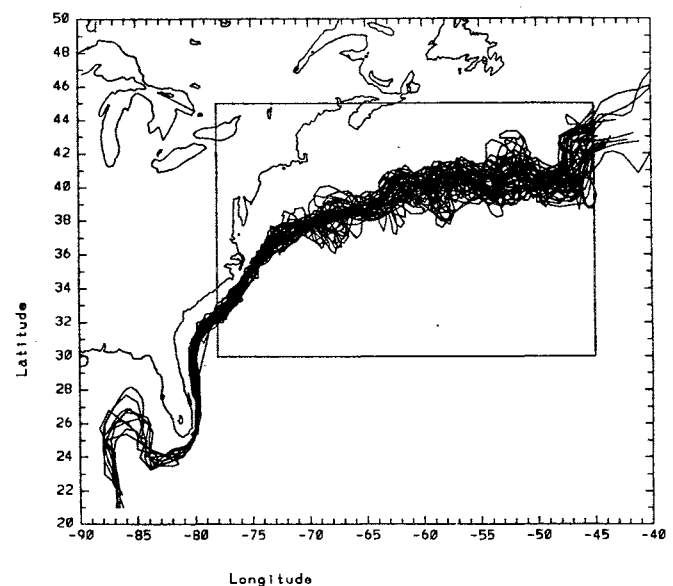
Figure 1 -- One year of weekly Gulf Stream axis positions. Inner box represents the domain of the forecast system.
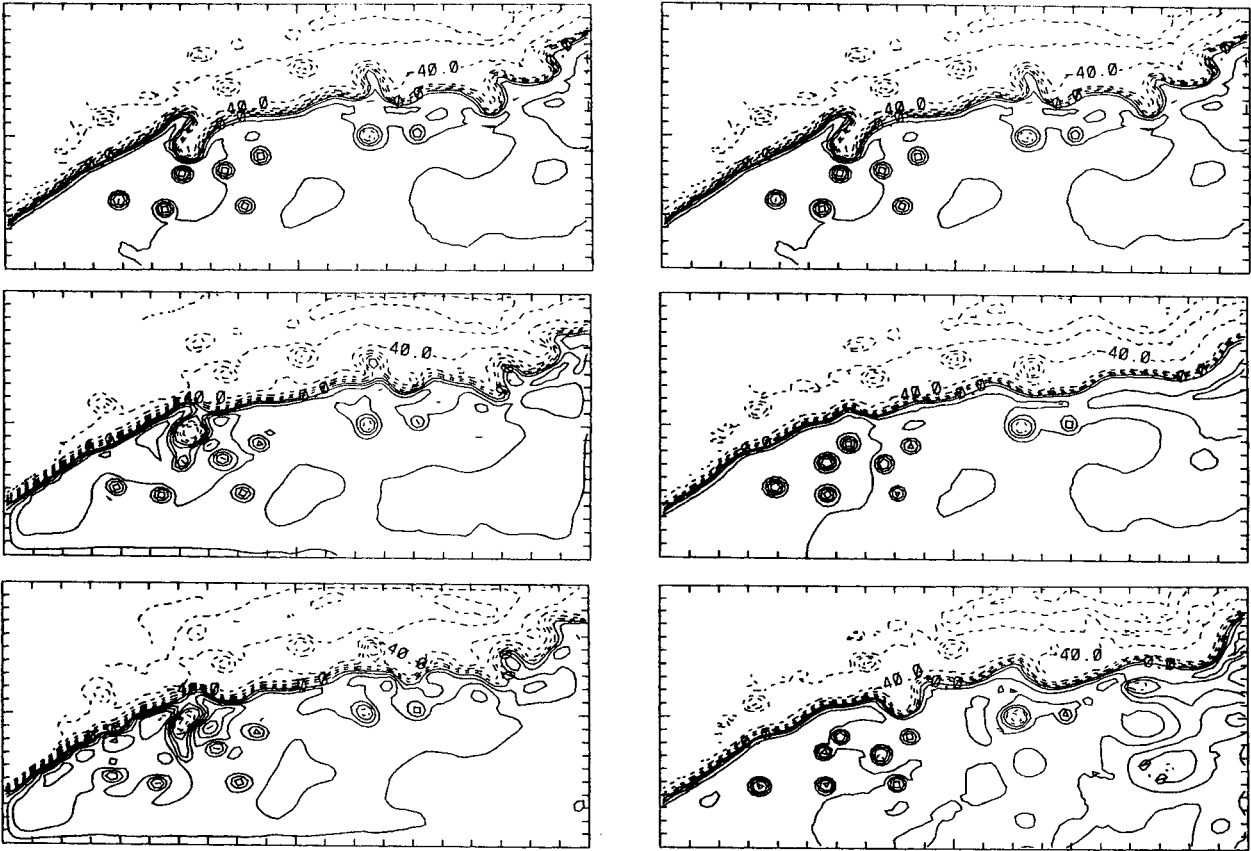
Figure 2-- Sample forecast (left) and verification (right) initialized on 6 May 1987 (top) and forecasted for 13 May (middle) and 20 May (bottom).
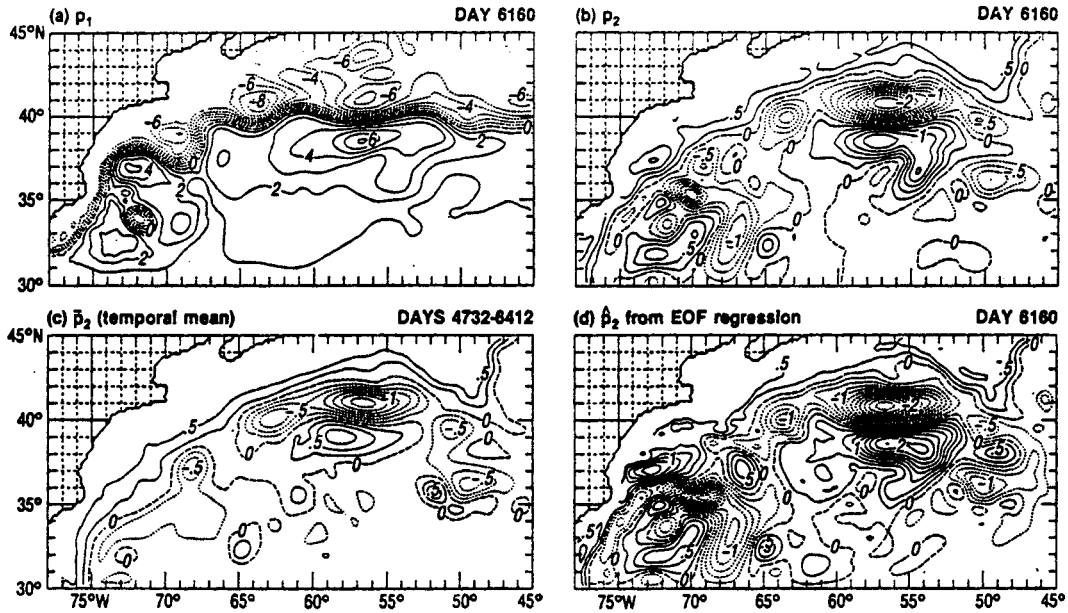
Figure 3-- Statistical estimation of subthermocline pressure (p2) from surface pressure (p1) for the Gulf Stream.

TRANSMISSION OF THE INFORMATION OF UNDERSEA TEMPERATURE USING A MOS-1 DCP

Hiroshi Suzuki* and Akira Kuroiwa**

* Tokyo University of Fisheries, Japan
** Fisheries Agency, Ministry of Agriculture, Forestry and Fishery, Japan

ABSTRACT

This paper describes the first test on the transmission of sea temperature distributed vertically in the sea using the Data Collection System(DCP) of the Marine Observation Satelite MOS-1.

We thought of measuring the vertical distribution of undersea temperature by well known expendable bathythermograph XBTs and to send the data of the sea temperature at the depth of down to 700 m through the sattelite MOS-1. After arranging a proto-type DCP with a XBT, transmitting model data were sent from a land point. Then the next experiments were carried out on a small boat at sea in Sagami Bay and on a research ship belonging to Fisheries Agency. On her research voyage around the Japan Islands some XBT probes were launched from the ship and the data were sent and received at the Earth Observation Center successfully.

1. INTRODUCTION

Information about underwater sea temperature is being requested by many fishermen and concerning companies. It is, however, very complicated work to obtain the vertical distribution of sea temperature around the fishing ground where they operate. Therefore, many research ships observe the sea temperature by using underwater thermometers, bathy-thermograph and so called CTD in order to send the data to the authorities.

XBT is one of the very useful oceanic instruments which are able to measure the sea temperature at the depth of down to about 1,000 m or more after being launched from the ship.

After arranging a proto-type DCP with a XBT, transmitting model data were sent from a land point. Then the next experiments were carried out on a small boat at sea in Sagami Bay. For the following half year the DCP was brought to a research ship belonging to Fisheries Agency. Around the Japan Islands some XBT probes were launched from the ship, where CTD observation was done. The data received at the Earth Observing Center EOC were compared with the data obtained by the CTD observation. Transmission and receipt were satisfactory.

This was done by the the Association of Fisheries Electronics commissioned by Fishery Agency as a NASDA's MOS-1 DCS verification project.

2. MOS-1 AND THE DCP

2.1 MOS-1 and Planned XBT Type DCP

The MOS-1 sattelite comes around over every day at almost the same ship's apparent time.

The data obtained by the XBT are converted to digital ones, coded and added by suitable CRC check bits. Data Collection System on the satelite MOS-1 receives the data and retransmits them by SHF waves towards the Earth Observation Center EOC in Saitama prefecture.

The first point of discussion was how to measure the temperature and other data in deep sea layer automatically and to send them to the DCS on the satelite in the required format. Table 1 shows the planned sensors and types of Data Collection Platform DCP; their merits and demerits are in the matrix.

Sensor type is classified in three kinds: thermister chain, up and down type thermometer and expendable bathythermograph. And the types of DCP are a moored buoy, a drifting buoy and an on-board-type.

Table 1 Classification of sensors and DCP type.

Type of DCP / Sensor	Moored-buoy DCP	Drifting-buoy DCP	On-board type DCP
Thermister chain	Low cost; limited to a specific point of measurement; incapable of obtainining so many data:	Low cost; being obstructive to the ships undergoing:	Difficult to be towed by ships; incapable of obtaining so many data:
Up and down type thermometer	Difficult to get data at the depth of 100 m and beyond:	Complicated mechanism; difficult to measure at deep sea layer and avoid collision damage:	Requires larger devices to measure at the same depth as XBT type; Difficult auto-mechanism:
Expendable Bathy thermo-Graph XBT type	Unsuitable for a research in wide waters; measurement the more costly, the deeper the layer:	Vertical dis-triution of sea temp. is obtained; Capable of in-vestigating in wide sea waters; most profitable to the satellite DCS:	Possible to utilize the conventional type of XBTs; low cost transmis-sion:

After discussing which type should be adopted in the MOS-1 DCP sensor, the conclusion reached is to utilize the XBT Drifting type for test on land and on board.

Figure 1 presents a flow chart of new MOS-1 system application.
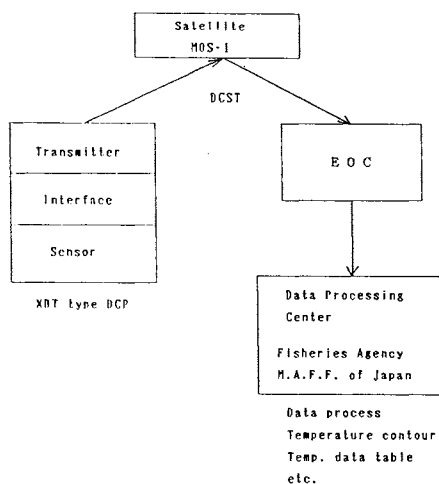
Figure 1. The situation of XBT type DCP in
MOS-1 data collection system flow

Figure 1 shows our XBT type DCP indicated in MOS-1 data collection system flow. The XBT type DCP sensor aquires sea temperature data at any depth while descending after being launched from the platform. The data are fed to the interface, where they are A-D converted to be processed and tranmitted toward the MOS-1 DCST. Then it relays the signal to the EOC. The center provides the data to the first user in a form of Computer Compatible Tape CCT or a floppy disc with the fixed XBT positions where the data were transmitted.

The first user may be called an information service center. There the data in the CCT or the floppy disc are analyzed, calculated for obtaining temperature contours around the fishing grounds.

2.2 Data Format

Figure 2 shows the pulse train of the DCP. The first frame constructed by a 256-bit-pulse after non-moduration part of 120 ms and a protocall of 48 bits is transmitted in one of two assigned VHF band frequencies in every 60 seconds.

M   Month
D   Date
H   Hour
D (i)   Depth
T (i)   Temperature
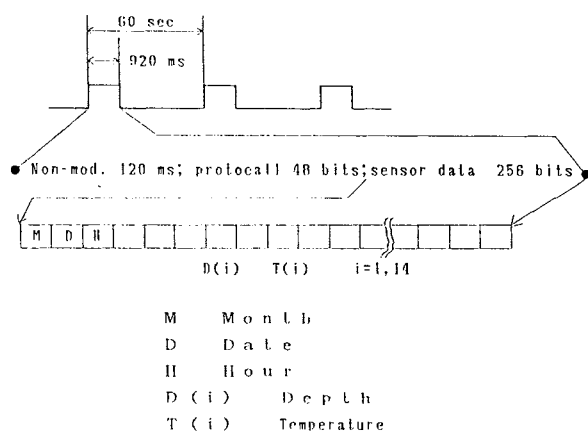
Figure 2. Pulse train of the DCP

Since the satellite is usually viewed over for several minuites, at least 8 frames in a group can be received by the DCST on the MOS-1. Our data were limited within 8 frames or less.

Sensor data of 256 bits are constructed by the data specifying month, day, time followed by the data of the sea temperature and the depth measured. The frame 2 and the rest are constructed by the data of depth and temperature only. The data group is transmitted repeatedly toward the MOS-1 during the time when the satellite passes over.

3 Experimental Results

After the electronic test in the firm, the XBT type DCP was brought out to a land place, and transmission test and receiving test at the EOC were carried out successfully.

3.1 Field Test in Sagami Bay

The first field test was done in the Sagami Bay near mid-Japan Island on a small boat.

Table 2 Receiving rate of the XBT type DCP.

Date	Pass No.	Transmitted number of frames	Received number of frames	Receiving rate
18 Aug.	7	20	19	95%
	24	27	23	85%
19 Aug.	8	22	21	95%
	25	23	20	87%

Table 2 shows the receiving result at the time. The receiving rate in the table 2 is the rate of received number of the frame to that of transmitted frames. This depends upon the degree of the elevation angle of the satellite in the orbit of the MOS-1 defined by the corresponding pass number.
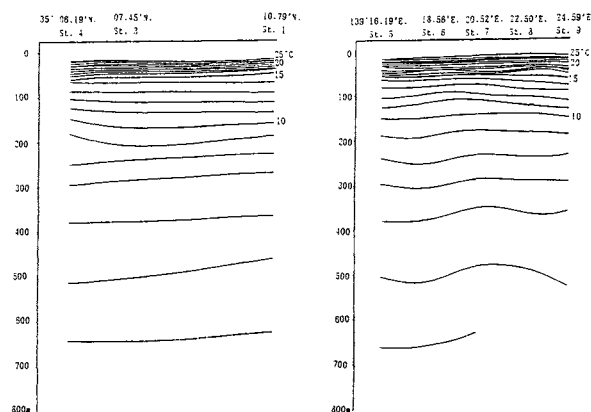
Figure 3. Vertical temperature contours
along the longitude of 139°E.
(left) and latitude of 35°N.
(right) in Sagami Bay

If the transmitted frame number is equal or more than 8, all temperature data from the surface to the maximum depth layer, in this case 760 m, are transmitted and considered to be received without failure.

Figure 3 shows vertical section of temperature contours along the longitude of 139°E. and along the latitude of 35°N. in Sagami Bay obtained by the MOS-1 DCS data from the XBT type MOS-1 DCP.

3.2 Japan's Neighboring Waters

The experiments were carried out in Japan's neighboring waters around the Japan island by using a research ship belonging to Fisheries Agency for a few month. The ship engaged in usual oceanograpic observation including CTD observation.
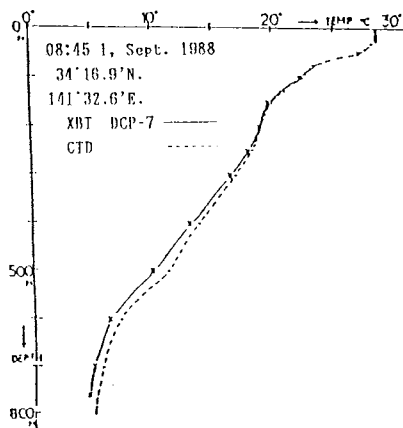
Figure 4 Comparison between the XBT type DCP and CTD Temperature data.

Figure 4 shows the comparison between the XBT type DCP and CTD data. It is obvious that there are some differences between them. Strictly speaking even though they both tried to measure the temperature at the same position, it is nearly impossible that the XBT type DCP and the CTD probe should come to the exactly same point. In addition to this we should bear inmind the instrumental errors in measuring depth and temperature.

3.3 Position Fix and the Problem

Oceanic observation demands accurate observing position. From this point of view, our XBT type DCP re-examined. Best resolution would be that the DCP carries a self contained position fix system. If the observing waters are in the area of radio navigational service, proper type of radio navigation receiving instruments are available, for example Loran C, A, NNSS, Decca and GPS etc. Fortunately, MOS-1 DCS has a position fixing system. Our project was granted to have a result of MOS-1 Verification Program conducted by NASDA.

Position error of the DCP was checked with a precisely known land position. The observation was carried out from 20th of April to 4th of July 1988. Mean position obtained from the MOS-1 DCS was deviated from the true position to 75 m northward and 58 m eastward.

65 % probable error circle became 489 m in the radius. It was proved that it is ver yuseful for us to observe the vertical dis -tribution of sea temperature using XBT typ eMOS-1 DCP.

4. FUTURE VIEW

Though a XBT type DCP for MOS-1 was developped as a prototype and tested at sea, it is not always faultless itself; it has some problems. When a small floating buoy with many XBTs is used, the launching of the XBT becomes difficult on the buoy rolled and pitched by the sea waves. Larger buoy may obstruct the way of ships, and costs much.

Automatic launching mechanism should be developped as soon as possible. The buoy can be set adrift at a position on the water often situated in an upper stream of sea current. The buoy will flow with the current, and launching could be attained automatically by a timer, for example once a day.

Another problem is that the position given from NASDA is that of the time when the DCP transmitted the radio waves of the data. The floating buoy moves with the sea current, so there comes a difference between the position of observation by lauched XBT and the position when the DCP transmits the radio waves toward MOS-1 DCS, because the time the satellite come sover evey day at about the same apparent time.

It is strongly desired that the DCS of MOS-1 should have more quantity of data frames. Position fixing of the DCP was very useful for the users.

ACKNOWLEDGEMENT

REFERENCES

Association of Fisheries Electronic:
Report of MOS-1 utilization system, 1986.
A.F.E.:
Report of MOS-1 utilization system, 1987.
A.F.E.:
Report of MOS-1 utilization system, 1988.

INVSTIGATIONS OF THE BOTTOM BOUNDARY LAYER'S DYNAMICS WITH THE HELP OF POP-UP SELF-CONTAINED STATIONS

E. A. Kontar, S. L. Soloviev, T. A. Demidova

P. P. Shirshov Institute of Oceanology USSR Academy of Sciences, USSR

Abstract

The benthic layer, being one of the most interesting with respect of hydrophysical phenomena, has not been well studied. Knowledge on the benthic layer characteristics, especially dynamic parameters, determined mainly by current velocity, is important for the correct interpretation of different oceanological data.

In this paper an analysis of benthic layer dynamics based on results of direct measurements of horizontal velocity components at 2.5-25 m above the bottom, and on concurrent measurements of benthic water temperature is presented Pop-up self-contained stations have been deployed 21 times at depths from 730 to 5,125 m for durations from 2 to 36 days on the bottom of Pacific and Atlantic oceans and Mediterranean sea.

1. Introduction

The Laboratory of Seismology of the P.P.Shirshiv Institute of Oceanology of the USSR Academy of Sciences in cooperation with specialized ins-titutions has developed an autonomous bottom pop-up seismological stations ADS-8 and ADS-M meant for studying seismicity of deep-water areas in the world Ocean /4, 14/.

The pop-up seismological stations of the ADStype have a high positive buoyancy, and therefore, in addition to the seismograph, they can carry some other meters forinstance, the "Potok" self-contained digitial current-and-temperature meter, manifac-tured by the USSR Academy of Sciences' Oceanological Design Department, was the firgt used meter. For the Labora-tory of Seismology studying water currents in the bottom boundary layer is important because of two reasons: to understand the mechanism,by which such currents produce noice in a seismograph; to try to record tsunamis at the open sea.

But apart from mentioned seismological interests benthic processes are now a major challenge for oceanologists in general.

"Potok" meters were out to work first in the spring of 1986, but it was not usefull until after the spring of 1988 when the time intervals for averaging current and temperature values sampling had been reduced from 15-30 minutes to 225 sec (sometimes even to 112 and 28 sec) and the exposure of the seabottom instruments extended to 36 days, that valuable scientific results began coming in.

2. BENTHIC CURRENTS OVER THE FIELDS OF MANGANESE NODULES IN THE NORTH-EASTERN PACIFIC OCEAN

Two stations were placed over the transform faults Clarion and Clipper-ton and the Guatemalan deep-water basin in February-March, 1988.They were equipped with sediment traps, "Potok" meters and instruments for measuring salinity, temperature, water pressure (STD) and content of oxygen dissolved in water (O_2). The stations operated at 5,000 and 3,600 m, respectively. The study areas are known as abundant in manganese nodules covering gently sloping sides of the abyssal hills.

Measurements showed variation both in STD values and O_2 content and in the benthic dynamic characteris-tics. A benthic storm lasting longer than 48 hours, with the benthic cur-rent speed, averaged over intervals of 0.5 h, reaching 13.5 cm/s, was recorded within a 36-day range /1/. The storm was found to be related to a deep-penetrating synoptic vortex /2/, and the facies conditions of

Manganese nodules formation were fo-
und to be associated with benthic dy-
namics /3,9/. The Manganese wos found
to be coming to the Guatemalan deep-
-water basin from the Galapagos rift
but not from the central part of the
Pacific ocean, as it had been suppo-
sed aerlier.

3. "Warm" Benthic Storms off

Crete Island

During the July 1988 sea-bottom
seismological experiment off Crete
Island,three stations ADS-M equiped
with "Potok" meters placed at 2.5 m
above the sea-bottom were put in ope-
ration. Stations were placed: at the
depth of 1,780 m on the south-eastern
slope of Grete Island (A),at the depth
of 1.530 m in the Kassos strait (B),
and at the depth of 1.745 on the Rodos
submarine ridge limited by the Pliny
trench on the south (C).

Station B within a week recorded
10 benthic storms, whose duration
took 15% of the records time. The cu-
rrent speed during the storms rose
sharply from the meter's sensitivity
threshold (3 cm/s) to 4.4-8.5 cm/s.
During one of the storms, unlike any
of the others, the water temperature
was found to rise stepwise to 0.4°C.
Station A recorded a similar storm
but in a different time. Station C
did not register any thermodynamic
processes on the sea-bottom /13/.

Petrological analysis of the de-
posited suspended sediments from the
trap at one of the stations,alongside
with some other considerations, have
led us to claim that the sea-bottom
stations have recorded some turbidity
currents generated above them, in the
upper parts of the submarine slopes.
This means that an essentially new
mechanism for vertical water exchange
in the World Ocean and oxygen trans-
fer to sea depths sesms to have been

discovered /10, 11, 12/.
The "cold" storms recorded by
station B apper to be relics of some
complex system of counter-currents in
the Kassos strait.

4. 12-hours-long migrations of the

Canary and Mauritanian currents

A station fitted with a "Potok"
meter was placed in July-August, 1988
on the submarine slope of the African
continent, 85 km west of the Cap Blan
in the Atlantic Ocean and worked a
week. It happened to lie on the borde-
line between the warm Mauritanian cu-
rrent flowing along the coast from
south to north and the cold Canary
current flowing something west of it
from north to south. The benthic cur-
rents, sometimes as fast as 26 cm/s,
were found to change their direction
steadily twice during 24 hours (with
a period of 11-13 hours) from north-
north-east to south-west, with a
± 0.2°C temperature change invariably
accompanying it /7/. This movement of
the borderline, as records of sea-bo-
ttom station show, is no smooth-flo-
wing process but a result of the in-
tervention of the cold masses of the
Canary currents into the warm waters
of the Mauritanian current (wich co-
ntributes to the wellknow phenomenou
of the Canary upwelling) /5/.

5. Near-bottom currents in a seismica-

lly active area of the Atlantic Ocean

In August 1988, three stations
ADS-M fitted with "Potok" meters at
2.5 m above the bottom were placed in
the seismically active Azores-Gibral-
tar belt of the Atlantic ocean. The
stations were instally at a depth of
3.300 m on the top of a submarinv(1),
at a depth of 4.250 m on the slope the

submarine mountain (2), and at a depth of 5.100 m on the bottom of deep-water basin (3) /8/.

Measurements showed variation in the benthic dynamic characteristics. The benthic current speed, averaged over intervals of 225 s, reaching 15.0 cm/s was recorded within a 13-day interval by stations 1 and 2. Station 3 did not register any near-bottom current with the speed more then the meter's sensitivity /6/.

6. Change of current speed with depth in the bottom boundary layer

In September, 1988, two stations were dropped on the submarine ridge Reykianes, south of Iceland.They were 100 m apart, one, as usual, equipped with a "Potok" meter, in 2.5 m from the bottom, the other one with a string of "Potok" meters deployed 5, 10, 15 and 25 m above the bottom. The stations were at work for four days. According to their records, the bottom boundary layer was in a very unstationary state, because at different horizons the time when currents become stronger or weaker do not coincide. But at the same time, at all horizons a few benthic storms were found to occur synchronously, with the speed of water motion increasing when approaching to the bottom.

7. Benthic currents in the Mediterranean deep-water basins

Pop-up stations of the ADS' type with 1 to 5 "Potok" meters were placed during October-November, 1989, in 10 study areas within the system of the Hellenic trenches and the Crete deep-water basin. A steady mass transfer, with the benthic current up to 8 cm/s, was recorded (at a depth of 5.125 m) in the Ionic trench.The wa-

ter temperature in the bottom boundary layer in the Ionic sea was found abnormally high. A steady anticyclonic circulation, with the speed of the stream on the periphery of the whirl up to 16 cm/s, was recorded in the Crete basin (at depths of 2.00-2.200m).

Referencec

1. Demidova T.A., Kontar E.A. On the near-bottom currents in the region of ferromanganesian nodules development //Doklady Akademii Nauk SSSR, 1989, 308(2), 468-472 (in Russian).
2. Demidova T.A., Kontar E.A., Sokov A.V. On the nature of the benthic storm in the Pacific // Doklady Akademii Nauk SSSR, 1990, 310(3), 706-711 (in Russian).
3. Dietrich P.G., Kontar E.A. Morphologisch-fazielle Einflüsse auf die Manganknollenführung im aquatorialen Nordpazifik// Zeischrift für Angewandte Geologie, 1989, band 35(6), 161-165.
4. Kontar E.A. Free-emerging systems for geological and geophysical reserch of the Ocean. Nauka, 1984, 152 p. (in Russian).
5. Kontar E.A. Experimental study of bottom boundary layer in the area of the Atlantic Canarian upwelling// Doklady Akademii Nauk SSSR, 1989, 309 (2), p. 456-460 (in Russian).
6. Kontar E.A., Grosul A.B., Savostin Yu.M. On near-bottom current in the Azores-Gibraltar region of the Atlantic Ocean // Oceanology, 1990, 30(1), p. 48-52 (in Russian).
7. Kontar E.A., Grosul A.B., Savostin Yu.M. On dynamic parameters of benthic layer in the rigion of Canarian upwelling // Atmospheric and oceanic physics, 1990, 26 (4), p.362-366 (in Russian).
8. Kontar E.A., Levchenko D.G., Soloviev S.L. Near-bottom currents in a seismically active area of the Atlan-

tic ocean // Doklady Akademii Na-
uk SSSR, 1990, 310 (5), p.1231-
1235 (in Russian).

9. Kontar E.A., Murdmaa I.O., Skor-
niakova N.S., Soltanovsky I.I.
Study of local variability of ma-
nganese nodules on the bottom of
the Pacific ocean with the help
of tree-fall samplers// Geology
and Prospecting, 1989, 11, p.74-
84. (in Russian).

10. Kontar E.A., Soloviev S.L. Obse-
rvation of possible small turbi-
dity currents in bottom boundary
layer SE of Grete Island // Anna-
les Geophysical, 1989, Special
issue, p. 24.

11. Kontar E.A., Soloviev S.L. On the
bottom storms in the Mediterrane-
an sea // Doklady Academii Nauk
SSSR, 1989, 309(5), p.1215-1218
(in Russian).

12. Kontar E.A., Soloviev S.L. Evi-
dence for a new phenomenon in the
benthic layer in a seismically
active region of the Mediterrane-
an// Oceanology International'90,
Brighton, 6-9 March 1990, 2, p.
p.21-36.

13. Kontar E.A., Soloviev S.L., Gro-
sul A.B., Savostin Yu.M. Measu-
rements of currents in near-bot-
tom layer of the Mediterranean
sea // Oceanology, 1989, 29(6),
p. 928-934 (in Russian).

14. Soloviev S.L., Kontar E.A., Dozo-
rov T.A., Kovachev S.A. ADS-8 - a
deep sea bottom pop-up seismolo-
gical station// Fizika Zemli,
1988, 9, p.75-85 (in Russian).

TARGET PARAMETER ESTIMATION BY USE OF A LINEAR-PERIOD-MODULATED SIGNAL AND PULSE SHARPENING WITH LATERAL INHIBITORY CONNECTIONS OF CONSTANT-Q FILTERS

W. Mitsuhashi, H. Kohno, R. Takeuchi and H. Mochizuki

The University of Electro-Communications, Chofu, Japan

Abstract

Bandpass filters uniformly distributed along the log-frequency axis are designed to organize a bank of constant-Q filters, on a model of the mammalian auditory systems. It is demonstrated that a linear-period modulated signal is well adapted to the design of the constant-Q filter bank system. For precise estimation of the range and velocity of moving targets, a phase sensitive model with the constant-Q filter bank is proposed. Results of numerical experiments show that unbiased range estimates can be obtained even if a target moves with rather a high velocity. It is found that the accuracy of the proposed method in target parameter estimation is superior to that of the conventional envelope detection system. It is also observed that lateral inhibitory connections between the filter outputs enable us to improve the sharpness of output amplitude.

1. Introduction

RADAR or SONAR are usually installed on moving vehicles or used to obtain information on moving targets. One of the main parameters to be estimated is the range between the observing system and the targets, and the other is the range rate(velocity) due to relative motions.

Since electro-magnetic wave is used in RADAR system, the Doppler effect caused by target motion is almost negligible. Even in the case where the frequency modulation is adopted to improve the system performance on the range resolution, the ratio of the frequency sweep width to the center frequency of emitted signals is usually relative small. Thus we can treat the Doppler effect simply as a linear frequency shift proportional to the target velocity.

On the contrary, the Doppler effect cannot be ignored in SONAR system because of the relative slow speed of sound propagation compared to target velocities. In addition, time–bandwidth product of frequency modulated SONAR signals is generally so large that we must consider that not only the frequency but the frequency sweep rate of the emitted signal is also altered by the target motion. For accurate estimation of target parameters, therefore, it is highly important how to design the signal not to be affected by the Doppler effect.

It is widely known that the linear frequency modulated(**LFM**) signal had been developed for increasing the average power capability in peak power limited RADAR systems[1]. As a direct consequence of the capability, target range resolution has been improved by the **LFM** technique[2]. The **LFM** signal has, however, an ambiguous property associated with error coupling in simultaneous estimation of range and velocity. Thus the target range can not be measured accurately with the **LFM** signal if the target velocity is unknown. In the same manner, velocity estimates are also ambiguous with inaccurate range estimates. Consequently, it has been necessary to eliminate the error coupling in target parameter estimation.

For removal of the error coupling, the ambiguity function of the emitted signal is required in general to be localized on a small area near the origin of estimating error space. For this case, however, a large number of matched filters(or correlation detectors) will be necessary for estimation in wide range of parameter values.

A linear period modulated(**LPM**) signal, the period of this signal increases linearly with time, has been developed as one of the Doppler tolerant signals[3], and it has been pointed out that the **LPM** signal has a typical feature of the location sounds produced by the **FM** bat[4]. The ambiguity function of the **LPM** signal has

a ridge on the axis of velocity error – that is, target range error is almost negligible – with approximately flat amplitude. Utilization of the **LPM** signal will consequently permit us to realize unbiased estimation of the range of a moving target.

In the present paper, we have proposed a measurement system by use of an **LPM** signal to measure the range and velocity of moving targets. This system is basically composed of a bank of constant-Q filters followed by time delay devices which eliminate non–linear spectral phase components of a received echo. The configuration of the proposed system is modeled on the early level of the mammalian auditory systems.

2. Backgrounds

2.1 The Echo Reflected From a Moving Target[5]

Emitting a signal $u(t)$ as a location sound to a point target that moves with constant velocity v_o, we obtain a returning echo reflected from the target

$$e(t) = \sqrt{s_o} \cdot u(s_o \cdot [t - \tau_o]), \tag{1}$$

where τ_o is the propagation delay time between the sound emitter and the moving target, and s_o denotes time compression or expansion of the echo waveform due to the Doppler effect. In the above expression, $\sqrt{s_o}$ is necessary in order to account for the fact that the signal energy does not changed under the signal transformation caused by the Doppler effect.

In Eq.(1), We have assumed that when the reflection occurred just at $\tau_o/2$, the distance from the emitter to the target was exactly r_o. In this situation, the following relationships hold:

$$\tau_o = \frac{2r_o}{c} \quad \text{and} \quad s_o = \frac{c - v_o}{c + v_o}, \tag{2}$$

where c is the velocity of sound propagation. Thus the measurement of the range and the velocity of a moving target is reduced to the problem to estimate two parameters which correspond to a shift of the time origin(τ_o) and a time scale factor(s_o) on the observed echo waveform.

2.2 Linear Period Modulated Signal[6]

An **LPM** signal within time $t > 0$ is defined[6] as

$$\begin{aligned} u(t) &= a(t) \cdot e^{j \cdot b \log t} \\ &= a(t) \cos(b \log t) + j \cdot a(t) \sin(b \log t) \\ &= u_r(t) + j \cdot u_i(t), \end{aligned} \tag{3}$$

$$u_r(t) = a(t) \cdot \cos(b \cdot \log t)$$
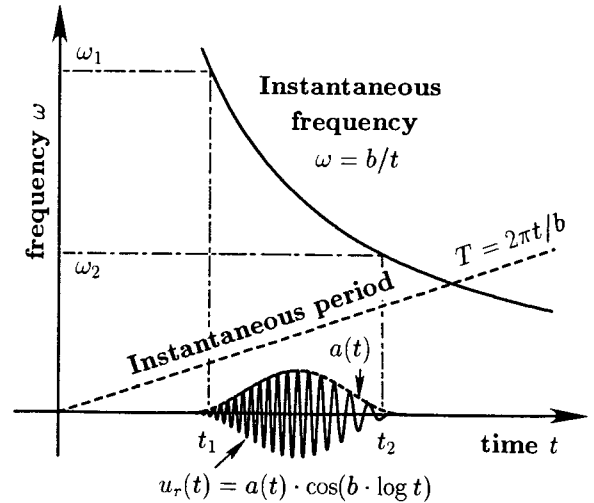
Figure 1: An **LPM** waveform and related parameters

where the envelope $a(t)$ is a relatively slowly varying time function in contrast with the phase $b \log t$. We can determine both the center frequency and the frequency bandwidth of this signal by controlling the position of $a(t)$ properly on time axis. The parameter b is closely related to a frequency modulation rate and, as will be shown in a later section, is used to determine the measurable range of target velocities. A simple example of the **LPM** waveform and related parameters are shown in Fig.(1).

Differentiating the signal phase in Eq.(3) with respect to time t yields the instantaneous frequency ω as

$$\omega = \partial b \log t / \partial t = b/t. \tag{4}$$

If the Doppler effect on the envelope $a(t)$ is assumed negligible, substitution of Eq.(3) into Eq.(1) leads to the expression

$$\begin{aligned} e(t) &= \sqrt{s_o} \cdot a(s_o \cdot [t - \tau_o]) \cdot e^{jb \log(s_o \cdot [t - \tau_o])} \\ &\simeq e^{jb \log s_o} \cdot u(t - \tau_o). \end{aligned} \tag{5}$$

The instantaneous frequency of the echo signal is thus written by

$$\tilde{\omega} = b/(t - \tau_o) \tag{6}$$

and equivalent to Eq.(4) except the delay time τ_o. This indicates that correlation between the emitted signal and the returning echo is still higher even if the target moves with a high velocity. Consequently the output amplitude in correlation detection of the **LPM** echo is nearly flat over the wide velocity range.

—58—
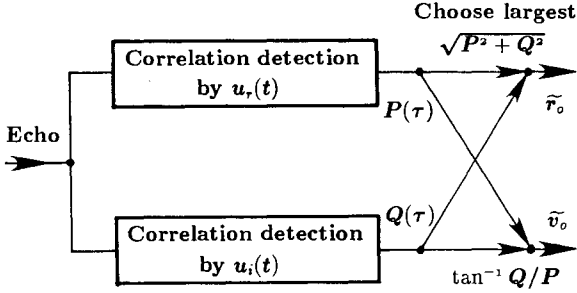
Figure 2: A conventional configuration for coherent correlation detection system.

2.3 Range and Velocity Measurement by Coherent Correlation Detection[6]

A signal to be emitted actually in SONAR problems will be a real signal. Thus, selecting only the real part of Eq.(3), we may rewrite Eq.(5) as

$$
\begin{aligned}
e(t) &= \cos(b\log s_o) \cdot u_r(t - \tau_o) \\
&\quad - \sin(b\log s_o) \cdot u_i(t - \tau_o).
\end{aligned} \tag{7}
$$

This equation indicates that two parameters to be estimated(the propagation delay τ_o and the time scale factor s_o) are contained in the echo signal separately in terms of time shift and amplitude modulation. One can also find that, in spite of an emission of the real part $u_r(t)$, the observed echo is composed of $u_r(t)$ and $u_i(t)$, weighted by $\cos(b\log s_o)$ and $\sin(b\log s_o)$ respectively. A coherent correlation detection system with the reference signals $u_r(t)$ and $u_i(t)$, therefore, permits us to estimate these two parameters separately.

A schematic diagram of coherent correlation detection system is illustrated in Fig.(2) and the system output is written as

$$
\int e(t) \cdot u^*(t - \tau)dt = P(\tau) + jQ(\tau), \tag{8}
$$

where * denotes complex conjugation. The real and the imaginary part in the right hand side of Eq.(8) can be expressed in terms of correlation functions as follows:

$$
\begin{aligned}
P(\tau) &= \cos(b\log s_o) \cdot \phi_{rr}(\tau - \tau_o) \\
&\quad - \sin(b\log s_o) \cdot \phi_{ir}(\tau - \tau_o), \tag{9} \\
Q(\tau) &= \cos(b\log s_o) \cdot \phi_{ri}(\tau - \tau_o) \\
&\quad - \sin(b\log s_o) \cdot \phi_{ii}(\tau - \tau_o), \tag{10}
\end{aligned}
$$

where, for example, $\phi_{rr}(\tau)$ denotes the auto–correlation function of $u_r(t)$ as

Phase $\Phi(\tau)$ and Envelope $A(\tau - \tau_o)$
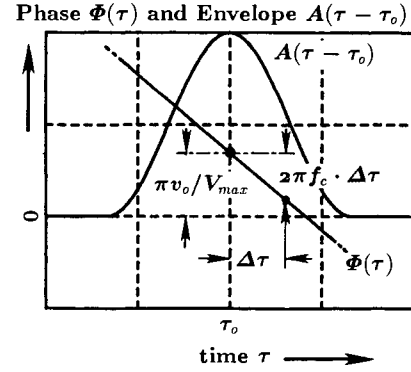
Figure 3: Phase shift and envelope of coherent correlation detector output as a function of delay error.

$$
\phi_{rr}(\tau) = \int u_r(t)u_r^*(t - \tau)dt, \tag{11}
$$

and ϕ_{ri} also denotes the cross–correlation function between $u_r(t)$ and $u_i(t)$, given by

$$
\phi_{ri}(\tau) = \int u_r(t)u_i^*(t - \tau)dt. \tag{12}
$$

These correlation functions have the following relations:

$$
\phi_{rr}(\tau) = \phi_{ii}(\tau) = A(\tau) \cdot \cos 2\pi f_c \tau \tag{13}
$$

$$
\phi_{ir}(\tau) = -\phi_{ri}(\tau) = A(\tau) \cdot \sin 2\pi f_c \tau, \tag{14}
$$

where f_c and $A(\tau)$, are the mean frequency and the envelope, respectively, of the auto–correlation function of the emitted signal $u(t)$.

If the velocity of target motion is much slower than the sound propagation speed, then the following approximation holds:

$$
\log s_o = -2v_o/c. \tag{15}
$$

Substitution of Eq.(13) and (14) into Eq.(9) and (10), and use of Eq.(15), yields the following expressions:

$$
\begin{aligned}
P(\tau) &= A(\tau - \tau_o) \cdot \cos(2bv_o/c - 2\pi f_c[\tau - \tau_o]), \tag{16} \\
Q(\tau) &= A(\tau - \tau_o) \cdot \sin(2bv_o/c - 2\pi f_c[\tau - \tau_o]). \tag{17}
\end{aligned}
$$

Thus we can finally obtain the relations

$$
\sqrt{P^2(\tau) + Q^2(\tau)} = A(\tau - \tau_o) \tag{18}
$$

and

$$
\begin{aligned}
\Phi(\tau) &= \tan^{-1}[Q(\tau)/P(\tau)] \\
&= 2bv_o/c - 2\pi f_c[\tau - \tau_o]. \tag{19}
\end{aligned}
$$

Eq.(18) indicates that, regardless of the target motion, maximum amplitude of the output envelope is obtained at the propagation delay time τ_o, and we can measure the target velocity v_o from Eq.(19) because the output

−59−

phase at τ_o is proportional to v_o. While we can estimate the propagation delay time without any a priori knowledge on the velocity, the precise estimation of τ_o must be required for the velocity measurement, because the phase in Eq.(19) varies with gradient $-2\pi f_c$ in respect to the delay estimation error($\Delta\tau = \tau - \tau_o$). Fig.(3) illustrates the envelope and the phase shift of the coherent correlation detector output as a function of delay estimation error.

3. Range and Velocity Measurement based on the Mammalian Auditory Systems

In the previous section, we described a coherent correlation detection system for a LPM echo to estimate the range and velocity of a moving target. It is doubtful, however, whether a correlation detector, which requires calculation of correlation between the location sound and the returning echo, is implemented in the auditory systems. In order to realize an equivalent function to the coherent correlation detection, we will propose a model to measure the range and velocity of a moving target by simulating the frequency selecting mechanism observed in the mammalian auditory systems.

3.1 A Bank of Constant-Q Filters

It is known that frequency analysis is coarsely performed in the early level of audition and the logarithmic frequency axis is developed along the basilar membrane. If we assume that the hair cells, which detect acoustical vibration, are distributed uniformly along the basilar membrane, the frequency analyzing function of these auditory mechanism can be simulated by a bank of constant-Q filters.

Applying a returning echo to the filter bank and eliminating its non-linear phase characteristics by delay compensation, we can realize an equivalent function to a 'matched filter' operation. If each filter is linear and time-invariant, time delay operation on the input is equivalent to that on the output. In this case, a matched filter is easily realized by selecting the center frequency of each filter so that all filters can be excited in phase, only at a certain time.

For the LPM signal, the phase ψ and the instantaneous frequency ω have the following relation:

$$\psi(\omega) = b \cdot \log(b/\omega). \tag{20}$$

If we choose the center frequency of each filter so that the emitted signal may have the phase of every 2π radians as illustrated in Fig.(4), the relation of the center frequency between the adjacent filters is given by
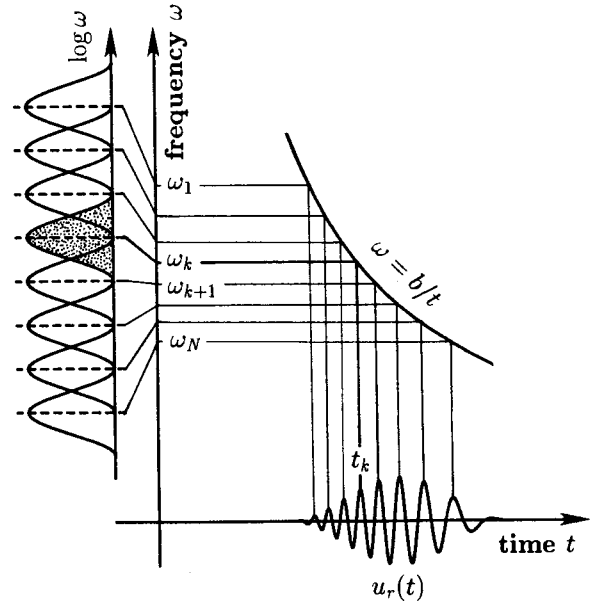
Figure 4: A design of center frequency distribution for a bank of constant-Q filters in accordance with the phase characteristics of an emitted LPM signal.

$$\omega_{k+1} = \omega_k \cdot e^{-2\pi/b}, \tag{21}$$

where the index k denotes the filter number. Fig.(4) shows that the filters are arranged at equal intervals along the logarithmic frequency axis. Thus the frequency characteristics can be uniformly distributed by the design of each filter to have the identical Q value.

Since the group time delay characteristics of a signal can be calculated by differentiating the spectral phase of the signal with respect to frequency, we obtain for the LPM signal as:

$$d_g(\omega) = b/\omega. \tag{22}$$

In order to satisfy the causality, a fixed constant delay must be added. The time delay for the filter with center frequency ω_k is then given by

$$d_k = d_0 - b/\omega_k. \tag{23}$$

Fig.(5) illustrates a schematic diagram of the proposed system composed of a bank of constant-Q filters followed by time delay devices. The output $P(\tau)$ in Eq.(16) can be simulated if a k-th filter has an impulse response defined by

$$h_{k,c}(t) = \exp(-a_k \cdot t) \cdot \cos(\omega_k t), \tag{24}$$

where $a_k = \omega_k/Q$. Similarly, the output $Q(\tau)$ in Eq.(17) is obtained with :

$$h_{k,s}(t) = \exp(-a_k \cdot t) \cdot \sin(\omega_k t). \tag{25}$$
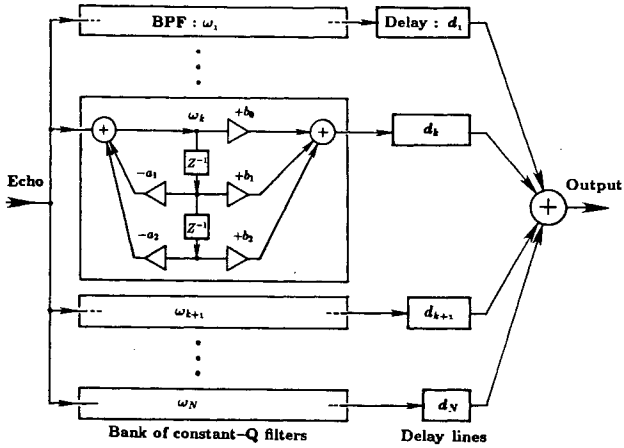
Figure 5: An equivalent function to a 'matched filter' operation is implemented with a bank of constant-Q filters followed by time delay devices

The quadratic implementation of the filter bank provides an equivalent to a coherent correlation detection system.

3.2 Phase Sensitive Model for Precise Estimation of Target Range and Velocity

Letting the frequency modulation rate b described in **2.2** be

$$b = \pi c/2V_{max}, \tag{26}$$

where V_{max} is the maximum range of measurable velocities, we can rewrite Eq.(19) as follows:

$$\Phi(\tau) = \frac{\pi}{V_{max}}(v_o - 2V_{max}f_c \cdot \Delta\tau) \tag{27}$$

where $\Delta\tau = \tau - \tau_o$ is estimation error in propagation delay time. It should be noted that the delay estimation error $\Delta\tau$ yields directly the velocity error $\Delta v = 2V_{max}f_c \cdot \Delta\tau$, and thus we must precisely estimate the propagation delay time for the accurate measurement of velocity.

Now let us divide the filter bank into two portions : the frequency bandwidth of each portion corresponds to the upper and lower half of the whole bandwidth, which have the mean frequency f_u and f_l, respectively. Output phases of both filter banks constructed independently in each frequency band are given as follows:

$$\Phi_u = \frac{\pi}{V_{max}}(v_o - 2V_{max}f_u \cdot \Delta\tau), \tag{28}$$

$$\Phi_l = \frac{\pi}{V_{max}}(v_o - 2V_{max}f_l \cdot \Delta\tau). \tag{29}$$

Thus we can obtain the delay and velocity estimates by solving above equations simultaneously. While it is

(a)

(b)
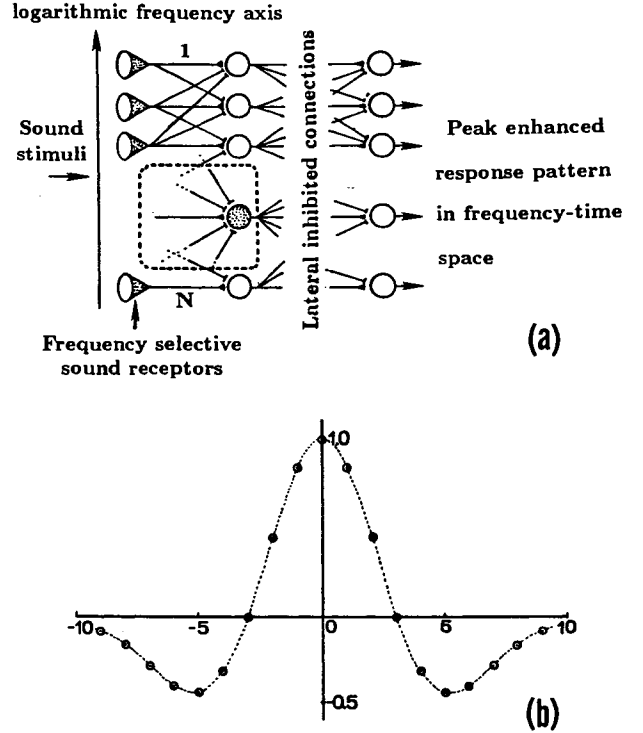
Figure 6: (a) : A model of laterally inhibited filter connections. (b) : An example of a weighting function in the filter connections : the abscissa corresponds to the difference of the filter number to be connected.

generally difficult to divide a correlation detector into two portions in frequency bandwidth, a bank of filters is easily divided into two frequency blocks with a slight modification to work separately within respective blocks.

3.3 Lateral Inhibitory Connection between the Filters

In **3.1**, we have offered the utilization of a bank of constant-Q filters modeled on the mammalian auditory systems. We assumed in the model that the auditory systems could perceive the phase information of the signal even in the case of ultrasonics. Since a quadratic implementation of the filter bank followed by the delay compensating devices can eliminate non-linear phase characteristics of the received signal, we can effectively compress the received signal in time duration.

Only for the purpose of pulse sharpening, however, a coherent process is unnecessary. A response pattern of the bank of constant-Q filters to a single echo signal will form a single hump with gradually decreased slopes — only one filter will produce the maximum response at a certain time, and the responses of adjoining filters decrease with the distance from the filter. These response patterns can be sharpened with second order

differentiation, which is equivalently formulated by lateral inhibitory connections(LIC) between the filters : a negative response must be suppressed to be zero. It is generally believed that the lateral inhibitory connections in the nervous system will give rise to a sharpening of sensory functions.

Fig.(6a) shows a model of laterally inhibited filter connections, and Fig.(6b) illustrates an example of weighting functions for the connections, which forms a "receptive field" of a filter : the abscissa corresponds to the difference of the filter number to be connected. The weighting function in this figure is calculated in accordance with second order differentiation of the Gaussian function with $\sigma = 3$: the width of a receptive field is approximately $\pm 3\sigma$, and we can control the sharpness of output responses by changing the σ value properly.

4. Numerical Experiments and the Results

A LPM signal was designed on the model of the location sound of the bat, *Epitesicus fuscus*, and was generated digitally with a sampling interval $2\mu s$. The instantaneous frequency of the signal was swept down from 55kHz to 25kHz, and the maximum range of measurable velocities, V_{max}, was set to 1m/s. Harmonic structures usually observed in the sounds of *Epitesicus* were not produced in this numerical experiment. Each of constant-Q filters was implemented with a second order IIR digital filter, and the Q value was set to 5π throughout the experiment.

The mean frequency f_c and the effective *rms* bandwidth B of the signal were calculated through the following definitions and became to 40.3kHz and 10.6kHz,respectively:

$$f_c = \frac{m_1}{2\pi} \text{ and } B = \frac{1}{2\pi}\sqrt{m_2 - m_1^2}, \tag{30}$$

where

Signal one-sided spectrum : $U(\omega)$, (31)

Signal energy : $E_u = (1/2\pi)\int_0^\infty |U(\omega)|^2 d\omega$, (32)

$$m_1 = \frac{(1/2\pi)\int_0^\infty \omega|U(\omega)|^2 d\omega}{E_u}, \tag{33}$$

$$m_2 = \frac{(1/2\pi)\int_0^\infty \omega^2|U(\omega)|^2 d\omega}{E_u}. \tag{34}$$

Using these definitions, *Cramér - Rao* lower bounds for error variance of the range and velocity estimation are given by [6]:
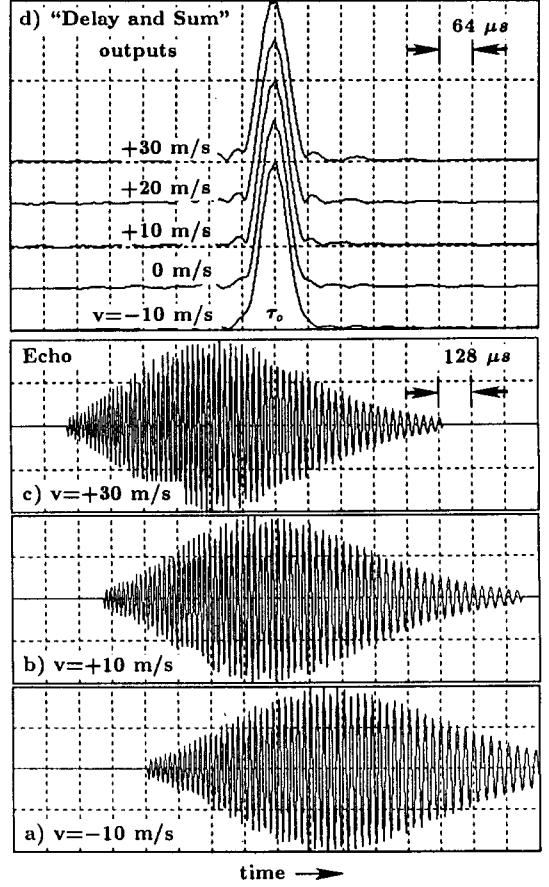
Figure 7: Doppler tolerant property. Target velocity is (a) : −10m/s, (b) : +10m/s, (c) : +30m/s. Output envelopes in (d) have the maximum value at the identical time, regardless of the velocity.

$$\sigma_\tau^2 \geq \frac{1}{(e_u/N_o)\cdot(m_2 - m_1^2)} \tag{35}$$

$$\sigma_v^2 \geq \frac{m_2}{(e_u/N_o)\cdot(m_2 - m_1^2)\cdot(\pi/V_{max})^2}. \tag{36}$$

4.1 Doppler Tolerance of the Proposed System

To examine whether the position of peak amplitude fluctuates in time or not under the influence of the time scale factor s_o, we have simulated echo signals reflected from a moving target with relative high velocities.

Fig.(7) illustrates simulated echo signals compared with the envelopes of compressed outputs. We can find clearly in this figure that the energy centroids of echo waveforms have shifted along the time axis according to time-compression or time-expansion caused by the target motions, while the peaks of output envelopes are fixed identically at the time τ_o. The Doppler tolerant property of the proposed system is consequently well confirmed.
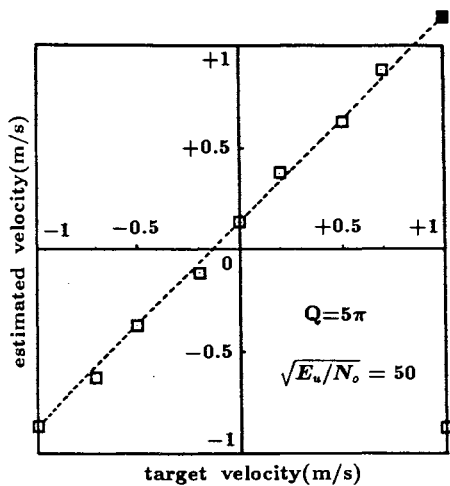
Figure 8: An experimental result of target velocity estimation. Biased estimates in this figure can be eliminated by the proper adjustment of filter 'Q' value.
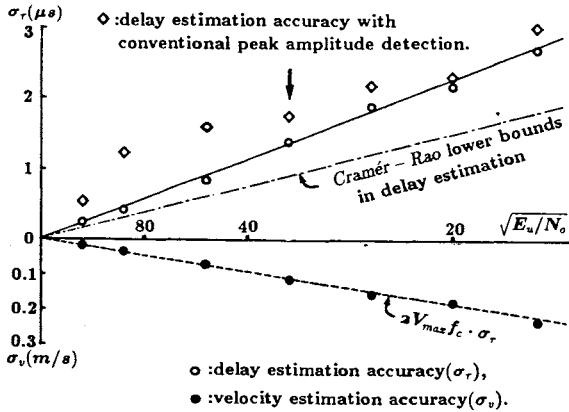
Figure 9: Dependence of estimating accuracy(σ_τ and σ_v) on the signal to noise ratio$\sqrt{E_u/N_o}$.

4.2 Estimating Accuracy

For a precise estimation of velocity, as described in **3.2**, we have divided the whole frequency band into two portions : upper and lower band were 55 – 40 kHz and 40 – 25kHz, respectively. Simultaneous solution of Eq.(28) and (29) permits us to estimate precisely the propagation delay time and the target velocity.

An example of results in velocity estimation is illustrated in Fig.(8). Although biased estimates are observed in this figure, we can eliminate the biased amounts by the proper adjustment of filter 'Q' value.

The accuracy in parameter estimation is generally evaluated with the square root of the estimation error variance. Fig.(9) plots the accuracy based on the proposed method, compared with *Cramér – Rao* lower

bounds, as a function of signal to noise ratio : $\sqrt{E_u/N_o}$, where N_o is the power spectral density of additive white Gaussian noise. The accuracy in delay estimation based on the envelope peak detection is also indicated in this figure. As a result, the accuracy of the proposed method is found to be superior to that of the conventional peak detection method.

4.3 Sharpening of Output Responses with the Lateral inhibited Filter Connections

Fig.(10) illustrates an example of response patterns of the bank of constant-Q filters to a single simulated echo signal. Fig.(11) shows response patterns to two separated targets – delay difference between two target is 0.3ms. The ordinates in these figures are the filter number, and correspond to the logarithmic frequency. Contour lines are plotted with every quarters of the maximum response, and we can roughly evaluate the time resolution through the width of the most inner contour line. A lateral inhibitory connection(LIC) between the filters is equivalent to the sharpening process along the log- frequency axis. For a pattern of which frequency varies with time, however, sharpening in frequency will imply an improvement in time resolution. These figures indicate that the repetition of LIC enables us to improve the sharpness along both frequency axis and time axis.

5. Conclusions

The numerical experiments indicate that the filter bank technique for target parameter estimation can work effectively as an equivalent of 'Matched filter' or correlation detection technique. Phase sensitive model for estimation of range and velocity can provide an improvement in estimating accuracy over that obtainable by conventional peak detection technique. The validity of lateral inhibitory connections for pulse sharpening is also proved. Further investigation is necessary, however, to eliminate the biased amount observed in the velocity estimation.

Acknowledgement
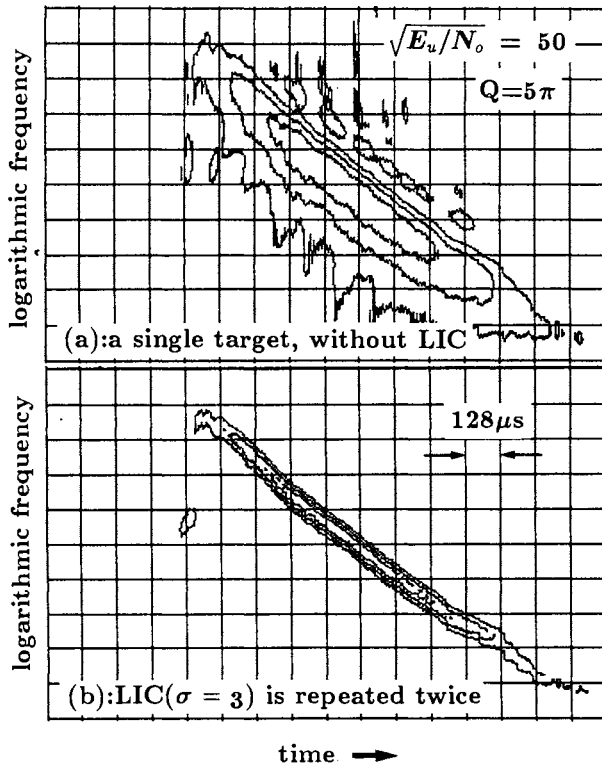
Figure 10: Response of the bank of constant-Q filters to a simulated echo signal. (a) : without lateral inhibitory connection, (b) : with lateral inhibitory connection repeated twice.
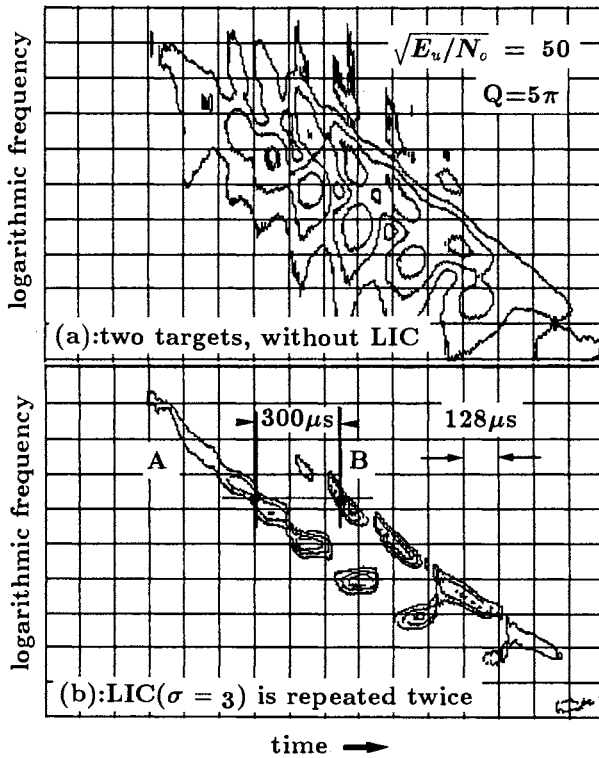
Figure 11: Response of the bank of constant-Q filters to two targets. (a) : without lateral inhibitory connection, (b) : with lateral inhibitory connection repeated twice. Delay difference between two targets A and B is 0.3ms

References

[1] C.E.Cook : "Pulse Compression – Key to More Efficient Radar Transmission," Proc. IRE, 48, 3, pp.310-316(1960)

[2] J.R.Klauder, A.C.Price, S.Darlington and W.J.Albersheim : "The Theory and Design of Chirp Radars," BSTJ, 39, 4, pp.745-808(1960)

[3] J.J.Kroszczyński : "Pulse Compression by Means of Linear-Period Modulation," Proc. IEEE, 57, pp.1260-1266(1969)

[4] R.A.Altes and E.L.Titlebaum : " Bat Signal as Optimally Doppler Tolerant Waveforms," J. Acoust. Soc. Am.,48, 4, pp.1014-1020(1970)

[5] E.J.Kelly and D.P.Wishner : "Matched Filter Theory for High-Velocity, Accelerating Targets," IEEE Trans. Military Electronics, MIL-9, 1, pp.56-69(1965)

[6] R.A.Altes and D.P.Skinner : "Sonar-velocity resolution with a Linear-Period Modulated pulses," J. Acoust. Soc. Am., 61, 4, pp.1019-1030(1977)

NOVEL CONFIGURATIONS FOR ACOUSTIC ARRAYS

Adam Zielinski and Lixue Wu

University of Victoria, B. C., CANADA

Abstract

A novel array of ring radiators is proposed which generates a symmetric search-light type narrow beam with greatly reduced sidelobes. A design procedure is detailed which benefits from existing design techniques developed for linear arrays. Obtained results are presented which shows possible reduction of sidelobes to more than 30 dB using a ring array with 10 elements.

1 Introduction

The circular piston is a widely used planar radiator [1]. One of the attractive feature of such a radiator is its symmetric directivity function with the first sidelobe level of 17.6 dB below the main lobe [2]. However, in some applications lower sidelobe level is desirable. In this paper, we propose an array consisting of ring radiators, which is capable of reducing the first sidelobe level below that of circular piston. A design procedure is described which benefits from the existing design techniques developed for linear arrays. The obtained results show that a reduction of sidelobes to more than 30 dB using a ring array with 10 elements is possible.

2 An Array with Ring Radiators

The directivity function of a planar, circular radiator with radius a and uniform sensitivity, placed in infinite rigid baffle is known to be [1]:

$$D_c(f, \theta, \psi) = a\frac{J_1[(2\pi a/\lambda)\sin\theta]}{(\sin\theta)/\lambda} \qquad (1)$$

where θ, ψ are elevation and azimuth angles respectively, λ is wavelength of the radiated signal and $J_1(\cdot)$ is the first-order Bessel function of first kind.

The directivity function of a ring radiator can be readily obtained by subtracting directivity functions

of two circular radiators [3].

We will consider an array formed by several concentric, contiguous (no gaps) ring radiators, each contributing to the overall directivity function with certain weighting coefficients c_i as illustrated in Figure 1 for three rings (for simplicity we will call the central, circular portion of the array also a ring).

The directivity function of an array with N ring radiators arranged in such a way can be written as

$$
\begin{aligned}
D(f, \theta, \psi) \;=\; & 2\pi a_0^2 c_0 \frac{J_1[(2\pi a_0/\lambda)\sin\theta]}{(2\pi a_0/\lambda)\sin\theta} \\
& + \sum_{i=1}^{N-1} c_i \left\{ 2\pi a_{i-1}^2 \frac{J_1[(2\pi a_{i-1}/\lambda)\sin\theta]}{(2\pi a_{i-1}/\lambda)\sin\theta} \right. \\
& \left. - 2\pi a_i^2 \frac{J_1[(2\pi a_i/\lambda)\sin\theta]}{(2\pi a_i/\lambda)\sin\theta} \right\} \qquad (2)
\end{aligned}
$$

where a_i are radii as indicated in Figure 1.

By varying the weighting coefficients c_i one can modify the overall function D to assume or to approximate a certain desired function D_d.
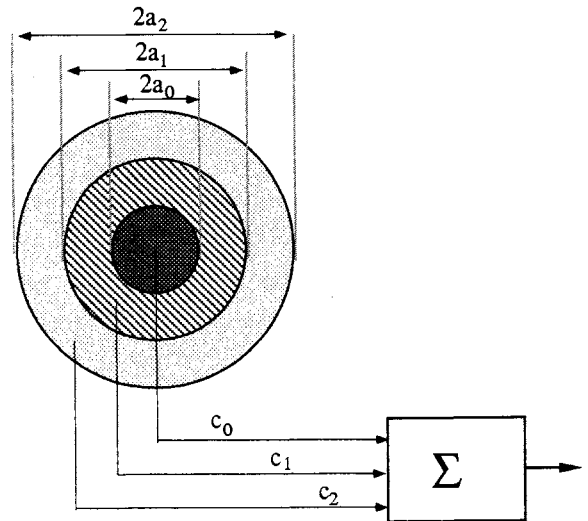
Figure 1: Geometry of an array with ring radiators

3 Design of an Array with Ring Radiators

The design technique for an array of ring radiators proposed here takes advantage of the techniques developed for linear arrays. Since linear array design is a mature and well-developed field, such approach offers obvious advantage.

3.1 Equivalent Linear Array of Ring Radiator

A linear array with N (even) elements spaced uniformly by d has the directivity function given by

$$D_l(u) = \sum_{j=0}^{N/2-1} A_j \cos(2j-1)u \qquad (3)$$

where $\{A_j\}$ are the weighting coefficients and

$$u = \frac{\pi d}{\lambda} \sin\theta \qquad (4)$$

The directivity function of ring radiator with radii a_i and a_{i-1} can be written as

$$
\begin{aligned}
D(f,\theta,\psi) &= D_r(u) \\
&= \pi a_i d \frac{J_1[(2a_i/d)u]}{u} \\
&\quad -\pi a_{i-1} d \frac{J_1[(2a_{i-1}/d)u]}{u} \qquad (5)
\end{aligned}
$$

Assuming infinite length of linear array, it is possible, by proper selection of weighting coefficients A_i, to obtain the directivity function of linear array equal to that of ring radiator, that is

$$D_r(u) = \sum_{j=0}^{\infty} A_j \cos(2j-1)u \qquad (6)$$

We will call such an array the equivalent linear array to ring radiator. Similar equivalency can be derived for a disc radiator with directivity function D_c given by Eq.(1).

We note that functions $\cos(2j-1)u$ are orthogonal in u-domain, namely that the inner product

$$
\begin{aligned}
&< \cos(2i-1)u, \cos(2j-1)u > \\
&= \frac{2}{\pi} \int_0^{\pi} \cos(2i-1)u \cos(2j-1)u\, du \\
&= \begin{cases} 1 & \text{for } i=j \\ 0 & \text{else} \end{cases} \qquad (7)
\end{aligned}
$$

Applying the inner product defined by Eq.(7) to the Eq.(6) we obtain

$$
\begin{aligned}
&\sum_{j=0}^{\infty} A_j < \cos(2j-1)u, \cos(2i-1)u > \\
&= < D_r(u), \cos(2i-1)u > \qquad (8)
\end{aligned}
$$

which leads to the explicit expression for A_i

$$A_i = \frac{2}{\pi} \int_0^{\pi} D_r(u) \cos(2i-1)u\, du \qquad i = 0,\ldots,\infty \quad (9)$$

3.2 Design of an Array of Ring Radiators by the Equivalent Linear Array Method

The equivalent linear array method for the design of array of ring radiators is basically a technique in which all ring radiators are represented by series of equivalent linear arrays. The directional response of the array of ring radiators is then the sum of directivity functions of all equivalent linear arrays. The equivalent linear array of a ring radiator has in principle infinite number of elements and associated weighting coefficients. In general, the amplitude of these coefficients is small for elements far away from the central of the array. It is therefore possible to truncate the equivalent linear array to finite number of elements by disregarding elements with small weighting coefficients. An equivalent linear array can also be defined for a circular array. It has been found that the weighting coefficient of linear array equivalent to circular array decreases more rapidly then that of ring array. This in turns introduces less error when the linear equivalent array is truncated. As an illustration of these findings shown in Figure 2 are radiation patterns of an disc radiator and its equivalent linear array truncated to 10 elements. We can see only a small error (at higher order sidelobes) introduced by this truncation. It is for this reason that we will carry our design using array of disc radiators. We can then modify such an array to the array of ring radiators with zero gap between rings having the same radiation pattern.
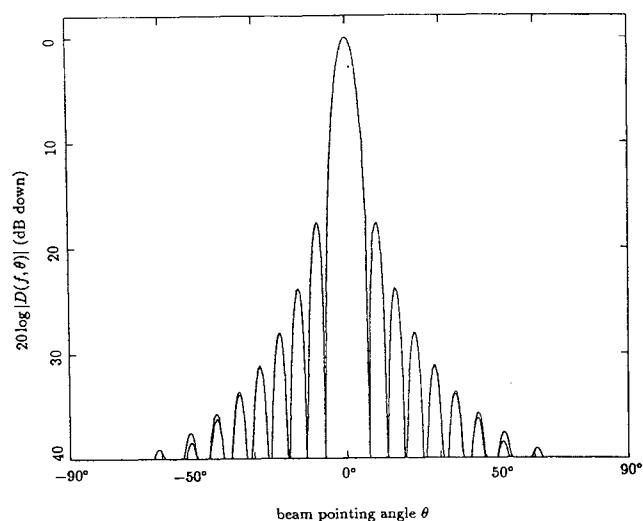
Figure 2: Beam patterns of a ring radiator and its equivalent linear array

We will demonstrate this equivalency by considering an array of stacked discs shown in Figure 3a. For the sake of exposition all concentric discs (or rings) are shown in a disassembled form. A disc radiator can be thought of as an assembly of concentric, contiguous ring radiators. This leads to equivalent stacked ring array shown in disassembled form in Figure 3b. Finally we can construct equivalent, single layer concentric ring array with suitable weighting coefficients as shown in Figure 3c. In general, for a given vector of weighting coefficient $\mathbf{w}_d$ associated with a stacked disc array, the vector of weighting coefficients $\mathbf{w}_r$ for equivalent single layer ring array, is given by
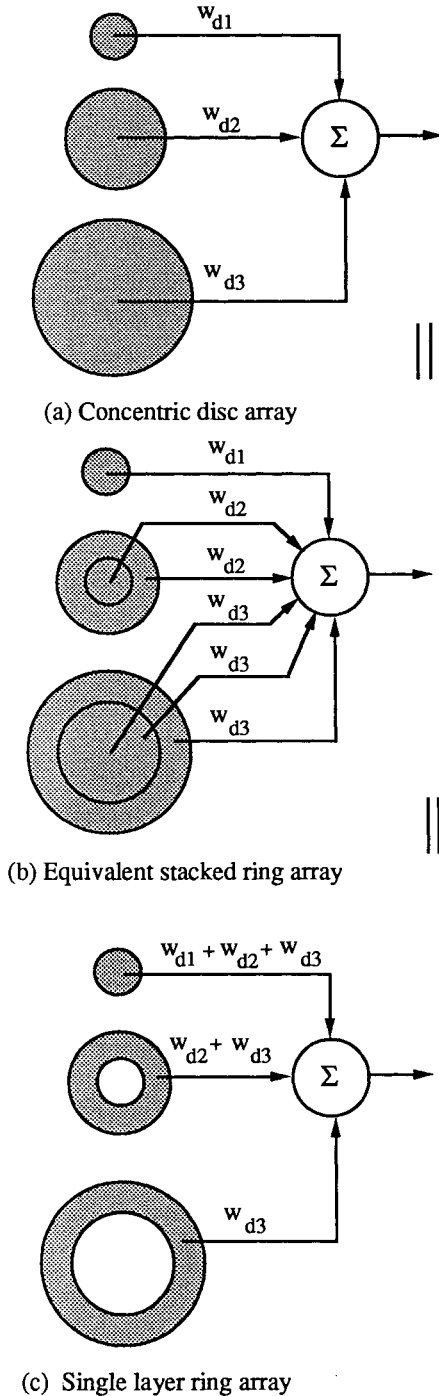
$$\mathbf{w}_r = \mathbf{A}\mathbf{w}_d \qquad (10)$$

where the elements of matrix $\mathbf{A}$ are

$$a_{i,j} = \left\{ \begin{array}{ll} 1 & \text{for } i \leq j \\ 0 & \text{else} \end{array} \right. \qquad (11)$$

The design procedure for obtaining the weighting coefficients for the array of ring radiators with zero gap between rings consists of the following steps:

1. Design a linear array of point radiators which produces a desirable form of directivity function (for example associated with Dolph-Chebyshev array), and therefore the N-dimensional column vector of weighting coefficients $\mathbf{w}_l$, spacing d, and size N of the array are given [5]. We will call such an array a *prototype*.

2. Consider a disc radiator and determine its radius in the follow steps:

   a) Select an initial value of r for the disc.

   b) Find equivalent linear array with spacing d of this disc. Such an array has in principle infinite number of elements (and associated weighting coefficients). However, it can be truncated to a finite size N_r without appreciable error in its radiation pattern. This can be done by neglecting coefficients with amplitudes less than a certain small percentage of the largest one. In general, N_r is an increasing function of r.

   c) Adjust $r = r_N$ such that $N_r = N$, and therefore the N-dimensional column vector of weighting coefficients $\mathbf{w}_N$ is formed

$$\mathbf{w}_N = \left[\begin{array}{c} w_{1,N} \\ w_{2,N} \\ \vdots \\ w_{N,N} \end{array} \right] \qquad (12)$$

3. Reduce the radius r_N of disc radiator until its equivalent linear array has the size of $N - 1$. The argumented vector of weighting coefficients $\mathbf{w}_{N-1}$ is then formed as

$$\mathbf{w}_{N-1} = \left[\begin{array}{c} w_{1,N-1} \\ w_{2,N-1} \\ \vdots \\ w_{N-1,N-1} \\ 0 \end{array} \right] \qquad (13)$$

(a) Concentric disc array

(b) Equivalent stacked ring array

(c) Single layer ring array

Figure 3: Identity of the array of disc radiators and the array of zero gap ring radiators

4. Repeat the step 3 to obtain equivalent linear array of size $N - 2, N - 3, \ldots, 1$ and form subsequent argumented vectors of weighting coefficients

$$\mathbf{w}_{N-2} = \begin{bmatrix} w_{1,N-2} \\ w_{2,N-2} \\ \vdots \\ w_{N-2,N-2} \\ 0 \\ 0 \end{bmatrix} \qquad (14)$$

$$\mathbf{w}_{N-3} = \begin{bmatrix} w_{1,N-3} \\ w_{2,N-3} \\ \vdots \\ w_{N-3,N-3} \\ 0 \\ 0 \\ 0 \end{bmatrix} \qquad (15)$$

etc.

5. Form the matrix of the weighting coefficients $\mathbf{W}$ as

$$\mathbf{W} = [\mathbf{w}_1, \mathbf{w}_2 \cdots \mathbf{w}_N] \qquad (16)$$

6. Solve the matrix equation

$$\mathbf{W}\mathbf{w}_d = \mathbf{w}_l \qquad (17)$$

to obtain the vector of weighting coefficients $\mathbf{w}_d$ of disc radiators.

7. The vector of weighting coefficients of ring radiators $\mathbf{w}_r$ is then found according to Eq.(10) by the matrix equation

$$\mathbf{w}_r = \mathbf{A}\mathbf{w}_d \qquad (18)$$

where the elements of matrix $\mathbf{A}$ is given by

$$a_{i,j} = \begin{cases} 1 & \text{for } i \leq j \\ 0 & \text{else} \end{cases} \qquad (19)$$

· This procedure does not result in final radiation pattern equal to the original radiation pattern of the prototype postulated in step 1, because of truncation error. It does however reproduce general trends of the required pattern. For example, increasing sidelobe suppression in the prototype leads to increased sidelobe suppression in the ring array.

To illustrate these points, we have performed an array design by applying the above design technique to a Dolph-Chebyshev linear array as a prototype with 30 dB sidelobe suppression [6]. The size of the prototype is 20 elements with spacing $d = \lambda/2$ which leads to 6° beam width (at 3 dB points). The resulting ring array has 10 elements and 10λ diameter. Table 1 gives the value of associated weighting coefficients. Its radiation pattern is shown in Figure 4. We can observe the first sidelobe suppression of approximately 23 dB. For comparison a radiation pattern of

a circular radiator of the same size is shown in Figure 5. Figures 6, 7 and 8 show radiation patterns of the ring arrays obtained by assuming 40 dB, 50 dB and 60 dB sidelobe suppression in the prototype. It can be seen that the reduction of sidelobes to more than 30 dB is possible using an array with 10 ring radiators.

TABLE 1

TABULATED WEIGHTING COEFFICIENTS OF THE ARRAY WITH RING RADIATORS

c_0	c_1	c_2	c_3	c_4
0.9202	0.9344	0.8785	0.9173	0.7718
c_5	c_6	c_7	c_8	c_9
0.8413	0.5616	0.7447	0.1110	1.0000
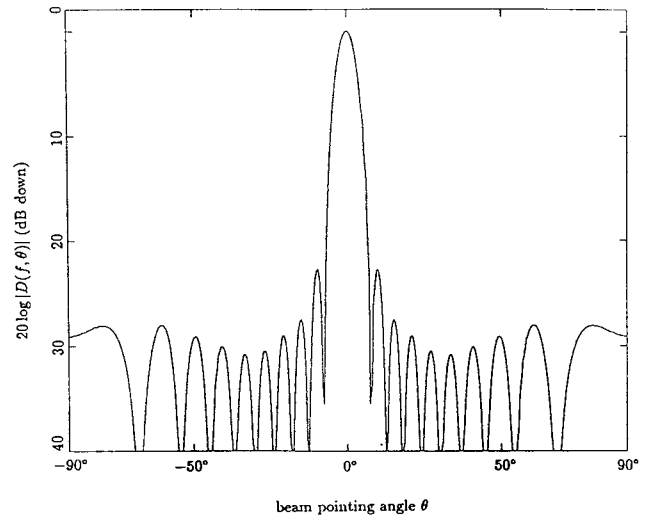
Figure 4: Beam pattern of an array with 10 ring radiators postulated 30 dB sidelobe suppression in the prototype
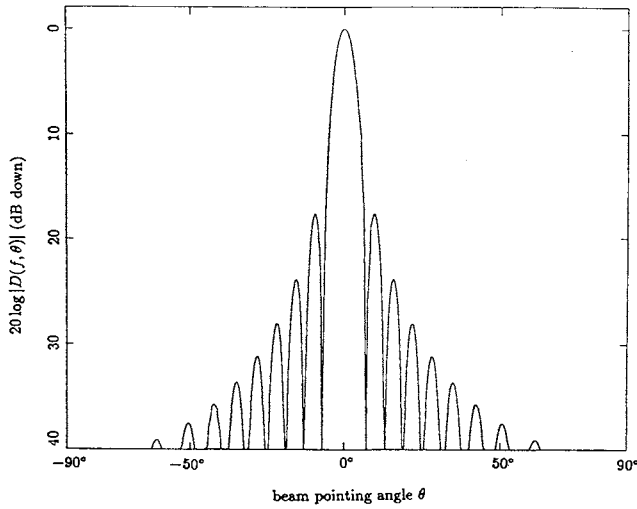
Figure 5: Beam pattern of a circular radiator with radius $a = 5\lambda$
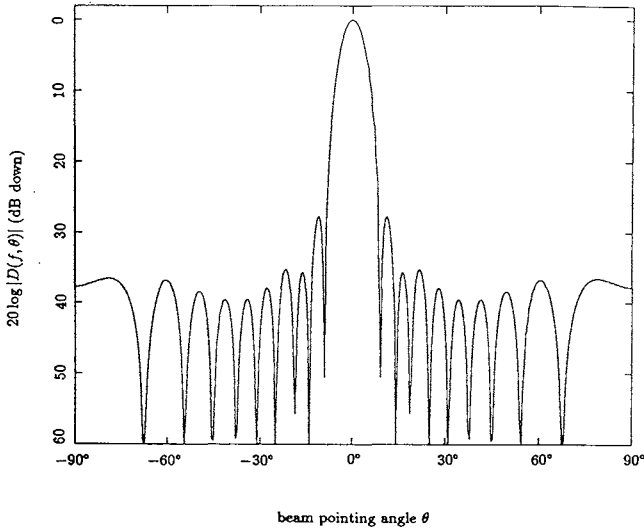
Figure 6: Beam pattern of an array with 10 ring radiators postulated 40 dB sidelobe suppression in the prototype
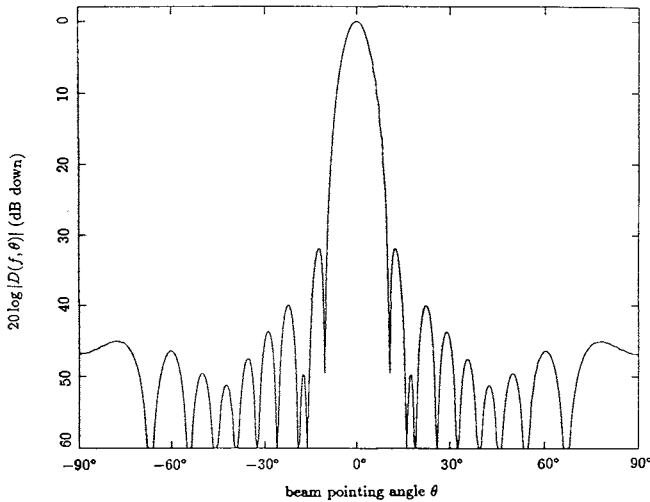
Figure 7: Beam pattern of an array with 10 ring radiators postulated 50 dB sidelobe suppression in the prototype
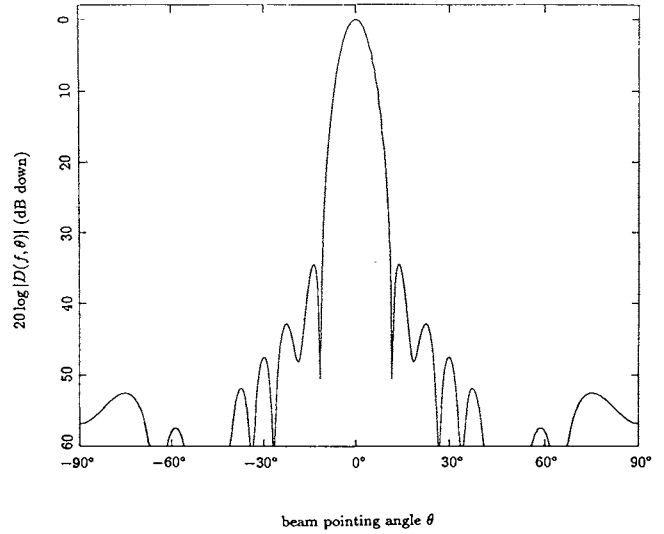
Figure 8: Beam pattern of an array with 10 ring radiators postulated 60 dB sidelobe suppression in the prototype

4 Other Configurations

Several other interesting three-dimensional array configurations are possible and some are described below. These will be investigated in future.

4.1 Helical Radiator

A three-dimensional configuration of an acoustic radiator which can be constructed using a piezoelectric wire is shown in Figure 9a. It is a helix made of N turns each of diameter D with spacing S between turns. The total length of the radiator is $L = NS$ while the total length of the wire is

$$L_n = NL_0 \tag{20}$$

where $L_0 = \sqrt{S^2 + C^2}$ is the length of the wire forming each turn and $C = \pi D$ is the circumference of the helix. Another important parameter is the pitch angle α which is the angle formed by a line tangent to the helix and a plane perpendicular to helix axis. The pitch angle is defined by

$$\alpha = \tan^{-1}\left(\frac{S}{\pi D}\right) \tag{21}$$

The beam pattern of the radiator can be varied by controlling the size of its geometrical properties compared to the wavelength.

Shown in Figure 9b is the simplified form of a helix radiator which can be used to analyze its radiation pattern. The beam pattern of such simplified structure is given by

$$D(f, \theta) = D_r(f, \theta)\frac{\sin[(N/2)\phi]}{\sin[\phi/2]} \tag{22}$$

where

$$\phi = 2\pi\left[\frac{S}{\lambda}(1 - \cos\theta) + \frac{1}{2N}\right] \tag{23}$$

The $D_r(f, \theta)$ in above equation represents the beam pattern of a single turn, and the rest part is the array factor of a linear array of N point elements.

To achieve maximum radiation intensity along the axis of the helix, the spacing S must be multiple of the wavelength. The operation of such an array is relatively insensitive to its dimensions, thus allowing for greater bandwidth [2].

(a) helix radiator   (b) its equivalent
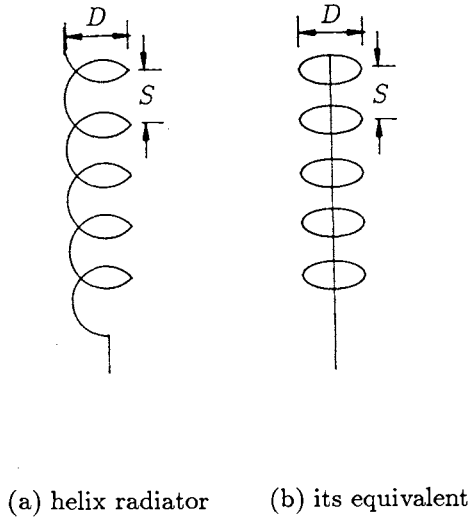
Figure 9: Helical radiator and its equivalent

4.2 Conical Spiral Radiator

Another possible geometrical configuration of an acoustic radiator is conical spiral. It has some desirable properties which can be used to design frequency independent radiator [2].

Such a radiator can be constructed by using piezoelectric wire or piezoelectric film. A conical spiral piezoelectric film radiator is shown in Figure 10a.

The shape of a nonplanar spiral can be described by defining the derivative of $g(\theta)$ to be

$$\frac{dg}{d\theta} = A\delta(\beta - \theta) \tag{24}$$

where $g(\theta)$ is a completely arbitrary function and θ is elevation angle. In above equation β is allowed to take any value in the range $0 \leq \beta \leq \pi$. For a given value of β, the above equation in conjunction with

$$r = e^{a\phi}g(\theta), \quad a = \frac{1}{K}\frac{dK}{dC} \tag{25}$$

describes a spiral wrapped on a conical surface.

The beam pattern of the conical spiral can be derived by representing the conical spiral by an array of N turns of uniform spacing which are placed along the z - axis as shown in Figure 10b. This simplified form can be used to derive and investigate its directivity function.

(a) conical radiator   (b) its equivalent
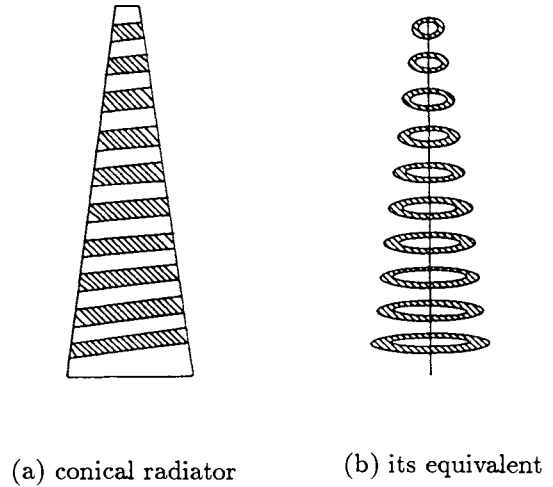
Figure 10: Conical spiral radiator and its equivalent

5 Conclusions

An equivalent linear array approach has been presented in the design of an array with ring radiators which is capable of reducing the first sidelobe level below that of circular piston. A design procedure is considered which benefits from the existing design techniques developed for linear arrays. The obtained results show that a reduction of sidelobes to more than 30 dB using a ring array with 10 elements is possible.

Acknowledgment

References

[1] R. J. Urick, *Principles of Underwater Sound for Engineering*, New York: McGraw-Hill, Edition 3, 1983.

[2] C. A. Balanis,*Antenna Theory Analysis and Design* New York: Harper & Row, 1982.

[3] V. M. Ristic,*Principle of Acoustic Device* New York: John Wiley & Sons, 1983.

[4] R. F. Harrington, *Field Computation by Moment Methods*, New York: Macmillan, 1968.

CONTINENTAL SHELF SURVEY PROJECT OF JAPAN

S. Kato*, S. Kasuga*, Y. Shimakawa*, Y. Kato* and H. Seta*

* Maritime Safety Agency, Tokyo, Japan

Abstract

The Hydrographic Department of Japan has been conducting the Continental Shelf Survey Project since 1983. The purpose of the project is to collect basic information on the Japanese continental shelf and to prepare bathymetric, geological structure, magnetic anomaly and gravity anomaly charts. Bathymetric, geological and geophysical surveys were carried out in survey areas each covering a 3° latitude by 2.5° longitude. The average spacing between survey track lines was 5 nautical miles. Areas of special interest were covered by closer tracks lines. Twenty boxes in the southern waters of Japan were surveyed by the end of FY 1989. These surveys revealed several interesting geological and geophysical features in the Okinawa Trough, Nanseisyoto Trench, central and northern part of the Philippine Sea, Sitito-Iozima Ridge and Ogasawara Plateau.

1. Introduction

The Hydrographic Department of Japan has been conducting the Continental Shelf Survey Project since 1983. The purpose of the project is to prepare bathymetric, geological and geophysical data of the exclusive economic zone and the continental shelf of Japan and to prepare Basic Maps of the sea in Continental Shelf Areas at the scale of 1 to 500,000[1][2].

Figure 1 shows the survey area of the project. Twenty boxes in the southern waters of Japan were surveyed by the end of FY 1989. This area covered the Okinawa Trough, Ryukyu arc-trench system, Daito Ridge group, Kyusyu-Palau Ridge, Sikoku Basin, Izu-Ogasawara arc-trench system and Ogasawara Plateau. The surveys revealed several interesting geological and geophysical characteristics.

This paper describes the geomorphological, geological and geophysical findings revealed by the survey in the southern waters of Japan.
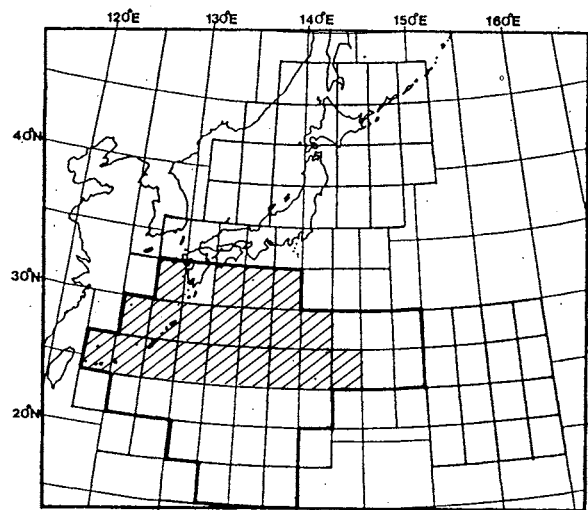
Figure 1 Survey areas and squares of the Continental Shelf Survey Project. Shaded area shows the surveyed squares until FY 1989. [1]

2. Outline of the Survey

The SEABEAM multi beam swath sonar system was used to acquire bottom depth. A single channel seismic reflection profiling system (air gun) and 3.5 kHz subbottom profiling system were used to obtain geological structure data. The geomagnetic and gravity data were also measured. All measurements were taken continually along ships track lines which were spaced 5 nautical miles apart. The track line configuration is shown in Figure 2.
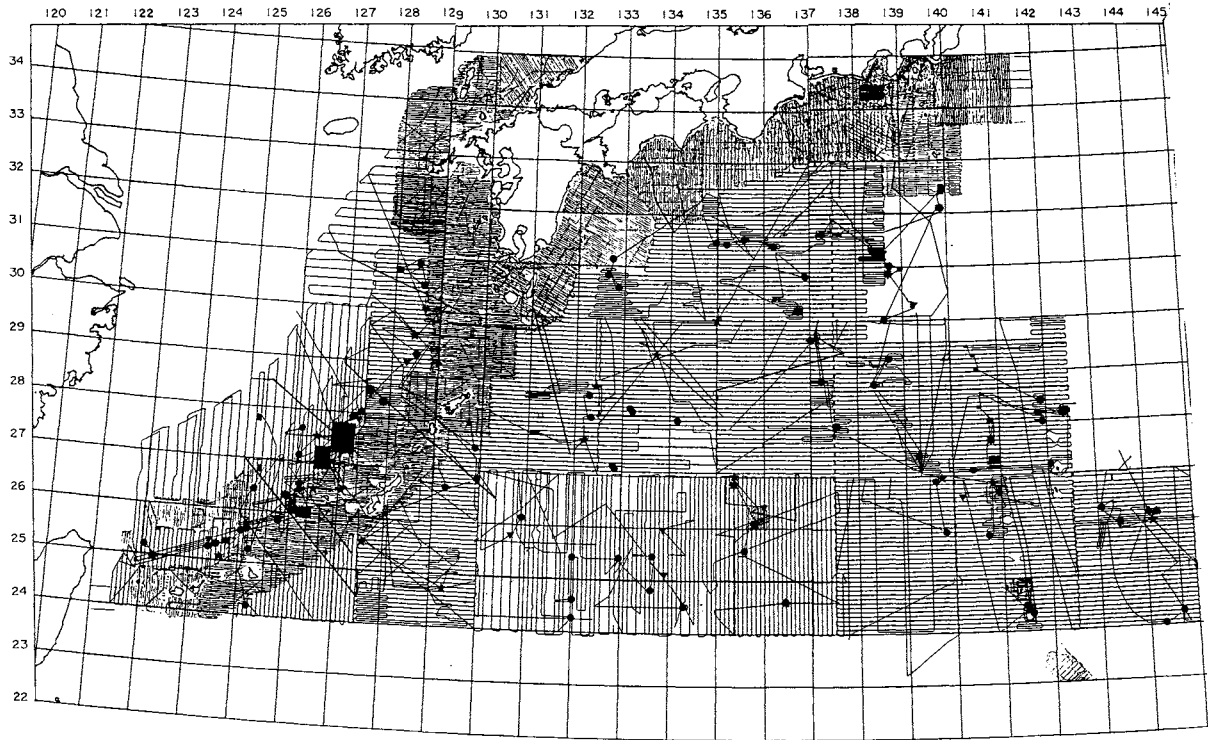
Figure 2 All survey tracks run by the Continental shelf Survey
Project. Dense track areas around Japan Island and
along the Ryukyu arc show tracks by previous survey
project.
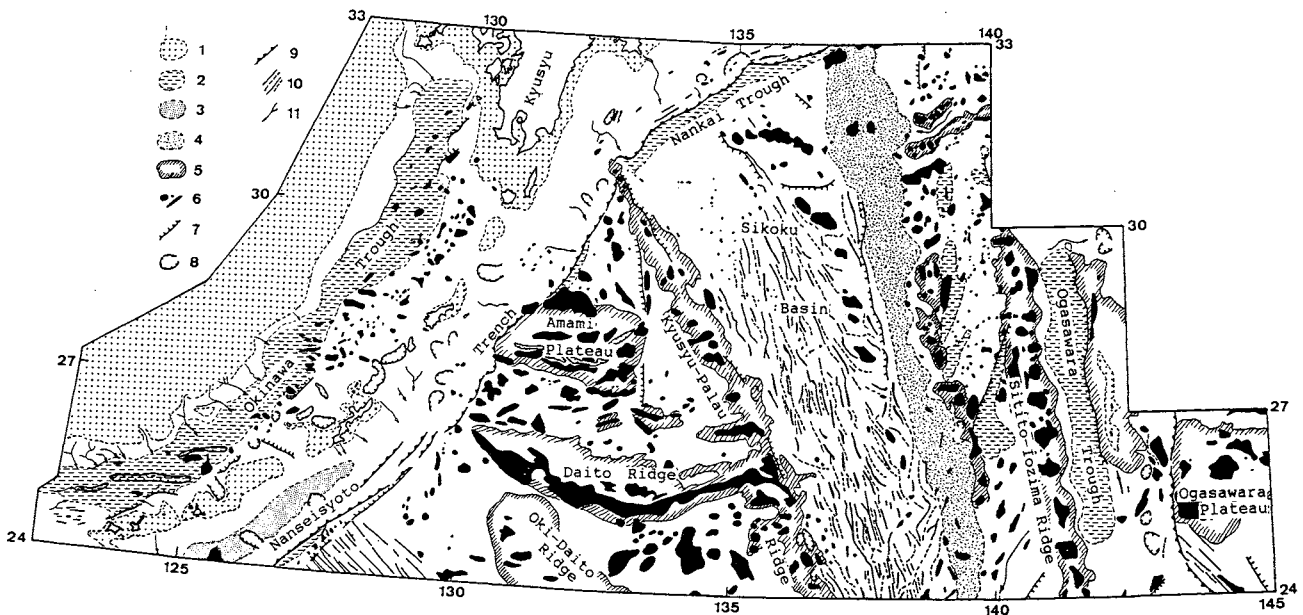
Figure 3 Geomorphological map of the southern waters of Japan.
1: Shelf and shallow waters, 2: Flat floor of trough,
trench and small basin, 3: Deep sea terrace, 4:
archipelagic apron, 5: Ridge and Plateau, 6: Seamount,
knoll and small ridge, 7: Escarpment, 8: small
depression, 9: Trust fault along trench axis, 10: Minor
ridge and trough, 11: channel and canyon.

Multi-channel seismic reflection profiling was conducted along the selected lines. Bottom sampling (dredge/core), heat flow measurement and bottom photographing were conducted at the special sites of interest.

Each survey area covers 3° latitude by 2.5° longitude. Three of these boxes are being surveyed each year. The survey results were compiled in the bathymetric, geological structure, geomagnetic anomaly and free-air gravity anomaly maps on a scale of 1 to 500,000. In the charts descriptions are many tectonic characteristics and the history of several ridges, basins, trenches in the area.

3. Geomorphological, geological and geophysical characteristics in the southern waters of Japan

Figure 3 is the geomorphological outline of the surveyed area. The area covers the northern part of the Philippine Sea plate and the boundary zone with surrounding plates.

3-1 Okinawa Trough

Ryukyu island arc-trench system consists of the Ryukyu arc and Nanseisyoto (Ryukyu) Trench. A active volcanic belt and a non-volcanic high elongate are at the axis of the island arc. Okinawa Trough is a long depression on the marginal sea behind the Ryukyu island arc. The deepest point is situated in the southwestern part of the trough. Water depth at that point is 2310 meters.

It is confirmed that the graben formed en-echelon pattern is composed of active faults in the trough axis at the middle and southwestern part of the Okinawa Trough. Knolls of igneous rocks were identified in the grabens.

The linear patterns of magnetic anomalies in the graben are attributable to the normal magnetization of the small ridges. Chemical examination and dating of rock samples recovered by dredging confirmed Quaternary arc-type volcanic activity in the trough.

The survey revealed the recent tectonic activity of the Okinawa Trough as subsidence of the basement accompanied by arc-type volcanism, faulting and sedimentation [3]-[7]. Figure 4 shows the isopack map of the upper layer of the Okinawa Trough.
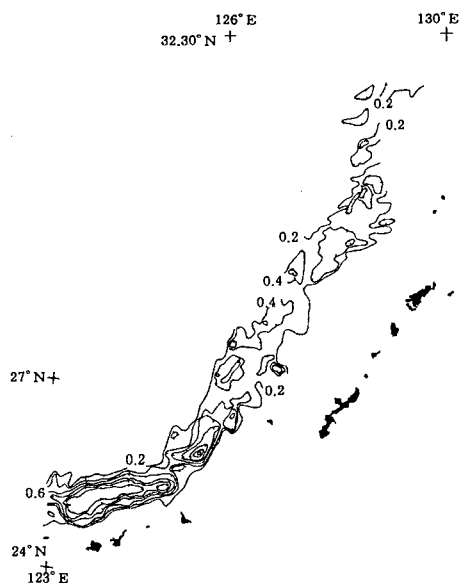
Figure 4 Isopach map of the upper layer (Ot-I and Eb-I formations) which deposited in the Okinawa Trough. Contour interval is 0.2 second in two way travel time. [6]

3-2 Nanseisyoto Trench

The Nanseisyoto Trench is the convergent boundary of the western part of the Philippine Sea plate subducting beneath the Ryukyu arc.

On the floor of Philippine Basin near the central part of the trench, minor ridges have been well developed accompanied by the geomagnetic lineation running in the same direction with these ridges. This implies that this basin is a marginal basin formed by expansion of the seafloor. A remarkable bathymetric lineation province is shown in Figure 3.

The large normal fault along the seaward side of the trench limits the northwest margin of the area where the minor ridges are developed. This fault may be fracture zone reactivated by the bending of the trench formation.

Short lineation in two directions mutually crossing almost orthogonally are recognized in the floor of the Nanseisyoto Trench. This 'mesh shaped' structure may be considered a composite of old minor ridge lineations and new bending faults lineations [8]. Figure 5 shows the mesh shaped structure in the central part of the Nanseisyoto Trench floor.
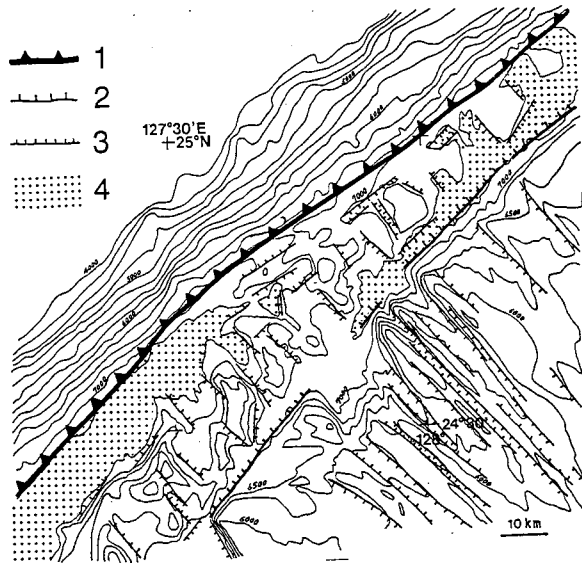
Figure 5 Mesh shaped structure in the Nanseisyoto Trench floor. 1: Thrust fault at the foot of landward slope, 2: Large normal fault, 3: Faults and lineaments, 4: Trench floor.

3.3 Ridges in the Philippine Sea

There are several ridges in the Philippine Sea. Kyusyu-Palau Ridge is a long ridge elongating in north-south direction which divides the Sikoku Basin and Daito Ridge group. Daito Ridge group consists of the Daito Ridge, Oki-Daito Ridge and Amami Plateau which extend in east-west directions.

The bathymetric trend of Daito ridge is ESE on its western half, whereas the eastern half of the ridge extends ENE. At the eastern tip of the ridge it is connected with the Kyusyu-Palau Ridge in topography. Oki-Daito Ridge extends in a NW-SE direction to the south of the Daito Ridge.

Magnetic anomaly distributions suggest that the Daito Ridge and Oki-Daito Ridge are composed of magnetic basement with intermediate to acidic rock properties, and several intrusive rocks with intermediate to basic properties. Free-air and Bouguer gravity anomalies indicate thick crustal structure below the two ridges.

These results support the idea that the two ridges are a remnant island arc [9][10].

3.4 Sikoku Basin

Sikoku Basin is a back arc basin limited by Kyusyu-Palau Ridge to the west, Izu-Ogasawara island arc to the east and Nankai Trough to the north (Figure 3).

Bathymetry of the Sikoku Basin is characterized by group of slightly curved small-scale minor ridges and troughs ranging 60 to 30 km in length. Remarkable alignments with NNW-SSE trends were found in the western half of the southern Sikoku Basin. The magnetic anomaly in the northern part of the basin were collected with distinct lineations parallel with bathymetric minor ridges and troughs. However, the amplitude of the magnetic lineation is reduced in the southern part of the basin.

The linear structures of bathymetry and geomagnetic anomaly suggests that the basin was formed by the process of sea floor spreading under an extensional stress perpendicular to the trend.

The east side of the Kyusyu-Palau Ridge slopes down to the Sikoku Basin. Several high escarpments are recognized along the slope. Figure 6 shows the steep eastward slope of the Minami Koho Seamount in the Kyusyu-Palau Ridge.

This steep slope is a fault escarpment and represents a remnant cliff of a rifted island arc that was formed immediately after the opening of the Sikoku Basin [11].

26°25'N
135°40"E

0   10   20km   26°00'N
                                  136°06"E
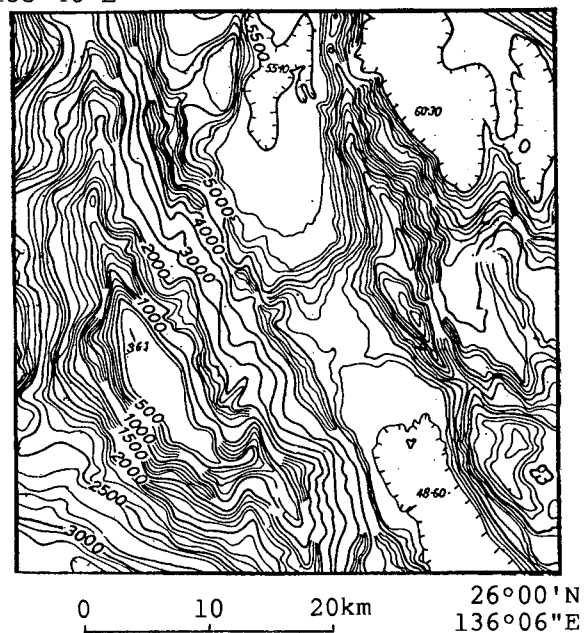
Figure 6 Bathymetric map of the Minami Koho Seamount. Contour interval 100 m.

3.5 Ogasawara Plateau

The Ogasawara Plateau is situated at the junction of the N-S trending Izu-Ogasawara - Mariana trenches and the E-W trending Michelson Ridge. The geomorphological features clearly indicate that the plateau is composed of four seamount blocks and three grabens.

A large number of NW-SE to NNW-SSE trending typical reverse faults were identified most parts of the plateau. On the other hand, typical normal faults, associated with tension in the surface of the subducting Pacific Plate, are recognized in the oceanward slope of the trench around the plateau.

The survey data indicate that a partial speed-down of the movement of the plate surface caused a congestion of seamount near the trench [12]. Figure 7 shows the palaeogeographic map of the Ogasawara Plateau.
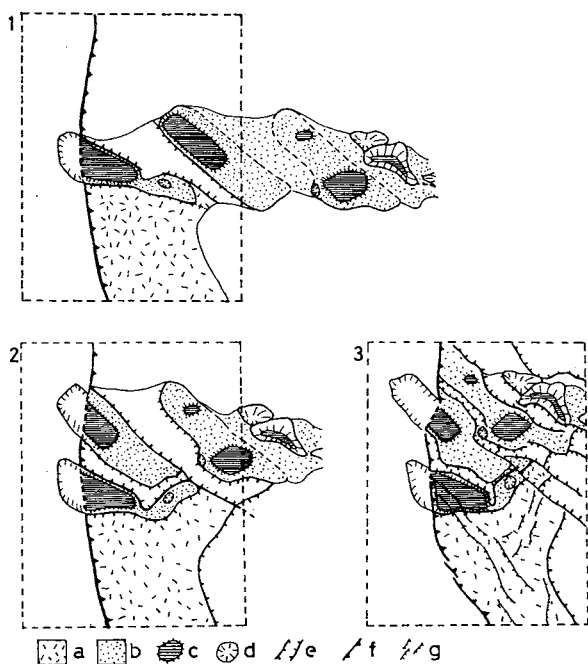
Figure 7 Palaeogeographic map of the Ogasawara Plateau. 1: Early Neogene, 2: Middle Neogene to Early Quaternary, 3: Recent, a: Marginal swell, b: Archipelagic apron, c: Guyot, d: Seamount with a rounded top or pinnacle, e: Graben, f: Trench, g: Fault. [12]

4. Conclusion Remark

The Continental Shelf Survey Project has prepared homogeneous and high quality bathymetric, geological and geophysical data in the exclusive economic zone of Japan and adjoining areas. These data leads to clalify the active geological process in island arc trench system and the geological and geophysical characteristics of the ridges and basins as the remnant of island arc and back arc spreading of the ocean floor.

References

1. Sato, T. and Oshima, S., "Continental shelf survey project of Japan", Int. Hydrog. Rev., Vol.65, p.41-63(1988)

2. Kasuga, S. and Kaneko, Y., "Transect of the Philippine Sea along 25°N", DELP News, No.26, p.21-24(1988)

3. Katsura, T., Oshima, S., Ogino, T., Ikeda, K., Nagano, M., Uchida, M., Hayashida, M., Koyama, K. and Kasuga, S., "Geological and geophysical characteristics of the southwestern Okinawa Trough and adjacent area", Rep. Hydrogr. Res., No.21, p.21-47(1986)

4. Oshima, S., Takanashi, M., Kato, S., Uchida, M., Okazaki, I., Kasuga, S., Kawashiri, C., Kaneko, Y., Ogawa, M., Kawai, K., Seta, H. and Kato, Y., "Geological and geophysical survey in the Okinawa Trough and the adjoining seas of Nansei Syoto", Rep. Hydrogr. Res., No.24, p.19-43(1988)

5. Kato, Y., Ogawa, M. and Oshima, S., "Stratigraphy of the Okinawa in the area west of Tokara Volcanic Island", Rep. Hydrogr. Res., No.25, p.123-131(1989)

6. Kato, Y., Ogawa, M. and Oshima, S., "Acoustic stratigraphy in the Okinawa Trough", Chikyu Monthly, Vol.11, No.10, p.591-596(1989)

7. Kato, Y., Oshima, S., Takanashi, M., Kato, S., Okazaki, I., Kasuga, S., Hayashida, M., Kaneko, Y. and Seta, H., "Geomorphological and geophysical characteristics around Ryukyu Islands", Chikyu Monthly, Vol.11, No.10, p.597-603(1989)

8. Kato, S., Kedo, K. and Kawai, K., "Mesh shaped structure in the Nanseisyoto Trench and tectonic line of the northern border of the Philippine Basin", Abstr. Seismol. Soc. Jpn., No.1, p.84(1987)

9. Iwabuchi, Y., Nagano, M. and Katsura T., "Geologic Development of Daito Ridge", Rep. Hydrogr. Res., No.21, p.49-64(1986)

10. Kasuga, S., Koyama, K. and Kaneko, Y., "Geomagnetic and gravity anomalies around the Daito Ridge", Rep. Hydrogr. Res., No.21, p.65-76(1986)

11. Kasuga, S., Iwabuchi, Y. and Kato, S., "Results of ocean bottom survey in the area connecting Sikoku Basin with West-Mariana Basin", Rep. Hydrogr. Res., No.22, p.113-134(1987)

12. Nagaoka, S., Uchida, M., Kasuga, S., Kaneko, Y, Kato, Y., Kawai, K. and Seta, H., "Tectonics of the Ogasawara Plateau in the western Pacific Ocean", Rep. Hydrogr. Res., No.25, p.73-91(1989)

MARINE GEOLOGICAL MAPPING PROJECTS OF JAPAN

Y. Okuda*, T. Moritani*

* Geological Survey of Japan

Abstract

Systematic marine geological mapping projects for the marine areas around Japan by the Geological Survey of Japan have been continued since 1974, when the R/V Hakurei-maru (1,821t), a geological and geophysical survey vessel, was constructed by the Japanese Government.

For the mapping projects, seismic reflection profiling survey, various sampling of sea bottom rocks and sediments, and geophysical survey such as gravity and geo-magnetic measurements have been systematically carried out as a routine work.

1. Introduction

Systematic geological and earth scientific investigation and information on the sea bottom of the offshore areas around the country are fundamental for the utilization, development and conservation of marine spaces, which will be more and more closely related to human activity in future. In this regards, the Geological Survey of Japan (GSJ) has been continuing the mapping survey and publication of marine geological maps.

Following several previous primary works of marine geological mapping by small survey boats, the systematic marine geological mapping projects around the Japanese islands by the GSJ started in 1974, when the R/V Hakurei-maru (1,821 gross tonnage), a geological and geophysical survey vessel, was constructed by the Japanese Government.

For the mapping projects, seismic reflection profiling survey and various sampling of sea-bottom rocks and sediments around the Japanese islands have been carried out as routine works in addition to other topographic and geophysical survey.

The first phase of the mapping projects between 1974 and 1978 accomplished publication of a series of regional geological maps (1:1,000,000) which entirely cover the area of continental margin around the Japanese islands. Several maps of this phase clarified the rough geological structures of the Japan, Ryukyu and Izu-Ogasawara Trenches, and the Nankai Trough, which include basic conception of accretion prisms there. Other results, also, revealed tectonic
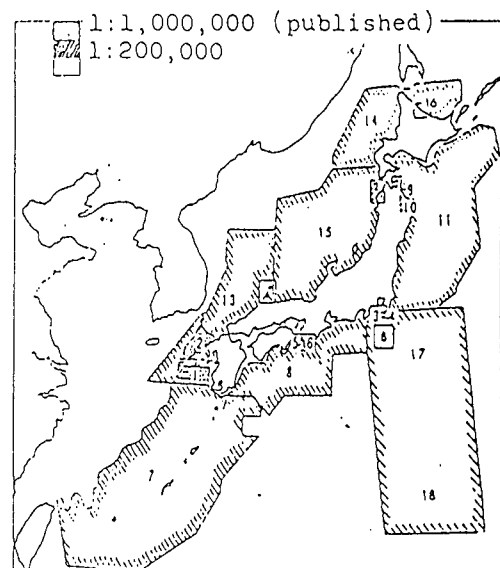
Fig.1 Areas of the marine geological maps for the continental margin of Japan, by the Geological Survey of Japan.

developments of back-arc basins and a part of marginal seas, such as the Okinawa Trough and the Japan Sea. These results were compiled into an offshore geological map (1:3,000,000) in 1983.

Succeeding the above works, more detailed geological mapping surveys at a scale of 1:200,000 have been continued until now, and it is expected to complete the present long term plan in around ten years. The purpose of the survey is to cover the whole area of continental shelf around the Japanese islands in 50 sheets of the detailed geological and sedimentological maps (1:200,000) using the base maps, the bathymetric charts of "Basic Maps of the Sea in Continental Shelf Areas" published by the Hydrographic Department, Maritime Safety Agency, Japan. Several tens of the sheets, mostly off northeastern and southwestern parts of the Honshuu Island, have been already published up to now.

In addition, the Geological Survey of Japan has been co-operating with inter-governmental organizations and several foreign countries for compilation of some offshore geological maps in several other categories to a ten million scale, such as the tectonic maps of the Circum- Pacific Mapping Projects and the sedimentary basin maps of CCOP.

2. R/V Hakurei-maru

The geological survey vessel, Hakurei-maru, was launched in March, 1974 and owned by the Metal Minig Agency, Japan. Since then, she has been chartered by the Geological Survey of Japan, the Deep Ocean Mineral Association, and the Japan National Oil Corporation for investigations of marine geology of the continental margin area around the Japanese Islands, the deep ocean floors of the Pacific Ocean, and the continental margin of the Antarctica.

The particulars of the Hakurei-Maru are as follows;

Length (o.a.)	86.95m
Length (p.p.)	77.0Um
Breadth (mld.)	13.40m
Depth (mld.)	5.3Cm
Draft (mld.)	5.00m
Gross tonnage	1,821.60T

Complement	55
Officers and crew	35
Scientists	20
Service speed	15.00kt
Trial speed	17.78kt
Cruising range	15,000 n.m.
Main engine	3,800ps X 230rpm X 1
Main generator	600 kW X 3
Propeller	
4 Bladed variable pitch type X 1	
Special equipment	Bow thruster 1 set

The vessel has five laboratories as Follows;

No.1 Laboratory : Geophysical laboratories equipped with depth recoder, subbottom profiler, seismic profiler, deep sea television, and others.

No.2 Laboratory : Wet laboratory for chemical analysis and photo-processing.

No.3 Laboratory : Semi-wet laboratory for geological sample processing.

No.4 Laboratory : Dry laboratory for geological sample analysis equipped with soft X-ray, and others

No.5 Laboratory : Geophysical data acquisition and processing laboratory.

The vessel is equipped with five main winches, three cranes, a gantry, and two gallows. These are conventionally used for geological sampling.
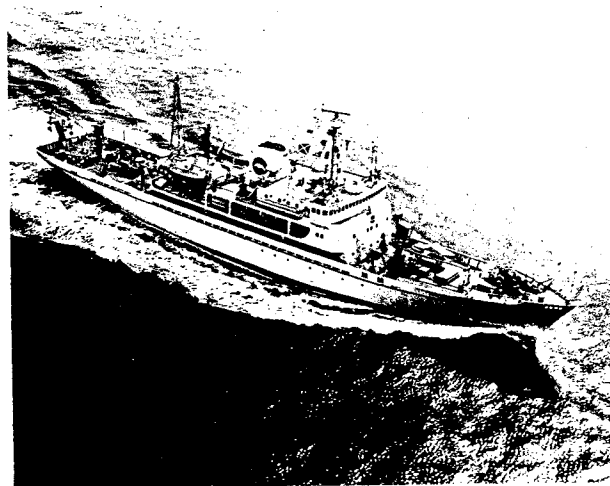
Fig.2 R/V Hakurei-Maru.

3. Survey Methods

For the regional geological mapping at a scale of 1:1,000,000, single channel seismic reflection survey, geomagnetic survey, gravity and sampling mainly by dredger and piston corer were carried out between 1974 and 1979.

The seismic data were obtained along the track lines at intervals of approximate 15 nautical miles. Then sampling sites were decided at suitable points based on the seismic reflection profiles for the stratigraphic correlations (Fig. 3).
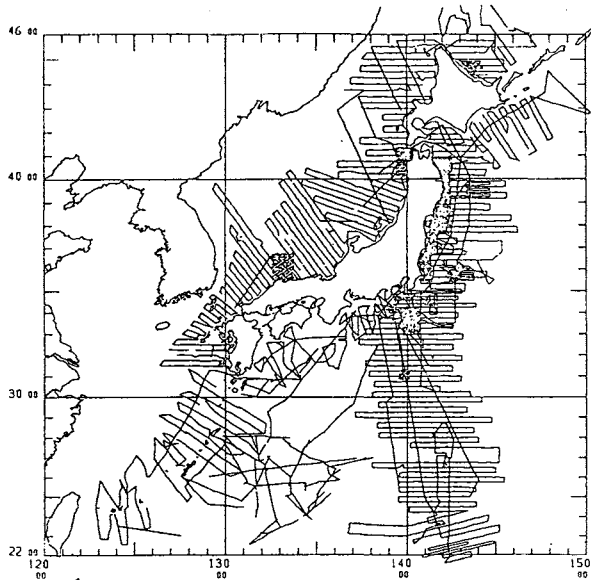
Fig.3 Track lines of the regional mapping survey (scal 1:1, 000,000) of the continental margin around Japan, by the Geological Survey of Japan.

For the deailed geological mapping and sedimentological mapping over laying the bathymetric maps of "Basic Maps of the Sea in the Continental Shelf Areas" (1:200,000), seismic reflection survey, and sampling mainly by grab sampler, dredger, piston corer have been carried out since 1974. Also, shallow marine drillings were carried out at some places by the submercible type rock drills, MD (Marine Drill) 300PT with and operational depth at 300m and penetration of 1m, and MD500H with an operational depth of 500m and penetration of 5 m.

The seismic and other geophysical data have been obtained along grid lines at intervals of two to five nautical miles (Fig. 4). Then, the sampling by grab sampler have been systematically carried out at the grid points with the space of two to five nautical miles (Fig. 5). Judging from these data, sampling by dredger, piston corer and shallow marine drilling have been carried out at suitable points for geological mapping (Fig. 6).
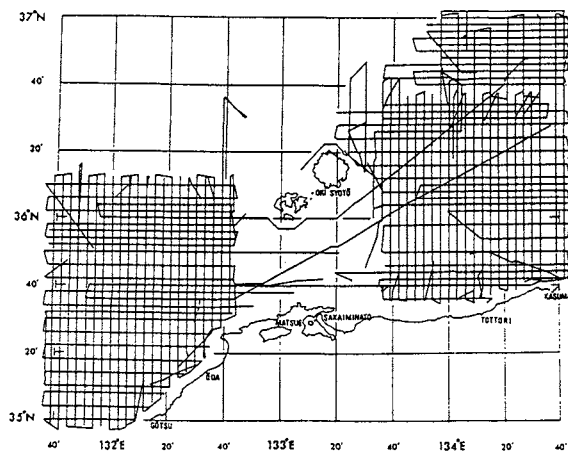
Fig.4 An example of track lines of seismic reflection and other geophysical survey for geological mapping (1:200,000).
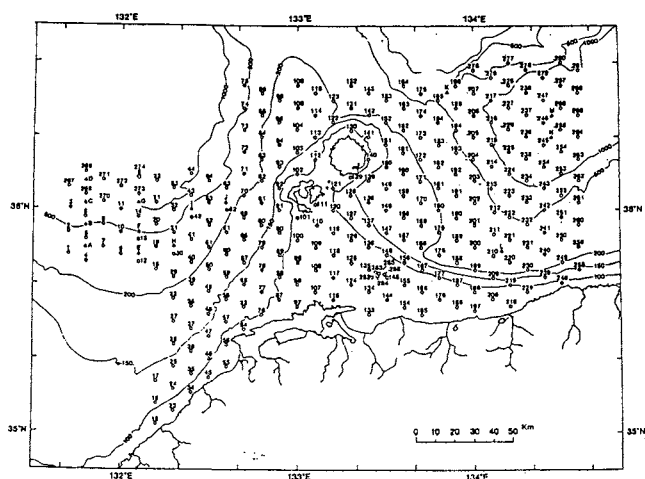
Fig.5 An example of grab sampling sites for sedimentological mapping (1:200,000).
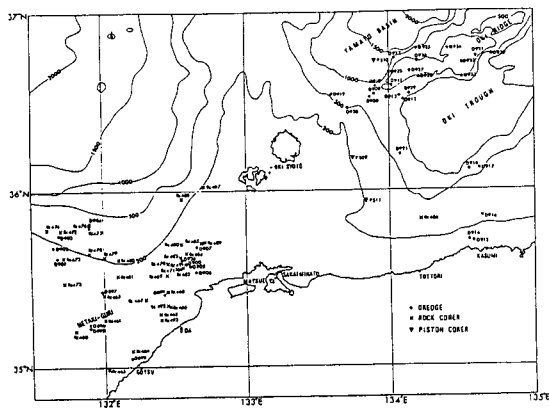
Fig.6 An example of sites of dredge, rock core and piston core sampling for geological mapping.
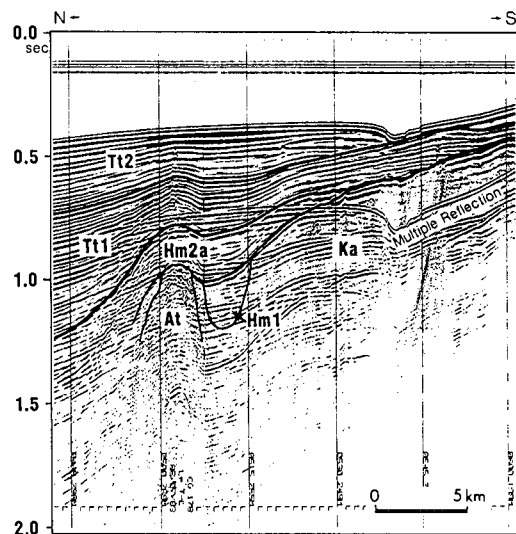
Fig.7 A single channel seismic profile.

4. Examples of the survey results

The single channel seismic reflection survey is convetionally carried out through the cruises to clarify the stratigraphy and geological structures in the sedimentary basins, and multi-channel seismic reflection survey and seismic refraction survey by sono-buoy and OBS are additonally carried out to grasp the physical characteristics such as seismic velocity.

Examples of the single channel seismic reflection profiles obtained off the Tottori area in the Southwest Japan and a multi-channel seismic profile obtained in the Oki Trough area are shown in Fig. 7 and Fig. 8 respectively.

Also, geophysical surveys such as gravity and geomagentic surveys are conventionally carried out through the cruises. Compiled data of the geomagnetic and gravity anomalies are shown in Figs. 9 and 10 respectively.

Various sedimetological analyses of sediments obtained by grab samplers are also carried out on board and in the laboratories. As an example, a soft X-ray photograph for sedimentary structure analyses of the sediment samples, which were taken on board, is shown in Fig. 11.
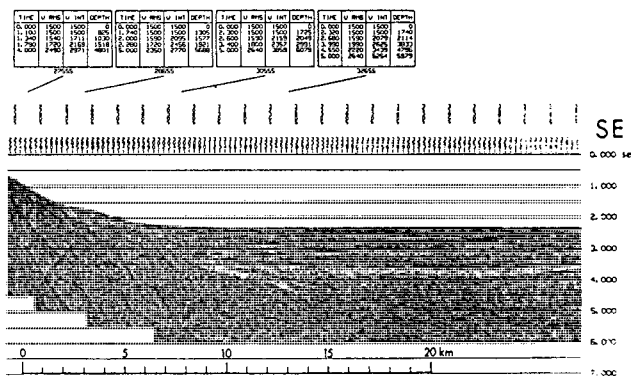
Fig.8 A Multi-channel seismic profile.
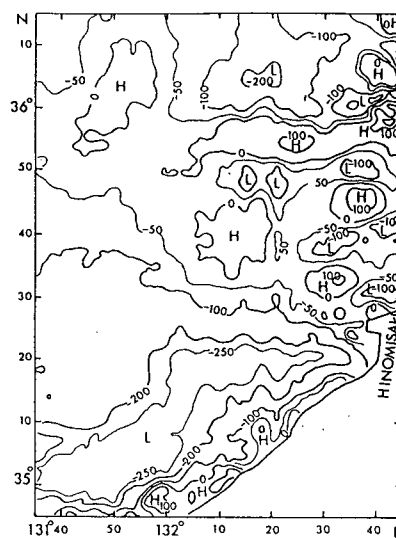
Fig.9 An example of magnetic anomaly map.
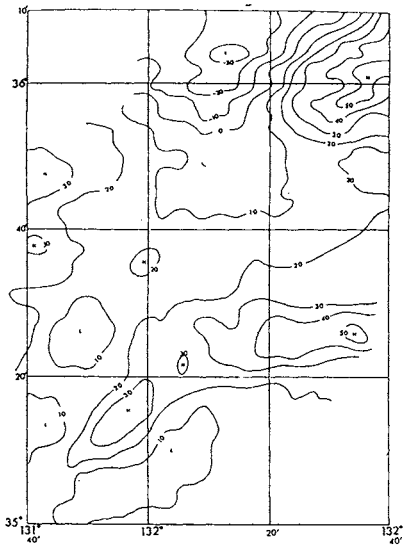
Fig.10 An example of free-air anomaly map (unit: mgal).

RC553

Fig.11 Soft X-ray photograph of a core sample.

5. Cruise Report and Geological Map Series

The preliminary results have been published in the cruise reports of regional geological mapping (1:1,000,000) within a few years after the cruises, and the geological and sedimentological maps have been published several years later. Usually, it takes three years to complete the drafts of the geological and sedimentological maps, and another year to print them out.

The cruise reports for the regional geological mapping (1:1,000,000) were presented in English in a series of the cruise reports (Nos. 5, 6, 7, 9, 10, 11, 13, 14, and 19) published by the GSJ.

The regional geological maps (1:1,000,000) were published in parts of marine geological map series (Nos. 7, 8, 11, 13, 14, 15, 16, 17, and 18. See Fig. 1).

These regional geological maps were summarized and incorporated in a geological map (1:3,000,000) published in 1983 (Marine Geological Map Series, no. 23)

On the other hand, most of the cruise results for the detailed geological and sedimentological mappings in quadrangle areas (1:200,000) have been presented in another series of cruise report written in Japanese by the end of the due fiscal year of the cruises, though several cruise reports were exceptionally published in English (Nos. 2, 3, 19).

The detailed geological and sedimentological maps (1 : 200,000) in quadrangle areas have been published in the series of marine geological maps several years later after the cruises as shown in Fig. 12.

It will take more fifteen years to complete the publications of the whole local detailed geological and sedimentological maps around Japan except Okinawa areas, if the geological and sedimentological survey by the Hakurei-maru for 40 days in a year as the current shiptime period will be secured in future.
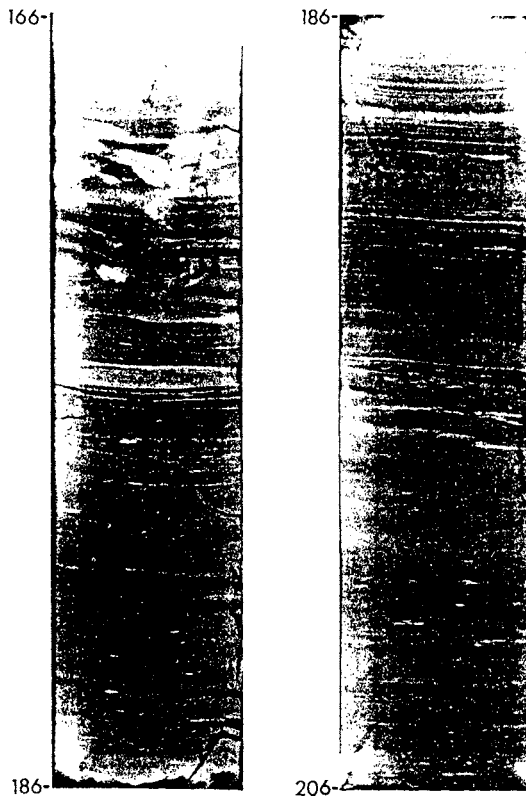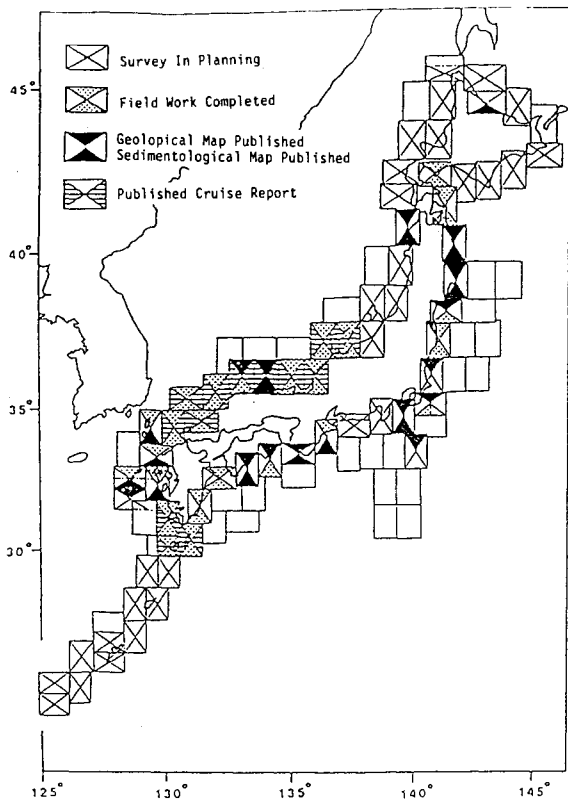
Fig.12 Coverage of marine geological
map (1:200,000) around Japan.

6. Sedimentary basins around Japanese Islands

Though the survey project is under going, above-mentioned geologic mapping surveys have clarified the general geologic settings off the Japanese Islands and the sedimentary basins around Japan (Fig. 13).

Generally speaking, fore-arc basins exist inside of the Chishima (Kurile), Japan, Izu- Ogasawara (Izu- Bonin) and Ryukyu Trenches and the Nankai Trough. At the Nankai Trough, typical accretionary prisms with imbricated structures can be recognized, and other trenches have, also, different types of accretionary prisms.

Complicated basin developments are considered in the areas of the Okinawa Trough, Izu- Ogasawara Ridges and the Japan Sea. These areas have complexed basins of the rifted, inter- -arc, and back- arc basins. Specially, inversion tectonics are recently discussed in the Japan Sea areas, due to the complicated tectonic

changes of the area in the Cenozoic era. While, the Okinawa Trough is considered to be changing from inter- -craton basin to rifted and back arc basins. Such areas are supposed to have high potential of continental types of hydrothermal ore deposits.
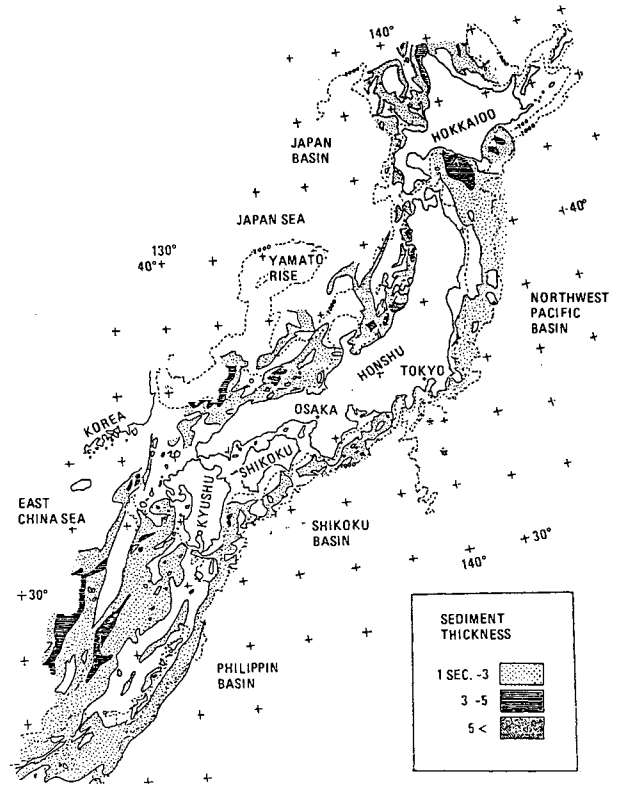
Fig.13 Distribution of sedimentary basins around Japan.

DIGITAL IMAGE PROCESSING TECHNIQUES FOR ENHANCEMENT AND CLASSIFICATION OF SEAFLOOR BATHYMETRY AND SIDE SCAN SONAR IMAGERY

T. B. Reed IV

Hawaii Institute of Geophysics University of Hawaii at Manoa Honolulu, Hawaii, U.S.A.

1. ABSTRACT

The recent growth in the production rate of digital side scan sonar images, coupled with the rapid expansion of systematic seafloor exploration programs, has created a need for fast and quantitative means of processing seafloor imagery. Computer-aided analytical techniques fill this need. A number of numerical techniques used to enhance and classify imagery produced by SeaMARC II, a long-range combination side-scan sonar and bathymetric seafloor mapping system have been developed. Three categories of techniques are presented: 1) pre-processing corrections (radiometric and geometric), 2) feature extraction, and 3) image segmentation and classification. Radiometric corrections include beam pattern/shading corrections, removal of gain changes, and contrast enhancement. Complete geometric corrections are made for towfish pitch, roll, and yaw, plus the cross-track distortion known as layover, caused by violation of the flat bottom assumption. The product of the pre-processing steps is a gridded data-base containing co-registered and corrected side-scan image intensity and seafloor bathymetry. Joint analysis of these two data sets greatly aids in the understanding of the seafloor geology, yielding the capability of discriminating images of similar appearance, but radically distinct geology.

1. INTRODUCTION

Side scan sonars have disclosed the location and, to some extent, the morphology of seafloor features but have provided little of the type of quantitative information necessary for lithologic identification. This quantitative imprecision, in contrast to the successes presently being enjoyed by the terrestrial remote sensing groups, stemmed chiefly from technical hardware problems resulting in a lack of seafloor image fidelity. Now, however, the application of objective digital image processing techniques to images of superior quality and uniformity makes possible a more quantitative approach in the analysis and interpretation of synoptic seafloor imagery.

1.1 The SeaMARC II System

SeaMARC II combines a conventional side scan sonar with a bathymetric mapping system in a single unit towed at depths of 100 m or less at speeds up to 10 knots (5 m/sec) (Figure 1). In water depths greater than 1 km, the system produces 10 km wide data swaths, permitting 100% coverage of over 3000 km of seafloor per day. A complete system description is given by *Blackinton et al.*, [1983].

Two parallel, inclined arrays are mounted on each side of the SeaMARC II towfish. The port arrays operate at 11 kHz and the starboard at 12 kHz to minimize cross-talk. By assuming a nominally flat bottom, and calculating the rate at which the outgoing pulse will have swept the bottom for cross-track distances from nadir to 5 km athwartships, the returning signal is divided into 1024 unequal intervals of time, each representing a 5-m-wide swath of the seafloor. Sampling rates are high for the near-nadir pixels and decrease in proportion to the cosine of the grazing angle. If the seafloor is in fact flat across-track, then this process will produce an image that is geometrically correct in horizontal range, but for ray bending effects. Cross-track topographic variations will however, result in image distortion. Specifics of this type of distortion, and remedies for it, are presented in section 2.

The SeaMARC II bathymetric information is acquired through the same transducers as the side scan data but is processed with different hardware and software. On transmission the transducer pairs on each side of the towfish are driven in parallel. On reception, each row in the pair is sampled independently. Therefore any signal incident upon the transducer at any angle off normal to the transducer face is detected at the two rows with a different phase lag, from which the depression angle θ of the reflector is calculated (Figure 2). By measuring the round trip travel time and assuming a sound speed of 1500 m/s, the slant range R to the reflector can be calculated. These values for R and θ are converted to across-track distance and depth for each reflector and contoured to produce a bathymetric map. Absolute accuracy of 2-3% of the water depth is nominal; relative accuracy is significantly better.
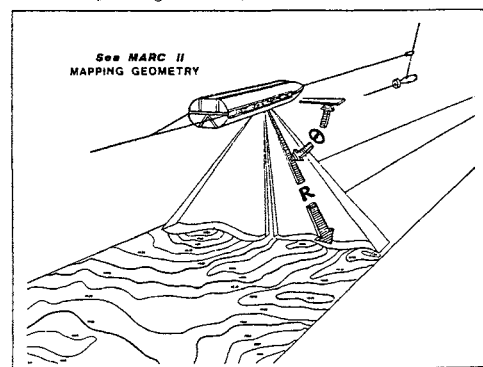
Fig. 1. SeaMARC II deployment configuration. Towfish depth ca. 100 m.

$$\sin \theta = \frac{C}{FD} \times \frac{\emptyset^{\circ}}{360^{\circ}}$$

C = ACOUSTIC VELOCITY
D = ARRAY SPACING
F = SIGNAL FREQUENCY
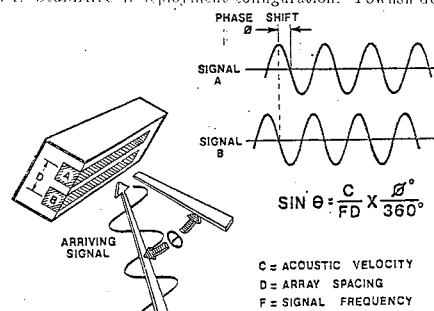
Fig 2. SeaMARC II phase inferometric bathymetry system.

2. PREPROCESSING CORRECTIONS APPLIED TO SEA MARC II DATA

A side scan sonar image is a two-dimensional display of pixels, each with an associated intensity, which attempts to model a physical realization of a four-dimensional process, namely, the interaction of sound with the seafloor. The dimensions of the process are the three Cartesian coordinates of space, which give the position and orientation of any reflector with respect to the sonar, and the fourth dimension of acoustic character (acoustic impedance and roughness). The image is an approximation of the bottom with various sources of errors. Preprocessing corrections should produce an image that is geometrically and radiometrically correct. Being geometrically correct implies that features are in their correct locations and represented by the same spatial distribution of picture elements irrespective of the slant range at which they are imaged. Being radiometrically correct implies that all contributions not indicative of actual changes in bottom acoustic character have been removed. Only when these two criteria are met can meaningful subjective or quantitative interpretations be conducted.

2.1 Radiance Transformations: Background Subtraction

Three radiometric artifacts are common to many side scan images (Figure 3). The first is the irregular band of high intensity pixels nearest to the ship's track (SeaMARC II plots strong reflectors as dark and shadows as light, so the images appears as negatives). The high intensity of these pixels is due to the contribution from near normal incidence specular and subbottom returns, which will only occur within the first few degrees from nadir. The second artifact consists of lines of high-intensity pixels parallel to the ship's track which represent surface reflections of the first bottom echo. The lines nearest the ship's track are peg-leg (down to the bottom, up to the surface, and back down to the towfish again) multiples. Similar dark linear features roughly parallel to the peg-legs but at the outside edges of the image are the first bottom multiples.

The third artifact is the swath of low-intensity pixels parallel to and located approximately 3 km athwartships of the ship's track on the starboard side. This diminution of intensity is caused by an irregularity in the beam pattern, which the angle varying gain (AVG) has not been able to correct. The AVG is designed to correct for beam pattern irregularities and the variation of backscatter intensity due to change in the angle of incidence over a uniform bottom. However, system problems or significant differences between the bottom being surveyed and the bottom from which the AVG was designed can result in severe image degradation.
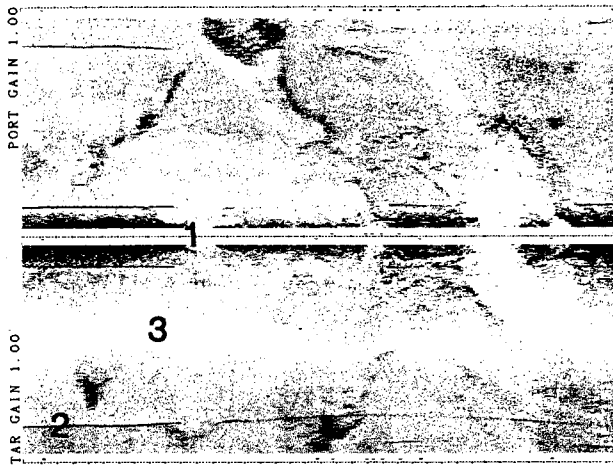
In our method, a parameter set is calculated for both port and starboard sides, consisting of an average pixel intensity (Figure 4a) for strips of the images representing strips of the bottom which would be subtended by 0.25° bins of the beam athwartships. These strips parallel the track of the ship and span the range of angles from nadir to the least depression angle. These averages should be taken along a representative portion of a mosaic so that variations in IV due to local geologic variations will cancel. The transformation is accomplished by multiplying every pixel in the image located at angle increment i by a factor P_i where

$$P_i = \overline{IV}/\overline{IV}_i \tag{1}$$

and $\overline{IV}$ is the average intensity value of the entire image under consideration and $\overline{IV}_i$ is the average intensity at the angle $i*.25°$. Comparison of Figures 3 and 4b shows the result of this transformation. The minimization of the three artifacts is evident, while the true geologic features are minimally affected. We refer to this correction as "background subtraction" as it is largely a correction based upon removal of the average image background.

Our method assumes that variations in pixel intensity due to geologic variability will be randomly distributed relative to the track of the ship and thus add destructively in the average as long as the data set is sufficiently large. As the parameter sets are normalized by the overall average of the image, the gain of the filter is independent of the geology or original gain settings. However, spurious features related to the operating system occur at fairly fixed depression angles, adding constructively in the along-track summation, and yielding estimates of systematically induced cross-track errors. Hence the specular reflections (constrained to near-nadir positions), the peg-leg multiples (constrained to a cross-track distance proportional to twice the fish depth), the surface multiples (constrained to a depression angle of 30°), and the beam pattern variations (by definition a function of angle and ray path bending) will all contribute significantly to the average cross-track profile.
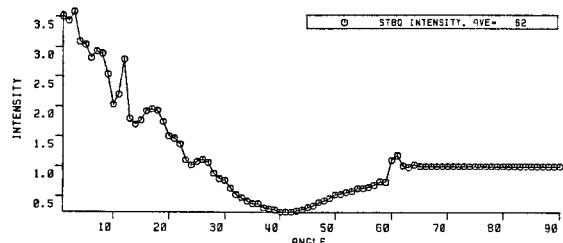
Fig. 4a. Plot of average pixel intensity verses look angle for the starboard half of the image shown in Fig. 2. Number 1 pixel is nearest the ship track. Note peaks at 1°, 12°, and 60° corresponding to the specular reflection, peg-leg, and surface multiples, respectively, and the trough about 42° corresponding to the null in the beam pattern.
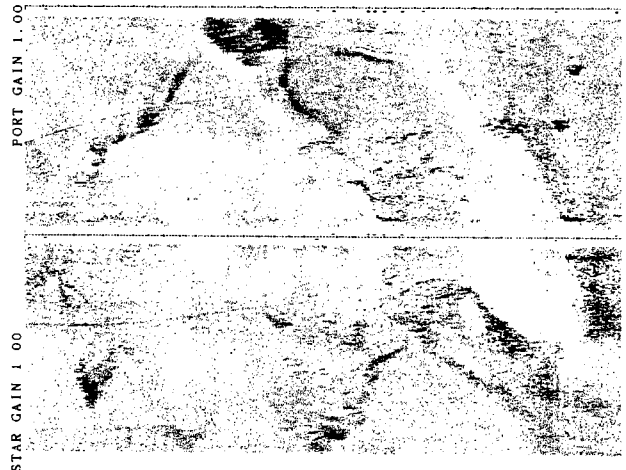
Fig. 4b. Image as shown in Figure 2 after background subtraction. Note removal of specular reflections, surface multiples, and shading problems.

Fig. 3. SeaMARC II side scan image, containing three types of errors: (1) high-amplitude near nadir specular returns; (2) peg-leg and first bottom multiples; and (3) swath of anomalously low intensity pixels on starboard side due to faulty beam pattern.

2.2 Geometric Rectifications: Layover

Layover refers to pixels which have been placed at the incorrect cross-track distance. Reflected side scan data from each "ping" (outgoing pulse) are acquired sequentially in time, i.e., linear in slant range. To convert this cross-track "slant range" image to a plan perspective usually requires that one assume that the bottom is flat across-track. The cross-track positions of the pixels are derived from knowledge of the travel time, approximate sound velocity, and nadir depth. Violation of this flat bottom assumption, as often happens, will result in topographic features being incorrectly positioned, or "laid over" (Figure 5). Thus reflections from points A and B in Figure 5, representing off-nadir troughs and peaks, are erroneously rotated along arcs of radii equal to their slant ranges to points A' and B' on the reference datum and consequently are imaged spuriously. The inward sloping faces of the trough and cliff have been foreshortened, and their boundaries have been misplaced.

Under the flat bottom assumption, side scan pixels are placed at a cross-track distance X equal to $(SR^2+TA^2)^{\frac{1}{2}}$ where SR is the slant range (sound velocity * arrival time/2) and TA is the towfish altitude (reference datum - fish depth). While the cross-track position may be wrong, the slant- range is correct. Our correction of this pixel position error is accomplished by interpolating a smoothed bathymetric profile at 5 m intervals, and determining the side scan pixel for which the slant range equals that of the nearest bathymetry point X,Z. The results of this transformation are shown in Figures 6, 7, and 8. Note how the axis of the valley, which appears curved in the raw image (Fig. 6) has straightened after processing (Fig. 7) to follow the actual morphology, as given by the bathymetry (Fig. 8). An obvious benefit of this rectification is that features are correctly placed on the image for interpretation and survey targeting.

The only assumption required by our layover correction method is that the side scan data be in the correct sequence athwartships, i.e., that there be no reflector at a cross-track distance X and elevation above the reference datum Z such that the travel time associated with it would be less than that for any reflector located at some $X<X$. This "correct sequence" assumption is a reasonable assumption for most geometries and bottom types, considering the relatively high altitude (height above bottom), typically greater than 20% of the swath width, at which SeaMARC II is deployed.

Accurately co-registering the side-scan image with the bottom bathymetry allows us to investigate relations between bottom topographic properties (slope, curvature, roughness, etc.) and image intensity. Figure 9 shows an example of modeling the seafloor surface given by the map in Figure 8 as a Lambertian surface, with a reflectivity given by the square of the cosine of the angle of incidence. While the image lacks significant detail present in the corrected side-scan image, it is clear that the Lambertian model does yield an adequate low-pass
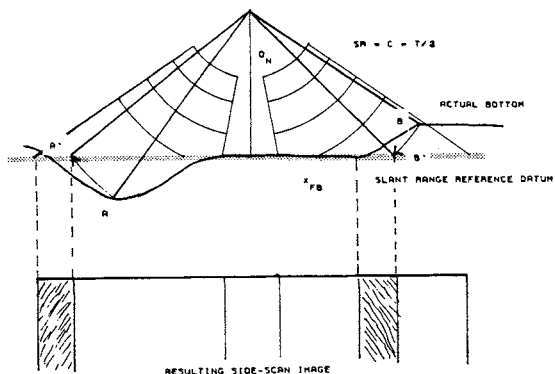
approximation of the component of reflectivity seen in side-scan images which might be due to terrain slope. In Figure 10, we have attempted to deconvolve this terrain slope effect from the side-scan image in Figure 8 by subtracting a portion of the slope amplitude from the side-scan amplitude on a pixel by pixel basis. The benefit of the resulting image is that the image intensity is now no longer a function of viewer position. In Figure 8, the mean image amplitude reverses polarity across the valley axis. It also reverses polarity from port to starboard, across the image centerline. These polarity reversals, due to changes in local angles of incidence, may confuse the observer and obfuscate the true geology. Removal of a portion of these slopes effects, as seen in Figure 10, correctly shows the similarity of the surface across both the valley axis and the track centerline, and allows the dynamic range of the output to be dedicated to geologic, rather than geometric, differences.
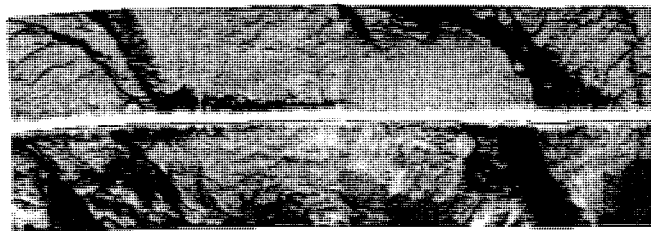
Fig. 6. Unprocessed side scan image corrected for slant range according to the "flat bottom" assumption.
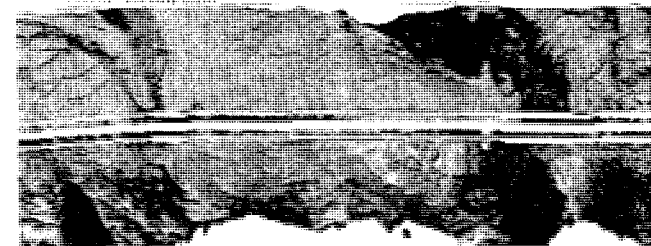
Fig. 7. SeaMARC II image after layover correction, as described in the text.
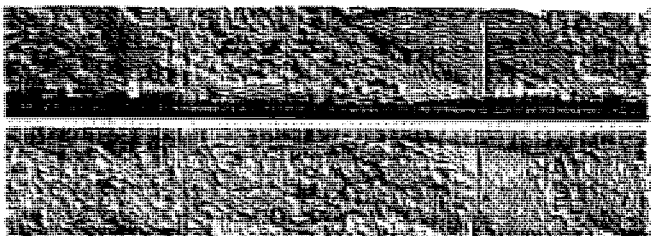
Fig. 8. SeaMARC II bathymetry for the image shown in Figure 6.
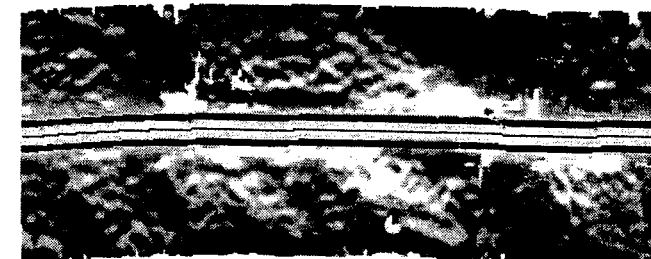
Fig. 9. Synthetic side-scan image, generated from SeaMARC II bathymetry and Lambertian shading.
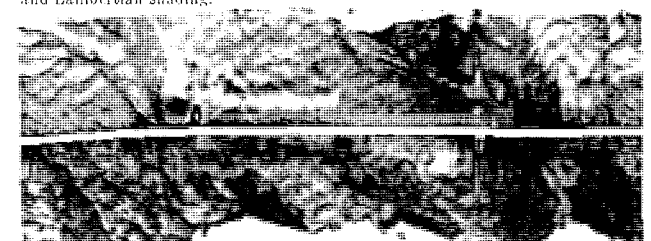
Fig. 10. Geometically corrected SeaMARC II image (fig. 7) minus the slope amplitude contribution (fig. 9).

Fig. 5. Slant range correction geometry. Nominal slant range correction assumes that the bottom is flat (reference datum). Topographic deviations from this reference datum will cause features to be imaged incorrectly, as shown by the compression of the inward sloping faces of the trough and cliff.

3. Feature Extraction

3.1 The Feature Vector

The chief purposes of remote sensing imagery are detection and discrimination. Although human observers are clearly capable of interpreting side-scan sonar imagery, the results are subjective, not necessarily repeatable, and often more indicative of the interpreter than the object. Statistical analysis of image texture provides an objective and repeatable means of identifying, distinguishing, and labeling surface types.

3.2 Texture

Texture is an innate property of all objects, which characterizes the closely interwoven relief of the surface. Texture is strongly stationary and independent of illumination. In this paper, we utilize the gray level co-occurrence matrix (GLCM) method of texture analysis [Haralick et al., 1973].

The GLCM method requires the creation of a secondary matrix from which second-order texture statistics are estimated. Specifically, let $F(x,y)$ represent the digital image over a rectangular domain $L_x = 1,2,...N_x$, $L_y = 1,2,...N_y$, quantized to N_g gray levels. Each GLCM is a square matrix of dimension N, whose entries $S(i,j;\theta,d)$ express the number of times there occurs in the image a pixel of intensity i neighbored by a pixel of intensity j in the direction θ, at distance d. The elements of the matrix are normalized by the total number of possible entries R for that direction and lag.

In order to insure that the texture signature of any given non-isotropic texture is not significantly altered by the angle at which it is imaged, these matrices are evaluated for values of θ equal to $0°$, $45°$, $90°$, and $135°$. Symmetry considerations allow neglecting the respective supplementary angles.

3.3 GLCM Features

Haralick et al. [1973] suggested 14 features which can be extracted from the GLCMs. Four of these statistics, ASM, CON, ENT, and AIDM, have been shown to be strong estimators of wavelength variations and to be insensitive to variations in either look direction or gain settings [Reed, 1987]. ISO, a feature of our own derivation, shows similar characteristics as the above four features. It is calculated as the sum of the differences of orthogonal GLCMs, and is a measure of the isotropy of the image. The means and ranges for these statistics are evaluated for unit lag. The resulting set of statistics forms a feature vector which describes the texture of that portion of the image over which the features were evaluated and by which that section of the image will be classified. To evaluate the texture of an entire image, the image is usually divided into rectangular cells referred to as "texels." To optimize the potential of this texture routine, these texels should contain at least NG^2 pixels, where NG is the number of gray levels to which the image has been quantized [Pratt, 1978] in order to maximize the possibility of measuring real image texture variations.

3.4 Texture Analysis - Applications

A SeaMARC II side-scan image of a submarine lava flow located 200 km NW of Vancourver Island is shown in Figure 11. The surrounding sediments are distal turbidites. The flow is flat-lying, except where it drapes over the fault to the northwest. To classify the image with the above-described texture algorithm, the image was first sub-divided into 2800 texels approximately 250 meters on a side, containing 294 pixels. The pixels in each texel were equal interval re-quantized to 16 intensity levels. Gray-level co-occurrence matrices were evaluated for each texel in four directions at unit lag (ca 40 m), and feature vectors were calculated as described above in 3.3. The 2800 length-6 vectors were classified via an un-supervised modified K-means algorithm [Reed and Hussong, 1989] to yield the 4 class thematic map shown in Figure 12. While the texture map may show us anything we could not have gathered from looking at the side-scan data, it does demonstrate the efficacy of the texture technique, and the numeric values of the texture vectors may yield information on relative surface roughnesses.
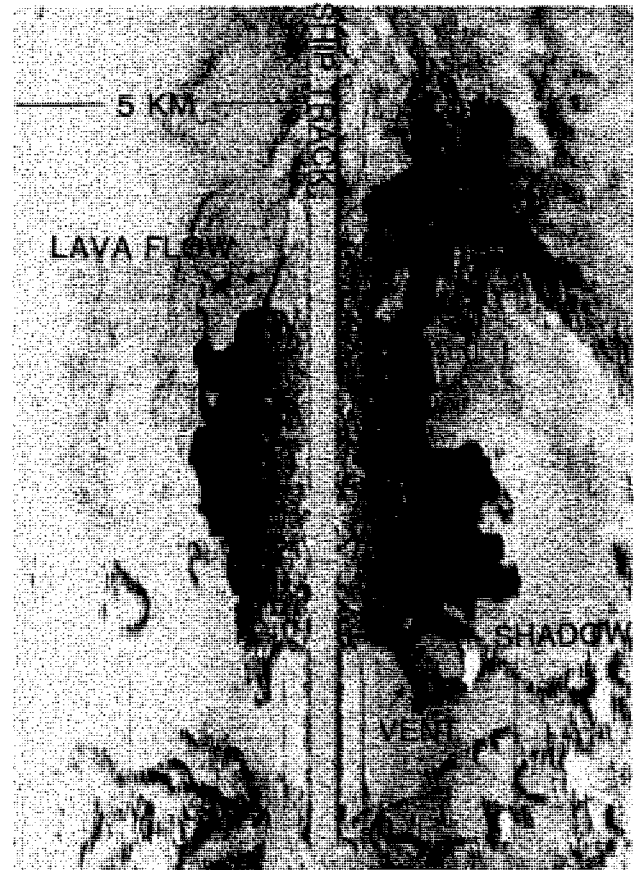
Fig. 11. SeaMARC II side scan sonar image of a lava flow, located 200 km NW of Vancouver. The linear feature in the top right corner is the Queen Charlotte transform fault scarp, with an associated down drop of several hundred m. Note the 100-m vent from which the flow may have emanated and its acoustic shadow.
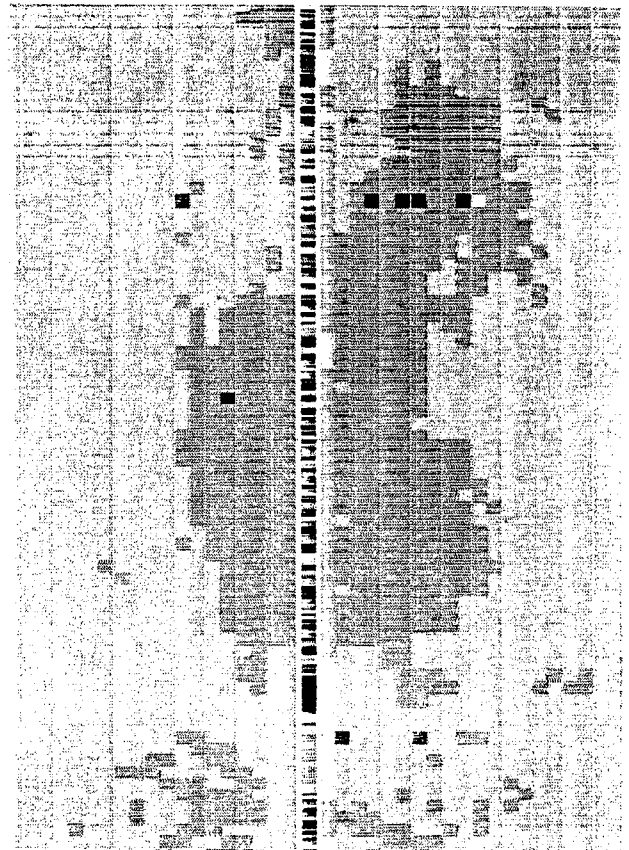
Fig. 12. Four class texture map of lava flow image shown in Figure 11.

The next application of texture analysis better demonstrates the strength of the technique for correctly making discriminations of which the human observer might not be capable. Figure 13 is a composite image, containing images from two separate surveys. The image on the right is half of the lava flow previously seen in Figure 11. The image on the left is of a Miocene dolomite from the Lima Basin, off Peru. The purpose of their juxtaposition in this figure is to demonstrate the difficulty of discriminating rock types on the basis of image intensity alone. The outcrops in each image half radically distinct physical and chemical, and lithologic properties, but they are virtually indistinguishable in the sonar images. Textural analysis can, as Figure 14 shows, distinguish the two. The image data from the two halves were concatenated to yield one digital image, which was subjected to texture analysis as described above for the lava flow alone. The resulting four class thematic map shown in Figure 14 demonstrates that the image of the dolomite is texturally distinct from that of the lava flow, and that the hemipelagic sediments surrounding the dolomite are distinct from the distal turbidites around the lava flow. While we admit that the apparent textural differences could be due to system differences, we note that both images were taken from the same side (starboard), in approximately the same water depth and seastate (ca. 2000 m, SS 2-3), at the same source power level and pulse length. The discriminatory capability remains valuable even if the differences are due partly to the system, as the images on their own are effectively indistinguishable without the texture analysis.

Fig. 13. Composite side-scan image, consisting of Miocene dolomite (left) juxtaposed with lava flow seen in Fig. 11. See text for details.
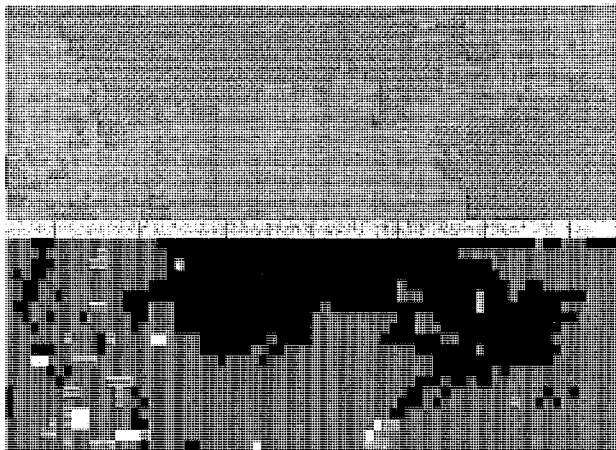
Fig. 14. Texture analysis of the composite image, showing the viability of image texture as an outcrop discriminant.

3.4 Region Growing -- ReGATA

The texel, the basic unit upon which the analysis is based, is assumed to contain a subset of the image data which possesses only one homogeneous texture, providing the texel is sufficiently large to capture the statistical nature of the texture. The probability of textural homogeneity of a randomly placed rectangle increases as the texel size decreases. The texel therefore can neither be shrunk below a minimum size without compromising the statistical validity of the textural analysis nor increased drastically without encountering an unacceptable number of mixed texels (mixels).

Rather than divide the image into a priori boxes which may or may not contain homogeneous patterns, we seek, via data-controlled decisions, a subdivision of the image into closed regions of limited spatial heterogeneity. One feature vector will then be used to represent each closed region. By allowing regions to grow to their natural boundaries, the probability of producing "mixels" is strongly reduced. As the regions will in general be larger than with the a priori texels, classification time will be reduced concomitant with the reduction in number of feature vectors.

The following describes the implementation of Region Growing and Texture Analysis (ReGATA) a bottom-up region-growing routine. SeaMARC II data are stored in records, line-interleaved-by-pixel. Two records, containing two pings of 984 port and 984 starboard pixels, are "read in." The data for port and starboard are subdivided into cells containing two lines of 16 pixels each. The mean intensity and variance are calculated for each of these 32-pixel cells. Two tests are then conducted. The first determines if the cell is reasonably homogeneous, in order to separate the cells into the categories of "region" and "boundary." Those cells which do not pass this test of limited heterogeneity are assumed to span two regions and hence are labeled as boundary cells.

The second test is the basis of annexation and region growing. The mean and variance of the cell under consideration is compared to the means and variances of region cells immediately adjacent in the west, northwest, north, and northeast directions. The logic of the comparison is that if two cells are neighbors and possess similar average value, they probably represent a uniform, connected surface in the object plane and hence should be annexed and similarly classified. As a region grows, its mean and variance are recomputed, and the pixels within the annexed cell augment the four GLCMs associated with the region. Upon closure texture vectors are calculated for all regions.

When the routine terminates at the end of the data file, all remaining open regions are closed by the routine and analyzed for texture. The resulting list of region-numbered, feature vectors are submitted to an unsupervised cluster analysis. The region numbers map the regions to the feature vectors in the clusters, and all pixels in all regions with similarly clustered feature vectors are mapped similarly.

3.5 Application of ReGATA

A SeaMARC II side-scan mosaic of the Alenuehaha channel, located in the Hawaiian Islands between the islands of Maui and Hawaii, is shown in Figure 15. Hand-smoothed 100-m bathymetric contours have been superimposed, along with labels for lithologies identified in goundtruthing efforts. The survey was conducted as part of an effort to determine bottom roughness to guide the placement of a underwater electric cable linking the geothermal power station with the rest of the Hawaiian Islands.

In our application of ReGATA, the side scan image of the channel (Figure 15) was re-quantized to 64 gray levels and subdivided into cells containing 32 pixels, for which the average intensities and standard deviations were calculated. A nonparametric, minimally distant means rule was used for region growing, with annexation occurring if the regions differed in their means by three levels or less. All closed regions containing five or more cells were analyzed for texture and hence had associated with them the six-dimensional feature vector. In the cluster analysis which followed, only those regions containing 100 or more cells contributed to the determination of the class centroids. Those regions containing fewer than 100 cells were then placed into the class from which their feature vector was minimally distant.

Bottom camera photographs and submersible observations allowed the determination of lithologies for a number of distinct image regions. Texture analysis of the image regions corresponding to the locations of the ground-truth data yielded mean feature vectors for use in a subsequent supervised minimum distance classification of the image. The resulting thematic map (Figure 16) containing eight classes, shown here in different tones of gray, corresponding to regions in the image containing the classes of lava flow, calcareous sand, exposed scarp, braided erosional channels, partially covered erosional channels, reef outcrop, sediment covered reef, talus slope, and "other". The final class is to allow for a null classification of those textured regions whose texture signatures exceed two standard deviations of the other defined classes.

While we have yet to be able to deterministically correlate image texture with surface roughness, there is some indication that texture does yield at least a relative measure of roughness. Figure 17 plots two of the components of the texture vector, contrast and isotropy, for the eight identified classes. We have also annotated the labels with estimates of roughness from the groundtruth observations. With the possible exception of the channelled talus slope, the lithologies show an increase in roughness paralleled by increases in the two features. Further work to quantify this proposed relation is clearly necessary, but the beginnings of the quantification of seafloor image analysis have been established.
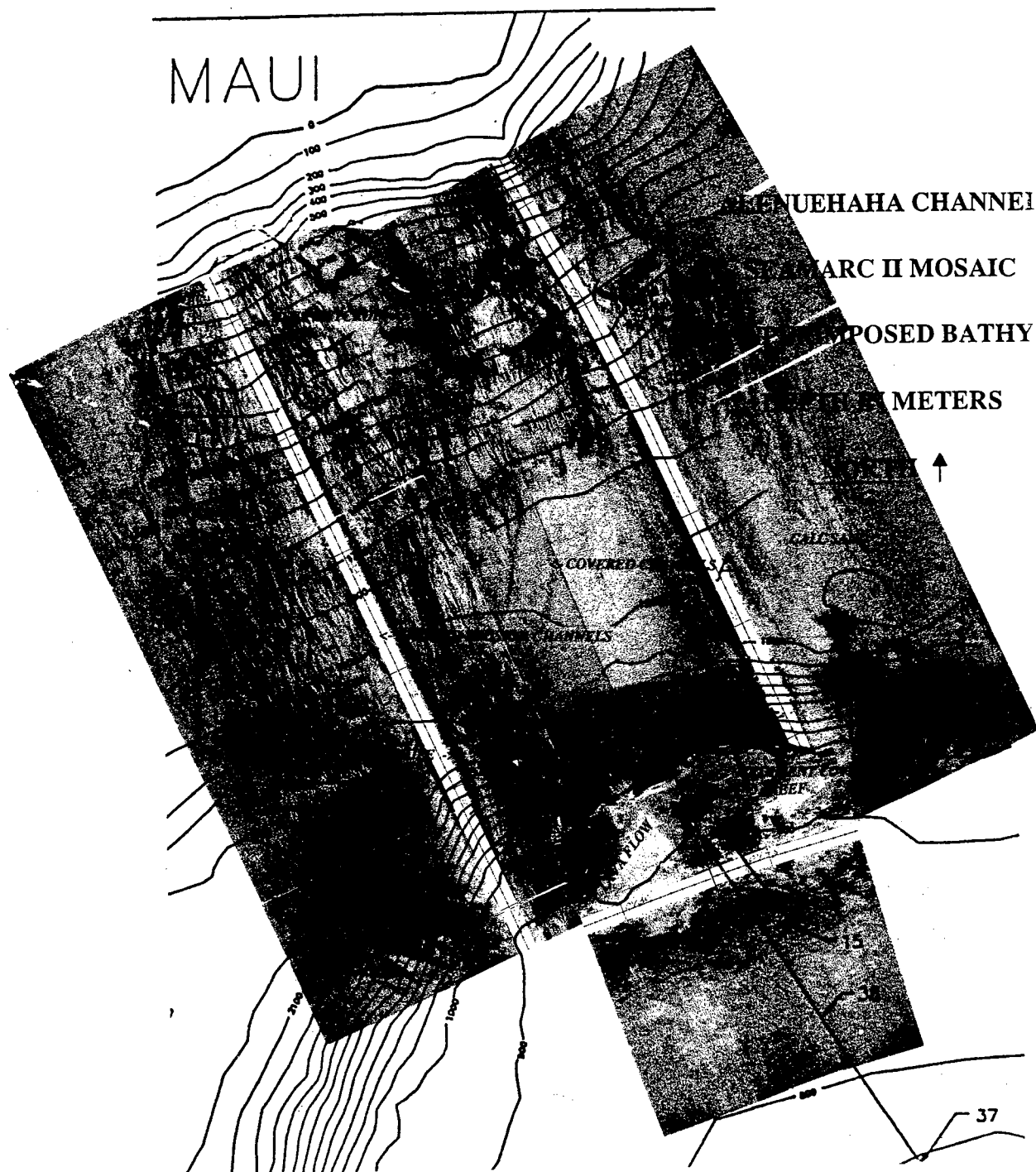
Fig. 15. SeaMARC II side-scan sonar mosaic of Alenuehaha Channel, in the Hawaiian Islands.

Fig. 16. Nine-class ReGATA texture map of the mosaic shown in Figure 15. See text for details.

4. CONCLUSIONS

Application of the above techniques to a variety of imagery resulted in both superior images for subjective and computer-aided interpretations. Although the use of marine acoustic data, which are strongly influenced by the low speed of sound in water and susceptability to ray path variations, is inherently more difficult than processing subaerial optical or radar images, we are confident that eventual increased quantification of seafloor data will permit widespread application of various airborne and satellite remote sensing techniques to the imaging and mapping of the seafloor.
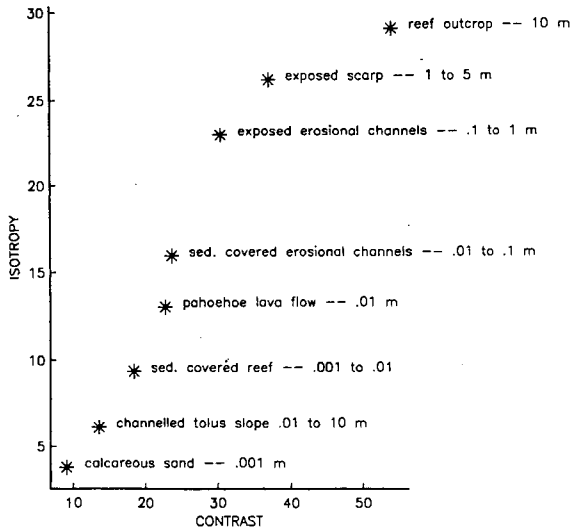
Fig. 17. Plot of two texture parameters (ISO vs. CON) for the eight lithologic classes in the texture analysis of the channel mosaic. Note that roughness, determined from bottom observations, increases with texture strength.

REFERENCES

Blackinton, J. G., D. M. Hussong, and J. Kosalos, First results from a combination side scan sonar and seafloor mapping system (SeaMARC II), in *Offshore Technology Conference, OTC 4478* pp. 307-311, 1983.

Haralick, R. M., K. Shanmugam, and I. Dinstein, Textural features for image classification, *IEEE Trans. Systems, Man, and Cybernetics. SMC-3,* 610-621, Nov., 1973.

Reed. T. B., IV, Digital image processing and analysis techniques for SeaMARC II side-scan sonar imagery, Ph. D. dissertation, Univ. of Hawaii, Honolulu, 1987

Reed, T. B., IV, and D. M. Hussong, Digital image processing and analysis techniques for SeaMARC II side-scan sonar imagery, *Jour. Geophys. Res.,* Vol. 94, pp. 7469-7490, June 10, 1989

USE AND CAPABILITY OF GPS IN MARINE APPLICATIONS

R. Santamaria* - A. Sposito* - S. Troisi*

Naval Universitary Institute- Naples- Italy

ABSTRACT

The paper addresses the aspects and the capability of GPS marine applications namely shipborne GPS applications.

A general view of the range of applications lead to consider at least three major kinds of them according to the required accuracy level.

One common problem to most shipborne applications lies in the mounting of the antenna. When it is mounted above the centre of gravity of the vessel, large antenna accelerations are implied; consequently recurrent cycle slips are produced, so that the precise phase method is strongly limited. Thus in this enviroinment the only pseudo-range method (absolute and relative) can be used. In the same way the mouvements themselves of antenna are wide enough to do not allow a precise determination of mobile trajectory.

Nevertheless to say that high accuracy shipborne applications need further instrumentation.

Finally kinematic applications and results as well as comparisons of kinematic models and some tests are discussed.

Background

The GPS was designed to provide quasi-istantaneous worldwide, all-weather three dimensional position fixes and speed information, plus precise time distribution with an accuracy of between 15 and 25 metres (100 metres under Selective Availablity). It will be used in its most accurate configuration PPS (Precise Positioning Service) by all the military services of USA, by NATO and by very few selected civil users. Otherwise a national and international civil use of the less accurate SPS (Standard Positionig Service) will be also available.

As a matter of fact the single-frequency C/A signal will be released to civil users only.

On the contrary the more precise dual-frequency P signals are destined exclusively for military applications.

Neverthless it also is true that there are potentially many more civil users than military ones requiring both the best possible accuracy and availability for their applications. Thus GPS limitations error sources and coverage limitations do mean a dramatic limitation for higher accuracy requirements in civil applications. Hence it follows that the use of carrier phase measurements instead of pseudo-range ones, the use of differential methods to reduce satellite and propagation errors, the use of

combined of both pseudo-range and carrier phase measurements for enhancing positioning accuracy and the use of integrated systems namely a combined use of GPS with external sensors such as inclination monitors or inertial navigation system, are all together to be considered.

Regarding the state-of-art GPS is expected to have an effettive worldwide 2-d positioning capability by 1990 and an effective 3-d positioning capability in 1993 just when with 21 satellites (18 satellites and 3 spares) the constellation will be declared fully operative. Finally it may be expected that the constellation will assume a definitive 24 satellites configurations in 1995.

1. GPS Marine Applications

1.1 - In marine applications besides considering requirements of accuracy, safety considerations as well as economic aspects also need to be contemplated.

Altough it is not possible to "closely" define the true concrete limit of required accuracy for each of marine applications a general view of their variety leads to consider at least three major kinds of them just according to the demand of accuracy level.

Following this "course" marine applications should be subdivided into: navigation in open waters, coastal channel navigation and hydrographic surveying.

Yet since the emphasis in the following will be on GPS marine applications namely shipborne applications, it will result more convenient to arrange the demanded accuracies along with achievable accuracy levels by using GPS.

1.2 - In such a way the shipborne applications can be subdivived as follows:

I - Low accuracy applications: tipically require 20 m to 30 m (1σ) they can be handled by absolute kinematic positioning model that is by a single receiver using pseudo-range measurements.
Thus the following shipborne applications will be fully satisfied in their demanded accuracy.

i) Navigation in open waters.
Most navigation tasks in oceanic phase are essentially represented firstly by skill to individuate and therefore to avoid possible hazards along the navigation path, in second place by providing accurate fixes in order to realize the shortest and safest route and consequently reducing strongly both transit time and operating cost.

In any case the accuracy level for safety corresponds to 1÷2 Km (1σ).

ii) Coastal channel navigation.
This navigation may be considered as that phase of it developing into coastal area and it will be required accuracy level for safety and search operations around 230 m (1σ); it also will correspond to 75 ÷ 100 m (1σ) in those particular cases obtaining benefits in resource exploitation.

II- Medium accuracy applications require 5 m to 10 m (1σ) they make use of the differential kinematic pseudo-range model. The following shipborne applications can satisfy their required accuracies.

i) Setting buoys. The accuracy range for setting navigational buoys is established with a tollerance from 10 to 30 m.

ii) Hydrographic surveying.
It is estimated that accuracy levels of 5 m in the immediate coastal area and 8 m in the areas out to approximately 100 miles are required respectively.

In addition to these applications it is worthy to contemplate.
iii) Narrow channel navigation.
Considering difficulties for large vessels to manouver quickly the accuracy for navigation in such environment is required exstremely high; actually accuracies of 4m to 10m are estimated necessary.

iiii) Harbor to harbor approach phase and river navigation.
Even large oceanic going ships navigate in harbors and rivers and given either their inability to alter course or stop quickly or likely congested areas, here navigational requirements for safety are 4 m to 10 m (1σ) as well; in particular for river navigation the requirement is for continuous 3 m to 5 m accuracy relative to the centre of the channel.

Nevertheless to say that except just few cases generally shipborne applications require the determination of fix and velocity in _real time_ thus a data link must be established between the GPS reference station and the user (also known as Differential data links) when real time differential kinematic positioning modes are employed.

III- High accuracy applications require tipically 0.5 m to 2 m (1σ). They can be handled by using either differential phase, differential combined, or differential integrated kinematic model.
Typical shipborne applications requiring the above said accuracy range are given as below:

i) Oil rig moves.
As regarding to oil rig moves two distinet steps have to be considered. The first step is marked by manoeuvring operations to get the establishedlocation. Theother one is represented by checking the final position and obviously the accuracy level required is much higher in this case.
The interesting areas are usually covered by radionavigation systems. Unfortunately, however the radionavigation systems of high accuracy and reliability have very limited range and need installation and maintenance of shore stations therefore the possibility of using satellite navigation systems allowing precise positioning are considered carefully.
At the time of writing the final position is obtainedby TRANSIT differential technique

(translocation technique) which requires, however, a 2 days period in addition to a post-processing phase to assure the accuracy demanded. Then it is clear the huge advantage when using a real time differential system as GPS. Indeed the use of GPS will enable the users not only to perform a real time differential system but also to achieve a 2 m accuracy level when averaging just after a one hour period.

ii)Three dimensional seismic surveys and gravity surveys.
Really GPS will have an impressive impact on the effectivness of shipborne applications such as geophysical surveys which could not be fittingly handled by conventional instrumentations.
The seismic gravity or magnetic data being recorded have no meaning without precise knowledge of the position where these data were acquired. In addition gravity data acquiring also demands precise knowledge of ship's motion to compensate for motion-induced accelerations. Not long ago an accuracy range of 50 to 100 m was considered enough sufficient provided that the relative positions of seismic data points along the ship's path were known to 2 ÷ 5 m. Nowadays there is a requirement for continuous navigational accuracy around 2 ÷ 5 m (1σ).
At the same way velocity accuracies of 10 cm s_{-1} or also better are required in marine gravity surveys in order to bound error in the Eotvos correction below 1 m Gal.

2. - Kinematic positioning models.

Only a brief overview of model equations is given as one can found detailed descriptions including mathematics elsewhere [3], [7].
The following model equations as addressed below may be considered in shipborne applications.

A. - Absolute pseudo-range kinematic positioning model

$$p = \rho + c(dt - dT) + d_{ion} + d_{trop} + d_\rho \qquad (1)$$

B. - Differential (relative) kinematic positionig models

B1. - Pseudo-range model

$$\Delta p = \Delta \rho - c(\Delta dT) + \Delta d_{ion} + \Delta d_{trop} + \Delta d\rho \qquad (2)$$

B2. - Carrier phase model

$$\delta\Delta\phi = \delta\Delta\rho - c\delta\Delta dT - \delta\Delta d_{ion} + \delta\Delta d_{trop} + \delta\Delta d\rho \qquad (3)$$

C. - Combined differential (relative) kinematic positioning model.

In this case both model equations (2) and (3) are utilized together.

D. - Integrated differential (relative) kinematic positioning model
External sensors can be used to aid GPS such as inclination monitors, ship's log and gyro Mini Ranger, and also Inertial Navigation Systems (INS$_s$).
In each of equations the quantities shown represent:

p, ρ : pseudo-range observation and geomet-
        ric distance respectively, between
        satellite and receiver

dt, dT : clock errors of satellite and receiver respectively; both are expressed in seconds

$d_{ion}, d_{trop}, d\rho$: range errors due to ionospheric refraction, tropospheric refraction, and to inaccurate ephemerides respectively, all of them expressed in metres.

c : is the speed of light expressed in metres/sec.

Δ : single differences between two receivers namely reference station and mobile user

δ : single differences between epochs.

2.1 - Benefits and limitations.

In the model A the two main limitations on accuracy are due to orbital and atmospheric effects. Even if it will be possible to remove ionospheric effects by using dual frequency signal unmodelled ionospheric effects contribute strongly to the error budget. A standard model can be used as far as tropospheric effects computing.

By contrast the satellite clock error which can be assumed known as computed from the broadcast message of navigation is pratically ignored in the equation.

However it has the huge advantage to enable a real time navigation by using only one receiver.

Unfortunately either for the prospected reduction of accuracy due to introduction of both Selective Availibility (SA) and Anti-Spoofing (A-S) or for too high noise level in pseudo-range measurements the method is limited to low accuracy applications.

In differential (relative) kinematic positioning models the advantage of removing or greatly reducing common or correlated errors such as selective availibility, satellite clock errors, satellite ephemeris (orbital) errors, and atmospheric errors, between a known static reference station and a mobile remote user, is attained. Any instantaneous change determined continuosly by GPS in the coordinate values of reference station can be monitored and transmitted as corrections to the mobile user namely GPS navigator.

When phase measurements are used a noise level two order of magnitude smaller than pseudo-range measurements is yielded [7] so even better accuracy is achievable. In any case the absence of cycle slips is needed. Just the solution of the cycle slip problem presents particular difficulties in shipborne kinematic positioning applications.

Therefore to control positioning errors produced by cycle ships, pseudo-range measurements are combined whith phase measurements so all of the adavantages of differential technique are preserved and C - model equation is produced. Several and sometimes sophisticated methods have been proposed and tested. One must however realize that the detection of cycle slips will be made obtainable by filtering technique provided that they are not correlated with errors in the pseudo-range measurements.

3. - Antenna mounting and multipath in shipborne applications.

Most experiences have verified that cycle slips occur frequently during acceleration and deceleration periods.

Then the antenna mounting becomes considerable enough. Actually when it is mounted above the center of gravity of the vessel, large antenna accelerations are implied, consequently reccurrent cycle slips are produced so that the precise phase method

is strongly limited. Thus in this enviroinment the only pseudo-range methods A and B1 (absolute and differential pseudo-range methods) can be used in real time shipborne applications namely in navigation. In the same way the mouvements themselves of antenna are wide enough to do not allow a precise determination of vehicle's path.

In any case if the antenna is shaded and loss of phase lock regards one satellite only the accuracy level is determinated by the strength of the geometry of remaining satellites. On the other side if loss of phase lock concerns all satellites simultaneuosly, a discountinuity of vehicle's measured path will be implied.

The integrated model in addition to the advantages of previous models so far examined will allow not only to overcome the cycle slip problem but also to yield better overall trajectory; in fact by time difference phase more and better reliable informations on the change in vehicle's position between consecutive epoch are attained.

3.2 - Multipath

GPS limitations, among others, depend on multipath and imaging effects which in shipborne applications may be considerable because of metal superstructure of a ship. Hence design of antennas along with development of techniques for strongly minimizing indesiderable effects produced must be taken into account.

By contrast use of antennas with high-gain near the horizon is required to reduce satellite outages. On the ground of recent results the conical spiral antenna seems to suit particularly for shipborne applications as to positioning problems.

As for the type of measurements a rule of thumb establishes that multipath effects are about 10% of the signal wavelength thus code measurements are affected more than carrier phase measurements [3].

Cases such as the total loss of overhead satellites signal and the situation with less than four satellites in view due to terrain shading are both examples in which the use of C- model can be well suited to handle them. Yet with a potential loss of phase lock on all satellites simultaneously the C - model use can't greatly improve the accuracy more than that achievable by B - model namely about 3 m with P - code and 10 m with C/A - code [4].

4. - Experimental results.

It is worthy to emphasize that when using GPS in differential mode, however accuracy level also depends on length of baseline namely there will be a degradation of accuracy as the distance from the ground reference station increases.

Neverthless with a geometrically strong network of reference stations an accuracy level of the order of a few metres should be assured over an area the size of the North sea.

Results coming from a differential GPS test conducted to verify the final position of an oil rig move show an accuracy less than 2.5 m (1σ) with a baseline of some 200 miles, as well as a better accuracy around 1 m is attained with a very short baseline [2].

Another marine experiment [9] confirms an accuracy of 2 m in each of two horizontal compenents.

A particularly interesting shipborne application either because it was realized under various sea states or because of the suitable software employed is the test conducted, with a 10 m hydrographic survey

launch, by Lachapelle et al. [5]. The velocity of the launch was 15 knots and the wind reached also 20 knots during the trials. External accuracies (rms) of 2 m or better in each of two horizontal components were attained.

5. – Conclusion.

The use of external sensors becomes necessary to realize higher degree accuracies and greater reliability in shipborne applications. Moreover integrated GPS/INS (Inertial Navigation System) system even if more expensive and complex than other integrated systems is, however, the most reliable just for it enables users to realize both precise interpolation between GPS fixes and accurate velocity informations.

Altough higher accuracies of the order of tens of centimetres have been declared possible to yield by many authors; test results at present do not confirm these hopes. Indeed at least two important aspects have to be examined in our opinion.

Firstly it is worthy to emphasize that imaging to achieve the above said accuracy order only by using more and more sophisticated mathematical models and filtering techniques would be fully useless without planning both the feasibility of a further reduction of error sources-due to atmospheric and ephemeris effects- and above all the elimination of frequent losses of phase lock.

Secondly the present poor number of GPS satellites do not allow completely realiable experimental trialsat sea. In addition the shortness of periods, during which kinematic positioning models should be employable restricts strongly their diffusion, so the potential market is at its turn dramatically limited and differential kinematic models for example are used mostly to calibrate other radionavigation systems.

REFERENCES

1. CANNON M.E., SCHWARZ K.P., WONG R.V.C., 1986. Kinematic positioning with GPS an analysis of road tests. Proceedings of fourth International Geodetic Symposium on Satellite Positioning. The University of Texsas at Austin, pp. 1251- 1267.
2. HERVING K., 1989. Diffstar a differential GPS System in the North Sea, Proceedings of NAV 89, Satellite Navigation RIN, LONDON October 1989.
3. KING R.W., MASTERS E.G., RIZOS C., STOLZ A., COLLINS J., Surveying with GPS. The University of NSW, Kensington, NSW AUSTRALIA.
4. LACHAPELLE G., FALKEMBERG W., CASEY M., 1986b. Use of phase date for accurate differential GPS kinematic positioning. Proceedings of PLANS '86 I.E.E.E.
5. LACHAPELLE G., FALKENBERG W., CASEY M., KIEMMAND P. 1989. Hydrostar: A computer Program for accurate GPS Real-Time Kinematic Differential Positioning. Lighthouse, Edition 39, Spring 1989, CANADA.
6. Radio Navigation Systems Economic and Planning. Analysis, Final Report. Volumes 1, 2 and 3. Prepared for Office of telecommunications Policy by Computer Sciences Corporation, 1977.
7. SANTAMARIA R. 1985. La tecnica interfonometrica applicata ai satelliti GPS - Atti, Torre del Greco -I-.
8. SANTAMARIA R., SPOSITO A., BUONOCORE B., 1990. Il Posizionamento di precisione ed il GPS - Istituto Italiano di Navigazione - ROMA.
9. SEEBER G., SCHUCHARDT A., WUBBENA G., 1986. Precise positioning results with TI4100 GPS receivers on moving platforms. Proceedings of Fourth International Geodetic Symposium on Satellite Positioning, the University of Texas at Austin, pp. 1269-1285.

TSUNAMI AMPLITUDES FROM LOCAL EARTHQUAKES IN THE PACIFIC NORTHWEST REGION OF NORTH AMERICA

G. T. Hebenstreit*, T. S. Murty**

* Science Applications International Corporation, Virginia, U.S.A.
** Institute of Ocean Sciences, Sydney, British Columbia, Canada

Abstract

Maximum tsunami amplitudes that will result from major earthquakes in the Pacific Northwest region of North America are considered. The modelled region encompasses the coastlines of British Columbia, Washington, and Oregon. Three separate models were developed for the outer coast and one model for the system consisting of the Strait of Georgia, Juan de Fuca Strait, and Puget Sound (GFP model). Three different source areas were considered for the outer coast models and the resulting tsunami was propagated to the entrance of Juan de Fuca Strait. Using the output from the outer models, the GFP model was run. The results showed that large tsunami amplitudes can occur on the outer coast whereas inside the GFP system, unless the earthquake occurs in the system itself, no major tsunami will result.

1. Seismological Background and Historical Tsunami Data

The Cascadia subduction zone lies off the west coast of the North American continent. It extends from the Mendocino fracture zone (roughly 40°N) to the Queen Charlotte Sound region of British Columbia (roughly 52°N). The Cascadia subduction zone is actually made up of four features: the Gorda South Plate, the Juan de Fuca Plate, the Explorer Plate, and the Winona Block. The boundaries between each of these sections consist of transverse fracture zones running seaward from the continent. A series of ridges mark the western extent of the Juan de Fuca Strait region.

In recent years, considerable controversy has arisen as to the tectonic nature of the Cascadia subduction zone. The basic question is whether or not the region can be considered to be a true subduction zone in which the oceanic (Juan de Fuca) plate is being driven downward under the denser continental (North American) plate. Initially, this question might seem puzzling since the historic record for the Pacific coast in this region contains almost no evidence that large ($M_s > 7.0$)

earthquakes have occurred. Earthquakes of this magnitude are typical of active subduction zones. Indeed, the lack of such evidence has removed the Juan de Fuca Plate region from consideration for many years, as a subduction zone.

In the past decade, however, a number of papers have been published which examine this very question. None of these papers really provide a definitive answer, but many of them provide a line of argument which makes it difficult to dismiss out of hand the possibility that active subduction is indeed taking place in the Juan de Fuca region. A series of papers (Heaton and Kanamori, 1984; Heaton and Hartzell, 1986, 1987) discuss the full range of the arguments, as does the paper by Rogers (1988). Although the skeleton of the arguments in favour of subduction will be presented here for completeness, the reader is urged to examine the reference provided for more detailed explanation.

In general, the argument in favour of subduction can be summed up by saying that various characteristics of the region conform more or less closely to the characteristics found in other, more active, subduction zones throughout the world. Such features as the relatively shallow offshore trench system, the lack of strong, free-air gravity anomalies, the presence of active Quaternary volcanoes, the seismic quiescence in the area, the reported convergence rate of the plates, and even the young age of the presumably subducting lithosphere can all be found in other young, strongly coupled, seismically active subduction zones in the Pacific basin. The fact that very large subduction earthquakes ($M_w > 8$) have occurred in other, similar subduction zones, makes it logical to speculate that earthquakes of that magnitude could also occur over quite long recurrence times in the Cascadia subduction zone (Heaton and Hartzell, 1986).

As indicated above, the arguments for the existence of the Cascadia subduction zone are compelling, but not conclusive. However, one fact is inescapable. If the area does indeed have the potential for experiencing large thrust earthquakes of the sort associated with

active subduction, then a major seismic risk is posed for the western regions of Canada (Vancouver island) and the United States (Washington and Oregon). A number of major cities (Vancouver and Victoria, British Columbia; Seattle and Tacoma, Washington; Portland, Oregon) are located close enough to the Cascadia subduction zone so that a major or great earthquake could cause severe ground shaking. Such an event would probably be quite catastrophic in heavily urbanized areas.

A second, less generally recognized, seismic hazard also exists, however. Large or great thrust earthquakes occurring under the sea surface always pose the threat of generating local tsunamis. These waves could be quite destructive in both large and small population centres along the shore. The purpose of this study is to examine two facets of this threat: (a) that posed to the outer coasts of Canada and the United States as the result of possible earthquakes in the Cascadia subduction zone and (b) to examine the tsunami threat to the GFP region.

Tsunamis are long, surface gravity waves generated by the sudden displacement of large volumes of water. The displacement is usually caused by thrust-type submarine earthquakes, although coastal landslides, submarine slumps, and volcanic eruptions have also produced tsunamis. The mechanism can be pictured quite simply. If the bottom moves upward, it pushes with it a volume of water that rises above the rough equilibrium state known as mean sea level. The ocean surface cannot support this 'bulge', but instead starts to return to equilibrium. The result is that surface waves begin to spread outward from the site of the disturbance. If the volume of water disturbed is very large, as is often the case in thrust-type earthquakes, the waves leaving the source will have very long wavelengths and will be able to propagate long distances and still retain significant portions of their initial energy. As the waves, which move very quickly in the open ocean, reach shallow water, they begin to slow down. A portion of the energy which had been propagating horizontally is converted into vertically directed energy. The result is that the waves begin to grow and can reach extreme heights by the time they reach the shoreline. If enough energy was pumped into the waves at the source and if the transition from deep ocean floor to shallow coastal waters is rapid enough, the waves striking the coast can be terribly destructive.

The threat from a tsunami is always two-fold. Coastal areas close to the source are always at risk since the waves which propagate into and along shore do not have time to lose much of their energy. Distant areas can also be at risk from the extremely large events which generate waves with enough initial energy to survive a basin-scale travel path. The tsunami events which produce destructive waves on a basin-wide scale are the most commonly known, but in truth, local tsunamis have historically caused more death and destruction since even a small (in terms of wave length and energy) tsunami can be a threat near the source area.

The historical record contains a number of incidents in which significant tsunami wave activity was recorded along the North American coast as a result of distant tsunamis. Because the coastal network of tide stations operated by the U.S. National Ocean Service (NOS) has only been expanded in the years since World War II, most of the data available dates from 1946. From 1946 to 1964, a total of five destructive distant tsunamis produced measurable wave heights in coastal areas around the Cascadia subduction zone. It should be noted that reported wave heights are taken from tide gauge records, which tend to underestimate extreme wave heights. Also, the gauges tend to be widely scattered and cannot provide a true picture of the pattern of water level along any given stretch of coast.

Table 1 shows maximum tsunami wave heights for a number of locations along the Pacific coast in the Cascadia subduction zone. The events listed occurred in a variety of locations. The April 1946 tsunami was generated by a fairly small earthquake (M = 7.4) in the central Aleutian Islands. The November 1952 tsunami originated off the Kamchatka Peninsula in the Soviet Union. The March 1957 tsunami came out of the eastern Aleutians. The May 1960 tsunami was generated by a major earthquake off southern Chile. The March 1964 tsunami was generated by the Prince William Sound (Alaska) earthquake. The first three events did little damage along the British Columbia, Washington, Oregon, and northern California coasts. The 1960 event caused surprisingly considerable damage in Crescent City, California. It is clear that the 1964 event, whose source was closes to the study area, caused much damage in both the United States and Canada.

It is clear from this sampling of historical data that the coastline bordering the Cascadia subduction zone can be susceptible to tsunami damage. Hebenstreit and Bernard (1985) showed that coastal submarine topography plays a major role in determining how tsunami energy is distributed along any stretch of coastline. With the exception of Crescent City, distributions have been roughly uniform along the entire coast. This would indicate that incoming energy from locally generated tsunamis would also spread out fairly evenly along the coast.

The historical record for local tsunamis in this area is almost non-existent. This is not surprising in view of the lack of seismological evidence for major earthquakes. Soloviev and Go (1984) described briefly two or three small tsunamis which apparently were generated by earthquakes on Vancouver Island and the Queen Charlotte Islands. None of these tsunamis caused any significant damage. Lockridge and Smith (1984), in their chart of tsunamis in the Pacific Ocean, show a large earthquake and tsunami generated in the Strait

Table 1. Maximum recorded wave heights (m) along the Pacific coast for five tsunamis.

Location	1946	1952	1957	1960	1964
Tofino, British Columbia	0.57	0.60		1.38	2.43
Port Alberni, British Columbia					>5.10[a]
Victoria, British Columbia	0.21	0.36			1.44
Neah Bay, Washington	0.36	0.45	0.30	0.72	1.41
Friday Harbor, Washington				0.18	0.69
Seattle, Washington					0.24
Astoria, Oregon			0.15	0.30	0.72
Crescent City, California	1.77	2.04	1.29	3.27	>3.90[b]

[a] Gauge record incomplete, wave height estimated
[b] Maximum excursion before gauge destroyed

Sources: U.S. Department of Commerce (1953); Salsman (1959); Symons and Zetlet (undated report); Berkman and Symons (undated report); Wilson and Torum (1972); Spaeth and Berkman (1972)

of Georgia in 1946. Significant waves were generated along the inner coasts between Vancouver Island and the British Columbia mainland but it is likely that the source motion was caused by slumping rather than seismic uplift (Rogers and Hasegawa, 1978).

The most intriguing evidence for local tsunami activity in the Canadian subduction zone has come from a number of studies of recent (Holocene) sediment deposits along the outer coasts of Washington and Oregon. Atwater (1987) reported evidence for at least six subsidence episodes in the last 7,000 years. In all cases, vegetated coastal lowlands have been buried by intertidal mud. In three of the episodes, patterns of sand sheets lying atop the buried lowlands could be explained by inundation due to tsunamis and the resulting shoreward transport of sand. Reinhart and Bourgeois (1987), Atwater et al. (1987), Hull (1987), and Darienzo and Peterson (1987) point to additional evidence for subsidence and possible tsunami-related flooding in the past 1,000 years. Heaton and Snavely (1985) studied several legends from Indian tribes in the Pacific Northwest and determined that at least some of them could be viewed as describing tsunami behaviour. As is the case with the evidence for active subduction, the sedimentary and anthropological arguments are compelling enough to require further study but not conclusive enough to prove the point.

The historical tsunami record indicates that the outer coasts in the Cascadia subduction zone are vulnerable to tsunami activity. The seismic evidence indicates that local subduction-type earthquakes, which can often be tsunamigenic, are a possibility in the region. The tsunami record is essentially non-existent for local events, and so it is not possible to estimate from observed data the nature of the threat posed by local events.

One approach to an examination of this type of problem is the use of numerical models to simulate possible events. This technique has been used in a number of cases (for example, Hebenstreit and Whitaker, 1981; Hebenstreit and Gonzalez, 1985; Houston et al., 1975; Kowalik and Murty, 1984; Dunbar et al., 1989a, 1989b) to examine the general tsunami threat to specific coastlines from either distant or local sources. The procedure used in these model studies is generally as follows:

– develop a working set of specifications for the type of sea floor uplift likely to result from a 'typical' thrust earthquake in the source area,

– use the sea surface disturbance which would result from the earthquake as the initial conditions for a wave propagation model based on some form of the classical long wave equations,

– use the equations to track the waves as they leave the source and propagate toward coastal areas, whether they are across the basin (as in Houston et al., 1975, and Kowalik and Murty, 1984) or close to the source area (as in Hebenstreit and Whitaker, 1981, and Hebenstreit and Gonzalez, 1985),

– examine, using whatever criteria seem most useful, the nature of the threat that the waves pose to the target coastline.

This technique has proven quite valuable for conducting generalized threat estimates. Since actual earthquake uplift patterns and observed tsunami data are usually not available, the results of such a model study can only be looked upon as qualitative rather than quantitative. Realistic predictions of tsunami wave height or runup height cannot be obtained from such studies although the results can be quite useful in estimating the magnitude of the threat without dealing with specifics.

Besides the present study, only three other model studies of tsunami threat in the Juan de Fuca Strait area have been completed. One

(Garcia and Houston, 1975) estimated tsunami runup in the Puget Sound area resulting from distant tsunamis originating in the Aleutian Trench. The purpose of this study was to establish 100- and 500-year runup maxima for insurance purposes. Maximum estimated wave runup in Puget Sound was on the order to 2-2.5 m.

Houston and Garcia (1978) reported a similar study for the outer coasts. Their 100- and 500-year tsunami heights were derived for tsunamis generated in the Aleutian Trench and in the Peru-Chile Trench. Notice that predicted elevations of 2-3.5 m above mean sea level (MSL) are common along the entire coast for the 100-year tsunami.

The third study (Dunbar *et al.*, 1989a, 1989b) examined the threat to the outer coasts of British Columbia from tsunamis originating in Alaska, Chile, the Aleutian Islands, and Kamchatka. Wave amplitudes in excess of 9 m were predicted at several locations along the coast, the most vulnerable regions being the outer coasts of Vancouver Island, Graham Island (Queen Charlotte Islands), and the central coast of the British Columbia mainland.

The subject matter described in the present paper represents the first organized effort to examine the effects of local tsunamis for the area under study. The methodology outlined above is used in order to examine the focusing of tsunami energy along the Pacific coastline of the Cascadia subduction zone. It does this by following wave energy from the source areas into shallow coastal waters and determining from calculated wave heights the relative levels of energy likely to reach portions of the coasts. No attempt at modelling runup or inundation is made in this study since the purpose is not a detailed analysis of any given area but a general picture of which regions are most likely to be threatened.

2. SPECIFICATIONS OF THE TSUNAMI SOURCE MOTION

In order to start the wave propagation process, we must impose some sort of displacement pattern on the sea surface in the area chosen as the generation region. Any pattern will serve to begin the wave process but it is physically more realistic and satisfying to use a pattern that is at least a reasonable approximation to the type of displacement caused by thrust-type earthquakes. Several models of free surface (in this case, sea floor) displacement caused by earthquakes have been developed. The one used in this study was developed by Mansinha and Smylie (1971). It is a point source displacement model in which the rupture motion is described as a collection of point sources over the extent of the fault plane and the contribution due to the vertical motion of each point is integrated over the plane to produce a total displacement pattern. All that the model requires are estimates of the

depth, length, width, dip angle, and vertical slip of the source, and a displacement pattern can be calculated.

The ocean is a compressible fluid so that a sudden vertical displacement of the bottom should cause the water column to compress slightly, as well as to rise. However, for the purpose of tsunami modelling, we usually assume that any motion of the sea floor is mirrored in a corresponding motion of the sea surface, without regard to compressional effects. The effect is probably small enough to ignore and the reality is that we never know enough about the sea floor motions, which generate a tsunami, to evaluate the magnitude of the effect.

It should also be noted that earthquakes are never instantaneous events, but take place over a finite period of time as the rupture across the source area. The model equations do include provision for a time-dependent source motion. Again, however, our relative ignorance of the mechanics of the source motion allows us to assume that it is, indeed, instantaneous. Hammack (1973) showed that most of the energy transfer from the earthquake.to the tsunami takes place in the first 60 seconds of the motion. Thus, this assumption is reasonable.

Once the tools, the wave propagation model and the source model, have been assembled, the next step is to define the source parameters. The Juan de Fuca Plate region spans 800-900 km of the Pacific coast of North America. It is possible that a subduction earthquake could occur anywhere along the length of this zone. Modelling every possible event would require a great deal of computer time and effort. Fortunately, it is possible to invoke a few simple arguments to allow us to reduce the simulations down to an easily manageable number.

Heaton and Hartzel (1986) have divided the Cascadia subduction zone into three subzones. The northernmost zone consists of the Explorer Plate, the southernmost zone of the Gorda South Plate, and the intervening Juan de Fuca Plate makes up the remaining zone. Rogers (1988) includes the Winona Block in his reckoning of the structures that make up the Cascadia zone but the likelihood of subduction earthquakes in that complex is unclear.

Following Heaton and Hartzell's definition of the Cascadia subduction zone, the Gorda South Plate (shortened to Gorda Plate for convenience) is the smallest of the three main zones, being only 150-200 km long. It is subducting at a rate that is possibly 25% slower than the Juan de Fuca zone (3.3 cm/yr versus 4.0 cm/yr according to Heaton and Hartzell (1986) and may be less likely to experience subduction earthquakes. Indeed, Spence (1988) suggest that subduction under the Gorda Plate has effectively stopped. However, in the absence of evidence to the contrary, it seems prudent to examine an event in this zone. Rogers (1988) provides

estimates of the various source parameters for all of the zone he examined. For the Gorda zone, he suggests a fault width of 100 km, a length of 150 km, and a vertical displacement under maximum rupture of approximately 3.0 m. Using Wyss' (1979) relationship for maximum expected magnitude,

$$M = \log(\text{length} \times \text{width}) + 4.15, \qquad (1)$$

this fault could produce an earthquake of magnitude 8.3.

The Explorer Plate is somewhat larger than the Gorda Plate (200 km) although the width of the fault can also be estimated at 100 km. Rogers estimates a vertical displacement of 2.0 m (maximum Wyss magnitude of 8.5). Riddihough (1984) estimates that this plate is subducting at a much slower rate than the Juan de Fuca Plate (as low as 2 cm/yr) although it is not clear what this means in terms of its potential for subduction earthquakes.

The Juan de Fuca Plate is on the order of 800-900 km long. It is subducting at a rate of 4-4.5 cm/yr. Of the three areas being examined, it is probably the one most likely to experience large subduction zone earthquakes. A rupture along the full length of the plate would produce a magnitude in the range of 9.1. One difficulty with such an event, however, is that the rupture would have to 'turn the corner' along the Washington coast. Although this is not completely unreasonable, it would seem more likely that the plate would be subject to two separate ruptures, one in the northern half and one in the southern half. Either such event, given a length of roughly 400-450 km, would have a magnitude of roughly 8.8. Rogers (1988) estimates that the vertical displacement of a rupture in this region would be on the order of 18 m.

In order to use the Mansinha-Smylie model, the dip angle of the fault plane and the depth of the fault must be specified. Heaton and Kanamori (1984) indicate that the Juan de Fuca Plate is dipping at approximately 10° below the North America plate. We will use this value for all of the events studied. For convenience, an arbitrary focal depth of 30 km was chosen.

Contours of seafloor uplift, calculated using the Masinha-Smylie model were superimposed on contours of bottom topography (m) for each of the tsunami-generating source areas. In all cases, the model indicates that uplift will take place offshore with some subsidence on land. This is, of course, the typical pattern observed in such major subduction events as the 1960 Chilean earthquake and the 1964 Alaskan earthquake. Since the wave model does not attempt to simulate wave runup on dry land, no land-based subsidence is taken into account in the calculations. Because of difficulties involved in producing the 0.0-m uplift contours (due to a peculiarity of the plotting package used), only positive uplift values are

shown. The plots are done in a rectangular coordinate space rather than in more conventional Mercator or Azimuthal coordinates. This does induce some distortion in the plots, but could not be avoided, since the contouring program used to generate the plots is not able to function in anything except rectangular coordinates.

Although four source motions were described above, only three are considered here: the Gorda Plate, the southern end of the Cascadia zone, and the northern end of the Cascadia zone. The placing of the uplift pattern for the Explorer zone proved to be close enough to that of the northern end of the Cascadia zone that no additional information was derived from the Explorer simulation. Only the three distinct cases will be examined in detail.

The bathymetric data were taken from the DBDB5 world bathymetry data base, obtained from the National Geophysical Data Center in Boulder, Colorado. This data base provides depth values for the world oceans at 5-min resolution in both latitude and longitude. This full resolution is used in the simulations. The Juan de Fuca Strait has been foreshortened because a separate model (the GFP model) was used to propagate the tsunami into the Juan de Fuca Strait and then into Puget Sound and the Strait of Georgia.

The primary goal of this study is to examine the distribution of tsunami wave energy along the coast as the result of the various source motions. In order to accomplish this, a number of coastal recording points were assigned for the course of each simulation. These points usually correspond to the last ocean grid point in the model before a land boundary is encountered. Successive water elevation values at these points were monitored and the highest positive value calculated during the simulation was stored for later analysis. Simulations were run for approximately 4 model hours with a time step of 22.5 s. The 4-h period was judged to be long enough to avoid excessive internal reflections from the rather irregular coastline, especially along Vancouver Island. The resolution of the model is coarse enough so that some of these reflections can contain numerical noise, especially in bays which are only one or two grid points wide.

3. FORMULATION OF THE OUTER COAST MODELS

The first tool needed is a set of equations to simulate the generation and propagation of the surface waves from their source to the threatened coastal areas. It is quite probable that the full detail of the tsunami generation in the locality of the source can only be completely described by nonlinear equations of motion which take into account not only the gravitational and advective forces acting on the sea surface but also bottom friction, vertical accelerations, and higher order forces. Two problems with simulations based on such equations make them

less attractive than mathematical rigor might imply. One is that the numerical solution of such equations tends to be quite time-consuming and expensive (in terms of machine time and, when applicable, dollars). This problem can, of course, be overcome by using large, fast machines and having a large computer budget. The second, more fundamental problem is that no one has yet been able to sufficiently verify that the use of fully nonlinear equations provides any significant improvement over more simple, linear or, at best, weakly nonlinear equations. The data, in the form of easily replicated, well-constrained, historical observations simply are not available. The useful, though undocumented, rule-of-thumb in the tsunami modelling community is that linearized models probably depict correctly up to 90% of the detail of tsunami behaviour. For this reason, the equations used in this study are derived from the linear equations of motion and continuity for long ocean surface waves. The only nonlinear terms included in the equations concern the bottom friction which acts on the waves as they propagate.

The model used in this study was originally developed to simulate the behaviour of storm surges as they propagate onto the continental shelf. The model was developed at Texas A&M University in the 1970's but was never documented (R.E. Whitaker, personal communication). The model is set in the coordinate system of a spherical earth, which makes it ideal for studying propagation of waves over long distances (such as the 5-10° of latitude which encompass the Cascadia subduction zone). The simulation grid is laid out along lines of latitude and longitude, and grid spacing is in minutes rather than kilometres, as would be the case in a Cartesian coordinate system. Because of the long distances covered, Coriolis forces are taken into account in the equations.

The numerical model used in this study is base don the inviscid, vertically integrated, linear equations of motion for the propagation of long waves (*i.e.*, waves whose length, λ, is much larger than the depth, h, of the water in which they propagate). These equations, in spherical coordinates, are

$$\partial_t U - fV + ghR^{-1}\partial_\theta\eta = 0 \qquad (2)$$

$$\partial_t V + fU + gh(R\sin\theta)^{-1}\,\partial_\theta\eta = 0 \qquad (3)$$

$$\partial_t(h + \eta) + (R\sin\theta)^{-1}\,[\partial_\phi V + \partial_\theta(U\sin\theta)] = 0 \qquad (4)$$

with

$$U = \int_h^\eta \dot{u}\,dz, \qquad (5)$$

and

$$V = \int_h^\eta v\,dz. \qquad (6)$$

Note the lack of a vertical velocity component, w, implying neglect of vertical accelerations. Note also the presence in (4) of a $\partial_t h$ term. This is the term through which

time-varying bottom displacements generate sea surface deformations.

The variables in these equations are defined as:

U = horizontal transport in the southward (θ) direction per unit width,
V = horizontal transport in the eastward (ϕ) direction per unit width,
t = time,
f = Coriolis parameter (f = $2\Omega\cos\theta$, where Ω = angular velocity of the earth),
g = acceleration due to gravity,
h = depth of water below MSL,
R = radius of the earth,
η = displacement of the free surface from mean sea level (MSL)
z = 0 at MSL,
ϕ = longitude measured eastward from 0° at Greenwich.
θ = co-latitude i.e., measured from 0° at the North Pole.

The notation ∂_x denotes partial differentiation with respect to the subscripted variable.

Numerical solutions to Equations (2 to 4) are obtained by using a finite-difference analog to these continuum equations. The code used is a modified version of a model originally developed to simulate the propagation of storm surges in coastal waters. The fact that it has been proven useful in shallow water simulations makes its application in this project quite attractive.

The general approach used in the model is to integrate Equations (2) through (4) over time using the multi-operational, alternating direction implicit (ADI) algorithm. A staggered computational mesh, is used in the numerical model formulation. At each cell, $\eta_{i,j}$ at time $n\Delta t$ is the average anomaly over the cell area centered at $i\Delta\phi$, $j\Delta\theta$ where Δt is the time increment and $\Delta\phi$, $\Delta\theta$ are increments in longitude and latitude, respectively. The transport $V_{i,j}$ is taken at the centre of the left-hand face and $U_{i,j}$ is taken at the centre of the lower face. The depths are defined at the same locations as the η's.

Two types of boundaries occur along the edges of the model grid: shoreline boundaries and open-ocean boundaries. Different boundary conditions are applied in each case.

Since, in this study, we are not concerned with predicting coastal runup and inundation zones, we can require that waves striking the coasts be fully reflected. This can be expressed, in terms of the velocity component perpendicular to the shore, as

$$u_n = 0 \quad \text{at land boundaries.} \qquad (7)$$

Setting the normal component of velocity to zero at the coastal boundary implies that no wave energy crosses the shore onto dry land.

At open-ocean boundaries (that is, when the region defined by the model grid ends not on dry land but in water) we require that wave energy approaching the boundary from within the model area pass through the boundary without reflection. This is referred to as a radiation-type condition. One way that it can be expressed is

$$\partial_t \eta = -c[R^{-1}(\cos\delta)\partial_\theta\eta \ (R\sin\theta)^{-1}(\sin\delta)\partial_\phi\eta]. \quad (8)$$

Here, c is the wave phase speed approximated by $c = [g(h + \eta)]^{1/2}$, and δ is the angle of incidence between the direction of wave propagation and open boundary.

The boundary condition expressed in (8) is satisfactory as long as the angle of incidence of the outgoing waves is known. If the outgoing waves are plane (i.e., the wave front has no curvature), then it is possible to determine δ quite readily. In the situation being modelled, however, the waves are not plane. Instead, they spread radially outward from the source zone and still have a definite curvature when they cross the open boundary. Reflected waves from the land/sea boundaries also add to the confusion. Techniques for calculating the angle of incidence at every point along the boundary at every time step would wind up taking more computation time than the finite-difference calculations themselves (Bennett, 1976).

A technique for taking into account the radially spreading nature of the waves leaving the source area was developed by Mungall and Reid (1978). The assumption is that the waves can be considered to be radiating outward from the point source and that each open ocean boundary point is located a distance r_b from that point. Then the radiation condition can be expressed as

$$U_b^r = c\eta b + \frac{c^2}{2r_b}\int_0^t \eta_b \ dt, \quad (9)$$

Where U_b^r is the outward transport in a radial direction. The time integral on the right-hand side takes into account the spreading of the wave front. Mungall and Reid showed that this condition could be used effectively even if the origin of the waves is not a point but a well defined region. Hebenstreit et al. (1980) used this boundary condition in their study of tsunami interactions in the Hawaiian Islands.

4. EARLY EARTHQUAKE SIMULATIONS FOR THE OUTER COAST

4.1 Gorda Plate Case

The results from the Gorda Plate simulation are, in many ways, typical of the results from all of the simulations made in this study. The extreme wave heights are found along the coastal zones within the source uplift zone, while the elevations tend to taper off (although not uniformly) to the north and south of the immediate area of the uplift. A

total of 45 coastal recording points were used in the simulation. One useful procedure for measuring relative tsunami threat is to identify those sections of the coast which receive wave energies which are higher or lower than the mean level of energy (as depicted by wave elevations) seen along the coast. This procedure accomplishes two things: it keeps the discussion in relative terms and it avoids the appearance of wave height predictions. This latter point is especially important in a study such as this, which is based on hypothetical source motions. The results showed that the distribution of maximum values is by no means regular. It is quite possible to have wide variations from one coastal point to the next. This is fairly typical of this type of simulation and is physically realistic. The local bottom topography tends to play a major role in the distribution of energy in a case like this, with some short sections of coast amplifying incoming energy, while others dissipate it.

The segment of the coast near Crescent City, California and southern Oregon receive the highest levels of energy in this simulation. This is, of course, in line with the extreme wave activity observed at Crescent City during historical distantly-generated tsunamis, especially when contrasted with coastal locations to the north. To much can be made of this similarity, however, since it does lie within the source zone.

4.2 Cascadia South Case

A total of 75 coastal recording stations were used in this simulation. Again, as in the Gorda Plate simulation, the extreme values are found along the coast within the source region. The entire coast from mid-Oregon to central Washington (Grays Harbor and north) receives wave energy higher than the overall mean for the coast. note that the mean value for this simulation is just below 6.0 m, so that even the locations below average receive wave heights on the order of 2.0 m and higher. It seems clear that a closer study of specific areas along this coast should be undertaken.

The results reinforce the impression of a general spreading out of the tsunami energy within the source zone. Note that above average values occurred in central Washington, although the main concentration lies farther south.

4.3 Cascadia North Case

The uplift pattern for this case faces most of the coast of Vancouver Island although the model grid extends to southern Washington. The coast of Vancouver Island is highly irregular, being laced with fjordic inlets along most of its length. The model topography is not capable of resolving all of these inlets although a number of the major ones, such as Barkley Sound (at about 48°50'N) and Nootka Sound (at about 49°15'N) are included. Although a portion of Queen Charlotte Strait does appear in the model

bathymetry, no attempt to model waves entering that area was intended in this study.

Here, 100 coastal stations are monitored. Even though the initial uplift pattern was essentially the same as that used in the Cascadia South case, the mean value of maximum calculated elevations is over.

5. CONCLUSIONS

The conclusions to be drawn from this type of study are fairly straightforward, at least at first glance. If the sizes of the earthquake sources used in the simulations are realistic, then the portions of the North American coastline falling within the source regions are highly susceptible to destructive tsunamis. This seems to be true for the entire coastline along the Cascadia subduction zone since no major 'shadow zones', which may be protected from waves due to offshore topography, were apparent in the simulations.

Because of the hypothetical nature of the choice and specification of these sources, we cannot in any way begin to examine issues such as how high the waves would be or how long they would persist. However, a study such as this does open the doors to a well-established, easily controlled form of study for examining specific target areas. Now that it is clear that the entire coast can be considered subject to a local threat, rather than just specific localities, more detailed studies of individual areas can be undertaken. For example, once a specific areas has been chosen for study, detailed simulations can be developed based on the cases studied here. A series of calculations, covering a wide range of possible source magnitudes and the resulting tsunamis, can be performed to assess the range of threats facing the area. These can range from the worst-case, catastrophic tsunami to a smaller, but still locally dangerous event. A catalogue of risk levels, base on the land use patterns of the target area, can be developed for future planning.

The results of this study also raise a number of technical issues that can be addressed in the future. One question is why it appears that the dominant energy distributions are more or less confined to the immediate source area. In other tsunami-prone areas of the world, most notably southern Chile, wave energies have followed a somewhat different pattern in which secondary concentrations of energy have been found at some distance north of the immediate source zone (Hebenstreit and Whitaker, 1981). The wave elevations in these secondary zones are usually noticeably higher than those seen in the intervening coastal areas. It is possible that the simulations used in this study did not span enough of the coastline to allow for the development of these secondary concentrations.

A second issue concerns the behaviour of the waves in the many inlets that dot the western coastline. As stated at the beginning, the simulations were not designed to address these types of detailed questions, and yet they do have a bearing on the level of tsunami threat posed to the coast. If the inlets act as amplifiers for the incoming energy, then even relatively small tsunamis could prove quite destructive.

REFERENCES

Atwater, B.F. 1987. Evidence for great Holocene earthquakes along the outer coast of Washington state. *Science*, 236: 942-236.

Atwater, B.F., A.G. Hull, and K.A. Bevis. 1987. Aperiodic Holocene recurrence of widespread, probably coseismic subsidence in southwestern Washington. [Abstract], *EOS*, 68(44): 1468.

Bennett, A.F. 1976. Open boundary conditions for dispersive waves. *J. Atm. Sci.*, 33: 176-182.

Berkman, S.C., and J.M. Symons. (Undated). The tsunami of May 22, 1960 as recorded at tide stations. Coast and Geodetic Survey, U.S. Department of Commerce, Washington, D.C.

Darienzo, M., and C. Peterson. 1987. Episodic tectonic subsidence recorded in late-Holocene salt marshes, northwest Oregon. [Abstract], *EOS*, 68(44): 1469

Dunbar, D., P. LeBlond, and T.S. Murty, 1989a. Evaluation of tsunami amplitudes for the Pacific coast of Canada. *Progress in Oceanography* (In press).

Dunbar, D., P. LeBlond, and T.S. Murty, 1989b. Maximum tsunami amplitudes and associated currents on the coast of British Columbia. *Sci. Tsunami Hazards*, 7(1): 3-44.

Garcia, A.W., and J.R. Houston. 1975. Type 16 insurance study: tsunami predictions for Monterey and San Francisco Bays and Puget Sound. U.S. Army Engineers Waterways Experiment Station Technical Report H-75-17, Vicksburg, Mississippi, NTIS: AD-A018-421. 271 pages.

Hammack, J.L. 1973. A note on tsunamis: their generation and propagation in an ocean of uniform depth. *J. Fluid Mech.*, 60(4): 769-799.

Hansen, W. 1956. Theorie zur Errechnung des Wasserstandes und der Strömungen in Randmeeren nebst Anwendungen. *Tellus*, 8: 287-300.

Heaton, T.H., and S.H. Harztell. 1986. Source characteristics of hypothetical subduction earthquakes in northwestern United States. *Bulletin of the Seismol. Soc. Amer.*, 76(3): 675-708.

Heaton, T.H., and S.H. Harztell. 1987. Earthquake hazards on the Cascadia subduction zone. *Science*, 236: 162-168.

Heaton, T.H., and H. Kanamori. 1984. Seismic potential associated with subduction in the northwestern United States. *Bull. Seismol. Soc. Amer.*, 74(3): 933-941.

Heaton, T.H., and P.D. Snavely, Jr. 1985. Possible tsunami along the northwestern coast of the United States inferred from Indian traditions. *Bull. Seismol. Soc. Amerc.*, 75(5): 1455-1460.

Hebenstreit, G.T., and E.N. Bernard. 1985. Azimuthal variations in tsunami interactions with multiple-island systems. *J. Geophys. Res.*, 90(C2): 3353-3360.

Hebenstreit, G.T., E.N. Bernard, and A.C. Vastano. 1980. Applications of improved numerical techniques to the tsunami response of island systems. *J. Phys. Ocean.*, 10: 1134-1140.

Hebenstreit, G.T., and F.X. Gonzalez. 1985. Preliminary model results of the 1985 Chilean tsunami. [Abstract], *EOS*, 66: 962.

Hebenstreit, G.T., and R.E. Whitaker. 1981. Assessment of tsunami hazard presented by possible seismic events: near-source effects. Technical Report SAI-82-651-WA, Science Applications, Inc., McLean, Virginia. NTIS:PB83-102665.

Houston, J.R., and A.W. Garcia. 1978. Type 16 insurance study: tsunami predictions for the west coast of the continental United States. U.S. Army Engineers Waterways Experiment Station Technical Report H-78-26, Vicksburg, Mississippi, NTIS:ADA063663. 69 pages.

Houston, J.R., R.W. Whalin, A.W. Garcia, and H.L. Butler. 1975. Effect of source orientation and location in the Aleutian Trench on tsunami amplitude along the Pacific coast of the United States. U.S. Army Engineers Waterways Experiment Station Technical Report H-75-4, Vicksburg, Mississippi, NTIS:AD-065-090. 54 pages.

Hull, A.G. 1987. Buried lowland soils from Willapa Bay, southwest Washington: further evidence for recurrence of large earthquakes during the last 5000 years. [Abstract], *EOS*, 68(44): 1468-1469.

Kowalik, Z., and T.S. Murty. 1984. Computation of tsunami amplitudes resulting from a predicted major earthquake in the Shumagin seismic gap. *Geophys. Res. Let.*, 11: 1243-1246.

Lockridge, P.A., and R.H. Smith. 1984. Tsunamis in the Pacific Basin (1900-1983). Wall chart published by the National Geophysical Data Center and World Data Center A for Solid Earth Geophysics, Boulder, Colorado.

Mansinha, L., and D.E. Smylie. 1971. The displacement fields of inclined faults. *Bull. Seismol. Soc. Amer.*, 61: 1433-1440.

Mungall, J.C.H., and R.O. Reid. 1978. A radiation boundary condition for radially-spreading non-dispersive gravity waves. Texas A&M University, Department of Oceanography, Ref. 78-2-T. 63 pages.

Reinhart, M.A., and J. Bourgeois. 1987. Distribution of anomalous sand at Willapa Bay, Washington: evidence for large-scale landward-directed processes. [Abstract], *EOS*, 68(44): 1469.

Riddihough, R. 1984. Recent movements of the Juan de Fuca Plate system. *J. Geophys. Res.*, 89(B8): 6980-6994.

Rogers, G.C. 1988. Magathrust potential of the Cascadia subduction zone. *Can. J. Earth Sci.*, 25(6): 844-825.

Rogers, G.C., and H.S. Hasegawa. 1978. A second look at the British Columbia earthquake of June 23, 1946. *Bull. Seism. Soc. Amer.* 678(3): 653-676.

Salsman, G.G. 1959. The tsunami of March 9, 1957 as recorded at tide stations. Technical Bulletin No. 6, Coast and Geodetic Survey, U.S. Department of Commerce, Washington, D.C.

Soloviev, S.L., and Ch.N. Go. 1984. Catalogue of tsunamis on the eastern shore of the Pacific Ocean. [Translated into English], Canada Institute for Scientific and Technical Information, National Research Council, Ottawa.

Spaeth, M.G., and S.C. Berkman. 1972. The tsunamis as recorded at tide stations and the seismic seawave warning system. In *The Great Alaska Earthquake of 1964: Oceanography and Coastal Engineering,* 38-110. National Academy of Sciences, Washington, D.C.

Spence, W. 1988. Anomalous subduction and the origins of stresses at Cascadia. Presented at the Workshop on Evaluation of Earthquake Hazards and Risk in the Puget Sound and Portland Areas, Olympia, Washington, 12-15 April, 1988.

Symons, J.M., and B.D. Zetler. (Undated). The tsunami of May 22, 1960 as recorded at tide stations: preliminary report. U.S. Coast and Geodetic Survey.

U.S. Department of Commerce. 1953. The tsunami of November 4, 1952 as recorded at tide stations. Special Publication No. 300, Coast and Geodetic Survey.

Wilson, B.W., and A. Torum. 1972. Runup heights of the major tsunami on North American coasts. In *The Great Alaska Earthquake of 1964: Oceanography and Coastal Engineering,* National Academy of Sciences, 158-180, Washington, D.C.

Wyss, M. 1979. Estimating maximum exceptable magnitude of earthquakes from fault dimensions. *Geology*, 7: 336-340.

MODELING TSUNAMI FLOODING

Charles L. Mader

Joint Institute for Marine and Atmospheric Research University of Hawaii, Honolulu, HI., U.S.A.

Abstract

Tsunami waves and their interaction with local topography were numerically modeled using the SWAN code which solves the shallow water long wave equations. New flooding and graphics capabilities have been added to the code. The SWAN code was used to model the interaction of waves with a site of well documented topography near the Mauna Lani Resort on the South Kohala Coast on the Island of Hawaii. The calculated results agree with the results obtained using the procedures developed and applied for flood insurance purposes by the U. S. Army Corps of Engineers and the recent JIMAR study at the University of Hawaii of tsunami evacuation zones for the site. Flooding may be modeled for complicated three-dimensional topography using the SWAN code.

Tsunami Hazard Evaluation

The magnitude of the tsunami hazard at any land site depends on the expected extent of inundation of the land by tsunamis at the site, expected water depths and velocities within the inundation zone, and the exposure of persons and property within the potential inundation zone. There is no definite upper limit to the power of tsunamis approaching a coastal site. Tsunami hazard must be expressed in terms of expected average recurrence intervals or frequencies. What is expected in the future can be judged only on the basis of what has occurred in the past. The power of tsunamis that have approached the coast can be estimated from the extent of inundation and the runup heights on land. All estimates of tsunami hazard are site-specific and based on runup heights of historic tsunamis.

In the last decade procedures have been developed and applied for flood insurance purposes by the U. S. Army Corps of Engineers[1]. These procedures built upon historical wave height data compiled at the University of Hawaii and utilized a numerical model to synthesize the maximum tsunami wave crest as a function of frequency of occurence. This information was used to develop the inundation maps as part of a National flood insurance program.

The resulting highly synthesized wave heights from the flood insurance program with additional historical inputs provide reasonably authentic worst-case tsunami wave heights as a function of frequency of occurence. Usually the wave heights fall within the envelope of the 1946, 1957 and 1960 tsunami events. To determine the tsunami evacuation zones the wave is then "runup" on the shore at selected points using a one-dimensional model described by Bretschneider and Wybo in reference 2 and Cox in reference 3. Critical factors in the inundation calculation include accurate topographic information and surface roughness. A contour line is drawn between points thus generated, representing the maximum probable inundation. Where possible it is compared with historical inundation information, flood insurance map lines and adjusted if warranted.

The study site chosen was a region with well documented topography near the Mauna Lani Resort on the South Kohala Coast on the Island of Hawaii. For the study site, the 200-year tsunami wave height 200 feet inland was estimated by Curtis and Smaalders[4] to be 10 feet using the techniques described. This corresponds to a wave height of about 8.5 feet above mean sea level at the shoreline and a wave height of 8.1 feet in 30 feet of water. This results in a wave amplitude (peak to trough) of 16.2 feet which is expected to occur once in every 200 years or has a 0.5 percent chance of being equalled or exceeded this year or any other year. Such a wave will result in 10 feet inundation at the site using the standard one-dimensional runup model for a surface roughness Manning "n" of 0.0325.

The surface roughness for typical Hawaiian terrain is described in reference 2 and 5. A Manning "n" of 0.0325 corresponds to a roughness characteristic of lava and grass with isolated trees. An "n" of 0.04 corresponds to many trees, boulders and high grass. The maximum inundation changes by only 30 feet out of 400 over this range of the roughness parameter in the site region.

Roughness in the numerical model in the *SWAN* code is described using the De Chezy friction model. The De Chezy coefficient depends not only on the bed roughness but also on the depth. The De Chezy coefficient is related to the Manning "n" by the depth to the 1/6 power. While not directly comparable, for the depths in the site region a De Chezy friction constant of 50 results in about the same friction effect as a Manning "n" in the 0.03-0.04 range.

The Numerical Model

The tsunami waves and their interaction with the study site topography were numerically modeled using the *SWAN* code which solves the shallow water long wave equations. It is described in detail in the monograph *Numerical Modeling of Water Waves* [6].

The long wave equations solved by the *SWAN* code are

$$\frac{\partial U_x}{\partial t} + U_x \frac{\partial U_x}{\partial x} + U_y \frac{\partial U_x}{\partial y} + g \frac{\partial H}{\partial x}$$

$$= FU_y + F^{(x)} - g\frac{U_x(U_x^2 + U_y^2)^{1/2}}{C^2(D + H - R)},$$

$$\frac{\partial U_y}{\partial t} + U_x \frac{\partial U_y}{\partial x} + U_y \frac{\partial U_y}{\partial y} + g \frac{\partial H}{\partial y}$$

$$= -FU_x + F^{(y)} - g\frac{U_y(U_x^2 + U_y^2)^{1/2}}{C^2(D + H - R)},$$

and

$$\frac{\partial H}{\partial t} + \frac{\partial (D + H - R)U_x}{\partial x} + \frac{\partial (D + H - R)U_y}{\partial y} - \frac{\partial R}{\partial t} = 0,$$

where

U_x	= velocity in x direction (i index)
U_y	= velocity in y direction (j index)
g	= gravitational acceleration
t	= time
H	= wave height above mean water level
R	= bottom motion
F	= Coriolis parameter
C	= coefficient of DeChezy for bottom stress
$F^{(x)}, F^{(y)}$	= forcing functions of wind stress and barometric pressure in x and y direction
D	= depth.

As described in the monograph, the *SWAN* code has been used to study the interaction of tsunami waves with continental slopes, shelves, bays and harbors such as Hilo harbor.

The *SWAN* code has been used to study the interaction of tsunami waves with continental slopes and shelves, as described in reference 7. Comparison with two-dimensional Navier-Stokes calculations of the same problems showed similar results, except for short wavelength tsunamis.

The *SWAN* code was used to model the effects of tides on the Musi-Upang estuaries, South Sumatra, Indonesia, by Safwan Hadi.[8] The computed tide and water discharge were in good agreement with experimental data.

The *SWAN* code was used to model the large waves that were observed to occur inside Waianae harbor under high surf conditions in reference 9. These waves have broken moorings of boats and sent waves up the boat-loading ramps into the parking lot. The numerical model was able to reproduce actual wave measurements. The *SWAN* code was used to evaluate various proposals for decreasing the amplitude of the waves inside the harbor. From the calculated results, it was determined that a significant decrease of the waves inside the harbor could be achieved by decreasing the harbor entrance depth. Engineering companies used these results to support their recommendations for improving the design of the harbor.

The effect of the shape of a harbor cut through a reef on mitigating waves from the deep ocean was studied using the *SWAN* code in reference 10. It was concluded that a significant amount of the wave energy is dissipated over the reef regardless of the design of the harbor. The reef decreased the wave height by a factor of 3. The wave height at the shore can be further decreased by another factor of 2 by a "V"-shaped or parabolic bottom design.

Other examples of applications of the *SWAN* code are presented in reference 11. They include the wave motion resulting from tsunami waves interacting with a circular and triangular island surrounded by a 1/15 continental slope and from surface deformations in the ocean surface near the island. The effects of a surface deformation in the Sea of Japan similar to that of the May 1983 tsunami was modeled. The interaction of a tsunami wave with Hilo Bay was described.

The *SWAN* code was used to model the effect of wind and tsunami waves on Maunalua Bay, Oahu as described in reference 12. The model reproduced the observed wave behavior at various locations in the bay for a 4 foot south swell with a 15 second period. A study was performed of the effect of an enlarged and deeper channel. The code was used to model the interaction with Maunalua Bay of waves outside the bay having periods of 15, 30, 60 seconds and a tsunami wave with a 15 minute period. Wave amplitudes of 1 to 6 feet

were considered with tides from mean lower low water to high tide (a 1.8 foot range). The same wave profiles within 10% were calculated at various locations studied throughout the bay for the current and the proposed bay with a larger and deeper entrance channel. The small difference between the current and the proposed bay varied with the wave period. The largest difference was found for the 30 second wave.

The 15 minute period tsunami wave doubled in amplitude as it passed over the bay and was highest at high tide. Severe flooding in the regions near the shore line was predicted. The tsunami effects were unrelated to channel configeration.

The calculated wave behavior at any location in the bay was a strong function of the entire bay with a complicated and time varying pattern of wave reflections and interactions.

Application of the Numerical Model

The *SWAN* code was used to model the interaction with the study site on the South Kohala Coast on the Island of Hawaii of waves having 15 minute and 30 minute periods. The waves were directed parallel to the shoreline for maximum effect. The tsunami wave amplitude (peak to trough) in 30 feet of water was 16.2 feet which is expected to occur once in every 200 years or has a 0.5 percent chance of being equalled or exceeded this year or any other year. Such a wave will result in 8 to 10 feet inundation at the site. The effect of roughness of the terrain on the flooding was described using a De Chezy coefficient of 50 which is equivalent to the Manning "n" of 0.0325 to 0.04 used in the JIMAR and flood insurance programs.

The space resolution in the numerical model grid was 50 feet. The numerical calculations were performed at 0.5 second intervals. The calculations were performed on an IBM PS/2 Model 80 computer using a special version of the *SWAN* code that includes flooding and the new Mader Consulting Co. graphics package called MCGRAPH. A calculation required 1 to 6 hours of computer time.

The picture and line contour plots of the topography for the site are shown in Figure 1. The interaction of the 200-year tsunami with the site topography is shown in Figures 2 and 3. The picture and line contour plots show the ocean flooding the land to the 9-10 foot level and inundating the land between 300 and 400 feet from the shoreline. These results agree with the results obtained using the procedures developed and applied for flood insurance purposes by the U. S. Army Corps of Engineers and the recent JIMAR study at the University of Hawaii of tsunami evacuation zones for the region. We conclude that flooding may be modeled for complicated three-dimensional topography using the *SWAN* code.

References

1. James R. Houston, Robert D. Carver, Dennis G. Markle, "Tsunami Elevation Elevation Frequency of Occurrence for the Hawaiian Islands," Technical Report H-77-16, U. S. Army Engineer Waterways Experiment Station, Vicksburg, Miss. (1977).
2. C. L. Bretschneider and P. G. Wybo, "Tsunami Inundation Prediction," Proceedings of 15th Coastal Engineering Conference (1976).
3. Doak Cox, "Potential Tsunami Inundation Areas in Hawaii," Hawaii Institute of Geophysics Report No. 14 (1961).
4. George D. Curtis and Mark Smaalders, "A Methodology for Developing Tsunami Evacuation Zones," Proceedings of International Tsunami Symposium 89 (1989).
5. C. L. Bretschneider, H. J. Krock, E. Nakazaki and F. M. Casciano, "Roughness of Typical Hawaiian Terrain for Tsunami Run Up Calculation," University of Hawaii Department of Ocean Engineering report (1988).
6. Mader, Charles L. *Numerical Modeling of Water Waves,* University of California Press, Berkeley, California (1988).
7. Charles L. Mader, "Numerical Simulation of Tsunamis," Journal of Physical Oceanography, Vol. 4, pp. 74–82 (1974).
8. Safwan Hadi, "A Numerical Tidal Model of Musi-Upang Estuaries." A dissertation submitted to Oceanography Department of University of Hawaii (1985).
9. Charles L. Mader and Sharon Lukas, "Numerical Modeling of Waianae Harbor," Aha Hulikoa Hawaiian Winter Workshop Proceedings (January 1985).
10. Charles L. Mader, Martin Vitousek, and Sharon Lukas, "Numerical Modeling of Atoll Reef Harbors," Proceedings of the International Symposium on Natural and Man-Made Hazards, Rimouski (1986).
11. Charles L. Mader and Sharon Lukas, "*SWAN* – A Shallow Water, Long Wave Code: Applications to Tsunami Models," Joint Institute for Marine and Atmospheric Research report JIMAR 84–077 (1984).
12. "Oahu Intraisland Ferry System - Draft Environmental Impact Statement," State Department of Transportation, Harbors Division (1988).
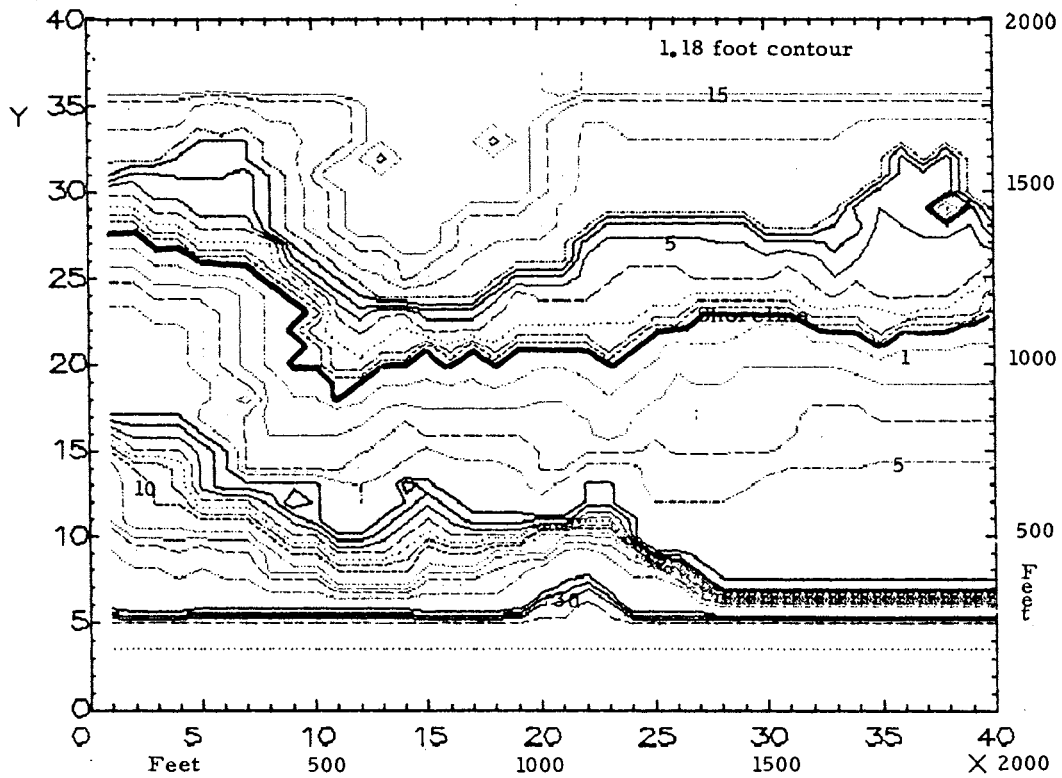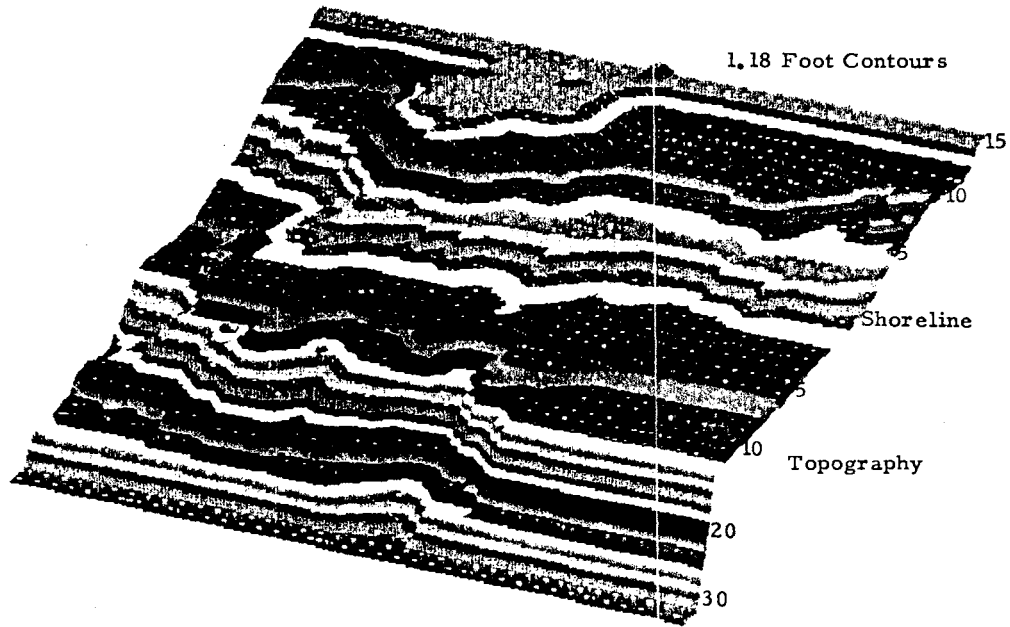
Fig. 1 The site topography showing the area above and below sea level. The contour interval is 1.18 feet.
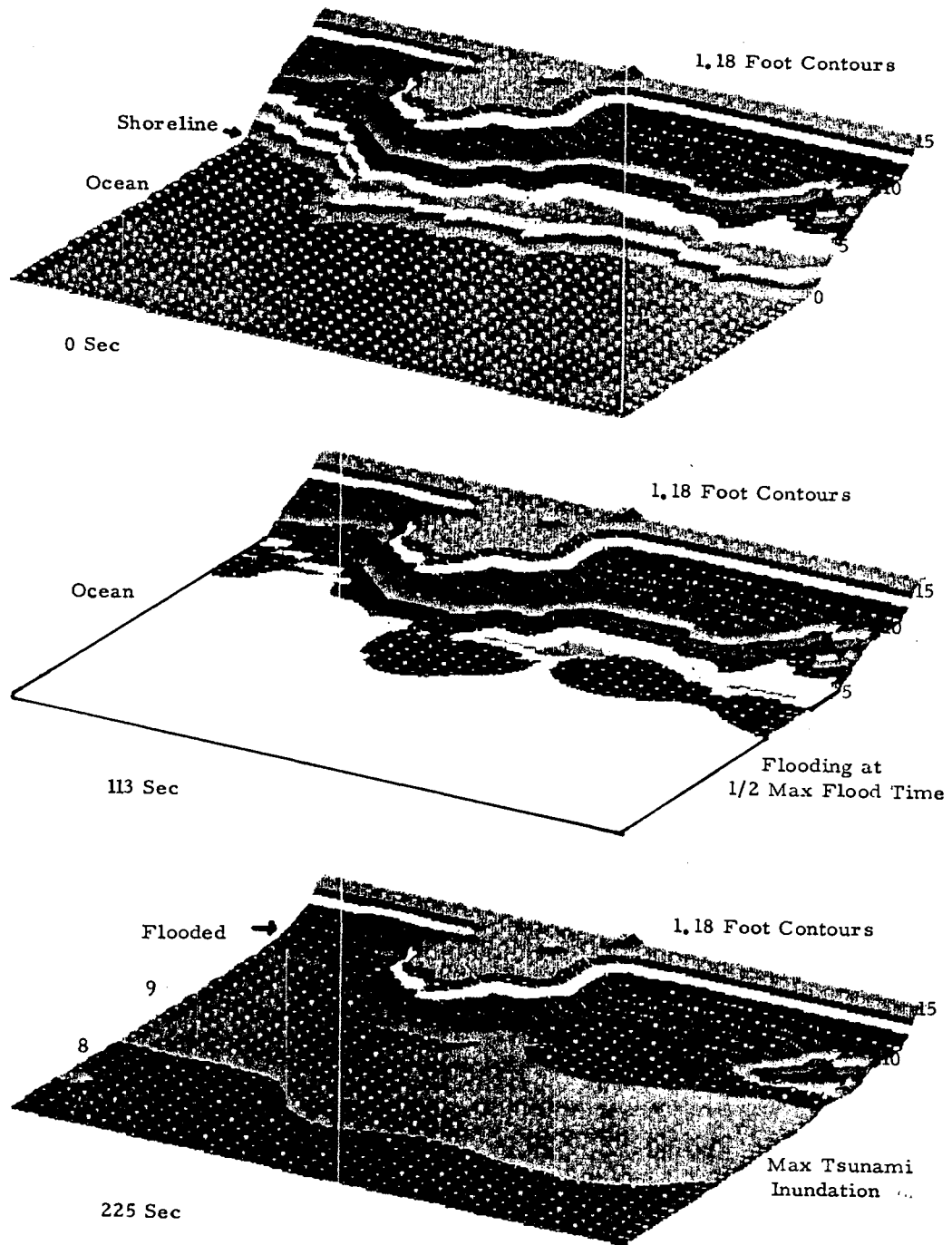
Fig. 2 The ocean surface and land topography at 0, 113 and 225 seconds (time of maximum tsunami amplitude). The ocean surface contours change color according to the surface height. Flooding to the 9-10 foot level is shown. The contour interval is 1.18 feet.
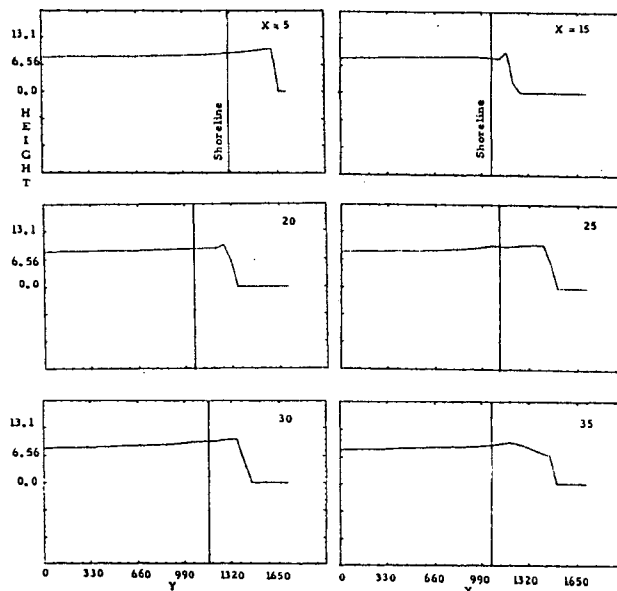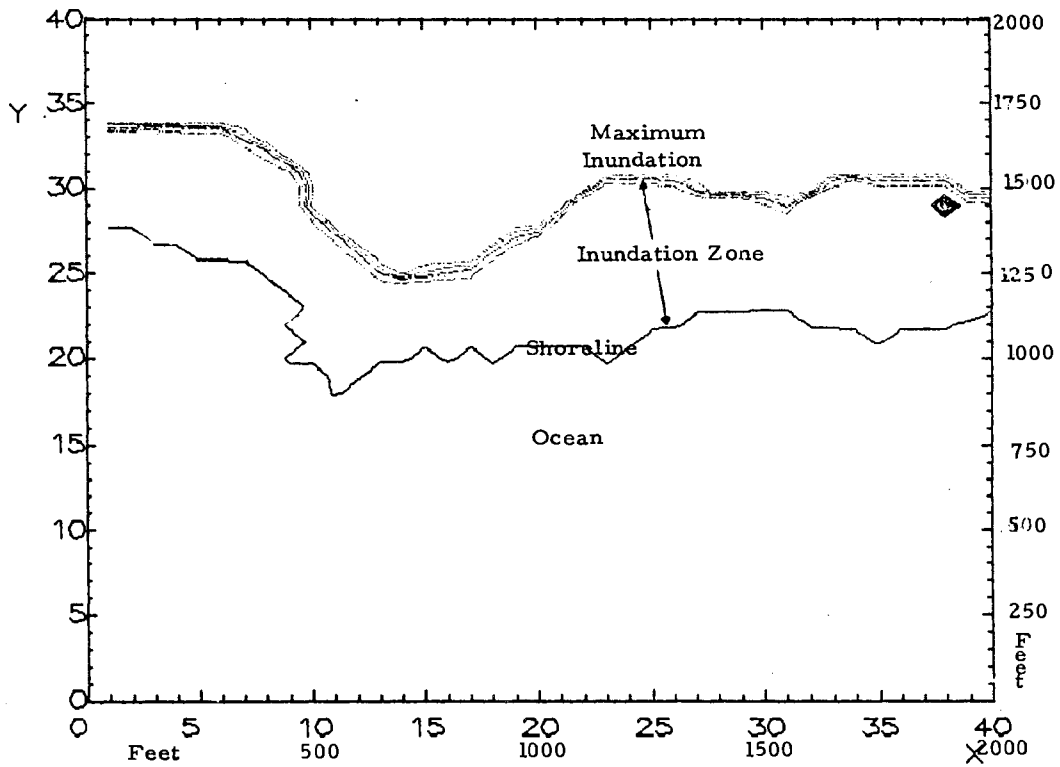
Fig. 3 Cross sections in the Y direction (perpendicular to shoreline) of the water
height. The cross sections are thru the X axis at the X values listed on each
graph. The location of the normal shore line is shown for each cross section.

COMPUTER GRAPHICS FOR THE STUDY OF TRANSOCEANIC PROPAGATION OF TSUNAMIS

F. Imamura*, T. Nagai**, H. Takenaka**, N. Shuto*

* TOHOKU Univ., Sendai, JAPAN
** Tech. Res. Inst., OHBAYASHI Corp., Tokyo, JAPAN

ABSTRACT

The 1952 Kamchatka tsunami and the 1960 Chilean tsunami are simulated in the whole Pacific Ocean. Agitation of the ocean after passage of the major part of the tsunamis is shown well through a computer-graphics-aided animation.

1.INTRODUCTION

According to historical data, tsunamis are generated, once in 1.5 years on an average along the fringe of the Pacific ocean. Although numerical simulations have been considered a useful means to understand the analyse the movement and propagation of tsunamis in the Pacific Ocean, an ordinary computer could not be used, because of its insufficient speed of computation and limited size of memory. A super computer gives satisfactory solutions, if its ability of vector operation is fully used and if a new numerical technique is introduced to reduce the CPU time and memory size.

A super computer creates a huge amount of information, only a few of which has been used in the analyses in past. If used in an animation visualized with the aid of computer graphics, all the computed results vividly reproduces a tsunami. An animation is useful for a better understanding. Sometimes it leads us to new findings. The present paper discusses first the new technique to reduce the computing time and memory on keeping the accuracy of computation. Second, two tsunamis are computed with this technique. Third, the system for graphics is stated.

2. NUMERICAL MODEL

2.1 Numerical Dispersion

According to Kajiura(1970), the dispersion effect is not negligible in the leading waves in the transoceanic propagation of tsunami. The linear Boussinesq equation with the Coriolis force, therefore, should be used in numerical simulations of tsunami propagation in the ocean. Then, even with a super computer it is difficult to meet this condition because the dispersion term which is partial differential term of the third order requires a huge computing time.

An alternative to the linear Boussinesq equation is the use of the numerical dispersion term which is inevitably introduced in the discretized linear long wave equations. Provided that the linear long wave equations are discretized with the Staggered leap-frog scheme, the first term of the discretization error has the same effect as the physical

dispersion term if the following ratio takes a value close to unity [Imamura and Shuto,1989].

$$R.D.=\sqrt{\frac{\text{numerical dispersion}}{\text{physical dispersion}}} = \frac{\Delta x}{2h}\sqrt{1-K^2} \quad (1)$$

where Δx; spatial grid length, Δt; time step size, $K=Co\Delta t/\Delta x$; the Courant number, Co; celerity of the linear long waves, h; water depth.

2.2 Governing Equations

Set of equations of the linear long wave theory is given as follows in the latitude-longitude coordinate system, with the Coriolis force included.

$$\frac{\partial \eta}{\partial t} + \frac{1}{R\cos\phi}\{\frac{\partial M}{\partial \lambda} + \frac{\partial}{\partial \phi}(N\cos\phi)\} = 0$$

$$\frac{\partial M}{\partial t} + \frac{gh}{R\cos\phi}\frac{\partial \eta}{\partial \lambda} - fN = 0 \quad (2)$$

$$\frac{\partial N}{\partial t} + \frac{gh}{R}\frac{\partial \eta}{\partial \phi} + fM = 0$$

where ϕ and λ; latitude and longitude, R; radius of earth, η; elevation of water surface, M and N; discharge in the direction of λ and ϕ, respectively, f; Coriolis parameter.

An example of the effect of the numerical dispersion is shown in Figure 1, in which of the water surface elevation are compared for the 1964 Alaska tsunami at 3.5 hours after its generation. The upper figure is the result with the linear long wave equations with the R.D. value of 1.1 and the lower the result with the linear Boussinesq equation. Except for a small region along the Aluetian Islands, results coincide well with each other.

2.3 Grid length and CPU Time

In order to carry out the computation of high quality, the following three condition should be taken into consideration, provided that Eq.(2) are discretized with the staggered leap-frog scheme. The first is to use the numerical dispersion as discussed above, the
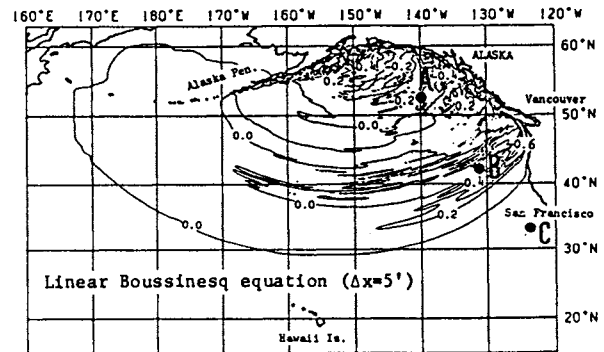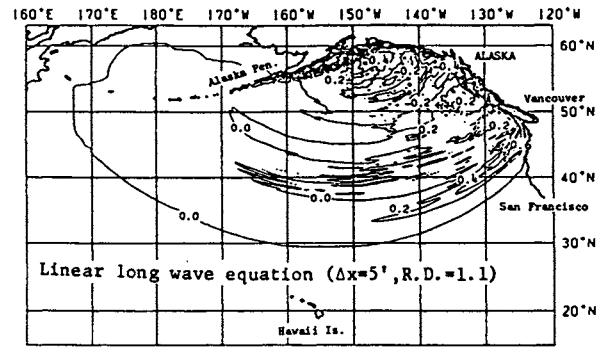
Fig.1 Contours of water surface elevation at 3.5 hour for the 1964 Alaska tsunami

second not to deteriorate the computed wave profile and the last to ensure the stability of computation.

1. R.D. value = 1.0
2. $\Delta x/L < 1/20 - 1/30$
3. $Co\Delta t/\Delta x < 1.0$

where L; length of the major wave component.

Corresponding to $\Delta t=10$ or 20 seconds, the spatial grid length is selected as 5' for 4,000m (R.D.=1.1) or 10' for h=5,000m (R.D.=1.56).

With its vectorization function, a super computer reduces the CPU time to 1/100 compared with the ordinary high-speed computer. The linear long wave equations requires 1/4 the CPU time and half the memory size compared with the linear Boussinesq equation.

3. SIMULATION FOR DISTANT TSUNAMIS

3.1 The 1952 Kamchatka tsunami

Table 1 gives the fault parameters of the earthquake, from which the initial profile of the tsunami is calculated in a usual way.

Figure 2 is a series of the bird's-eye view of the water surface elevation at one-hour interval. The direction of dominant energy propagation is normal to the long axis of the earthquake fault. On the continental shelf along the Aluetian and Kuril trenches, a part of tsunami energy propagates as edge waves.

The tide records and computed results are compared at Kushiro, Hokkaido, Japan as the time series in Fig.3(a) and as the power spectra in Fig.3(b). From the latter comparison, it is evident that the frequency components higher than 10 min. are not adequately reproduced in the numerical simulation. This is due to two reasons. First, the spatial grid length in the computation is not fine enough to reflect the effect of the local topography. Second, the shallow water theory should be used in the nearshore zone.

t=0hr
t=1hr
t=2hr
t=3hr
t=4hr
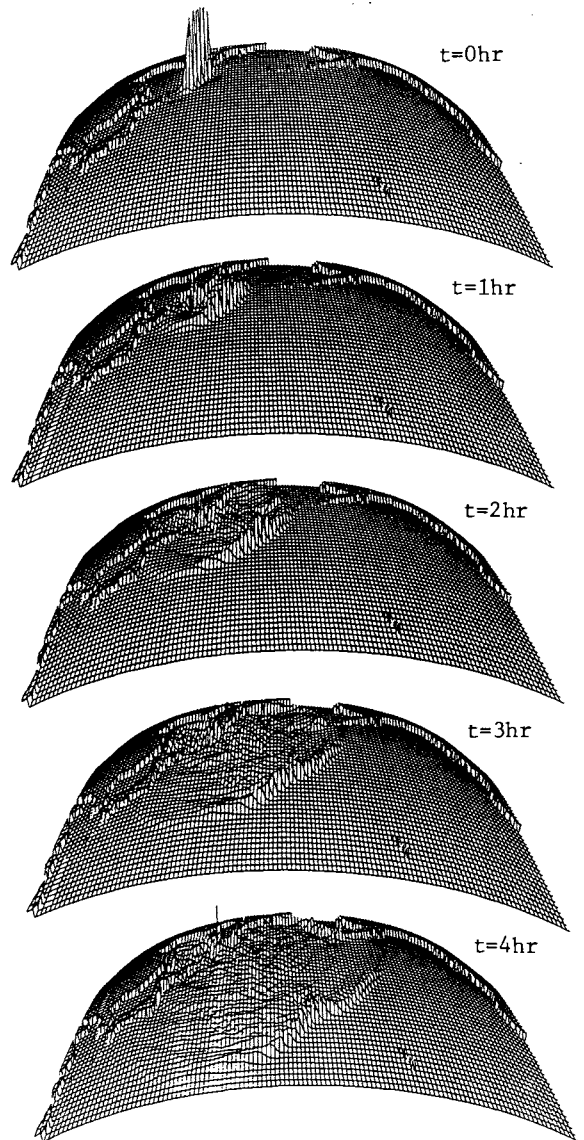
Fig.2 Bird's-eye views of the 1952 Kamchatka tsunami
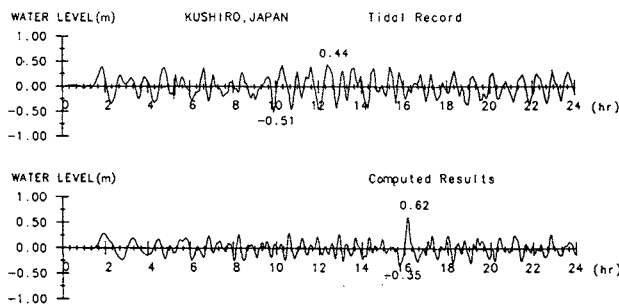
Fig.3a Comparison of tide record with computed result at Kushiro,Japan for the Kamchatka tsunami
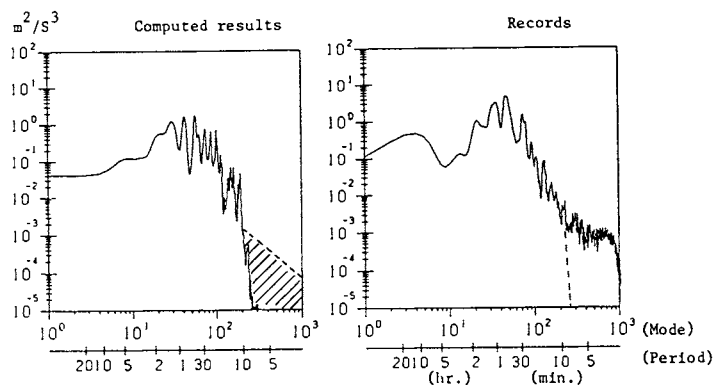
Fig.3b Comparison of power spectra between the computed result and measured at Kushiro, Japan for the Kamchatka tsunami

3.2 The 1960 Chilean tsunami

This is one of biggest tsunami in the Pacific Ocean. Figure 4 shows the position of the tsunami front at one-hour interval. At the beginning, the tsunami spreads nearly circularly around its source. Near and beyond the Hawaiian Islands, the tsunami is affected by topography makes it change its direction of propagation toward Japan and Kamchatka.

Another topographical effect is the trapping of the tsunami around islands.

Figure 5 shows the share of propagating and trapped energy. The continental shelf of South America traps 40% of the tsunami source energy. Then Polynesian, Hawaiian and other islands cause the decrease of the propagating tsunami energy by trapping and reflection. As a result, 25% of the original energy arrives at Japan. The fact that the tsunami is reflected and entrapped by islands is well understood with the aid of an animation described below.

Overall agreement of the computation is evaluated in terms of Aida's K and κ values [Aida,1978]; the geometric mean of the
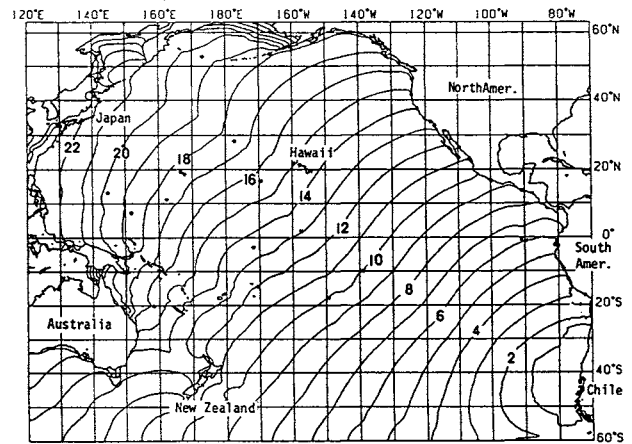
Fig.4 Propagation pattern of the wave front of the 1960 Chilean tsunami
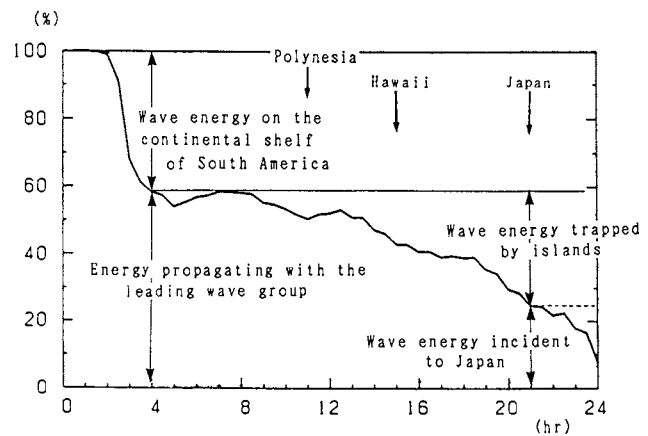
Fig.5 Change in shares of tsunami energy with the travelling time

Table 1 Parameters of fault models of distant tsunamis

Length	Width	Depth	Dip direction	Dip angle	Dislocation	Slip angle
650km	200km	30km	N34°E	30°	5m	110°
800km	200km	53km	N10°E	10°	24m	90°
500km	300km	20km	S85°E		7m	66°

upper; 1952 Kamchatka, middle; 1960 Chile, lower; 1964 Alaska

Table 2 Aida's K and κ in the Pacific ocean

	Arrival time K	κ	First wave height K	κ	Maximum wave height K	κ
South Amer.	1.60	1.56	1.05	1.35	1.60	1.69
Middle Amer.	1.07	1.04	1.01	1.64	1.15	2.01
North Ameri.	1.07	1.05	1.24	1.62	0.77	2.61
Alaska	1.00	1.14	1.10	1.44	0.78	1.48
Hawaii&Polyn.	1.02	1.06	0.69	2.20	0.54	2.77
Australia&N.Z.	1.12	1.05	0.95	1.75	0.42	2.22
Micronesia	1.06	1.03	0.62	1.82	0.85	1.64
Phill.&Taiwan	1.10	1.04	0.56	1.23	0.92	2.89
Japan	1.08	1.04	0.60	2.81	0.66	1.49
Total Average	1.11	1.21	0.93	1.91	0.78	2.44

measured-to-computed tsunami characteristics and the corresponding deviation. Table 2 summarizes the result for each and whole regions. The arrival time, for which K and κ are 1.11 and 1.21, is simulated reasonably well. For the first and maximum wave heights , the averaged values of K are 0.93 and 0.78, suggesting that the total tsunami energy is reasonably well. On the other hand, values of κ, 1.91 and 2.44, suggest that the original energy distribution had better be corrected. For the further detailed study, the shallow water theory and the finer grid length are required in the nearshore zone.

4. COMPUTER GRAPHICS

A full use of the computed data can be possible through editing the data into animation. There are several ways of presentation.

The simplest expression is an animation of the sequence of contours of water surface elevation such as shown in Fig.1. If colours are assigned to particular values of the water surface elevation, an animation becomes easier to be understood. When the transoceanic propagation is discussed, this kind of

animation is good enough for an overall understanding of a tsunami in the wide whole ocean. Among several phenomena, tsunamis entrapped around islands are very clearly but only qualitatively shown by this kind of animation. After the passage of the major portion of a tsunami, the whole ocean is agitated long by reflection and trapping by islands. When the area of concern is very wide, this kind of animation is better.

An animation of pictures in the bird's-eye view like Fig.2 supplies more quantitative informations. It gives a good presentation of the major tsunami energy, if well designed with a properly selected view angle. On the

other hand, water surface disturbances left behind the major is not expressed well in this kind of animation, because the wave height is not large and the wave pattern is very complicated. In addition, tsunamis which enter the sheltered areas such as behind peninsulas are not expressed well. The view angle should be changed in this case. When the area of concern is very wide, this kind of animation is only useful to understand the major movement of a tsunami.

If the area of concern is not wide, an animation in the bird's-eye view is one of the powerful means not only to understand but also to find the movement of a tsunami under the strong effect of local topography.

Figure 6 summarizes the flow from the computation to the final output, video tape. It consists of three stages. The first stage is the numerical computation. A super computer (NEC SX-1EA) was used. The results were once stored in discs. The local net work (Insernet) was used to transport the stored records to the work station (SUN 4/260) which is for the second stage to interpret the computed results to picture images with assigned colours. The results of the second stage were also once stored in discs. The last stage was the recording. Each scene was picked up from the discs of the second stage, displayed with
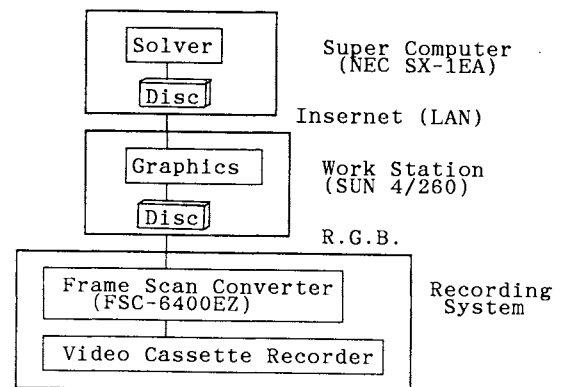
Fig.6 System and flow of the computer-graphics

the aid of the frame scan converter (FSC-6400EZ) and recorded on video tapes.

The CPU time to reproduce 40 real hours for the 1960 Chilean tsunami was 31 min. 27 sec. with NEC SX-1EA, with the time interval $\Delta t=10$sec.. For computer graphics, 6 pictures per 1 real hour, i.e., 240 pictures in total, were selected. It took 1 min. to colour a picture with the aid of SUN 4/260. In the animation, 240 pictures were shown in 24 seconds in total.

5. CONCLUSIONS

The propagation of two tsunamis in the Pacific Ocean is simulated with the linear long wave equations. On discretizing, three conditions are taken into consideration. One of them, the R.D. value (or Imamura number) ensures inclusion of the dispersion effect through numerical truncation errors.

In case of the 1960 Chilean tsunami, 40% of the initial energy is entrapped on the continental shelf along South America and 35% of it is reflected by and entrapped around islands in the ocean. This causes the agitation in the whole Pacific Ocean after the passage of the tsunami. A computed-graphics-aided animation helps to show very vividly but qualitatively and understand this situation.

REFERENCES

1. Kajiura,K, "Tsunami source, energy and the directivity of wave radiation", Bull.Earthq. Res.Inst., vol.48, pp.835-869 (1970).
2. Imamura,F. and N.Shuto, "Tsunami propagation simulation by use of numerical dispersion", ISCFD-NAGOYA 1989, pp.406-411 (1989).
3. Aida,I.,"Reliability of a tsunami source model derived from fault parameters", J.Phys.Earth, vol.26, pp.57-73 (1978).

SOME PROPERTIES OF SMALL TSUNAMIS OBSERVED IN THE PACIFIC COAST OF NORTH EAST JAPAN ON OCT. 29 AND NOV. 2, 1989

Kuniaki Abe*, Masami Okada** and Yoshinobu Tsuji***

* Niigata Junior College, Nippon Dental University
** Meteolorogical Research Institute
*** Earthquake Research Institute, Tokyo University

Abstract

We estimated sources of tsunamis observed at tide stations along the Pacific Ocean of the northeastern Japan on Oct.29 and Nov.2, 1989. The sources were determined by the use of refraction diagram method in the assumption of a simultaneous generation with the earthquake. In the next step we carried out numerical experiments on vertical displacement fields derived from fault models consistent with the sources as a first approximation and found the best fit model comparing the calculated waveforms with the observed ones by try and error method.

The numerical experiments revealed some characteristic properties of these tsunamis. The first is a source location on the sea bottom topography corresponding to the turning points of equi-depth lines. The second is a rapid decrease of the maximum amplitude at an epicentral distance of about 300 km. The third is an observation of small negative wave preceding the main positive wave, observed at tide stations near the source. This small initial wave of negative phase is explained by a thrust fault of low dip angle.

Introduction

Seismic activity increased at the north western part in the Pacicic Ocean off the Sanriku district of north east Japan from Oct.27 to Nov.30, 1989. In the period two biggest earthquakes generated tsunamis. It was reported by Japan Meteolorogical Agency that the former was an earthquake(M=6.5) having the origin time of 14h 25m on Oct.29(JST) and the epicenter of N39 34', E143 47' and the focal depth of 20 km, and the latter was an earthquake(M=7.1) having the origin time of 3h 25m on Nov.2(JST), the epicenter of N39 50', E143 47' and the focal depth of 0 km. The former generated a very small tsunami which was observed at the Sanriku coast. On the other hand the latter generated a small tsunami, which was observed at the coast of Hokkaido and the Sanriku coast.

It is shown by Aida(1978) that a numerical experiment is effective to reproduce the observed waveforms of tsunami on the fault model. We can study characteristic properties of these tsunamis on the numerical experiment.

Source determination

We collected copies of tide gage charts recording these tsunamis by mail. Assuming an simultaneous generation of tsunami with the earthquake we can obtain travel time of tsunami initial wave and initial wavefronts by an inverse refraction diagram method on a computer or compass. Identifying the initial wave with the beginning of rise in the main positive wave we obtain the initial

wavefronts as shown in Fig.1,2. In these figures numerals accompanying with the front lines correspond with station numbers as listed in Table 1. A distribution of initial wavefronts obtained for the larger tsunami shows a moderate divergence. In general it tends for them to be determined inside with the increase of travel time. This tendency is related with the decrease of resolution due to the increase of travel time. As for the result it is remarkable that source regions were determined in the area in which equi-depth lines are not straight. In the source area of the former tsunami we can find a turning point of equi-depth line of 3000 m and in that of the latter tsunami we can find a curved equi-depth line of 2000 m.
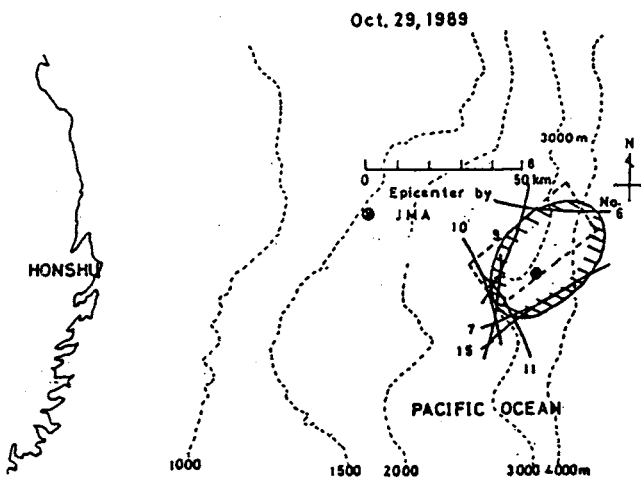
Fig.1
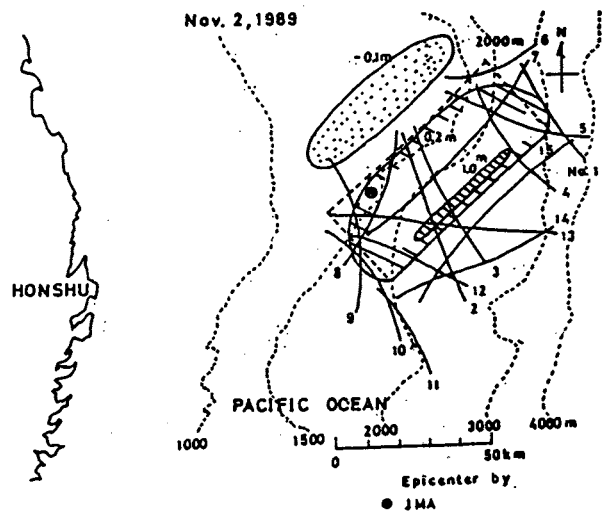
Fig.2

No.	Obs.Station	Oct.29	Nov.2
1	Hanasaki		59
2	Kushiro		55
3	Tokachi		55
4	Syoya		48
5	Urakawa		47
6	Mutsuogawara	46	41
7	Hachinohe	58	53
8	Kuji	44	38
9	Miyako	30	25
10	Kamaishi	29	26
11	Ofunato	35	
12	Miyagienoshima		41
13	Ayukawa		53
14	Soma		80
15	Onahama	66	69

Tsunami Travel Time(min)

Table 1

Fault Models

Parameter	Oct.29	Nov.2
Length(km)	40	70
Width (km)	20	35
Depth (km)	20	1
Dip angle(deg)	30W	30W
Strike (deg)	N50E	N50E
Dislocation(m)	1	2.2
Moment($\times 10^{26}$dyne·cm)	2.4	16

Table 2

In the next time we seek a fault model explaining the collected wavefronts by try and error. The vertical displacement field is calculated on the assumed fault parameters((Mansinha and Smylie,1971). Pure dip slip is assumed. The obtained vertical displacement fields are shown with the fault planes projected on the ground surface in Fig.1,2. Fault parameters of the best fit model are shown in Table 2.

Numerical experiment

Numerical experiments were carried out on the vertical displacement calculated from the fault model. The basic equation is a linear long wave theory. The finite difference equation is used with grid interval of 5 km and time step of 10 sec. Starting from the initial conditions derived from the fault model as shown in Table 2, we obtained time histories of water level and particle velocity for 2 hours.

Reducing the astronomical tide from the original records we compared the observed waveforms with the calculated ones. The results are shown in Fig.3,4. The fitness of calculated waveforms in the tsunami model on Nov.2 is better than that on Oct.29. The difference is related to the source size because the larger
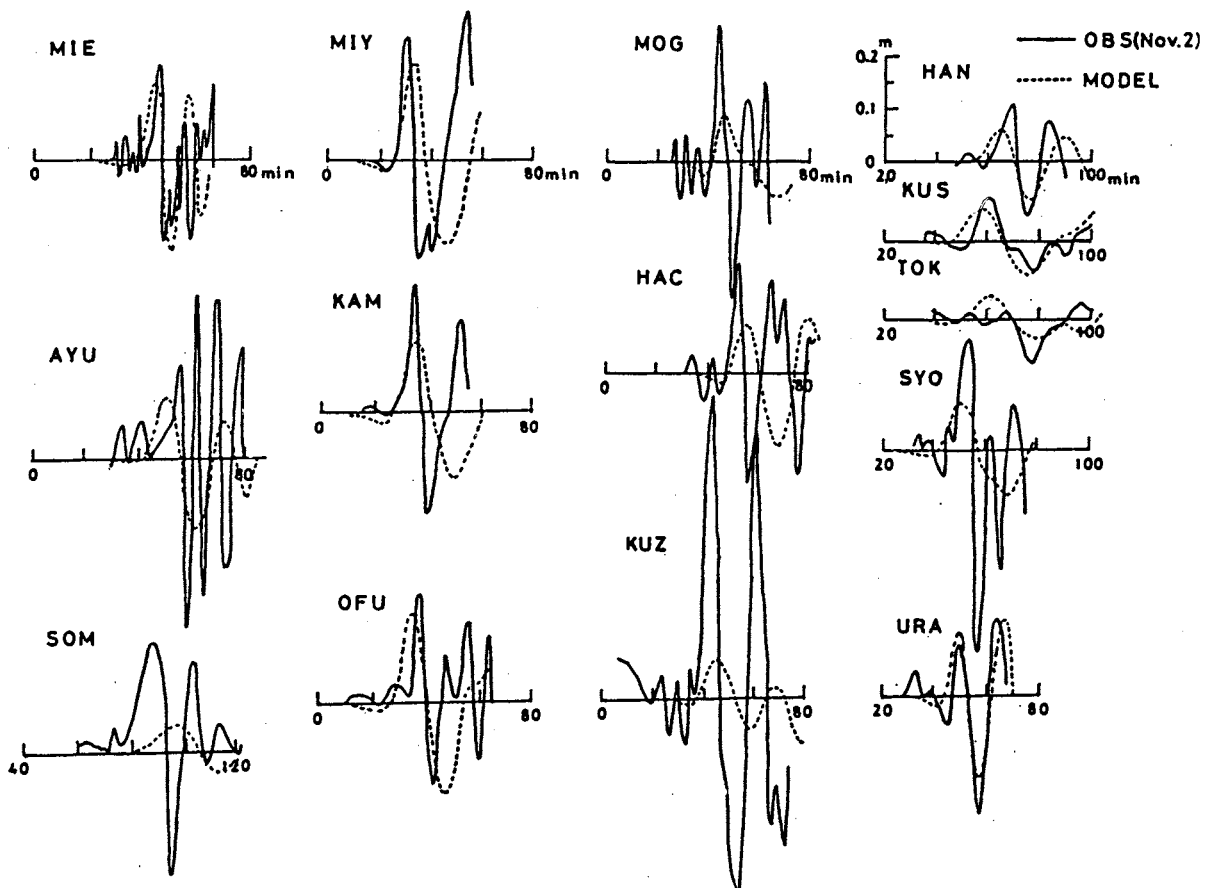
Fig.3
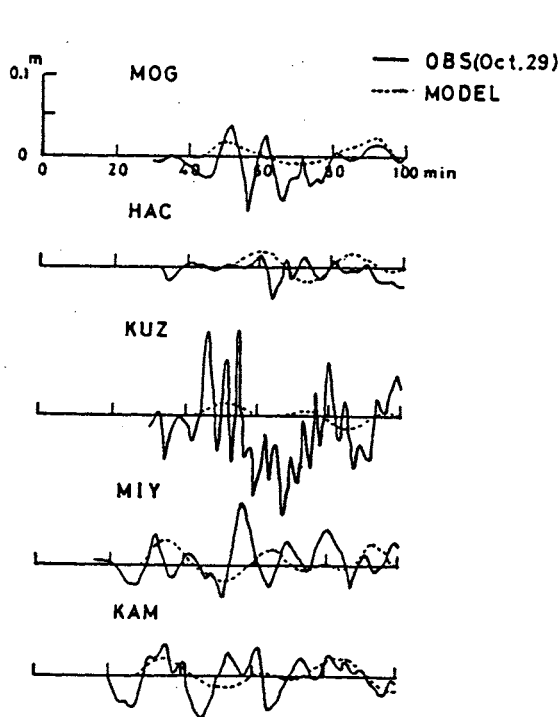
Fig.4
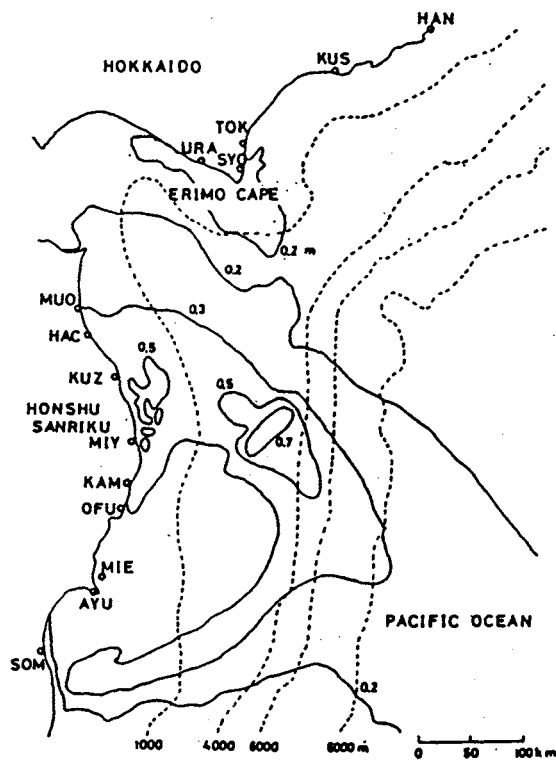
Fig.5

source size is more exactly reproduced under the same grid interval. It is noticed that a tide gage installed outside the bay such as the station, Miyagi-enoshima(MIE), shows the observed record approximately fitting the model. This fact suggests that a reason of unfitness is found in the seiche excited in the neighborhood of tide stations.

The maximum elevations for the tsunami on Nov.2, are shown in Fig.5. The figures shows an energy concentration to the Erimo Cape in Hokkaido and south part of the Sanriku coast in Honshu. It is considered that these concentrations preceded to an increase of decreasing ratio of the maximum amplitude observed with the epicentral distance of 300 km.

Thus we can explain tsunami sources with these models. Finally we mention negative waves preceding the first positive waves. We can point out the negative wave arriving before the arrival of the first positive waves in Miyako(MIY). This phase is characteristic to a thrust fault of low dip angle. The observation shows that the tsunami was generated by the thrust fault of low dip angle.

References
Aida,I.,Reliability of a tsunami source model derived from fault parameters,J.Phys.Earth,26,57-73,1978.
Masinha,L. and D.Smylie,The displacement fields of inclined faults,Bull.Seismol.Soc.Amer.,61,1433-1440,1971.

HEIGHTS OF HISTORICAL TSUNAMIS ON THE COAST OF KATA BAY IN OWASE CITY AND ITS PROPER OSCILLATIONS

Yoshinobu Tsuji*, Takashi Yanuma*, Siniti Iwasaki**

* Earthquake Research Institute, University of Tokyo, Japan
** Hiratsuka Branch of Oceanographic Studies, National Research Center for Disaster Prevention, Japan

Abstract

Kata Bay, in Owase City, Mie Prefecture, was attacked by four huge tsunamis in 1707, 1854, 1944 and in 1946. Detailed survey of inundation heights of those tsunamis was made and found out that at some particular villages on the coast tsunami height was higher than that at another villages in the bay for every tsunami.

The proper oscillation modes of the bay were numerically calculated by matrix method. It was clarified that, the places where inundation height becomes higher for every tsunami are just situated at the places of antinodes of fundamental or secondary modes of the proper oscillations of the bay.

Fig. 1 Diagram of earthquake-tsunamis in the southern sea area off Kanto, Tokai, and Nankai districts since the 14th century. Full lines show the extent of coasts heavily hit by tsunamis. Black circle with an arrow shows the location of Kata bay. In the present study we discuss the 1707 Hoei, the 1854A Ansei-Tokai, the 1944 Tonankai, and the 1946 Nankai tsunamis.

1. Introduction

Kata Bay is located in Owase City, Mie Prefecture, on the south east coast of the Kii Peninsula, in the central of the Honshu Island, the mainland Japan. The mouth of the bay opens south to the Pacific Ocean.

Huge earthquakes occurred in 1707, 1854, and in 1944 in the sea region of south east off the coast of the Kii Peninsula, and accompanied with those earthquakes huge tsunamis were always generated. Those tsunamis are called 'Hoei', 'Ansei-Tokai', and 'Tonankai' Earthquake-Tsunamis, respectively. As the bay stands just facing to the source area, severe damages took place for every tsunamis.

In 1946 another gigantic earthquake called 'Nankai Earthquake' occurred off the western coast of the Kii peninsula, and tsunami with height two or three meters hit the bay.

Musha(1942 to 1949) collected old documents of historical earthquake tsunamis and published them in four

volumes of collected materials.
Tsuji(1981) also collected and
published newly discovered old
documents of historical earthquakes in
the district of the Kii Peninsula.
Catastrophes of the historical tsunamis
in the villages of Kata bay are
described in some documents introduced
on those collected materials. We
selected the articles about Kata bay,
and made measurement of the tsunami
height in almost all villages on the
coast of the bay.
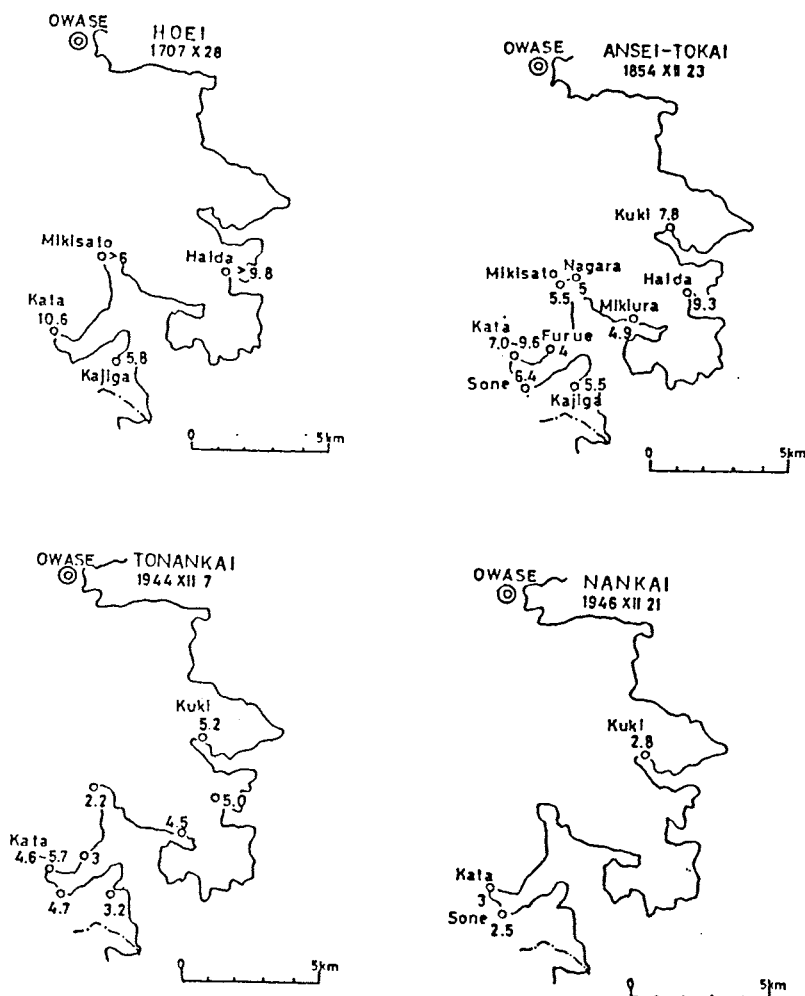
Fig. 2 Heights(m) of the 1707 Hoei, the
1854 Ansei-Tokai, the 1944 Tonankai,
the 1946 Nankai tsunamis in Kata Bay.

2. Survey of Inundation Heights of Historical Tsunamis in Kata Bay

Survey of inundation height of
historical tsunami along the coast of
Mie prefecture had been made in first
by Hatori(1978)[3], but he did not
enter the coast of Kata bay due to the
limit of surveying days.

In the present study, we stayed
there for four days, made precisely
identification of place names described
in the old documents on the present
maps of the residential area, collected

legends from old persons, and on the
basis of those informations measured
inundation height.
　　Fig 2. shows inundation height of
the historical tsunamis. Kata bay has
shape of a cross inside. Kata and Sone
villages are located on the innermost
coast of the western branch bay, and
Mikisato and Mikiura are situated in
the northern and the eastern branch
bays.
　　Sea water climbed up to 10.6m, and
9.6m at Kata village in the 1707 and in
the 1854 tsunamis, respectively, and
in contrast that, at Mikisato in the
northern branch bay, height of only 5
to 6 meters was recorded. Also in the
eastern branch, tsunami height of only
4.9 meters was of measured.
　　As for the tsunami of 1944 and 1946,
we obtained many direct witnesses from
old inhabitants. Most of houses
submerged in the bay in the time of the
1944 Tonankai Tsunami and the
distribution of inundation height is
shown in Fig 2c. For this case also
the highest tsunami was recorded at
Kata village in the western branch bay.
　　The 1946 Nankai Tsunami did not bring
heavy damage to the villages. Only in
the villages of Kata and Sone in the
western branch bay sea water flooded in
the residential area, and houses were
submerged above the floor there.
　　It should be noticed that, tsunami
height was always in the maximum at the
innermost part of the western branch
bay.

3. Calculation of Proper Oscillations in inner bay

　　Various types of numerical
simulations of tsunami propagation are
made by many tsunamists. Most of them
are the method of finite difference
method in which the basic differential
equations of motion in two directions
and of mass conservation are re-write
into difference equations and time
integrations are made step by step in
leap frog method. In the recent years,
this type of calculation has been
developed very precisely such that
individual buildings are separately
distinguish in the used grid scheme.
Probably, uneven inundation height
above mentioned can be numerically
simulated by using powerful force in
such a time integration by the leap
frog method.
　　But to see inundation height
distribution as Fig 2, we may suppose
that uneven height is essentially
influenced by the proper oscillations
of the inner bay.
　　In the case that the shape of bay or
lake is simplified such as one

dimensional channel, rectangle, or circle, it is easily to solve the eigenvalue problem and period and pattern of oscillation are analytically obtained.

Hidaka(1931)[4] obtained the solution of oscillation of an elliptic bay with uneven bottom by using Ritz's method.

Loomis(1966)[5] introduced a method of numerical analysis on bay or lake oscillations by solving eigenvalue problem of matrix.

In the present study we use the Loomis' method, and obtained the solution of the eigenvalue problem of bay oscillation for Kata Bay.

We assume that wavelength of tsunami is sufficiently long in contrast to depth of sea, and neglect the terms of non-linear, viscosity, and rotation of the Earth. We have the equation of tsunami propagation as,

$$\frac{\partial^2 \eta}{\partial t^2} = g \nabla \cdot (H \nabla \eta) \qquad (1)$$

where η is sea surface displacement, g is acceleration of the gravity, $H(x,y)$ is depth, and nabla operator ∇ is two dimensional (in x- and y-directions) one.

We also assume that η changes periodically as $\eta = z \exp i\omega t$, then we have

$$-\omega^2 z = g \nabla \cdot (H \nabla z) \qquad (2)$$

We re-write (2) in difference style as,

$$-\omega^2 z_{i,j} = \frac{g}{(\Delta x)(\Delta y)} \{ (\frac{H_{i,j} + H_{i+1,j}}{2} z_{i+1,j} + \frac{(H_{i,j} + H_{i-1,j})}{2} z_{i-1,j}$$
$$+ (\frac{H_{i,j} + H_{i,j+1}}{2} z_{i,j+1} + \frac{(H_{i,j} + H_{i,j-1})}{2} z_{i,j-1}$$
$$- (2H_{i,j} + \frac{H_{i+1,j} + H_{i-1,j} + H_{i,j+1} + H_{i,j-1}}{2}) z_{i,j} \} \qquad (3).$$

where suffix i, and j is the orders of grid cells in x-, and y-directions. We make re-numbering grid cells in one dimensional with removing grid cells of land area, and re-write the suffix as 1,2,... k for z and H. k is the total number of the grid cells of sea region. Then (3) is deformed as

$$A z = -\omega^2 z \quad (z \equiv \begin{pmatrix} z_1 \\ \vdots \\ z_k \end{pmatrix}) \qquad (4)$$

where A is a square matrix arranged the coefficients in (3) and has the size of k x k.

Boundary condition for the coastline is given by assuming that wave is perfectly reflected there. On calculation we regard the coastline as a mirror, then the boundary condition is automatically satisfied. Thus we have,
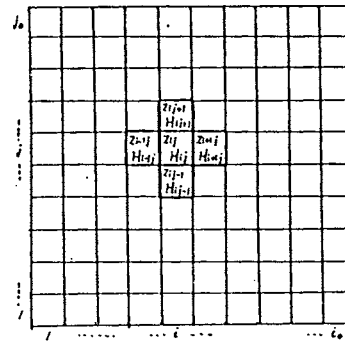
Fig. 3. Grid mesh with order of suffixes.

$$\frac{\partial \eta}{\partial n} = 0 \qquad (5).$$

As for the boundary condition on the mouth of bay, Murty(1984)[6] proposed various typed ones. In the present study, we simply assumed that water level keeps zero on the open boundary, and so,

$$\eta = 0 \qquad (6).$$

This assumption is equivalent to that depth of the outside of the bay is assumed to be infinitive and that sea water can be supplied instantaneously in any amount.
Actually depth of outside of the bay is finite, and sea water can not be supplied instantaneously, and so, actual periods of individual mode oscillations would be slightly longer than those obtained numerical analytically.

Only five non-zero value appears in each line of matrix A in (4) in maximum. All non-zero values are situated within the band with width of i_{max}, and so we need not keep full memory of k x k for expression of A. We can use Jacobi's eigenvalue calculation subroutine in band matrix, which is generally equipped at any computing center.

We tried to make program in FORTRAN IV for personal computer PC-9801VX(NEC) and big sized computer of HITAC-280H in Earthquake Research Institute, University of Tokyo. It was clarified that as for the personal computer, limit of number of sea grid cells k is 300, and for big sized computer, limit of k is about 6,000 in considering memory size and general CPU time.

4. Result of Eigenvalue Analysis

We used grid mesh covering Kata Bay with cell size 180m x 180m.
The proper periods of the first, second and third modes is 21.5, 10.3, and 8.93 minutes, respectively. The pattern of each mode is shown in Fig 6.
The first mode with period of 21.5 minutes has only one nodal line at the bay mouth, and whole the bay oscillates in the same phase. For this mode, wave height at Kata, the innermost point of the western branch bay is about 10 to 15% higher than that at Mikisato, in the north branch, and 40% higher than that at Mikiura in the eastern branch.
The second mode has two nodal lines. One is situated at the bay mouth and the other is situated at the joint of the western branch bay. Sea level in the western bay oscillates in the opposite phase with that in another
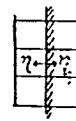
Fig. 4 Boundary condition on coastline
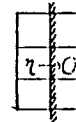
Fig. 5 Boundary condition for bay mouth

parts of the whole bay. Absolute value of the wave height at Kata, the innermost of the western branch is 15%, and 120% higher than that at those of the northern and eastern bays, respectively.

We may recognize that the fact that tsunami height always takes maximum at the villages on the innermost coast of the western branch bay as we described above, can be explained by that in this bay, the proper oscillations for the fundamental(first) and/or second modes are easily induced by the coming tsunami and that the distribution of tsunami height is strongly reflected by the pattern of the proper oscillations.

The third mode with period of 8.93 minutes has three nodal lines; one is at the bay mouth, the second and the third are at the joints of the western and northern branch bays. For this mode main wave motion is going and returning of water between in the northern and eastern branches, and western branch hardly contributes to the motion. Wave height is not high at the innermost of the western bay, and the pattern of the third mode does not agree with the actual height distributions of historical tsunamis.

5. Discussion

We can recognize that the distributions of height of tsunami of the historical tsunamis in Kata bay agrees with the pattern of the fundamental and the second mode of the proper oscillations of the bay. Generally speaking, low order modes of oscillations are apt to induced more eminently than higher ordered ones. Especially, it is not too much to say that the most part of the induced motion by tsunami is that of the fundamental mode. We can say that tsunami height distribution can be explained basically by induction of the fundamental and/or the second mode of the bay.

Induction of the low ordered mode is, roughly speaking, independent to the condition of coming tsunami, and so, at the points where amplitude of the proper oscillation of some low ordered mode is bigger than another part of the bay, inundation height will also be higher for future tsunamis. But in the special case that period of coming tsunami nearly agreed with period of some mode of inner bay, the oscillation will be stimulated extremely caused by the resonance. In such special case, particular higher order mode oscillation pattern may be strongly induced in the bay.

Ratio of tsunami height at the innermost point of the western branch
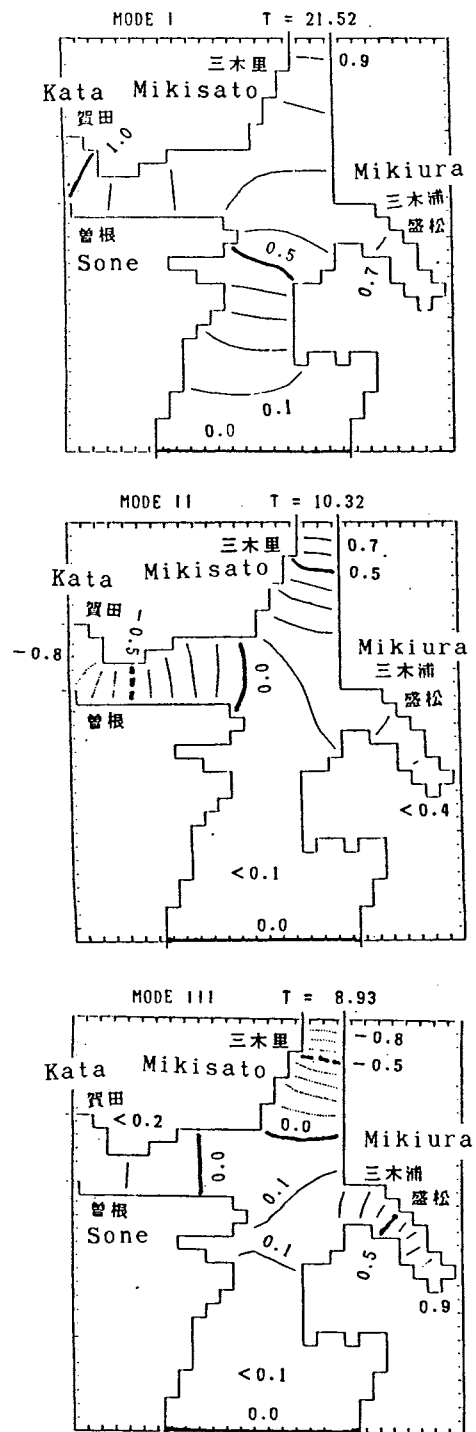
Fig. 6 Analytically calculated proper oscillation of Kata Bay for the first, the second, and the third modes

bay to that of the northern branch is 1.4 to 1 for the 1854 Ansei-Tokai Tsunami and 1.6 to 1 for the 1944 Tonankai Tsunami, and so the difference of tsunami height is greater than that of the calculated proper oscillation modes. This difference can not be well explained now. And it can also be pointed out as a future problem that the period of second and third mode are close to each other, 10.3 minutes and 8.93 minutes respectively, and so both modes oscillations are considered to be equally induced, but is it reasonable to consider that only 2nd mode was developed and 3rd mode was not developed.

References

1. Musha, K., Historical materials on earthquakes in Japan(revised edition, in Japanese), 4 volumes, I:1942, II and III:1943, Meihosha Press, IV:1949, Mainichi-Shinbunsha Press.
2. Tsuji, T., Historical materials on earthquakes and tsunamis in Kii Peninsula(in Japanese), National Res. Cent. for Disaster Prevention, pp392(1981).
3. Hatori, T., Field investigation of the Tokai Tsunamis in 1707 and 1854 along the Mie coast, east Kii Peninsula, Bull. Earthq. Res. Inst., 53, 1192-1225(1978).
4. Hidaka, K., The oscillations of water in spindle and elliptic basins as well as the associated problems, Mem. Mar. Sci. Div., MS Rep., 28, 47-79,.
5. Loomis H.G., Some numerical hydrodynamics for Hilo Harbor, Inst. Geophys. Univ. Hawaii, HIG-66-7(1966).
6. Murty, T.S., "Storm Surge - Meteorological Ocean Tides", Dep. of Fisheries and Oceans, Sci, Infor. and Publications Branch, Ottawa, pp897.

A NOTICE ON CHILEAN TSUNAMIS IN THE NORTHWESTERN PACIFIC

S. Nakamura*

* Kyoto University, Japan

Abstract

A notice is given for predicting the most hazardous events of Chilean tsunamis on the coasts in the northwestern Pacific. A dynamical possibility of cyclic tsunami hazards is also discussed on the basis of the planetary effect as one of the triggers for the events. In this work, a key to the present status of the existing tsunami warning systems are introduced and notifyed first. Then, the published tsunami catalogs and the newly revealed materials are noted as the references for learning to prepare a catalog of the trans-Pacific tsunamis which had been generated off the south America. After that, the author concentrats his interest to the most hazardous events in the catalog. Referring to the catalog of the most hazardous events caused by the Chilean tsunamis, the author considers possiblility of a cyclic property of the hazardous events in relation to the effects of the solar activity, the planets in the solar system, the lunar ascending tide and the Earth's pole tide. A part of this notice could be helpful for short-term and long-term predictions and protection plannings of the most hazardous events.

1. Introduction

This work is a notice to the most hazardous events caused by the Chilean tsunamis on the coasts in the northwestern Pacific. As is well known, the 1960 Chilean tsunami was one of the most hazardous tsunamis on the coasts near the antipode of the tsunami source. This event was a trigger to form a Pacific Tsunami Warning Center. This event has raised a problem to consider what is the most effective way to predict the hazardous trans-Pacific tsunamis which hit the coasts of the Japanese Islands located in the north western Pacific. With the above notice, the author considers what is necessary to protection and warning of the events. This work must be possibly a mile-stone for the

tsunami warning and protection works if we could establish a reasonable prediction of the most hazardous tsunamis generated near at the antipode. In this work, the tsunami catalogs are overviewed with the author s remark first. Then, the author concentrates his interest to the most hazardous Chilean tsunamis which had hit the coasts of the Japanese Islands located in the northwestern Pacific. These tsunami catalogs give us an information about what had been happened at the events in the past, though it is hard to find what had been the essential troggers of the events on the basis of the scientific scopes. The author now notes possible cycle existence of the most hazardous Chilean tsunamis in relation to the solar activity, the effects of the planets in the solar system, the lunar ascending tide and the Earth's pole tide. If the author's notice is reasonable, it could be utilized for the warning and public protection works planning in future.

2. Tsunami Warning System

The United States had suffered in 1945 by the Alaskan tsunami without any aware of the hazards on the Californian coasts. And, the coasts of the Japan Islands in the northwestern Pacific had hit by the 1960 Chilean tsunami which had caused the most significant hazards on the coasts which were near the antipode of the tsunami source. These experience made us to establish the present Pacific Tsunami Warning Center for the circum-Pacific seismic zone. The function of this Center is aimed to be well organized for the short-term prediction or warning of any tsunamis which hit any part of the coasts facing the Pacific.

On the other hand, the International Tsunami Information Center(ITIC) was settled at Honolulu which has been maintained by the U.S. National Ocean and Atmospheric Administration(NOAA) for the International Oceanographic Commission(IOC) after the UNESCO's

support. The membership of the IOC International Co-ordination Group for the Tsunami Warning System in the Pacific(ITSU) now comprises of the interested states, i.e., Australia, Canada, Chile, China, Columbia, Cook Islands, Democratic People's Republic of Korea, Ecuador, Fiji, France, Guatemala, Indonesia, Japan, Mexico, New Zealand, Peru, Philippines, Republic of Korea, Singapore, Thailand, U.K. Hong Kong, U.S.A., U.S.S.R. and West Samoa in 1989(1). The above tsunami warning functions have been promoting a more reasonable and effective practice with an improved prediction technique which must be completed in near future.

3. Tsunami Catalogs

By the time in 1990, we have many of the published tsunami catalogs in the world. One of the first english editions must be prepared by Iida et al.(2) in 1967. In U.S.S.R., Soloviev and Gao have published the tsunami catalog in the western Pacific (3) in 1974 and the tsunami catalog in the eastern Pacific(4) in 1976. These two of the Russian edition are including the compiled descriptions from the local surveys. One of the japanese editions about the tsunamis and earthquakes must be, for example, 'Dainippon-Zishin-Shiryo' which had been edited by Tayama(5) in 1904 after Professor Fusakiti Ohmori at that time. One of the recent editions is published by Watanabe(6) in 1985 in japanese. Local tsunami catalogs must have been composed in every hazardous areas respectively. For example, Iida has composed a brief catalog of the tsunamis in Japan and its neighboring countries(7) in 1984. As for the Mediterranean and the Atlantic, tsunami catalogs has been edited by Galanopoulos(8) in 1960, Ambraseys(9) in 1967, Caputo and Faita(10) in 1982 and Moreira in 1982(12), in 1984(13) and in 1985 (14). Vita-Finzi and King(15) have explored in 1985 seismicity around the 1981 Corinth earthquakes and examined its geomorphological evolution which has traced over the last 40 000 years, though no detail is introduced in this work. Now, the author concentrates his interest to the trans-Pacific tsunamis observed on the northwestern coasts of the Pacific. This main purpose is to get a dynamical understanding of possible cycle of the most hazardous events caused by the Chilean tsunamis even though the locations of the tsunami sources had been distant enough to the suffered coastal zones. At the past events of the Chilean tsunamis, no one had felt any seismic signal in advance or any precursor which make them to consider their ways to protect or mitigate their coastal activities by theirselves. This state is unchanged even at this time, so that it is necessary to consider problems as seen in this work.

4. Hazardous Tsunamis Generated off South America

A chronological table of the Chilean tsunamis and of the trans-Pacific tsunamis generated off the south America was prepared by Nakamura(16) in 1988. In his table, it is clarified that the locations of the hazardous tsunamis off the South America are also effectively hit the coasts in the northwestern Pacific. For example, the locations of the tsunami sources are off Ecuador, off Lima, off Peru(Collao), off Valparaiso, off Iquique, off Coquimbo, off Atakama and off Valdivia. The biggest tsunami events which were in a category of the case exceeding 20 meters tsunami height, had left the records of the big tsunamis in the Hawaii Islands as well as those in the Japanese Islands. These could be briefly listed as follows, i.e.,

a) 1586   off Lima, Peru(28 m).
b) 1837   off Valdivia, S.Chile(big tsunami).
c) 1868   N.Chile(21 m).
d) 1877   off Iquique, Chile(23 m).
e) 1960   off Valdivia, S.Chile(25 m).

The above five events had affected those on the coasts of the Hawaii Islands, though we know that the maximum tsunami height was 6 m at Hilo in 1837, 3.6 m at Hilo in 1906, 3.6 m at Maui and 1.5 m at Hilo in 1906, 2.1 m at Hilo in 1922, and 10.5 m at Hawaii in 1960, respectively.

Including the above five events, the trans Pacific tsunamis off the South America had made to leave the records and documents on the Japanese Islands, especially on the coasts of the eastern Japan. As for the coasts of the south and west Japan, the minor effects had been recorded. Nevertheless, the author has to be aware that the above five events were very hazardous on the coasts of almost all of the Japanese Islands facing the northwestern Pacific. Now, it is essential to clarify that any dynamical understanding of cyclic severe tsunami hazards caused by the trans-Pacific tsunamis. If this cycle is understood on the basis of dynamical scope, it is useful to consider an effective warning and an effective plan for tsunami protection works.

At present, we have a detailed reconaissance report about the 1960 Chilean tsunami which had hit the Japanese Islands and which had caused the unexpected severe hazards in the coastal zones even though the tsunami source was located at a distant location on the Earth. There must be the other reports which includes what had been happened and observed on the coastal zones at the 1960 Chilean tsunami. In this work, the author feels it necessary to get any hypothetical understanding of the cycle of the Chilean tsunamis not only in the scope of historical chronology but in the scientific scope.

5. The Most Hazardous Chilean Tsunamis

According to the chronological table of the Chilean tsunamis prepared by Nakamura (16) in 1988, the five tsunamis introduced above were taken to be very hazardous in Hawaii and in the Japanese Islands. With a more careful understanding of the table, the 1960 Chilean tsunami affected in the wide range of the coastal zones in the northwestern Pacific. A quite similar event to the 1960 tsunami is the 1837 tsunami. Although, there have left only a limitted documents about the 1837 tsunami. As for the south Japan, people seems to have been in a stage of famine around in 1837 and the trace of the 1837 Chilean tsunami is not found by this time except the districts including the Sanriku coast in the eastern Japan facing the Pacific. Now, the author tends to believe that the 1837 Chilean tsunami could be almost same to the 1960 Chilean tsunami in the effects found on the coasts.

As seen above, the time interval between the 1960 and 1837 Chilean tsunami is 123 years. This time interval is not so far from the time interval of 121 years.

It is well known that the climate variations are significant in the 11-years solar cycle, for example, as Mori(17) noticed in 1981, and that, the 11-year term is also detected in the sea level variations, for example, as Currie(18) pointed out it in 1981. Now, the author is wondering to manipulate the time interval numerically in order to understand why the time interval should be 123 years in this case. One idea must be the value of 121 as a square of 11. This seems suggesting that the most hazardous Chilean tsunami has a cycle of the eleven times of 11-years with an allowance of two or three years. Although, there is no dynamical reason with any agreeable understanding. In the author's understanding, the 11-years cycle variations of the climate and the sea levels could be related directly to the solar activity which affects the solar radiation on the Earth's surface as to supply heat energy in the tropical zone to drive the Earth's fluids. Nevertheless, it is hard to consider that the solar activity can be directly effective to the priodicity of the interested tsunami events which are generated the earthquakes undersea.

As for seismic cycle, one of the U.S. scientists proposed a hypothetical report on higher possibility of earthquake occurrence around the two equinoxes in a year in a scope of statistics of seismic activity. After a time elapse, the author has informed that Rundle et al.(19) reported in 1989 about Scholtz's argument on no-periodicity of earthquakes.

Even though, the author's interest is in an effect of the solar activity to the tsunamis. The 11-years cycle of the solar activity had been pointed out as the sun spot number variations, for example, by Maunder(20) in 1922, by Hale(21) in 1924, by Stix(22) in 1989, by Tayler(23) in 1989 and by Nakamura(24) in 1989.

6. Effects of the Planets

If the cycle of the Chilean tsunamis in the northwestern Pacific could be predicted at a time interval of about 121 years, there must be some dynamical reason which has never been clarified.

Now, the author tries to consider problem of a simplified astronomical two-body with some assumption for a convenience of a consideration. The established knowledge on astronomy tells us that the solar year cycle of the Jupiter is 11.861 years and that of the Saturn is 29.443 years. Most of each planet must be effective more or less for the elastic deformation of the Earth's crust in a concept. The effect must be a function of the mass ratio of the interested two planets. The mass ratio of the Jupiter to the Earth is about 318, which suggests that a part of the variations of the Earth's motion must be in a period of the Jupiter's solar year cycle. Similarly, the Saturn's effect could be considered. Minor effect could be expected for the solar year cycle of, for example, the Mars, the Uranus, the Neptune or the Pluto. Here, now, the above is simply a notice referring to the solar year cycle of each planet in the solar system. When there is no dynamical support, the above notice can simply be a numerical manipulation.

As for the Saturn, its solar year cycle about 118 years seems to be able to interact to intensify its attractive effect to the Earth when a time meets to the Jupiter's ten cycles, that is, 118 years. This 118 years could be acceptable for the 121 or 123 years time interval of the Chilean tsunamis with an allowance of five years.

At this time, the author can not escape out of the application limit of the astronomical two-body problem. Even if a numerical manipulation looks to be reasonable it is simply a presupposition without any dynamical understanding. Hence, it is necessary to make clear that the Chilean tsunamis cycle is existing and this cycle can be dynamically related to the astronomical factors. Then, the author's concept should be confirmed whether it is reasonable in the scope of astronomy. In order to confirm this, he has to stand again at the starting line of the astronomy which could be overviewed a text book written by Obi(25).

7. Luni-Solar Interaction

By this time, it is not yet clar that the effects of the planets in the solar system to an expected 121 or 123-years Chilean tsunamis. One of the recent interesting publications must be in the scope of this work because it concerns on long-term changes in the rotation of the Earth in the period of 700 B.C. to A.D.1980. This problem has been undertaken, for example, by Hide(27) in 1984 and by Stephanson and Morrison(28) in 1984. However, it seems that this would not give any expected trigger for the dynamical background of the periodicity of the most hazardous Chilean tsunamis.

Now, the author has to write that no direct application of the astronomical knowledge can not give any expected answer, and there seems to be little possibility of a simple application of the results on the rotation of the Earth for the author's aimed conclusion. Nevertheless, there must be any reason for the time interval of the 121 or 123-years.

As we are familiar to the Sun and the Moon, there must be some information which supports a 121 or 123-years cycle. Here, one of the long-term lunar cycles are introduced for the author's consideration. That is to consider the lunar ascending nodal tide. This tide seems not to be taken as one of the effective factors for the periodicity of the most hazardous Chilean tsunami in the northwestern Pacific at a glance.

Now, the author considers an interaction between the two cycles. The one is the cycle of the lunar ascending nodal tide and the other is the 22-years cycle of the solar activity. These frequencies can be obtained easily, i.e., the frequency of the lunar ascending nodal tide is

$$f_1 = (\ 1/18.6\ )\ \ y^{-1}.$$

The frequency of the 22-years cycle of the solar activity is

$$f_2 = (1/22)\ \ y^{-1}.$$

When the values of f_1 and f_2 are evaluated as

$$f_1 = 0.0537\ \ y^{-1},$$

and

$$f_2 = 0.0455\ \ y^{-1},$$

then, we have the two other frequencies as a modulated result after an interaction of the two components of f_1 and f_2. That is, the one is the component with a frequency given by the sum of f_1 and f_2. The other is the component with a frequency given by the difference of f_1 and f_2. Those are

$$f_+ = f_1 + f_2\ ,$$

and,

$$f_- = f_1 - f_2,$$

respectively. Then, the values of the two frequencies f_+ and f_- are given as follow;

$$f_+ = 0.0992\ \ y^{-1},$$

and,

$$f_- = 0.0082\ \ y^{-1}.$$

These frequencies approximately corresponds to the following values in period, i.e.,

$$T_+ = 1/f_+ = 10.08\ \ y,$$

and,

$$T_- = 1/f_- = 121.95\ \ y,$$

respectively.

The period of T_+ is approximately 121.95 years. This period is almost same to the time interval of the most hazardous Chilean tsunamis 123 years with an allowance of about two years. It is easily seen that the 22-years cycle can be taken as a doubled 11-years solar cycle. Nevertheless, no remark is given about this long-term cycle in the climatological and geophysical variations by Hayami(29) in 1967.

As for Brückner cycle of 35 years, there is a negative remark about its deterministic cycle after referring to the appearances an the Earth's surface. This remark is given by Wadati(30) in 1979. Wadati has noticed that the Brückner cycle can not be exactly periodical after his studies about the state of the Alpine Glaciers, of the river freezing in the Soviet Union, of the water level variations in the Caspian Sea, of tree-ring growth rate, of agricultural crops and of the other interested processes.

As stated above, the Brückner cycle must be aperiodical. This cycle must be reduced after a statistical analysis of some features surrounding Brückner as a variation with an avaraged period of 35 years. Hence, there must be any reason for the variations. As far as we try to take it meaningful that the 35-years cycle is preveiled in many processes found on the Earth' surface, it could be one idea to take the 35-years cycle as a doubled 18.6-years cycle with an allowance of two or three years. With this, there must be a dynamical reasoning of the Brückner cycle even though the idea must be acceptable as an approximate consideration.

8. Effect of the Pole Tide

As seen above, it looks as if reasonable to take a 121-year cycle as an interaction of the 22-years solar cycle and the lunar ascending nodal tide with the cyclic period of 18.6-years.

At this time, the author feels it necessary to consider the other factors which govern the 121 or 123-years cycle of the most hazardous Chilean tsunamis.

By this time, the pole tide has observed by Chandler(31),(32) in 1901. The pole tide has been discussed by Haurbich and Munk(33) in 1959 and by Maximov(34) in 1970. The dynamics of the pole tide has been taken as a variations of the Earth's latitude. The related works has been undertaken, for example, by Larmor(35) in 1915, by Jeffreys and Vincente(36),(37) in 1957 and by Haubrich and Munk(33) in 1959 . This pole tide of the Earth is taken as caused by the mutation of the Earth's axis of the Earth's rotation in a period of 14 months.

When we accept that a solar year of the Earth is 12 months and the pole tide is 14 months in cycle, an interaction of the two makes two modulated cycles. If we consider this interaction in similar way to that for the interaction of the 22-years solar cycle and the lunar ascending nodal tide as stated in the last section, it is easy to get the modulated freqencies. The two modulated frequencies tell us the two modulated cycles of 7-years and 0.58 year. The 7-years cycle is found in the fields related to climate though no details are discussed in this work.

Successively, an interaction of the above 7-years cycle and the 11-years solar cycle induces the other two modulated cycles of 4.28-years and 19.25-years. The one of these cycles is approximately same to the five-years cycle found in the climatological processes. This can not be in interest to the present author's work. The other one is the 19.25-years cycle. This cycle is nearly same to the 18.6-years cycle of the lunar ascending nodal tide. As far as we trust these cycle to be deterministic, a bold expected cycle can be reduced by the same way to get two modulated frequencies as a result of an interaction of selected two cycles appeared above.

Thence, the 19.25-years cycle modulates the 22-years cycle to expect a 154-years cycle. This 154-years cycle can not be a supporting factor to the existence of the 121 or 123-years cycle at this time.

A triple 7-years cycle modulate the 19.25 years cycle to expect a 231-years cycle. Although, this 231-years cycle could be same to the doubled 121-years cycle with an 11-years allowance.

A triple 7-years cycles may modulate the doubled 11-years cycles to expect a 462-years cycle. This 462-years cycle is same to the doubled 231-years cycle. This 462-years cycle can be taken as a quater 121-years cycle with an allowance of 22 years.

The 18.6-years cycle interact to the 19.25-years cycle to expect a modulated cycle of 496-years. This 496-years cycle can be taken as a quater 121-years cycle with an allowance of 12 years.

With the above result, the author thinks it necessary to remind that the 11-years cycle is obtained as a result of a statistical processing of the data of the solar activity. The 11-years solar cycle is not necessarily deterministic. So that, the above expected 231, 462 or 496-years cycle could be a measure of the existing long-term cycles. The second harmonics of the above three cycles could be a 116, 231 or 248-years cycle, and the third harmonics could be a 77, 154 or 165-years cycles. The fourth harmonics could be a 58, 115 or 123-years cycle.

A numerical manipulation has given the 123-years cycle as the fourth harmonics of the above 496-years cycle. Even though, this fourth harmonics of the 123-years cycle could be faintly effective for the 123-years cycle of the most hazardous Chilean tsunamis.

After all, the author thinks it possible to consider several long-years cycles of the intersted events. However, it is hard to give any dynamical understanding for the intersted long-years cycles with considering the potentials of the planets in the solar system. In addition, it is true at present in need to confirm whether such long-years cycles could be effective for the interested tsunami hazards.

9. Conclusions

The author has noticed about the Chilean tsunamis in the northwestern Pacific. This problem has a close relation to the short-term and long-term prediction of the forthcoming trans-Pacific tsunamis as the cause of the most severe coastal hazards. The existing warnig system should be ready to work its expected function. Possible cycle of the Chilean tsunamis in the Japanese Islands is considered and discussed. A 121-years cycle of the Chilean tsunamis must be reasonable even as a hypothetical result.

References

1. International Tsunami Information Center, "Tsunami Newsletter", Vol.22, No.1, 19p. (1989)
2. Iida, K., Cox, D., and Pararas-Carayannis G., "Preliminary catalog of tsunamis in the Pacific", Univ.Hawaii, HIG-67, Data Report No.5, ca 200p. (1967)
3. Soloviev, S.L., and Gao, Ch.N., "Katalog tsunami na zapadnom poberezie Tixogo Okeana", Akad.Nauk USSR, Izdat.Nauk,310p. (1974)
4. Soloviev, S.L., and Gao, Ch.N., "Katalog tsunami na vostochnom poberezie Tixogo Okeana", Akad.Nauk USSR, Izdat.Nauk,202p. (1976)
5. Tayama,M., "Dainippon-Zishin-Shiryo", Shinsai-Yobo-Chosa-Kai Report No.49, part A and B, 606p.and 595p. (1904)
6. Watanabe, H., "Nippon-Higai-Tsunami-Soran", Univ.Tokyo Press, 216p. (1985)
7. Iida, K., "catalog of tsunamis in Japan and its neighboring countries", Special Report, Aichi Inst.Tech., 52p. (1984)
8. Galanopoulos, A.G., "Tsunamis observed on the coasts of Greece from antiquity to present time in the broad Aegean region", Annali di Geofisica, Vol.13, Nos.3-4, p.369 (1960)
9. Ambrasey, N.N., "Data for investigation of the seismic sea wave in the eastern Mediterranean", Bull.Seism.Soc.Am., Vol.52 No.4, p.895 (1962)
10. Caputo, M., and Faita, G.F.Q., "Statistical analysis of the tsunamis of the Italian coasts", J.Geophys.Res., Vol.87, No.2, p.601 (1982)
11. Caputo, M., "Prime catalogo dei maremoti delle coste Italiane", Atti della Accademia Nazionale dei Lincei, Memorie, Serie VIII, Vol.XVII, Sezione I, Fascicolo 7, Roma, 355p. (1984)
12. Moreira, V.S., "Seismotectonics of Portugal and its adjacent area in the Atlantic", Techtonophysics, Vol.117, p.85 (1985)
13. Moreira, V.S., "Seismotectonoca de Portugal continental e regiao Atlantica adjacente", Instituto Nacional de Meteorologia e Geofisica, Lisboa, 29p. (1982)
14. Moreira, V.S., "Seismicidade historica de Portugal continental", Revista do Instituto Nacional de Meteorologia e Geofisica, Lisboa, 79p. (1984)
15. Vita-Finzi, C., and King, G.C.P., "The seismicity,geomorphology and structural evolution of the Corinth area of Greece", Phil.Tr.R.Soc.Lond., A314, p.379 (1985)
16. Nakamura, S., "The 1837 Chilean tsunami in the northwestern Pacific", La mer, Tome 26, No.1, p.81 (1988)
17. Mori, Y., "Evidence of an 11-year periodicity in tree-ring series from Formosa related to the sunspot cycle", J.Climat., Vol.1, p.345 (1981)
18. Currie, R.G.,"Amplitude and phase of the 11 yr term in sea level: Europe", Geophys. J.Roy.astron.Soc., Vol.67, p.547 (1981)
19. Rundle, J.B., Julian, B.R. and Turcotte, D.L., "Are earthquakes deterministic or chaotic?", Trans.Am.Geophys.Union(EOS), Vol.70, No.40, p.880 (1989)
20. Maunder,W., "The sun and sunspots", Monthly Not.Roy.astron.Soc., Vol.82, p.534 (1922)
21. Hale, G.E., "Sunspots as magnets and the periodic reversal of their property", Nature, Vol.113, No.2829, p.105 (1924)
22. Stix, M., "The sun", A and A Library, Springer-Verlag, 390p. (1989)
23. Tayler, R.J., "The sun as a star", Quartery J.Roy.astron.Soc., Vol.30, No.1, p.125 (1989)
24. Nakamura, S., "Subarctic interrelation between annual mean sea level and tree-ring growth rate", Trans.Am.Geophys.Union (EOS), Vol.70, No.43, p.1051 (1989)
25. Obi, S., Kosai, Y., and Moriyama, F., "The solar system", Geoscience Series No.1, Kyoritsu-Pub., Tokyo, 248p. (1976)
26. Nakamura, S., "The 1837 Chilean tsunami in the northwestern Pacific", La mer, Tome 26, No.1, p.81 (1988)
27. Stephenson, F.R. and Morrison, L.V., "Long-term changes in the rotation of the earth: 700B.C. to A.D.1980", Phil.Trans. Roy.Soc.Lond., Series A, Vol.313, p.47 (1984)
28. Hide, R., "Rotation in the solar system", Royal Soc., London, 186p. (1984)
29. Hayami, S., "A.D.1650-An age from darkness to dawn", Annuals Disaster Prevention Res.Inst., Kyoto Univ., No.10A, p.1 (1967)
30. Wadati, K., "Encyclopedia of Meteorology", the 4th ed., Tokyo-Do, Tokyo, 704p. (1979)
31. Chandler, S.C., "On a new component of the polar motion", Astron.J., No.490 (Vol.21, No.10), p.79 (1901)
32. Chandler, S.C., "On the new component of the polar motion", Astron.J., No.494 (Vol.21, No.4), p.109 (1901)
33. Haubrich,Jr, R., and Munk, W., "The pole tide", J.Geophys.Res., Vol.64, No.12, p.2373 (1959)
34. Maximov, I.V., "Geophysichekii cili i vodi okeana", Godromet.Izdat., Leningrad, 447p. (1970)*
35. Larmor,J., "The influence of the oceanic waters on the law of variation of latitudes", Proc.London Math.Soc., Ser.2, Vol.14, p.440 (1915)
36. Jeffreys, H., and Vincente, R.O., "The theory of mutation and the variation of latitude", Monthly Not.Roy.astron.Soc., Vol.117, p.142 (1957)
37. Jeffreys, H. and Vincente, R.O., " The theory of mutation and the variation of latitude: The Roche model core", Monthly Not.Roy.astron.Soc., Vol.117, p.162 (1957)

* Japanese edition:
   Takano, K. and Endoh, M., "Chikyu, tsuki, taiyo ni yoru Kaiyo, Kikou no chouki hendo", Tokai Univ.Press, Tokyo, 358p. (1974)

TRACES OF TSUNAMI IN MARSH DEPOSITS OF THE SENDAI PLAIN, NORTHEAST JAPAN

K. Minoura*, S. Nakaya**

* Tohoku University, Japan
** Hirosaki University, Japan

Abstract

A particularly destructive train of tsunami generated by the Japan Sea Earthquake of May 26, 1983 surged over the coast of Northeast Japan. It caused destruction and death in coastal area. The tsunami induced characteristic sedimentary processes on the exposed Japan Sea coast. Three kinds of sedimentation depending on the hydraulic scale of the tsunami were recognized, and each of them left its own characteristic deposits which remain in sedimentary succession preserving remarkable sedimentary facies.

Cored samples taken from the coast areas in Sendai have been examined for detecting traces of ancient tsunamis. Sedimentological and geochemical analyses on the samples reveal that thin sand layers similar to those developed by the Tsunami of the Japan Sea Earthquake are found in the drilled cores. Radioisotopic ages of the sandy layers are exactly equivalent to the dates of ancient tsunamis documented in historical materials.

1. Sedimentary processes caused by tsunami

Depositional processes conduced by the Tsunami of the Japan Sea Earthquake can be summarized in the following three categories [1].

{Type A}
A large volume of seawater was carried ashore by the tsunami. Advancing waves transported voluminous materials of beaches and dunes as well as artificial constructions landward in a moment. A seaward return of the water following coastal flooding resulted in accumulation of suspended materials in the shoreface region forming submerged longshore bars.

Fig. 1 Simplified expression of depositional processes caused by the Tsunami of the Japan Sea Earthquake. O: Offshore, S: Shoreface, E: Estuary, C: Channel, L: Lagoon, D: Dune field, F: Fluvial.
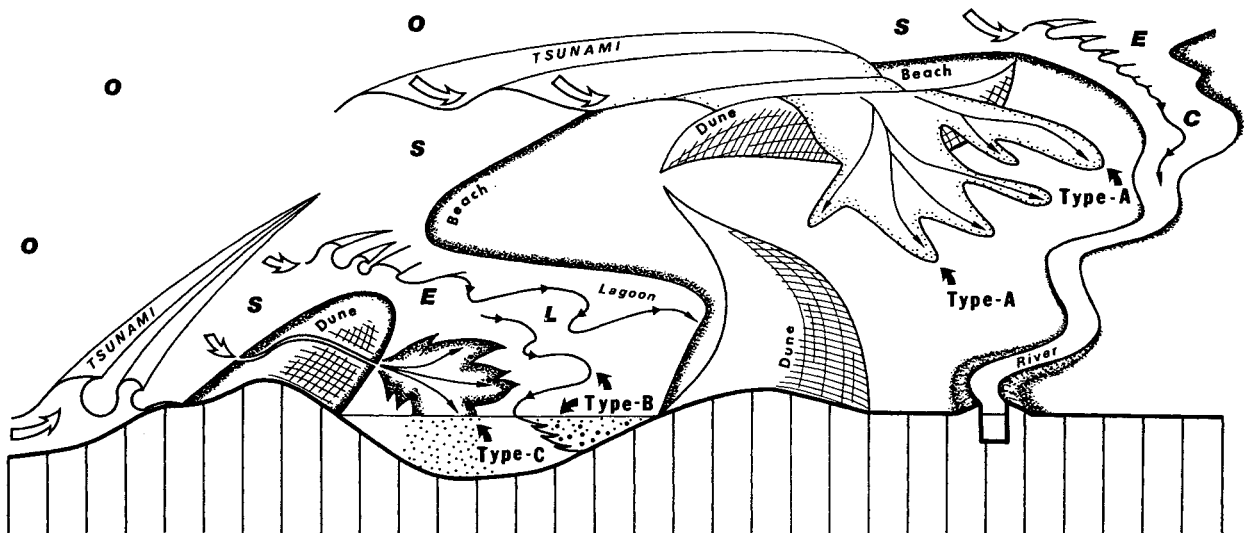
(Type B)

The tsunami invaded the inter-tidal lake and deeply eroded buried deposits. Molluscs and their shells were sorted out from the deposits by sediment agitation and then transported to shallower places on the opposite side of the lake.

(Type C)

Seismic shocks exceeding seismic scale V cracked beaches and dunes. Incoming seawater rushed into an inter-dune pond through the cracks as a result of the rapid rise of water level. Sand grains of beaches and dunes taken in the seawater were transported to the pond in a suspension form and deposited there in a thin sand layer. The seawater remained for a long period in the deeper layer of the pond, from which some chemical materials were moved into superficial sediments in different ways.

Fig. 1 schematically illustrates depositional processes caused by the tsunami. Each process is expected to be caused by any tsunamis depending on scale and recorded in sedimentary successions.

Three representative columns of subsurface deposits are shown in Fig. 3, illustrating vertical facies changes (left) and mud contents (right). Some sandy layers and a sheet of felsic airborne tephra were found in each column. These thin layers are traceable laterally for a long distance as shown in Fig. 3. Grayish white tephra, dated AD 870-934 [2], can be traced throughout the section (Fig. 3). Each sand layer, scarcely including muds, is composed of well-sorted medium to fine sand originated mainly from dunes. The layer found at the highest horizon in coastward section, overlies peaty deposits, filled up topographic undulations. The sedimentary feature proves an unconformity below the sand layer.

Judging from the sedimentary facies and distribution of the sand, all the layers were developed by tsunami. The wide distribution of sand layers signifies very large in scale of tsunami, which caused sedimentation process of Type A.

2. Traces of tsunami in marsh deposits of the Sendai Plain

We set up a base line at right angles to the shoreline of the Sendai Bay (Fig. 2). Subsurface deposits were drilled at several points along the line. Every columnar samples is 2 m in length. Variations and the lateral continuation of sedimentary facies were also observed on trench walls along the Base line.

Fig. 2 Location map of the Sendai Plain. Borehole samples were drilled along a base line (L) at right angles to the coast. S1 to S3: Representative borehole sites.
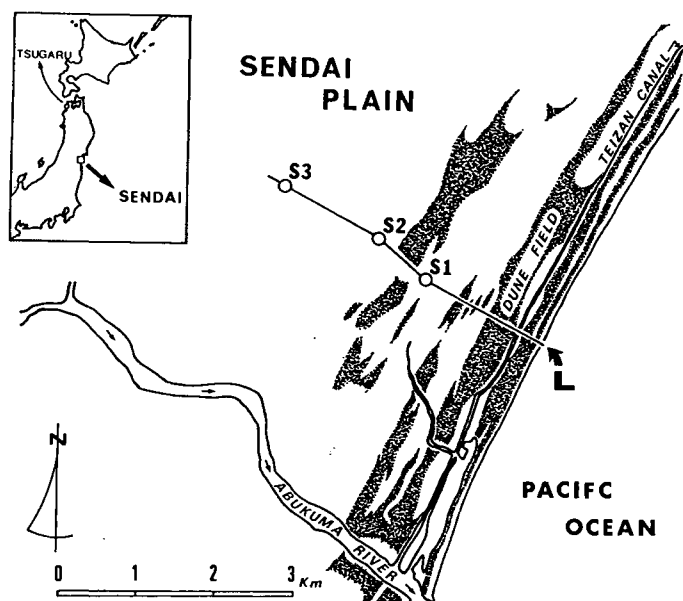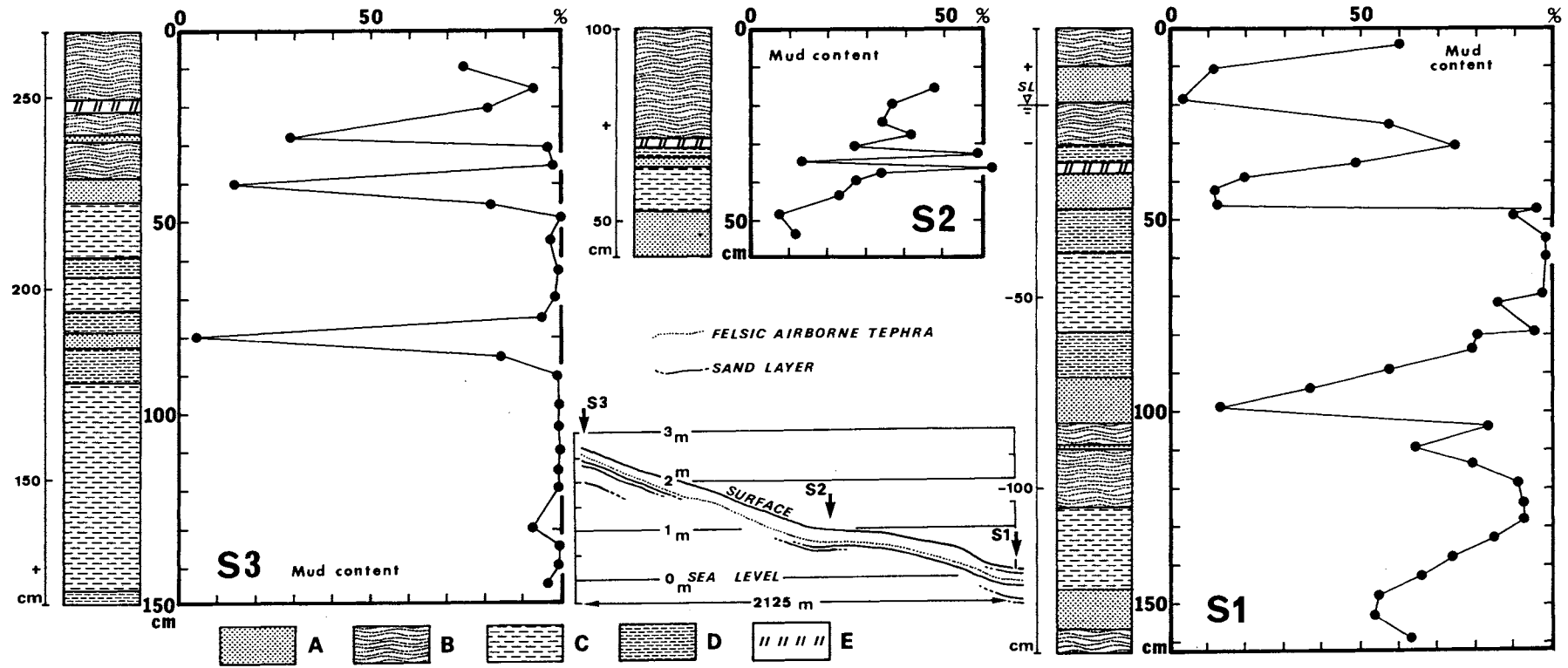
Fig. 3   Sedimentological results from drilled samples, S1,
S2   and S3.   Each column includes several thin sand   layers
poor in   mud contents.   A: Clean sand, B: Peaty   mud,   C:
Silty mud, D: Peat, E: Felsic tuff.

3. Ages of tsunami deposits

Fig. 4 shows the change in ^{14}C dates of sediments of column S1 with depth. All the isotopic dates fit a straight line, which reveals that sedimentation has progressed continuously but clean sands accumulated intermittently, interrupting ordinary deposition during these 3,000 years. Supposing that the sedimentation rate was constant, the period of time represented by the unconformity can be estimated by the parallel transfer of the regression line along the horizontal axis in Fig. 4. Calculation shows a hiatus spanning the time interval over 380 years.

The estimated age of the upper two sand layers of column S1 are AD 1630 (±20) and AD 870 (±20) respectively. The ages exactly agree with those of the ancient tsunamis recorded in historical documents, which describe the enormous tsunami attacked the coast in the late 9th century (AD 869), causing heavy surf damage and great loss of life [3]. The trace suggesting younger age is correlative with the great catastrophe happened in the 17th century (AD 1611) which surge over the coast of the Sendai Plain with waves exceeding 6 m in height [3]. Both of them followed large submarine earthquakes of magnitude 8 or more centered in the forearc region off the coast of southern Sanriku [3].

Each trace of the tsunami is recognized in column S1 at an interval of about 55 cm, which means that large-scale tsunamis caused by off-shore submarine earthquakes surged over the coast nearly every 800 years. It has made clear that the last large-scale tsunami took place nearly four hundred years ago (AD 1611). I seems that the inhabitants in the coastal area will be secure from a serious catastrophe wrought by an enormous submarine earthquake for next four hundred years.

References

1. Minoura, K., and Nakaya, "Changes of sedimentary environment in and around the Lake Jusan", In K. Sasaki (ed.), Tsugaru Jusanko (Lake Jusan in Tsugaru District). Hopposhinsha Press. P.91 (1988)
2. Yamada, I., and Shoji, S., "Holocene airborne tephra distributed in Miyagi Prefecture", J. Soil Fert. Soc. Japan. Vol. 52, p.155 (1981)
3. Watanabe, T., 1985, "Comprehensive bibliography on tsunamis of Japan", University Press of the Univ. Tokyo. 260p. (1985)
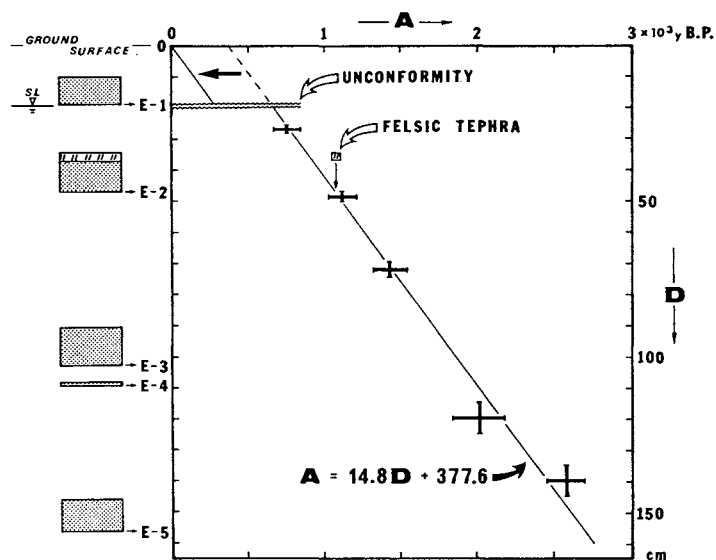
Fig. 4 Radiocarbon ages (A) as a function of depth (D) in column S1. Symbols are the same as in Fig. 3. A thick arrow shows the direction of parallel transfer of the regression line. E-1 to E-5: Base of sand layer, SL: Mean sea level.

A METHODOLOGY FOR DEVELOPING TSUNAMI INUNDATION AND EVACUATION ZONES

george D. Curtis

Joint Institute for Marine & Atmospheric Research

University of Hawaii, Hawaii, U.S.A

Abstract

Tsunami research should culminate in saving lives and reducing property losses. The warning systems have been functioning reasonably well, and rapid evacuation of susceptible areas is the essential follow-on. Careful delineation of such areas is necessary and improved methods and procedures have been developed to do so. These are described, in detail, comparisons are made with other methods, and lessons and conclusions are drawn.

Introduction

The primary goal of tsunami research is to save lives and reduce property losses. Rapid evacuation of susceptible coastal areas upon a warning is a standard procedure. Definition of such areas has progressed from "low-lying areas" through "up to 50 feet above sea level" to inundation/evacuation zones somehow developed and depicted on published maps. Hawaii is among the few areas in the Pacific which has mapped evacuation zones, but these are incomplete and obsolescent, dating from 1961. Clearly, there was need to apply the years of tsunami research in this area, for the benefit of this--and other--areas. More formalized methods to determine runup and inundation were at hand, and the Civil Defense helped obtain funding to develop new evacuation maps.

A primary motivator was the rapid population buildup in coastal areas. In some locales, the population density is high enough that there was a major concern whether evacuation of the denoted areas is feasible in the limited time available, Curtis, [1]. Unlike hurricane evacuation, the time is generally only two hours. Thus, maps with the narrowest feasible (but safe) zones, as well as clear evacuation routes were needed.

The Problem

Table I depicts the primary factors involved in tsunami hazard mitigation. The existing zones (circa 1961) published in the telephone directories for each island, were developed utilizing an estimate of total wave energy. This was represented by a 50 ft wave approaching the island and sloping down 1% from the 10 ft depth line. Actual inundation history was used in only a few, well documented areas such as Hilo [Cox, 2]. However, in roughly the last decade, procedures were developed and applied for flood insurance purposes by the U.S. Army Corps of Engineers [Houston, et al, 3]. These procedures built upon historical wave height data compiled at the University of Hawaii and utilized a numerical model to synthesize a tsunami wave height contour. After considerable revision, this information was used with work by Bretschneider [4], to help develop a set of inundation maps as part of a National flood insurance program. The maps are only concerned with water depths which produce property damage, and also include the effect of stream floods and in a few areas, storm surges.

Table I

MITIGATION OF TSUNAMI HAZARDS

PEOPLE	STRUCTURES
WARNING + EVACUATION + EDUCATION	ACCURATE ZONATION INSURANCE STANDARDS BUILDING CODES

IMPROVE WARNING SYSTEM BY:

- BETTER EVALUATION OF SEISMIC EVENT (LONG PERIOD, AUTO EVAL., ETC.)
- BETTER, RAPIDLY ACCESSIBLE DATA ON CONDITIONS & HISTORY ENROUTE TO LOCATION (198 PAPER)
- DEEP OCEAN SENSORS (HIG/JTRE-PMEL)
- QUANTITATIVE PREDICTIONS; LEAD TIME
- BUT - NEVER A MISS OF A DAMAGING EVENT

IMPROVE EVACUATION BY:

- REDUCE SIZE OF EVACUATION AREAS; CONSIDER POPULATION INCREASE & ROUTES
- PREPARE PUBLIC & OFFICIALS & PROCEDURES
- CONSIDER PRIORITY AND SELECTED AREAS
- IMPROVE LEAD TIME BUT REDUCE UNNECESSARY EVACUATION
- LOCAL TSUNAMIS NOT INVOLVED

PROGRAMS:

- MONITOR TSUNAMI WAVES IMPACTING HAWAII
- PREPARE TO EVALUATE RUNUP AFTER AN EVENT
- PROPOSE PROJECTS TO IMPROVE/RESOLVE PROBLEMS LISTED ABOVE
- ADVISE STATE AND COUNTY CIVIL DEFENSE AGENCIES
- EDUCATE AND EXCHANGE INFO; PUBLISH JOURNAL
- PREPARE BETTER EVACUATION MAPS

Evaluation

We were able to gather a team to advise on the work which included several investigators in the tsunami field, notably Doak Cox, who produced the 1961 maps and had conducted post-event surveys from 1946 on.

In addition to the 50 ft*, 1% slope procedure, and the Corps of Engineers method, other approaches have used a variety of formulas or assumptions for determining inundation once a coastal wave height is somehow determined.

Table II

CALCULATION OF RUNUP (R) AND INUNDATION (I.L.)

- ONE DIMENSIONAL SCHEMES
- SINGLE WAVE, INDEFINITE PERIOD(S)
- MAX. WAVE HEIGHT AT SHORELINE KNOWN OR ASSUMED (h)
- ON-SHORE TOPOGRAPHY KNOWN

HOUSTON AND GARCIA (1974): $R \cong h$

CAMFIELD & STREET (1967) - EXPERIMENTAL-
  SIMILAR FOR SLOPES OF $\sim 8°$

KONONKOVA & REIHRUDEL (1976): $<8°$, $R \cong h$; $>8°$, $R>h$

FREEMAN & LE MEHAUTE (1964) - THEORETICAL-

$$\frac{R}{h_s} = \frac{6}{1 + \frac{32g}{C_h^2 S}} \qquad WHERE: \quad \begin{array}{l} C_h \ IS \ CHEZY \ COEF. \\ (VARIES \ W/DEPTH) \\ h_s = SURGE \ HEIGHT \end{array}$$

SPEILVOGEL (1975) - THEORETICAL - DIVIDED
  CALCULATIONS BY WAVE/SURGE RATIOS AND SHOWED DIFFERENCES
  W/BORE; R may be much greater than h.

BRETSCHNEIDER & WYBRO (1976) DEVELOPED A FLUID FLOW FORMULA
FOR A CHANNEL TO BE USED FOR TSUNAMI RUNUP:

$$h_2 = h_1 - \left[tan\,\theta + \frac{n^2 g \, F^{2/3} - \frac{1}{3}}{(1.486)^2} \right] \left[\frac{F^2}{2} + 1 \right]^{-1} \Delta X$$

(ADOPTED BY CORPS OF ENGINEERS)

MADER (1989): USING NON-LINEAR SHALLOW WATER WAVE MODEL WITH
  SWAN CODE - RUNUP OFTEN MUCH HIGHER THAN ABOVE; VARIES
  WITH PERIOD.

Our Approach

We choose to use the highly synthesized wave heights of [3] with additional historical inputs and conservative statistics to provide a reasonably authentic worst-case wave height contour around the islands. Since the values in [3] are based on a (least-mean squares) probability, we used a 200 year "return time" to ensure safety. The contour is checked to ensure it includes the envelope of all credible data we have from the 1946, 1957, and 1960 events; this should be so since [3] is based largely on our data set.

*Note: Due to the large usage of historical data, all cited values are maintained in the English system.

It was found necessary to set out a few definitions to ensure consistency and to list precepts basic to the work; these are shown in Tables III and IV. As procedures were developed and verified, they were summarized in a brief manual [5] for use by those doing or reviewing such work. A handbook produced by the Corps of Engineers and based on [3] and [4] codifies the calculations [6].

Table III

TSUNAMI PROJECT
Definitions, 5/8/89

Inundation line (limit) - the inland limit of wetting, measured horizontally form the MSL line. Where MLLW was used, it should be converted to the MSL line. (Move inland to an elevation 0.7 ft. higher). The vegetation line is sometimes used as a reference. If it can be determined that it is more than 10 ft. from the MSL line, adjust; otherwise, ignore.

Maximum Expectable Inundation - The inland limit of the highest expectable tsunami from any direction, at high tide.

Runup (height) - the elevation of the ground above MSL that the water will reach. This is usually not equal to the wave height, or inundation depth, at the shoreline.

Wave height (h) - the height of the (highest) wave, at or re the MSL shoreline. In the absence of other information, may be considered to be measured 200 feet inland. Tide gages show wave height in harbors, which may be significantly different from runups. May be converted from another reference level (if significant) by assuming a 1% slope and/or a 0.7' MSL/MLLW correction (Hawaii approximation).

Table IV

TSUNAMI PROJECT
Precepts 12/2/88

MEASUREMENTS - should be in feet and referenced to MSL. If other units are used, they must be referenced or noted.

SOURCE OF DATA - should be from the first reference, if available, should be noted with tsunami date, envelope, extrapolated, calculated, estimated, etc.

SYMBOLS - per the following list:

h	-wave height at shoreline*
R	-runup height*
IL	-inundation limit*
IL_{100};R_{100};etc	-values calculated for a 100 year return time (note this time is only a general approximation)
IL_E	-inundation limit of worst actual measured/calculated tsunami values.

CHARTS, DIAGRAMS, TABLES - should be dated and initialed, and follow the above precepts.

Estimation of Maximum Expectable
Inundation Limit--Procedure

Using two dimensional (transects or profiles normal to shoreline) method; appropriate except for bays and where good historical inundation records are available:

--assemble available records of maximum runups and/or wave heights. Calculate synthesized wave height for 200 year return time. Compare, and use most credible; add high tide (MHHW) correction as needed. Determine probable point where wave was recorded, or use 200 ft. point.

--determine topography along the profile from best available, large-scale map. Draw profile in segments.

--Estimate friction coefficient for each segment, using photos, surveys, and observations with established guidelines.

--"Runup" the wave on the shore, using numerical or graphical solutions [6]. Transfer point to map.

--Repeat for transects wherever topography, wave heights, or surface changes.

--Connect the points, following contours of the land. Review carefully; revise if warranted by additional information.

Table V lists the primary factors involved in such evaluations.

Meetings of the other tsunami specialists and others involved were held to coordinate and verify procedures, data, sources, etc. Other organizations--Corps of Engineers, Federal Emergency Management Agency, and State and County Civil Defense Agencies--were involved and contributed or cooperated in planning and carrying out the work.

In addition to determining the best methodology and procedures, the initial phase of the project included assembling all historical data and pertinent references. We were able to accomplish this effectively for our area, because most of the information, though scattered, was still within the University of Hawaii since so much tsunami research had been done here. We hope to maintain this material in retrievable form for future use.

Table V

DETERMINATION OF MAXIMUM EXPECTABLE INUNDATION

VARIABLES

- WAVE HEIGHT
  - . REFERENCE LEVEL (MSL, MLLW, ETC.)
  - . SOURCE (HISTORICAL, CALCULATED, MODEL)
  - . REFERENCE LOCATION (SHORELINE, 200'INLAND)
- WAVE TYPE
  - . (BORE, NON-BORE, PERIOD)
- TOPOGRAPHY
  - . SLOPE (S) (1,2,3, INCREMENTS)
  - . ACCURACY (10', 20', 40', CONTOURS, EST., ETC.,)
  - . SURFACE(S) (MANNING'S "N" - FRICTION)
- RETURN TIME (100, 200 YEAR, ENVELOPE ONLY)
- METHODS
  - . COX (HEIGHT AND SLOPE)
  - . BRETSCHNEIDER ET AL (USUAL)
  - . HOUSTON (WINDWARD OAHU)
  - . HISTORICAL LIMIT (HILO)

VALIDATION

- MINIMAL HISTORICAL
- FLOOD INSURANCE, RATE MAPS (VARIOUS PROBLEMS)
- CONSERVATISM/JUDGEMENT

PURPOSE

- PUBLIC (TELEPHONE DIRECTORY, ETC.,): ZONES
- CIVIL DEFENSE (STATE & COUNTY): LINES AND ROUTES

An important task, which is still not complete to our satisfaction, is validating the models and procedures used. In drawing a critical line such as needed here, one must lean toward a conservative approach when in doubt, although the goal is to be realistic. Thus, considerable effort has been expended to determine valid wave heights and locations, and in particular, to find reliable concurrent records of wave heights and runup height or inundation limit. Surprisingly, there are very few examples of such data. For those few, our results have proven to be fairly accurate and always conservative.

The major source of error or confusion, and one which other investigators should note carefully, is confusion in historical accounts between wave heights and runup. Much of the concern about accuracy hinges on validity of the historical "runup" data. As mentioned, it is often not clear whether it was: a) measured at the shoreline (h), b) measured some 200 ft inland, c) measured as a runup height on land, re MSL (R), or d) extrapolated back to the shoreline from a runup level and listed as wave height. A great deal of time is spent guessing at such matters; all too often the conclusion is to assume the level is a wave height at 200 ft, as a conservative approach, although is may well have been a swash mark on the side of a hill, much higher than the actual wave near the shore on which the calculations were based. Houston [3] tried to resolve this by assuming that all such records applied 200 ft inland. Unfortunately, Cox, the source of the 200 ft assmuption [7] and many of the measurements, feels that this is frequently not the case, and should not be assumed.

In fact, the numerical (computer) method developed by the Corps of Engineers which combined and codified Houston's wave height determinations and Bretschneider's runup formula embedded the 200 ft standard so it is automatic. We made a modification to locate the wave height (h) at any desired point, and so treat each area specifically, with considerable judgement. The 200 ft. is always available as a conservative default.

The Product

Figure 1 is an example of a wave height, inundation, and runup problem. A typical worksheet used to maintain the data in one area is also shown along with the map of that area. Note that both historical and calculated levels are shown, along with records and comments. Both the data and the inundation limit on the map are reviewed by (at least) a second person as a final check for currency, completeness, accuracy, and reasonableness. For example, if there is any indication a bore has developed in that area, has the bore and non-bore runup been evaluated? (We use the higher). Has the zone been annotated to flag on-going shore developments such as construction of a marina?

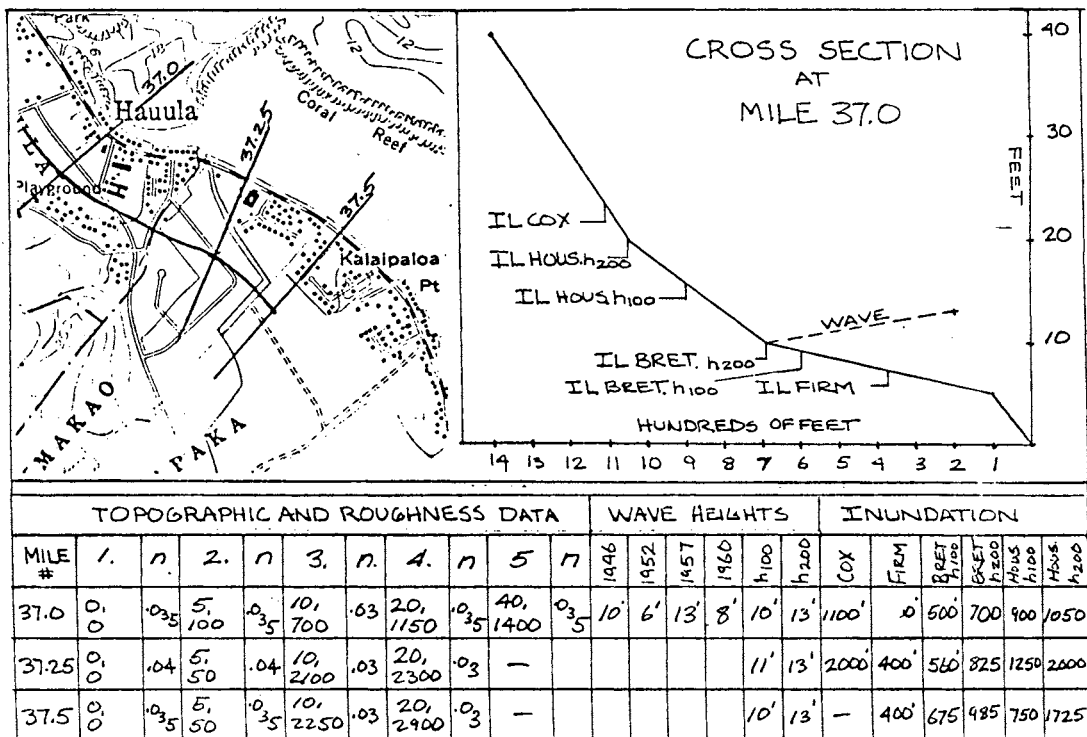	TOPOGRAPHIC AND ROUGHNESS DATA										WAVE HEIGHTS						INUNDATION					
MILE #	1.	n.	2.	n.	3.	n.	4.	n	5	n	1946	1952	1957	1960	h100	h200	Cox	Firm	Bret h100	Bret h200	Hous h100	Hous h200
37.0	0,0	.035	5,100	.035	10,700	.63	20,1150	.035	40,1400	.035	10'	6'	13'	8'	10'	13'	1100'	0	500'	700'	900	1050
37.25	0,0	.04	5,50	.04	10,2100	.03	20,2300	.03	—						11'	13'	2000'	400'	560'	825'	1250	2000
37.5	0,0	.035	5,50	.035	10,2250	.03	20,2900	.03	—						10'	13'	—	400'	675'	985'	750	1725

Fig 1 - Example of wave height, inundation, and runup data, with worksheet and typical transects on map.

The resulting inundation map is provided to the civil authorities for conversion to an evacuation map. We have worked with police, highway, and public works staff as well as Civil Defense (emergency management) people in setting the final line and zone size. It is important that such lines not only be inland of the expectable inundation, but they be recognizable to the public: a road, park boundary, wall, etc. On occasion, we have aided evacuation by putting the line clearly on the shore side of a road, thus leaving it open for traffic.

These maps--in less detail--will appear in the next issue of the phone directory for each island, replacing the older ones. Figure 2 is an example of the savings in evacuation area afforded by the refinements of the present work; the smaller zone is all that will appear in the final maps.

A seldom-considered source of variation is found in the compilation of historical records. The thorough collection of wave heights for Hawaii by Loomis used in (5) shows values for several events, clumped at discrete locations. At many such locations, the measurements were actually made at various points in the general area. Observers have often noted the large variations in runup which occurs within a given area. Therefore, unless we are able to "unclump" the listed values, we tend to ignore the smaller values, and smooth the assumed maximum wave contour.
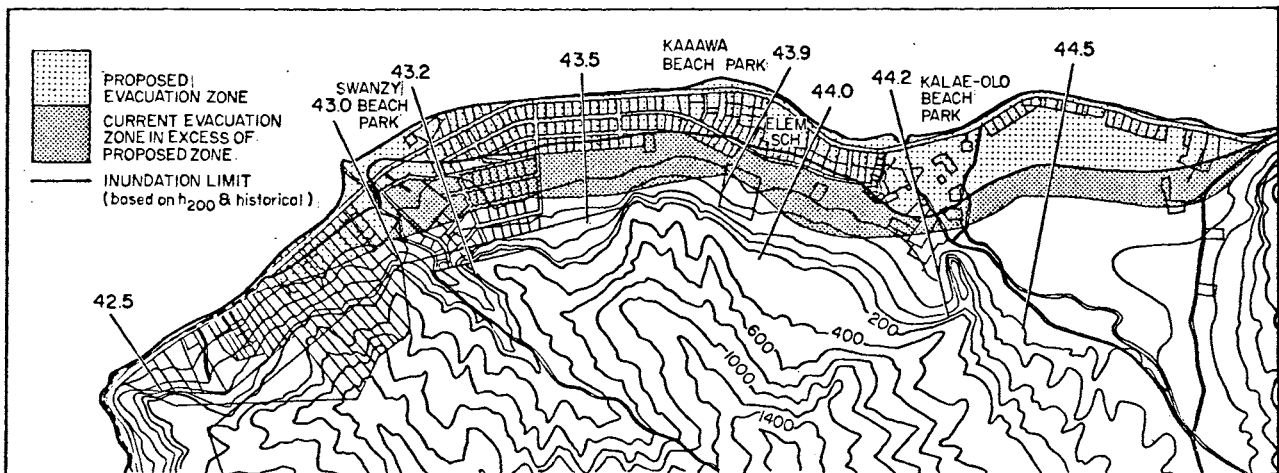
Fig 2 - Contour map with old and new evacuation zones overlaid. The inundation line is also shown; the smaller zone is all that will appear in the final maps.

Discussion-Inundation

In addition to these factors, knowledge of the actual topography and surface roughness sets limits on the accuracy of calculations and the resolution of final plots. In practice, there is again a tendency to be conservative and use smaller friction factors (Mannings "n" or Chezy coefficient). We do not set "n" closer than .005 for these reasons. And, we do not report wave heights closer than 1 ft (or 0.5 m).

In addition to checking our results with what actual values we could find, we have been examining comparisons with other models and methods. The work done in the past, like ours, has been regrettably lacking in historical verification, and experimental results have had varied agreement with theory. Some of the reasons noted include problem of comparison with tide gauge records (the peaks are filtered), the h vs. R problem discussed earlier, and scaling (viscosity problem, etc) factors in lab experiments.

We have made comparisons for both hypothetical and real configurations with fluid flow models developed by Mader [8]. These models permit a full three dimension treatment of an embayment, and take wave period into account. In one example [evaluation of an area near Mauna Lani] having shoreline slopes the order of 4%, the agreement was reasonably good. A comparison with an older three dimensional model [9] is included in the transect shown in Fig. 1; it shows flooding much in excess of anecdotal reports and other analyses.

Additional studies of various models of tsunami flooding are in progress at JIMAR. More information on these are to be presented in another paper, at this conference.

Evacuation-Conclusion

All conclusive results must be applied in context of evacuation, to achieve our original object of protecting lives. Moving the line upslope to the physical evacuation line provides an additional margin of safety, but in a few strategic locations it may help to avoid conservatism, i.e., where a route is needed or final evacuation can be postponed. Minor flooding, as in heavy rain or winter storms may not be a real hazard, if a road provides an important egress, for example. "Vertical evacuation" may be used in some areas; concrete buildings in high density areas can provide safe shelter if people move to the third floor or higher.

In some instances, tsunami-zoned maps have been used for hurricane evacuation. This is reasonable to expect if nothing else is available, but there are enough differences in the effects and the time available, that different zonation and criteria should be used. The FEMA flood insurance rate maps (FIRM) currently include some hurricane flooding; unfortunately it is not differentiated from stream and tsunami flooding, and its derivation (historical or theoretical) is not stated. It should also be noted that the FIRM zones usually stop at a 4 ft depth, were greatly revised in many areas in the last few years, and are intended only for structural protection.

We feel that these revised tsunami inundation maps will aid in the next evacuation in these islands, and the same process should be applied to the same goal--to protect lives--in other coastal areas. If there is one other lesson to be learned from this work, it is to obtain more and better data on wave height and inundation when the next significant (not necessarily major) tsunami occurs. Only that way can we refine our final results, with safety.

References

1. Curtis, George and William Adams, "Needs and developments in tsunami monitoring," Science of Tsunami Hazards, vol 3, no. 1, 1985.

2. Cox, Doak, "Potential tsunami inundation areas in Hawaii," Hawaii Institute of Geophysics Report No. 14, University of Hawaii, 1961.

3. Houston, J. R., R. D. Carver and D. G. Markle, "Tsunami-wave elevation frequency of Occurance for the Hawaiian Islands," Technical Report H-77-1, U.S. Army Engineer Waterways Experiment Station, Vicksburg, Mississippi, 1977.

4. Bretschneider, C. L. and P. G. Wybro, "Tsunami inundation prediction," in Proceedings of the 15th Coastal Engineering Conference, ASCE, 1976.

5. Curtis, George, "Tsunami inundation/evacuation line and zone selection procedure," JIMAR Memo dated Dec 9, 1988.

6. Corps of Engineers, "Manual for determining tsunami sunup profiles on coastal areas of Hawaii," M. & E. Pacific Inc., 1978.

7. Cox, Doak, "Locus of tsunami frequence distribution," University of Hawaii Environmental Center, SR:0021, 1978.

8. Mader, Charles, Numerical Modelling of Water Waves, University of California Press, 1988.

9. Houston, J. R. and H. Lee Butler, "A numerical model for tsunami inundation," Technical Report HL-79-2, U.S. Army Engineer Waterways Experiment Station, Vicksburg, Mississippi, 1979.

FAST DETERMINATION OF TSUNAMI GENERATION MECHANISM

Augustine S. Furumoto* and S. Yoshida**

* University of Hawaii, Hawaii, U.S.A.
** Tokyo Gakugei University, Japan

Abstract

Comparisons were made between the 1957 and 1986 tsunamigenic earthquakes off Andreanof Islands and between the 1960 and 1985 tsunamigenic earthquakes of Chile. The difference in size of the rupture areas correlates well with the energy of the generated tsunamis: the larger the rupture area, the greater the tsunami damage in distant shores.

For the Tsunami Warning System a reliable estimate of the rupture area will be a very advantageous bit of information for decision as to issue a warning or not. Body wave inversion and surface wave analysis are mutually confirming methods that can be used within the time constraints of a tsunami watch.

1. Introduction

During a tsunami watch, the decision to issue a warning can be greatly facilitated if there were methods to distinguish between a Pacific wide tsunami and a local tsunami by using seismic data. By Pacific wide tsunami we mean a tsunami that can cause damage at distances of thousands of kilometers away from the earthquake epicenter; a local tsunami is one that is destructive within two hundred kilometers of the epicenter. Such a distinction, if possible, is highly desirable because issuing a tsunami alert without necessity disrupts the economic and cultural life of tens of millions of people.

2. Background Information

From hindsight we find that Pacific wide tsunamis were generated by earthquakes with much larger rupture zones than earthquakes that generated local tsunamis. The lengths of rupture zones of Pacific wide tsunamis are the following:

1946	April	1	Aleutian	?	
1952	November	4	Kamchatka	700	km
1957	March	9	Andreanof	1100	
1960	May	25	Chile	1200	
1964	March	28	Alaska	800	

Meanwhile, within the past fifteen years, the number of earthquakes that have generated local tsunamis are numerous.

1976	August	16	Mindanao	Ms = 8
1977	August	19	Sumbawa	Ms = 8
1979	December	12	Ecuador	Ms = 7.7
1983	May	26	Japan	Ms = 7.8
1985	March	3	Chile	Ms = 7.8
1985	September	19	Mexico	Ms = 8.1
1986	May	7	Andereanof	Ms = 7.7

Rupture zones of these had lengths less than 250 km.

Surface wave magnitude is not a good discriminant to recognize Pacific wide tsunamis. Moment magnitude is not useful because we cannot determine moment magnitude within the short duration of a tsunami watch. Mantle magnitude as proposed by Talandier and Reymond (1988) is claimed to be equivalent numerically to moment magnitude, but there are a few difficulties with mantle magnitude.

3. Methods for Discrimination

As a discriminant between a Pacific wide tsunami and a local tsunami, we propose the determination of dimensions of rupture area from seismic data, within the real time constraints of a tsunami watch, by surface wave analysis and body wave inversion.

To test the discriminant methods, we found two pairs of earthquakes that are most appropriate. The first pair, the 1957 and 1986 earthquakes that occurred off Andreanof Islands in the Aleutians, had epicenters within a few tens of kilometers of each other, but rupture length of the 1957 earthquake was 1100 km long, while the 1986 earthquake had a rupture length of roughly 240 km from aftershock distribution (Boyd and Nabelek, 1988). The 1957 tsunami caused extensive property damage in the Hawaiian Islands while the 1986 tsunami, though detected on maregrams throughout the Pacific, did negligible damage, even in the Aleutians. The disruption of economic and cultural life caused by the issuance of a tsunami warning in the 1986 event was considerable and far from being negligible. The other pair of earthquakes were the

Chile earthquakes of 1960 and 1985. The rupture length of the 1960 earthquake was 1200 km long (Wada and Ono, 1963), while that of 1985 was about 150 km. The 1960 tsunami caused deaths and destruction as far away as Japan. Although the 1985 tsunami caused no damage, the magnitude of the 1985 earthquake was 7.8 with considerable destruction on land in Chile. No tsunami warning was issued for the 1985 earthquake, fortunately.

4. Surface Wave Analysis

In 1961 Ben-Menahem proposed the method of directivity to determine the length of a rupture zone. He showed that the ratio of the spectra of Rayleigh waves R_1 and R_2 is expressible as directivity which is a function of three parameters: rupture length, rupture velocity and the angle between the rupture direction and direction of wave propagation. The great advantage of the directivity method is that a long period seismogram with sensitivity to 400 second period from only one station is necessary for the analysis.

A record from the strain meter at Yasato Station in Japan were obtained and analyzed. Figure 1 shows the R_1 record and Fig. 2 the R_2 record for the 1986 Andreanof earthquake. Figure 3 is a plot of the ratio of the spectra of R_1 and R_2. Figure 4a is a plot of the directivity function with a rupture length of 1100 km, rupture velocity of 2 km/sec and angle of 20 degrees between rupture direction and wave direction, while Fig. 4b is the directivity for rupture lenth of 80 km with other parameters being the same as the 4a case. The 80 km rupture length fits the data. A plot of aftershocks by Boyd and Nablek (1988) showed a rupture area of 240 km by 150 km. It may be that the aftershock area did not correspond to the rupture area for this earthquake.

For the Chile earthquakes, the rupture length for 1960 was 1200 km (Wada and Ono, 1963) and that of 1985 was 150 km by our determination.

The surface wave method is a quick and dirty method for discrimination during the time limitation of a tsunami watch. If the ratio of spectra shows a cluster of peaks and troughs in the 400 second period area, then the rupture area is in the range of 700 to 1200 km range. If the cluster is near the 150 second period section, the rupture length is roughly 250 km. If in the 70 second range, then the rupture area is in the range of 100 km.

In spite of the late arrival of the R_2 wave, the analysis can be completed to be in time for the decision to issue a warning or not. With appropriate scanning device to read seismograms and properly tailored software for spectral analysis, surface wave analysis can be done in 15 minutes.
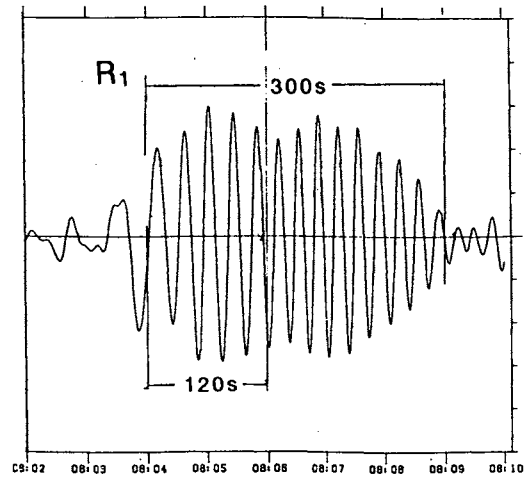

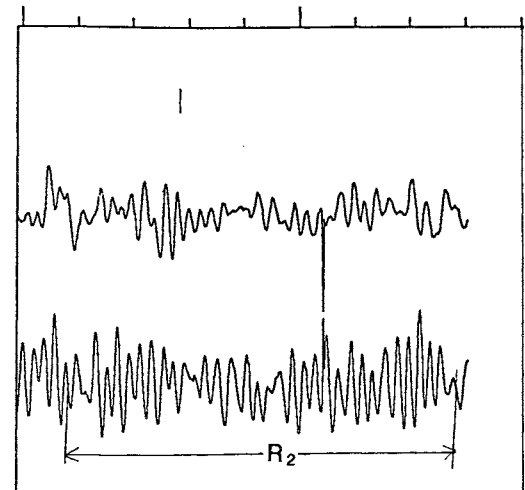Fig.1. R_1 wave from the 1986 Andreanof earthquake on Yasato Staion.
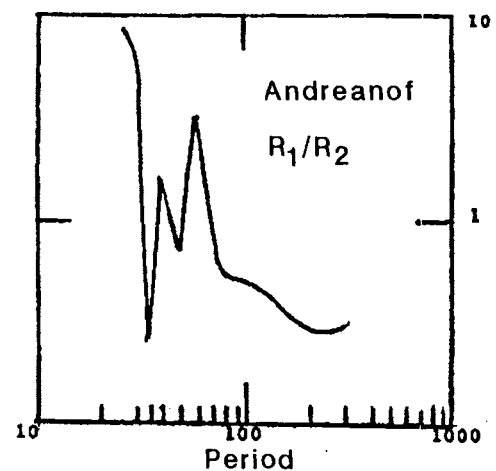

Fig.2. R_2 wave on Yasato record.
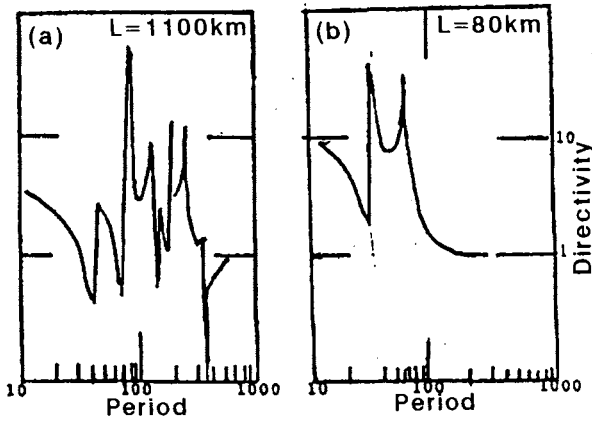

Fig.3. Spectral ratio R_1/R_2.

Fig.4. Directivity functions for rupture lengths 1100 km (a) and 80 km (b).

5. Body Wave Inversion Mehod

To estimate a length of rupture area from body waves, we apply a waveform inversion technique. By an inversion method we obtain the slip distribution on a fault plane that minimizes a misfit of the synthetic seismograms to the data.

To analyze in real time, we express a fault model in terms of linear parameters. A large fault plane is placed in the xy-plane; the x-axis is parallel to the strike direction and the origin is taken as the rupture initiation point. The fault plane should be taken much larger than the rupture extent inferred from the magnitude and the surface wave analysis. We divide the fault plane into $M \times N$ subfaults with length Δx and width Δy. Letting $x_m = m\Delta x$ and $y_n = n\Delta y$, mn-subfault occupies the region $x_m - \Delta x/2 \leq x \leq x_m + \Delta x/2$, $y_n - \Delta y/2 \leq y \leq y_n + \Delta y/2$. Approximating each subfault by a point dislocation source placed at the center of the subfault, we assume the slip time function $D_{mn}(t)$ at the mn-subfault as

$$D_{mn}(t) = 0 \qquad t < T_{mn}$$
$$= \sum_{l=1}^{k-1} D_{mnl} + D_{mnk}/\tau \ (t - T_{mn} - (k-1)\tau)$$
$$T_{mn} + (k-1)\tau \leq t \leq T_{mn} + k\tau$$
$$= \sum_{k=1}^{K} D_{mnk} \qquad t > T_{mn} + K\tau \qquad (1)$$

with

$$T_{mn} = \sqrt{x_m^2 + y_n^2}/V_r$$

D_{mnk} $(k = 1, 2, .., K)$ are the model parameters of which values are determined by the inversion and V_r is a rupture velocity. From the inversion solution for the final slip distribution, $\sum_k D_{mnk}$, we can find the length of the rupture area. Since the estimated slip depends on the assumed value of V_r, we will obtain least squares solutions for various values of V_r and choose the solution leading to the best fit among them as our preferable solution. By modeling the slip function as Eq.(1), we can take account of variation in local rupture velocities as well as variation in slip functions. For example, the

slip function with $D_{mnk} = 0$ for $k = 1, 2$ may correspond to delayed rupture by 2τ. This expression for the slip function is based on Olson and Apsel (1982).

The synthetic P-wave at the station x_j radiated from our fault model is given by

$$F(t, x_j) = \sum_{mnk} D_{mnk} f_{mn}(t - T_{mn} - (k-1)\tau, x_j) \quad (2)$$

where $f_{mn}(t)$ is the elementary wave from the mn-subfault with unit slip and a rise time of τ. We calculated $f_{mn}(t)$ on the basis of the ray theory assuming that it is composed of direct P, pP, and sP phases. Attenuation effects and instrumental response were taken into account.

Introducing smoothing and positivity constraints to stabilize the problem, we determine values of the model parameters D_{mnk} that yield the best to the data. The inversion scheme is almost the same as Yoshida (1989).

To test this method, we first inverted the long-period P-waves (sampling interval = 1 sec) from the 1985 Chile earthquake recorded by the Global Digital Seismograph Network (GDSN). We assumed the hypocenter is 33.155°S, 71.980°W, depth 33 km reported in Preliminary Determination of Epicenter and the fault plane is strike=N11°E, dip=25°, and slip anlge=110°, which was determined by Dziewonski et al. (1985). In Fig.5, we show the equal-area projection of the focal sphere (the lower hemisphere) and the GDSN stations used for the inversion. Considering a fault of 680 km length and 160 km width, we assumed $M = 17$, $N = 4$, $\Delta x = \Delta y = 40$ km, $K = 5$, and $\tau = 6$ sec. Thus the number of the model parameters is $M \times N \times K = 340$. The vertical component seismograms of 200 sec at ten stations were inverted. Testing for the rupture velocities of 1.5, 2.0, 2.5, and 3.0 km/s, we obtained the best fit when $V_r = 3.0$ km/s. The total computational time for obtaining the least squares solutions for the four values of V_r was about 15 minutes. Figure 6 shows the comparison of the observed and the synthetic seismograms for the preferable solution with $V_r = 3.0$ km/s and Fig.7 shows the contours of the final slip on the fault plane. The estimated model has three high slip areas with a length of 240 km, which is somewhat larger than the estimation of 150 km by the surface wave analysis. The length of the twohigh slip areas south of the hypocenter is about 150 km; this region may correpond to the rupture area
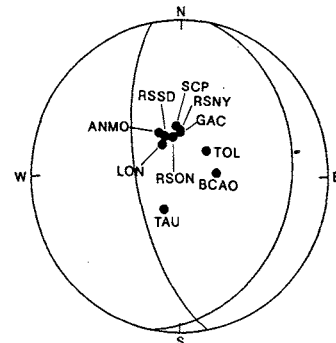
Fig.5. Equal-area projection of the focal sphere (the lower hemisphere) and the stations used for the body wave inversion of the 1985 Chile earthquake.
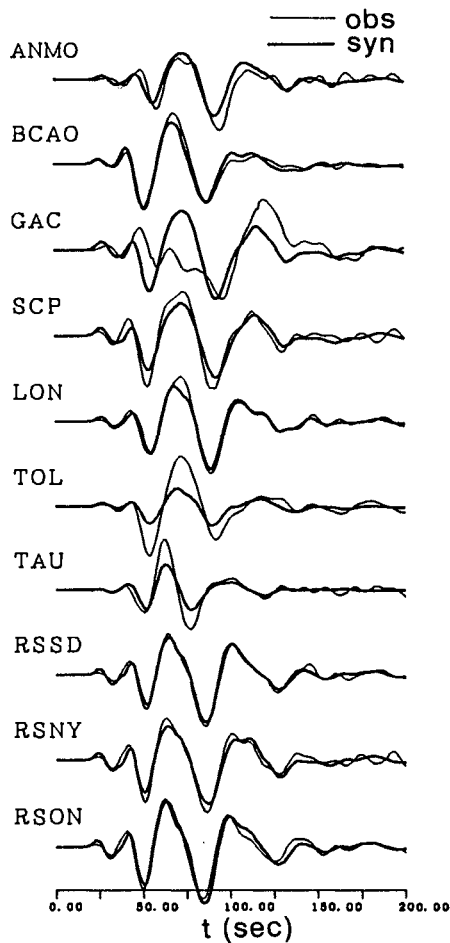
Fig.6. Comparison of the observed (thin line) and the synthetic (thick line) seismograms calculated for the inversion solution of the 1985 Chile earthquake.

estimated from the surface waves.

Next we studied the 1986 Andreanof earthquake in the same way. When we assumed $V_r = 2.0$ km/s, we obtained the solution yielding the best fit. Figure 8 shows the estimated slip distribution. It is found that the length of the high slip area is about 80 km, which is the same estimated by the surface wave analysis.

6. Evaluation

During a tsunami watch, in addition to the parameters that are routinely obtained, the mantle magnitude and the parameters of the rupture area should be obtained. Both methods we propose for rupture parameter determinations can be completed within 30 minutes. We point out that in the cases we have studied, one method confirms the other.

During a tsunami alert, once the size of the rupture area has been determined, we can use main frame computers and calculate the distribution of tsunami amplitude across the Pacific as the tsunami progresses. Software for such computation is already available. We can predict the expected damage at distance shores.

What we propose entails the installation of strain meters, preferably those very similar to the one at Yasato Station, at the Pacific Tsunami Warning Center or nearby.

Fig.7. Contours of the estimated slip for the 1985 Chile earthquake. The contour interval is 0.2 m. The synthetic seismograms from this model are shown in Fig.6.

Fig.8. Contours of the estimated slip for the 1986 Andreanof earthquake.

References

1. Ben-Menahem, A., 1961. Radiation of seismic surface waves from finite moving sources, *Bull. Seism. Soc. Am.*, **51**, 401-435.
2. Ben-menahem, A., 1963. Source mechanism from spectra of long period surface waves, 2. The Kamchatka earthquake of November 4, 1952, *J. Geophys. Res.*, **68**, 5207-5222.
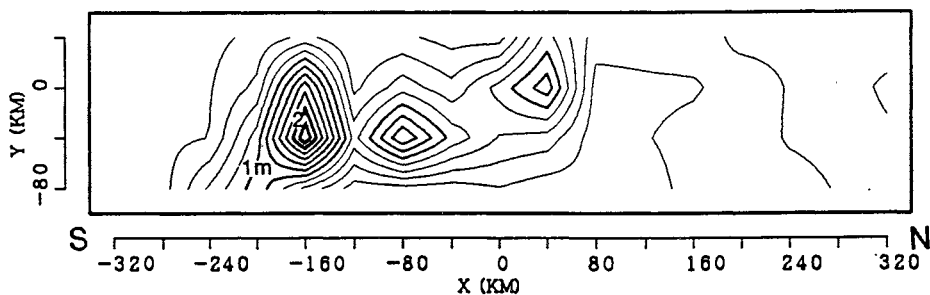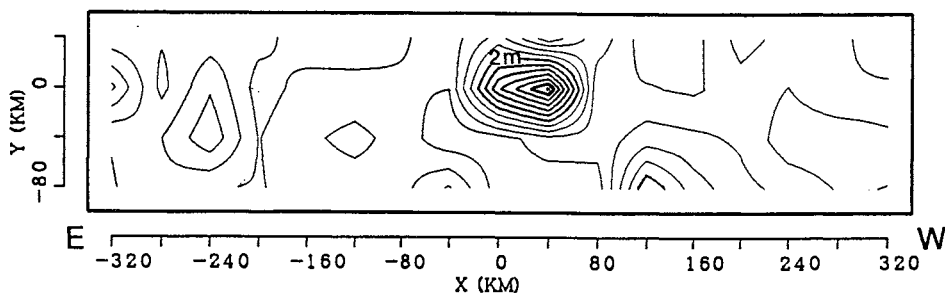3. Boyd, T. M., 1984. Characteristics of seismicity associated with the 1957 ($M_w = 9.1$) Aleutian Island earthquake, (abstract), *Trans. Am. Geophys. Un.*, **66**, 298.
4. Boyd, T. M. and Nabelek, J. L., 1988. Rupture process of the Andreanof Islands earthquake of May 7, 1986, *Bull. Seism. Soc. Am.*, **78**, 1653-1673.
5. Dziewonski, A. M., Franzen, J. E. and Woodhouse, J. H., 1985. Centroid-moment tensor solutions for January-March 1985, *Phys. Earth Planet. Inter.*, **40**, 249-258.
6. Olson, A. H. and Apsel, R. J., 1982. Finite faults and inverse theory with applications to the 1979 Imperial Valley earthquake, *Bull. Seism. Soc. Am.*, **72**, 1969-2001.
7. Talandier, J. and Reymond, D., 1988. A new approach for a quick estimation of the seismic moment, magnitude M_m, *Natural and Man Made Hazards*, 109-124, Reidel Pub. Co.
8. Wada, T. and Ono, H., 1963. Source mechanism of the Chilean earthquake from spectra of long period surface waves, *Zisin, ser* II, **16**, 181-187.
9. Yoshida, S., 1989. Waveform inversion using ABIC for the rupture process of the 1983 Hindu Kush earthquake, *Phys. Earth Planet. Inter.*, **56**, 389-405.

SOURCE CONFIGURATION AND THE PROCESS OF TSUNAMI WAVES FORMING

An, G. Marchuk, V. V. Titov

Computing Center, Siberian Division of the USSR Academy of Sciencies, Novosibirsk, USSR

Abstract

The first stages of tsunami waves forming by two-dimensional surface displacement are still not clear enough. In this paper authors made the attempt to describe theoretically and confirm conclusions numerically the process of tsunami waves generation by rectangular positive and negative initial ocean surface displacements. The main result of the paper is the proof of the focussing point existance for combined plus-minus initial displacement where abnormal tsunami wave height can be registered.

1. Introduction

The most important role for parameters of tsunami wave in near-source zone have bottom relief (bathymetry), form and location of the source. But the importance of these factors in different cases is not equivalent. Characteristics of the wave, coming from a distant source mainly depend on its size and peculiarities of the bathymetry between source and observation point. Near tsunami source the main role in wave signal forming plays distribution of the initial surface displacement in it. It is well known for the shallow water theory that in one-dimensional case positive surface displacement generates positive (rise) tsunami wave without any negative wave train behind it. But two-dimensional rectangular initial surface elevation generates tsunami wave having after the leading positive wave some negative train. So we see that the second dimension is responsible for negative waves in tsunami wave train (case of positive source).

2. Wave focussing

Let's consider rectangular positive initial surface displacement having maximum height at the central point. On the figure 1 one can see the numerically calculated behavior of the water level (marigram). Maximum value of water level here was at the initial moment. Then level was coming down to zero and have stopped. In one-dimensional case that would be the end of the process, but here after some time interval (it is equal to wave travel-time from short boundaries of the source) level began to coming down again till some minimum value, which verifies from minus 1 (square source) to zero (very very long source). If we change up and down of this picture
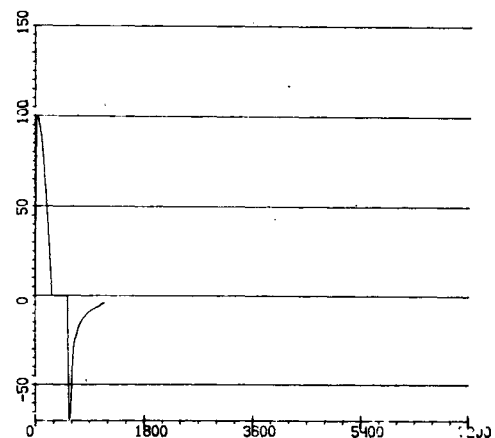

Fig.1 Behavior of the sea
level in the center
of rectangular source.

we'll obtain the marigram in the center of rectangular negative source. So we have find that short sides (boundaries) of the positive rectangular source are working like generators of negative tsunami waves and in the case of negative initial surface displacement - as generators of positive waves.

Let introduce the concept of focusing as a simultaneous arrival of tsunami waves from different sources or parts of the initial wave front to the point named focus. For regions with constant depth location of the focus can be easily find geometrically using comparison of distances.

Now let's return back to spatial tsunami sources. Usually real tsunami source is combination of positive and negative displacements. Some approach to reality is so called plus-minus source which consists of two symmetric rectangular parts with surface displacements of opposite signes. If we will consider the kinematic picture of generation and propagation process in case of plus-minus source (fig.2), we will see that on the straight line coming through centers of both parts $S1$ and $S2$ there exists point M (the focus) where positive waves from the center of the positive part $S2$ and short boundaries AB and EF of the negative part arrive simultaneously.

about abnormal high tsunami amplitude (as compared with the case of positive initial source) in the neighborhood of the focus. On the figure 3 water surface in two moments of the propagation process is drawn. One can easily see positive waves coming from short boundaries of the negative part (sides AB and EF on the fig.1).

(a)

(b)
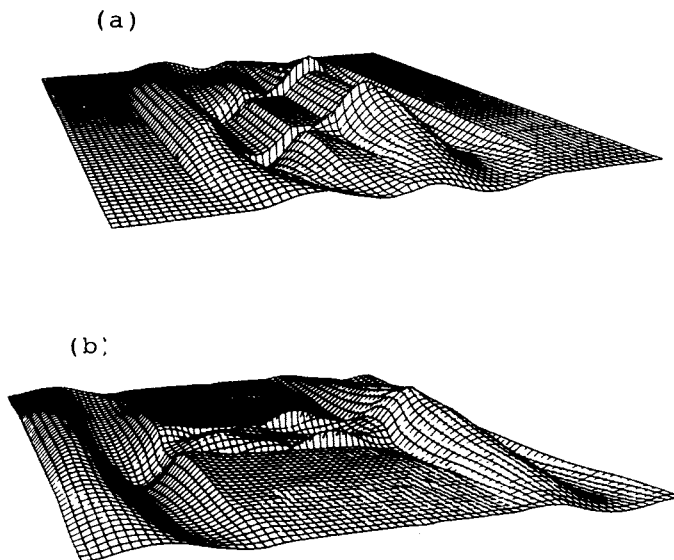
Fig.3 Form of the water surface 328 (a) and 657 (b) sec after the start of the propagation process.

Looking through the distribution of the maximum surface level along the straight line coming through centers of both parts of the initial surface displacement it is possible to see the area with maximum amplitudes higher than half a meter (initial height in the source was 1 m). The same distribution for positive source of the same rectangular form and height has no maximums outside the source (dotted line on fig.4).

Comparisson of the maximum wave heights in the neighborhood of the focus gives one and a half times growth of the wave height there for rectangular plus-minus source as compared with the positive initial surface elevation of the same amplitude (+1 m) and form.

Fig.2 Location of the focus for plus-minus initial surface displacement.

At the focusing point M we can expect increasing of the wave height. Numerical simulation of this problem (generation of tsunami waves by plus-minus source) have confirmed our statement

Application to tsunami zoning

So we see that after generation of tsunamis by the source which has rise and fall parts (at the initial moment of time) there can exists the focus, where abnormal high tsunami can be registered. It is clear that for some
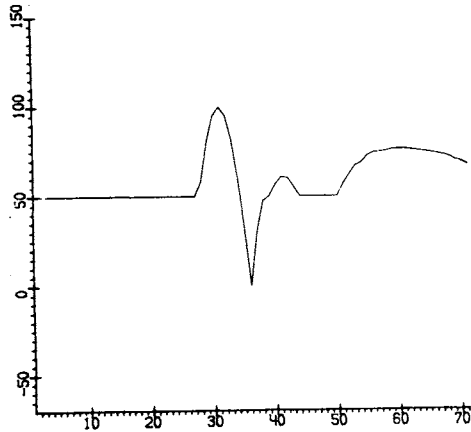
Fig.4 Distribution of maximum
      wave heights for plus-
      minus   and   positive
           sources.

location of the described plus-minus
source the focus can be located close
to the coasline. In this case in the
coastal points near this focus abnor-
mal high tsunami waves can be registe-
red. If we take a fixed point on the
coastline it is not difficult to
obtain potentially dangerous location
(dangerous for the neighborhood of the
fixed point) of plus minus tsunami
source using isochrone technique. If
the center of the positive part of the
source and short sides of the negative
part are located on the same iso-
chrone (travel times from our coastal
point are the same) in this given
point we will register the focal amp-
lification of the wave height. Let us
consider sloping bottom relief near
the straight coastline. In this case
it is possible to build isochrones
using analytical approach. Above the
sloping bottom wave rays are cycloids
which parametrically can be expressed
as [1]:

$$x = c_1 (t - \sin t)$$
$$y = c_1 (1 - \cos t)$$

where the radius of the cycloid c_1
is derived for every pair of start and
end points. Assume that the bottom
iclination angle is equal to α , so
at the distance y_* off shore depth
H will be expressed

$$H = y^* \, tg \, \alpha \quad .$$

Let M be the fixed point on the
coasline and the initial point of the
coordinate system. X - direction along
the coastline, y - off shore. From the
point (a,b) to the coastal point M
tsunami travel time will expressed [1]

$$T_1 = \frac{\sqrt{2c_1}}{\sqrt{g \cdot tg \, \alpha}} \cdot arccos(1 - b/c_1) \, ,$$

and from the marine point S with
coordinates $(0, b_1)$ travel time is
expressed as

$$T_0 = \frac{2b_1}{c_s + c_m} = \frac{2b_1}{\sqrt{g \cdot b_1 \cdot tg \, \alpha}} \qquad (2)$$

Here C_s and C_m are tsunami velocities
at points S and M ($C_m = 0$). Our aim
is to find the form of isochrones for
our coastal point M . From condition
of equality of both times T_1 and T_0
we can find correlation between quan-
tities a,b and b_1.

$$\frac{2b_1}{\sqrt{g \cdot b_1 \cdot tg \, \alpha}} = \frac{\sqrt{2c_1}}{\sqrt{g \cdot tg \, \alpha}} \cdot arccos(1 - \frac{b}{c_1}) (3)$$

and finally

$$b_1 = \frac{c_1}{2}(arccos(1-b/c_1))^2 \qquad (4)$$

From wave ray equations (1) we can
find the value of parameter t in the
point (a,b)

$$t^* = arccos(1 - b/c_1) \qquad (5)$$

and then we obtain equation which
ties together a , b and c_1

$$a = c_1(arccos(1-b/c_1) - \sin arccos \, t^*) (6)$$

Using equations (4) and (6) it is
possible to derive the connection bet
ween a, b and b_1 which independent on
c_1. Now for every value b_1 it is
easy to find values a and b for
dense enough set of values
arccos($1 - b/c_1$) from zero to 2π .
It is interesting that the form of
obtained isochrone is independent on
time and bottom inclination, but it
linearly depends on offshore distance
b_1. For $b_1 = 1$ from obtained expres-
sions one can find that the width of
isochrone (fig. 5) is close to 1.28 ,
and it intersects coastline in points
(±0.318,0). Finally it is necessary
to say that tsunami travel time from
each point of this isochrone expressed

—158—

by formula (2). Broken line on the figure 5 shows us the possible location of plus-minus tsunami source which produces wave focusing in point M .

Kurils. After drawing of isochrones we can easilly choose the location of one of the possible plus-minus tsunami sources which was used for numerical computations of tsunami propagation process. Method of numerical simulation was based on nonlinear shallow-water equations

$$H_t + (Hu)_x + (Hv)_y = 0 ,$$

$$u_t + uu_x + vu_y + gH_x = gD_x ,$$

$$v_t + uv_x + vv_y + gH_y = dD_y ,$$

where $H(x,y,t)$ - the whole depth from ocean bottom to surface, $D(x,y)$ - bathymetry of the region, $u(x,y,t)$, $v(x,y,t)$ - waver velocity components, g - gravity acceleration. The difference between H and D is surface displacement from undisturbed level. Numerical atgorithm is based on splitting method. More details about this numerical algorithm one can find in [2]. Numerical experiment in Nothern Kurils region gives one and a half times growth of tsunami waves height near the shore for plus-minus source as compared with positive tsunami source with the same initial height. On the figure 6 the comparison of distributions of maximum tsunami wave heights along the coastline is shown. Here vertical lines mean maximum wave heights from one meter plus-minus source and the curve shows the distribution of maximum tsunami heights from one meter positive source. It is clear that plus minus source with negative part towards the shore produces rather

Fig.5 Form of the isochrone for the costal point M above the sloping bottom. Broken line shows potentially dangerous location of the plus-minus tsunami source.

In regions with real bathymetry isochrones for coastal (or any other) points can be build only using numerical computations. For example authors carried out this procedure for Nothern
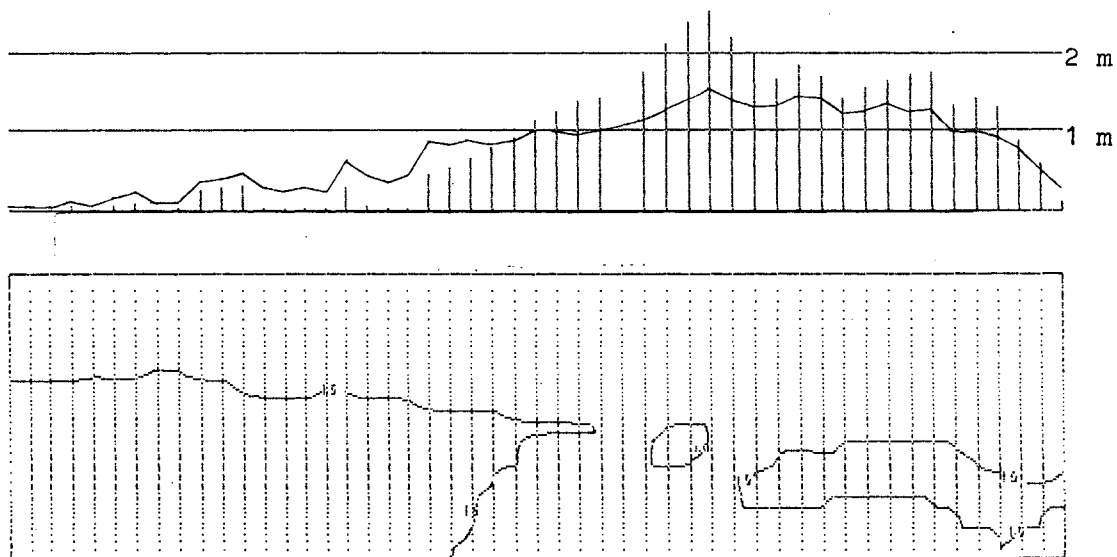
Fig.6 Distribution of computed maximum tsunami wave heights along the coast of Nothern Kurils with and without focusing.

high tsunami waves in the neighborhood of the coastal focusing point.

Let's do one more step to reality. Real tsunami sources generally consist of two parts (rise and fall), but instead of rectangular these positive and negative parts usually have ellipsoidal form.

Let's simulate the situation which has taken place during Japan sea tsunami May 26, 1983 near Akita coast. In that case tsunami source had rise and fall parts. Maximum elevation in the source was about 3.5 meter and minimum initial water level in negative part near minus half a meter. Location of
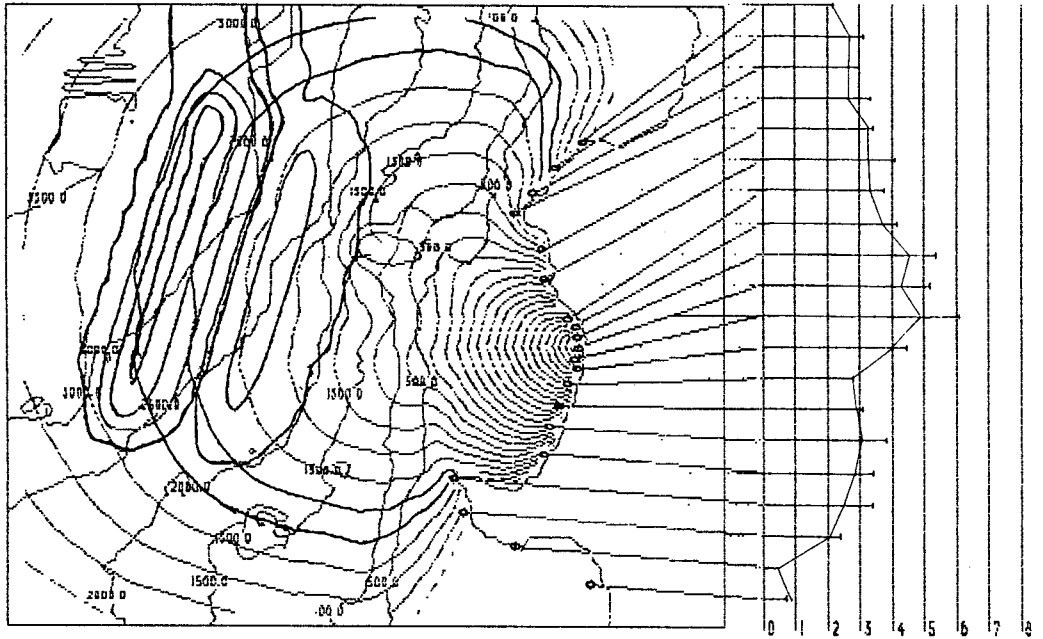
Fig.7 Location of tsunami source near Akita prefecture coast. In the right part distribution of maximum tsunami wave heights is shown. Points give us computed heights for full source and the curve - for the source without negative part.

this source which was used in numerical modeling is close to real one.This follows from comparison of computed first wave arrival times with the real

data. On the figure 7 one can see that the center of the positive part of our initial surface displacement and short boundaries of the negative part locate
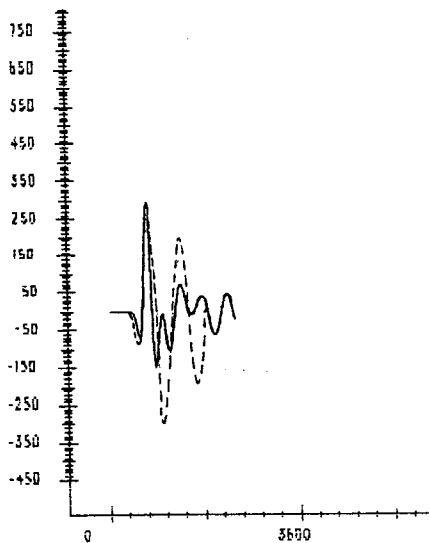
Fig.8 Comparison of real data [3] (broken line) and computed marigram in Fukaura.
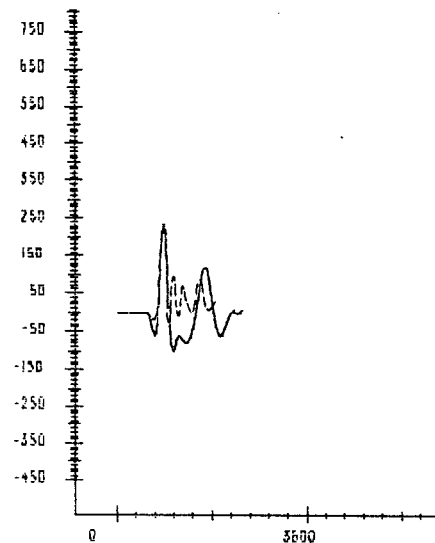
Fig.9 Comparison of real and computed marigrams for the point on Oga.

on the same isochrone which was built for the coastal point with maximum registered tsunami heights. Distribution of maximum wave heights along the coastline is very similar to the real tidal data. The same we can say about tsunami arrival times and first cycles on marigrams (figures 8 and 9). So our conclusion on this matter can be formulated as follows: during Japan sea tsunami in 1983 great tsunami wave heights near Minehama village were the result of the wave focusing too. This is confirms by results of numerical simulation of this event with the initial surface displacement without negative part. Distribution of wave heights in this case is drawn as a curve. Comparison of distributions gives the large enough difference in focal area (near Minehama village).

4. Conclusions

If the initial tsunami source have rise and fall parts there exists some point out of the source where abnormal wave heights can be registered. This happens as a result of mutual interaction of positive tsunami waves coming from different parts of initial surface displacement. Sometime this focal point can be located near the coastline and this situation can increase the damage on the shore.

References

1. Marchuk, An.G., Chubarov, L.B. and Shokin, Yu.I.,"Numerical modeling of tsunami waves",Siberian branch "Nauka" publishers, Novosibirsk, USSR, 175 p., (1983)
2. Titov, V.V.,"Numerical modeling of tsunami propagation by using variable grid", Presented at the International Tsunami Symposium, Novosibirsk, USSR, 1989, (to appear).
3. Satake, K., Okada, M. and Abe, K., "Tide gauge responce: measurements and its effect on tsunami waveforms",Proceedings of PACON 88, Honolulu, Hawaii p. OST6/9, (1988)

A SEMI-ANALYTICAL AND SEMI-EMPIRICAL METHOD FOR THE EVALUATION OF TSUNAMI GENERATING EFFICIENCY DUE TO LANDSLIDES PLUNGING INTO THE WATER BODIES.

S. I. Iwasaki

National Research Center for Disaster Prevention, Japan

ABSTRACT

On tsunamis generated by landslides plunging into water bodies, the generating efficiency was fixed by the comparison of linear theory with laboratory experiments and field observations. Waves were generated by the impacts of the slides at the water surfaces and the submerged movements of the landslides in the water. At the water surface, about 8-15% of the kinematic energy of the sliding body was transformed into the wave energy. In total, the efficiency was about 26%.

1. INTRODUCTION

About 90% of causes of tsunamis is submarine earthquakes, other 10% is landslides, volcanic eruptions, rock or ice falls and so on. In particular, submarine landslide induced tsunamis are not accompanied with so-called foreshocks as in the case of earthquakes and volcanic eruptions. And tsunamis generated by landslides plunging into water bodies can occur in inland lakes and reservoirs where normally considered to be safe for such disastrous water waves. Predicting the wave heights of various dimensions and speeds of the slides for site hazard evaluation purposes is of clear importance.

For the estimation of the heights of tsunamis generated by landslides, one of the bases is WIEGEL's [1] laboratory experiment. One of the conclusions was "about 1% of the initial potential energy(net, submerged) is transformed into the wave energy." Based on this conclusion, STRIEM&MILOH [2] calculated the wave height assuming the generated wave is one dimensional solitary wave and compared with the historical data. But, they committed simple mistake in the calculation of the solitary wave energy. MURTY [3] reported the submarine landslide induced tsunami occurred on April 27, 1975, in Kitimat Inlet, British Columbia. Inversely evaluated efficiency from the observational data and correct solitary wave energy is 32.2%. This value is far from the WIEGEL's conclusion. It is suggested that WIEGEL's result could not be applied simply to all of the landslides-induced tsunami evaluations. Iwasaki([4],[5]), introducing the concept of Virtual Mass(Added Mass), reconstructed the data of WIEGEL's experiment and showed the maximum efficiency was 10% through the numerical simulations and the linear theory(KAJIURA, [6]).

In this paper, tsunamis due to landslides plunging into the water bodies were investigated. Generation

mechanism of the tsunamis divided into two stages , impact at the water surfaces and submerged movements of the sliding bodies in the water. Using the conclusion of IWASAKI [4], generating efficiency at the water surface was fixed.

2. TSUNAMI GENERATING EFFICIENCY DUE TO LANDSLIDES PLUNGING INTO THE WATER BODIES

Using the data derived from a U.S. Army engineer Waterways Experiment Station(WES) model study of Lake Koocanusa, Montana(DAVIDSON & WHALIN, [8]), and a Western Canada Hydraulic Laboratories, Ltd. (WCHL) model study of Mica Reservoir, British Columbia(WCHL. [9]), SLINGERLAND & VOIGHT [7] presented a empirical formula

$$\log(\eta_{max}/d)=-1.25+0.71\cdot\log(K.E.) \quad (1)$$

where η_{max} is the maximum wave amplitude at a standard distance r/d=4.0 directly in front of a slide, d is the average depth off shore from slide site, r is the radial horizontal distance from the point of slide impact and K.E. is the nondimensional slide kinematic energy. Fig.1 shows the empirical formula and laboratory experimental data denoted by black squares(WES) and dots(WCHL). Confidence limits at the 95% level are indicated by dashed lines. The back calculations of slide-induced tsunamis that occurred in Lituya bay, Alaska and Disenchantment bay, Alaska are also shown in Fig.1. Informations of both slides are shown in Table-1.

Table-1 Parameters concerning the slides of Lituya Bay and Disenchantment Bay.

	Vo (c m^3)	ρ (g/cm^3)	Vf (cm/sec)	d (cm)
LITUYA BAY	3.1×10^{13}	2.7	$5.6 \sim 6.9 \times 10^3$	1.2×10^4
DISENCHANTMENT BAY	2.9×10^{13}	1.0	$6.0 \sim 8.3 \times 10^3$	8.0×10^3
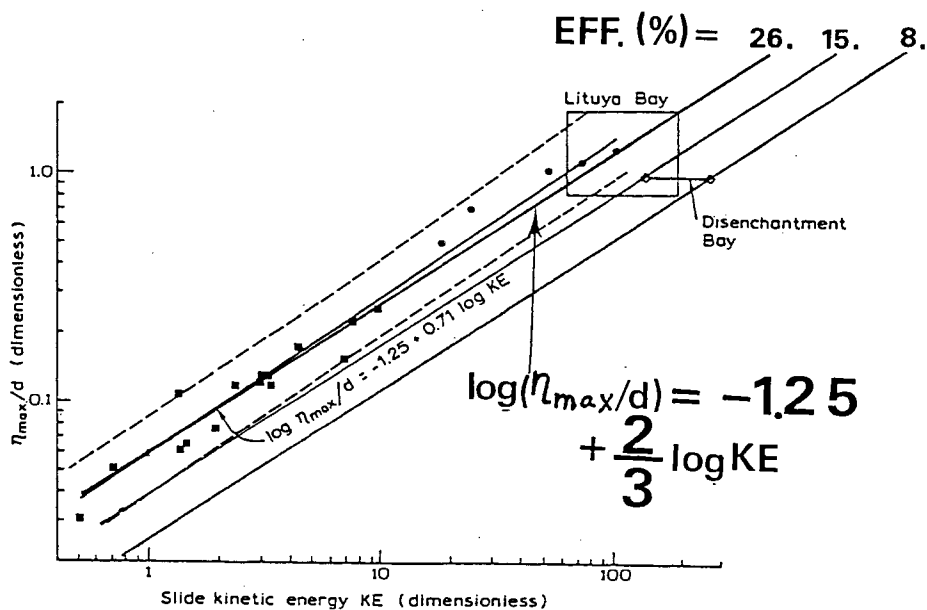
Fig.1 Plots of maximum wave amplitude versus slide kinematic energy (after SLINGERLAND & VOIGHT, [7]). Efficiency is constant along each bold solid line.

We, now, assume the generated wave had the solitary wave characteristics and consider the one dimensional propagation. The energy of solitary wave per unit width is expressed as follows

$$E_s=(8/3)\cdot \rho_w \cdot g \cdot d^3 \cdot \gamma \sqrt{\gamma /3} \qquad (2)$$

$$\gamma = \eta_{max}/d$$

where ρ_w denotes the density of the water and g the gravitational constant. In the experimental conditions, the wave propagated through a 180° arc. Then, the total energy is(see, Fig. 2)

$$W.E. =E_s\cdot \pi \cdot r \qquad (3)$$
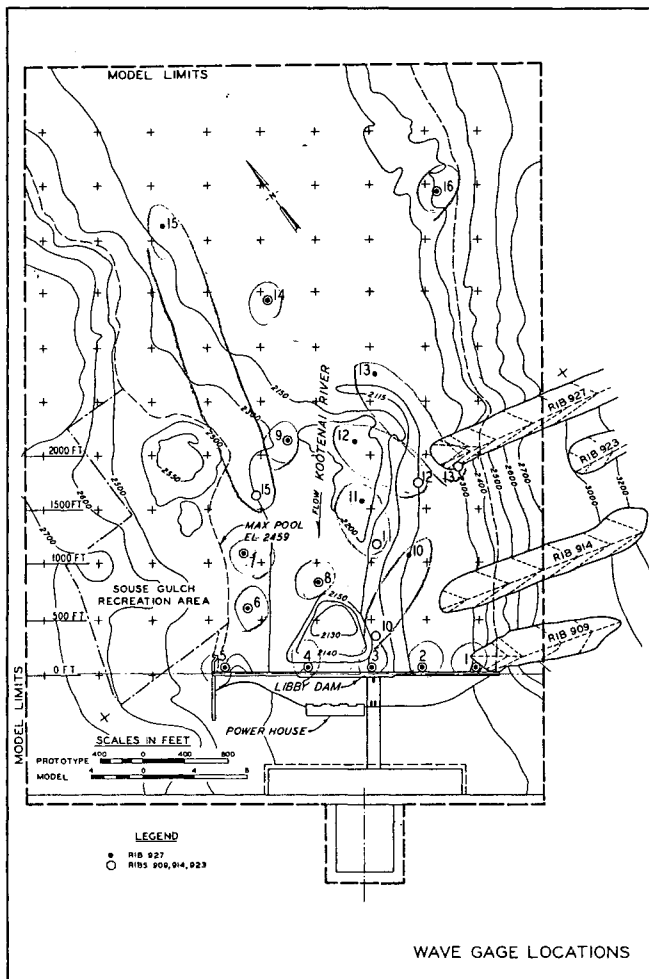
Fig. 2 Laboratory experimental set up of WES (after DAVIDSON & WHALIN, [8])

And, slide kinematic energy is

$$E_k=(1/2)\cdot \rho_s \cdot V_o \cdot V_f^2 \qquad (4)$$

where ρ_s denotes the density of the material of landslides, V_o the volume of the slide and V_f the final velocity of the slide. Nondimensional form of (4) is

$$K.E. =E_k/(\rho_w \cdot d^3 \cdot g \cdot d) \qquad (5)$$

There is little difference if the coefficient of log(K.E.) is changed from 0.71 to 2/3 in the equation (1) (see Fig. 1, bold solid line).

$$log(\gamma)=-1.25+(2/3)\cdot log(K.E.) \qquad (6)$$

Substituting (2) into (3) yields

$$log(W.E.)=log(8\pi /3\sqrt{3})+log(\rho_w \cdot g \cdot d^3)$$
$$+log(r) +(3/2)log(\gamma) \qquad (7)$$

Substituting (6) to (7) and after some algebra we get

$$(W.E./E_k)=0.26 \qquad (8)$$

Efficiency can be defined along the line of incline 2/3 in Fig. 1. In the experimental conditions mentioned above, the efficiency is about 26%.

3. GENERATING EFFICIENCY AT THE WATER SURFACE

It is suggested from Fig. 1 that tsunami generating efficiencies rather low for the Disenchantment Bay slide compared with that for the Lituya Bay slide. The reason of this difference can be considered as follows. The material of the Lituya Bay slide was soil($\rho =2.7g/cm^3$) but the material of the Disenchantment Bay slide was glacier($\rho =1.0g/cm^3$). So that, according to IWASAKI [4] ,for the case of Lituya Bay, the slide generated

tsunami even in the water at the maximum efficiency 10%. But, for the case of Disenchantment Bay, the fallen glacier did not generate tsunami in the water.

To confirm this speculation, we assume the virtual landslide, that is, whose K.E. is the same with that of the Disenchantment Bay glacier and density ρ is the same with that of the Lituya Bay slide (see Table-2). The range of K.E. of the Disenchantment Bay fallen glacier varies from 130 to 249 depending on the estimation difference of the final velocity. In Fig.3, A and B indicates the point of K.E.=130 and K.E.=249, respectively.

If the 10% of the potential energy lost in the water of the virtual slide was transformed into the wave energy, then,

the points A and B move to A´ and B´ as shown in Fig.3. This tendency are considered to be reasonable compared with the experimental data. The real values exist between A and A´ or B and B´. The Disenchantment Bay fallen glacier is thought to have the effect for the tsunami generation only at the water surface. Then, we can evaluate the generating efficiency due to the impact at the water surface by the method mentioned in section 2. The result is about 8-15% of the kinematic energy of the slide was transformed into the wave energy at the water surface as shown in Fig.1.

Table-2 Parameters of the slides of Disenchantment Bay, prototype and virtual slide.

	V_0 (cm^3)	ρ (g/cm^3)	d (cm)	KE (non-dim.)	η max/d
Prototype A	2.9x10^{13}	1.0	8.0x10^3	130	0.96
B				249	0.96
Virtual Slide A	1.1x10^{13}	2.7	8.0x10^3	130	1.30
B´				249	1.30

$$\log(\eta_{max}/d) = -1.25 + \frac{2}{3}\log KE$$
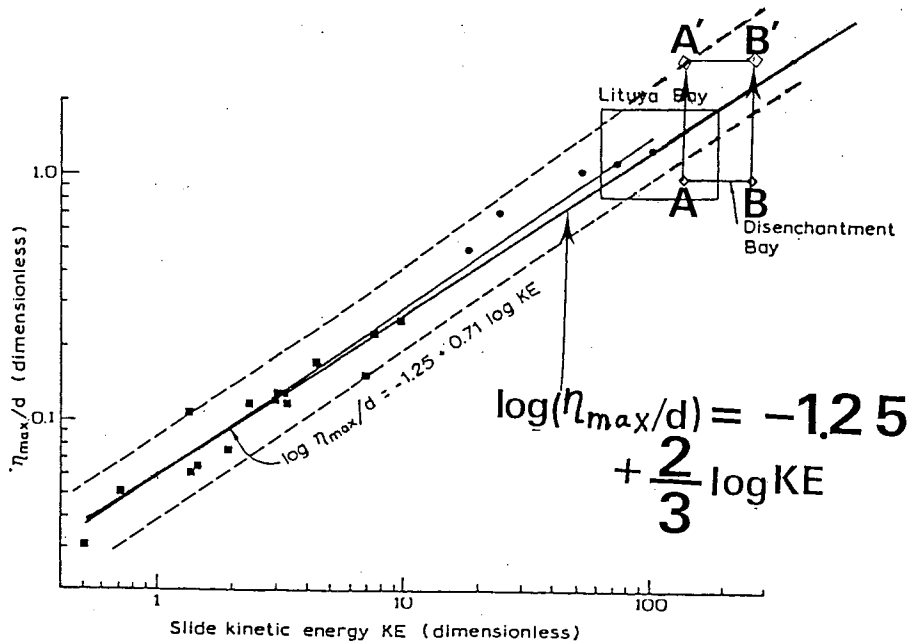
Fig.3 The same figure as Fig.1, but the points A,B correspond to the cases of prototype slide and A´,B´ correspond to the cases of virtual slide of Disenchantment Bay, respectively.

4. CONCLUDING REMARKS

On tsunamis generated by landslides plunging into the water surfaces, following results are found.

1. Generation mechanism is divided into two stages, that is, impact at the water surface and submerged movement of the sliding body in the water.

2. For the evaluation of the generating efficiency, it is essential to know the values of kinematic energy, potential energy lost in the water and density of the slide.

3. It was found by the semi-analytical and semi-empirical method that about 26% of the kinematic energy of the slide was transformed into the wave energy in the cases of the both laboratory experiments(WES and WCHL).

4. At the water surface, about 8-15% of the kinematic energy of the slide is transformed into the wave energy.

5. REFERENCES

1. WIEGEL, R. L., "Laboratory studies of gravity waves generated by the movement of a submerged body," Trans. Amer. Geophys. Union, 36, 759-774, 1955.

2. STRIEM, H. L. and T. MILOH, "Tsunamis induced by submarine slumpings off the coast of ISRAEL," International Hydrographic Rev., 53, 41-55, 1976.

3. MURTY, T. S., "Submarine slide-induced water waves in Kitimat Inlet, British Columbia," J. Geophys. Res., 84, 7777-7779, 1979.

4. IWASAKI, S. I., "Generation of surface waves due to submerged disturbances - II," Proc. of the fall meeting of the Ocean. Soc. of JAPAN, 200-201, 1986. (In Japanese)

5. ----------, "On the estimation of a tsunami generated by a submarine landslide-Summary," Proc. of the International Tsunami Symposium, 134-138, 1987.

6. KAJIURA, K., "The leading wave of a tsunami," Bull. of Earthq. Res. Inst., 41, 535-571, 1963.

7. SLINGERLAND, R., and B. VOIGHT, "Evaluating hazard of landslide-induced water waves," J. of Waterways, Port, Coastal and Ocean Division, ASCE, 108, ww4, 504-512, 1982.

8. DAVIDSON, D. D. and R. W. WHALIN, "Potential landslide-generated water waves, Libby Dam and Lake Koocanusa, Montana," Technical Report, No. H-74-15, U. S. Army Engineering Waterways Experimental Station, Corps of Engineers, Vicksburg, Miss., 1975.

9. Hydraulic Model Studies, Wave action generated by slides into Mica Reservoirs(British Columbia), Western Canada Hydraulic Laboratories, Vancouver, Canada, 1970.

APPLICATIONS OF FUZZY ALGORITHM TO CONTROL OF AUTONOMOUS UNDERWATER VEHICLE

Naomi Kato

Tokai University, Shimizu, Japan

ABSTRACT

This paper presents the applications of fuzzy algorithm to guidance and control of autonomous underwater vehicle (AUV) in terms of intelligence of machines.

A good combination of the hardware and software is indispensable to the perfectly autonomous control of AUV. As to the hardware, a new type of AUV named FLIPPER and a new concept of underwater survey system proposed by the author et al. are referred. As to the software, control architecture of FLIPPER has hierarchical structure consisting of attitude control with decoupling of motion, guidance, navigation, path planning and communication.

The attitude control, the guidances for seabed survey, rendezvous with unmanned, underwater station (UUS), pipeline survey are numerically simulated by use of fuzzy algorithm.

1. INTRODUCTION

Future targets of R & D of ROVs will be focused on intelligence of ROVs, cooperative working between a group of ROVs and support vessel, and long-term mission. Of various types of ROVs, AUV is suitable for deep water survey and light working because of no troubles caused by umbilical cables and of a little consumption of power.

This paper presents ongoing work about AUV and the underwater survey system [1,2] from the viewpoints of above-mentioned targets. The author proposed a new type of AUV named FLIPPER (see Fig.1) performing a stable oceanographic undersea investigation on a prearranged course as well as underwater survey system as shown in Fig.2.

Control Configured Vehicle (CCV) technology was adopted for the attitude control decoupling some components of the motion. Fuzzy algorithm was applied to the guidance as a step of intelligence of AUV.

AUV in general has shortcomings about power and communication compared with tethered ROV. Not only to overcome these shortcomings, but also to perform cooperative and long-term missions by a group of AUVs, proposed underwater survey system has an UUS having the missions of docking AUVs, charging or replacing AUVs' batteries, exchanging information in the shed of UUS, and watching AUVs. This paper deals with (1) the situation of fuzzy algorithm in terms of intelligence of machines, (2) control architecture of AUV, (3) application of fuzzy algorithm to attitude control of AUV with CCV modes and (4) application of fuzzy algorithm to guidance on a prearranged course, collision avoidance maneuver, rendezvous of AUV with UUS and pipeline survey using vision.

2. INTELLIGENT MACHINES AND CONTROL ALGORITHMS

According to rapid expanse of automation in the fields of machinery control and process control in recent years, the control targets have been more complicated, but more advanced, more various, more flexible control functions have been needed as well. As the corresponding control system to such circumstances, autonomously distributed control system is more desirable than centralized control system. In addition, cooperative man-machine system is also desired. In the autonomously distributed control system, functions, performances, data, processes, sensors, system management, resources and so on are distributed to perform intelligent tasks such as measurement, congnition, inference, evaluation, judgement and operation. In the cooperative man-machine system, informations such as natural languages, characters and pictures are transferd from human beings to machines to obtain the support of decision making from the machines having the system for knowledge data base, inference and learning.

There are three control algorithms so far for the construction of the autonomously distributed control system and the cooperative man-machine system, namely knowledge-based algorithm[3], neural network [4] and fuzzy algorithm [5].

Of three algorithms,fuzzy algorithm is aimed at realizing the intelligent machine capable of human-friendly information management and working. The fuzzy algorithms have been successfully applied to various fields of industry in Japan,for instance, autopilot of subway and water purification plant for drinking water. The fuzzy algorithm based on subjective linguistic rules with fuzziness is applicable to ill defined problems where logical algorithms cannot be applied to. As relevant matters,the comparison of fuzzy control with usual other controls i.e. PID control and optimal control is shown in Table 1.

3. UNDERWATER SURVEY SYSTEM AND CONTROL ARCHITECTURE OF FLIPPER

There are three progress stages of autonomous control of AUV according to communication bandwidth,i.e.1) acoustic linked [6] ,2)supervisory [7], and 3) perfectly autonomous. A good combination of the hardware with the software is indispensable to the third stage. The main problems of the hardware are 1)power sourses with long-term performance , 2)communication [8], 3)parallel multi-processor[9] capable of parallel multi-task,and 4)optimum hull form closely related with missions[1]. On the other hand,those of the software are 1)machine intelligence using parallel multi-processor for cognition of circumstances and action, 2) distributed control architecture ,and 3) cooperative tasks by a group of ROVs.

3.1 UNDERWATER SURVEY SYSTEM

To solve the first two problems of the hardware, the author proposed the concept of an underwater survey system consisting of a mother ship,a launcher,a UUS,a group of AUVs and underwater position system. The mission of each subsystem is as follows.
(1)Mother Ship
A total decision and strategy are made on the mother ship. Power is supplied to the launcher and UUS through a cable.Sampled data by AUVs are transformed to the mother ship during the docking of AUV in UUS. Mother ship watches the locations of the subsystems by an underwater acoustic position system.
(2)Launcher
In launching and recovery of the launcher, UUS mates with it housing AUVs in the sheds. It enables UUS to do rapid and easy operation between the

mother ship and a target depth.
(3)UUS
UUS is connected to the launcher with neutrally buoyant cable to protect the transmission of the mother ship motion in waves to UUS. UUS has the missions of housing of AUVs,power supply to AUVs and information transfer between AUVs and the mother ship. UUS is equipped with the sheds for AUVs,docking system and dynamic positioning system for the attitude control of UUS by thrusters. The battery charging or exchanging system and the data transformation system on UUS make it possible for AUVs to operate for a long period.

3.2 CONTROL ARCHITECTURE OF FLIPPER

An optimum hull form was designed focusing on the realization of two types of CCV decoupling modes,i.e. (1)a constant pitch angle and a constant vertical speed in the longitudinal plane and (2)zero roll angle a constant yaw angle in the lateral plane under the conditions of design speed of 2 m/sec and the length of 2 m. The designed submersible(Fig.1) has an all movable forward horizontal wing,a rear horizontal wing with a pair of rudders rotating simultaneously in the same direction, and upper and lower vertical tails with a pair of rudders rotating independently.

Rough sketch of control architecture of FLIPPER is shown in Fig.3. The control architecture has hierarchical structure consisting of attitude control, guidance, navigation, path planning and communication. The attitude control and guidance are described in details as follows.
(1)Attitude control
Three CCV modes are used for the attitude control, i.e. a)α mode for constant vertical speed and constant pitch angle ,b)An mode for constant vertical speed and constant pitch angular velocity, and c)β mode for zero roll angle and constant yaw angle. Those target magnitudes are input from the guidance process. This attitude control process is performed asynchronously with the guidance process. accelerometers,a rate gyro and a magnetic compass are used as sensors for the attitude sensing.
(2)Guidance
This process has six modules. Table 2 shows the modules of guidance,the corresponding CCV modes and sensors for the navigation.

4. DECOUPLING OF MOTION FOR ATTITUDE CONTROL

We consider the decoupled control system where the number of output variables is equal to that of input variables and that of target input variables and where a one-to-one

correspondence between output variables and target input variables is satisfied. The decoupling of motion for attitude control is an essential point for the construction of distributed control system of AUV because guidance which lies in the upper layer on the attitude control can be performed independently from the attitude control.

In the author's earlier paper [1] the control law of decoupling of motion was based on a state feedback of modern automatic control theory which belongs to a linear system. However,this control law has disadvantages about the parameters of matrixes describing dynamic system and disturbances such as tidal current. That is,when the form of AUV is changed,the parameters must be improved. In addition, when tidal current flows, a feedforward control must be added to CCV controller to eliminate the state magnitudes caused by tidal current. Or an adaptive control with a system of parameter identification including disturbances must be installed.

On the other hand,the application of fuzzy algorithm to CCV controller has the following advantages.
(i)The description of dynamic system is not needed,independent of linearity of the system.
(ii)It has robustness against disturbances.
(iii)Even when the form of AUV is changed,improvement of fuzzy rules is not necessary for the decoupling of motion in essential.

4.1 Control Algorithm for α Mode

We construct two sets of fuzzy rules. One is a set of fuzzy rules for input variables of the difference between present vertical speed of AUV and the target vertical speed,and the time differential of the vertical speed,and for output variable of operational magnitude of rudder angle $\Delta\delta$ w for the control of vertical speed. The other is a set of fuzzy rules for two input variables of pitch angle and pitch angular velocity ,and for output variable of rudder angle $\Delta\delta$ p for the control of pitch angle. From these two output variables,the forward horizontal wing angle δ a(t) and the rear horizontal rudder angle δ e(t) at time t are expressed using the variables at previous time (t - Δ t) as

$$\delta \text{ a(t)} = \delta \text{ a(t-}\Delta \text{ t)} + \Delta\delta \text{ w} - \Delta\delta \text{ p}$$
$$\delta \text{ e(t)} = \delta \text{ e(t-}\Delta \text{ t)} + \Delta\delta \text{ w} + \Delta\delta \text{ p}$$
$$(1).$$

Fig.4 shows an example of the simulation where the target vertical speed and the pitch angle are taken as 0.3 m/s and 0° ,respectively and the time interval is 0.1 second. In the figure, w denotes vertical speed,θ pitch angle, q pitch angular velocity.

5. SEABED SURVEY

5.1 Altitude-Keeping Control and Collision Avoidance Maneuver in the Longitudinal Plane

The main target of the control strategy for seabed survey (Fig.5) is to keep the pitch angle of FLIPPER zero and to keep the altitude from seabed constant as long as possible, infering risk of collision with seabed and forward obstacles by fuzzy rules.

The degree of risk of collision J_θ is infered by the fuzzy rules based on the informations of altitude sonar and forward obstacle search sonar. The inputs of the inference are

$$\Delta \text{ h} = \text{h} - \text{h}_\theta , \ \Delta \text{ l} = \text{l} - \text{l}_\theta \qquad (3)$$

where h denotes altitude from seabed,l denotes distance to forward obstacle ,h_θ and l_θ are taken as 5 m and 20 m,respectively.

After the inference of J_θ ,the control strategy is separated into three flows:
(1)When J_θ is greater than zero the degree of risk of collision is judged to be high. The collision avoidance maneuver is taken by use of An mode of CCV modes,of which target pitch angular velocity is obtained from fuzzy rules about J_θ as input variable and pitch angular velocity as output variable.
(2)When J_θ is equal to zero,the altitude-keeping control is taken by use of α CCV mode having zero target pitch angle and the target vertical speed which is obtained from fuzzy rules about Δ h and d(Δ h)/dt as input variables and the vertical speed as output variable.
(3)When J_θ is less than zero,the difference between the target altitude and the measured altitude by the sonar is judged to be large. The altitude-keeping control is taken by use of An CCV mode having constant target vertical speed and constant target pitch angular velocity.

As an example of simulation of above-mentioned guidance,a sinusoidal seabed is taken. The wave length is 40 m,the wave height is 3m and the maximum slope angle is 13° .In the simulation attitude control was performed every 0.1 second and guidance is done every 1 second with the running speed of FLIPPER of 2 m/s and with the target altitude from seabed of 5 m. The result of Fig.6 shows that the target altitude of 5 m and the target pitch angle of 0° are almost attained.

5.2 Course-Keeping Control in the Lateral Plane

The course to be runned on is

prearranged in the path planning layer of the control architecture. The location and the azimuth of AUV are measured every one second by a Long-Base Line acoustic position system and a magnetic compass. The strategy of the guidance is as follows.
(1)β mode of CCV modes for zero roll angle and a yaw angle is performed.
(2)AUV runs straight from a corner to the next corner and changes the course when it runs into the region of the circle having the center at the edge.
(3)When the location of AUV running a corner to the next corner is off the prearranged course,the fuzzy algorithm is applied.

Two methods for output variable are considered against two input variables of the minimum distance between the present location of AUV and the prearranged course to be runned on and its time differential.

(i)The yaw angle to be turned to from the present azimuth of AUV is obtained as an output variable. This angle plus the present azimuth of AUV is input to the CCV controller.

(ii)The variation of the yaw angle is obtained from fuzzy rules. The yaw angle to be turned to is taken as the sum of the variation of the yaw angle.

The former method is used when the azimuth of AUV is the main target although a off-track remains in case a tidal current flows in the transverse direction against the course of AUV. On the other hand,the latter method is used when the off-track is the main target although off-angle from the azimuth of the prearranged course to be runned on remains in case there exists a tidal current in the transverse direction against the course of AUV.

6. RENDEZVOUS OF AUV WITH UNDERWATERSTATION

We consider two steps of guidance for rendezvous of AUV with UUS ,i.e. rough guidance and precise one. The rough guidance is defined from an original point of AUV to an appointed point which lies on the straight line elongated from the center line of UUS(see Fig.7). The precise guidance is performed from the appointed point to the entrance of UUS. α mode in the longitudinal plane and β mode in the lateral plane of CCV control modes are performed for the attitude control both during the rough guidance and during the precise one.

6.1 Rough Guidance

When the location of AUV running straight is off the prearranged course,the fuzzy algorithm is applied both in the longitudinal plane and in the lateral plane.

In the longitudinal plane,input variables for fuzzy rules are the minimum vertical distance between the present location of AUV and the prearranged course and its time differential,while the output variable is vertical speed which is input to CCV control as the target input. The target pitch angle is taken to be equal to that of prearranged course.

In the lateral plane,input variables for fuzzy rules are the minimum lateral distance between the present location of AUV and the prearranged course and its time differential,while the output variable is yaw angle to be turned from the present azimuth of AUV. This angle plus the present azimuth of AUV is input to CCV control as the target input.

6.2 Precise Guidance

The entrance of UUS is equipped with four transponders to measure the off-track distances both in the longitudinal plane and in the lateral plane from the prearranged straight course between the appointed point and the entrance of UUS. AUV is ,on the other hand,equipped with transmitter and receiver. As shown in Fig.8, the transponders P_3 and P_4 are located in X'-Z_0 plane and P_1 and P_2 in X'-Y' plane. The off-track distances Δy and Δz in X'-Y plane and in X'-Z_0 plane,respectively, are obtained as follows.

$$\Delta y = (R_1^2 - R_2^2) / 4 \cdot l_0$$
$$\Delta z = (R_3^2 - R_4^2) / 4 \cdot l_0 \qquad (4)$$

The control routine after that is the same as the rough guidance.

6.3 Numerical Simulation

An example of numerical simulation is shown in Fig.9,where the attitude control was performed every 0.1 second, the rough guidance every 1 second and the precise one every 0.1 second at the running speed of FLIPPER of 2 m/s.

7. PIPELINE INSPECTION

Computer vision which realizes human visual ability by machine is one of the most important fields in robotic researches. The computer vision for cognition of circumstances in underwater technology can be used to carry out surveys,inspections and workings. However,few researches about it have been made [10,11]. The difficulties are due to software for pattern recognition and hardware for sufficient fast computation for real time operation.

Here, a simple example for pattern recognition is taken,that is, pipeline inspection where the diameter of pipeline is known a priori and AUV swims along the pipeline with constant

altitude and constant lateral
distance from pipeline based on the
information of computer vision.
Fig.10 shows an example of video
pictures about pipeline inspection taken
by CCD camera mounted on a underwater
towed vehicle in North Sea. By
filtering and binarization of the
video picture (256×256 picture
elements ,64 gray levels),Fig.11 is
obtained,where clear edges of pipeline
are detected. The procedure of the
guidance of AUV along the pipeline is as
follows.
(1) Two linear equations of the edge
lines are obtained by least square
method.
(2) The distance lp between the location
of camera and the point P in Fig.12
is approximately obtained from
the vertical view angle of the
camera ,the length of Dp' in the
picture and the real diameter of
pipeline Dp.
(3) The altitude from seabed hp is
obtained as follows .

$$\Delta \theta v = \Delta q/lp$$
$$hp = lp*\sin(\theta v +\Delta \theta v) + Dp/2 \qquad (5)$$

where θv denotes tilt angle of
camera, Δq the distance between
the center of picture and the
center of pipeline (Fig.12).
(4) Relative yaw angle of AUV ϕp is
interpolated by use of
relationship between ϕp and angle
τ between the center line of
pipeline and the vertical center line.
(5) The lateral distance Sp is obtained
as follows.

$$Sp = lp*\cos(\theta v +\Delta \theta v)*\sin(\phi p +\theta h) \quad (6)$$

where θh denotes pan angle of
camera.
(6) Using the target altitude hp₀ and
the target relative lateral
distance Sp₀ ,

$$\Delta hp = hp - hp₀ ,\Delta Sp = Sp - Sp₀ \qquad (7)$$

are obtained.
(7) In the longitudinal plane,guidance
and control of AUV are performed
using fuzzy rules for guidance of
which input variables are Δhp
and its time differential and the
output variable is vertical speed
which is input to CCV attitude
controller having the target pitch
angle of 0' .
(7) In the lateral plane,the input
variables of fuzzy rules for
guidance are ΔSp and its time
differential. The output variable
is yaw angle to be turned from
the present azimuth of AUV is input
to CCV control as the target
input.

Fig.13 shows an example of numerical
simulation where hp₀ and Sp₀ are taken
as 1.0 m and 1.5 m,respectively,and

initial values of hp nd Sp are taken as
2.0 m and 2.5 m,respectively.

References

1. Kato,N.,and Kouda,S.,"Attitude Control
and Navigation of Unmanned,Untethered
Submersible", Proceedings of the 8th
International Conference on Offshore
Mechanics and Arctic Engineering,
Vol.6, p.89(1989)
2. Kato,N.,and Endo,M.,"Guidance and
Control of Unmanned,Untethered
Submersible for Rendezvous and Docking
with Underwater Station",OCEANS'89,
Vol.3,p.804(1989)
3. Feigenbaum,E.,"The Art of Artificial
Intelligence",Thomes and Case Studies
of Knowledge Engineering,IJCA15(1977)
4. Rumelhart,D.E.,and McClelland,J.L.,
"Parallel Distributed Processing",MIT
Press(1986)
5. Zadeh,L.A.,"Fuzzy Sets",Information
and Control,Vol.8,p.338,1965
6. Borot,P.,and Brisset,L.,"ELIT Project:
A Concrete and Impending Stage for
Autonomous ROVs",ROV '88,UTC,
Intervention,p.577(1988)
7. Sheridan,T.B.,"Supervisory Control:
Problems,Theory and Experiment for
Application to Human-Computer
Interaction in Undersea Remote
Systems",MIT Technical Report,
MIT(1982)
8. Suzuki,M.,Nemoto,K.,Tsuchiya,T.,and
Nakanishi,T.,"Digital Acoustic
Telemetry of Color Video Information",
Oceans '89,Vol.3,p.893(1989)
9. Durham,J.,Gillcrist,B.,and Heckman,P.
Jr.,A Testbed Processor for Embedded
Multi-Computing",Proceedings of 6th
International Symposium on Unmanned
Untethered Submersible Technology"
(1989)
10. Nguyen,H.G.,Heckman,P.Jr.,and Pai,A.
L.,"Real-Time Pattern Recognition for
Guidance of an Autonomous Undersea
Submersible",Proc.IEEE International
Conference on Robotics and
Automation,p.1767(1988)
11. Lane,D.M.,Chantler,M.J.,Robertson,E.W
.,and McFadzean,A.G.,"A Distributed
Problem Architecture for Knowledge
Based Vision",Distributed Artificial
Intelligence,Ed.M.Huhns,Pub.Morgan
Kaufman (1989)
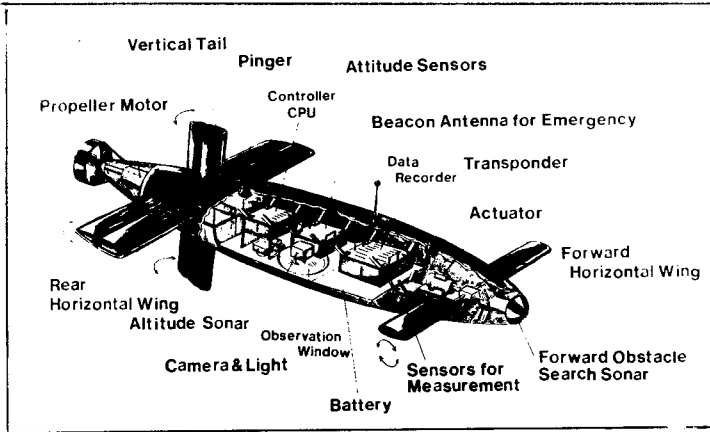
Fig.1 Structure of AUV(FLIPPER)
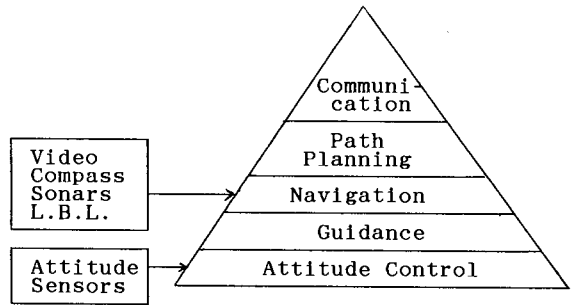
Fig.3 Control architecture of FLIPPER
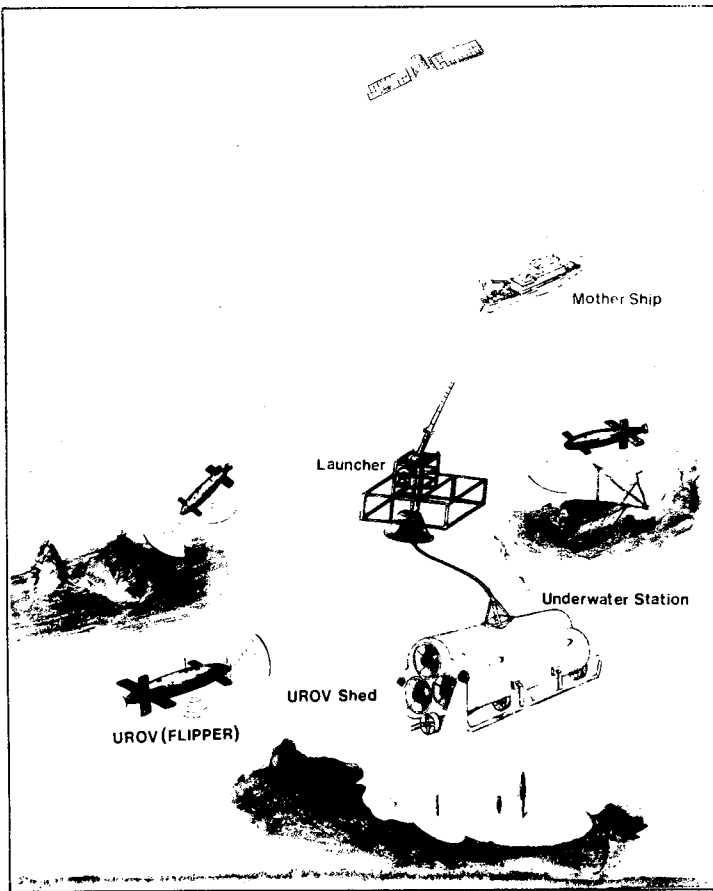
Fig.2 Concept of underwater survey system
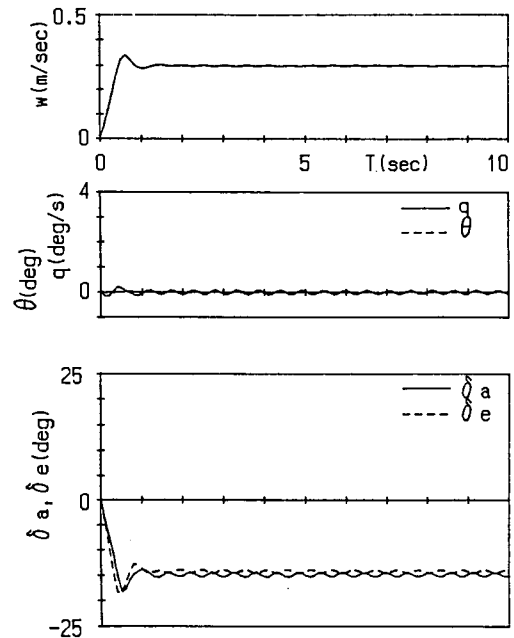
Fig.4 CCV attitude control modes
        α mode(w_1 = 0.3 m/s, θ_1 = 0
                                            deg.)

Table 1. Comparison of fuzzy control with other ones

Type	Relation between input and output	Production of algorithm	Tuning
Fuzzy control	A small number of outputs from a large number of measured data through reasoning	Linguistic rule based on operation data	Improvement of rules judging from output data
PID control	Single input and single output	Choise of PI or PID	Tuning of gain judging from oscilatory output
Optimal control	Multi-output from multi-input through linear matrix opration	Based on dynamic model of object	Improvement of weight matrix

Table 2. Modules of guidance, CCV modes for attitude control and sensors for navigation

Module	Items	CCV modes	Sensors for navigation
Bottom survey	·Altitude-keeping control from sea bed (longitudinal plane)	α mode An mode	Altitude sonar Forward obstacle search sonar
	·Course-keeping control (lateral plane)	β mode	Long-base line Magnetic compass
Depth-keeping control	·Depth-keeping control (longi.)	α mode	Depth sensor
	·Course-keeping control (trans.)	β mode	Long-base line Magnetic compass
Rendezvous & docking with underwater station	·Rough guidance Course-keeping control (longi.& trans.)	α mode β mode	Long-base line Magnetic compass
	·Precise guidance Course-keeping control (longi.& trans.)	α mode β mode	A transmitter & receiver on AUV 4 transponders on UUS
Object following	·Relative altitude keeping control(longi.)	α mode	Video vision (Altitude sonar & F.O.S. sonar)
	·Relative course keeping control (trans.)	β mode	Video vision Compass (L.B.L.)
Arrival at start point	·Course-keeping control (longi.& trans.)	α mode β mode	Depth sensor,Altitude sonar,L.B.L.,Compass
Emergent ascent	·No control (drop of ballast)		
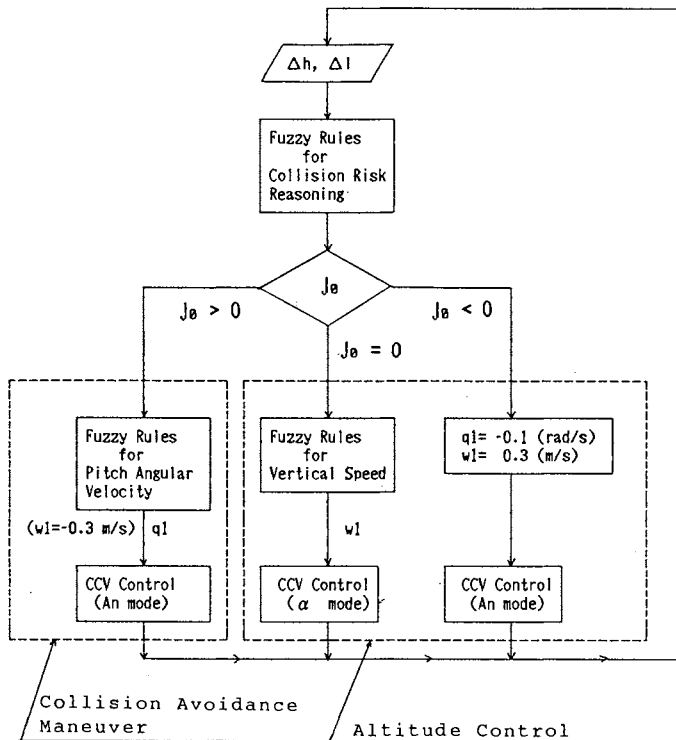
Fig.5 Control strategy for seabed survey in the longitudinal plane
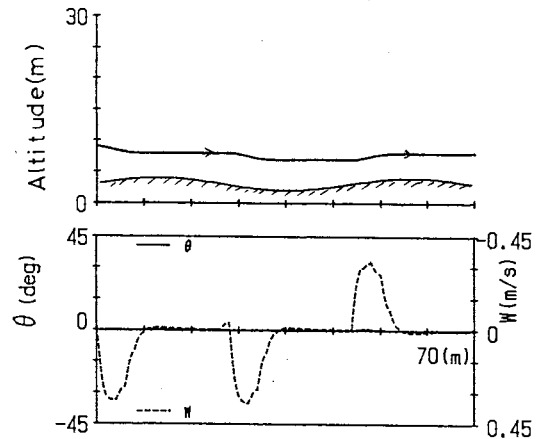
Fig.6 Simulation of altitude-keeping control and collision avoidance maneuver in the longitudinal plane
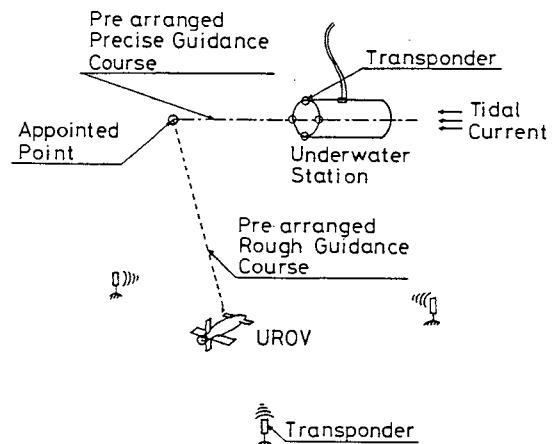
Fig.7 Conceptional view of guidance of AUV to UUS
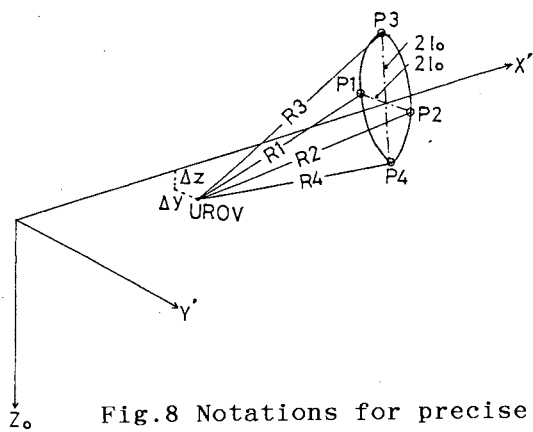
Fig.8 Notations for precise
guidance

Fig.9 Simulation of guidance and
control of AUV to UUS

Fig.10 A video picture of pipeline on
seabed

Fig.11 Binarized picture

Fig.12 Notations for pipeline survey
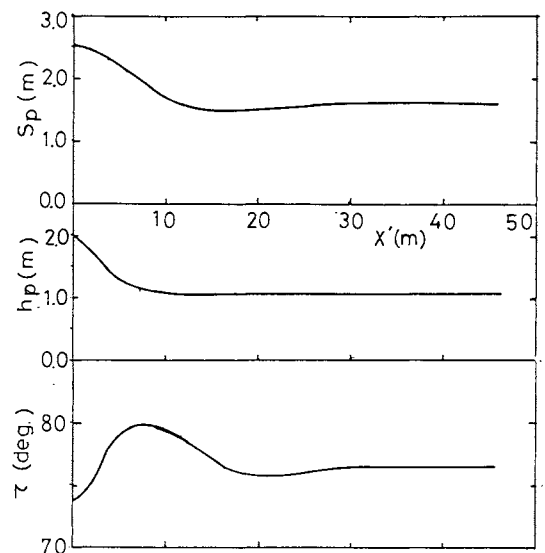
Fig.13 Simulation of pipeline survey

DEVELOPMENT OF 6,500M MANNED RESEARCH SUBMERSIBLE "SHINKAI 6500"

Shinichi Takagawa*, Kenji Takahashi*, Hideyuki Morihana**, Nobuhiko Watanabe**

* Japan Marine Science and Technology Center (JAMSTEC), Japan
** Mitsubishi Heavy Industries, Ltd, (MHI), Japan

Abstract

Japan has developed a new manned research submersible "SHINKAI 6500" whose maximum operating depth is 6500 meters. Its maximum depth capability is the deepest in the world except those of the bathyscaphe submersibles which have already retired.

"SHINKAI 6500" was built by Kobe Shipyard & Machinery Works of Mitsubishi Heavy Industries Ltd. (MHI) and marked 6465m and 6527m dives in the Japan Tranch during the sea trials with the support vessel "YOKOSUKA" in August 1989. After the successful trials, it was delivered to Japan Marine Science and Technology Center (JAMSTEC) in November 1989.

This paper presents the result of the sea trials, the history of the development program and the features of the "SHINKAI 6500".

Photo 1. "SHINKAI 6500" Recovered After Trial Dive

1. Sea Trials of "SHINKAI 6500"

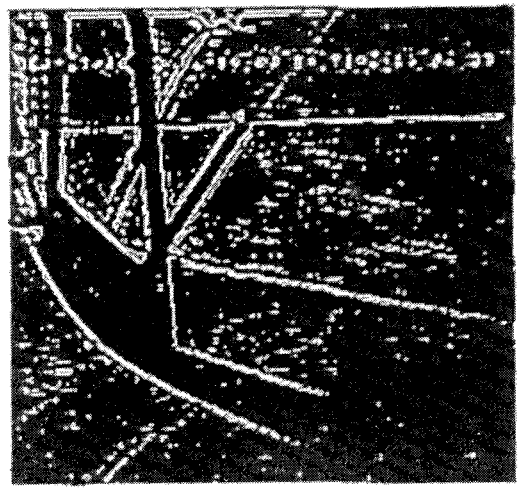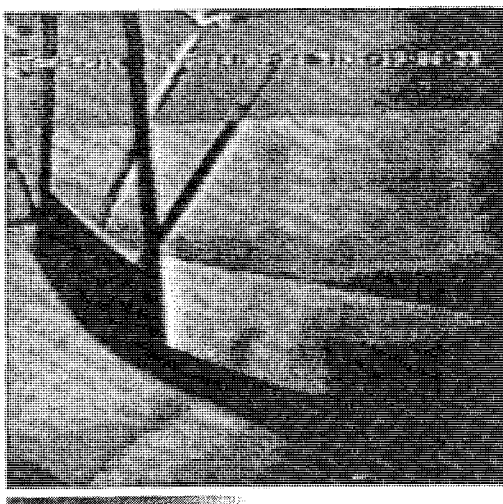On August 10th and 11th 1989, the manned research submersible "SHINKAI 6500" marked 6,465m and 6,527m trial dives in the Japan Trench about 240 km off the Sanriku coast of the Japan's main island. This is the final goal of the research and development of the manned deep research submersibles in Japan. At the same time, it is the real start of the new program to explore the deep oceans in 1990's.

Japanese scientists have successfully carried out many studies and researches on biologies and geophysics using the submersible "SHINKAI 2000" which was built in 1981 and has the depth capability of 2,000m deep. However, "SHINKAI 2000" covers only 30% of the Japan's 200nm exclusive economic zone. So they anxiously have been looking forward toutilizing the new submersible for their current uprising studies, diving to the depth of 6,000m or more.

The series of the sea trials of "SHINKAI 6500", supported by its own support vessel "YOKOSUKA" which was built by Kawasaki Heavy Industries Ltd. (KHI), began on April 1989 and continued for for about four months. Prior to the sea trials in March 1989, "YOKOSUKA" completed her own sea trials andwastransferred to the pier of Kobe Shipyard of MHI, where "SHINKAI 6500" was loaded on board "YOKOSUKA" and the combination tests interfacing

"SHINKAI 6500" and "YOKOSUKA" were extensively carried out for about a month. During these tests, launching and recovery system, battery charging control system, acoustic positioning system and acoustic communication system were carefully clarified with their functions and performance.

In the sea trials of final construction stage, "SHINKAI 6500" successfully conducted 29 dives during scheduled five test periods. The first period was consisted of six dives up to 100m deep around Kii Straight. The main objective at this period was the training of the operators.

The second period also included six dives up to 500m deep. Propulsion system, ballasting system and maneuverability were verified systematically at this period.

Successively the third period conducted six dives to 1,250m and 2,000m deep. These divings were conducted at Kii Straight up to 1,250m deep and at Kumano Nada up to 2,000m deep. Three transponders were deployed down to the sea floor and Long-Baseline (LBL) navigation system was checked. Also ballasting and trimming system and acoustic navigation and communication system were tested and verified.

The fourth periodn was composed of five dives to 3,000m(Zenisu Ridge), 4,000m and 5,000m(Nankai Trough) deeps. The whole subsystems were successfully tested there. Advanced to these dives, LBL calibration with three transponders and ocean
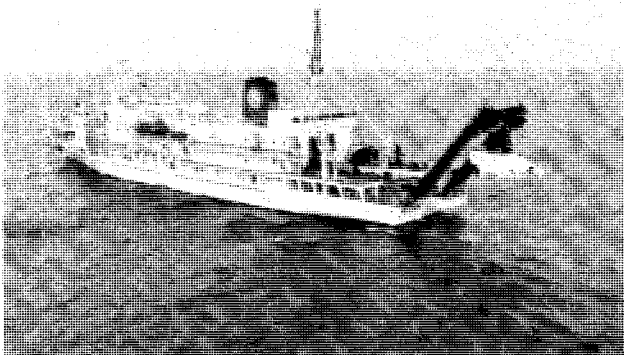
Photo 2. "SHINKAI 6500" and Support Vessel "YOKOSUKA"

floor contour mapping with the multi-narrow-beam echo sounder were conducted by "YOKOSUKA".

The final period included six dives. Three 6,000m deep dives and following two 6,500m deep dives were conducted at the slope of the Japan Trench about 240km off north-east coast of the Japan's main island. Although the 6,500m deep diving tests were postponed by four days because the Typhoon No.13 severely attacked the diving area, the function and performance of the total system of "SHINKAI 6500" were evaluated greatly and it marked 6,527m deep diving record which is the deepest one of the world ones besides those of bathyscaphes of tens of years ago.

On the way back to Kobe, "SHINKAI 6500" made an extra dive at the former 1,250m deep dive site to recover the transponder which could not be released from the bottom. Finding out and releasing it using manipulators, "SHINKAI 6500" accomplished this mission successfully.

The results of these sea trials were satisfactory and the designed performances were suc-

Photo 3. Deep sea holothurian *Kolga kumai* at 4,835m deep by TV Camera of "SHINKAI 6500"
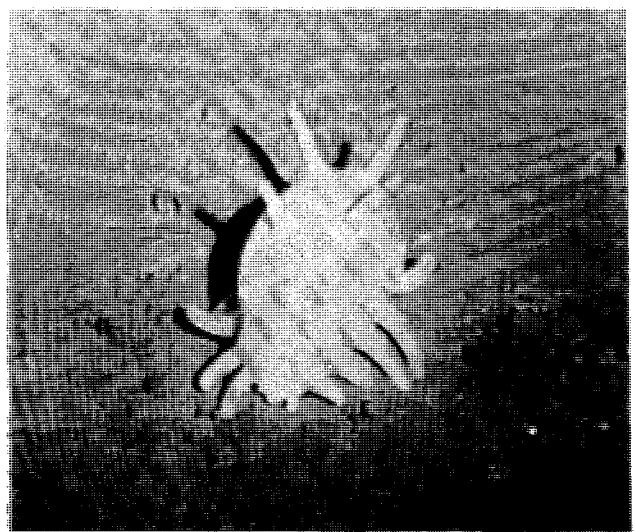
Photo 4. Deep sea holothurian *Scotoplanes globoa* at 6,527m deep by TV Camera of "SHINKAI 6500"

Photo 5. A Rat-tail at 6,527m deep by TV Camera of "SHINKAI 6500"

Period	Site	Depth
1st	#1	25-500m
2nd		
3rd	#2	1250m
	#3	2000m
4th	#4	3000m
	#5	4000m
	#6	5000m
5th	#7	6000m
	#8	6500m

Fig.1 Trial Diving Sites of "SHINKAI 6500"

cessfully achieved. Also "SHINKAI 6500" proved its expected depth capability and reliability. Some software bugs found in acoustic positioning system of both the submersible and the support vessel were carefully amended within the following maintenance duration. The cause of releasing failure of the transponder was also located and the re-

leasing mechanisms of all the transponders were modified.

On 28th November 1989, the completed "SHINKAI 6500" was delivered to JAMSTEC. After one year training of the pilots and the crew of the support vessel, JAMSTEC is planning to start the research dives from 1991.

2. The History of "SHINKAI 6500" Development Program

In 1969, reflecting the world trend to the ocean development, an advisory board for the prime minister of Japan submitted the report on the general policy and program of ocean development in Japan. In the report the necessity of the development of a 6,000m class manned deep research submersible was insisted as a most critical issue. This actually initiated the development of the manned research submersibles in Japan.

The research and development on the several key technologies were started with the support of some funds of Japan Marine Machinary Development Association (JAMDA), Ministry of Transportation and some private ship-building companies. Those technologies included pressure hull, buoyancy material, batteries, hydraulic system, navigation system and so on.

In 1971 JAMSTEC was established as a national center for ocean development under the supervisory of Science and Technology Agency (STA) of Japan. Thereafter, JAMSTEC has conducted the research and development program of deep research submersibles in Japan.

In 1977 the advisory board of STA and JAMSTEC reviewed and evaluated the status and achievements of the research and development program and state-of-the-art technologies. Consequently it was decided to develop a 2,000m manned research submersible as an important interim step to the final goal of the 6,000m class submersible. Thus the 2,000m deep manned research submersible "SHINKAI 2000" and its support vessel "NATSUSHIMA" were built in 1981 to accumulate construction technologies and operation experiences. JAMSTEC has operated this "SHINKAI 2000" system for more than eight years and It has has made more than 450 dives by the end of 1989. The precious operation experiences on these system was systematically utiliized to design and construct the new submersible.

After the completion of "SHINKAI 2000" system, JAMSTEC and the ship-building company were still obliged to make their research and development efforts in such key technologies as titanium alloy pressurehull, syntactic foam of binary mixture glass-micro-baloon, oil-filled inverter and so on in order to realize the new deeper submersible. In the following year of 1983 JAMSTEC carried out a final feasibility study on 6,000m manned research submersible. The results were most promising, verified by uprising needs and modern technologies.

In their consideration in 1984 JAMSTEC made two important decisions on the planning and design of the new submersible. One is as for its maximum depth capability. As the national supervisory board declared, 6,000m maximum depth capability had been considered to be quite reasonable because almost all ocean floors are not deeper than 6,000m and 97% of oceans in all over the world are cov-

ered by 6,000m depth capability. The recent progress in geophysical researches, however, revealed the importance to survey the trenches deeper than 6,000m. According to the theory of plate techtonics, the Pacific Ocean Plate is subducting under the Eurasian Plate on the site of these trenches. The movement makes a large scale energy release that would cause catastrophic earthquakes and tsunamis. Even through these global dynamics should be investigated in the trenches around Japan, it is really the most critical issue of world geophysical scientists. With this concern, the maximum operating depth of the new submersible was decided to be 6,500m.

The other decision was on the material of the pressure hull which was the heaviest component of the submersible. There were two candidates, 10Ni-8Co ultra-high yield strength steel and Ti-6Al-4V ELI titanium alloy. The properties of both materials were investigated and evaluated by a special committee established by JAMSTEC. Reflecting the high strength weight ratio and resistance property to sea water, the titanium alloy was finally selected.

The preliminary design of the new submersible was started in 1985. As the same verification program, the study of the arrangement with a mock-up model and a scaled model strength test of titanium pressure hull, collapsing after cyclically pressurising, were carried out in a systematic manner. After these verification tasks with satisfactory results, JAMSTEC and MHI started the construction of the 6,500m deep manned research submersible in 1987.

One of the big events in the process of "SHINKAI 6500" construction was performed in the United States of America. The rule of the Japanese Government on the safety of manned submersible requires to test the pressure hull under extra hydrostatic pressure of 1.1 times of the maximum operating pressure. As for "SHINKAI 6500" the maximum operating pressure is equivalent to 680kg/cm^2(9,670psi) and the test pressure is 748kg/cm^2(10,640psi). Al-
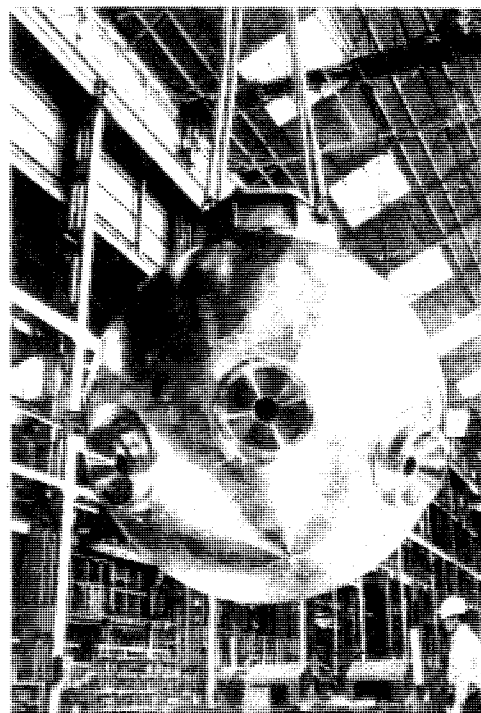
Photo 6. The Pressure Hull of "SHINKAI 6500"

Table 1 Particulars of "SHINKAI 6500"

Dimensions	Length (overall): abt. 9.5m Breadth (moulded): 2.7m Depth (moulded): 3.2m	Thrusters	Main : Oil-filled IM 5.2kw×1set Vertical : Oil-filled IM 1.4kw×2set Horizontal: Oil-filled IM 0.7kw×1set
Weight in Air	abt. 26 ton	Weight and Trim Adjustment	Main Ballast Tank : 1.3m³ × 2 Variable Ballast Tank : 300kg Descent/Ascent Ballast: 1,270kg Mercury Trim System : ±10°
Maximum Operating Depth	6,500m		
Complement	3 persons	Hydraulics	Pressure Compensating System 140kg/cm² ×12 ℓ /min
Payload in air, excluding crew, cameras, manipulators	200kg	Navigation System	Positioning: Sync. Pingers, LBL Transducer Alt. Sonar, Gyro Compass etc.
Life Support Duration	9hr & 5days		
Maximum Speed	2.5 kts		Communication:UQC Telephone, Radio etc.
Pressure Hull	Material: Ti-6Al-4V ELI Inside Diameter: 2.0m Viewports: 120mmdia × 3	Observation & Research	Manipulator, Grabber, Acoustic Imaging Sonar, TV Cameras etc.
Main Battery System	Oil-filled AgO-Zn: 440Ah×108V×2sets	Emergency Use	Jettisoning of heavy items Emergency Battery Emergency Breathing Apparatus Rescue Buoy

Fig.2 General Arrangement of "SHINKAI 6500"

though JAMSTEC has a pressure test tank with the capacity up to 1,560kg/cm² (22,200psi), its inside diameter of 1.4m is too small to test the pressure hull of the "SHINKAI 6500". Therefore, it was transported overseas and tested with the test facility of David Taylor Research Center (DTRC) of the U.S. Navy in Carderock, MD near Washington D.C. In advance to the transportation to the U.S.A., the completely assembled pressure hull was fully instrumented with strain gauges in Japan in order to save the time and sent to Washington D.C. by air. The wiring to the data acquisition equipment, pressurising operation and precise strain measurement were carried out by DTRC. The pressure tests proved the integrity of the spherical pressure hull structure on April 1988 in schedule.

On January 1989, the new submersible was launched at Kobe Shipyard of MHI and was named as "SHINKAI 6500". In the following summer, the sea trials with the support vessel were successfully performed as described previously.

JAMSTEC is going to operate "SHINKAI 6500" and the support vessel "YOKOSUKA" for training dives in 1990 and for mission dives from 1991.

3. Features of "SHINKAI 6500"

The particulars and the general arrangement of "SHINKAI 6500" are shown in Table 1 and Fig.2 respectively. And the list of manned deep research submersibles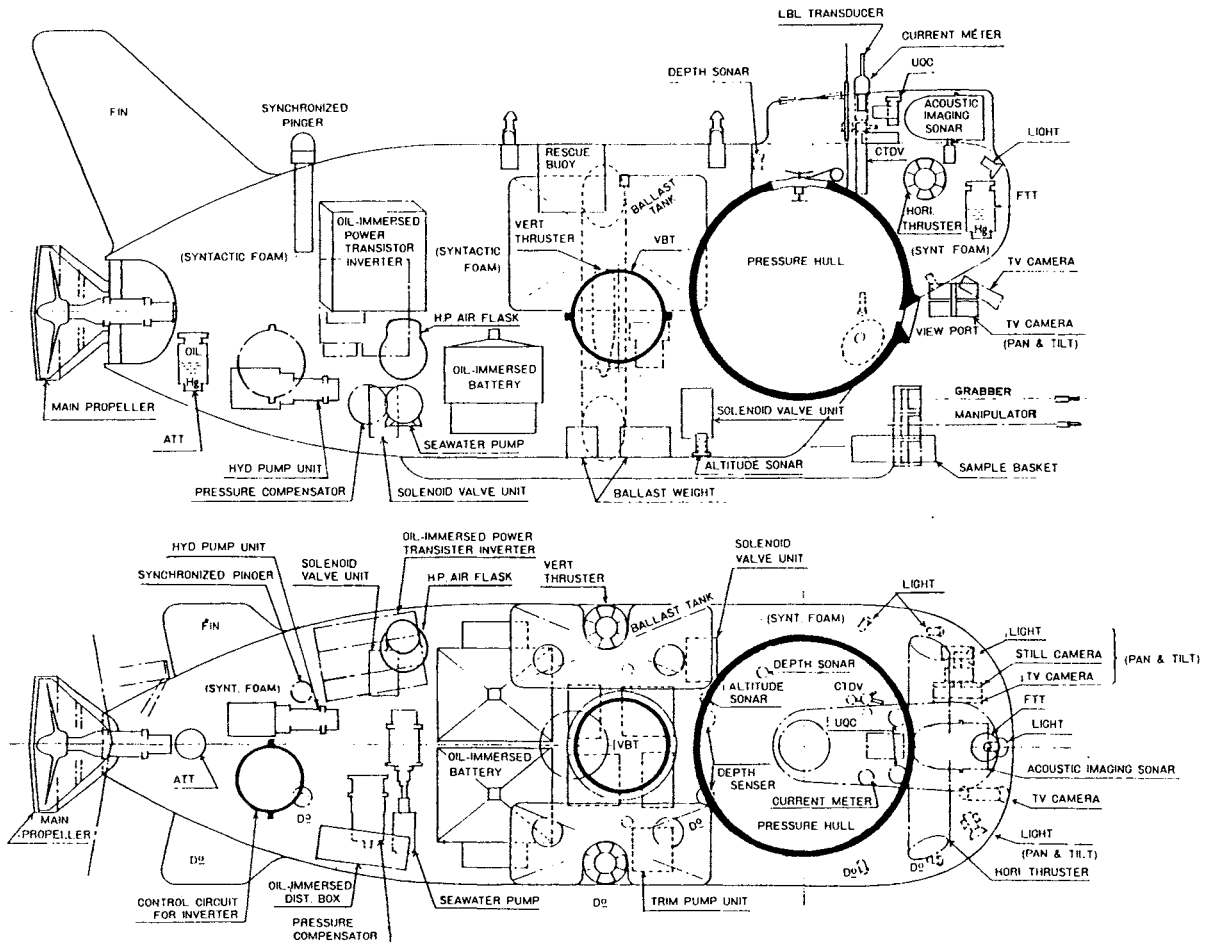 operational today in the world are shown in Table 2. Currently "SHINKAI 6500" is the deepest submersible operational today. Some features of "SHINKAI 6500" will be descirbed in this section.

Table 2 Manned Research Submersibles of 2,000m or Deeper Depth Capability

Name of Country	Name of Submersible	Maximum Operat. Depth(m)	Dimension LxBxD(m)	Weight in air (ton)
USA	TURTLE	3,000	7.9x3.7x3.7	24
	ALVIN	4,000	7.0x2.6x3.8	17
	SEA CLIFF	6,100	9.6x3.7x3.7	26
France	CYANA	3,000	5.7x3.0x2.1	9
	NAUTILE	6,000	7.6x2.7x3.2	18
USSR	MIR-I	6,000	7.8x2.9x3.2	19
	MIR-II	6,000	7.8x2.9x3.2	19
Japan	SHINKAI 2000	2,000	9.3x3.0x2.9	23
	SHINKAI 6500	6,500	9.5x2.7x3.2	26

3.1. The 6,500m Depth Capability

As described before, most ocean floors are not deeper than 6,000m. There are, however, many trenches deeper than 6,000m around Japan. It is very important for Japanese scientists to make surveys of the slopes of these grounds especially for their geophysical studies. For instances, a schematic profile of the east-west section of Japan Trench north-east off the Japan's main island is shown in Fig.4. The plate below the bottom

of Pacific Ocean is moving from east to west and subducting under the Eurasian Plate along the margin of the land. The subduction causes bending of the plate and many faults on the slope of trench in the depth of 6,200m or deeper. These faults are considered possibly to result in large scale earthquakes and tsunamis which will suffer Japan seriously. On the slope of the opposite side in the trench, there used to be big landslides which would suggest the creation of the basic foundation of Japan Island. "SHINKAI 6500" will dive to 6,500m deep and make surveys on these spots not only in Japan Trench but also the following ones, the slope of Kuril Trench, Izu-Ogasawara Trench, Mariana Trench, Ryukyu Trench and others.

The 6,500m depth capability can cover 96% of the Japan's 200nm exclusive economic zone. "SHINKAI 6500" expands the ability to explore the deep ocean more than three times that of "SHINKAI 2000" in both depth and area.
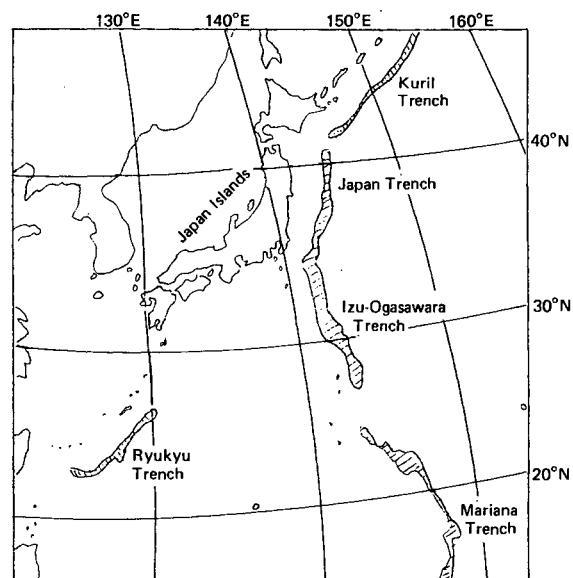
Fig.3 Location of Trenches around Japan
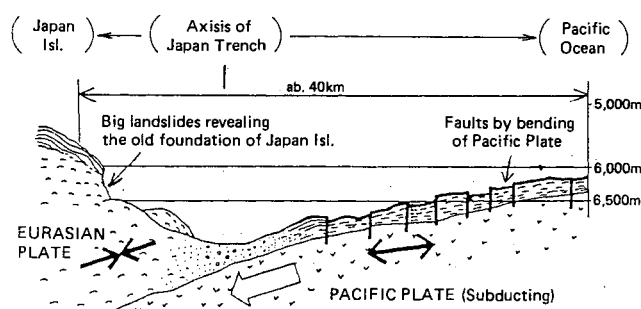
Fig.4 Schematic Profile of Japan Trench

3.2. Size and Weight

It is most important to make a submersible small in size and light in weight because of the ease of handling while launching and recovery and also its maneuverability in water with restricted power. Among the 6,000m class submersibles, "SHINKAI 6500" is almost the same in size and weight as Turtle of U.S.Navy, but is heavier than Nautile of France or MIRs of USSR. The design phylosophy and regulation on performance, safety and reliability

are different in each countries, which has an influence in making the basic specification for size and weight.

In a fundamental design, the size and weight are planned to be the same as those of "SHINKAI 2000" because the operational experiences of "SHINKAI 2000" are to be beneficially adopted to the new submersible. To achieve this target, all kinds of efforts were made in the technologies of many fields.

For the weight saving, based on the laborious research and development, the pressure hull of Ti-6Al-4V ELI titanium alloy was adopted instead of ultra-high strength steel. The design procedure of titanium alloy hull was verified through the series of model tests on creep property, cyclic pressurising and collapse strength. At the same time the fabrication and assembly procedure of titanium alloy hull were established by the trial production of a full-size proto type model. Thus hot press forming of the titanium hemispheres, electron beam welding for thick titanium sections and precise three dimensional machining to improve the sphericity were systematically developed.

On the other side, the property of buoyancy material has a great effect on the size and weight of the submersible. The syntactic foam with binary mixture composition of glass microballoons was developed and applied. The specific gravity of the new buoyancy material is reduced to 0.54, that is nearly the same to that of "SHINKAI 2000" in spite of the higher collapse strength by nearly doubled.

"SHINKAI 6500" has inverters to change the direct current of the batteries to the useful alternate one as "SHINKAI 2000" has. Inverters of "SHINKAI 2000" were settled in the pressure vessels because of fragile electric components. The weight of the pressure vessels could apparently increase enormously as the operating depth comes to 6,500m. To avoid this, new inverters with electric components which could operate in high pressure environment were developed. The main circuits of the inverters, consisting of power transistors, capacitors, reactors and so on were put into the oil to consist the pressure compensated structures. As a result, only the control circuits are accommodated in a pressure vessel to realize a considerable weight saving.

Consequently the size of "SHINKAI 6500" was kept to almost the same as the "SHINKAI 2000" and its weight was only aobut 10% more than that of "SHINKAI 2000".

3.3. Maneuverability

The maneuverability of "SHINKAI 6500" was studied and planned on the basis of the evaluation of the operational experiences of "SHINKAI 2000". The electrically driven induction motors, controlled efficiently by inverters, were proved to be satisfactory in controlability, noise and also in reliability. Thus all motors equipped in "SHINKAI 6500" are electrically driven ones.

The main propulsion thruster at the stern makes the submersible travel at maximum 3 knots in ahead and trails by 80 degrees in right and left side to increase the traversing and turning capability while that of "SHINKAI 2000" is limited to 60 degrees.

The auxiliary thruster system of "SHINKAI

6500" was greatly modified from that of "SHINKAI 2000". "SHINKAI 2000" has a pair of auxiliary thrusters extruded on the both sides at midship which turn in vertical plane, changing the direction of the thruster horizontally or vertically. This system inconveniently requires some time lag to change the direction and its extruded thrusters burden some fear to be entangled by ropes and fishing nets abandoned in the sea. "SHINKAI 6500" has a pair of ducted vertical thrusters on the both sides and also a ducted horizontal thruster at the bow forehead. Although this system brought some increase in length and weight of the vehicle, those problems pointed out for "SHINKAI 2000" could be elimitated. By the collaboration of the main propulsion thruster steered to the maximum inclined degrees and the horizontal thruster to deny her yaw moment, "SHINKAI 6500" can traverse sideways keeping almost the same heading, as shown in Fig.5. This property will be very useful to make investigations especially along steep cliffs.

These four thrusters could be controlled with two joysticks on a portable control box.

Main thruster 25 kgf
Steering angle 80 deg.
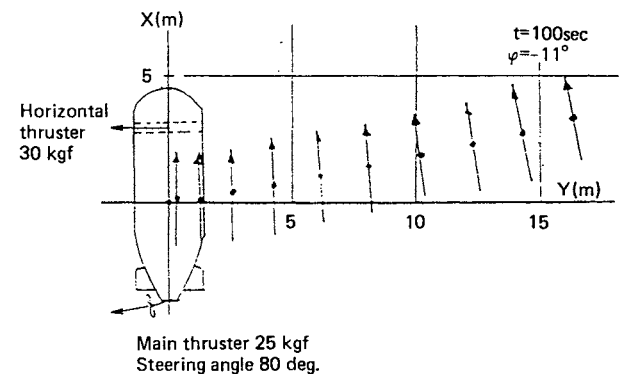
Fig.5 Lateral Movement of "SHINKAI 6500" by Calculation

3.4. Observation and Research Equipment

The observation and research equipment with "SHINKAI 6500" are thoroughly furnished. Manipulator and grabber work as right and left hand of the submersible respectively. The manipulator has master-slave control mechanism, having a bilateral force-feedback grip as its seventh axis which is designed to perform delicate tasks. The grabber is controlled with joystick and especially assigned to perform rather heavy works. Both arms are powered by electro-hydraulic servo system.

The two TV cameras are of broadcast-use class with high horizontal resolution of 450 lines. One of the TV cameras is equipped with zooming function and is mounted on a pan&tilt table with still camera, 1kw halogen lamp and strobo-flash so that the TV camera works as a view finder of the still camera.

The three dimensional acoustic imaging sonar was intensively developped to figure out and observe obstacles in rather long distance beyond the range of light transmission. The sonar generates a narrow pencil beam with two cross-fan (emitting and receiving) beams scanning with high speed to perceive active reflection of targets which composes three dimensional images. Fig.6 shows the schematic beam pattern of the observation sonar. The detective range capability is just over 100m.

The payload capacity of "SHINKAI 6500" comes

up to 200kg excluding those of the crew and fixed equipment as manipulators and cameras. the power source of AC100V and DC108V electricity and hydraulics are available specially for payload equipment.

(1) Longitudinal cross section

(2) Elevation

(3) Horizontal cross section
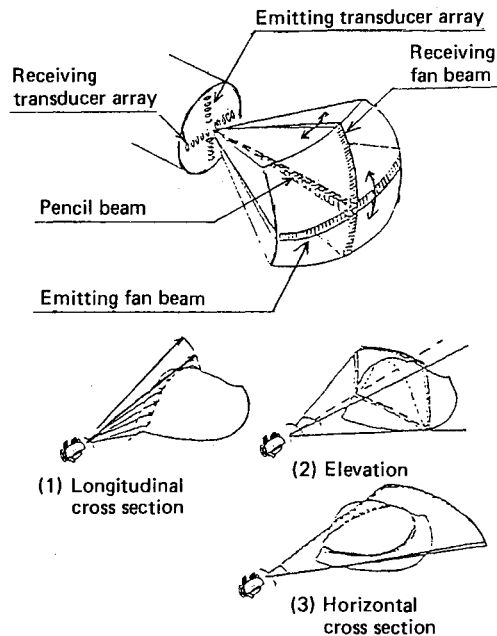
Fig.6 Principle of the Acoustic Imaging Sonar

3.5. Acoustic Positioning System

In "SHINKAI 6500" system, the location of the submersible is acoustically monitored by both the support vessel "YOKOSUKA" and the submersible itself, while location of "SHINKAI 2000" is attained only by the support vessel "NATSUSHIMA". Apparently, the undersea locating brings about a lot of benefit in operation efficiency and position accuracy to realize a high quality research.

"SHINKAI 6500" has a pair of synchronized acoustic pingers which interogate a pulse signal of the frequency of 6.6kHz, accurately synchronized to the clock of the support vessel. On the other hand, the three transponders on the sea bed respond to the signal emitting the individually assined signals of 6.9, 7.2 and 7.5kHz. The transducer on "SHINKAI 6500" receives these signals from each transponders and the precise location of the vehicle is to be calculated and displayed instantly using LBL nets. The rationality and high accuracy of the underwater positioning system is successfully verified in the sea trial of the system.

4. Conclusion

JAMSTEC has completed "SHINKAI 6500" system, consisting of a fully developped submersible and its support vessel, and is going to operate this system from 1990. At this moment, Japan has joined to the nations which operate 6,000m class manned research submersible, following to the U.S.A., France and USSR.

It is, however, still an important issue for us to achieve the effective and useful exploration and researches of prosperous deep oceans, taking advantage of these excellent systems. Now the fruitful accomplishment of the studies and researches in the field of biology, microbiology, geology, geophysics, marine mineral resources and so on are highly expected.

References

1 Takagawa, S. et al, '6,500m Deep Manned Research Submersible "SHINKAI 6500"', Oceans '89, Vol.3, pp741-746 (1989)
2 Takagawa, S. et al, 'Japanese 6,500m Deep Manned Research Submersible "SHINKAI 6500" system', Techno-Ocean '88, Vol. II, pp250-258 (1988)
3 Nakanishi, T. et al, 'Japanese 6,500m Deep Manned Research Submersible Project', Oceans '86, Vol.5, pp1438-1442 (1986)

LONGITUDINAL MOTION CONTROL OF FREE SWIMMING VEHICLE BY NEURAL NET

T. Fujii*, T. Ura*

* Institute of Industrial Science, University of Tokyo, Japan

Abstract

The off-line supervised learning method and the self-organizing method are introduced to construct a neural net controller for an AUV(Autonomous Underwater Vehicle). These methods are applied to longitudinal motion control of a free swimming vehicle "PTEROA"[1,2].

Two neural net controllers are constructed through off-line supervised learning[3] with reference to the teaching motions which are generated through numerical simulations with linear feedback controller and Fuzzy controller. It is shown that both constructed nets can operate the vehicle appropriately in numerical simulations and free swimming tank tests.

To make the control system more flexible to cover variation of vehicle dynamics and environment, newly developed SONCS(Self-Organizing Neural-Net-Controller System)[4] is introduced. A neural net controller is generated adaptively by SONCS according to a specific evaluation of motion of the vehicle with minimum pre-knowledge about the vehicle dynamics. Experimental results show that SONCS succeeded in organizing the adequate controller with several times of adaptation .

1. Introduction

Parallel processing and flexible adaptability of neural nets are suitable characteristics for realizing control systems for AUVs. As a neural net executes through parallel distributed process, it can deal with multiple data simultaneously and redundantly. And by learning it can be organized and adjusted to the controlled objects and environmental conditions.
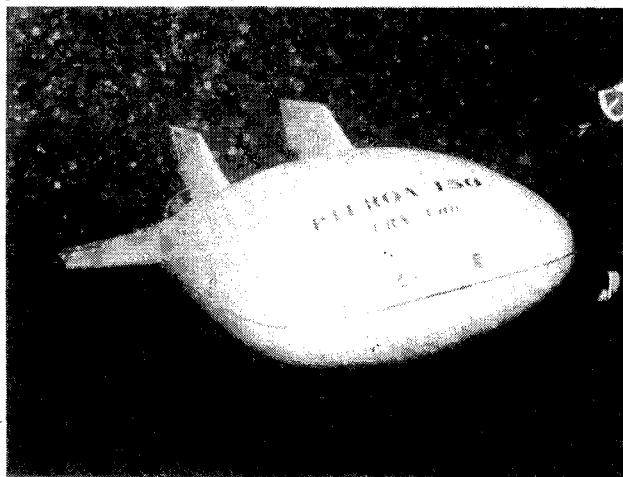
In this paper, two methods for construction of neural nets are introduced to control the longitudinal motion of a free swimming vehicle "PTEROA"[1,2], which is now in the stage of development at the Institute of Industrial Science, the University of Tokyo. Both methods are examined through numerical simulations and free swimming tank tests.

2. Free Swimming Vehicle "PTEROA"

The mission of "PTEROA" vehicle is to take pictures of the sea bed along a measurement line. The vehicle consists of a body, elevators, stabilizing fins, rudders and a pair of thrusters. The body is designed to generate lift force so that the vehicle can glide from the surface to a target point on the bottom. A prototype, named "PTEROA150", of $150cm$ in length and $220kg$ in dry weight has been constructed (cf. Figure 1). The longitudinal motions of the vehicle such as pitching and heaving are controlled with a pair of elevators. The equations of longitudinal motion of the vehicle were investigated by towing tank tests and numerical analysis[1]. Dynamic behavior of the vehicle

Fig.1 PTEROA150 Vehicle
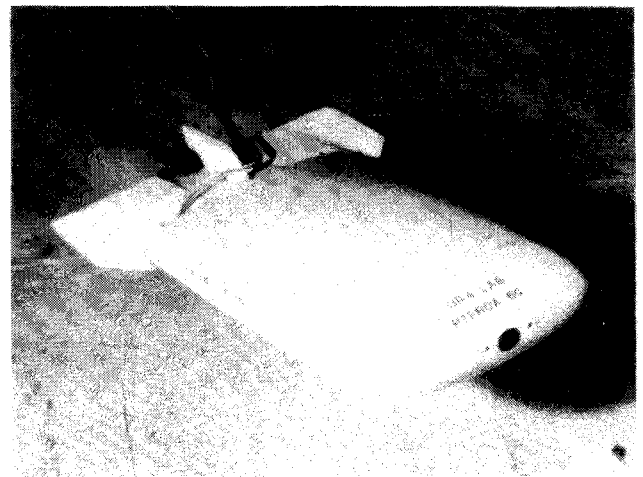
Fig.2 PTEROA60 Vehicle

Fig.3 Block Diagram of Experimental System

Fig.4 The Connectionist Model
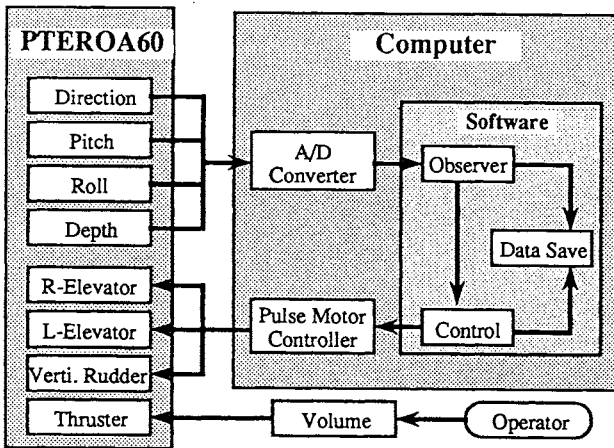
can be calculated on the basis of them.

In this paper, a small test-bed "PTEROA60"[5] shown in Figure 2 is used as the controlled object to examine the applicability of the neural net. The principal dimensions of "PTEROA60" are shown in Table 1. The vehicle is equipped with depth sensor, 2-dim inclinometer, a pair of elevators to trim and a thruster. Since the dimension of the vehicle is too small to be self-contained, an umbilical cable links the vehicle to the computer on the surface. The block diagram of experimental system of "PTEROA60" vehicle is shown in Figure 3.

3. Mathematical Model of Neural Net

The multilayered neural net, which is called as the Connectionist Model[6], is used as a mathematical model in this paper. It consists of some layers including several neurons in each layer (cf. Figure 4). When the connection between the neurons in the same layer doesn't exist, the processing of the i-th neuron of the n-th layer is given by:

$$
\begin{aligned}
u_i{}^n &= \sum_j w_{ij}{}^{n-1} x_j{}^{n-1} + h_i{}^n , \\
x_i{}^n &= f(u_i{}^n) ,
\end{aligned}
\tag{1}
$$

where $u_i{}^n$ is the membrane potential, $w_{ij}{}^{n-1}$ is the synaptic weight of the connection between the j-th neuron of the $(n-1)$-th layer and the i-th neuron of the n-th layer, and $h_i{}^n$ is the threshold value. $f(u)$ is a monotonous increasing function defined by:

Table 1 Dimensions of PTEROA60

Length of body	: L	0.6 m
Width Over All	: BOA	0.39m (0.65L)
Width of Body	: B	0.3 m (0.5L)
Thickness of Body	: T	0.18m (0.3L)
Displaced Weight	:$\nabla \rho$ g	17.45 kg
Center of Buoyancy	: XB	0.243m (behind the leading edge)
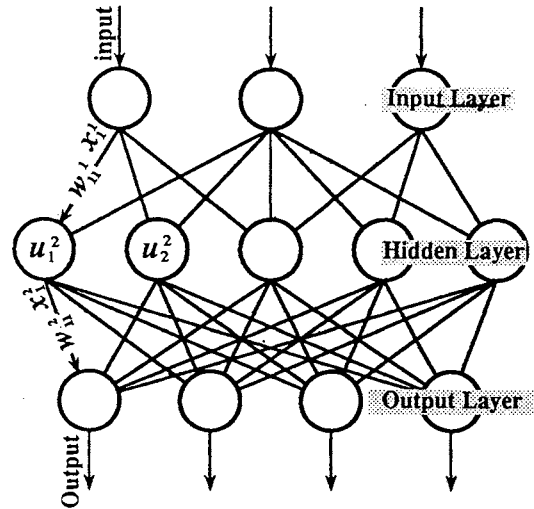
$$
f(u) = \begin{cases} u & : \text{input layer,} \\ 1/(1 + exp(-u)) & : \text{others.} \end{cases}
\tag{2}
$$

The following Error Back-Propagation[6] is adopted as a learning method. Let the potential function E represent the summation of the output errors as:

$$
E = \frac{1}{2} \sum_i (t_i - o_i)^2 .
\tag{3}
$$

Here, o_i is the output of the net corresponding to a certain set of inputs and t_i is the desired output given by the teaching motions. Each synaptic weight $w_{ij}{}^n$ should be changed by $\Delta w_{ij}{}^n$ to minimize E according to:

$$
\Delta w_{ij}{}^n = -\eta \frac{\partial E}{\partial w_{ij}{}^n} .
\tag{4}
$$

Let $\Delta w_{ij}{}^n(p)$ be the value of changing in the p-th step of learning. It can be given by:

$$
\Delta w_{ij}{}^{n-1}(p + 1) = \eta \delta_i{}^n x_i{}^{n-1} + \alpha \Delta w_{ij}{}^{n-1}(p) ,
\tag{5}
$$

where $\delta_i{}^n$ is the error signal. η and α are parameters to determine the rate and momentum of learning, respectively. From Eq.(1), (2) and (3),

$$
\delta_i{}^n = \begin{cases} (t_i - o_i)f'(u_i{}^n) & : \text{output layer ,} \\ f'(u_i{}^n) \sum_k \delta_k{}^{n+1} w_{ki}{}^n & : \text{others.} \end{cases}
\tag{6}
$$

4. Off-line Learning System of Neural Nets

In order to get a neural net for controlling longitudinal motion of the vehicle, learning should be carried out with reference to desired maneuvering actions. This procedure is:

1) Get motion data of typical maneuvering actions.

2) Make teaching samples including a certain number of sets of inputs and desired outputs derived from maneuvering actions.

Fig.5 Learning System for Neural Net
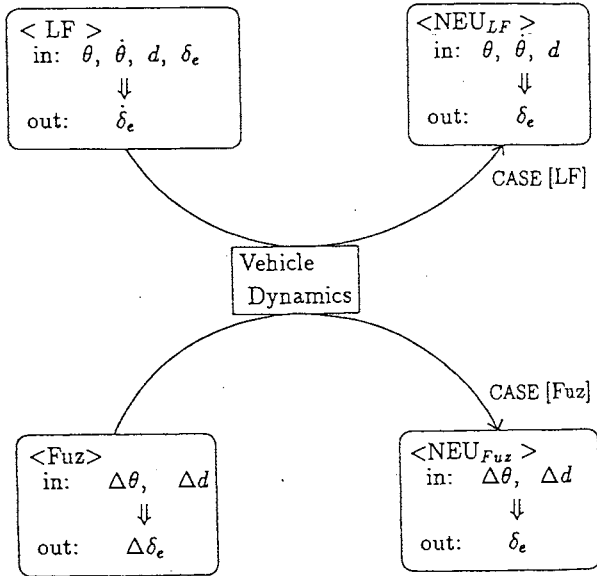
LF=Linear Feedback Control
Fuz=Fuzzy Control
NEU_{LF}=Neural Net Learned from LF
NEU_{Fuz}=Neural Net Learned from Fuz

θ_0 : Steady State Pitch Angle
d_0 : Depth to Dive

Elevator

Fig.6 Untethered Vehicle in Free Swimming

3) Update the synaptic weights by Back-Propagation Method.

To get typical maneuvering actions of PTEROA vehicle, the following two controllers are selected as teachers (cf. Figure 5).

CASE[LF] :Linear feedback controller of pitching motion considering depth of the vehicle.

CASE[Fuz]:Fuzzy controller considering the changes of pitching angle and depth.

The teachers should control the vehicle, at first, in numerical simulations to provide typical maneuvering actions. The I/O systems of these controllers are shown in Table 2. The pitching angle θ, the depth d and the trimming angle of elevators δ_e are defined as illustrated in Figure 6. Two types of neural net denoted by $[NEU_{LF}]$ and $[NEU_{Fuz}]$ are constructed through learning with reference to two teaching samples by [LF] and [Fuz]. The I/O systems of the nets are also represented in Table 2.

Fig.7 Teaching Sample by Linear Feedback Controller

4.1 Learning Process

CASE [LF]:To calculate the feedback gains of the teacher [LF], required parameters were determined through the limit cycle tests of the vehicle in a towing tank[5]. The targets of control are depth d_0 and horizontal steady swimming angle of pitch θ_0(cf. Figure 6). A maneuvering action with [LF] is shown in Figure 7. Here the initial condition of this simulation are $\theta = 0rad$, $d = 1m$ and $\delta_e = -0.1rad$ and the targets are $\theta_0 = 0.049rad$ and $d_0 = 3m$.
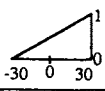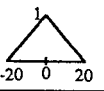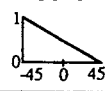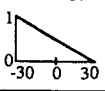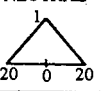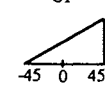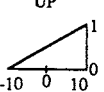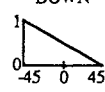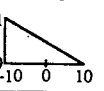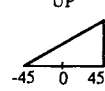
Table 2 Input and Output of Controller

CASE	Teacher Controller		Neural Net		
	Input	Output	Input	Output	Neurons in Hidden Layer
[LF]	$\theta - \theta_0$, $\dot{\theta}$ $d - d_0$, $\delta_e - \delta_{e0}$	$\dot{\delta}_e$	θ, $\dot{\theta}$, $d - d_0$	δ_e	5
[Fuz]	Δd, $\Delta \theta$	$\Delta \delta_e$	Δd, $\Delta \theta$	δ_e	5

Fig.8 Fuzzy Algorithm

Fig.9 Teaching Sample by Fuzzy Controller

CASE [Fuz]: A teaching sample with [Fuz] is derived from the result of a numerical simulation of control with [Fuz], which is constructed so as to maneuver the vehicle to decrease the changes of depth and pitching angle in every $1sec$ (cf. Figure 8). Inputs to the controller [Fuz] are the changes of depth Δd and pitching angle $\Delta \theta$. An output is the incremental trimming angle of the elevators $\Delta \delta_e$ at every $1sec$. Membership functions of each rules are tuned to attain the ability at least to let the vehicle swim horizontaly in the simulation. The result of the numerical simulation with [Fuz] is shown in Figure 9, where the initial conditions of this simulation are $\theta = 0.2rad$, $d = 1m$ and $\delta_e = 0rad$.

4.2 Numerical Simulations

CASE [LF]: Figure 10 shows a result of the simulation of control by [NEU$_{LF}$] on the same conditions as the teaching samples of Figure 7. Though there remains about $15cm$ of the deviation of depth, it can be

said that the net has almost equivalent ability to the teacher [LF]. Figure 11 shows another example when the initial depth and the target depth are $3m$ and $1m$, respectively. This result also indicates that the net can control the vehicle well even outside the range of input values which have been taught.

It should be noted that the inputs of the net don't include explicitly the pitching angle of steady swimming. As the output of the net is the absolute elevator trimming, the neural net, therefore, involves the information about the horizontal steady swimming and dynamics of the vehicle. This is one of the fascinating advantage of this control system.

CASE [Fuz]: Figure 12 shows a result of the simulation of control by [NEU$_{Fuz}$] on the same condition as the teaching samples of Figure 9. It is remarkable

Fig.10 Simulation of Control by [NEU$_{LF}$]-(1)
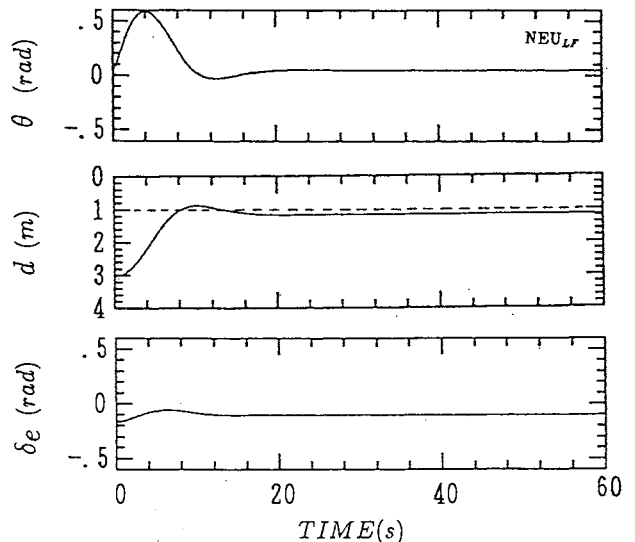
Fig.11 Simulation of Control by [NEU$_{LF}$]-(2)
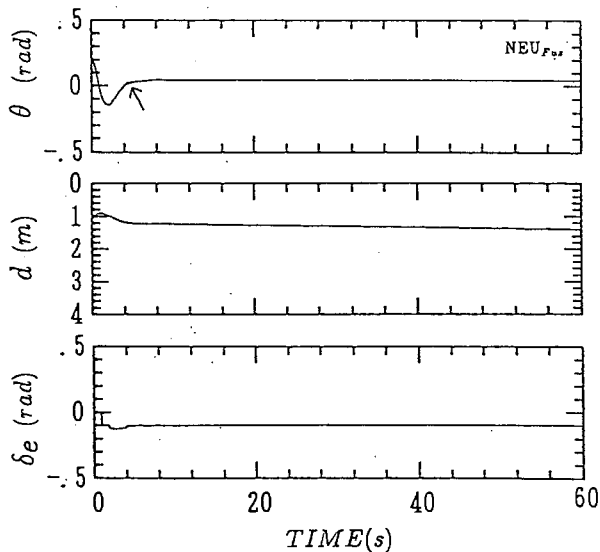
Fig.12 Simulation of Control by [NEU$_{Fuz}$]
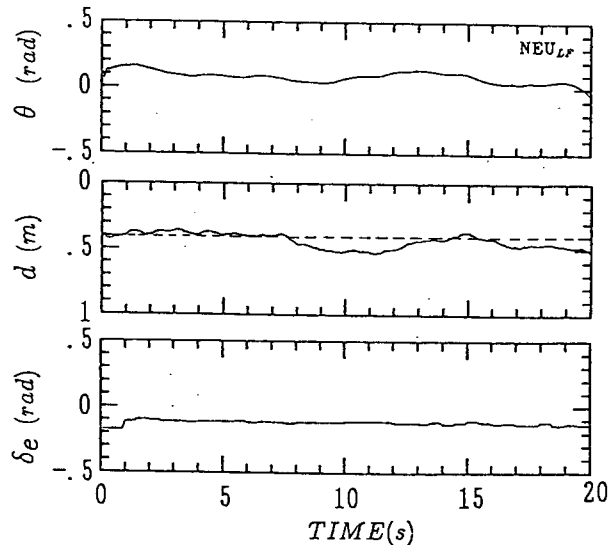
Fig.13 Experimental Results of Control by [NEU$_{LF}$]

Fig.14 Experimental Results of Control by [NEU$_{Fuz}$]
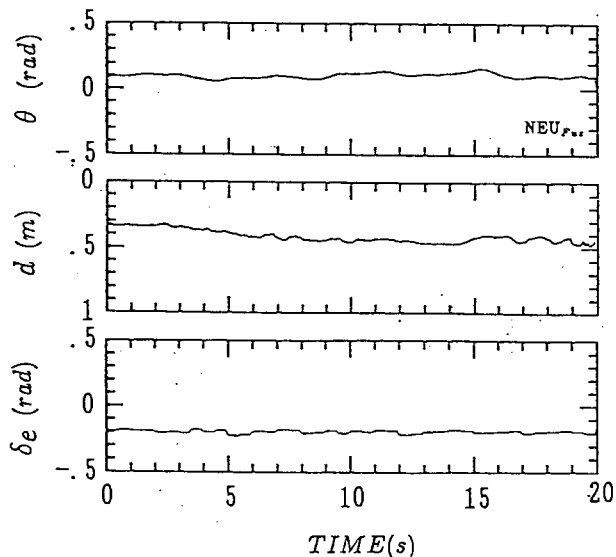
Fig.15 Experimental Results of Control by [Fuz]

that the net reduces the oscillation of the pitching motion, which is inevitably induced when controlled by the teacher [Fuz].

In this case, the inputs of the net are same as the teacher controller [Fuz], but the output is the angle of the absolute elevator trimming, which is not equal to that of the teacher. This also means that the net involves the information about dynamics of the vehicle.

4.3 Free Swimming Tank Tests

In the practical environment there exists considerable amount of disturbance which reduces the stability of motion of the vehicle. It consists of mechanical and electrical noise of actuation and sensing, and unsteady flow, etc. In order to investigate the effectiveness of the neural nets in the practical environment, free swimming tank tests are carried out with "PTEROA60" vehicle in the circulating water tank. This tank has $1.8m \times 1m$ test section and flow velocity is fixed at $0.7m/sec$ in all the tests.

Figure 13 shows a result of the test controlled by [NEU$_{LF}$] with a target of depth $0.4m$, and represents that the developed controller [NEU$_{LF}$] succeeded in letting the vehicle swim very stably.

Figure 14 and 15 show results with [NEU$_{Fuz}$] and the teacher [Fuz], respectively. It should be emphasized that [NEU$_{Fuz}$] succeeds in controlling the vehicle in such an environment where the teacher [Fuz] fails.

4.4 Robustness Against Disturbance

Since [Fuz] has been mainly tuned by means of human decisions and doesn't involve the information about the dynamics of the vehicle, [Fuz] failed to control the vehicle in the test basin as illustrated in Figure 15. It is interesting that [NEU$_{Fuz}$], which has been constructed with the samples derived from [Fuz], succeeds in controlling in the same environment. This indicates that the controller [NEU$_{Fuz}$] is more robust against the unknown disturbance than [Fuz].
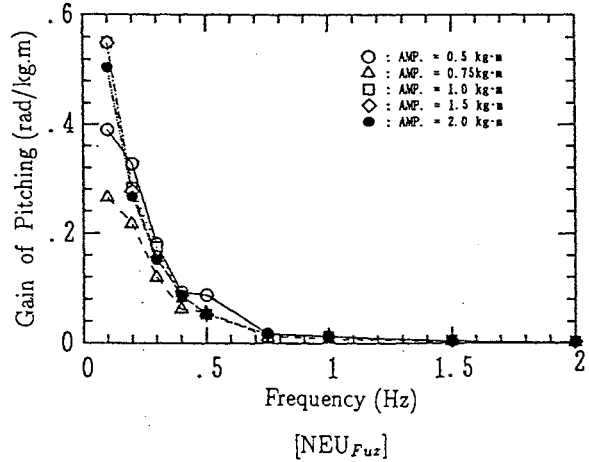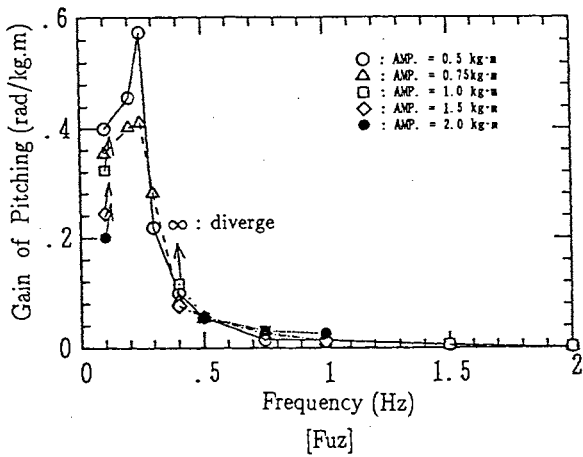
Fig.16 Response of the Control System against Disturbance

In order to compare the characteristics of $[NEU_{Fuz}]$ and $[Fuz]$, the response of the control systems to the forced oscillation is calculated by numerical simulations, namely the vehicle is subjected by sinusoidal pitching moments. Figure 16 shows the level of the response of the vehicle. The amplitudes of pitching motion divided by that of the applied moment are plotted versus frequency. The controller $[Fuz]$ has a clear peak at about $0.2Hz$. The response level diverges to the infinity at that frequency when the amplitude of the moment is more than $1.0kgm$. On the other hand, the controller $[NEU_{Fuz}]$ doesn't have such a peak. It can be said that the controller $[Fuz]$ has the tendency to make the pitching motion unstable under the existence of disturbance with certain frequency and amplitudes. $[NEU_{Fuz}]$ does not inherit this demerit owing to the characteristic of the logistic function in Eq.(2). It can be concluded that the distinguished difference between $[Fuz]$ and $[NEU_{Fuz}]$ in the experimental results is caused by the difference of characteristics against disturbance of low frequency in the flow of the circulating water.

5. Development of SONCS

As mentioned above, a neural net can be organized as a controller by off-line learning with some specific teaching samples. The off-line learning method, however, has following difficulties for implementations.

1) The net can't follow the variation of the vehicle's dynamics caused by changes of environment and a state of motion.

2) When learning is proceeded only through computer simulations, the equation of motion of the vehicle should be known accurately.

When dynamics of the vehicle cannot be obtained in advance, a kind of adaptive control system is needed to generate an appropriate controller automatically according to real dynamics of the vehicle. Here, the SONCS(Self-Organizing Neural-Net-Controller System)[4] is introduced to deal with this problem.
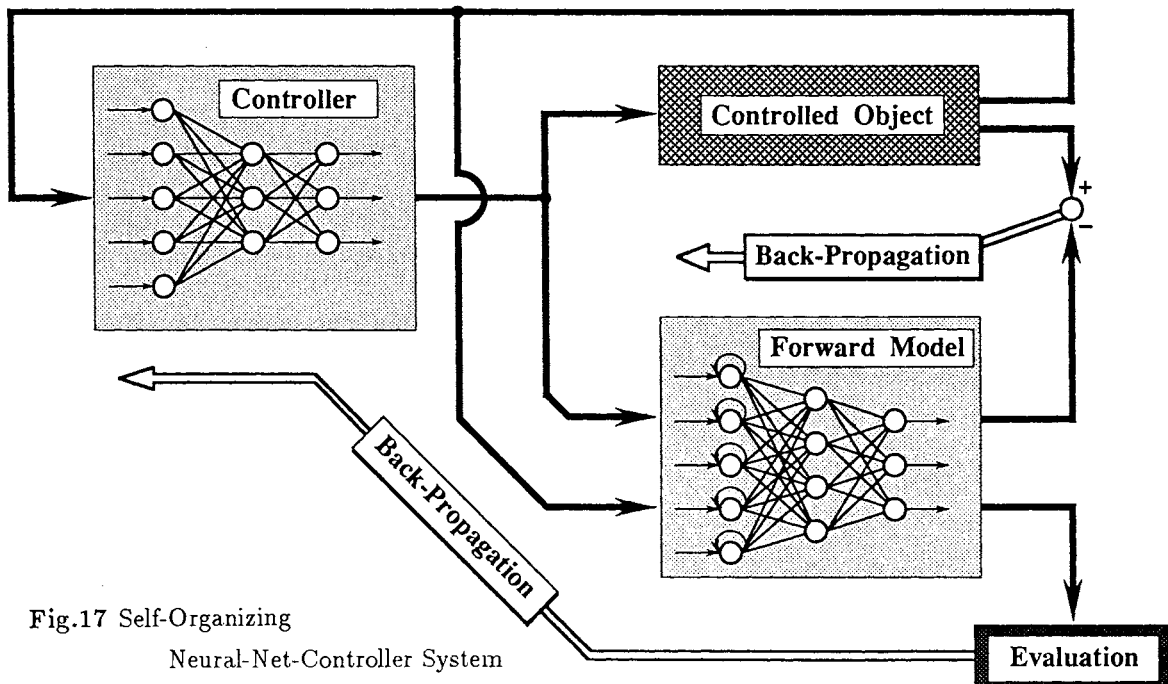
Fig.17 Self-Organizing
Neural-Net-Controller System

The SONCS consists of three subsystems(cf. Figure 17):

1) Controller Network [cnet] : for controlling the vehicle,

2) Forward Model Network [enet] : for referring the state variables,

3) Evaluation and Adaptation Mechanism : for adapting the controller network and forward model network.

The basic concept of this system is to adapt the controller network according to backward propagated signals derived from the evaluation of the vehicle's motion expressed by the forward model network. This adaptation can only be carried out by regarding two subnetworks as one network.

5.1 Introduction of Forward Model

In order to generate and to adjust the controller adaptively, it is necessary to establish a subsystem which can represent the dynamics of the vehicle. For this issue, a neural net which expresses the forward dynamics of the vehicle is introduced in the SONCS. This net is called "Forward Model Network" (cf. Figure 18). The inputs of the net involve state variables of the vehicle at the previous time step and corresponding control inputs. The outputs of the net are state variables at each time step.

Generally, the Connectionist Model which have only the connections between the neurons in the different layers can express only static relations between the input and the output patterns of the signals. The order of appearance of the patterns in the inputs cannot have any specific meaning. In order to deal with the time historical order of the state variables and control inputs, recurrent connections are fitted to the forward model nets in the input layer(cf. Figure 18). As the output function of the neurons in the input layer are identical (cf. Eq.(2)), these connections explicitly make effects of the preceding state of the neurons as follows:

$$
\begin{aligned}
O_i(t) &= \mu_i\, O_i(t-1) + I_i(t) \\
&= \mu_i{}^t\, O_i(0) + \sum_{\tau=0}^{t-1}\mu_i{}^\tau\, I_i(t-\tau) .
\end{aligned}
\tag{7}
$$

Here $I_i(t)$, $O_i(t)$ and μ_i are the input, the output and the synaptic weight of the recurrent connection, respectively, of the i-th neuron in the input layer.

5.2 Evaluation and Adaptation

The synaptic weights of the controller net can be updated so as to reduce the specific evaluation potential E^* about the motion of the vehicle. The updating value $\Delta w_{ij}{}^n$ of the synaptic weights can be calculated as:

$$
\Delta w_{ij}{}^n = -\varepsilon\,\frac{\partial E^*}{\partial w_{ij}{}^n} ,
\tag{8}
$$
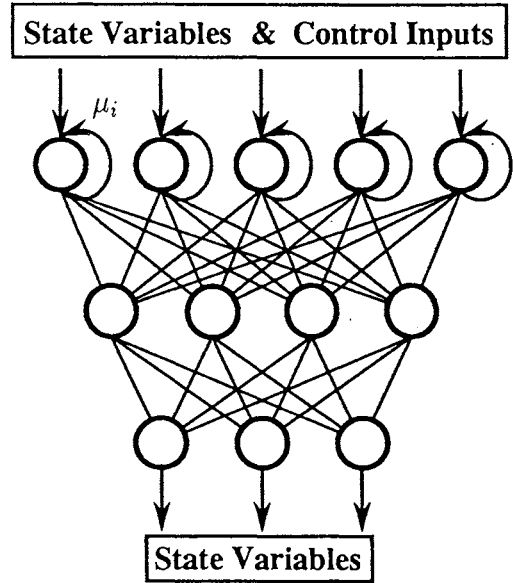
Fig.18 Forward Model Network

where ε is a constant to determine the rate of updating. When E^* is defined as:

$$
E^* = \frac{1}{2}\int^t (\mathbf{x}-\mathbf{x_t})^T\,(\mathbf{x}-\mathbf{x_t})\,dt ,
\tag{9}
$$

the controller net comes to get the ability to let the state vector $\mathbf{x}$ of the vehicle correspond to the desired state $\mathbf{x_t}$ when the updating process progresses.

When a controller network and a forward network are connected with each other, they can be treated as a large single network as shown in Figure 17. On the assumption that the forward model is accurate enough, their outputs is considered to be equal to the state variables of the vehicle.

To modify the forward model network, their synaptic weights are updated with reference to the inputs and outputs of the vehicle in order to decrease the modelling error in normal way.

By substituting the outputs of the forward model for the state vector $\mathbf{x}$ in Eq.(9) and by regarding the desired state vector $\mathbf{x_t}$ as the teaching signal, the evaluation potential is equivalent to the time-integral of the output-error function in Eq.(3) of the whole network. Therefore, updating of all synaptic weights in the controller network can be carried out simultaneously by the same procedure as the Back-Propagation Method. The propagated error signals based upon the evaluation of motion are calculated through the whole network and the weights are updated only in the controller network.

5.3 Organizing Process of Controller

As mentioned above, it is possible to organize the controller which is able to let the vehicle converge to the desired state using developed SONCS. In practical environment, the following two schemes for ignition should be included in the system.

1) Setting the initial values of the synaptic weights.

2) Getting the motion data to make the Forward Model.

From practical point of view, it is dangerous to start the organizing process with no information about the vehicle. During initiation of the synaptic weights of the controller network and generation of motion data, the motion of the vehicle should be kept within appropriate range.

For this purpose, the process which is initiated by Fuzzy controller is introduced as illustrated in Figure 19. Since the structure of Fuzzy controller is more understandable for users than neural nets, it is easy to make the rules for control according to only qualitative knowledge about the vehicle's action and motion. It should be noted that, for this purpose, the controller is not necessary to be tuned up, because the issue of this controller is to control the vehicle in reasonably safe state. So that, this controller is called as premature Fuzzy controller in the following.

Using premature Fuzzy controller as an igniter, on-line organization of the controller network can be proceeded as follows(cf. Figure 19):

A. **Pre-Learning** : making the initial controller network through learning from the motion controlled by premature Fuzzy controller.

B. **Forward Modelling** : making the forward model network through learning from the motion controlled by premature Fuzzy controller.

C. **Evaluation and Adaptation** : adapting the controller network through evaluating the motion and updating the forward model network simultaneously with reference to the inputs and outputs of the vehicle using the whole system.

6. Application of SONCS to PTEROA60

6.1 Premature Fuzzy Control

Premature Fuzzy controller for initiation is defined by the algorithm shown in Figure 20. The rules are so simply tuned that the vehicle just swim in the tank. The inputs of this controller are the variations of depth Δd and pitching angle $\Delta \theta$ in $0.1sec$ at the control timing. An output is the incremental trimming angle of the elevator $\Delta \delta_e$ at every $1sec$. Figure 21 shows the experimental result of motion of the vehicle controlled by this premature Fuzzy controller. On the basis of these motion data, the following SONCS's process is carried out through free swimming.

Fig.20 Fuzzy Algorithm (Version 2)

Fig.19 Organizing Process of the Controller
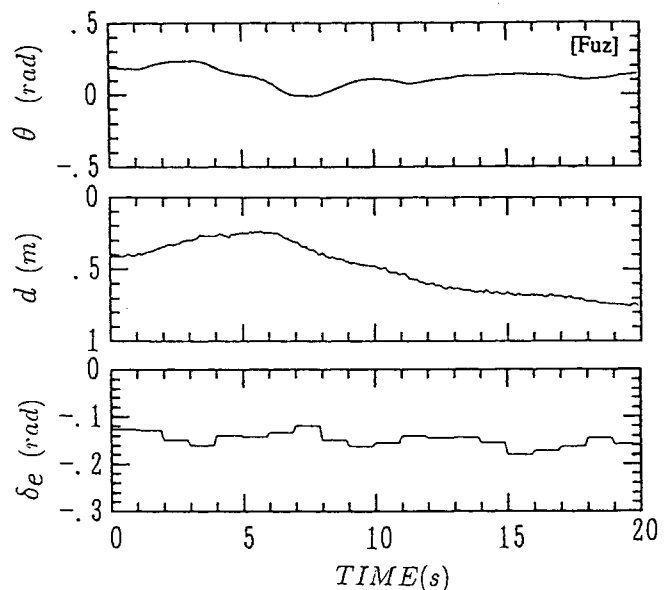
Fig.21 Experimental Results of Control
by Premature Fuzzy Controller

7.2 Pre-Learning

Inputs of [cnet], which represents the controller network, are $\theta(t),\dot{\theta}(t),d(t),\dot{d}(t)$ and $\delta_e(t-1)$, and an output is $\delta_e(t)$. 500 times of learning are carried out with 40 sets of teaching data which have been made from 20 sets of the initial motion data and their negative patterns for reduction of the time for calculation. Figure 22 shows the experimental result of motion of the vehicle controlled by this initial [cnet]. It can be said that [cnet] has come to get the almost equivalent ability to the premature Fuzzy controller's.

7.3 Forward Modelling

As the targets of control are given in regards to $\theta(t)$ and $d(t)$, two forward model networks are made correspondingly from experimental motion data. They are denoted by [enetθ] and [enet$d$] in the following. Inputs of these networks are $\theta(t-1),\dot{\theta}(t-1),d(t-1),\dot{d}(t-1)$ and $\delta_e(t)$. Though these nets can be combined into one network, they are intentionally divided in order to make the system understandable and to reduce the time for learning. To get [enetθ] and [enet$d$], 3000 times and 1000 times, respectively, of learning are carried out with a set of motion data for $20sec$. The outputs of the [enetθ] and [enet$d$], which are illustrated in Figure 23, shows good agreement with the original motion. It can be said that the accurate models of the dynamics of the vehicle have been established in these forward model networks. Here all the weights of the recurrent connections μ_i is equals to 0.9. As these forward models are accurate enough, the updating process of these models will not be carried out in the following experiments.

7.4 Evaluation and Adaptaion

Let's introduce the following two quadratic integrals about θ and d.

$$\begin{cases} E_\theta{}^* = \dfrac{1}{2}\int^t(\theta-\theta_0)^2 dt, \\[2mm] E_d{}^* = \dfrac{1}{2}\int^t(d-d_0)^2 dt. \end{cases} \qquad (10)$$

The evaluation potential for updating the controller network is defined as:

$$E^* = E_\theta{}^* + E_d{}^*. \qquad (11)$$

The initial [cnet] and [enet]s are combined to construct the whole system as shown in Figure 24. [cnet] should be updated so as to reduce E^*.

Figure 25 shows the experimental results of motion of the vehicle controlled by updated [cnet] after every adaptation. Figure 26 shows decrease of the value of E^* through the adaptation process. Adaptation of [cnet] are carried out for 4 times on condition that $\theta_0 = 0.1 rad$ and $d_0 = 0.5m$. Here the rate of adaptation ε is 0.2. It is clearly shown that [cnet] is gradually getting the ability

to keep θ and d in desired values. After four times adaption, [cnet] has come to be able to let the vehicle swim stably with desired θ and d. It is demonstrated that the proposed SONCS is available in a practical environment to organize the controller of the AUV.
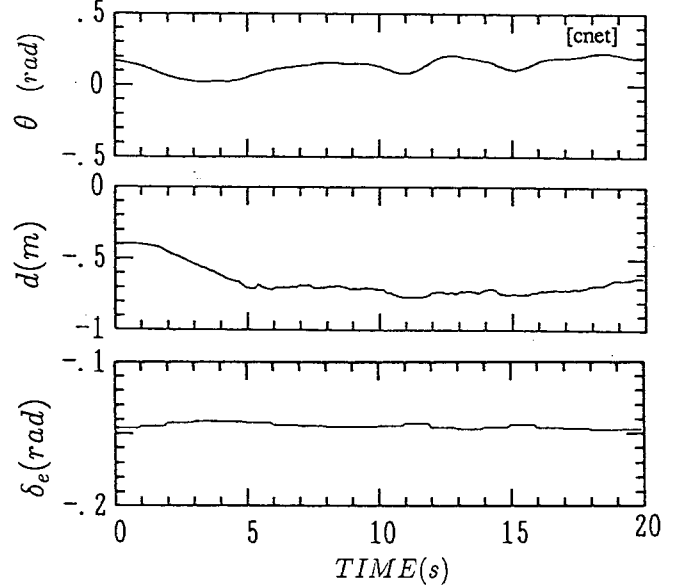
Fig.21 Experimental Results of Control by Initial [cnet]
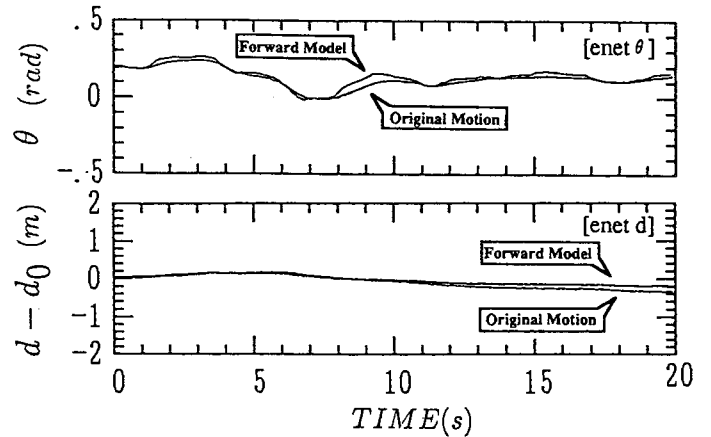
Fig.22 Output of Forward Model Networks
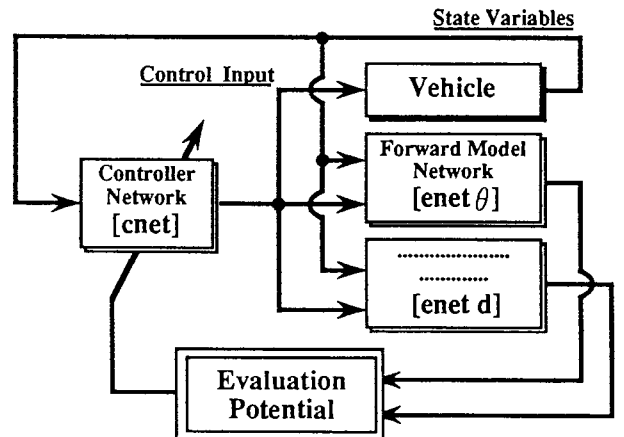
Fig.23 SONCS for PTEROA Vehicle
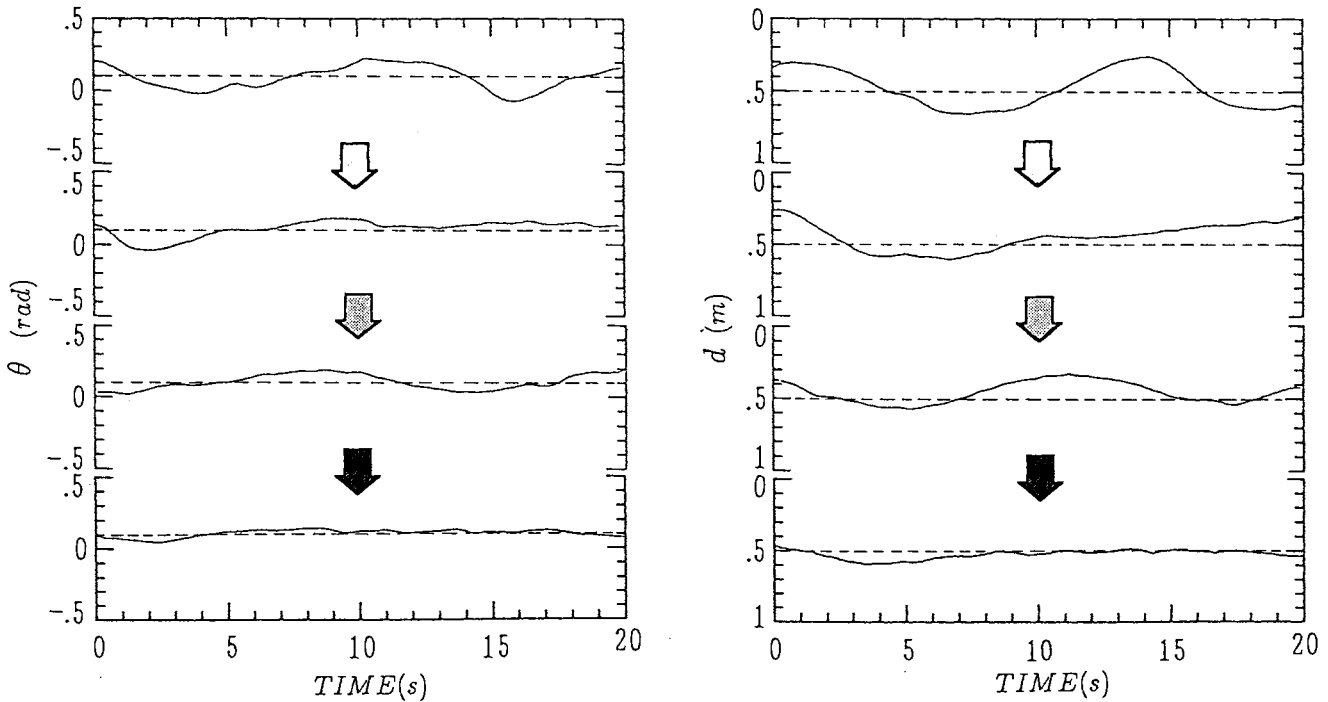
Fig.24 Progress of Adaptation of Controller
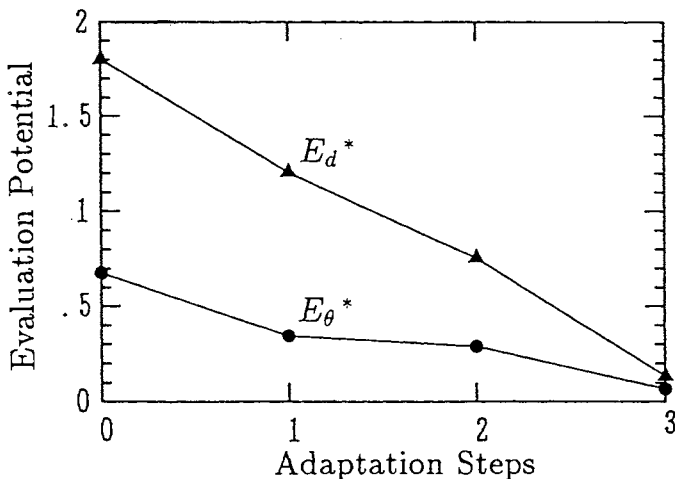
Fig.25 Decrease of Evaluation Potential

8. Concluding Remarks

Two types of control systems for AUVs based on neural nets, i.e. the system with off-line supervised learning and SONCS, are introduced in this paper. Both systems are examined through the application to a free swimming vehicle "PTEROA" and showed good performance. Results can be summarized as follows:

1) Neural nets can obtain equivalent ability to the teacher controller with sufficient steps of learning.

2) The controller net can have robustness and flexibility because of fascinating characteristics which neural nets originally have.

3) the proposed SONCS have a great possibility to make highly reliable and robust control system for underwater vehicles.

References

[1]T.Ura and S.Otubo : "Gliding Performance and Longitudinal Stability of Free Swimming Vehicle", Proceedings of PACON88, Honolulu, HI, 1988, pp.OST1/10-18

[2]T.Ura : "Free Swimming Vehicle "PTEROA" for Deep Sea Survey", Proceedings of ROV '89, San Diego, CA, 1989, pp.263-268

[3]T.Fujii and T.Ura : "Neural Nets for Controlling Longitudinal Motion of AUV", IEEE Journal of Oceanic Engineering, July 1990 (to be published)

[4]T.Fujii and T.Ura : "Development of Motion Control System for AUV Using Neural Nets", Proceedings of IEEE Symposium on Autonomous Underwater Vehicle Technology, Washington DC, 1990 (to be published)

[5]T.Ura and T.Fujii : "Feasibility Study on Gliding Submersibles (6th Report : Free Swimming Tank Tests)", Monthly Journal of Institute of Industrial Science, University of Tokyo, Vol.41, No.9, 1989, pp.33-36 (in Japanese)

[6]D.E.Rumelhart, J.L.McClelland and The PDP Research Group : "Parallel Distrbuted Processing, Volume 1 : Foundations", The MIT Press, Cambridge, MA, 1986

FIELD TESTS ON AQUATIC WALKING ROBOT FOR UNDERWATER INSPECTION

M. Iwasaki, J. Akizono, T. Nemoto, O. Asakura

Port and Harbour Research Institute, Ministry of Transport, Japan

Abstract

Aquatic walking robot named "AQUAROBOT" has been developed. Main purpose of the robot is to carry out underwater inspecting works accompanied with port construction instead of divers.

This robot has two main functions. One is the measurement of the flatness of rock foundation mound for breakwaters by the motion of the legs while walking. The other is the observation of underwater structure by TV camera.

AQUAROBOT is six-legged articulated "insect type" walking machine. Operation is fully automatic because this robot is so-called intelligent mobile robot. The working depth is up to 50m.

AQUAROBOT has an ultrasonic transponder system which is long base line type as a navigation device. It also has an underwater TV camera with ultrasonic ranging device at the end of the manipulator on the body.

Through the field tests, the performance of the robot was proved to be sufficient for the practical use.

Test results are as follows.

Walking speed is 6.5m/min. on the flat floor in the test pool and 1.4m/min. on the irregular rubble mound in the sea. In the case of navigation, the positioning accuracy is within +21cm. The robot can measure the flatness of rubble mound by the motion of the legs with the same accuracy as divers.

key words: walking robot, underwater application, inspection work

1. Introduction

The underwater inspection works accompanying port construction are carried out by manual labor of divers. However, the efficiency and safety of underwater activity are not sufficient because underwater condition is austere. Increasing risks and lower working efficiency of port construction work at deeper sea area and shortage of divers make the situation worse. Therefore, it is necessary to develop the underwater inspection robot.

The robot which carries out the underwater inspection work taking the place of divers should have good stability, positioning ability and the ability to move on uneven seabed. Compared with free-swimming type, the bottom-reliant type is good for this purpose. We selected walking type, not wheel type or crawler type or archimedian screw type, as the underwater inspection robot.

Fig .1 is schematic view of AQUAROBOT measuring the flatness of rubble foundation mound.

We started this project from 1984 and have made 3 models up to now. The 1st one made in 1985 is an experimental model for overground test. The 2nd one made in 1987 is a prototype. The 3rd one made in 1989 is light-weight type.

In this paper, the walking test of prototype in the sea is mentioned.
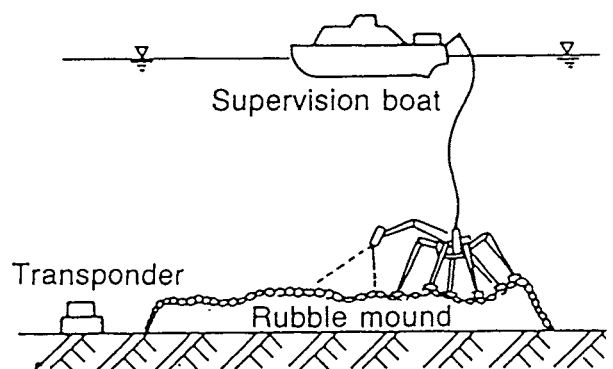
Fig.1 Schematic view of measurement of rubble mound by AQUAROBOT

2.Outline of AQUAROBOT

2.1 Hardware

AQUAROBOT is six-legged articulated "insect type" walking machine. Each leg has three articulations, and they are driven semi-directly by DC motors which are built inside the leg. The articulations are mechanically independent to each other.

All the motions are controlled by a tiny lap-top micro computer (CPU 80286), which makes the robot be able to walk on irregular rough terrain. The measurement of the profiles of seabed is possible by recording the motion of the end of the legs while it walks.

AQUAROBOT can walk in any direction without changing its quarter and can turn within its own space. Each leg is equipped with a tactile sensor on its end and there are two inclinometers, a gyrocompass, and a pressure sensor in the body.

The prototype model has 150cm legs and weighs 857kgf. It can be operated 50m deep in the sea. A manipulator for underwater TV camera with ultrasonic ranging device is mounted on the body. The robot is connected by optical/electric cable of 100m long to the control unit on mother ship.

Prototype has an ultrasonic transponder system which is long base line type as a navigation device. It also has an underwater TV camera with ultrasonic ranging device at the end of the manipulator on the body.

Main dimensions and the positions of the sensors are shown in Fig.2 and the specifications in Table 1.
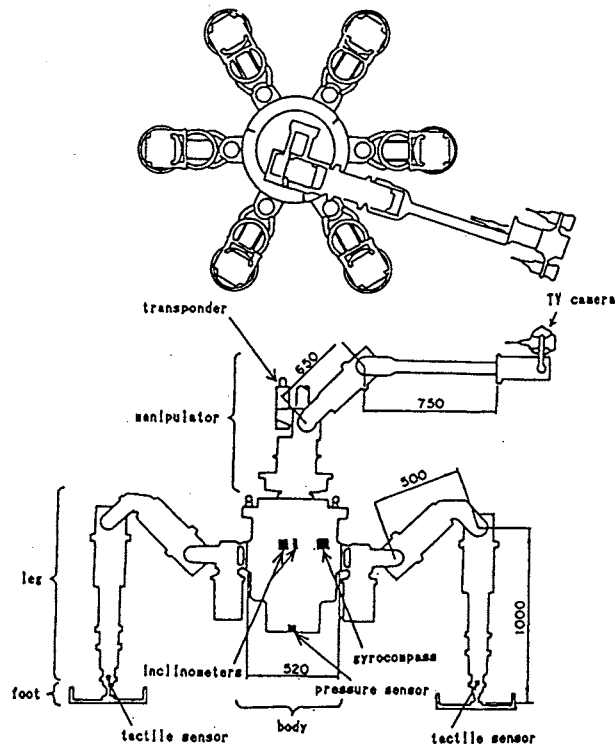
Fig.2　Dimensions and sensors of AQUAROBOT

type	axis-symmetric 6-legged insect type walking robot
articuration drive method	semi-direct drive by DC servo motor
control method	software control by micro computer
main material	anti-corrosive alminum
weight	857kgf(in the air) 440kgf (in the water)
sensors	6 tactile sensors, 2 inclinometers 1 gyrocompass, 1 pressure sensor
terrain roughness	±35cm max.
watertightness	50m deep
purpose of practical robot	measurement of flatness of rubble mound observation of underwater structure supervision of underwater construction work

Table.1　Specifications of prototype

2.2 Software

The control program consists of operating program and walking algorithm program which are independent of each other. They are interfaced by a robot language. The calculation for linear interpolation and synchronization of motor rotation is processed in the real time by this robot language.

Operation is quite easy. Operator just input walking direction and walking distance when not navigated, or X and Y coordinate values of the destination when navigated. In both case, AQUAROBOT walks on irregular terrain autonomously utilizing informations from sensors with the body kept horizontal.

The state and the motion of AQUAROBOT is shown on the computer display all the time.

3. Field test

3.1 Test place

Field test was carried out at Izumi working area in Kamaishi Port of Iwate Prefecture on February 14-23, 1990.

Test area, which is 42 77m wide, is next to the caisson yard for Kamaishi Bay Breakwaters. It is the place for temporary storage of completed caisson until final submersion at the projected place. Average water depth is about 24m and the sea bottom is rubble mound which was leveled by the rubble leveling machine developed by 2nd District Bureau of Port Construction in Yokohama.

AQUAROBOT was submerged on the sea bottom being hung by crane barge. Photo.1 shows AQUAROBOT walking on the test area.
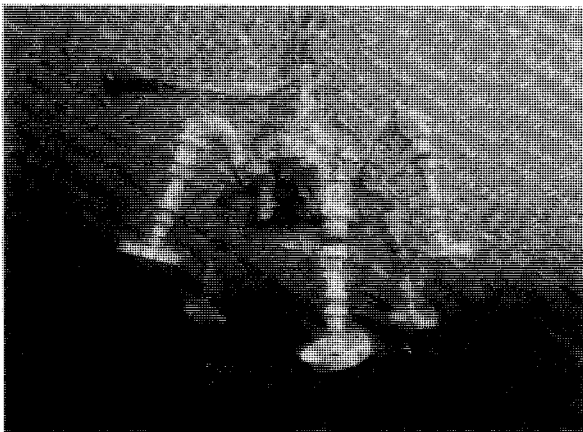
Photo.1 Walking 25m deep in the sea

3.2 Procedure of Test

In this field test, accuracy of navigation, walking speed, error of flatness measurement, maneuverability, are mainly investigated to examine the adaptability of AQUAROBOT for the practical use.

Navigation test is done by walking from one point to the other point where the location is measured previously. These points are landmarked by steel plates of 0.9 1.8m. AQUAROBOT is navigated by transponder system at every two step. Frequency of ultrasonic wave is 40-70kHz. The accuracy of transponder system alone is +10cm at the measuring distance of 300m.

Relative height of walking terrain is measured by summing up the motions of the legs. Absolute water depth of terrain is achieved by calibrating the relative height by the values of pressure sensor recorded at the starting point and the finishing point of walking.

4. Test Results

4.1 Navigation

The test result is shown in Table 2. All the values are measured by transponder system. Error is within +21cm. In addition to this, when AQUAROBOT reached the destination, it is observed that the robot is just on the steel plate from the view of underwater TV camera.

pulse output speed	step width (cm)	step height (cm)	commanded destination (cm)	measured destination (cm)	error (cm)	walking speed (m/min.)
1/3	15	35	X 34821	X 34816	-5	0.61
			Y -7251	Y -7284	-13	
1/3	20	35	X 35029	X 35044	+15	0.67
			Y -8232	Y -8218	+14	
1/2	15	35	X 34821	X 34822	+1	0.67
			Y -7251	Y -7249	+2	
1/2	20	35	X 35029	X 35037	+8	0.76
			Y -8232	Y -8231	+1	
1/2	20	25	X 32810	X 32811	+1	1.27
			Y -7371	Y -7350	+21	
1/2	20	25	X 33000	X 32981	-19	1.43
			Y -7500	Y -7504	-4	

Table 2 Accuracy of navigation and walking speed

4.2 Walking speed

Walking speed depends on the step height, step width, and pulse output speed from micro computer. Walking speed is also
shown on the Table 2. Maximum walking speed is about 1.4m/min.

4.3 Flatness measurement

An example of measurement is shown in Fig.3. The maximum difference is 56cm. Considering the roughness of this area is +30cm from the 30cm pitch measurement by divers, the measured value is proper.
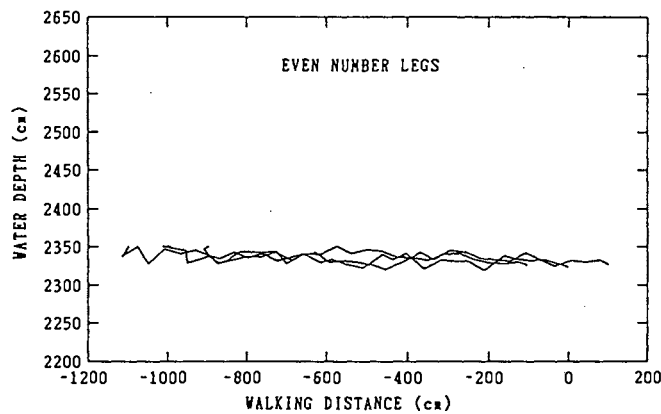
Fig.3   Result of flatness measurement

4.4 Automatic area scanning

For the practical use in the near future, the software for fully automatic operation is developed. When the operator just input the coordinate values of 4 vertex of projected area and measuring interval before operation, AQUAROBOT will generate walking lines shown in the left of Fig.4 and will walk along those lines automatically.

The actual walking line is shown in the right of Fig.4. In this case, walking distance is 95m and walking time is 72min. without down time of navigation system, so average walking speed is 1.32m per min.

4.5 Walking test on the sand

Walking test on the sand terrain is additionally carried out on the sandy sea bottom around the rubble mound. No problem can be observed compared with the walking on rubble mound except the water was made muddy when the foot touches the sea bottom.

5.Conclusion

Although the number of research on walking robot is increasing, the perfor-

mances of walking robot for overground use seems to be insufficient for practical use. However, AQUAROBOT is proved to have sufficient ability for practical use through the field test. AQUAROBOT is expected to become the first practical walking robot.

The technology of AQUAROBOT can be applied for the other severe conditions than underwater, such as space, radio active, and so on.

References

Mineo Iwasaki et al., 1987, 'Development on Aquatic Robot for Underwater Inspection', Report of the Port and Harbour Research Institute Vol.26 No.5, pp.393-422

M Iwasaki et al., 1988, 'Development on Aquatic Robot for Underwater Inspection', Proceedings of the 5th In-International Symposium on Robotics i Construction, JSCE, Vol.2, pp.765-774

J Akizono et al., 1989, 'Development on Aquatic Robot for Underwater Inspection', Proceedings of 4th Interna-n tional Conference on Advanced Robotics
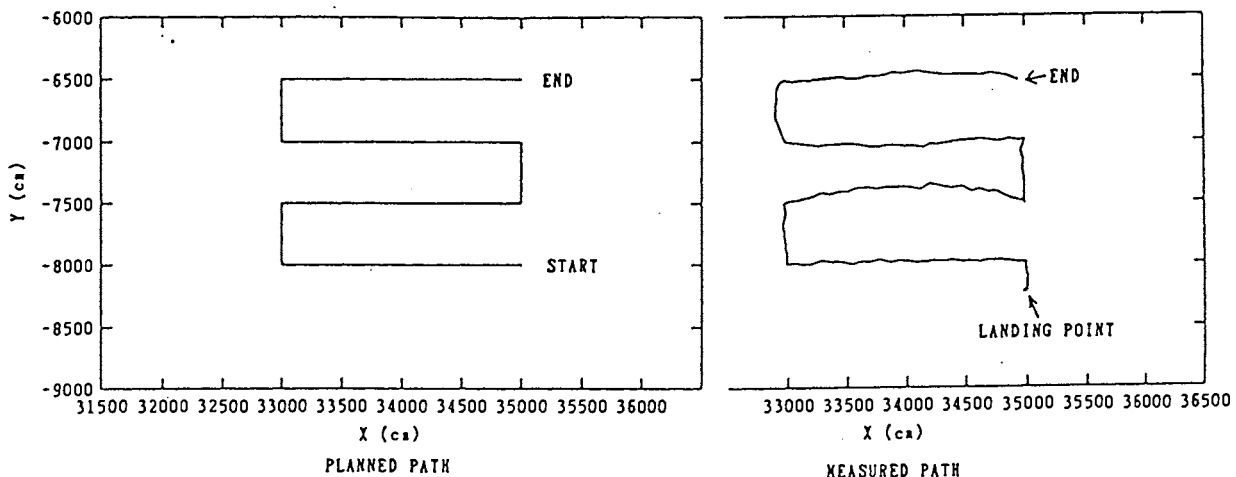
Fig.4   The planned and measured path of area scanning

AUTONOMOUS UNDERWATER VEHICLE OF THE INSTITUTE OF MARINE TECHNOLOGY PROBLEMS, USSR ACADEMY OF SCIENCES

M. D. Ageev

Institute of Marine Technology Problems, USSR

Abstract

In the report one of the latest Institute models – the Autonomous Underwater Vehicle (AUV) MT-88 – is described. The vehicle is a multipurpose underwater informative robot assigned for various works in the field of oceanology. AUV is program-controlled, a program is input before the vehicle launch and has acoustic link correction. The vehicle trajectory can be either arbitrary and spatial at hydrophysical measurements or disposed in the bottom vicinity at photo- and telesurveying. Acoustic Positioning System (APS) guarantees AUV location. The vehicle is equipped with measuring instruments,TV and still cameras. The following report presents AUV construction and on-board systems structure peculiarities. Natural experimental results and further prospects are also discussed here.

1. Introduction

The future of underwater technologies,especially of those assigned for deepocean regions, belongs to robotized systems. An informative underwater robot, or,according to terminology accepted, Autonomous Underwater Vehicle (AUV) is the simplest representative of such system.

The staff of the Institute of Marine Technology Problems has been developing this trend since 1972. First vehicles "Skat" and "Skat-Geo" designed for operations at shelf depths permitted us to realize the problems of this new field of science and enginee-

ring as well as to gain primary experience. The vehicle "Skat" shown in Fig.1 comprised originally two large hulls, thus forming a catamaranlike construction. Gradually some extra devices arranged in small containers were added. "Skat-Geo" proved to have a rather large number of said containers (Fig.2,3). This caused the idea of a

modular construction. Propulsor system comprising four stern propulsors is another success of early works. Its advantages are pointed below. At last I can't but mention one more"discovery". Vehicles with such body configuration reveal a strong screening effect in the bottom vicinity. At the command of descent the vehicle slides over flat bottom at distance of 0.2...0.3 m. As a matter of fact, such a planed body configuration is probably expedient for vehicles assigned for operation in the bottom vicinity(recall a flounder) though it is not always convenient to realize, due to a number of construction and exploitation problems. The vehicles "Skat" and "Skat-Geo" were tested and used in experimental works in the Sea of Japan,the White Sea and Lake Baikal.

Further on deepwater AUVs were developed. The first model was tested at utmost depth in December 1980, depth of 5,970 ms was reached. Considerable experience of AUV exploitation has been gained for recent years thus permitting us to affirm that the Autonomous Underwater Vehicle is the effective and perspective means of ocean investigation and exploration. Even at present state of development(and capabilities of progress are non-limited) they can be used not only for simplest works such as, for example, bottom

overall photographic survey but for more complicated operations as well. Carried out by means of AUV the investigation of the submarine "Komsomolets" sunk in spring 1989 serves an example.

2. AUV MT-88 General Description

AUV MT-88 photo taken during tests is presented in Fig.4, its scheme — in Fig.5. The vehicle has a traditional body configuration formed, however, with buoyancy units and fairings.Basic equipment is disposed in 14 containers small in dimensions.The body is subdivided into several sections.Thus there occur wide modifying possibilities.

Though being autonomous, AUV combined with Acoustic Positioning System (APS) and carrier ship equipment form an integral information control system with interacting components controlled by operator.

A carrier ship disposes of a control post comprising a central electronic computer, transceiver units of APS and acoustic link, recording and other devices. Ship kit functions consist in providing pre-launch AUV control and program input; reflecting AUV and ship movement in real time scale; AUV operation correction by acoustic link; reading out and preliminary processing of data from on-board vehicle storage devices after AUV recovery.

Both constructive elements and communication devices of separate electronic units have been unified. On-board vehicle instruments with unified controllers have a common communication channel that permits to vary on-board systems structure and improve separate systems, outboard electric connections being kept invariable.Programs input before the vehicle launch, data reading out after its recovery and vehicle operation in towed mode (at tests) are conducted over the same channel.

The vehicle descent and ascent are carried out by utilizing cast-iron ballasts. AUV descends with 2 ballasts, one of them being thrown off when set water-level is reached, the other — when the operation program is over.The AUV movement in this mode of operation

is spiral and uncontrolled, the vehicle tangage being 60-70°. The vertical descent and ascent rate is about 4 km/hr. With depth of 4-5 kms the deviation of descent point from launch one doesn't usually exceed 200...300 ms. At set water-level the vehicle has positive buoyancy in the order of 3...5 kgf.

The propulsor system tested before is applied in the vehicle. It consists of 4 main propulsors installed in the AUV stern at an angle of about 20° relative to the vehicle longitudinal axis. Motors rotation velocities being controlled,such system permits to form a thrust arbitrary in direction, thus providing the vehicle fast-acting and good manoeuvrability. Simplicity and homogeneity are also the system advantages. Instead of one velocity and two positional servo-systems(one propulsor with controlled velocity, two rudder turn gears) four identical velocity systems are utilized. It is possible to use only 3 propulsors but some inconveniences arise inthis case.One big screw is sometimes considered to be more effective than four small ones.It is exactly so if you don't take into account a number of factors. It was pleasant for me to find in [2] the arguments for a multi-screw system. The analysis of dynamics of the vehicle with similar propulsor system is given in [1]. The vehicle velocity gradually changes to 1.2 m/s. Reverse is also provided for emergency cases.Once this rate was realized in the situation when the vehicle had got (strung)on a thin metallic construction not detected by an obstacle avoidance sonar.

2.1 AUV MT-88 Main Features Assignment

- Bottom cartography and survey;
- Geophysical and geodetic works;
- Deep-water minerals prospecting;
- Oceanological measurements;

Characteristics

- Rated water depth — 6,000 ms
- Maximal speed — 1.2 m/s
- Underwater endurance — 6 hours
- Mass — 1 tonne
- Overall dimensions — 3.8x1.15x1.1 ms
- Power source — 16 cells,
  silver- zink battery — 100 A hours

MT-88 main units and devices disposition is presented in Fig.5.The containers in which the instruments are disposed are made of high-strength aluminium alloy, the containers destruction pressure being 750 kgf/cm^2 , that guarantees safety factor of 20%. It is, probably, quite enough for unmanned vehicles.Free space between the containers is filled with syntactic foam. Containers hermetic lead-ins are connectors with glass insertions. External joints are accomplished with conductors placed into flexible pipes filled with oil. Pressure compensators are utilized to keep little redundant pressure. In Fig.6,7,8 some elements and structures are shown as examples.

The vehicle works the following way. By means of cable it is connected up to ship electronic computer through a hermetic connector.The vehicle systems control is carried out and the operation program is input. The cable disconnected, the vehicle is launched. While launching it is characterized with negative buoyancy, so after launching by a crane and releasing hook it easily descends, and this operation is of no difficulty, even in frosty weather. When planned depth is reached the first ballast is thrown off.

APS permits to follow the descending vehicle and to fix the deviation of reaching point from the program-planned one. Transmitting the corresponding commands to the vehicle over the acoustic link one can move it to the necessary point.After that the vehicle starts working according to the program.At a corresponding command the program can be corrected during the vehicle movement. The program over, at command of ascent or in case of emergency the vehicle throws off the second ballast and ascends. The carrier ship approaches the point of the vehicle expected ascent, radio- and light beacons on the vehicle are used for search. The vehicle recovery on board a ship is really a more complicated task than its launch as it demands the presence of people in the pneumatic boat for connecting slings.

The cable is connected up to the vehicle after its installation on the deck, data is read out and the vehicle is operated.

3. Control System

The vehicle is controlled by central processor unit (CPU) which works out program commands, interacts with all the vehicle electronic units, reacts to telecontrol signals, provides the vehicle systems control and proper commands in emergency cases. Information exchange between the vehicle systems is realized over the common main line.

The vehicle orientation control system structure is more or less traditional. The movement control in horizontal plane is carried out through comparison of data taken from a fluxgate or gyro compass to the course set by CPU. To damp oscillations, a signal of the gyro angular velocity transducer is included into feedback circuit. A control channel in vertical plane has two operation modes - the ones of reaching set depth or set altitude. In the first case a program-set depth value is compared with a depth-meter signal, in the last one a feedback signal is produced by an echo-sounder. Signals from a tangage transducer and a gyro angular velocity transducer are extra-used. Transducer signal transfer coefficients are chosen so as to achieve the best dynamic qualities of the control system.

Obstacle avoidance has been conducted by the present time in the vertical plane, with the help of three sonars, their beams directed down, forward and at an angle of 45°. Their signals are adjusted to provide safe vehicle movement over the rough bottom, at set distance from it. The said system proved to be effective enough in most of real situations. In the AUV MT-88 program-set is the capability to realize the improved adaptive control system with spatial obstacle avoidance (see [3] - the report for the present congress). The system has been modelled in the electronic computer, its testing and debugging in the sea are planned for 1990.

4. Navigation System

AUV location from a carrier ship is

provided by Acoustic Positioning System (APS) in real time scale. The system operates the following way. AUV equipment includes a timer synchronized with a carrier ship timer. Quartz generators accuracy makes 10^{-8} that guarantees distance calculation error not exceeding 1 metre, due to generators drift. Both vehicle and carrier ship periodically (periods being different) excite bottom transponders. Thereby the slant ranges between the carrier ship, the vehicle and the transponders are determined and thus the carrier ship's and the vehicle's coordinates are calculated.

The vehicle on-board positioning system includes a log, a compass, a tangage transducer and provides numerical calculation of the vehicle location. Errors accumulation stipulates the above-mentioned system imperfection. It is clear that dead reckoning data correction in accordance with APS data is demanded. In the AUV MT-88 the Integrated Positioning System (IPS)has been realized, in which the combined data processing is provided [4]. IPS tests are planned for 1990.

Now the work is being done to equip AUV with Inertial Navigation System (INS) which will operate also combined with APS. Modern INS use in low-speed apparatus is expedient only together with APS. Really, the equivalent error of AUV velocity determination at gyroes drift in the order of 10^{-3} deg/hr makes 0.06 mile per hour(that is about 100 m/hr), that considerably exceeds the error permitted and APS error in favourable hydrological conditions. At the same time, APS operation in the vicinity of rough bottom is not always stable, prolonged signal losses (for 10-15 minutes) are possible. In these situations INS keeps working out data of AUV location. It is expected, however, that in case of AUV when the exciting accelerations are very little (to 10^{-2}g),the industrial aviation type INS will reveal more accuracy than standard one for flight conditions.

5. Experimental Results

The AUV MT-88 was tested in summer

1988 and in spring 1989. Tests were carried out in the Sea of Japan near Vladivostok. The main difference between MT-88 and its prototypes consisted in electronic equipment considerable renewal. Thus the main task was the instruments debugging, amplification coefficients optimization in control channels, all devices operation control.

In September 1989 MT-88 was used in experimental investigation of regions of iron-manganese nodules bedding, by the contract with the industrial society "Dalmorgeologia". Works were conducted in the Pacific, in the vicinity of ridges Clarion and Clipperton, at depth of 4.5 kms. We were to carry out bathymetric, photographic and TV surveying of a bottom area. Due to AUV precise stabilization over the bottom, TV and photo surveying quality proves to be higher than in case of towed vehicles. Moreover, AUV is more effective in detailed investigation of comparatively small bottom areas. In contrast to autonomous vehicle, towed one needs much time expenditure for tacking, especially at big depths. Bottom photo examples taken during work are presented in Fig.9. Works were carried out from the ship "Geolog Pyotr Antropov". Launch-recovery operations were accomplished with the help of A-frame. We find them rather complicated even in favourable weather conditions, due to board height at the stern (6 ms). However, with board height of 2-3 ms and crane derrick utilization, the vehicle's launch and recovery are possible even at sea state four.

6. Conclusion

The experience of the AUV development and experimental exploitation accumulated by the Institute staff is the evidence of the fact that even at present stage of technology, AUVs provide costeffective bottom investigation carrying out, for example, on purpose of minerals prospecting and survey.

In the report many results of my colleagues – scientists and engineers

of the Institute, are accumulated.They
all are co-authors of the work which
would have never been accomplished if
it were not for their enthusiasm.

References

1. Autonomous Underwater Vehicles/
   M.D. Ageev, B.A. Kasatkin, L.V. Ki-
   selyov: Sudostroyeniye, 1981.
2. C.A. Gongwer, Relationships for
   Self-propelled Underwater Vehicles
   in Steady Motion, Intervention'89
   Conference.
3. A.V. Inzartsev, L.V. Kiselyov,
   O.Yu. Lvov, Underwater Robot Motion
   Adaptive Control, PACON'90.
4. M.D. Ageev, L.V. Kiselyov,
   A.Ph. Shcherbatuk, Integrated Posi-
   tioning System of Underwater Robot,
   Intervention'90 Conference.
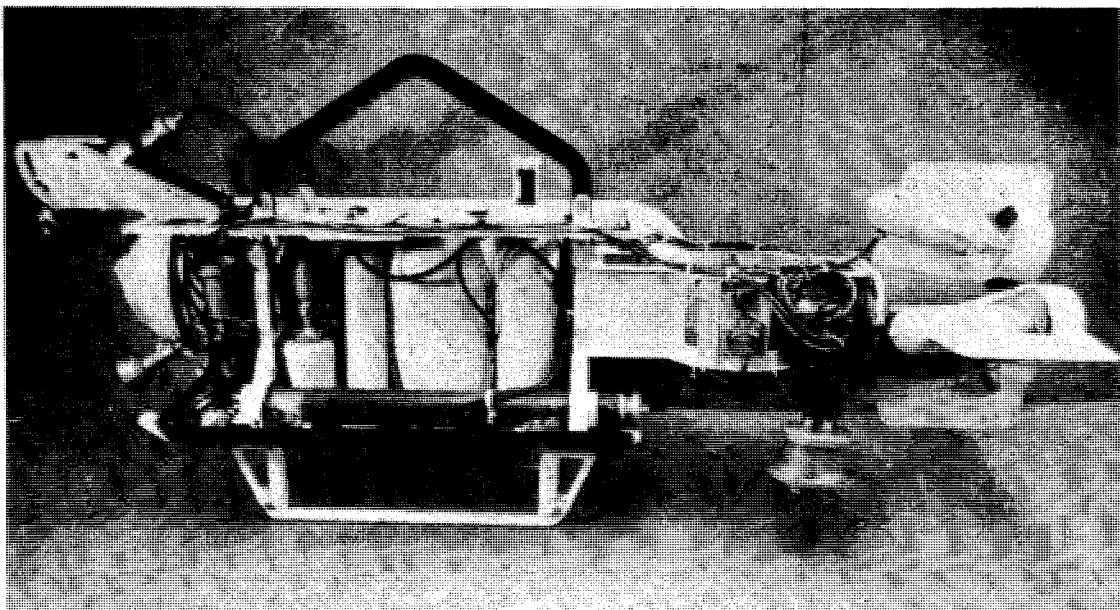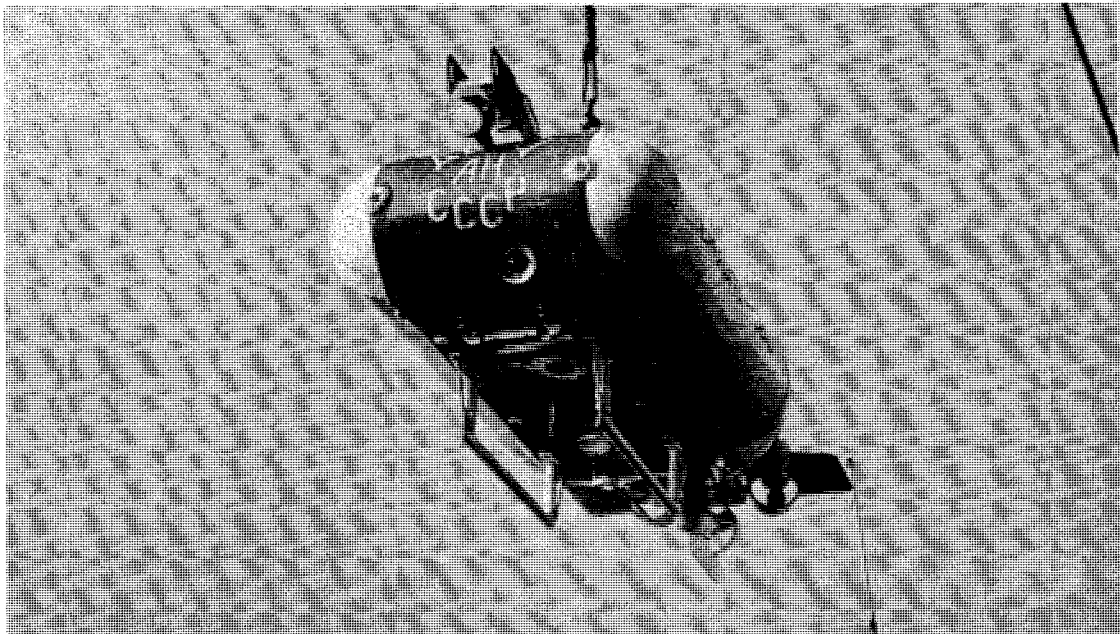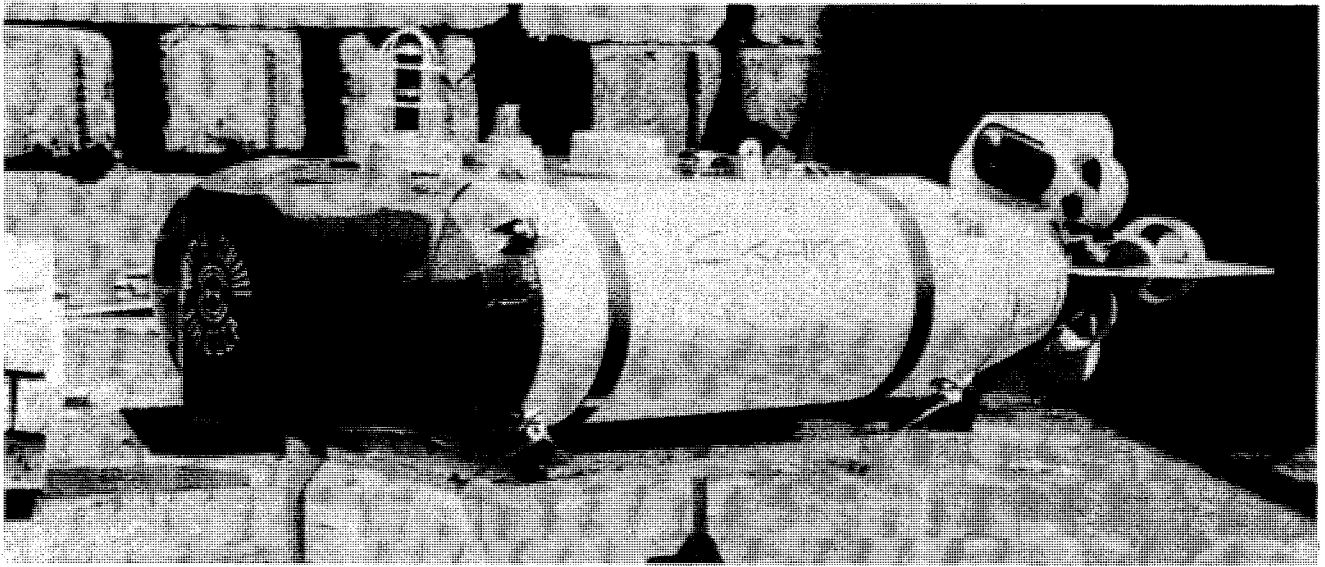
Fig.1. AUV Skat.   Fig.2,3. AUV Skat-Geo.

Main battarry

SS Sonar and measuring
units . sections

Radio and light
beacons

Ballast
weights

Trusters
oft section

Control and navigation
systems sections

Still camera

Nose section: TV camera,
obstacle avoidance sonar
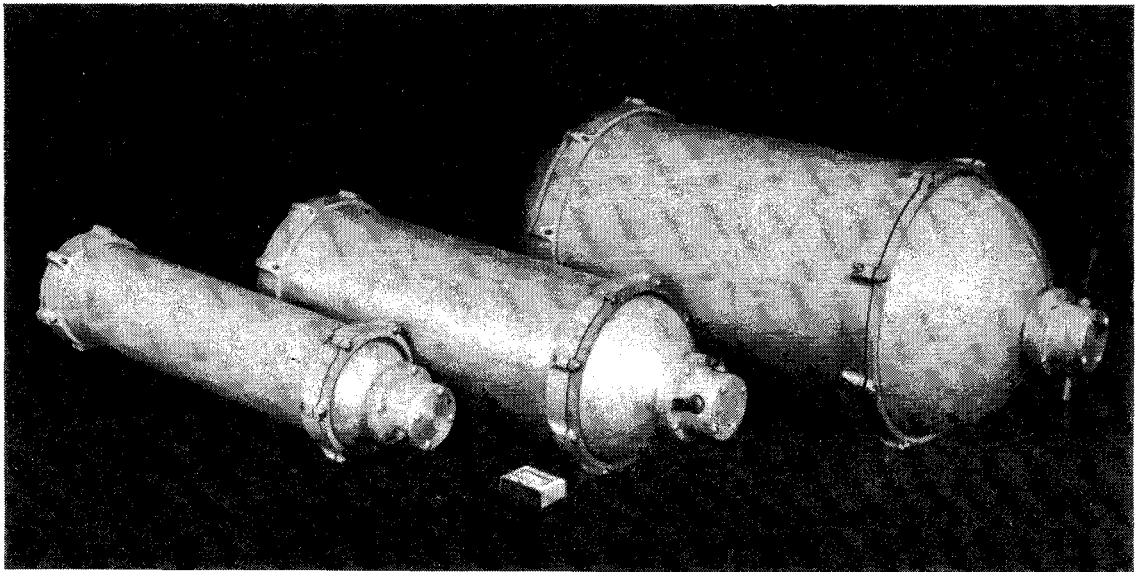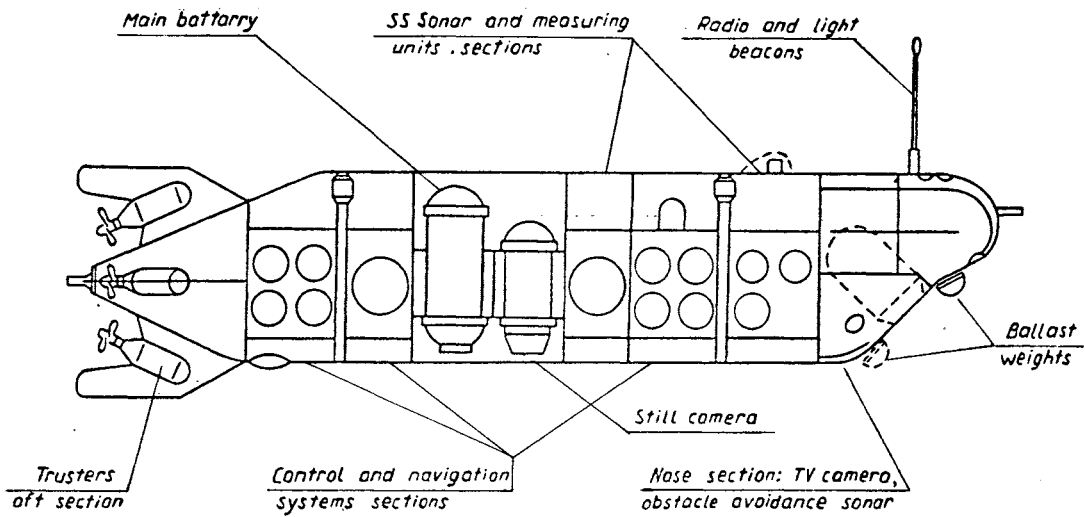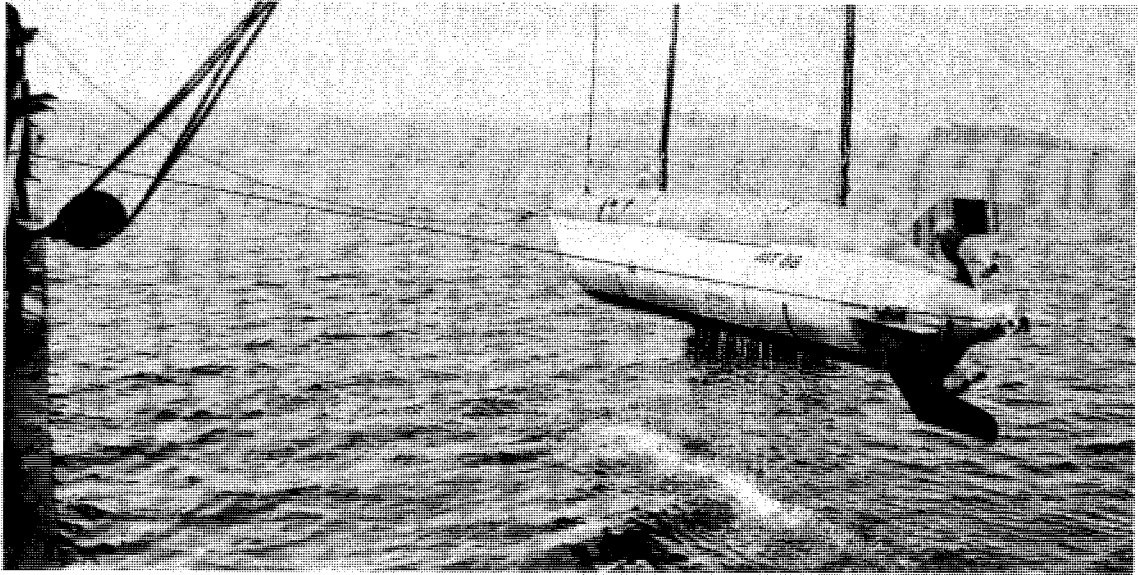
Fig.4,5. AUV MT-88.

Fig.6. Pressure Containers.
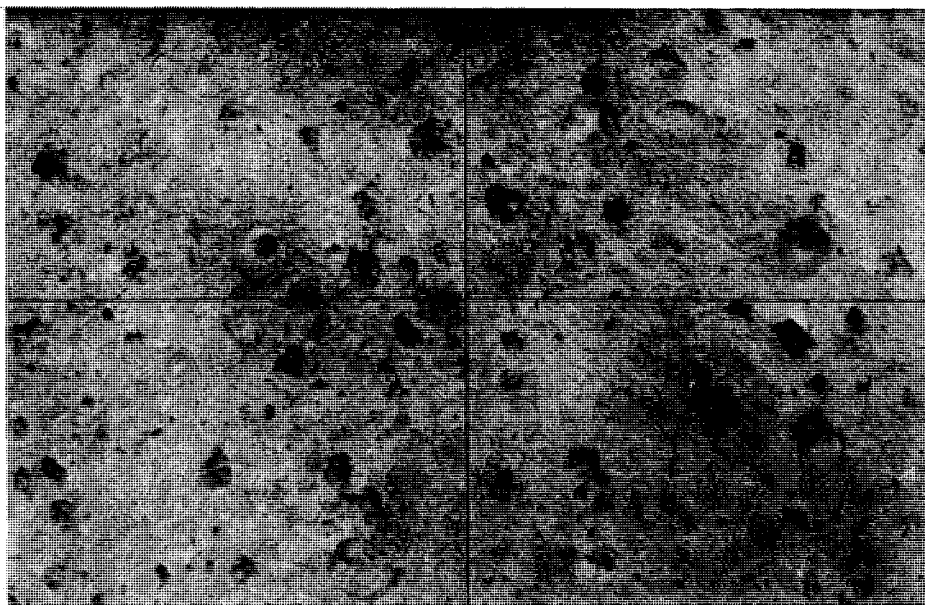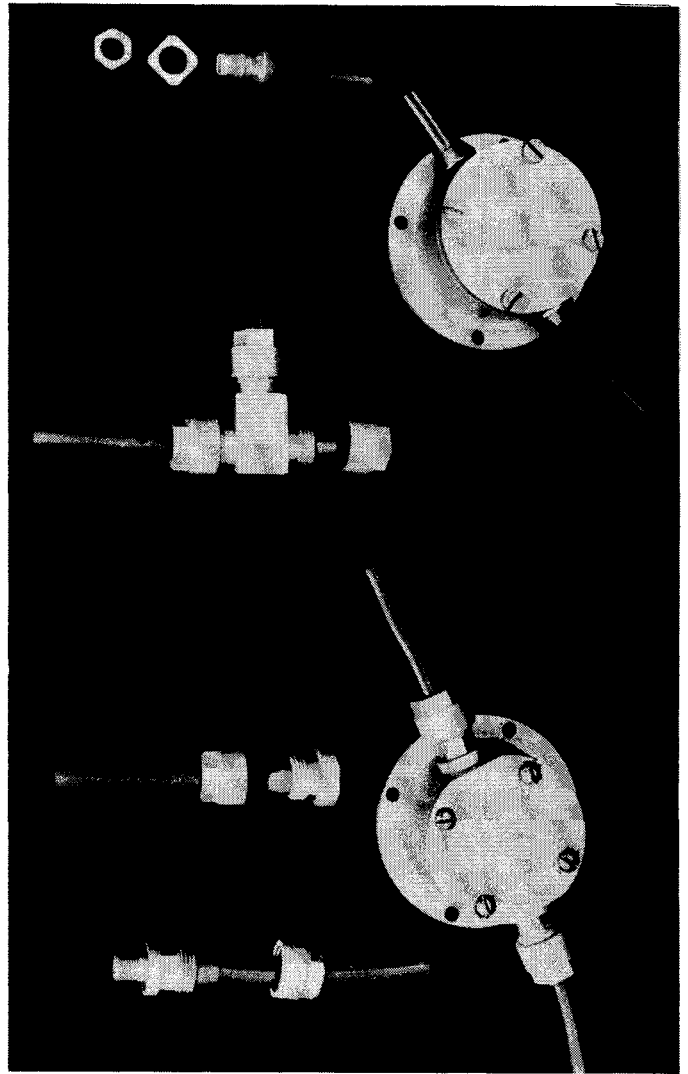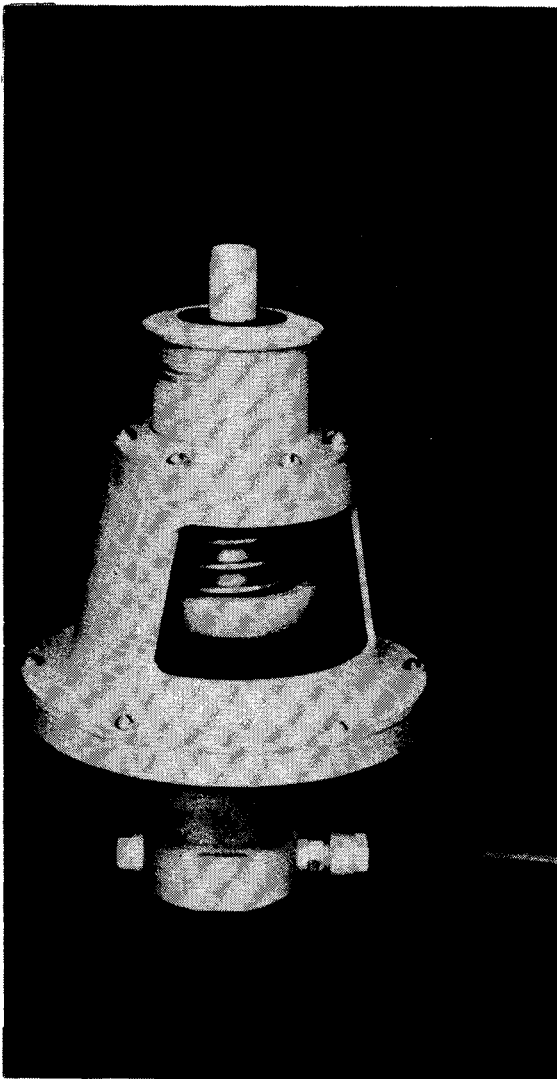
Fig.7. Pressure Compensator.
Fig.8. Elements of electric
connections.

Fig.9. Bottom photo taken by AUV MT-88,
depth 4.5 kms, height 3.0 ms.

POP-UP CARRIER WITH WATER BALLAST CELL FOR UNDERSEA RESEARCH

T. Trayanov

Institute of Oceanology, Bulgaria

Abstract

The results on making and experimenting a pop-up carriers with water ballast cell by Laboratory of Oceanographic devices of Institute of Oceanology in Varna are exhibited in this paper.

In basis of experiments (natural dimensions) carried out in a deep towing tanks in the Institute of Ship Hydrodynamic in Varna, were determined the hydrodynamic resistances of the pop-up carriers.

1. Design and mode of function

The advantages of pop-up carriers using ballast cell with water are well known. They are low price; don't throw out iron, steel, lead and/or concrete on sea bottom; the processes of taking ballast (by submerging), establishing of neutral buoyancy or the blowing the water ballast could be easily controlled.

The disadvantages of water ballast are the following: low specific weight and limited working depth, because of the high density of gases for blowing the water ballast [1].

Technological and economical calculations together with ergonomic considerations of dimensions and weights of pop-up carriers with water ballast cell demonstrated itself to be the most advantageous, when the compressed air is blowing at depth up to 200 m. By greater depths are used gas generating substances, e.g. lithium hydrates (LiH).

In case of shallow water seas, as the Black Sea and the Baltic, the vertical circulation is mostly expressed in the 0 - 200 m layer that is the productive zone of Black Sea. That is why using pop-up carriers with water ballast cell is justified for these depths.

A new moment in the application of water ballast pop-up carriers is the possibility of carring-out investigation and sampling in an intact water body by the physical field of the research vessel.

It has been elaborated in the Laboratory of

Oceanographic devices a pop-up carriers (Fig. 1) which consists of water ballast cell 1, connected with piping to hermetic body 3, to these pipes being fixed rosette 2 of electromagnetically guided water samples. In the foremost part of ballast cell is contained a signal device 6.

Hermetic body 3 contains of a measuring and recording apparatus and a block controlling the sinking. There are sensors for conductivity 4, temperature 5 and depth. Ballast cell 1 is fitted with superior and inferior controllable valves and corresponding preventing valves. At the superior part the pop-up carrier ends with lifting hook 7.

The working scheme with the pop-up carrier with water ballast cell is given in Fig. 2. Arriving at the preferred research point, the pop-up carrier is lowered to the water surface with empty ballast cell (pos. 8).
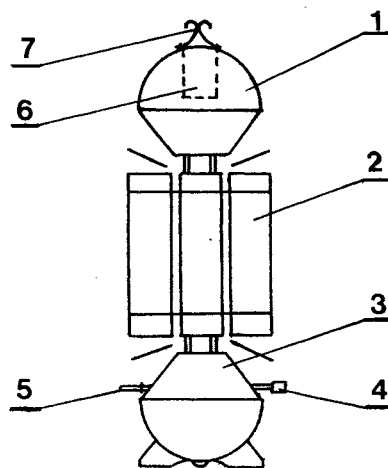
Fig. 1 General view of a pop-up carrier with ballast cell:

1 - ballast cell; 2 - rosette of water samplers; 3 - hermetic body; 4 - conductivity sensor; 5 - temperature sensor; 6 - signal device; 7 - lifting hook.
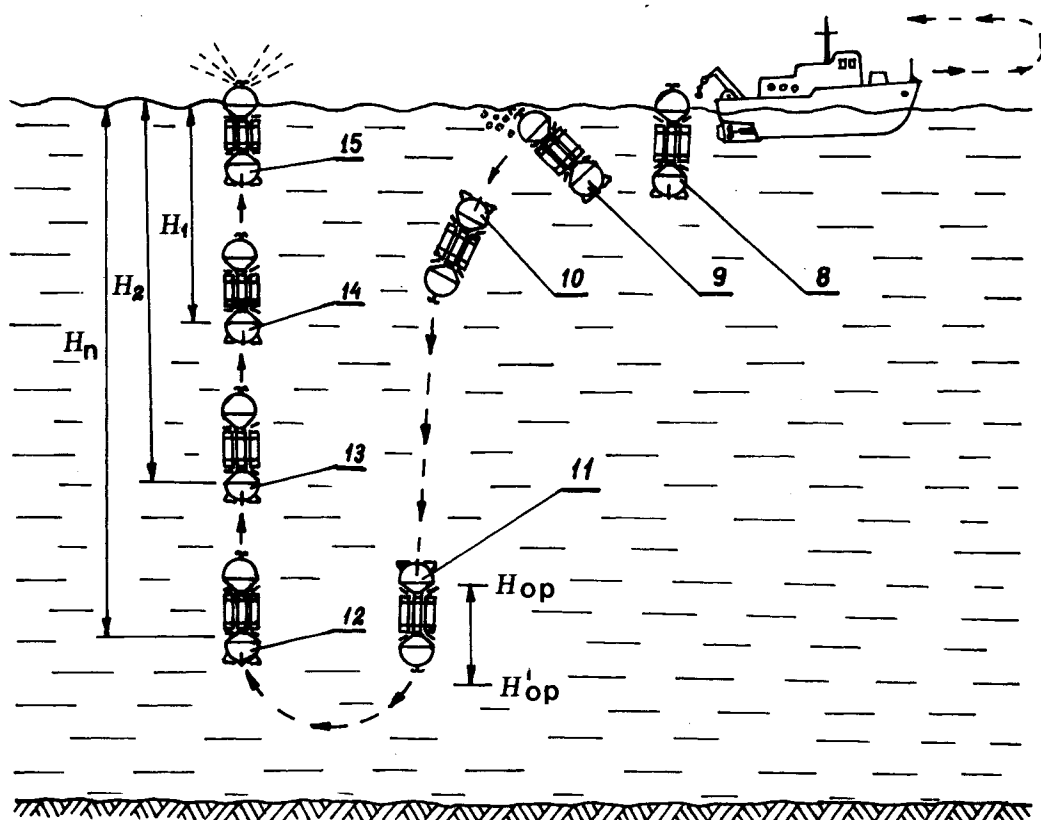
Fig. 2 Working scheme of succseding operations:
8 - lowering the pop-up carrier; 9 - begining to fille the ballast cell; 10 - turning about it axis; 11 - activating the ballast blowing system; 12, 13, 14 - sampling water probs; 15 - emerging at the surface.

The vessel navigates to some distance from which the physical field doesn't exert impact on measuring and representativiness of samples to be taken. After determines its location, that of the carrier and the direction of superficial drift, by radio signal or by gradient timer the controllable valves are activated and the ballast cell begins to be filled (pos. 9). The pop-up carrier turns about its axis and begins to sink (pos. 10). After few seconds a pressure sensor emits a signal and the controllable valves close. At the marginal depth H_m (pos. 11) is activated the ballast blowing system. In eventual defect of the system at the depth H'_m enters in action a doubling ballast blowing system.

By sinking, the conductivity, temperature and depth are measured. During the process of transition, when the carrier is inverted, a microprocesor system by selected criteria determines the depths from which samples are to be taken, when the pop-up carrier emerges, e.g. from the layer of temperature fall.

Arriving at the depth H_n (pos. 12) the first sample is taken; at the depth H_2 (pos. 13) is taken another sample and arriving at depth H_1 (pos. 14) a sample is taken with the last water sampler.

After emerging at the surface (pos. 15), a radio signal and light signal are given to make a quick detection of the carrier [3].

The pop-up carrier we constructed hase the following technical data:

Length of carrier	- 1200 mm
Diameter max	- 300 mm
Weight in air (without ballast)	- 28 kg
Ballast (sea water)	- 12 l
Operating depth	- 200 m
Speed of submerging and emerging	- 0.8-1.2 m/sec.

The rosette is equipped with four two liter water samplers.

2. Hydrodynamic investigations

The hydrodynamic characteristics of the pop-up carrier are defined experimentally for 10 combinations for front and lateral resistance depending on whether the water samplers are opened or closed. Of these, two combinations have been mounted light streamlined on the rosette with water samplers. For determining the front resistance are achieved at velocities up to 1.9 m/sec, and the lateral one - up to 1.5 m/sec.

The values of the dimensionless coefficients Cx and Cy are defined also. For velocity ranges of 0.5 - 1.2 m/sec the values of Cx can be assumed as constant (Cx = 0.52) and fall in the empirically defines limits of 0.34 for convex hemisphere to 0.89 for a circular cylinder by ratio of l/d = 4 [2].

The stability of the dimensionless coefficient Cy for lateral resistance could be admitted for the range of 0.5 - 1.4 m/sec.
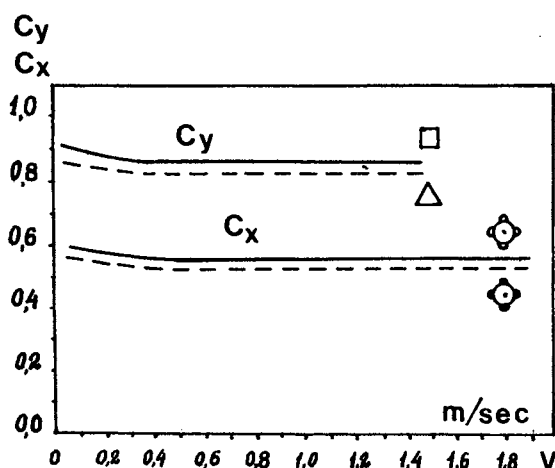
Fig. 3 Resistance coefficients of front and lateral streamlining of the carrier;

□ - with open water samplers;
△ - with closed water samplers;
◈ - with 4 open water samplers;
◈ - with 4 closed water samplers;

By given forces of resistance, weight and operating depth the velocity of submerging and emerging can be calculated, and the whole cycle of emerging and submerging too.

$$Tc = ts + \frac{Hop}{Vs} + \frac{Hop}{Vr} + ttp \qquad (1)$$

where:

Tc - whole cycle time (min.);
ts - time of filling of the ballast cell (sec);
Vs - speed of submerging (m/sec);
Vr - speed of emerging (m/sec);
Hop - operating depth (m);
ttp - time of transition process for blowing water ballast (sec).

By testing pop-up carriers in Black Sea a mean speed of submerging/emerging of 0.875 m/sec was found.

Conclusions

The pop-up carrier with water ballast cell, working after the above scheme is lowered in the sea without ballast which simplifies operating with it. The presence of a regulating system for submerging

helps to exclude the vessel impact in movement on measuring and on taking samples. The mounted microprocesor permits sample taking from scientifically important water layers.

References

1. Kontar', E. A., "Free falling systems for geological and geophisical research in world ocean", Moscow, "Nauka" (in Russian), p. 117 (1984)
2. Kochin, H. E., Kibbel, I. A. and Rose, N. V., "Theoretical hydromechanics", Moscow, "Fizmatizdat" (in Russian), app. 5 (1963)
3. Trayanov, T. K., "Pop-up carrier", Patent application № 89973, Peoples Republic of Bulgaria (in Bulgarian) (1989)

UNDERWATER ROBOT MOTION ADAPTIVE CONTROL

A. V. Inzartsev, L. V. Kiselyov, O. Yu. Ivov

Institute of Marine Technology Probelms, USSR

Abstract

Most problems solved by underwater robots, or Autonomus Underwater Vehicle (AUV), require motion organization in the seabed vicinity. The vehicle must manoeuvre actively to compensate environment disturbances and to avoid obstacles, their location being unknown as a rule. The control algorithm intended for these purposes and designed for the AUV "Sea Lion" (MT-88) is described.

Introduction

The problem of vehicle motion control in the seabed vicinity can often be reduced to reaching a target point in unexplored environment. Motion spatial character stipulates tracing algorithm specificity, demanding, besides target point reach, a number of requirements in program trajectory form to be satisfied, as follows:

- Minimal power and time expenses must be guaranteed, the trajectory being correspondingly minimal in length;

- AUV motion trajectory must in many cases be equidisant to seabed relief, it must follow relief profile along the equidistant motion trace;

- Environment perturbations and forces disturbances (buoyancy, steadiness) varying are to be compensated when equidistant moving;

- Limitations for maximal possible tangage caused by vehicle main propulsors must be taken into consideration.

Carrying out such type of trajectories requires AUV simultaneous manoeuvre in horizontal and vertical planes. Motion control in the underwater robot MT-88 is accomplished by an on-board computer coupled with a block of five acoustic sonars. At each control cycle the trajectory is calculated a step in advance that permitted to create a comparatively simple algorithm with little single control cycle. The approach adopted doesn't imply surface scanning and leads to the simpler task of relief approximation by planes sections calculated through sonar data. Herein surface parameters determining subsequent motion direction are calculated for each step within direct visibility. In other words AUV total trajectory can be presented as a series of segments, each optimizing the way relative to adjacent plane elements approximizing visible relief surface in a certain trajectory point. Thus, the following operation succession is carried out for a single control cycle:

- surface parameters determined ;
- motion direction calculated ;
- motion towards calculated "optimal" straight line organized.

1. Surface Parameters Determination

Let us present the surface as a function $Z(x, y)$ in Cartesian coordinates system. The vehicle position is set by the point Pa over the surface $Z(x, y)$. When creating a relief model we shall study the forms, their minimal dimensions exceeding those of AUV. We substitute function $Z(x, y)$ in the point (Pax, Pay) for its first differential, i.e. approximate the surface in the point locality by a tangent plane with a normal vector $N = (Nx, Ny, Nz)$ and displacement D.

Surface parameters are determined in coordinates system $Axyz$ connected with AUV body. Sonar sighting lines have constant orientation in this system. We

admit Dl, Df, Dr, Db, Ds for measuring vectors of left, front, right, bottom and slanting sonars correspondingly.

Left (right), slanting and front sonars are used to identify plane relief surfaces discovered ahead along the motion trace. Thereby two planes are identified for which left and right sonars data, correspondingly, is applied. The normal vector of each plane is expressed by the corresponding vector product:

$$N = [(Df-Dl) * (Df-Ds)]$$
$$N = [(Dr-Df) * (Df-Ds)]$$

A group of sonars including left (right), slanting and bottom ones are used in all the rest cases when there occurs no obstacle along the travel trace. The normal vector of each plane is calculated for this group the following way:

$$N = [(Dr-Db) * (Ds-Db)]$$
$$N = [(Ds-Db) * (Dl-Db)]$$

Surface normal mean value in the given point is calculated by two normal vectors, thereafter plane displacement D is determined for said point.

2. Travel Direction Finding

Assume the longitudinal axis of AUV in the point Pa to be oriented in the direction of velocity vector V. We express range to the bottom determined in the direction E perpendicular to AUV longitudinal axis. Suppose the vehicle list to be zero, "equidistant" vector is found through the following equation system:

$$V * E = 0$$
$$E * [K*V] = 0$$
$$(Pa+E)*N + D = 0$$

where K is the vector (0,0,1). The system solution can be presented as functional dependence E=E(Pa,V).

Let's find travel direction "optimal" for the present plane. It is generally known that a line of minimal length connecting two surface points is a geodetic one. The main geodetic line normal coincides in every point with the surface normal, each point being crossed by a single line in the definite direction. Thus, it is necessary to satisfy two requirements for AUV trajectory to be geodetic:

- AUV must be perpendicularly oriented to the surface normal in every point;

- the angle included between direction to the target A and travel direction being determined L must be minimal. In other words, the trajectory must lie in the plane crossing A and N.

The abovementioned conditions result in equation system:

$$|L| = 1$$
$$A + t*N = L$$
$$N*L = 0$$

Hence, $L = (A-N*(N*A))/SQRT(1-(N*A)^2)$.

Moreover, the trajectory achieved must meet the following requirements: the distance to the bottom must equal datum E = const. So one more equation system is to be solved:

$$|E(P,L)| = E$$
$$P = Pa + t*N$$

where the second system equation is applied to determine the starting point P of vector L. The calculated starting point P and vector L uniquely define the "optimal" straight line.

When solving said system, no restrictions were imposed on Lz (i.e. tangage increase). It was specially done to simplify L and P cyclic calculation procedure. As a result of calculations we can obtain Lz corresponding to tangage angle exceeding the permissible value. Therefore, on getting the result we should check up whether threshold T set for tangage PSI is exceeded.

In case |PSI+arcsin(Lz)| < T is not satisfied, the permissible direction is to be recalculated on condition that Lz = sin(T*sign(Lz)-PSI). The other vector L components can be found by solving the following system:

$$|L| = 1$$
$$N*L = 0$$

3. Motion Organization

3.1 Motion in Horizontal Plane

To get out arbitrary initial position to a determined equidistant segment we create the condition supervising included angle ALPHA between vehicle longitudinal axis direction and vector L, and distance DELTA from vehicle to equidistant, exactly speaking, to its projection on longitudinal horizontal plane.

It is expedient to carry out hitting to the equidistant by means of circular movements. Two AUV position variants relative to the adopted

projection are possible:

a) vehicle "head" to projection. In this case direct hit to equidistant by circle is possible.

b) vehicle "stern" to equidistant. The situation implies preliminary vehicle turning with maximal possible angular velocity, until point a) is realized.

If the condition $|DELTA| < d$ is satisfied, control is carried out through DELTA and ALPHA displacements. Strictly speaking, this motion "in a tube" proves to be principal, since after hitting to equidistant value DELTA fluctuates about zero.

3.2 Motion in Vertical Plane

To organize underwater robot control in longitudinal vertical plane, a regulator with etalon and predictive models is used which provides vehicle real and programmed motion proximity.

The following steps are realized for adaptive regulator synthesis:

− constructing etalon motion model setting controlled object desired behaviour;

− carrying out predicted motion based on state vector measurement of cotrolled object;

− forming control minimizing Euclid norm of difference of predicted and etalon motion.

The controlled object is described in terms of state space by the differential equations system:

$$\dot{X} = A*X + B*U + R, \qquad (1)$$

where $X = [Ψ, \dot{Ψ}, Ʋ, H]$ is object state vector in vertical plane;
Ψ − tangage;
$\dot{Ψ}$ − tangage velocity;
Ʋ − trajectory angle ;
H − depth;
A − 4 x 4 dimension matrix;
B − 4 dimension vector ;
U − scalar control;
R − generalized disturbances vector composed of external physical disturbances and disregarded object model errors.

We set etalon motion X in the same forms as real motion (1) but having constant parameters A and B, not taking into account external disturbances:

$$\dot{Xe} = A*Xe + B*Ue \qquad (2)$$

State vector X is easy-measured in time tact moments $t[k]=k*T$, where T is measuremed procedure discretization period. Scalar control U at "k"-th step

of process $(k-1)*T < t < k*T$ is constant and equals $U[k]$.

We introduce predicted motion Xp, its model differing from real motion (1) in the presence of predicted disturbance Rp:

$$\dot{Xp} = A*Xp + B*U + Rp \qquad (3)$$

the initial condition $Xp[k]=X[k]$, where $X[k]$ is state vector in moment of time $t[k]$.

Equation system (2) and (3) solving is done by numerical integration with period T.

Disturbance vector can be determined through analysis of travelled trajectory part $X[k]$, $X[k-1]$... As for predicted disturbance, we calculate it by linear extrapolation:

$$Rp = 2*R[k] - R[k-1], \qquad (4)$$

where $R[k]$, $R[k-1]$ are mean disturbance values at $t[k]$ and $t[k-1]$ travel steps.

Control $U[k]$ providing predicted (3) and etalon (2) motion proximity results from the following condition:

$$|| Xp[k+1] - Xe[k+1] || = min\ U[k+1]$$

$$0.5*Q*U*U + 0.5*(Xp[k+1]-Xe[k+1])^T * G*(Xp[k+1]-Xe[k+1]) = min\ U[k+1] \qquad (5)$$

where Q − weihting coefficient;
G − positively defind diagonal matrix;
Object control is found in the form:

$$U[k+1] = Ue[k+1] - L^T * (X[k]-Xe[k]) - S*Rp$$

where $Ue[k+1] = C^T * (Xe[k]-Xz[k])$ − etalon linear control;
$L(A, B, G, Q, T)$, $S(A, B, G, Q, T)$ − weighting vector determined in (5) ;
C − feedback weighting vector;
Xz − program trajectory;
$Xz1[k] = Ψz[k]$ − program tangage formed by the abovementioned algorithm;
$Xz2[k] = 0$,
$Xz3[k] = 0$,
$Xz4[k] = Hz[k]$ − program depth.

Program depth Hz is formed based on ranges found by sonars Di, $i = 1...5$ and program stabilization height Dz:

$$Hz[k] = H[k] + CD^T * D[k] - 5*Dz[k]$$

where $D[k] = (Dl, Df, Dr, Db, Ds)$ − distances vector by sonars;
CD − angular cosines vector (angles between Db and corresponding sonars).
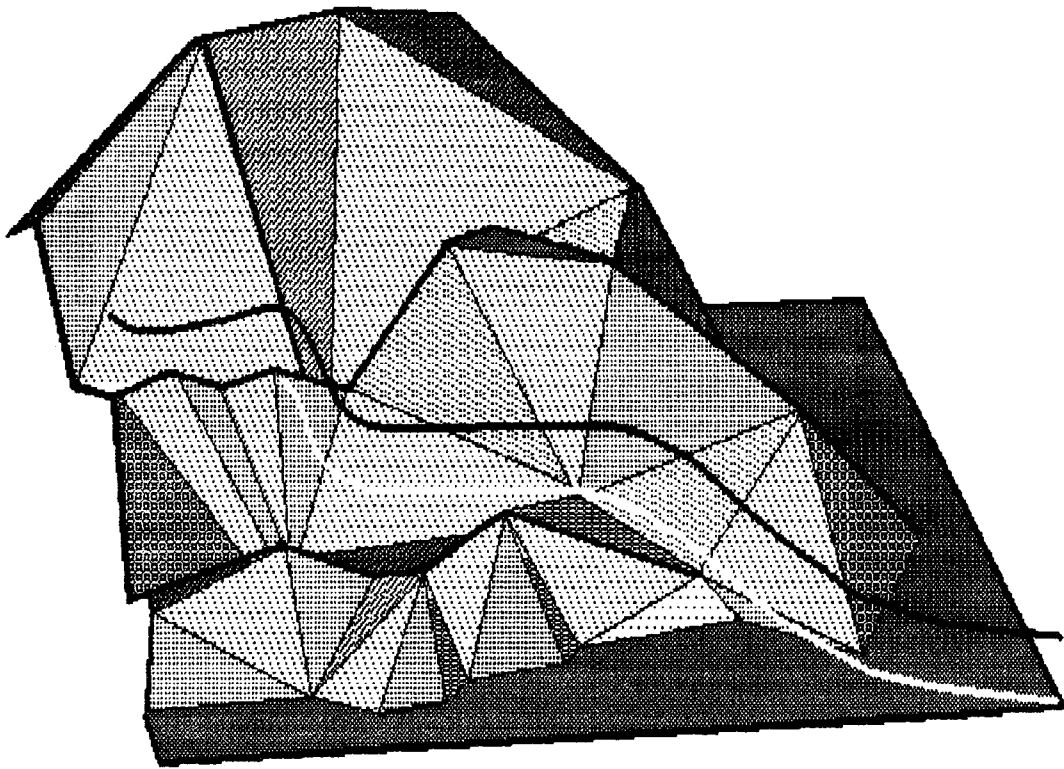
Fig.1 Isobath trajectory part
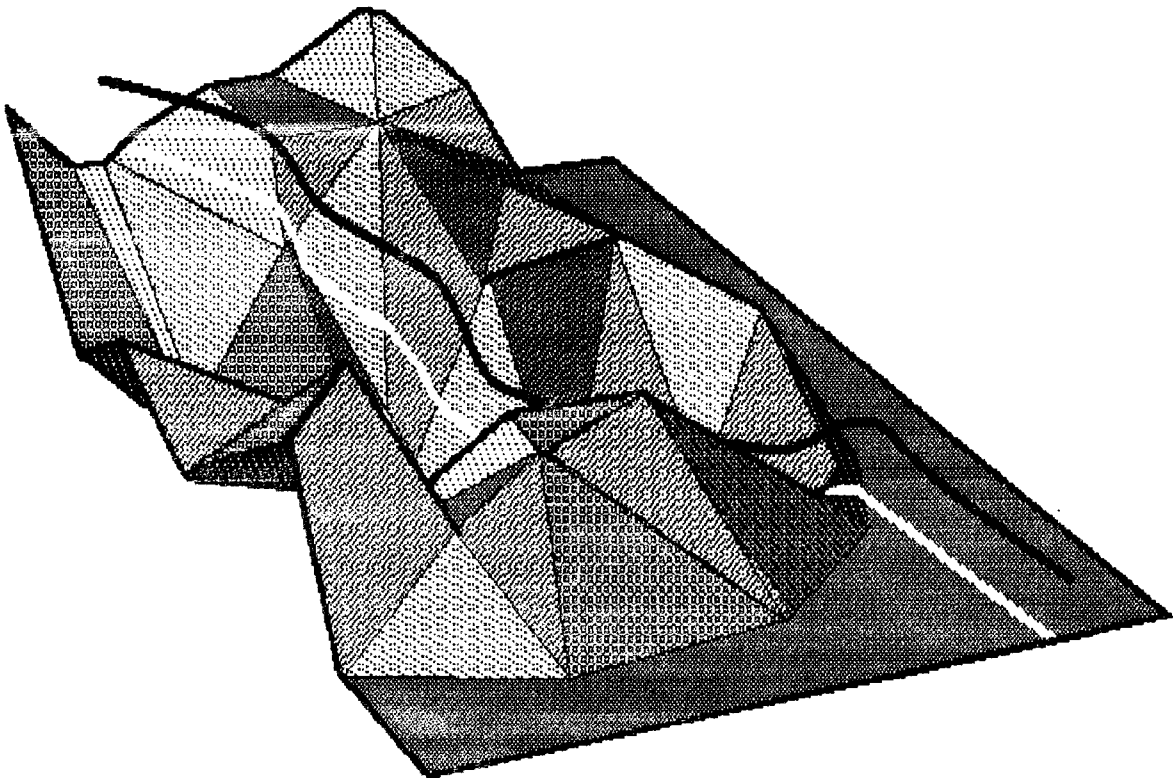
Fig.2 Final trajectory part

4. Motion Simulation in Computer

Control algorithm investigation was carried out by means of mathematical simulation. Model structure comprises environment model (3D relief surface), vehicle sonar system model, vehicle kinematic and dynamic models and motion control model. Some results illustrating algorithm operation are presented in Fig.1 and 2 demonstrating two fragments of one motion.

Fig.1 presents a still of relief surface projected on plane OXY in a form of square. Blackening degree of surface elements in inverse proportional to angle of view value at which this or that surface area is visible to the observer. In the selected model scale relief height makes 60 ms, motion height set for AUV is 10 ms, starting point in lower right angle. Finishing point is located so that slope is in the vehicle motion path. As it is shown in Fig.1, slope

steepness being little, AUV travelled to the target along equidistant in the vertical plane. When the steepness sharply increased, the vehicle started horizontal manoeuvring, moving by isobath trajectory, and thus, avoiding the obstacle from the left. To demonstrate it more clearly, we showed except the main trajectory its projection to relief.

Fig.2 illustrates the final trajectory part, finishing point being in the right angle. Projected area makes 120 x 120 ms in dimensions. AUV is first seen to lower in the gently sloping crater, thereafter - manoeuvre into the cavity between two heights. The height nearest to observer covered a part of trajectory with itself. Having passed the cavity the vehicle descended serpentinelike to the base plane (as slope stepness didn't permit stright movement). On reaching flat seabed, AUV continued travelling to target along straight line.

HIGH PERFORMANCE HYDROFOIL CATAMARAN

Masakazu Kaji*

* Kawasaki Heavy Industries, Ltd., Japan

Abstract

A high performance hydrofoil catamaran is being developed by Kawasaki Heavy Industries, Ltd. The hydrofoil catamaran consists of two sidehulls and fully submerged hydrofoils placed between the sidehulls, and it is supported by both hydrofoil lift and sidehull buoyancy. The hull form is designed to be thin to reduce the wave making resistance and the wave exciting force, and the foil is designed to have a high aspect ratio to increase the ratio of the lift to drag.

Provided with an active control system, the ship controls the motions of heaving, pitching and rolling, and relative bow height in order to achieve superior seakeeping performance including comfortable ride in rough sea.

As a result of investigations including tank tests, the hydrofoil catamaran has been found attractive to a high speed cargo ship, passenger ferry, car ferry, etc.

The resistance, ship motion and other characteristics of the ship are presented in this paper.

1. Introduction

To respond to the need for high speed transportation, a high performance ship is being developed. The targets of this development are as follows:

1. Adaptable to large ships (max. full loaded weight of abt. 3000 t) as well as small ships
2. High speed (max. speed of abt. 40 knots)
3. Low resistance
4. Superior seakeeping performance
5. Technically simple system
6. Low construction cost

As a result of feasibility study on various conventional ship forms, it has been found that the hydrofoil catamaran, whose weight is supported by both hydrofoil lift and hull buoyancy, is more suitable for the above targets. Tank tests were carried out to investigate resistance in still water and waves, ship motions and loads in waves and maneuverability, and the structural analysis was also made.

As a result of these investigations, it has been confirmed that this concept is feasible.

2. Configuration of Concept

The hydrofoil catamaran has twin sidehulls with fully submerged hydrofoils mounted in tandem between the sidehulls as shown in Fig.1.

The ship is supported by both hydrofoil lift and hull buoyancy.

HYCAT [1], HC-200 [2], HC-2000 [3], etc. were designed on the nearly same concept as the above one.

The percentage of hydrofoil lift is determined taking account of resistance and ship motions in rough sea. The sidehull form is designed to be thin to reduce the wave making resistance and the wave exciting force. The foils have a high aspect ratio to increase the ratio of the lift to drag.

As the ends of the foil are connected to the sidehulls, the sidehulls work as endplates of the foil, which reduces the induced drag.

Also, the foil is used as a structural tie between the sidehulls to reduce the stress on the hull.

When the foil is used as a structural tie, the structural weight of the foil increases because the load acting on the foil becomes severe, that is, wave loads acting on the sidehulls are transmitted to the foil in addition to member loads of lift, cross flow drag, etc. But the hull structural weight can be decreased. Therefore the weight of the hull with foils is made lighter than that of the conventional catamaran.

Center struts are provided to decrease the bending moment acting on the foils. The strut can be used as a vertical rudder.

As a propulsion system, the propeller is adopted because the propulsive efficiency of the propeller is superior to that of the water jet as shown in Fig.2 [4] in the speed range of this concept.

The engine, propeller shaft, gear, etc. are installed inside the sidehulls. Therefore the form of the sidehulls may not be the most suitable in view of resistance, especially in the case of a small-size ship, but less propulsive horse power is required than in the adoption of the water jet propulsion system or other systems because of the higher propulsive

efficiency of the propeller.

This concept ship is self-stabilizing because statical stability in heave, pitch and roll are kept by the sidehulls only. Superior seakeeping performance is also achieved in the rough sea condition because ship motions are controlled by the control system using the hydrofoils.

A small high-speed ship is designed as shown in Table 1 and Fig.1 to investigate this concept.

Table 1 Particulars of prototype ship

Lpp Bmax D			26.0m 13.0m 4.8m
Foil borne	d Disp. Lift F. Vs	abt. abt.	2.0m 70t 100t 35kts
Hull borne	d Disp Lift F.	abt.	3.5m 170.0t 0t
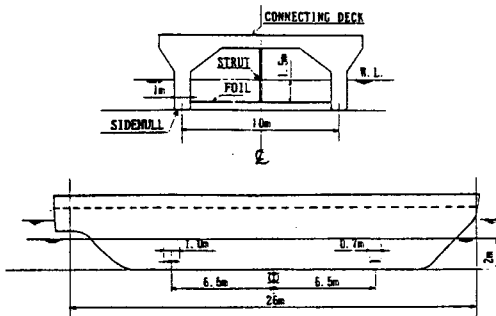
Fig. 1 Configuration of hydrofoil catamaran

SPEED (KNOTS)
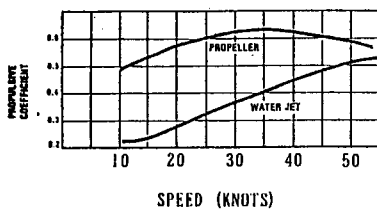
Fig. 2 Propulsive Coefficient
(From Ref. [4])

In the case of the small high-speed ship, the higher the ratio of the dynamic lift is, the lower the resistance and the better the sea-keeping performanace becomes. The size of the sidehulls is made minimum enough to install the propeller shaft, gear, etc.

As a result, the percentage of the dynamic lift is about 59%, and that of the buoyancy is about 41%.

3. Tank Test

To confirm various performances of this concept ship experimentally, the tank tests were carried out at Akashi Ship Model Basin in 1987. Resistance tests, ship motion tests, wave load tests and PMM tests were conducted.

In this paper, the resistance and ship motion tests out of these tests are described.

The aims of the resistance tests are to estimate the total resistance of the prototype ship shown in Table 1 and to establish the technique to predict the resistance of this concept ship.

And the aims of the ship motion tests are to ascertain that the ship motion can be decreased by active control and to confirm the validity of the ship motion prediction theory.

At the resistance tests, scale models of 1/10 and 1/20 were used, and at the ship motion tests a scale model of 1/10 was used. Particulars of the models are shown in Table 2.

The ship speed of the prototype ship is 35 knots, but the motion tests were carried out at the speed of 25 knots based on the full scale ship because of the speed limit of the towing device. The area of the foil of the model ship is determined to be 1.50 times as large as the designed value to get the designed dynamic lift at this test speed.

As hydrodynamic characteristics of the foil are very important for this concept ship, both models are designed so that the dynamic lift and the drag of the foil can be measured separately from the hull to analyze the hydro-dynamic force of the foil.

Table 2 Tank test model

		MODEL I (RESISTANCE TEST)	MODEL II (MOTION TEST)
Scale		: 1/20	1/10
L B max d		1.30 m 0.65 m 0.10 m	2.60 m 1.30 m 0.20 m
FOIL		NACA 643 - 618	NACA 643 - 618
FORE	SPAN CHORD t/c	0.45 m 0.035m 0.18	0.90 m 0.105m 0.18
AFT	SPAN CHORD t/c	0.45 m 0.035m 0.18	0.90 m 0.15 m 0.18
WEIGHT XG lcb Radius of longitudinal gyration		— — — —	176.5 kg 0.376m 0.095m 0.806m

3.1 Resistance

The resistance test was carried out in the condition of the hull being fixed and the attack angle of the foils being changed according to the ship speed. The resistance and the lift of the whole hull and those of the fore and aft foil were measured separately.

The coefficients of the total resistance of the 1/20 scale model including the foil drag are presented in Fig.3 as a function of Froude number based on volume $(Fn\nu=V/\sqrt{g\cdot\nabla^{1/3}})$.

At Froude number below 2.0, the total resistance coefficient (C_T) decreases nearly in proportion to Froude number. At the high Froude number over 2.0, the ratio of C_T reduction to Froude number becomes small. At the high Froude number, therefore, it is better to increase the percentage of the foil lift supporting the ship in order to decrease the resistance.

$$C_T = R_T/\tfrac{1}{2} \cdot \rho \cdot V^2 \cdot \nabla^{\frac{2}{3}}$$
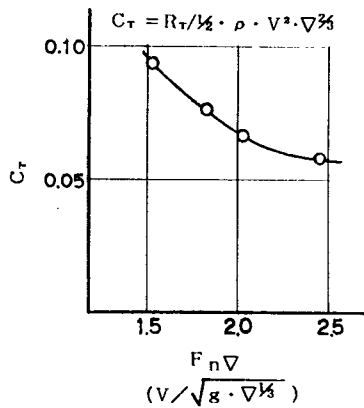
Fig. 3 Total resistant coefficient

In the case of the prototype ship in Table 1, the designed Froude number is 2.44, and so the resistance can be decreased by the increase of the percentage of the foil lift supporting the ship and the decrease of the size of the sidehull. In this case, a propeller, which has higher propulsive efficiency than any other system, can not be adopted because of inadequate space in the sidehulls to install the propeller shaft, gear, etc. and as a result the propulsive horse power increases more than that of the prototype ship in Table 1.

Fig.3 shows that a suitable Froude number for this concept is about 2.0 or below, which means this concept is especially advantageous to a large size high speed ship.

The resistance of the ship in Table 1 is calculated based on the tank test results and its components are shown in Table 3.

Because the sidehull form is designed to be thin and the foils with high aspect ratios (12.85 for the fore foil and 9.0 for the aft foil) are used, both the percentage of the wave making resistance and that of the foil drag are small.

On the other hand, the frictional resistance is much larger than other components.

In a high-speed ship, measures to decrease the frictional resistance are very important.

Table 3 Drag breakdown

HULL	VISCOUS	FRICTION	46 %
		OTHERS	8 %
	WAVE		12 %
	WIND		3 %
FOIL & STRUT			31 %
TOTAL			100 %

3.2 Motion

The motions are controlled by the use of the hydrofoils supporting the ship as described in "2. Configuration of Concept".

Three controlling modes are adopted as shown below:

(1) Platforming mode
    To get comfortable ride by decreasing ship motion.

(2) Contouring mode
    To keep a constant relative bow height between the bow and the water surface in order to prevent slaming at high waves.

(3) Bank mode
    To bank the ship to make co-ordinate turn.

Regarding the longitudinal motion both in an uncontrolled condition and in a platforming control condition, the outline of the ship motion prediction theory, comparison between experimental values and theoretical ones, and comparision of ship motions between this concept and a conventional displacement type monohull ship are described in this section.

The tank tests were carried out with the pitching and heaving motion being free and the surging motion being fixed both in the uncontrolled condition and in the controlled condition.

The purposes of this tank tests are to examine the motion prediction theory in both conditions, and to investigate relations between control gain and the motion. Various control gains are used in the motion control tests to investigate the above relations and so the control gain is not the most suitable in view of decreasing the ship motion as much as possible.

The state feedback control method is applied as shown in Fig.4 Block diagram.
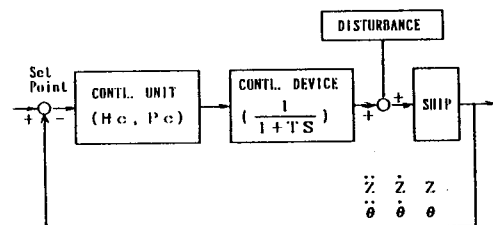
$$H c = K_{31}\ddot{Z} + K_{32}\dot{Z} + K_{33}Z$$
(Control force for heaving motion)

$$P c = K_{61}\ddot{\theta} + K_{62}\dot{\theta} + K_{63}\theta$$
(Control moment for pitching motion)

Fig. 4 Block diagram

The ship motion equation on the frequency domain in the open loop condition is shown below.

The coordinate system is a right-handed rectangular coordinate system.

The coordinate system moves horizontally in the direction of the mean course of the ship with the mean speed of the ship.

$$(M+A_{33})\ddot{Z}+B_{33}\dot{Z}+C_{33}Z+A_{35}\ddot{\theta}+B_{35}\dot{\theta}+C_{35}\theta=F_3 e^{i\omega t}$$

$$(I_5+A_{55})\ddot{\theta}+B_{55}\dot{\theta}+C_{55}\theta+A_{53}\ddot{Z}+B_{53}\dot{Z}+C_{53}Z=F_5 e^{i\omega t} \quad (1)$$

Here Z and θ are the displacement of heave and pitch respectively, M is mass, I_5 is

inertia about pitching motion, Aij is added mass or inertia, Bij is the damping, Cij is restoring constant, F_3 and F_5 are the complex amplitude of heaving force and pitching moment respectively.

The following hydrodynamic forces and hydrostatic force are considered in the above ship motion equations (1).

(a) Hydrodynamic force obtained under non-lifting potential flow assumption
(b) Lift
(c) Viscous damping force (cross flow drag)
(d) Restoring force (hydrostatic force)

The strip method is used to calculate the hydrodynamic force in (a).
The boundary value problem is solved by the source technique with the interaction between the sidehulls being considered.
The lift of the hydrofoil in (b) is calculated in consideration of memory effect.

The Theodorsen function C(K) stands for the memory effect of the hydrofoil due to free voltex in an unsteady condition [5][6][7].

$$C(K) = \frac{H_1^{(2)}(K)}{H_1^{(2)}(K)+jH_0^{(2)}(K)} \qquad (2)$$

$$= F(K) + jG(K)$$

K : Reduced frequency

$H_n^{(2)}$: Hankel functions of the second kind

The diagram of this function is shown in Fig.5. Relations between the wave length (λ) and the reduced frequency (K) of the aft foil of the prototype ship in Table 1 are also shown in Fig.5.
The wave length is made nondimensional by the ship length (L).
As seen from Fig.5, this concept ship is operated in the wave frequency bound greatly influenced by the memory effect due to free voltex.
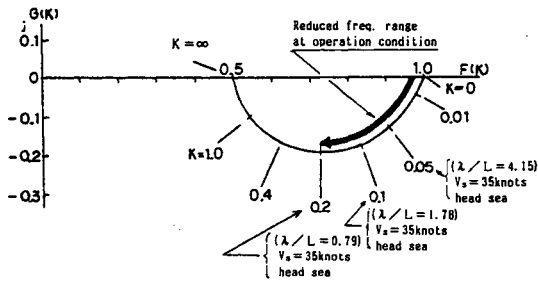
Fig. 5 Theodorsen function

Therefore the ship motions in both the uncontrolled and the controlled conditions are affected by the memory effect of the hydrofoil. Comparison between experimental and calculated values of heaving and pitching motions in the uncontrolled condition is shown in Fig.6 and Fig.7. The ship speed is 25 knots and the wave direction (χ) is head sea (180°).

The amplitude of heaving motion (Za) and that of pitching motion (θa) are presented as a function of the wave length (λ).
And these three are made nondimensional by the wave amplitude (ζa), the wave slope ($k_0\zeta$a) and the ship length (L) respectively.

To know the degree of the memory effect on the ship motion, the calculated values without the memory effect are also presented in those figures. (Fig.6 and Fig.7)

Good agreement between the experimental and calculated values with the memory effect is achieved. On the other hand, the calculated values without the memory effect are different from the experimental ones. Therefore the memory effect of the hydrofoils affects the ship motion greatly.
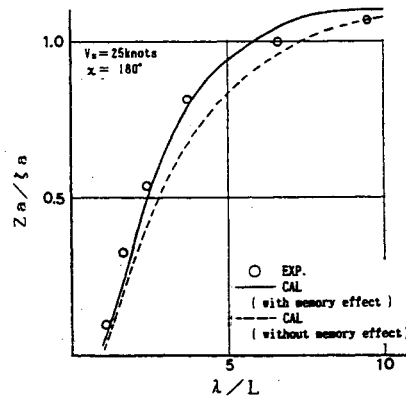
Fig. 6 Heaving motion amplitude
in uncontrolled condition
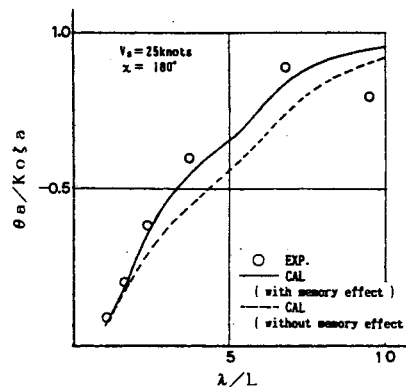
Fig. 7 Pitching motion amplitude
in uncontrolled condition

In the conventional SWATH ship with control foils, as the ratio of the hydrodynamic lift of the foils to the total hydrodynamic force is very small, the calculated values well agree with the experimental ones without any consideration of the memory effect of the foils [8].
In this concept ship with large foils, however, it is important to consider the memory effect so as to predict the ship motion.
Comparison between experimental and calculated values of the vertical acceleration per unit wave amplitude at the bow and the

stern is shown in Fig.8 and Fig.9. The unit of acceleration is gravity acceleration g (9.1 m/sec^2). Both values agree with each other well.
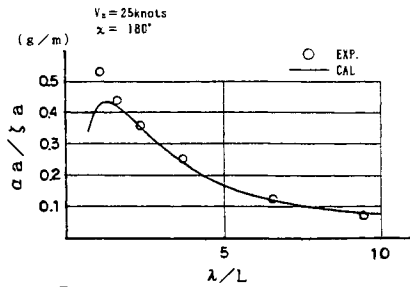
Fig. 8 Vertical acceleration at FP in uncontrolled condition
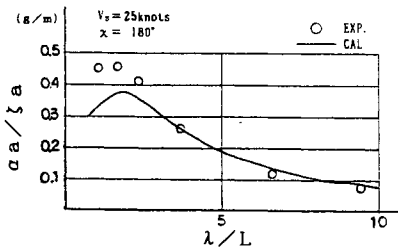
Fig. 9 Vertical acceleration at AP in uncontrolled condition

The control method is a state feedback control, and acceleration, velocity and displacement of heave and pitch are feedback variables as shown in Fig.4 Block diagram. The closed loop motion equation in frequency domain is shown below.

$$\begin{pmatrix} H_{33} & H_{35} \\ H_{53} & H_{55} \end{pmatrix} \begin{pmatrix} Z \\ \theta \end{pmatrix} = \begin{pmatrix} F_3 \\ F_5 \end{pmatrix} - \frac{1}{1+j\omega T} \begin{pmatrix} CK_{33} & CK_{35} \\ CK_{53} & CK_{55} \end{pmatrix} \begin{pmatrix} G_{33} & 0 \\ 0 & G_{55} \end{pmatrix} \begin{pmatrix} Z \\ \theta \end{pmatrix} \quad (3)$$

H_{ij} : Hydrodynamic Coef. of hull and hydrofoil

F_i : Wave exciting force

$\frac{1}{1+j\omega T}$: Control device (1st order lag)
  T : Time constant

CK_{ij}: Memory effect coef. of control surface

G_{33} : Heave control gain

G_{55} : Pitch control gain

The characteristics of such control devices as the actuators and the flaps are replaced approximately by the 1st order lag.

Ckij are coefficients due to the memory effect of the foils.

CK_{35} and CK_{53} mean the pitch control force becomes disturbance to the heaving motion and the heave control force becomes disturbance to the pitching motion. In case the reduced frequencies of the both foils are same, both CK_{35} and CK_{53} equal zero. Therefore it is necessary to determine the control gain with much consideration of the memory effect.

Comparison between the experimental and calculated values of the heave, pitch and acceleration in the controlled condition is shown in Fig.10, Fig.11, Fig.12 and Fig.13 in the same way as in the uncontrolled condition.

As seen from these figures, the experimental values agree with the calculated ones very well. In the controlled condition as well as in the uncontrolled condition, validity of the theory is confirmed.

The motion performance of this concept ship is evaluated by this theoretical calculation.

The response functions of the vertical acceleration at the bow, the pitching and heaving motion of this concept ship of total weight 170 t type described in Table 1 calculated by this theory are shown in Fig.14, Fig.15 and Fig.16.

Calculation conditions are the ship speed of 35 knots and the wave direction of head sea(χ=180°)
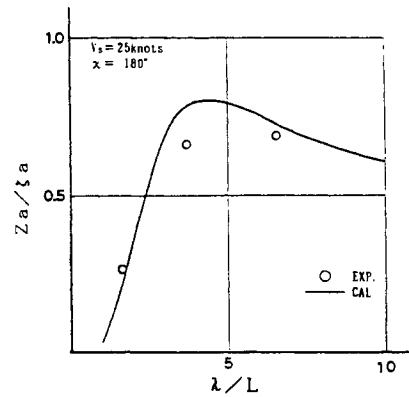
Fig. 10 Heaving motion amplitude in controlled condition
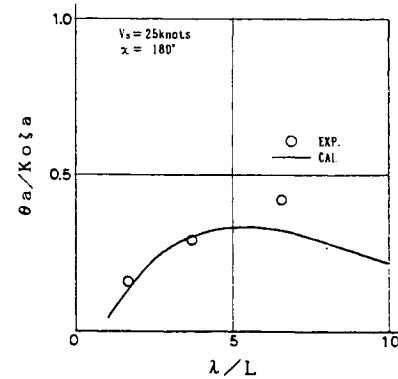
Fig. 11 Pitching motion amplitude in controlled condition
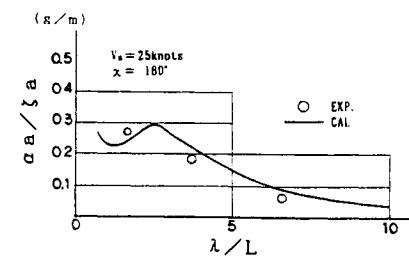
Fig. 12 Vertical acceleration at FP in controlled condition
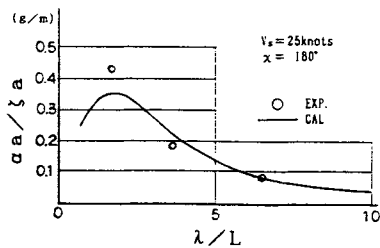
Fig. 13 Vertical acceleration at AP
in controlled condition

To compare these values with those of the displacement type monohull ship, the response functions of the monohull ship (L = 38.57 m, ∇ = 168 m^3, ship speed = 34.96 knots) shown in Ref. 9 are added in the above figures.

This concept ship has much smaller motion than the displacement type monohull ship even in the uncontrolled condition, and besides this motion can be more decreased by control. This concept ship has superior seakeeping performance.
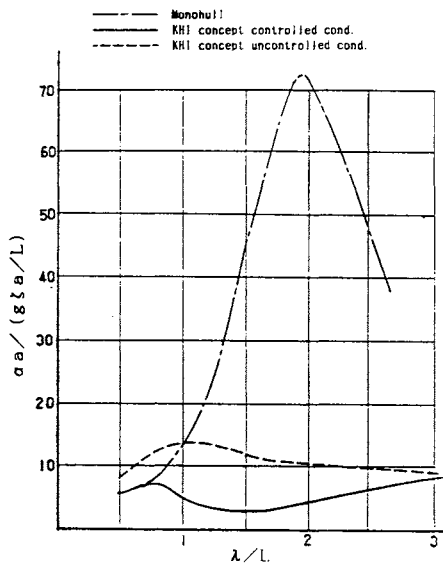
Fig. 14 Comparison of acceleration at FP
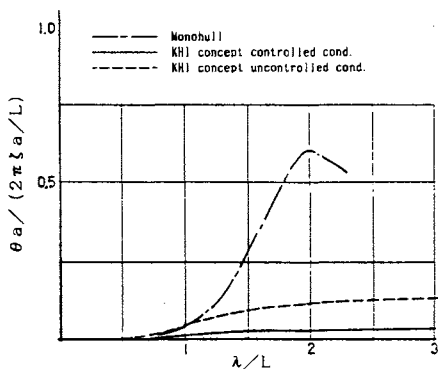
Fig. 15 Comparison of pitching motion
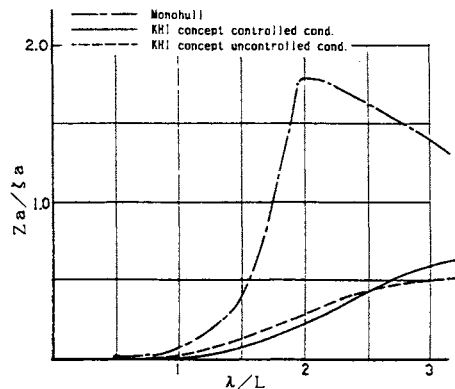
Fig. 16 Comparison of heaving motion

The aim of this control system is to decrease acceleration. Therefore, as it is more efficient to make the pitching motion smaller than the heaving motion, the control gain is determined so that the pitching motion can be decreased more than the heaving motion. If the aim of the control is to make the heaving motion much smaller, the heaving motion in the controlled condition can be decreased more.

4. Hull Structure

It is necessary especially for this concept ship to increase the structural reliability and to lessen the hull weight as much as possible. So the hull must be designed based on the accurate loads and structural model.

The structural analysis system was established as shown in Fig.17.

The hull structure of the prototype ship was analyzed by the above system using a 3-D panel model in Fig.18. The structural characteristics of this concept ship were understood clearly.
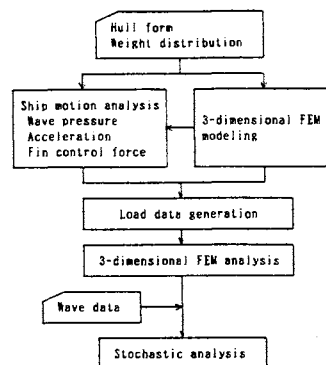
Fig. 17 Rough flow of analysis
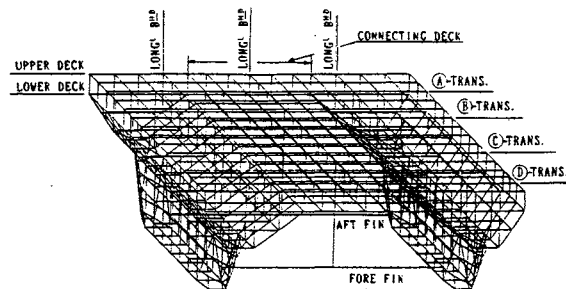
Fig. 18 Model configuration

The split force, yaw connecting force, racking force and torsional moment are important loads for the design of the structure as well as in the conventional catamaran. However, the structural responses of this concept ship to the above loads are quite different from those of the catamaran.

As the foil is used as a structural tie between the sidehulls (original model), the stress on the hull due to these loads becomes about one third of that acting on a model, where the foil is not used as a structural tie (separated foil model) as shown in Table 4 [10]. Structural behavior of the separated foil model is nearly the same as that of the conventional catamaran.
Therefore, the hull weight can be decreased from that of the conventional catamaran.
As the hydrofoils are important structural members, they must be designed by analyzing fatigue, buckling, etc. to get high reliability.

Table 4 Comparison of typical stresses of original
model (A) vs. separated foil model (B)

KIND OF STRESS	WAVE CONDITION	STRESS RATIO (A/B)
DECK TRANS. AXIAL STRESS (a)	$\chi = 90°$ $\lambda/Lpp = 1.0$	2.7
DECK TRANS. BENDING STRESS (b)	$\chi = 120°$ $\lambda/Lpp = 1.5$	3.0
DECK TRANS. SHEAR STRESS (c)	$\chi = 30°$ $\lambda/Lpp = 0.75$	2.5
SIDE SHELL SHEAR STRESS (d)	$\chi = 30°$ $\lambda/Lpp = 0.75$	1.3
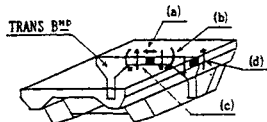
5. Outline Design of Cargo Ship

As a result of the investigations, this concept ship has been found to be more suitable for large ships of total weight from 1,000 t to 3,000 t. Two cargo ships are designed as examples of the application of the large ship. The particulars and the artistic impression are shown in Table 5 and Fig.19 respectively. The ships are designed on the condition that the full load draft in harbor is below 6.0 m and the ship width of type 1 is below 18 m and that of type 2 below 25 m.

The transport efficiency of this concept ship type 1 and type 2 is shown in Fig.20. This figure was made by plotting values of this concept ship, SWATH ships and the high speed displacement type monohull ship into the figure in Ref. [11].

Transport efficiency is defined as the ratio of the work done by total weight of ship (W) travelling at speed (V) to the total power (P), whose measurement is introduced by Gabrielli and Von Karman.

Regarding the ship speed around 40 knots, one of the targets of this concept, the displacement type monohull ship has the best transport efficiency and this concept ship has the second best efficiency. But as seakeeping of the monohull ship is inferior at the speed around 40 knots, this ship doesn't seem to be suitable for a high speed merchant ship.

Table 5 Particulars of prototype ship

Type	type 1 [Full loaded weight 1,700t type]	type 2 [Full loaded weight 2,700t type]
Dimension		
Lpp	65.00 m	75.00 m
Bmld	18.00 m	25.00 m
Dmld	8.00 m	11.00 m
dmld (foil borne)	4.00 m	4.00 m
dmld (hull borne)	5.80 m	6.00 m
Lift (foil borne)	700 t	800 t
Disp. (")	1,000 t	1,900 t
Dead weight	900 t	1,300 t
Full loaded weight	1,700 t	2,700 t
Vs	40 knots	40 knots
Main engine	Gas turbine	Gas turbine
Propeller	CPP	CPP
SHP	60,000 PS	90,000 PS
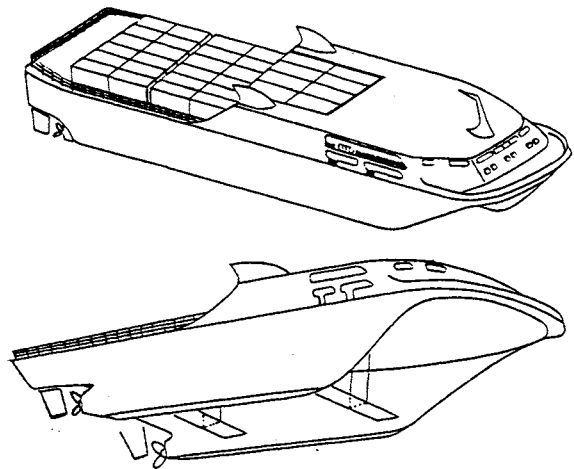
Fig. 19 Artistic impression
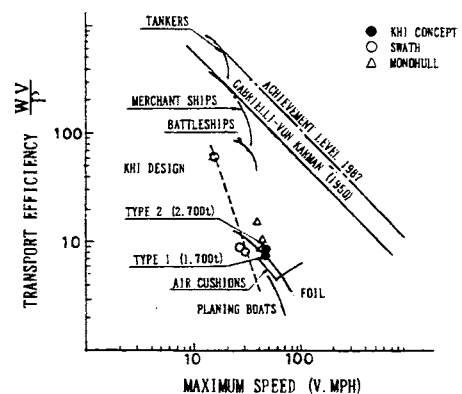
Fig. 20 Transport Efficiency Spectrum

Significant values of the vertical acceleration at the bow of this concept ship type 1 are presented as a function of significant wave height ($H_{1/3}$) in Fig.21. The unit of acceleration is gravity acceleration (g). ISSC spectrum is used and sea condition is a long crested irregular wave whose direction is head sea. Ship speed is 40 knots. The relation between the significant wave height $H_{1/3}$ (m) and wave mean period T (sec.) is assumed to be $T = 3.86\sqrt{H_{1/3}}$.

At the significant wave height of 4.0 m, the significant value of the acceleration is about 0.18 g. In this acceleration, only 10% persons get seasick during 4 hours. Therefore there is no problem in operation of this concept ship in rough sea [4].
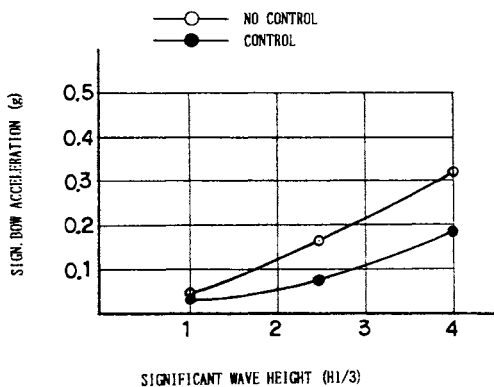
Fig.21 Significant value of the vertical acceleration at the bow (Type 1)

6. Conclusion

The technique to predict resistance and ship motion, and the structural analysis system have been established for this concept ship.

As a result of investigations, it has been found that this concept ship is more suitable for large size high speed ships of the weight from 1,000 t to 3,000 t.

This concept has the following superior characteristics:
(1) An attractive power to displacement ratio in the 35 - 40 knots speed region.
(2) Superior seakeeping performance.
(3) Large deck area to be designed according to trade requirement.
(4) Low construction cost.
(5) Design and construction by well-known technology.

The draft of this concept ship in harbor condition is deeper than that of the displacement type monohull ship of the same size. But it is 6.0 m at the deepest in a ship of the size of our target. So there seems to be no problem.

A high speed container ship, cargo ship, car ferry, passenger ferry, etc. are the most suitable for this concept.

References

1. D.E. Calkins, "HYCAT: Hybrid Hydrofoil Catamaran Concept" AIAA-81-2079 1981

2. Hideaki Miyata, "Development of a New-Type Hydrofoil Catamaran (1st Report: Confirguration Design and Resistant Properties)" JSNA JAPAN Vol.162, 1987

3. Hideaki Miyata, "Development of a New-Type Hydrofoil Catamaran (3rd Report: Design of a Large-Scale System and its Hydrodynamical Properties)" JSNA JAPAN Vol.166, 1989

4. Capt. Robert J. Johnston, "Mordern Ships and Craft, CHAPTER V HYDROFOIL" P187, NAVAL ENGINEERS JOURNAL Feb. 1985 SPECIAL EDITION

5. R.L. Bispling, H. Ashley and R.L. Halfman, "Aeroelasticity. Addison-Wesley.

6. T. Nishiyama, "Unsteady Hydrofoil Theory, Part 1 Characteristics of hydrofoil moving at constant speed under sinusoidal waves" JSNA JAPAN, Vol.112, 1962

7. T. Nishiyama, "Unsteady Hydrofoil, Part 2 Characteristics of Hydrofoil Performing Heave and Pitch while Moving at Constant Forward Speed in Still Water", JSNA, Vol.112, 1962

8. C.M. Lee, "Prediction of Motion, Stability, and Wave Load of Small-Waterplane-Area, Twin- Hull Ships" SNAME, Vol.85, 1977

9. Lindgren, H. and Williams, A. "Systematic Tests with Small, Fast Displacement Vessels, Including a Study of the Influence of Spray Strips", SNAME, Diamond Jubilee International Meeting, 1968

10. M. KAJI, "Wave Pressure Acting on Hydrofoil Catamaran and Strucutral Response", Journal of the Kansai Society of Naval Architects, JAPAN, No.211, 1989

11. Peter J. Mantle, "Cushion and Foils", SNAME, Spring meeting, 1976

DEVELOPMENT OF A WING IN GROUND EFFECT CRAFT MARINE SLIDER: μ SKY-1 AS A HIGH SPEED BOAT

Syozo Kubo, Toshio Matsuoka* and Tetuya Kawamura

Faculty of Engineering, Tottori University Tottori, JAPAN
* Kobe Shipyard & Machinery Works, Mitsubishi Heavy Industries Ltd., Kobe, JAPAN

Abstract

An experimental WIG craft named **Marine Slider: μ sky-1** was developed, constructed and evaluated as a high speed boat. The craft had ram wing configuration. Its size was 4.4m long, 3.5 m wide and 2.0 m high. The total weight of the craft was 295 kg. It was propelled by an air propeller driven by a 64 hp engine. The craft was constructed by CFRP honeycomb to achieve its light weight. The tail unit was constructed by aluminium pipes covered by cloth. The control system of the craft was an elevator and, air and water rudders. The water rudder was linked to the air rudder. The craft had no control device for roll, because it had enough stability for roll by the ground effect. When the craft turned to right or left, it slided horizontally instead of bank turn. The engine power was controlled by a throttle lever operated by the left hand. The take-off speed of the craft was 66 km/h and its maximum speed was 82 km/h. Results obtained from a series of test runs suggested that the WIG was a promising candidate of a high speed boat of the next generation.

1. Introduction

Many pacific countries are consisted of islands, e.g., Japan, Philippine, Indonesia, etc. In these countries, one of serious problems is transportation beyond sea. In Japan they are constructing tunnels under sea and long bridges over sea. These facilities are very effective for the transportation beyond sea. The most important demerit of them is their costs, which are too huge for almost all countries or areas. It is true in Japan also. In fact, peoples in an area of relatively thin population or on islands relatively far from the main islands are suffering from lack of a suitable method of transportation beyond sea.

Table 1. 10 Big Islands in Japan (excluding 4 main islands)

Name	Area (km²)	Population (x1,000)	Distance (km)
Okinawa	1,211	1,122	550
Amakusa	860	182	3
Sado	857	88	30
Amami	718	86	300
Tsushima	692	52	120
Awaji	590	172	4 or 2
Yakushima	500	16	70
Tanegashima	447	47	43
Fukue-jima	327	57	100
Tokunoshima	248	35	350

Distance means the distance from a main island.

Amakusa and Awaji are connected to main islands by bridges. The largest island in Japan is Honshuu. Hokkaido is 20 km off from it, and connected by a tunnel. Kyuushuu is only 1.2 km off from Honshuu, and has the second large population. Then it is connected by a tunnel to Honshuu. The distance between Honshuu and Sikoku is 7 km. Now 3 routs are going to

connect by huge bridges. On the other hand, 8 big islands in Table 1 and other islands will not be connected to a main islands by tunnels or bridges.

The most popular method of marine transportation is using ships. Throughout the human history, it is the most economic method of transportation. It will be used in future too, especially for transportation of raw materials and many heavy products. In spite of the great merit of ship, it is not enough for other purposes, say, passengers transportation, mail, personal use, general use, etc., because of its relatively slow speed. In old days, ship was relatively a speedy craft in all

Table 2. Short History of Transportation Methods

1761 Canals for river ships.
1807 Steam ship.
1829 Steam locomotive.
1839 Ship with a screw propeller.
1863 Underground rail way.
1869 Suez Canal.
1889 Automobile.
1895 Electric locomotive.
1901 Ship with a steam turbine.
1906 Bus.
1908 Mass-production of cars.
1912 Ship with a Diesel engine.
1930 Motor Boat.
1933 Airliner.
1955 Jet airliner.
1960 Shinkansen.
     Hydrofoil.
     ACV.
1976 SST.
2000? Linear Motor Car.
----

countries. Speed of other crafts, e.g., cars, trains and aircrafts, has been increased in 19th- and 20th-centuries. Speed of ships too has been increased in this time. But the rate of increase was relatively smaller than those of other crafts. From this fact, we needs now a speedy marine craft.

In many developing countries and areas, the needs is also very strong for a good transportation craft on water. The development of an area is usually carried out along a river or other water sources, because water is one of

Table 3. Order of Cruising Speed of Transportation Methods
----
pedestrian	4 km/h
coach	15
bicycle	15
river ship	20
ocean ship	50
motor boat	70
hydrofoil	80
hovercraft	100
normal train	100
car and bus	100
super express train	300
commuter airplane	300
linear motor car	500?
jet airliner	900
SST	2,000
----

important factors for every development. The access way to such a place is unfortunately very limited. Usual river ship is too slow to use passengers transportation. Aircraft including helicopter is very useful but too expensive and too difficult to ordinary persons working in such a place. They use cars and some other similar work machines for their construction. They can maintain machines complicated like as a car or so. But it will be difficult to maintain machines like as an aircraft. In a short words, they need a car on the water surface.

Many attempts have been done to increase the speed of ships. The first attempts was the design of hull shape. Methods to reduce the wave drag followed. A great improvement has been achieved by using planing beyond the hump speed. This introduced, however, two difficult problems. One of them was reduction of payload. The other was the shock of water surface. Hydrofoil was a revolutionary technique to increase the ship speed. The speed is, unfortunately, not enough high to satisfy many users of these crafts. Besides this, there are difficult problems of cavitation, spray and interaction of water flow between the free surface, when the speed of ship is increased. In spite of these difficulties, attempts to reduce ship drag and increase its speed are continuing. These efforts will give a more economic

ship in future.

Wheels are not suitable to use on water, even though they are very good tool on land, because the water surface is many times deformable than the earth surface. From the fact, we find that our new craft must have a small pressure on the water surface. Weight of a craft can not reduced in a large amount. The new craft must have a large ˙area though which the craft is supported by the water surface.

One of simple methods to have a speedy marine craft is to run in the sky instead of on the sea or in the. sea. The density of the air is about 1/800 of that of sea water. This is the reason why an aircraft is so speedy.

Air Cushion Vehicle (ACV) satisfies the above requirements. It is surely a good method of transportation on the water surface. But we must recognize the fact that ACV has its speed limit. ACV is lifted up from the surface by its air cushion. If ACV's speed is increased, the air cushion will be blown off at some speed. In practice, it will be unstable at a slower speed than that limit. ACV has also many practical problems. The present authors consider that ACV has a special characters suitable for transportation of heavy object on a weak basement. It is not suitable for a high speed transportation. The reason that ACV has been considered as a candidate of the high speed craft on sea will be the fact that there was no other suitable craft for the purposes.

Aircraft is attractive method of transportation beyond the water. We know, however, that the aircraft is not so common in transportation between islands. There must be some reasons. The present authors estimate the reasons as follows:

1. Aircrafts are too much expensive.
2. Control of aircrafts is too difficult for an ordinary person.
3. Maintenance of aircrafts is too difficult for daily use.
4. Aircrafts are too dangerous when an accident will happen.
5. Maintenance of airfields is too expensive and difficult

for daily use.

Our new craft should be free from these shortcomings.

2. Characteristics of WIG

If we want to travel in a high speed, it is not necessary to fly at a high altitude. The altitude of 1 mm is enough high, if it is possible to continue. In the theory of airplane wing, we know the effect of ground, which is an effect that the lift increases and the drag decreases when the wing is in the vicinity of the ground surface. This effect is favourable for our purpose. WIG is a craft using the effect.

WIG can fly only at a height of less than 10 % of its aerodynamical dimension, which is usually wing span or chord length. From the fact, WIG can not fly freely in 3-dimensional open space. It can travel only in a narrow layer adjacent to the surface. Its motion is restricted in a quasi 2-dimensional layer. This is important limitation of WIG. From other side of view, the limitation is not always a demerit. By the restricted motion, many mechanisms of WIG can be simplified. The WIG engine is, for example, simpler than that of the airplane. It is as simple as a car engine. The engine of the airplane is complicated by the reason that the airplane must experience vertical turn, spin, diving, etc. The engine must work in all these tangled motions. On the other hand the car engine will stop when the car is upside down. Carburetors, fuel pumps, sparkplugs and many other parts of the airplane engine are necessarily complicated and delicate. Besides this, an airplane engine must be light weight. All these difficult engineering problems are originated to the free 3-dimensional motion. Another example is the fact that we need not a pressurized cabin because we travel only near region adjacent to the sea surface. The pressurized cabin causes again many complicated problems for engineers. At first, the cabin must be completely shielded against possible air leak. Second, a

suitable air conditioning system is required for air supply to the cabin. Third, the structure of the cabin must be proof against possible fatigue caused by a cyclic loading of pressure change in each flight. By simple mechanisms, we will be able to construct a WIG in a reasonable cost. The maintenance of WlG will be also easy and in a low cost.

Running cost of WIG is also lower than that of an aircraft. A wing in ground effect has better efficiency than that at a high altitude. This means better fuel consumption of WIG than that of an aircraft. The control of WIG is easier than that of an airplane. The cost for pilot training is smaller for WIG than for an aircraft. The cost for maintenance is also small. WIG is therefore more economic than the aircraft.

The quasi 2-dimensional motion of WIG is easier to control than the free 3-dimensional motion of an aircraft. The situation resembles that of a motor car or a motor boat.

The source of the difficult maintenance of an aircraft is caused by its complicated engine, a number of movable parts, weak structure and its wing extended in a large extent. Aircraft engine must work in every situation of free 3-dimensional motion and in every circumstance including a high temperature at a low altitude and a low temperature and pressure at a high altitude. A number of moving parts is necessary to satisfy not only its low speed flight of take-off but also its high speed flight. Our WIG does not need all of these complicated mechanisms. Weak structure is common to WIG and air-craft, because they need light weight. Span of WIG can be reduced in considerable order by making use of the ground effect.

Now we will consider about safety. The most dangerous phenomenon of an aircraft is fall down in an accident. When a craft falls down from a high altitude, it is accelerated by the gravity force. The normal altitude of WIG is less than a few meter. WIG will be not accelerated during its fall. The second fact is that the impinging angle of WIG to the surface will be less than 10 degree. This means that WIG is hard to be broken, turned to upside down or crashed. Among all, low altitude flight will give passengers a feeling of safety. We need not airfields to operate WIG. We can use not only a harbour but also a sea shore and a river bank, because the drought of WIG is very small due to its light weight.

Cruising WIG does not touch the surface of ground or sea. It does not suffer from surface suspended objects or sea weeds. It can run over the sea surface, flat surface of ice, snow covered land, muddy surface and sand-bank. It is a new path of transportation. WIG and ACV are sharing the area.

3. Classification of WIG

In the 50 years history of WIG research, many types of WIG had been proposed and tested. We classify these following their plan view (see Fig.1).

1. Flying Boat Type (Fig.1a)
A craft of this type has hull, main wing and tail units separately, just like as an ordinary flying boat. This type is suitable for a high speed craft, because the wing area is relatively small. We can design the main wing without a serious interaction between other elements of the craft. The type is thus suitable to a large craft of high performance. A number of concepts of huge machines have been proposed based on this type.

2. Lippisch Wing Type[1] (Fig.1b)
This type has a special wing so-called "Lippisch Wing", whose plan form is an inverted triangle with a negative dihedral angle. The inventor of this wing was Alexander Lippisch, the famous designer of sail plane and aircraft, especially the inventor of the delta wing. A very high performance was reported on the aerodynamic characters of the wing. An experimental craft was constructed in USA at first. After the time, development of this type craft has been continued in West Germany. In USSR, CLST[1] has
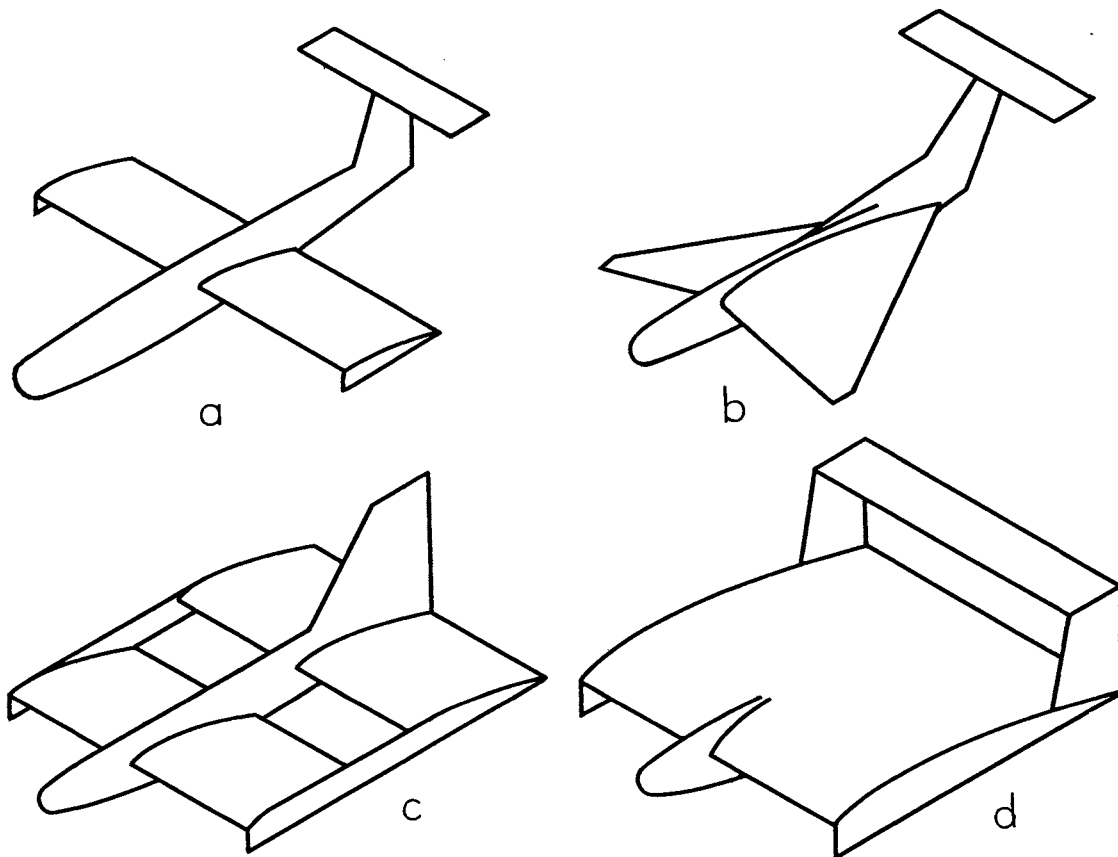
Figure 1. Classification of WIG
a: Flying Boat Type, b: Lippisch Wing Type, c: Tandem Wing Type,
d: Ram Wing Type.

been continued their effort on developing WIGs of this type. CSSRC[4] in China is also developing models for practical use of this type. This type is now the most popular type of WIG.

3. Tandem Wing Type (Fig.1c)

This type has two wings, the front wing and the rear wing. It has no horizontal tail wing. This type has been investigated by Günter Jörg[1] who was a designer of the aircraft of vertical take-off and landing in West Germany.

4. Ram Wing Type (Fig.1d)

This type has a big wing extended from the nose to tail of the craft. This is the simplest type of WIG. It has relatively large wing area. Thus it is suitable for a slow craft. One of famous WIGs of the ram wing type is RAMESES-I[2] which was developed in USA in 1975. This craft can, even today, satisfy our requirements except its pitching stability. The problem of pitch-up has been a serious problem of WIG of ram wing

type from the time of the first WIG by Kaario[3] Many experimental crafts including RAMESES-I have been given up by the difficult problem of controlling the pitch-up. This is a real problem of WIG for the practical use.

4. **Marine Slider: μ sky-1**

Many experimental WIGs have been constructed and tested. Many persons are continuing their effort to develop machines for practical use.

At the beginning of our development of a new WIG, we directed our outline of development to design a craft of practical use and of mass production, if possible. On the other hand, WIG is not enough popular in daily life. We decided that the new craft should satisfy items as follows.

1. The craft must fly at a low altitude steadily and safely.
2. Slow take-off speed is favourable.
3. A compact craft is favourable.

4. The craft must be clearly different from an aircraft.
5. The control of the craft must be definitely easier than that of an aircraft.

The items 1 and 4 were required by the reason that the new craft had a role of a demonstrator of WIG. The items 2 and 5 were considered for easy translation from motor boat to WIG. This requirement would be also favourable for safety development of a new craft. It is not so difficult to increase the cruising speed of the craft up to about 200 km/h. The item 3 was set from the stand point that handling of a water airplane was not enough favourable because of its large size, especially its long wing. For personal use and general use, handling on the water or on the shore is very important. This includes the area of storage or harbour.

By these requirements, the type of the new craft was decided to be a ram wing type. By the item 2, the craft must have a large wing area. The most compact type of WIG is the ram wing type, which can satisfy the items 3 and 4. Item 5 will be satisfied by any kind of WIG except its pitching stability. Therefore, our target was to develop a new craft similar to or better than RAMESES-I without pitch-up.

We have many advantages than the developers of RAMESES-I by the following reasons.

1. We can obtain a suitable engine today, because high performance light engines have been improved considerably.
2. We can use many kind of good materials, e.g., FRP, special cloths, specially treated aluminum pipes, etc. to design a light structure.
3. We can use many electronic devices for sensors and controls, etc.
4. We can obtain many parts of mechanisms, e.g., propeller, reduction gear, instruments, flexible tube, water pump, etc., from the market for marine sports goods, ultra-light airplanes and small hover crafts.

5. We can expect a considerable market for marine sports.

Our solution for the pitch-up problem was mainly 2 ways. One of them was the use of a cambered wing instead of the flat wing of RAMESES-I. The cambered wing
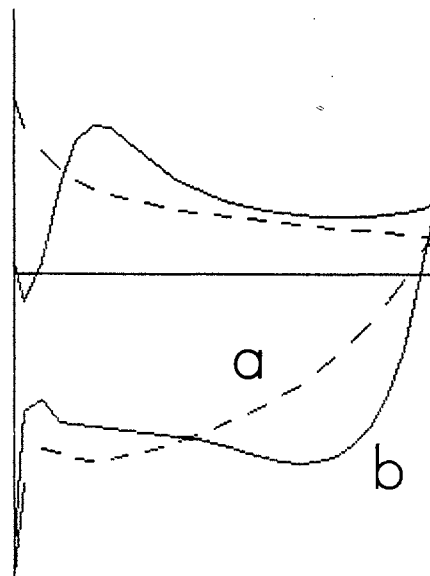
Figure 2. Pressure Distributions of (a) flat wing and (b) cambered wing.

brought us a mild pressure distribution on the upper surface of the wing instead of a peaky distribution of a thin flat wing. We see the ground effect as a high pressure at the rear half part of the lower surface.

Another way was position of air screw. It was set at the upper rear side of the wing and in front
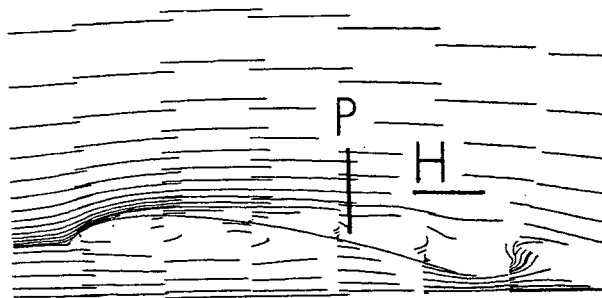
Figure 3. Position of Propeller and Tail Units

of tail units. The positions of the propeller is shown by P, and the horizontal tail by H in Fig.3. The propeller accelerated the air at the upper rear part of the wing, which was otherwise easily separated from the surface of the wing. By the effect, the phenomenon of stall became mild and was practically controlled by pilots. The elevator and rudder in the propeller slip stream were very effective especially at a low speed. This was unexpectedly effective for the pitch-up control, because the phenomenon used to happen at a low speed of take-off.

We named the craft thus developed **Marine Slider**: μ **sky-1**. **Marine Slider** is the general name of our WIG and μ **sky-1** is the individual type name. A photography of μ **sky-1** is shown in Fig.4. Its top view and side view are shown in Fig.5. Its principal particulars are shown in Table 4.
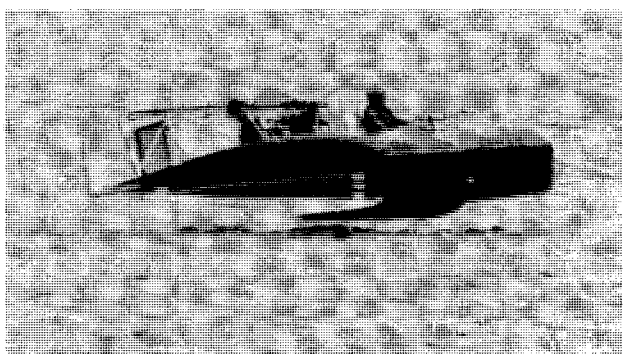
Figure 4. μ sky-1 in Flight

Table 4. Principal Particulars of μ sky-1

```
-------------------------------------------
Length overall:        4.4 m
Width:                 3.5 m
Height overall:        2.0 m
Wing Area:            14.0 sq.m
Wing Loading:         20.4 kg/sq.m
Weight, empty:         225    kg
        maximum:       295    kg
Installed power: 64 hp. (ROTAX 532)
Propeller: Fixed pitch 4 blades
Passengers:            1
Take-off speed        66 km/h
Cruising speed        82 km/h
Hull:                 CFRP
Wing:                 CFRP
Tail units: cloth + aluminum pipes
-------------------------------------------
```
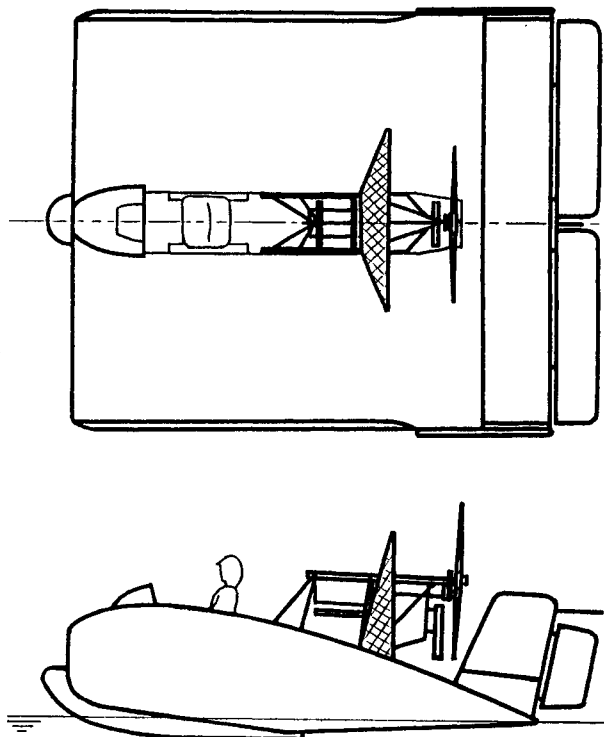

Figure 5. Top and Side View of μ sky-1.

We compare these particulars to those of RAMESES-I. The size of μ sky-1 is about 70 % of RAMESES-I. Its weight is 84 %. The wing area is 44 %. Then the wing loading is about 2 times of that of RAMESES-I. The cruising speed is thus increased. The engine power is 2 times larger than that of RAMESES-I. The most significant difference between μ sky-1 and RAMESES-I is the rigidity of the two crafts. μ sky-1 is almost rigid. On the other hand, RAMESES-I is flexible. μ sky-1 shows that the success of RAMESES-I was independent of its flexible structure. We conclude from the fact that WIG of ram wing configuration can have a rigid structure, which is necessary for a construction of large vehicle.

We made the first test run of μ sky-1 at March in 1988. A series of test runs had been carried out from the time. We learned from the results that the design of its hull should be reconsidered to give better performance on ship mode. After suitable reformation, another

series of test runs had began in November of that year. In this time, our μ sky-1 achieved a long jump. After about 300 test runs, μ sky-1 succeeded a complete continuous flight of 1 km long at an altitude of about 50 cm. During the test runs, many technical data were also measured by runs of remote control. From the successful flight, about 40 test runs had been carried out.

Our μ sky-1 satisfied the item 1; flight at a low altitude. Low take-off speed and compact size were also realized as shown in Table 4 and Fig.5. It is enough slow and compact in comparison with an aircraft. The craft has, in practice, no tendency of pitch-up. Therefore, the control of μ sky-1 is definitely easier than that of an aircraft. Our μ sky-1 satisfies all requirements and supports the possibility of practical use of WIG.

We are now developing a new 2-seater model; μ sky-2, for sports and light purposes. Its details are out of scope of this paper.

4. WIG in Future

From scientific or technical point of view, there is no essential problems to design a WIG of 20-50 seats cruising less than 200 km/h. Many small problems of engineering nature is naturally left for future investigation. A craft of this class will be very useful in many countries including pacific countries. It will be used for passenger transportation in a short or middle range, safe and comfortable tour around beautiful islands, many purposes of area developments, etc.

When we consider a craft of this class, we should keep in mind the fact that more severe requirements will be imposed on developers. One of them will be the economic efficiency. To improve the efficiency, we must have a knowledge about performance of WIG wing. This suggests us that systematic data must be piled up just as the data of wing sections of aircraft. It is not so easy to obtain such data in a short period. Numerical simulations will help us to find out an optimum configura-

tion of a WIG, if we can develop a suitable method of simulation. The other one difficult problem will be to decide the limit and improve the ability of operation at rough weather or sea state. This problem is consisted in many complicated factors. Usual approach to answer this problem has been to accumulate practical data for every crafts now in service. We have no such amount of data for WIG at present. They will be accumulated day by day, when WIG will be used even for restricted purposes.

We can count out many other serious problems related to WIG operation. The present author think that these problems are unavoidable to a machine of revolutionary new characters. These will be solved step by step by the effort of persons related to individual problems.

Development of a larger craft of higher performance is essentially possible. Naturally it needs an amount of effort in many fields concerned. We conclude that WIG has a big possibility of new transportation method on the water surface.

References

1. Jane's High-Speed Marine Craft and Air Cushion Vehicles 1989, pp.419-428.
2. R.W.Gallinton, H.R.Chaplin, F.H.Krause, J.A.Miller & J.C.Pemberton, Recent Advances in Wing-in-Ground Effect Technology, AIAA/SNAME Advanced Marine Vehicles Conf., 76-874, 1976, 9.
3. R.G.Ollila, Historical Review of WIG Vehicles, J.Hydronautics, 14, 3, 1980, pp.65-76.

STATE OF THE ART OF SWATH IN JAPAN

H. Yagi*, S. Shibahara**

* Mitsui Engineering & Shipbuilding Co., Ltd., Japan

Abstract

This paper outlines the features of Small WaterPlane Area Twin Hull (SWATH) vessels, and reviews the technical aspects to be considered during design and construction stages. The construction record in Japan is presented covering the hull particulars and performance.

Key design parameters of SWATH are discussed comparing their merits and demerits. The various performance of SWATH vessels including speed and motion in waves is presented.

Finally, consideration of future application to commercial use is discussed referring to its technical merit.

1. Introduction

Small Water Plane Area Twin Hull (SWATH) or Semi-Submerged Catamaran (SSC) is one of the advanced marine vehicles. The concept was acquainted more than a century ago, and at present it is in a stage of application to commercial use.

In Japan, the research of SWATH was initiated by Mitsui Engineering & Shipbuilding Co., Ltd. at the beginning of 1970s [1]. It was just before the construction of the U.S.Navy's first 190- ton SWATH vessel "Kaimarino".[2]

The development work at Mitsui was followed by the Japanese first experimental 11-meter vessel "Marine Ace" in 1977 under the sponsorship of Japan Marine Machinery Development Association (JAMDA). The commercial fast passenger ferry "Seagull" was constructed in 1979 and extensive sea trials were carried out. [3] Since then, many commercial applications have been made in Japan, leading the trend of realizing the more-advanced high performance vessels.

In this paper, the technical development of SWATH is reviewed, focusing on the design and construction in Japan.

2. General Features of SWATH

SWATH has a lot of advantageous features in its performance but has inherent delicate points in design and construction due to its hull form. In this section, such points are listed with the related merits and demerits.

2.1 Sustension system

Fig. 1 shows the relation of weight sustension for various advanced vehicles. The weight of SWATH is supported by static buoyancy similar to the conventional displacement type ship. It is, however, very common to utilize the hydrodynamic lift in order to control the posture of the vessel and dynamic motion in waves taking the advantage of small water plane area.

On the other hand, SWATH is fairly sensitive to weight change, and therefore, design and construction is to be carried out with best care.
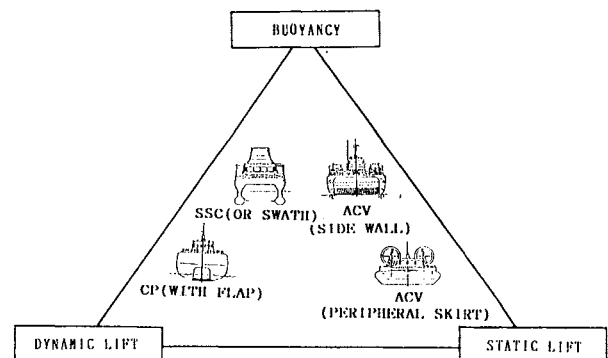
Fig. 1 Weight Sustension Diagram

2.2 Hull form

SWATH is composed of three major parts of hull. The lower hull is torpedo-like body under the water. Strut is the surface piercing streamlined hull located on the lower hull.

A pair of struts is located in parallel. The upper hull connect the two struts well above the water line.

The cross deck arrangement enables to afford a wide and flush deck area for usage of various purposes, such as accommodation, working space, etc.

The most important feature of SWATH performance is its superb seaworthiness attributable to the small water plane struts. It is, generally, quite advantageous that SWATH has a very long natural period which is far beyond those of encountering waves in ocean. This hull arrangement makes it possible to maintain the ship motion minimum even in rough seas. This feature also results in the minimum speed loss in wave.

2.3 Structure

The twin hull arrangement of SWATH is subjected to different wave forces from those which will occur to monohull. In the design, the transverse strength is the key factor.

Due to the limited data of the actual vessels, SWATH has to be designed not on rules but on analysis. It is, therefore, required to be based on the proper design wave loads estimated from the model tests, theoretical calculation results and actual ship data.

Analytical tools are also important for the design by analysis. Combined method using the hydrodynamic tool and structural analysis is used in the practical design.

2.4 Outfitting

The most unique point is the outfitting of propulsion system in SWATH.

Due to the limited space in lower-hull, it is required to make arrangement of various machineries well in compact.

There are two possibilities for the location of main propulsion engine arrangement: (1) on cross deck, or (2) in lower-hull.

With respect to driving system, there is also alternatives: (1) direct, or (2) indirect electric system.

2.5 Applications

Reflecting the various features of SWATH, suitable application of this type of vessel is fairly wide: Passenger vessel with comfortable ride in rough seas, research vessel with stable working condition, and ferry boat with high operability etc. Another application is the oceanographic survey vessel taking the advantage of low level of noise emitted in the sea in addition to the superior motion characteristics in waves. It is reported that SWATH vessels for application to large oceanographic vessels are being constructed in the U.S.A.[4] and Japan.[5]

3. Construction Record of SWATH in Japan

The construction record of SWATH in Japan is shown in **Table 1**. Ten vessels were constructed so far, and nine vessels are in active operation.

The length of the vessels ranges from 11 to 53 meters.

Fig.1   MAIN PARTICULARS OF THE SWATH BUILT IN JAPAN

NAME	MARINE ACE	SEAGULL	KOTOZAKI	OHTORI	KAIYO	MARINE WAVE	SUN MARINA	BAY QUEEN	SEAGULL 2	DIANA
KINDS	EXPERIMENT	HIGH-SPEED PASSENGER	HYDRO-GRAPHIC SURVEY	HYDRO-GRAPHIC SURVEY	SUPPORT FOR UNDERWATER WORK	CABINE TYPE LUXURY BOAT	SALOON TYPE LUXURY BOAT	MULTI-PURPOSE WORKING	HIGH-SPEED PASSENGER	PARTY BOAT
COMPLETION	1977	1979	1981	1981	1985	1985	1987	1989	1989	1990
L.O.A. (m)	12.35	35.9	27.0	27.0	60.0	15.1	15.05	18.0	39.3	20.8
L.P.P. (m)	11.0	31.5	25.0	24.0	53.0	11.95	11.925	15.9	33.7	15.9
BREADTH (m)	6.5	17.1	12.5	12.5	28.0	6.2	6.4	6.8	15.6	6.8
DEPTH (m)	2.7	5.85	4.6	5.1	10.6	2.75	2.75	2.8	6.8	2.8
DRAFT (m)	1.55	3.15	3.2	3.4	6.3	1.6	1.6	1.6	3.25	1.6
GROSS TON(T)	—	670	250	250	2849	19	19	39	567	52
PAYLOAD OR COMPLEMENT	20 P	402-446	abt. 36 T	abt.36 T	860 T	17 P	33 P	40 P	410 P	40 P
STRUT TYPE	TWIN/SINGLE	SINGLE	SINGLE	SINGLE	SINGLE	SINGLE	SINGLE	SINGLE	SINGLE	SINGLE
HULL MATERIAL	AL	AL	STEEL/AL	STEEL/AL	STEEL	FRP	FRP	AL	AL	AL
MAX.SPEED(KTS)	17.3	27.1	20.5	20.6	14.0	18.2	20.5	21.6	30.6	19.2
MAIN ENGINE (PS x NO.)	GASOLINE 200PSx2	DIESEL 4050PSx2	DIESEL 1900PSx2	DIESEL 1900PSx2	DIESEL/ELEC. DG 1250KWx4 MTR 850KWx4	DIESEL 275PSx2	DIESEL 300PSx2	DIESEL 470PSx2	DIESEL 2650PSx4	DIESEL 370PSx2
PROPELLER	F.P.P.	F.P.P.	C.P.P.	C.P.P.	C.P.P.	F.P.P.	F.P.P.	F.P.P.	F.P.P.	F.P.P.
FIN CONTROL	AUTO	AUTO	MANUAL	MANUAL	MANUAL	AUTO	AUTO	AUTO	AUTO	AUTO

Fig. 2 shows the trend of size of SWATH vessels. Regarding ship size, the maximum is the support vessel for underwater work experiment "Kaiyo" owned by Japan Marine Science Technology Center (JAMSTEC). In terms of the speed, the vessels are divided into two categories : "High" and "Low" speed vessels as shown in **Fig. 3**. "Kaiyo" is the only case of low speed vessel whose design speed is below the last hump of resistance. High speed vessels are mainly for the passenger ferry and slow speed vessels for research purposes. Other typical phenomenon is that the construction of small size SWATHs are becoming popular for leisure use.
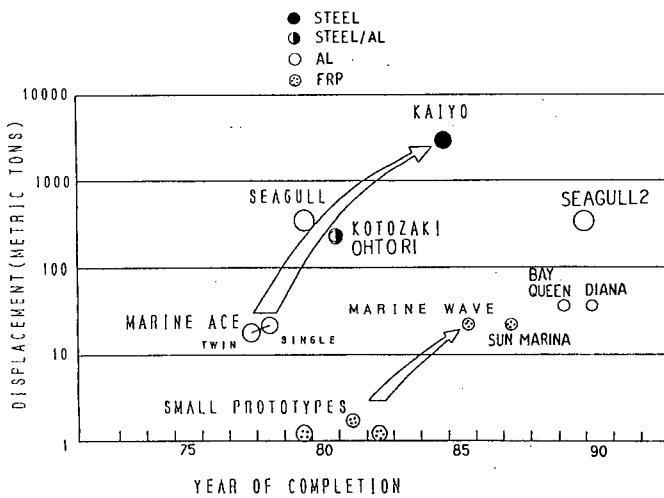
Fig. 2 Trend of Size of SWATH
Completed

FROUDE NUMBER
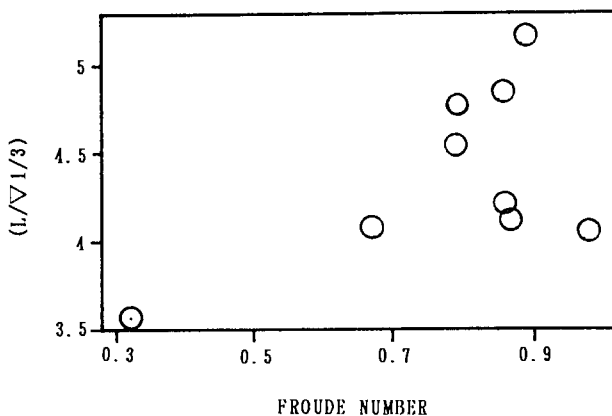
Fig. 3 Speed and Hull Parameter

4. Key Technical Features

4.1 Selection of Strut Type

There are two types of struts in the SWATH design, namely;

    1) Single strut per demi-hull type
    2) Twin strut per demi-hull type

The selection is made considering the requirements for stability, speed performance and structural design for their operation. In Japan, the single strut per demi-hull is dominant. There is only one case in which the experimental vessel was built with twin strut per demi-hull and then converted into single strut for the purpose of comparative evaluation of the two types of struts. Model test results of resistance comparison between the two types of struts are shown in **Fig.4**, on "Marine Ace". In this case, single type is superior to that of twin over the whole speed range investigated.
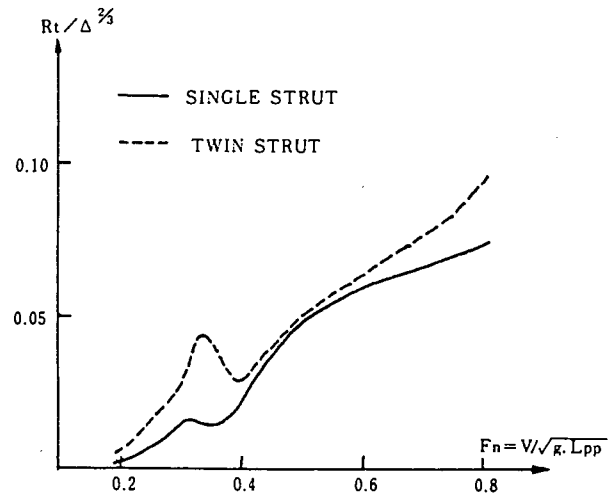
Fig. 4 Comparison of total Resistance Between Twin and Single Strut

4.2 Consideration of Propulsion System

1) Prime mover

For the total ship design, the impact of main engine weight upon a SWATH vessel is more significant than in the case of a conventional vessel. Therefore, the selection of main engine is most important, especially for the vessel of small sized or high speed type. Any prime mover should be selected considering its size and weight suitable for the best arrangement of machinery. The most compact and powerful engine is gas turbine. But, its application was made only to the experimental ship "Kaimarino" in the U.S.A.. The installed engines in Japan are high speed diesel except the experimental ship "Marine Ace" which is equipped with two gasoline engines. This is mainly due to the economic consideration.

In terms of weight per unit output, the installed engines ranges from 2.6 kgf/kW to 7.1 kgf/kW depending on the type and manufacturer. Future development of a lighter and compact engine is strongly requested.

2) Driving system

Driving machinery system is categorized into the two types:
A) direct drive by diesel prime mover
B) indirect drive electric motor drive

Among the direct drive system, two types of power transmission systems are utilized so far: straight shaft system and Z-shaft system. At the early stage of SWATH design, Z-type system was installed on "Seagull" and "Kotozaki" as shown in **Fig. 5**.
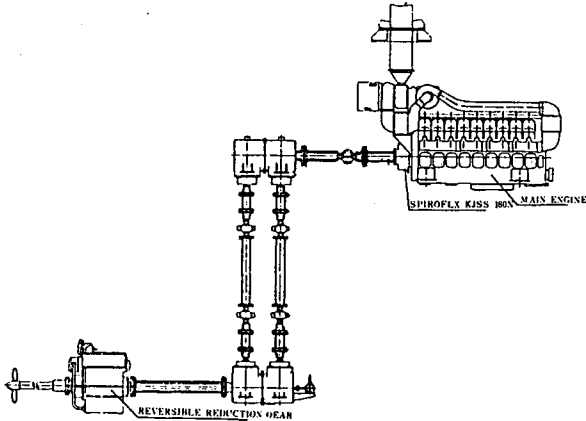
Fig.5 Z-Drive Transmission system

For the purpose of weight reduction, easy maintenance and minimum transmission loss, it became popular to utilize straight shaft system, allowing some rake in propeller and shaft . In the case of straight shaft system, the arrangement of the machinery system is very much restricted from the weight distribution and the limit of propeller efficiency.

Another design aspect is the proper arrangement of joints of shaft having rather long shaft, and careful design study and construction are required. The very recent application of new main engine/gear system is noteworthy. In the "Seagull 2" , 2 sets of 16 cylinders engines exert the shaft horse power of 2 x 2680 PS (1971 kW) per shaft. The arrangement is shown in **Fig. 6**.
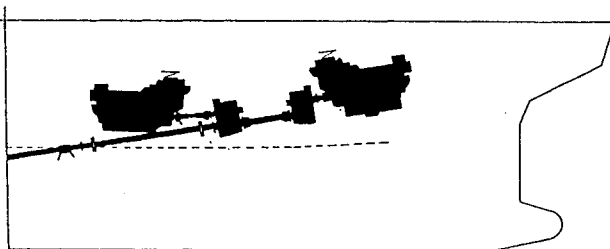
Fig. 6 Engine Arrangement of "Seagull 2"

It is to be noted that the engine arrangement in the lower hull is possible in design but causes some dif-ficulty in daily maintenance at site.

The use of electric power drive is mainly for the research vessels in which cost and weight penalty shall be covered by the merit obtained from the system. One of the possible applications is the oceanographic field having low noise emission from the hull surface.[6],[7]

3) Propeller

In the selection of total propulsion system, CPP or FPP is also to be taken into account in terms of propeller noise and controllability of the ship. The research vessels "Kaiyo" and "Kotozaki" are installed with CPP and the other vessels are with FPP.

In the case of "Kaiyo", CPP is used as a propulsor for the dynamic positioning system combined with bow and stern thrusters.
CPP increases the controllability of vessel. But there is a possibility that propeller noise at decreased pitch is rather high compared with that of FPP.

In terms of controllability of ship, SWATH with FPPs has enough moneuverability for usual maneuvers by using twin rudder and propeller. In addition, slight benefit of propeller efficiency is expected in FPP.

4.3 Structural design

Regarding the structural design, the ISSC conference in 1988 discussed the SWATH design as a novel design concept, and review of structural design was made reflecting the increased construction of SWATH vessels.[8] Therefore, progress in the design method will be expected.

1) Hull materials

Material selection is done based on the displacement hull weight ratio. Generally, aluminum alloy and FRP are suitable for small ships due to its strength/weight ratio. Steel including high tensile steel is suitable for rather large sized vessels. **Table 2** shows a comparison of materials used for SWATH. FRP usage is to be carefully done for not only keeping the strength but also weight control during construction due to the weight sensitivity of SWATH.

Table 2   Comparison of Hull Materials

Kind	Steel	Aluminum	FRP
Strength/Weight	Small	Large	Medium
Weight	Heavy	Light	Medium
Uniformity	High	High	Low
Cost	Low	High	Low
Labor/ton	Low	High	Low

2) Design method

The key factor of structural design is the estimation of wave loads. Estimation is made based on the theoretical calculations and model test results.[9].[10]

Notwithstanding such approaches, the measurement results on actual vessel should be carefully evaluated to validate the methodology. A comparison of side force in beam sea and time history of wave fluctuation pressure are made in **Fig. 7** and **Fig. 8** respectively.[11] It is very important to note that side force is maximum at a time when a SWATH vessel is at rest in beam sea as shown in **Fig. 8** that is well illustrated by the measured record on actual vessels.

Structural analysis is usually made by using 3-dimensional FEM. Sample model of midship part is shown in **Fig. 9**. For the future design, wave load estimation will become more accurate. In addition, strength assessment based on reliability will be applied, that is different from the present deterministic one based on safety factor.[12] This approach is rational for SWATH vessels because of the present stage where the actual vessels are in a very limited number.
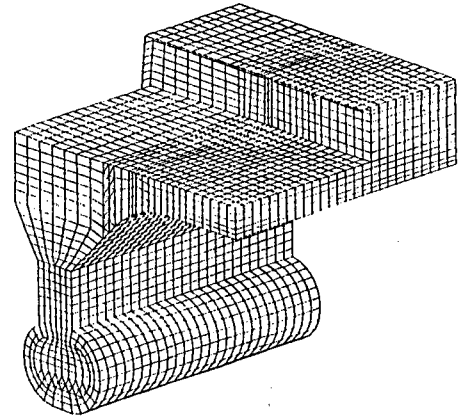
Fig. 9 FEM Model of Midship Part

4.4 Fin control system

All of the vessels are equipped with fin control system in order to enhance the seaworthiness. Two pairs of fins are arranged at port and starboard, fore and aft inward lower hull.The aft fin type is selected to be canard or flap depending on the operation mode.

In the case of a slow speed SWATH, fixed fins (non-movable) are used at the rear part for stabilizing and damping the ship motion. The initial setting of fin angle is made based on the model test results or theoretical stream lines calculation.

The method of control is divided into two categories:

1) Automatic control
2) Manual control

High speed type of SWATH is generally controlled by automatic mode and low speed by manual mode, judging from the operability of the vessel. **Fig. 10** shows the effectiveness of the control system for "Seagull 2" and **Fig.11** for "Bay Queen".
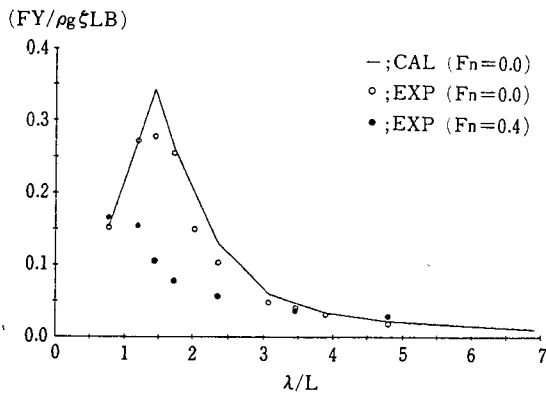
Fig. 7 Side Force Acting on SWATH
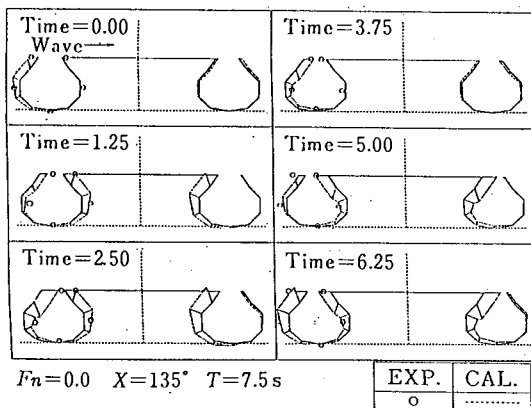
Fig. 8 Pressure Distribution and Its Time History
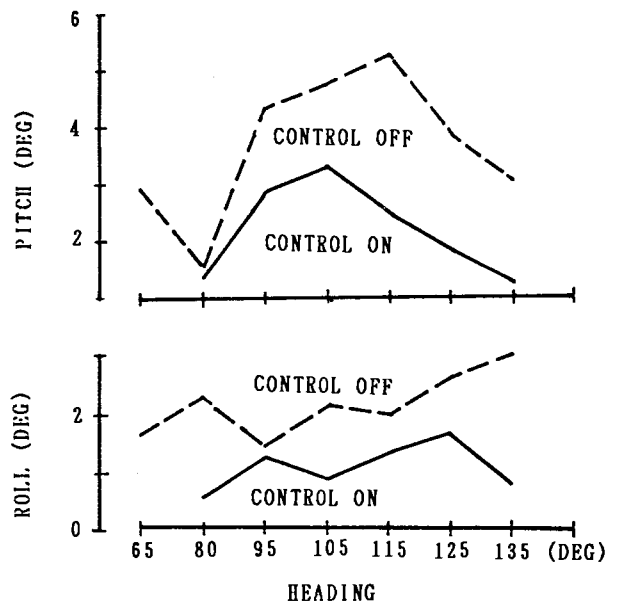
Fig.10 Effect of Fin Control System on Motion of "Seagull 2"
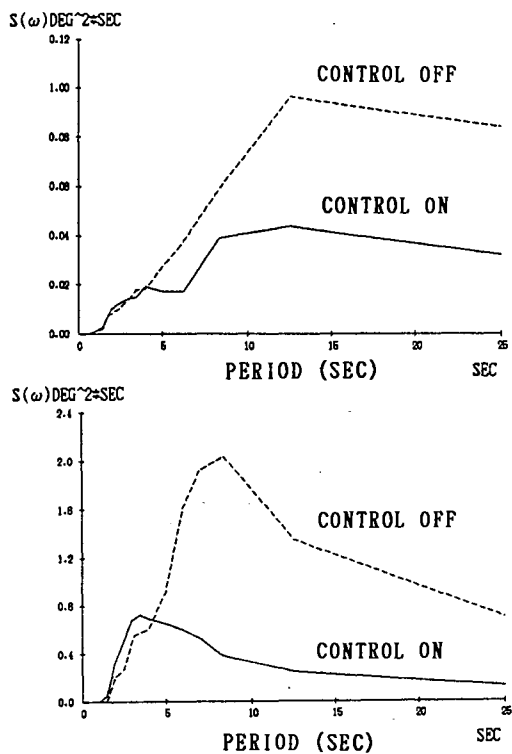
Fig. 11 Effect of Fin Control System on Ship Motion of "Bay Queen"

As clearly seen in these figures, the adoption of fin control system **decreases the ship motion in waves and** enhance the habitability especially for passenger vessels.

4.5 Speed performance

SWATH has, inevitably, rather large wetted surface area compared with mono-hull or conventional catamaran. However, the required horse-power index is less than that of mono-hull as far as small sized high speed vessel is concerned as shown in **Fig.12.**
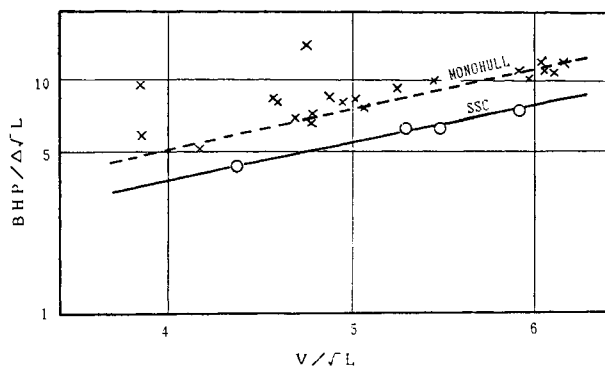
Fig. 12 Speed Power Relation of SWATH and Mono-Hull1

Speed in waves is generally decreased due to the limit of acceptable acceleration and/or to the hull resistance increase. SWATH can maintain the loss of speed in waves to the

minimum extent. An example of actual operation record of "Seagull" is shown in **Fig. 13.** As shown in this figure, speed loss of 30-meter long ship in sea state 5 is about 5 percent in speed.
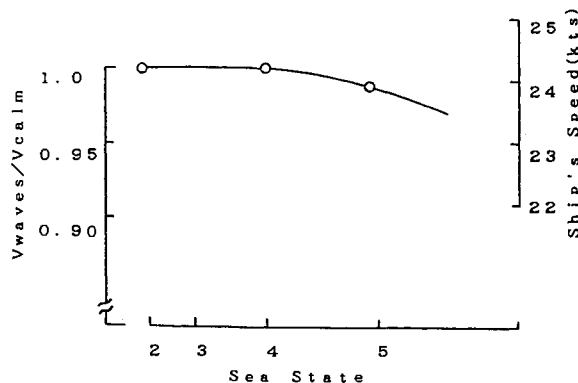
Fig. 13 Speed Loss in Waves of "Seagull"

4.6 Motion in Waves

On some vessels fins are not automatically controlled. Even if fins are not controlled, the motion response is very small compared with conventional vessel with similar size. Some examples of motion response of "Kaiyo" is shown in **Fig. 14** and **Fig. 15** for rolling and bow vertical acceleration, respectively. In these figures, tank test results and theoretical calculation results are also shown.
The actual ship data covers wide wave range from very calm to the rough seas with wave height of about 9 meters. The response are plotted for four speed ranges from zero to 13 knots.
The measured significant value of rolling is about 10 degrees at 8 meters wave height. Regarding acceleration, less than 0.2 g is measured at 8 meters wave height. These results well support the activity of the researchers onboard.
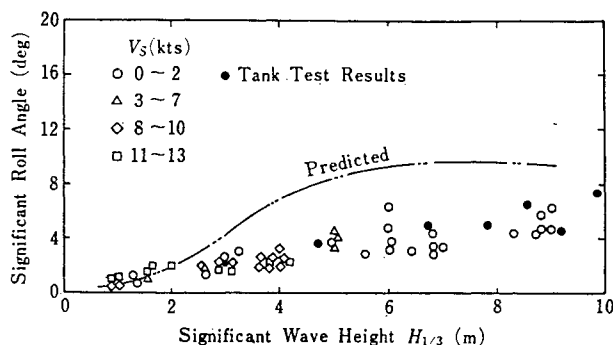
Fig. 14 Rolling Motion of "Kaiyo"
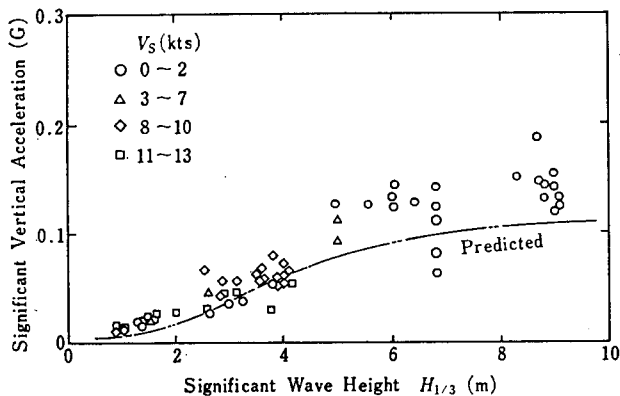
Fig. 15 Acceleration at F.P. of
"Kaiyo"

5. Future Prospect

The requirement for high quality
marine transportation in Japan will
increase, reflecting the trend of
economic growth and public demand. In
terms of passenger transportation, a
comfortable and regular service system
is becoming to be required even for
islands in remote ocean because there
are many inhabited islands around the
main land. In addition, the use of
ships for marine leisure is becoming
popular. Therefore, the application
of SWATH vessel will be expanded in
future.

Generally, the keen interest in
oceanographic research and survey
requires a more efficient platform
supporting the researcher's activity
at sea. This is not limited to Japan
but is a global trend. The SWATH type
of vessel will afford stable and com-
fortable laboratories on site even in
rough seas, and contribute to ac-
celerate the research activity.

The SWATH vessel is one of the most
promising vessels for future applica-
tion to the marine transportation of
light density cargo such as passenger.
The key technology of SWATH vessels is
mainly weight- oriented, and
breakthrough in materials and propul-
sion equipment will make it possible
to design ships with various kinds of
functions besides the present use.

6. Concluding Remarks

The technology of the SWATH type
vessels were reviewed mainly form the
aspect of their design and construc-
tion. In future, a wide variety of ap-
plications is expected, taking advan-
tage of their superior performance in
waves. The most promising and advan-
tageous field will be passenger
transportation and also the support of
oceanographic or geographic research.

References

1. Oshima, M.,et.al., "Development of
   Semi-Submerged Catamaran (SSC)",
   AIAA/SNAME A.M.V.C., No. 79-2019,
   1979
2. Lang, T.,et.al. "Design and Develop-
   ment of the 190-Ton Stable Semi-
   Submerged Platform (SSP)", Trans.
   ASME Paper No. 73-WA/   Oct-2
3. Narita, H.et al., "Design and Full
   Scale Test Results of Semi-
   Submerged Catamaran (SSC) Vessel",
   IMSDC '82, April, 1082
4. Covich, P., "SWATH T-AGOS Production
   Design", AIAA No. 86-2384, Sept.,
   1986
5. "Ship of the World", November, 1988,
   Page 191 (In Japanese)
6. Mitsuhashi,K., et. al., "Underwater
   Radiated Noise Signature of
   the Semi-Submerged Catamaran (SSC)",
   Mitsui Engineering &
   Shipbuilding Co., Ltd., Technical
   Bulletin No.114, April
   1982.
7. Amitani, Y., et. al., "Study   for
   Reduction of Underwater
   Noise Radiated from 'Kaiyo'", Tech-
   nical Report of JAMSTEC,
   No.14, 1985
8. Report of Committee V-4, "Novel
   Design Concept-SWATH", ISSC88,
   August, 1988, Vol.2
9. Kobayashi, M., Shimada, K., "Dynamic
   response Analysis of Marine
   & Offshore Structures (DREAMS)",
   Mitsui Engineering & Ship-
   building Co., Ltd. Technical Bul-
   letin No. 126, October 1985
10. Niho, O., Nishimura, K., "Recent
    Developments in Structural
    Design of Merchant ships", Mitsui
    Engineering & Shipbuilding
    Co., Ltd., Technical Bulletin No.
    138, October 1989
11. Murotsu, Y., et. al., "Structural
    Systems Reliability Assess-
    ment of Semi-Submerged Catamaran",
    to be presented at the
    Spring Meeting of the Society of
    Naval Architects of Japan,
    May 1990

NUMERICAL DETERMINATION OF THE LIFT DISTRIBUTION OF HIGH SPEED CRAFT

Yasushi Yoshida*, Tamotsu Nagai**

* Technical Research and Development Institute, Japan Defense Agency, Japan
** Kanagawa Institute of Technology, Japan

Abstract

This paper describes the numerical method to obtain the lift distribution of a high speed craft having vee- or wave-shaped bottom with chine under the planing condition, which is applicable to the initial design.

The free surface of water is first determined by applying the impact theory to motion analysis of two-dimensional hydrodynamical model dropped on the still water with the velocity equal to the vertical speed component of model speed.

The longitudinal dynamic lift distribution is determined by the momentum change theory, considering this free surface. The change of dynamic lift to static lift at the planing speed is obtained, which enables designers to presume change of center of buoyancy. Also the pressure distribution at each transverse section is obtained by Bernoulli's equation, considering wetted wedge's spread. The numerical results are reasonably compared with the actual craft records, and model test data showing the good correspondence.

Nomenclature

W : potential function, $W = \phi + i \psi$

ϕ : velocity potential

ψ : stream function

i : imaginary unit

Z : complex variable, $Z = x + i y$

u : x-direction velocity

v : y-direction velocity

U : $U = \sqrt{u^2 + v^2}$

$\bar{v}$: wedge cross section's downward speed

ζ : rise of free surface

ζ_∞ : ζ at infinite distance, i.e. depth of keel from water line at a transverse section (see Fig. 4 and 5)

$\dot{\zeta}$: upward velocity of free surface

t : time variable

c : maximum half-width of wetted wedge (see Fig. 2)

$\lambda(c)$: spread coefficient of a wedge width, $\lambda(c) = d \zeta / d c$

a_i ($i = 1,2,3,\cdots$) : unknown coefficients composing $\lambda(c)$

F_∇ : Froude number, $F_\nabla = V / \sqrt{g \cdot \nabla^{1/3}}$

V : speed of model

g : gravity acceleration

∇ : displacement of model at $V = 0$

Δ : displacement weight of model at $V = 0$ in N

R : total resistance in N

m : virtual mass $m = K \rho \pi c^2 / 2$, where $K = 1$ in this case according to H.Wagner's virtual mass [1]

ρ : fluid density

n : dynamic lift at a transverse section of model for unit length normal to the section in N/cm

N : total dynamic lift in N, sum of n

Ns : total dynamic lift by spray in N

s : static lift at a transverse section of model for unit length normal to the section in N/cm

S : total static lift in N, sum of s

τ : angle between water line and keel line at a point on keel, $\tau = \tau' + \theta$

τ' : trim

θ : angle between water line and tangent at
     a point on keel

p : dynamic pressure on the bottom hull along
     a transverse direction in N/cm^2

P_∞ : fluid pressure at infinite distance in
     N/cm^2

F(t) : Bernoulli's coefficient

1. Introduction

Theoretical analyses about high speed crafts are quite few concerning systematic model tests. [2],[3] At the planing condition, induced dynamic lift causes the hull to rise and hence its wetted surface area decreases. This will result in the decrease of resistance coefficient $R/\{(\frac{1}{2})\cdot \rho V^2 \nabla^{2/3}\}$. This phenomena are the inherent property of high speed crafts different from displacement type ships such as destroyers etc..

In this report, the dynamic lift distribution is obtained by applying the impact theory to the motion analysis for a wedge's two-dimensional hydrodynamical model which was dropped on still water. The dropped wedge causes the initial water line to rise. Its free surface is first determined. Then obtained are the longitudinal dynamic lift distributions together with dynamic pressure distribution at each transverse direction.

The numerical results are reasonably compared with actual craft records, and also with model test data showing the good correspondence. By this method, therefore, we can determine (1) the lift distribution of hull, (2) the ratio of dynamic lift to static lift, and (3) the traveling center of buoyancy at the initial design phase.

2. Relation between Resistance and Trim at Each Crusing Condition

Three crusing conditions such as displacement, semi-planing, and planing conditions are discussed below.

(1) Displacement condition

The stern sinks gradually to the lowest point from Froude numbers 1.0 to about 1.5, and increasing trim τ' from about 100 minutes to about 200 minutes. There are few cases the bow sinks

at low speed up to about $F_\nabla = 0.5$, but then the bow gets upward. Under these conditions, the total resistance R increases undulatingly, and makes the last hump on the total resistance coefficient at about $F_\nabla = 1.0$. Near around this last hump, the wave making resistance will become the maximum. Experimental data show that the larger trim, the larger becomes total resistance coefficient. [3]

(2) Semi-planing condition

The stern continues to rise from the lowest position after the last hump from $F_\nabla = 2.0$ up to 2.5, and the draft becomes still water condition. As the hull will get greater trim reaching about 300 minutes, the wetted area and total resistance coefficient decrease. At this condition small quantity of dynamic lift appears.

(3) Planing condition

The dynamic lift appears remarkably beyond about $F_\nabla = 2.5$. As increase in Froude number from about 2.5 up to 3.5, the stern rises back to the point of initial draft at rest and goes further up. Its trim τ' decreases than that of semi-planing condition, and keeps ups and downs about 300 minutes and about 150 minutes. This causes both wetted surface area and total resistance coefficient become small. The total resistance consists of frictional resistance, wave making resistance, and spray making resistance. Test data indicate that total resistance coefficients decrease as trim's increase, showing reverse compared with that of the previous displacement condition. [3] (see Fig.1)

Since the planing condition is the typical characteristics of high speed crafts, the theoretical analysis is now carrid out.

First of all, a spread coefficient of a wedge width will be expressed in mathematical form, which was used by H.Wagner. [1]
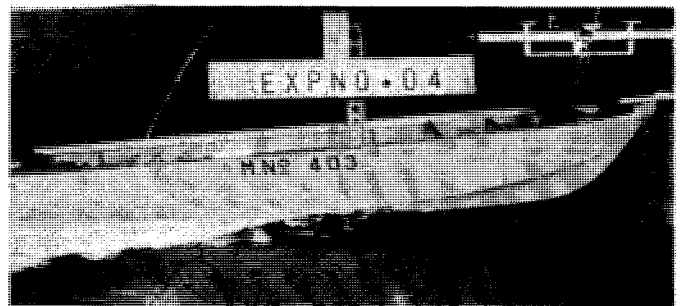
Fig.1 Planing at $F_\nabla = 3.5$

3. Formulation of Free Surface during Impact

3.1 Spread Coefficient of a Wedge

During the two-dimensional wedge's impact a-gainst water the free surface of water rises near the wedge. [1],[4]-[6] To determine the free surface, we need spread of the width at the point c on wedge surface, and hence $\lambda(c)$ will be introduced as a polynominal equation

$$\lambda(c) = \sum_{i=1}^{n} a_i c^{i-1} \qquad (1)$$

where $a_1 \neq 0$, and $a_2 = a_3 = a_4 = a_5 = \cdots = 0$ mean vee-shaped wedge. With arbitrary coefficients of a_i any shaped wedges are determined. Since each transverse section of the hull requires a wave-shaped wedge, we used five a_i coefficients (i = 1,2,3,4,5) to fit the shape of wedge. To analyze the planing condition, wedge's impact phenomena are applied. Speed V of model consists of $V \sin \tau$ normal to the keel line and $V \cos \tau$ parallel to the keel line. The velocity normal to the keel line will be used to calculate the dynamic lift, because fluid phenomena normal to the keel line are similar to those of the wedge's impact model.

We determine the free surface by using H.Wagner's method, and then the dynamic lift are followed.
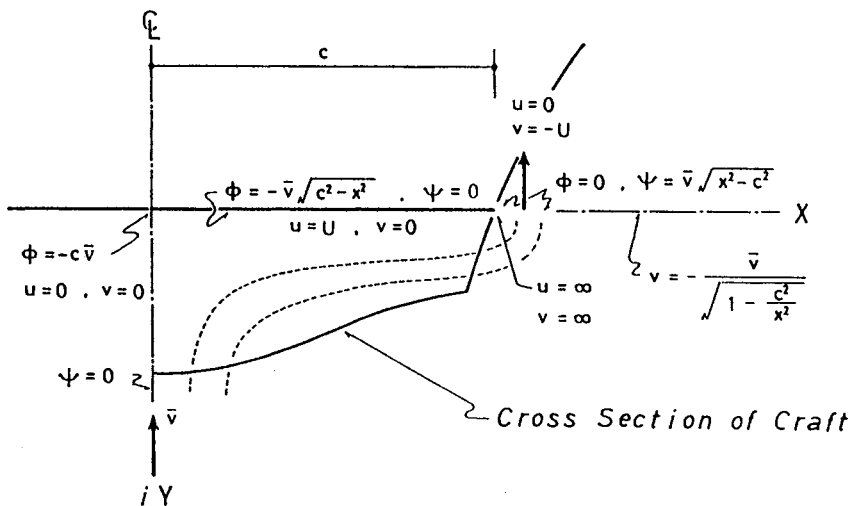
3.2 Determination Method of Free Surface

The free surface and the rise of bow of model ($\Delta = 788.06$ N) at planing condition $F_{\nabla} = 3.5$ are shown in Fig.1. Assumptions of analysis are given below :

(a) ideal fluid

(b) neglect of g's effect against impact load

(c) symmetrical two-dimensional flow

During planing with speed V, the transverse section normal to the keel line moves downward with speed $\overline{v}$. Supposing that hull is staying, fluid around the section will move upward with speed $\overline{v}$ as shown in Fig.2. Considering a number of horizontal layers having half width c within the section, this each layer will be supposed to have fluid with speed $\overline{v}$ upward. In such a fluid field, we try to obtain the free surface. A layer will be made successively from the apex of the section while moving downward. The layer's right end moves along the surface of wedge, which is the spray root. In the right half plane x > c of Fig.2, there are the free surface ranges. The potential function in this fluid field of layer W is given by the rising speed of the surface $\overline{v}$

$$W = \phi + i\psi = i\overline{v}\sqrt{z^2 - c^2} \qquad (2)$$

The boundary condition of ϕ, ψ, u, and v are given in Fig.2. Since $\phi = 0$ means the range x > c,

$$\psi = \overline{v}\sqrt{x^2 - c^2}$$

$$\qquad (3)$$

then,

$$v = -\frac{\partial \psi}{\partial x}$$

$$= \frac{-\overline{v}}{\sqrt{1-(c/x)^2}}$$

$$\qquad (4)$$

This v results in the

$\phi = -\overline{v}\sqrt{c^2-x^2}$, $\psi = 0$

u = U , v = 0

$\phi = 0$, $\psi = \overline{v}\sqrt{x^2-c^2}$

u = 0
v = -U

$\phi = -c\overline{v}$
u = 0 , v = 0

u = ∞
v = ∞

$v = -\dfrac{\overline{v}}{\sqrt{1-\dfrac{c^2}{x^2}}}$

$\psi = 0$

Cross Section of Craft

Fig.2 Flow Field

rise of free surface ζ at t, causing
the wedge half width to spread up to c
after the apex contacts with the water.
ζ is given by

$$\zeta = - \int_0^t v \, d t \qquad (5)$$

Now if $\lambda(c)$ is defined as

$$\lambda(c) = \frac{d \zeta / d t}{d c / d t} = \frac{\dot{\zeta}}{d c / d t} \qquad (6)$$

Then Eq.(5) becomes such as ·

$$\zeta = \int_0^c \frac{\dot{\zeta}}{\sqrt{1-(c/x)^2}} \cdot \frac{\lambda(c)}{\dot{\zeta}} d c$$

$$= \int_0^c \frac{\lambda(c) d c}{\sqrt{1-(c/x)^2}} \qquad (7)$$

Since Eq.(7) excludes time t term, ζ is a
function of only c variable.

Required is that ζ at c moves along the
wedge's contour or cross section. To satisfy this
requirement the least sqare method is applied at
selected points. Unknown coefficients of a_i in
Eq.(1) are now obtained. A computer program for
the multiple regression analysis is used for this
calculation. [2]

3.3 Obtained Results ·

12 points from keel to chine, and 6 points from
chine to deck side are selected to determine 5
a_i, satisfying the boundary condition within 3 %
error.

The free surface is calculated at each wetted
ordinate of the hull, but around the midship ordi-
nate at one-fifth distance between each ordinate
in order to search the peak of the dynamic lift.
Number of ordinate of 2.5 m model is defined
as 0 at the bow and 10 at the stern.

As an example, the relation between c and
$\lambda(c)$ at Ord.6 is obtained in Fig.3. This
$\lambda(c)$ should be substituted into Eq.(7) to get
ζ at the points x > c . Up to the infinite
distance, this ζ should be assembled successively
to determine the free surface. Obtained free sur-
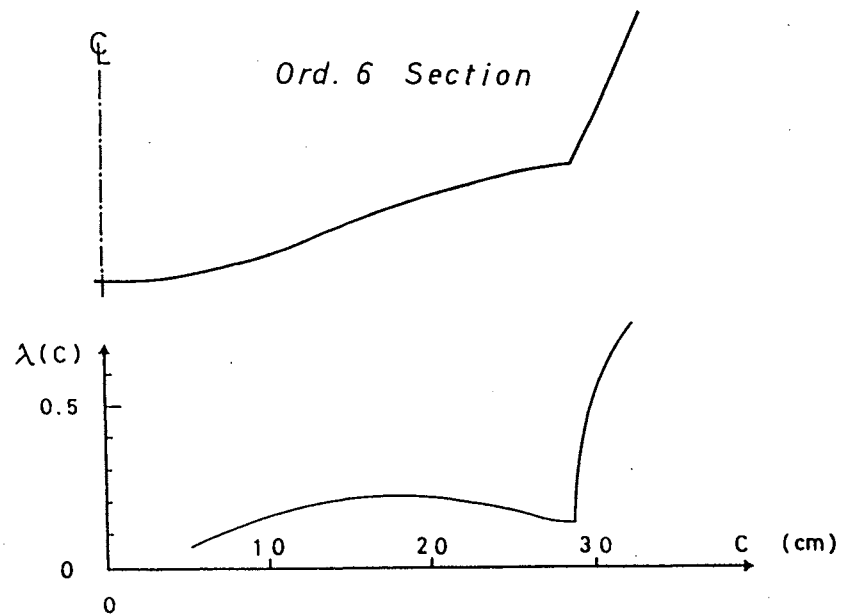
Fig.3   c and $\lambda(c)$ at Ord.6

faces are shown in Fig.4, in case of hull dis-
placement Δ = 788.06 N for each Froude number
F_{∇} = 2.5, 3.0, 3.5. Also the case of Δ = 588.40
N is shown in Fig.5. These figures show the
change of the free surfaces upward corresponding
to the decrease of Froude numbers. A cross point
of the hull side with the surface is considered as
the source of spray. This point may be called as
spray root. The special case occurs at chine,
which is the discontinous point on the contour
showing nearly the same point of a spray root, as
the case of F_{∇} = 3.5 in Fig.4. Calculations
for the wetted chines were all done by 2 steps :
as the first step the surface having its origin at
the chine like this special case was determined,
and then additional water rise ζ was calculated
on its first surface.

Based on these spray roots, the dynamic lift
will be obtained.

4. Dynamic Lift along the Lengthwise Direction

4.1 Formulation

Dynamic lift n normal to the keel line will be
given as the change of momentum. [1],[4]-[6]

$$n = \frac{d}{d t} (m \dot{\zeta}) \qquad (8)$$
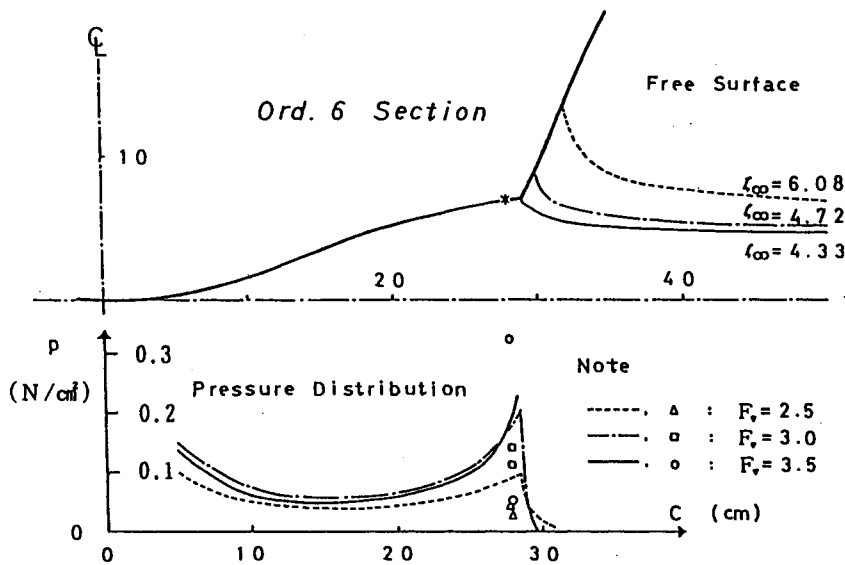
Fig.4　Free Surface and
Pressure Distribution
at Ord.6 (Δ = 788.06 N)
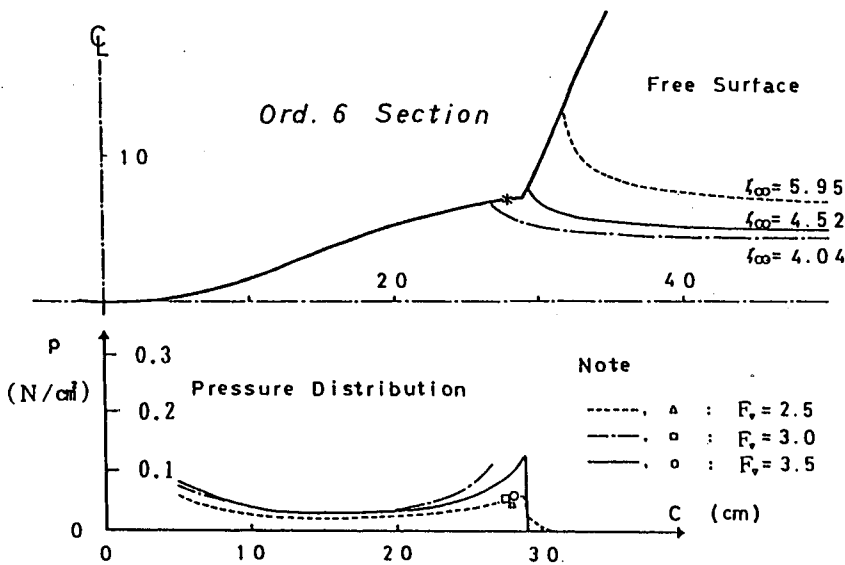
Fig.5　Free Surface and
Pressure Distribution
at Ord.6 (Δ = 588.40 N)

$\ddot{\zeta} = 0$　because of hull's constant speed can be substituted into Eq.(8). This n results in the following non-dimensional form.

$$\frac{n}{c\left(\frac{1}{2} \cdot \rho \, \dot{\zeta}^2\right)} = \frac{2\pi}{\lambda(c)} \qquad (9)$$

This form is made by $\frac{1}{2} \cdot \rho \, \dot{\zeta}^2$ of dynamic pressure and c of half width. These can be determined by the following ways.

(1)　c
Based on the trim at a planing condition,

$$\zeta_\infty = \lim_{x\to\infty} \int_0^c \frac{\lambda(c)\,dc}{\sqrt{1-(c/x)^2}}$$

$$= \int_0^c \lambda(c) \, dc \qquad (10)$$

(2)　$\dot{\zeta}$
As a downward speed normal to the keel line,

$$\dot{\zeta} = V \sin \tau \qquad (11)$$

4.2　Obtained Results

Dynamic lifts, n, in N/cm obtained by Eq.(9) are shown in Fig.6 and 7 corresponding to Δ =788.06 N　and 588. 40 N, with number of ordinate on abscissa, where Ord.0 means the cross of the keel line with the chine line and Ord.10 the keel end.

The amount n becomes large around Ord.3, starting from the contact point with water surface. This is due to large τ value around Ord.3, comparing τ value between Ord.5 and Ord.10. Hence, the amount n becomes large due to the effect of $\dot{\zeta}$ by Eq.(9). Then, the dynamic lift around bow range becomes larger with higher speed and larger keel curvature.

The maximum n appears near midship, where $\lambda(c)$ of Eq.(9) is small. This means that to obtain larger dynamic lift near midship we need smaller deadrise angle, and larger c of Eq.(9). The peak value of n appears again around Ord.8, because of small $\lambda(c)$ as shown in Fig.6 and 7.

These figures show that the larger dynamic lift is brought corresponding with larger Froude num-

Fig.6 Dynamic Lift and Static Lift

(Δ = 788.06 N)

Fig.7 Dynamic Lift and Static Lift

(Δ = 588.40 N)

4. 3 Static Lift along the Lengthwise Direction

Static lifts, s ,in N/cm which are buoyancies, are shown in Fig.6 and 7 corresponding to Δ = 788.06 N and 588.40 N. As static lifts change corresponding to the cross section area under water surface, the amount of static lifts increase from the bow through the stern with decrease in Froude number. (see Fig.6,7 and Table 1)

Table 1 Ratio N / (N+S)

Δ in N	F_{∇}	Lift in N		$\dfrac{N}{N+S}$
		N Dynamic Lift (sum of n)	S Static Lift (sum of s)	in %
788.06	2.5	261.7	430.8	38
	3.0	351.8	330.3	52
	3.5	354.2	276.4	56
588.40	2.5	155.0	398.3	28
	3.0	196.1	267.2	42
	3.5	250.0	269.6	48
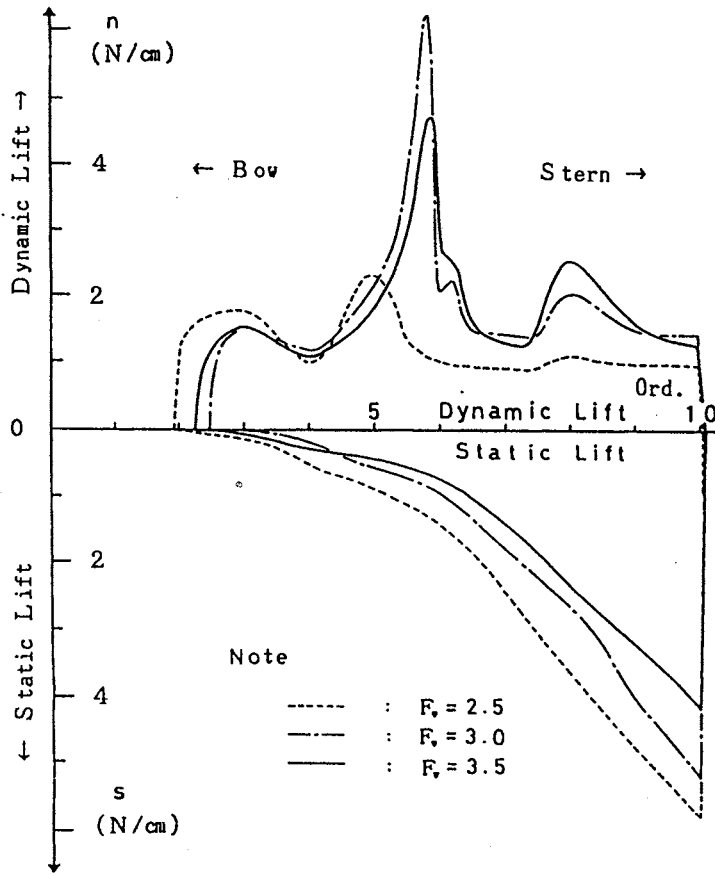
Also, the dynamic lift due to spray Ns, which is the sum of the dynamic lift distribution due to spray, is roughly given by deducting both dynamic and static lifts by water, N (sum of n),S (sum of s) from the weight of the model Δ, as shown in Table 2. This table indicates that at F_{∇} = 3.5 the dynamic lift is a 65 % share of the total lift N + Ns + S ,and the dynamic lift due to spray Ns is a 31 % share of the dynamic lift N + Ns in case of Δ = 788.06 N.

Table 2 Ratios of Lifts

Δ in N	F_{∇}	Lift in N			(N+Ns)/ (N+Ns +S)	Ns/ (N +Ns)
		N Dynamic Lift (sum of n)	Ns Spray Lift	S Static Lift (sum of s)	in %	in %
788.06	2.5	261.7	96.5	430.8	45	27
	3.0	351.8	106.0	330.3	58	23
	3.5	354.2	157.5	276.4	65	31
588.40	2.5	155.0	35.1	398.3	32	18
	3.0	196.1	125.1	267.2	55	39
	3.5	250.0	68.8	269.6	54	22
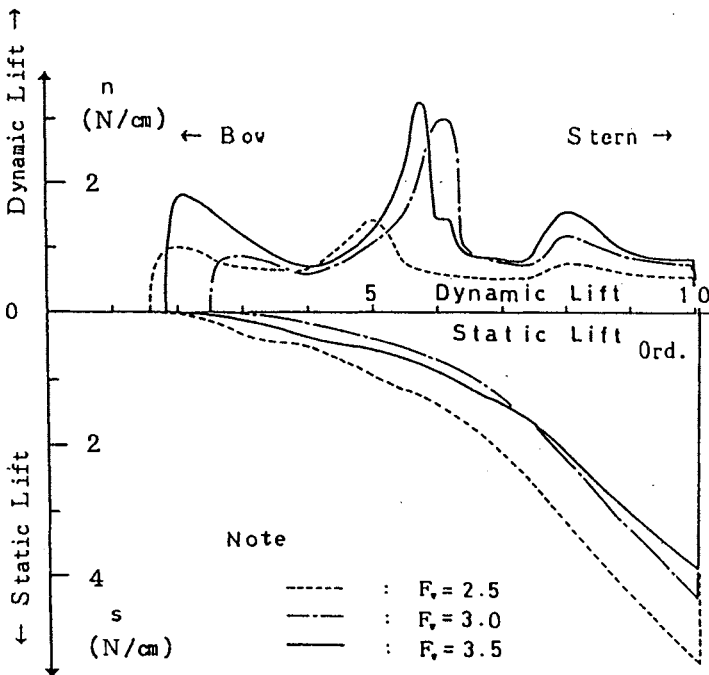
Then, the dynamic pressure distribution on the bottom hull along a transverse direction will be analyzed.

5. Dynamic Pressure Distribution on the Bottom Hull along the Transverse Direction

5. 1 Formulation

Bernoulli's equation is expressed neglecting external force,

$$\frac{P}{\rho} = - \frac{\partial \phi}{\partial t} - \frac{U^2}{2} + F(t) , \qquad (12)$$

where $F(t)$ is Bernoulli's coefficient as

$$F(t) = \frac{U^2}{2} + \frac{P_\infty}{\rho} \qquad (13)$$

In Fig.2, a uniform speed at the infinite distance U equals to a wedge cross section's downward speed $\overline{v}$, i.e. $U = \overline{v}$. Hence $F(t)$ is

$$F(t) = \frac{\overline{v}^2}{2} + \frac{P_\infty}{\rho} \qquad (14)$$

Both ϕ and U calculated under the layer in Fig.2 are substituted into Eq.(12). Considering fluid pressure P_∞ at the infinite distance of Eq.(14) as zero and using condition $d\dot{\zeta}/dt = 0$, p will be obtained.

$$p = \frac{\rho \overline{v}^2}{\lambda(c)} \left[\frac{1}{\sqrt{1-(x/c)^2}} \right.$$

$$\left. - \frac{\lambda(c)}{2\{(c/x)^2-1\}} + \frac{\lambda(c)}{2} \right] \qquad (15)$$

Using Eq.(15) the pressure distribution on the bottom hull was determined. Pressure distributions of Ord.6 section for Froude number from 2.5 through 3.5 were shown in Fig.4 and 5 in case of $\Delta = 788.06$ N and 588.40 N, having the maximum at the position close to the spray root. At the other sections, the same distribution patterns were obtained as that at Ord.6 section. It is

considered that these phenomena are similar to those of seaplanes. [7],[8]

5. 2 Measured Pressure at Near-by Chine Line

Pressure distributions for an actual craft were measured at Ord.6, showing good correspondence in distribution between calculated results by Eq. (15). [9] (see Fig.8)
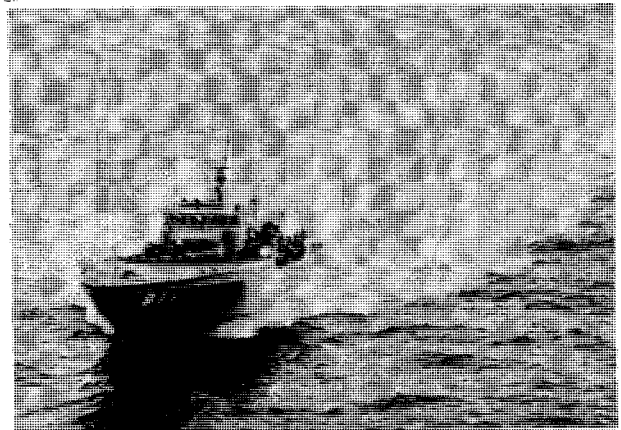
Fig.8 Recording by Actual Craft

On the other hand, model tests were carried out to measure pressure at a point close to the chine line, where pressure becomes the maximum. The manometer is installed at this point, as marked " * " shown in Fig.4 and 5. This marked point is 11 mm forward from Ord.6 and 10 mm inside from the chine line.

The measured values are plotted by marks " Δ ", " $\square$ ", and " $\bigcirc$ " in these figures, showing good tendencies around the calculated curves by Eq. (15). The two cases show us being non-convergent at $F_\nabla = 3.0$ in Fig.5 and $F_\nabla = 3.5$ in Fig.4.

Computer program in our calculation is briefly given as follows.

6. Computer Program

```
          ( Start )
              |
   -------------------------
   |        input          |
   |  Cross section etc.   |
   -------------------------
              |
   -------------------------
   |  Spread coefficients  |
   |  λ(c) of Eq.(1)       |
   -------------------------
              |
             Ⓐ
```

```
         Ⓐ
┌─────────────────────────────┐
│   Free surface of Eq.(7)    │
└─────────────────────────────┘
               │
┌─────────────────────────────┐
│   Dynamic lift of Eq.(9)    │
└─────────────────────────────┘
               │
┌─────────────────────────────┐
│ Pressure distribution at a  │
│      section of Eq.(15)     │
└─────────────────────────────┘
               │
┌─────────────────────────┐
│   Results               /
│                        /
└───────────────────────/
               │
        ( E n d )
```
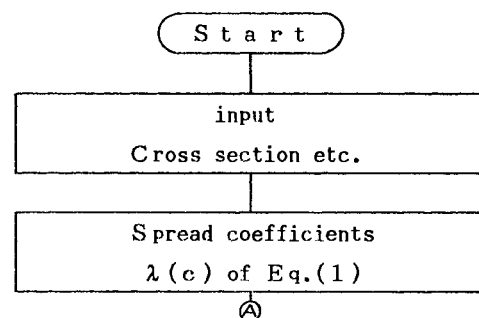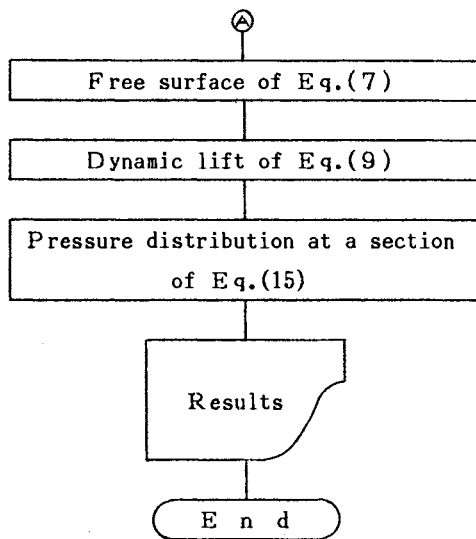
For each cross section, using this program calculations were pursued concerning relation between c and $\lambda(c)$, plotting free surface up to the infinite distance, dynamic lift, and pressure distribution on the bottom hull.

Conclusions

A numerical method is presented to get lift distributions of vee- or wave-shaped bottom hull with chine under the planing condition.

(1) In the theoretical analysis, the two-dimensional impact model of a wedge is used in order to estimate approximately the free surface during impact, then, the use of change of momentum on this results to dynamic lift distributions along the ship length.

(2) The pressure distributions on the bottom hull along the transverse direction are also obtained by Bernoulli's equation with the spread coefficients of wedges conforming to the bottom hull.

(3) These distributions are compared with experimental data, showing reasonable coincidencies between them.

Finally we are grateful to many members of Japan Tank Test Committee of the Society of Naval Architects of Japan for their valuable discussions.

References

1. Herbert Wagner, "Über Stoss- und Gleitvorgänge an der Oberfläche von Flüssigkeiten", Zeitschrift für Angewandte Mathematik und Mechanik, Band 12, Heft 4, Aug.1932

2. Tamotsu Nagai, Hirotsugu Tanaka and Yasushi Yoshida, "Statistical Analyses of Model Test Results in Still Water", Jour. Soc. Naval Arch. of Japan, Vol.137, Jun. 1975

3. Yasushi Yoshida, Tamotsu Nagai, "Principal Component Analysis and Factor Analysis referring to Model Test Results in Still Water of High Speed Craft", Jour. Soc. Naval Arch. of Japan, Vol.140, Dec. 1976

4. Tamotsu Nagai, Yasushi Yoshida, "Numerical Method to obtain the Lift Distribution of High Speed Crafts", Technical Research and Development Institute, Japan Defense Agency, TR－A－816, Dec.1980

5. Tamotsu Nagai, Yasushi Yoshida, "The Free Surface of a Omega-Plane Type High Speed Claft under the Planing Condition", First Division of Japan Tank Test Committee, Report No.51－6, 19 Feb.1980

6. Yasushi Yoshida, Atsushi Shintani, "The Dynamic Pressure of a Omega- Plane Type High Speed Craft under the Planing Condition", First Division of Japan Tank Test Committee, Report No.52－3－9, 27 Jun.1980

7. Tamotsu Nagai, Tatsumi Sakurai and Junsei Nagai, "Test Result of Bottom Pressure Distribution of STOL Seaplane Model", Jour. Japan Society of Aerospace, No.179, Vol.16, Dec.1986

8. Tamotsu Nagai, Masami Hamamoto and Hisanao Ito, "Determination of Wave Impact Loads", Technical Research and Development Institute, Japan Defence Agency, TR－586, May 1974

9. Tamotsu Nagai, "On the Strength Calculation of All-Welded Aluminium Alloy High-Speed Craft during Slamming", Committee of Light Metals for Shipbuilding Industry, Committee Report No.14, Jun. 1969

MODEL TESTS OF STEPLESS AND STEPPED PLANING BOATS WITH DEEP VEE HULL

T. Hori*, J. Fujisawa*, N. Hirata*, I. Saito*, J. Hasegawa*, M. Makino*, M. Yamaguchi**

* Ship Research Institute, Japan
** Technological Research Association of Techno-Superliner, Japan

Abstract

The report presents some results of resistance tests in smooth water by four models of stepless and stepped planing boats, which have hull forms of deep vee. The stepless planing boat is called "Toreka 26", which has 7.95 m in an overall length. The model has 1/6 scale. The resistance test was performed with some changes of displacement and longitudinal centre of gravity. The test with vertical and horizontal variations of towing positions was, too, performed in order to check the effect on resistance and running trim.

The resistance tests were performed by three models of planing boats of the same hull form of deep vee with steps in the same manners as the stepless model.

In analysis of rise of model at running, some effects on surface elevation and sinkage by the towing carriage were noticed. These effects was constant under the speed about 4m/s of the towing carriage and surface elevation were not constant with time over that speed of towing carriage.

Finally, resistance, trim and rise of four models were presented with some con siderations.

1. Introduction

The planing hull form is extensively used for recreational craft, pilot boat, coast guard vessel, military patrol craft, racing boats and work boats for offshore industry. The following range of geometric and operational parameters are typical for existing planing hull designs:

Length overall	4 –	60 m
Length-to-beam ratio	3 –	7
Displacement	5 –	600 long tons
Speed	20 –	60 knots

The planing hull is designed for operation in the high speed range $Fn > 1.0$ (Froude number Fn is $V/SQRT(gL)$; V: the velocity, g: gravity acceleration, L: length overall). The hull form is characererized by:

A. Sharp chines and transom stern,
B. Straight buttock lines,
C. Bottom deadrise, increasing rapidly in the bow area,
D. Fine entrance waterlines

These characteristics of hull form of planing boats have been improved in viewpoints of induction of flow separation at the stern and along the sides, and reduction of impact loads in waves, reduction of low speed resistance.

When the planing hull is driven beyond the displacement ship speed range, it develops positive hydrodynamic bottom pressures. As the hydrodynamic lift increases with increasing speed, the amount of hydrostatic buoyancy decreases accordingly. In the planing condition, it is said that the flow separates from the transom and chines, and the resistance-to-displacement ratio is essentially constant for a given trim angle.

The high-speed resistance will be the least with the least angle of deadrise. However, in order to attain good directional stability and good turning characteristics, some deadrise is necessary. Recently large deadrise is considered better in order to run in rough water. If the seakeeping qualities are considered important and the deadrise angle are selected large, the performance qualities in the smooth water are worse than those with small deadrise angle. There are some methods for improvement of performance and one of them would be the boats with steps on the planing bottom.

There are some data of resistance tests and propulsion tests by the model for the high-speed boats in Japan but usually the model size are small about 0.8 m. And there are quite a few cases of model tests for planing boats, specially with steps.

Therefore, the Ship Research Institute had cooperation test program about planing boats with the Boat Association of Japan together and measured resistance in the large towing tank by large models with stepless and stepped planing boats, which have large angle of deadrise β of 20 degrees at the aft end.

There are some discussion of estimation method for the performance and correlation between results of model and full scale of a high-speed craft. Concerning to the model tests in the towing tank, the resistance test by planing boat models have been performed since about 50 years ago by National Advisory Committee for Aeronautics for seaplanes. In 1963, E.P. Clement and D.L. Blount presented their paper on the resistance of a systematic series of planing hull forms, generally known as the TMB Series 62 [2]. All of the considered hull forms had a constant deadrise of 12.5 degrees. In 1982, J.A. Keuning and J. Gerritsma presented the paper which showed the performance of planing boats with a deadrise angle of 25 degrees [5]. About the stepped planing boat, there are a few publications and one of them is that E.P. Clement and J.D. Pope presented in 1961 some graphs with some angles of deadrise of 0, 5, 10, and 15 degrees for performance prediction and design [1].

Savitsky et al. showed some explanation about model test technique for planing boats [4]. There remain some problems to investigate the procedure of estimation of performance or phenomena at high-speed fluid around hull.

So here resistance test by large models was performed in order to know the running attitude and trim of stepless and stepped planing boats, which were towed with free to heave and pitch. Moreover, the test was performed with vertical and horizontal variation of towing points.

It is requested to have a chance of full scale measurement in future to get correlation factor between model and full scale size.

2. Stepless and Stepped Models

The planing boat, considered here, is called "TOREKA 26", which has length overall of 7.95 m in full scale and maximum speed about 50 knots. The craft was built of carbon-fiber reinforced plastic in 1981. The deadrise angle at aft end is about 20 degrees. This hull form is stepless. Figure 1 shows the body plan of the craft. The craft has two spray strakes in each side. Table 1 shows the principal dimensions.

The model size should be selected within the limits given by the tank boundaries and capabilities of the test facility as large as possible to minimize scale effect. The towing tank in the Ship Research Institute, used for these resistance tests, has length of 400 m, breadth 18 m, depth 8 m and the towing carriage can run with speed over 10 m/s. Around the critical speed of the tank (SQRT(gH) ; g:gravity acceleration, H:the depth of the tank; 8.9 m/s in the tank), there occurs shallow water effects on the performance of model. To reduce shallow water effect, the model length should be smaller. It was requested that the the maximum speed of model should be 7.0 in Froude number $F\nabla$ based on the displacement and the weightiest displacement should be 2.0 tons in full scale. Therefore, the model was decided to have scale ratio 1/6 and the length overall 1.325 m.

It is said that the model length should be smaller than one-half of the tank width to reduce tank wall effects. The tank is enough wide to satisfy this condition.

The model was made of wood with transverse frame structure. It is important to pay attention to the vertical edges of the chine in order to promote

separation. Also, the transom is slightly recessed to promote flow separation at the stern.

Fig.2 shows the profiles of 4 models, one of them has no step, and others have steps. Each step has height of 50 mm in full scale. The stepless model is called "M1". The model "M2" has only one step afterward from the midship. The models "M3" and "M4" have two steps, as shown in Figure, one of which is afterward from the same position of the midship as the model "M2". The second step of model "M3" is at 33.3% of the length overall forward from the aft end and one of model "M4" is at 25%.

The resistance tests were measured with 3 conditions of displacement weight of 1.30, and 1.65, 2.00 ton (full scale) and 3 conditions of longitudinal center of gravity LCG of 25 % length overall and 30 %, 35 %.

The displacement was adjusted by fixed ballast inside of the hull. The LCG of the model was carefully controlled by balancing the fully equipped model in air.

A towing setup is given in Fig.3. The model was fixed in roll, yaw, sway and surge but free to heave and pitch during all tests. The model was towed on the propeller shaft line, which was estimated to have an angle of 5 degrees with the base line of the craft from the aft end. At all running trim conditions, the apparatus was manually adjusted vertically with help of a displacement censor to coincide with the shaft line. The towing force was measured not on the shaft line but on the horizontal component. The rise was recorded at the position near the aft end with the servo-motor displacement sensor and the running trim was recorded by an electric inclinometer.

When the model tests is performed in the towing tank, there are some measuring problems as towing points. The test with vertical and horizontal variations of towing points was, too, performed in order to check the effect on resistance and running trim. Fig.4 shows the towing points which are selected to compare the effect on the performance. As to the basic measurements, the point A was taken. In order to examine the effect by the vertical positions of tow, three points were selected as A, B and C, and for horizontal positions, three points selected as B, D and E. In the Figure, D' and E' are shown

as the the vertical positions on the line between A and C.

3. Effect by the Towing Carriage

The towing tank is used usually to measure the performance in the smooth water and waves for the conventional low-speed vehicles. The performance of the high-speed vehicles as air cushion vehicles, high-speed catamarans and hydrofoils have been measured in the tank. The model of the planing boat was, however, not yet measured in this towing tank. This experiment is the first test for planing boats with high-speed as $F\nabla$ =7. Therefore, it was necessary to check circumstances of the tank and the testing apparatus and system for test of planing boats.

The ITTC report shows some effect upon wave by the towing carriage. It says that, during model test of high-speed vehicles, the aerodynamic force due to the towing carriage may distort the free-water surface such that the model trim, heave, and resistance will be affected.

It is usually assumed that the water surface is constant and wave formation travels with the towing carriage. The data of the wave heights are usually measured at a fixed location along the length of the towing tank as a function of time while the carriage (without a model attached) travelled down in the tank. These data is considered the waves generated by the carriage as like those of the ship model. When the wave heights are measured at some different locations along the length of the tank at the runs of the carriage, these wave formations should be quite closed to one and almost the same.

During measurements of heaving of model at running, however, the records on heaving were noticed changing and not constant with time. This phenomena did not occur at the low-speed of the towing carriage but occurred in the high-speed range. Therefore, it was thought necessary that this phenomena should be checked by runs of towing carriage without the model attached.

In the case of large and full models as like tankers, there were some discussions of some effect upon performance by a wave generated at the acceleration time of the carriage with the model. When the carriage starts with constant

acceleration, then the solitary wave is generated by the accelerated models and this solitary wave progresses with the specific velocity of the tank (SQRT(gH)).

Therefore, this solitary wave can affect the performance of the model but after several seconds of a running time with a constant velocity, the solitary wave is far from the running carriage, and the effect from the wave is a little because the velocity of carriage is slower than the progress velocity of the solitary wave. And the slow acceleration was applied to the speed control system of the carriage and afterwards there is no problems of the tests for large and full models.

While the surface deviation was measured from the carriage during a run in high speed range without the model attached, the surface deviation was not constant as shown in Fig.5. Figure shows the surface variation under the carriage during runs with three speeds. When the speed of carriage is slower than about 4.0 m/s, the surface elevation under the carriage shows almost constant. In these cases, if the surface elevation is measured at the any other position of the carriage fore or aft, the surface variation is not different with time. While the speed is over that speed (two cases of speed 6.648 m/s and 9.685 m/s is shown here in the figure), the elevation is not constant with time and if surface elevations are measured at some other points of the towing carriage fore and aft, they are different each other. It would be thought that the surface variation is configured by a kind of a solitary wave in the towing tank and the wave progresses with the speed of SQRT (gH) and the wave would be growing with time.

Some surface elevations are thought to be generated by aerodynamic force of the towing carriage. And the velocity of wave of surface elevation are quite close to the speed of the towing carriage in the high-speed. Therefore, it is thought that the wave should affect the performance of models.

Therefore, it is necessary to measure the free-surface deviations under the carriage and specially around the setpoint of model during the run of the carriage without the model attached. This is based on the assumption that the wave elevation is generated mainly by the running carriage and not by the model. But when the model generates a larger wave of the same speed, then it is difficult to distinguish the wave of models. At least, it is necessary to measure the wave of the running carriage without a model attached and consider the wave in analysis of performance. In each run of different velocity of the carriage, it is necessary to measure the surface deviation. These data apply to one specific towing carriage and may and may not apply to others. Based on the data, it is recommended that the results appropriately applied to test procedures and the analysis of the data.

Under the towing carriage, the surface elevation was measured but not the wave slope because of lack of measurement time. It is necessary to measure the slope of the surface elevation and check the towing force by the effects of surface elevation slope.

4. Results of Resistance Test

The following quantities were measured for a given displacement and LCG position.

    a. Towing speed
    b. Total resistance in the direction of towing velocity, i.e., the horizontal component of the towing force
    c. Rise and sinkage of the model at a position near aft end
    d. Trim angle of hull relative to base line, and
    e. Photograph of model underway.

Adding to above, the video camera was used during the measurements. The following quantities are usually measured but here was not:

    f. Wetted pressure area from underwater photography, and
    g. Whisker spray area from visual observations

The resistance tests of the stepless model were performed with three displacement weights and three longitudinal centers of gravity. The tests of models with steps, which has the same hull form of deep vee, were performed in the same manners as the stepless model.

Fig.6 shows the example of the results, i.e., resistance-to-displacement ratio and running trim, mean rise of the model "M1" of 1.65 ton and LCG 30 % length overall. The running trim indicates the angle between the base line of the craft bottom and the horizontal line. The initial trim at stop is included with the running trim. The re-

sistance-to-displacement ratio are shown increasing as the speed increase.

At slow speeds, the weight of the craft is mainly supported by hydrostatic buoyancy, and above $F\nabla=1$ the hull experiences a hydrodynamic lift which increases with speed in the same way as the hydrostatic buoyancy decreases. The rise of medium between fore and aft ends indicates the beginning of a positive contribution of hydrodynamic lift. Figure shows that the model rises over the speed of $F\nabla=1$ and gets to the maximum at about $F\nabla=4$.

These results are obtained by the tow of 5 degrees to the base line and the rise are results with planing force and the towing force. The vertical component of towing force Fz is given as follows:

$$Fz = R \tan(\tau + 5) \qquad (1)$$

where R : resistance, i.e., horizontal component of tow force
τ : running trim in degree
From the results of the model test, the vertical component Fz is around 3 % of the displacement in the high-speed range over $F\nabla=3$.

Fig.7 shows the results of comparison of the 4 models in the case of the displacement 1.65 ton and LCG 30 % of L. The results of the model "M2" shows less resistance than those of the model "M1". The case of the model "M3" and "M4" with double steps have less resistance. The running trim is less than optimum (about 4 degrees) and, therefore, the resistance would be a little larger in general.

Some porpoising phenomena occurred in the case of 2.00 ton and LCG 25 % of L of "M2" and weak porpoising phenomena in the cases of 1.30, and 1.65 ton with LCG 25 % of L of the same model. It is thought that in these phenomena, the testing apparatus had some effects on porpoising oscillation. In the cases of "M1", "M3" and "M4", any porpoising did not occur.

Fig.8 shows the results of the cases by horizontal and vertical variation of the towing points. There are small changes in the resistance and running attitude by the horizontal variation. As the towing point moves from aft to fore, the running trim shows a little increases and the resistance decreases in the high-speed range. This is because the model was towed upwards along the shaft line and the model rose a little on the towing point.

In the case of vertical variation of towing points, the resistance increases and the rise and running trim decreases, as the towing points are higher. As the position of tow is higher, tow force increases and, then the pitching moment by the tow force increases to bow down, and acts less running trim and less rise.

It depends upon the testing apparatus and in some cases it is impossible to tow the model at the exact point and therefore it is necessary to know the effect on the performance of the towing points.

5. Consideration

It is said to the total resistance RT of a planing hull is the sum of the following components;

$$RT = RWF + RWB + RP + RS + RV + RAP + RAA \qquad (2)$$

Where RWF = wavemaking resistance
RWB = wavebreaking resistance
RP = pressure or induced drag
RS = spray resistance in whisker spray area
RV = viscous resistance in pressure area
RAP = appendage resistance, including struts, shafts, rudders, water scoops, interference drag, etc.
RAA = aerodynamic drag. Dependent upon frontal area of superstructure and fineness of bow. In model tests, the superstructure is usually omitted.

The spray resistance is negligible in the preplaning speed range and the remaining components of resistance are identical to those for displacement ships with their usual dependence upon Froude number and Reynolds number.

For a planing hull with straight buttock lines aft, the following simple relationship exits when planing:

$$RWF + RWB + RP = \triangle \tan\tau \qquad (3)$$

Where $\triangle$ = displacement weight
τ = trim angle
so that the hydrodynamic resistance RH of an unappended hull operating in the planing conditions is:

$$RH = \triangle \tan\tau + RV + RS \qquad (4)$$

and the first term on the left side is called pressure drag and the sum of the second and third terms is total viscous drag.

Fig.9 shows the results of model "M3", for example, as resistance-to-displacement ratio versus running trim with a parameter of speed. In low speed range, the results are lower than pressure drag component because the speed range are the displacement ship speed zones. In high-speed range, there shows planing conditions and the running trim is lower than a specific trim angle at which the drag is a minimum (maybe about 4 degrees) and therefore the resistance is large.

Fig.10 shows the total resistance coefficients versus the running trim with parameter of speed. The total resistance coefficients are expressed by displacement volume and speed. These results show similar among those model because those models have the same deadrise angles.

Because the drag of planing hulls is sensitive to running trim angle, consideration should be given to the pitching moments created by the lift and drag of the steps. It is thought that the steps at the bottom would have some effect on planing area and trim and would make close to the optimum planing trim of about 4 degrees if the step can control planing area and aspect ratio by the positions and heights of steps with balance of LCG position and propelled force.

6. Conclusion

High-speed crafts are designed with many data of experience and experiment. It is considered too expensive to perform some experiments with a large scale model in the towing tank. Therefore, while the designers would like to get or check the performance of the craft, they used to have full-scale measurements but usually the results is dependent on the circumstance as wind and wave, current. The data by full-scale measurements would be more complicated and therefore difficult to find some small changes of performance and to distinguish some effects among the performance.

In this paper, some results show that the step can have some effect on planing area and trim. If full scale measurement is performed, it would be too difficult to distinguish the differences.

In future, the model test technique for planing boats will be examined with-

in the boundary conditions and capability of the tank, and variations of steps will be examined with some full scale measurements.

References

1. Clement, E.P., and Pope, J.D., "Stepless and Stepped Planing Hulls-Graphs for Performance Prediction and Design", DTMB Report 1490 (1961).
2. Clement, E.P., and Blout, D.L., "Resistance Tests of a Systematic Series of Planing Hull Forms", Transaction SNAME, Vol.71 (1963).
3. Savitsky, D., "Hydrodynamic Design of Planing Hulls", Marine Technology, Vol.1, p.71-95 (1964).
4. Savitsky, D. et al., "Status of Hydrodynamic Technology as Related to Model Tests of High-Speed Marine Vehicles", David Taylor Naval Ship R&D Center Report DTNSRC-81/026 (1981).
5. Keuning, J.A. and Gerritsma, J., "Resistance Tests of a Series of Planing Hull Forms with 25 Degrees Deadrise Angle", I.S.P. Vol.29, No.337 (Sept. 1982).
6. 17th ITTC Report of the High-Speed Marine Vehicle Committee (1984).

Table 1 Principal Dimension

		Craft	Model
L_{OA}	(m)	7.95	1.325
B_{nX}	(m)	1.90	0.317
B_{Cn}	(m)	1.40	0.233
B_{CR}	(m)	1.65	0.275
β_n	(deg.)	29.74	
β_R	(deg.)	19.86	
Scale		6	
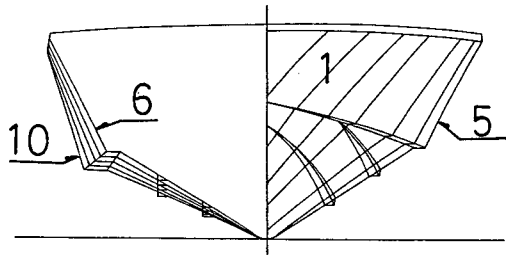
Fig.1 Body Plan of "TOREKA 26"

Fig.2 Profile of Models

Number : % of L

Fig.3 Towing Setup

Number : % of L
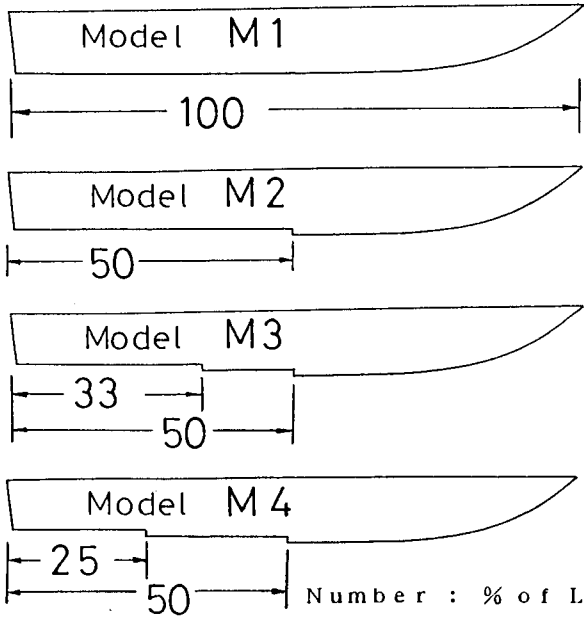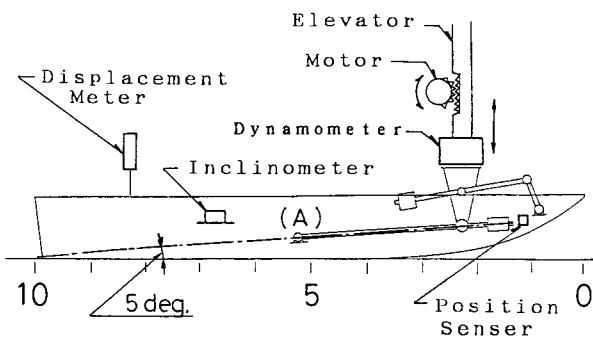
Fig.4 Towing Points
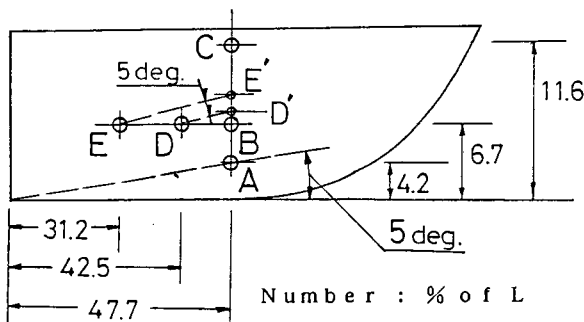
Number:Velocity
       of Carriage,m/s
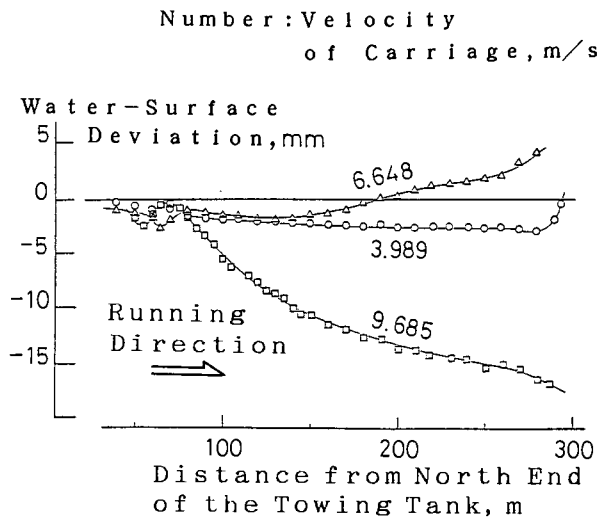
Fig.5 Water-Surface Deviation
      under the Running Carriage

Model M1

Fig.6 Results of M1 with
      △=1.65ton and LCG/L=0.30
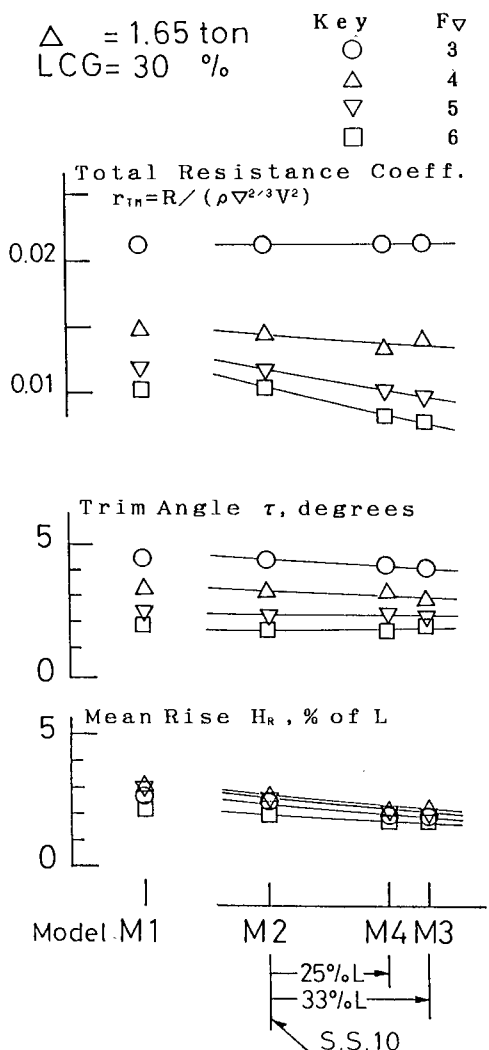
Fig.7 Comparison of 4 Models
    of △=1.65ton and LCG/L=0.30
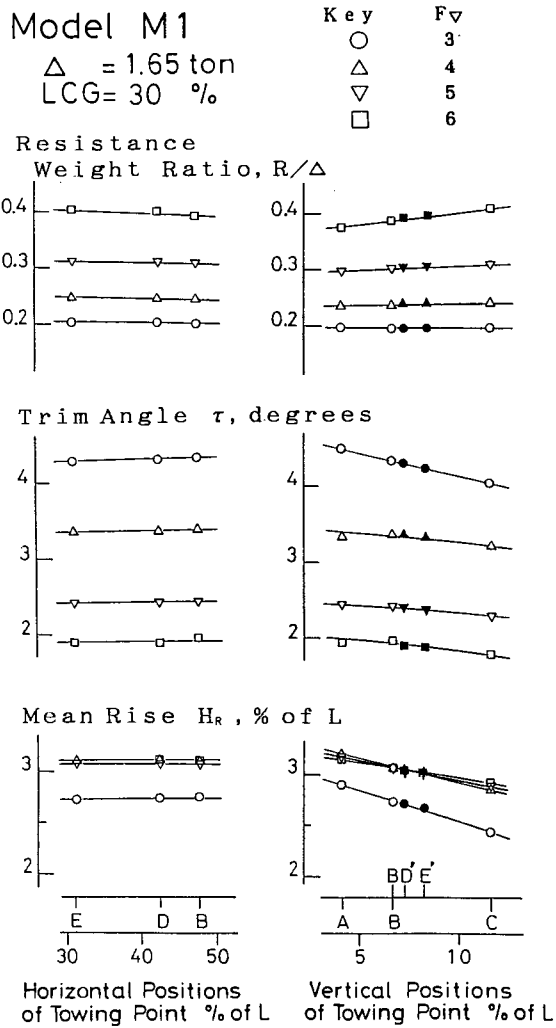
Fig.8 Results of M1 by Horizontal
    and Vertical Valiation of
    Towing Points
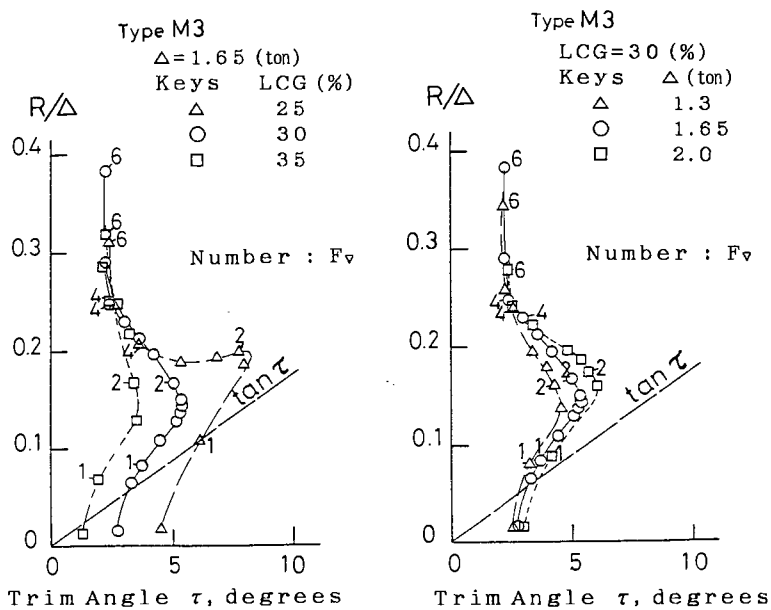
Fig.9 Resistance-to-Displacement Ratio
    versus Running Trim of M3
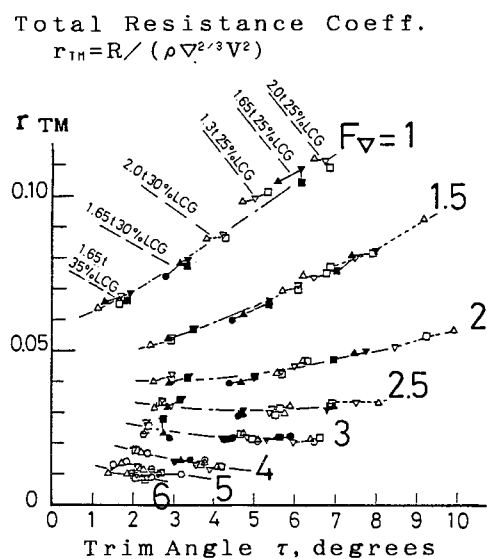
Fig.10 Total Resistance
    Coefficients

DEVELOPMENT OF A SUPPORT VESSEL "YOKOSUKA" FOR 6,500M DEEP MANNED RESEARCH SUBMERSIBLE "SINKAI 6500"

Shinichi Takagawa*, Toshiyuki Nakanishi*, Toshio Tsuchiya*, Masatoshi Ohyama**,
Takeo Iimori**, Tadashi Sano**

* Japan Marine Science and Technology Center (JAMSTEC), Japan
** Kawasaki Heavy Industries, Ltd., Japan

Abstract

Since 1981, Japan Marine Science and Technology Center (JAMSTEC) has operated a 2,000m deep manned research submersible "SHINKAI 2000" with its support vessel "NATSUSHIMA" for a deep underwater survey up to 2,000m.

In addition, JAMSTEC completed a new support vessel "YOKOSUKA" in April 1990 for supporting a new 6,500m deep manned research submersible "SHINKAI 6500", as well as a future 10,000m deep class unmanned remotely operated vehicle (10K ROV).

"YOKOSUKA" is capable of providing various support services for the submersible and 10K ROV, including transportation, launching and recovery, underwater navigation support, and maintenance and replenishment, and also capable of undertaking a deep sea bottom survey and an oceanographic research by herself, using the latest advanced and improved equipment over the former "NATSUSHIMA".

This paper describes an outline of "YOKOSUKA" and her features, and in particular the acoustic features which make her one of the most quiet and the most modern research vessel afloat today.

Introduction

"YOKOSUKA" was designed and built by Kobe Works of Kawasaki Heavy Industries, Ltd. She has a displacement of about 4,000tons on the design draught of 4.5m, a legngth of 105m and a beam of 16m.

The propulsion system is conventional diesel engine driven. Total maximum output of main engine is 6,000PS(BHP) giving a service speed of 16.7 knots at 85% of the maximum output with 15% sea margin. She has two controllable pitch propellers and twin rudders, and is equipped with one bow thruster of 8 tons nominal thrust, which provides high maneuverability throughout the operational speed range. The cruising range is about 9,500 nautical miles. She has also a pair of bow thruster gates in order to avoid air bubble inclusion to the sea water which may disturb the performances of acoustic systems.

The complement of researcher is 12, and there are 45 officers and crews operating the vessel and handling the submersible onboard. General arrangement and principal particulars of "YOKOSUKA" are shown in Fig.1 and Table 1 respectively.
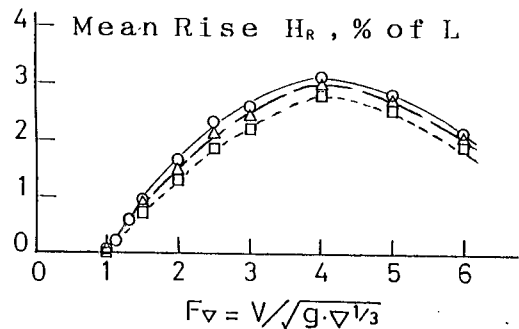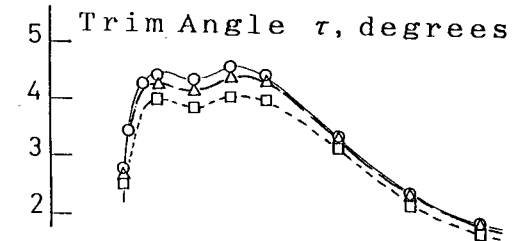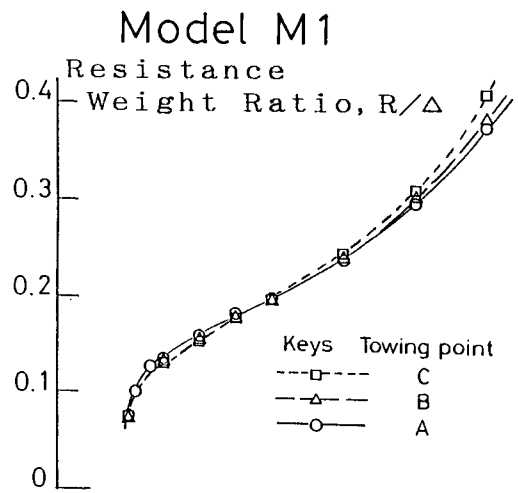
Equipment onboard "YOKOSUKA" to support the activities of "SHINKAI 6500" includes:

① A large A-Frame crane at the stern end for launching and recovery of the submersible. It is remotely controlled at the aft wheel house.
② An acoustic navigation system.
③ An underwater telephone system.
④ A local control and display system which are centralized in the command and information center on the bridge.
⑤ A supply and maintenance system in a large hangar.
⑥ A multi-narrow-beam echo sounder for efficient preliminary survey of the area where the submersible will be operated.
⑦ A Doppler current profiler to measure the current directions and velocities upto 400m deep.
⑧ Several apparatuses for analyzing and storing of collected data and samples.
⑨ A space to mount a container for a deep-tow system and a variety of instrumentations.
⑩ The fitting arrangement and the power supply required for future installation of equipment for 10K ROV handling has been fully considered. 10K ROV will carry out preliminary surveys of the area in which the manned submersible will dive and will be used for submersible rescue operations.

"YOKOSUKA" is classified by Nippon Kaiji Kyokai (NK) and conforms their standards for class C ice-strengthened structures except propellers.

Features

1. Reduction of Underwater Noise Radiated from the Hull

There is no method other than underwater acoustics for the communication, positioning and information exchange between the support vessel and the submersible. In order to obtain satisfactory performances on these underwater acoustic system, major effort was expended on noise reduction during the design and construction and the effort resulted in "YOKOSUKA" as an extremely quiet vessel. This performance was proved during the final phase of the sea trials in which the 6,500m deep manned research submersible "SHINKAI 6500" dove to 6,527m deep, the world record for the advanced
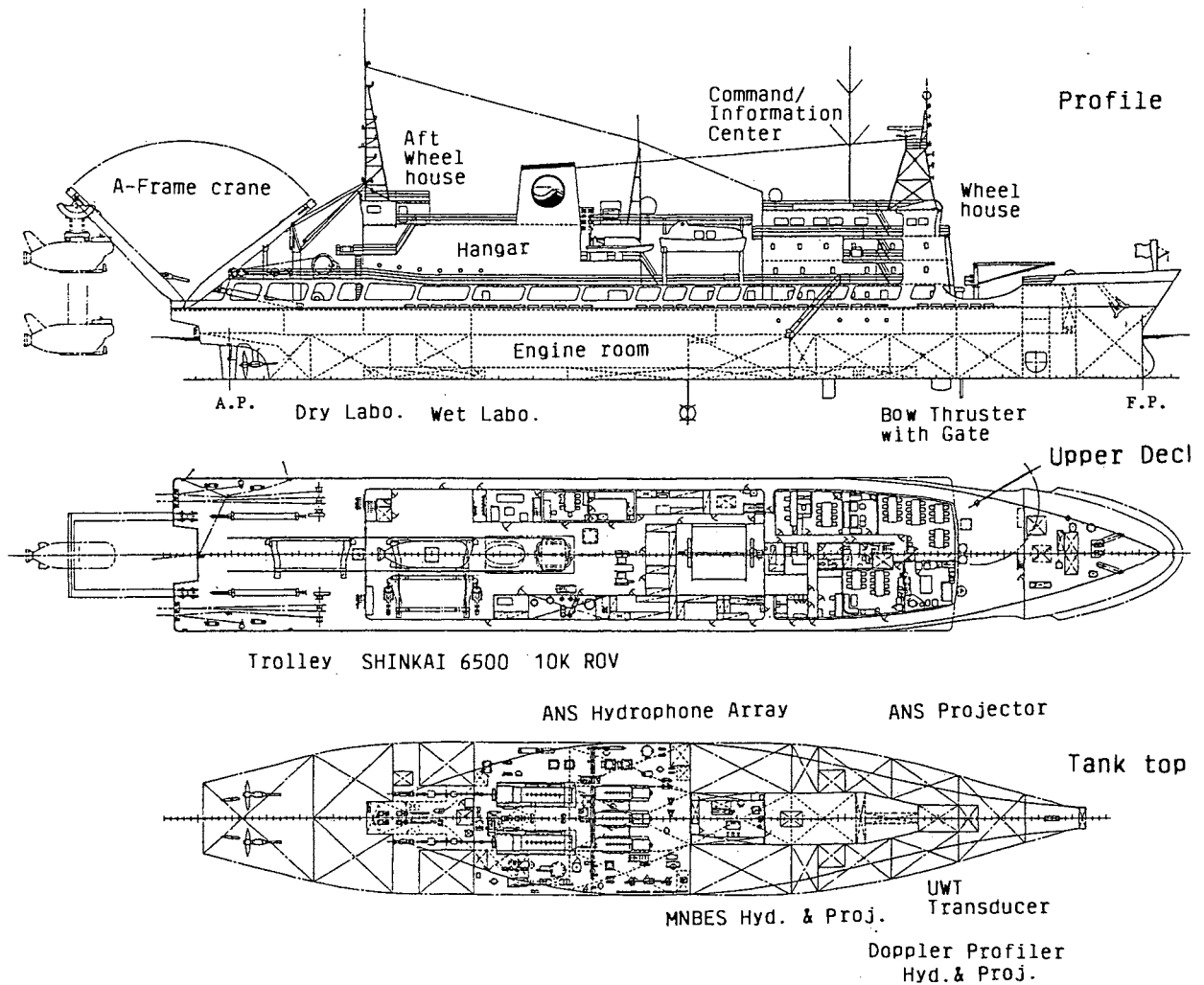
Fig. 1. General Arrangement of "YOKOSUKA"

Class	NK (MO)	Main Engine	Diesel, 3,000PS at 600 rpm x 2
Flag	Japanese	Main Generator	Diesel, 740kw x 3
Length O.A.	105.22 m	Propeller	CPP, 3mDia x 2
Length P.P.	95.00 m	Bow Thruster	8-ton thrust x 1
Breadth Mld.	16.00 m	Thruster Gate	Hydraulic x 2
Draught Mld.	4.50 m	Aux. Boiler	1,500kg/h x 1
Dead Weight	1,183 tons	Distilling Plant	15 ton/day x 2
Gross Tonnage	4,439 tons	Launch/Recovery System	2-rope, 2-point suspension by Stern A-Frame Crane
Service Speed	16.7 knots		
Cruising Range	9,500 miles	Launch/Recovery Condition	Sea State 4
Trip Duration	40 days(10 days of navigation and 30 days of research)	A-Frame Crane Capacity	28.5/10 ton x 21/42 m/min x 2
Crew Complement	57(including 12 researchers)	Date of Completion	April 10, 1990

Table 1. Principal Particulars

manned submersible.

The following paragraph describes some of the major features for reduction of noise in "YOKOSUKA".

1.1. Target Level of Noise Radiation

A ship radiates various type of noises. Typical examples are shown in Fig.2. Among them, structure-borne noise caused by the vibration and noise of the main engine and auxiliary machinery, and noise directly radiated from the propellers are the most influential ones for the underwater acoustic system.

From this point of view, the target level for the hull and propeller noise reduction was determined to secure the S/N (signal/noise) ratio which was required for the acoustic instruments of the support vessel.

There are two operating mode for "YOKOSUKA". The first is normal cruising mode and the second is the supporting mode, i.e. in a speed of less than 4 knots under sea-state 4 or less, in which "YOKOSUKA" supports the diving of the submersible. The effort on underwater noise reduction was focused on the second condition.

In this case, the target of the underwater acoustic noise level was set up at -35dB as refering 1 microbar/ Hz at 10kHz at the acoustic instruments as shown in Fig.3. This level is lower by 10dB than that of the quiet vessel "NATSUSHIMA", the support vessel of the 2,000m manned research submersible "SHINKAI 2000". In order to achieve this
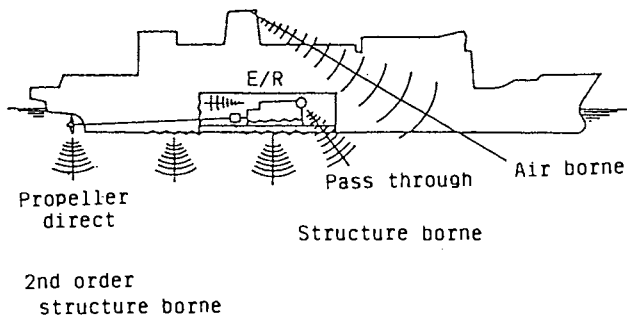
Fig.2. Various Noise Radiation Routes
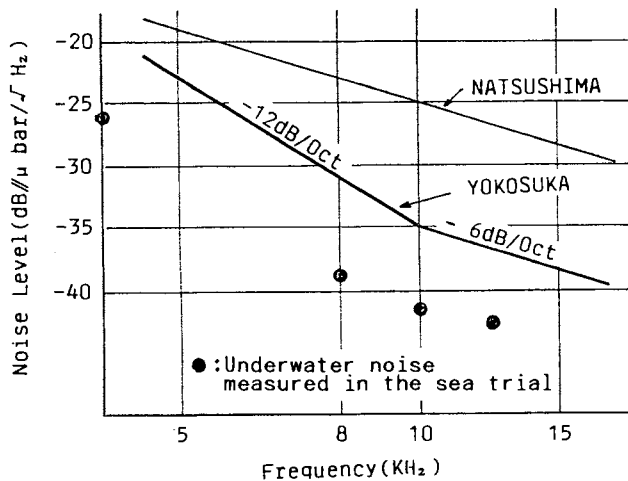
Fig.3. Allowable Upper Limit of Radiated Noise (Submersible Support Condition)

target, highly precise noise predictions were made on the basis of the noise reduction techniques applied to "NATSUSHIMA" and confirmed by various model tests and measurements.

1.2. Propeller Noise Reduction

As for propeller radiation noise, it is strongly connected with the occurrence of the propeller cavitation. In order to grasp the correlation between the cavitation noise and the operating conditions of an actual propeller, the propeller noise of "NATSUSHIMA" was measured, and also in order to grasp the correlation of cavitation noise between the full scale and the model propellers, the cavitation test using a geometrically similar model propeller with controllable pitch was carried out.

From these measurements, it was found that there were combinations of propeller blade angle and revolution which gave minimum propeller noise, and that the optimum combinations changed in accordance with the ship speed. Also it became clear that a slight occurrence of face cavitation caused a rapid increase of propeller noise.

"YOKOSUKA"'s propellers and its operating conditions were investigated widely from the view point of minimum occurrence of cavitation using the above mentioned results and the following countermeasures were adopted on "YOKOSUKA" and her propellers.
① Adoption of 5-blade, large diameter and lower revolution propeller.
② Adoption of improved propeller geometry with highly skewed and tip-unloaded pitch distribution.
③ Improvement of wake distribution around the propeller.

Propulsion constrol system was also evaluated from the view point of low propeller noise operation of a support vessel having a wide propeller working range. As a result, the follwoing system was selected.
① Adoption of 2-speed changeable reduction gear (Low speed for supporting operation and high speed for normal operation).
② Adequate engine telegraph program setting for combination control of the propeller blade angle and revolution.

1.3. Structure-Borne Noise Reduction

The principal way to reduce noise is to use quiet machinery at first and then to suppress the tranmission. For this purpose, various noise sources in "NATSUSHIMA" were measured and analized quantitatively. Then a new underwater noise prediction method using Statistical Energy Analysis (SEA) for the structure-borne noise has been established so as to realize various noise suppression measures. To reduce the noise, the followings were considered in the design stage.
① To select low noise and low vibration main engines and auxiliary machinery on the basis of those acoustic target level.
② To select adequate vibration isolation mounting arrangement.
③ To reduce the hull vibration throughout all transmissive routes of vibration.
④ To reduce underwater hull vibration levels, which should in turn reduce the noise radia-

tion by the hull.
⑤ To reduce air-borne sound which becomes a source of underwater radiated noise.
⑥ To select an adequate position for installation of machinery so as to make the distances to the acoustic devices longer.

Several measures taken are summarized as follows to reduce the noise emission from machinery and equipment onboard as well as the hull structures.
① The main engine and the reduction gear were mounted on a common bed which was supported by several V-shaped vibration isolation rubber mounts. A flexible coupling was installed between the propulsive shaft and reduction gear to absorb the discrepancies of shafting alignment caused by the vibration of engine and reduction gear. Also air acoustic insulation hoods were installed on the reduction gear and the supercharger of the main engine.
② The diesel generators was mounted on massive and rigid middle-bases using rubber mounts. Then the middle-bases were mounted on the same type rubber mounts as illustrated in Fig.4. This double mounting system gave an attenuation over 35dB (acceleration level) at high frequency range.
③ In addition to the careful selection of the machinery and equipment, all major rotating and reciprocating machinery were mounted on vibration isolators, and pipings and wirings to this equipment were decoupled by the use of flexible coupling and isolation mounts.
④ In order to reduce the noise transmission through the structures, vibration dampers were applied to the interior of the hull. These dampers consist of epoxy resinous viscoelastic cement which was painted and fitted to the inside shell in the engine room, to the interior of tanks, to the inside shell near the bow thruster and to supporting foundations of the major machinery.
⑤ The sound absorbing insulation wall of about 100 mm thick which consisted of rubber and rock wool was installed to the side shell and the transverse bulkhead in the engine room. This gave an attenuation over 15dB (sound pressure level).

The noise tests during the sea trial demonstrated the full attainment of the reduction target as shown in Fig.3. "YOKOSUKA" also proved that its hull and propeller noise would not adversely affect acoustic equipment, and the above mentioned countermeasures for noise reduction were adequate.

2. Underwater Navigation Supporting System

2.1. Function of the System

The system is provided with two functions. One is a preliminary environmental and topographical surveys of the sea and these surveys are carried out from the sea surface prior to the submergence research. The other is a navigation supporting for the submersible during the diving research activities.

At the preliminary surveys, various data of interested sea area such as water depth, bottom topography and vertical profile of water temperature are to be obtained. Using these data, items such
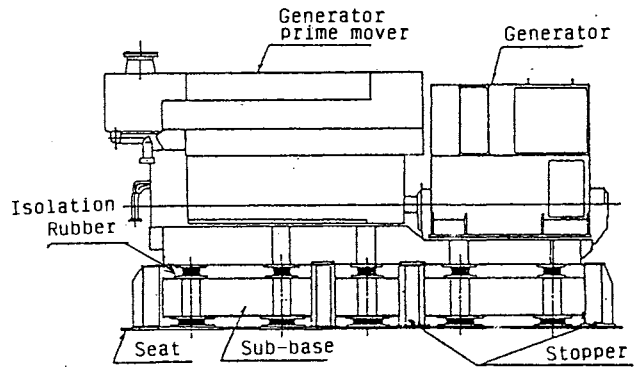
Fig.4. Double Mounting System for Generator

as the position, characteristics of the target area, position of particular targets, position of the obstacles or dangerous topography, predicted acoustic ray propagation chart and so on are analized and details of the coming legs and safe and efficient diving research activities are planned.

The function of supporting the diving of the submersible has been so designed that they can provide the useful informations as listed below, by obtaining most of them throughout the period of diving.
① The accurate absolute position of the support vessel (LONG, LAT) as well as the relative position of the submersible to the support vessel can be obtained. Using these informations adequate informations including proper instructions can be given from the support vessel to the submersible in accordance with the predetermined research plan.
② Reference points for the acoustic positioning can be set upon the sea bottom, thereby the correct position of the support vessel and the submersible in relation with the reference points can be measured accurately on board. Then the support vessel can provide proper guidance to the submersible with highly reproducible position information to the reference points.
③ The motions of other vessels located adjacent to the support vessel can be so analysed that she can issue anti-collision supporting informations to the submersible to insure safety during the surfacing operation.
④ Mutual communication means between the support vessel and the submersible can be provided.
⑤ The support vessel can continuously record and store navigation tracking data of the submersible during the underwater research operations.

2.2. Major System Components

This system consists of the Hybrid Radio Navigation System, Automatic Radar Plotting Aid, Underwater Acoustic Navigation System, Underwater Telephone System, Multi-Narrow-Beam Echo Sounding System, XBT and Total Control and Display System etc. as illustrated in Fig.5. The advanced acoustic and electronic technologies are applied to each equipment so as to meet the requirements of increased service range in proportion to the diving depth of the submersible.

The following paragraph describes some of the major features of the components in the system.

SURFACE POSITIONING
HYBRID NAVIGATION SYSTEM
* GPS/NAVSTAR
* NNSS
* LORAN-C
* DECCA
* GYRO COMPASS

INTEGRATED CONTROL & DISPLAY
TOTAL CONTROL AND DISPLAY SYSTEM
* FULL GRAPHIC DISPLAY
* X-Y PLOTTER
* VOICE RECORDER
* COMMUNICATION CONTROL PANEL

INFORMATION EXCHANGER
MULTI-PURPOSE COMPUTER
  NETWORK SYSTEM
* μ VAX II
* DISK
* TAPE

UNDERWATER TRACKING AND
  LOCATION
ACOUSTIC NAVIGATION SYSTEM
* SSBL
* LBL
* DEEP OCEAN TRANSPONDER

RADAR PLOTTING
* RADAR
* ARPA

OCEAN ENVIRONMENTAL RESEARCH
* XBT
* DOPPLER PROFILER

BOTTOM GEOLOGICAL RESEARCH
MULTI-NARROW-BEAM ECHO SOUNDER

COMMUNICATION
UNDERWATER TELEPHONE
VHF RADIO TRANSCEIVER

Fig.5. Underwater Navigation Supporting System

2.2.1. Acoustic Navigation System

This system can provide underwater position locating functions combined with transponders deployed on the sea bottom. The system can locate the position of the support vessel, the submersible, the transponders and towed objects, and the results are plotted on an X-Y plotter or graphically displayed on a multi-purpose display unit in the command and information center.

As for measuring method, advanced SSBL is adopted together with advanced LBL for underwater position location. Advanced SSBL system using 4x4 elements planar hydrophone array is applied in lieu of conventional type to detect various acoustic reply signals with high S/N ratio.

Also a synchronous pinger system was introduced to the submersible for position locating by the support vessel in order to avoid the lack of signal reception at the submersible due to the large noise level emitted from the submersible. Signals are received by the SSBL receiver, and the relative position of the submersible to the support vessel can be determined.

2.2.2. Underwater Telephone System

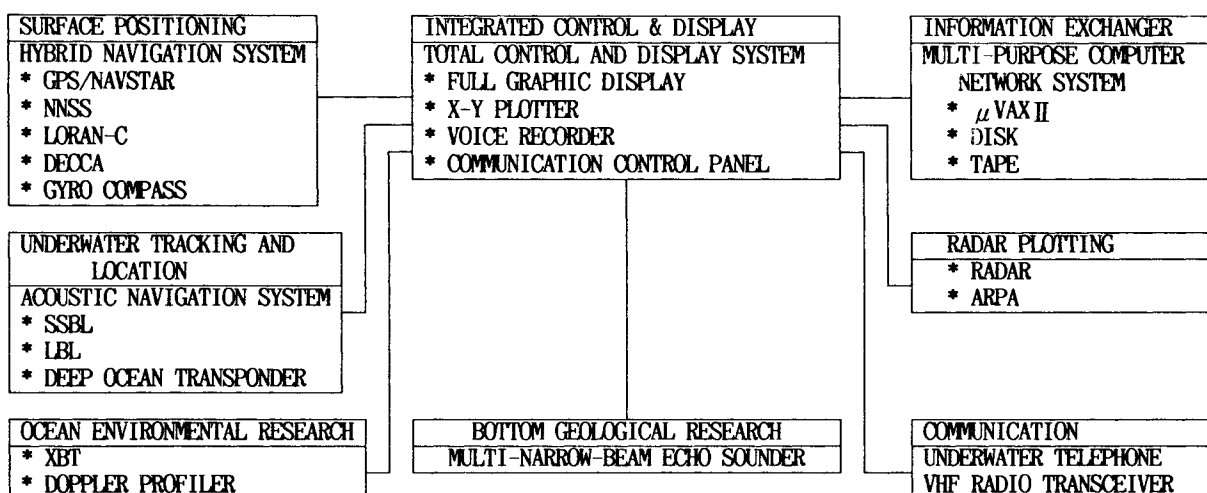This system is the only means for mutual communication between the submersible and the support vessel.

The communication is made either through vocal or keying signals. The underwater telephone consists of the beam steering system for both transmitting and receiving in order to improve the S/N ratio. By 3x3 elements planar array transducer, two kinds of directivity patterns (wide and narrow) are prepared. A wide beam or a narrow beam is set in downward direction, and another eight narrow beams in circumferential direction. The most suitable beam is selectable automatically or manually toward the relative direction of the submersible, and thus clear communication can be maintained anytime.

2.2.3. Multi-Narrow-Beam Echo Sounder(MNBES)

Safe and efficient diving of the submersible requires a detailed sea bottom topography chart of the target area. In order to obtain the sea bottom topography, "YOKOSUKA" is equipped with MNBES

which can measure the maximum depth of 11,000m. This is the first bathymetric survey system made in Japan especially designed for deep sea application.

To enhance the searching capability, the search beam width has been set to 2 degrees and 45 pieces of preformed beams have been adopted. Thus one scan of the signal gives 45 pieces of depth data over 90 degrees right-to-left range, nearly twice as wide as the perpendicular water depth. The depth data thus obtained are plotted as a real time contour map on the X-Y plotter or displayed on the color display monitor for topographical survey.

During official sea trials, "YOKOSUKA"'s MNBES drew a clear depth contour map of the sea bottom about 9,600m deep in the Izu-Ogasawara Trench as shown in Fig.6. It was also confirmed at the final sea trial of the "SHINKAI 6500" system that the depth reading at the landing point of the submersible and the depth indicated by contour map agreed very well. Also it was confirmed that the countermeasures for reducing underwater radiated noise were good and the thruster gates were remarkably effective for protecting the MNBES from bubbles flowing around its receiver and transmitter embedded on the hull bottom.

2.2.4. Hybrid Radio Navigation System

High-precision surface positioning is indispensable for efficient and safe diving. It is also necessary in addition to the underwater positioning by the acoustic navigation system for the tracking and recording of the underwater position of the submersible.

The latest version of navigation sensors, i.e. GPS/NAVSTAR, NNSS, Loran C, DECCA, Gyor Compass and Doppler Profiler, are adopted and each data obtained is automatically processed by a multi-purpose computer system, by which the present location of the vessel can be determined accurately and continuously. As a second function of this Hybrid Radio Navigation System, a route tracking capability combined with the steering system is provided.

2.2.5. Automatic Radar Plotting Aid(ARPA)

Based on the information obtained from two sets of radar, the movements of vessels adjacent
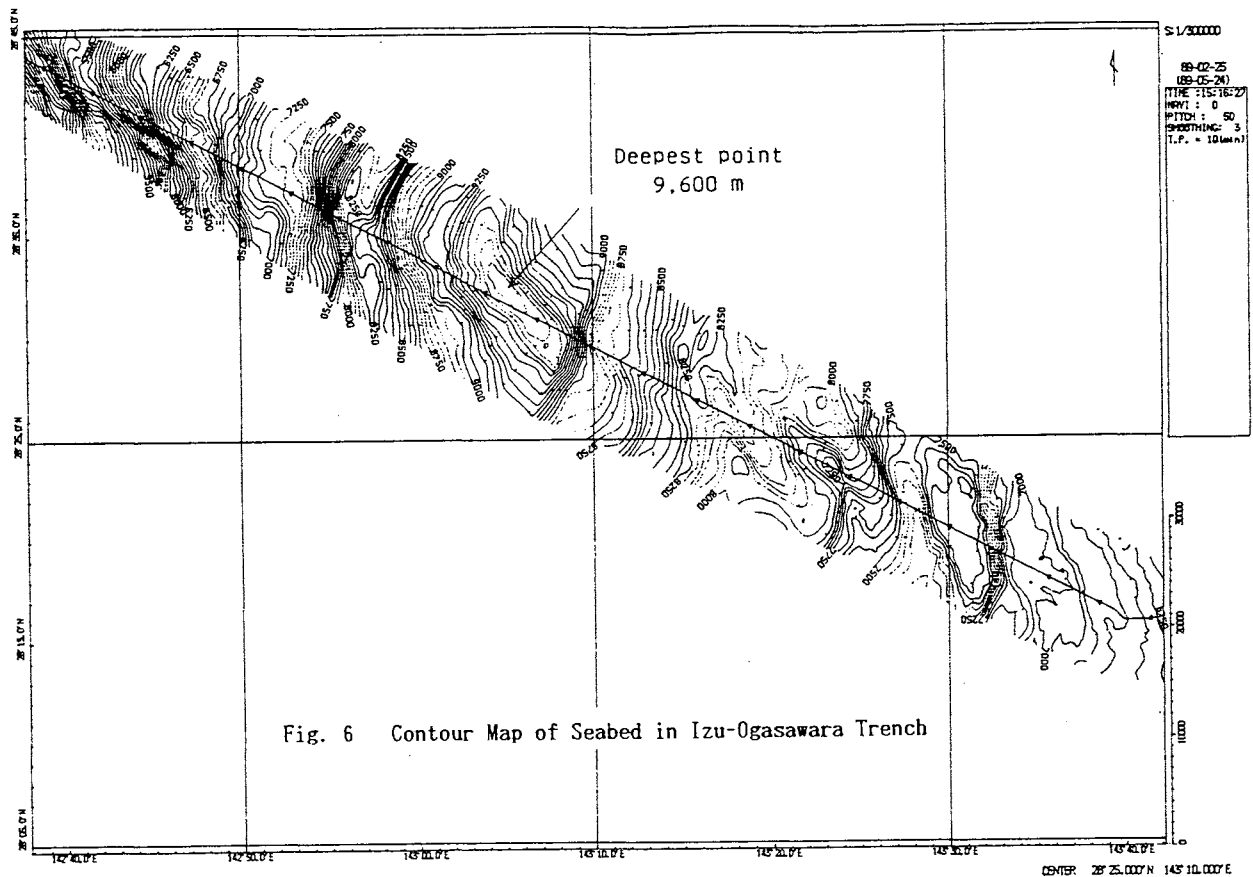
Fig. 6   Contour Map of Seabed in Izu-Ogasawara Trench

to the support vessel can be analysed by the ARPA. The data obtained by ARPA are sent to the Total Control and Display System, where the movements of vessels together with the underwater information is displayed on the color display system.

2.2.6. Total Control and Display System

As for control, commanding and monitoring of the underwater activities, various kinds of surface and underwater informations are integrated and centrally displayed on the CRT screen, etc. This system is a digital processing full graphic CRT display system and has the following displaying and controlling functions.

Major displaying items:
① Position display pattern consisting of earth fixed plan view, support vessel and/or submersible centered plan view, vertical section view, etc.
② Various status informations consisting of equipment status.

Major controlling items:
① VHF radio/Underwater Telephone remote operation and voice recording.
② Acoustic Navigation system remote operation with character display and keyboard.

3. Intelligent Computer Network System

For efficient and rationalized data processing onboard, "YOKOSUKA" is provided with a multi-purpose computer system that consists of two DEC Micro Vax Ⅱ
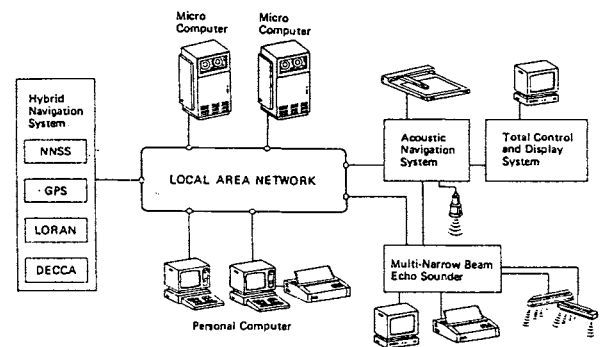
Fig. 7. Multi-Purpose Computer Network

central processing units as illustrated in Fig. 7. This system is the core of an onboard local area net work (LAN) for intelligent data handling and has the following features.

① Measured data and navigation information can be obtained on a real-time basis through the input, output, arithmetic operations and registration of data concerning the Hybrid Radio Navigation System and Multi-Narrow-Beam Echo Sounder.
② Data obtained by the system can be supplied to the wheel house, the command and information center, the aft wheel house, laboratories, researcher's private cabins, instrumentation containers, study rooms and others. Researcher's cabins and study rooms are equipped with servers of personal computers and VAX terminals for access to the LAN system.

③ The computer system can also be used for scientific and technical calculations to enable researchers to process data when necessary.

④ The system is linked to the INMARSAT through a modem for data communications allowing data to be transmitted and received between "YOKOSUKA" and shore contacts.

⑤ Redundancy is maintained by mutual backup between the two central processing units.

4. Rationalized Launch and Recovery System

The launch and recovery operation of the submersible in waves is very difficult because the substantial difference of the hull dimensions between the submersible and the support vessel, hence their oscillation characteristics in waves differ from each other and the complex and large relative motion appears in irregular waves at the actual operation area.

This problem has been solved through the adoption of the shock absorbing method using flexible nylon hoisting ropes and the ram tensioners arranged between the hoisting winchs and the A-frame crane to follow the relative motion. Also the adoption of the self-mating type lifting device in the A-frame crane system is remarkably useful when recovering the submersible from the wavy sea surface.

This system has been adopted on "NATSUSHIMA" and now it has proved satisfactory throughout several hundreds of operations. "YOKOSUKA" is equipped with the same type launch and recovery system as "NATSUSHIMA" but it is designed to permit operations even in sea state 4 condition.

To reduce time and manpower for this operation including preparation work onboard, the following measures are adopted.

① "YOKOSUKA" is planned to be a twin screw vessel with a bow thruster and controllable pitch propellers considering her good maneuverability in low speed condition such as launch and recovery operations.

② To reduce the rolling motion of "YOKOSUKA" in such operating condition, a Flume type anti-rolling tank is provided on the second deck level near the midship of the vessel.

③ To minimize the swinging motion of the submersible in hanging condition from the upper beam of the A-frame crane, four holding lines are connected to the submersible each of which is driven by an auto-tension winch. This is useful especially in landing operation of the submersible onto the trolley.

④ The transportation of the submersible between the hangar and working area of the A-frame crane is carried out using the trolley driven by a winch. Also a transverse shifting mechanism of the trolley is provided in the hangar considering the retrofitting of the 10K ROV on "YOKOSUKA".

⑤ To facilitate attaching the expendable ballast of steel plates to the submersible, a semi-automatic ballast loading system is provided.

5. Other Features

① The submersible is accommodated in the midship hangar. In the hangar there are some spaces for maintenance and replenishment such as supporting machinery room including battery charger /discharger, maitenance rooms for machinery and electronic equipment.

② As for analysis and storage of collected samples, there are three laboratories onboard, and a large refrigerator, cryogenic freezer, microscope, rock cutter, video editing device etc. are provided there.

③ For oceanographic survey, the XBT system which is capable of measuring sea water temperature profile up to 1,800m deep in maximum and weather satellite receivers for NOAA and HIMAWARI are provided.

Prospect and Acknowledgement

"YOKOSUKA" embodies a variety of new ideas developed through experiences with similar vessels. All members concerned in this project expects the "YOKOSUKA" as well as "SHINKAI 6500" and 10K ROV (in the near future) to make important contributions to deep sea research, oceanographic survey and ocean development not only in Japan but also in the world.

The authors wish to acknowledge the valuable advices and cooperations given by the members concerned in the planning, design and construction.

APPLICATION OF TRANSDUCER WITH FLEXIBLE FILTER FOR MEASURING PORE PRESSURE IN SEABEDS

Yoshihiko Maeno* and Keiji Tokutomi**

* Maizuru College of Technology, Japan
** Kyowa Electric Instruments CO., LTD., Japan

ABSTRACT

This paper described an application of the pore pressure transducer with the newly developed flexible filter, which enable us to measure pore pressure in many types of deposits, minimizing phase lag and damping in measurements. The phase lag between the naked transducer and the filtered one is observed in our laboratory experiments, in which high-density porous porcelain filters or metal filters are employed. The phase lag and damping due to typical metal, ceramic, and plastic filters were reviewed. The superiority of the newly developed flexible filters was confirmed. Moreover the applications of flexible filters were reported.

INTRODUCTION

Under an ideal condition, even though there is no problem with the response of a pore pressure transducer, the measurements can easily be affected by the condition of the environment where the instrument is installed, and this causes some problems. For example, even if the filter and the filling chamber were completely filled with degassed water, air bubbles could be produced in the chamber after installation of the measuring equipment due to the activity of organic matter or microorganisms. Also, seawater or underground water in the vicinity of the sensor might enter the chamber through the filter. Especially with a porous-type filter, air bubbles are likely to stick to the filter or enter the fluid-filling chamber between the filter and the pressure-gauge diaphragm. Once the air bubbles enter the equipment, they will not come out of the filter in most cases. Thus, the air bubbles which adhered to the filter or entered the chamber greatly affected the volume factor of the pore pressure transducer, and greatly influenced error factors in dynamic measurements of pore pressure.

In consideration of the above-mentioned points, the filters used in pore pressure transducers should satisfy the following conditions: (1) distillation of degassed water and assembly of the pore pressure transducer in degassed water at the measuring site are unnecessary, (2) it has a simple structure which can accommodate the properties of the soil of the ground, and (3) installation in the ground is easy. We therefore developed a new type of flexible filter. This filter enables us to suppress production of air bubbles, and even if bubbles are produced, the structure does not allow the bubbles to accumulate easily in the fluid-filling chamber which is located between the filter and the pressure-gauge diaphragm based on the following reasons. (1) The filter is a combination of a board having small pores and copolymerized resin mesh, (2) the strength is comparable to conventionally used metal filters, and (3) the mesh is chemically stable. Furthermore, the filter must be structurally simple, and the combination can be changed easily in accordance with the properties of the nature of the soil, such as the diameter of the sand grains.

EXPERIMENTAL METHOD FOR FILTERS

Characteristic tests of the filters for pore pressure transducers were conducted mainly by means of a low-cycle pressure device. Among the filters tested this time, the flexible filters developed in this research were subjected to an application test in a laboratory wave simulator tank.

The characteristics tests were already conducted for the many types of filters, e.g., typical metal filters, ceramic filters, plastic filters and newly developed flexible filters. In this paper the phase and damping are quantitively evaluated for the flexible filters. The detailed informations are found in Maeno & Tokutomi(1989). Table 1 shows the basic characteristics of the typical filters.

Figure 1 shows the parts and the structure of the pore pressure transducer used in this test.

Table 1. Basic characteristics of typical filters.

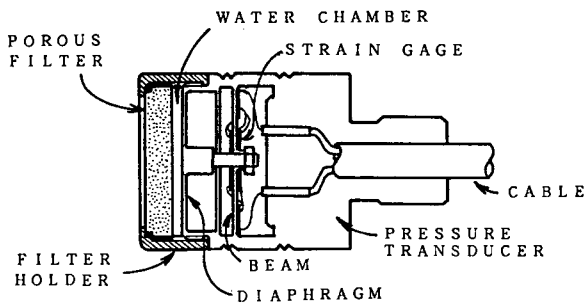| Kind of filter	Metal			Flexible Porous ϕ 0.5 p=1 100# × 3
Average pore size (μ m)	2	10	100	92
Mesh ratio (%)	44	44	33	9.7
Kind of filter	Ceramic			
Average pore size (μ m)	2.0	1.4	6.8	3.6
Appearant mesh ratio (%)	22	36	21	36

Fig. 1. Structure of pore pressure transducer.

The structure of the newly developed flexible filter is shown in Figure 2.
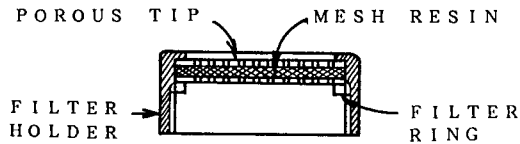
Fig. 2. Structure of flexible filter.

Various types of filters fixed into filter holders were degassed by means of a vacuum pump before the tests so that the filter pores would be completely filled with degassed water for an ideal condition. In order to study the influence of air bubbles on the response quantitatively, we used four types of metal filters and carried out tests for the two following cases: one with air bubbles in the filter, and the other with air bubbles in the chamber between the filter and the pressure-gauge diaphragm. Furthermore, comparative tests of flexible filters with typical metal filters and ceramic filters were conducted under normal installation conditions of a pore pressure transducer. Figure 3 lists the test conditions for metal filters.

In calculating the response magnifications, we designated the peak values of probability densities of amplitudes as the mean value of the peak-to-peak amplitudes. With regard to the definition of response magnification, the value of each pore pressure transducer was indicated in percentage based on the values of the standard pressure gauge.
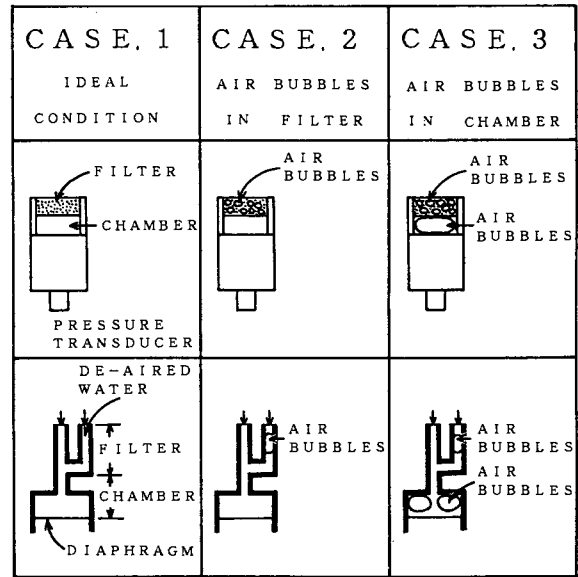
Fig. 3. Schematic drawing of test conditions for metal filters.

PHASE AND DAMPING DUE TO FILTERS

(1) Completely Degassed Conditions

The considerable phase lag and damping due to ceramic filters were observed even in completely degassed conditions. Figure 4 and 5 show the relationship between the phase lag and frequency, and frequency response. According to the results, the pore size of the ceramic filters was especially small and pores were sparsely distributed. Therefore, already at 0.5Hz, a phase lag of -15 degrees to -54 degrees was observed. In the case of the filter which showed the effects and whose pore size was 2μm with 2% porosity at frequencies higher than 5Hz, the phase was canceled by the wave in the next phase. Similarly, in response magnifications, at 0.5Hz, it was damped by 95%, or in the worse case, by 43%. Damping increased rapidly with the increase in the pressurizing frequency.

In order to confirm the superiority of the newly developed flexible filters, all of pore pressure transducers were examined under an ideal condition without being subjected to influences of air bubbles.

With flexible filters, although we did not take any special care such as filling them with degassed water, response magnifications and phase lags were not affected at all.

Test results of metal filters did not indicate any damping of response due to frequency. In the case of the filter with 2μm pore size, phase lags of -0.1 degree at the frequency of 0.5Hz, and -3.6 degree at 20Hz were observed. Since pore sizes of plastic filters are large, frequency did not affect the response or phase lag.
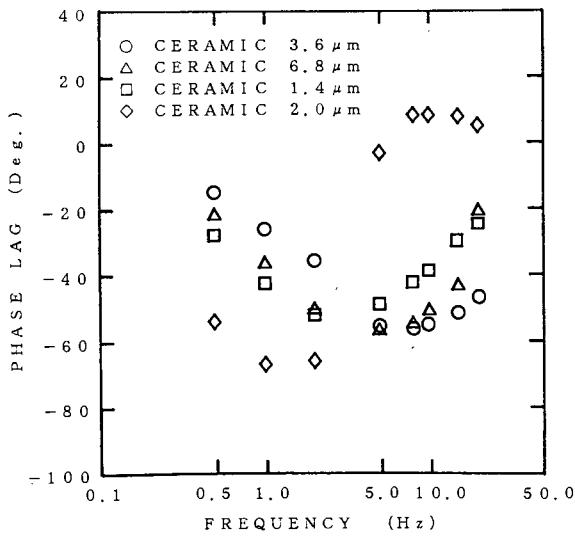
Fig.4. Phase lag due to ceramic filters.
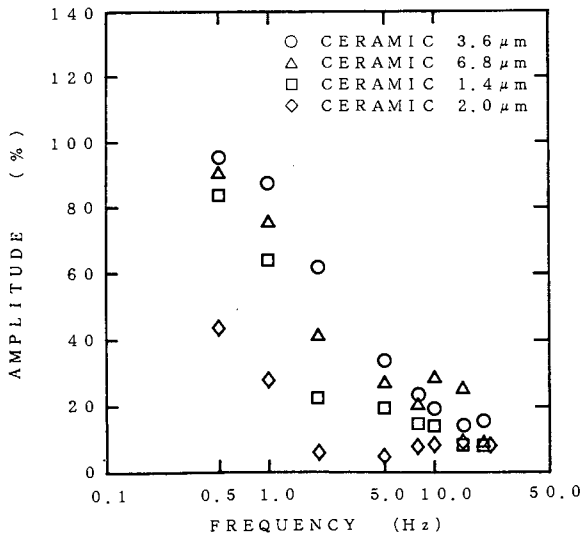
Fig.5. Response by ceramic filters.

(2) Phase and Damping due to Air Bubbles

As mentioned above, air bubbles cause the severe influences on pore pressure response. In this research, to recreate an actual situation in a laboratory, we assumed the following two cases. In one case, air remained as bubbles in 50% of the pores, i.e., in 0.60cm³ of the filter volume, and in the other case, the entire filling chamber of 0.254cm³ capacity between the filter and pressure-gauge diaphragm was filled with air.

The following is the result of the experiment simulating the case in which air bubbles entered only the filter. When a filter whose pore size was 2μm was used, a phase lag of approximately 20 degrees maximum occurred at the frequency of 20Hz. It was verified that the phase lag produced by all types of filters was nearly 5 times as much as the phase lag produced when the filter was filled up with degassed water.

The response magnification was affected by the entry of air bubbles, but damping was only about 5% maximum. This can be explained as follows. Pore channels leading to the fluid-filling chamber have multiple paths, and even if air bubbles entered some of these channels, the others could still be connected to the chamber and function as water channels. Therefore, pressure is conducted via water, which is an incompressible fluid, through these channels.

When air bubbles entered the fluid-fillling chamber, those behave just as a damper because of their compressibility. Combining the pressure loss due to capillary friction, far greater influence than estimated was observed. At a frequency higher than 5Hz, in the case of the filter with the pore size of 2μm, the waveform was considerably distorted by the next wave train. The damping was only several percent. Figure 6 and 7 show the results of the test.
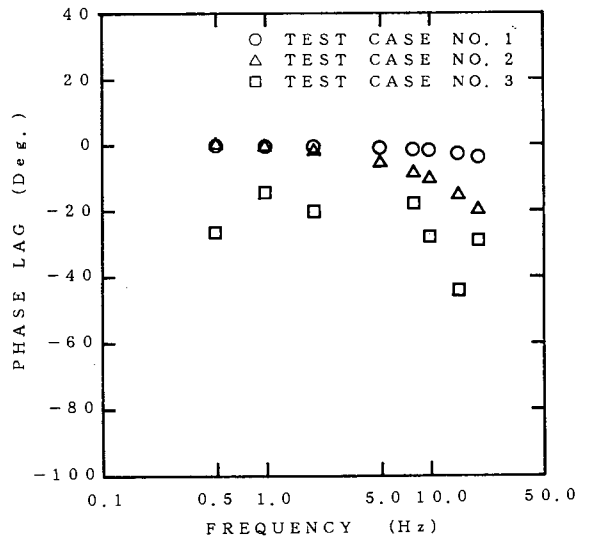
(a) Metal filter with pore size 2μm
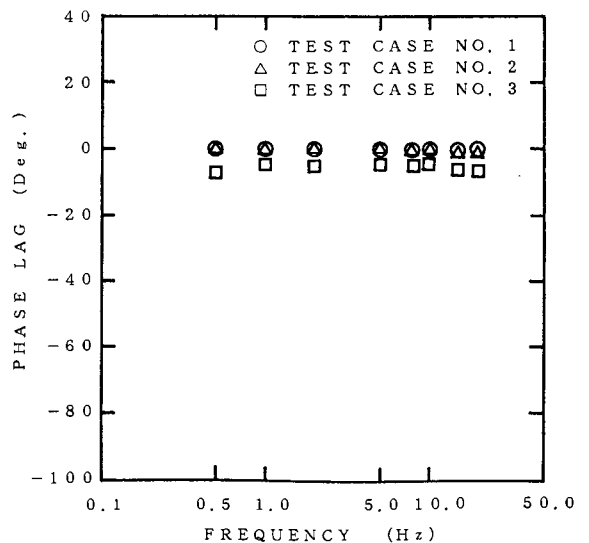
(b) Metal filter with pore size 100μm

Figure 6. Phase lag by metal filters.

—260—

(a) Metal filter with pore size $2\mu m$

Fig. 8. Phase lags for various filters.
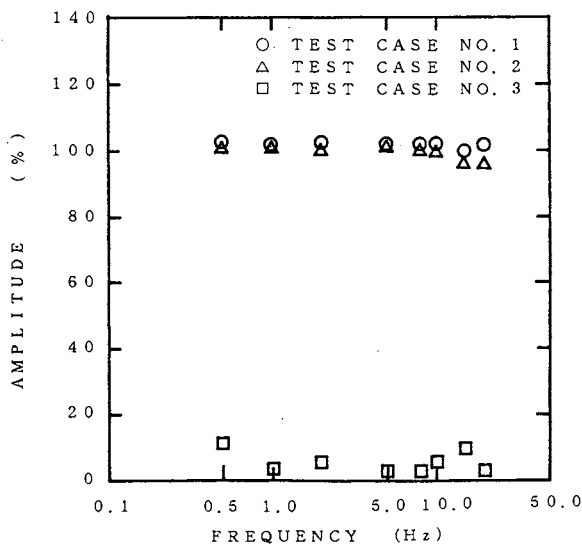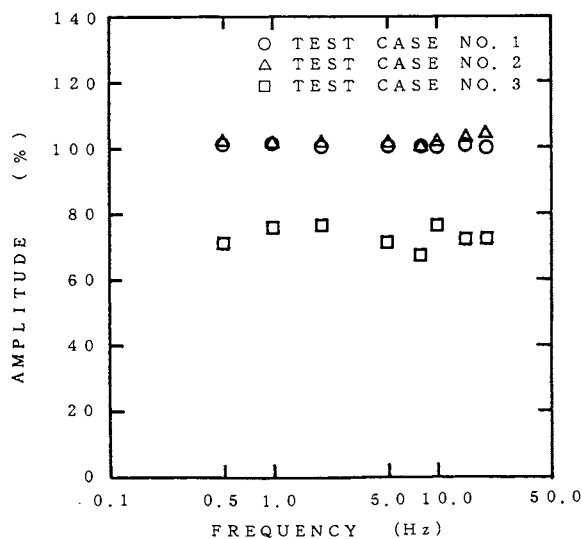
(b) Metal filter with pore size $100\mu m$

Fig. 7. Response of metal filters.
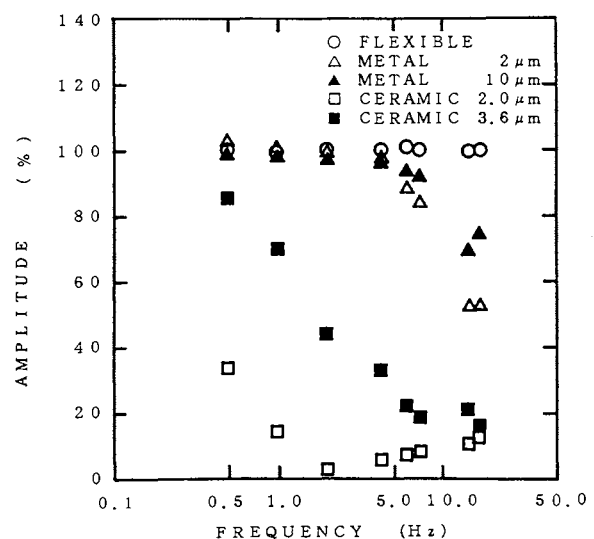
Fig. 9. Response of various filters.

(3) Normal Installation Condition

We assembled various filters with the greatest care in water which was boiled and then cooled by assuming the actual situation of use of the equipment without using a vacuum pump, and carried out an experiment. Figure 8 and 9 show the results of the test. When assembling a metal filter, we included a very small number (about $0.01cm^3$) of air bubbles into the fluid-filling chamber.

The flexible filters are stable and present no problem for practical use. Their response also presented no problem. Thus those are proved to be easy to handle.

In order to measure the wave phenomena within 5% of error, only the phenomena whose frequency ranges are less than 5Hz can be followed when metal filters with pores of either 2 μm or $10\mu m$ are used. With regard to the phase lag, a problem already develops at a relatively low frequency of 0.5Hz.

With respect to the ceramic filters, the response magnification was already approximately 30% to 85% at the low frequency of 0.5Hz, while the phase lag of this filter was rather large, ranging from about 75 degrees to 20 degrees. These results indicate that ceramic filters were unsuitable for the dynamic measurements of pore pressure.

TRANSMISSION OF PRESSURE IN SAND BEDS

(1) Experimental Set-Up and Conditions

The experiments were conducted in a wave tank installed at the Department of Civil Engng., Maizuru College of Technology. This wave tank can generate waves whose periods range from 2.16 to 0.63 second and whose heights extend up to 20cm.

A sand bed measuring 40cm x 9m was prepared in the wave tank and, as shown in Figure 10, a pore pressure transducer and a earth pressure transducer were embedded in the sand bed 3cm from the surface; pore pressure and earth pressure were then measured. Parallel to these measurements, wave pressure was measured at the surface of the sand bed and pore pressure was measured at 5 locations, i.e., 2, 10, 20, 30, and 40cm from the surface of the sand bed. The wave height was also measured at the top of the pressure transducer by means of a capacitance-type wave height meter.

The sand used in the experiments was collected at the Nabae Shore of Takahama, Fukui, which has been used in all experiments reported by the authors. Physical properties of the Nabae sand are shown in Table 2. The details of the experiments are given in the paper by Maeno (1988).

(2) Pressure Attenuation in Sand Beds

Before studying the effective stress in the surface layer of sand beds, we need to study the development of pore pressure in sand beds.
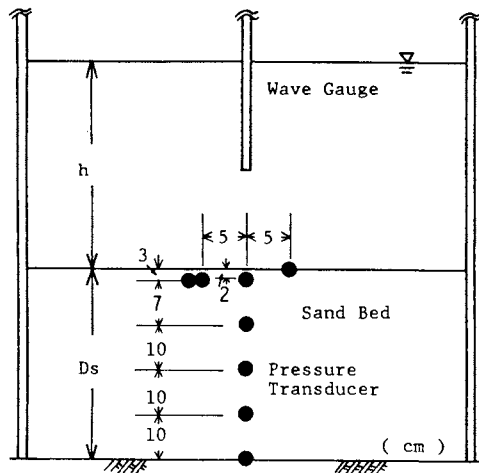
Fig. 10. Set-up of pressure transducers.

Table 2. Properties of Nabae sand.

Uniformity coefficient	1.53
Specific gravity	2.70
Permeability	0.023cm/s
Effective grain size	0.114mm
Average grain size	0.160mm

Many measurements of pore pressure have been conducted; however, the selection of the filters used in pore pressure transducers to separate earth pressure from the pore fluid pressure remains a problem. In addition, many other issues such as the frequency of the measurements and particular characteristics of soils at the measurement sites must be taken into consideration. Below, we discuss the attenuation of pressures in sand beds, using the flexible filters developed by the authors.

The basic characteristics of the flexible filters are described by Maeno and Tokutomi (1989); however, the commonly used metal filters and ceramic filters show great attenuation of pore pressures even for wave frequencies below 1Hz. Here, since the newly developed flexible filters are used, we assume that there is no attenuation of pore pressures under normal conditions.
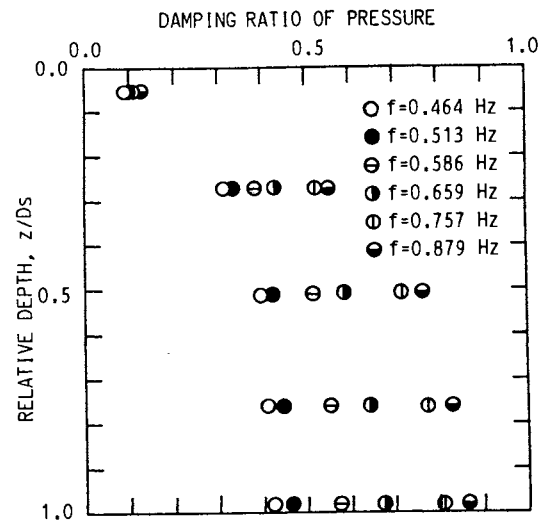
Fig. 11. Relationship between attenuation of pore pressures and frequencies.
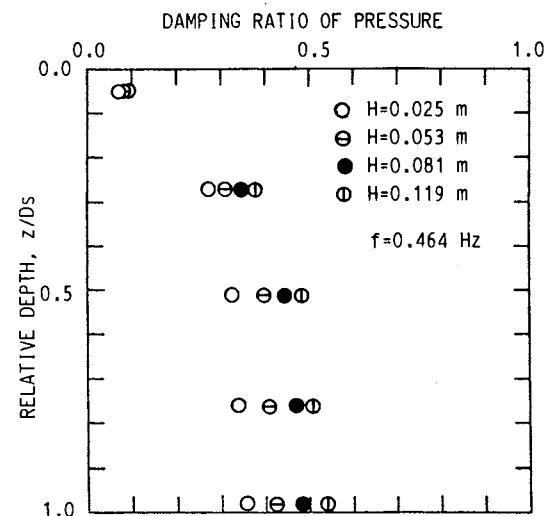
Fig. 12. Relationship between attenuation of pore pressure and wave height.

Figure 11 shows the attenuation of amplitude of pore pressures in the sand beds for different frequencies; as the frequency increases, pore pressures attenuate. This tendency increases as the depth of the sand layers increases.

Figure 12 shows the relationship between the amplitude of pore pressure and the wave height for f=0.464Hz. As shown, the amplitude of pore pressure was highly attenuated with the increase of wave height. These results are in agreement with the results reported by Maeno and Hasegawa (1985).

(3) Phase Lag of Pressure Transmission

The next issue we must consider is that of phase characteristics of pressure transmission in sand beds. It is known that the wave pressure fluctuation at the surface of sand beds is not transmitted into sand beds instantaneously, thus, it is necessary to evaluate the phase characteristics.

Figure 14 shows the relationship between the phase angle of wave pressure fluctuations at the surface layer of sand beds with the wave profile, and the frequency. According to the figure, in each case, the phase angle increased with an increase in the frequency. In other words, as the frequency increased, the phase angle increased.

In the same way, Figure 15 shows the relationship between the phase angle of pore pressure fluctuations with wave profiles, and the frequency. According to the figure, at a depth of 2cm in the sand, the points are scattered but there is a tendency for the phase angle to increase with the frequency. However, the tendency is minimal compared with the fluctuation in the phase angle near the surface of the sand bed. As the depth increases, the phase angle tends to decrease with the increase in the frequency. Then, this trend intensifies as the depth increases.

Fig. 13. Phase lag of pore pressures.

Figure 13 shows the phase difference between the fluctuation of the water surface (hereafter abbreviated as wave profile) and pore pressure at different depths for various wave conditions. In the figure, phase lags are considered positive. As shown, with an increase in the depth, the phase angle increases. When the fluctuation of the pressure at the surface of the sand bed and the pore pressure at 2cm from the surface are compared for many cases, the phase angle between the pore pressure obtained at 2cm from the bed surface and the wave profile is smaller than the phase angle between the wave pressure fluctuation and the wave profile. Contrary to the general trend in which the phase angle increases monotonously with the increase of the depth of the sand layers, complicated phase characteristics were obtained near the surface region in the sand bed. This indicates that the surface of the sand bed received different wave influences compared with other deeper regions.

Fig. 14. Phase angle between wave pressure fluctuations and wave profiles.
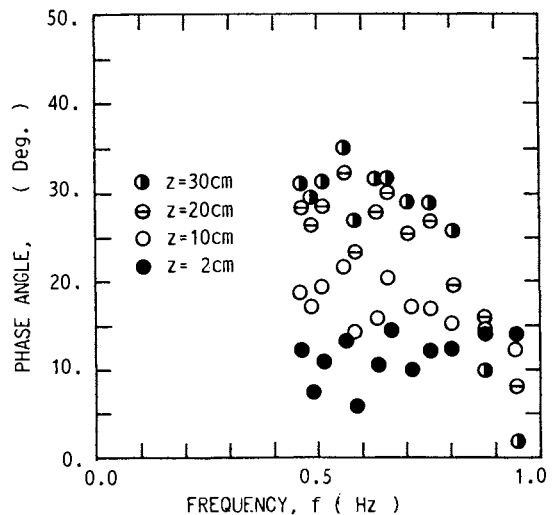
Fig. 15. Phase angle between changes both in pore pressure and in water surface

Figure 16 shows the relationship between the phase angle of fluctuation of wave pressure and the wave profile, and the wave height at f=0.464Hz. According to the figure, the phase angle at the surface of the sand increases with the wave height. Thus, phase fluctuation due to wave height was observed.

Figure 17 shows the relationship between the phase angle of the pore pressure fluctuation and wave profiles, and the wave height at f=0.464Hz. According to the figure, the phase angle in the sand bed increased with the wave height, as was the case for the surface layer of the sand. The tendency seems to be that the phase angle remains constant regardless of the depth of sand. In this respect, the result is different from that whereby the difference in the phase angle with respect to frequency increased with the depth.
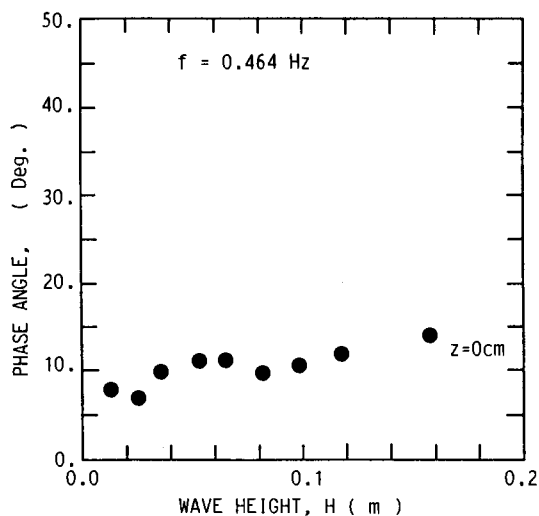
Fig. 16. Relationship between the phase
angle of the wave pressure and
wave profile, and the wave height.
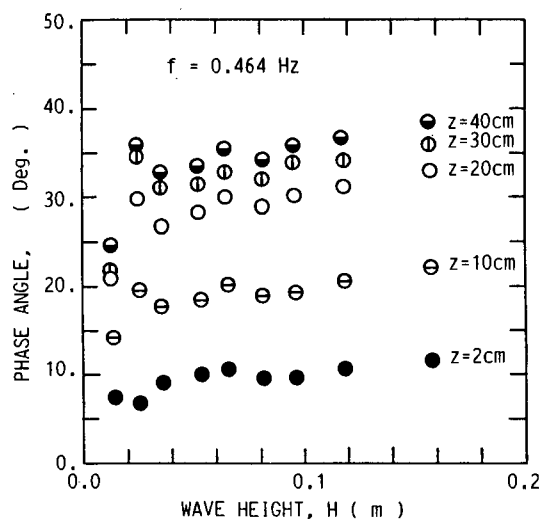
Fig. 17. Relationship between phase angle
of pore pressure and water
profile and wave height.

CONCLUSIONS

From the evaluation of the points described above, we reached the following conclusions:

(1)   The newly developed flexible filter outlined in this research is easy to handle in comparison with conventional filters; also, its characteristics are stable. Using this kind of filter, we confirmed that pore pressure in the sand bed of the sea bottom can be measured accurately because the filter damping of the phase lag or response is reduced to a minimum.

(2)   When air bubbles entered into the filter only, the influence was not large, but when they penetrated into the fluid-filling chamber between the filter and the pressure-gauge diaphragm, a considerable phase lag and response damping were produced, even though the volume of the entered bubbles was small.

(3)   The attenuation of pressure in sand layers increases with frequency and wave height.

(4)   The phase lag of pressure fluctuation in sand beds becomes pronounced with the increase in the frequency and the increase in wave height. Furthermore, near the surface of the sand bed, due to the effect of roughness of the boundary between water and sand bed, phase disturbance develops.

ACKNOWLEDGMENT

REFERENCES

Maeno,Y., and Hasegawa,T.(1985), "Evaluation of Wave-Induced Pore Pressure in Sand Layer by Wave Steepness," Coastal Engineering in Japan, JSCE, Vol.28, pp.31-44.

Maeno,Y., and Tokutomi,K.(1989), "Characteristics of flexible filter for pore pressure transducer," Proc. of IAHR Workshop on Instrumentation for Hydraulics Laboratories, Ontario, pp.105-119.

Maeno,Y., and Tokutomi,K.(1989), "Measurements of Wave-Induced Pore Pressure by Flexible Filter," Proc. of IAHR Workshop on Instrumentation for Hydraulics Laboratories, Ontario, pp.121-134+1.

Maeno,Y.(1989), "Effects of Energy Loss near Bed Surface on Wave-Induced Pore Pressure in Sand Layer," Proc. of the 21st Int. Conf. on Coastal Eng., Malaga, pp.1842-1856.

DYNAMIC CHARACTERISTICS OF THE HYDRODYNAMIC FORCE TESTING MACHINE USING LINEAR MOTOR

T. Kawanishi*, J. Karita**

* Nihon University, Japan
** Shinkou Denki Co., Japan

Abstract

The authors developed new testing machine of hydrodynamic forces using linear motor. The testing machine using linear motor is used for measurement of added mas, damping force of hydrodynamic models. This paper reports the theoretical and experimental results of dynamic characteristics of hydrodynamic testing machine. The theoretical and experimental values agree where the vibration velocity are low.

1.Introduction

Testing machines for hydrodynamic forces can be divided into towing test machines, on which hydrodynamic damping forces are measured while towing model ships, and forced vibration test machines, on which hydrodyanmic added mass forces and viscous damping forces are measured by vibrating the models. While high-speed towing test machines using the United States, Britain, France and Germany, there have been no forced vibration test machines equipped with linear motors. The authors have used a linear inductions motor as the thrust source on a hydrodynamic force testing machine to reduce a linear driving force in an attempt to reduce the amount of distortion on the shapes of the vibration waves and to create large vibration amplitudes. The outline, composition and results of vibration tests on this machine have been discussed in the two previous reports1,2).

The study reported here deals with the thrust force characteristics on hydrodynamic force testing mahines, such as the accleration and displacement, vary according to the sizes and shapes of the test models attached. There is a need to estimate the weight of the model in air, added mass in water and underwater damping forces prior to the test and to set the command singnals for output of the predetermined acceleration and displacement from numerical calculations. Here, analysis models and equations of motion are calculations of the characteristics implemented. The calculation results are compared with the test results and clarification is made of the relationship between displacement and the various numerical values of the command voltage.

2. Analysis

2.1 Outline of Test Machine

The linear motor hydrodynamic force testing machine is shown in Figure 1. The machine consists of a water channel, a linear motor, a control device, a frame for the machine, a displacement detector, an acclerometer and a supporting frame for the test model.

A short primary, induction linear motor was used. The motor consists of the primary "moving part" on the feeder side and the secondary "fixed part". The moving part creates travelling magnetic fields, which gives rise to an eddy current in the fixed part through electromagnetic induction. A thrust force is created between the magnetic field due to the eddy current and that due to the moving part.

The moving part consists of a 161.7 N, 3 phase 6 pole coil and an iron core, while the fixed part is made up of a 5 mm thick aluminium conductor plate and a steel plate. The specifications of the linear motor are as follows – phases:3, voltage: 200 V, frequency: 50 Hz, synchronous speed: 6.6 m/s, pole pitch: 66 mm, thrust force: 435 N, load factor: 0.1, current: 24 A, length: 34.3 cm, width: 15.8 cm, height: 6.6 cm, weight: 165 N, gap between moving and fixed parts :3 mm. The fixed part is located underneath the moving part

and the moving travels along on a carriage. the carriage weight 269.5 N and is supported with 12 hard resin rollers. A transistor-driven vector-control PWM inverter was used for the power source and control devices. As there was no feedback control, slight tension was applied to the two ends of the carriage with elastic bands to prevent drifting of vibration positions.

The linear motor is fixed to the carriage and connected to the model via the carriage and the load cell. Coefficients of the hydrodynamic force, such as those for the added mass and the damping force, are calculated from the reaction force applied to the model.

2.2 Assumptions and Analysis Model

The following assumption were made in creating the analysis model.
1) The linear motor is used in an area with low velocity and the thrust force is constant against the velocity.
2) The thrust force is proportional to the command voltage.
3) The rolling friction of the rollers supporting the linear motor is small enough to be negligible.
4) The wave making resistance due to the waves created by the model is negligible.

5) The hydrodynamic added mass coefficient and hydrodynamic damping force coefficient of the model are not dependent on the frequency.

The analysis model of the linear motor hydrodynamic test Figure 2. Here, F is the thrust force, M the total mass of the moving part, C the hydrodynamic damping coefficient of the test model and K the spring conatant of the elastic bands for maintaining the carriage in a neutral position. The mass of the moving part is the total of the masses of the linear motor, the carriage, the load cell for measurement of forces, the supporting frame for the test model and the test model itself, together with the hydrodynamic added mass.

2.3 Equation of Motion and Analysis

The equation of motion, taking in the inertia force, damping force, restitutive force of the spring on the basis of the analysis model, will be as follows, Here $h(\dot{X})$ is the hydrodynamic damping force expressed by $C|\dot{X}|\dot{X}$, which is proportional to the square of the velocity, While ω is the angular frequency.

$$M\ddot{x} + h(\dot{x}) + Kx = F \sin \omega t \qquad (1)$$

The equation is a non-linear differential equation which contains an item for the square of the velocity based on hydrodynamic damping[3]. Assuming that the solution is close to a sine wave, the equation may be expressed as follows.

$$x(t) = X \sin(\omega t - \phi) \qquad (2)$$

By substituting Equation 2 into equating the respective sine and cosine items on the left and right sides, the following equationis obtained.

$$-M\omega^2 X + KX + \frac{1}{\pi}\int_0^{2\pi} h(\omega X\cos\theta)\sin\theta d\theta = F \cos\phi \qquad (3)$$

$$\frac{1}{\pi}\int_0^{2\pi} h(\omega X\cos\theta)\cos\theta d\theta = F \sin\phi \qquad (4)$$

By expressing this as

$$H(\omega X) = \frac{1}{\pi}\int_0^{2\pi} h(\omega X\cos\theta)\cos\theta d\theta \qquad (5)$$

the following equation can be obtained from Equations 3 and 4.

$$KX = M\omega^2 X \pm \sqrt{F^2 - H(\omega X)^2} \qquad (6)$$

$$\sin\phi = H(\omega X)/F \qquad (7)$$

$H(\omega X)$ is then obtained from $h(x)$.

$$H(\omega X) = \frac{4}{\pi}\int_0^{\frac{\pi}{2}} C\omega^2 X^2 \cos^3\theta d\theta = \frac{8C}{3\pi}\omega^2 X^2 \qquad (8)$$

X and ϕ are obtained by substituting the above into Equation 6.

$$X = \frac{M}{2D}\sqrt{\sqrt{1 + \frac{2F}{M\omega^2}} - 1} \qquad (9)$$

$$\phi^{-1} = \sin\left(\frac{8C\omega^2}{3\pi F}\right) \qquad (10)$$

Here, $D = 8C/3$.

3. Vibration Characteristics Test

3.1 Measurement of Displacement and Acceleration

The displacement of the linear motor is measured by sight from the measure attached to the side of the rail. A servo type accelerometer is used for measurement of the acceleration at low frequencies. The specifications for this are - maxium acceleration: 2 G (19.6m/s), measurement frequency range: 259 Hz from DC. The acceleromter is attached to the upper part of the carriage for the linear motor. The accelerometer is surrounded by aluminium and steel plates to shut out the electromagnetic noise from the linear motor.

3.2 Test Method

In the vibration characteristics test, basic wave signals were inputted from the signal generator and tests were made on the relationship between the excitation periods and load weights and between displacement and acceleration. It is known from the results of the static thrust force characteristics test described in the previous report that F=158E, where E is the voltage of the command signal and F the thrust force. The vibration characteristics test was implemented with the command voltage ranging between 0 to 2 V and the period between 0.1 and 10 seconds. As a load, a column with a length of 0.489 m and a diameter of 0.048 m was attached horizontally to the supporting frame for the model and placed in the water. Since the resistance coefficient4) of the column is 0.82 , the hydrodynamic damping coefficient D of the model will be 0.489*0.048*0.82*1000/2. The 1000 here is the density of water.

4. Calculated Values and Results of Characteristics Test

4.1 Displacement Characteristics

The characteristics of the displacement amplitude against the command voltage with the period as a parameter is given in Figure 3. The displacement amplitude is expressed as the distance between peaks and troughs. It can be seen from Figure 3 that the displacement increases with the

increase in command voltage and the priods. The curves are disrupted in the parts with low command voltage and long periods. This is because the linear motor comes into contact with the ends of the rail. There is close correspondence between the theoretical and experimental values. The maximum displacement of 3.6 m is reached when the command voltage is 0.5 V and the period 9 seconds.

4.2 Acceleration Characteristics

The characteristics of the acceleration amplitude against the command voltage with the periods as a parameter is given in Figure 4. The acceleration increases in proportion to the command voltage. Figure 5 is the characteristics of the velocity against command voltage. The test results agrees more or less with the theoretical values but difference begin to appear with velocity of over 0.8 m/s. It is thought that at these speeds Assumption 1 no longer stands as the velocity of the linear motor exceeds 0.8 m/s. There is a need to implement characteristic calculations using equations of motion which allow for a wider range of velocitys.

5. Conclusion

The conclusions drawn from the test results might be summarised as follows.

1) An analysis model for a linear motor hydrodynamic force test machine was created and the solution to the equation of motion was obtained. The application range of the equation was asertained by comparing the results of the analysis and the experiment.

2) The theoretical and experimental values agree closely where the vabration velocitys are low, indicating that accurate calculations of the vibration characteristics can be made using the equation of motion.

References
1) Toshimasa Kawanishi, Norimasa Takagi, Takashi Kato, Juzi Karita Basic Characteristics of Hydrodynamic Force Testing Machine using Linear Motor The Institute of Electrical Engineers of Japan ,Comm. of Lineardrive LD-88-25 1988.10

2) Toshimasa Kawanishi, Norimasa Takagi, Takashi Kato, Juzi Karita, Yuzo Takakado Basic Characteristics of Hydrodynamic Force Testing Machine using Linear Motor (No.2 Load Test) The Institute of Electrical Engineers of Japan , Comm. of Lineardrive LD-89-7 1989.2
3) Yoshikazu Sawaragi Nonlinear Vibration p.117-120 Kyoritsu Pab.
4) Akira Shima ,Ryozi Kobayashi hydrodynamics p.122-123 Maruzen Pab.
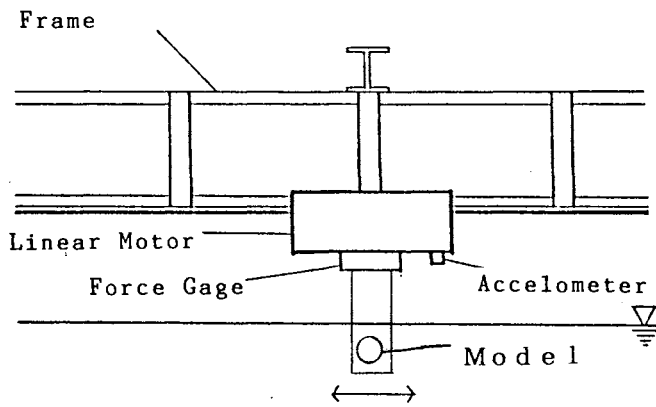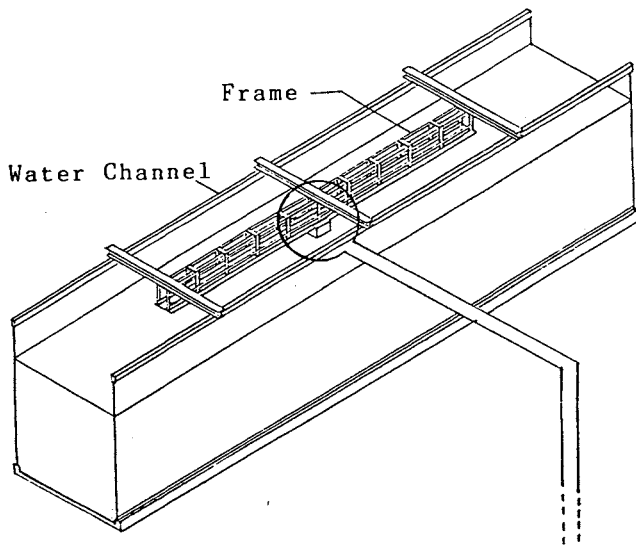
Figure 1 Hydrodynamic Force Testing Machine
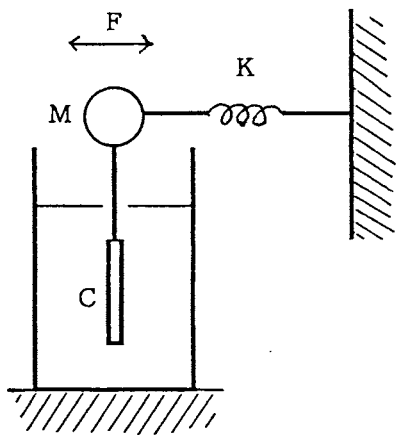
Figure 2 Analysis Model
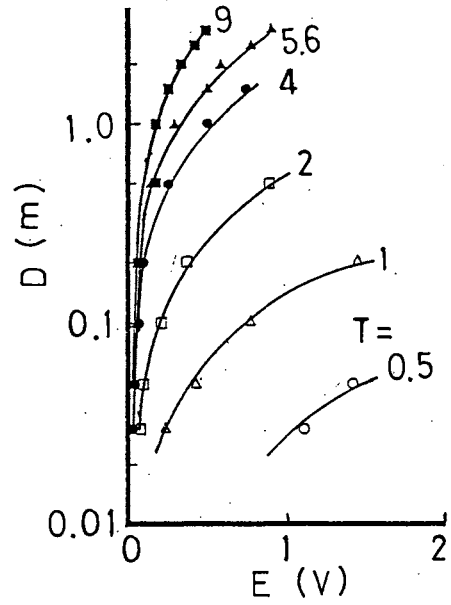
Figure 3 Displacement Characteristics
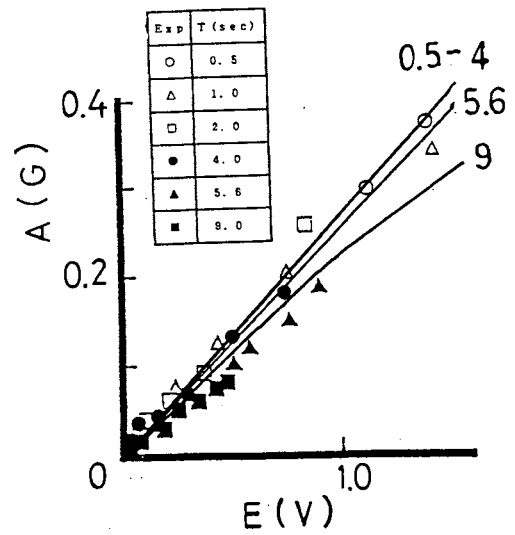
Figure 4 Acceleration Characteristics
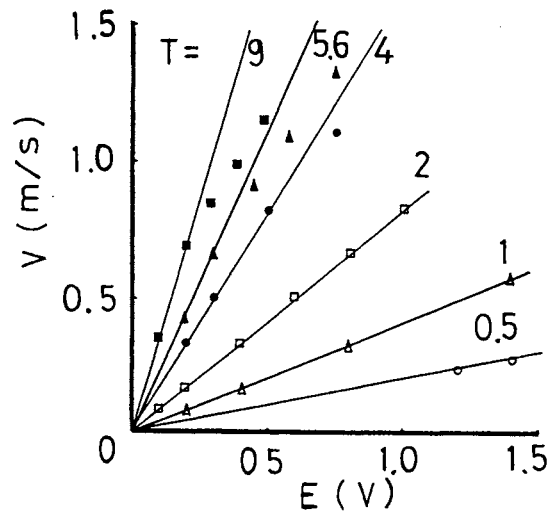
Figure 5 Velocity Characteristics

THE PERFORMANCE OF A WATER-HEAD TYPE WAVE GENERATOR

Hisao Tanaka*, Masaaki Kuroi*

* Hitachi Zosen Corporation, Japan

Abstract

The most important performance required for the wave generators in leisure pool facilities is that they can make large solitary waves suitable for surfing. In the previous paper(Ref.1), the authors developed a water-head type wave generator which can make such waves. They predicted maximum wave height based on conservation law of mass, but the result was unsatisfactory.

In this paper, the different approach is adapted. The wave generator is regarded as a kind of energy transformation system, and maximum wave height is predicted on the basis of energy conservation law. Consequently, the prediction results of wave height has shown good coincidence with the experiment. The efficiency of energy transformation has also investigated experimentally.

1. Introduction

Recently, there is a great demand for marine leisure facilities of high quality. It is important not only for leisure facilities near waterfronts, but also for ones on land. In fact, leisure pool facilities constructed in the last several years have high quality. Most of these facilities provide some water-sliders or wave generators. As to wave-generator, demands for ones which can make large steep waves suitable for surfing are increasing. Large solitary waves observed near seashore are suitable for surfing, it seems to be very difficult to make such waves with a conventional wave generator. Large solitary wave like tsunami, that is a most typical one, is generated as the result of large energy concentration on the free surface or on the bottom in a short time. However, conventional type wave generators, which are flap type, plunger type, and pneumatic type ones, transforms supplied energy into wave energy. That can not accumulate large energy in advance. When the conventional type wave generator makes large solitary wave, the movable part like flap plate must be driven in a way that large energy is concentrated near the free surface. For the purpose of such movement, scale of the equipment must be large, and power supply must also be enlarged. Taking a case of flap plate type wave generator as an example, it can be shown that the scale becomes very big. It is necessary to equip 2.2m length hydraulic pressure cylinders to generate 2m height waves in water channel of 6m water depth. Further, maximum supplied power is about 220kW per 1m width of flap plate(Ref.2). This example shows that conventional type wave generators can not satisfy the economical requirement for construction or for maintenance.

With this view in mind, we developed a new type wave generator which can make a large steep solitary wave easily. This paper describes the mechanism of the equipment, and a relationship between the supplied energy and the maximum height of wave generated.

2. System of Wave Generator

The system arrangement of the water-head type wave generator is shown in Fig.1. This equipment has a main water tank which has an opening under water, an exhaust valve, a suction valve, and an exhaust pump or an exhaust fan. A process of wave generation is as follows; (1)The suction valve is closed and the exhaust valve is opened. (2)Water level in the tank rises as the pump exhausts the air. (3)Exhaust pump is stopped and suction valve is opened in an instant, when the water surface in the tank is the required level. (4)After water in the tank flows out, a large solitary wave is generated. In fact, mechanism of this type wave generators consists of two parts; first one is an accumulation process of static potential energy to generate a large wave, and latter is a concentrated radiation process of energy near free surface when water in tank falls freely. So, when
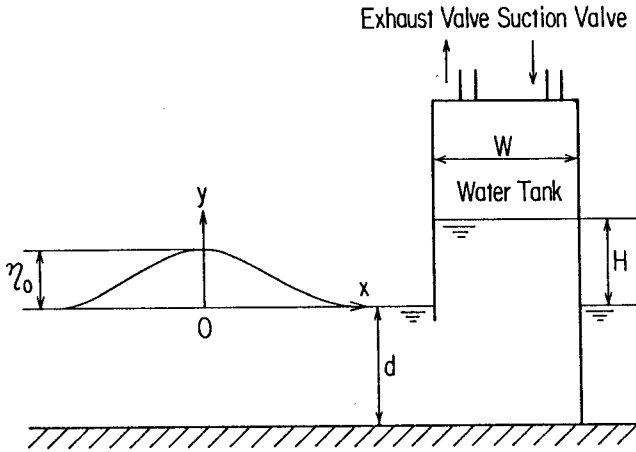
Fig. 1 Notaion and coordinate system

this equipment generates a large solitary wave, it is not necessary to be large scale. And, supplied power is not so great, too.

3. Prediction of Wave Height

In the recent report of the authors, maximum height of a solitary wave generated was predicted on the conservation law of mass, where mass of water in tank and mass of a solitary wave are to be equivalent. But, the obtained result did not seem to be reasonable, because maximum wave height was proportioned to both the square of water height in tank and the square of width of tank. In here, Considering a principle of this wave generator, the authors predict maximum wave height on the conservation law of energy on the assumption that generated waves can be considered approximately cnoidal waves or solitary waves which are special cases of cnoidal wave. Because waves generated by this equipment are large one in finite depth water.

As shown in Fig. 1, let the origin of coordinate system be taken at the center of a solitary wave on the level water line, and X and Y axis's be the horizontal and vertical coordinates. Y-axis is taken positive into the upward. The coordinate system is moving with the solitary wave. η_0, L, d, means maximum wave height on level water line, wave length, and water depth, respectively. Under the assumptions those are $d/L \ll 1$ and $\eta_0/d \ll 1$, it is possible to solve two dimensional potential problem accompanied with non-linear free surface conditions with regular perturbation method, and to obtain profile and velocity of cnoidal or solitary wave, and velocity distribution in fluid (Ref. 3). It is assumed here that the generated waves can be regarded as solitary waves for simplification of the following calculation.

A profile of a solitary wave is described as

$$\eta \cong \eta_0 \text{sech}^2\left(\sqrt{\frac{3\eta_0}{4d^3}}\, x\right) \tag{1}$$

And, u that means horizontal velocity in fluid is described as

$$u \cong \eta_0 \sqrt{\frac{g}{d}}\, \text{sech}^2\left(\sqrt{\frac{3\eta_0}{4d^3}}\, x\right) \tag{2}$$

where g means acceleration of gravity. Vertical velocity in fluid is negligible, since it is a very small amount compared with horizontal one.

When potential energy of water in tank is completely transformed into potential energy Ep of solitary wave and into kinematic energy Ek of it,

$$U = E_P + E_K \tag{3}$$

must be realized. Solitary wave's potential energy Ep is represented

$$\begin{aligned} E_P &= \rho g \int_{-\infty}^{\infty} \int_0^{\eta} y\, dy\, dx \\ &= \frac{1}{2} \rho g \int_{-\infty}^{\infty} \eta^2 dx \\ &\cong \frac{1}{2} \rho g \eta_0^2 \int_{-\infty}^{\infty} \text{sech}^4\left(\sqrt{\frac{3\eta_0}{4d^3}}\, x\right) dx \\ &= \frac{4}{3} \rho g \sqrt{\frac{\eta_0^3 d^3}{3}} \end{aligned} \tag{4}$$

by using of wave profile (1). Also kinematic energy Ek is represented approximately

$$\begin{aligned} E_K &= \frac{1}{2} \rho \int_{-\infty}^{\infty} \int_{-d}^{\eta} (u^2 + v^2)\, dy\, dx \\ &\cong \frac{1}{2} \rho g \eta_0^2 \int_{-\infty}^{\infty} \text{sech}^4\left(\sqrt{\frac{3\eta_0}{4d^3}}x\right) dx \\ &= \frac{4}{3} \rho g \sqrt{\frac{\eta_0^3 d^3}{3}} \end{aligned} \tag{5}$$

where it is considered that vertical velocity is negligible.

Comparing with Eq. (4) and Eq. (5), we can recognize that potential energy and kinematic energy are approximately equal each other. We get total energy of solitary wave as

$$E_P + E_K = \frac{8}{3} \rho g \sqrt{\frac{\eta_0^3 d^3}{3}} \tag{6}$$

form Eq. (4) and Eq. (5). We also get water potential energy in tank accounted from level water as

$$U = \frac{1}{2} \rho g H^2 W \tag{7}$$

where H denotes water head from level water and W denotes width of water tank.

When we substitute Eq. (6) and Eq. (7) for Eq. (3), and solve for η_0, we can get an expression of predicted maximum wave height as

$$\eta_0 = \left(\frac{27}{256}\right)^{\frac{1}{3}} \frac{H^{\frac{4}{3}} W^{\frac{2}{3}}}{d} \tag{8}$$

In short, maximum wave height of solitary wave is proportioned to 4/3 power of water head in tank. Further, maximum wave height is also proportioned to 2/3 power of width of tank. So, as for the comparison between a wider tank and a taller one, it shows that the latter is possible to generate a larger solitary wave than the former.

4. Experimental Results

The result of experiment to verify the prediction result shown in the foregoing section is described in this section. Wave generation experiments were carried out at two dimensional experimental channel(total length is 14m and width is of Osaka University.

4.1 Wave Profile

The generated wave profile is shown in Fig. 2. when initial water head is H=0.3m.
Water depth is 0.2m and width of tank is 0.25m. Fig. 3 shows the comparison between measured wave profile in Fig. 2 and calculated one in Eq. (1) which maximum wave height is same to the observed one. Solitary wave is going from the right to the left both in Fig. 2 and in Fig. 3.

Measured wave profile is slightly unsymmetrical about the center of solitary wave on the whole. Specifically, although the calculated profile is exactly symmetrical, the fore half part of observed profile is larger than that of calculated one, and after half part of observed profile is smaller than that of calculated one. On the whole, the observed wave profile is very similar to the calculated one. So, it is reasonable that the observed wave is approximately considered as a solitary wave.
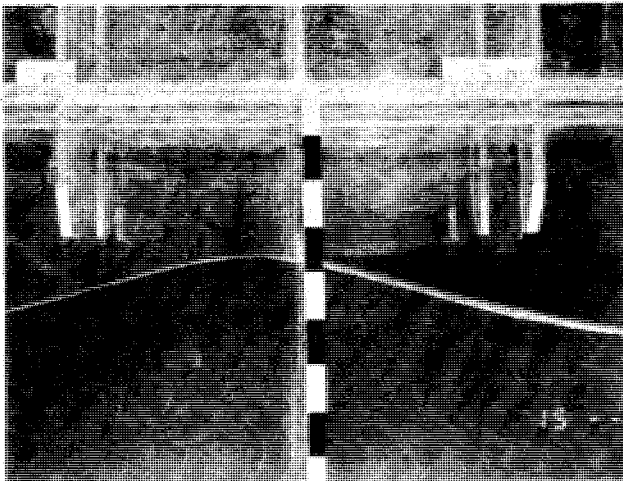
Fig. 2 Observed wave profile
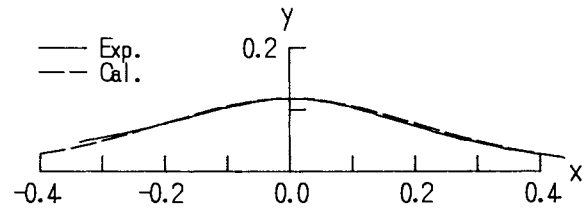
Fig. 3 Comparison of wave profile between experiment and calculation

4.2 Maximum Wave Height

Next, relation between maximum wave height and dimension of water tank or water head or water depth is described. The wave generation experiments were carried out in following conditions; width of water tank W is 0.125m, 0.250m, 0.500m, water depth in channel d is 0.2m, 0.4m, and initial water head in tank is varied from 0.02m to 0.70m.

Initial water head H and measured maximum wave height η_0 in various conditions are shown in Figs. 4~8. When maximum height of a solitary wave is small compared with water depth, it advances without the modification of wave profile. But, it is known that a solitary wave is modified and leads to breaking when the relative wave height η_0/d is larger than 0.83 (Ref. 4 & 5). Hence, the measurement results which are not accompanied with wave breaking, are only mentioned in Figs. 4~8.

Since maximum wave height was predicted to proportioned to the 4/3 power of water head H as stated before, we chose the relation between H and written in the form of

$$\eta_0 = AH^n$$

and we obtained experimental curves by using of method of least squares. These are also shown in Figs. 4~8. In these results, maximum wave height are proportioned to the 4/3 power of water head H independently of water depth and width of tank. So, it is considerable that the predicted maximum wave height is almost correct when it is based on the conservation law of energy.

To clarify this relation moreover, Fig. 9 shows the plotting of $(H^{\frac{4}{3}} \cdot W^{\frac{2}{3}})/d^2$ against η_0/d. the plotted points are on the one line. So, the relationships between wave height, water head, tank width, and water depth become as

$$\frac{\eta_0}{d} \propto \frac{H^{\frac{4}{3}}W^{\frac{2}{3}}}{d^2}$$

which consists with Eq. (8).
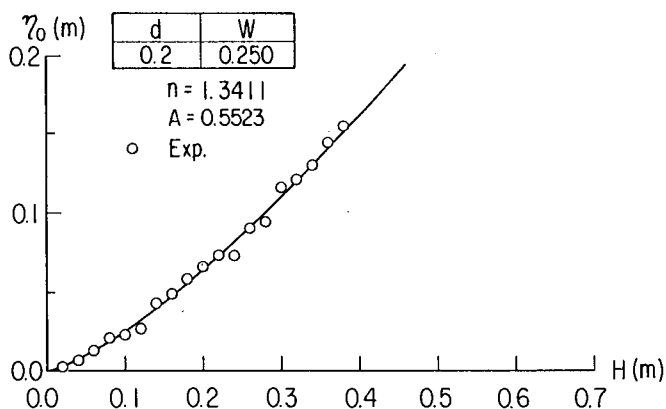
Fig. 4 Measured maximum wave height
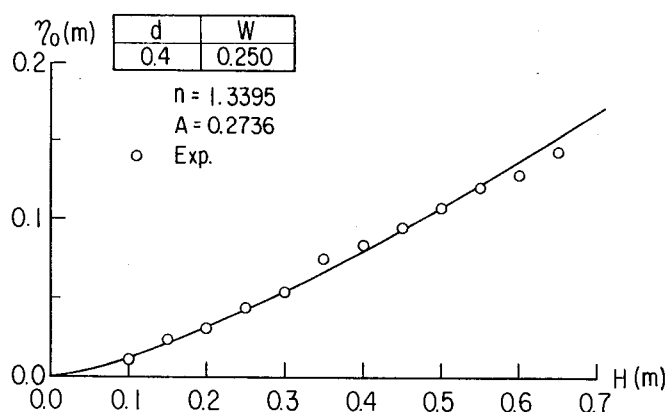
Fig. 7 Measured maximum wave height
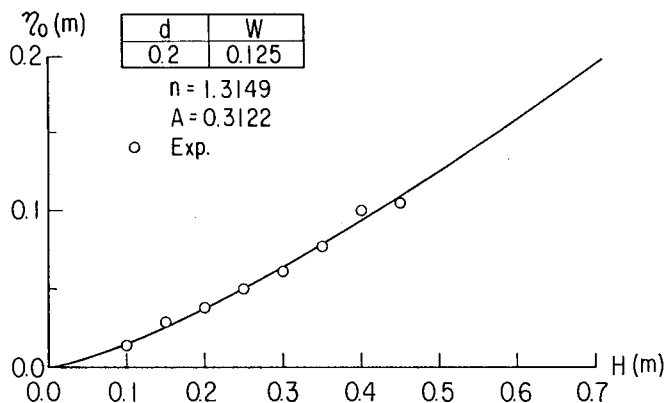
Fig. 5 Measured maximum wave height
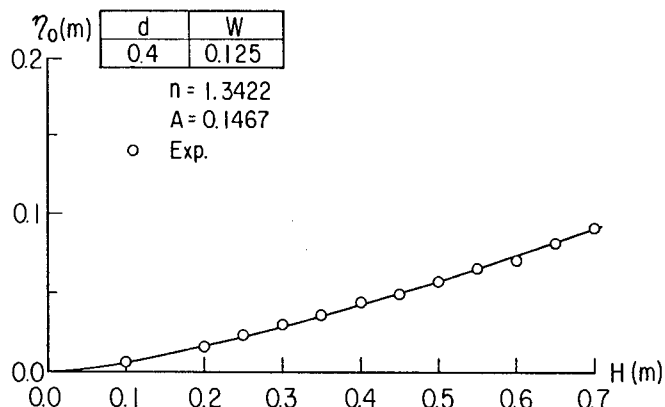
Fig. 8 Measured maximum wave height
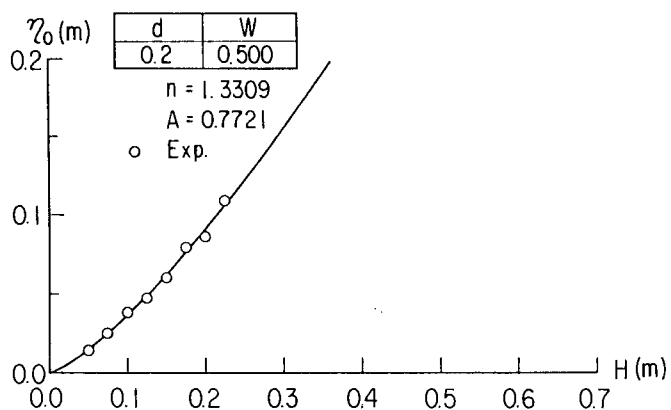
Fig. 6 Measured maximum wave height

4.3 Efficiency of Energy Transformation

We adapted the assumption to obtain Eq. (8) that potential energy in water tank is wholly transformed into solitary wave's energy. But it seems that energy loss exists actually in the process of wave generation, because the large vortex like shown in Fig. 10 are generated near by the opening of water tank when water flows out from tank. This observed fact suggests that a part of supplied energy disappears as head loss cause on viscosity. Accordingly, the relationship between supplied energy and wave's energy is mentioned as

$$\beta U = E_P + E_K \qquad (9)$$

where β means efficiency of energy transformation, Eq. (8) can be expressed as

$$\eta_0 = \beta^{\frac{2}{3}} \left(\frac{27}{256}\right)^{\frac{1}{3}} \frac{H^{\frac{4}{3}} W^{\frac{2}{3}}}{d} \qquad (10)$$

Applying method of least squares for the experimental results shown in Fig.9, we can get β =0.433. This means that half part of the supplied energy vanishes caused by viscous energy loss and by the other loss.

Considering total head loss in the internal flow is usually treated about 0.5, or a large vortex is observed near by the opening of the water tank, we can conclude that the predicted value of β is appropriate in a way. But it is very difficult to predict the exact efficiency of energy transformation theoretically, because the flow around the opening of tank seems to consists of the complex of bending tube flow, nozzle, and jet flow.

Fig.10 Observed flow pattern near water tank

Fig. 9 Measured maximum wave height in dimensionless expressions

	d	W
○	0.2	0.250
△	0.2	0.125
□	0.2	0.500
×	0.4	0.250
Y	0.4	0.125

4.4 Improvement of water tank form

We can recognize in Fig.10 that a large vortex, which seems to be caused by the separation of flow at the edge of the opening, is flowing out when a wave is generated. Since it seems to be reasonable that the energy loss mentioned above is caused by the generation of such large vortex, improvement of water tank form is carried out by using of some appendages attached to the opening edge.

Three kinds of appendages, which are expected to reduce the energy loss at the opening, are shown in Fig.11. Fig.12 shows measured maximum wave height against water head when these appendages are attached to the edge of the opening. Comparing the measured wave height between three kinds of appendages, we can not find any large

Fig.11 Shape of appendages
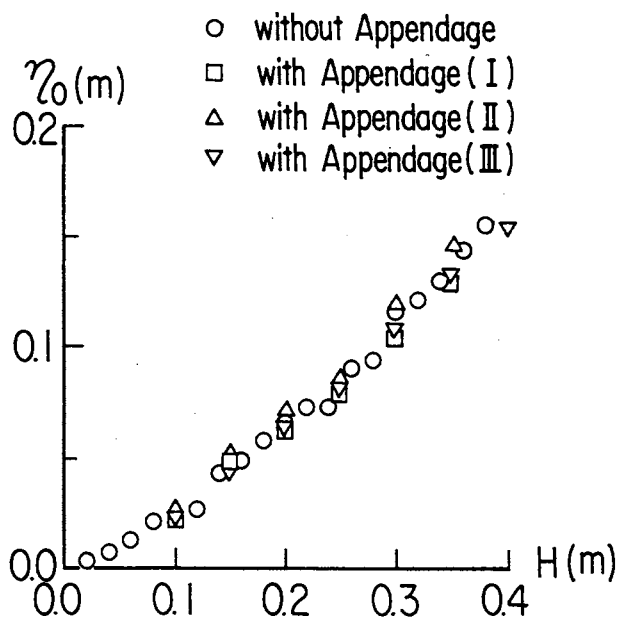
Fig.12 Measured maximum wave height
      with appendages

difference, however we observed and recognized accurate differences of flow in the experiment.

So, it seems that it is necessary to transform the whole shape of water tank to improve the efficiency of wave generation.

5. Concluding Remarks

In this paper, the authors introduced system of the water head type wave generator, and discussed the performance of it with attention to energy conservation law. The authors also discussed the improvement of the water tank form to save supplied energy. The following is a summary of the contents.
(1) A wave generated by this equipment is closely similar to a solitary wave.
(2) On the basis of energy conservation law, predicted maximum height of generated wave is proportional to the 4/3 power of water head in tank and the 2/3 power of tank width. This theoretical prediction indicates good incidence with the experimental results.
(3) When some appendages are attached to water tank, these do not contribute the improvement of the efficiency of wave generation.

Reference
1) H. Tanaka, et al. : On Wave-Maker of Large and Steep Solitary Waves Suitable for Surfing, Proc. of 8th. Ocean Engineering Symposium, 1988 (in Japanese)
2) H. Tanaka, et al. : On the performance of a Water-head type wave generator, Jour. of Kansai Society of Naval Architecture, vol. 211, 1989 (in Japanese)
3) G. B. Whitham: "Linear and Non Linear waves", John Wiley & Sons, 1974
4) H. Yamada: On the highest solitary wave, Rep. of Research Institute of Applied Mechanics, vol. 5, 1957
5) M. S. Longuett-Higgins et al. : On the mass, momentum, energy and circulation of a solitary wave II, Proc. of Royal Society of London, A340, 1974

RESISTANCE TESTS OF "MARINE EXPRESS"-
AN UNDERWATER TRAIN

Wataru Koterayama*, Yusaku Kyozuka*, Masaru Inada*, Nobuyoshi Fukuchi**, Toshiaki Ohta***

* Research Institute for Applied Mechanics, Kyushu Univ.
** Dept. Naval Architecture, Faculty of Eng., Kyushu Univ.
*** Dept. Civil Eng., Faculty fo Eng., Kyushu Univ.

ABSTRACT

This reports model experiments on an underwater train called the "Marine Express" which is now under study and development as part of the "Marine Express Project". Resistance tests on powering of the train were carried out as a first step using a 1/17th scale model, and resistance components such as the friction between the wheels and guideway, skin-friction of the body surface, and those due to the existence of the guideway were considered. The residual resistance obtained by subtracting the friction between the wheels and guideway from the total resistance was found to fit well with the estimation formula of the skin-frictional resistance of the flat plate with the form factor.

1 Introduction

This paper deals with the resistance tests of an underwater train now being studied as part of the "Marine Express Project" of Kyushu University begun in May 1989.

The "Marine Express" is a linear motor-driven rapid transfer system being developed for use both on land and in the water. This type of transport would offer the benefit of providing direct access to a floating airport or a floating city, thus avoiding the need to transfer to another system. Another merit would be its provision of a stable means of conveyance in the ocean which would be free from the effects of storms.

Research groups involved in the project are segregated into those working on train development, guideway system, station development and ocean environmental aspects. This particular report is on train development and pertains to the resistance of the Marine Express when it travel in water; estimation of the power required at a given speed is also dealt with. These resistance tests are thought to be the first in the world on an underwater train. Among the factors considered were how the existence of the guideway and the clearance between the body and the guideway affect resistance of the Marine Express.

2 Model and Experimental Setup

Experiments were conducted in a maritime water tank ($L \times B \times d = 80m \times 8m \times 3.5m$) of the Tsuyazaki Sea Safety Laboratory of the Research Institute for Applied Mechanics, Kyushu University. A guideway $40m$ in length was constructed about $1m$ below the surface of the water, and resistance tests were carried out under two condition: with and without the guideway.

Figure 1 shows dimensions of a $1/17th$ scale model of a prototype of the actual Marine Express, while principal dimensions of the full model and the actual train are shown in Table 1. There are two prototype trains each with eight pairs of wheels and bearings as shown in Figure 1. Figure 2 is a picure of the model taken on the ground.

The experimental setup for the resistance tests with the guideway is shown in Figure 3. The model train was towed by a stainless steel wire, and total resistance was measured by two load-cells through fore- and aft-struts. Resistance of the body was obtained by subtracting the resistance of the struts from the total resistance.

Figure 4 shows the experimental setup for tests without the guideway, in which the model was sup-

ported by four struts and the total resistance was measured by one load-cell. Figure 5 is a top view of the experimental setup without guideway.

The Measured data contained some noise, mainly emanating from the discontinuity of the guideway which was constructed in twenty units of $2m$ length. Resistance was, therefore, determined by averaging the recordings excluding the acceleration and deceleration portions. Figure 6 is a picture of an experiment with guideway taken in water, where white dots denote air bubbles blown from the bottom of the tank.

3 Components of resistance of the model

The resistance of the model can be separated into the following four components as:

$$R_T = R_0 + R_1 + R_2 + R_3 \qquad (1)$$

where

R_T : Total resistance

R_0 : Frictional resistance between wheels and guideway

      (independent of velocity)

R_1 : Skin-frictional resistance of the body

      (proportional to velocity squared)

R_2 : Pressure resistance due to existence of the guideway

      (function of velocity)

R_3 : Resistance due to the shear flow in the narrow clearance between body and guideway

      (linear with velocity)

R_0 is dependent on the friction of the wheels and ball- bearings, and linearity of the guideway. It was determined from the results of low speed tests and assumed to be independent of the forward velocity.

R_1 is the skin-frictional resistance without the guideway as for a ship or airplane, and is estimated by the following equation.

$$R_1 = \frac{1}{2}\rho S V^2 (1 + K) C_F \qquad (2)$$

where

ρ : density of water, V : velocity

S : area of body surface, K : form factor

C_F : coefficient of skin-friction of flat plate

There are several formulas for C_F ; we applied Schlichting's formula for the turbulent flow as:[1]

$$C_F = 0.455/(\log R_n)^{2.58} \qquad (3)$$

where

$R_n = VL/\nu$: Reynolds number

L : length of model

ν : coefficient of kinematic viscosity
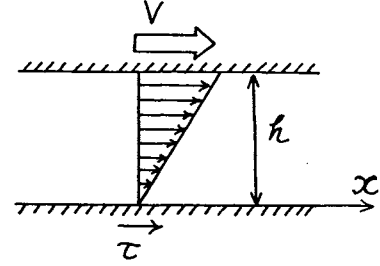
R_2 and R_3 are components of resistance which are due to the guideway, but R_3 can be estimated by the analysis of Quette flow in the narrow clearance between the body and the guideway. As shown in above Figure, shear stress on the wall for $dp/dx = 0$ is given as follows, using the coefficient of viscosity (μ) :

$$\tau = \mu V/h$$

Then, R_3 may be estimated simply as

$$\left. \begin{aligned} R_3 &= \tau A \\ &= \mu V A/h \end{aligned} \right\} \qquad (4)$$

Substituting values of the present experimental condition for $h = 3.5 \times 10^{-3}$ (m) and $V = 1.0(m/s)$, we obtain $R_T = 10.4g$. Therefore, we may conclude that the resistance due to the shear flow in the clearance between the body and guideway is negligible compared with other components.

4 Results and Discussion

Figure 7 shows the total resistance of the model and four struts without the guideway; the resistance of the struts alone is also plotted, so that the resistance of the model alone is obtained by subtracting that of the struts. Although the area of the wet part of a single strut is rather small ($b \times d = 0.05m \times 0.74m$) , the resistance of the four struts accounts for almost half of the total.

Figure 8 shows the total resistance with the guideway, and that of two struts alone; two clearances,

3.5mm and 6.0mm, between the body and the guideway provided two resistance curves in the figure.

The final results of resistance coefficients, in which frictional resistance R_0 is excluded in the tests with the guideway, are shown in Figure 9. Solid lines denote the resistance coefficient of the flat plate, and a dotted line denotes the resistance coefficient by the Prandtl-Schilichting formula in the transition flow as:

$$C_F = 0.455/(\log R_n)^{2.58} - A_t/R_n \qquad (5)$$

where A_t is a function of the point of separation of the flow; A_t is assumed as 1500 in this figure.

Experiments on the velocity under $0.5m/s$ might give results reflecting the transition flow from the turbulent flow, and show the same tendency as eq.(5)

The clearance effect on the resistance coefficient doesn't seem as large in these experiments as had been expected by eq.(4)

Resistance coefficients of velocity greater than $0.75m/s$ are roughly parallel to the solid line. Therefore, the form factor K is determined by eq.(2), and obtained as:

$$\left.\begin{array}{l} K = 0.20 \quad \text{without guideway} \\ K = 0.40 \quad \text{with guideway} \end{array}\right\} \qquad (6)$$

The difference of K with or without guideway is attributable to the change of the flow field around the model due to the existence of the guideway.

5   Powering of the Actual Marine Express

From the above model tests, let us estimate the power required for actual Marine Express, the principal dimensions of which are shown in Table 1. Frictional resistance between the wheels and guideway need not be conordered since there is no contact bercause of the utilization of the linear motor and the actively controlled fins. Wave resistance is also ignored.

Including the correction of the skin-frictional resistance due to roughness of body surface, total resistance and the coefficient are given as follows:

$$\left.\begin{array}{rcl} C_T &=& (1+K)C_F + \Delta C_F \\[2mm] R_T &=& \dfrac{1}{2}\rho SV^2 C_T \end{array}\right\} \qquad (7)$$

Estimation of the effective horsepower(EHP) for several velocities is shown in Table 2, where $\Delta C_F =$

0.56×10^{-3}, $K = 0.40$ and a sea water temperature of $15°C$ are assumed.[2]

6   Conclusion

In summary, our conclusion drawn from the above experiments are:

(1) Effect of the guideway on the resistance of the Marine Express occurred as the change of the flow field around the body, and the form factor of frictional resistance became almost double that without the guideway.

(2) Resistance due to shear flow in the clearance between the body and guideway was as small as had been expected by a simple analysis of Quette flow. However, this clearance may affect the vertical force and moment of the body.

(3) Estimation of power required for the actual Marine Express was made with correction of body surface roughness included. The Marine Express offers advantages over conventional surface ships operating at higher speed because it is free from the wave-making resistance.

References

1) Schlichting, H. : Boundary-Layer Theory, Sixth Edition, McGraw-Hill Book Company. (1968)

2) Kansai Zousen Kyoukai : A handbook for ship design, Fourth Edition, Kaibundou. (1983)(in Japanese)

1,470

Vertical Wing   Vertical Wing   Oblique Wing

Guideway

Horizontal Wing   Horizontal Wing

PLAN

182

206

Guide Roller

Guideway

Guide
Bearing   Guide Bearing

120
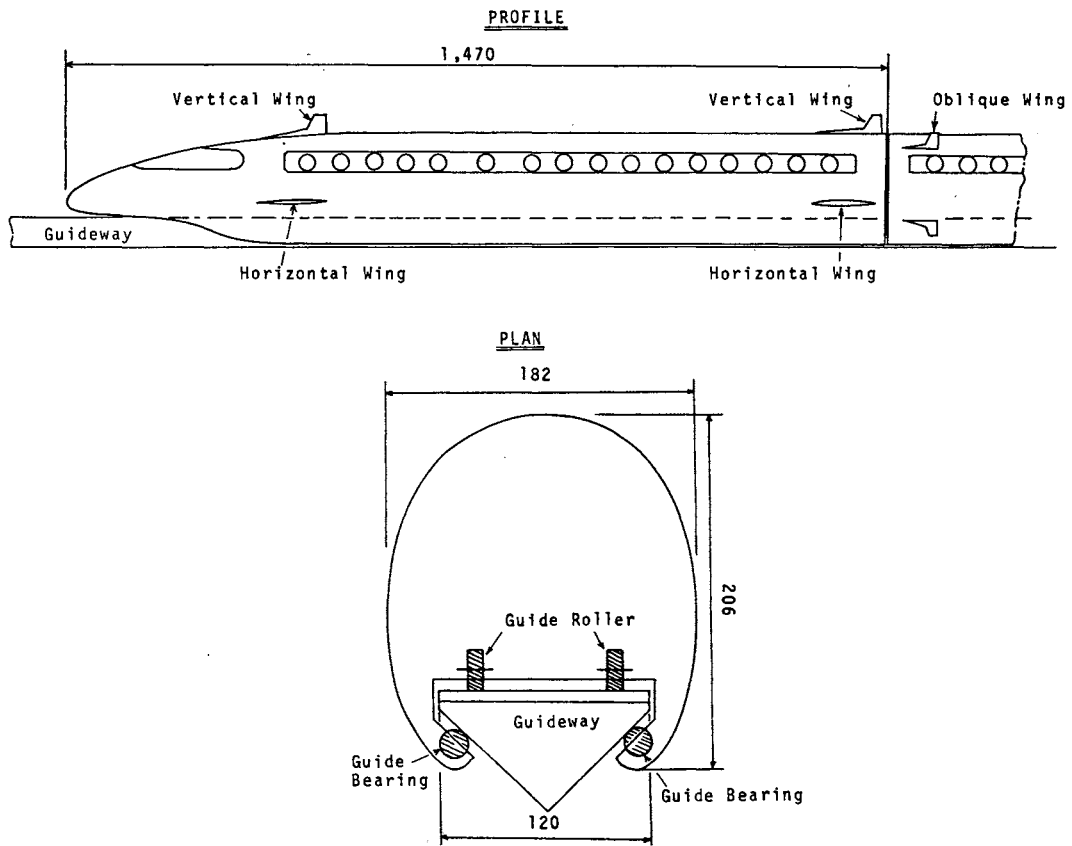
Figure 1 Model of the Marine Express

Table 1 Principal particular of the model

		Model	Actual
Length	(m)	2.94	50.0
Breadth	(m)	0.18	3.1
Displacement Volume	(m^3)	0.0667	327.7
Weight in air	(Kg)	69.1	—
Weight in water	(Kg)	2.4	—
Body surface	(m^2)	1.94	561.0
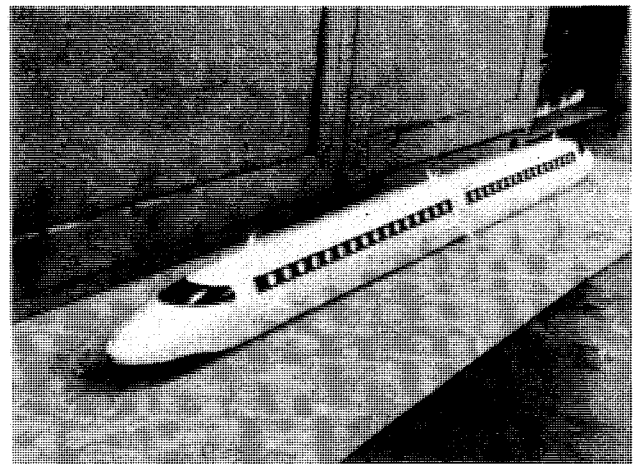
Figure 2 Picture of the model
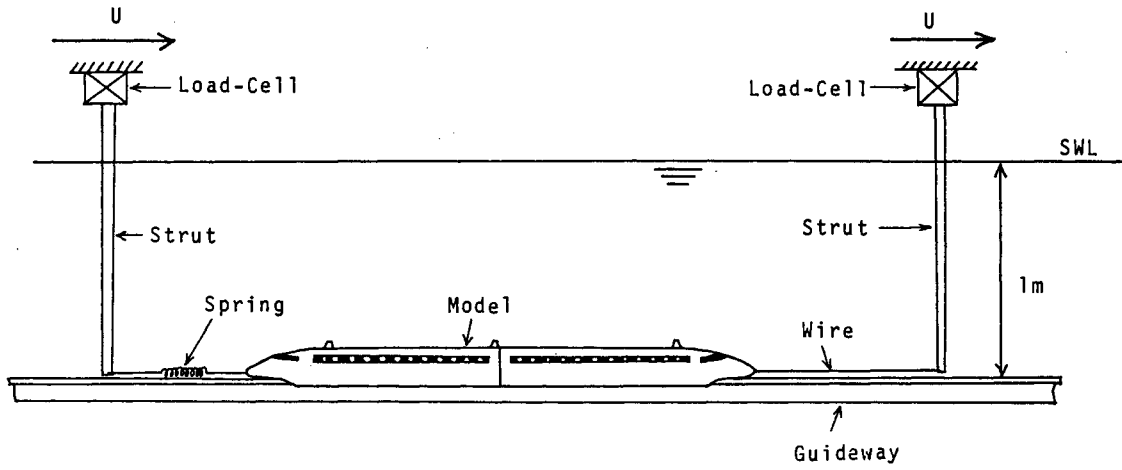
Figure 3 Experimental setup with guideway
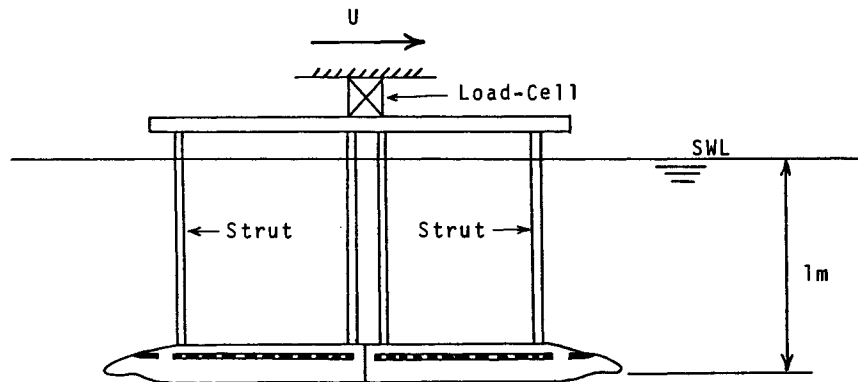
Figure 4 Experimental setup without guideway
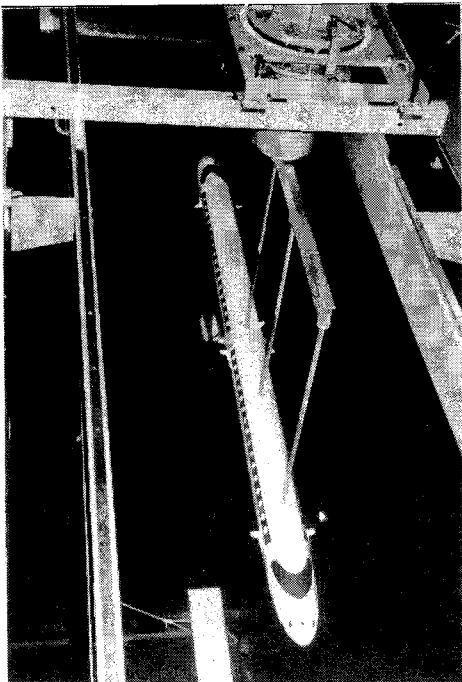
Figure 5 Picture of experimental setup without guideway
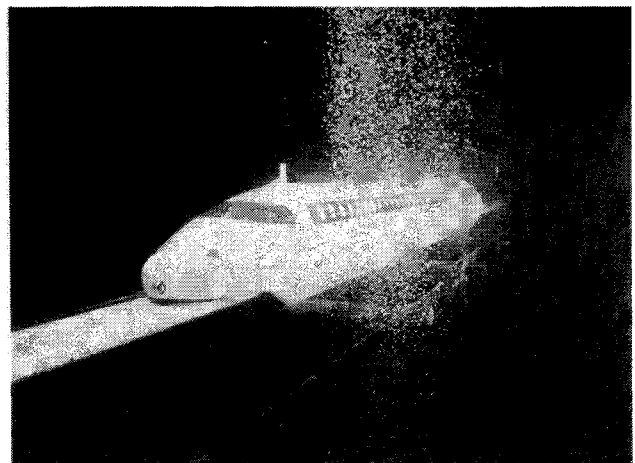
Figure 6 Picture of an experiment with guideway
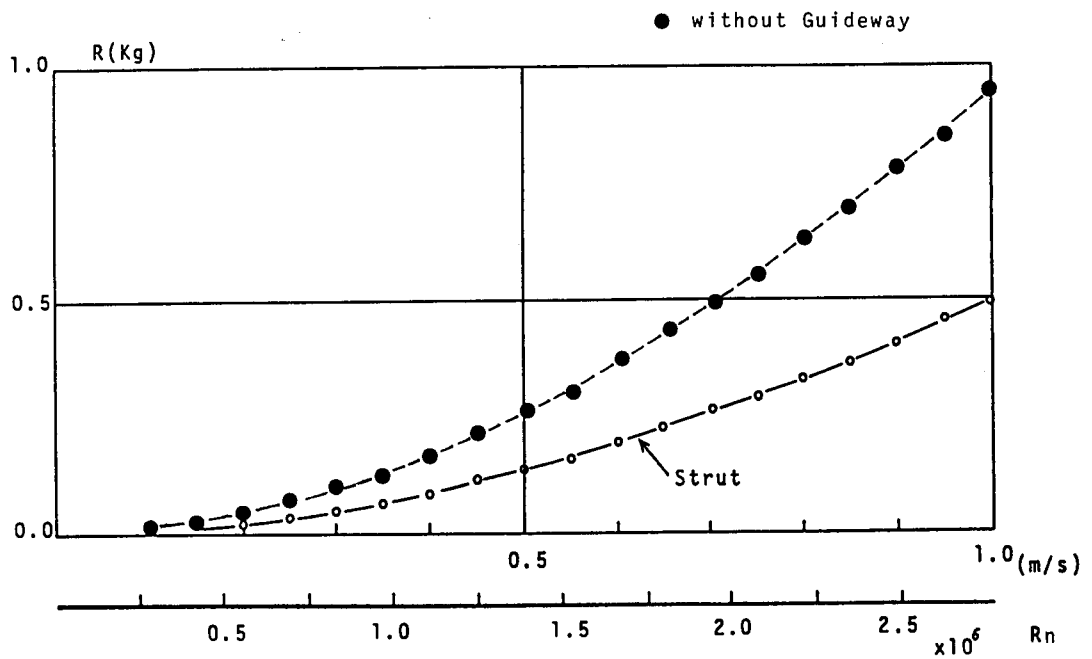
Figure 7 Measured resistance without guideway
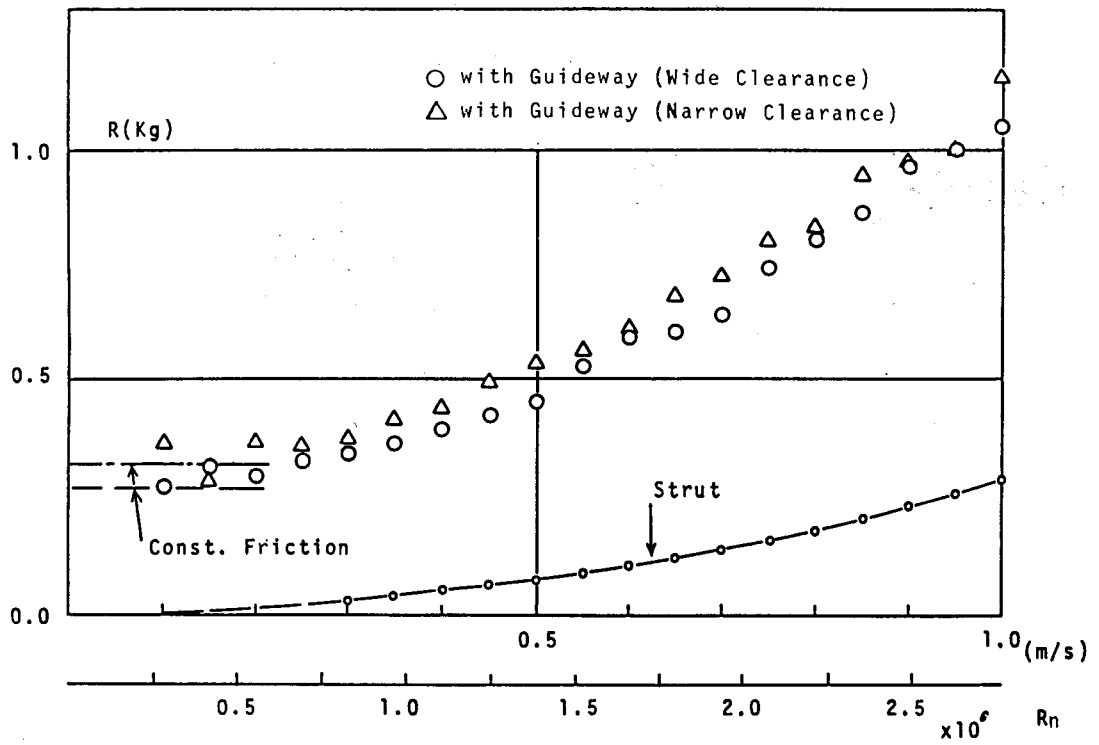
Figure 8 Measured resistance with guideway
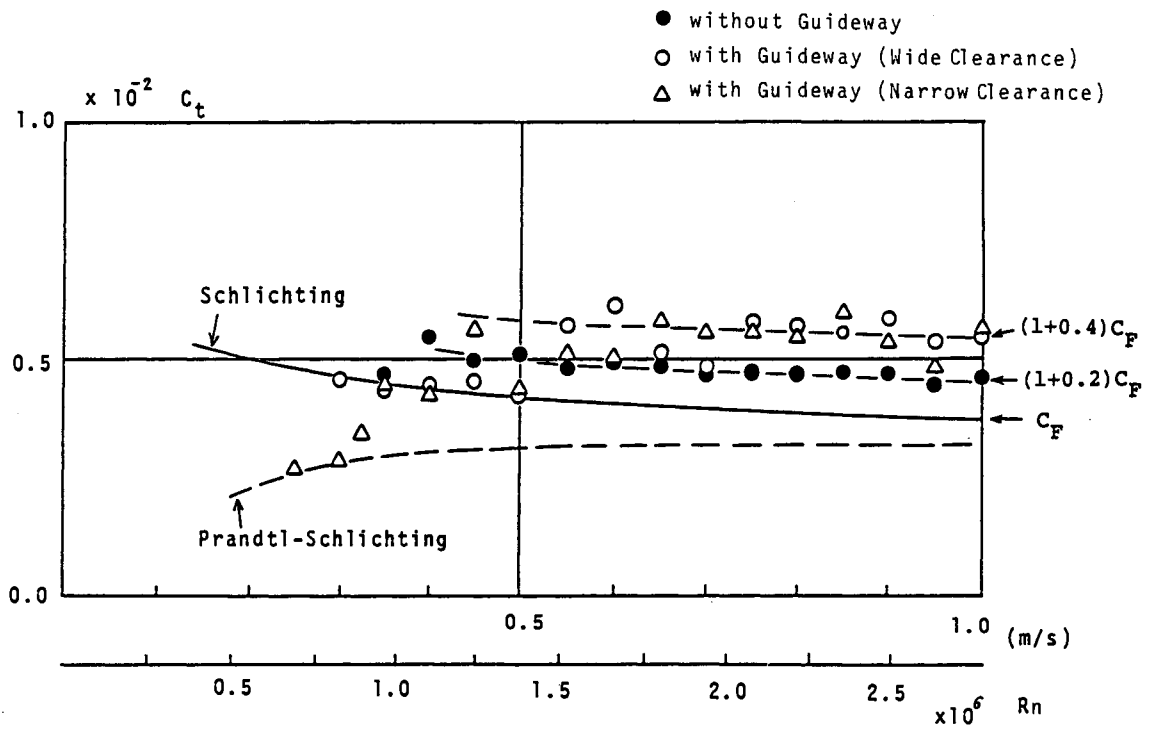
Figure 9 Coefficient of total resistance of the Marine Express

Table 2 Estimation of effective horse-power(EHP) of the Marine Express

$V(Km/h)$	$V(Km/s)$	$C_T(10^{-3})$	$R(Kg)$	EHP
40	11.11	2.981	10799	1600
50	13.89	2.913	16486	3053
60	16.67	2.859	23301	5178
70	19.44	2.815	31224	8095
80	22.22	2.777	40240	11923

A FIELD STUDY OF SWASH OSCILLATION ON A GENTLE BEACH FACE

Susumu Kubota*, Masaru Mizuguchi** and Mitsuo Takezawa*

* College of Science and Technology, Nihon Univ., Japan
** School of Science and Technology, Chuo Univ., Japan

Abstract

Swash oscillation on a gentle beach was measured using a photographical method involving 16 mm memo-motion cameras. The results showed that beach conditions were dissipative and ordinary wind waves, ranging in frequency between 0.2 Hz and 0.06 Hz, lost their energy by breaking in the surf zone and on the swash slope. Long-period waves with frequencies below 0.06 Hz formed on-offshore standing waves, and these waves primarily governed the swash oscillation characteristics.

1. Introduction

To determine swash oscillation characteristics on natural beaches a field experiment was carried out. Another paper in these Proceedings [1] described and discussed swash oscillation measurement techniques and showed examples of observation from a swash zone with a steep slope. In that paper, it was established that long-period waves from on-offshore standing waves which have an anti-node at the swash slope, and the properties of the standing waves primarily governed the characteristics of the swash oscillations. An attempt to separate the waves observation in incoming waves (incident waves) and outgoing waves (reflected waves) was done. In this paper, the theoretical background for the wave separation is briefly summarized and results from field observations from a swash zone with a steep slope are described.

2. Theoretical Background for Separating of Incoming Waves and Outgoing Waves.

2.1 Method Based on Linear Small-amplitude Long Wave Theory

Applying linear small-amplitude long-wave theory, Guza et al. [2] derived the following expressions

$$\eta_I = \frac{1}{2} \left\{ \eta + \alpha \left[\frac{h}{g} \right]^{1/2} u \right\} \qquad (1)$$

$$\eta_R = \frac{1}{2} \left\{ \eta - \alpha \left[\frac{h}{g} \right]^{1/2} u \right\} \qquad (2)$$

where η, η_I, and η_R are the water surface elevation of the observed, u is the water particle velocity, g is the acceleration due to gravity, h is the water depth, and α is a constant. The constant α has a value of unity theoretically. However, in analyzing data a somewhat different value on α may be selected to accomplish optimal separation.

2.2 Method Based on Linear Small Amplitude Wave Theory

Assuming that the measured waves can be expressed as a sum of sinusoidal waves with different frequencies, Kubota et al. [3, 4] obtained;

$$\eta_I = \frac{1}{2} \left\{ \eta + \sum_{i=1}^{N} \frac{1}{H_i} (C_i \cos \sigma_i t + D_i \sin \sigma_i t) \right\} \qquad (3)$$

$$\eta_R = \frac{1}{2} \left\{ \eta - \sum_{i=1}^{N} \frac{1}{H_i} (C_i \cos \sigma_i t + D_i \sin \sigma_i t) \right\} \qquad (4)$$

$$\left. \begin{array}{l} H_i = \dfrac{\sigma_i \cosh k_i (h+z)}{\sinh k_i h} \\[2mm] \sigma_i^2 = g k_i \tanh k_i h \end{array} \right\} \qquad (5)$$

where t is the time, z is the vertical distance with the origin of the coordinate system taken at the still water surface, $\sigma = 2\pi/T$, $k = 2\pi/L$, T is the wave period, L is the wave length, and C, and D are the Fourier coefficients.

2.3 Method Based on Quasi-nonlinear Small Amplitude Long Wave Theory

Applying nonlinear small amplitude long wave theory, Kubota et al. [3, 4] obtained the following appropriate equations for the incident and reflected wave:

$$\eta_I = \frac{1}{2}\left\{\eta + \alpha u\left[\frac{h}{g}\right]^{1/2}\frac{h}{h-\eta}\right\} \quad\text{...............} \quad (6)$$

$$\eta_R = \frac{1}{2}\left\{\eta - \alpha u\left[\frac{h}{g}\right]^{1/2}\frac{h}{h-\eta}\right\} \quad\text{...............} \quad (7)$$

3. Field Observation

The field experiment discussed in this paper was carried out on July 30 1987, at Hazaki beach facing the Pacific Ocean, located at the southern part of Tokai Coast about distant 100 km from Tokyo(see Fig. 1). A research pier belonging to the Hazaki Oceanographical Research Facility, the Port and Harbor Research Institute, Ministry of Transportation, is located here for facilitating field studies in the nearshore zone. the field observations were carried out using the pier as a platform for the 16 mm cameras. The average tidalrange at the beach is about 1.2 m and the beach slope is considered to be gentle. the beach is composed of sand with a grain size in the range of 0.1 to 0.5 mm. the median grain diameter on the swash slope was around 0.18 mm.

A stick array consisting of 31 target marker iron bars, placed at an interval of 1 m, was installed normal to the shoreline, about 30 m south of
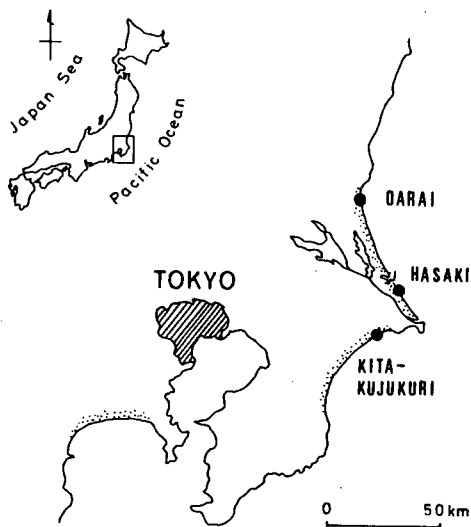
Fig. 1 Location map of experimental site.

the pier. In extension of the array line going seaward, five poles were installed for the wave measurement. The poles at St.4 and St.5 were equipped with a capacitance-type wave gage and an electromagnetic current meter were equipped. a run-up meter(see Takezawa and Kubota(1990) [1]) was located approximately 50 cm south of the array. During the experiment, a few persons were engaged in adjusting the height of the supporting devices of the capacitance wire. figure 2 shows the beach profile plan-form, and the arrangement of the instrumentation. Photo 1 shows the stick array and 16 mm cameras located on the pier. Four sets of 16 mm memo-motion cameras were set up on the pier, where two sets photographed the stick array
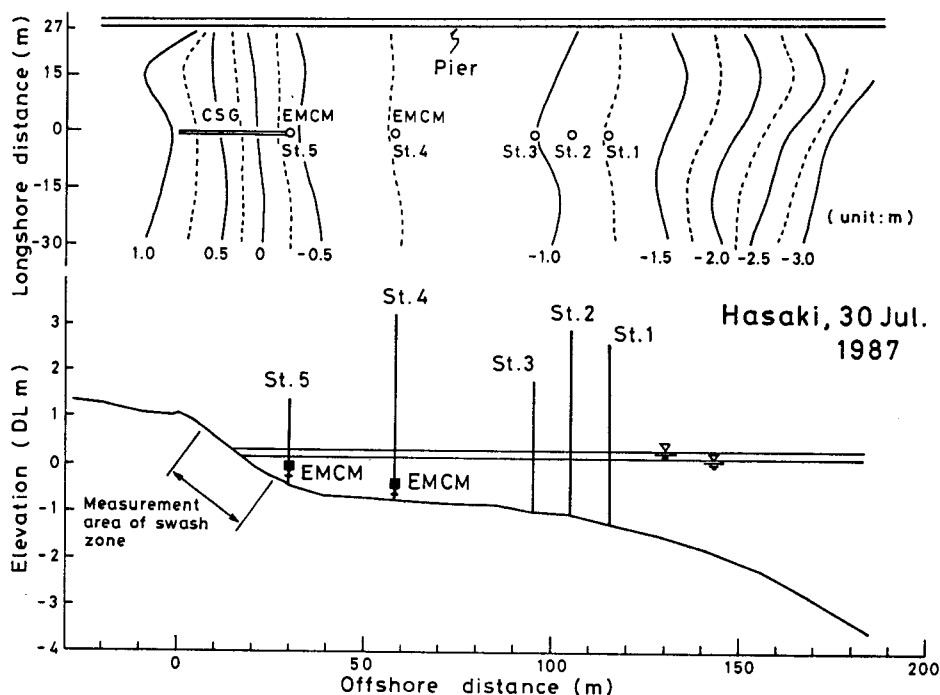
Fig. 2 Beach profile, and arrangement of instrumentation.
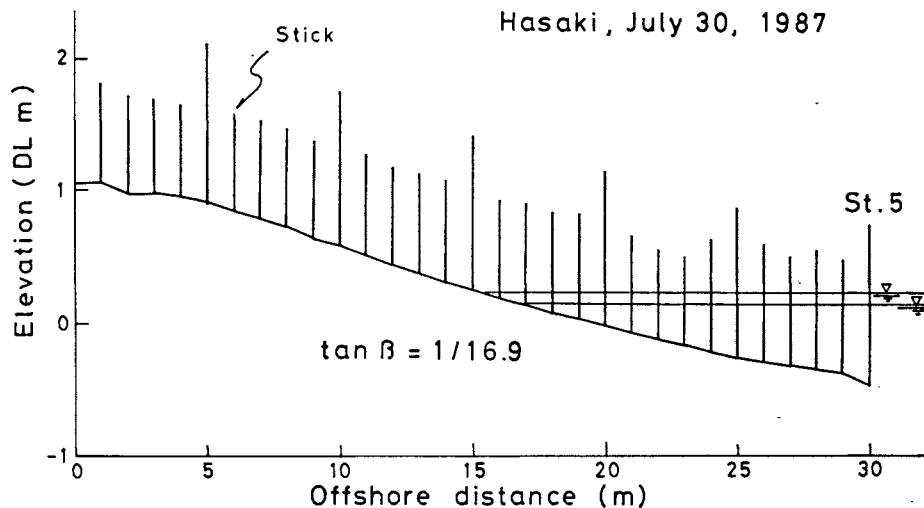
Fig. 3 Assumed compound slope for the swash zone.
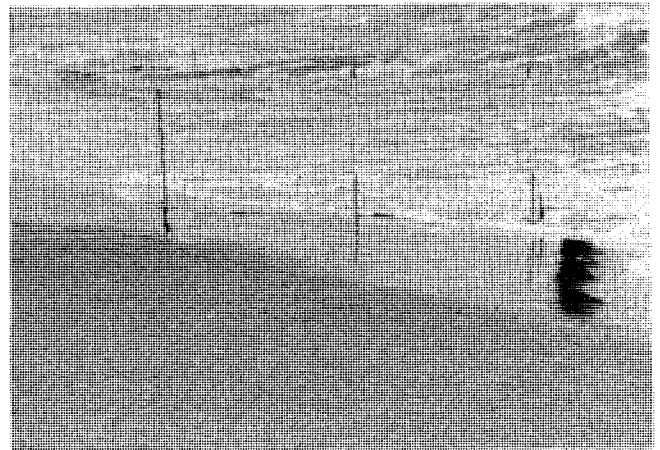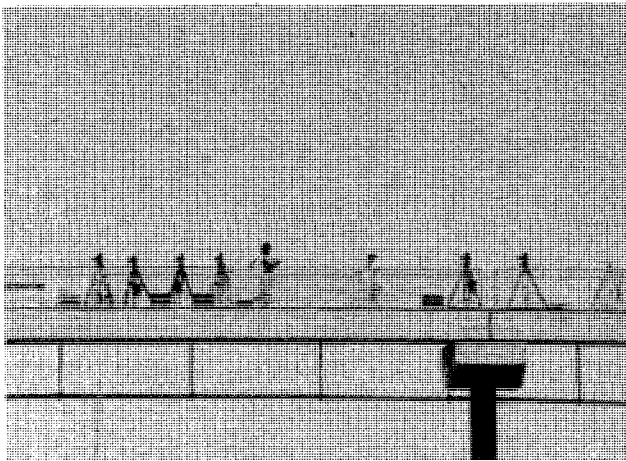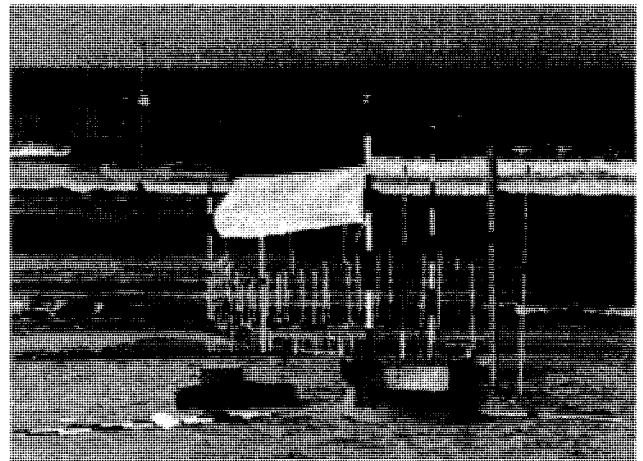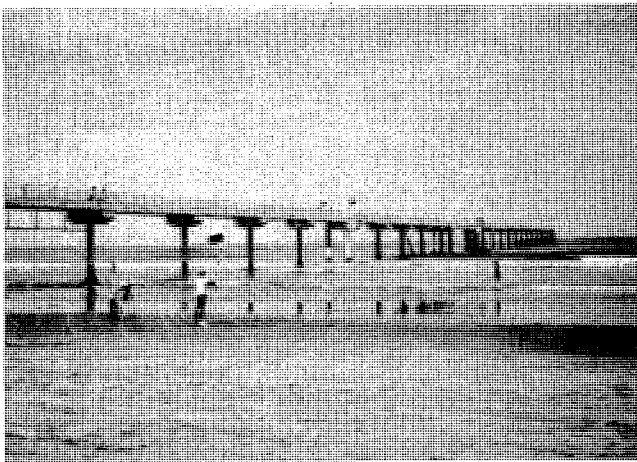
Photo 1   Stick array and run-up meter.

and the other two sets photographed the poles in the sea. The measurements started on 17:15 and ended 18:31, with seventy six minutes of data collected. During the measurements, the tide rose about 20 cm. The average breaker line was located near St.2 and an average breaking wave height of 0.95 m and a wave period of 12.1 s were recorded. The waves broke as the plunging type. The methods for data recording and processing are the same as presented by Takezawa and Kubota[1] in these Proceedings. However, in the present experiment video cameras were not employed.

4. Results and Discussion

Results obtained with the 16 mm cameras and from the current meter measurements are described next. Figure 3 shows the beach profile of the swash zone.
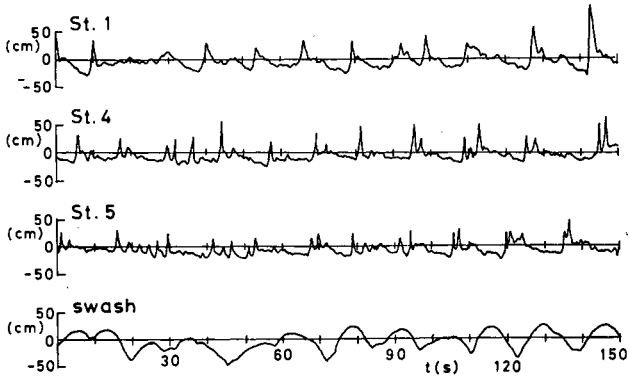
Fig. 4 Time series of raw data.

4.1 Raw Data

Figure 4 displays a portion of the measured sea surface variation at Sts. 1, 4, 5, and at the swash slope. Station 1 was located near the break point, whereas St. 4 and St. 5 were in the surf zone. At Sts. 4 and 5, small waves occurred between the primary individual waves (compare Mizuguchi(1982) [5]). These waves are probably caused by the wave breaking. The passage of the primary individual waves are easily follows from St. 1 to St. 5. However, the relatively smaller primary individual waves are not possible to from St. 5 up to the swash even though this could be done for the larger primary waves. A large wave following a smaller wave travels fast-er, eventually catches up, and passes the preceding wave running up the swash slope. A small wave running up after a large proceeding wave is prevented from traveling up the slope by the large wave beginnings to swash down. These are the reasons why relatively small waves disappear on the swash slope.

Table 1 gives statistically representative waves of the adjusted data by zero-down crossing method.

Table 1 Statistically representative waves.

Hasaki, 30 Jul., 1987

Station number	Depth h (cm)	No of waves	Wave height					Wave period			
			H_{rms} (cm)	H_{mean} (cm)	H_{max} (cm)	$H_{1/10}$ (cm)	$H_{1/3}$ (cm)	T_{mean} (s)	T_{max} (s)	$T_{1/10}$ (s)	$T_{1/3}$ (s)
St. 1	145	394	59	51	129	108	85	9.6	12.1	11.8	11.3
St. 2	121	408	61	55	132	103	87	9.3	14.0	10.9	11.8
St. 3	114	442	54	48	116	86	74	8.6	22.1	12.6	11.6
St. 4	93	486	41	37	82	64	55	7.8	10.4	12.0	10.7
St. 5	76	476	33	30	70	52	45	7.9	17.1	16.4	12.7
Swash	0	226	42	40	80	64	55	16.6	35.7	26.8	21.1

(adjusted data, zero-down crossing method)

4.2 Distribution of Wave Height and Period

Figure 5 shows the distribution of wave height and period defined by the zero-down crossing method at St. 1 and St. 4 and for the swash oscillation. Adjusted data implies the removal of the tidal rise of 20 cm assuming a
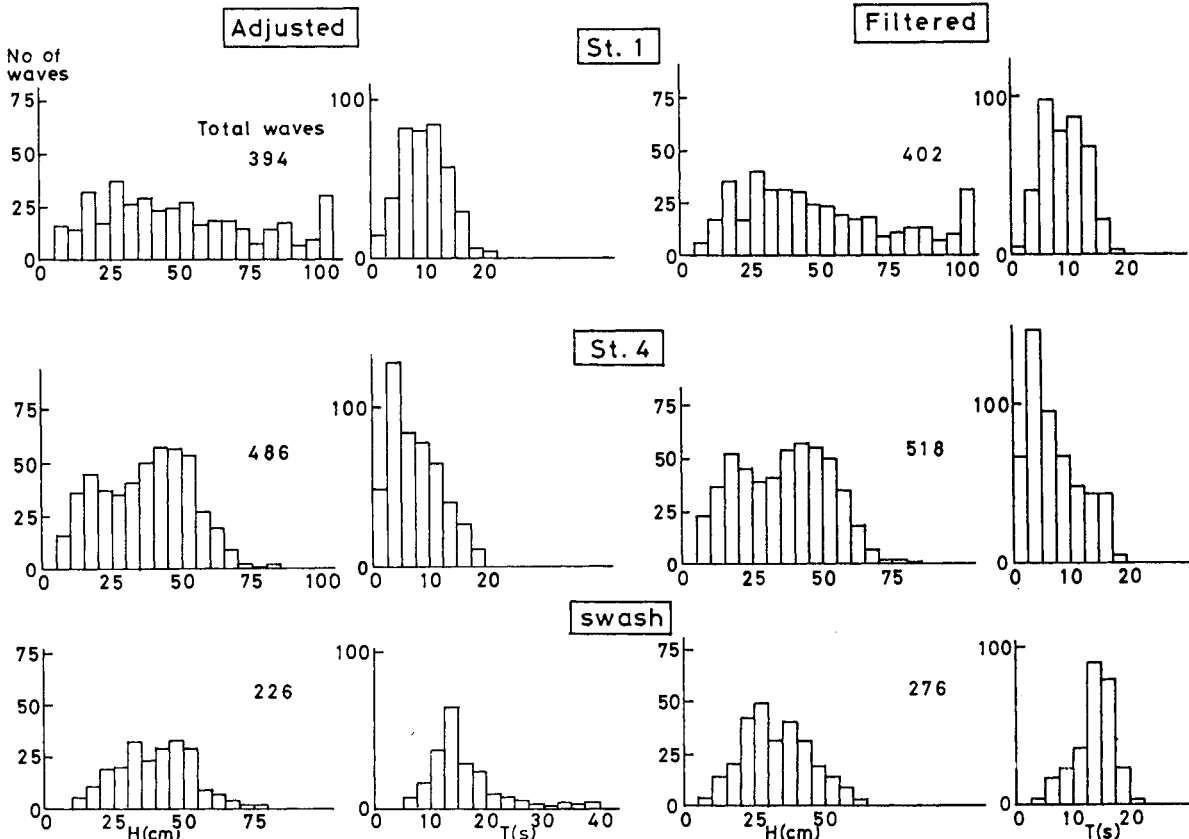
Fig. 5 Distribution of wave height and period.
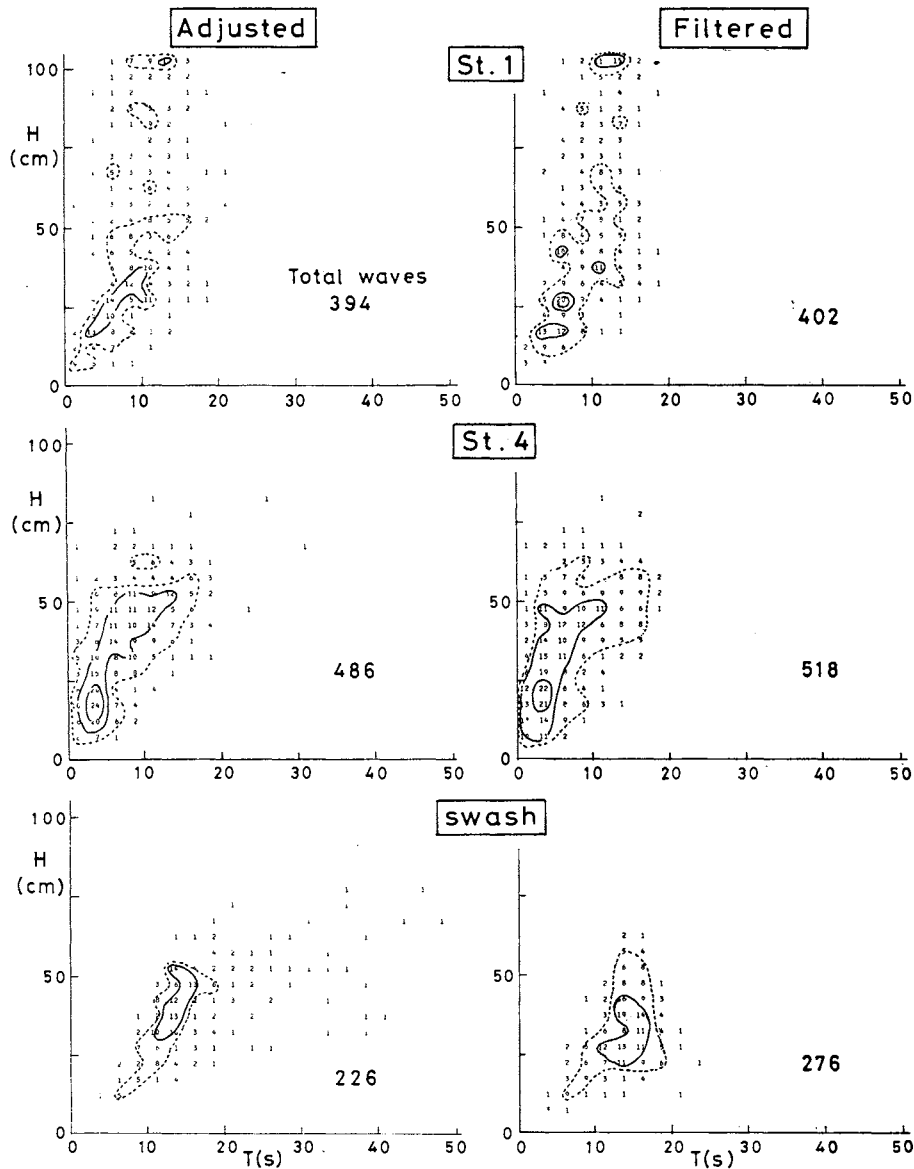
Fig. 6 Joint distribution of wave height and period.

parabolic curve and filtered data was obtained by high-pass filtering with a cut-off frequency of 0.05 Hz. The wave height distributions at St.1 and St.4 are similar to what is commonly observed in the surf zone. The distribution of St.1 located at the break point are more spread out towards higher waves. the distribution at St.4 located in the surf zone is bimodal and the two peaks appear at either side of the average wave height [6]. The change in the number of identified waves is the same as for the steep beach [1]. The number of waves increases in the surf zone, whereas the number considerably decreases on the swash slope, the number of identified waves in the filtered data also increases, the wave height distribution for the swash oscillation regarding the filtered data is similar to the unfiltered data.

Figure 6 shows the joint distribution of wave height and period at St. 1

and 4, and for the swash oscillation. At St. 4 located in the surf zone, a strong correlation is recognized in the domain of small wave heights and short periods. This phenomenon is usually observed in the surf zone.

The spread of the wave height distribution toward higher waves in the swash oscillation was much wider than what was observed at a steep beach such as Oarai beach, although the wave conditions were different during respective observation. In the present experiment wind waves dominated whereas swell reviled for the experiments at Oarai Beach. A remarkable difference compared to the steep beach at Oarai is to be found in the joint distribution if the swash oscillation for the filtered data. No correlation was found in the range of small wave heights and short periods. It seems as if there is no correlation between wave height and period. Establishing the reason for
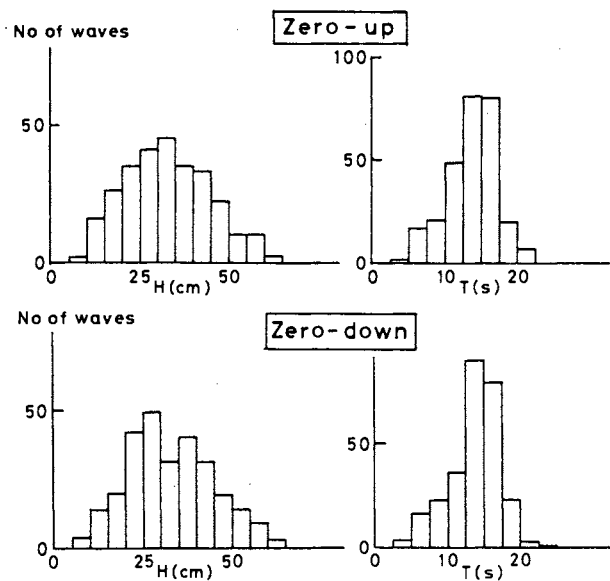
Fig. 7 Comparison of distribution of wave height and period using the zero-up and zero-down crossing method.
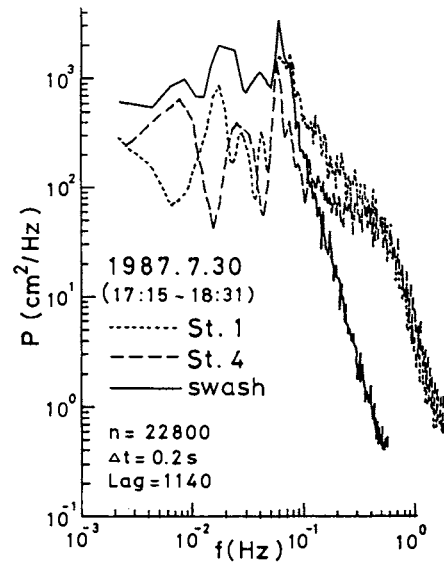
Fig. 8 Power spectral density function.

this difference in results is deferred to future work.

Figure 7 shows a comparison of the distribution of wave height and period for the filtered data using the zero-up and zero-down crossing method. No significant difference was found between the distributions.

4.3 Spectral Analysis

Figure 8 shows the power spectral density function of the sea surface variation at St. 1 and 4, and for the swash oscillation. In the range between 0.06 Hz and 0.7 Hz, the power at St 4 was considerably smaller than the power at St. 1. This implied that waves in that range break and lost their energy as they propagated from St. 1 to St. 4. At around 0.06 Hz the power at Sts. 1 and 4 Where of the same order. Figure 9 illustrates the cross-spectral function of the water surface elevation and the on-offshore component of the water particle velocity at St. 4.

In the phase function a change in phase from + to - is encountered at around 0.06 Hz, corresponding to a coherence close to unity. Based on these observations it is inferred that long period waves appeared in the form of standing waves in the range from 0.06 Hz to the lower frequency range. At around 0.03 Hz there is a pronounced minimum in the coherence function and an abrupt change in phase. A maximum in power is also identified at around 0.03 Hz as seen Fig. 8. Below 0.03 Hz the coherence is nearly unity and the phase difference is $\pi/2$. It is con-

cluded that perfect on-offshore standing waves, implying no breaking, appear in the range below 0.03 Hz for the slope studied. In the range 0.03 to 0.06 Hz partial on-offshore standing waves will be formed.

Figure 10 displays a portion of the resolved waves and Figure 11 shows the spectral power density function for the resolved waves at St. 4 and 5, and for the swash oscillation. At both stations 4 and 5 the power of the reflected waves begin to increase around 0.1 Hz going toward lower frequencies. The phase function in Fig. 9 experiences a distinct change at around 0.01 Hz. Thus, the partial standing waves become effective around 0.1 Hz. Figure 12 shows the joint distribution of wave height and period for observed, incident and reflected waves at St. 4. The distribution for the observed and resolved incident waves are similar. Reflected long-period waves only affect the wave conditions in the surf zone to a lesser degree.
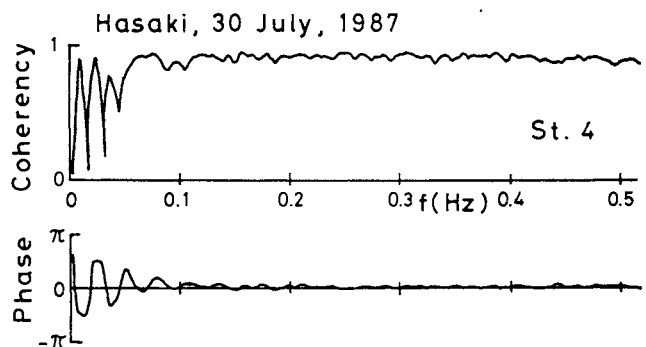
Fig. 9 Cross spectrum between sea surface elevation and on-offshore component of water particle velocity at St. 4.

-287-

Fig. 10 Example of resolved incident and reflected waves.

1987. 7.30
(17:15~18:31)
.... swash
---- St. 5 η_I
—— St. 5 η_R

n= 22800
Δt= 0.2s
Lag =1140

1987.7.30
(17:15~18:31)
.... swash
---- St. 4 η_I
—— St. 4 η_R
n={22800 (swash)
    18950(St.4)
Δt=0.2s
Lag={1140 (swash)
     947 (St.4)

Fig. 11 Power spectral density function of resolved incident and reflected waves.

HASAKI 87, 7.30
St.4
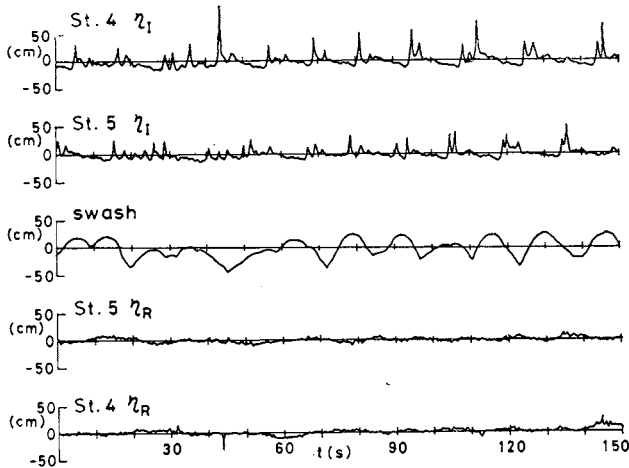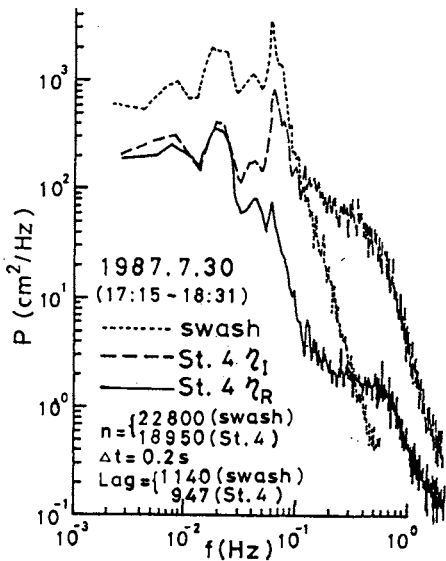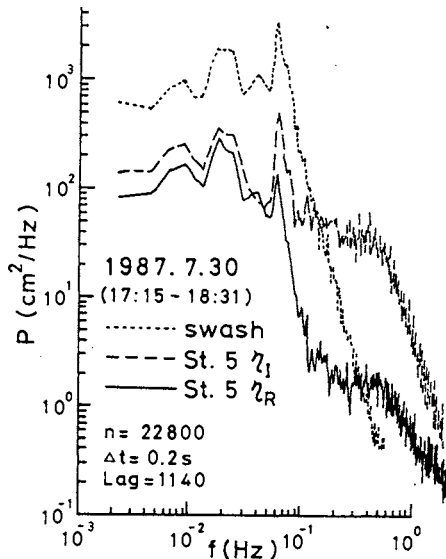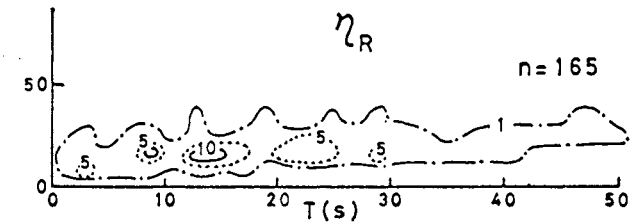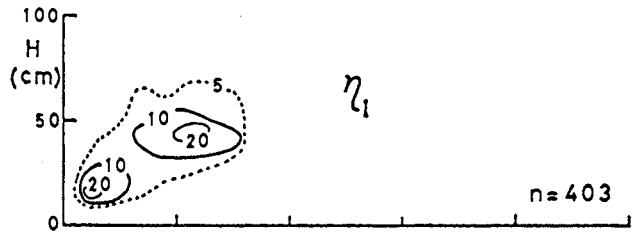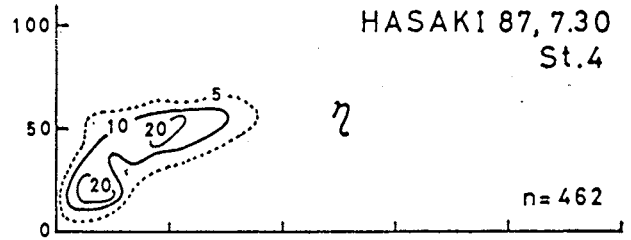
Fig. 12 Joint distribution of wave height and period for observed, and resolved incident and reflected waves.

5. Conclusion

The field observations may be summarized:
1. Waves in the frequency range above 0.1 Hz loose the energy due to breaking and no significant reflection to the offshore takes place.
2. Waves in the frequency range below 0.03 Hz or on-offshore standing waves. These standing wave do not break on the swash slope.
3. Waves in the range between 0.3 Hz and 0.1 Hz may form partially standing waves.
4. No correlation was found between wave height and period in the joint distribution of swash oscillation.

6. Acknowledgements

References

1. Takezawa, M., and Kubota, S., "A field study of swash oscillation on a steep beach face", Pacific Congress on Marine Science and Technology - PACON90, (1990).
2. Guza, R. T., Thornton, E. B., and Holman, R. A., "Swash on steep and shallow beaches", Proc. 19th Coastal Eng. Conf., ASCE, pp. 708-723(1984).
3. Kubota, S., Mizuguchi, M., Hotta, S. and Takezawa, M., "Reflection on natural beaches", Proc. 36th Coastal Eng. Conf., JSCE, pp. 119-123 (1989), (in Japanese).
4. Kubota, S., Takezawa, M. and Mizuguchi, M., "Reflection from swash zone on natural beach", Proc. 23rd Coastal Eng. Conf., ASCE, (1990), (in press).
5. Mizuguchi, M., "Individual wave analysis of irregular wave deformation in the nearshore zone", Proc. 18th Coastal Eng. Conf., ASCE, pp. 485-504(1982).
6. Hotta, S., and Mizuguchi, M., "A field study of waves in the surf zone", Coastal Eng. in Japan, Vol. 23, pp. 59-80(1980).

A FIELD STUDY OF SWASH OSCILLATION ON A STEEP BEACH FACE

Mitsuo Takezawa*, Susumu Kubota* and Nagatomo Nakamura*

* College of Science of Technology, Nihon Univ., Japan

Abstract

In order to record swash oscillation on a beach a measuring system encompassing 16 mm memo-motion cameras, capacitance-type wave gages, and a video camera was developed. Using this system the swash oscillation on a steep beach face was measured. The observed results showed that the swash oscillation is governed by on-offshore standing waves and that the wave characteristics in the surf zone is partly determined by superposition of incident and reflected waves.

1. Introduction

The characteristics of swash oscillation on natural beaches is of great importance in connection with coastal engineering works such as predicting beach deformation, designing coastal structures, and stabilizing the back-shore zone. However, the properties of swash oscillation are not fully understood mainly because accurate measurements are difficult to perform on natural beaches. Attempts to measure has already been made by several investigators, and for their specific purpose the methods employed gave satisfactory results. The authors in the present paper developed a measuring system which combines electrical and visual techniques. Utilizing this system, measurements of swash oscillation were carried out on natural beaches. Valuable results were obtained, and the purpose of this paper is to describe the measuring system and characteristics of swash oscillation on a steep beach as elucidated from measurements obtained with this system. Field observations were carried out during the summer of 1987 and 1988, of which results based on the data obtained in 1987 were reported in the Proceedings of the 21st International Conference on Coastal Engineering ([1], pp. 151-165) Mainly results from the observations in 1988 are described in this paper.

2. Techniques for Measuring Swash Oscillation on Natural Beaches

Techniques for measuring swash oscillation on natural beaches can be divided into two categories with respect to the method employed. One method involves the use of wave gages, resistance-type or capacitance-type (for example, Sawaragi and Iwata[2]), stretched parallel to and above the sand surface at a constant height. The other method is to employ 8 mm or 16 mm movie cameras (for example, Mizuguchi [3]) and/or video cameras (Holman and Guza[4]), photographing the water surface along target markers.

Both methods have their advantages and disadvantages. In general the resistance-type wave gage is superior to the capacitance-type regarding sensitivity. However, the latter has better stability and durability than the former. A common problem associated with electrical wave gages is the need to support the wires at a constant height above the sand surface, since the swash slope is not plane and changes in the sand surface elevation will take place for every swash occurring. Also, the gages require verification or calibration, normally done with visual methods. Eight millimeter movie cameras have been employed from the early stage of research for calibrating electrical methods or for obtaining data directly. Sixteen millimeter movie cameras have also been used due to the superior resolution compared to the 8 mm cameras. The recording time with 8 mm and 16 mm cameras is limited by the film length. Recently, as an alternative to film cameras, Video Cameras have been employed for research purposes. However, the resolution of a video camera is lower than that of a 16 mm camera even though high-quality video cameras are appearing on the commercial market.

3. Measurement Method Employed

The system developed in this study is a combination of the conventional methods, the electrical and visual measuring technique, improving or modifying their respective ability for the specific use. The measuring system consists of capacitance-type wave gages, 16 mm memo-motion cameras, and a high quality video camera which recently became commercially available. The leading edge of the water on the swash slope is detected by a capacitance-type wave gauge which is stretched parallel to and above the sand surface at a constant height by using supporting rods installed at fixed interval (Hereafter this wave gauge is referred to as the run-up meter, CSG in Fig. 2). The water surface is also photographed by the camera system, which utilize 16 mm memo-motion cameras, enabling choice of an arbitrary shutter interval with a minimum time interval of 0.1s, directed at target marker sticks installed along the swash slope. A set of cameras is employed in each photographing direction to be run alternately. By changing film in the cameras not currently used, a continuous synchronized record without time limitation may be obtained. The 16 mm memo-motion camera system was originally developed and employed for studying nearshore waves in the field. Results from these experiments can be found in, for example, Hotta et al. [5] and Ebersole and Hughes [6]. The system was applied to the swash oscillation measurements with some modifications particular to this study. In order to take large and sharp pictures for highly accurate data analysis the 16 mm cameras were used with maximum zoom. It could also be necessary record the wave conditions for wide angles, for which a video camera was prepared. Data from the video camera may be substituted when the 16 mm camera or the run-up meter is malfunctioning, although the accuracy will be less. A large advantage of the system is to ensure the collection of accurate data, also greatly reducing the risk of loosing data if an instrument is not working properly.

4. Field Observations

Field observations were carried out in August 29, 1988, at Oarai beach facing the Pacific Ocean, located about 100 km north of Tokyo. Oarai beach is at the northern end of the Kashima Coast and is bounded by a commercial harbor. Groins were constructed here to protect the harbor from sand entrainment from the south, thus sand accumulates at the south side of the groins. The observation site was located approximately 2.0 km south of
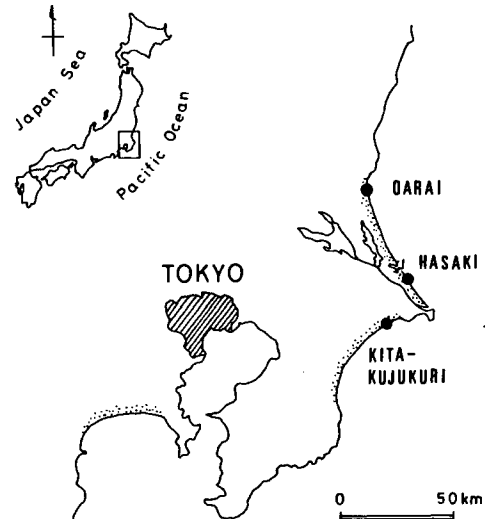
Fig. 1 Location map of experimental site.
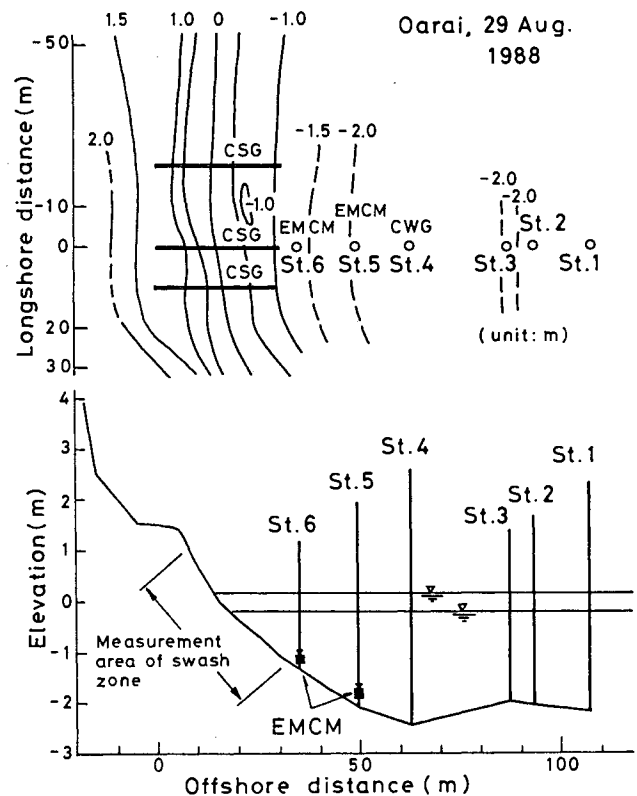
Fig. 2 Beach profile, and arrangement of instrumentation.

the largest groin (Fig. 1). The observation site in 1988 was at the same location as in 1987. However, the beach profile was somewhat different as compared to 1987. The sand in the swash zone was well sorted with a median diameter of 0.45 mm and a sorting coefficient, defined as $S=d_{75}/d_{25}$, where dp is the grain diameter at which p percent of the sand weight is finer, of around 1.25. Figure 2 shows the beach profile and the arrangement of the instrumentation.

In the swash zone, the run-up meter was stretched normal to the shoreline. The wire was held at a constant height of 2 cm above the sand

surface by supporting rods installed at an interval of 2 m.   A plastic scale was pasted to each supporting rod.   In order to keep the wire at a constant height, two men were engaged in adjusting the movable supporting device of the wire to follow the sand surface fluctuations.   The length of the wire was 20 m which covered the entire swash zone during the experiment.   For photographic recording by the 16 mm cameras, an target stick array consisting of 41 iron bars painted yellow was installed parallel to the wave run-up meter and 50 cm beside it.   The interval between target sticks was 50 cm.   Photo 1 shows the stick array and the run-up meter.

Four sets of 16 mm cameras were prepared for the experiment.   Two sets of cameras were placed on a scaffold, elevated at the midpoint of the swash zone approximately 50 m south of the stick array, for photographing the waves from the side.   The other two sets of cameras were placed on a scaffold elevated at the berm crest to photograph target poles installed in the surf zone to record sea surface variations at the poles.   A capacitance-type wave gage with a measuring

range of 4 m in the vertical and a two-component electromagnetic current meter (EMCM) were attached to target poles St. 6 and 5.

During the measurements the sea was rather rough and the average breaking wave height and period determined by visual observation were 130 cm and 7.5 s.   The waves mainly broke as the spilling type.   Because of the rough sea conditions no target pole could be installed outside the break point. Therefore, no data where obtained for the shallow water region were non-breaking conditions prevailed.   The tide was rising and an increase in water level of 36 cm was recorded during the experiment.

The measurements started at 14:00 and ended at 15:41, with a sampling interval of 0.2s.   A total number of 30,400 data points were collected for analysis.   The output from the electrical instruments were recorded on an open-reel type digital data recorder with simultaneous monitoring by a chart recorder.   The tape recorded was directly transformed to a mainframe computer for further analysis.   The leading edge of the water in the swash

Photo 1   Stick array and run-up meter.
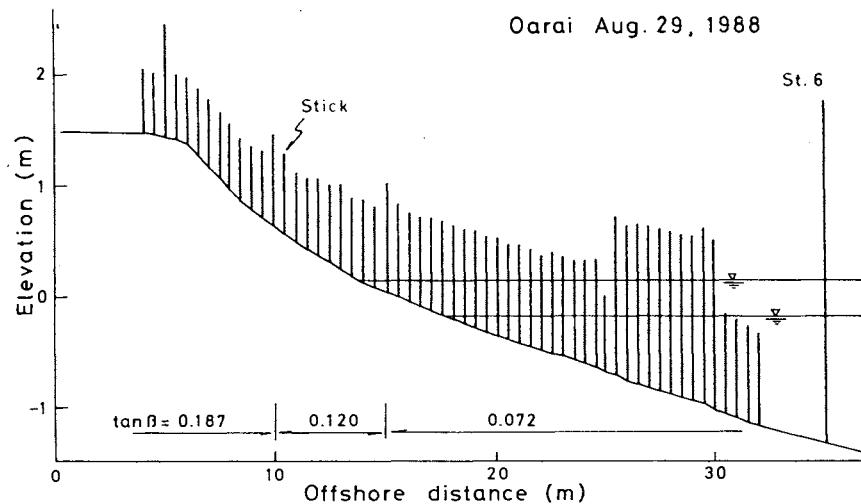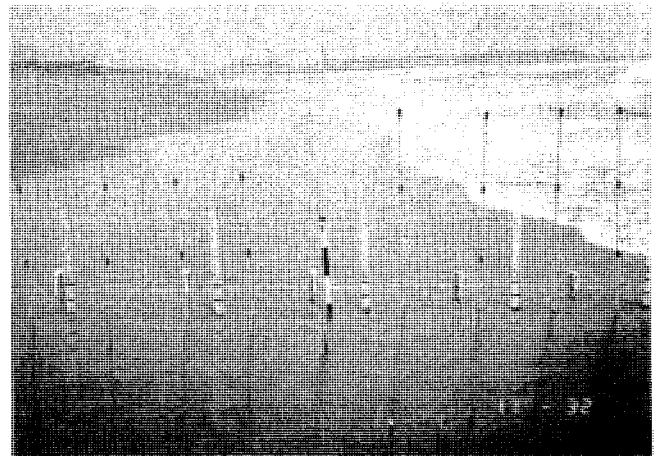
Fig. 3 Assumed compound slope for the swash zone.

zone as recorded on the 16 mm film was read as the horizontal distance from a reference point on the 16 mm film analyzer using an ultrasonic digitizer graph pen system. After digitizing, the data were transferred to a floppy disk on a micro computer. The horizontal distance was transformed to a vertical distance by assuming that the swash zone could be schematized as a compound slope consisting of three straight lines (Fig. 3). The location of the sea surface at the poles, to be used for wave height analysis, was measured as the vertical distance from the top of the poles using the same data processing instruments and procedures as for the swash oscillations.

5. Results and Discussion

5.1 Raw Data

Figure 4 shows a portion of the recorded sea surface variation at Sts. 1, 5, and 6 and at the swash slope. It is possible to follow the passage of primary individual waves [7] from St. 1 to the swash zone. The phase velocity of each primary individual wave between Sts. 1 and 5, and between St. 5 and St. 6 is constant and agrees with the theory for linear long waves in shallow water using the average water depth between two measuring stations[1]. Station 1 located at the shoreward end of the breaker zone recorded waves which were decaying in height after breaking together with waves which did not break at the average break point but instead increased in height due to shoaling. There are a few small waves between the primary individual waves as can be seen at Sts. 5 and 6. Some of these small waves were reflected waves from the shore which could be clearly observed as outgoing waves by viewing the film. Some of the waves were due to disturbances in connection with wave breaking. These waves influenced the distribution of wave height and period in the surf zone as described in the next section. Table 1 gives statistically representative waves of the adjusted data by zero-down crossing method.

Table 1 Statistically representative waves.

Oarai, 29 Aug., 1988

Station number	Depth h (cm)	No of waves	Wave height					Wave period			
			H_{rms} (cm)	H_{mean} (cm)	H_{max} (cm)	$H_{1/10}$ (cm)	$H_{1/3}$ (cm)	T_{mean} (s)	T_{max} (s)	$T_{1/10}$ (s)	$T_{1/3}$ (s)
St. 1	182	668	101	93	186	155	134	6.8	7.0	8.0	7.9
St. 2	185	672	95	88	202	140	123	6.8	9.3	8.1	8.0
St. 3	164	658	94	87	200	141	122	6.9	10.4	8.4	8.0
St. 4	214	710	.73	68	135	105	94	6.4	11.4	8.7	7.9
St. 5	174	818	58	53	137	95	80	5.6	19.4	7.2	7.0
St. 6	122	787	59	53	127	98	81	5.8	8.6	7.6	7.0
Swash	0	379	64	58	146	114	90	12.0	23.3	17.4	16.0

(adjusted data, zero-down crossing method)
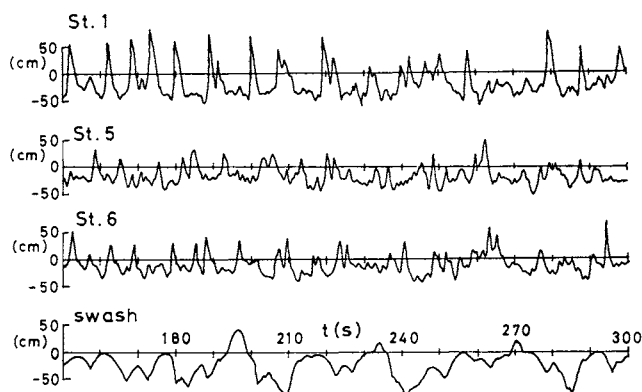
Fig. 4 Time series of raw data.

5.2 Distribution of Wave Height and Period

A wave by wave technique was employed when analyzing the wave data. The distribution of wave height and period are discussed here. The tidal trend was first removed from the original time series of raw data by assuming a parabolic curve. Hereafter the time series with the tidal trend removed will be referred to as the adjusted data. The long-period sea surface fluctuations (long-period waves), not easily recognized in the offshore or nearshore zone, become significant and affect waves near the shore line. The waves of interest are wind waves or swell in the range between 5-20 s. A high-pass filter which cuts off frequencies less than 0.06 Hz was applied to the data when the influence of the long-period waves was not studied. Data processed in this manner are called the filtered data.

Fig. 5 shows the distribution of wave height and period defined by the zero-down crossing method for St. 1, and St. 5, and for the swash oscillation, encompassing both adjusted and filtered data. The distribution for the adjusted data indicates that the peak frequency of the wave height at St. 1 shifted to a lower height at St. 5, implying wave height decay. The number of short-period waves increased at St. 5 as compared to St. 1. For the swash oscillation, both the distribution of wave height and period were skewed to the right side (the peak frequency becomes lower than the average frequency). A remarkable fact is the wide range of the period distribution.

The number of identified waves are different at each measuring station, being largest at St. 5 and smallest for the swash oscillation. These results may be understood by studying the sea surface variation in Fig. 4.

Regarding the distribution, it was not possible to relate the distribution
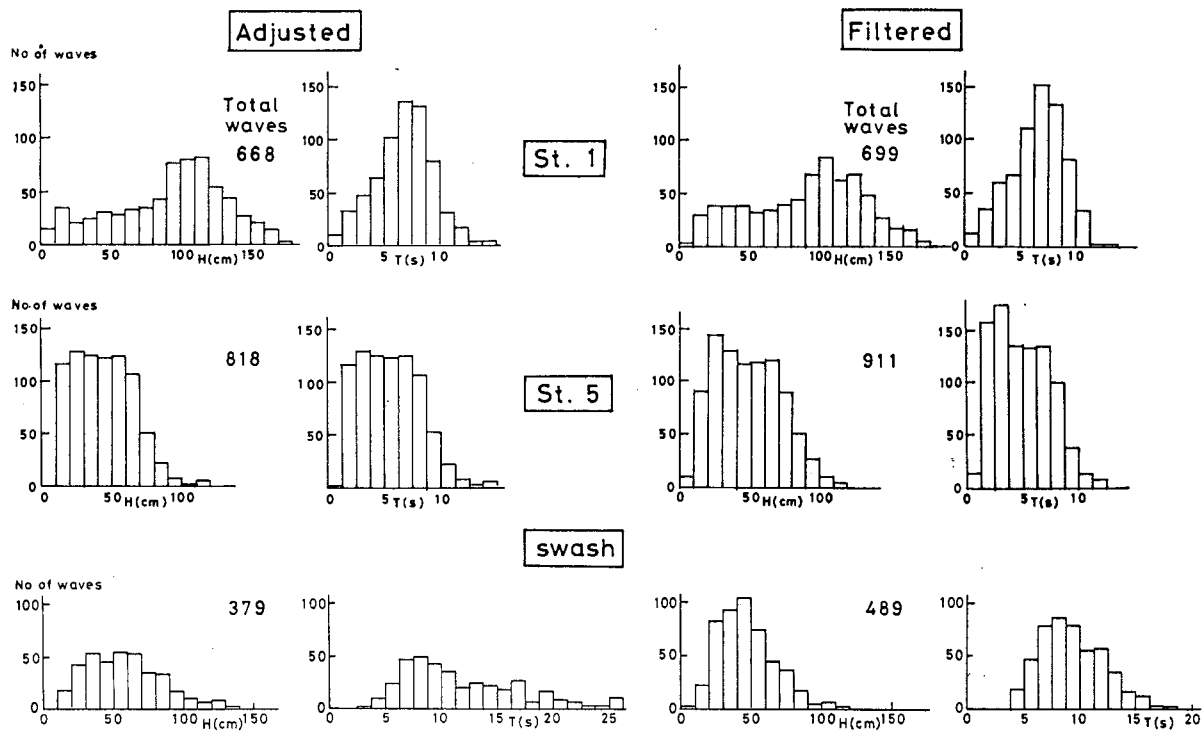
Fig. 5 Distribution of wave height and period.

at a specific measuring station to that at another station because the number of waves forming the distribution was different, even though the primary individual waves could be identified at each station. A more thorough discussion of this problem may be found in Mizuguchi [3, 7].

For the filtered data, the number of identified waves increase at every measuring station compared to the adjusted data. This is explained by the effect of the long-period fluctuations of the sea surface on the individual waves. The removal of the long-period fluctuations of the sea surface results in an increase in the number of waves identified by the zero-downcrossing method. It should be noted that when comparing distributions the effect of long-period fluctuations becomes more conspicuous near the shoreline. The distribution of the waves in the swash for the filtered data becomes a distribution skewed to the right much like a Rayleigh distribution. Results from observations carried out in 1987 [1] showed that the distribution of wave height and period skewed to the left (the peak frequency was higher than the average frequency). This difference could possibly be attributed to the sea conditions but it is not clear at this point. Further examination of the data is needed and this work will be carried out in the near further.

Figure 6 shows the joint distribution of wave height and period at St. 1 and 5, and for the swash oscillation, for which the marginal distributions

were considered in the preceding paragraphs. The distribution at St. 1 located in the breaker zone exhibits two maxima which was characteristic for the breaker zone. In the distribution of the swash oscillation there is a strong correlation in the domain of small wave heights and short wave periods. This distribution also had two maxima.

Figure 7 shows a comparison of the distribution of wave height and period for the filtered data using the zero-up and the zero-downcrossing methods. No significant difference could be found between these methods.

5.3 Spectral Considerations

Figure 8 shows the power spectral density function of the sea surface variation at Sts. 1 and 5, and for the swash oscillation. At Sts. 1 and 5, the main power is in the range from 0.09 Hz to 0.2 Hz (0.09 < f < 0.2 Hz), where f is the frequency. The power at St. 5 is considerably smaller than that at St. 1. This decrease in the power spectral density function is probably due to energy loss in connection with wave breaking in the surf zone. The power of the swash oscillation in the range above 0.15 Hz is considerably smaller than at Sts. 1 and 5, and vice versa in the range below 0.15 Hz. At Sts. 5 and 1, significant minima in the power spectral density function alternately appear in the range below 0.065 Hz. This alternate change in power is not observed for the swash oscillation.
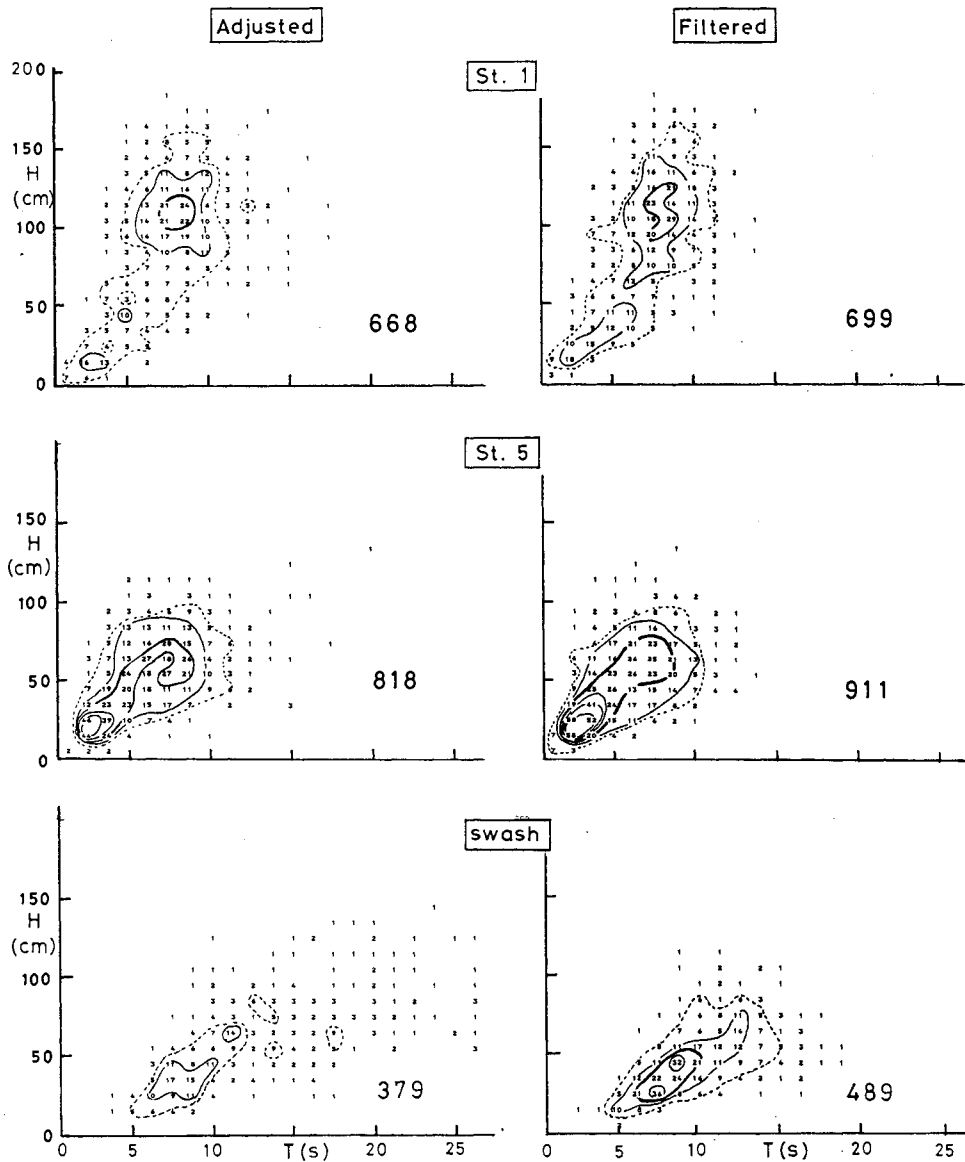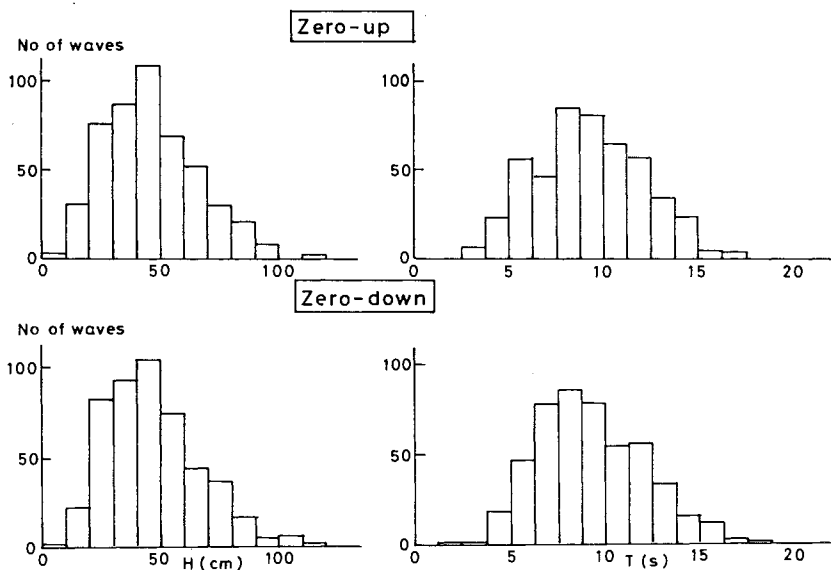
Adjusted

Filtered

St. 1

668

699

St. 5

818

911

swash

379

489

Fig. 6 Joint distribution of wave height and period.

Zero-up

No of waves

No of waves

Zero-down

Fig. 7 Comparison of distribution of wave height and period using the zero-up and zero-down crossing method.

1988.8.29
(14:00～15:16)
······ St.1
--- St.5
── swash

n = 22800
Δt = 0.2 s
Lag = 1140
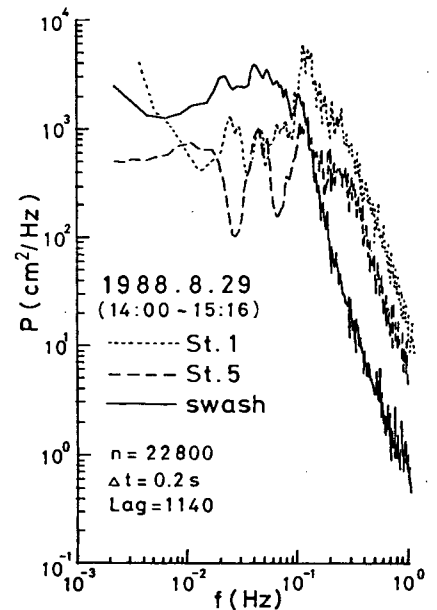
Fig. 8 Power spectral
density function.

This implies that the low frequency waves are on-offshore standing waves, which have an anti-node at the swash slope. Figure 9 shows the cross-spectral function between the sea surface elevation and the on-offshore component of the water particle velocity at St. 5. An abrupt drop in coherence and a
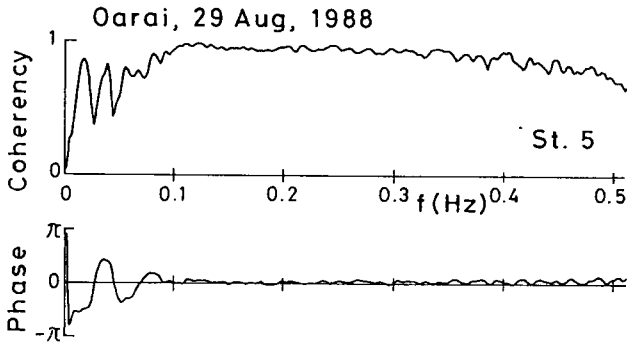
Fig. 9 Cross spectrum between sea surface elevation and on-offshore component of water particle velocity at St. 5.
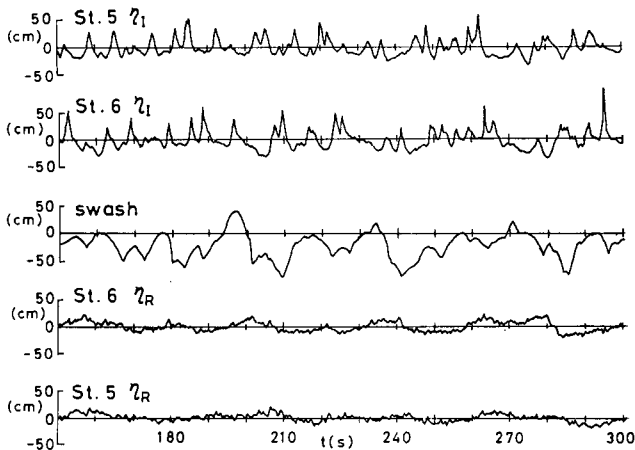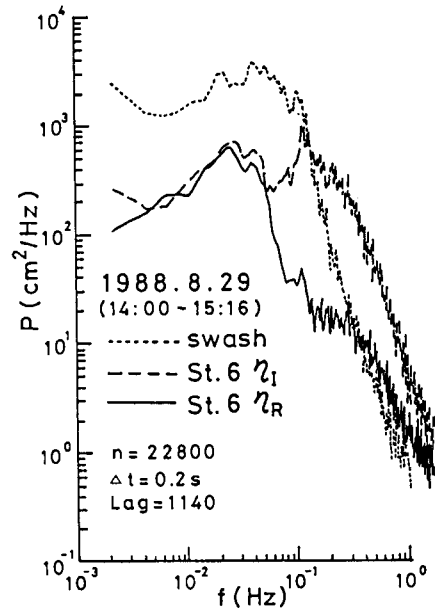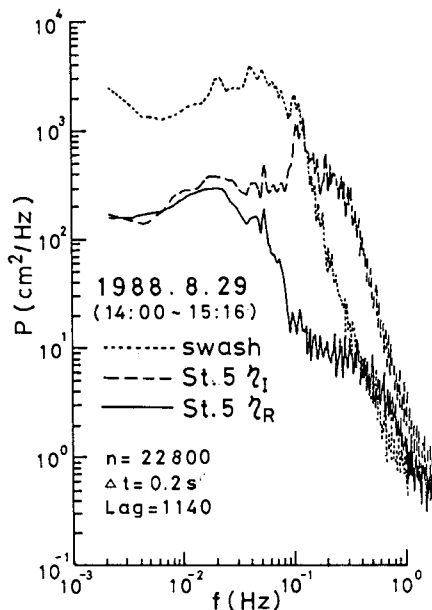
Fig. 10 Example of resolved incident and reflected waves.

sudden change in the phase function at corresponding frequencies are characteristic features of two-dimensional standing waves. The frequency at the fourth zero-crossing counting from the zero in the phase function is around 0.07 Hz and the coherence function is about 0.07 Hz, whereas the coherence function in the region below 0.07 Hz is close to 1.0. In Fig. 8, a pronounced minimum in power at St. 5, and a peak in power at St. 1 occurs around 0.07 Hz. Based on these facts it is inferred that waves below 0.07 Hz form perfect two-dimensional standing waves. The fifth zero-crossing in the phase function is located around 0.09 Hz. The power of the swash oscillation becomes greater than that of St. 5 and St. 1 around 0.09 Hz. Thus, it may be assumed that waves ranging between 0.07 Hz to 0.09 Hz probably form two-dimensional partially standing waves, which implies that waves break on the slope and a part of the incoming energy is lost by breaking but a part of the energy returns to the offshore as reflected waves. Waves with a frequency above 0.07 Hz are expected to break on the slope and dissipate energy.

The next step in the analysis was to separate the incident and reflected waves. Details of the separation method is described in another paper in these proceedings (see Kubota et al.). The separation was done using a method involving quasi-nonlinear long-wave theory. A part of the separated waves is shown in Fig. 10. The dominance of the short-period waves in the incident wave train disappeared in the reflected waves. Figure 11 shows the power spectral density function for the swash oscillation, and for the separated incident and reflected waves at St. 5
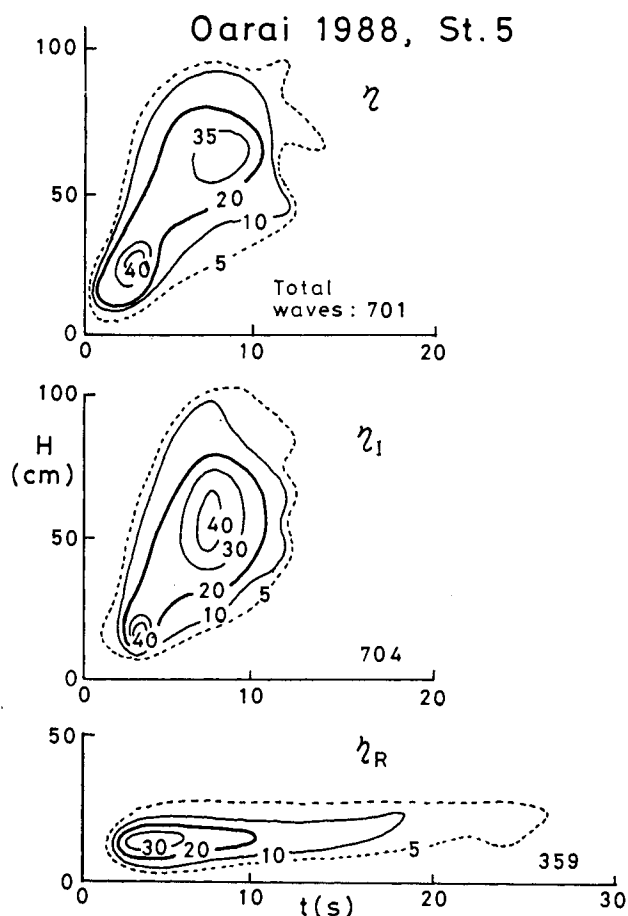
Fig. 11 Power spectral density function of resolved incident and reflected waves.

Fig. 12 Joint distribution of wave height and period for observed, and resolved incident and reflected waves.

and 6. The main power of the incident waves is in the range between 0.1 Hz to 0.2 Hz. These waves are ordinary wind waves coming from the offshore. The power spectral density function of the reflected waves increases in the range between 0.065 Hz to 0.09 Hz with decreasing frequency, and the power of the incident and reflected waves is almost the same. These observations support the former inference that waves lower than 0.065 Hz will form perfect two-dimensional standing waves which does not break on the slope, and the waves ranging between 0.065 Hz and 0.09 Hz will be two-dimensional partially standing waves of which some break on the slope.

Figure 12 shows the joint distribution of wave height and period for the observed, incident, and reflected waves at St. 5. The distribution clearly shows the wave field character-istics as inferred previously. High-frequency waves loose their energy due to breaking and disappear in the re-flected wave field. The middle-range frequency waves partially break on the slope and loose some of their energy, whereas the remaining energy returns to the offshore. Low-frequency waves form on-offshore standing waves without any

breaking on the slope. The long-period waves not identified in the incident wave field emerge in the reflected wave field.

Concluding Remarks

The developed measurement system functioned satisfactorily during the experiments reported in this study. However, during other field experi-ments carried out by the same authors, mechanical problems in connection with the operation of the 16 mm cameras or malfunctioning of the run-up meter oc-curred. Sometimes the capacitance wave gage did not work for considerable time periods because dust in the water ad-hered to the wire and changed the output with elapsed time. Wire wave gages may not work well during rough sea conditions. Under such circum-stances visual methods are highly useful. No successful field observa-tions of swash oscillation under severe storm conditions have been reported yet. The next task is to develop a method enabling observations during severe storm conditions.

Acknowledgements

References

1. Takezawa, M., Mizuguchi, M., Hotta, S., and Kubota, S., "Wave run-up on a natural beach", Proc. 21st Coastal Eng. Conf., ASCE, pp. 151-165 (1988).
2. Sawaragi, T., and Iwata, K., "A non-linear model of irregular wave run-up height and period distributions on gentle slopes", Proc. 19th coastal Eng. Conf., ASCE, pp. 415-434 (1984).
3. Mizuguchi, M., "Swash on a natural beach", Proc. 19th Coastal Eng. Conf., ASCE, pp. 678-694 (1984).
4. Holman, R. A., and Guza, R. T., "Meas-uring run-up on a natural beach", Coastal Engg. Vol. 8, pp. 129-140 (1984).
5. Hotta, S., Mizuguchi, M., and Isobe, M., "Observations of long period waves in the nearshore zone", Coastal Eng. in Japan, Vol. 24, pp. 41-76 (1981).
6. Ebersole, B. A., and Hughes, S. A., "DUCK 85 PHOTOPOLE EXPERIMENT", U. S. Army Corps of Engrs., WES, Miscel-laneous paper, CERC-87-18, 62p, (1987).
7. Mizuguchi, M., "Individual wave analysis of irregular wave deforma-tion in the nearshore zone", Proc. 18th Coastal Eng. Conf., ASCE, pp. 485-504 (1982).

WAVES IN FRONT OF PERMEABLE SLOPING SEA WALLS

Daijiro Nagasawa*, Susumu Kubota*, Shintaro Hotta*, and Mitsuo Takezawa*

* College of Science and Technology, Nihon Univ., Japan

Abstract

The swash oscillation on a sloping sea wall made of step-shaped concrete clocks was measured together with the waves in front of the sea wall. From the obtained data, it was inferred that ordinary wind waves in the period range 5-10 s, which contain the main power of the incoming waves, formed partially on-offshore standing waves, and that the incident waves were reflected at a high rate offshore the sea wall.

1. Introduction

The construction of sloping sea wall consisting of precasted concrete blocks where permeability or roughness is increased have recently become popular in Japan. The main purposes of this type of construction are to reduce the wave run-up height and to prevent local scour occurring at the foot of the sea wall. Furthermore, wave induced beach change in front of the sea wall is reduced by decreasing the rate of reflection. The properties of swash oscillation on the permeable slope of a sea wall are not fully understood, although limited observations from laboratory experiments and field measurements have been reported. In order to obtain a data record long enough in time to determine the statistical quantities of waves on a sea wall and to predict the rate of reflection from a sea wall, a field study was carried out on a sloping sea wall constructed of step-shaped concrete blocks. During the field experiment and in the processing of the data some problems were encountered. A 16 mm camera experienced mechanical problems and a portion of the data record could not be used, even though data from a video camera could be substituted into the interrupted record. The output voltage of the run-up meter got lower with time elapsed caused by the adhering of dust in the sea to the capacitance wire.

During the data processing, malfunctioning of a film digitizer occurred and some roles of film will to be digitized again. At present, the films have not been completely digitized and further analysis will be carried out for that portion of the data. Thus, since limited amount of data are available for analysis at this point, the results in this report should be considered preliminary. Results from the complete analysis will be reported in the near future.

2. Field Observation

The field study was carried out on may 6, 1989, at Nakayari beach facing to the Pacific Ocean, located at the norther end of the Kujuukuri Coast at a distance of about 80 km from the Tokyo (see, Fig. 1). At this beach the sloping sea wall was continuously constructed using different kinds of concrete blocks in a section of several hundred meters along shore.

The portion of sloping sea wall investigated in this study was constructed by a step-shaped concrete
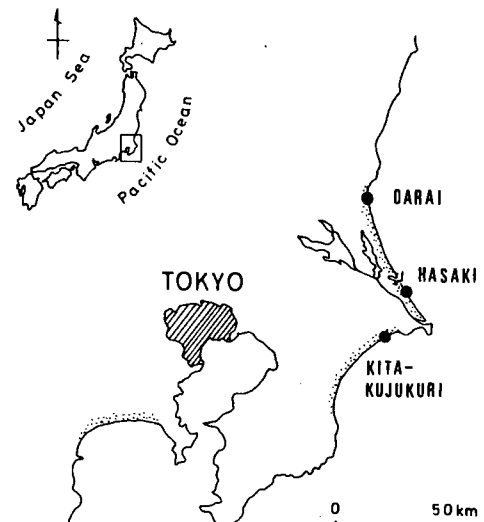
Fig. 1 Location map of experimental site.

block called "Cross Akmon Float Type" as shown in photo 1. The slope of the sea wall was 1/3. A target maker stick array for photographing the wave run-up was prepared on the slope normal to the sea wall. The interval between the sticks was not constant since the sticks were installed in the gaps of the concrete blocks. The horizontal distance between the sticks varied between 1 and 1.5 m. Along the seaward extension of the stick array, six poles were installed to be used for wave measurements. A capacitance-type were gage (run-up meter) was also stretched along the stick array. Figure 2 illustrates the beach profile, plan, and the arrangement of instrumentation. At Sts. 3 and 4, an electromagnetic current meter and a capacitance-type wave gage were also attached. Figure 3 shows and enlargement of the sea wall slope and the stick array. There sets of 16 mm memo-motion cameras were employed in the experiment. Two sets were prepared on the top of the sea wall to photograph the poles located in
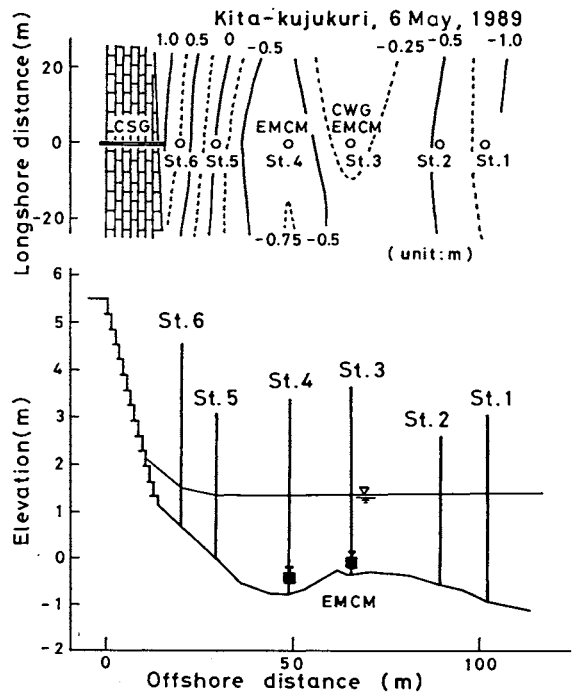
Fig. 2 Beach profile, and arrangement of instrumentation.
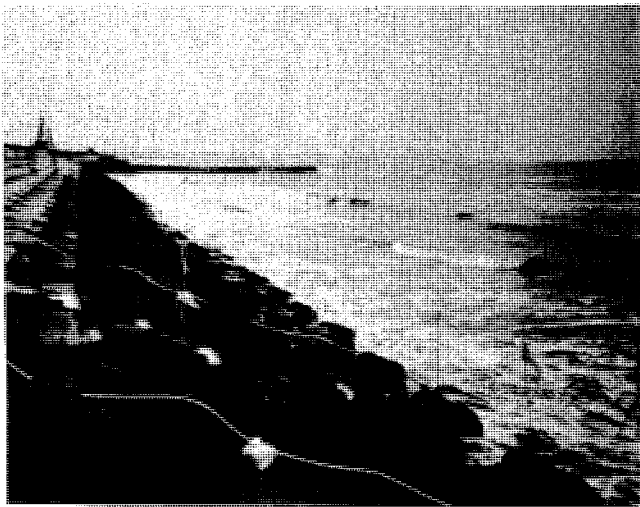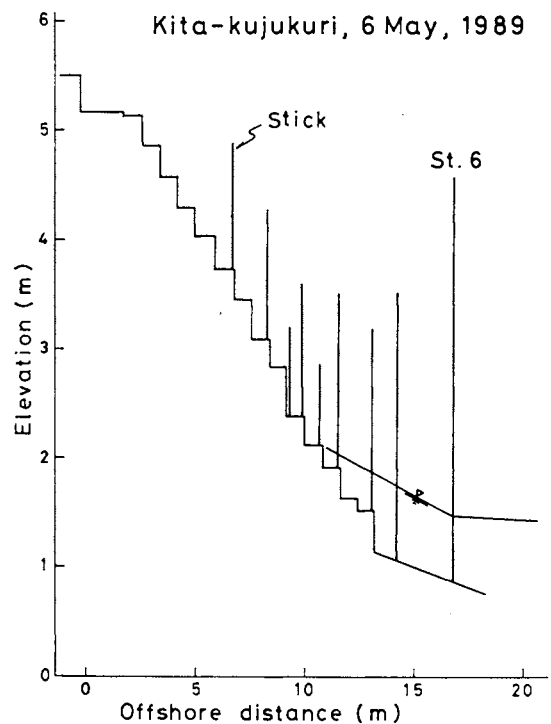
Fig. 3 Assumed compound slope for the swash zone.

the sea, providing information of the wave conditions seaward of the sea wall. A scaffold was elevated at the midpoint of the slope approximately 30 m south of the stick array to photograph the waves on the slope from the side. Swash oscillation of the water surface along to the stick array were recorded by a pair of 16 mm film cameras placed on the scaffold at a shooting interval of 0.2 s.

Photo 1 Stick array and run-up meter.

The data recording system and the procedures used in the data processing are described in Takezawa and Kubota [1] included in these Proceedings. The data collection started at 16:40 and ended at 17:40, giving an experimental duration of 50 min. The measurements were performed immediately before and after high tide and no appreciable change in tide level was observed. The average breaker line was located between Sts. 2 and 3. The breaker-type was plunging and incident wave direction was almost normal to the shoreline.

3.1 Raw Data

Figure 4(a) shows a comparison of the swash oscillation data obtained by the 16 mm cameras and the run-up meter. The broken line gives the oscillation as recorded by the 16 mm cameras and in this case the time series of the swash had a step-type character corresponding to the slope of the sea wall. The recorded profiles are approximately the same using the cameras or the run-up meter However, there is a tendency that the profile crests recorded by the 16 mm cameras are higher than those recorded by the run-up meter, whereas the troughs given by the 16 mm cameras are lower than those given by the run-up meter. At the present stage, analysis have not been completed to provide information on how to deal with the step-shaped wave profiles, and which data should be used for determining the wave characteristics. For sake of convenience, the swash oscillation data obtained by the run-up meter will be employed in the present analysis. Detailed discussion pertaining to the both data sets and associated results are deferred to future work.

Figure 4(b) displays a portion of the sea surface elevation recorded at Sts. 2, 3 and 4, and for the swash oscillation. The passage of the wave crests for primary individual waves [2] may easily be followed from St. 2 to the swash on the slope. At St. 3 and St 4, many small waves can be identified between the primary waves. Those waves were generated in connecting with the wave breaking and reflection from the sea wall slope. In front of the sea wall it was often observed that reflected waves encountered incoming waves, being combined into one wave which rapidly increased in height, and broke almost instantaneously, resulting in large disturbances of the water surface.

Table 1 gives statistically representative waves of the adjusted data by zero-down crossing method.
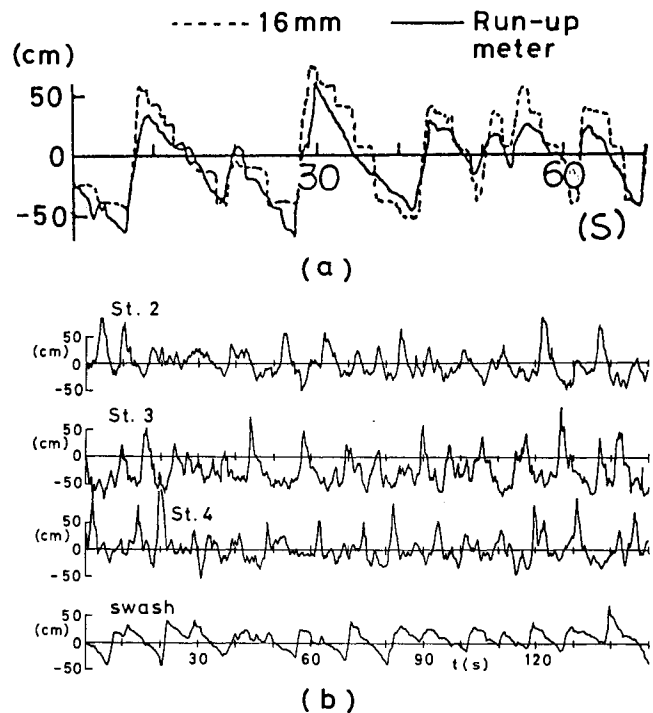
Fig. 4 Time series of raw data.

Table 1 Statistically representative waves.

Kita-kujukuri, 6 May, 1989

Station number	Depth h (cm)	No of waves	Wave height					Wave period			
			H_{rms} (cm)	H_{mean} (cm)	H_{max} (cm)	$H_{1/10}$ (cm)	$H_{1/3}$ (cm)	T_{mean} (s)	T_{max} (s)	$T_{1/10}$ (s)	$T_{1/3}$ (s)
St. 2	191	483	69	61	169	126	98	6.3	9.3	9.1	8.6
St. 3	178	505	53	46	130	94	76	6.0	8.7	8.9	7.9
St. 4	214	541	63	56	172	116	91	5.6	4.8	8.3	7.6
St. 5	141	589	61	55	133	107	87	5.1	5.5	8.4	7.4
St. 6	74	617	62	56	162	106	86	4.9	6.4	7.0	6.1
Swash	0	363	81	75	163	127	109	8.3	3.2	12.6	11.4

(adjusted data, zero-down crossing method)

3.2 Distribution of Wave Height and Period

Figure 5 shows the distribution of wave height and period defined by using the zero-down crossing method. The number of waves identified for the adjusted data at St. 3 is large. The reason for this may be the interaction between outgoing and incoming waves as described before. The number of waves defined at St. 2 for the adjusted and the filtered data is almost the same. Station 2 was located at a position where waves increased in height due to shoaling and the small waves induced by wave breaking did not appear between the primary waves, even though large waves sometimes broke. The wave height of the standing waves rapidly decreased with distance offshore [3]. Station 2 was located at a considerable distance from the sea wall and therefore it is inferred that the long period waves, which formed the standing waves, only influenced the wave field at St. 2 to a lesser degree.
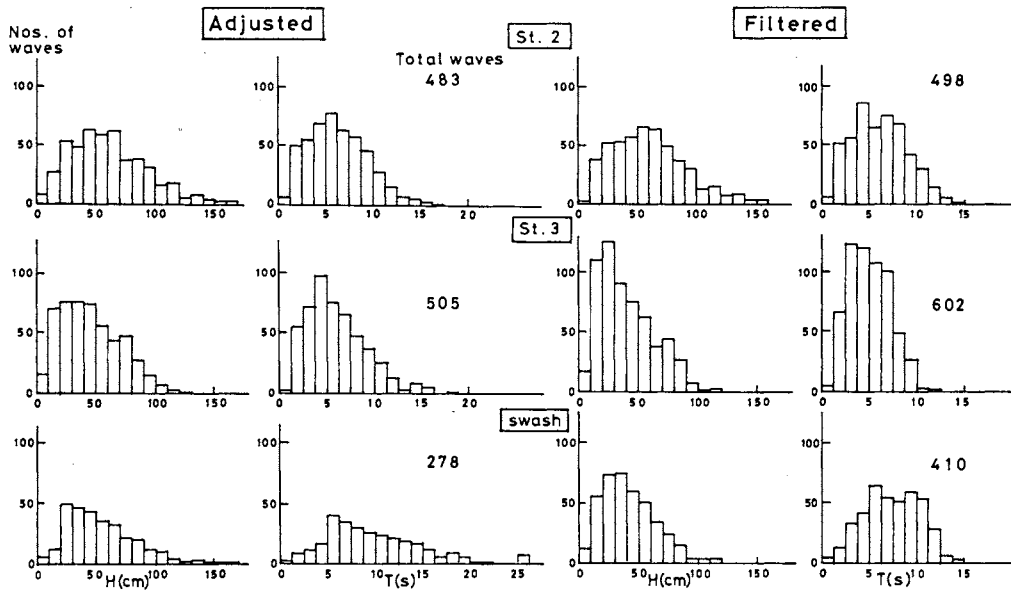
Fig. 5 Distribution of wave height and period.

Figure 6 shows the joint distribution of wave height and period at Sts. 2 and 3, and for the swash oscillation. At St. 3, there is a strong correlation between wave height and period in the region of small of wave heights and periods. However, the correlation between wave height and period is weak for the swash oscillation.

Figure 7 illustrates the differences obtained in the identified wave height and period when using the zero-down crossing method. It is not possible to find any significant differences.

3.3 Spectral Consideration

Figure 8 shows the power spectral density function of the sea surface elevation at St. 2, St. 3, and the swash oscillation. The power at St. 2 and St. 3 is almost of the same order at a frequency around 0.07 Hz. The power at St. 3 is smaller than that at St. 2 in the range from 0.07 Hz to 0.3 Hz. This probably due to energy loss mainly generated by wave breaking as the waves propagate from St. 2 to St.3. Figure 9 shows the cross spectral density function between the sea surface elevation and the on-offshore component of the water particle velocity at St.3. In Fig. 9, a remarkable difference is noted as compared to what is observed on natural beaches, for example at Oarai Beach[1] and Hazaki Beach[4], reported in other papers in these Proceedings. Changes in the sign of the phase function and corresponding depression minima in the coherence function often appeared in the frequency range below 0.16 Hz. This implies that waves had a frequency of 0.16 Hz form on-offshore standing waves. Abrupt changes in the phase function
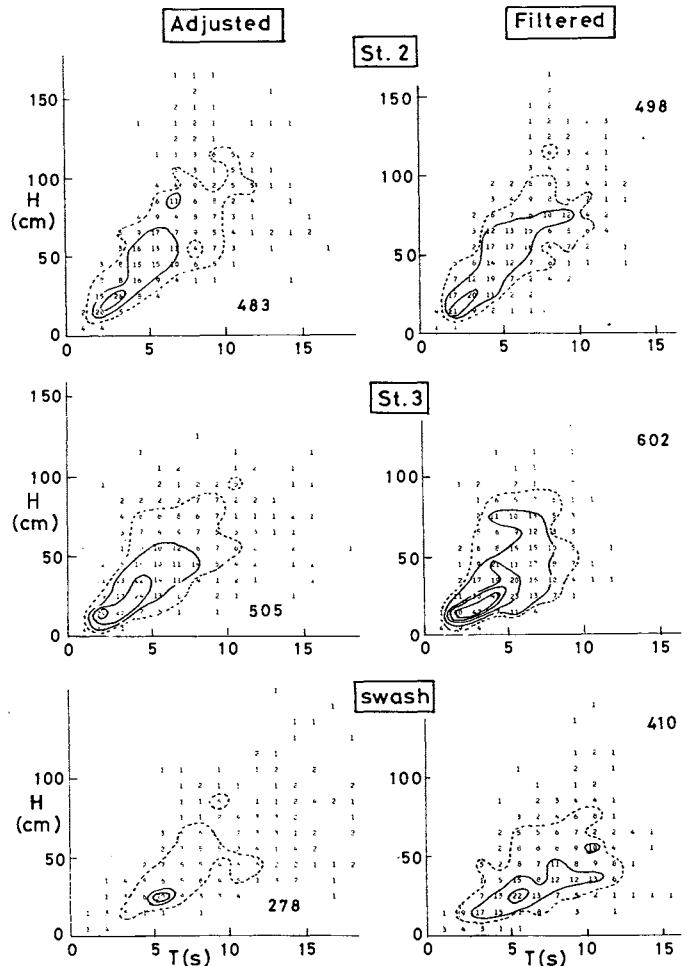
Fig. 6 Joint distribution of wave height and period.

and pronounced minima in the coherence may be found in the frequency range below 0.07 Hz. The change in phase and the corresponding minimum in the coherence are in the range 0.07 Hz to 0.16 Hz, even though the minimum in the coherence function is small.
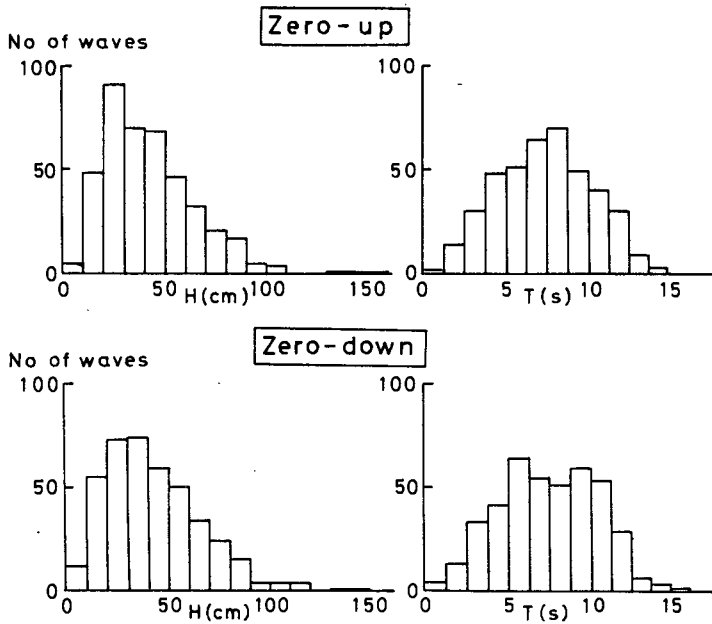
Fig. 7 Comparison of distribution of wave height and
period using the zero-up and zero-down
crossing method.
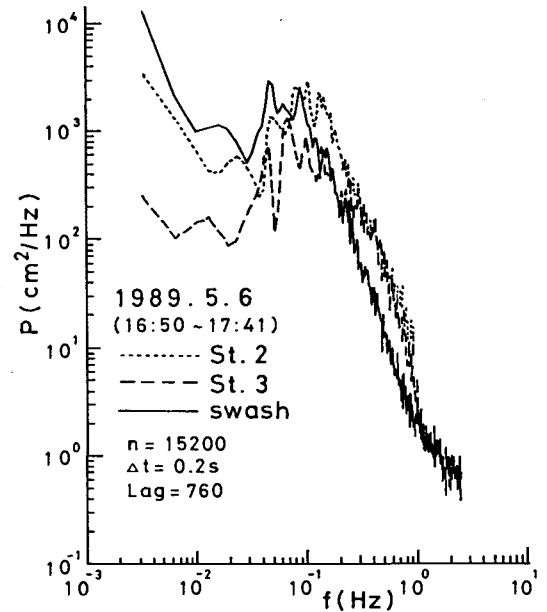
Fig. 8 Power spectral
density function.

Figure 10 displays a portion of the resolved incident and reflected waves by using the method of quasi-nonlinear long standing theory [4, 5]. Incoming and outgoing primary waves may easily be identified. Figure 11 shows the power spectral density function of incident and reflected waves at St. 3 and St. 4, and the swash oscillation. The power of the incident and reflected waves becomes roughly the some at 0.07 Hz. The power of the reflected waves decreases in the frequency range from 0.07 Hz to 0.7 Hz. However, the rate of reduction is smaller than that on natural beaches. This fact means that incident waves in the range from 0.07 Hz to 0.7 Hz were highly reflected. Further more, it is difficult to find a frequency where the power of the re-flected waves begin to increase, indi-cating that partially standing waves are forming.

From the above considerations, it is inferred that waves below 0.07 Hz from on-offshore standing waves, and waves in the range from 0.07 Hz to 0.16 Hz form partially standing waves expe-riencing breaking, but with a high rate of energy returning to the offshore.

Figure 12 shows the joint distri-bution of wave height and period for observed, incident, and reflected waves at St. 3. The distribution of the incident waves has two maxima as may be found in the breaker zone on natural beaches. The distribution of the reflected waves shows that waves in the period range of 5 to 15 s, which were ordinary wind waves, were reflected to the offshore with a rather high waves height.
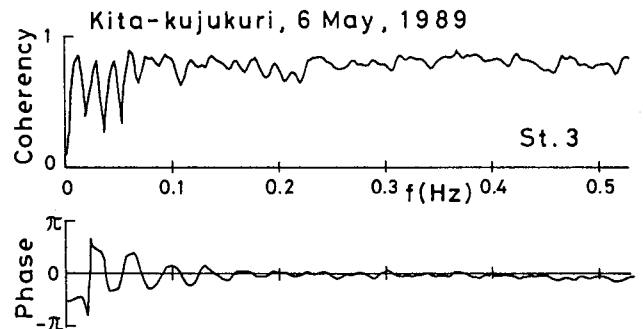
Fig. 9 Cross spectrum between sea surface
elevation and on-offshore component
of water particle velocity at St. 3.
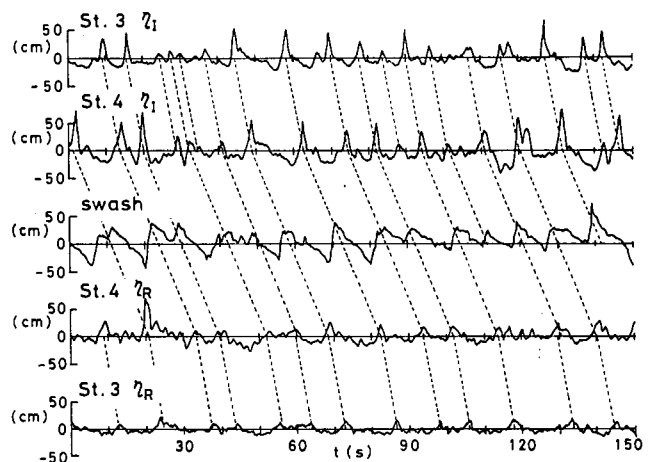
Fig. 10 Example of resolved incident and
reflected waves.

3.4 Rate of Reflection

The rate of reflection may be determined as the ration between the
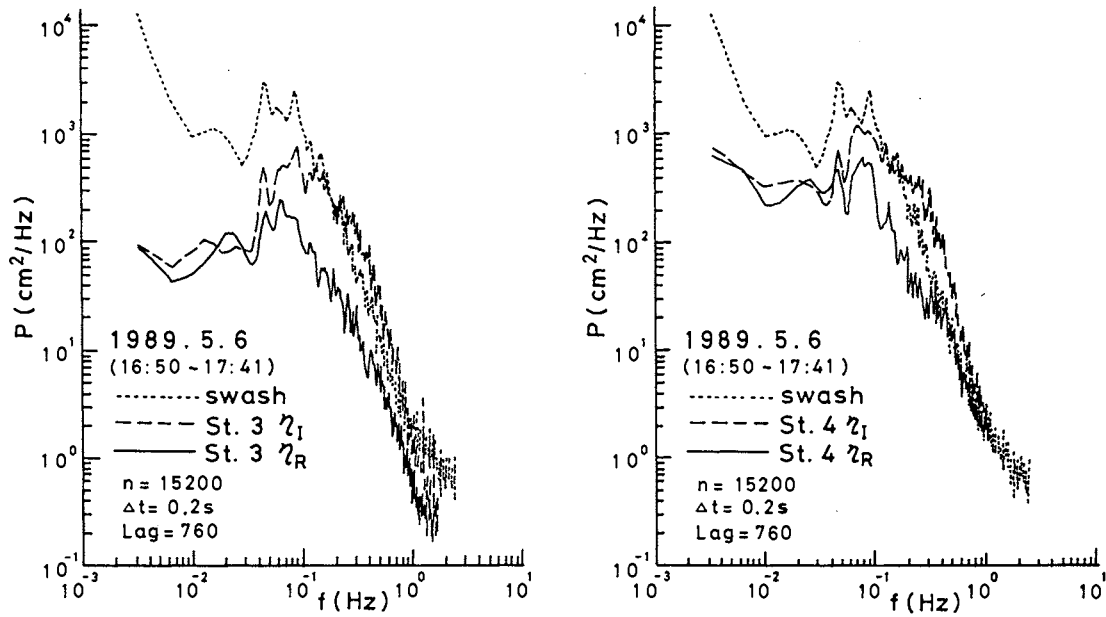
Fig. 11 Power spectral density function of resolved incident and reflected waves.

reflected and incident wave heights (defined as the reflection coefficient) for the primary waves. However, incident wave usually experienced wave height deformation by shoaling, braking, and dissipation in the surf zone. These phenomena are not taken into the present consideration when separating incoming and outgoing waves. The reflection coefficient of primary waves obtained by Kubota et al. [6] for a steep natural beach face provided unexpectedly high values. They suggested that further examination regarding an appropriate definition of the reflection coefficient was needed. The results from the reflection coefficient calculations will be presented after data have been analyzed in detail.

The ratio of the square root of the mean sea surface variation of the reflected and incident waves, which implies, an average reflection coefficient, were 0.48 at St. 3 and 0.59 at St. 4. These values approximately agrees with those obtained by TakeKzawa et al. [6] on a steep swash slope, but are somewhat larger than what have been obtained in laboratory experiment.

4. Concluding Remarks

The measuring system which was successfully employed on natural beaches experienced some difficulties when used on the concrete block slope of a sea wall. One problem was adhesion of dust to the capacitance wire, resulting in a lowering of the output voltage. The wire had to be occasionally cleaned up and careful verification of the data had to be perform. The moving sand which is transported up and down in the swash probably cleans up the
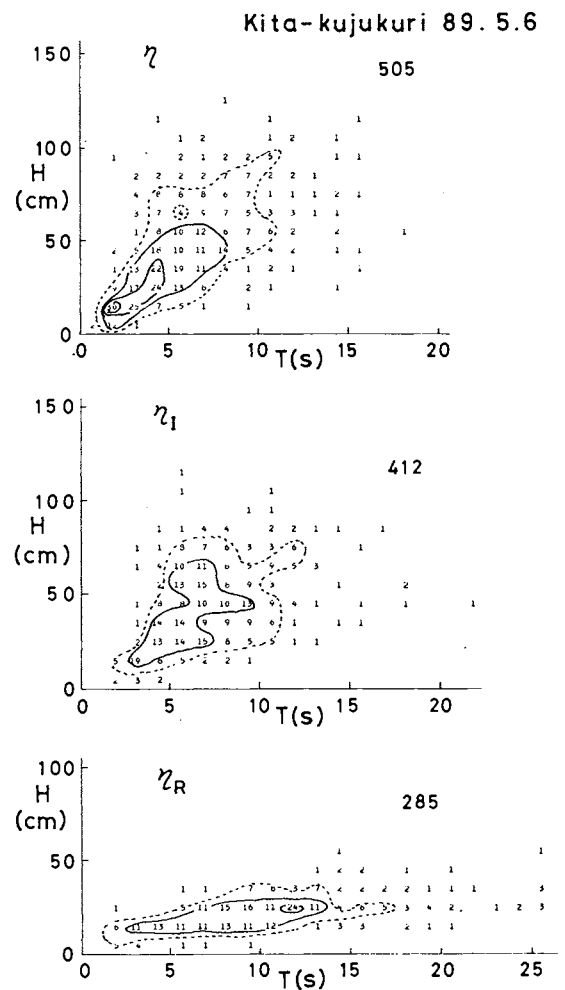
Fig. 12 Joint distribution of wave height and period for observed, and resolved incident and reflected waves.

dust adhered to the wire on the sandy
swash slope. The sea wall slope stud-
ied had an irregular configuration in
both the offshore and longshore direc-
tion. When digitizing the 16 mm film,
deciding the location of the water's
edge during down swash was especially
difficult. In future field studies of
swash oscillation on artificial con-
crete clock sea wall slopes, further
improvement of the measuring system
will be made to allow more detailed
analysis than what was carried out for
the present data.

5. Acknowledgements

References

1. Takezawa, M., and Kubota, S., "A field
   study of swash oscillation on a
   steep beach face", Pacific Congress
   on Marine Science and Technology -
   PACON90, (1990).
2. Mizuguchi, M., "Individual wave
   analysis of irregular wave deforma-
   tion in the nearshore zone", Proc.
   18th Coastal Eng. Conf., ASCE,
   pp. 485-504(1982).
3. Hotta, S., Mizuguchi, M., and Isobe,
   M., "Observations of long period
   waves in the nearshore zone",
   Coastal Eng. in Japan, Vol. 24,
   pp. 41-76(1981).
4. Kubota, S., Mizuguchi, M., Takezawa, M.
   "A field study of swash oscillation
   on a gentle beach face", Pacific
   Congress on Marine Science and
   Technology - PACON90, (1990).
5. Kubota, S., Mizuguchi, M., Hotta, S.
   and Takezawa, M., "Reflection on
   natural beaches", Proc. 36th Coastal
   Eng. Conf., JSCE, pp. 119-123
   (1989), (in Japanese).
6. Takezawa, M., Mizuguchi, M., Hotta,
   S., and Kubota, S., "Wave run-up on
   a natural beach", Proc. 21st Coastal
   Eng. Conf., ASCE, pp. 151-165(1988).

INSTANTANEOUS ELECTROMAGNETIC MEAN SEA LEVEL ······ IEMSEL

Qiu Xing Ya, Shen Yi Shin

Tongji University, China

Abstract

Although the work frequency of Radar altimeter is microwave·band, but owing to the atmosphere refraction, the beam brings deviation, so, the measured distance is not the vertical distance, and the beam illuminated point drifts off the sub-astral point, therefore, the measured wave-high is not accurate, In order to improve the measureing accruacy, there are several error correction formulas and the position revision method of illuminated point are presented in this artical.

It is valuable of the beam refraction correction and illuminated point deviation revision of the Radar altimeter to the ocea platform engineer, tide prediction, marine survey and military.

Introduction

An elevation survey in geoscience Which was presented for the first time in 1966, is now being realized, in fact, the satellite altimetry is an reverse levelling method, the accuracy can be in centimetre order if this method is used to measure the hight of the seawave.

In the general method of the elevation survey, the altitude is ueasured upward from the geoid (geodetic datum), but in the satellite altimetry, the reference datum is the stable platform in orbit of known altitude, and the measurement, is from that platform vertically downward.

The measurement of this vertical distance is carried out by the Nadir pointed Radar on that stable platform, and the platform is assumed to be the reference system of motion, the antenna axis (actually the electrical axis) of Radar is always pointing to the Nadir celestial sphere.

The Radar wouks at UIIF, and transmission pulse, in which the pulse Width is 10, 100 ns 250 rpps toward the earth (or sea surface). In the measurement of the sea surface, vertical distance measured by tht Radar altimeter is the "Instantaneous vertical distance" . The difference between the rms of the measured vertical distance of the whole sea area and the altitude of the satellite is defined to be, "Instantaneous Electromagnetic Mean Sea Level" . evidenty, the Instantaneous Electromagnetic Mean sea level· (IEMSL) is related to the mean sea level and the geodetic datum, the relation is as following,

$$h_g = h_s - h_a - \Delta h \quad \cdots\cdots\cdots\cdots \quad (1)$$

in which

h_g ─── altitude from the geodetic datum;

h_s ─── distance from the satellite to the mass center of the earth;

h_a ─── altitude of the satellite from the ellipsoid;

Δh─── dynamic effect due to sea.

The mcthematic and phyic meaning of above formula is abvious due to the

epual gravitation force, the sea
surface has a particular characteris
to maintain in epuillibrium state, so
the result of the measurement offered
by the geodetic levelling, this relation
is represented straightforward in the
following figure 1.
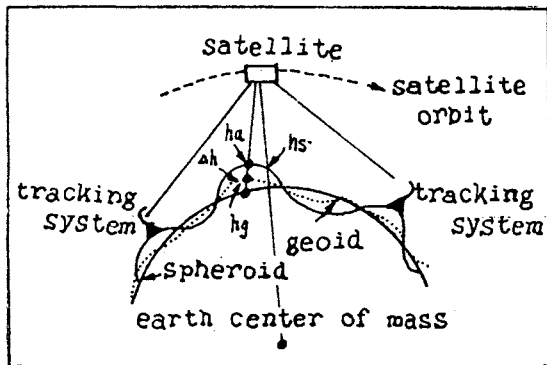
figure 1   determine geoid

From the IEMSL which is obtained
from the measurements of sea dynamic,
through data processing and correction,
we can obtain the mean sea level
indirectly, is more realistic than the
mean sea level obtained from the tide
observation, and is more actual.

Of course, the main contribute of
the satellite altimetry is not noly
limited this point, it spread over the
research to a series of all the physical
phenomenon of the sea, such as ocean
current, ocean geology, we can get more
accurate data from the satellite
altimety in these area.

But, in this apaer, we only deal
with the accurate calculation of the
"IEMSL" and the actual measurement
point position.

■ Determination of the IEMSL

● Vertical distance & it's accuracy:
The classical formula of pulse
ranging method is

$$D = 1/2 \cdot c \cdot \Delta t \qquad (2)$$

in which
D ——— distance obtained from the
Radar beam ranging (arc

distance) noted as. $\hat{D}$.
C ——— transmission velocity of the
electromagnetic wave in space
(C_0/η, C_0: light velocity in
the vacuum, η: refractive
index of the atmosphere);
Δt ———— time delay between the
received of return wave and the
transmitted pulse.
for improvement the accuracy of the
ranging, it is adapted generally that in
every ranging time element , more
measurement is to be taken, and them
get the average the result, i.e.

$$\hat{D} = (\hat{D}_1 + \hat{D}_2 + \text{———} + \hat{D}_n)/n \qquad (3)$$

in the equation
n ——— an integel greater than 1 (i.
e. n>1).
From equation (2), the accuracy in
every ranging $\hat{D}_1 \sim \hat{D}_n$ is related to
measurement of Δt, that is the accuracy
of Δt determine the accuracy of the
IEMSL, the input data of the Radar
altimeter, except the original data of
the target, is the time (i. e. the delay),
which is consist of three parts. The
first part is $\Delta_1 t$, it is defined as the
time difference between the trigger time
from the transmitter to the antenna,
it's value is:

$$\Delta_1 t = 6 \cdot 980 \cdot 10^{-6} \cdot 2 \cdot h_a/c \qquad (4)$$

in which
ha ——— height of the satellite;
c ——— electromagnetic wave speed.
The second part $\Delta_2 t$ is the time
delay induced by the execution time of
the software in the altitude tracer,
it's value is

$$\Delta_2 t = 73.5 \text{ ms} \qquad (5)$$

The third part $\Delta_3 t$ is propagation
delay of the electromagnetic wave, it
equal to the one way transition time i.
e.

$$\Delta_3 t = h_a/c \qquad (6)$$

All the above time delay is to
increase the measured time, so , the

total correct calculation of the time mark should be:

$$\Delta t = \Delta_1 t - \Delta_2 t - \Delta_3 t$$

$$= - (6 \cdot 980 \cdot 10^{-6} - 2 \cdot h_a / c$$

$$- 73.5 \cdot 10^{-3} - h_a / c$$

$$= h_a / c - 79.38 \cdot 10^{-3}$$

$$\cdots\cdots\cdots\cdots (7)$$

From Eq. (4). (6). (7), the time delay Δt is related to h_a, then, the revising of h_a can be obtained from the revising of Δt, vice versa. .

● The calculation of the revising value of the ranging due to the instable of electromagnetic wave proapgation velocity.

It is proved in experiment that the speed of the electromagnetic wave is related to the transimission medium and it's density. To say it move correctly, the pulse energy of the altime ter after it transverse the outer space will passing through the ionosphere, troposphere and stretosphere, the speed in passing there are not equals each other, and then the Δt will be varies due to the value c is not a constant!

Differentiate eq. (2) which respect to c, and keep the other value in the right of the equation to be unvaried and after conversing the value to the resultant increment, we get:

$$\Delta h_{ac} = h_a \cdot \Delta c / c \quad\cdots\cdots\cdots\cdots (8)$$

On the other hand, the propagation velocity of the radio wave in the atmosphere is related to refraction index of atmosphere, that is $c = c_0 / \eta$ and $\eta = \sqrt{\varepsilon}$. The recent value of c is $c_0 = 299,79245 \pm 1.2$ m/s (η: atmospnere refraction index, ε = aielectric constant of atmosphere), under the condition, $\eta_0 = 1.0003245$. differentiate above equation with respect to η and after changing it into the ultimate increament, we can obtain

$$\Delta c = c_0 / \eta^2 \cdot \Delta \eta \quad\cdots\cdots\cdots\cdots (9)$$

substitute the Δc in this equation and

the c in the prior to eq. (8), we get

$$\Delta h_{ac} = -h_a \cdot \Delta \eta / \eta \cdots\cdots\cdots\cdots (10)$$

If the unit of Δh_{ac} is meter, h_a is in kilometer, and consider that $\eta = 1$, then the baove eqation can be simplified to the following form, that is

$$\Delta h_{ac} = - \Delta \eta \cdot h_0 \cdot 10^{-3} \quad Km$$

$$\cdots\cdots\cdots\cdots (11)$$

in the Radar measurement, the $\Delta \eta$ in above equation, can be obtained as the difference value from the refraction index of each atmosphere layer as (see figure 2)

$$\Delta \eta = (\Delta \eta_0 - (\Delta \eta_1 + \Delta \eta_1) / 2)$$

$$+ (\Delta \eta_0 - (\Delta \eta_2 + \Delta \eta_3) / 2)$$

$$+ (\Delta \eta_0 - (\Delta \eta_3 + \Delta \eta_4) / 2)$$

$$+ \cdots\cdots, \quad\cdots\cdots\cdots\cdots (12)$$

atmosphericl layer
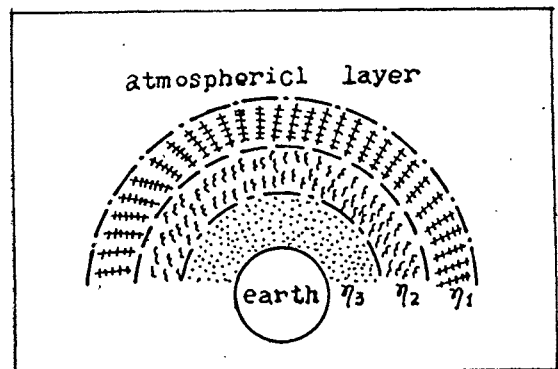
figure 2

and the $\eta_1, \eta_2, \eta_3, \cdots$ can be obtained from the data in the meteorological observation, and the $\Delta \eta_1, \Delta \eta_2, \cdots$ can be calculation from the forulas presented by p.m. Г oucheha in 1950, that is

$$\Delta \eta_1 = P_1 / T_1 \cdot (105.5 + K_1 / P_1$$

$$\cdot (5709 / T_1 - 14.5))$$

$$\Delta \eta_2 = P_2 / T_2 \cdot (105.5 + K_2 / P_2$$

$$\cdot (5709 / T_2 - 14.5))$$

$$\begin{aligned}&\cdots\cdots\cdots\cdots\cdots\cdots\cdots\cdots\cdots\cdots\cdots\cdots\cdots\cdots\\&\cdots\cdots\cdots\cdots\cdots\cdots\cdots\cdots\cdots\cdots\cdots\cdots\cdots\cdots\\&\cdots\cdots\cdots\cdots\cdots\cdots\cdots\cdots\cdots\cdots\cdots\cdots\cdots\cdots\\&\hspace{3cm}\cdots\cdots\cdots\cdots\quad(13)\end{aligned}$$

in which

P_1, P_2 --- pressure of the first & second layer atmosphere;

T_1, T_2 --- absolut temperature of the first & second layer atmospaere;

K_1, K_2 --- absolute temperature.

● Ranging error induced by the jitter of the modulated pulse's leading edge

Although the repetation frequency of Radar altimeter is highly stable, but the high frquchey leading edge of transmitter outpdt is jitter when the modulator is triggered by pulae (due to flutter of the leading edge of modulated pulse grented by the modulator tube) , then this error is generating in ranging. The experience expression that the Radar for using hard modulation tube, the Jitter can be controlled within the order $0.1 \sim 0.02$ μs that mean the ranging error can be controled within range of $1.5 \sim 3m$, in addition, this jitter increased to the order of a few tenths of 1μs, if the modulator adapte soft modulation tube, and the induced ranging error is more!

● Error due to pulse compression technology

In the Radar of new type, most of them adapt the "pulse compression" technology, in the Radar using liner frqency modulation system, two ranging error can be generaled, one is the distance error h_{ad} which is induced from the dopplor frequency of the returned signal and can be expressed as:

$$h_{ad} = 150 \ \tau \ f_d/B_s \quad\cdots\cdots\cdots\cdots\quad(14)$$

in which

τ --- pulse width of the input signal (befor pulse compression);

B_s --- width of the signal spectrum at 3db point;

f_d --- Doppler freqeency.

● Altitude error is caused that due to the position error of the satellite orbit

Because of the radial orbit error is a relative large error as compared with the error in the geod leveling, special attention should be given to this error.

We can analyse the relative error for every orbit, the influence of error of the station position error, error of the gravitation field model, error of refration etc. , these error are proportion to the altitude. Investigate these orbit, it can optimize the orbit altitude calculation at every pass of the satellite. These error can be reduced 10 cm after correction.

● Vertical distance error due to direction pointing error

Even if the altitude measurements if very correct, but if the beam direction pointing get error, the vertical distance ranging get error to do, this error is noted as Δh_{ad}.

The Nadir point direction can be determinated by the antenna direction characteristic patter, direction pointing error can be determinated by analyse the trailling edge of the return signal (see figure 3.) If there is error in the
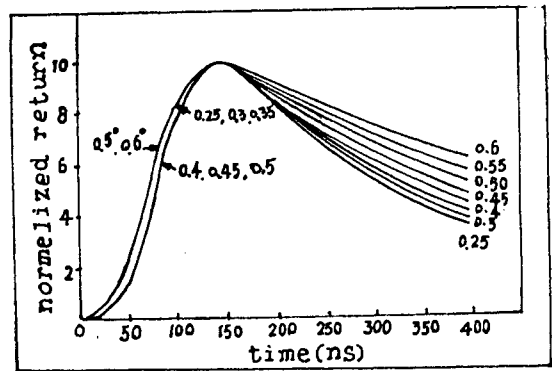
figure 3

pointing, there is the distortion in the amplitude (variation in slope), the system is more sensitive to the direction pointing error when the direction angle of the antenna is small. than the pulse width, because of the bad influence to the front of the return signal caused by the direction point error. So, it is valuable to improve the accuracy in the ranging and altitude measured.

We know from the figure 3, the trailing edge of the return pulse is most unsensitive with respect to surge of the sea surface, then it is properly be chosen as to determine error of direction pointing accuracy. Through the

correction of this error, the residual error in the pointing can be reduced to about 10 cm, i. e.

$$\Delta h_{ad} = 10 \ Cm \quad \cdots\cdots\cdots\cdots \quad (15)$$

● Vertical distance error due to multi -path propagation

The side lobe wave can also be reflected by the sea surface when the direct reflect wave is superposed with the reflectionwave of the side lobe. In results, the signal to be fluctuation and the energy center of the superposed signal is then shifted as with respect to the energy ecnter of the direct reflected signal. The average value of this error is

$$h_{an} = R_c \cdot \sin\theta \cdot h/ \sqrt{G_{st}} \quad \cdots\cdots\cdots\cdots \quad (16)$$

Where

R_c —— refraction coefficient of the sea surface;

h —— altitude of the antenna center from the sea surface;

G_{st} —— power ratio of the signal

θ —— beam incidence angle.

● Error in the data transmission system and measureing-reading, digitizing

If the output of altimeter is digital not an analogous, the data transimission system, measureing-rading system and digitizing do not create any error, but , there is still exists error in the digitizing. The neasureing error is related to the minimum unit in digitizing, the ranging syatem should be setting-up at ground before lauching into orbit. The residual error after setting-up is called as "normaling error" (i.e. normaliztion error), the accruacy of zero setting is restricted by the measurized interval. so, the normalized error can not be less tnan the measurized error.

● Error due to the targetal dynamic

The sea state always ever-changing, the wave surge hight which mean the equivalent reflective areo, of the Radar altimeter varies also. this causes amplitude fluctuation. But this fluctuation is random, so it called as "amplitude noise" . It makes the intensity of the reflected wave varing.

To say in principle, due to the automatic controlled circuit (AGC) in the instrument, the amplitude fluctuation of target did not cause ranging error, but depend on essentially how width on the band-widh of AGC circuit, ánd whether dynamic range of it is large enough or not! even though, the AGC can not cancel the error thoroughly, in actual there remains little, but it does not influence the determination of the "IEMSL" and can be neglected.

● Measureing error due to the sea surface influence

The wave on the sea surface can cause an error in the measureing, the deviatin is between the true mean sea level and the actually measurd ses level, this error is small, but it's mathematics model can not be given and the accurate correction not also, it can only be estimated.

The data of the sea surge altitude can be obtained by analyse the leading edge of the reflected wave sigbal as it does in the ordinary Radar. The ranging resolution is related to pulse width. higher ranging resolution can be obtained with narrow pulse. The width of pules is as narrow as 2~ 3 ns in the recent Racar, and the resolution is well than 10 cm, and the error of the influence by sea surface is estimatedas 0.7 m or more, i. e.

$$h_{aoc} = 0.75 \ m \quad \cdots\cdots\cdots\cdots \quad (17)$$

finally, we get;

$$h_a = D - \Delta h_{ac} - \Delta h_{ad} - \Delta h_{ab} - \Delta h_{am} - \Delta h_{aoc} - 1.5 \ m \quad \cdots\cdots\cdots \quad (18)$$

■ Determination of the position at which the IEMSL, is actually measured

In this section, we shall discuss the determination of the position of marker point while the sea area of the IEMSL is measured when all the vertical distance error and the estimete or calculation of the correction value is achieved.

The error revision various have been discovered in the referenec varions. now

I shall presentation my self-work effort. and I hope that this effort have contribution to PACON 90-convention.

In general, the actual position of the ocaea area is not useful, but, in the some special reverse altitude measuring point, provide an accurate position is practical useful to the platform engineer and the surveyer, for example, provide the maximal sea wave hight of some special econmic value place and it's accurate position.

In the figure 4, assumption "S" is satellite instantaneous position in the space, and the "S'" is subastral
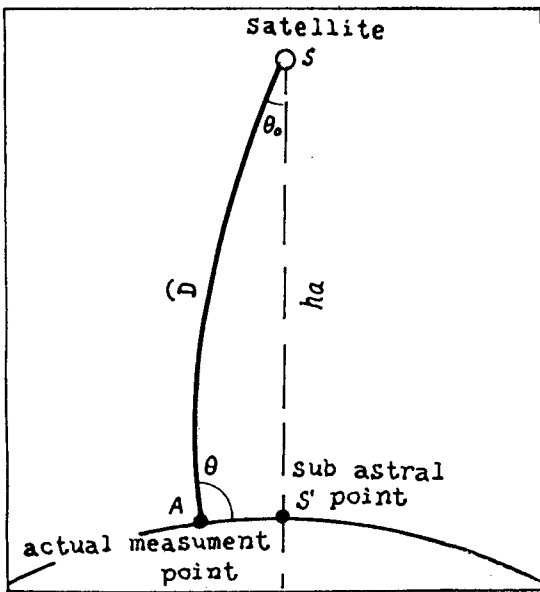
figure 4

point position to satellite, then the geography coordimation of "S'" can be obtainted by following two formlas

$$\sin(\phi)_{s'} = \sin(u) \cdot \sin(i);$$

$$tg(\lambda_{s'} - \lambda_N + (2\pi/T_e) \cdot (t-t_{N1})$$

$$= tg(u) \cdot \cos(i) \quad \cdots\cdots\cdots (19)$$

Where

$\phi_{s'}$ —— geography latitude of the subastral point;

$\lambda_{s'}$ —— longtitude of the subastral point

u —— the argment of latitude point;

i —— an incillination of satellite orbit;

λ_N —— longtitude of the latitude

point,

Te —— equal to earth's rotational period of a sidereal day;

t_{N1} —— the time of satellite across pass latitude point in first.

To say from theory, the position of the measrued point by Radar altimeter beam illumibation should be the position of subastral point, but the actual position of measuring point offset the subastral pointdue due to the beam curved by refrection, therefor, we wust be shift the position of subasiral point by means of above formulas, as such, we can geting true instantaneous position of the measuring point, get from figure 4.

$\widehat{D}$ —— the are distance measured by Radar altimeter;

h_a —— approximate vertical distance which corrected by errors to the arc distance D.

in the spherical trigonometer $\triangle ASS'$,

$$\cos(\widehat{AS'}) = \cos(\widehat{D})\cos(h_a) + \sin(\widehat{D})\sin(h_a) \quad \cos\theta_0$$
$$\cdots\cdots\cdots\cdots (20)$$

in which , the D, h_a is known, and the θ_0 is angleal between the start point of beam ray and vertical line, it's computation formula is

$$\cos\theta_0 = a\eta_0\cos\theta / \eta (a+h) \cdots (21)$$

where

a —— the raius of earth;

h —— the hight of ray;

θ —— the angle between the beam ray and the horizon;

η_0 ——the refraction index of atmosphere at ground.

so, the actual position of beam illumina tional point is:

$$\phi = \phi_{s'} \pm AS'$$
$$\left.\begin{array}{c} \\ \\ \end{array}\right\} \quad \cdots\cdots\cdots\cdots (22)$$
$$\lambda = \lambda_{s'} \pm AS'$$

the ± sign above formula depend on the direction of the satellite flying and earth rotation, arc distance can be obtainted by solution the eq. (20).

The eq. (22) only apply to the

equatoral orbit or polar orbit, but, following formula can be fit to any orbit which . an incillination of satellite orbit is small than 90° , i,e.

$$\phi = \phi_{s'} + 180 \cdot (\overset{\frown}{As'}) \cdot \sin(i) / (a \cdot \pi)$$

$$\lambda = \lambda_{s'} + 180 \cdot (\overset{\frown}{As'}) \cdot \cos(i)$$
$$/ (a \cdot \pi \cos(\phi))$$
$$\cdots\cdots\cdots\cdots (23)$$

in which

i ─── an inciliantion of satellite orbit;

a ─── the equatorial radius of earth.

● Refereneo

S. H. Laurila: 《Electroic survey & navigation 》 1967

A STUDY BY SUN GLITTER ON SEA SURFACE

Maki Enomoto, Manabu Kato and Jun Takahana, Toshimasa Kawanisi

College of Science & Technology, Nihon University, Japan

1. Preface

For the comfortable living on the coast or sea, psychological and physical effects to the various environmental conditions peculiar to the sea such as shaking, salt, wind, wave sound, temperature and humidity, and light must be considered. When we turn our attention to the optical environment, we can notice the spicular-reflected light of the sea surface by sun, which is a major factor different from on land, on the sea of fine days.

This is called the sun-glitter and is an important visual environment factor peculiar to the seascape. This is caused by the spicular-reflection of light on the sea waves and has numerous brightening points with frequently and extremely changing luminances, and changes its aspect in accordance with the weather and the position of the sun[1]. The beautiful golden or silver glittering in the evening is called "The Load to Happiness" in other words and gives comfortable feeling to man[2]. On the other hand, the glaring glitter in the daytime seems to be given an eye fatigue or temporary visual acuity drop as well as an discomfort feeling because of high luminances. The psychological and physiological phenomena due to light stimulus like this are called "glare" with the former as "discomfort glare" and the latter as "disability glare". "The glare" is the most important factor which dominates the quality of visual environment[3].

The purpose of the present study is to evaluate the relation between the physical value and psychological affect of discomfort and comfort glare (here after called glare). Using an image analysis apparatus enabled us to discover a method of classification for the physical properties of sun-glitter.

2. Outline of Experiment

This experiment was conducted on a clear December day at the Makuhari Coast in Chiba Prefecture(fig.1). A total of 13 readings were taken at 3° intervals (about 20 minutes apart) beginning at 12 noon.

2-1. Outline of Image Analysis Apparatus

a. Measurement System

Fig.2 indicates the block diagram of measurement system and tab.1 indicates details of each equipment.
The luminance distribution appears as an illuminance distribution on image space on CCD camera "XC-77"(SONY-MADE) through the 16(mm) standard lens.
A video signal which is directly proportional to an illuminance distribution is transmitted from a CCD camera. And the video signal is converted into the luminance signal of 64 tone by analog digital converter of image processing board "FDM-4"(PHOTORON-MADE).
This converted image is analyzed by a personal computer "PC-9801VM-21"(NEC-MADE).

b. Character and Correction of Each System

The spectral responsivity of CCD camera largely differs from the standard relative luminous efficiency V( ) which is indicated in fig.3. Therefore, We used a color correction filter "No.102"(KODAK-MADE) and an infrared-rays-cut-filter"IR".
As a result, there is only 5-9% difference between the results of this correction and the standard relative luminous efficiency.
Fig.4 show the relativity of the incident luminance and the reference voltage on the image processing board

according to the F-number of a camera.
The light source for fig.4 was the
lambertian surface made out of a white
acrytic board lighted by an incandescent
lamp form the rear. As a result, their
relation was proportional.
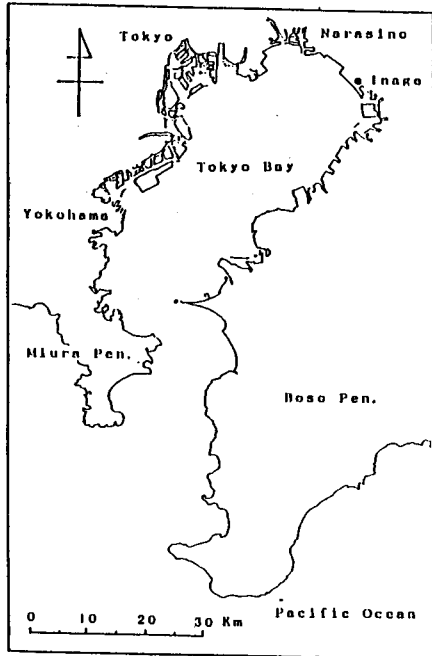
Fig.1 Measurement Point
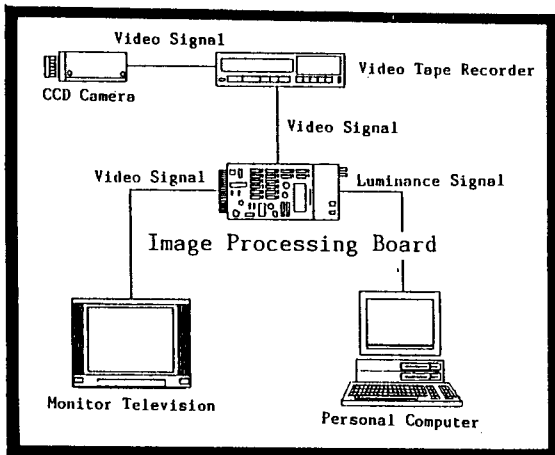
Fig.2 Block Diagram of Measurement System

Tab.1 Machine Parts and Specifications

CCD Camera	Camera Tube Spesification	: Solid State Image Specification (Type of Interline)
	Camera Tybe Area	: 8.8×6.6[mm] (size of 2/3in.)
	Effective Picture Elements	: 768(H)×493(V)
	S/N Ratio	: More Than 50[db]
	Camera Corrector	: γ =1
16[mm]Standard Lens	Horizontal Angle of View	: 30.40°
	Vertical Angle of View	: 23.18°
Image Processing Board	Resolution	: 256×256
	A/D Converter	: 6 Bits , 64Tone
	Sampling Time	: Image/Time 1/50[sec]
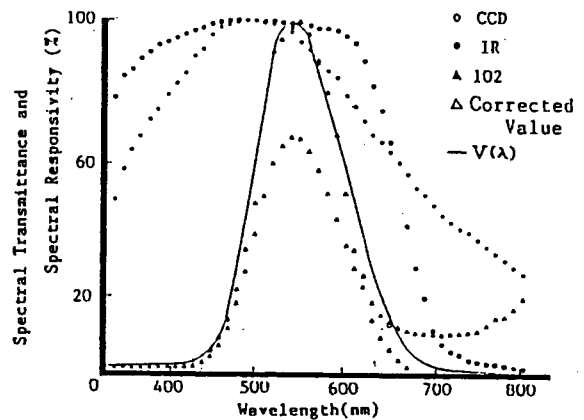
Fig.3 Relative Luminous Efficienty Curve
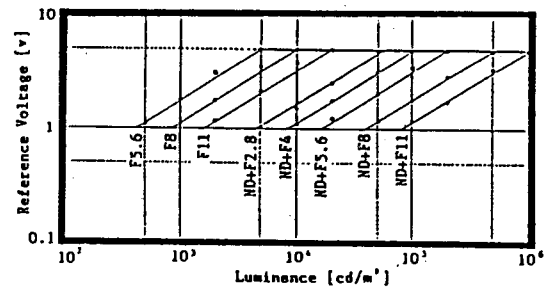
Fig.4 Rataion of Luminance and Referenc Voltage

2-2.   Measurement of Physical Value

   We measured the following four
physical values which were predicted to
have an affect on glare and the direct
sunlight ratio.

a.   Sun-Glitter Luminance

   The sun-glitter luminances is an
index of light intensity and we measured
the maximum luminances by scanning the
sun-glitter part with a luminance meter
of visibility angle 1°.

b.   Luminance Ratio

   This is an index indicating the
grade of contrast to the circumferential
sea surface and we calculated it as the
ratio of the sun-glitter luminances over
the   maximum   luminances   of
circumferential blue sea surface.

c.   Configuration Factor

   This is an index indicating the
apparent size of the reflected image and
we calculated it as the ratio of area
over the visual field area, using sea
surface photograph taken by a fisheye
camera set vertically to the sea
surface.

d. Luminance Distribution

The luminance distribution is an index of a grade of irregular luminances in a visual field investigated and an important physical value on discussion of glare. We calculated the amount of scattered luminances distribution by obtaining the image data of the luminances distribution of the sea surface with an image analysis apparatus using CCD camera, as the index indicating the grade of luminances variation. Fig.5(a) shows eight stages of simulated color indications of the luminances distribution of the sea surface investigated. We obtained the luminances ratio distribution as shown in fig.5(b) by performing an image operation to extract luminances difference between neighboring picture elements. After that, we made Lorentz diagram from this image histogram to numerically indicate the concentration of distribution and calculated the amount of scatter.

e. Direct Sunlight Ratio

This is an index to indicate an incident ratio of direct sunlight at the time of measurement and we obtained an illumination ratio of direct sunlight of horizontal plane at the daytime with an illumination meter.

3. Result and Consideration

We classified the weather conditions for each measurement by the sun-glitter luminances shown in fig.6 and the variation of direct sunlight ratio.

In the measurement under 10 percent of direct sunlight ratio, we classified D1 and D2 as the clouded sky because the sun was covered by cloud, Y1 and Y2 as the evening because the direct sunlight was diminished by the air with under 10° of the sun altitude regardless of fine day and the others S1 to S9 as the blue sky.

When the sun-glitter of each measurements was classified by physical value, the relationship of luminances and solid-angle projection ratio is shown in fig.7, and the relationship of luminances ratio and luminances distribution is shown in fig.8. As a result, type A consisting of sun-glitter on the clouded sky and evening concentrated in the territory of weak luminances and small reflection plane. At the blue sky, it has larger reflection image and amount of scattering in the case of 30° to 20° sun

altitude, having B and C types with different luminances and contrast. Type D with 20° to 10° sun altitude has very strong luminances and contrast, but smaller sun-glitter, because of slender pattern of reflection image, than other sun-glitter of the blue sky. The result of classification is shown in tab.2.

(a) Luminance Distribution   (b)Luminances Ratio Distribution
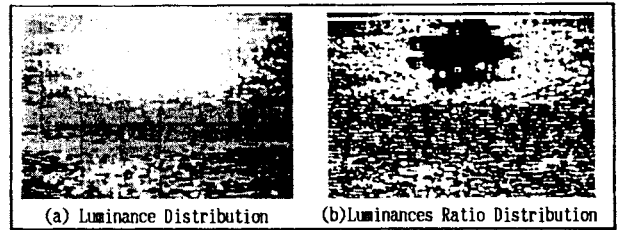
Fig.5 Example of Image Analysis
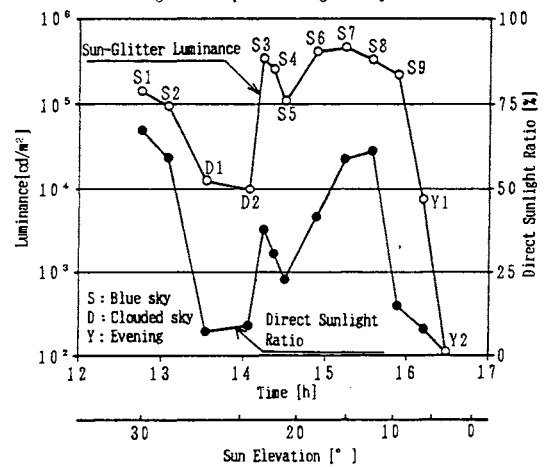
Fig.6 Varies of Sun-Glitter Luminance
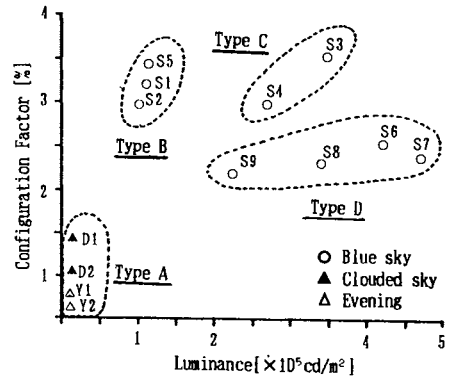
Fig.7 The Relation of The Sea Surface Reflection Luminance and The Configuration Factor
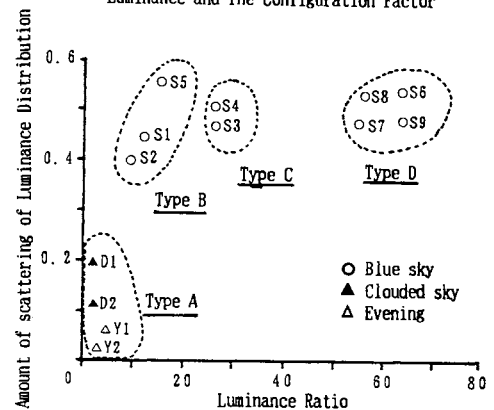
Fig.8 The Relation of The Sea Surface Reflection Luminance Ratio and Luminance Distribution

Tab.2 Classification of Sun-Glitter by Physical Value

Type	The Sea Surfac Investigated	Physical Value of Sun-Glitter		
		Luminance,Luminance Ratio	Reflection Image	Amount of Scattering
A	D1,D2,Y1,Y2	Very Low	Small	Small
B	S1,S2,S5	Low	Large	Large
C	S3,S4	Strong	Large	Large
D	S6,S7,S8,S9	Very Strong	Small	Large

References

1) Maki Enomoto, Toshimasa Kawanisi, and Wataru Kato : Measurement of Luminance Distribution on the Sea Surface for Comfortable Living Space , OCEANS'88 Proceedings Vol.2 by M.T.S. and I.E.E.E. , Oct , 1988, P276-281.
2) Motoaki Kishino : Some Ploblems of Light Near Sea Surface , Marine Science , Vol.4 , No.9 , P11 , 16,Sep,1972
3) The Illumination Engineering Institute of Japan : Better Lighting , P76 , 1977

ROV '90- A TECHNOLOGY REPORT FROM VANCOUVER, BRITISH COLUMBIA

Robert L. Wernli

Naval Ocean Systems Center San Diego, California, USA

ABSTRACT

ROV '90 was held in Vancouver, British Columbia, Canada during 25-27 June, 1990. Due to the closeness of that conference to the PACON '90 conference, it was not possible to prepare a written manuscript for the PACON conference proceedings. Therefore, it was decided to give an oral presentation in the Special Session on "News Events." The ROV '90 Proceedings will cover these topics in detail, and can be obtained from the Marine Technology Society, ROV Committee, P.O. Box 61149, San Diego, California, 92126, USA.

This presentation will summarize the most significant information presented at the ROV '90 conference in the areas of ROV applications, operational experience, and emerging technologies.

The ROV '90 conference technical sessions included 67 papers from 12 different countries. Subjects to be discussed will include combined operations of ROVs and manned submersibles, cable burial with the SCARAB IV, and Canada's new SPIRIT autonomous vehicle program. Subsea intervention will include the latest ROV applications by STATOIL and Saga Petroleum and vehicle handling system designs. New applications for ROVs will address physical security, harbor defense, manganese nodule mining, oceanographic exploration, and tunnel inspections. Emerging technologies will address micronavigation, manipulators and control systems, tactile sensors, acoustic and fiber optic communications and ceramic pressure housings.

DEVELOPMENT OF INTEGRATED MARINE SURVEY SYSTEM AND APPLICATION FOR MARINE CONSTRUCTION WORKS

Tadashi Matsumoto and Masafumi Sakai

Taisei Corporation, Tokyo, Japan

Abstract

In marine development, especially marine construction work, an understanding of ocean phenomena is important. This understanding, however, has been lacking in the past due to undeveloped oceanographic observation technology. Recently, such technology allows us to collect and analyze various oceanographic data. In the future, the need for accurate oceanographic information will multiply paralleling the development of marine construction technology.

Our system was developed in anticipation of future needs. It covers information processing steps ranging from the collection of oceanographic information to its analysis and evaluation.

The system can simultaneously measure and analyze boat positioning, current, depth, seabed topography, sea temperature and other environmental factors in an integrated manner. Such data allows predictions and assessments of the marine environment through simulated tests. The system realizes high-precision and high-quality of data by the most recent ultrasonic and electronic innovations.

This paper describes the design of this system together with various applications to marine construction.

1. Introduction

A new national land development policy is being put forward in Japan --- a policy befitting the central world economy in the 21st century. The expansion of highway and transportation networks, including such projects as the Trans-Tokyo Bay Highway and construction of the Honshu-Shikoku Bridges, forms the main axis of this policy which is designed to cope with internationalization, as exemplified by the New Kansai International Airport and by the growth of Tokyo into a major world capital. The 4th national comprehensive development plan has been also put forward against this background, giving a large-range point of view and leading various ministries and agencies to develop a range of water-front renovation concepts, such as the "Marine Community Polis Concept", and the "Aquamarine Plan".

These examples indicate that land development in Japan cannot be discussed without considering the sea, and in fact most large-scale projects at the moment, including power stations, are planned for offshore site. However, conditions in marine areas differ greatly. Also, technical considerations range widely from planning, design, and construction stages through to maintenance after completion.

Given this situation, an important aspect of marine development is the dissemination of data on marine conditions. The work involved is continuous through the processes which begin with planning, so every effort must be made to obtain adequate data of an appropriate accuracy.

Conventional methods of data accumulation suffer from problems of accuracy and processing time, and the data is not readily usable because different readings are all taken separately. The marine survey system introduced here was developed specifically for the type of applications described, and it is a comprehensive system encompassing the entire range of user's needs.

2. Present Status of Marine Development and Outstanding Problems

2.1 Plans for Large Marine Structures

At the present time, plans for large marine structures are continually being announced and built. The Honshu-Shikoku Bridges, such as the Seto Bridges completed in 1988, the Akashi Kaikyo Bridge, and the Kurushima Kaikyo Bridge, are progressing, and New Kansai International Airport Project which is an offshore airport, the Trans-Tokyo Bay Highway including a tunnel and offshore artificial island, and the deep breakwater in Kamaishi Port are now under construction. Each of these large marine developments has its own unique site conditions and technical problems. For example, while the Honshu-Shikoku Bridges is a project necessitating marine construction at great depth and in extremely swift tidal currents, the Trans-Tokyo Bay Highway must be constructed in ultra-soft ground. Description of representative large-scale projects presently underway in Japan follows.

The Akashi Kaikyo Bridge is to be 3,910 m long, linking Honshu and Awaji Island and it will be the world's longest suspension bridge when completed. Fig. 1 outlines the project, in which undersea operations are necessary for the main-tower foundations 2P and 3P. The laying-down caisson method is being used for construction of these foundations, and this method involves marine construction techniques such as seabed excavation, caisson towing, mooring and submerging of the caisson, scouring protection work, and concrete placement.

The bridge site is subject to extremely difficult condition; 50 m-deep water and tidal currents of over 9 knots. Under these conditions, one requirement of the project is investigation and estimation of tidal currents and velocity, precise measurement of the seabed topography, etc. In addition, measurements over a long period of time are needed to control the excavated surface during construction and to control scouring after completion, and this constitutes an extremely difficult problem.

Fig. 2 shows the Kurushima Bridge project. In particular, undersea operations are difficult in 5P foundation. The marine construction work at this location may be undertaken using methods employed for the Akashi Kaikyo Bridge. Not only is the tidal current extremely fast (maximum of 7 knots just as with the Akashi Kaikyo Bridge), but also the current is complex because of the many islands shown in the figure. Also, since the topography is steep, information from marine surveys plays a very important role in the selection of the route and in the implementation of the construction plan.

The detailed construction plan is presently being drawn up based on data from surveys.

① Seabed Excavation ② Towing Caisson to the site ③ Mooring and Submerging ④ Scouring Protection ⑤ Concerte Placement
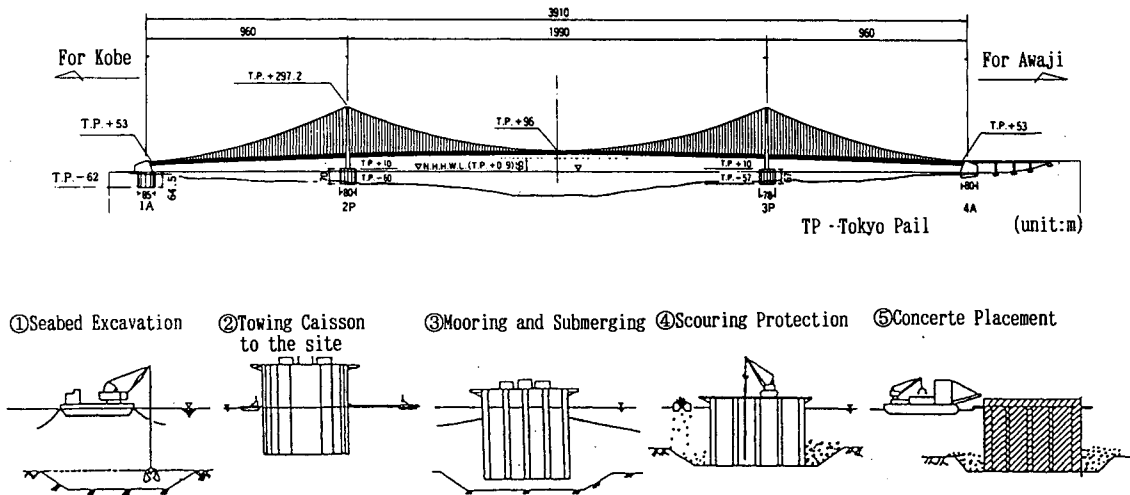
Fig.1 Outline of Akashi Kaikyo Bridge
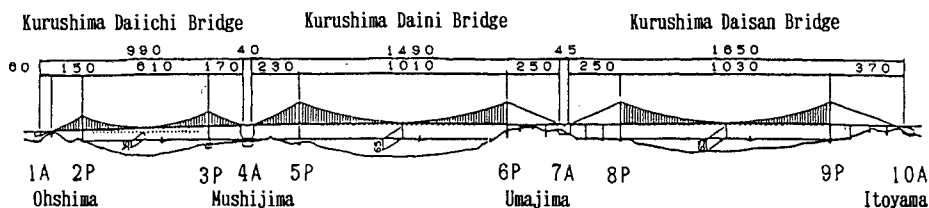
Fig.2 Outline of Kurushima Kaikyo Bridge (unit:m)

The New Kansai International Airport project involves the creation of an artificial island (500 ha in Phase I and 1,200 ha in Phase II) as shown in Fig. 3 about 5 km offshore from Senshu. The seabed is an accumulation of ultra-soft material 20 m thick, so sophisticated measurement techniques are needed to cope with problems of sinking, pollution control, etc.
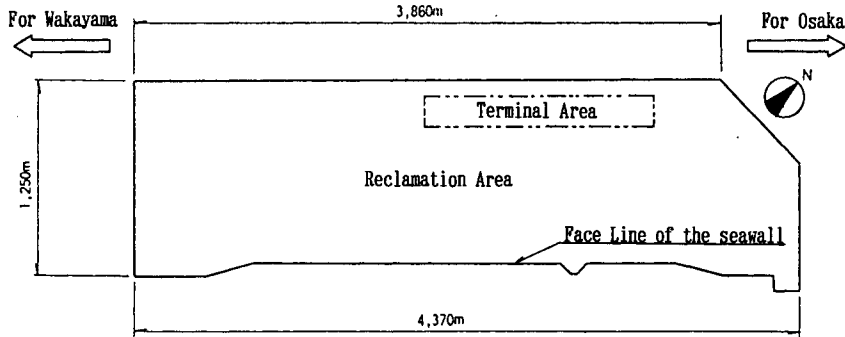
Fig.3 Outline of Kansai International Air Port (PHASE I)

The Trans-Tokyo Bay Highway has a total length of about 15 km, and it will join Kawasaki and Kisarazu. It consists of a tunnel section and a bridge as shown in Fig. 4 On the Kawasaki and Kisarazu sides artificial islands will be constructed for ventilation purposes.

The artificial island on the Kawasaki side will have a cylindrical concrete wall structure as large as 100 m in diameter. Since construction will be on ultra-soft ground, a variety of measurements are required including monitoring of marine pollution and measurement of the completed shape of the excavations.
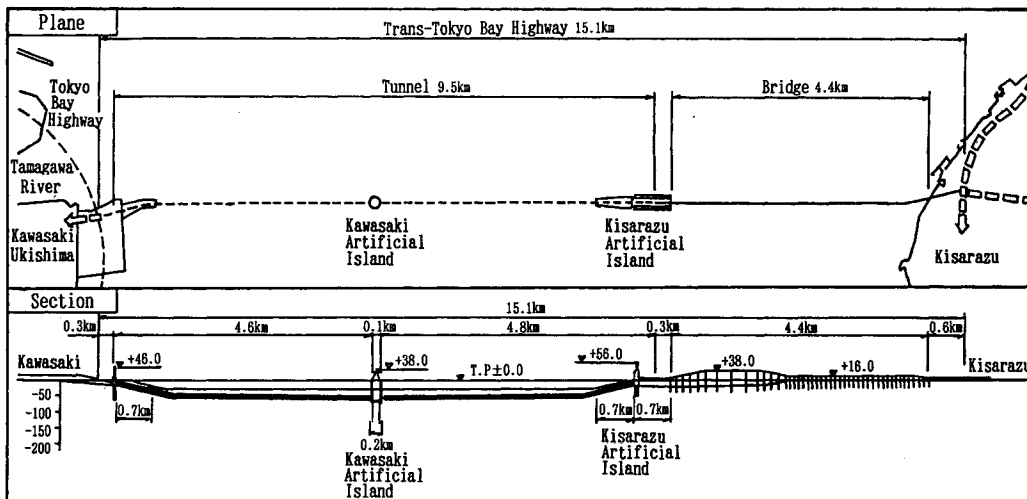
Fig.4 Outline of Trans-Tokyo Bay Highway

The Kamaishi Port Breakwater at the mouth of the bay will be the largest breakwater in Japan when completed, and will be constructed in 60 m of water as shown in Fig. 5. The caisson will be a huge structure 30 m in width and 33 m in height. The mound section will also be 7 million m^3 in volume, a massive structure equivalent in size to the world's largest rockfill dams. The control and measurement of the height and configuration of this mound during construction is considered of utmost importance.
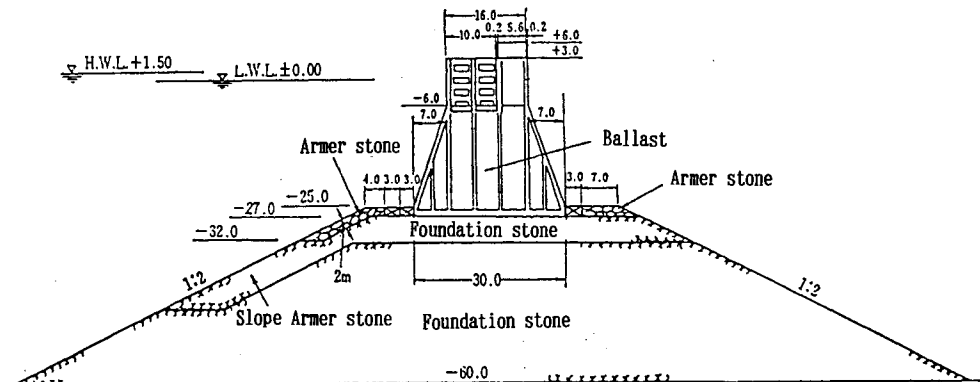
Fig.5 Outline of Kamaishi Harbor's Break Water in deep water (unit:m)

2.2 Waterfront Development Projects

Several Japanese ministries are presently proposing outlines for the re-development of coastal areas, and the major cases are shown in Table 1.

Besides these, many municipalities have also announced their own plans for development of coastal areas, actively moving into this field of construction. All the projects described will require appropriate measurements and forecasts of marine conditions (tidal currents, waves, water temperature, etc.) in coastal areas.

Table 1 Marine development projects proposed by major ministries and agencies

Ministry or agencies	Project	Description
Ministry of Transport	Offshore artificial island and concept	Feasibility studies have been conducted in five districts, i.e. off Kisarazu, Yokohama, Shimizu, Tamano-Kurashiki and Shimonoseki. Proposals include the construction of large-scale artificial islands, many of which are expected to be the reclamation type though some will be floating bodies.
	Marine town projects (MTP)	Waterfront development projects in provincial ports and harbors aiming at activating regional economies. Many of the projects involve recreation related development as a whole. Surveys have been conducted on 11 projects in 1986-1987.
	Coastal resort projects	Waterfront development projects of the marine recreation type including marinas, artificial beaches, fishing wharfs in addition to marine amusement facilities based on the private sector, restaurants, etc. Surveys were conducted on five projects in 1986.
	Port Renaissance 21	Making use of private sector vitality, waterfront development projects at ports and harbors relatively near urban areas are being implemented. The nucleus of these projects includes, for example, land-based facilities such as fish markets, convention facilities, etc., and port and harbor development projects of conventional type including new wharfs, etc. as related facilities.
Ministry of Construction	Coastal community zones (CCZ)	Waterfront development projects over areas extending 2 km from the beach. Development of recreation facilities by the introduction of private sector vitality. Surveys were conducted on 12 beaches in 1987.
	Marine multi-zone (MMZ)	Although no specific development areas have been chosen, the concept includes construction of sea control structures for effective utilization of the sea itself. This idea is in the basic research-stage, and is similar to the "quiet sea" concept of the Ministry of Transport in which a calm sea area behind an offshore artificial island is fully utilized.
Ministry of International Trade and Industry	Marine community polis	Surveys were conducted on most of the case study areas jointly with the offshore artificial island concept, which include Kashima, Yokosuka-Shimizu, Tamano-Kurashiki, etc.
Ministry of Agriculture Forestry and Fisheries	Marinovation	Aims at sophistioation of the fishery industry. Projects will cover a wide range including development of fishing equipment, methods of fishing, distribution, fishing areas, fishing ports, fishing villages.
Science and Technology Agency	Aquamarine	Surveys have been conducted to see what new technological development can be applied to sea area development. The need for development of new equipment has been emphasized. These ideas are not directly connected to actual projects. However, the "Okhotsk Program" set forth in this concept is scheduled to be implemented by Hokkaido.

2.3 Demands for Marine Measurements

As has been stated, the importance of environmental surveys and evaluation of the effects of construction is more important than with land-based development projects. Preliminary surveys for environmental assessment and as the basis for drawing up design and construction plans have taken on more weight. There is also a desire for sophisticated construction management methods where sea conditions are severe.

Judging from the present condition of marine survey technology, however, although measurement tools have improved along with advances in electronics, there appear to be a number of problems; the users' point of view in areas such as data collection and processing methods, and these must be solved.

Basically users want marine information that is abundant but accurately and readily available, and they would like data that can be quickly updated, or even available in real time.

The marine survey system introduced here was developed to meet these needs. The aim is "Sophistication of Information Processing in Marine Surveys" from analysis, evaluation through to simulation forecasts using collected information.

3. Characteristics of the New Marine Survey System

3.1 Problems with Conventional Methods

Where quantitative surveys and analysis of the sea is required, it is necessary to make use of all the various information available. Under present circumstances, it is difficult to obtain simultaneous readings of general marine observations (tidal current, seabed topography, water temperature, salinity, etc.).

Also with the measuring instruments generally used, there are various restrictions on the quality of the data collected. For example one problem with the conventional instrument for measuring water depth is that information can only be obtained at a point inprediately below the boat (depth sounder) while the position of the boat cannot be recorded simultaneously. Thus users cannot expect highly accurate measurement control of the completed configuration during excavations nor accurate monitoring of scouring.

With regard to the measurement of tidal currents, conventionally fixed instruments have been used and so data is only obtained at a single position. Consequently, when the particular sea area needs to be measured, a large number of instruments is needed at great effort and expense.

Judging from in a different way, conventional marine surveys have had to sacrifice basic conditions such as "the same position" and "the same time" due to various restrictions, such as sensors, instruments, and information processing techniques. To make the information highly usable and to facilitate accurate construction management in the future, it is necessary to systematize use of the measuring equipment.

3.2 Characteristics of Integrated Marine Survey System

This system aims at comprehensive collection and use of data such as "current velocity", "water temperature", "topography", "geology", as shown in Fig. 6, which was independently measured and used conventionally.

The comprehensive range of information is recorded onto magnetic tape and quickly processed by main-frame, from which output is obtained. The computer can also make various estimations from the data using simulation software.

As explained, one objective of this system is to process information through the entire construction period from survey, analysis and evaluation through to estimating. The features of this system are as follows:

a) The necessary data can be obtained through a real-time operation from a boat, making marine information available over a wide area in a short time.

b) Each measurement can be combined as necessary with any other and is recorded on magnetic tape for the same location and the same time.

c) The data obtained can be quickly processed using a main-frame through off-line operation, making it possible to carry out forecasting by simulation analysis, etc.

d) Sophisticated modern instruments make it possible to carry out surveys such as topography surveys to an accuracy previously impossible.

e) The system can be applied to various management operations from planning to construction.
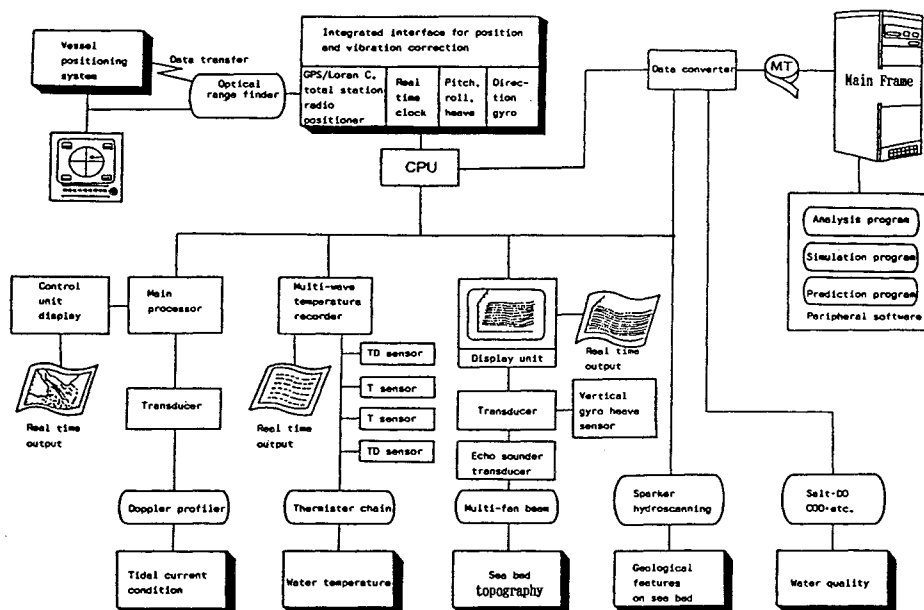
Fig.6 Integrated Marine Survey System

4. Component Technology

Let us introduce the main component technologies used in this system. The first area is boat position and guidance technology, the second is tidal current condition measurement using ultrasonics and information processing, and the third is detailed examination of the seabed topography by means of multi-fan beams.

4.1 Boat Position and Guidance Technology

To accurately locate the boat on the sea is fundamental to surveys. Since the boat is moving continually due to the effects of tidal currents, waves, etc, in addition to the normal forward motion of the boat itself, it is necessary for a time record to be kept that is linked to other information. This system incorporates a boat position measurement system and a subsystem which guides the boat to the designated sea area or survey line. Presently, the boat's position is measured using radio observation of position or an optical range-finder, and the information obtained is fed into the system. In survey work carried out so far, the system has been extremely successful, particularly where tidal currents are strong, since the captain can confirm his position while steering along the survey line.

In cases where very accurate positional information is called for, as in the examination of seabottom topography, the total station method using an optical range-finder is very effective. In this method, as shown in Fig. 7, the three-dimensional position X, Y, and Z of the target boat are measured using an optical range-finder on the shore, and this information is then converted into optical signals which are returned to the boat as boat position information for boat guidance. The optical range-finder is an extremely accurate instrument with an accuracy several centimeters per kilometer. Since this system also directly measures the elevation of the boat, no tidal level correction needs to be made as was the case with conventional measurements, so it is a good technique for application to seabed topography measurements.
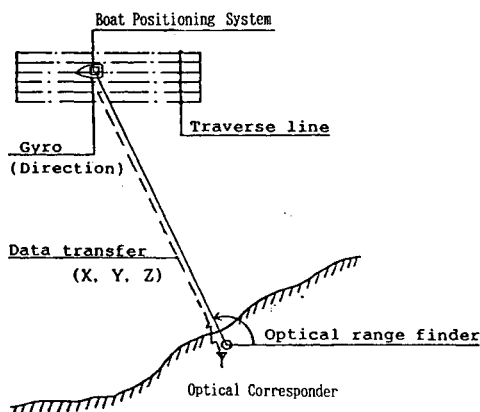
4.2 Tidal Current Condition Measurement Using Ultrasonics and Information Processing

Unlike the direct measurements (by propeller) in systems, this is a non-contact method using ultrasonic waves. As shown in Fig. 8, an ultrasonic pulse is emitted underwater from a transmitter equipped in the ship's side. Part of this pulse is returned after reflecting off objects in the water (plankton, etc.). The frequency of the reflected signal is shifted in proportion to the relative velocity of the object. This phenomenon is known as the Doppler effect, and measurement of this frequency shift can yield the current velocity vector. As shown in Fig. 8, this system emits 60° angle ultrasonic pulses in four directions perpendicular to each other, and combining those signals for translation into velocity means that the effects of movement such as rolling, pitching, etc., can be eliminated, and a three-dimensional vector of current velocity in X, Y, and Z directions is obtained. This system is capable of measuring the current velocity vector in 16 layers simultaneously at the rate of once every 30 seconds while the boat is under way, and the results are output in real time as shown in Fig. 9. Thus this system surveys the current direction and current velocity from on-board and by combining this data with precision positional information, the current conditions over the entire designated sea area can be accurately measured within a short period. The data is recorded on magnetic tape, and using a main-frame, plane cross section, of current conditions as well as the current direction, current velocity distribution and time series changes at any point can be constructed.
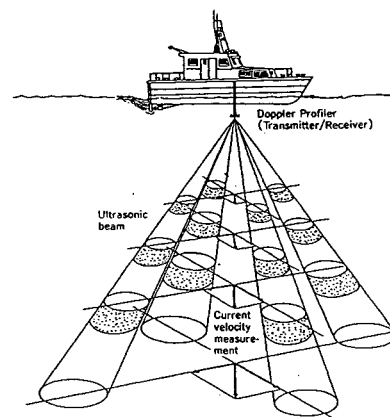
Fig.8 Doppler Profiler
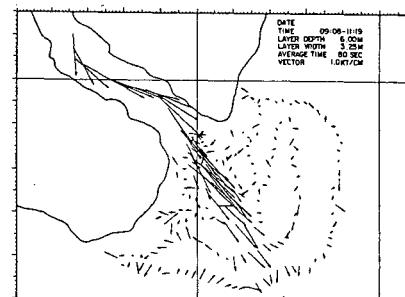
Fig.9 RealTime Output of Tidal Current

Fig.7 Boat Positioning by Total Station

4.3 Examination of the Seabed Topography by means of Multi-Fan Beam

Conventionally, seabed topography surveys were conducted using a single-beam echo-sounder, which was unable to measure the seabed as a plane (water depth information was obtained as single point only) and as the beam was wide problems remain to be solved from the viewpoint of accuracy.

The multi-fan beam, on the other hand, transmits a fan-shaped beam at right angles to the direction of boat motion as shown in Fig. 10, picking up signals by instantaneous scanning. The system measures and records the depth of water (seabed topography) continuously and over a plane area.

Fig. 11 shows the multi-fan beam method of measurement. It is possible to make measurements over a width of more than 3-times the water depth in one scan (when the scanning width is 120°), so a three-dimensional view of seabed topography can be obtained by making measurements continuously. In addition, contours, etc. (refer to Fig. 12-14) can be checked in real time on the boat.

This system has made it possible not only to survey the completed shape of civil engineering work, (surveys of mounds and excavations, for example) but also to measure scouring near a structure, as shown in Fig. 15.

Fig.10 Principle of Multi-Fan Beam

Fig.11 Seabed Topography Survey by Multi-Fan Beam
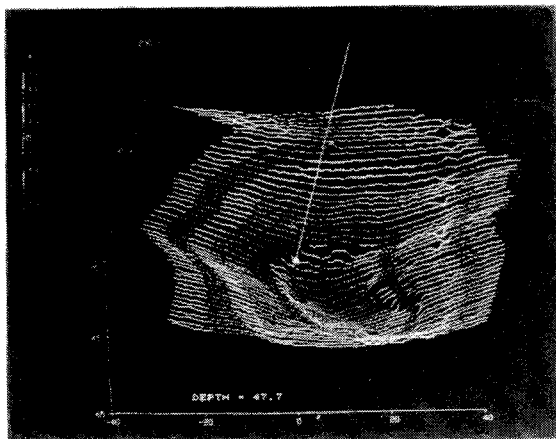
Fig.12 Three-dimensional View of Seabed
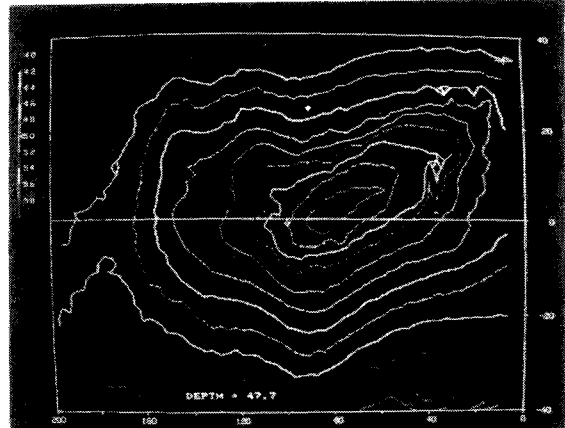
Fig.13 Seabed Contour
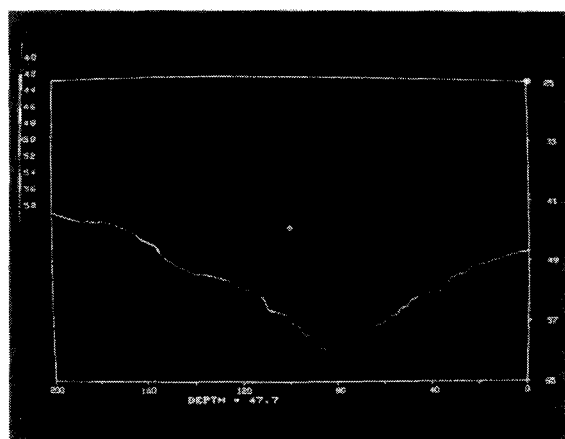
Fig.14 Seabed Cross Section
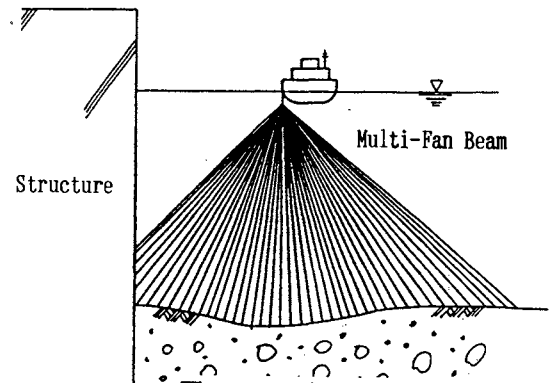
Fig.15 Scouring Survey

5. Application and Use

This system has brought together various measurements into a unified time and location framework, which is the basis of a comprehensive survey system which can cope with quick real time operation. Environmental assessments or forecasts can also be undertaken using the highly sophisticated processing and data available.

This is a comprehensive processing system for marine information of construction from survey, planning, and design through to construction management.

In particular, the availability of real time information has made it possible to perform construction management of unprecedented accuracy. With regard to the analysis of the environmental assessment, the effectiveness of the system has been freely utilized in estimating diffusion, including the monitoring of diffusion of hot water effluent. The system has been used in as many as ten projects,

proving its workability. The following are major projects in which the system was used:

(1) Sea area survey for the Akashi Kaikyo Bridge of Honshu-Shikoku Bridge Authority.

(2) Survey of the route for a sea-crossing bridge.

(3) Environmental assessment for the siting of power plants.

(4) Preliminary environmental survey prior to laying a submarine pipeline.

(5) Evaluation of SS diffusion analysis due to excavation.

(6) Scouring survey at a power plant intake.

(7) Construction management of marine construction work.

Table 2 shows further possible uses for the system.

Table 2 Use of the integrated marine survey system

Use	Description	Remarks
Current Condition Survey	Continuous measurement of three-dimensional current over wide area. Observation of output is real time.	It is possible to measure the current velocity in 16 layers at maximum in the direction of water depth.
Environmental assessment survey	Obtaining the information required for environmental assessment, such as current conditions, water quality, seabed geology, etc., and evaluation of the data.	Continuous measurement of composite data and simulation analysis.
Location planning	Construction planning for structures based on measurement data in the case of power station siting and bridge routes, etc.	Application of measured data and simulations forecasting total currents.
Highly accurate managements of construction work	By continuously measuring in three dimensions the completed shape of a mound of underwater excavation to great accuracy, real time management can be realized.	Highly accurate mapping system.
Survey of diffusion of hot water effluent	Simultaneously observes and measures multi-layer water temperature and multi-layer current conditions. Software analysis by means of simulations.	Hot water effluent diffusion simulation program.
Pollution diffusion survey	Measurement of extent of diffusion and distribution of pollution resulting from dumping sand or gravel and dredging. Interpolation software by means of simulations.	Making use of reflected intensity of ultrasonic waves.
Survey of fishing grounds	Survey and analysis of the conditions, topography, and layer temperatures of fishing grounds.	It is possible to survey fish shoals.
Survey of drifting sand and scouring	Periodic measurement of minute fluctuations in seabed topography.	Highly accurate mapping system.

References

1) "Wide Sea Area Marine Survey System" by Tadashi Kanzaki and Gentaro Kai, from Report of Civil Engineering Planning Committee, issued in 1984 by the Japan Society of Civil Engineers.

2) "Visualized Technology of Marine Informations and Data" by Tadashi Kanzaki and Genrato Kai, from Civil Engineering, Vol. 40, No. 2, issued 1985.

3) "Wide Sea Area Marine Survey by Upgraded Systematized Method" by Tadashi Kanzaki, from lectures provided for members of Japan Coastal Fishery Development Association, in June 1985.

4) Report on Development and Joint Study on Precise Survey Technology for Current Condition Along Coastal Area" by the Japan Marine Science & Technology Center and Taisei Corporation issued in March 1984.

5) "Water Temperature Distribution Measurement with Towing Type Sensor Chains" by Toshiaki Hara and Gentaro Kai, from Sensor Engineering (Vol. 4, No. 8) issued in August 1984.

A NEW OCEAN MEASUREMENT USING ADCP TOWED VEHICLE

W. Koterayama, A. Kaneko, M. Kashiwagi, M. Nakamura

Abstract

The ADCP (Acoustic Doppler Current Profiler) is a powerful instrument that can measure three dimensional vertical profiles of ocean currents and it is sometimes mounted on a research vessel. The data obtained by using the system of ADCP and a research vessel are affected by motions of the research vessel induced by surface waves, the cabitation noise generated by the ship's propeller, and bubbles entrained under the ship's hull. We developed a towed vehicle system for housing ADCP in order to eliminate these obstructions.

The towed vehicle developed is depth and roll controllable. The length of the towing cable is 800m. The height, breadth and length of the towed vehicle is 1.5m X 2m X 2m. The weight is 360kg in air. The maximum towing velocity is 12 knots.

On-site experiments in Kuroshio showed the good performance of the towed vehicle and the good accuracy of the data obtained.

1. Introduction

The Acoustic Doppler Current Profiler (ADCP) is developed for measuring the detailed vertical profile of ocean currents.

The accuracy of ADCP is guaranteed when it is mounted on sea bottom [1].

A few oceanographers made an attempt at using ship board ADCP [2], which enable us to collect high density data of current velocity in time and space. They reported that ship motions due to surface waves have serious adverse effects on the ADCP data.

For avoiding surface waves which cause bad effects on collected data, under water vehicle is suitable. The ideal vehicle for housing ADCP might be free-swimming one for excluding the effect of surface waves completely, but we want to collect ocean data in a wide area of the sea and it prompt us to choose the towed vehicle system.

We developed a towed vehicle system DRAKE" (Depth and Roll Adjustable Kite for measuring Energy flux of Kuroshio) of which main wings and the tail wings are controled automatically to maintain the operation submerged depth and roll stability. To minimize the pitch motion, the best towing point is selected through the theoretical consideration.

In this report, the structure of DRAKE and results of on-site experiments are described.

2. Concept of DRAKE-ADCP system

In Fig.1 the schematic diagram of DRAKE system for ocean measurements is shown. The sensors housed in DRAKE are CTD (Conductivity, Temperature and Depth) sensor and the acoustic doppler current profiler (ADCP). ADCP is a powerful instrument that can measure vertical profiles of ocean currents.
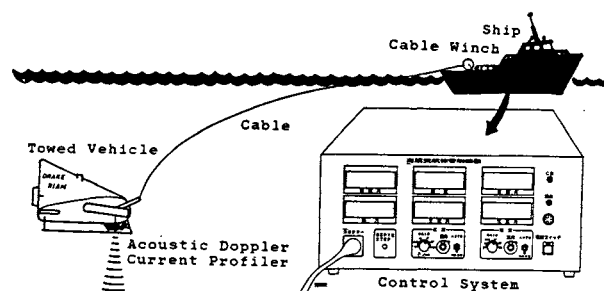
Fig.1 Schematic diagram of DRAKE and ADCP system

We choose a product of RD Instruments as the current profiler of which specifications is in Table 1.

The physical configuration of ADCP is shown in Fig.2. The length of ADCP is 1.8m and the weight in air is 80kg.

Table 1 Specification of ADCP

Acoustic frequency	150kHz
NO. of Acoustic beam	4 beams
Range of current measurement	250m/400m
Velocity range	10m/s
Number of depth cells	128
Accuracy	0.5cm/s
Dirrection accuracy	2°
Measurement interval	1~64kping

The operation principle of ADCP is described as follows [3]; The ADCP operates by transmitting short acoustic pulses into the water along the lines of position defined by one or more highly directional transducers. Four vertically inclined beams are used as illustrated in Fig.3. Backscattered sound from plankton, small particles, and small scale inhomogenities in the water is received by the transducer with a Doppler frequency shift proportional to the relative velocity between the scatterers and the transducer. A time series of measurements of the Doppler frequency shift after sound transmission produces a range segmented picture (or profile) of the water flow velocity versus range along the lines of position defined by the four beams. By knowing the precise beam geometry, three orthogonal current velocity components for each "depth cell" are computed by combining the measurements from any three of the four beams. Normally only the horizontal current profile is recorded as North & East current components as a function of depth. Each depth resolution cell represents the average current velocity through a horizontal "slice" of the water column in the region bounded by the four beams.

In the case that the instrument attitude and heading change within the measurement interval, the ADCP compensates the measured velocity data for each ping for instrument tilt and heading prior to vector averaging.

Due to the operation principle and on-site experiments [1], we can rely on the accuracy of ADCP mounted on sea bottom or on the stable platform. In the case that the ADCP is housed in a vehicle which is oscillated by external forces, the accurate measurement of ADCP attitudes is essential because the all collected data are transformed into North and East current component in ADCP by using the measured data of the attitudes and direction. For measuring the attitudes of ADCP, pendulum type tilt meters are used and they are disturbed by the accelerations of ADCP. Therefore the accelerations of motions of the vehicle must be minimized.
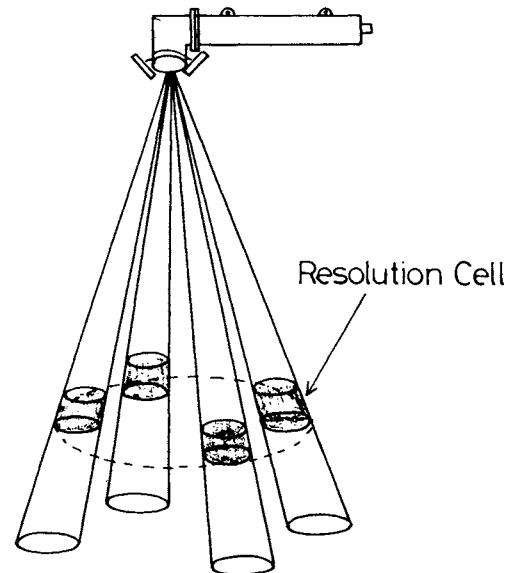
Fig.3 Illustration of resolution cell of acoustic beam of ADCP
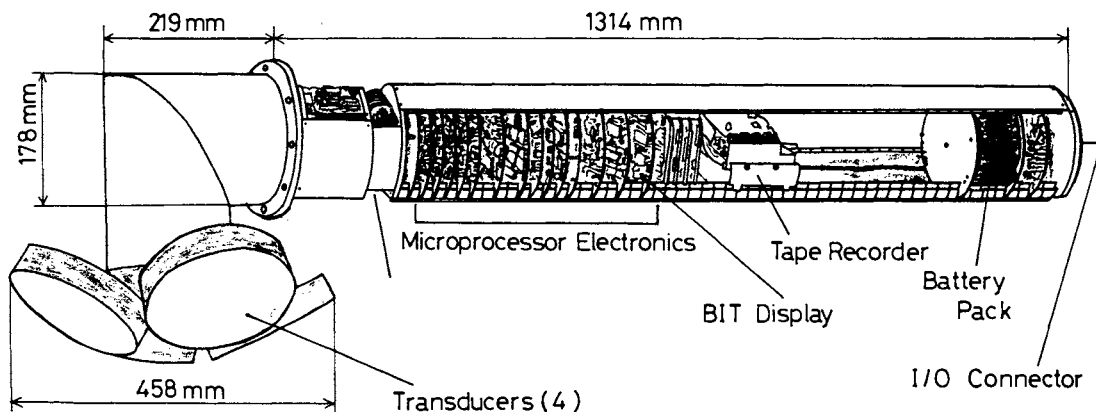
Fig.2 Physical configuration of ADCP

We have developed DRAKE system for the purpose of

o measuring ocean currents accurately even under severe sea states,
o collecting the data at wider range of the depth than the covering range of ADCP
o reducing the influence of cavitation noise generated by the ship's propeller,
o eliminating interference caused by bubbles entrained under ship's hull and
o using ADCP on unspecified research vessel.

The second, the third, the fourth and the fifth purpose will be achieved by just introducing the towed vehicle with the towing cable of an adequate length. For the purpose of the first one, motions of DRAKE must be minimized by designing the most suitable hull shape and a control system because of above mentiond reason. In addition to that, mother ship speeds must be measured accurately because the data of the current velocty obtained with ADCP are those relative to DRAKE and they should be transformed into the velocty relative to Earth by subtracting the advance speed of DRAKE. ADCP can measure its own velocity relative to Earth by bottom tracking in shallow water, but in deep water other methods of navigation must be used. Loran-C system is adopted in present experiments, but in future we plan to use the Grobal Positioning Sytem, which is much more accurate than Loran-C.

3. Structure of DRAKE

In Fig.4 we show a picture of DRAKE. The hull of DRAKE is made of Fiver Reinforced Plastic (FRP). The shape is stream line contour and its deep vertical contour is intended to increase the damping- and added mass-force for the roll in order to diminish the high frequency roll which is hard to control by horizontal tail wings. The main wings are symmetrical NACA 0010 airofoil Profile. The lower part contains ADCP and CTD sensor, so the shape of lower part is designed so as not to obstruct the acoustic beam of ADCP and the flow inlet for CTD sensor.

The towing cable is double armoured one with a pair of electric power conductors for supplying the electric power for sensors and ten signal conductors.

In Table 2 we show the principal dimensions of DRAKE system.
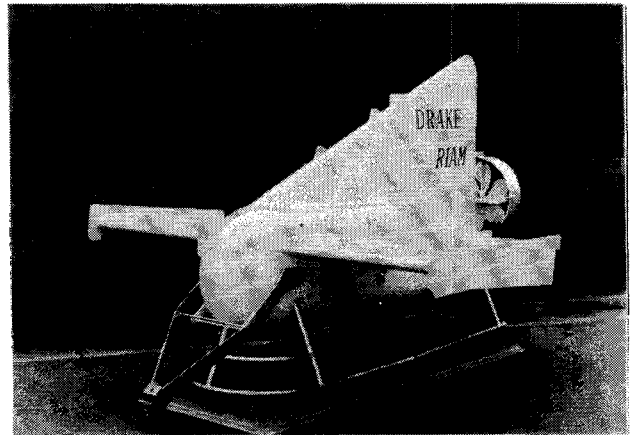
Fig.4 Figure of DRAKE

Table 2 Principal dimensions of DRAKE and towing system

DRAKE	
Operating depth	0~300m
Dimensions	L=2m, W=2m,H=1.5m
Air Weight	360kg
Towing Velocity	5~12knot
Depth control	By main wing
Roll control	By horizontal tail wing
Instrumentation	ADCP, CTD sensor
Towing cable	
Length	800m
Diameter	12.9mm
Breaking tension	9 ton
Conductors	Power conductor 1 pair Signal conductor 10
Cable winch	
Weight	2060kg
Dimensions	1.8m×1.8m×2.0m
Maximum reeling tension	1.5 ton
Maximum stopping tension	2.3 ton

In Fig.5 the perspective of DRAKE is shown. The impeller set at the tail end is coupled to a hydraulic pump and provides power for the actuation of main- and horizontal tail- wings. The idea of using a stream-driven impeller to generate hydraulic power is introduced in the development of "Batfish" by the Bedford Institute of Oceanography [4].

As shown in Fig.6, the electro-hydraulic actuator system is composed of a hydraulic pump driven by the impeller, oil filter, servomotor valves for controling wing actuaters. The control signals for the wing actuaters are sent from the controller set on a mother ship through the towing cable.
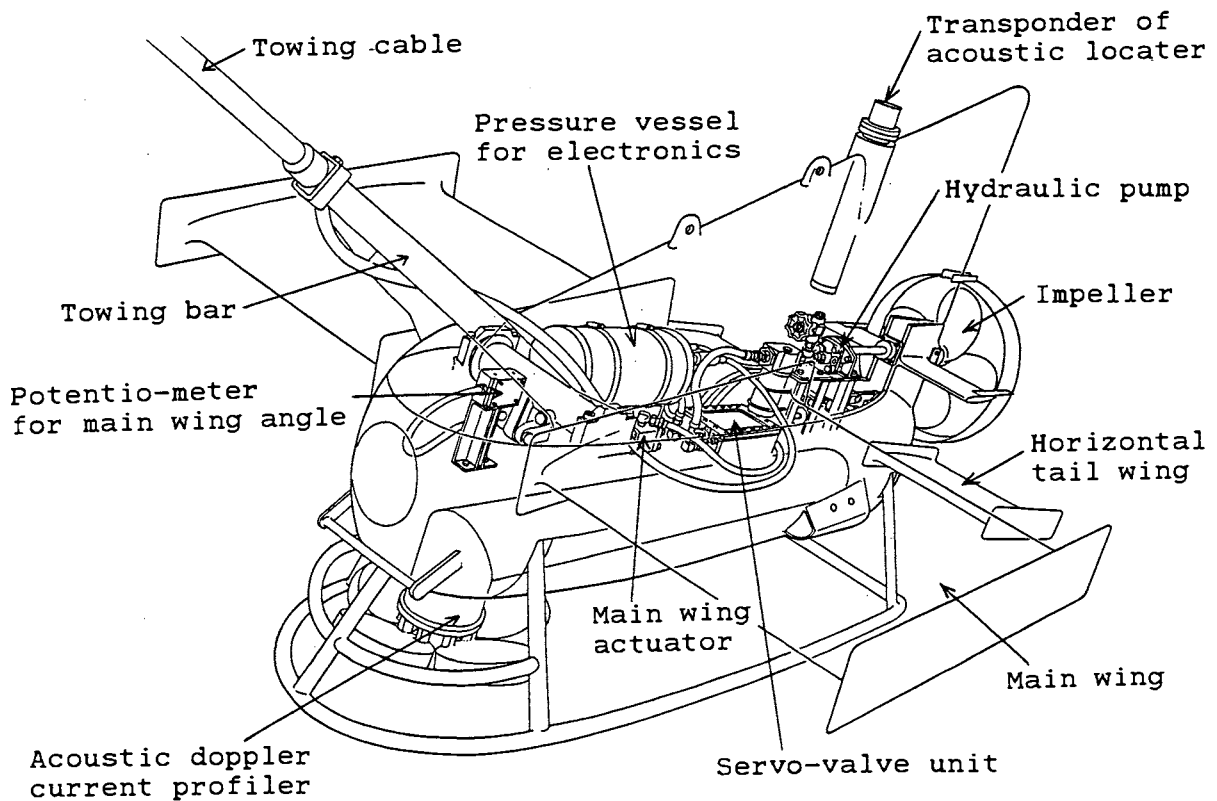
Fig.5 Perspective of DRAKE
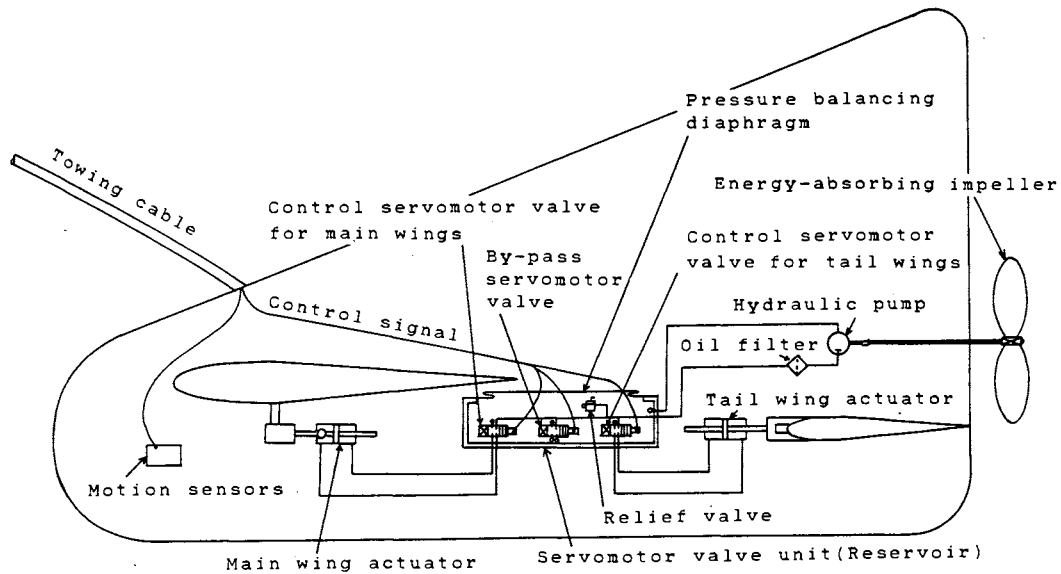
Fig.6 Schematic view of control system and hydraulic
circuit of DRAKE

4.On-site experiments

An on-site experiment was carried out to confirm the performance of DRAKE and the accuracy of the numerical simulation technics developed for estimation of motions of DRAKE and to show the validity of DRAKE-ADCP system in ocean measurements.

In Fig.7 the sea area for the experiments is shown. It is near the Tanegashima and the OKINAWA which are located south west part of Japan and near the Kuroshio. The submerged depth of DRAKE is measured with a pressure transducer mounted at the pressure vessel for electronics set inside the body where the pressure is equal to the outside static pressure. The pitch and roll angle are measured with a

pendulum type clinometers. The angles of main wings and horizontal tail wings are measured with potentiometers. The towing line tension is measured with a tension meter set at the towing winch on the quater deck of the mother ship. The location of DRAKE relative to the mother ship is measured with the acoustic locator system.

In Fig.8 the view of an experiment is shown. Expriments were carried out by a chartered ship of 500ton. The deployment of DRAKE was carried out with a hoist crane set on the quarter-deck of the mother ship and the towing winch is also set on the quater-deck.

Fig.8 A view of an experiment

In Fig.9 the static characteristics obtained from experiments are shown. The abscissa is the desired submerged depth of DRAKE. Hydrodynamic coefficients of DRAKE used in calculations were estimated from model experiments [5].

The circles indicate experimental results of main wing angle and the solid line is its calculated result. The squares and broken line show results of trim of DRAKE. The double circles and one dot chain line are the attack angle of main wings relative to the uniform flow. The triangles and two dot chain line are the results of the tension at the towing winch. This figure indicates the good accuracy of theoretical estimations in the static problem.

Fig.7 Sea area around Kuroshio
for experiments
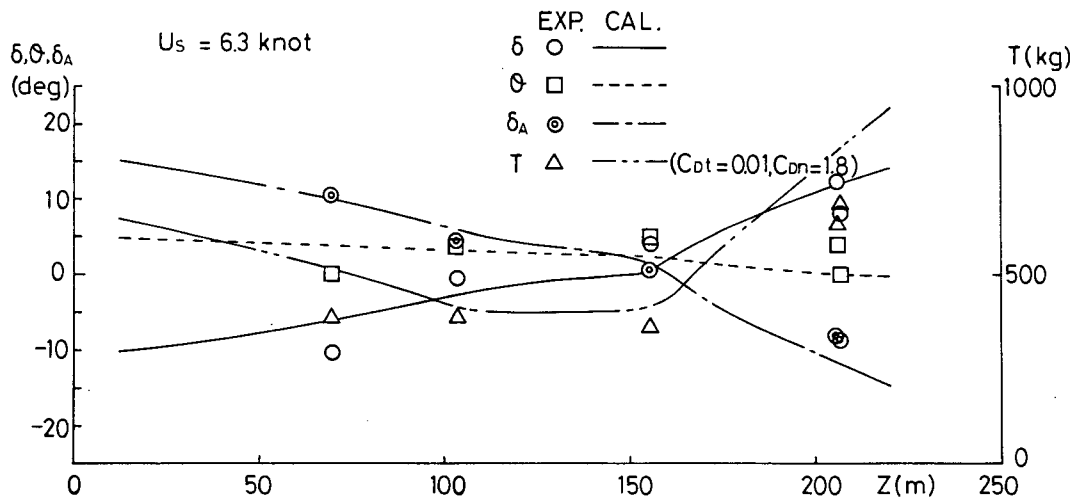
Fig.9 Static characteristics of DRAKE (6knot,Experimental results)

In Fig.10, we show time series of motions of DRAKE. The towing speed of this case is 12knots. The motions of mother ship caused by surface waves induce tension variations of the towing cable, and they cause motions of DRAKE. The calculation results indicated by broken lines in the figure are obtained by using three dimensional lumped mass method for cable dynamics and six-degree-freedom equation for motions of DRAKE [5]. T indicates the towing tension. Z is the submerged depth or heave of DRAKE, δ is the main wing angle, γ is the horizontal tail angle. The measured and calculated values of the amplitude of heave and roll of DRAKE is almost zero, but the measured value of the pitch is greater than expected one. We used a pendulum type sensor for measuring the pitch of DRAKE, therefore, the accelaration of the surge has a great effect on the measured value of the pitch. If we want to avoid this effect, we have to use the gyroscope type motion sensor for measuring the pitch of DRAKE. We can use it for measuring the motions of mother ship, but it is difficult to use it for DRAKE because it requires the great amount of electric power and space. The theoretical calculations suggests that the pitch angle is much smaller than the measured one.

In Fig.11 we show the comparisons between the power spectrums of motions of ship and DRAKE. The heave and roll of DRAKE are much smaller than those of the mother ship, but the pitch of DRAKE is rather greater than that of the ship. We have to improve the measuring system of the pitch of DRAKE. We did not measure the surge, sway and yaw of DRAKE, but the theoretical analysis suggests that the sway and yaw of DRAKE is much smaller than those of the mother ship, the surge of DRAKE is smaller than that of ship but it is greater than the sway

or yaw and the ratios of motions of DRAKE and the ship decrease with the increase of the incident wave height.
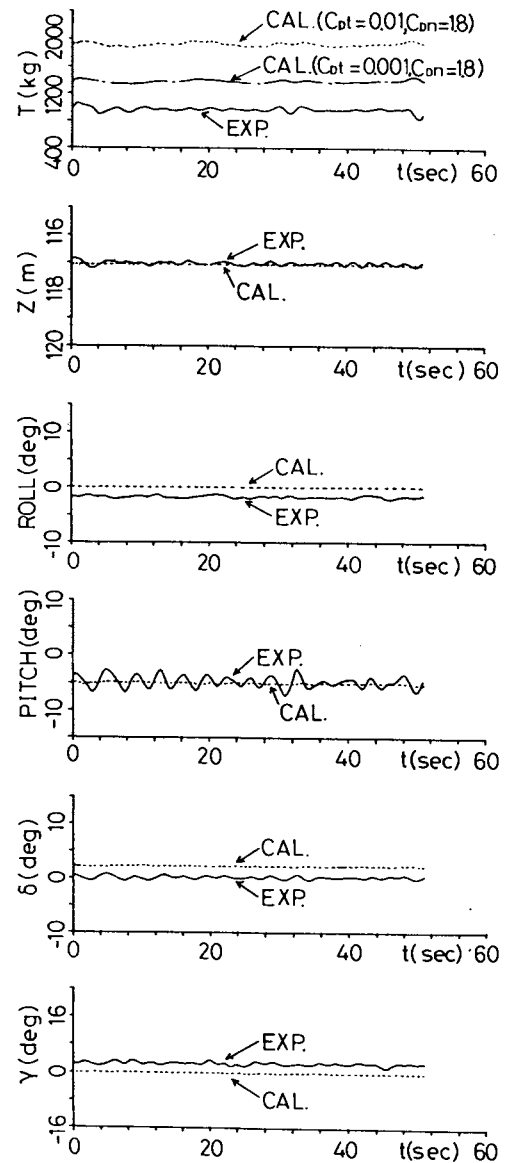
Fig.10 Time series of motions and towing tension of DRAKE (Experimental results)
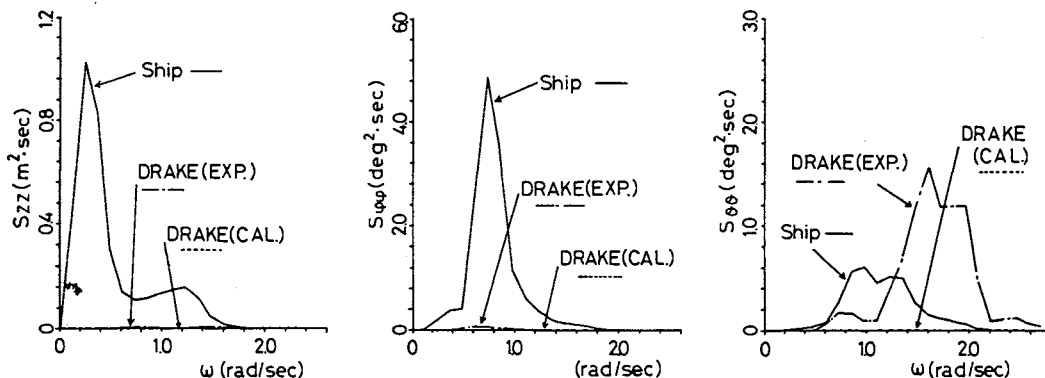
Fig.11 Power spectrums of motions of mother ship and DRAKE (Experimental results)
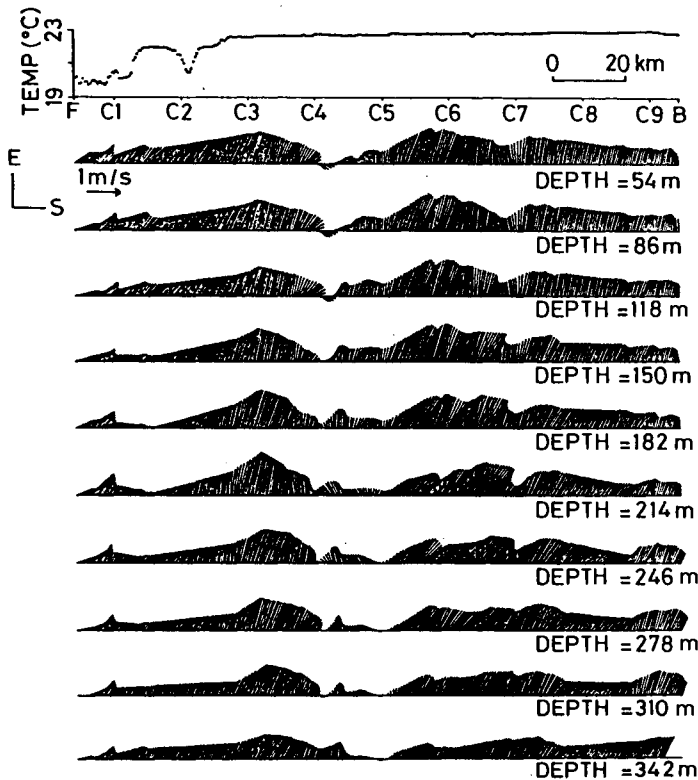
Fig.12 Velocity distribution of the Kuroshio
obtained by using ADCP and DRAKE system

Fig.13 Submerged buoy system
for ocean measurements

In Fig.12 we show the velocity distribution of the KUROSHIO obtained with DRAKE and ADCP system. The disturbances in the velocity distribution are caused by the small ilands. The velocity distribution in an ocean current are usually obtained from the geostrophic calculation by using the measured vertical profile of water temperature and salinity. This procedure is indirect and ,therefore, the results are considered to be suspicious. We have developed submerged buoy systems which can measure the current velocity at several points along the mooring line [6]. We can collect the continuous velocity data for one year or more by using this submerged buoy system (Fig.13). The submerged buoy system has an advantage over the towed vehicle system with ADCP in the view of the continuous measurement. The data obtained with the towed vehicle and ADCP are excellent in the point of the spatial continuity. The towed vehicle system with ADCP and the submerged buoy system are complementary to each other in the measurements of ocean currents.

5.Conclusions

An on-site experiment was carried out to confirm the performances of a towed vehicle system with ADCP. The main conclusions obtained from the experiments are written as follows;
1) Motions of the towed vehicle are much smaller than those of the mother ship.
2) The depth and roll of the towed vehicle are controled perfectly even in the high speed towing.
3) The calculated results obtained by using the three dimensional numerical simulation technique show good agreements with experimental results.
4) The towed vehicle system with ADCP is very useful for measurements of ocean currents.

Acknowledgment

References

1. Lhermitte, R., "Doppler sonar observation of tidal flow", Journal of Geophysical Research, No.88(1982)
2. Joyce, T.M., et al, "Shipboard acoustic profiling of upper ocean currents", Deep-Sea Research, No.903(1982)

3. RD Instruments,"A catalog of acoustic doppler current profilers".
4. Dessureault, J.G., "-Batfish- A depth controllable towed body for collecting oceanographic data," Ocean Engineering Vol.3(1976)
5. Koterayama, W., et al, "Motions of a depth controllable towed vehicle," The proc. of the 7th International Conference on Offshore Mechanics and Arctic Engineering(1988)
6. Kawatate, K., et al, "A subsurface buoy system for measuring the Kurosio" proc. of the 5th International Conference on Offshore Mechanics and Arctic Engineering(1986)

MARINE RESOURCE DEVELOPMENT

THE SERUM BACTERICIDAL ACTIVITY: A POSSIBLE INDICATOR AS CRUSTACEAN HEALTH CONDITIONS

R. Ueda, H. Sugita, Y. Deguchi

Department of Fisheries, Nihon University, Tokyo, Japan

Abstract

Serum bactericidal activity of Japanese spiny lobster Panulirus japonicus, which was reared under various conditions, was examined. The activity was influenced by low salinity of rearing water while water temperature ranging from 13 to 28℃ and starvation for 14 days did not cause effective decrease or increase of the activity. Additionally, effect of transportation on the bactericidal activity varied with transporting media, including air, seawater and sawdust. These results suggest that the serum bactericidal activity of coastal Crustacea changed according to the physiological condition of animal individuals, and possibly become an indicator as crustacean health conditions. Moreover, an electron microscopic observation revealed that the serum bactericidal activity of the Japanese spiny lobster is attributed to a lytic phenomenon.

1. Introduction

Marine Crustacea include a lot of economically important species, some of which are cultured in many countries including Japan. In intensive farms, however, diseases often occur and result in serious losses. It, therefore, seems to be of significant importance to obtain the information on the health condition of culture animals.

Many invertebrates possess humoral and/or cellular defense mechanisms such as agglutinin, bactericidin and phagocytes [1-5]. We already reported that Japanese coastal crustaceans possess naturally occurring both agglutinin and bactericidal activity against bacterial cells in their hemolymph [6]. The present study was undertaken to evaluate the serum bactericidal activity, as an indicator of health conditions of crustaceans, which were exposed under various environmental conditions.

2. Materials and Methods

2.1 Animals

Specimens of Japanese spiny lobster Panulirus japonicus (85 to 132 g body weight) were caught by gill nets around Shimoda, Shizuoka Prefecture, Japan. All alive specimens were transferred to the Shimoda Marine Laboratory, Nihon University and acclimated in the aerated-running seawater tanks (200 to 1000 l in capacity) for at least three days prior to the experiment.

2.2 Serum Preparation

After body surface of each specimen was swabbed with 70% ethanol, hemolymph was collected by a sterile syringe from the pericardial sinus, and then transferred into a sterile test tube. Serum was obtained by allowing the hemolymph to clot and breaking the cloting with a sterile glass stick, followed by centrifugation at 4000 rpm for 15 min.

2.3 Preparation of Bacterial Cells

Vibrio sp. V-8 strain, which was isolated from the gut content of a shore crab Plagusia dentipes, was used as the target cell since the previous study [7] indicated that this strain reacted strongly with coastal crustacean sera. The strain was aerobically incubated on PYBG agar [5] at 25℃ for 2 days. After being harvested by centrifugation, cells were washed three times with PBS (pH 7.0) and then prepared at the concentration of 5×10^4 cells/ml in 2% NaCl-PBS.

2.4 Assay Method for Bactericidal Activity

To determine the bactericidal activity, 0.1 ml of alive bacterial suspension was added to 0.7 ml of 2% NaCl-PBS plus 0.2 ml of serum, and the mixture was incubated at 25℃ for 2 hr. Control, in which the same volume of the bacterial suspension was added to 0.9 ml of 2% NaCl-PBS, was also incubated similarly. The surviving bacteria were counted on the PYBG agar after incubated at 25℃ for 2 days. The bactericidal activity was calculated as the $\log_{10}$ CFU (colony forming units per ml) in the control minus the $\log_{10}$ CFU with serum.

2.5 Effect of Various Rearing Conditions on Serum Bactericidal Activity

To determine the effect of water temperature and starvation on serum bactericidal activity, animal specimens were reared for 14 days at the water temperature ranging from 13 to 28℃, with or without the feeding. Both before and after the experiment, hemolymph was withdrawn from each specimen.

To analyze the effect of low salinity of the rearing water on serum bactericidal activity, animals were exposed to 70% seawater and reared for 14 days at 20℃. Hemolymph was withdrawn at 0 and 18 hr, and 14 days after the experiment. Moreover, health index of specimens was measured simultaneously according to Nishimura et al. [8].

To determine the effect of alive transportation on the bactericidal activity, animals were stored in the container including air, seawater or sawdust as transporting media, and transported 280 km for 8 hr by an automobile. Both before and after transportation, hemolymph was withdrawn from each animal specimen.

2.6 Ultrastructure of Bacterial Cells Reacted with Spiny Lobster's Sera

A transmission electron microscope was used for analysis of serum bactericidal phenomenon. At 0, 15, 30 and 60 minutes after the Vibrio sp. V-8 strain reacted with the Japanese spiny lobster's serum, the mixture was fixed for 3 days at room temperature according to Ueda et al. [9]. Some samples were also fixed by Kellenberger's method [10] to observe fine structure of DNA. These were followed by dehydrated with a graded series of ethanol, embedded in epoxy resin according to Ueda et al. [9] and analyzed by using a Hitachi HS-9 transmission electron microscope.

3. Results

3.1 Effect of Water Temperature and Starvation on Serum Bactericidal Activity

Serum bactericidal activity, against the Vibrio sp. V-8 strain, of the Japanese spiny lobster which were reared for 14 days at various water temperatures, with or without feeding, is shown in Table 1. It was found that the activity was not significantly influenced by the water temperature ranging from 13 to 28℃ while the starvation for 14 days may slightly influence the activity, except for the specimen kept at 20℃.

Table 1. Serum bactericidal activity against the Vibrio sp. V-8 strain, of the Japanese spiny lobster reared for 14 days at various water temperatures, with or without the feeding

Water temp.	Feeding	0 day	14 days
13℃	Fed	2.40±0.29*	2.18±0.21
	Starved	2.05±0.57	1.73±0.61
20℃	Fed	1.93±0.55	2.11±0.50
	Starved	2.07±0.79	2.07±0.63
25℃	Fed	2.33±0.26	2.19±0.16
	Starved	1.79±0.72	1.40±0.68
28℃	Fed	1.80±0.74	1.75±0.62
	Starved	1.77±0.53	1.35±0.84

*Mean ± standard deviation of bactericidal activity of 5 specimens.

3.2 Effect of Low Salinity on Serum Bactericidal Activity

Serum bactericidal activity, against the Vibrio sp. V-8 strain, of the spiny lobster which were reared in 70% seawater for 14 days, is shown in Table 2. At 18 hr after a total of 18 specimens of the animal were exposed to 70% seawater, 15 specimens showed the decrease in serum bactericidal activity or died whereas the activity of three remaining specimens increased. After 14 days, only three specimens could recover their activity to the initial level. Fig. 1 shows that there was positive relationship between the increasing activity and the rising health index in the 14 day-specimens while the activity varied with the specimen, even, at the same stage of health index.

Table 2. Serum bactericidal activity against the Vibrio V-8 strain, of the Japanese spiny lobster at 0 and 18 hr and 14 days after the exposure to 70% seawater

Specimen	0 hour	18 hours	14 days
1	3.04 (A) [*1]	2.87 (B)	2.08 (A)
2	2.51 (A)	0.41 (D)	2.45 (A)
3	2.08 (A)	– [*2] (E)	–
4	2.19 (A)	2.57 (D)	1.31 (D)
5	3.04 (A)	2.87 (B)	– (E)
6	0.86 (A)	0.51 (D)	– (E)
7	3.04 (A)	– (E)	–
8	2.16 (A)	0.44 (D)	0.33 (D)
9	2.16 (A)	2.87 (C)	2.49 (A)
10	3.04 (A)	1.87 (C)	0.86 (D)
11	3.12 (A)	2.39 (D)	– (E)
12	3.12 (A)	– (E)	–
13	3.12 (A)	0.73 (C)	– (E)
14	2.34 (A)	– (E)	–
15	1.79 (A)	1.85 (C)	2.05 (A)
16	2.97 (A)	1.00 (D)	0.71 (C)
17	2.87 (A)	1.08 (C)	1.72 (B)
18	3.12 (A)	1.85 (B)	1.77 (A)

[*1] Bactericidal activity (Health index according to Nishimura et al. [8] : A, very active; B, active; C, weak; D, moribund; E, died).
[*2] Not determined.
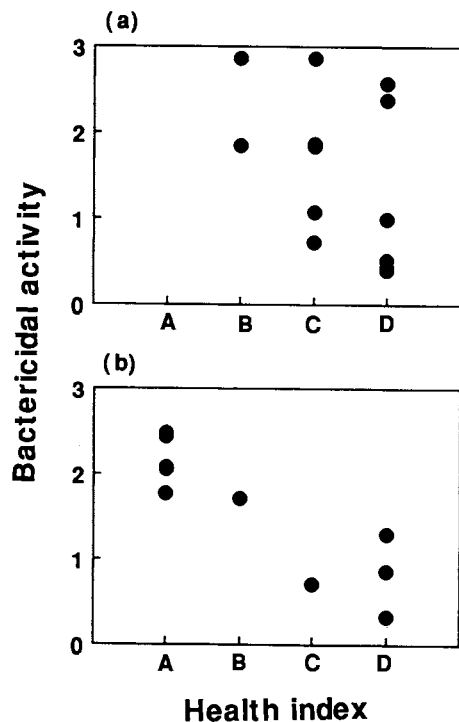
Fig. 1. Serum bactericidal activity against the Vibrio sp. V-8 strain at different stages of the health index of the Japanese spiny lobster exposed to 70% seawater: (a) 18 hr and (b) 14 days after the animals were exposed to 70% seawater.

3.3 Effect of Transportation on Serum Bactericidal Activity

Serum bactericidal activity, against the Vibrio sp. V-8 strain, of the spiny lobster which were transported by an automobile in three defferent media is shown in Table 3. The activity was not significantly influenced when the animals were stored in the seawater but decreased prominently in the specimen stored in the sawdust and only the air.

Table 3. Serum bactericidal activity against the Vibrio sp. V-8 strain, of the Japanese spiny lobster transported by an automobile

Medium in container	Before transportation	After transportation
Seawater	1.82±0.97[*]	1.83±1.06
Sawdust	2.15±0.94	1.48±1.16
None (air)	2.09±0.86	1.30±1.09

[*]Mean ± standard deviation of 8 specimens.

3.4 Ultrastructure of the Bacterial Cells Reacted with Spiny Lobster's Sera

Ultrastructure of bacterial cells at 0, 15, 30 and 60 minutes after reacted with the serum from Japanese spiny lobster is shown in Photos 1-6.

At time zero (control): the cell wall was covered with a cell coat, perhaps lipo-polysaccharides, and the cytoplasm was filled with ribosomes (Photo 1).

After 15 minutes of tratment: the cell coat disappeared, and the cell wall was partly broken and high density-masses appeared in the cytoplasm (Photo 2). The Kellenberger's fixation [8] strongly indicated that the high density-mass was the aggregate of DNA (Photo 3). Moreover, some vacuole-like structures and round structures were observed in the cytoplasm and on the cell wall, respectively. The fact that these materials possess the multi-lamellar structure strongly suggests that they were phospho-lipids (Photo 4).

After 30-60 minutes of treatment: The ribosomes and aggregates of DNA were partly melted and decreased. Both the cell wall and membrane were partly broken, resulting in the flux of DNA and cytoplasm (Photos 5 and 6).

—335—

4. Discussion

In the previous paper [6], we reported that Japanese coastal Crustacea possess naturally occurring both agglutinin and bactericidin, as self-defense agents, in their hemolymph. However, these activity varied significantly with the specimen, thereby suggesting that these activity correspond to the physiological condition of animal specimens. In the present study, therefore, the Japanese spiny lobster reared in various suspected stressful conditions, were examined for the serum bactericidal activity as an indicator of crustacean health conditions.

As shown in Tables 1-3, the bactericidal activity was influenced by the low salinity (70% seawater) of rearing water and the alive transportation after stored in the sawdust and only the air as transporting media, whereas the activity was influenced significantly neither by the water temperature ranging from 13 to 28℃ nor the starvation for 14 days. These results suggest that the low salinity of rearing water and the alive transportation become stressers for coastal crustaceans. Spencer et al. [11] reported that the gill NaK-ATPase activity of coastal crabs increased when the animals were exposed to diluted seawater. This result reveals that the diluted seawater was stressful for the Crustacea.

As shown in Fig. 1, it was found that there was positive relationship between the increasing activity and the rising health index in the 14 day-specimens whereas such relation was not observed at 18 hr after the experiment. Nishimura et al. [8] reported that the health index of Japanese spiny lobster decreased first and then recovered after 18 hr of exposure to diluted seawater if the animal specimen could adapt to the environment. As a result the 14 day-specimens can be divided into two types: (i) adapted specimens (A and B of health index) and (ii) stressed ones (C and D). These results suggest that the serum bactericidal activity of Japanese spiny lobster changes according to the physiological conditions of animal specimens, and can become an indicator as crustacean health conditions. Farther studies along those lines are now in progress.

On the other hand, there was no information on the mechanism of the bactericidal phenomenon although much were known that Crustacea possesses the bactericidin in their hemolymph [2-4].

In the present study, therefore, the ultrastructure of the bacterial cells after reacted with the lobster's serum were examined by electron microscopy. As shown in Photos 1-6, the lytic phenomenon of bacterial cells was observed with the degradation of DNA and the melting of cell wall and cell membrane. This result indicated that the serum bactericidin of Japanese spiny lobster is a lysozyme as reported in other invertebrates [12].

References

1. Johnson, P.T. and Chapman, F.A., "Comparative studies on the in vitro response of bacteria to invertebrate body fluids II. Aplysia californica (sea hare) and Ciona intestinalis (tunicate)", J. Invertebr. Pathol. Vol.16, p.259 (1970)
2. Pistole, T.G. and Britko, J.L., "Bactericidal activity of amebocytes from the horseshoe crab, Limulus polyphemus", J. Invertebr. Pathol. Vol.31, p.376 (1978)
3. Evans, E.E., Cushing, J.E., Sawyer, S., Weinheimer, P.F., Acton, R.T. and McNeely, J.L., "Induced bactericidal response in the California spiny lobster, Panulirus interruptus", Proc. Soc. Exp. Biol. Med. Vol.132, p.111 (1968)
4. Stewart, J.E. and Zwicker, B.M., "Natural and induced bactericidal activity in the hemolymph of the lobster, Homarus americanus: products of hemocyte-plasma interaction", Can. J. Microbiol. Vol.18, p.1499 (1972)
5. White, K.N., Ratcliffe, N.A. and Rossa, M., "The antibacterial activity of haemocyte clumps in the gill of the shore crab, Carcinus maenas", J. Mar. Biol. Ass. U.K. Vol.65, p.857 (1985)
6. Ueda, R., Sugita, H. and Deguchi, Y., "Naturally occurring agglutinin and bactericidal activity in the hemolymph of coastal crustacea", Proceedings of the Second Asian Fisheries Forum. p.461 (1990)
7. Sugita, H., Tanaami, H., Kobashi, T. and Deguchi, Y., "Bacterial flora of coastal bivalves", Bull. Jpn. Soc. Sci. Fish. Vol.47, p.655 (1981)
8. Nishimura, K., Yoshida, K. and Saitoh, M.,"Tolerance of low salinity water by the Japanese spiny lobster, Panulirus japonicus", Suisanzoshoku. Vol.20, p.79 (1972) (in Japanese)
9. Ueda, S., Ishii, N., Matsumoto, S., Hayashi, K. and Okayasu, O., "Ultrastructural studies on surface lining layer (SLL) of the lungs: part II", J. Jap. Med. Soc. Biol. Interface. Vol.14, p.24 (1983)

10. Kellenberger, E., "The tenth of the society for general microbiology (W. Hayes and R.C. Clowes ed.)", Microbial Genetics, Cambridge at Univ. Press. (1960)
11. Spencer, A.M., Fielding, A.H. and Kamemoto, F.I., "The relationship between gill NaK-ATPase activity and osmoregulatory capacity in various crabs", Physiol. Zool. Vol.52, p.1 (1979)
12. Anderson, R.S. and Cook, M.L., "Induction of lysozymelike activity in the hemolymph and hemocytes of an incect, Spodoptera eridania", J. Invertebr. Pathol. Vol.33, p.197 (1979)
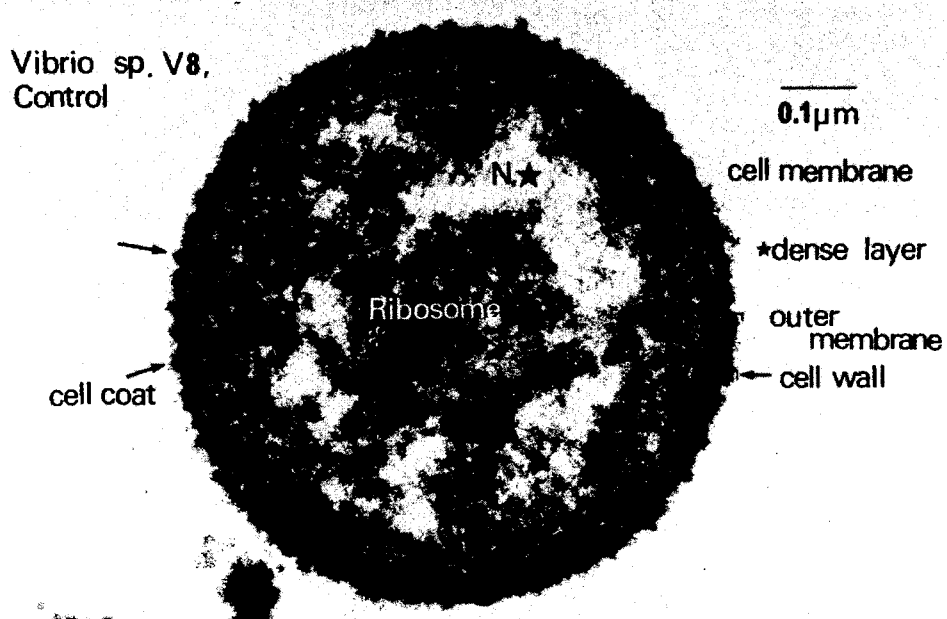
Photo 1. Ultrastracture of the Vibrio sp. V-8 strain (control).
★N: nuclear region.
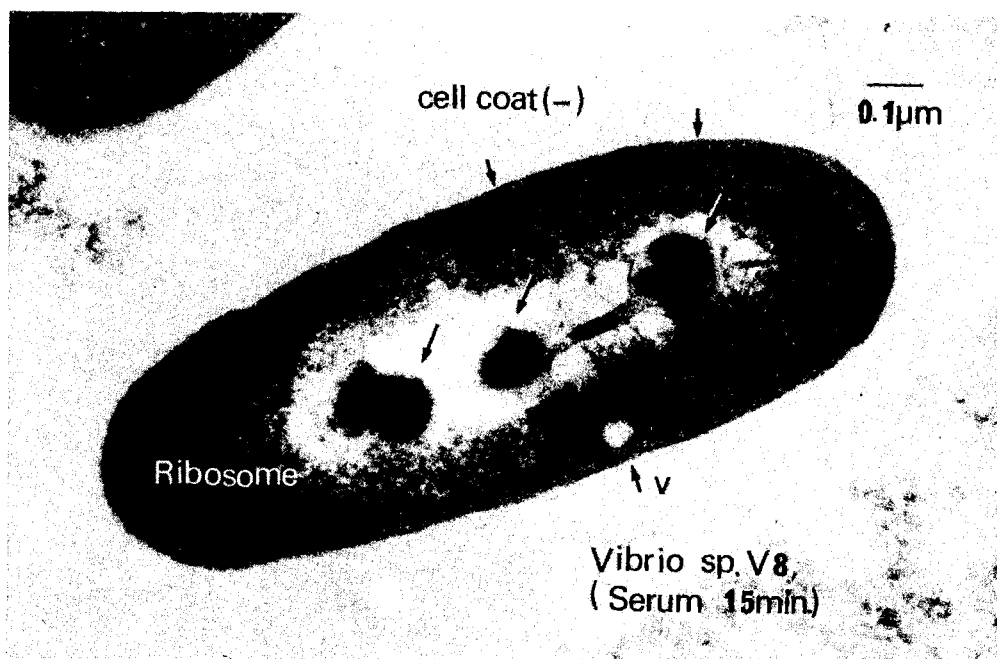
Photo 2. Ultrastructure of the Vibrio sp. V-8 strain at 15
minutes after reacted with the serum of the Japanese
spiny lobster. V: vacuole-like structure.
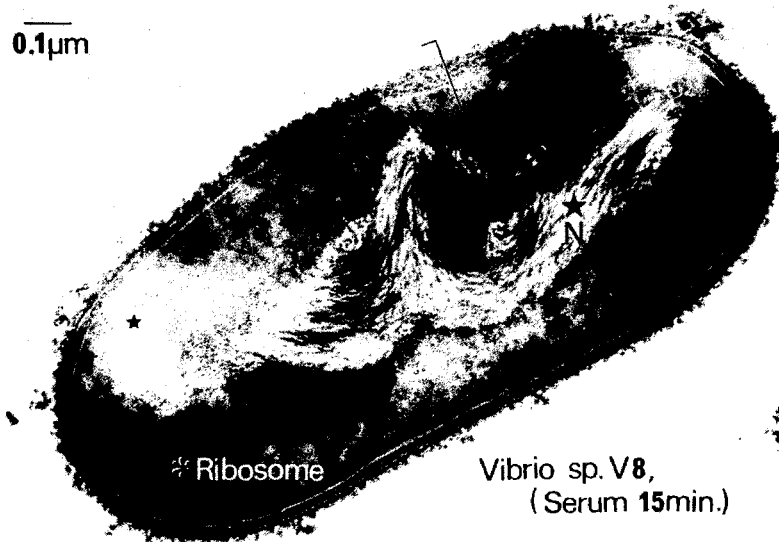
photo 3. Ultrastructure of the Vibrio sp. V-8 strain which were
          fixed by Kellenberger's method [8] , at 15 minutes after
          reacted with the serum of the Japanese spiny lobster.
          ★N: nuclear region. Arrow shows the aggregate of DNA.
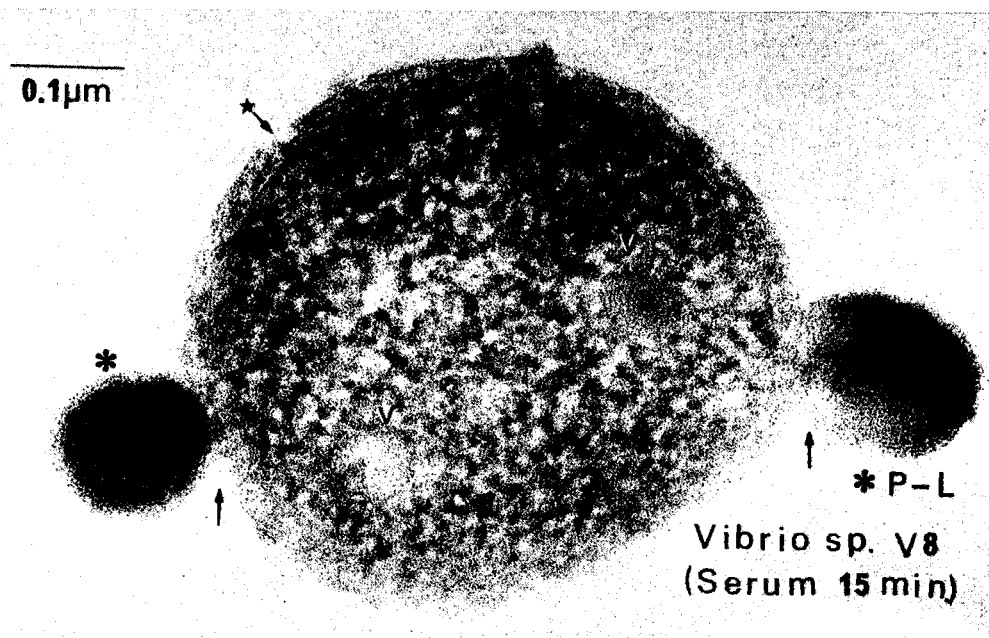
Photo 4. Ultrastructure of the Vibrio sp. V-8 strain at 30
          minutes after reacted with the serum of the Japanse
          spiny lobster. V: vacuole-like structure; *: phospho-
          lipids. Arrow shows that cell wall was partly broken.

—339—

0.1μm

Ribosome + DNA

DNA

N★

Vibrio sp. V8, (Serum 60min.)
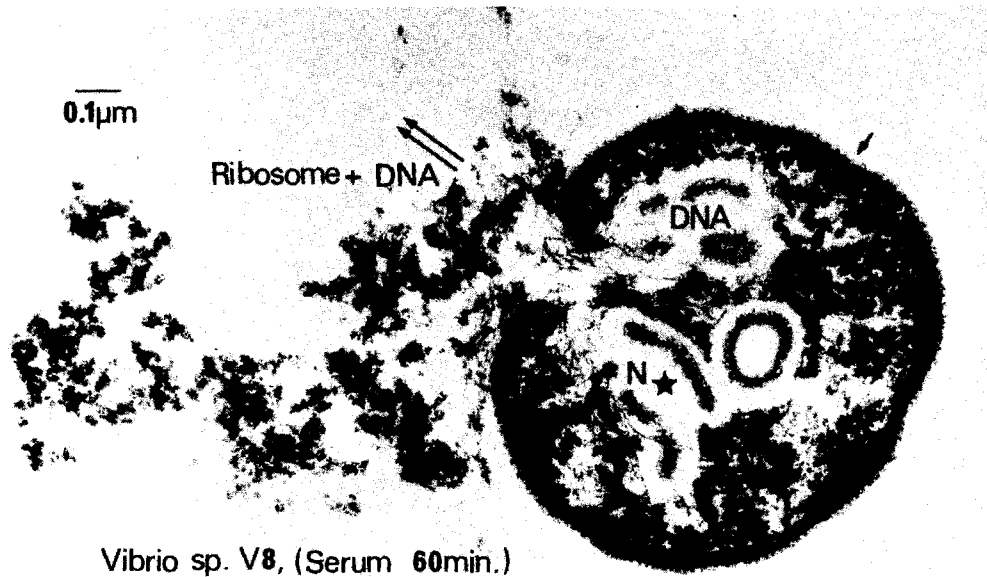
Photo 5. Ultrastructure of the Vibrio sp. V-8 strain at 60
minutes after reacted with the serum of the Japanese
spiny lobster. ★N: nuclear region. Arrow shows the
out-flow of both ribosomes and DNA.

Vibrio sp. V8,
(Serum 30min.)

DNA

cell coat

N★

0.1μm
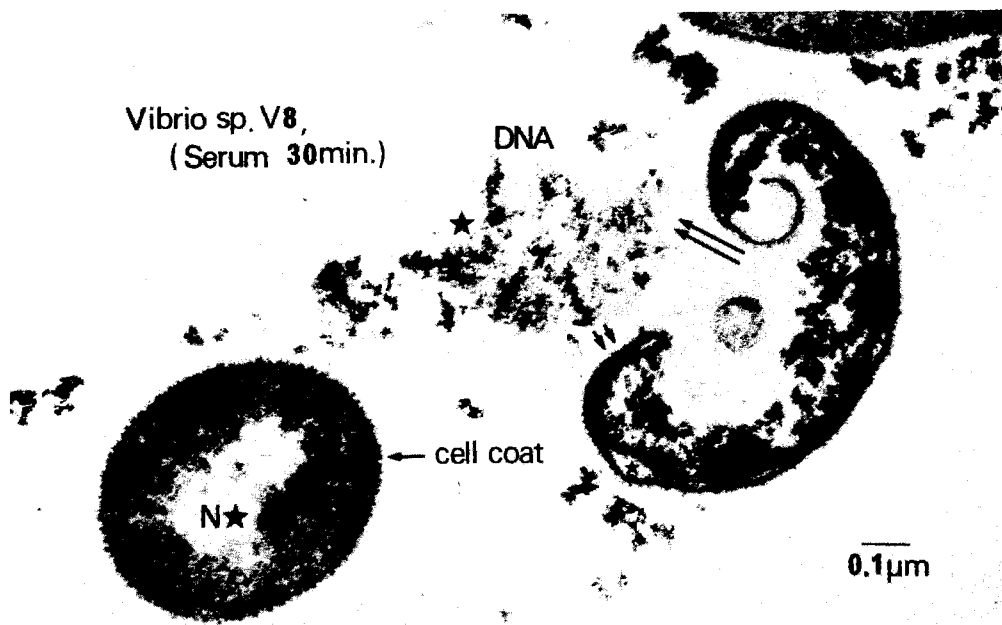
Photo 6. Ultrastructure of the Vibrio sp. V-8 strain 30 minutes
after reacted with the serum of the Japanese spiny
lobster. ★N: nuclear region.

A STUDY ON ARTIFICIAL FISHREEF STRUCTURE IN SHALLOW WATER

Kenji Arai

Fisheries Laboratory Kawasaki Office Mikuniya Corp., Japan

ABSTRACT

The shallow water in the Japan set up the artificial fish reefs of the goverment's policy start to 1959 from continuation . The fishes schooling system of artificial fish reef was not a definite , many students state various opinion . However , the effect (many fishes schooling) of artificial fish reef recognize fishermen . Several type artificial fish reefs in the Niigata and Shizuoka Pref., obseved to SCUBA (self-contained underwater breathing apparatus) diving on fish fauna . The observation was each artificial fish reef , underwater recorded on the position , total length , number of fishes . The each fish species was division type of observation fish species , convesion weight from total length . An artificial fish reef was total volume 27 ,32 ,50 m³ (inside are empty) , unit volume of fish school at 196 to 42 kg/m³ . The fish school volume on an artificial fish reef have been thinkable the inside structure than the total volume and the outside structure .

METHODS

The examine was diving observation of fish school at several type artificial fish reef in the shallow water Ohgata Town Niigata Pref. and Maisaka Town Shizuoka Pref.(Fig.1) .

The artificial fish reefs in the shallow water Ohgata Town befor the 1 year set up the sand bottom , Poly-con type fish reefs 4 set (27 m³ type 2 set , 32 m³ type 2 set , Fig.2) ,Trapezoid type artificial fish reefs 2 set (1 set 25 m³, Fig.3) .   A Poly-con type artificial fish reef was inside small and large structure .

The Sonicylindrial type artificial fish reefs 2 set (1 set, 150 m³,Fig.4), and a Poly-con type artificial fish reef (155 m³, Fig.2) at observation dived , depth 46 m set up on the sand bottom in the Ohgata Town shallow water .

The artificial fish reef in the shallow water Maisaka Town Shizuoka Pref. set up on the sand bottom , Ordinary artificial fish reef (1 place, 100 pieces , 337.5 m³, Fig.5) after 1 to 3 years set up depth 30, 36, 37 m of 3 places , the Poly-con type artificial fish reefs set up depth 46 m (1 set 423 m³, Fig.2), 36 m 2 set (1 set 124 m³, Fig.2) .

The observation of fishes went to a artificial fish reef point on fishing boat , after mooting , tow persons diver at the same time , the

subject diving to observed fish fauna etc. .
The observation was on the artificial fish reefs
inside and around within 5 m , each fish species
observed number of fishes , total length ,
attracted position etc. . In the water
observation recorded on the white vinyl chloride
board by pencil , at the same time take a
photograph of artificial fish reef on fish fauna
attracted .

The artificial fish reef structure by
observation result was examination different
from fish species and fish school volum , study
on artificial fish reef structure of fish fauna
many attracted .

Fig.2　Poly-con type artificial fish reef (merchandise name) :
Industrial waste of polyethlene sheet fragment and heat up
sand made compress cast on mold in the with poly-con board
of height 1.05 m , width 1.05 m , thick 0.05 m , and
poly-con pollar inside steel pipe of height 0.06 m , width
0.06 m , leength 5.5 m . Consequently , poly-con type
artificial fish reef putt together total volum to 5 m³
from 423 m³ , height 1~10 m .
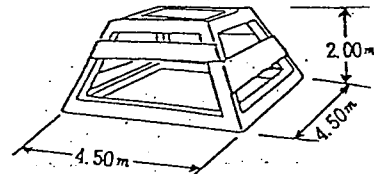
Fig.1　Fish school obseved to diving , Artificial fish reef
position in the Ohgata Town Niigata Pref.
and the Maisaka Town Shizuoka Pref. shallow water

Fig.3　Trapezold type artificial fish reef (merchandise name) :
Cement concrete mad cast on mold in the plant .
Trapezold type artificial fish reef putt together total
volum 50 m³ , height 2.0m .
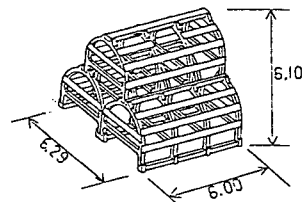
Fig.4　Semicylindrial type artificial fish reef (merchandise
name) : Cement concrete mad cast on mold in the plant .
Semicylindrial type fish reef putt together total volum 300
m³ , height 5.5 m .
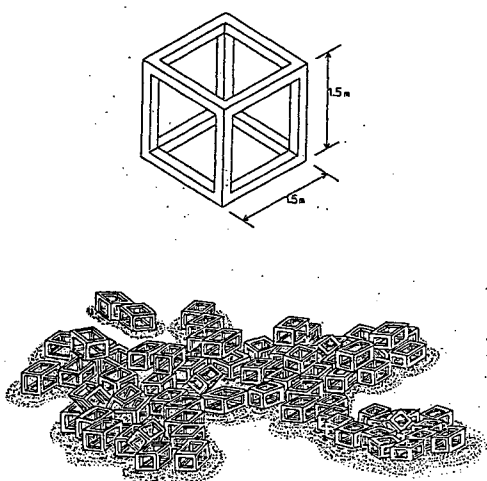
Fig. 5 Ordinary artificial fish reef : Cement concrete mad cast
on mold in nearby a fishing port yard .
A ordinary artificial fish reef was about 3.4 cubic meter ,
inside empty cube . Many ordinary artificial fish reef
randam sunk on the sink point , randam piled up high .

RESULT

(1).Ohgata Town Niigata Pref.

Ohgata Town Niigata Pref. in the shallow water
of the artificial fish reefs was depth 26 , 46 ■
of 2 point (Fig. 1) , the enviroment
conditions of current etc. from the monotonous
shore line was about the same .   Diving
observation was three times in June , July ,
August , each artificial fish reefs dived two to
six time .

The observation result not damage to
artificial fish reefs .   The artificial fish
reefs set up the bottom of the depth 26 ■ fine
sand , 46 ■ soft sand , that around the bottom
exist as ditch at depth 0.5 to 0.7 ■ , width 2.0
to 3.0 ■ .

The current at observation diving was the flow

of June about SW to NE , July NE to SW or SW to
NE , August SW to NE along a depth contour.

The observation fish fauna of each artificial
fish reefs have been observed on each 8 to 18
species , total 28 species .   The observation
fishes was division type from behavioure of
Migrant fishes , Settlement fishes , the Other
fishes .

The depthe 26 ■ of artificial fish reefs Ⅰ to
Ⅴ have been observed Ⅰ on 16 species (M.f. 3
species, S.f. 7 species, t.O.f. 6 species) , Ⅱ
on 11 species (M.f. 2 species, S.f. 6 species,
t.O.f. 3 species) , Ⅲ on 17 species (M.f. 3
species, S.f. 11 species, t.O.f. 3 species) ,
Ⅳ on 18 species (M.f. 3 species, S.f. 11
species, t.O.f. 4 species) , Ⅴ on 12 species (
M.f. 3 species, S.f. 5 species, t.O.f. 4 species
) , observation fishes at Ⅴ of Settlement
fishes was few .   The depth 46 ■ of artificial
fish reefs have been observed Ⅵ on 13 species (
M.f. 3 species, S.f. 7 species, t.O.f. 3 species
) , Ⅶ on 8 species (M.f. 2 species, S.f. 4
species, t.O.f. 24 species) , artificial fish
reefs Ⅵ and Ⅶ differ from observed Settlement
fishes .   Clupeidae and Trachurus japonicus of
Migrant   fishes   ,   Sebastes   schlegeli   ,
Hexagrammos otakii and Thamnaconus modestus of
Settlement fishes have been observed on the
artificial fish reefs Ⅰ to Ⅶ .

July , each artificial fish reefs of depth 26
■ stock the sea with Pagrus major fry (juvenile
stage of artificial culture) number of 5,000 ,
after when have been observed behavioure of
Pagrus major fry.   Pagrus major fry attacted to
the center of artificial fish reefs , when
schooling on near bottom (Fig. 6) .   Pagrus
major fry many school up within 3 ■ sphere , the
outside school within 10 ■ , up the current of
artificial fish reefs was twice as many school
as down the current .   The artificial fish
reefs attracted upper the current of Trachurus
japonicus (total length 20 cm) , inside of
Sebastes schoegeli .   Pagrus major fry swiming

near bottom the artificial fish reefs , fry have not attacked of the other fishes . <u>Pagrus major</u> fry have an attacked of artificial fish reefs inside at <u>Sebastes schlegeli</u> and 30 cm or more bottom upper the current at <u>Trachurus japonicus</u> . August , <u>Pagrus major</u> fry had escaped from this artificial fish reefs , when have been not observed .

The environment conditions in July observation have been mesured of underwater illumination (incident light , catoptric light) and water temperature (Table 2) . The weather was cloudiness , mesure time 12:30 , the degree of transparency 20.0 , underwater illumination kown both incident light and catoptic light from 0 to 5 m the most absorption . The same water temperature most descended from 0 to 5 m .
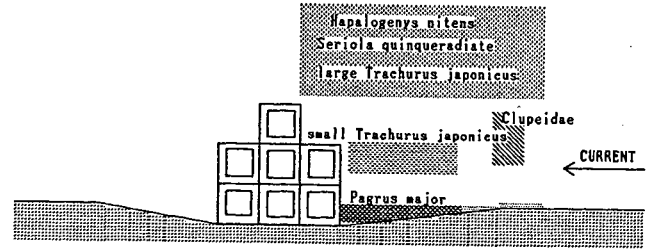
Fig.6   Artificial fish reef on fish fauna attracted observation stock the sea with Pagrus major fry (juvenile stage of artificial culture) .

Table 2   Underwater illumination and water temperature of observation point

depth   :   25.0m

the degree of transparency :   20.0

Depth	Incident light	Catoptric light	Water temperature
0 m	9,200 lux	250 lux	26.8 ℃
1	8,600	230	
2	7,800	220	
3	7,500	200	
4	7,300	150	
5	7,200	148	25.5
6	7,200	136	
7	7,100	128	
8	7,000	122	
9	6,800	113	
10	6,600	108	24.7
11	6,400	102	
12	6,200	97	
13	6,000	93	
14	5,800	89	
15	5,600	85	
16	5,200	82	
17	5,000	80	
18	4,900	78	
19	4,800	76	
20	4,400	74	23.8
21	4,300	73	
22	4,100	73	
23	4,000	72	
24	3,900	72	
25	3,600	71	23.6

Table 1   Artificial fish reef of every type observed fish species in Ohgata Town Niigata Pref.

Species	Artificial fish reef						
	I	II	III	IV	V	VI	VII
Clupeidae	☆	☆	☆	☆	☆	☆	☆
Trachinocephalus myops	○						
Trachurus japonicus	☆	☆	☆	☆	☆	☆	☆
Seriola quinqueradiata	☆		☆	☆	☆		
Seriola dumerili						☆	
Apogon semilineatus			◎	◎			
Apogon doederleini			◎	◎		◎	
Epinephelus septemfasciatus		◎	◎				
Stereolepis ischinagl						◎	
Hapalogenys nitens	◎		◎	◎			
Pagrus major	◎	◎	◎	◎	◎		◎
Oplegnathus fasciatus	◎	◎	◎	◎	◎	◎	
Ditrema temmincki						○	
Pterogobius zacalles	○	○		○	○		
Pterogobius zonoleucus					○		○
Pterogobius elapoides							○
Sagamia geneionema	○					○	○
Gobiidae	○		○	○	○		
Sebastes inermis				◎	◎		
Sebastes thompsoni				◎	◎		◎
Sebastes schlegeli	◎	◎	◎	◎	◎	◎	◎
Synanceiidae			○			○	
Hypodytes rubripinnis	○			○			
Hexagrammos otakii	◎	◎	◎	◎	◎	◎	◎
Paralichthys olivaceus	○						
Pleuronectidae			○				
Stephanolepis cirrhifer	◎			◎			
Rudarius ercodes			○		○		
Thamnaconus modestus	◎	◎	◎	◎	◎	◎	◎
Number of species	16	11	17	18	12	13	8
Number of Observation	6	3	5	5	5	2	2

note : ☆ : Migrant fises . ◎ : Settlement fishes . ○ : The others fishes
I : Poly-con type artificial fish reef 35 m³ (the inside of small structure) .   II : Poly-con type artificial fish reef 35 m³ (the inside of large structure) .   III : Poly-con type artificial fish reef 27 m³ (the inside of small structure) .   IV : Poly-con type artificial fish reef 27 m³ (the inside of large structure) .   V : Trapezoid type artificial fish reef 50 m³(1 set, 25 m³, the inside of large structure).   VI : Poly-con type artificial fish reef 155 m³ (the inside of small structure).   VII : Somicylindrial type artificial fish reef 300 m³ (1 set, 150 m³,the inside of large structure) .

(2).Maisaka Town Shizuoke Pref.

Maisaka Town Shizuoka Pref. in the shallow water of the artificial fish reefs set up on the sand bottom of depth 30 to 40 m , after set up from 1 to 3 year , observation diving was 1 to 3 time .

Poly-con type artificial fish reef of I set up on the depth 45 m 1 set 423 m³ , around the exist as ditch at depth 0.65 to 0.8 m , width 1.0 to 4.2 m .

Poly-con type artificial fish reefs of II set up on the depth 36 m 2 set , 248 m³ , around the bottom exist as ditch at depth 0.5 to 0.7 m , width 1.4 to 2.5 m .

Ordinary artificial fish reefs of Ⅲ set up on the depth 36 m 100 piece , 337.5 m³ , a diameter about 20 m range at intensively , around the bottom exist as ditch depth 0.6 to 1.1 m , width 1.8 to 2.8 m .

Ordinary artificial fish reefs of Ⅳ set up on the depth 37 m 100 piece , 337.5 m³ , a diameter about 15 m range at intensively , around the bottom exist as ditch depth 0.7 to 0.8 m , width 1.0 to 1.5 m .

Ordinary artificial fish reefs of Ⅴ set up the depth 30 m 100 piece , 337.5 m³ , a diameter about 18 m range at intensively , around the bottom exist as ditch depth 1.0 to 1.5 m , width 2.5 to 4.2 m , this reef was not protruding bottom .

The observation fishes of each artificial fish reefs have been observed Ⅰ on 19 specis (M.f. 3 specis , S.f. 11 specis , t.O.f. 5 specis) , Ⅱ on 22 specis (M.f. 2 specis , S.f. 9 specis , t.O.f. 11 specis) , Ⅲ on 16 specis (M.f. 2 specis , S.f. 8 specis , t.O.f. 6 specis) , Ⅳ on 29 specis (M.f. 4 specis , S.f. 15 specis , t.O.f. 10 specis) , Ⅴ on 21 specis (M.f. 3 specis , S.f. 8 specis , t.O.f. 10 specis) , Ⅳ at observation fishes most many .

The ordinary artificial fish reefs of same scale and same structure differ at observed fishes .   A large size artificial fish reef not attracted large fish school .
Parapristipoma triineatum of Migrant fishes , Giniistius zonatus , Sebastiscus marmoratus and Thamnaconus modestus of Settlement fishes have been observed on the artificial fish reefs Ⅰ to Ⅴ .

Table 3   Artificial fish reef of every type observed fish species in Maisaka Town Shizuoka Pref.

Species	Ⅰ	Ⅱ	Ⅲ	Ⅳ	Ⅴ
Dasyatis akajei		◇			
Plotosus lineatus		◇			
Gymnothorax kidako		◇		◇	◇
Clupeidae	☆				☆
Trachurs japonicus	☆			☆	☆
Seriola quinqueradiata			☆	☆	
Apogon semilinetus	◎	◎	◎	◎	◎
Apogon doederleini		◎			
Apogonidae	◇				
Lateolabrax japonicus		◎		◎	
Epinephelus septemfasciatus	◎	◎	◎	◎	
Epinephelus moara				◎	
Lutjanus kasmira					◇
Lutjanus monostigma					◇
Franzia squamipinnis	◇		◇		
Parapristipoma trilineatum	☆	☆	☆	☆	☆
Plectorhynchus cinctus	◎	◎		◎	
Plectorhynchus pictus				◎	
Pagrus major			◎	◎	
Acanthopagrus schlegeli	◎				◎
Kyphosus lembus		◇			
Oplegnathus fasciatus	◎	◎	◎	◎	
Cirrhitichthys aureus				◇	◇
Goniistius zonatus	◎	◎	◎	◎	◎
Pomacentridae					◇
Choerodon azurio		◇	◇	◇	◇
Pseudolabrus japonicus					◇
Thalassoma cupido					◇
Labroides dimidiatus	◇	◇			◇
Labridae	◇				
Platax orbicuralis		◇			◇
Microcanthus strigatus			◇	◇	
Pomacanthus imperator			◇	◇	◇
Chaetodon auripes	◇	◇			
Chelmo rostratus				◇	
Heniochus acuminates	◇	◇		◇	
Siganus fuscescens			◎		
Sagamia geneionema				◇	◇
Prionurus scalprus	◇			◇	◇
Sebastiscus marmoratus	◎	◎	◎	◎	◎
Pterois lunulata				◎	
Sebastes inermis	◎			◎	◎
Hexagrammos otakii				◎	
Parlichthys olivaceus			◇		
Stephanolepis cirrhifer		◎			
Thamnaconus modestus	◎	◎	◎	◎	◎
Canthigaster rivulata		◇		◇	◇
Number of species	19	23	16	29	21
Number of Observation	1	3	2	2	2

note : ☆ : Migrant fishes . ◎ : Settlement fishes . ◇ : The others fishes
Ⅰ : Poly-con type artificial fish reef 1 set, 632 m³
Ⅱ : Poly-con type artificial fish reef 2 set, 248 m³ (1set, 124 m³)
Ⅲ : Ordinary artificial fish reef 100 piece, 337.5 m³
Ⅳ : Ordinary artificial fish reef 100 piece, 337.5 m³
Ⅴ : Ordinary artificial fish reef 100 piece, 337.5 m³

DISCUSSION

Ohgata Town Niigata Pref. and Maisaka Town Shizuoka Pref. both in the shallow water of the artificial fish reefs at observed fish fauna , the observation fishes sorted out division type (Table 4) .   The division type weight estimated each fish for total length .   Each artificial fish reefs compared unit volum of fish school .   The observation fishes of each artificial fish reefs examined of Index of diversity and Degree of overlap .

Morishita's Index of diversity

$$\beta = \frac{N(N-1)}{\Sigma ni(ni-1)} \qquad \cdots\cdots (1)$$

Morisita's Degree of overlap (1959)

$$C\lambda = \frac{2\sum\limits_{i=1}^{s} n_{1i} \cdot n_{2i}}{(\lambda_1 + \lambda_2) N_1 \cdot N_2}, \quad 0 \leq C\lambda \leq 1 (\pm) \quad \cdots \cdots (2)$$

$$\lambda_1 = \frac{\sum\limits_{i=1}^{s} n_{1i}(n_{1i}-1)}{N_1(N_1-1)}, \quad \lambda_2 = \frac{\sum\limits_{i=1}^{s} n_{2i}(n_{2i}-1)}{N_2(N_2-1)}$$

Diving have been observed fish estimate weight , unit volum of fish school and Index of diversity shown table 5 , Degree of overlap at table 6 . Total observation fish volum many most of Ⅲ on 196.8 kg and then Ⅰ on 132.6 kg , Ⅵ on 118.9 kg , Ⅳ on 100.6 kg , half of Ⅲ was the other . The unit volum of fish school many most of Ⅲ on 7.3 kg/m³ and then Ⅳ on 4.2 kg/m³ , Ⅰ on 4.1 kg/m³ , other was below 1.5 kg/m³ . The total size attracted most fish school on small seze of artificial fish reefs .

The same size of artificial fish reefs attracted most fish school inside small structure . The Index of diversity , observation fishes attracted most at Ⅲ, Ⅰ, Ⅵ, Ⅳ more than 3.45 , when few attracted at Ⅱ, V, Ⅶ not more than 2.6 , simple fish fauna .

The Degree of overlap , same depth higher at Ⅰ to V , differ depth lower at Ⅵ to Ⅶ . The artificial fish reefs between Ⅵ to Ⅶ higher , that said fish fauna attracted decide from depth of possibility hint .

The artificial fish reefs in the shallow water Maisaka Town Shizuoka Pref. have been observed at most observation fishes of Ⅳ on 585.2 kg and then Ⅱ on 505.9 kg . The unit volum of fish school many most of Ⅱ on 2.0 kg/m³ and then Ⅳ on 1.7 kg/m³ , half of the other . The Index of diversity number higher differed from Ⅳ 4.24 to Ⅱ 3.21 . The construction of same unit at Ⅲ , Ⅳ and V differ observed result from differ accumulation . Poly-con type artificial fish reefs of Ⅰ and Ⅱ not attracted most fishes at large unit size . Degree of overlap , Poly-con type artificial fish reef of

depth 45 m and ordinary artificial fish reefs of depth 30 m at fish fauna attracted decide from depth of possibility .

The artificial fish reefs on attracted fish fauna effected of decision facter from depth .

The artificial fish reefs of most fish fauna attracted from total size than inside structure . Small unit higher piled up more effective .

The larger artificial fish reef unit attracted few fish fauna , same 400 m³ of artificial fish reef , 1 unit of less than 40 m³ said many set up artificial fish reefs.

Table 4   Division type of observation fish species

Type	Fish species
DASYATIS AKAJEI - Type	Dasyatis akajei .
GYMNOTHORAX KIDAKO - Type	Gymnothorax kidako .
PAGRUS MAJOR - Type	Hapalogenys nitens . Pagrus major . Oplegnathus fasciatus . Ditrema temmincki . Lutjanus kasmira . Lutjanus monostigma . Franzia squamipinnis . Plectorhynchus cinctus . Plectorhynchus pictus . Acanthopagrus schlegeli . Kyphosus lembus . Pomacentridae .
SEBASTES SCHLEGELI - Type	Epinephelus septemfasciatus . Stereolepis ischinagi . Sebastes schlegeli . Synanceiidae . Hypodytes rubripinnis . Cirrhitichthys aureus . Goniistius zonatus . Siganus fuscescens . Prionurus scalprus . Sebastiscus marmoratus . Pterois lunulata . Epinephelus moara .
PLATAX ORBICURALIS - Type	Platax orbicuralis .
SEBASTES THOMPSANI - Type	Apogon semilinetus . Apogon doederleini . Sebastes inermis . Sebastes thompsani . Apogonidae . Microcanthus strigatus . Chaetodontoplus septentrionalis . Pomacanthus imperator . Chaetodon auripes . Chelmo rostratus . Heniochus acuminates .
PARALICHTHYS OLIVACEUS - Type	Paralichthys olivaceus . Pleuronectidae .
HEXAGRAMMOS OTAKII - Type	Trachinocephalus myops . Hexagrammos otakii
SERIOLA QUINQUERADIATA - Type	Trachurus japonicus . Seriola quinqueradiata . Seriola dumerili . Lateolabrax japonicus . Parapristipoma trilineatum .
PSEUDOBLENNIUS COTTIDES - Type	Pterogobius zacalles . Pterogobius elapoides . Pterogobius zonoleucus . Sagamia geneionema . Gobiidae . Choerodon azurio . Pseudolabrus japonicus . Thalassoma cupido . Labroidae . Labroides dimidiatus .
SARDINOPS MELANOSTICTA - Type	Clupeidae .
SILLAGO JAPONICA - Type	Plotosus lineatus
THAMNACONUS MODESTUS - Type	Stephanolepis cirrhifer . Thamnaconus modestus . Rudarius ercodes . Canthigaster rivulata .

Table 6   Observation each artificial fish reef on fish fauna attracted between degree of overlap in the Ohgata Town shallow water

	Ⅰ	Ⅱ	Ⅲ	Ⅳ	V	Ⅵ	Ⅶ
Ⅰ	–	0.574	0.939	0.809	0.954	0.778	0.783
Ⅱ	0.574	–	0.631	0.853	0.586	0.319	0.105
Ⅲ	0.939	0.631	–	0.912	0.992	0.585	0.548
Ⅳ	0.809	0.853	0.912	–	0.875	0.442	0.510
V	0.954	0.586	0.992	0.875	–	0.302	0.556
Ⅵ	0.778	0.319	0.585	0.442	0.302	–	0.819
Ⅶ	0.783	0.105	0.548	0.510	0.556	0.819	–

Table 5 Diving have been observed fish species number and weight at the
artificial fish reef in the Ohgata Town shallow water
(a number of observation mean)

Type		Artificial fish reef						
		I	II	III	IV	V	VI	VII
Migrant fishes		3	2	3	3	3	3	2
	(kg)	63.1	27.7	94.0	70.3	61.0	18.7	25.0
Settlement fishes		6	6	11	11	5	7	4
	(kg)	65.5	14.3	102.6	30.2	15.4	99.6	19.9
the Other fishes		7	3	3	4	4	3	2
	(kg)	4.3	0.4	0.1	0.1	0.4	0.5	-
Total		15	11	17	18	12	13	8
	(kg)	132.6	42.4	196.8	100.6	76.8	118.9	44.9
Unit volum of fish school kg/m³		4.1	1.3	7.3	4.2	1.5	0.7	0.1
Index of diversity		3.45	2.28	4.43	3.62	2.39	4.74	2.60

note : Upper paragraph , Observed fish species number . Lower paragraph ,
Convesion weight from observed fish total length .
I : Poly-con type artificial fish reef 32m³(the inside of small structure).
II : Poly-con type artificial fish reef 32m³(the inside of large structure).
III : Poly-con type artificial fish reef 27m³(the inside of small structure).
IV : Poly-con type artificial fish reef 27m³(the inside of large structure).
V : Trapezoid type artificial fish reef 50m³. VI : Poly-con type artificial
fish reef 155m³(the inside of small structure). VII : Semicylimdrial type
artificial fish reef 300m³.

Table 7 Diving have been observed fish species number and weight at the
artificial fish reef in the Maisaka Town shallow water
(a number of observation mean)

Type		Artificial fish reef				
		I	II	III	IV	V
Migrant fishes		3	2	2	4	3
	(kg)	56.8	413.9	135.0	321.0	158.0
Settlement fishes		11	9	8	15	8
	(kg)	94.8	82.2	98.5	255.5	93.7
the Other fishes		5	11	6	10	10
	(kg)	2.4	9.9	24.6	8.7	13.4
Total		19	22	16	29	21
	(kg)	154.1	505.9	258.1	585.2	265.1
Unit volum of fish school kg/m³		0.4	2.0	0.8	1.7	0.8
Index of diversity		4.08	3.21	3.53	4.24	3.32

note : Upper paragraph , Observed fish species number . Lower paragraph ,
Convesion weight from observed fish total length .
I : -45m Poly-con type artificial fish reef. II : -36m Poly-con type
artificial fish reef. III : -36m Ordinary artificial fish reef. IV : -37m
Ordinary artificial fish reef. V : -30m Ordinary artificial fish reef.

Table 8 Observation each artificial fish reef on fish fauna attracted
between degree of overlap in the Maisaka Town shallow water

	I	II	III	IV	V
I	-	0.649	0.655	0.682	0.492
II	0.649	-	0.943	0.939	0.452
III	0.655	0.943	-	0.825	0.525
IV	0.682	0.939	0.825	-	0.424
V	0.492	0.452	0.525	0.424	-

REFERENCES

1). Niigata Pref. examination room (1985, 5) :
The artificial fish reefs in the Niigata
Pref. shallow water of synthesis study and
social work .
2). Edited by Osamu Sato (1984, 10) :
Artificial Reef
Corp. Kouseisya Kouseikaku

STUDY ON GENERATION OF UPWELLING WITH ARTIFICIAL RIDGES "SUPER RIDGES" MADE OF HARDENED COAL ASH BLOCKS

M. Oki*, T. Suzuki*, M. Kusabuka*, T. Sugihara**, Y. Kasai**

* Hazama Corporation, Japan
** Tokyo Electric Power Co., Inc. Japan

ABSTRACT

The world's major fishing grounds are maintained by natural upwelling, which enables nutrients in the sea water to rise from the seabed to the photic region and so increases primary production. The study reported here was concerned with the creation of new fishing grounds, where sea water upwelling will be generated by installing artificial ridges named "Super Ridges" on the seafloor. Coal ash, which has been used up until now to be disposed of mainly on reclaimed land, is effectively utilized as the principal materials of these ridges. This report outlines the "Super Ridges" project and discusses the technical problems involved in implementation of the project.

1. INTRODUCTION

Japan faces the problem of decreases in catches on coastal fishing grounds due to restrictions on fishing within the 200 mile-zones in many countries and decreasing fishing resource due to water pollution from coastal reclamation and industrial effluent, as well as overfishing. The situation calls for development of new coastal fishing grounds.

At the same time, Japan, which is the second largest energy consumer in the world after the USA, is rapidly turning from oil to coal power generation to avoid becoming too dependent on a single energy source and thus ensure a stable energy supply. As a result, the electric power output of coal-fired thermal power plants has already reached 13 GW as of 1989, and that level is expected to double within the next 10 years.

Coal-fired thermal power plants produce coal ash at an annual rate of approximately 360,000 tons per 1 GW of power, which must somehow be disposed of. At present, most of the coal ash is used as materials for reclamation of coastal areas. Although more effective uses for coal ash have been developed, there is no market for it in such large quantities.

This concept of artificial ridges called "Super Ridges" has been proposed to solve both of these problems. These ridges feature a newly developed hardened product made from coal ash. They are constructed on the sea bottom in areas with poor fishing resources to improve these fishing grounds.

2. UPWELLING FISHING GROUNDS

Coastal areas off California (west coast of USA), Peru and Algeria are well known as good upwelling fishing grounds. The upwelling is, in many cases, generated by winds. As shown in Fig .1, the wind along the coast generates surface currents away from the coast on Ekman's wind driven current theory, and this causes sea water at the bottom in the deep sea area (deep sea water) to move up towards the surface following the topography. Through this process, the upwelling carries deep sea water up towards the surface. In general, deep sea water contains rich
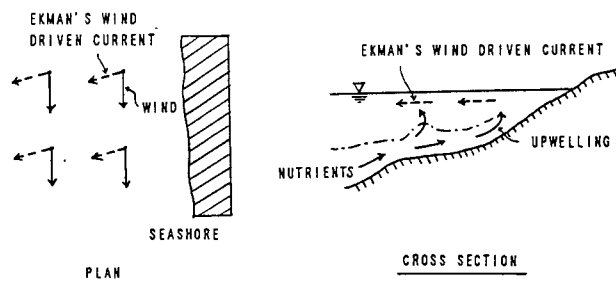
Fig. 1. The model of upwelling generated by the wind

nutrients, such sea water produces plank-
tons when exposed to sunlight. The large amount
of plant planktons so generated becomes the fo-
undation of a food chain in the sea, leading
ultimately to an increase in the fishing resou-
rces.

In addition to wind-generated upwelling fis-
hing grounds mentioned above, there are many
smaller fishing grounds generated by local cur-
rents. In Japan, current-generated upwellings
are found around islands (e.g. Hachijojima), in
channels (e.g. Naruto Strait) and at other loc-
ations. A detailed study on current-generated
upwellings was conducted on the Shiomaki Reef
in Yamaguchi Prefecture by Uekita, Nakamura,
Hideshima et al .[1), and the various interest-
ing findings from the study were reported. The
study indicated that this type of upwelling is
generated by differences in the pressure betwe-
en the slow current in the bottom layer and the
fast current in the surface layer when the curr
ent flows over the reef.
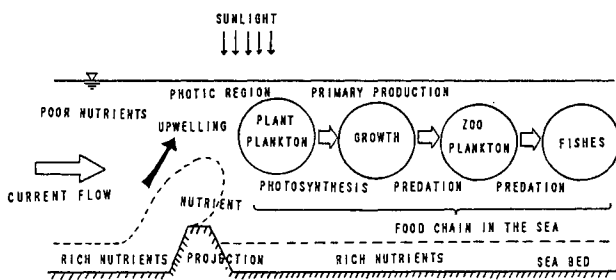
Fig. 2. The simplified mechanism of biological
production by current-generated upwell-
ing

3. LARGE-SCALE ARTIFICIAL RIDGES "SUPER RIDGES" EMPLOYING NEW HARDENED PRODUCTS

To illustrate the process of constructing
artificial ridges "Super Ridges" using coal ash,
let us assume that a 1 GW coal-fired thermal
power plant is located on the coast, and that
the area has a sand/mud bottom with less fishi-
ng resources. A further assumption is made that
all the coal ash discharged by power plants is
used as raw materials. Cement with water and
admixture is mixed with coal ash to make hard-
ened materials.

In this case, several construction methods
are possible, however let us assume that blocks,
as the hardened material weighing 100 tons each,
are continuously manufactured and stacked close
by. The power plant discharges 1,000 tons of

coal ash per day, to make 17 blocks per day.
These blocks are piled up to a height of 35 m
on the seabed 100 m below surface to form a
Super Ridges as shown in Fig. 3. In case of 10 m
and 80 m wide ridge at the top and bottom resp-
ectively with 200 m length, approximately 280,
000 m^3 volume of the ridge will be required.
The total quantity of coal ash discharged in 30
years will be 11 million tons, from which appr-
oximately 11 million m^3 of hardened coal ash
can be produced. Using these to construct ridg-
es with 66% voids, the approximately 23 km len-
gth of ridges can be created.

When currents in the sea crash against the
Super Ridge, new upwelling will be created,
bringing up nutrients near the seabed to the
photic region of the area where sunlight can
reach. Planktons will increase feeding on the
nutrients and subsequently a new fishing ground
will be created.
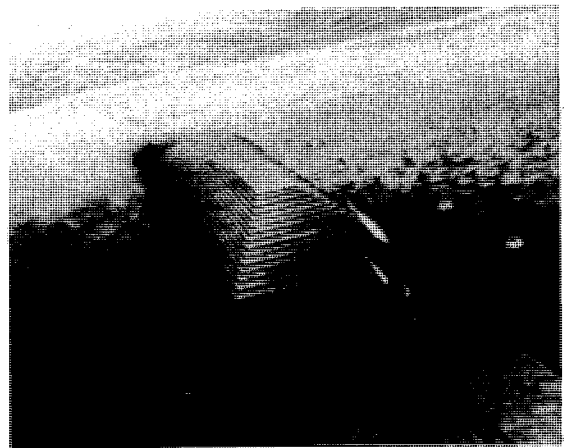
Fig. 3. The image of Super Ridges

4. TECHNICAL PROBLEMS IN IMPLEMENTATION OF CONCEPT

4.1 Serviceability of Hardened Coal Ash Blocks

The authors have been engaged in research on
new hardened blocks using coal ash as its main
component in order to make effective use of
coal ash and, through development of an admixt-
ure, which contributes greatly to harden coal
ash, have succeeded in producing high-strength
hardened coal ash blocks at reasonable costs.

Fig. 4. shows the relation between the ratio
of cement C/(F + C) and the compressive streng-
th of the blocks and a comparison is made betw-
een the cases with and without the newly devel-

oped admixture. It can be seen from the figure that the strength of the hardened blocks can be controlled by adjusting the ratio of the cement and that in all cases use of the new admixture was effective to obtain higher strength of hardened blocks.
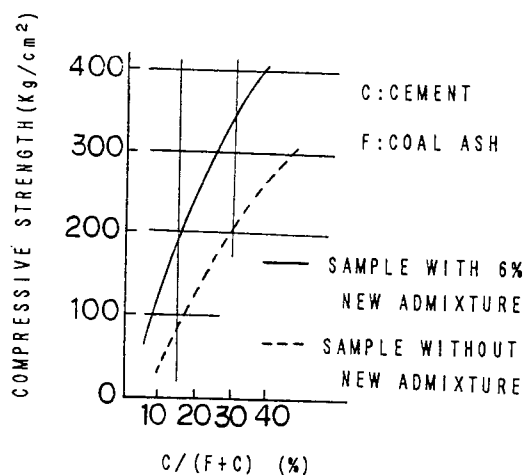
Fig. 4. The relation between the ratio of cement and the compressive strength

Core samples were taken from a hardened coal ash block which had been sunk in the sea for two years to investigate their resistance to seawater. Their compressive strength was 453 kgf/cm^2 and no signs of deterioration were observed in X-ray diffraction analysis and SEM observation.

The results of the elution test are given in Table 1. The values for hardened coal ash block and concrete satisfied the safety standards set by the Environment Agency of Japan-

Table 1. Results of elution test

(Unit :mg/l)

Analysis Items	Samples		detection Limit	Safety Standars
	Hardend Coal Ash block	Concrete		
Cadmium and Compounds	not detected	not detected	0.01	≦0.01
Cyanide Compounds	″	″	0.2	not detected
Organophosphoric Compounds	″	″	0.1	″
Lead and Compounds	″	″	0.1	≦0.1
Hexavalent Chromium	″	″	0.05	≦0.05
Arsenic and Compounds	″	″	0.05	≦0.05
Mercury and Compounds	″	″	0.0005	≦0.0005
Alkyl Mercury Compounds	″	″	0.0005	not detected
PCB	″	″	0.0005	″

ese government. This is thought to be because the hexavalent chromium contained in the coal ash as well as in the cement was solidified by the cement and the water, then was stabilized. Since the safety standards set by the Environment Agency are as stringent as water quality standards under the Water Supply Law, hardened coal ash blocks can be reckoned to be as safe as concrete to living organisms.

In Fig. 5, a comparison is made of compressive strengths and raw material costs between hardened coal ash block and ordinary concrete. A coal ash is designated an industrial waste, they don't have a reasonable price. If the price of the coal ash is subtracted from the costs, the cost of the materials for hardened coal ash blocks will be a third that for ordinary concrete of the same strength.
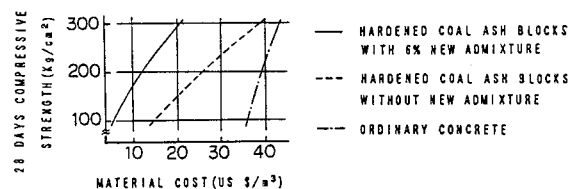
Fig. 5. The relation between the compressive strength of blocks and the raw material cost

4.2 Biological Productivity of Deep Sea Water Containing Rich Nutrients

Culture tests of plant planktons were carried out in order to examine the productivity of nutrients in deep sea water.

(1) Test Method

Marine chlorella (Chlorella sp.), which is commonly found in eutrophicated sea zones, was used for the test. Water samples were taken from depths of 0.5 m and 80 m for surface and deep sea water, respectively. The results of water quality analysis are shown in Table 2. The deep sea water sample contained 5 times as much NO_3-N, twice as much T-N and 1.5 times as much PO_3-P as the surface water sample. After the samples were filtered using 1 μm glass filters, 5 mixtures with different proportions of surface and deep sea water were prepared (ratios of surface to deep water - 1:0, 3:1, 1:1, 1:3, and 0:1). The sample mixtures (700 m each) were placed in flasks and to these marine chlorella of a constant density (5.2 x 10^4 cells/m each) were added. These were left for 16 days in the apparatus as shown in Fig. 6.

Table 2. Results of water quality analysis

Analysis Items		Surface Water Sample	Deep Sea Water Sample
Water Temperature (℃)		21.9	20.1
pH		8.2	8.1
DO	(ppm)	6.2	5.5
Salt	(‰)	35.4	35.0
COD	(mg/l)	1.0	1.2
NH_4-N	(μg.at/l)	not detected	0.15
NO_2-N	(μg.at/l)	〃	not detected
NO_3-N	(μg.at/l)	2.8	14.8
T-N	(μg.at/l)	10.7	21.2
PO_3-P	(μg.at/l)	1.5	2.0

LIGHT SOURCE (A FLUORESCENT LIGHT)

AIR
ALUMINUM FOIL
PUMP
FLASK (1ℓ)
HEATER
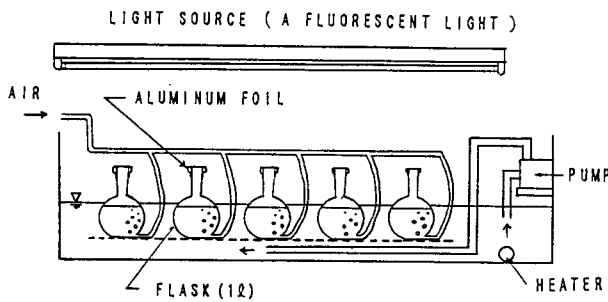
Fig. 6. The apparatus of culture test for chlorella

(2) Results and Observations

Fig. 7 shows the increase of chlorella with the passage of time. It can be seen that the breeding ratio of the chlorella increases with the proportion of deep water in the sample mixtures and it means that the primary productivity is higher for deep sea water containing rich nutrients than for surface water with less nutrients.

	SURFACE WATER	:	DEEP SEA WATER
O	1	:	O
●	3	:	1
×	1	:	1
△	1	:	3
▲	O	:	1

THE PASSAGE OF TIME (days)
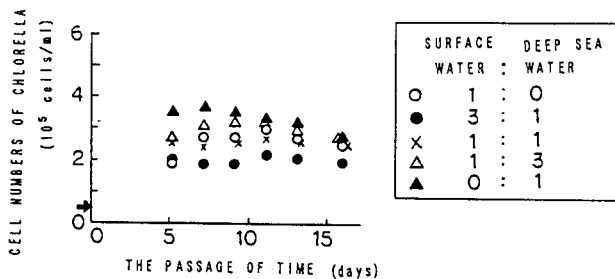
Fig. 7. The increase of chlorella with the passage of time

4.3 Generation of Upwelling with "Super Ridges"

When the nutrients-rich deep sea current collides with the "Super Ridges", deep sea wa-

ter is carried to the photic region near the surface through generation of separated vortices at the summit of the ridge and consequent mixing and diffusion of surface and deep sea water. The effects of parameters, such as the height and slope angle of the ridge, the current velocity and the difference in density between surface and deep sea water, were investigated by generating density stratified flow in a two-dimensional experimental waterway.

The items investigated included the following.
a. Relation between height(D) of Super Ridges and rise of deep sea water
b. Relation between slope angle(R) of Super Ridges and rise of deep sea water
c. Relation between current velocity(V) and rise of deep sea water
d. Relation between density difference($\Delta \rho$) and rise of deep sea water.

(1) Test Method

The density of the sea water at the surface off the coast of Kanto Region in Japan is 1.0-240 to 1.0246 g/cm^3, while that at 100 m below surface is 1.0254 to 1.0258 g/cm^3, giving a density difference of 0.0012 to 0.0014 g/cm^3. In the experiment, the density difference was created by using fresh water for the surface water and salt water for the deep sea water. It was assumed that only the deep sea water contained nutrients. The salt water as deep sea water was coloured and measurements were taken of how far the deep sea water would be made to rise by the Super Ridges.

(2) Results and Observations

The relation between the height (D) of the Super Ridges and the rise (Zu) of the deep sea water is shown in Fig. 8. The values for D and Zu are made dimensionless by the water depth (h). The results indicate that Zu/h increases with D/h.

Fig. 9 shows the relation between the slope angle (R) of the Super Ridges and the rise(Zu) of the deep sea water. It is to be observed that the effect of R is not particularly great however the Zu reaches its maximum value when R is between 50 and 60 degrees. It is not feasible from the point of view of actual construction to raise R above 60 degrees.

Fig. 10 shows the relation between current velocity (V) and rise of deep sea water. The results indicate that the value for Zu/D increases with V.
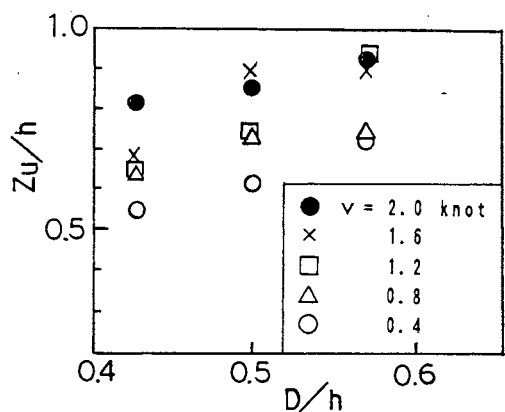
Fig. 8. The relation between the hight(D)
of the Super Ridges and the rise(Zu)
of the deep sea water

Fig. 9. The relation between the slope angle(R)
of the Super Ridges and the rise(Zu)
of the deep sea water
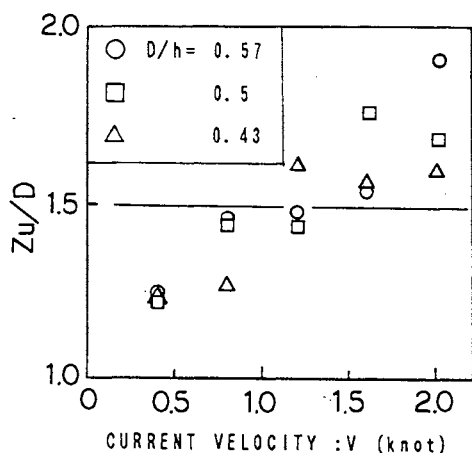
Fig. 10. The relation between current velocity
(V) and the rise(Zu) of deep sea water

Fig. 11 shows the relation between the density difference ($\Delta\rho$) and rise of deep sea water (Zu). Tests were implemented setting $\Delta\rho$ at 0, 0.001, 0.002 and 0.004g/cm^3. On the side of the Super Ridges facing the current, the greater the density difference, the more likely it was for the deep sea water to be retained, while on the downward side of the Super Ridges, the smaller the density difference, the greater the rise. Separated vortices were observed at the summit of the ridges when $\Delta\rho$ was 0, 0.001 and 0.002g/cm^3.

DISTANCE FROM THE SUPUR RIDGE
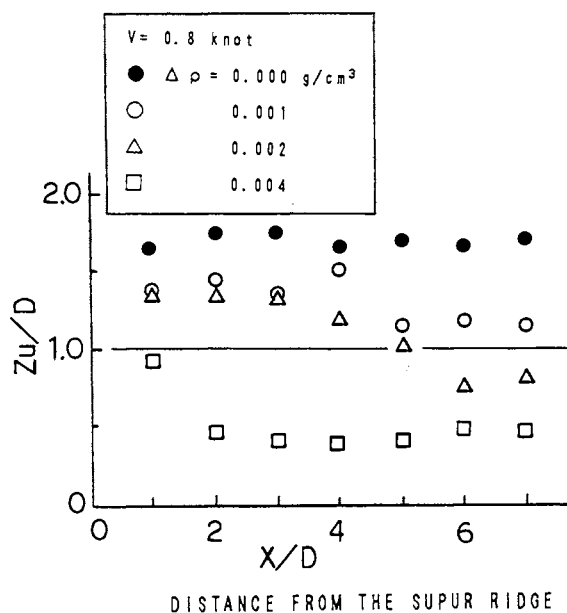
Fig. 11. The relation between the density
difference($\Delta\rho$) and rise(Zu)
of deep sea water

4.4 Numerical Analysis

In many cases, the vertical distribution of nutrients density in the sea water is triangular, as shown in Fig. 12. Through numerical analysis, the quantity of nutrients from deep sea water levels which will be carried to the upper photic region due to the influence of the Super Ridges, was studied. As an analysis method, a turbulent flow model utilizing a k-ε equation was adopted. The cases of the analysis are shown in Table 3. For case 1, conditions corresponding to the hydraulic test mentioned in the previous section were given. For case 2, conditions were given, assuming a triangular distribution for the nutrients density. The results of the calculation are shown in Fig. 13. This figure shows, using a vertical distribution,

the quantity increased of nutrients density. The analysis proved that, in case 2, a large quantity of nutrients around the seabed would be carried up to the photic region due to the influence of the Super Ridges.

NO$_3^-$+NO$_2^-$ (μ g at/l)

PO$_4^{---}$ (μ g at/l)
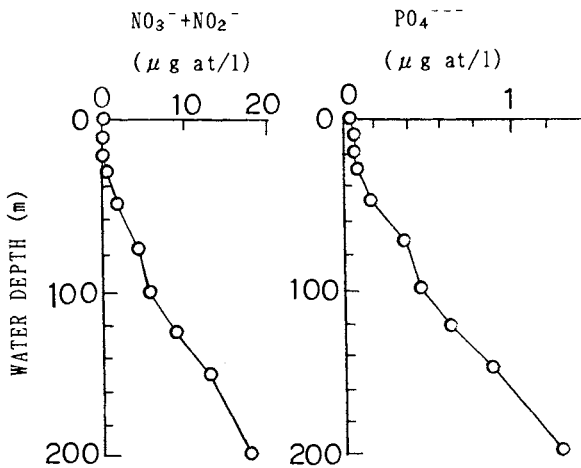
Fig.12 An example of the vertical distribution of nutrients density (around the Izu Islands, Japan)[4]

Table 3 Analysis case

CASE No.	VERTICAL DISTRIBUTIO OF SEA WATER DENSITY (g/cm^3)	VERTICAL DISTRIBUTION OF NUTRIENTS DENSITY PO$_4$-P (μ g at/l)	CURRENT VELOCITY (knot)
1	100m 10m 1.0 1.001	0 0.5	1.0
2	100m 1.0 1.001	0 0.5	1.0

Notes; It assumes that water depth is 100m and (PO^4-P) density at 100m depth is 0.5 μ g at/l according to Fig.12.

D/h=0.4
R=60 deg.

CASE 2

CASE 1

THE QUANTITY INCREASED OF NUTRIENTS DENSITY (μ g at/l)
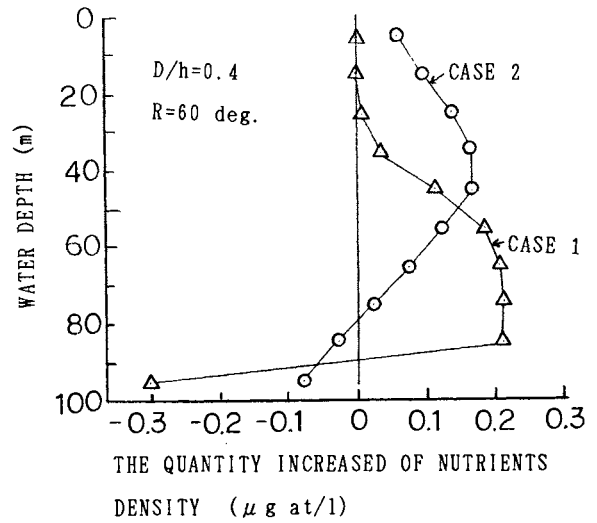
Fig.13 Results of the calculation

5. CONCLUSION

1) With the existence of a newly developed admixture, high-strength hardened coal ash blocks were produced at reasonable costs.
2) Hardened coal ash blocks satisfy the Japanese safety standard of the elution and are safe for living organisms.
3) The primary productivity is greater in deep sea water than in surface sea water.
4) Factors contributing to the upward movement of deep sea water are; height of Super Ridges, current velocity and density difference between the surface and deep sea water.
5) The results of the numerical analysis also indicate that the Super Ridges are contributing to carrying a large quantity of nutrients up to the photic region.

6. FUTURE TASKS

1) Investigations have been made on generation of upwelling with Super Ridges in two-dimensional terms. Since, in reality, the three-dimensional vortices around the Super Ridges will also be a factor of upwelling, three-dimensional investigations will need to be implemented.
2) In order to evaluate beforehand the effect of the Super Ridges, experiments need to be implemented, taking account of the nutrients density distribution, sea water density distribution, current velocity distribution and the shape of the seabed at the actual proposed sea area.

REFERENCES

1. Uekita, Nakamura, Hideshima :"Observation of
   the Upwelling Occurring Behind the Large Re-
   ef in Case of Shiomaki." Bulletin of Nation-
   al Institute of Fisheries Engineering. No.5
   1984

2. Suzuki :"A Concept of Large-Scale Artificial
   Ridges Using a New Hardened Product Made
   from Coal Ash."
   Ocean Space Utilization '85, 1985

3. Taniguchi, Suzuki, Shimomura, Oga, Nagataki
   : "Applicability of High-Volume Fly Ash Con-
   crete to Marine Structures." 3rd Inter. Con-
   ference on Fly Ash, Silica Fume, Slag & Nat-
   ural Pozzolans in Concrete Supplementary
   papers. 1989

4. Takahashi, Koike, Ishimura, Saino, Furuya,
   Fujita, Hattori and Ichimura : Upweeling
   plumes in Sagami bay and adjacent water aro-
   und the Izu Islands , Japan, J.Oceanogr.Soc.
   Japan, Vol.36, pp.209~216, 1980

DEVELOPMENT OF NEW TYPE OF ARTIFICIAL STEEL REEFS ACCEPTABEL TRAWL FISHERY

K. Sekita*, T. Saitou*, K. Miki** and N. Kato**

* Nippon Steel Corporation, Sagamihara City, Japan
** Nippon Steel Corporation, Tokyo, Japan
*** Tokai University, Shimizu City, Japan

Abstract

Recent efforts have been made to replenish depleted coastal fishing grounds through the development of artificial reefs. Because such reefs are being situated in deeper waters, the following requirements must be met.

1) They must be larger.
2) They must be able to function in trawl fishing areas.
3) They must attract large numbers of fish.

Because the reefs must be larger, they must also be both stable and strong enough to bear hydrodynamic forces related to this increase.

Secondly, the reef must be of a nature which avoids entanglement in drag nets.

Finally, because of hydrodynamic fluctuations caused by the reef, involving flows and eddies, the ability to attract fish must remain a consideration.

In consideration of these requirements, two types of artificial steel reefs were designed. Simulated net-catching and hydrodynamic tests were carried out in currents and towing tanks, and this paper describes these tests and their results.

1. Introduction

While the Fishery Agency and other organizations are carrying out development projects for coastal fishing grounds in waters off the Japan Sea coast, the development of fishing grounds based on artificial reefs is moving forward aggressively. This work is focussed on placing larger such reefs in deeper water, and also the development of steel reefs which will increase fishery resources is being sought.

The use of concrete for artificial reefs has an extensive track record good, but steel reefs have many advantages as listed below:

(1) The weight per bulk of the structure is low. This facilitates transportation and installation. In addition, steel reefs are affected less by conditions of soil and topography of seabed and the risks of them being buried, washed away, or capsized is small.

(2) Steel reefs are easier to manufacture, and the design can be chosen more freely. Since steel reefs can be made larger, more complicated and in better combinations, the functions of the reef can be improved to suit specific catch types and fishing grounds.

(3) A high fish yield can be expected. Sunken ships and other steel marine structures have been known to attract fish. Dissolved[1] iron (Fe ions) may possibly contribute to the increase of plant plankton in the seawater according to laboratory tests.

Work on steel reefs has been chiefly carried out by the Kozai Club[2] and each steel maker has developed products of its own.

Nippon Steel has also developed the reef for shallow waters and convex/cubic type steel reefs for deep waters that are resistant to entanglement by gill nets. Subsequently, we have come up with two new dome-type steel reefs that prevent the entanglement of trawl nets, which were realized by taking measurements of the hydrodynamic, observing the ambient flow and simulating net-entanglement.

Fig. 1 shows two different reefs. Type A is based on the old convex design and helps to prevent interference with nets, while type B is designed to have an overall curved structure.

2. Shape and Structure of the New Steel Reef

Small trawl nets and offshore trawl nets are widely used around the coast of Japan at depths of 30 to 200 meters. This creates a wide range of applicable depth, from shallow waters up to 50 meters deep and to deep waters of 50 to 200 meters. The fish to be farmed were tentatively chosen to be seabed species. The shape and structure of the new reef were determined on the following grounds.

Table 1 Shape and structural characteristics of the new reef

Objective	Shape
Prevention of net entanglement	Low periphery is slightly tapered. Point-symmetric, plane-wise.
Adjustable height to suit water conditions at different locations.	Tapered in two tiers.
Generation of riser currents.	An umbrella-like panel is installed inside, and the top of the reef has hole directly above the panel.

Of these shape determinants, top priority was given to the prevention of net entanglement, and a point-symmetric structure was employed so that a trawl net could be drawn over the reef in any direction. As explained later, the reef is shaped such that it is smaller than the maximum rise angle of its bottom edge so as not to entangle trawl nets. As the height of reef is important, a 2-tier tapered shape was chosen. This prevents sufficient height being obtained as in the case of types, so a hole is introduced at the top and an umbrella added inside to generate an upwelling flow driven by the current. This structure creates an apparent height. As a whole, the reef is a polygonal pyramid and with many holes around the bottom to allow the entry of seabed species. The space between openings is smaller than the outer diameter of the sinker, and other fittings on a trawl net's ground rope.
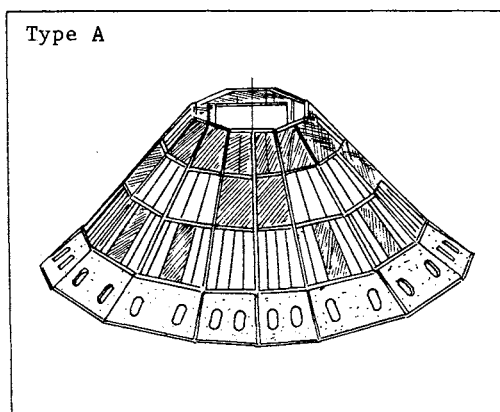
3. Net-Entanglement Simulation

A basic experiment was first carried out in which a model trawl net was pulled over an inclined board to see if a change in the bottom edge angle is effective in preventing net entanglement. Next, models of types A and B were examined for entanglement-prevention qualities with a trawl net typically used in water with a depth of about 50 m.

The large wave-generating tank (68m long, 2.5m wide, 2m deep) which also has a tow cart, at our Sagamihara Research & Engineering Center was used.

3.1 Method of Experiment

The model net shown in Fig. 3 was fixed to the tow cart and three values of the space X at its entrance were tested (20cm, 50cm, 120 cm). In the case of the reef models, the model was positioned in the direction of the center line or in a line away from the center line (Y = 0.25 cm).

Reef models of types A and B were used, and each was 50 cm in diameter.

Experiments with inclined board

To confirm resistance to net entanglement resulting from different bottom edge angles, we used an inclined board 150 cm wide as shown in Fig. 2. The inclination of this board could be changed in 5° increments.

The influence of the bottom edge angle on entanglement characteristics was observed by recording the action of the trawl net model over the inclined board using a video camera as shown in Fig. 2 The cart speed was constant at 0.3 m/s and the inclination was changed from 25° to 90°.

Experiment with reef model

The effectiveness of the new steel reefs in preventing trawl net entanglement was observed by recording with a video camera the motion of
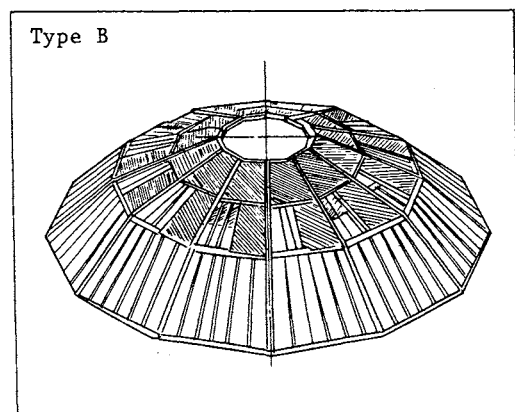
Fig. 1 New steel reefs

the model trawl net over 1/30 scale models of the reefs, which were placed on the tank bottom with no clearance as shown in Fig. 3.

Table 2 shows the cart speed as an experimental parameter and the equivalent actual towing speeds based on Tauchi's comparative rule[3].

Table 2 Towing speed

Actual	Model
1.4 knots	0.3 m/s
1.0 knot	0.1 m/s

3.2 Results and Discussion

Experiments with the trawl net model over the inclined board yielded the following results with changes in inclination C°.

The trawl net towed smoothly if C was between 25° and 50°. When C was increased to 70°, slight catching of the net was observed at the top. When C was raised to 90°, the inclined board was shifted by the entangled net.

These findings demonstrated that a change in the angle of the bottom edge or a change in height was important as far as net-entanglement was concerned. The reef characteristics affecting net entanglement, however, also include the height, plane shape, elevation, shape of structural members and the openings. These factors will have to be considered in addition to the bottom edge angle.

When type A was swept away by the trawl net, the net slid smoothly over the model's outer edge. (Photo. 1)

As for type B, the present shape allowed the net to sweep smoothly over the reef. While the space between the slits on the bottom edge is larger than the sinker diameter (1.2 cm), the trawl net moved with no trapping of the sinkers by the slits. As a result, the type B design is seen to have overall qualities of net-entanglement prevention. (Photo 2.)
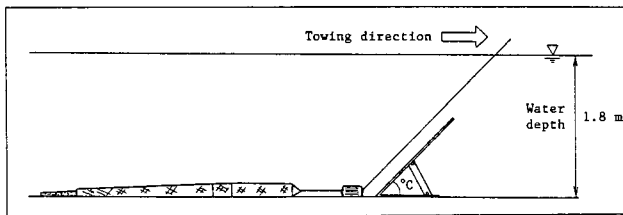
Fig. 2 Experiment with inclined board
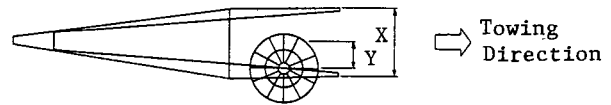
Fig. 3 Experiments with reef models
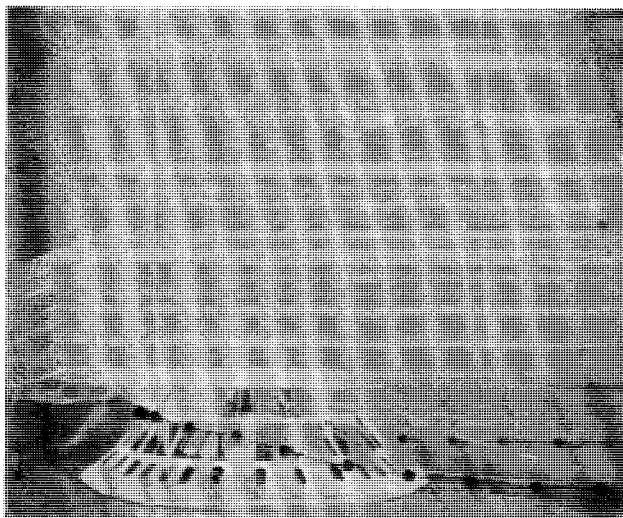
Photo 1 Type A
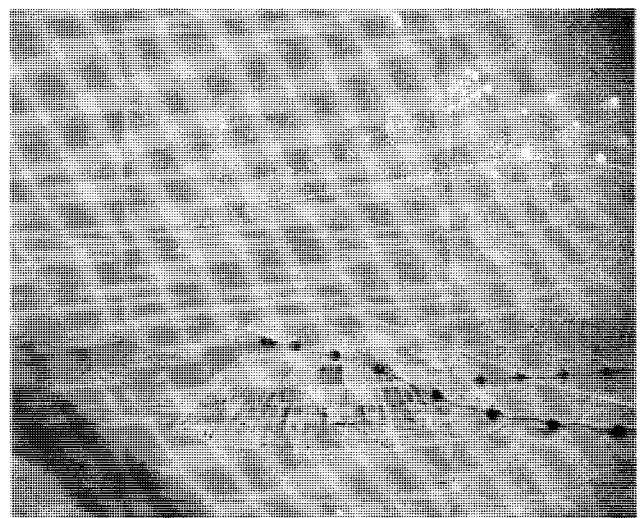
Photo 2 Type B

4. Measurement of Fluid Rresistance and Observation of Ambient Flow Conditions

Here, the horizontal force and capsizing moment acting on the steel reef model were measured to examine its stability in seabed currents and to determine the drag coefficient which is an important design factor.

Next, the ambient flow speed vector was measured and the flow, made visible with a dye, was observed to study the effects of such flow conditions as riser currents, propagation of flow speed changes and eddying.

The experiments were carried out in a 2-impeller, vertical-circulation, upright water tank located in Ship Research Institute of Tokai University' oceanography department. Table 3 shows the performance and specifications of this tank.

Table 3 Specifications of experimental water tank

Observation section	2.8m long, 1.4m wide, 1.15m deep
Measurable flow speed	0.2-1.3 m/s (2.0 m/s)
Uniformity of flow speed distribution	±2%
Observation windows	One side window 1.5m x 0.7 m Two bottom windows 0.5m x 0.5m

The model used in the experiments was scaled down to 1/30th and was made of brass. The experiments were based on Froude's law.

Table 4 shows the model dimensions and flow speeds in the experiment.

Table 4 Dimensions of model

		Actual	1/30th scale model
Outer diameter (mm)		15,000 mm	500 mm
Height	Type A	6,150 mm	205 mm
	Type B	3,750 mm	125 mm
Flow speed		1.1-7.1 m/s	20-130 cm/s

4.1 Experimental Method

Horizontal force/capsizing moment

To measure the horizontal force and capsizing moment applied to the reef model by the flow, a temporary bottom was introduced in the circulation tank's observation section. A 3-component load cell was attached inside the temporary bottom to measure the horizontal force (Fx) and the moment (My) around the detector center.

The water depth in this experiment was 90 cm. The flow speed was changed adjusting the impeller speed and the main flow was set using a Prandtl-type pitot tube.
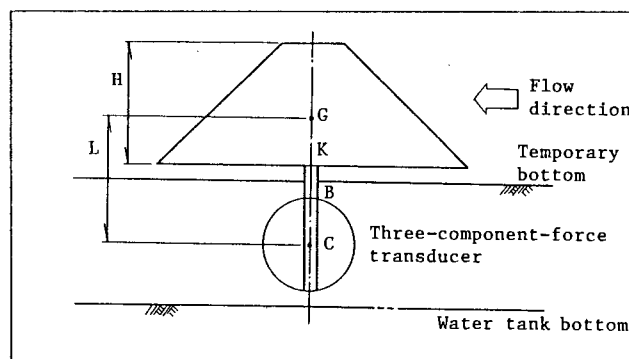
Fig. 4 Method of horizontal force/capsizing moment measurement

Flow velocity vector

The flow velocity vector around the model under these conditions was measured using a 5-hole pipe current meter with a globular head measuring 6 mm in diameter. It was attached to a traversing device with 5 degrees of freedom.

The points of measurement were laid out 0, 10, 20, 30, 40, 60, 80, and 100 cm from the model center on the down stream side, 0, 20, and 40 cm from the center and right of the flow and at heights of 10, 20, 30, 40, and 50 cm from the temporary bottom in the vertical direction (up to 40 cm, in the case of type B).

Here, the pitot tube was used to set the main flow to a constant speed of 0.74 m/s (equivalent actual speed, 4.05 m/s).

Observation of flow conditions

To observe the flow, a fluorescent dye, Neo Color Red (Tanner Co., Ltd.), was injected. Dye was injected carefully through a 3.3 mm OD pipe so that it entered the flow smoothly. Dye was injected in front of the model and behind it, over the model and also 10 cm away from the center line. Developments were recorded using a video camera.

4.2 Results and Discussion

Drag Coefficient, coefficient of capsizing moment

The drag coefficient (C_D) and coefficient of capsizing moment (Cm_y) are expressed by the equations below.

$$F = \frac{Wo}{2g} C_D A v^2$$

$$My = \frac{Wo}{2g} Cm_y A GK v^2$$

where, F: Horizontal force
My: Capsizing moment

A: Area over which pressure is applied
v: Flow velocity
GK: Height of center of gravity above bottom surface.

In the experiments, C_D1, the drag coefficient based on the total reef area (A1) projected on the plane perpendicular to the flow direction and C_D2, the drag coefficient on the total reef area (A2) excluding openings projected on the plane perpendicular to the flow direction, were derived. Similarly, moment coefficients, Cm_y1 and Cm_y2, were obtained.

Fig. 5 shows the drag coefficient and moment coefficient of type A. As illustrated, both coefficients are nearly constant values with the flow velocity. Negative values of moment coefficient mean that the reef is tending to vertically turn against the flow direction. These results indicate that the reef is stable in the flow and is very resistant to capsizing.

Table 5 shows the average of all experimental cases. It is seen that C_D2 ranges from 1.1 to 1.3. Since the structure consists of boards and squares, this value is equal to or larger than the drag coefficient[4] of a board. On the other hand, the drag coefficient of all structural members (front, middle and rear) calculated[5] three-dimensionally by

using current velocity components in the slope direction, on the assumption that drag coefficients of all members of the reef were the same, turned out to be approximately 0.57, suggesting it was much smaller than the drag coefficient of board. That is, the rear members inside the reef are seldom exposed to the flow road.

Table 5 Drag Coefficient

		Type A	Type B
C_D1		0.53	0.37
C_D2		1.07	1.32
C_DA	Model	383 cm^2	157 cm^2
	Actual	34 m^2	14 m^2

Flow velocity vector

Fig. 6 shows the flow velocity vector at reef center on the plane perpendicular to the flow direction. At the reef center, a rising flow is generated in the vertical direction with a flow velocity roughly 25% that of the main flow.
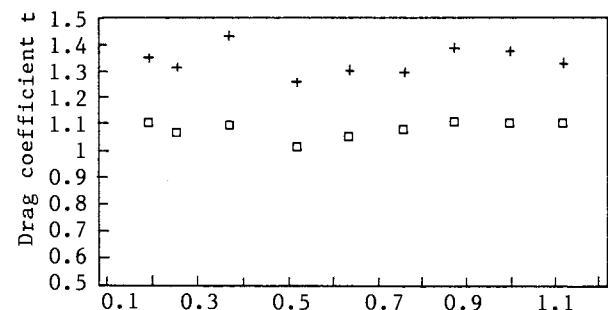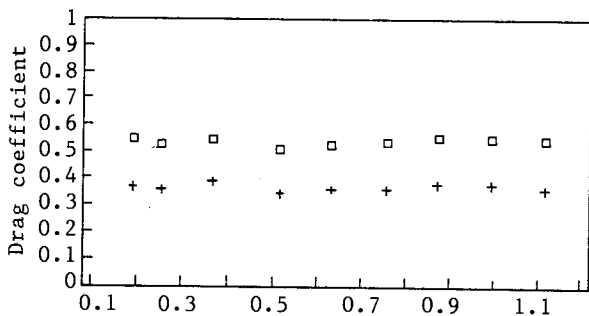
Drag coefficient C_D1
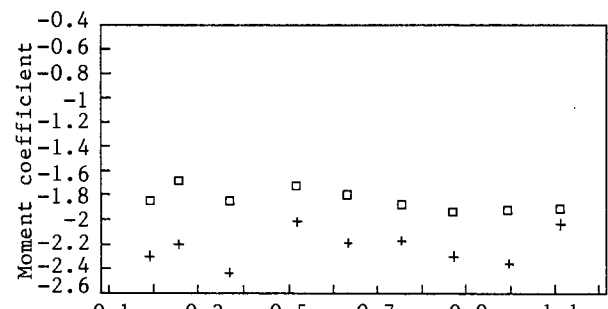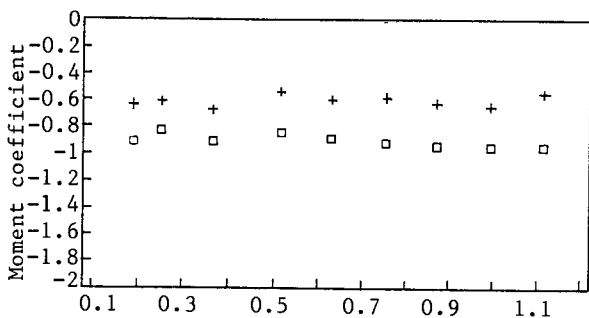
Drag coefficient C_D2

Capsizing moment coefficient Cm_y1

Capsizing moment coefficient Cm_y2

Fig. 5 Drag coefficient and capsizing moment coefficient

To the rear of the model, an _immeasurable area of eddies is formed[6]. The dimension of the area along the flow direction is three times that of the height, and this area is larger in the case of type A than type B.

In addition, the recovery of velocity loss in the flow direction is slower in the case of type A. Flow velocity at a height roughly 5 times that of the model was much lower than the main flow velocity.
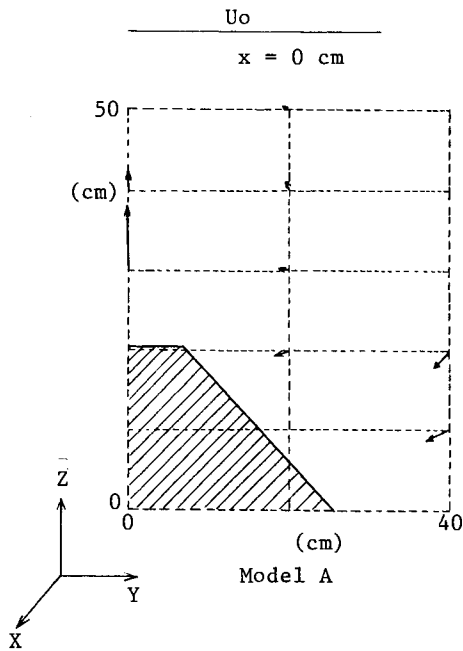
Fig. 6 Flow velocity distribution

As Photo 3 shows, it was confirmed that dye injected near the bottom of reef models types A and B flowed through the models and welled up through the top hole.

The dyed flow reaches a height up to 1.5 times higher than the model and diffusion of the dye due to passage through the reef model was confirmed.

It was also shown that the settling of the dye takes place to the rear of the reef model.

5. Conclusion

From a series of experiments carried out on the new reef, the following conclusions can be drawn.

(1) The capsizing moment coefficient and drag coefficient were derived to calculate the hydrodynamic forces acting during placement. As a result, it was discovered that the capsizing moment had a minus value in the flow and the drag coefficient was small. Thus the risk of a capsize or slippage is extremely small.

(2) It was confirmed that there was upwelling current through the top hole and eddying to the rear of the reef. Because of the influence this will have on the flow environment, a fish-gathering effect can be expected.

(3) The trawl net model and its fittings slid along the reef model's bottom edge. Sliding of the surface of the model also occurred higher on the reef. Therefore, the reef can be expected to be entanglement resistant.
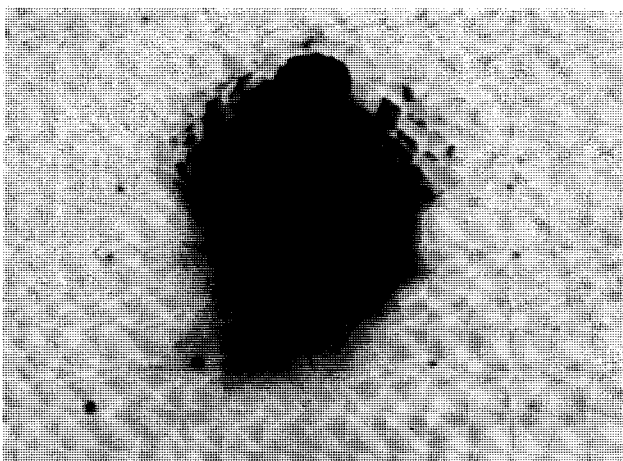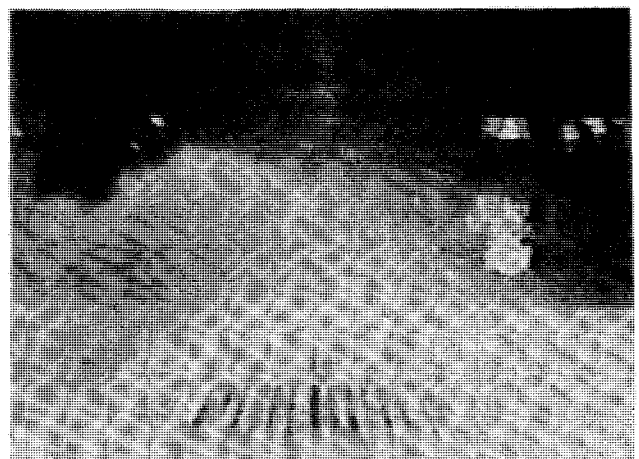
Type A   Type B

Photo 3 Observed flow conditions

References

1. Matsunaga, K., "The Effect of Steel Reefs - I, II, III, IV", The Japanese Society of Scientific Fisheries (1989)

2. Kozai Club, Steel reef, Nov. (1977)
3. Osawa, Y., Koyama, T., Nomura, M., Mori, K., Tawara, Y. and Senga, K., "Basic Study on the Net Construction of Trawl Nets by Model Experiment", Bulletin of National Research Institute of Fisheries Engineering, No. 8 March (1987)
4. DnV, "Rules for the Design Construction and Inspection of Offshore Structures, Appendix B Loads (1977)"
5. Sekita, K., "Laboratory Experiments on Wave and Current Forces Acting on a Fixed Platform", OTC Paper No. 2191, Houston, TX. (1975)
6. Kato, N. and Yamaguchi, M, "The Vortex on a Submerged Solid of Revolution", 2nd International Symposium on Ship Viscous Resistance Goteborg, Sweden (1985)

PREDICTION METHOD FOR RESISTANCE AND INCLINATIONS OF A FLOATING TYPE NET-CAGE MOORING BY A SINGLE LINE IN CURRENT

H. Maeda*, T. Yokoyama**, H. Makita*** and S. Miyajima*

* Institute of Industrial Science, University of Tokyo, Japan
** Mitsubishi Electric Corporation, Japan
*** Corporation of Niigata Steel Engineering, Japan

Abstract

The present floating type net-cage is moored by a single line in a proper submerged depth in order to cultivate fish. Then it is important to predict its resistance and position in current.

In this paper, a reasonable prediction method for its resistance and inclination is investigated. The square and octagonal types are tested in the experiment. First, resistance of a plane net in various attitude is measured. Secondly, experiments of 3-D nets are carried out. Finally, tensions and inclinations of a mooring line of the net-cage model are measured, when it is moored by a single line in uniform flow.

The authors propose to predict resistance of a plane net in any attitude according to Tauchi's method by using modified C_d and resistance of 3-D net in attitude by using τ (interaction among plane nets), and calculate inclination and tension of a mooring line of a net-cage in uniform flow.

1. Introduction

As offshore aquacultural facilities, floating type net-cage moored by a single line is proposed. It has advantages of changing proper submerged depth as to sea temperature or surroundings, reducing construction cost, and having a small occupancy of the sea. While, it is necessary for design to know resistance of a net-cage, tension of a mooring line, its motion and its attitude in severe surroundings of coastal current and waves. But analytical methods of these are not solved yet.

This net-cage consists mainly of such members as nettings, frames, floats and a mooring line. In general, total resistance is obtained by summing up resistance of every member. As for frames or floats, it is possible to predict its resistance by D.N.V. rules[1] etc. based on strip theory. But as for nettings, a prediction method for its resistance is not clear with some respects. Tauchi[2] predicts total resistance of the netting considering a twine as a cylinder acted by normal velocity of flow. About the field of fishery engineering, Tauchi's method[3] or Nakamura's method[4][5] is used as practical prediction method. Nakamura's method is summarized in a design guidance called "Orange Book" for a man of affairs. Nakamura predicts total resistance of the netting choosing simple projected area as representative area and as $C_d=1.0$.

Many studies of resistance of a plane net considering interference among twines have been done very actively. Imai[6], Osawa[7] and Konagatani[8] made accurate experiments and proposed experimental equations about an actual netting. And Miyazaki[9] investigated the influence of Reynolds number. But by these equations, resistance of plane net in any attitude can't be predicted accurately.

As for resistance of a 3-D net, Miyazaki made an experiment about netting-bags and mentioned that it was practically established to sum up resistance of very small nets. Nakamura propose an approximate prediction method about cube or cylinder type net-cage. He considers the wake effect of its upstream side face on its downstream side face. As for inclination of a 3-D net moored by a single line, Nakamura predicts from the ratio of its surplus buoyancy to drag force of a net-cage without being inclined. The effect of its inclination on resistance is not considered. Above two respects have not been studied enough.

In this paper, three problems have become subjects to solve as follows; a) how to predict resistance of a plane net in various attitude. b)whether summation principle of resistance of plane nets is applicable for a 3-D net. c)how to predict tensions and inclinations of a mooring line of the net-cage model.

The test is performed in the following three steps; 1)resistance of a plane net, 2)resistance of 3-D nets 3)tensions and inclinations of a mooring line of the net-cage model. It is assumed that velocity distribution in current is uniform in depth. As result authors have proposed a prediction method for its resistance and inclinations in current.

2. Experiment on a plane net

2.1 A sample of plane net

A sample of plane net is named No.1. It has the following specification; Tetron knotless netting, a diameter of a twine:d=2.0mm, a mesh size:$2l$ =34.0mm, hanging angle:δ =45deg., mesh numbers is 19*19, Imai says that the value of the coefficient is not depending on mesh numbers, when mesh number is more than 6*6.

2.2 Testing procedure

The testing net is fixed on the gate shaped frame in any attitude. Experimental angle α on which a 3-D net makes to flow direction is 0 to 90 deg., which corresponds to inclination of a net-cage. In various velocity from 0.2 to 0.6m/s, resistance to 3-component are measured by 3-directional load cell fixed on a top plate of the frame. Resistance values of the plane net are obtained by subtracting resistance of the frame from its measured values of the plane net and the frame.

2.3 Experimental analysis and result

(1) Calculating C_d by Tauchi's method

From the experimental results, the authors calculate a drag coefficient C_d of a piece of twine according to Tauchi's method. When uniform flow vector V(u,v,w) acting on the plane net fixed on xyz-coordinate system, xyz-directional forces (F_x,F_y,F_z) are expressed as follows;

$$F_x=C_d*Funi*S*(d/1)*2u/\sin(2\delta)$$
$$F_y=C_d*Funi*S*(d/1)* v*\cot(\delta)$$
$$F_z=C_d*Funi*S*(d/1)* w*\tan(\delta) \qquad (1)$$

where Funi=ρ $V^2/2$, ρ :density of water, S:the netting area and (u,v,w):unit vector of flow. Total resistance R is expressed as $\sqrt{F_x^2+F_y^2+F_z^2}$. C_d is calculated from the experimental values of resistance R.

$$C_d=\frac{R \text{ (experimental value)}}{Funi*S*(d/1)*\sqrt{4u^2/\sin(2\delta)+v^2*\cot(\delta)+w^2*\tan(\delta)}} \qquad (2)$$

Figure 2.1 shows that calculated results, and comparison of α' with C_d. The authors define originally that α' is an angle between flow velocity vector and the plane of net.

(2) Modified C_d

As shown in Fig.2.1, C_d obtained from the experimental results are very scattered on the contrary to Tauchi's assumption. When α' is over about 20deg., C_d is considered as constant. But when α' is less than about 20deg., C_d is proportion to the angle α' . Its physical reason is interaction among twines. Then the authors define H' is an angle when interaction happens, and propose to use two different C_d in two regions, α' >Θ' and α' <Θ' respectively. From experimental results it is decided that Θ' of Net No.1 is 20deg.. When α' >Θ' , it is decided C_d=1.59 from average value. When

α' <Θ' , it is decided that the first order formula of α' for C_d is C_d=0.04*α' +0.79. from a least square method. Like this, an approximate formula of α' for C_d considering interaction among twines is named as a modified formula.

2.4 Comparison with other predicted values

The authors compare the experimental values with predicted values by other researchers by making total resistance R nondememsional as follows;
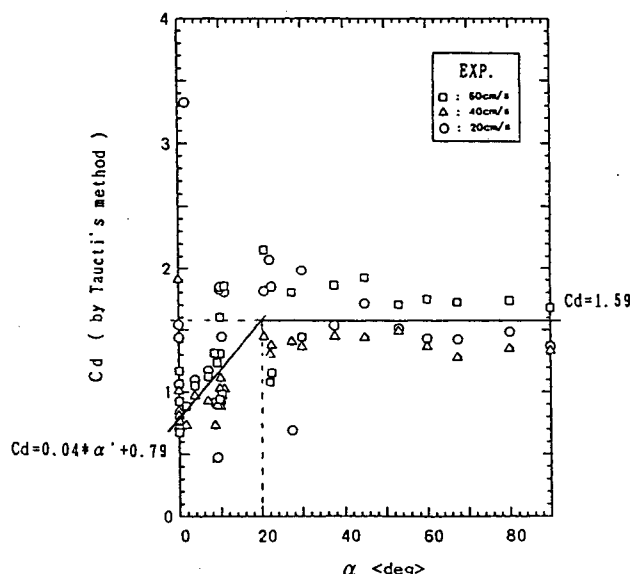
Fig. 2.1 Relationship of α' and Cd of the net No.1 from its experimental resistance.
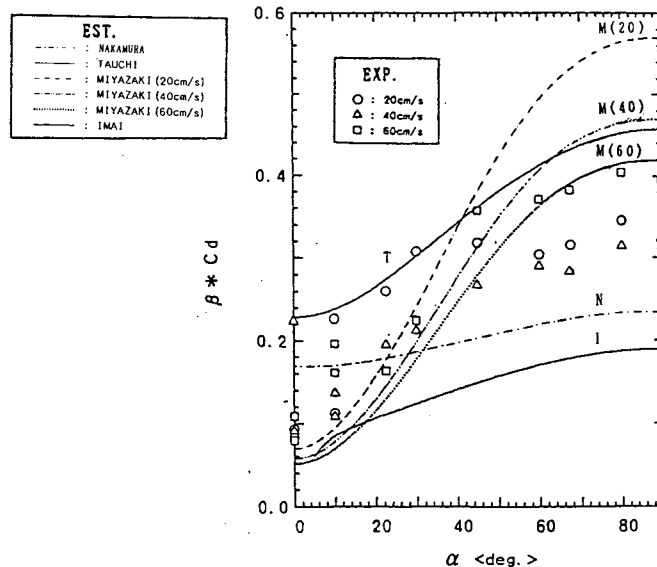
Fig. 2.2 Relationship of α and dimensionless R(total resistance) of the net No.1 and comparision of its experimental values with predicted ones.

$\beta *C_d=R/(\rho SV^2/2)$ (3)

where β is the ratio of projected area to the netting area. The authors choose $\beta *C_d$ as nondimensional values as common with predicted methods by each researcher. Its results are shown in Fig.2.2. There are some differences in predicted values by each researcher. The order of magnitude of predicted values is Miyazaki(20cm/s), Tauchi(C_d=2.0), Miyazaki(40cm/s), Miyazaki (60cm/s), Nakamura(C_d=1.0), Imai(circular tank and knotless net). The experimental values stand in the middle of all predicted values.

3. Experiment of 3-D nets

3.1 Models of 3-D net
Cube and Octagonal 3-D nets of 30cm scale in length of side are tested. They are netting members of (a)Cube(30) and (b)Oct.(30) each other, and made of Net No.1. The numbers in brackets represent scale length of the models.
3.2 Testing procedure
A frame fixed on the 3-D net is a rectangular frame, which is 710mm in height, 710mm in width and 560mm in length, and is made of pipes of 13mm radius. The 3-D net is fixed on the frame for its angular side to face to the flow direction in its lying attitude. Experimental angle α on which a 3-D net is changed from 0 to 90deg., which corresponds to inclination of a net-cage. In various velocity from 0.2 to 0.8m/s, its drag and lift forces are measured by 3-component load cell fixed on a top plate of the frame. Resistance values of a 3-D net are obtained by subtracting resistance of the frame from its measured values of the 3-D net and the frame.

3.3 Experimental result
Experimental results are shown as white marks in Fig.3.1. As shown in Fig.3.1, the maximum is at α=45deg. and the minimum is at α=90deg.. The maximum is 1.5 times of the minimum. The angle has a large correction factor on drag.

3.4 τ of 3-D net
It is defined that τ is the ratio of a resistance value of a 3-D net to a total resistance value of plane nets. Here the former resistance value is obtained by the experiment. The latter resistance value is obtained by summing up resistance values of
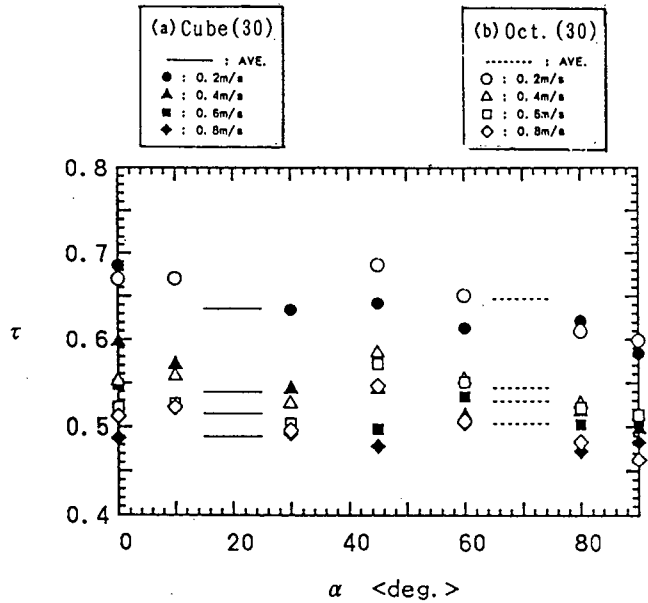
Fig.3.2 Relationship of α and τ of 3-D net of Cube(30) or Octagonal(30) model.
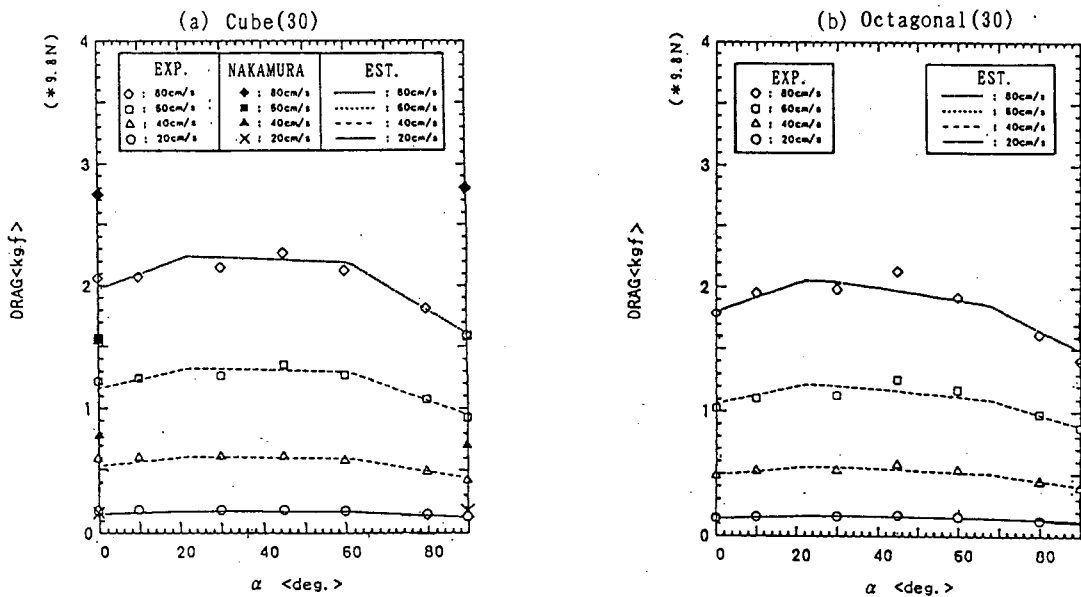
Fig.3.1 Relationship of α and drag force of 3-D net of Cube(30) or Octagonal(30), and comparision of drag force between its experimental values and estimated ones.

each plane net calculated by Tauchi's method using the modified Cd formula. Its results are shown in Fig.3.2.

This figure shows that τ is nearly equal at the same velocity. As the velocity is bigger, τ becomes smaller and converge to about 0.5 of both Cube(30) and Oct.(30) models.

4. A single point mooring test

4.1 Test models

As shown in Fig.4.1 and Table 4.1, the authors choose four types as experimental models. (a) and (b) are cube and octagon of 30cm scale in length of side. (a) and (c) are cube of 30cm and 45cm scale in length of side. (b) and (d) are octagonal of the same scale, but made of different nets. (a), (b) and (c) are made of Net No.1. (d) is made of a small scale net for a model.

4.2 Testing procedure

The authors set a ball float of 50mm radius on the top of each model, and moor it by a single line through a pulley. In uniform flow from 0.1 to 0.5m/s, the authors observe their motion, and measure inclinations(α,γ) and tensions of a mooring line. Here α is inclination of the main body. γ is inclination of a mooring line. As for Oct.(30) and Cube(45), velocity distributions around each model are measured. The direction of measured velocity is the flow direction in far field(X-direction).

These models are about 1/100 scale of a real object. Basically their inclinations are decided from the ratio of surplus buoyancy to drag. Buoyancy of a model is converted into 10^4 times about a real object, because its drag is proportional to its netting area.
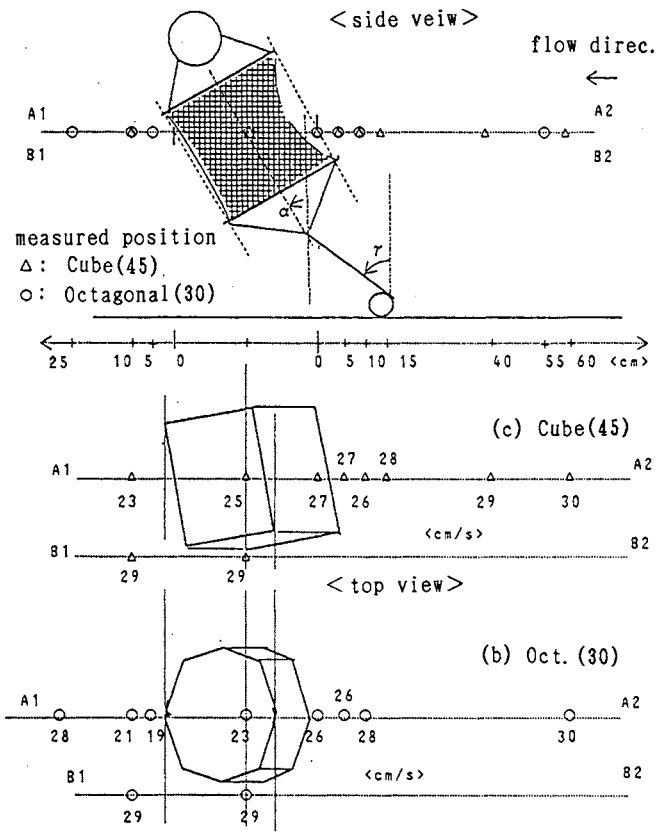
Fig.4.2 Schematic veiw and velocity ditributions around each model of Cube(45) and Octagonal(30) moored by a single line in uniform flow(30cm/s).

(a) Cube(30) (b) Oct.(30) (c) Cube(45) (d) Oct.(T)

unit<mm>
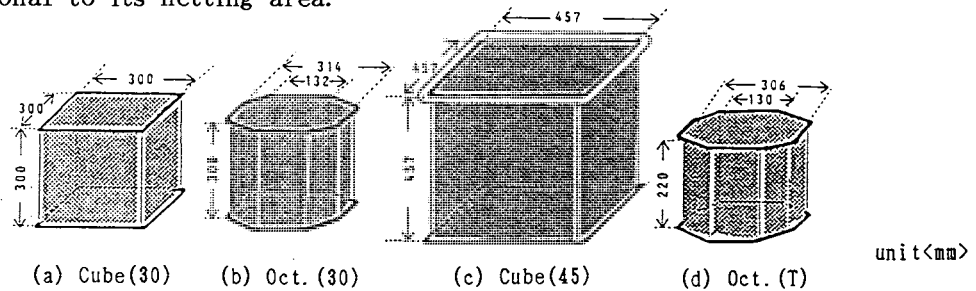
Fig.4.1 Outline of net-cage models.

Table 4.1 Specification of net-cage models.

Model type	kind of net	Size and shape of net Upper net	Side net	Frame members shape and weigh	Floats shape and buoyancy	Total weight in air
(a)Cube(30)	Tetron Knotless (Net No.1) lozenge mesh d= 2.0mm 2l=34.0mm	300mm*300mm δ=45°	300mm*300mm	Circular bar 4mmϕ*302mm*4 117g*2	a ball(100mmϕ) 480g	415g
(b)Octagon(30)		side length of Oct.:132mm, δ=45°	132mm*300mm	Circular bar 4mmϕ*136mm*8 102g*2	a ball(100mmϕ)	365g
(c)Cube(30)		457mm*457mm δ=45°	457mm*457mm	Circular bar 4mmϕ*460mm*4 117g*2	a ball(100mmϕ)+ Circular bar(4mmϕ *465*4), 1027g	415g
(d)Octagon(T)	Nyron sheet bend d= 0.3mm 2l=11.1mm	side length of Oct.:132mm. δ=38.5°	132mm*300mm lozenge mesh δ=28.5°	Circular pipe 5mmϕ*302mm*8 26g*2	a ball(100mmϕ)	180g

4.3 Experimental result
(1) Motion observation
When a net-cage model is moored in flow, it is inclined slowly at its static stable position but such unstable motion as slow oscillation doesn't appear.

(2) Velocity distribution
Velocity distribution around Oct.(30) and Cube(45) models in uniform flow(30cm/s) is shown in Fig.4.2. As for each model, 87% or 90% velocity is measured before the front net of each model, 77% or 83% velocity is inside of it, and 67% or 77% velocity is behind back net of it.
(3) Tension and inclination
On the experiment, T(tension of a mooring line) F_U(surplus buoyancy) and γ (inclination of a mooring line) are measured. D(drag force) and L(lift force) are calculated from the following formulas. These results are shown in Fig.6.2 and Fig.6.3.

$$T*\sin(\gamma)=D$$
$$T*\cos(\gamma)=F_U+L \tag{4}$$

5. Prediction for resistance

5.1 Prediction method
The process of the presented prediction method for resistance is shown as follows;
(step1)Divide a 3-D net(netting member of a net-cage) into plane nets.
(step2)Predict resistance of each plane net by Tauchi's method using the modified C_d.
(step3)Predict resistance of a 3-D net by summing up resistance of each plane net and being multiplied by τ.
(step4)Predict resistance of other members as frames, float and so on by D.N.V. rules.
(step5)Add the resistance of other members to that of a 3-D net, then it makes the total resistance of a net-cage.
In this method, it is important how to decide the modified C_d and τ.
As for (a), (b),and(c), Method.1 is applied, which uses the modified C_d formula obtained from experimental results. As for (d), the modified C_d formula is not known. Method.2 is expressed as an example method applied to such a case. Miyazaki's method suits a small scale net of the model(d) best. Each constants are decided as follows;
1)Prediction for C_d of a twine
<Method.1>Use C_d=1.59 from experimental results.
<Method.2>Determine C_d by Miyazaki's method. C_d=16*$R_e^{-0.28}$, R_e=V*h/ν , h=(l sinδ cosδ)/2
2)Prediction for the modified Cd formula
<Method.1>Use the modified C_d formula obtained from experimental results.
<Method.2>Obtain C_d at α' =0, Θ' and 90 by Miyazaki's method, and determine the modified C_d formula. Θ' is an angle when interaction happens. Θ' is obtained from Imai's method. At the case of sheet bend knot netting, Θ' =6*$\sin^{-1}$(d/2l cosδ)
3)Prediction for τ
Use its average value of each model at each

velocity from experimental results as τ.
4)Prediction for C_d of other members
Use C_d=0.5 about a sphere, C_d=1.2 about a cylinder.

5.2 Predicted results of a 3-D net
As for Cube(30) and Oct.(30), resistance of a 3-d net is calculated according to Method.1. Predicted results are shown by curved lines in Fig.3.1, and agree well with experimental results except near α=45deg..

6. Prediction for inclination and tension

6.1 Prediction method
The authors considers simplified model of 2-D dynamic system as shown in Fig.6.1 ,and set up equilibrium equations for force and moment acting on a net cage model. Here three conditions are assumed as follows; a net-cage is not deformed, resistance acts on each members(nettings, floats, frames) independently, and a mooring line is straight and have no weight.
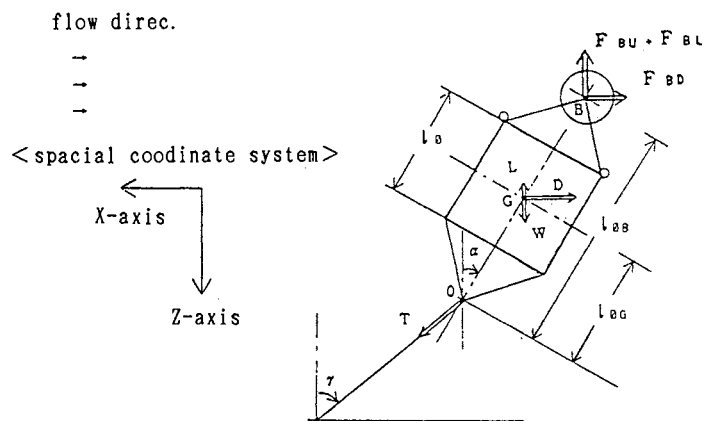
Fig.6.1 Outline of 2-D dynamic system of a net-cage model with floats, which is moored by a single line in uniform flow.

From equilibrium for force of X-direction and Z-direction,

$$F_1(\alpha,\gamma)=\{T_0*L(\alpha)\}*\tan(\gamma)-D(\alpha)-F_{BD}(\alpha)$$
$$=0 \tag{5}$$

From equilibrium for moment around the 0-point of the fulcrum,

$$F_2(\alpha) =[l_{OB}*\{W-L(\alpha)\}-l_{OB}*\{F_{BU}+F_{BL}(\alpha)\}]$$
$$*\tan(\alpha)-\{l_{OG}*D(\alpha)+l_{OB}*F_{BD}(\alpha)\}$$
$$=0 \tag{6}$$

Where constants and variables are as follows;
Constants of length; l_{OB}:length of 0B, l_{OG}:length of 0G, l_0:longitudinal length of the main body, 0:fulcrum point of the main body, G:the center of gravity, B:the center of buoyancy,
Constants of force; F_{BU}:buoyancy of floats, W:weight of the main body in water, T_0(=F_{BU}-W):initial tension of a mooring line,

Variables; α:inclination of a main body, γ:inclination of a mooring line, D(α):drag of a main body, L(α):lift of a main body, $F_{BD}(\alpha)$:drag force of floats, $F_{BL}(\alpha)$:lift force of floats.

First, equation(6) is solved for α by Newton-Raphson's method. Secondly, γ is obtained by substituting its converged solution α into equation(5).

6.2 Predicted result

As for each four type model on the experiment, their inclinations and tensions of a mooring line are predicted. Resistance acting on a net-cage is calculated by Method.1. As for Oct.(T), resistance is calculated by Method.1 and Method.2. Each constant is fixed as shown in Fig.6.2. As for Cube(30) and Cube(45) models, present predicted results are compared with Nakamura's predicted

results. The calculated results of inclinations(α,γ) are shown in Fig.6.2. Then Calculated results of drag and tension are shown in Fig.6.3. The comparison of this predicted results with experimental results is shown Table 6.2.

As for Cube(30) and Oct.(30), predicted results agree well with experimental results.

As for Cube(45), predicted results of inclinations and force is underestimated a little compared with experimental results. Its main reason seems to be due to underestimate τ.

As for Oct.(T), predicted results by Method.2, agree well with experimental results. On the other hand, predicted results by Method.1 is underestimated compared with experimental results. Its principal reason seems to be underestimate C_d and τ.

Table. 6.1 Specification of constant values
to use for the prediction formulas.

Constants Model type	Total Weight in water: W	Surplus buoyancy of floats: F ʙu	Total surplus buoyancy: T ʙ	lₐ	Length lₐₐ	lₐₑ
(a)Cube(30)	260g	480g	220g	30.0cm	29.0cm	54.0cm
(b)Octagon(30)	215g	480g	265g	30.0cm	29.0cm	55.0g
(c)Cube(45)	442g	1027g	585g	45.5cm	37.5g	69.0g
(d)Octagon(T)	100g	180g	380g	23.0cm	28.5cm	48.0cm

(a) C u b e (30)

(b) O c t . (30)

(d) O c t . (T)
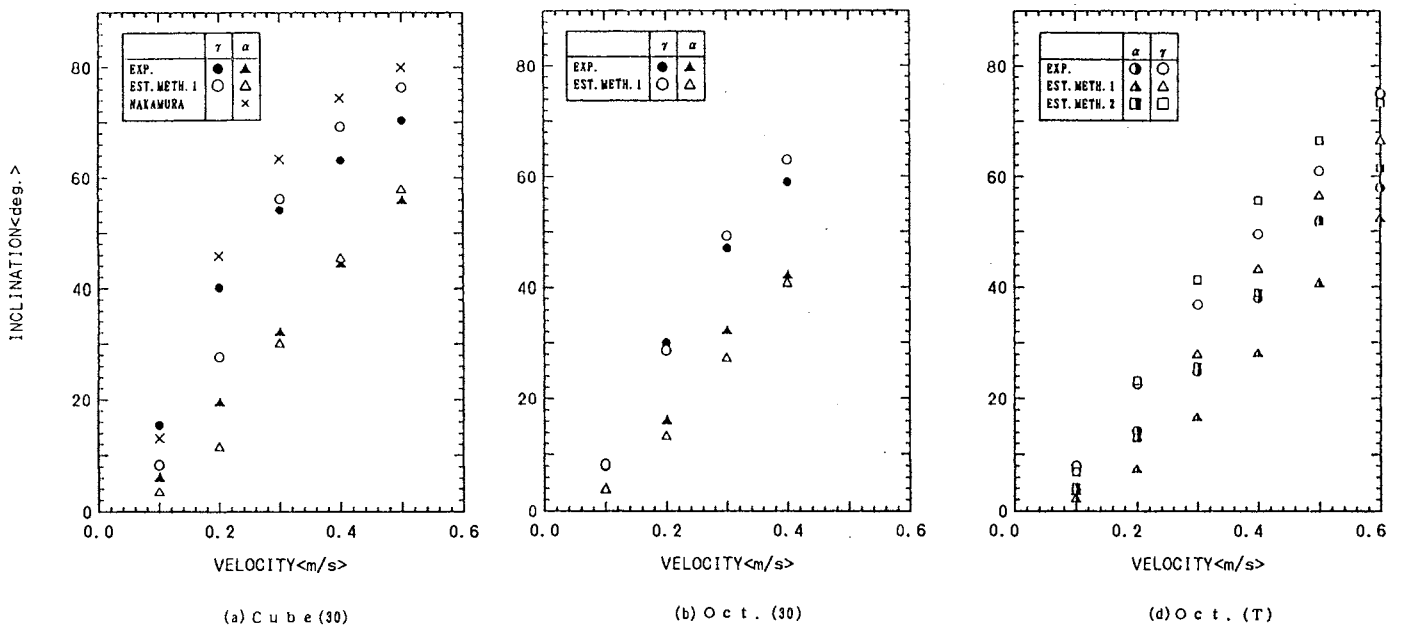
Fig. 6.2 Relationship of velocity and inclination (α, γ) of each net-cage model, and comparision between experimental values and predicted ones.

(b) O c t . (30)   (c) C u b e (45)   (d) O c t . (T)
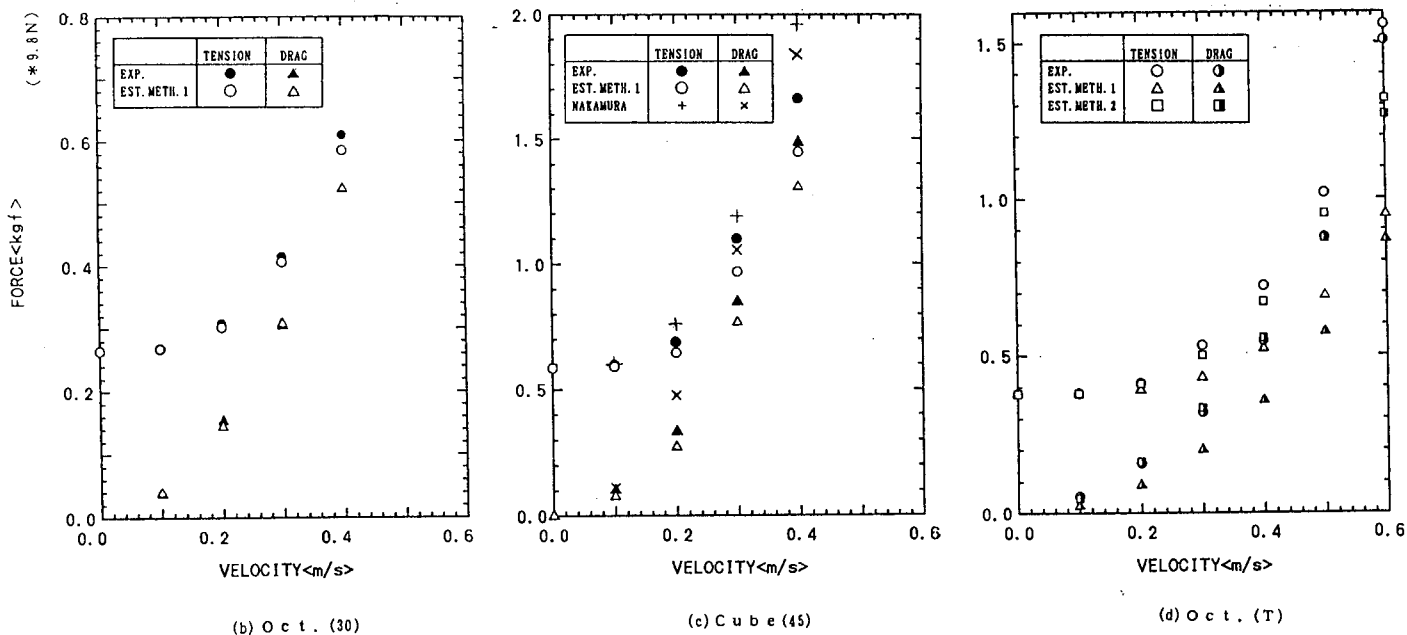
Fig. 6. 3 Relationship of velocity and tension of leg or drag force of each net-cage model, and comparision between experimental values and predicted ones.

Table. 6. 2 Comparision of predicted values to experimental ones.

Comparision / Model type	Comparision of force		Comparision of inclination	
	Tension	Drag	γ	α
(a) Cube(30)	○underest.	○underest.	○overest.	○overest.
(b) Octagon(30)	◎very good	◎very good	○overest.	○overest.
(c) Cube(45)	△underest.	△underest.	△underest.	△underest
(d) Octagon(T)	×underest.	×underest.	×underest.	×underest.
	○good	○good	○underest.	○underest.

7. Discussion

7.1 Present prediction method

The authors investigate two coefficients of C_d and τ, in order to predict resistance acting on a net-cage. τ is defined of a coefficient to correct resistance for interaction among plane nets. As another correction factor, η is defined of a coefficient to correct resistance for deformation of 3D-net. By using these coefficients, the authors show an idea to predict resistance of a net-cage in Fig.7.1. In this paper, It is possible to predict to <3> in Fig.7.1 from model experiment. Each coefficient is discussed.

(1) Drag coefficient C_d

Some experimental formulas are proposed and reliable. From these it is possible to obtain its modified Cd formula and predict

(Predicting resistance) (Predicting coefficince) (Considering facter)

<1> Predicting Cd of a twine

<2> Resistance of a plane net --- Modifying Cd <Cosidering interaction among twines on the same plane net>

<3> Resitance of a small scale mode of a net-cage --- Preicting τ <Considering interaction among distant plane nets>

<4> Resistance of a real scale model net-cage --- Modifying τ <Considering scale effect>

<5> Resitance of a real net-cage --- Predicting η <Considering deformation>
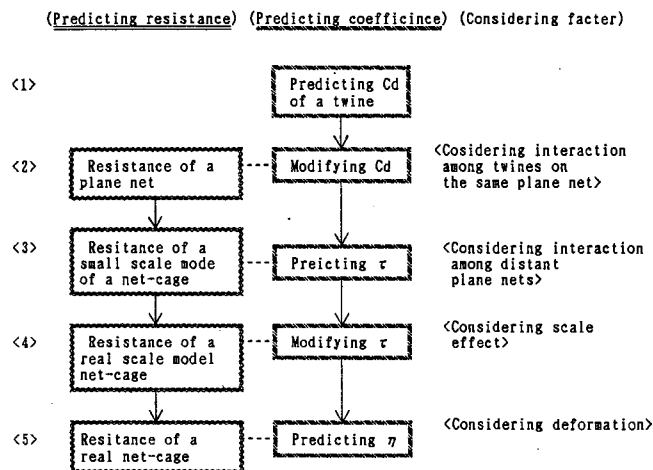
Fig. 7. 1 Outline of the method to predict resistance of a net-cage in uniform flow.

resistance of a plane net in any attitude. Such an example is Method.2.

But from results of Sec.2.4, predicted results by each method fluctuate. It is expected to develop a more reliable C_d formula for any given condition.

(2) Correction factor τ for 3-D interaction

It is considered that velocity decrease before the front net of the cage corresponds to the blockage effect, and decrease velocity in its middle or behind its back net corresponds to the wake effect. The correction factor τ depends mainly on these effect.

As the velocity is big enough, τ converges to a constant value, and the shape and angle of the models don't have important role for τ. Then the effect of its scale and solidity becomes important in order to predict resistance of a real net-cage.

(3) Correction factor η for deformation

The present net-cage is difficult to deform, because buoyancy of floats pull the cage up, and tension of a mooring line pulls it down. From experimental results, the effect of η is negligible for the present case.

(4) Inclination

From experimental results as shown white marks in Fig.3.1, The maximum is 1.5 times of the minimum. The effect of its inclination can't be ignored. Then present prediction method by iteration is useful in order to predict inclination and drag.

7.2 Method by Orange Book

As shown in Fig.6.2 and Fig.6.3, predicted results by Nakamura are close to experimental results in safety side. The authors discuss its reasons and problems.

(1) Modified C_d

Nakamura uses C_d=1.0, which underestimates C_d at $\alpha' >20$, and overestimates C_d at $\alpha' <20$ compared with experimental values. But in average predicted C_d by Nakamura is near experimental values in spite of considering τ not enough.

(2) Correction factor τ

Figure 3.1 shows predicted resistance values of 3-D net of Cube(30) by Nakamura at α=0 and 90. Predicted values by Nakamura are about 1.8 times of experimental values. Its reason is due to considering the effect of τ not enough. The authors note problems as follows; not considering the effect of blockage, how to select plane nets influenced by the wake, and confining the effect of momentum loss to the inside of a net-cage.

(3) Inclination

Nakamura predicts its inclination from the ratio of its surplus buoyancy to drag force of a net-cage without being inclined.

Figure 3.1 shows that predicted drag values by Nakamura at α=0 is close to experimental values of the inclined cage.

From above reasons, Nakamura's predicted values of inclination and force are near experimental values in spite of considering the effect of τ not enough and not considering interaction among twines on a same plane and the effect of inclination.

8. Conclusion

In this paper, the authors proposed a prediction method for resistance of a net-cage, tension and inclination of a mooring line in current. The predicted values agree well with experimental values. It was be proved that its inclination can be calculated from resistance of a net-cage. As for its resistance, it was proved to be predicted from two factors as follows; 1)modified C_d: it is a drag coefficient of a twine considering interaction among twines on the same plane as hydrodynamic characteristics of a plane net. 2)correction factor τ: it is a factor considering interaction among plane nets as hydrodynamic characteristics of a 3-D net. Some researchers are working on the problem of 1). But the problem of 2) is not investigated enough. The knowledge mentioned about 2) is important to make clear the hydrodynamic characteristics of a net-cage in future.

As for Orange Book, it was confirmed that its prediction method is useful in practice, though its way of thinking has problems due to the lack of the consideration of characteristics of 1) and 2).

As future problem, the scale effect of τ is important. It is necessary to collect experimental data of full scale net-cage and its physical interpretation.

References

1. Det Norske Veritas :Rules for Classification of Mobil Offshore Units Pt.3 Ch.1 Sec.4(1984)
2. Tauchi,M. :Bull.Japan.Soc.Sci.Fish. Vol.3, 1-4(1934)
3. Tauchi,M. :"Practical Fishery Physics", Kouseisha-Kouseikaku(1963)
4. Nakamura,M. :"Design Guidance of Structures for Coastal Fishing Ground Improvement and Development Act, Chap.14 aquacultural Fishery", Japan.Soc.Conservation of Fishery Resources(1978)
5. Nakamura,M. : "Fisheries Engineering", Kogyo-Jijitsushinsha(1980)
6. Imai,T. :Fundamental Studies of the Fluid Dynamical Resistance on the Plane Netting, Mem. Fac. Fish. Kagoshima Univ.(1986)
7. Osawa,Y. :Studies on Resistance of Plane Net against Flow of Water(3), Inst. Fish. Engn.(1985)
8. Konagatani,T. and Kawakami,T. : Resistance of Plane Net set Parallel to Stream(2), Journ. of Japan. Soc. Sci. Fish. (1971)
9. Miyazaki,T. :Basic Investigations on the Fishing Nets,(1)~(7), Journ. of Tokyo Univ. Fish.(1964)
10. Kawakami,T. :" Introduction to Analysis for Fishery", Kouseisha-Kouseikaku(1981)

EXPERIMENTAL STUDY ON THE MAN-MADE UPWELLING GENERATION STRUCTURE

K. Inaba*, J. Nakamura**, S. Hosono***. N. Takagi****, M. Sakuta*****

* Nihon University Graduate School, Japan ** Shimizu Corporation, Japana
*** Ohbayashi Corporation, Japan **** Facilities for Aquaculture Section National Research Institute
of Fisheries Engineering, Japan ***** Nihon University, Japan

Abstract

The workable area and level of this coastal fishing ground indicates that the areas suitable for fishing within Japanese waters have a water depth of 200 m or less and said to have an area of some 130,000 Km^2. however, according to the records from 1982 to 1986, areas made workable amount to some 1,000 Km^2, and if this area is added to the areas already in use of 1,000 Km^2, we will have a total workable area of some 12,000 Km^2. However, the current fishing ground utilization ratio is about 9.2%. Thus as far as the coastal area is concerned, sea areas nine times as large as the current fishing ground can be opened up as future fishing grounds.

The authors have paid attention to this utilization of deep layer water by means of an upwelling flow, and have intended on reclaiming fishing ground which has the same function as a natural upwelling fishing ground, by generating artificial and regional upwelling .

This report clarifies the characteristics of deep water, through research on single-and twin-type structures, reviewed a newly develop-ed structure. Their development techniques are also described.

1. Introduction

Currently, the annual haul by Japan is about 11 million tons, of which some 7 million are hauled within the 200-mile zone off Japan, and about 3 million tons are hauled within the 200-mile zone of foreign countries. However, the advent of the "200-mile exclusive fishing zone problem" has made it difficult to fish within the off-shores of foreign coun-tries, namely, we are forced to select between abandoning fishing within foreign coastal zones which have thus far been opened up by us or continuing by paying heavy taxes. As a result, we have been forced to make up the haul of some 3 million tons obtained within the 200-mile zones of foreign countries by fishing in Japanese coastal areas, and thus the Japanese marine products industry is planning on converting the "fish-catching" industry into a "fish-growing" industry.

Now,let us look at the 200-mile fishing zone within Japanese waters. Although the land area of Japan is relatively small at about 380,000 Km^2, the area of her 200-mile fishing zone measures about 4.5 million Km^2, which is the seventh largest fishing ground in the world. If we limit our attention to this coastal fish-ery zone of Japan, the sea area termed the "coastal fishery zone" amounts to some 400,000 Km^2, and its haul reaches some 3 mil-lion tons, which account for nearly one half of the haul within the 200 mile zone of Japan..By opening up the Japanese coastal zone in this way, considerable expansion of fishery produc-tion can be achieved.

Here, let us consider the necessary fishing ground reclamation from the viewpoint of "growing and nurturing a fishery." The growing and nurturing of a fishery can be broadly divided into "farm cultivation" and "seed cultivation." Farm cultivation includes fishing ground reclamation, and artificial reefs have been laid. Such activities can be termed as fishing ground reclamation, centered on hauling, studied from the standpoint of the effects of fish-gathering. On the other hand, seed cultivation is aimed at

the maintenance and expansion of resources 1) by managing fish, etc., when their dissipation is the highest, by artificial protection and breeding and 2) by releasing fish, etc., to more habitable environments. In the environment after release, however, mainteance of a balance of the ecology becomes important such as the food chain, etc. Many juveniles, after being released, find a food shortage in the sea area, thereby causing the sea area to become uninhabitable and making expection of an increase in fish impossible. However, the breeding method until fish mature to adulthood, as in cultures, cannot be said to be a very sound method, because of sea pollution due to fish feed and an imbalance between the quantity of feed given and the ultimate quantity of fish haul.

In view of the above, we want to create a habitable environment based on a natural rule and desire to achieve fishing ground reclamation 1) as a field where the propagation of fish and growing of juveniles can be positively achieved and 2) as a production fishing ground which can be viewed macroscopically. One of the examples of such a fishing ground reclamation which comes to mind is the upwelling sea area known as a good natural fishing ground and a high production area. Ryther estimated fish production, when he classified the ocean into open sea, coastal zone and upwelling zone, and clarified that, although the area of the upwelling zone accounts for only 0.1% of the total ocean area, its production is equivalent to 1/2the total ocean fish production. The reason for such high fish production in the upwelling zone is that deep water enriched with ocean nutrient salts are transported to the bright zone, resulting in a brisk generation of phytoplankton, improvement in primary ocean productivity and increases in sequentially-higher-order life forms.

Next, the generation mechanism of upwelling is shown. The generation mechanism of upwellng is divided into the eolian and orographic type. Fig. 1-1 shows main upwelling zones in the sea near Japan.

First, eolian upwelling (coastal upwelling) is explained. As the Ekman transport theory shows, surface waters, as a whole, in oceans of the rotating earth are transported to the Northern Hemispere at right angles and rightward to leeward. Therefore, when a southern (northern) wind blows along the east (west) coast on the lands of the Northern Hemisphere, the layer of surface water near the coast is transported offshore. Then, this surface layer water transported offshore is made up of lower layer water transferred to the upper layer, because one side of the sea is the coast, thereby generating coastal upwellng. As examples, offshore California on the eastern fringes of the Pacific Ocean and from offshore Chili to Peru in South America are well-known for this upwelling phenomena.

Orogrraphic upwellings are found around islands, around capes, on submarine mountain ranges, and around banks. There upwellings are generated regionally by submarine bottom topography and tides/currents. Examples of such upwellings are found in Pandara Attol, Izu-Oshima andthe sea zone around Miyake is.

In view of the above, the authors have paid attention to this utilization of deep layer water by means of an upwelling flow, and have intended on reclaiming fishing ground which has the same function as a natural upwelling fishing ground, by generating artificial and regional upwelling. Thus the authors have, through research on single-and twin-type structures, developed the artificial upwelling generation structure show in Fig. 1-2.

This report clarifies the characteristics of deep water, corrects the defects of structures shown in Fig. 1-3 and reviews a newly developed structure. Their development techniques are also described.

2. Test Method

The test was carried out by using the circular stream cistern (20 x 0.6 x 1.0 m) of the Department of Oceanic Architecture & Engineering at the Narashino Campus of Nihon University, School of Science and Technology.

In this test, a flow was visualized in order to measure the flow condition around the structure and the upwelling effect of the structure. Still cameras and VTR were used for recording purposes. As a method of visualization, a day flow tracer method was used. For coloring, meth-

ylene blue and rhodamine B were used. To estab-
lish similarity, the test was conducted accord-
ing to Froude's similarity. The upwelling rate
was defined as shown blow. For measuring flow
velocity, a propeller current meter and an
electromagnetic current meter were used.

3. Upwelling Generation Mechanism
of Upwelling Structure

The upwelling generation mechanism of the
structure proposed here has the same features as
the aforementioned circular stream cisterm. The
flow, which overflowed the top of the structure
installed in the flow, generates a large eddy in
the wake zone, and a negative pressure zone is
generated eddy. The flow which has passed
through the interior of the structure is con-
verged on by the fence, before the flow reaches
the water passage inside the structure. Simulta-
neously when the flow changes to an upward flow,
a suction phenomenon occurs due to the negative
pressure, which has been caused by the eddy at
the top. The flow which has passed through the
interior of the structure further rises and,
together with the transfer flow, becomes
upwelling.

Characteristics of Deep Water

This Chapter clarifies the characteristics
of deep water containing ample nutrient salts,
which become the determining factor in ocean
primary production through upwelling, and de-
scribes the effects of deep water on production.
a) High Nutrition Quality

Deep water has ample quantities of nutri-
tious chlorine necessary for the growth of
photosynthesizing algae, and its composition is
stable.
b) Cleanliness

Deep water has a low dissolved organic con-
centration and also has a stable composition.
There are but few parasites and little marine
fouling which live on sea foods, and disease,
germs and other bacteria are also sparse.
c) Low Water Temperature Property

It has stable physical and chemical proper-
ties at low water temperature.

Nutrient salts in deep water contain partic-
ularly large quantities of nitrate, phosphate
and silicate. The composition of nutrient salts,

expressed in atoms, in the seas around Japan
have been reported to be about 14:1:36 for N:P:
S. 1) This ratio is fairly stable regardless of
the depth and sea areas in question, and there-
fore, if the concentration of nitrogen nitrate
is used as an index of nutrient salts in this
report. Here an example of the productivity of
deep water is given. Fig. 3-1 shows the vertical
distribution of nutrient salts in the sea around
Izu-Oshima. There is little nutrient salt from
the surface to a depth of 30 m, and concentra-
tion suddenly increase at depths between 30 and
80m, until at a depth of 80 m, nitrogen nitrate
concentration reaches 10 μg/l. At a depth of 80
m or below, nutrient salt concentration gradual-
ly increases, as depth increases.

Fig. 3-2 shows the result of phyoplankton
culture, using sea water at various depths in
the sea around Izu-Oshima. In sea water from the
surface down to a depth of 40 m, phytoplankton
do not propagate, but at a depth of about 40 to
100 m, propagation suddenly increases, as the
depth increases. At a depth of 100 m or below,
it can be seen that even if depth increases,
propagation in quantity does very much. From
Figs. 3-1 and 3-2, therefore, it can be said
that 10 μg/l or above is sufficient for a
nitritic nitrogen concentration in deep water to
be used as an index in the propagation of
phytoplankton. In this way, a high correlation
exists between nutrient salt concentration and
primary productivity. Examples of vertical
distributions of nutrient salt concentrations in
other sea areas where orogreaphic upwelling
occurs are shown in Fig. 3-3 to 3-6. From these
results, trend can be seen that 1) at a depth of
80 to 100 m, nitrogen nitrate concentrations
reach about 10 μg/l, 2) at a depth of 100 to
200 m, nutrient salt concentrations gradually
change and 3) at a depth of 200 m or below,
nutrient salt concentrations stabilize.

Therefore, the authors define biologically
productive deep water as "sea water in which
inorganic nutrient salts exist at a nitrate
concentration of 10 μ g/l at a depth below the
bright zone, where photosynthesizing algae such
as phytoplankton find difficulty in growing."

4. Folded-surface type Upwelling Generation Structure

4.1 Outline of test

The cross section and paramenters of this structure are shown in Fig. 1-3.

this structure is developed through tests and research on single and twin types. In this chapter, the results of hydraulic test are shown whereby the optimum dimensions and shape were understood under the conditions shown in Table 4-1, and also the optimum shape of the structure itself is shown.

4.2 Results and Discussions

Figs. 4-1, 4-2, and 4-3 shown the rising rations for the respective resistance board angles (θ_3, θ_4) of throttling angles of (θ_1, θ_2)=(10°, 40°) (θ_1, θ_2)=(20°, 50°) and (θ_1, θ_2)=(30°, 60°) respectively. The ordinate represents the upwelling rate and the abscissa represents the ratio between 1) height H_2 from the cistern bottom to the bottom edge of the throttling board and 2) resistant board height H_3 vertical height ratio H_1/H_2 at that time are shown in Table 4-2. Therefore, when the upwelling rate viewed from H_1/H_2 is taken into consideration, it has been clarified that the optimum shape of this structure will have:
Throttling angle   :

(θ_1, θ_2) = (30°, 60°)
Resistance board angle :

(θ_3, θ_4) = (20°, 50°)
Vertical height ratio :

$$H_2/H_3 = 1.0$$

Fig. 4-4 shows a typical photo showing the test results of the optimum-shaped model.

5. Cube Structure (Non-directional)

5.1 Outline of Test

When it is considered to install a folded-surface-type structure in the actual sea are, it is desirable to install the structure so that it will perpendicularly intersect the flow at the sea area. The flow condition in the actual sea area, however, is considerably complex, because reciprocating flows such as tidal flow exist, although there is a predominant flow direction. Further, in submarine construction work at great depth, the execution of work taking into consideration such directionality is very difficult.

In view of the above, the necessity has arisen for developing an artificial upweling structure which will not be governed by the directionality of flow. In view of the above, the authors here have proposed the cube structure shown in Fig. 5-1 on the basis of the results of tests so far conducted. To comprehend appropriate model dimensions, it has been arranged that both the height of the outside board H_1 and the height of the inside board H_2 can be increased in height at three stages, and hydraulic model tests have been conducted, using respective height ratios and main dimensions as parameters, to examine the optimum shape of the structure. Fig. 5-2 shows the cross section of the model.

5.2 Results and Discussions

Fig.5-3 shows the upwelling rate obtained by the height ratio of the inside board H_3 to the outside board H_1. Fig. 5-4 shows the upwelling rate obtained by the height ratio of the inside board H_3 to the outside board H1, when the flow direction is changed by 45°. Fig. 5-5 shows the upwelling rate obtained by the height ratio of the outside board H_1 to the inside board H_3, when flow direction is changed by 45°.

Table 5-1 shows, as a test result, the upwelling rates and a mean upwelling rate.

As a trend. Fig. 5-3 TO 5-5 indicates that the upwelling rate is within a range of 150 to 200%, and the shape which gives the greatest upwelling effect is obtained when the outside board is low and the inside board is high. For the influence on an upwelling effect, height H_3 of the inside board becomes a parameter, and as the height ratio increases, the upwelling rate also tends to increase. Viewed as the mean upwelling rate from Table 5-1, directionality, even though it is slight, has appeared. The optimum shape is shown in Fig. 5-6.

6. Multi-direction Upwelling Structure (Cylinder Structure)

6.1 Outline of Test

According to the hydraulic test results of the cube structure, it is clearly inferior in its upwelling effect to the folded surface type structure. Also from the views of work execution and economy, the former structure seems to be

lacking practicality. Further, the cube struc-
ture has shown slight directionality. In view of
the above, the authors here have taken into con-
sideration the loss in upwelling efficiency and
the effects of fish-gathering reefs, and pro-
posed a cylindrical, non-directional upwelling
structure.

Its model consists of a combination of the
open and fence unit. Through combination of
these two units, the height and open area of the
structure can be changed. Further in order to
find the optimum shape, a hydraulic test has
been conducted using height H_1 of the open unit
and height H_2 of the fence unit as shown in
Fig. 6-1.

6.2 Results and Discussions

Fig. 6-2 shows the upwelling rate due to
changes in the ratio of open unit H_1 to fence
unit height H_2.

Fig. 6-3 shows the upwelling rate due to
changes in the ratio of fence unit H_2 to open
unit height H_1.

Fig.6-2 and 6-3 indicate that even if the
fence unit is raised higher than open unit
height H_1, no upwelling effect can be obtained,
and the upwelling rate tends to lower, and the
trend that even if the open unit is raised
higher than the fence unit height H_2, no
upwelling effect is obtained, and H_1/H_2 lowers
within a vicinity of 2.0 times. Therefore, the
opimum shape isthe type shown in Fig. 6-4.

Viewed from Table 6-1, it can seen that this
cylinder structure barely has directionality.
This will become clearer, if this structure is
compared with the cube structure.

7. Conclusion

Development methods and hydraulic model
tests of upwelling structures ranging from the
single type to the current cylinder structure
containing the fishreef effect have been de-
scribed. Ultimately, the upwelling effect which
was obtained by the folded-surface-type struc-
ture was lost by adoption of nondirectionality,
but the authors have proposed an economical and
practical cylindrical fish-reef-type model. In
the future, the authors will select the most
suitable reclamation sea area for the use of the
cylinder-type structure and to lay it in an

actual sea site.

Therefore, the authors would like to show
below the conditions which must be satisfied in
order to reclaim fishing-ground with an artifi-
cial upwelling structure at a depth of 200 m or
below.

1) There should be a water mass, which has usa-
ble deep water or equivalent characteristics
(nitrogen nitrate concentration of 10 μ g/l or
above) in the vicinity of the fishing-ground re-
clamation area. Particularly within coastal re-
gions, sea areas where marine bottom ravines
interlace would be advantagous.

2) This upwelling structure requires an appro-
priate flow velocity of sea water in order to
raise water using tide and current energy.

3) It is possible to artificially create the
same function as that of the upwelling flow
generated in natural sea area, but it is impos-
sible to actually realize the same scale of
upwelling found in natural sea areas. Therefore,
the artificial upwelling structure should be
installed near naturally occurring upwelling
areas to assist through natural upwelling.

4) The purpose of deep water utilization lies
in the expansion of primary productivity of sea
areas. Therefore, an efficient conversion to
phytoplankton is necessary. For this purpose, a
stagnation time for sea water of a few days is
necessary, and it is required that a stagnant
sea area near the upwelling zone be setup.

Ideally application of an upwelling structure
within an enclosed area is desirable for enabl-
ing the expansion of primary productivity and
the promotion of sea water exchange.

Table 4-1　case of expriment

throttling board angle (θ_1, θ_2)		$(10^\circ, 40^\circ)(20^\circ, 50^\circ)(30^\circ, 60^\circ)$
resistant board angle (θ_3, θ_4)		$(10^\circ, 40^\circ)(20^\circ, 50^\circ)(30^\circ, 60^\circ)$
distance of models	H_2/H_3	0.4, 0.5, 0.6, 0.65, 0.7, 0.75, 0.8, 0.95, 1.0, 1.25, 1.3, 1.5
	H_2/B	1.0
velocity (cm/s)		5, 8, 11, 14, 17, 20, 25, 30
the depth (cm)		50

Table 4-2 th results of expriment

(θ_1, θ_2)	(θ_3, θ_4)	upwelling rate (%)	reached high (cm)	H₂/H₃
(10° ,40°)	(10° ,40°)	306	22	0.8
	(20° ,50°)	347	25	0.6
	(30° ,60°)	368	25	0.4
(20° ,50°)	(10° ,40°)	318	30	0.8
	(20° ,50°)	323	30	0.6
	(30° ,60°)	341	31	0.6
(30° ,60°)	(10° ,40°)	306	33	1.0
	(20° ,50°)	323	40	1.0
	(30° ,60°)	324	35	0.6

Table 5-1
upwelling rates

type	angle	upwelling rate (%)
A	0°	187.8
	45°	168.9
B	0°	185.6
	45°	162.2

Table 6-1
average of percentage

	angle	upwelling rate(%)
cubu model	0°	169.3
	30°	168.4
cylinder model	0°	187.8
	45°	168.9
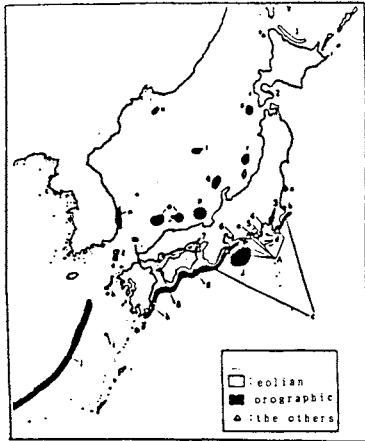
Fig. 1-1 The main upwelling zone in the sea near Japan
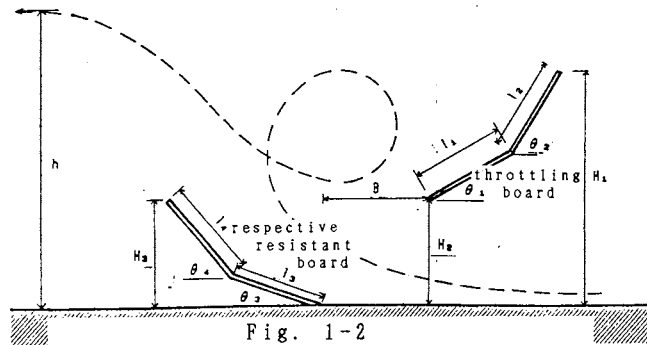
Fig. 1-2
upwelling generation structure
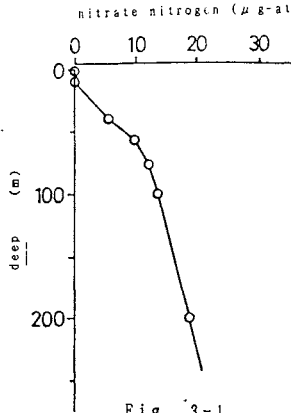
Fig. 3-1
vertical distribution of nutrient salts in the sea around Izu-oshima
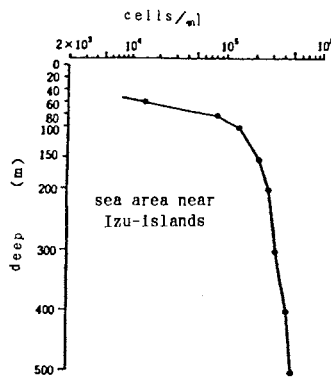
Fig. 3-2
result of phyoplankton cultore
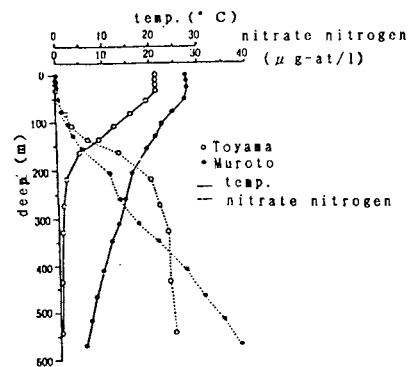
Fig. 3-3
vertical distribution of nutrient salts in the sea around Muroto and Toyama
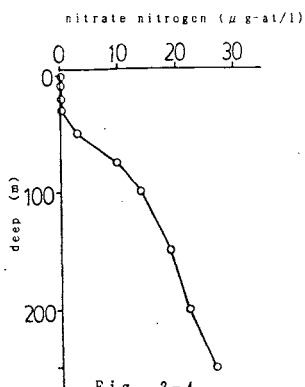
Fig. 3-4
vertical distribution of nutrient salts in the sea around Bousou
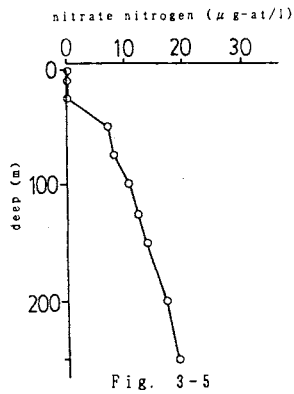
Fig. 3-5
vertical distribution of nutrient salts in the sea around Toi-misaki
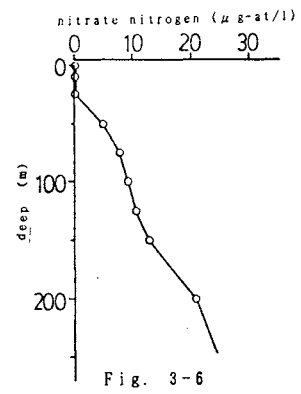
Fig. 3-6
vertical distribution of nutrientsalts in the sea around Shiono-misaki

upwelling rate (%)
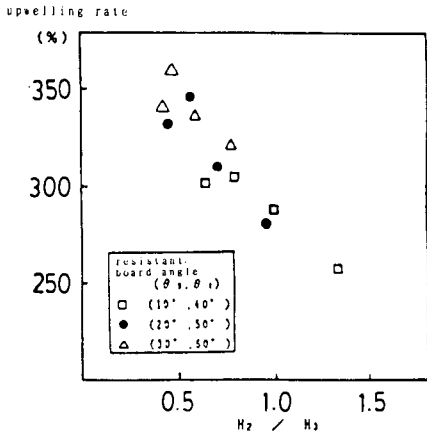
Fig.4-1 relation between eate of lift and expriment model [(θ₁,θ₂)=(10° ,40°)]

upwelling rate (%)
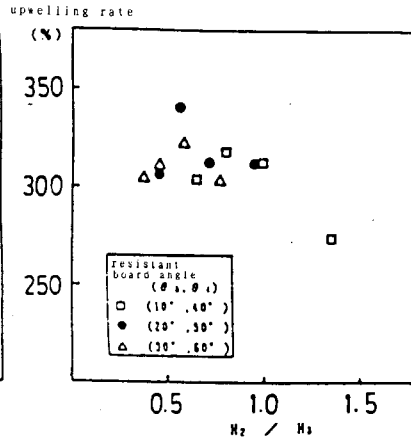
Fig.4-2 relation between eate of lift and expriment model [(θ₁ , θ₂)=(20° ,50°)]
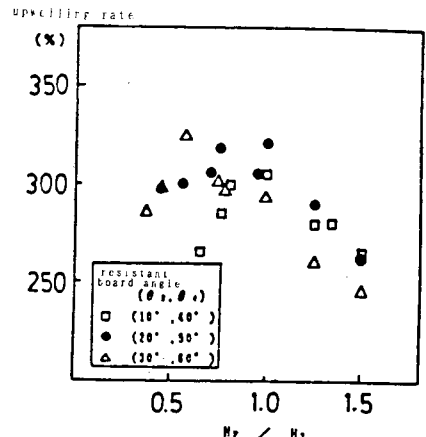
upwelling rate (%)

Fig.4-3 relation between eate of lift and expriment model [(θ₁,θ₂)=(30° ,60°)]
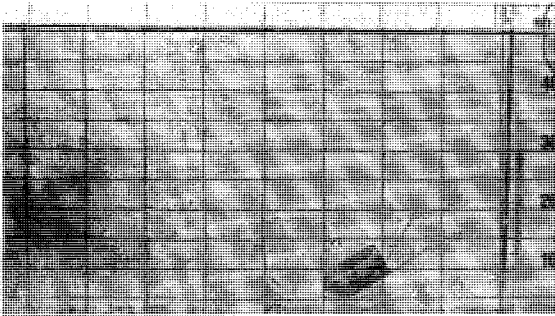
Fig. 4-4 the test results of the optimumshaped model
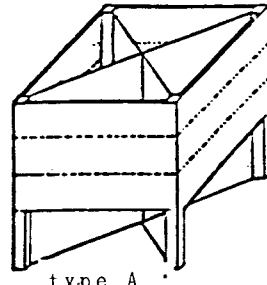
type A   Fig. 5-1 test models   type B
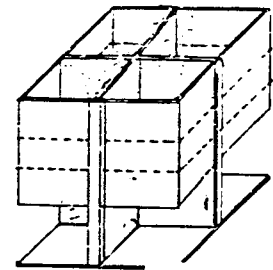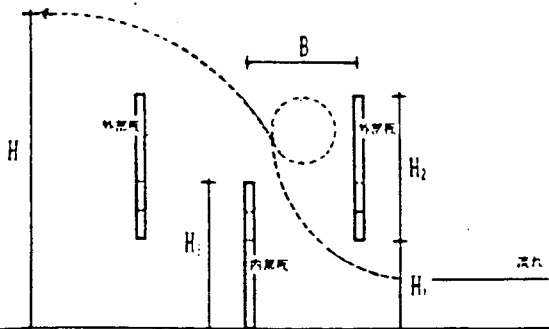
Fig. 5-2 section of model
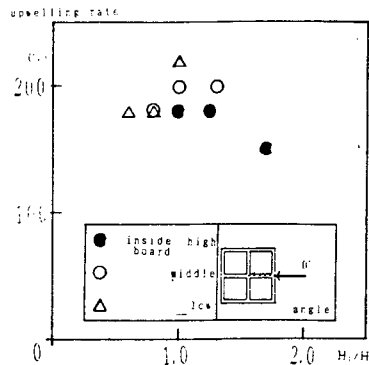
upwelling rate

Fig. 5-3 the upwelling rate obtained by the height ratio of the inside board
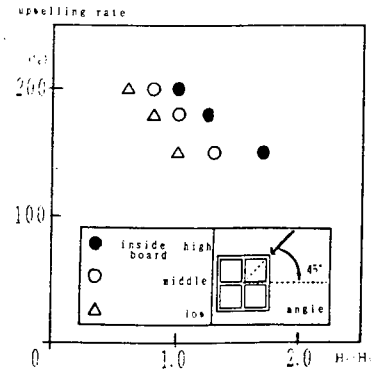
upwelling rate

Fig. 5-4 the upwelling rate obtained by the height ratio of the inside board
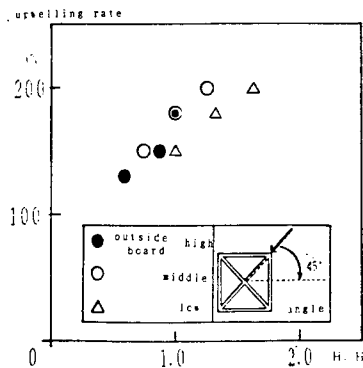
upwelling rate

Fig. 5-5 the upwelling rate obtained by the height ratio of the outside board
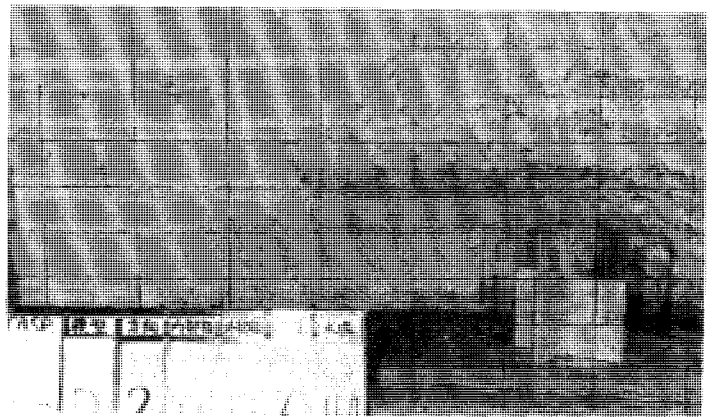
Fig. 5-6 the test results of the optimumshaped model
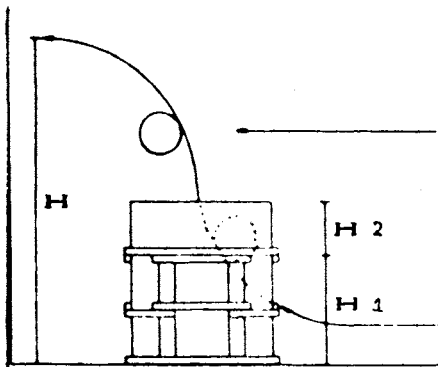
Fig. 6-1
cylinder structure model
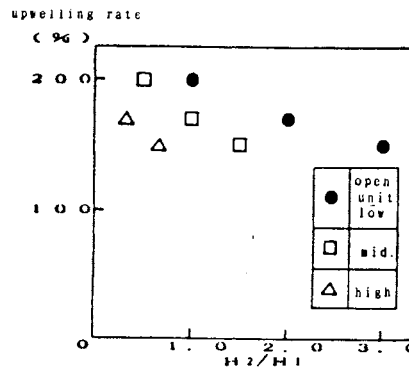
Fig. 6-2
the rate of H₁ to H₂
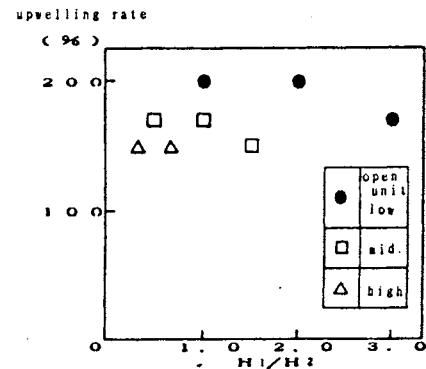
·Fig. 6-3
the rate of H₂ to H₁
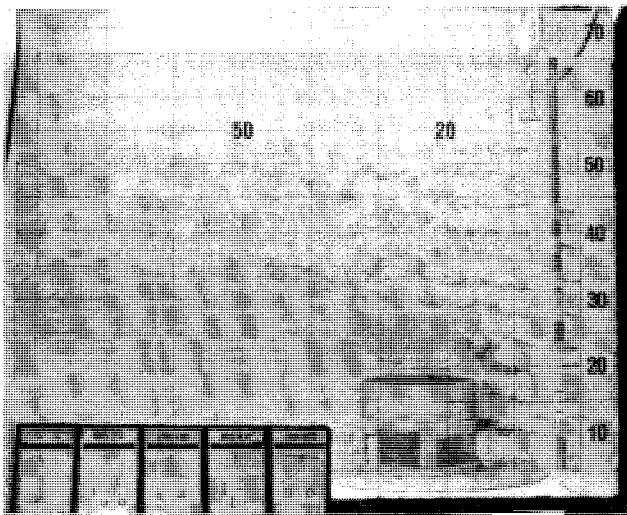
Fig. 6-4 the test results
of the optimumshaped model
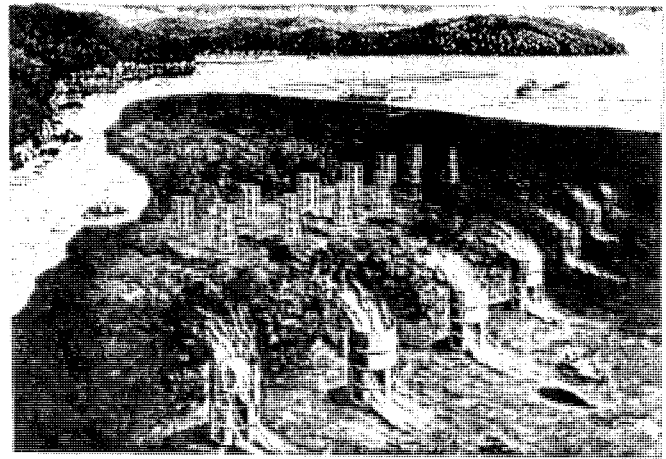
Fig. 7-1
An Image of the Fishing-ground using the
Man-made Upwelling Generation Structure

References

1) A. Naito: "Search and Utilizationof Marine
Biological Resources, CMC Co., March, 1986

2) T. Toyota and T. namajima:
"Bio-environmental
Characteristics of Ocean DeepWater – New
Resource for Bio-production, "Ocean Science
and Technology Center, Test and Research
Report Jamstecture 16,1986

3) T. Tsuzuki and T. Nakao:
"Marine En vironmental Characteristics at
Natural Upwelling Zone, " Suisan-Doboku,
Vol. 22 No.2 (Through-No.44), March, 1986

4) Marine Indaustry Research Society:
"Research Report on Fishing-ground Haul
Improvement Techniques by Ocean Ranch System,"
Aug. 22, 1986

5) Meteorological Agency:
"Marine Meterials by Meteorological Agency,"
No.77, 1985

6) S.Kawashima, Y.Takagi and M.Sakuta:
"research on Fold-surface-type Upwelling
Generation Board (No.1) and
(No.2),"Proceedings of the Arch. Inst. of
Japan Symp., Aug., 1985

7) S.Kawashima, Y.takagi, M.Sakuta and S.Hosono:
"Research on Folded-surface-type Upwelling
Generation Board (No.3), lbid., Ocyober, 1986

8) Marine Industrial Research Society:
"Marine Ranch News," Vol. 2, Mar., 1986

9) T. Shimazu and A. Setoguchi:
"Coastal Upwelling alog soto-Bo Coastal
Region, " Suisan-Doboku, Vol. 23, No.1
(Through-No.45), Nov., 1986

10) T. Nemoto:
"Coastal Upwelling and Plankton," Coastal
Marine Research Note, Vol.15, No.2, Feb., 1978

BASIC STUDIES ON LIFTING OF MANGANESE NODULES BY AIR-LEFT-PUMP

Takayuki Saito, Fumio Kiyono, Tetsuo Yamazaki, Yasuo Tomishima, Takashi Usami

National Research Institute for Pollution and Resources, Japan

1. INTRODUCTION

The Agency of Industrial Science and Technology has started the large scale project of research and development of Manganese Nodule Mining System since 1981.

Manganese Nodule Mining System consists of total system (mainly mining ship), collector system, lift system, machinery handling system, and measurement & control system.

National Research Institute for Pollution and Resources takes charge of fundamental study which is necessary to develop the lifting system and collector system and to establish operation method of these systems.

In this project an ocean mining test is planned at sea of the southeast of Hawaii in the last year of the project. At the ocean mining test the water depth is over 5,000 m and lifting system will be operated under the severe natural condition, such as a rapid change in the weather.

To give a full role to the lifting system's ability under such conditions, it is necessary to estimate the performance of lifting system by computer simulation and to establish the operating method forward to the ocean mining test.

In this research, at first, the floating velocity of manganese nodules which is necessary for constructing fundamental equations was measured and an empirical formula was deduced.

Next, fundamental equations for three phase flow were constructed by using this formula.

Then the result of simulation was compared with the result of pilot plant test in which a 200m vertical water tank was used.

2. MEASUREMENT OF FLOATING VELOCITY OF MANGANESE NODULE

2.1 MEASUREMENT METHOD

The terminal velocity was obtained by the following method.

A particle was dropped into the acrylic pipe filled with water. The time during the particle passed through two measurement sections was measured by a watch.

Terminal velocity was calculated from the length between measurement sections and the time to pass through.

Inside diameter of acrylic pipe was 600mm, and the length between measurement sections was 1.14m.

The measurement of floating velocity of particles was done by using the apparatus shown in fig.1. The test pipe is acrylic pipe which inside diameter is 150mm and, length is 3m equipped with pressure taps at the 1500mm interval.
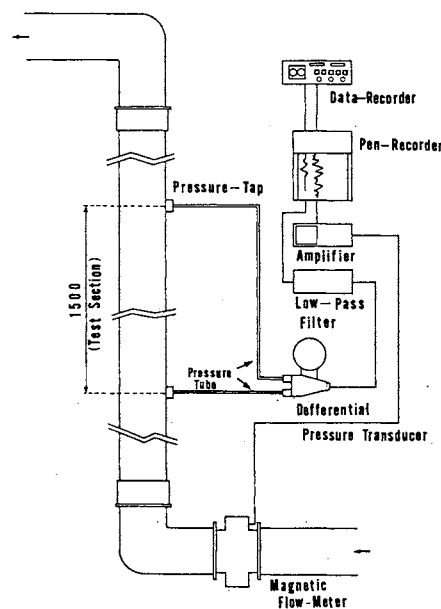
Fig. 1   Schematic diagram of Equipment for Floating Velocity

The water was supplied to the test pipe from a head tank which height is 20m and inside diameter is 3m. The flow of water was controlled by the valve which was equipped under the head tank. The velocity was measured by magnetic flow meter, and pressure drop was measured by a differential pressure transducer.

Particles which weight were measured in advance were put into the pipe. The valve was opened slowly to supply water in the pipe. The particles began made to float gently. The velocity at which the whole particles floated was adopted as the floating velocity.

2.2 RESULT OF EXPERIMENT AND CONSIDERATION

2.2.1 TERMINAL VELOCITY

The measurement result of the terminal velocity of a particle was shown in table 1.

Table 1 Physical Propaties of Solid Particles

Solid	ds(mm)	Ll(mm)	Ls(mm)	Ld(mm)	Sf	Ws(gr)	Ss	Vsf(m/s)	Vsh(m/s)	CD	Rep
Gravel	37.5	52.6	26.9	42.6	0.70	72.40	2.61	1.020	0.950	0.758	3.48×10^4
S.N-1	40.1	45.8	32.0	42.2	0.85	65.70	1.94	0.792	0.788	0.785	2.95×10^4
S.N-2	42.0	44.3	39.1	41.8	0.91	75.80	1.96	0.838	0.830	0.750	3.20×10^4
S.N-3	42.3	48.6	37.6	42.1	0.83	78.80	1.99	0.807	0.786	0.842	2.15×10^4
Rubber ball	41.8	41.8	41.8	41.8	1.00	44.90	1.17	0.365	0.482	0.698	1.39×10^4
Mn (ISs)	32.7	49.0	21.9	41.3	0.47	38.30	2.03	0.457	0.461	2.110	1.73×10^4
Mn (ISs)	36.1	54.2	26.0	37.5	0.57	50.10	2.04	0.589	0.577	1.410	2.42×10^4
Mn (SEr)	36.6	41.7	35.2	36.7	0.89	51.90	2.02	0.837	0.778	0.697	3.18×10^4
Mn (SEr)	56.0	64.0	55.8	59.3	0.89	169.00	1.82	0.903	0.798	0.737	5.84×10^4
Mn (Sr)	19.6	25.5	16.3	19.7	0.75	8.23	1.98	0.502	0.497	1.030	6.21×10^3
Mn (Sr)	26.7	29.6	24.9	26.8	0.85	19.50	1.95	0.681	0.652	0.698	2.04×10^4
Mn (Ss)	25.7	34.5	21.0	25.6	0.71	17.00	1.86	0.517	0.523	0.975	8.38×10^3
Mn (Db)	46.6	55.6	45.0	49.1	0.85	92.60	1.72	0.784	0.708	0.714	4.17×10^4
Mn (Db)	48.0	69.9	40.6	45.0	0.70	112.00	1.93	0.692	0.655	1.220	3.78×10^4
Mn (Db)	63.7	73.1	62.1	64.9	0.88	258.00	1.89	0.904	0.795	0.907	6.56×10^4
Mn (Ds.r)	36.0	50.4	29.1	38.1	0.67	51.40	2.08	0.635	0.618	1.390	1.45×10^4
Mn (Ds.r)	43.2	61.5	34.1	48.3	0.63	88.90	2.05	0.665	0.621	1.470	1.82×10^4
Mn (Ds.r)	54.0	77.3	43.9	63.0	0.63	169.70	2.03	0.707	0.638	1.510	2.42×10^4
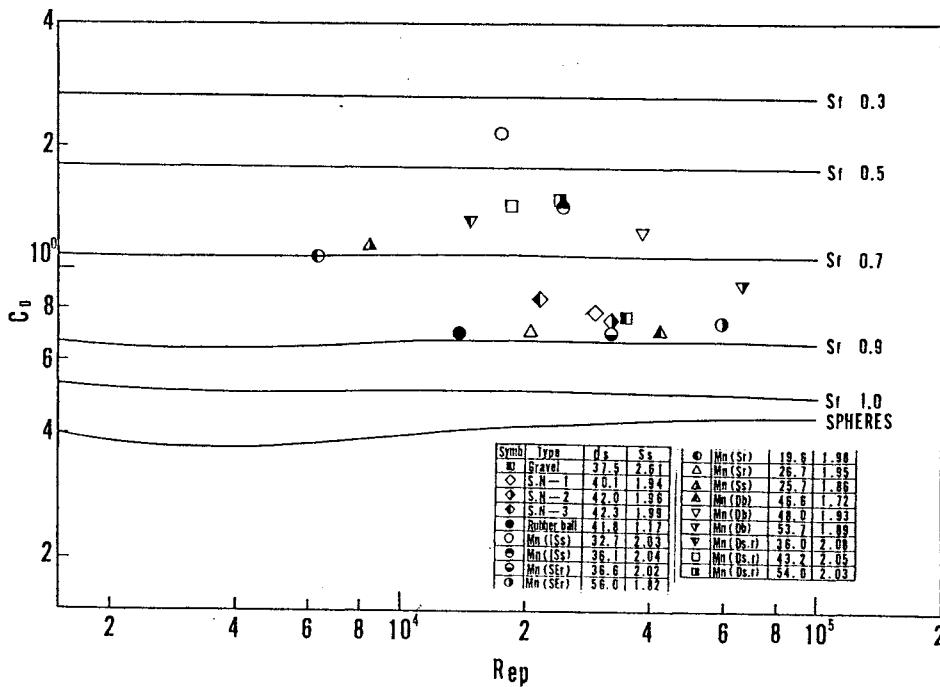
Fig.2 Relationship between Rep and Cd

Drag coefficient and particle Reynolds Number were calculated by using following equations.

$$C_D = (4/3)\{gd_s(\rho_s - \rho_w)\}/V_{sf}^2 \qquad (1)$$

$$R_{ep} = d_s V_{sf} / \nu \qquad (2)$$

Fig.2 was the relations of Cd and Rep on the logarithm graph. Solid lines show the relation of Cd and Rep in the case that the shape factor proposed by Albartson was used as a parameter.

Fig.2 showed that the particles used in the experiment belonged to the Newtonian region and the particles which have complex figure and complex property of surface as manganese nodule showed the same tendency as other particles if arranged by the shape factor.

It was clear from the definition of the shape factor Sf that Sf was equal to the ratio between the projected area toward settling direction and the area of section perpendicular to that projected area and Sf seemed to be the ratio of the representative length of the projected area to the representative length of section perpendicular to that projected direction.

Sf was thought to show the relation of location between the settling posture and the point of separation.

Though the drag force is the sum of the pressure drag and the frictional drag, in the Newtonian region the pressure drag occupy the most part of the drag force.

The pressure drag was decided by the projected area of particle toward settling direction, and in the Newtonian region the location of the point of separation is constant.

In addition,thinking the physical meaning of shape factor Sf, the ratio of drag coefficient of nonspherical particle to that of spherical particle was rearranged by using a correct coefficient in which shape factor and property of surface were considered.

The relation between Cd/Cds and Sf was shown in fig.3. From this figure it is found that there is a linear relation between Cd/Cds and Sf if plotted in a logarithm sheet.

This relation was represented approximately as following equation.

$$C_D = 1.427 C_{Ds} S_f^{-1.65} \qquad (3)$$

In the region of this experiment the drag coefficient of a spherical particle is 0.4 constantly, so equation (3) was rearranged as following equation.

$$F_r = 1.46 S_f^{0.825} \qquad (4)$$

here

By deforming equation(4) still more, next equation was obtained.

$$V_{sf} = 1.46 S_f^{0.825} \sqrt{gd_s(S_s - 1)} \qquad (5)$$

Fig.4 and fig.5 were obtained by rearranging the experimental data using equation(5). In fig.4 average value of each sample was plotted. In fig.5 average value of each group was plotted. Calculated value agree with measurement value very well.

Fig.3 Relationship between Cd/Cds and Sf
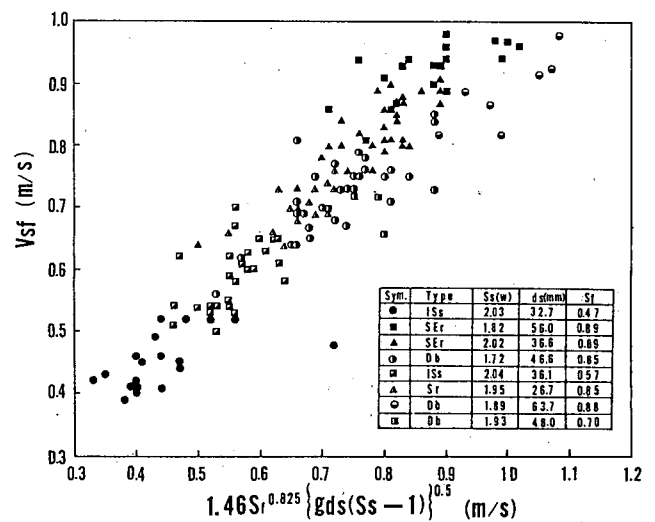
Fig.4 Comparison of Experimental Value and Calculated Value on Terminal Velocity
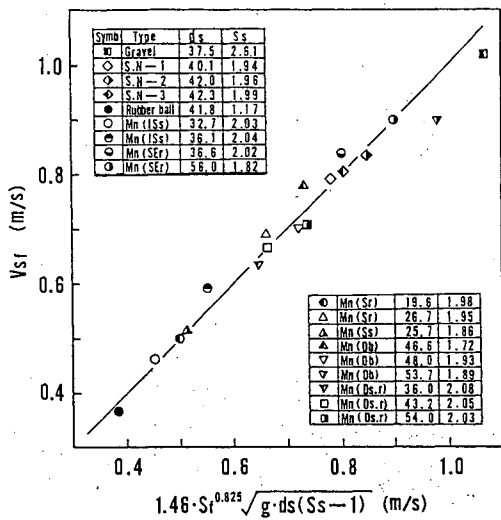
Fig.5 Comparison of Experimental Value and Calculated Value on Terminal Velocity

2.2.2 HINDERED SETTLING VELOCITY

As the result of rearranging the experimental data by the ratio of the settling velocity and the ratio of diameter ds/D, the hindered settling velocity was represented as following equation approximately.

$$V_{sh}/V_{sf} = 1 - (d_s/D)^2 \qquad (6)$$

And using equation(5) and (6), above equation rearranged to following equation.

$$V_{sh} = \frac{1.46\{1 - (d_s/D)^2\}S_f^{0.825}}{\sqrt{gd_s(S_s - 1)}} \qquad (7)$$

Comparison of the calculated value with the experiment value was shown in fig.6.
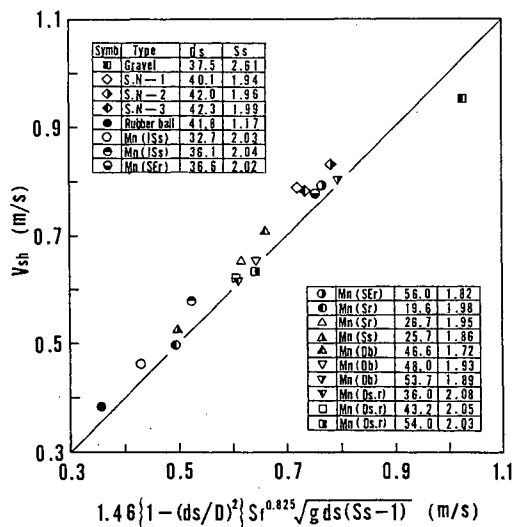
Fig.6 Comparison of Experimental Value and Calculated Value on Hindered Settling Velocity

2.2.3 FLOATING VELOCITY OF PARTICLES

Floating state of particles in this experiment was recognized to be different from that of very small size particles. In the case of small particles the particles distributed uniformly in the pipe, on the other hand particles in this experiment flowed as the projected area to the flow direction is maximum shown in fig.7.
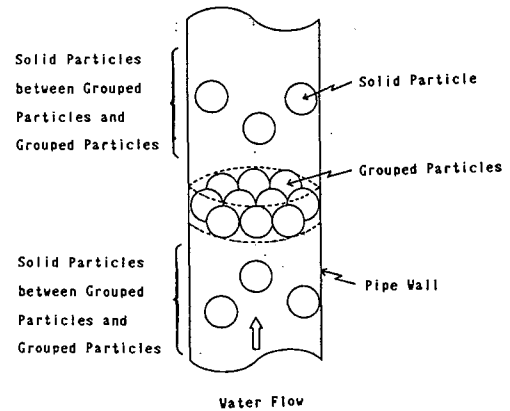
Fig.7 Floating Model of Solid Particles

In addition the particles were arranged as they occupied the maximum area of the cross section of the pipe. Several groups of the particles were formed in the pipe and the condition of floating was maintained by means of exchange of the particles between these particles groups and the space between those groups.

It was found that the floating condition of particles was affected by the arrangement of particles in the pipe as well as the property of particle, wall effect et al.

Relation of the floating velocity of the particles Vf and the concentration was shown in fig.8.

Fig.8 Relationship between Floating Velocity and Cs

Vf decreased rapidly as the concentration increased in the low concentration region but in the high concentration region the rate of decrease of Vf got small and the linear relation appeared between Vf and Cs. Solid line of fig.8 was drawn based on the calculation of Noda's equation.[2] But these results of calculation differed from this experimental result. That was due to the difference of the floating state between Noda's experiment and this experiment.

In this research it was found that the results of experiment were arranged by introducing shape factor Sf as following equation.

$$V_f/V_{sh} = \sqrt{S_f^{5.38Cs}} \exp(-4S_f C_s)/ \quad (1 + C_s) \tag{8}$$

The comparison of calculation results to measurement results was shown in fig.9. Equation(8) can estimate Vf accurately.

Fig.9 Comparison of Experimental Value on Vf/Vsh

3. SIMULATION

3.1 FUNDAMENTAL EQUATIONS

Simulation model which is based on the equation of motion was composed by taking account of the result of 200m pilot plant test. Model shown in fig.10 was assumed.

By applying momentum equation for incompressible fluid to the section between face 1 and face 2, and momentum equation for compressible fluid to the section between face 2 and face 3, equation (9) and (10) were obtained.

$$dP_\emptyset + (\gamma_{m\emptyset}/2g)d(V_{m\emptyset}^2) + \gamma_{m\emptyset}dx + f_{r\emptyset}dx = 0 \tag{9}$$

$$dP_3 + d(V_{m3}^2 \gamma_{m3}/2g) + \gamma_{m3}dx + f_{r3}dx = 0 \tag{10}$$

Fig.10 Air-Lift-Pump Model

3.2 DEFINITION OF EACH VARIABLE

3.2.1 SUPERFICIAL VELOCITY OF MIXTURE

Superficial velocity of solid-liquid mixture and superficial velocity of air-solid-liquid mixture are defined as follows.

$$V_{m\emptyset} = \{(1 - C_{s\emptyset})V_{ls\emptyset} + C_{s\emptyset}V_{s\emptyset}\}/A \tag{11}$$

$$V_{m3} = \{AV_{m\emptyset} + Q_{g\emptyset}(P_a/P)\}/A \tag{12}$$

3.2.2 SPECIFIC GRAVITY OF MIXTURE

$$\gamma_{m1} = C_{s\emptyset}\gamma_s + (1 - C_{s\emptyset})\gamma_l \tag{13}$$

$$\gamma_{m3} = f_{a3}\gamma_a + (1 - f_{a3})\{(1 - C_{s1})\gamma_l + C_{s1}\gamma_s\} \tag{14}$$

3.2.3 VOLUMETRIC CONCENTRATION OF SOLID PARTICLE

Equation(15) which express the relation between particle supplying concentration and concentration in pipe was deduced by considering local velocity, local concentration, and drift velocity of solid phase and liquid phase.

$$\{V_{s\emptyset}/(V_{s\emptyset}+V_{l\emptyset})\}/C_s = (C_{sr}V_{Tr})/(C_{sr}V_{Tr}) + C_{sr}V_{sdr}/ \{C_{sr}(V_{s\emptyset}+V_{l\emptyset})\} \tag{15}$$

3.2.4 MEAN VOID FRACTION OF THE THREE PHASE FLOW

If the method of Zuber and Findly was expanded to the three phase flow and the drift velocity was constant in cross section of the pipe, the void fraction was calculated by a following equation.

$$f_{a3} = \{(P_a/P)(Q_{go}/A\}/[\{AV_{m\emptyset}+$$

$$(P_a/P)Q_{go}\}/(k_f A)+V_{ad3}] \quad (16)$$

3.2.5 VOLUMETRIC CONCENTRATION OF SOLID PARTICLE AT THE CROSS SECTION OF THE THREE PHASE FLOW

Applying same method as above, the volumetric concentration is expressed as a following equation.

$$C_{s3} = \{(P_a/P)(Q_{go}/A\}/[\{AV_{m\emptyset}+$$

$$(P_a/P)Q_{go}\}/(k_f A)+V_{sd3}] \quad (17)$$

3.2.6 PRESSURE DROP OF THE THREE PHASE FLOW

Empirical equation concerned with pressure drop coefficient and the modified Frude number are used.

Here a and b is coefficient and index decided by the flow pattern.

$$(\Delta P_{f3} - \Delta P_{f2})/(C_s \Delta P_{f2}) =$$

$$(\alpha/\lambda_{1R})[V_{mR}^2 \sqrt{C_D}/$$

$$\{gD(\gamma_s/\gamma_1 -1)\}] \quad (18)$$

3.3 CALCULATION METHOD

Taking account of the transition of the flow pattern, a function by which a section is divided automatically was provided in program.

Runge-Kutta method was adopted to solve the differential equation. Convergence of the calculation was judged by comparing the pressure of upper end of the top section with the atmospheric pressure.
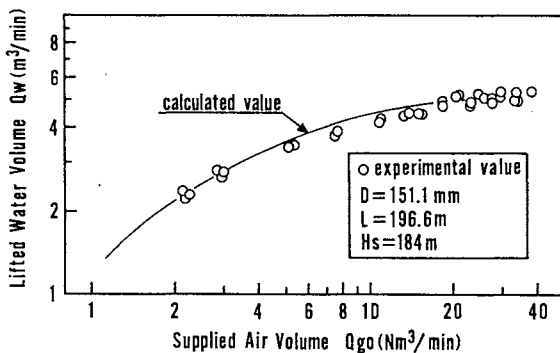
Fig.11 Example of Calculation Results for Lifted Water Volume

3.4 RESULTS OF CALCULATION

Taking the case that the depth of air inlet was 184m, the comparison between calculation result of lifted water volume and experimental result was shown in fig.11.

In other case, the lifted water volume and the tendency of curve which showed lifted water volume for air supply agreed with experimental result very well, so the simulation program was considered to be appropriate.

The comparison between calculation result of lifted slurry volume and experimental result in the case that the depth of air inlet was 184m was shown in fig.12.
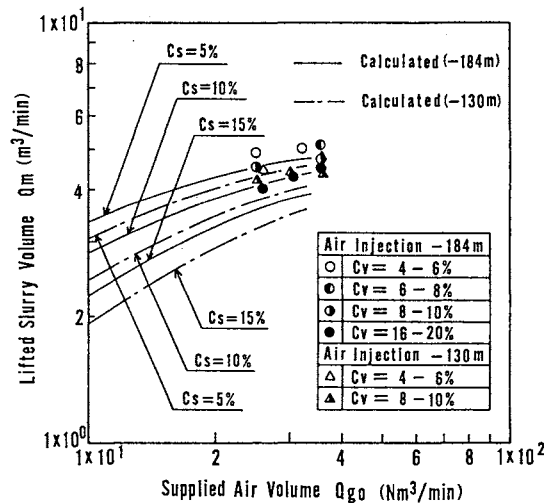
Fig.12 Example of Calculation Results for Lifted Slurry Volume

Though the calculation result of lifted slurry volume is smaller than the experimental result, tendency of lifted slurry volume for air supply, rate of drop of lifted slurry volume accompanied with increase of slurry concentration and effect of the depth of air inlet showed good agreement with experimental result.

So this simulation model was considered to be reasonable in the case of three phase flow. The difference between the calculation result and the experimental result was thought to be due to the evaluation of particle concentration and pressure drop at three phase flow.

4. CONCLUSION

In this research, at first the floating velocity of manganese nodule was measured.

As a result following equation was obtained.

$$V_f/V_{s\infty} = \sqrt{S_f^{5.38Cs}}\exp(-4S_fC_s)/$$

$$(1 + C_s) \quad (8)$$

Secondly, using this equation a simulation model was constructed to evaluate the lifting capacity.

Lastly, comparing the calculation result with the experimental result of 200m pilot plant test, both results agreed very well.

REFERENCES

1)Report No.12, Subcmm, on Sedimentation, Inter-Agency Committee on Water Resources, Minneapolis, Minn. 1958
2)Karoku NODA, et al, J. Mining & Metallurgical Inst. Jap. , Vol. 86, No. 981, pp13-18

NOMENCLATURE

Cd   drag coefficient
Cds   drag coefficient of particle
ds   equivalent settling velocity diameter
Fr   Froude number
fa   void fraction
g   gravitational constant
L_{ℓ} length of particle
Ls   breadth of particle
L_d thickness of particle
Rep   particle Reynolds number
Sf   shape factor
Vsf   terminal velocity
Vsh   hindered settling velocity
Vf   floating velocity
ρ_s density of particle
ρ_w density of liquid
ν coefficient of kinematic viscosity
Vad   drift velocity
P   static pressure
Pf   friction loss
γ specific weight
A   cross sectional area of the pipe
V   velocity
ζ coefficient of inlet loss
λ friction factor
t_u hold up ratio
D   pipe diameter
Q   flow rate
Cs   spacial volume concentration of solid
P   pressure loss

SUBSCRIPT

1   liquid
g   gas
s   solid
0   solid-water 2-phase flow
2   air-water 2-phase flow
3   air-water-solid 3-phase flow
o   normal condition
a   in atmospheric condition
m   mixture
r   at arbitrary radius

ENGINEERING PROPERTIES OF DEEP-SEA MINERAL RESOURCES

T. Yamazaki, Y. Tomishima, K. Hanada, K. Tsurusaki

National Research Institute for Pollution and Resources, Japan

Abstract

Deep-sea manganese nodules, massive submarine polymetallic sulfides, and cobalt rich manganese crusts, which have been found in large quantities at basins and seamounts of the Pacific, have been considered as future potential resources for Au, Pt, Ag, Cu, Pb, Zn, Ni, Co, and Mn.

Among these, mining technology of manganese nodules has been developed these twenty years by several countries and groups, but there still remain some problems in designing a commercial miner. The other two resources have just been in stages of feasibility study for exploitation. Almost nothing is known, however, in order to evaluate their trafficability and excavatability.

Some physical and engineering properties of these three mineral resources, which are essential factors for design of their mining systems, are introduced and summarized in the study. Fundamental design concepts of their mining systems are proposed. Some subjects to be solved are also presented.

Nomenclature

A : contact area

A_p : projected area

c : vane shear strength

d : distance between loading point

F_a : adhesive resistance

F_c : cutting resistance

F_f : frictional resistance

F_s : separating resistance

F_t : total resistance from sediments

f_p : nodule pick-up force per unit area

k_a : adhesive coefficient

k_c : cutting coefficient

k_f : frictional coefficient

N : number of observed data

n : porosity

P : contact pressure

P_1 : load at failure

r : coefficient of correlation

S : cutting area

S_c : compressive strength

S_t : tensile strength

s : standard deviation

V : volume

W_o : dried weight in air

W_s : saturated weight in water

W_w : saturated weight in air

w : water content

x : observed data of x axis

$\bar{x}$: average of data of x axis

y : observed data of y axis

ρ_s : solid density

ρ_d : density under water saturated condition

ρ_w : density of water

1. Introduction

Manganese nodules are widely distributed on soft deep-sea sediments at water depths of 4,000 to 6,000 m. They have been considered as a future strategic metal resource because they are rich in manganese, copper, nickel, and cobalt. Mining technology of manganese nodules has been developed these twenty years by several countries and groups [1, 2, 3], but there still remain some problems in designing a commercial miner. Fundamental engineering properties of manganese nodules and deep-sea sediments are reviewed and updated in the paper. In concluding these characteristics, a design concept for driving and excavating mechanisms of nodule miner is discussed.

Massive submarine polymetallic sulfides have been worthy of attention these ten years. They are formed by hydrothermal processes associated with spreading centers of plate techtonic activity. They contain considerable amounts of gold, silver, lead, zinc, etc.. Their general distribution characteristics are shown in Table 1 comparing with the other resources. From engineering view point, however, they are the least known of the deep-sea resources to date [4]. Some physical and engineering properties of their samples are introduced in the paper. An important information is requested for their resource assessment.

Cobalt rich manganese crusts lately have become a center of interest because they include several metals having top priority such as cobalt, manganese, and platinum. Crusts which include considerable percentage of cobalt have been found at water depths between 800 and 2,400m, coating island slops, seamounts, and tops of guyots. Their distribution characteristics are also summarized in Table 1. Very little engineering data has been published until now [5, 6, 7, 8]. Fundamental physical and engineering properties of crusts and their substrates are introduced in the paper. Some important considerations for the design of mining system and problems to be solved are presented as well.

2. Engineering Properties

2.1 Nodules

Considering the distribution aspects, geotechnical properties of deep-sea sediments are very important factors for the design of nodule miner. Many data have been measured with box core samples on board. Vane shear strength, cone penetrating resistance, and water content which were measured in nodule dense area during the GH83-3 Cruise [9] are summarized in Table 2. The water content is defined by the following equation:

$$w = \frac{W_w - W_o}{W_o} \times 100 \qquad (1)$$

Nodule abundance, nodule size distribution, and nodule pick-up force are also important factors. Data obtained during the Cruise are shown in Figs. 1 - 3. The abundances and the size distribution were obtained from nodules sampled by free fall grabs. The pick-up force was measured with nodules sampled by a box corer. Nodule pick-up force per unit area is defined by the following equation:

$$f_p = \frac{W_s + F_s}{A_p} \times 100 \qquad (2)$$

2.2 Polymetallic Sulfides

Density, porosity, and P wave velocity were measured as the physical properties with the same test piece which was saturated by water in a vacuum water pot for 48 hours. Then the weights in water and in air under water saturated condition were measured. After being dried at 105 degrees Celsius for 24 hours, the weight in air under fully dried condition was measured. The saturated density and the porosity were calculated using the following equations respectively:

$$\rho_d = \frac{W_w}{(W_w - W_s) / \rho_w} \qquad (3)$$

$$n = \frac{W_w - W_o}{W_w - W_s} \times 100 \qquad (4)$$

Compressive strength, tensile strength, Young's modulus, Poisson's ratio, Shore hardness, and micro-Vickers hardness were measured as the engineering properties. Because quantity of samples was not sufficient, it was difficult to core standard cylindrical test pieces. Therefore, rectangular column test pieces in about 20 mm x 20 mm x 40 mm were used for uni-axial compressive strength measurements, and irregularly shaped test pieces for point load tensile strength measurements. The tensile strength is calculated using the following equation [10]:

$$S_t = 0.9 \, P_1 / d^2 \qquad (5)$$

Samples from Gorda Ridge at East Pacific Rise [11] and Izena Calderon at Okinawa Trough [12] were tested. The results are summarized in Table 3 comparing with the results of Kuroko ores which are expected as old massive submarine polymetallic sulfides.

2.3 Crusts

Considering the distribution aspects, physical and engineering properties of crusts themselves and those of their substrates are important factors for the design of crust mining system. Measured items and methods of physical and engineering properties are almost the same as massive submarine polymetallic sulfides. But, because crusts and some of their substrates were too weak and quantity of samples was not sufficient, it was difficult to get even rectangular column type test pieces. Therefore, a substitutional method using irregularly shaped test pieces for compressive strength measurement was chosen. In order to avoid size effect, fragmental specimens with weight ranging from 30 to 50 grams in water saturated condition were used for the tests. The compressive strength was calculated from the ordinary uni-axial load testing method using the following equation [13]:

$$S_c = 5.26 \ P_1 \ / \ V^{2/3} \tag{6}$$

Samples from the equatorial region of the Central Pacific, the south east and the south west regions of Marcus Island, and around Okinotori Sima Island were tested. The results of measurements are summarized in Table 4. Frequency distribution of the density, the compressive strength, and the tensile strength were shown in Figs. 4 - 6.

3. Discussion

3.1 Nodules

Deep-sea sediments are treated like ideal clay from results of undrained and unconsolidated tri-axial compression tests [14]. The shear strength is, therefore, the most important geotechnical property. It affects bearing capacity, settlement, cutting resistance, etc.. The other important property is the sensitivity. Sensitivity value of three which is the average in Table 2 is the margin between usual and sensitive clay. For example, relatively lower critical bearing capacity is expected when the sensitivity is higher than three [15].

Total resistance acting on a nodule miner caused by deep-sea sediments are presented by the following equation from the results of previous researches [16, 17]:

$$F_t = F_c + F_f + F_a \tag{7}$$

$$\text{where} \quad \begin{aligned} F_c &= k_c \ c \ S \\ F_f &= k_f \ P \ A \\ F_a &= k_a \ c \ A \ . \end{aligned}$$

The shear strength has major role in this equation, too. The coefficients shown in Table 5 mean that it is a principal design criterion to reduce cutting resistance.

In order to recover much nodules from miner track, it is required to remove nodules in advance with the tracking. It means that the sediments on the track are disturbed prior to the tracking. Because of high sensitivity of sediments it is difficult to expect what is the probability of strength reduction. This would make control of miner driving difficult. Hence it follows uncertainty of miner path.

The same kind of trade-off relationship is appeared between the contact pressure of miner and the negative pressure generated by hydraulic nodule pick-up device. Balancing these trade-off factors is an important design concept of a commercial miner.

3.2 Polymetallic Sulfides

Solid density of polymetallic sulfides which is calculated from the following equation is close to that of Kuroko ore, but the porosity is higher than that of Kuroko

ore:

$$\rho_s = \frac{W_o}{(W_o - W_s) \ / \ \rho_w} \tag{8}$$

The difference of the porosity causes the low values of the compressive strength, the tensile strength, and the Shore hardness.

It is considered from these results that the conventional technique for medium hard rock will be adaptable for excavating mechanism as examined in previous feasibility studies [18, 19]. Mining system itself is, however, affected by dimensions of massive ore body. Deposit distribution sizes of spread on sea floor and of depth below the sea floor are required for the resource assessment and the design of mining system.

3.3 Crusts

Considering the result of density measurement, 1.9 g/cm^3 is preferable for average density of crust, although 1.8 g/cm^3 was adopted in the previous feasibility study of crust mining [20]. Gravity separation in ore dressing would be useful because about 60 % of the distribution of substrates in density is not overlapped with the one of crusts. On the other hand, strength difference between crusts and their substrates is probable to be used for excavation and dressing.

Some correlations are expected from the results of measurements. The relationships between the engineering properties of substrates are shown in Figs. 7 - 9. They show feasibility of utilizing these correlations for estimation of engineering properties of substrates. When data accumulation of the engineering properties becomes sufficient, accurate estimation of substrate characteristics seems to be possible.

Quantitative evaluation of crust thickness, coverage, and surface microtopography by visual and/or acoustic means are also very important informations both for the exploration and for the exploitation.

4. Conclusions

Engineering properties of manganese nodules and deep-sea sediments are summarized. Shear strength and sensitivity of sediments become key factors for design of commercial miner. Balancing some trade-off factors is considered to be an important design concept of a commercial miner.

Porosity of massive submarine polymetallic sulfides is higher than that of Kuroko ore. The conventional technique for medium hard rock will be applicable for sulfide excavating mechanism. Information

about dimensions of massive ore body is desired to design whole mining system.

Average density of cobalt rich manganese crusts under water saturated condition is 1.9 g/cm^3. Density and strength differences between crusts and their substrate are very important factors for design of excavating and dressing systems. Some useful correlations are observed between engineering properties of substrates. Quantitative information about crust distribution characteristics are also required.

References

1. Takahara, H., Handa, K., Ishii, K., and Kuboki, E., "Research and development project of manganese nodule mining system in Japan", Proceedings of 16th Offshore Technology Conference, Paper No.4782, (1984)
2. Tolefson, D. C., Latimer, J. P., and Kaufman, R., "Design consideration for a commercial deep ocean nodule mining system", Proceedings of 5th Offshore Mechanics and Arctic Engineering, Vol.2, pp.470-480, (1986)
3. Bernard, J., Bath, A., and Greger, B., "Analysis and comparison of nodule hydraulic transport systems", Proceedings of 19th Offshore Technology Conference, Paper No.5476, (1987)
4. Crawford, A. M., Hollingshead S. C., and Scott, S. D., "Geotechnical engineering properties of deep-ocean polymetallic sulfides from 21°N, East Pacific Rise", Marine Mining, Vol.4, No.4, pp.337-354, (1984)
5. Cruickshank, M. H., and Paul, R. C., "Characterization of seabed rocks for mine planning in the EEZ", Proceedings of 18th Offshore Technology Conference, Paper No.5236, (1986)
6. Larson, D. A., Tandanand, S., Boucher, M. L., Olson, M. S., Morrell, R. J., and Thill, R. E., "Physical properties and mechanical cutting characteristics of cobalt-rich manganese crusts", Bureau of Mines Report of Investigations 9128, (1987)
7. Yamazaki, T., Tsurusaki, K., Tomishima, Y., and Handa, K., "Preliminary study on engineering properties of cobalt rich manganese crusts", Proceedings of TECHNO-OCEAN'88 International Symposium, Vol.1, pp.74-80, (1988)
8. Yamazaki, T., Tomishima, Y., Handa, K., and Tsurusaki, K., "Fundamental study on remote sensing of engineering properties of cobalt rich manganese crusts", Proceedings of 9th Offshore Mechanics and Arctic Engineering, Vol.1, Part B, pp.605-610, (1990)
9. Tsurusaki, K., and Yamazaki, T., "Manganese nodule research cruise in the Penrhyn Basin, Central Pacific", Mining and Safety, Vol.30, No.10, pp.524-542, (1984), (in Japanese)
10. Hiramatsu, Y., Oka, Y., and Kiyama, H., "Rapid determination of the tensile strength of rocks with irregular test piece", Journal of the Mining and Metallurgical Institute of Japan, Vol.81, No.932, pp.1024-1030, (1965), (in Japanese)
11. Malahoff, A., "Comparison between Galapagos and Gorda spreading centers", Proceedings of 13th Offshore Technology Conference, Paper No.4129, (1981)
12. Halbach, P., Nakamura, K., Wahsner, M., Lange, J., Sakai, H., Käselitz, L., Hansen, R.-D., Yamano, M., Post, J., Prause, B., Seifert, R., Michaelis, W., Teichmann, F., Kinoshita, M., Märten, A., Ishibashi, J., Czerwinski, S., and Blum, N., "Probable modern analogue of Kuroko-type massive sulphide deposits in Okinawa Trough back-arc basin", Nature, Vol.338, No.6215, pp.496-499, (1989)
13. Protodyakonov, M. M., "New methods of determining mechanical properties of rocks", Proceedings of International Conference on Strata Control, Paris, Paper No.C 2, (1960)
14. Tsurusaki, K., Handa, K., and Yamazaki, T., in preparation, "Geotechnical properties of deep-sea sediments from potential manganese nodule mining areas"
15. Yauchi, K., and Asakawa, Y., "Soil mechanics", Shokokusya, Tokyo, p.229, (1968), (in Japanese)
16. Reece, A. R., and Grinsted, T. W., "Soil mechanics of submarine ploughs", Proceedings of 18th Offshore Technology Conference, Paper No.5341, (1986)
17. Yamazaki, T., Tsurusaki, K, and Handa, K., "Experimental study of adhesion appearing between plate and clay", Proceedings of 8th Offshore Mechanics and Arctic Engineering, Vol.1, pp.573-579, (1989)
18. Cruickshank, M. J., and Zippin, J. P., "A development scenario for mining in the Gorda Ridge area", 16th Offshore Technology Conference, Paper No.4779, (1984)
19. Kaufman, R., "Conceptual approaches for mining marine polymetallic sulfide deposits", Marine Technology Society Journal, Vol.19, No.4, pp.50-56, (1985)
20. Halkyard, J. E., "Technology for mining cobalt rich manganese crusts from seamounts", Proceedings of OCEANS'85, Vol.1, pp.352-374, (1985)

Table 1 Distribution characteristics of manganese nodules,
massive submarine polymetallic sulfides, and cobalt
rich manganese crusts

	Nodules	Polymetallic sulfides	Crusts
Depth	4,000-6,000m	1,200-3,500m	800-2,400m
Topography	Flat sea bottom	Spreading center of rise, back arc, etc.	Island and seamount slopes Top of guyots
Substrate	Sediments	Basalt Metamorphic rock	Basalt Hyaloclastite Limestone
Morphology	Nodule	Chimney and mound on sea floor	Crust (Nodule)
Deposit aspect	Coverage:<75% Abundance: <40kg/m^2	Massive ore tens million m^3	Thickness:<20cm Coverage:<100% Abundance: <200kg/m^2
Metal content	Co :< 0.5% Mn :<35 % Fe :<25 % Ni :< 2 % Cu :< 2 %	Fe :<40 % Cu :<15 % Pb :<25 % Zn :<50 % Au :<15 ppm Ag :< 1 %	Co :< 2 % Mn :<35 % Fe :<25 % Ni :< 1 % Cu :< 0.5% Pt :< 2 ppm

Table 2 Geotechnical properties of deep-sea sediments

Depth (cm)	Vane shear strength (gf/cm^2)						Sensitivity	Cone penetrating resistance(gf/cm^2)			Water content (%)		
	Undisturbed			Remolded									
	Ave.	Max.	Min.	Ave.	Max.	Min.	Ave.	Ave.	Max.	Min.	Ave.	Max.	Min.
4	14.3	28.3	6.1	4.8	8.5	2.7	3.0	68	156	40	293	353	200
10	26.0	38.2	18.4	8.5	11.9	5.1	3.1	165	227	100	257	304	221
16	31.1	47.7	14.3	10.5	16.0	4.8	3.0	194	245	97	250	335	191
22	34.5	58.7	11.9	12.4	22.5	5.1	2.8	243	332	90	239	300	176
28	35.4	52.9	14.3	13.9	25.9	6.5	2.6	277	330	120	231	291	168
34	30.0	36.5	15.7	11.6	16.4	6.8	2.6	246	298	130	212	254	150
40	30.2	36.5	17.7	11.2	13.3	7.8	2.7	205	313	125	211		

Table 3 Engineering properties of polymetallic sulfides

	Izena Caldelon						Gorda Ridge	Kuroko ores
	A	B	C	D	E	F		
Density(g/cm^3)	2.94	3.87	2.73	2.32	2.82	1.88	3.14	4.13-4.75
Solid density(g/cm^3)	4.63	4.55	4.49	4.25	4.71	3.64	4.68	4.18-4.89
Porosity(%)	37	15	39	45	40	48	33	0-3
P wave velocity(km/sec)	3.4	3.5	3.1	1.9	2.3	1.8	3.7	3.4-4.7
Compressive strength(MPa)	24.0	38.2	21.0	3.45	6.37	3.13	9.06	84-144
Tensile strength(MPa)	2.23	4.09	3.04	0.61	0.80	0.14	0.09	2.0-13.4
Young's modulus(GPa)	21.9	35.2	18.5	5.7	7.8	22.5	24.5	39.5-62.6
Poisson's ratio	0.15	0.28	0.47	0.31	0.27	0.31	0.35	0.25-0.38
Shore hardness	10.2	18.3	14.6	1.6	9.4	5.2	x	32.5-38.9
Micro-Vickers hardness	162	218	154	x	59	x	x	176-226

Table 4 Summary of engineering properties of crusts and their substrates

	Crusts	Substrates
Density (g/cm^3)	1.65-2.17	1.44-2.92
Porosity (%)	43-74	7-69
P wave velocity (m/sec)	2090-3390	1760-5860
Compressive strength (MPa)	0.5-16.8	0.1-68.2
Tensile strength (MPa)	0.1- 2.3	0.0-18.9

Table 5 Coefficients of deep-sea sediments

k_c	k_f	k_a
8.2	0.12	0.08

N = 149
x̄ = 13.8
s = 11.2
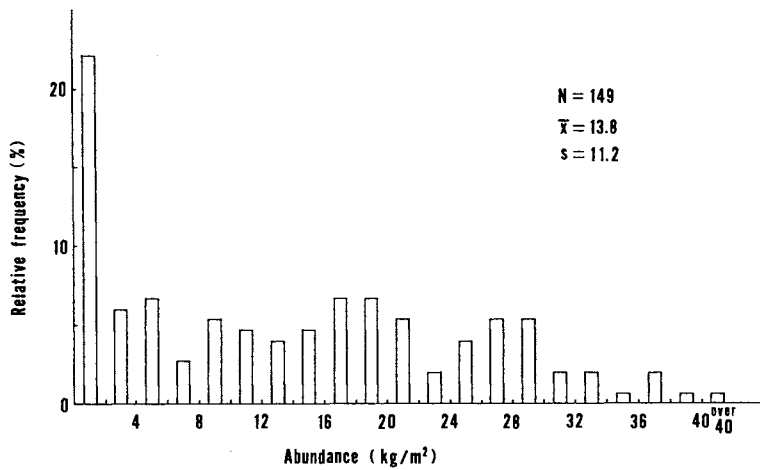
Fig. 1 Frequency distribution of nodule abundance

N = 6200
x̄ = 2.4
s = 1.4
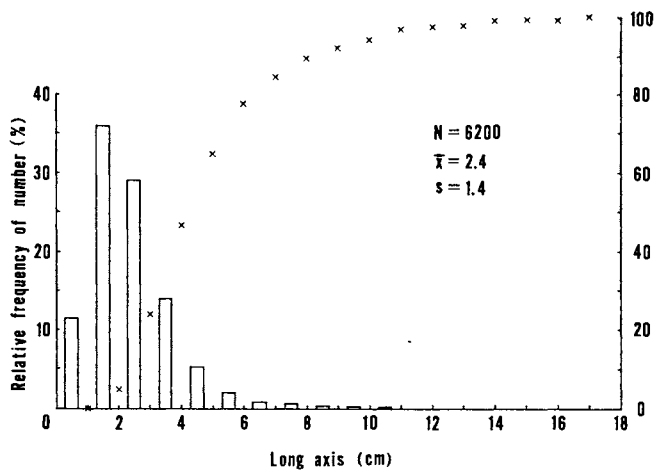
Fig. 2 Frequency distribution of nodule size

N = 141
x̄ = 7.4
s = 2.6
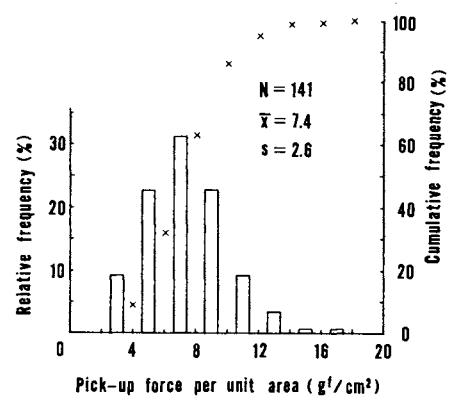
Fig. 3 Frequency distribution of nodule pick-up force

N = 196
x̄ = 1.90
s = 0.09

N = 150
x̄ = 2.17
s = 0.34
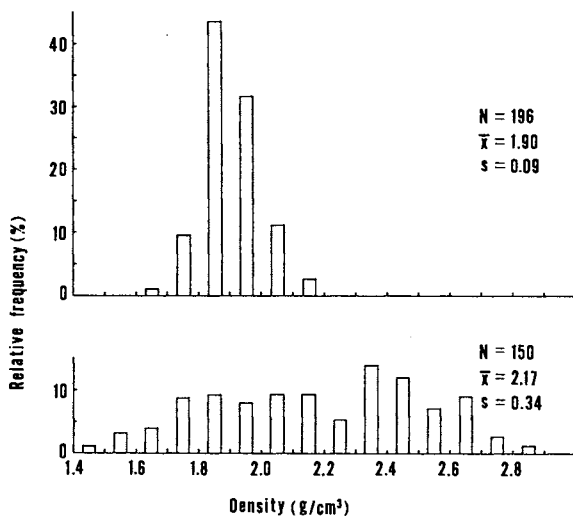
Fig. 4 Frequency distribution of density of crusts and their substrates

Crusts
N = 122
x̄ = 3.86
s = 2.99

Substrates
N = 106
x̄ = 13.4
s = 14.8
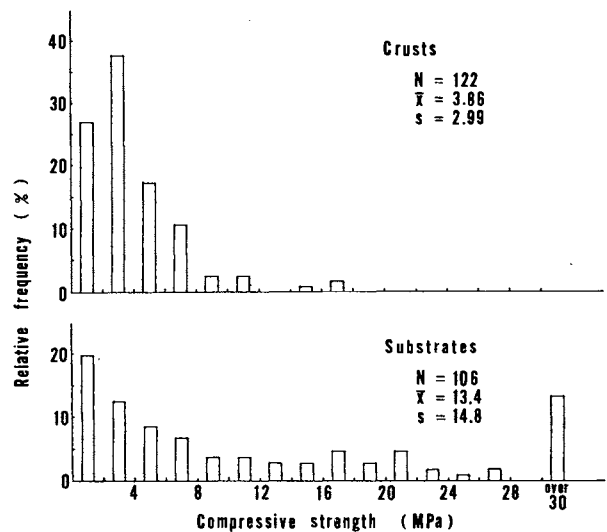
Fig. 5 Frequency distribution of compressive strength of crusts and their substrates

-391-

Fig. 6 Frequency distribution of tensile
strength of crusts and their
substrates
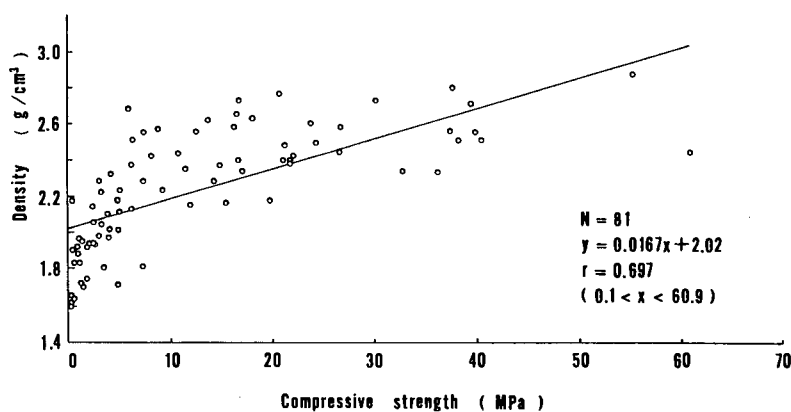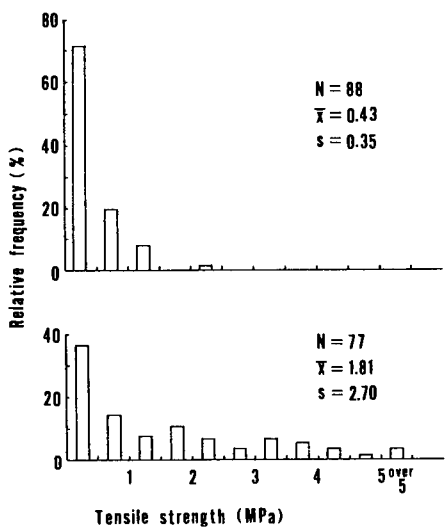
Fig. 7 Relationship between compressive
strength and density of substrates
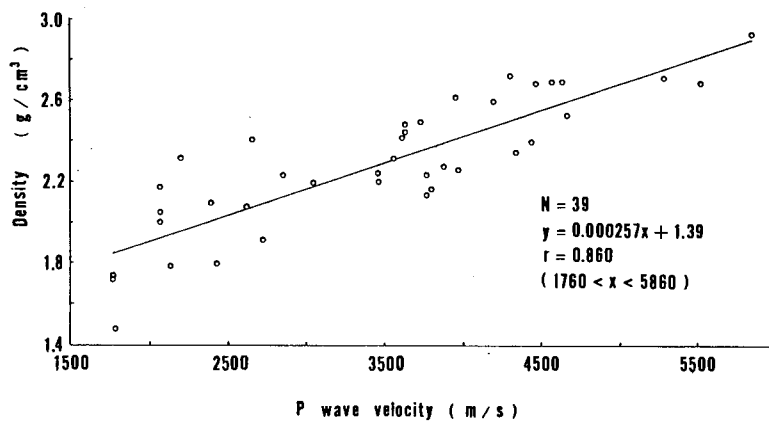
Fig. 8 Relationship between P wave velocity
and density of substrates
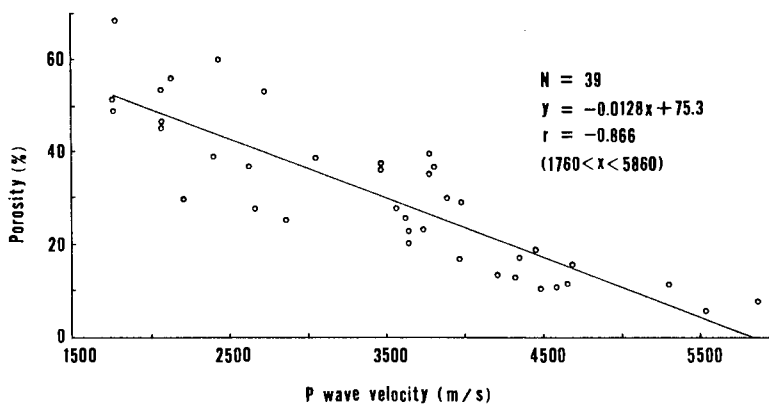
Fig. 9 Relationship between P wave velocity
and porosity of substrates

THE DRAG AND ADDED-MASS COEFFICIENTS OF VARIOUS BUFFERS VIBRATING AXIALLY IN WATER

K. Aso*, K. Kan*, H. Doki*, and M. Mori*

* Akita University, Japan

Abstract

In order to analyse the longitudinal vibration of a pipe-string for mining mineral resources at deep-sea bottoms, the fluid forces acting on the buffer and pump-module attached to the pipe-string must be evaluated in advance.

In this study, first, a new method was developed for determining the drag and added-mass coefficients of a buffer vibrating axially, and then both coefficients for various shapes of buffers were determined. The results obtained on the spherical buffer-models proved to be in fairly good agreement with those by Sarpkaya and showed the validity of the new method. Furthermore, the results of other buffer-models indicated that there was a good correlation between those coefficients and Keulegan-Carpenter number, K_c, and that as K_c increases, the drag coefficient decreases exponentially and the added-mass coefficient increases or decreases linearly according to the shapes of the buffer-models.

Nomenclature

A = amplitude of longitudinal vibration of buffer-model
A_R= resonance amplitude of vibration of model
a = amplitude of forcing displacement
a_R= amplitude of forcing displacement in resonance
C_d= drag coefficient
C_m= added-mass coefficient
$\bar{c}$ = coefficient of equivalent linear damping
D = diameter of model
$F(t)$ = fluid force due to the ambient water
$G = g_1 + g_2$
g_1, g_2 = coefficients of structural damping of springs
$K = k_1 + k_2$
K_c= Keulegan-Carpenter number
k_1, k_2 = spring constants
L = length of model
$M = m + C_m m_a$
m = mass of model
m_a= mass of the water displaced by model

R_e= Reynolds number
S = the maximum cross-sectional area
t = time
U_m= the maximum velocity of vibrating model
x = displacement of model from the equilibrium position
x_0= forcing displacement
ρ = density of the ambient water
ν = coefficient of kinematic viscosity
ω = circular frequency of forcing displacement
ω_R= resonance circular-frequency of forcing displacement

Introduction

For mining mineral resources from deep-sea bottoms, a pipe-string is needed to connect the mining ship on the sea surface with the collector or miner on the seafloor. Furthermore, the string must be equipped with the pump-modules for pumping the mineral resources up to the ship and with the buffer which regulates the slurry-density of ore-fluid mixture in the pipe-string and plays a role of the weight to stabilize the mechanical behavior of the string. Hence, the longitudinal and lateral vibrations of the string, which are caused by the ship-motions, must be analysed for the design of the above mining system. Besides, to analyse these vibrations the fluid forces acting on the pump-modules and buffer must be evaluated, and to calculate these forces by Morison's formula [1], the drag and added-mass coefficients for the pump-modules and buffer vibrating in water must be known in advance.

Up to the present, those coefficients pertaining to spheres, cylinders and plates in vibrating flow have been studied by many researchers [2~5]. However, the coefficients for more complicated shapes of buffers or pump-modules have not been reported yet.

In this study, the drag and added-mass coefficients of various buffers vibrating axially in water were determined by the following method which was developed by the authors. First, considering the shape-effect

of a buffer on the longitudinal vibration of the above-mentioned pipe-string, various buffer-models, which were sphere, cylinder, cylinders with semi-spherical or conical ends, cylinder with rugged side,etc., were selected.

Second, a model attached axially to a vertical spring was vibrated longitudinally in still water by a vibrator which provided the top of the spring with a sinusoidal displacement. Then, the drag and added-mass coefficients were analysed by introducing experimental values of amplitudes and frequency in the resonance into the theoretical solution of a spring-mass-damper system.

The results obtained on the spherical models were compared with those by Sarpkaya [3] in order to examine the new method, and both results proved to be in fairly good agreement. Furthermore, all results indicated that there was a good correlation between the drag or added-mass coefficient and Keulegan-Carpenter number, but no clear correlation between those coefficients and Reynolds number.

Method for Determining C_d and C_m

The method for determining the drag and added-mass coefficients, C_d and C_m, which has been developed in this study, is composed of the following experimental and theoretical procedures.

Experimental Procedure

The experimental apparatus used in this study, as is shown in Fig.1, is composed of a cylindrical water-tank, a vertical spring with

1 Water Tank
2 Window
3 Vibrator
4 Line-Sensor Camera
5 Electronic Camera
6 Spring
7 Test Piece
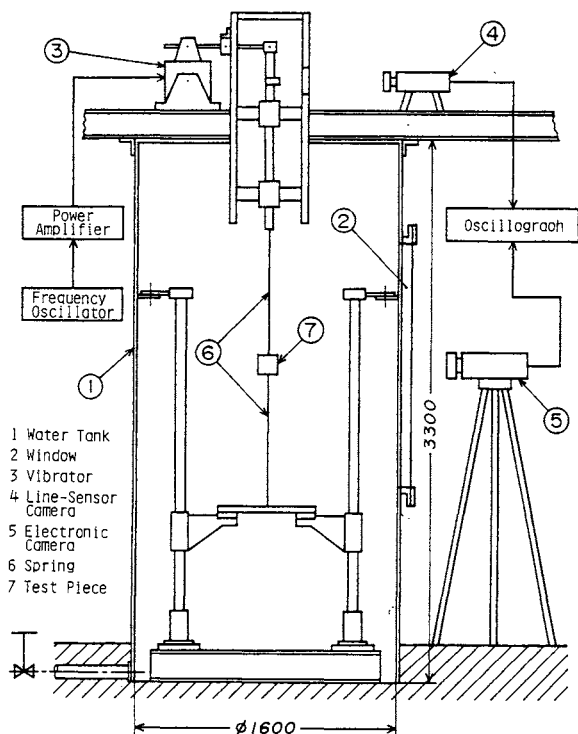
Fig.1 Experimental apparatus

a buffer model, a vibrator and measuring devices. At the central axis of the tank whose diameter and height are 1.6m and 3.3m respectively, a vertical spring with a buffer-model is set. After the tank is filled with water, the top of the spring is provided with a sinusoidal forcing-displacement by an electro-magnetic vibrator, causing the model a longitudinal vibration. Then, the forcing displacement and frequency are measured by the line-sensor camera (made by Matsusita) and the response amplitude of the model is measured by the electronic camera (made by Zimmer) through the window of the tank. At the same time, these three quantities are recorded by an oscillograph. Finally, the resonance circular-frequency, ω_R, the resonance forcing amplitude, a_R, and the resonance response-amplitude, A_R, are obtained. Here, it must be mentioned that in order to prevent the lateral vibration of the model, the spring is stretched in advance by a certain quantity, in which a buffer-model is vibrated longitudinally. Furthermore, the spring constants and structural-damping coefficients of springs are determined by the method of logarithmic decrement applied to the experimental results of free longitudinal-vibrations of the model. The spring constants of springs used in this experiment are 15~800 N/m and their coefficients of structural damping are 0.5×10^{-3} ~60.0×10^{-3} N·s/m.

Analytical Procedure

Defining the mass of a buffer-model as m, the structural-damping coefficients of the springs above and below the model as g_1 and g_2 respectively, and the corresponding spring constants as k_1 and k_2 respectively, the analytical model of this problem can be shown in Fig.2. In this figure, $x_0 (= a \sin\omega t)$ is the forcing displacement applied at the top of the spring, and $F(t)$ represents the fluid force due to the ambient water.

Thus, the equation of motion for this problem can be expressed as follows:

$$m\ddot{x}+g_1(\dot{x}-\dot{x}_0)+g_2\dot{x}+k_1(x-x_0)+k_2 x=-F(t). \qquad (1)$$

Moreover, $F(t)$ is represented by Morison in the following form [1]:
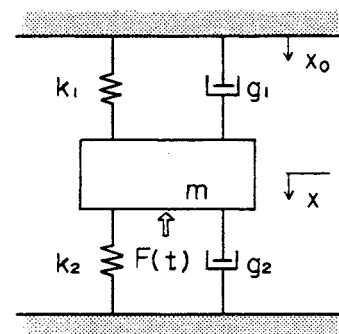
Fig.2 Analytical model

−394−

$$F(t)=C_m m_a \ddot{x}+0.5\rho C_d S \dot{x}|\dot{x}|\ ,\qquad(2)$$

where C_m is an added-mass coefficient, m_a is the mass of water displaced by a buffer-model, ρ is the density of the ambient water, C_d is a drag coefficient, S is the area projected to the plane perpendicular to the direction of vibration of the model (the maximum cross-sectional area of the model).

Here, the second term of the right-hand side of Eq.(2) could be linearized, and the equation can be rewritten in the form:

$$F(t)\simeq C_m m_a \ddot{x}+\bar{c}\ \dot{x}\ ,\qquad(3)$$

where $\bar{c}$ is the coefficient of the equivalent viscous damping. Assuming the vibration of a buffer-model as a harmonic motion, which is $A\sin(\omega t+\phi)$, and equating the work done by the equivalent damping force pertaining to $\bar{c}$ during one cycle of vibration of the model with that by a drag force due to the ambient water during the same cycle of vibration, $\bar{c}$ is represented as follows:

$$\bar{c}=4\rho S C_d A\omega/3\pi\ .\qquad(4)$$

Now, defining the following quantities:

$$M=m+C_m m_a,\ G=g_1+g_2\ ,\ K=k_1+k_2\qquad(5)$$

and introducing the relation, $x_0=a\sin\omega t$, into Eq.(1), the following equation is obtained.

$$M\ddot{x}+(G+\bar{c})\dot{x}+Kx=g_1\ a\omega\cos\omega t+k_1\ a\sin\omega t\ .\qquad(6)$$

Then, the steady-state solution of Eq.(6) can be expressed as follows:

$$x=A\sin(\omega t+\phi)\ ,\qquad(7)$$

where ϕ is a phase angle, and the amplitude A is shown in the following equation:

$$A=\frac{\sqrt{g_1^2+(k_1/\omega)^2}}{\sqrt{(K/\omega-\omega M)^2+(G+\bar{c})^2}}\ a\ .\qquad(8)$$

Furthermore, substituting Eq.(8) into Eq.(4), and rearranging the resulting equation with respect to C_d and M, the following equation is obtained.

$$\left(\frac{4A\omega S\rho}{3\pi}\right)^2 C_d^2+2\left(\frac{4A\omega S\rho}{3\pi}\right)GC_d+G^2$$
$$+\left(\frac{K}{\omega}-\omega M\right)^2-\left(\frac{a}{A}\right)^2\left\{\left(\frac{k_1}{\omega}\right)^2+g_1^2\right\}=0\ .\qquad(9)$$

On the other hand, the resonance circular-frequency, ω_R, that corresponds to the frequency, at which the amplitude of the model becomes maximum, can be determined by differentiating Eq.(8) with respect to ω.

$$\omega_R=\sqrt{-\left(\frac{k_1}{g_1}\right)^2+\sqrt{\left(\frac{k_1}{g_1}\right)^4-\left(\frac{k_1}{g_1}\right)^2\left\{\frac{(G+\bar{c})^2}{M^2}-\frac{2K}{M}\right\}+\left(\frac{K}{M}\right)^2}}\qquad(10)$$

Besides, introducing the relations of Eqs.(4) and (5) into the equation (10), and rearranging the resulting equation with respect to C_d and C_m, the following equation is obtained.

$$\left(\frac{4A_R\omega_R S\rho}{3\pi}\right)^2 C_d^2+2\left(\frac{4A_R\omega_R S\rho}{3\pi}\right)GC_d+G^2$$
$$+\omega_R^2(m+C_m m_a)^2\left\{\left(\frac{g_1\omega_R}{k_1}\right)^2+2\right\}$$
$$-2K(m+C_m m_a)-\left(\frac{g_1 K}{k_1}\right)^2=0\ .\qquad(11)$$

Next, the substitutions of the quantities in the resonance into Eq.(9) give the following equation:

$$\left(\frac{4A_R\omega_R S\rho}{3\pi}\right)^2 C_d^2+2\left(\frac{4A_R\omega_R S\rho}{3\pi}\right)GC_d+G^2$$
$$+\left\{\frac{K}{\omega_R}-\omega_R(m+C_m m_a)\right\}^2-\left(\frac{a_R}{A_R}\right)^2\left\{\left(\frac{k_1}{\omega_R}\right)^2+g_1^2\right\}=0\ .\ (12)$$

Therefore, substituting the experimentally-obtained values of ω_R, a_R and A_R into Eqs.(11) and (12), and solving the simultaneous equation composed of these two equations, the drag and added-mass coefficients, C_d and C_m, can be obtained.

Results and Discussions

According to the above-mentioned method, the drag and added-mass coefficients for various buffer-models have been determined. The buffer-models used in this study are shown in Fig.3, which indicates six kinds of models; sphere (MODEL A), cylinder (MODEL B), cylinder with semi-spherical ends (MODEL C), cylinder with conical ends (MODEL D), cylinder with a

MODEL A   MODEL B   MODEL C

MODEL D   MODEL E   MODEL F
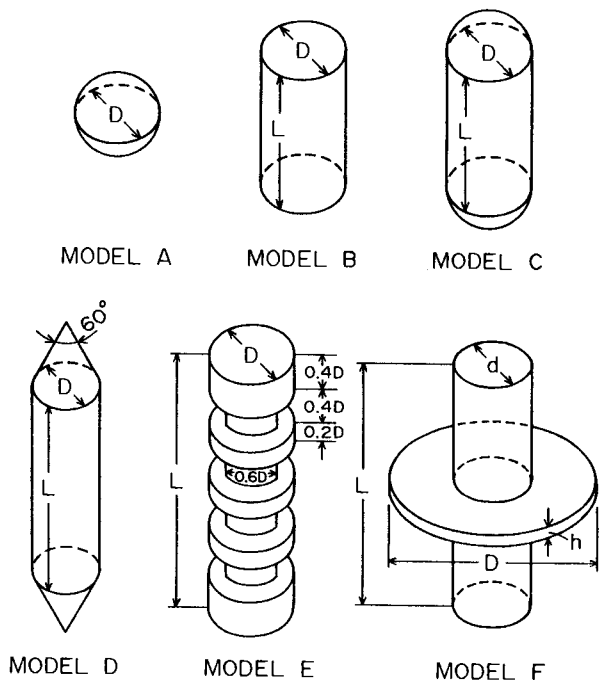
Fig.3 Buffer model

SPHERE				
D (mm)	38.2		25.5	
Symbols	■	□	▼	▽
f (Hz)	4.33~4.42	6.82~6.93	3.52~3.57	5.71~5.82
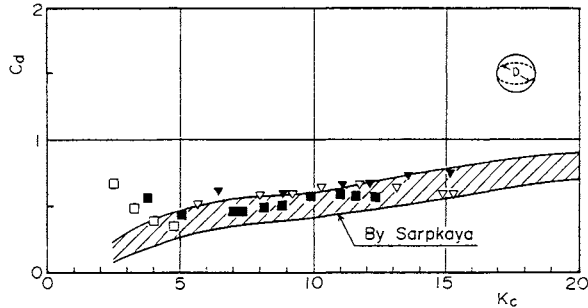
(a) Relationship between C_d and K_c
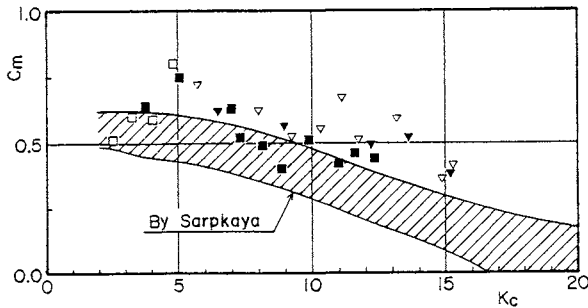
(b) Relationship between C_m and K_c

Fig.4 C_d and C_m for MODEL A (sphere)

rugged side (MODEL E), cylinder with a circular plate (MODEL F).

First, the coefficients for spherical models (MODEL A) were determined and compared with those obtained by Sarpkaya [3], who determined the coefficients by vibrating the ambient water. The results are shown in Figs.4-(a) and (b), the abscissas of which are Keulegan-Carpenter numbers [2]. The Keulegan-Carpenter number, K_c, is defined as $K_c = U_m T / D$, where U_m is the maximum velocity of a vibrating model and equals to $A\omega$, and where T is its period. From the figure 4-(a), it can be seen that the drag coefficients obtained in this study well coincide with those by Sarpkaya (shaded area), although a little difference can be seen in the range where K_c is less than 4. Figure 4-(b) shows a fairly well agreement between the added-mass coefficients obtained in this study and those by Sarpkaya. Here, it must be mentioned that Sarpkaya's added-mass coefficients in Fig.4-(b) were obtained by subtracting one from the original values to adjust them to the values pertaining to a vibrating model in the still water. Hence, it can be realized that the method developed in this study could be applicable for determining a drag and added-mass coefficients of a buffer-model considered in this study.

Second, the drag and added-mass coefficients for cylindrical buffer-models (MODEL B) with the aspect ratio (L/D) of 1 are shown in Figs.5-(a)~(d). Figure 5-(a)

CYLINDER ASPECT RATIO $L/D=1$									MODEL B
D (mm)	60.2		50.2		40.2		25.6		12.7
Symbols	●	○	▲	△	■	□	▼	▽	◆	◇
f (Hz)	4.80~4.95	8.13~8.23	6.25~6.39	10.98~11.20	2.27~2.36	8.25~8.48	2.75~2.80	4.81~4.85	6.00~6.28	10.39~10.76
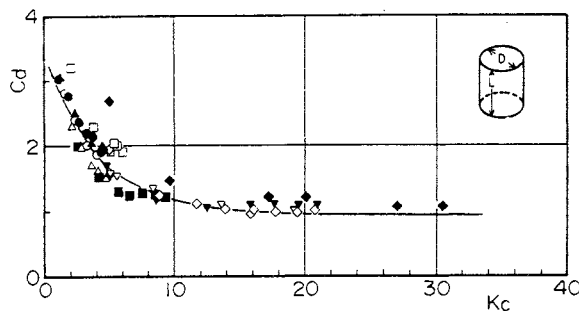
(a) Relationship between C_d and K_c
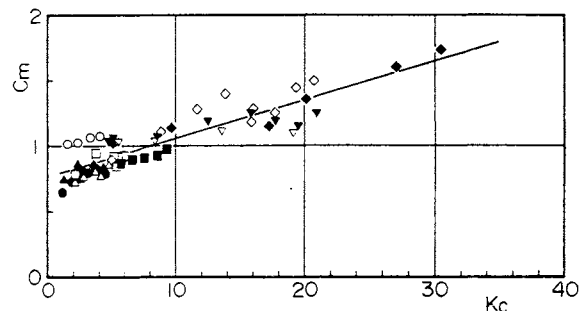
(b) Relationship between C_m and K_c
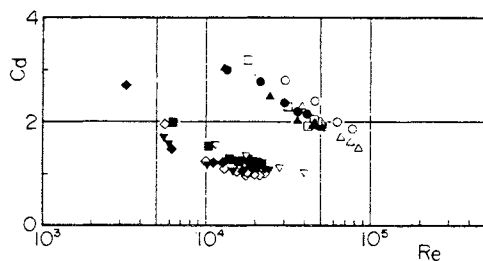
(c) Relationship between C_d and R_e
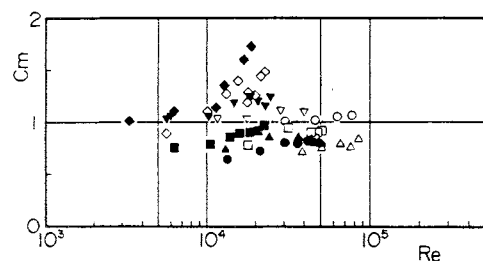
(d) Relationship between C_m and R_e

Fig.5 C_d and C_m for MODEL B (cylinder, $L/D=1$)

CYLINDER ASPECT RATIO							L/D=3
D (mm)	50.2		40.2		25.6		12.8
Symbols	▲	△	■	□	▼	▽	◆	◇
f (Hz)	2.37~2.40	6.57~6.87	3.25~3.29	9.77~10.07	2.80~2.86	4.98~5.08	4.00~4.01	6.54~6.57
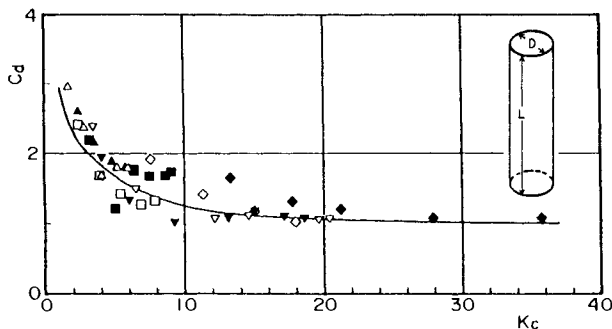
(a) Relationship between C_d and Kc
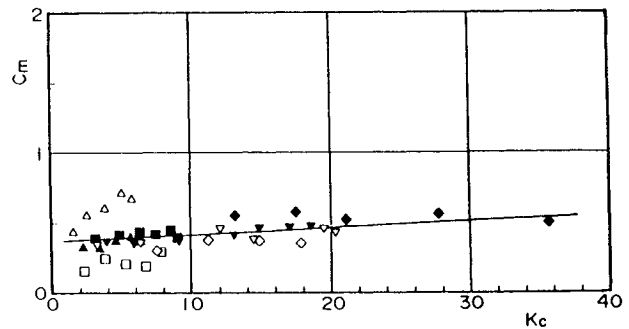
(b) Relationship between C_m and Kc

Fig.6 C_d and C_m for MODEL B (cylinder, $L/D=3$)

indicates the relationship between the drag coefficient, C_d, and the Keukegan-Carpenter number, Kc, while Figure 5-(b) does the relationship between the added-mass coefficient, C_m, and Kc. From these figures, it can be seen that there is a strong correlation between C_d or C_m and Kc. As Kc increases, C_d decreases exponentially and approaches the constant value (about 1.0) at $Kc \doteqdot 14$. Furthermore, C_m increases linearly as Kc increases. On the other hand, it can be realized from Figs.5-(c) and (d) that there is no clear correlation between C_d or C_m and the Reynolds number, R_e. This is true in cases of all buffer-models used in this study. Hence, the only relationship between C_d or C_m and Kc will be discussed in the following parts of this paper.

Figure 6 shows the relationship between C_d or C_m and Kc in case of the cylindrical buffer model (MODEL B) with the aspect ratio of 3. Figure 6-(a) indicates the same relationship between C_d and Kc as that mentioned before, and the values are almost the same as those of Fig.5-(a). Besides, Figure 6-(b) also indicates the same linear-relationship between C_m and Kc as that of Fig.5-(b). However, the values of C_m are less than those of Fig.5-(b), and the rate of increase of C_m with increasing of Kc is also smaller.

Third, the drag and added-mass coefficients for the cylindrical buffer-model with semi-spherical ends (MODEL C) are shown in Figs.7 and 8. From these figures, again it can be found that there are strong correleations between C_d and Kc as well as between C_m and Kc. Figures 7-(a) and 8-(a) show that the drag coefficient decreases exponentially as Kc increases, and approaches the constant value when Kc is about 7 in case of the aspect ratio of 1 and about 11 in case of the ratio of 3. The constant value is about 0.35 and less than the corresponding value for MODEL B. Figures 7-(b) and 8-(b) indicate

the linear relationship between the added-mass coefficient and Kc. These figures also show that the added-mass coefficient decreases as the aspect ratio increases and it slightly decreases as Kc increases, and that the values of this coefficient are smaller than those for MODEL B.

Fourth, the relationships between C_d and Kc as well as between C_m and Kc for the cylindrical buffer-model with conical ends (MODEL D) are shown in Figs. 9 and 10, which indicate the same strong-correlation between those coefficiens and Kc as that mentioned in the previous cases. Figures 9-(a) and 10-(a) show that as Kc increases, the drag coefficient decreases exponentially and approaches the constant value when Kc is about 6 in case of the aspect ratio of 1 and about 10 in case of the ratio of 3. Besides, this constant value is found to be about 0.30 and smaller than the corresponding value for MODEL C. On the other hand, the added-mass coefficient, as is shown in Figs.9-(b) and 10-(b), is smaller in case of larger aspect-ratio, and it decreases slightly and linearly as Kc increases. Moreover, the rate of the decrease is larger in case of larger aspect-ratio.

Fifth, the cylindrical model with a rugged side (MODEL E) was considered in order to reduce the longitudinal vibration of the offshore pipe-string with a buffer by increasing the drag force. Then, the drag and added-mass coefficients for this model were determined. The results obtained are shown in Fig.11, in which Figure (a) shows that the drag cefficient decreases exponentially as Kc increases and it approaches the constant value of about 2 when Kc is about 10. Hence, the buffer with the shape of MODEL E is found to provide a drag force which is about twice as large as that of the cylindrical buffer. In addition, the added-mass coefficient, as is shwon in Fig.11-(b), increases linearly as Kc increases, and both

MODEL C				
ASPECT RATIO	L/D=1			
D (mm)	50.0		30.7	
Symbols	▲	△	▼	▽
f (Hz)	3.23~ 3.27	5.47~ 5.61	2.85~ 2.93	5.00~ 5.05
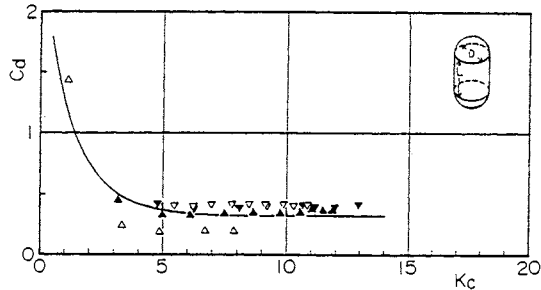
(a) Relationship between C_d and K_C
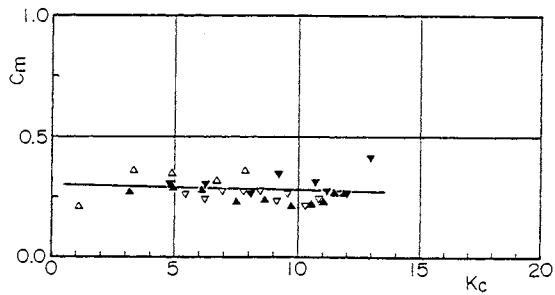
(b) Relationship between C_m and K_C

Fig.7 C_d and C_m for MODEL C (L/D=1)

MODEL C				
ASPECT RATIO	L/D=3			
D (mm)	50.1		30.9	
Symbols	▲	△	▼	▽
f (Hz)	3.74~ 3.82	3.77~ 3.82	2.13~ 2.15	3.50~ 3.53
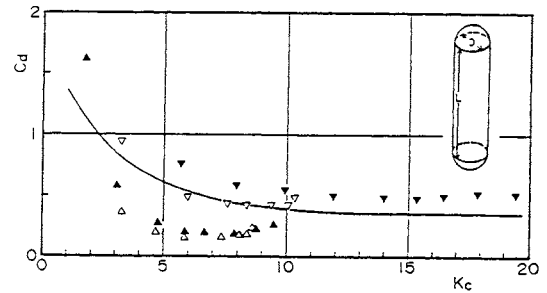
(a) Relationship between C_d and K_C
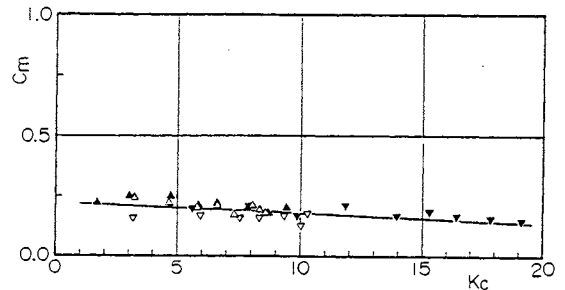
(b) Relationship between C_m and K_C

Fig.8 C_d and C_m for MODEL C (L/D=3)

MODEL D				
ASPECT RATIO	L/D=1			
D (mm)	50.0		30.1	
Symbols	▲	△	▼	▽
f (Hz)	3.32~ 3.35	5.52~ 5.54	2.98~ 3.01	5.10~ 5.17
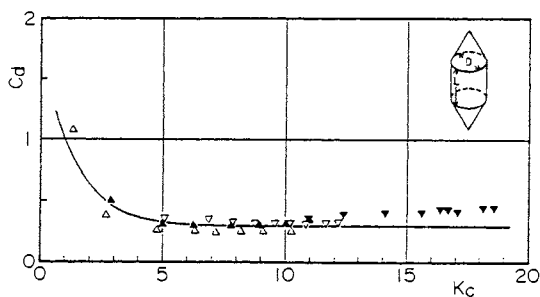
(a) Relationship between C_d and K_C
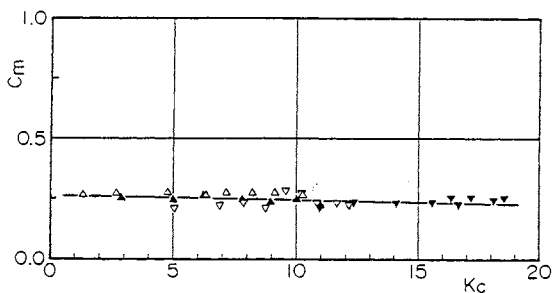
(b) Relationship between C_m and K_C

Fig.9 C_d and C_m for MODEL D (L/D=1)

MODEL D				
ASPECT RATIO	L/D=3			
D (mm)	50.1		30.1	
Symbols	▲	△	▼	▽
f (Hz)	3.78~ 3.82	3.88~ 3.92	2.16~ 2.18	3.63~ 3.65
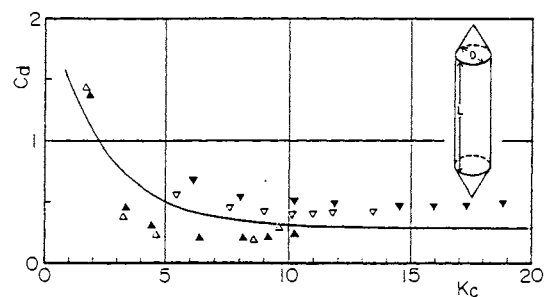
(a) Relationship between C_d and K_C
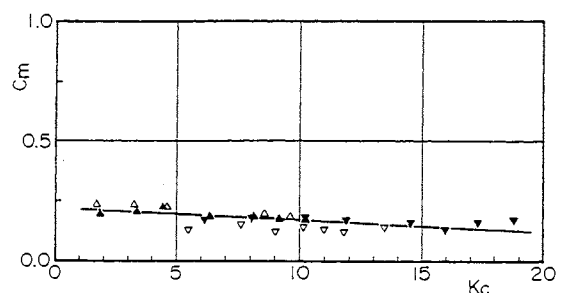
(b) Relationship between C_m and K_C

Fig.10 C_d and C_m for MODEL D (L/D=3)

MODEL E		
ASPECT RATIO L/D=3		

D (mm)	50.2		30.1	
Symbols	▲	△	▼	▽
f (Hz)	3.53 ~ 3.77	3.79 ~ 4.11	3.74 ~ 3.90	3.96 ~ 4.18
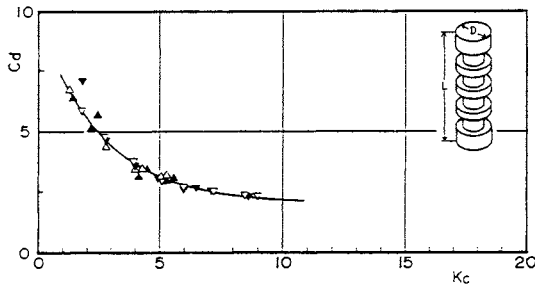
(a) Relationship between C_d and K_c
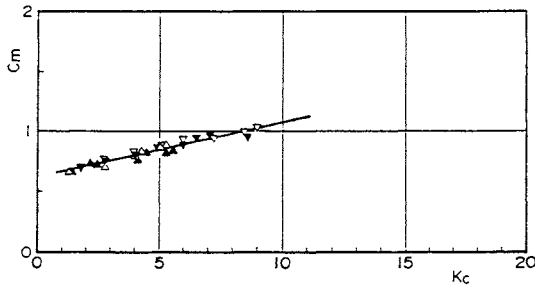
(b) Relationship between C_m and K_c

Fig.11 C_d and C_m for MODEL E (L/D=3)

the value and the rate of the decrease are greater than the corresponding ones for the cylindrical buffer shown in Fig.6-(b).

Finally, the cylindrical buffer-model with a circular plate (MODEL F) was considered in order to increase the drag force, keeping in the minimum increase of the buffer-mass. Then, the drag and added-mass coefficients for this model were determined. The relationships between these coefficients and K_c in cases of two ratios of D/d, which are 2 and 4, are shown in Figs.12 and 13. Figures 12-(a) and 13-(a) indicate that the drag coefficient decreases exponentially as K_c increases and that it approaches the constant value of about 1.5 when K_c is about 16 in case of the ratio (D/d) of 2 and about 10 in case of the ratio of 4. On the other hand, the added-mass coefficients in cases of these two ratios are shown in Figs.12-(b) and 13-(b). These figures show that the added-mass coefficient increases linearly as K_c increases, and that the rate of the increase as well as the value of this coefficient are larger in case of larger ratio of D/d.

Therefore, it can be realized that among the buffer-models considered in this study, MODEL F causes the largest fluid force, because its cross-sectional area, S, is much larger than others, although its drag coefficient is smaller than that for MODEL E, and because its added-mass coefficient is greatest

MODEL F	D/d=2	h=0.17d		
D (mm)	60			
Symbols	□	●	⊗	△
f (Hz)	17.09 ~ 17.63	11.88 ~ 12.03	9.29 ~ 9.30	4.94 ~ 5.05
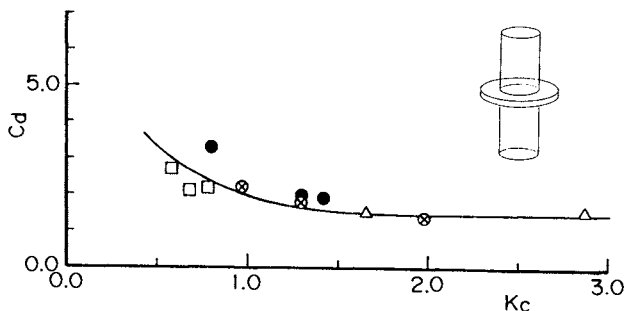
(a) Relationship between C_d and K_c
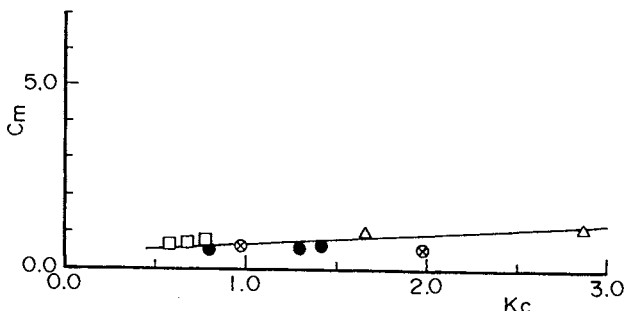
(b) Relationship between C_m and K_c

Fig.12 C_d and C_m for MODEL F (D/d=2)

MODEL F	D/d=4	h=0.17d				
D (mm)	120					60
Symbols	O	Φ	△	▲	■	▼
f (Hz)	7.34 ~ 7.37	8.01 ~ 8.18	4.97 ~ 5.43	5.11 ~ 5.25	3.33 ~ 3.88	2.53 ~ 2.62
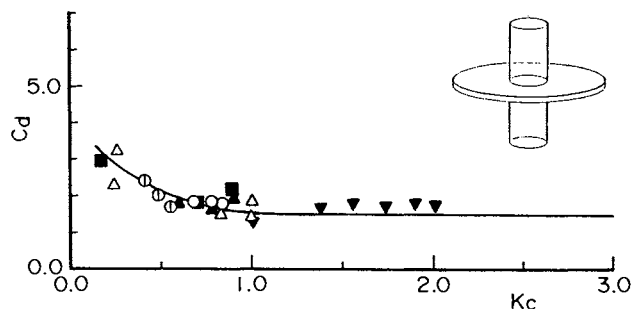
(a) Relationship between C_d and K_c
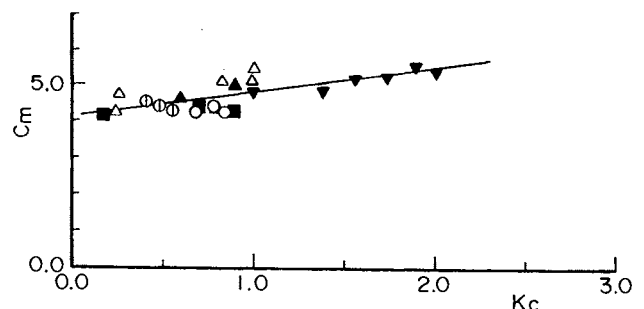
(b) Relationship between C_m and K_c

Fig.13 C_d and C_m for MODEL F (D/d=4)

of all. Thus, a buffer of MODEL F is more effective than others to reduce the longitudinal vibration of the pipe-string for mining mireal resources at deep-sea bottoms.

Conclusions

In order to analyse the longitudinal vibration of a pipe-string with a buffer for mining mineral resources at deep-sea bottoms, the fluid force acting on the buffer must be evaluated in advance. Furthermore, to determine this fluid force, the drag and added-mass coefficients for the buffer vibrating axially in water must be known.

In this study, first, a method for determining these coefficients was developed, and then the coefficients for six kinds of buffer-models, which are a sphere (MODEL A), a cylinder (MODEL B), a cylinder with semi-spherical ends (MODEL C), a cylinder with conical ends (MODEL D), a cylinder with a rugged side (MODEL E) and a cylinder with a circular plate (MODEL F), were determined.

The results obtained are as follows:

1. The results obtained on the spherical models proved to be in fairly good agreement with those by Sarpkaya [3] and shows the validity of the new method developed in this study, which is for determining the drag and added-mass coefficients of buffers vibrating in water.

2. There is a good correlation between the drag or added-mass coefficients of buffers vibrating longitudinally in water and the Keulegan-Carpenter number, K_c. However, there is no clear correlation between those coefficients and Reynolds number.

3. Except for the case of the spherical buffer-model, the drag coefficients decrease exponentially as K_c increases, and then the coefficients approach the constant values when K_c exceeds some values. These constant values are about 1.0 for MODEL B, about 0.35 for MODEL C, about 0.3 for MODEL D, about 2.0 for MODEL E and about 1.5 for MODEL F. Moreover, these values are almost independent of their aspect ratios.

4. There is a linear relationship between the added-mass coefficient and K_c. In the cases of MODEL B, MODEL E and MODEL F, the coefficients increase as K_c increases, and the rate of increase in the case of MODEL B is greater in smaller aspect-ratio. In the cases of MODEL A, MODEL C and MODEL D, however, the coefficients decrease as K_c increases and their rates of decrease are greater in larger aspect-ratio. Furthermore, the absolute values of the added-mass coefficients for the former models are greater than those for the latter models.

5. In order to reduce the longitudinal vibration of a pipe-string for mining mineral resources at deep-sea bottoms, such buffer-models as MODEL E and MODEL F are recommended, because they causes higher fluid forces than the other models. Among the buffer-models tested in this study, MODEL F is considered to be the most effective one for that purpose.

References

1. Morison, J.R., O'brien, M.P., Johnoson, J.W., and Schaaf, S.A., "The Force Excerted by Surface Waves on Piles," Petro. Trans. AIME, Vol.189, p.149-154 (1950)
2. Keulegan, G.H.,and Carpenter, L.H., "Forces on Cylinders and Plates in an Oscillating Fluid," J. Research of National Bureau of Standards, Vol.60, No.5, p.423-440 (1958)
3. Sarpkaya, T., " Forces on Cylinders and Spheres in a Sinusoidally Oscillating Fluid," Trans. ASME, J. Appl. Mech.,Vol.42, p.32-37 (1975)
4. Ueno, H., and Kataoka, E., "Fluid Forces on Plates Oscillating Vertically in Water with Finite Amplitude," Trans. JSME, Vol.44, No.386, p.3478-3486 (1978)
5. Ishiwata, R., and Ohashi, H., "Fluid Forces on Cylinders in Oscillating Flow," Trans. JSME, Ser.B, Vol.50, No.449, p.265-272 (1984)

APPLICABILITY OF MODERN CONTROL THEORY TO MARINE DEVELOPMENT

Y. Okano

The University of Tokyo, Japan

Abstract

This paper is to discuss or criticize the applicability of linear quadratic(LQ)-, adaptive-,Hardy space- and others-control theories to several problems in marine developments. The main subjects considered here are as follows.
1)The limits of Liner Quadratic Gaussian (LQG) control;
It has been suggested that dynamics of a pipe string for deep sea mining or a dynamic positioning system(DPS) of platform for petroleum development can be improved by LQG control. The LQG control system, however, involves an assumption that the spectrum of disturbance can be entirely known. It seems unpractical especially in oceanic environments. The author suggests,therefore, an application of the Hardy space control theory which became discussed eagerly in recent times.
2)The problem of adaptive control;
The model reference adaptive control system(MRACS) has been applied to sea-surface or submarine vehicles of various types. It must be noticed clearly,however, that the theory for MRACS excludes the effects of disturbances,and consequently that its considerable robustness should an important target.

Introduction

The so-called 'modern control theory' corresponds in a narrow sense to the theory developed in a vector space as well as in a time domain. It made a great progress in 1960s as a counterphase to the so-called 'classical control theory' or 'scalar control theory' based on analyses and syntheses exclusively in a frequency domain.

Thereafter,however, further developments in control theories and techniques have been offering different types of control strategies and consequently eliminating the borderline between the both theories (Table 1).

Table 1 Brief history of control theory

Periods	Trends	Items
1840-1900	creation of control theory followed by establishments of a series of stability criteria	Routh,Hurwitz and Lyapnov methods
1900-1945	recognition of similarity of feedback loops through analysis by differential equation	Nyquist method, Bode diagram, Ziegler- Nichols rule, PID algorithm,
1945-1960	synthesis of control loop by communication engineering	root locus method
1960-1970	control mathematics of state space concept	controllabi- lity, observability, optimal regulators (LQ,LQG) maximum prin- ciple, DP
after 1970	theories of various dynamic systems and computer simula- tion	MRA(CS), STR, fuzzy control, Hardy space control theory

Considering the theories appearing in this stage of developments as the 'modern control theory' in a broad sense, the author surveys and criticizes their applicability to several control problems to be encountered in different fields of marine developments.

The theories involve Linear Quadratic

Gaussian(LQG) Control, Model Reference Adaptive Control System(MRACS), Hardy Space Control, Fuzzy Control and so on.

Pipe String for Deep Sea Mining

A long pipe is an essential element of a method in hand for development of deep sea mineral resources, i.e. the manganese nodules, the hydrothermal deposits and the cobalt rich manganese crusts.
The pipe of a few score centimeter diameter and of 2000 to 5000 meter length can be more appropriately termed 'a pipe string'.

It seems almost impossible from an economical point of view, to test the behaviors or characteristics of the pipe strings with full scale in oceanic sites (Fig.1). It is reasonable therefore to try to get necessary information from simulation results based on the proper mathematical models of the systems.

Some of such informations are already available in the research works including those of the governmental project (1). Most of them, however, are concerned with pipe strength and string deformation or shape. Although the latter should be accepted as a static characteristic from a control point of view, dynamics of the string on the other hand have been scarcely discussed in the past researches.

It is clear that there exists a considerable dead time in the dynamic relation between the manipulated variable and the controlled one in case of a mining method with a towed or unsteared collector, where the mining ship moves to control swaths by towing a collector.
Systems involving a dead time have been investigated eagerly with revival of the 'Smith's method'. It remains far from practical conditions, however, to consider the control object as a 'black box' and suppose its linearity.

It is necessary, therefore, to construct a mathematical model of the whole system or the pipe string over its full length and to investigate dynamics of the whole system, which should be inherently expressed with distributed parameters.
A unique contribution (2) to this problem revealed several interesting behaviours, most significant one of which is that the dynamics can be improved by application of a thruster. The same result was thereafter obtained in the author's study applying a model with masses and springs or lumped-parametrizing the system.

It must be pointed out, however, that there appears a common problem concerning the both researches in their suggesting an application of an optimal regulator with an observer ,i.e. LQG control system. Two different aspects of the problem are to be discussed below.

Firstly, it does not seem necessarily practical that as a performance index function a quadratic form is applied, a principal concept of which is a trade off between the magnitude of manipulated variable and the control error or the transient behaviour of the control system.
In some cases otherwise it should be reasonable to apply a control in shortest time based on the Pontryagin's maximum principle.

Secondly it is not always realistic in the oceanic environments that the statistical property of disturbance is not only constant, but also known. It is, however, an indispensable assumption for LQG control
For a countermeasure to the above problem an application of the Hardy space control theory can be suggested, which became recently noticed and aims at maintaining a lower limit of compensation for arbitrary disturbances through evaluating the control error derived by the worst disturbance (3).

Engineering
Criteria   Behaviours

Strength ⌐————————⌐ Vibration

Hydraulic   Transient
Lifting   Response
Efficiency   (Dynamics)

Controllability   Deformation,
                          Shape
                          (Statics)
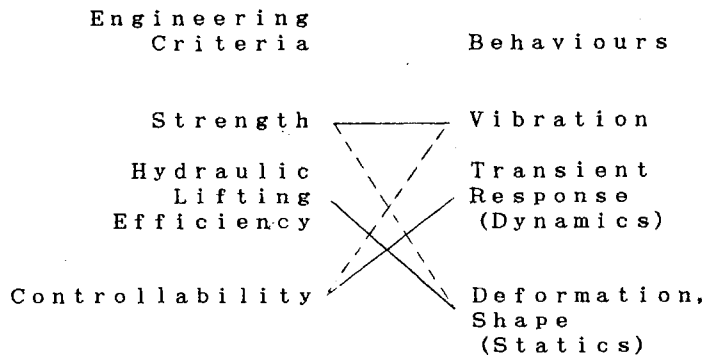
Fig.1 Relationships between
      the behaviours and the
      engineering criteria
      of the pipe string
      Note: Solid lines
            indicate more
            significant
            relationships than
            dotted ones.

The dynamic positioning system (DPS) can be constructed by non-interacting multiple loops each of which armoured with a conventional PID regulator.
On the other hand a more elaborate way is to apply an optimal regulator based on the vector control theory to the DPS, as it is inherently a multi-input and multi-output (MIMO) system.

Although it can be further suggested that the LQG control with Kalman filter should be applied, expected performances cannot necessarily be obtained because of the same reason as mentioned in 'pipe string' and an introduction of the Hardy space control theory would be also suggested.

Maneuverability, e.g. course stabilty or maneuverability indices, of ships has been usually evaluated by stability analyses and frequency response analyses. The former involves mainly the Routh-Hurwitz method.

Most of autopilots have been designed utilizing PID regulators based on the scalar control theory.
These systems, however, deteriorate their control performances in case of changing in ship dynamics or in environmental conditions.
In modern autopilots, therefore, they are applying the model reference adaptive control system (MRACS).

Stability _____ Maneuver-
Analyses   ability
   e. g. Routh-   of Ships
       Hurwitz
       Method

                         Phase
Feedback   Control
Control   in
   with   Wave Energy
PID Regulator   Conversion

Feedforward
   Control
                         Active
DPS   Control
                            of
Optimal   Marine
Regulators: ——————>   Structures
   LQ,
   LQG

Control
   of   Adaptive
Pipe   Controls: Autopilots
Strings   MRACS,
                            STR

                         Hardy Space
                         Control

                         Amenity
                         Control
Fuzzy Control————   of
                         Marine
                         Structures
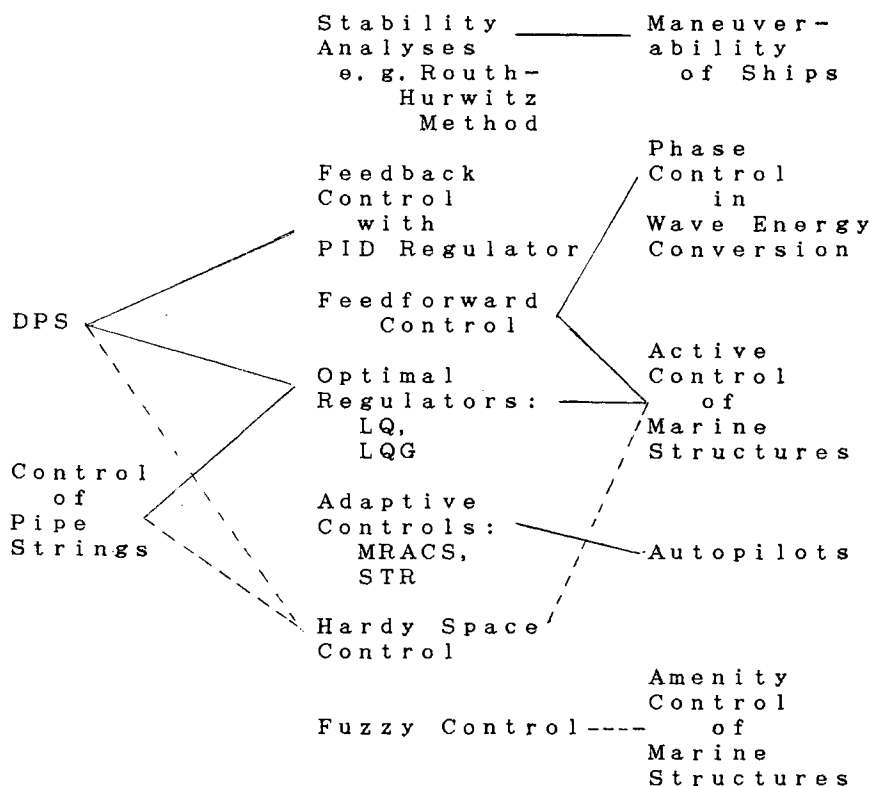
Fig.2 Examples in applications of controls to marine developments
      Note: The dotted lines indicate potential applications.

The theoretical background for MRACS excludes any existence of disturbances. This seems a considerable bottle neck for its application into oceanic practices. Although filters of different types have been suggested as countermeasures, the author expects further developments of investigations into the robustness of MRACS, some information of which has already been available.

The other type of adaptive control systems, i.e. the self tuning regulator (STR) has been applied also to autopilots.

Marine structures

A recent increase in scale of various marine structures has made it necessary to apply the so-called 'active control' for compensation of their dynamic responses to maritime disturbances.
The strategies of the control involve an open loop or a feedforward control and an optimal regulator or a state feedback (4).

The former necessitating some detection of disturbances cannot solely yield sufficient control performances because of its neglecting the disturbances not to be detected.
The latter with an observer also holds a problem in assuming the Gaussian property of disturbances.

Amenity of maritime structure

In the maritime structures designed for ocean space utilization, i.e. one of the main phases of up to date marine developments, the controlled variables involve those which appeal to the sense organs of human beings and on which consequently its amenity depends.

A typical one is 'dazzlingness' in lighting. Such a qualitative index can be conveniently expressed by degrees of its belongingness or membership to the fuzzy sets.

The control systems based on the fuzzy set theory have already been accepted by different industries, although their theoretical background, e.g. stability analysis has never been established.

Application of the fuzzy control to this field of marine developments therefore can be practically expected.

Conclusions

Mentioning several items of marine developments, the author discussed applicability of modern control theories to them. Figure 2 shows concretely the relations between the control theories or strategies and the different fields of marine developments.

References

1. e.g. Aso,K. and Kan,K., "Behaviour of a pipe string in the deep sea",Proc. of 5th OMAE, p.491 (1986)
2. Koehne,M., "Simulation and optimal control of hauling pipes in ocean mining systems", Proc. of 2nd IFAC MMM symposium,p.299 (1976)
3. Kimura,H., "From LQG to H ",J. of Soc. of Instr. and Control, Vol.29,p.1 (1990);in Japanese
4. Yoshida,K.,Suzuki,H. and Oka,N., "A trial of response control of tower-like offshore structures", J. Soc. Nav. Archit. Japan, No.161,p.271 (1987)

PLATINUM ACCUMULATION IN COBALT-RICH FERROMANGANESE CRUSTS

J. Wiltshire

Hawaii Undersea Research Laboratory, University of Hawaii, Honolulu, Hawaii, U.S.A.

Abstract

Sixty-nine bulk manganese crust samples from the Hawaiian and Johnston Island Exclusive Economic Zones and three U.S.G.S. standards were analyzed for their platinum contents. Platinum values ran as high as 2 ppm. Samples were analyzed by both standard fire assay and low temperature anion exchange techniques. The results showed a systematic undervaluing of platinum by the fire assay technique probably as a result of loss of loosely bound platinum spherules. A series of detailed stratigraphic micro-sections were run looking at platinum accumulation in different layers of a manganese crust collected at Schumann Seamount in the Southern Musicians Group. Two restricted stratigraphic zones of significant platinum accumulation were indicated. Electron microscope work showed the platinum to be in very small (average 60 micron) spherules, apparently deposited in rugose undulations on the crusts. These data suggest a cosmogenic origin for at least some of the older platinum. Platinum appears most favorably concentrated south of Johnston Island. Although the platinum is not of a mineable grade by itself, it is probably worth extracting from a crust mining operation designed to recover cobalt.

Introduction

During the 1970's the private sector spent several hundred million dollars on the development of deep ocean minerals, focusing primarily on manganese nodules. This in turn resulted in much government and academic study and major attention in the Law of the Sea Treaty. By 1982 the Law of the Sea Treaty had been caught in a stalemate with industrialized countries primarily because of its unfavorable ocean mining provisions. However, the treaty had established 200 mile Exclusive Economic Zones (EEZs) as part of common international law. In 1983, President Reagan formally declared the U.S. EEZ and charged the Department of the Interior with investigating its resource potential.

Building on earlier industrial efforts, the Minerals Management Service set up an innovative joint State/Federal Task Force with the State of Hawaii to examine cobalt-rich manganese crusts. These crusts had briefly been examined by industry but had not received the resources dedicated to nodules due to the more restricted geographic area in which the crusts are located. However, recent studies [11] show that crusts are worth $350/ton whereas nodules run only about $200/ton. Resource assessment was undertaken on six research cruises in the Hawaiian Islands and one in the Johnston Island area [7,12]. Analysis of the several hundred crust samples brought back from these expeditions yielded interesting data. The crusts had concentrations of cobalt four times those of nodules (in several cases over 1% Co). Nickel and ferromanganese concentrations were also in the economic range but copper concentrations were low. The water depths of optimum crust location varied from 700 to 1700 meters [19]. This makes the crusts much more accessible than the 4500 m deep nodule fields. In addition to the potential for new marine industry and the development of the EEZ, mining of cobalt-rich manganese crusts would offer to the U.S. a domestic source of at least two of the top five strategic minerals. Over 90% of the cobalt used in the U.S. is presently imported. Most of this cobalt comes from Zambia and Zaire. Cobalt is critical to the steel industry for such high temperature alloys as jet turbine blades. A similar situation exists for manganese with most imported from Brazil and Gabon.

Although a crust mining and processing industry would provide badly needed high-tech jobs in Hawaii and would secure a domestic source of critical minerals, it is unclear if such an industry would be economic. Several studies on this question have recently been completed. Unfortunately, the results are conflicting. Plasch et al. [16] using 1985 metal prices concluded that the value of the metals recovered from the crusts would be less than the cost of the mining operation. U.S. Bureau of Mines studies by Ritchey, Avery and Denton [17] indicate that other cobalt supplies will be exhausted by 2005 necessitating a price rise. This price rise will be sufficient to make crusts attractively economic by 2005. A Japanese study [10] maintains that a converted fishing vessel using the low budget continuous line bucket system [15], the only mining system currently tested on crusts, could sell the crusts directly to existing metal refiners at a 30% profit. However, U.S. ocean mining industry has no interest in this type of system (C. Welling, Ocean Minerals Co., personal communication, 1989).

In calculating these economics, value is only ever assigned to cobalt, nickel, copper and ferromanganese. Halbach and Puteanus [5] have discovered platinum concentrations in excess of 1 ppm in seamount crusts from the central mid-Pacific area. This is the same level of concentration as is found in numerous land deposits. At $500/oz. (rounded spring 1990 price) the additional value recovered from platinum could significantly enhance the value of the crusts.

The U.S. uses 50% of the world's platinum supply yet does not have any presently operational platinum mines. Half of the U.S. platinum consumption is going into automotive uses, particularly for catalytic converters. The use of platinum for such pollution control projects is rapidly increasing. New platinum uses such as cobalt-platinum superconductors are increasing in importance. One currently suggested design for cold-fusion reactors involves a palladium core wrapped in platinum wire. In order to meet these clearly increasing demands for this precious metal without increasing dependence on unstable foreign sources, the U.S. must develop domestic platinum sources. Given current economic studies which indicate that manganese crusts are probably near the marginal economic range at current prices, a possible secondary platinum ore is very significant. The inclusion of platinum may turn a potential resource into a marketable ore with the ability to handle many of the U.S. strategic minerals problems for three metals, cobalt, manganese and platinum, instead of just the former two.

Most platinum deposits on land do not occur in isolation. The most famous of these deposits, South Africa's Merensky Reef not only is the world's greatest source of platinum but it is also a significant source of palladium and ruthenium. The Sudbury complex in Canada is also a major platinum and palladium producer. However, the mineralogy of the platinum and palladium are different. The palladium tends to be associated with pentlandite $(Fe,Ni)_9S_8$ whereas the platinum is normally found in an iron-sulfide structure (pyrrhotite) or as platinum-iron alloys or their intergrowths [3]. Platinum values average 10 ppm in the Merensky Reef and 3.3 ppm in the Sudbury Complex [2]. Besides the platinum group elements, gold is often associated with deposits of this type.

Given these potentially very valuable associations, the suspicion that platinum was in fact concentrated in manganese crusts and the uncertain economics of the production of the crusts, we decided to investigate the nature of precious metals in manganese crusts. Using the collection of manganese crusts recovered during the Minerals Management Service sponsored cruises we selected 69 samples representing the Hawaiian Archipelago and Johnston Island for detailed analysis. These samples were analyzed by fire assay and and a specially devised anion exchange-atomic absorption technique. All samples were analyzed for platinum as well as gold, palladium and a standard suite of elements including Fe, Mn, Co, Ni, Cu, Ca, Mg, Ba, Al, Ti, V, K and P. The results showed platinum to be the only precious metal significantly concentrated in manganese crusts. Palladium and gold concentrations have been discussed elsewhere [18] and the other geochemical associations with the major

elements will be treated in more detail in a forthcoming paper (Wiltshire and McMurtry, in press). Therefore, the discussion which follows will focus on platinum. It will include an evaluation of the various methods of platinum analysis, an interpretation of the results of this initial work, a commentary on the possible meaning of these results and an evaluation of the direction future work in this area should take in the light of what has already been discovered.

Platinum Abundance

Figure one shows a histogram of the geochemical abundance distribution pattern for platinum. The general character of the graph is log normal. However, there is one particularly significant feature. The high end values are far greater in number than would statistically be expected. Although the average value is 317 ppb, a number of values are as high as 2 ppm. The values shown in figure one are a combination of fire assay results with secondary selective reanalysis by the anion exchange method. In general the anion exchange method gives higher (and more accurate) values for the reasons which will be discussed.

Platinum Frequency Distribution
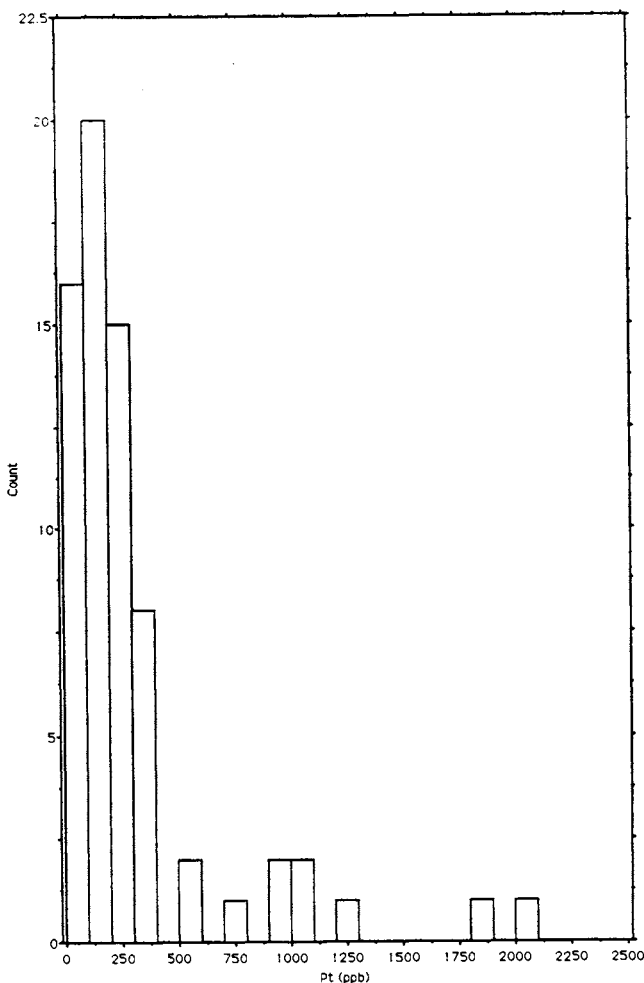
Fig. 1 A histogram of the number of samples with a given platinum abundance (in ppb).

PLATINUM DISTRIBUTION (in ppb)

180°

30°N — 30°N

363

64

278

776 254

170°W

284

37 51 185 133 228 120

160°W

531

375

96

186

180°

N

HAWAIIAN AND
JOHNSTON ISLAND EEZ

170°W

170°W

135

1090

187 2076

9040 993

1832

17°N 17°N

100 0 200km

111 1270

1052 266

160°W 412

160°W 17°N 17°N

170°W
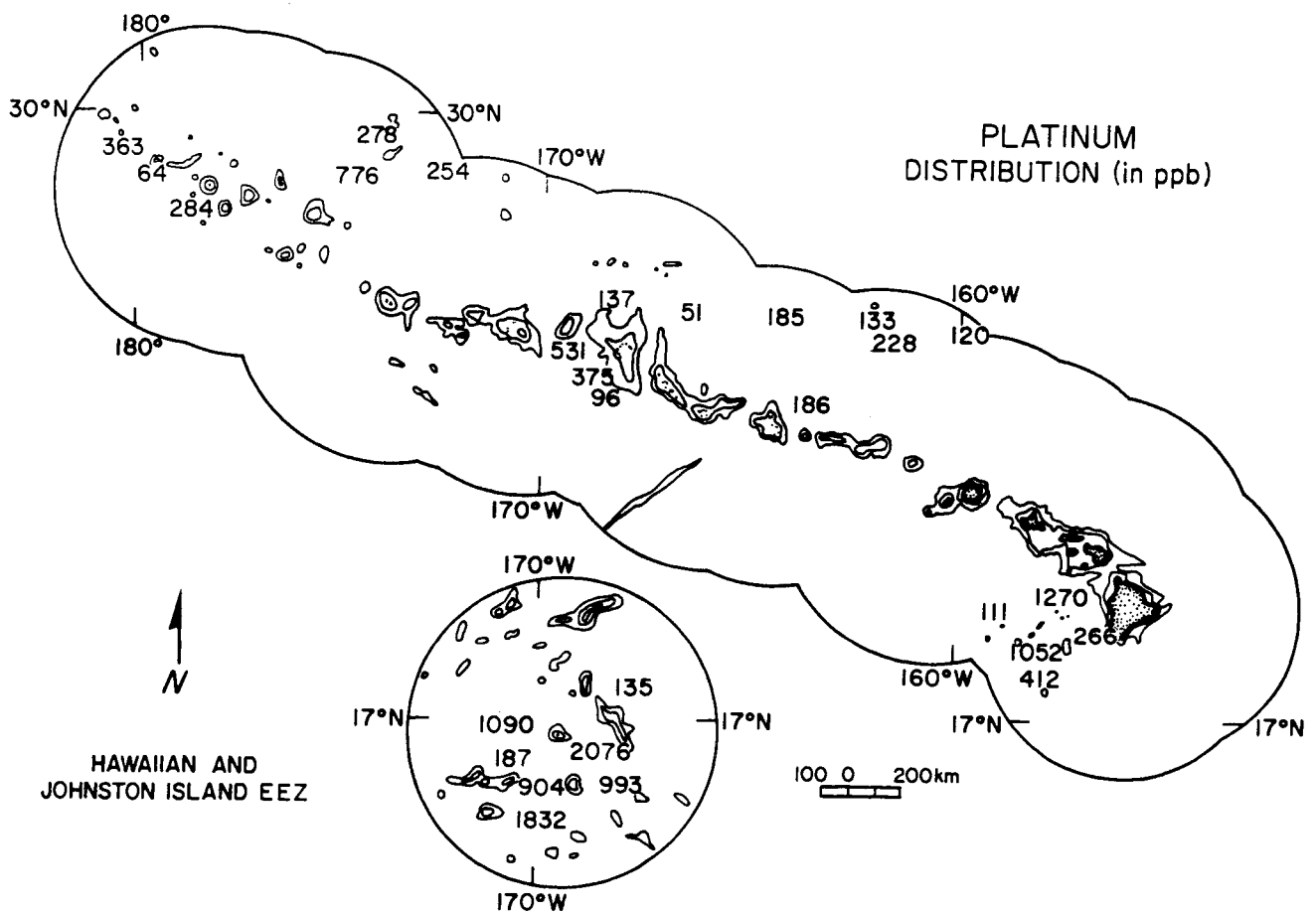
Fig. 2 The geographic distribution of platinum abundances (in ppb) in whole ground manganese crusts from the Hawaiian and Johnston Island EEZs.

Figure two shows the geographic distribution of the platinum values. This reveals some very interesting trends. This plot indicates specific areas of higher concentration. In general the areas of highest concentration are south of Johnston Island (16 degrees north) and in the southern part of the Hawaiian Archipelago (17 degrees north). Areas to the north whether on-axis or in the older off-axis seamounts do not show a noticeable concentration above a background level. The number of samples is not large enough to make an iron-clad correlation with latitude, but the trend certainly is apparent. The Johnston Island area in particular shows extremely elevated values. The question becomes whether Johnston Island is in some way unique or is simply the most southerly sample site.

In terms of economics, an area with consistent platinum abundances varying from 1 to 2 ppm with large tonnages is of mineable grade. Currently, the Sudbury meteorite impact structure is very profitably mined with an average grade of 3.3 ppm. New large tonnage deposits in Montana's Stillwater complex are being investigated for possible mining with platinum abundances in the vicinity of 1 ppm. Naturally, the cost of mining on land would be much lower than an offshore mining operation but then in any proposed crust mining scheme platinum would be a secondary target (a bonus) rather than the primary target on which the economics were based.

Geographic Variation of Platinum Abundance

The geographic data presented in figure two are intriguing. We anticipated a possible correlation between the platinum abundance and the age of the seamounts on which the crust is formed. The seamounts along the axis of the Hawaiian Ridge vary in age from zero at newly forming Loihi seamount, southeast of the Island of Hawaii, to 20 million years old at Midway. The seamounts off-axis are about 80 million years old. Within the limits of our data there is no trend favoring on or off axis seamounts or any evident relationship to age. A check was made to see if an age effect was masked by a relationship with water depth. Figure three shows a plot of platinum abundance versus water depth. These two parameters are clearly independent. Water depth has no genetic effect in the accumulation of platinum in manganese crusts.

It appears that a background value of platinum of several hundred parts per billion is relatively uniformly distributed throughout the area where crusts form. In addition, the areas south of the main Hawaiian Islands and Johnston Island have additional platinum raising their abundance values up to 2000 ppb, although some samples show no more than background platinum values.

Platinum Abundance Compared to Water Depth
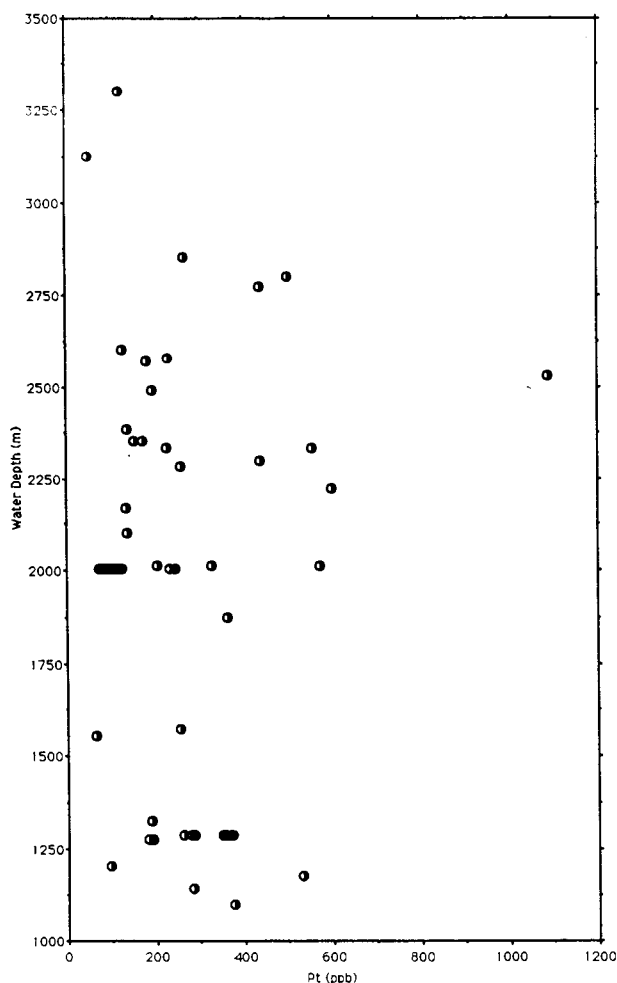
Fig. 3 Platinum abundances in manganese crusts
(in ppb) compared to the water depth (in m)
at which they were collected.

Detailed work on a scanning electron microscope (SEM) has revealed small spherules in the crust. These spherules are iron-rich but also appear to be a site of significant platinum concentration. Size, composition and ablation features from aerodynamic shaping point to these spherules as being of cosmogenic origin, most likely being the break-up products from an iron-nickel meteorite impact. If this is true it implies that the southern sites are closer to the area of meteorite impact or are at least more favorably located along the transport paths away from it. However, there is clearly a background platinum value which is not directly related to any single event or any specific geographic location. This suggests a relatively uniform marine chemical method for the incorporation of platinum into the crusts. Possible mechanisms will be briefly discussed later in the paper. More samples will be needed to resolve this controversy particularly from the Johnston Island and Northern Line Islands areas. To further complicate the problem the analysis of platinum in manganese crusts is very difficult and at least one of the traditional methods of analysis may seriously underestimate any cosmogenic component of the platinum accumulation. This will be discussed in detail.

Analytical Methods and Difficulties

A traditional approach to analyzing mining grade samples in ore bodies has been fire assay. This approach has been particularly widely used with precious metals, especially gold, platinum and palladium. The standard technique of lead fire assay involves fusing the material to be analyzed into a fire assay bead under high temperature in an open reaction vessel. This technique is acknowledged to result in the loss of certain platinum group elements, particularly osmium (which is lost as osmium tetraoxide). Some correction can be made for this using nickel sulfide as the collecting agent in the fire assay rather than lead [20]. Nonetheless, all of the fire assay techniques assume that the platinum group elements are tightly bound, typically in a sulfide mineral structure. Fire assay has not been known to be a problem with gold analyses. The majority of marine mineral samples are either sediments or oxide phases such as manganese nodules or crusts. Analysis of platinum and platinum group elements in these samples has frequently been ignored because of the difficulties involved with low abundances and sample loss [8,9].

Our initial set of analyses was by fire assay as described above. Following fire assay fusion and subsequent dissolution of the solidified melt in dilute hydrochloric acid, precious metal contents were measured with flameless atomic-absorption spectrophotometry. Numerous sample repeats were run both using identical powders and powders made from different subsamples of the same manganese crust dredge haul. The whole process was further calibrated using the U.S.G.S. manganese nodule standards, A-1 and P-1. All samples were run for Pt, Pd, and Au.

This technique appeared to be satisfactory for the Pd and Au [18] but seemed to somewhat underestimate the platinum. We have set up an analytical laboratory for platinum using a technique pioneered at Scripp's Institute of Oceanography by Hodge et al. [9]. In order to get an accurate platinum value, the matrix material should be separated from the analyte. The Scripp's technique accomplishes this and gets around the need for fire assay collection by concentration of the platinum through the use of anion exchange columns. The ground crust samples are dissolved in a series of sequential treatments with several acids in closed reaction vessels under conditions of moderate temperature (80-110° C). The resulting solution is then run through an anion exchange column (AG 1X2 resin) to concentrate and separate the platinum before final analysis. In order to avoid any possible contamination, the exchange resin is contained in Teflon acid-washed columns fitted with specially machined frets which allow flow through the columns at optimized rates for platinum extraction. Through experimentation, using different pH solutions, it is possible to take the platinum off the columns with very little wash acid. This effectively concentrates the platinum for the final analytical step. Final platinum abundance measurement is by graphite furnace atomic absorption spectrophotometry.

The key to this method is the tracing of the platinum through each stage of the process by the use of platinum-191, a radioactive isotope of platinum. In this way it can be guaranteed that correc-

tions can be made for any platinum loss. The radioactive platinum is made in the reactor at Oak Ridge National Laboratory and shipped to us by overnight express. Speed is critical at this juncture, as the short half-life of platinum-191 allows for only one month's worth of quantitative data. For this reason, only a selection of the initial fire assay samples have been rerun using this method.

If the platinum in manganese crusts is in fact in cosmogenic spherules, as the initial SEM results suggest, then subjecting the powdered crusts to intense heating in the fire assay analytical procedure could result in sample loss and a serious underestimation of the amount of platinum present. This is further exacerbated by the fact that the crusts are oxide minerals known to bind elements less strongly than their sulfide counterparts. If the platinum-rich spherules are simply sitting in the rugose structures of the crusts, chemically bound to the rest of the crust structure only through weathering and of very small diameter (60 microns), it would seem likely that they could be easily lost in the off-gassing associated with the fire assay technique. This would account for the fact that the few platinum values in the literature for manganese crusts indicate values only up to about 1 ppm [14] whereas we have measured values as high as 2 ppm using more sophisticated techniques.

In order to verify the suspected underestimates associated with the fire assay technique, 24 of the original 69 samples done by fire assay were reanalyzed using the anion exchange technique. The results are shown in figure four. This indicates that above 300 ppb, data taken by anion exchange are uniformly higher. Fire assay values average only 80% of anion exchange values but values may be as low as 45%. The 1:1 line shown on figure four would equally divide values if only experimental error were at the root. This is clearly not the case. Vertical lines join repeats of the same samples taken from different splits of the ground powder. This indicates that there is some external variation within samples. This is to be expected if discreet individual spherules are present. It is significant that at low platinum values (300 ppb and below) in

samples from the Northern Hawaiian Islands where presumably fewer spherules are present, there is almost no variation between sample repeats or between fire assay and anion exchange techniques. This documented variation between these two analytical techniques is indirect support for the significance of platinum-rich cosmogenic spherules in manganese crusts.

Mechanisms of Origin of Platinum in Crusts

Work by Halbach et al. [6] has shown that the manganese crusts are composed of two generations an older and a younger one. The platinum content of these two generations is different, generally considered to be significantly higher in the older or stratigraphicly lower generation [14]. The two generations are typically separated by a band of phosphate.

Halbach et al. [4] consider that the platinum in manganese crusts is derived from platinum dissolved in seawater. Unfortunately, because levels of platinum are usually extremely low in the marine environment, the behavior of platinum during continental weathering, transport, precipitation and concentration is poorly understood. It appears that platinum in seawater is largely in the form of chloride complexes. Of the chloride complexes, $[Pt(II)Cl_4]^{-2}$ may be the most dominant one [4].

In order to be incorporated into the manganese crust, the negatively charged platinum chloride complex would have to be adsorbed onto the crust surface. Unfortunately the manganese oxide mineral phases predominating in the crusts selectively scavenge divalently charged cations. To get around this Halbach et al. [4] propose the following redox reaction whereby the platinum chloride complex is broken up and incorporated into the crust as elemental platinum.

$$Mn^{+2} + [PtCl_4]^{-2} + 2H_2O \rightleftharpoons Pt^0 + MnO_2 + 4Cl^- + 4H^+$$
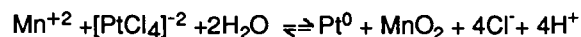
In order for this reaction to co-precipitate platinum and MnO_2 a large amount of Mn^{+2} must be available. Unfortunately, current concentrations of Mn^{+2} are at least an order of magnitude too low to accomplish this. Possible explanations include an expansion of the seawater paleo oxygen minimum layer during times of growth of the older crust generation. Such an expansion of the oxygen minimum layer would favor dissolved Mn^{+2} over MnO_2 and this could raise the Mn^{+2} concentration in seawater significantly. An alternate possible explanation is adsorption of $[PtCl_4]^{-2}$ onto positively charged amorphous iron hydroxide particles. However, as very few negatively charged species seem to be incorporated into manganese crusts and an enrichment factor of two million times (platinum concentration in crusts versus seawater) is present, this mechanism seems tenuous.

With only a seawater source model it is difficult to explain the significant variation in platinum accumulation between the two crust generations. The geographic variation of platinum creates another difficulty for the sole seawater origin of platinum. Possible explanations include changes in
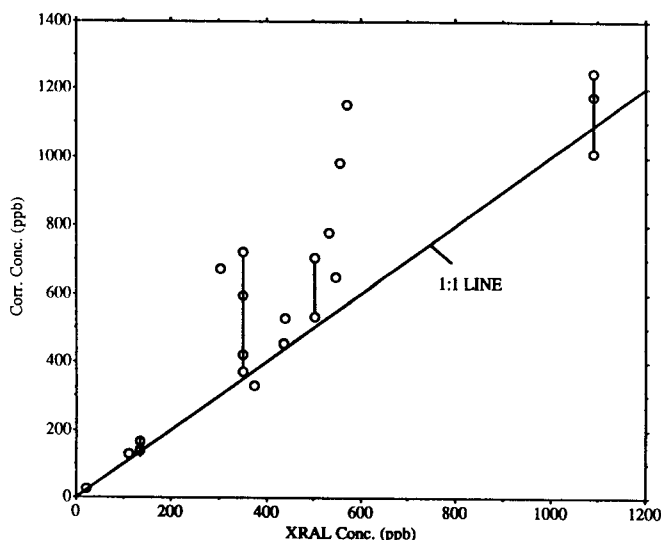

Fig. 4 A comparison of platinum concentrations (in ppb) obtained by fire assay from X-Ray Analysis Laboratories (XRAL) with corrected concentrations obtained by anion exchange.

platinum availability in seawater resulting from differing rates of continental erosion or differing bottom water properties over time resulting in varying amounts of platinum incorporation into the crusts. These explanations seem to us to be insufficient.

Preliminary work was therefore undertaken to investigate the exact disposition of the platinum in the crust matrix . A detailed profile was run over a well developed crust sample using a VG instruments laser ablation ICP mass spectrometer (plasma quad). This detailed analysis undertaken at 2 millimeter intervals in the crust, showed that in fact there were two areas within the older generation that had significant platinum concentrations. These concentrations were related to concentrations of iridium which had also been measured for this sample. The high platinum areas corresponded with the high iridium areas (G. McMurtry, personal comm.). Iridium concentration has been related to meteorite impact by Alvarez et al. [1]. A cosmogenic origin of platinum would account for its differing abundance in different stratigraphic parts of the crust.

A second piece of evidence comes from some preliminary scanning electron microscope (SEM) work on the crusts. SEM photos of an area of high platinum concentration show tiny spherules about 60 microns in diameter. These spherules are very Fe-Ni rich and appear to be the location of at least some of the elevated platinum content. Such spherules have been shown in the past to result from the disintegration of iron-nickel meteorites.

Koskevitch [13] investigated five such iron-nickel spherules from crusts collected in French Polynesia. These varied in diameter from 90 to 335 microns. In one case a nickel-platinum group element alloy was isolated as an inclusion in the spherule. Other workers have also recorded platinum as a discrete metallic phase in the spherules taken from deep sea clays with spot analyses as high as 45% Pt in the most platinum-rich part of the spherule [4].

These two pieces of evidence are very compelling, a distinct iridium association and abundant metallic spherules. Unfortunately, the bulk of the initial profile work represents one stratigraphic section taken from one sample on one seamount. Obviously, in order to meaningfully document this phenomenon the data base must be significantly expanded. This will involve additional work on the plasma quad as well as a great deal more SEM work.

Considerations for Mineability

A prime mining target would be characterized by crust of at least 1.0% Co, thickness averaging at least 5 cm, slopes less than 10%, smooth microtopography and platinum values of 1 ppm [11]. From the data taken to date, the area south of Johnston Island appears to be the prime candidate for further investigation. Of the factors contributing to a prime mining target, platinum accumulation is the least well understood.

A clear understanding of the origin and disposition of platinum is needed both to pick the highest grade site and to determine ore beneficiation techniques. If the platinum is cosmogenic, presumably this would imply a site near a meteorite

impact crater or along the trajectory path of ejecta. In terms of beneficiation, the size of the spherules could become of tremendous importance in the separation of the platinum from the rest of the crust. If the spherules are large enough they could be separated from the surrounding matrix by grinding to a given fineness. This could, for example, be particularly significant in grinding operations where the size of the particles was significant for later processing. Should the particles be ground at too large a size to isolate the spherules then a concentrated chemical attack might be required in a case where the spherules could have been more easily separated magnetically if the grinding had been finer.

In order to calculate an optimum grinding range, an accurate estimate of the size distribution of the spherules needs to be obtained. This will require detailed SEM work involving a statistically significant number of spherule counts. This needs to include both the numbers of spherules in given areas of a crust sample as well as the size of each individual spherule.

The geochemical profiling work on manganese crust stratigraphy has indicated a very strong correlation between platinum and iron in the one sample we studied in detail. By contrast, most of the other valuable metals in the crusts are directly related to manganese concentration. This unusual geochemical relationship may be an additional indication of the cosmogenic origin of the platinum.

If platinum is so closely correlated with iron because it is in iron-rich spherules and the spherules are magnetic, then magnetic separation could prove an effective beneficiation scheme. Magnetic separation is one of the cheapest means of ore beneficiation. If this technique could be used to concentrate the platinum, then the economic return from even relatively low grade platinum in the crusts would be greatly enhanced.

This scheme would ultimately rest on the weathering state of iron in the spherules. Halbach et al. [4] found many of the spherules to be magnetic. Other workers (G. McMurtry, personal comm.) feel that the majority of the spherules are too weathered to retain magnetic properties. This situation must be clarified. This will require detailed SEM analysis of a given crust sample. The sample will be ground to the size fraction of the spherules identified by the SEM. The resulting powder will be subjected to magnetic fields of different strengths. Samples of both the remnant powder and the powder separated by the magnet will be analyzed by the anion exchange method for their platinum content. In this way, the strength of the magnetic properties of the spherules and the possibility of magnetic platinum separation can be quantified.

Conclusions

The U.S. suffers considerably because of its forced dependence on foreign sources for certain key strategic minerals. Manganese crusts, if they can be economically extracted, could end this problem for cobalt, platinum and manganese. However, it is unclear under what conditions the crusts are economic. Platinum abundance is likely to be a meaningful factor in future calculations of the economic viability of manganese crust mining. It may prove to be the second most valuable metal in

the crusts. However, platinum is by no means uniformly distributed. Enriched areas up to 2 ppm are found south of Johnston Island whereas the general background appears to be several hundred ppb. It appears that the background platinum may have been incorporated by precipitation out of seawater where the most likely dissolved platinum species is a chloride complex. By contrast elevated concentrations are most likely to be reached by incorporating cosmogenicly derived Pt-rich spherules. These spherules are likely derived from the break-up of an iron-nickel meteorite. The spherules are very sensitive to the analytical technique used. It appears that standard fire assay may underestimate their abundance. Accurate platinum assessment can reveal the areas of most favorable occurrence, perhaps closest to meteorite impact sites, as well as information useful for optimizing grinding and processing schemes.

Additional detailed SEM and plasma quad profile studies are needed to firmly establish the disposition of the platinum in the crusts. These studies also need to cover the Northern Line Islands and Mid Pacific Seamounts in order to refine the limits of high platinum areas. An understanding of the results will make a crust industry more viable as it will stand on a firmer foundation. This in turn will offer to the U.S. the possibility of virtual independence from the threat of industrial disruption by unfavorable foreign sources for three of its most critical strategic minerals.

References

1. Alvarez L. W., Alvarez W., Asaro F, and Michel, H. V., 1980, Extraterrestrial Cause for the Cretaceous-Tertiary Extinction, *Science*, v. 208, p.1095-1108.

2. Geological Survey of Canada, 1947, Geology and Economic Minerals of Canada, third edition, Geology and Mines Branch, Ottawa, 357 pp.

3. Guilbert J and Park C., 1986, The Geology of Ore Deposits, W.H. Freeman, New York, 985 pp.

4. Halbach P. , C. Kriete, B. Prause and D. Puteanus, 1989, Mechanisms to Explain the Platinum Concentration in Ferromanganese Seamount Crusts, *Chemical Geology*, v.76 n.1/2 95-106p.

5. Halbach, P. and D. Puteanus, 1985, Cobalt-Rich Ferromanganese Deposits within the Johnston Island EEZ: Environmental and Resource Data, Technical University of Clausthal Report, Clausthal-Zellerfeld (F.R.G.), Nov. 1985.

6. Halbach, P. , F. Manheim and P. Otten, 1982, Co-rich ferromanganese deposits in the marginal seamount regions of the Central Pacific Basin - results of the Midpac '81, *Erzmetall*, vol. 35 no.9 p.447-453.

7. Helsley, C.E., B. Keating, E. De Carlo, G.M. McMurtry, M. Pringle, F. Campbell, L. Kroenke and P. Jarvis. 1985. Resource Assessment of Cobalt-Rich Ferromanganese Crusts within the Hawaiian Exclusive Economic Zone, *Hawaii Institute of Geophysics Report,* Honolulu, Dec. 1985.

8. Hodge, V., M. Stallard, M. Koide and E.D. Goldberg, 1986, Determination of Platinum and Iridium in Marine Waters, Sediments and Organisms, *Anal. Chem.*, v.58:6, p.16-20.

9. Hodge, V., M. Stallard, M. Koide and E. Goldberg, 1985, Platinum and Platinum Anomaly in the Marine Environment, *Earth and Planetary Science Letters*, v.72 p.158-162.

10. Japan Resources Association. 1986. The exploitation of cobalt-rich manganese crusts: Second Report (translated by Y. Masuda). Committee for Cobalt-Rich Crust Resources, Mar. 1986, Tokyo.

11. Johnson, C.J. and A.L. Clark (eds). 1986. Pacific mineral resources, physical economic and legal issues. East-West Center, Resources Systems Institute Proceedings, Honolulu, 639 pp.

12. Johnson, C.J., A. Clark, J. Otto, D. Pak, K. Johnson and C. Morgan. 1985. Resource assessment of cobalt-rich ferromanganese crusts in the Hawaiian Archipelago. Resource Systems Institute Report, East-West Center, Honolulu, May 1985.

13. Koskevitch, A., 1987, Presence de spherules cosmiques ferronickeliferes a platinoides dans un encroutement polymetallique sous-marine de Tuamotu, *C.R. Acad.Sci., Paris, Ser. II* , v.305 p.105-108.

14. Mangini A., P. Halbach , D. Puteanus and M. Segl, 1987, Chemistry and growth history of Central Pacific Mn-crusts and their economic importance, in (eds.) Teleki P, M. Dobson, J. Moore and U. von Stackelberg, Marine Minerals: Advances in Research and Resource Assessment, NATO ASI Series: Mathematical and Physical Sciences vol. 194 pp. 205 - 220

15. Masuda, Y. 1985. Continuous line bucket (CLB) mining systems. in P.B. Humphrey (ed.) Marine Mining: A New Beginning. State of Hawaii, Department of Planning and Economic Development, Honolulu, 61-71.

16. Plasch, B.S., W. Miklius and P. Leung. 1987. Manganese Crust Mining and Processing: Economic and Demographic Impacts. In Minerals Management Service, 1987, Draft Environmental Impact Statement, Department of the Interior, Washington, D.C., Cl-C22.

17. Ritchey, J.L., D.W. Avery, and D.K. Denton. 1986. Cobalt-rich manganese crust in the U.S. EEZ as a potential domestic source of cobalt. U.S. *Bureau of Mines IC*, Washington .

18. Wiltshire, J.C., 1989, Precious metal accumulation in manganese crusts from the Hawaiian and Johnston Island Exclusive Economic Zones, Proceedings of the Second Continental Margins Symposium, Bureau of Economic Geology, University of Texas at Austin.

19. Wiltshire, J.C. and C.L. Morgan. 1986. The potential for high-grading cobalt-rich manganese oxides in the Hawaiian Exclusive Economic Zone. Proceedings of the 2nd Pacific Congress on Marine Technology, Honolulu, Mar. 1986, p. MRM 3/13-19.

20. X-Ray Analysis Laboratories (XRAL), 1989, XRAL Schedule, 1885 Leslie St., Don Mills, Ontario, M3B 3J4

WAVE ENERGY ABSORPTION OF AIR CHAMBER MADE BY LARGE CIRCULAR PILE FOR USE OF LIGHT BEACON AND SHALLOW WATER INFLUENCE

F. Kitamura*, R. Inoue*, M. Iwai*

* Ship Research Institute, Japan

Abstract

A light beacon which is installed on the sunken rock as navigation aid has great difficulty in securing power supply because of its location. Therefore as power source for light beacon, utilizing wave energy which exists in its surroundings can be said to be very effective measures. Authors have already developed a so-called O.W.C. (Oscillating Water Column) type air chamber of wave activated generator attached around circular base of light beacon.

Now two types of air chambers making use of large circular pile are investigated by basin test, they are economical and easy to construct. 1/5 scale air chamber models are used in this test. One is made of circular tube with one part cut off to make wave intake. And another is like a upside-down tumbler supported by struts with a wave intake around it. The energy absorption efficiency (the ratio of absorbed energy to incident wave energy) of the former air chamber is about 50%, and the latter 25%. In spite of the low efficiency, the latter has the merit to maintain the same efficiency independent of wave direction.

Usually, water depth is shallow around sunken rock where light beacon is constructed, therefore, the decrease of wave height must be considered to estimate energy absorption. Here the decrease of absorbed energy is investigated. In this experiment, a 1/15 scale model is used.

1. Wave Energy Absorption Efficiency

1.1 Experimental Procedure

1.1.1 Experimental Model

Two types of air chamber models making use of large circular tube are illustrated in Fig.1, one is the pile type air chamber and the other is the strut type, and the former is also
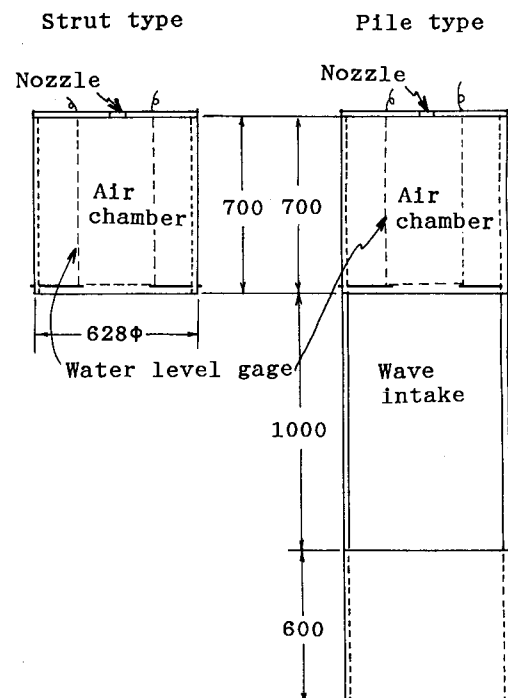
Fig.1 Air chamber models
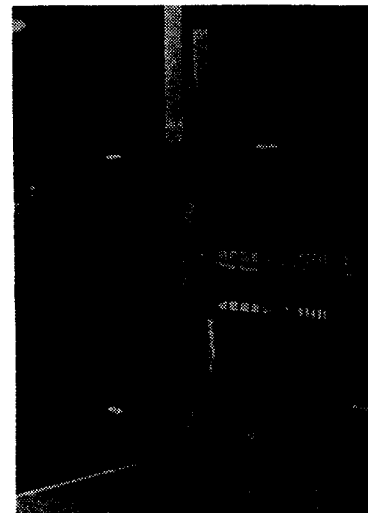
Photo 1 Pile type model

shown in Photo 1. Both models are 592mm in inner diameter, 18mm in thickness and made by vinyl chloride tube. Water plane area of these models are 2752cm^2. The pile type model has a wave energy intake of the height 1000mm and the open angle 180deg. This model reaches to water bottom. And then incident wave from intake is reflected by back wall, so the amplitude of inner water oscillation is enlarged.

By the way, the strut type has a shape of upside-down tumbler style, and supported by several struts. A part of incident wave is converted to inner water oscillation, and the rest of incident wave passes through the chamber. Then wave energy absorption is not so large, but does not change independent of wave direction.

The load for air chamber instead of air-turbines and electric generators is an air nozzle which is set on the top of air chamber. The load of air chamber is changed by changing the diameter of nozzle.
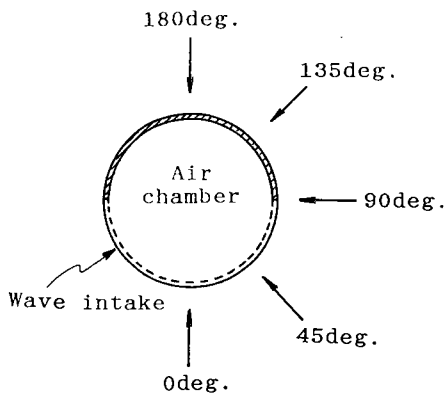
Fig.2 Wave incident angle

1.1.2 Experimental Conditions

In the experiment of the pile type air chamber, the influence of wave direction for energy absorption is mainly studied, and in the experiment of the strut type, the influence of front depth of air chamber is also studied. Fig.2 shows the definition of wave incident angle χ. The wave which comes straight to wave intake is χ=0deg., and backward i.e. the wave to back wall side is χ=180deg.

Table 1 shows the experimental conditions. The open ratio R means the ratio of nozzle area to air chamber water plane area. For both models, we investigate two cases of R=1/100 and 1/270.

The measurement items are incident wave height, inner water level and air pressure in the air chamber. Air pressure is measured at the top of air chamber using miniature water pressure sensor. And water level in air chamber is measured by two capacitance type wave height meters.

Table 1 Experimental conditions

	Pile type	Strut type
depth(cm)	180	
front wall depth(cm)	20	10, 20, 30
wave incident angle(deg.)	0, 45, 90, 135, 180	0
open ratio	1/100, 1/270	
wave height(cm)	5, 10, 15, 20	
wave period (sec.)	1, 1.5, 2, 2.5, 3	

These experiments were carried out at Ocean Structure Test Basin in Ship Research Institute, which has the width 28m, the length 40m and the depth 1.8m.

1.2 Results and Consideration

The energy absorption efficiency of air chamber η is generally defined by ratio of the wave energy absorbed in air chamber E_a to the wave energy E_i which comes in width of air chamber B. That is

$$\eta = E_a/E_i \qquad (1)$$

In regular wave, incident wave energy per air chamber diameter B is calculated by

$$E_i = \frac{1}{2}\rho g H_i{}^2 V_g B \qquad (2)$$

Here H_i is incident wave height and V_g the group velocity of wave. Next absorbed energy E_a is calculated by

$$E_a = \frac{1}{2}\omega z_0 p_0 A \qquad (3)$$

Here z_0, p_0 are amplitudes of the water level and the air pressure in the air chamber. A is the water plane area of air chamber. Fig.3 shows an example of wave energy absorption efficiency η of the pile type air chamber. Here open ratio is R=1/100, the front wall depth is d=20cm, wave incident angle is χ=0 and 180deg. When the wave incident angle is χ=0deg.,the efficiency is about 50% at maximum and as same as the case of sector type air chamber[1].When the wave comes opposite to the wave intake (χ=180deg.), the absorption efficiency drops to 25% at maximum.
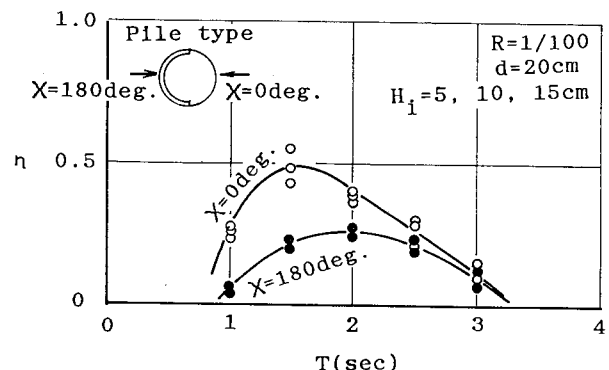
Fig.3 Wave energy absorption efficiency
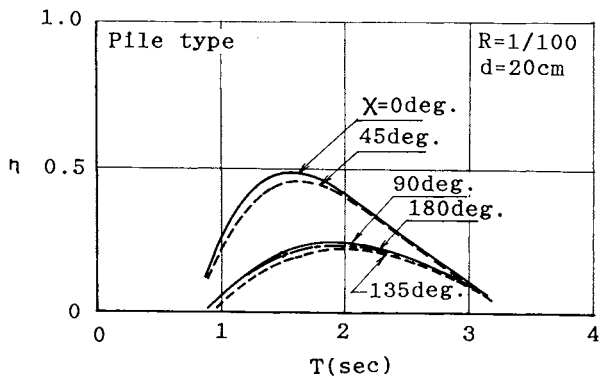
Fig.4 Influence of wave incident angle on wave energy absorption efficiency

Fig.5 Wave energy absorption efficiency of strut type

Fig.6 Comparison of wave energy absorption efficiency for full scale model
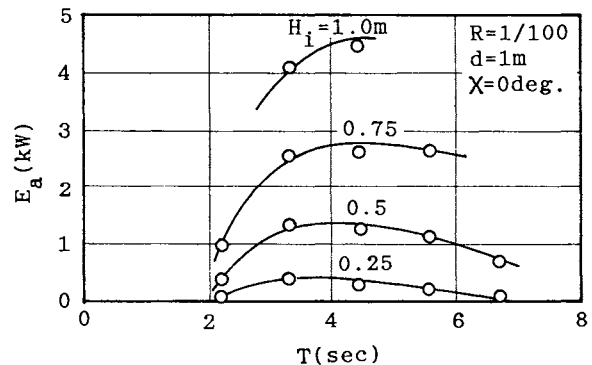
Fig.7 Absorbed energy estimated for full scale model

Fig.4 shows the comparison of mean measured data from $\chi=0$ to 180deg. The absorption efficiency is the same when incident angle is from $\chi=0$ to 45deg. But when incident angle exceeds $\chi=90$deg. the efficiency decreases steeply and does not change for the more incident angle. That is to say, the effect of back wall in the air chamber is useful until $\chi=45$deg. Therefore, if the wave direction changes under 90deg., good efficiency can be got by setting the wave intake to the most provable wave direction.

Fig.5 shows the absorption efficiency of the strut type air chamber according to the front wall depth. The shorter the front wall depth is, the greater the absorption efficiency is. But considering the change of water level by tide, the shorter one is not always advantageous, and there exists the best front wall depth[2]. The absorption efficiency of the strut type is nearly as same as that of the pile type when incident angle is from $\chi=90$ to 180deg. The comparison of the absorption coefficients of the pile type ($\chi=0$deg.) and the strut type is shown in Fig.6. The advantage of the pile type can be understood.

Fig.7 shows the absorption energy of 3m diameter pile type air chamber, that is calculated from model test under the assumption of Froude's law. The absorption energy is proportional to the square of the wave height. For 0.5m wave height, output energy is about 1.3kw. This output energy seems to be sufficient for power source of a light beacon throughout a year[2].

2.Shallow Water Effect

The absorbed energy and the absorption efficiency discussed above are that of deep sea condition. But reefs, where light beacons are constructed, are usually so shallow that we must consider the wave energy absorption in shallow water.

2.1 Wave Height Reduction

2.1.1 Experimental Procedure

The two dimensional water channel in Ship Research Institute is used for this test. This channel has the length 13m, the width 1m and the depth 1m. Making temporary bottom, the experiment of wave height decrease is carried out. The schematic view of this apparatus is illustrated in Fig.8. The scale ratio is 1/15.

In this experiment, the depths are 1m (without temporary bottom), 0.3m, 0.2m and 0.1m, and the shallow part is 7m long. The wave height at shallow part is compared with that at near front of wave maker. Waves used in this experiment are regular and their wave heights are 3, 5, 7cm, periods 0.6, 0.8, 1.0, 1.2, 1.4sec.
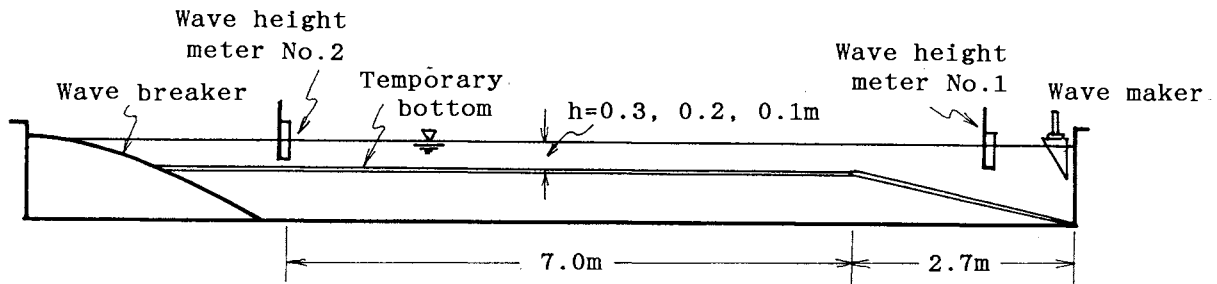
Fig.8 Experiment of wave height decrease

2.1.2 Results and Consideration

When waves come into shallow water part, they change their form, and the more shallow the depth is, the greater the change is. Fig.9 shows an example of wave form deformation in this experiment. The first wave form is of the incident wave at wave height meter No.1 in Fig.8. That is regular wave of 5cm wave height and 1.2sec. period. From second to fourth waves are wave forms at wave height meter No.2 and depths are h=30, 20, 10cm respectively. When depths are h=30, 20cm, transformation are not so large, but when h=10cm, the wave form changes seriously. These transformation coincide with the wave calculated from Stokes' wave of the third order. (refer to Fig.10.)

To investigate the wave height reduction by bottom friction, measurement results are compared with wave height reduction calculated by Bretschneider-Reid's formula[3]. That is

$$K_f = \frac{1}{1+\frac{64}{3}\frac{\pi^3 fH_i\Delta x}{g^2}\frac{h}{h^2}(\frac{1}{T^2})^2\frac{K_s^2}{\sinh^3(2\pi h/L_i)}} = \frac{H}{H_i} \quad (4)$$

Where, K_f; wave height reduction factor

f ; friction factor of bottom

H_i; incident wave height

H ; wave height

K_s; shallow water factor

And shallow water effect of finite amplitude wave is

$$K_s = K_{si} + 0.0015(\frac{h}{L_i})^{-2.8}\cdot(\frac{H_i}{L_i})^{1.2} \quad (5)$$

for $H_0/L_0 < 0.04$.

$$K_{si} = \frac{1}{[\{1+\frac{4\pi h/L_i}{\sinh(4\pi h/L_i)}\}\tanh(2\pi h/L_i)]^{1/2}} \quad (6)$$

Wave height meter No.1 (Incidence wave) H_i=5cm T=1.2sec

Wave height meter No.2
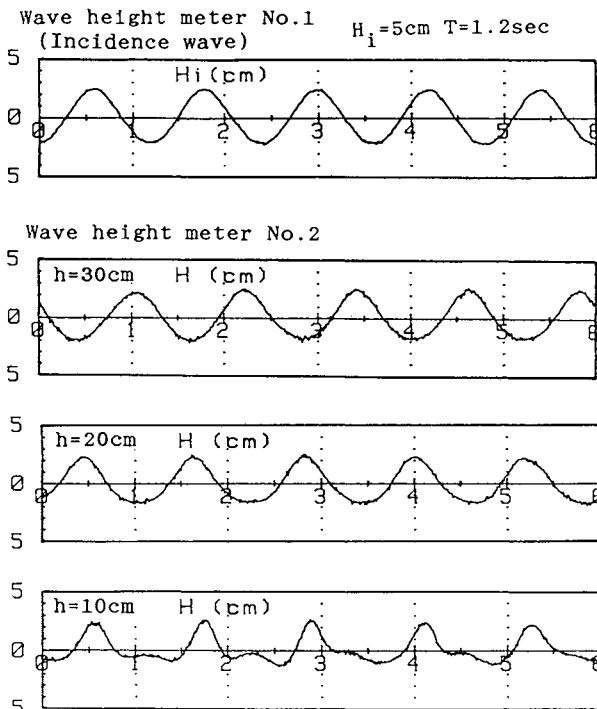
Fig.9 Deformation of wave
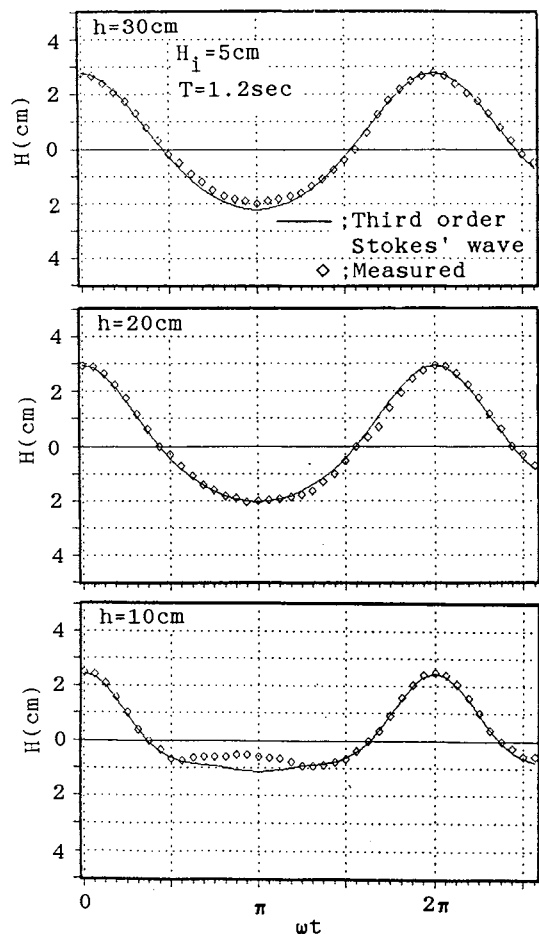
Fig.10 Comparison of wave form of calculation and experiment
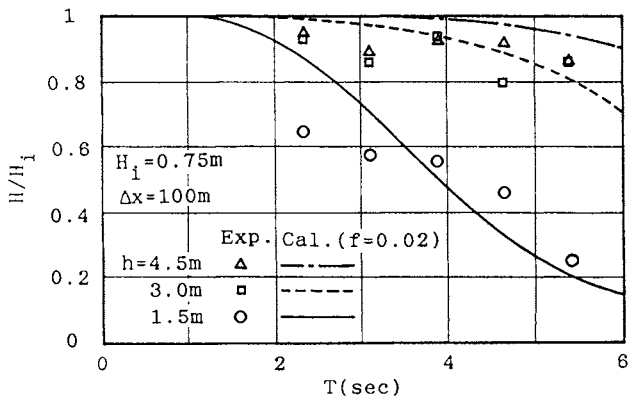
Fig.11 Wave height decrease

For example, Fig.11 shows the comparison of theory and experiments of the decrease of wave height H/H_i in the case of the sine wave of wave height $H_i=0.75m$ coming into the shallow water region of 100m long. In this calculation, the friction factor of bottom is supposed to be 0.02. The measured wave is expanded in Fourier series and its first term is used for wave height H.

2.2 Wave Energy Absorption Experiment

2.2.1 Experimental Procedure

The temporary bottom in two dimensional water channel is used for the energy absorption experiment. The scale ratio is about 1/15. The shallow part is 10m long and has a two dimensional air chamber at the end of the channel as shown in Fig.12. Fig.13 illustrates the air chamber model, which has the width 964mm, the depth 250mm, and the water plane area 2410cm². The load for air chamber, instead of air turbines and generators, is changed by changing the area of nozzle. The experiments are carried out under the conditions of R=1/100 and 1/270. The depths are 1, 0.3, 0.2 and 0.1m, here 1m water depth is the case of deep water condition. The waves are regular, wave heights H_i are 3, 5, 7cm, and periods are 0.6, 0.8, 1.0, 1.2, 1.4sec. The measurement items are the incident wave height, the water level and air pressure in air chamber. Air pressure is measured by using miniature water pressure sensor at the top of the air chamber and water level by two capacitance type wave meters.

Fig.13 Two dimensional air chamber model

2.2.2 Results and Consideration

Also in this experiments, wave energy absorption efficiency is expressed by formula(1). But in this case, incident wave energy E_i is measured at near front of wave maker. Absorption energy E_a is calculated by using formula(3). Therefore in this case, wave energy absorption efficiency is the ratio of energy absorbed by air chamber after passing through the 10m long shallow water part to that of incident wave.

Fig.14 shows an example of the change of wave energy absorption efficiency η for the change of the ratio of depth to wave length h/λ. The open ratio is R=1/100 and period T=1.2sec. Here the region where the ratio of depth to wave length exceeds h/λ=0.5, is deep water, and efficiency is η=75%. If depth decreases, η also decreases, but up to h/λ=0.25 the efficiency is almost as same as at deep water condition. If the depth more decreases, the shallow water effect develops, and the efficiency decreases steeply. The efficiency becomes η=70% at h/λ=0.15, η=60% at h/λ=0.1 and efficiency reduces to almost 0% at h/λ=0.05.
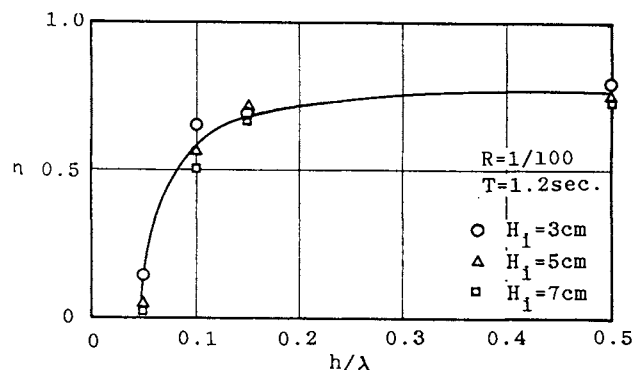
Fig.14 Relation between depth and wave energy absorption efficiency

Fig.12 Wave energy absorption experiment in shallow water

—417—
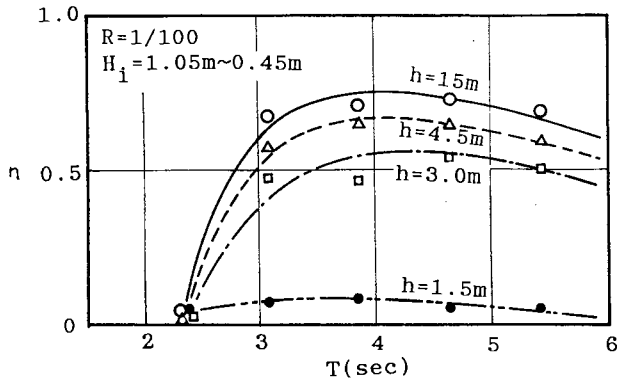
Fig.15 Wave energy absorption
efficiency as to wave period
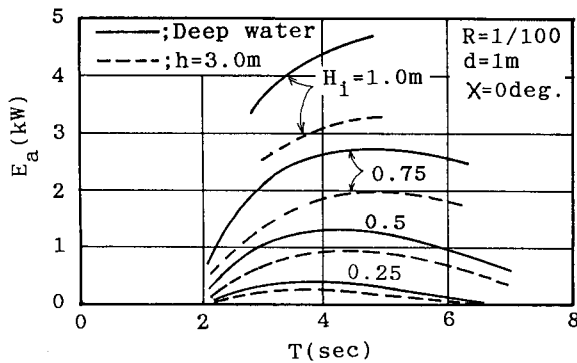
Fig.16 Comparison of energy absorption
efficiency of deep and shallow water

2.2.3 Shallow Water Effect to Absorbed Energy

Fig.15 shows the energy absorption efficiency for full scale model, calculated from mean value indicated in real line in Fig.14 for model test, as to wave period T. In this figure, depth 15m means deep sea, and this value η is that of deep sea condition. The values of the depth from h=4.5 to 1.5m are for shallow condition. Now, supposing the efficiency of the deep water (h=15m) to be 1, the efficiencies for shallow water are 0.9 for h=4.5m, 0.7 for h=3.0m and 0.1 for h=1.5m.

As mentioned above, the pile type air chamber at deep sea condition is sufficiently useful for power source for light beacons. But, where the depth is shallow, as shown in Fig.15, the absorbed energy decreases. Now, as shown in Fig.7, comparing the absorbed energy at deep water region with that at h=3.0m, the absorption efficiency decreases and becomes 70% of that of deep water condition. In Fig.16, the wave energy absorption efficiency decreases as indicated by broken line and it is doubtful whether it is sufficient for the power source of light beacons. Therefore to estimate the wave energy absorption, one must take the water level change by tide etc. into consideration.

3.Conclusion

The items discussed above can be put into order as follows.

(1) The maximum wave energy absorption efficiency of the pile type air chamber is 50% and that of the strut type is 25%.

(2) The pile type air chamber has an efficiency of 25% even if the wave come from backward of the wave intake. This value is as same as that of the strut type.

(3) The pile type air chamber has a same efficiency for the wave incident angle less than X=45deg. But for the greater incident angle, the efficiency reduces and for the wave which comes from sideward(X=90deg.) and straight backward (X=180deg.), the efficiency is the same.

(4) If the system is suitably designed and constructed, the wave activated generator system making use of circular pile seems to be useful.

(5) When the ratio of the water depth to the wave height is over h/λ=0.25, the wave energy absorption efficiency is the same as that of deep water condition. But it reduces to 0.8 times at h/λ=0.1 and becomes almost 0 at h/λ=0.05.

References

1. Inoue,R., Iwai,M., Yahagi,M. and Yamazaki,T. "Wave energy absorption characteristics of circular air-chamber for use of light beacon fixed on sunken rock" IUTAM Symposium, Lisbon,(1985)

2. Inoue,R., Iwai,M., Kitamura,F. and Katsuhara,M. "Power simulation of wave activated generator in waves for use of light beacon", Abstract of the 67th General Meeting of the Ship Research Institute, Tokyo,(1986)

3. Bretschneider,C.L. and Reid,R.O., "Modification of wave height due to bottom friction, percolation and refraction", B.E.B. Tech. Memo. No.45, (1954)

CONSTRUCTION OF A WAVE POWER EXTRACTING CAISSON BREAKWATER FOR FIELD EXPERIMENT AND ELECTRIC POWER GENERATION

Yoshimi Goda*, Katsumi Kanda**, Hideaki Ohneda**, Hiraku Odani**, Hiroshi Suzuki***, Masanori Hirano***, Shigeo Takahashi**

* Yokohama National University, Japan
** First District Port Construction Bureau, Ministry of Transport, Japan
*** Coastal Development Institute of Technology, Japan

ABSTRACT

The Ministry of Transport in Japan is conducting a field verification experiment of an OWC-type wave power converter. The converter is named the wave power extracting caisson and can be utilized as a caisson for vertical breakwater. The construction of the converter was completed in the fall of 1989. The electric generation and related measurements are now being carried out.

1. Introduction

Japan is surrounded by rough seas and is endowed with potential wave energy as shown in Fig. 1. The figure shows the estimated amount of average wave power coming to Japan. The total average wave power around Japan is 36 million kW, or one third of the total electric power produced in Japan. This amount corresponds to the mean rate of 7 kW per meter of the coastline, the total length of which is measured as 5200 km along the outer rim of Japanese island. The wave power is relatively high along the Japan Sea side as well as along the northern Pacific coasts.

Many organizations in Japan have been studying the wave power converters especially since 1973. Several devices were already put on sea trials. The Ministry of Transport (MOT) of Japan is also developing a fixed-OWC wave power converter called a wave power extracting caisson. This device can be used as caissons for composite-type breakwaters and sea walls, thus functioning as a breakwater and a wave power device at the same time. The combination of the wave power converter and the breakwater is expected to reduce the cost of power generation by the converter and also to increase the stability as the breakwater.

The wave power extracting caisson consists of a hollow case called an air chamber and an ordinary caisson supporting it. Figure 2 shows the cross section of the caisson on the rubble foundation. The front wall of an air chamber is a curtain wall with an opening so as to let waves enter inside. The wave action makes the water level in the air chamber oscillate up and down, the air in the chamber is compressed and expanded generating an air flow through a nozzle, and thus wave power can be converted into air power. A turbine set within the nozzle is rotated by the air flow, and electric current is yielded by the electric generator coupled to the turbine. This system is

Fig.1 Wave Power Around Japan

one of the Oscillating Water Column (OWC) type wave power converters. The Wells turbine is adopted for the wave power extracting caisson. This turbine has a special feature that it rotates in the same direction even with reciprocating air flow.
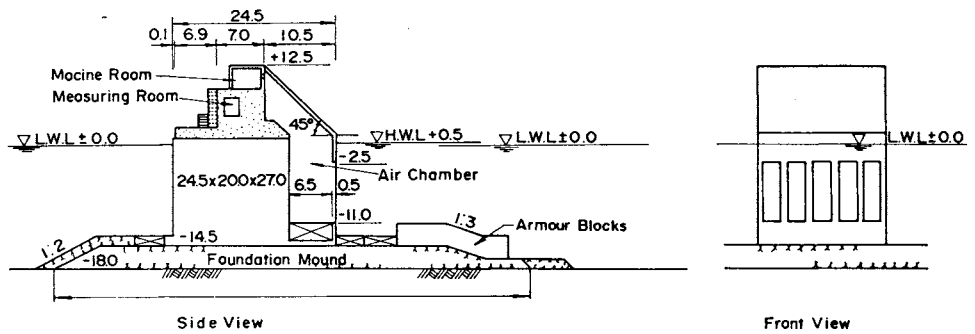
Fig.2 Cross section of Wave Power Extracting Caisson

The research and development work on the wave power converter is being carried out by a collaboration of the Port and Harbour Research Institute (PHRI), the First District Port Construction Bureau (FDPCB) and the Coastal Development Institute of Technology (CDIT) under guidance of the home office of MOT. The PHRI conducted basic research for 5 years from 1982[1]. The CDIT conducted survey and research including the feasibility study of wave energy utilization systems in fiscal years 1985 and 1986 in the form of joint study with twenty private enterprises[2]. The FDPCB has started a field verification study for the wave power extracting caisson breakwater since 1987 at Sakata Port[3]. The construction works of the caisson were finished in the summer of 1989. The turbine, generator and other electric apparatuses were also installed. Photo 1 shows the completed caisson at Sakata Port. The system started the electric power generation in the autumn of 1989. Photo 2 shows the on-land observation house and a tower illuminated by generated electric power.

This paper reports the construction of the system and the ongoing prototype test.

2. Outline of Field Verification Experiment

The field verification experiment is carried on at the Sakata Port as shown in Fig. 3. The Sakata Port is a major port facing the Japan Sea and comprises two parts of the Main Harbor Area and the North Harbor Area. The Second North Breakwater is currently under construction in the North Harbor Area, and one of the caissons in this breakwater was made as a wave power extracting caisson equipped with a turbine and a electric generator. Various measurements on wave pressures, air power and electric generation are

Photo 1 Completed Caisson at Sakata
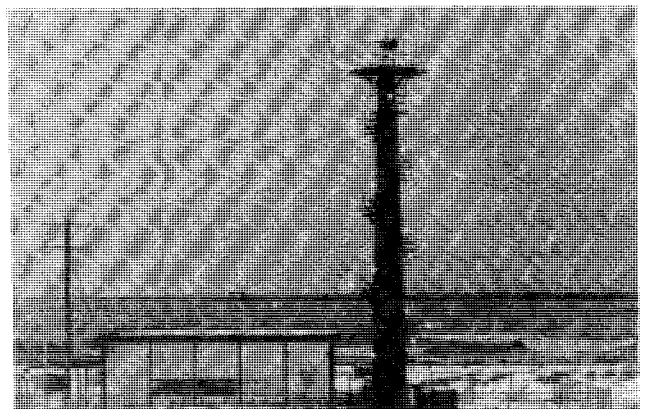
Photo 2 On-land Observation House and Tower with Lights
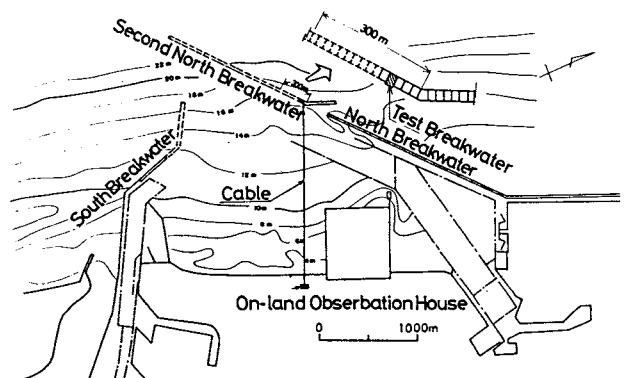
Fig.3 Location Map of Sakata Port

being made. The electricity generated by the system and the signals from various sensors are sent to an observation house on the land through an underwater cable. The data are recorded and simultaneously analyed in the house. The generated electricity is supplied to several apparatuses in the house for experimental utilization and demonstration.

The caisson is made of reinforced concrete and is installed on a rubble foundation as the conventional breakwater caisson. The caisson is quite large, because the water is deep (about 20 m) and the design wave is high with the significant wave height 10.2m (Hmax = 15.3m) and the significant wave period 14.5s. In this area, the sea is rough in the winter season and the power of about 20kW/m attacks the coast. However, the sea is very calm during summer.

The field experiment is divided into three portions:
i) Measurement of the stability of the caisson against storm waves,
ii) Measurement of the power generation,
iii) Use of the generated power.
The whole field experiment is being conducted by the FDPCB. In addition, "the Research Group on the Wave Power Extracting System Using Breakwaters" organized within the CDIT by twenty private enterprises is now in charge of the experiment on the power generation. Also, in order to smoothly carry out the field verification experiment and to ensure successful achievements, an technical advisory committee has been set up with various experts in the related fields (the senior author being the chairman).

The experiment began in 1987 and the wave power extraction started in the fall of 1989. Power generation and measurement are scheduled to continue for two years from 1989 to 1990, and the final report will be formulated in 1991.

3. Design of a Caisson for Field Verification Experiment

3.1 Basic shape of caisson

The caisson width is 24.5m, the air chamber width is 7m, and the crown elevation of caisson is 12.5m above the datum level as shown in Fig.2. The width of air chamber is an important factor that governs the efficiency of air output (air energy/wave energy). From laboratory experiments and theoretical analyses with "the thermodynamics and wave-kinematic

theory[4,5]", it has been confirmed that an air output efficiency is maximized by maintaining the ratio of the air chamber width to the wavelength within the range of about 0.1 to 0.2. The normal wave height and period considered for power generation in the caisson are $H_{1/3}$ = 2m and $T_{1/3}$= 6s, respectively. The width (7m) of air chamber corresponds to 13% of the wavelength of the significant wave. The crown elevation of the caisson is almost close to the design significant wave height. The elevation of the nozzle between the air chamber and the machine room was set to H.W.L. + $0.5H_{max}$ (= +8m), which was proposed based on the results of laboratory test in order to restrict the intrusion of sea water during extremely high waves. The air chamber is divided into 5 compartments, each with the width of 4m. Vent holes are made in the partitions between the five compartments so that they function as one air chamber.

3.2 Wave resisting design of caisson

This experimental caisson has a sloped upper portion, which reduces the horizontal component of wave pressure and increases the wave resisting stability of caisson by means of the vertical component of wave pressure. In order to make the wave overtopping almost the same as that of ordinary upright caissons, the crown elevation was made higher than the ordinary caissons; this enabled to locate the turbine nozzle at a raised elevation. Design wave pressure for the stability calculations of caisson are estimated by the extended Goda Formula with the pressure modification factors $_1$ = 1.0 and $_2$ = 0 considering the wave dissipating effect of the caisson, based on the results of laboratory experiments [6]. The wave pressure distribution is shown in Fig.4. The design air and wave pressure for the structural members in the air chamber is 1.0 w_0H_{max} as shown in Fig.5. In the figure w_0 denotes the specific weight of sea water.

3.3 Design of turbine-generator and valves

Figure 6 is a general view near the machine room where the turbine-generator is installed. The turbine-generator is centrally located there and two air flow regulating valves for adjusting the air flow to the turbine are also installed there. In addition, two pressure relief valves are provided there. The turbine is the Wells type with the diameter 1.3m, two of which are arranged in tandem as shown in Fig. 7. The electric generator is placed in the center between turbine

rotors. The generator is synchronous AC generator with the maximum output of 60kW and the voltage of 200 V.

The diameter of the turbine is much smaller than that of the optimum turbine matching with the air power from the air chamber, because of the limitation of research fund. Two dummy nozzles are installed to consume the extra air energy which is almost half of the total air power. The air power to the turbine is limited by the air flow regulating valves and the pressure relief valves. Power generation is stopped at the time of extremely large waves by fully opening the air flow valve (the air flow to the turbine is closed).

Figure 8 shows the air flow regulating valve. The valve is a rectangular box with a butterfly valve inside. The air flow can be controlled by the rotational angel of the butterfly valve. An electric actuator is equipped to move the butterfly valve. The actuator is usually controlled according to the signal of the rotation number of the turbine as programmed beforehand. For the conservative operation the valve opens by 1/4 of the full angle when the rotation number exceeds 1800 rpm and the valve closes by 1/4 of the full angel when the rotation number become lower than 1500 rpm. However for the standard operation the limit values of the rotation number are changed to 2000 rpm and 1700 rpm respectively. The air flow regulating valves are designed in such a manner that the total opening ratio of about 1/90 (proportion of the total cross-sectional area of the two air flow valves to the area of the air chamber) can be obtained when the air valve to the turbine is closed.

Figures 9 shows the pressure relief valve which is a vertical cylinder with a covering lid. The diameter of the cylinder is 80 cm and the height of the cylinder is 170 cm. If the air pressure in the air chamber exceeds the threshold pressure the relief valve opens and air leaks. The threshold pressure can be adjusted by the weight on the valve lid. The threshold pressure of the relief valve is set at 1 tf/m^2 for the left valve and 1.5 tf/m^2 for the right valve. The pressure relief valves have the total opening ratio of 1/120.

In addition to the pressure relief valves and the air flow regulating valves, two emergency valves are installed. The valve is a kind of guillotine type gate as shown in Fig.10. When the rotation speed of the
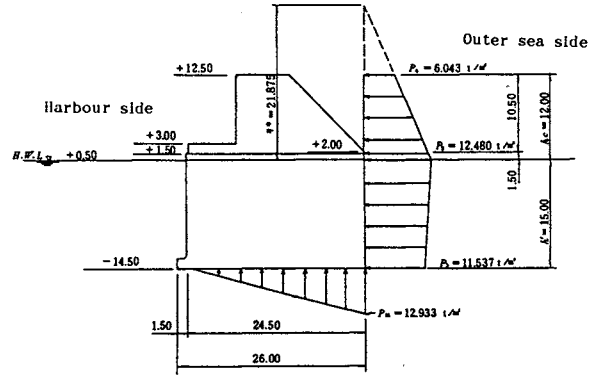
Fig.4 Design Wave Pressure of Caisson

p: Wave pressure intensity (t/m^2)
w_o: Specific weight of sea water (1.03 tf/m^3)
H: Design wave height (H_{max} = 15.3m)
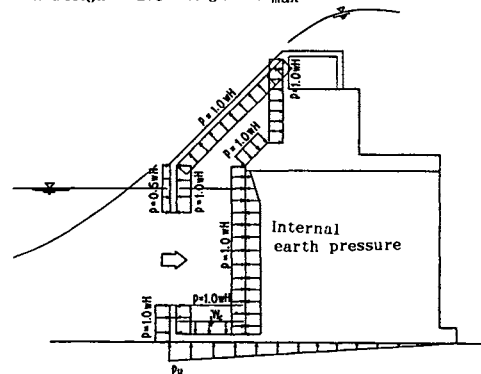
Fig.5 Design Wave Pressure in Air Chamber (during compressing wave)
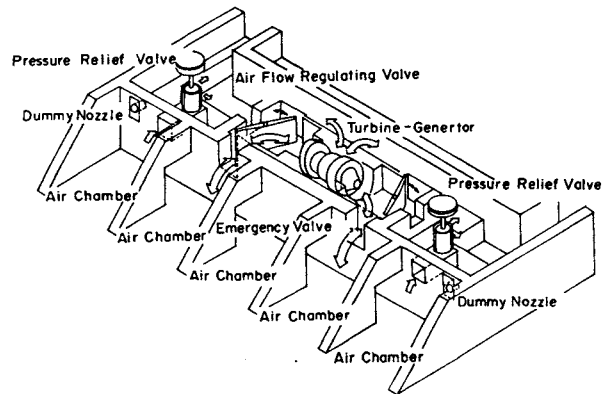
Fig.6 Plan View of Machine Room

unit : mm
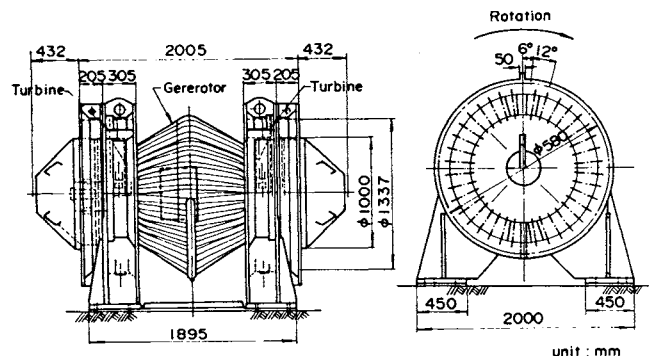
Fig.7 Turbine and Generator

turbine exceeds a certain value, the valve plate falls to close the opening to the turbine and at the same time to open a nozzle to machine room. The total opening ratio of the two nozzles is 1/70.

4. Construction Procedure

The wave power extracting caisson has a special shape compared with an ordinary breakwater caisson. Especially, the front wall of the air chamber is sloped and this makes the construction work more difficult. Moreover, a large wave force seems to act to the sloped wall. Therefore, a sufficiently high accuracy is required for building this sloped wall. The lower portion of the caisson was built on a floating dock and the upper portion was made at sea at a calm place in the harbor. The caisson completed up to the sloped portion was then towed out to the sea and installed on the foundation mound. Machine room and so forth for housing the turbine-generator was completed after installing the machines. Figure 11 shows the construction procedure for the caisson. Photos 3 and 4 show the towing of the caisson and the installation of the turbine-generator. Photo 5 shows the turbine during its assembly. The turbine rotor with the blades is seen in the photo.
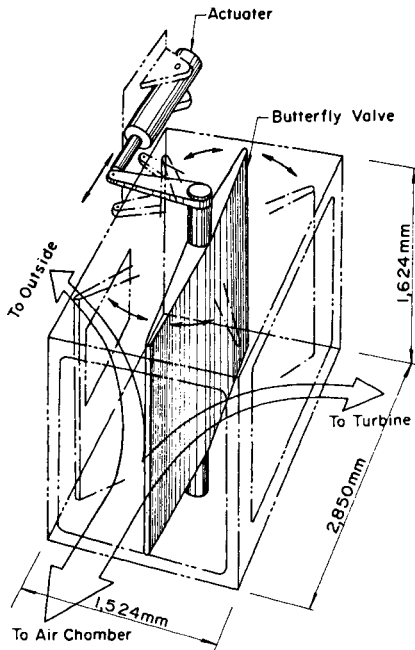
Fig.8 Air Flow Regulating Valve
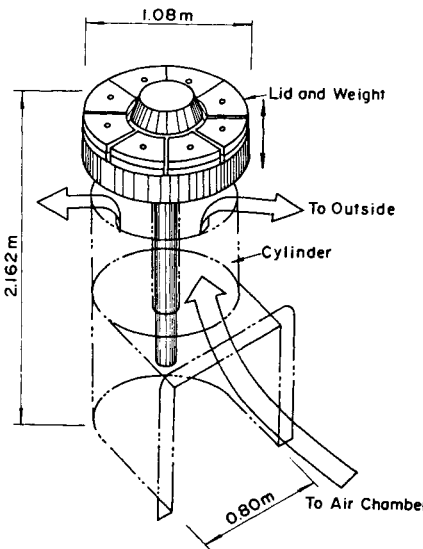
Fig. 9 Pressure Relief Valve
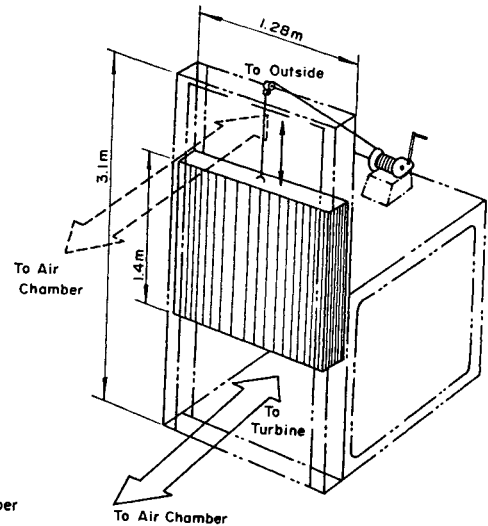
Fig.10 Emergency Valve
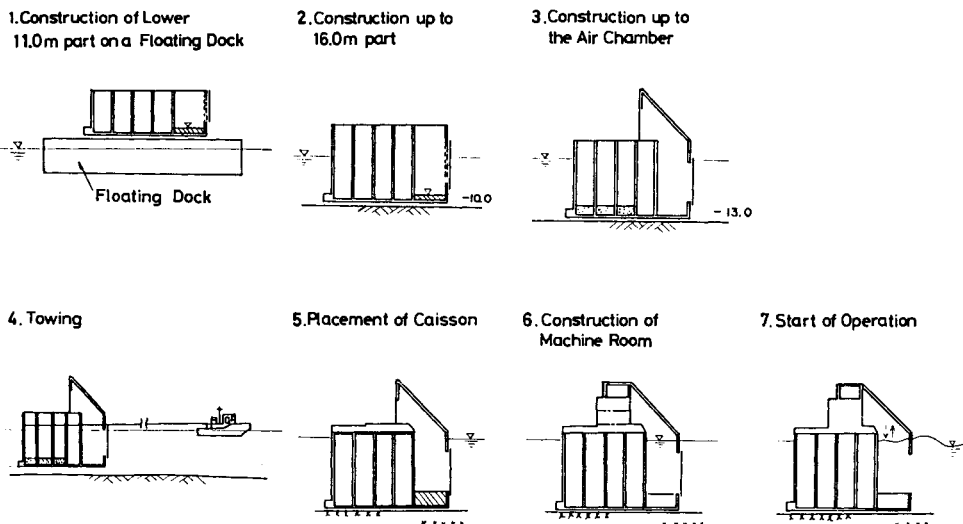
Fig.11 Construction Procedure for Wave Power Extracting Caisson Breakwater

5. Measurements

Various kinds of sensors are attached to the caisson and generator. Figure 12 shows the location of the sensors attached to the caisson. The data obtained are then amplified in the measuring room of caisson and are converted into optical digital signals and transmitted through an optical fiber cable to the on-land observation room. The data is analyzed in the observation room on real time and simultaneously recorded on magnetic tapes. Measurements are carried out for the following items:

1) Finding the wave condition by measuring the wave spectrum with an array of three wave pressure gauges and the ultrasonic wavemeter.
2) Verification of the stability of caisson by measuring the wave pressure and uplift.
3) Verification of the safety of structural members by measuring the stresses in reinforcing bars.
4) Verification of air output efficiency and power generating efficiency by measuring the air pressure and water level in air chamber, turbine speed, generated electric power, etc.

Photo 6 shows the operation room in the on-land observation house where the control panels of the turbine-generator and the system for data acquisition and analysis are placed. There are four personal computers in the room to analyze the data simultaneously. The first one is to find the incident wave conditions including directional spectrum, and the second one is to analyze the wave power conversion, the third one is to know the wave pressure and the stress on the caisson and the last one is to show the real time variation of the operation of the wave power conversion.

6. Power Generating Operation and Energy Utilization

Power generating operation is basically performed automatically, and electric power corresponding to the wave conditions can be obtained. At the time of large waves, the air flow regulating valve and pressure relief valve work in order to restrict the output below 60kW. The power generated by the system is transmitted through a cable to the on-land observation station. At the on-land observation station, load resistors are provided for consuming the power. Also provided is a system for branching the generated power without affecting the power
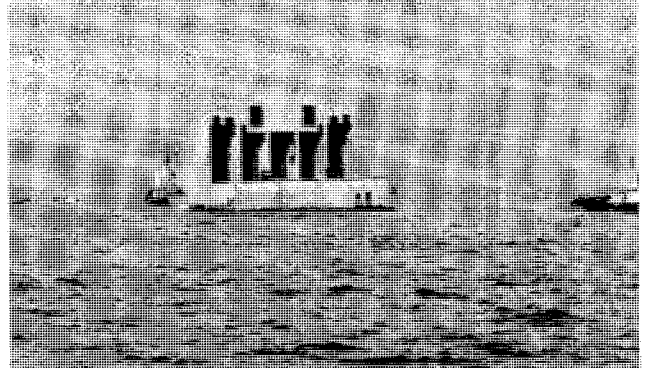
Photo 3   Caisson Being Towed
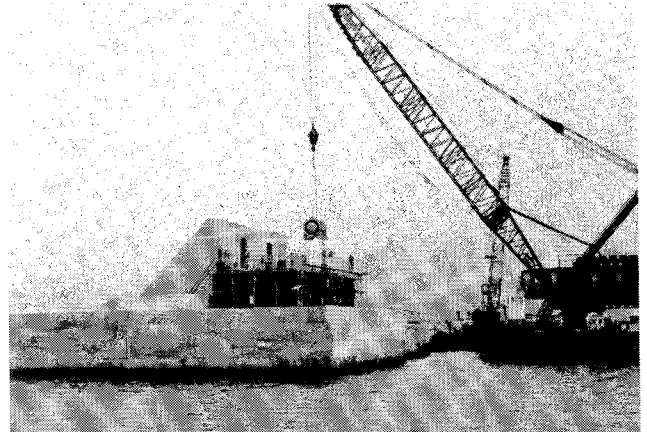
Photo 4   Turbine Being Installed on the Caisson
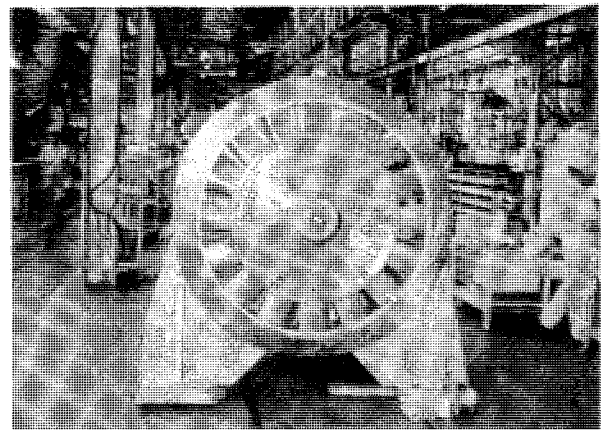
Photo 5   Turbine Being Assembled

Photo 6 Operation Room
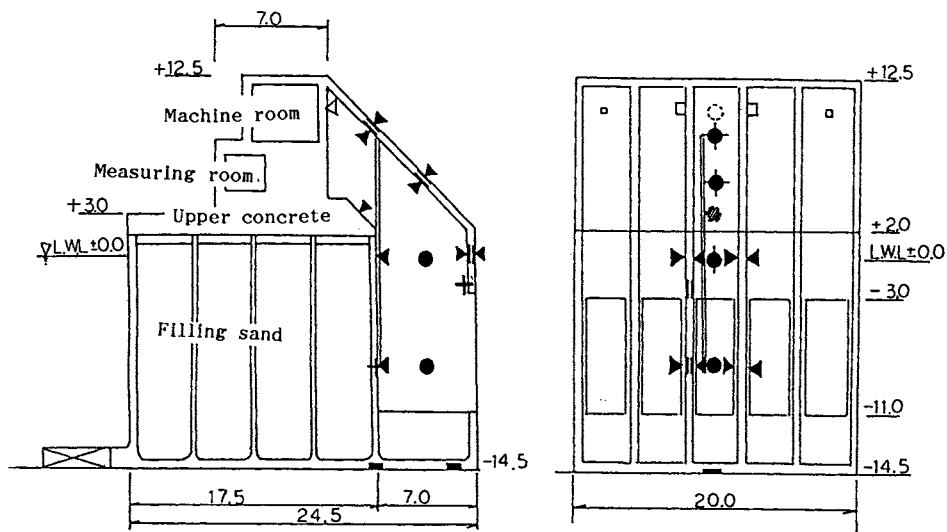
Items to be measured	Sensors	Place
Pressure in air chamber	Wave pressure gauges	○ ▷
Wave pressure in air chamber	Wave pressure gauges	
Wave pressure acting to frontface	Wave pressure gauges	● ▶
Uplift	Wave Pressure gauges	▬▬▬
Stresses in sloped wall	Reinforcing bar gauges	— ꟾ
Stress in partition wall	Reinforcing bar gauges	
Water level in air chamber	Step-type wave gauge	⟺
Incident wave height and wave direction	Ultrasonic-type wave gauge with wave pressure transducers	320 m away from caisson
Power generation	Turbine speed meter, wattmeter, voltmeter, etc.	Machine room

Fig.12 Location of sensors
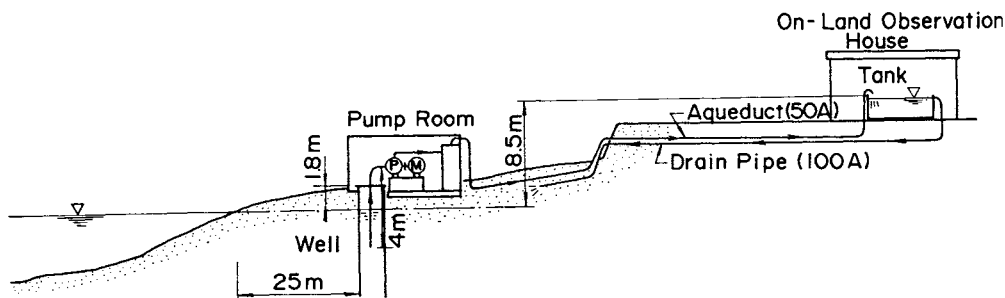
Fig. 13 Pump System

generating system. By using the branched electric power, the power utilization is demonstrated by various electric equipment. Figure 13 shows the water pumping system utilizing electric power from wave power. It was assured that the pump works smoothly although the frequency of electricity fluctuates. The tower in Photo 2 has forty 1kW-electric lights. The snow melting system and other apparatus to use the electric power are tested in the experiment.

The electric load is controlled in proportion to the third power of the rotation speed of the turbine and the load of 60 kW is set at 2000 rpm.

7. Results of the Experiment

The electric power by the system is being generated satisfactorily since December 1989. Figure 14 shows the sample of the experimental results. The average electric power during twenty minutes is plotted against the significant wave height. The calculated value by the thermodynamics and wave-kinematic theory is also shown in the figure. The solid line is the calculated value with the condition that the pressure relief valves and the air flow regulating values are closed. The dash-dotted line is the calculated value for the conservative operation (1500 rpm - 1800 rpm) and the dotted line is for the standard operation (

1700 rpm -2000rpm). By the standard operation the average electric power is about 20 kW and 40 kW when the significant wave height is about 2 m and 4 m respectively. The calculated value agrees well with the experimental values.

Figure 15 shows the maximum peak value of the pressure measured when the waves with the significant wave height of 7.3 m attacked the caisson. The estimated maximum wave height was 12 m. The measured air pressure is less than 1.0 $w_0 H_{max}$. The measured pressure confirms the design method of the caisson. The experiment is scheduled to continue till March 1991 and the results of the experiment will be reported subsequently.

REFERENCES

1. Takahashi, S.(1988): A study on design of a wave power extracting caisson breakwater, Report of Wave Energy Lab., Port and Harbour Research Institute, 337p.
2. Coastal Development Institute of Technology(1984): Report of the Comprehensive Study on the Utilization of Wave Energy. (in Japanese)
3. Goda, Y. et.al.(1989): Field Verification Experiment of a Wave Power Extracting Caisson Breakwater, - Design and Construction of the System and Plan for Its Test Operation-, International Conference on Ocean Energy Recovery, Hawaii.
4. Ojima,R. et.al.(1984): Theory and experiments on extractable wave power by oscillating water-column type breakwater caisson, Coastal Engineering in Japan, Vol.27,pp.315-326.
5. Takahashi,S. ,et.al.(1986): Turbine power by wave power extraction system with vertical breakwaters, Proc. of 5th OMAE, pp.553-559.
6. Takahashi,S.(1988): Hydrodynamic characteristics of wave-power-extracting caisson breakwater, Proc. of 21st ICCE, pp.2489-2503.
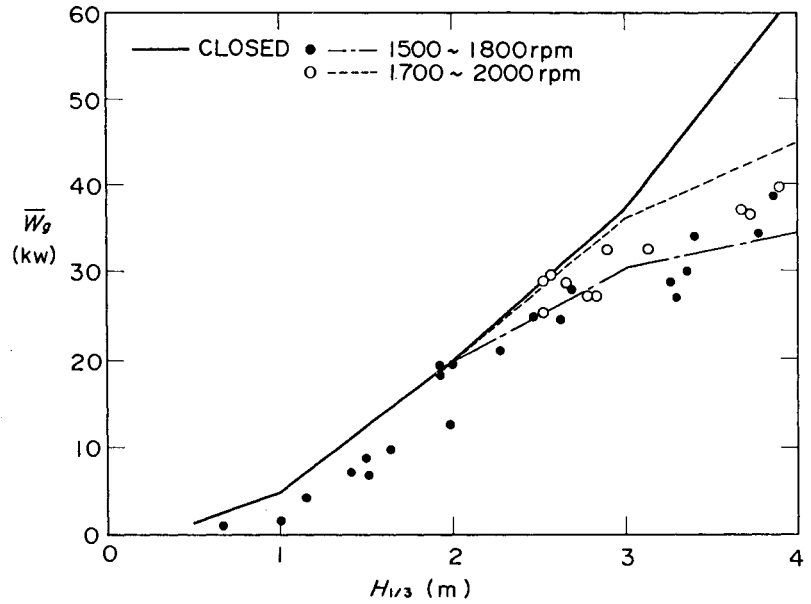
Fig.14 Average Electric Power Versus Significant Wave Height

Front View

Side View
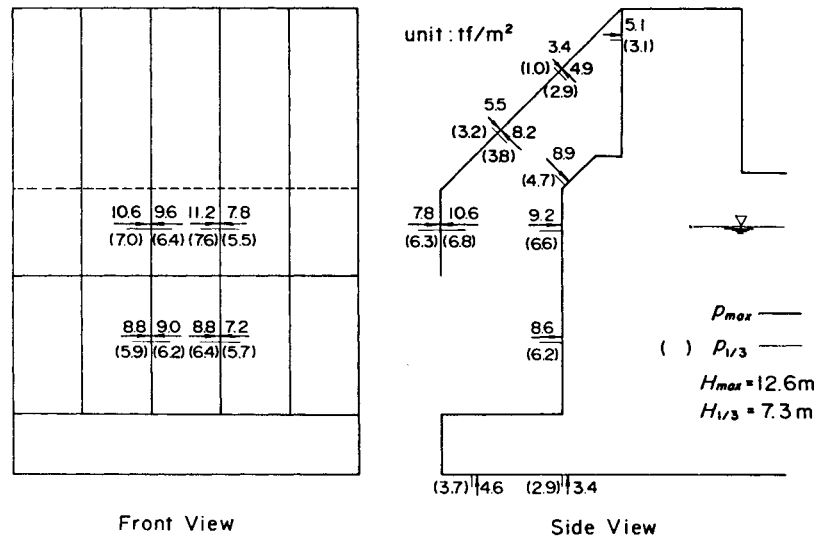
Fig.15 Measured Pressure by Storm Waves

DEVELOPMENT OF FLOATING TYPE WAVE POWER DEVICE.

Yoshio Masuda, Yosiyuki Outa

Ryokuseisha Corporation, Japan

Abstract

Small wave power generator was used for
navigational buoy,but it's power demand
increased. And so improvement study was done,
and efficiency of magnet generator was improved
from 40% to 80%,and capability of power supply
to load increased two times.

The other hand,ship shape$_\wedge$Normard buoy was
tested in water tank,it has characteristic of
low drag,and stable and high power generation.

In order to progress Backward Bent Duct Buoy
(BBDB), Professor McCormick Naval Academy
completed theoretical study. High output in
head sea,and forward movement by wave were
certified.

Large wave power generator was studied for
island and land use.
New Heller generator can supply constant Hz
in variable rotation speed of turbine by wave.
Double rotor Wells turbine was studied,it
will reduce jet noise of Wells turbine in
high rotation.

Using these development works ,power cost
is reduced to feasible value in large wave
power generator.

1. Introduction.

We reported a new floating type wave power
device Backward Bent Duct Buoy (BBDB) in
PACON 88.
Study was continued,it includes center pipe
navigational buoy,ship shape$_\wedge$NORMARD buoy
and large BBDB.
Water tank test was conducted in coopear-
ated with Ship Research Institute.
Theoretical study was conducted by Professor
McCormick US Naval Academy.
Electric generator study was conducted by
Takaba Kagaku Kougiyou and Heller Dejulio
Corporation.
Turbine study was conducted by Professor
Kaneko Saga University.
Floating type wave power generator
progressed for feasible use through these
studys.

2. Improvement of small wave power generator.

2-1 Need of study.

Small wave power generator was used for
power supply of navigational buoy from
1965 by Marine Safety Board in Japan.

Recently, power demand on the navi-
gational buoy increased by changing of
international regulation for navigational
light on buoy from 5 watts to 10 watts in
average electric consumption.

Therefore power up of wave power generat-
or is necessary.

Since wave power buoy uses a long
center pipe,oyster growing in the center
pipe disturbs water motion in the center
pipe.

It must be prevented without using pois-
onous paint.

It is difficult to change buoy's dimension,
power up must be done by improvement of
conversion efficiency.

Conversion efficiency of old type wave
power generator was about 21%.

        Valves efficiency-----95%
        Turbine efficiency----55%
        Generator efficiency--40%   total 21%.

Our study target of improvement of conversion
efficiency was about 49%.

        Valves efficiency-----95%
        Turbine efficiency----65%
        Generator Efficiency--80%   Total 49%

This study target looks like to be obtained by
Vareious study works,some of them is introduced.

2-2 Turbine.

There are three kind small turbine of
Impulse,Wells and Servonus for buoy use.
Their efficiency by constant air flow is
reported in reference 2 as follow.

Impulse------Peak efficiency 60%

Wells--------Peak efficiency 40%

Servonus-----Peak efficiency 30%

We adopted Impulse turbine for improved unit
from veiw point of high efficiency.

Impulse turbine was redesigned to change
it's rotor diameter from 200 mm to 250 mm.

New turbine with new electric generator is
showen in Fig 1.
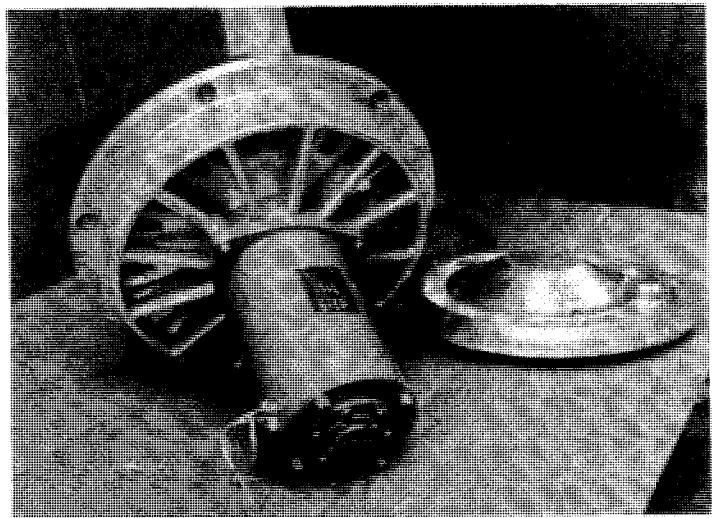
Fig.1 New turbine with Takaba Generator.

2-3 Electric Generator.

It was a difficult study to improve efficiency
of small electric magnet generator.

Improvement work of ordinary generator was done by
Ryokuseisha Corporation.

Special generator was studied by Takaba-Kagaku-
Kōgiyou Ltd.

Both studys improved generator's efficiency as
follows.

Ordinary generator--------to 65 %

Special generator---------to 80 %

Ordinary generator has a perpendicular magnet path
against rotor axis as same as ordinary design of
motor and generator.

Special generator has parallel magnetic path
against rotor axis,and high efficiency was obtained
by decreasing of iron loss and electric loss.

Ordinary high efficiency generator is now on practical use, and special generator finished blower test with turbine,but it is not yet tested on sea.

If the special generator becomes to practical use, the target of improvement will be completed.

2-4 Adoption of Bioclean.

There are many kind of anti-fouling paint,but poisonous paint is not adoptable from enviromental view point.

We tested bioclean paint produced by Chugoku Paint Ltd in our sea test of twin-hull Backward Bent Duct Buoy (BBDB).

Principle of prevention of fouling by bioclean is it's very high attach angle,and it rejects water on the surface and prevents fouling.

It has no poison,and it can keep it's function in long years.

It has two horizontal pipes (0.6 m in diameter,2.4 m in length), one pipe is painted by bioclean,and the other pipe is not painted by bioclean,it is painted by ordinary paint.

Bioclean test of twin hull BBDB was done half year (summer season) in Yura Turuoka-city (Japan sea), and after half year rest, it was tested half year in Mikawa Bay.

Total 1 year test concluded that it is quite effective to prevent oyster growing in the center pipe,there were no oyster growing in Bioclean painted pipe.

3. Study of new ship shape NORMARD buoy.

Several robot weather buoys are used in telemeter oceanographic data and weather data on sea.

Normard buoy is one of them,it is ship shape buoy. It is knowen that this buoy is useable in harzard ocean area since it is low drag force in high current condition.

Recently,1/10 model of this buoy with horizontal duct in it' bottom was tested on a small water tank of Japan Ship Research Institute.

3-1 General veiw of 1/10 model.

Fig.2 shows model dimension,it is 61.8 cm in length,30 cm in width,22 cm in hight and 6.6 Kg in weight.

It is constructed by Aluminium plate,and duct is fixed in the hull's bottom, duct's cross section is triangle. This model is moored in the water tank by small chain line. Fig.4 shows test veiw in the water tank.
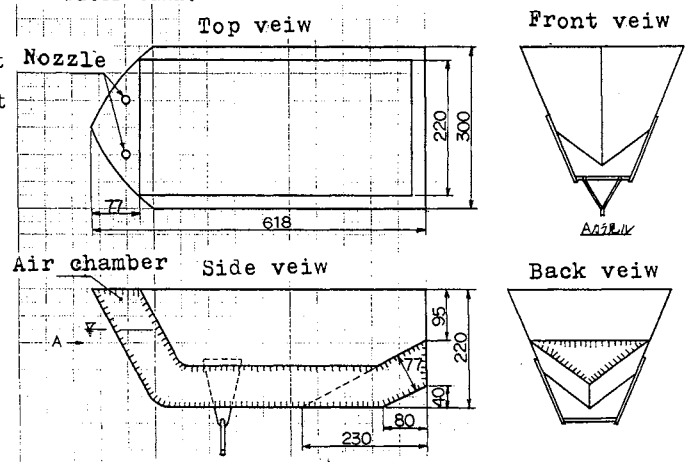
Fig2 Model dimension of Ship shape wave power buoy (Normard buoy type)
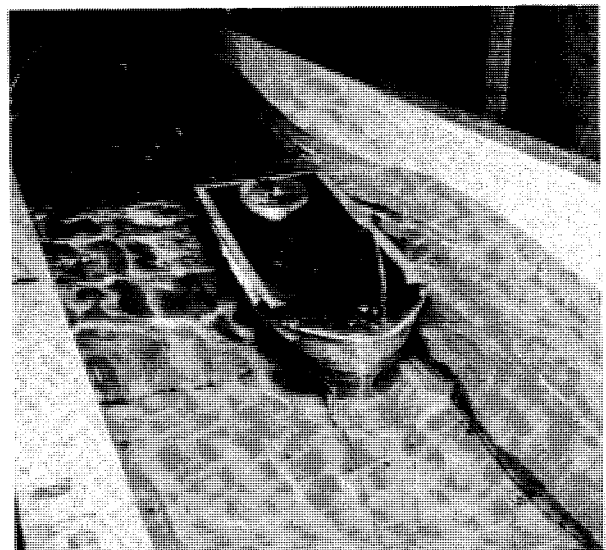
Fig.3 Water tank test veiw.

3-2 Test result.

(a) Air pressure ratio and air output by wave period.

Since model is very small, air pressure ratio is relatively low,but it is still higher than present center pipe buoy's data.

Peak air pressure ratio is obtained at 0.9 sec, and air output was 0.15 watts by 6 cm wave hight.

(b) Buoy motion.

When this Normard buoy model was tested on the same water tank without bottom horizontal water duct (no wave power absorption), dangerous rolling and other motion was observed, but there was no rolling and no dangerous motion in this test. We concluded that wave power generation and bottom. duct is quite effective to dump buoy's pitching and rolling motion by wave.

(c) Drag force in towing.

Drag force by towing was quite small, it was 0.15 Kg by 0.82 knot of towing speed.

3-3 Capability of Wave power NORMARD Buoy.

Based on model test result,Ship type Normard buoy (10 times larger than model, 6 m in length. 6 ton in weight) with wave power generator on deck, nd horizontal duct in bottom will have following characteristic.

(a) Electric power generation by 60 cm wave hight, 3 sec wave period in inland sea is expected as follows.

$$0.49 \times 0.15 \text{ watt} \times 10^3 \times \sqrt{10} = 222 \text{ watt}$$

But, 0.15 watts by 6 cm wave is test result by very small model with very short pipe length.

When I tested center pipe buoy in Meguro water tank, air output increased by increasing of center pipe length

Thinking these matter,500 watts electric power generation will be possible, and 50 - 100 watts power consumption will be possible.

(b) When this ship type buoy is moored in high current channel of 4 knot,drag force is calculated as follows.

$$0.15 \text{ Kg} \times (4/0.84)^2 \times 10^2 = 340 \text{ Kg}$$

It is about 0.3 of drag force of Center pipe, and there is no inclination of buoy.

Safety and high capability buoy can be expected.

4.Theoretical study result

Professor McCormick finished a theoretical study about BBDB (Self Propelled Backward Bent Duct Barge) as showen in Fig.4.
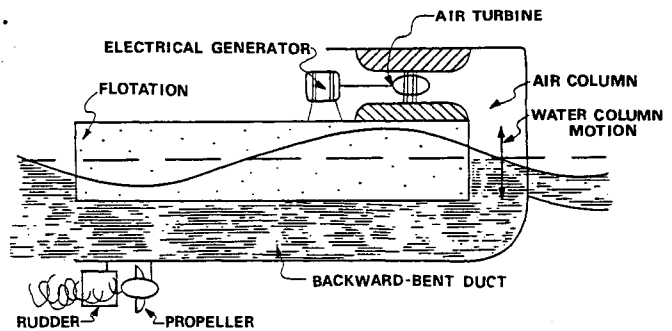
Fig.4 Schematic sketch of Self Propelled BBDB Barge.

4-1 Output difference by buoy's direction.

BBDB in head sea has 10 times higher output than BBDB in following sea and fixed BBDB in a following sea as showen in Fig.5.

As showen in Fig.5, peak output is a little longer than Wzc which is natural oscilation in horizontal duct,natural oscilation period Tz is calculated as follow.

$$Tz = 2\pi\sqrt{L/2 \ g}$$

In where L= Horizontal duct length.

g= 9.8 m/s

π = 3.14
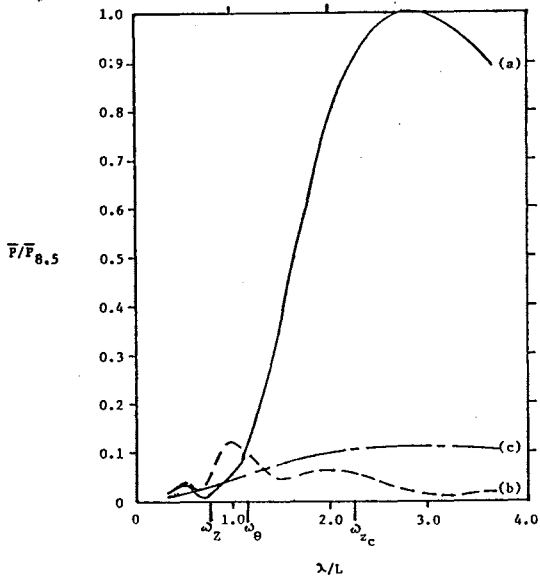
Fig.5 Normalized average converted power.

The maximum power for all wave periods,

which occurs at T=8.5 s. is used in the

normalization. The curves correspond to (a)

the BBDB in head (design) sea------,(b)

the BBDB in following sea--------and (d) a

fixed BBDB in following seas -- - ---.

For this comparison, BBDB's dimension is.

    Length----35.6 m.

    Beam------9.91 m.

    Displacment------500 metric ton.

    Duct cross section----- 2 m in hight.

                       19.8 m in width.

Conversion peak efficiency in head sea at 8.5

second is calculated 83%.

The reason of high output of head sea

condition is explained by phase relation

between pitching and water column movement

as showen in Fig.6.

4-(2) Forward speed.

    Standard barge and ship configurations is

drifted by wave,but BBDB has different
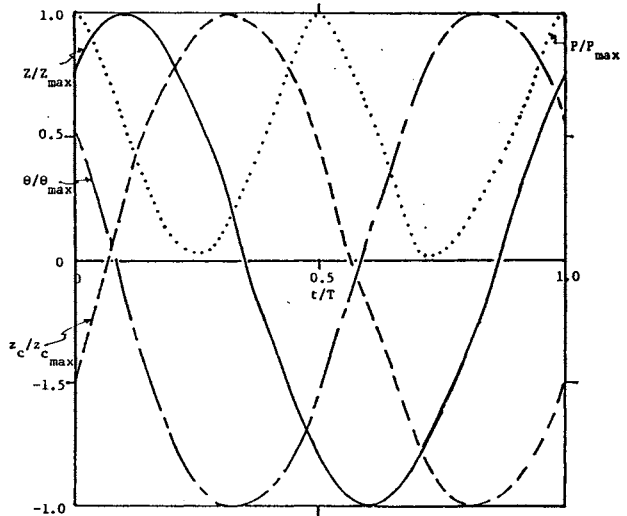
Fig .6 Normalized heaving,pitching,water

    column resonances and converted power.

    These are instantaneous valuesover one

    period for T=8.5 s,H=1.0 m and U-0.

characteristic of drift.

  It's drift seems to be positive,it has a

  tendency to go forward in wave.

  In order to check this behavior,Professor

McCormick made 1/20th scale model of 35,6 m

berge and tested in a wave tank. The

positive drift of the BBDB was verified.

This characteristic will increase of

safety mooring in high sea area,and also

it will bring some application for Self-

Propelled Barge by wave power in future.

5. Study for Large Scale Wave Power.
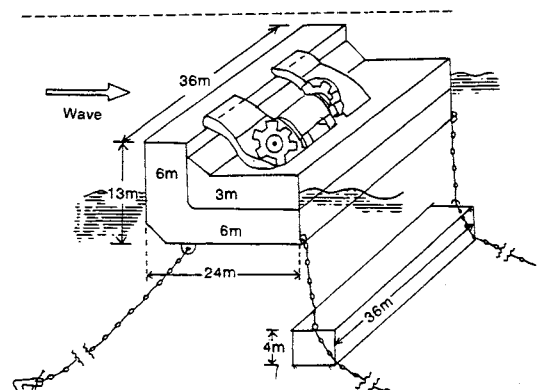
fig.9 Large BBDB wave power generator

Larger use is island and land power.

Figure 9 shows one design of BBDB for

island and land power.

Conversion efficiency of floating type

wave power device increased by adoptation

BBDB as showen in theoretical study, but

there are still problems in turbine and

generator design.

5-1 Study of double rotor Wells turbine.

Wells turbine needs no valve. It is very high

speed ,but there is a high frequency jet noise

at high rotation speed.

Double rotor Wells turbine was studied to

decrease noise and   strength problem of rotor

by Professor Kaneko Saga University.

case(A)   case(B)   case(C)
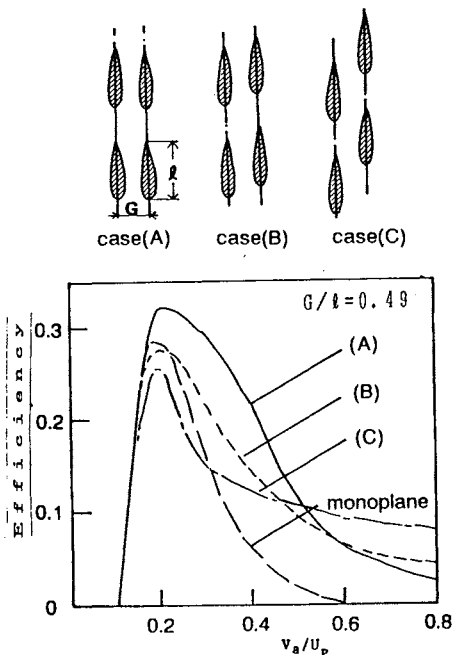
Fig.7 Bench test for biplane
         wells turbine.

Figure 7 shows the test result. Efficiency of

bi-plane was higher than monoplane in case of

(A), but biplane (A) has a poor self-starting

characteristic,therefore induction generator

is better to be combined with (A) arrangement.

On the other hand,rotation speed is decreased

to about half.

When Wells turbine is constructed by plastic

CRFRP(Carbon fiber),and it is estimated 2

million yen per 1 unit in case of 2 meter in

diameter.

5-2 Study of electric generator.

Conventional AC generator and induction

generator were used in Kaimei test,but AC

generator needs AC-DC-AC conversion to

connect to grid,it is high price.

Normal induction generator is constant speed,

fluctuated electric output can not be

smoothlized. Improvement of generator was most

difficult matter in wave poqer generation.

Fortunatly,US company,Heller-Dejulio

Corporation made the Heller generator which

can generate thesame frequency to grid in wide

speed range from base RPM with good efficiency

and powerfactor. It is said that 500 KW with

Wells turbine is ¥ 10 million .
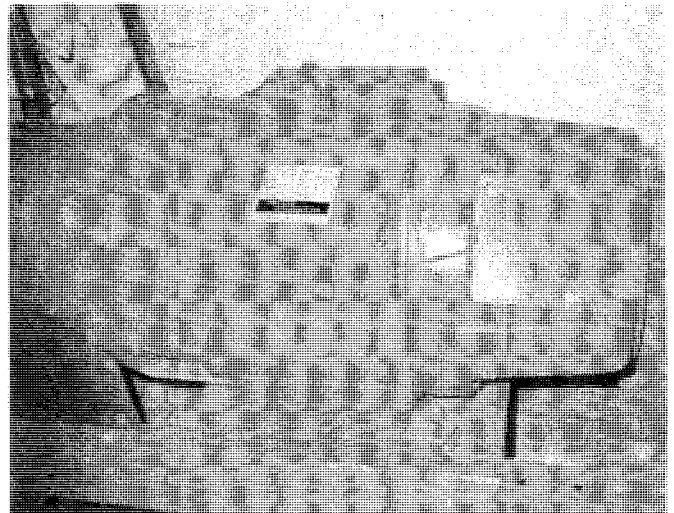
Fig.8:   15 KW Heller Generator.

Fig 8 shows 15 KW Heller Generator in his

test facility in Sanfrancisco.It is wound

type induction generator with capacitance

and resistance in rotor circuit.

It produced the same frequency (Hz) by

variable speed from base rpm to two times

rpm with good efficiency and power factor.

It is cheap enough for practical use,500

KW unit is ¥ 10 million .

5-(3) Calculation of Wave Power Cost.

Buoy hull (24 m in length,36 m in width

and 13 m in hight) is constructed by 12 mm-

8 mm steel plate,and 400 ton for hull.

In adition 60 ton for underwater bucket,

it can be constructed by ¥ 130 million

($ 2000/ton,¥290,000).

two units of 500 KW generator are installed

on the deck,it will need ¥ 40 million. In

addition,mooring needs ¥ 20 million. Cable and

it's laying needs ¥ 15 milluon. Transportation

and mooring opearation need ¥ 25 millon.

Contigency needs ¥ 10 million.total construction

cost will be ¥ 240 million in minimum.

using tank test data,efficiency of BBDB

of 24 m. with underwater bucket is estimated

as showen by solid line in Fig.10.

There are many high wave area,highest country

will be Newzeland.It is estimated 80-100 KW/m

in average through year. UK Ireland etc high

atitute from 40 degree to 50 degree area is

60-40 KW/m.propic island such as Hawaii is

20 -26 KW/m,but the other including Japan is

10- 15 KW/m.

Conversion efficiency from wave to air output

in 1 year can be calculated by energy

distribution in natural wave in 1 year and

conversion efficiency as showen in Fig 10.

In Hawaii case,it is estimated 59 %.
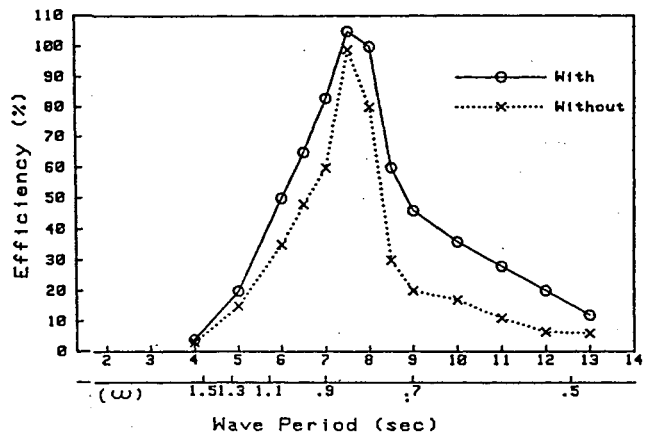
Fig.10   Efficiency of large BBDB of 24 m,

with and without underwater bucket.

BBDB's width is 36 m. Conversion efficiency

from air output to electricity by turbine and

generator is 0.6, and output power KW-h

produced by BBDB in 1 year is calculated as

follow for Hawaii where 26 KW/m in wave power

is expected.

26 KW/m x 36m x 24 h/d x 365 d/y x 0.59 x o.6

= 2,920,284 KWh/y

Expense per year of wave power generation is

10 % of construction cost by UK formula.

When BBDB in Fig.9 is used in Hawaii, power

cost is estimated as follows.

0.1 x 240,000,000 yen/ 2,920,284 KWh

= ¥ 8.2 / KWh = 5.6 cent/KWh

Since wave power is 2 - 4 times higher in UK
or Newzeland,power cost will be very cheap,
but it will be high such as 10 cent/KWh in
Japan etc.

4 CONCLUSION.

Recently,the progress of wave power generation
was delayed by energy situation,but several
important progress were done as follows.

(a) Small magnet generator was improved in
it's efficiency from 40 % to 80 %. This progress
will givea superiority of wave power for buoy's
power system against solar power.

(b) Ship type NORMARD buoy with wave power
generator will be very superior buoy in high
current and high sea area and also deep sea
use.

(c) Floating type wave power generator
renders less difficulty of site selection and
construction than shore fixed type.
Iexperienced test of floating large wave power
generator "Kaimei".The hull was found to be
excellent after 10 years use. Turbine and
generator experienced only minor problems.
A mooring and power cable to the shore all
remained intact. but conversion efficiency
from wave to air output of Kaimei was not good.
New floating buoy system BBDB increased
efficiency about 10 times than Kaimei,and
decreased hull size from 80 m to 25-35 m,and

decreased number of turbine and generator from
12 to only 1. power cost became to feasible by
these improvement.

6. REFERENCE

6-1   Y,Masuda. T,Yamazaki.Y,Outa Ryoku-
    Seisha Corp, Utilization of Wave Power
Generator for development of island country
    in the Pacific Ocean. PACON 88.

6-2 M,KATUHARA.Ship Research Institute.
    Impulse Wells and SAVONIOUS Air turbines
    for wave activated generator used at
    light beacons. PACON 88.

ON THE BEHAVIOR AND PERFORMANCE OF THE FLOATING OFFSHORE WAVE POWER DEVICE

H. Hotta

Japan Marine Science and Technology Center, Japan

Abstract

The method for estimation of the behavior and performance of the Floating Offshore WAve power Device (FOWAD) is described in this paper. FOWAD is one of the floating type wave power convertor, which is moored at the offing and it can absorbe the wave energy and create the calm sea area behind the device as a floating breakwater.

The motions of six mode of FOWAD in regular waves are estimated by the modified strip method, and the efficiency of wave power absorption is estimate by the modified thermodynamics and wave-kinematics method. Furthermore, the performance in the long and short crested waves are estimated by the method of superposition.

1. Introduction

Ocean has several kinds of natural energy resources, and wave energy is the most convenient energy resources in the ocean. Because the total amount of the wave energy is very huge and we can utilize it at most part of the coastal zone except in the bay However, the density of wave energy is not so high and the output of energy fluctuates with time. Nevertheless, the study on the utilization of wave energy is continued still now. Furthermore, we supporse that it will be more popular. Because, we should utilize the natural energy resources for supplyment of energy for the antipollution measure at the coast.

Japan Marine Science and Technology Center carried out the open sea tests for two types of proto type wave power devices up to this time. These are the floating attenuator type device "KAIMEI" [1][2][3] and the shore fixed type device "SANZE" [4]. As a result of the project of KAIMEI, we could confirm the possibility to utilize the wave energy, however the estimated value of the cost for the electrical generation was not so cheap and output power was not stable. In order to improve these shortcomings, JAMSTEC continued to research and develop on the new type of the wave power device.

As a result of this study, it was clarified that the floating terminator type device has most effective performance for the absorption of wave energy and the dissipation of the incident waves, if it will be moored at near coastline easily. The Floating Offshore WAve power Device (FOWAD) is one of this kind of devices [5].

2. Outline of FOWAD

FOWAD has several air chambers which can absorb the incident wave energy and convert to the other energy resources and several floating chambers has the ability to keep the buoyancy. Every air chamber has an orifice which can simulate the air turbine which is equiped on the full scale device, and it causes the damping force for vertical motion of the oscillating water column in an air chamber. Furthermore, FOWAD has some projecting walls and some bottom plates in order to increase the efficiency of energy conversion because of the phenomenon of "the harbour resonance" by the air chamber.

Usualy, FOWAD is moored by some catenary chain lines, and its longitudinal axis coinsides to the significant direction of wave crests at the offing like a the floating breakwater. A scheme of FOWAD under the condition of mooring is shown in Fig.1.

Most characteristic points of FOWAD are;

(1) The natural period of rolling and pitching are very long because of a

small GM due to the special arange-
ment of air chambers and floating
chambers.
(2) The projecting walls causes the
effect of "harbour resonance" [6]
even FOWAD is oscillated by waves.
(3) Heaving motion of FOWAD is very
small because of the damping force
due to some orifices.

3. Motion in Waves

3.1 Fundamental equation of Motion

When the FOWAD is moored and
oscillates in the regular waves, since
the coupling between heave and pitch
and between sway, yaw and roll are
remarkable rather than the coupling by
the surge, the equations of six modes
of motion are described as follows.

Heave and Pitch ;

$$a_{11}\ddot{z} + a_{12}\dot{z} + a_{13}z + a_{14}\ddot{\theta}_p + a_{15}\dot{\theta}_p + a_{16}\theta_p = F_H \left.\right\}$$ (1)
$$a_{21}\ddot{z} + a_{22}\dot{z} + a_{23}z + a_{24}\ddot{\theta}_p + a_{25}\dot{\theta}_p + a_{26}\theta_p = M_p$$

Sway, Yaw and Roll ;

$$a_{31}\ddot{y} + a_{32}\dot{y} + a_{33}y + a_{34}\ddot{\psi} + a_{35}\dot{\psi} + a_{36}\psi$$
$$+ a_{37}\ddot{\phi} + a_{38}\dot{\phi} + a_{39}\phi = F_y$$
$$a_{41}\ddot{y} + a_{42}\dot{y} + a_{43}y + a_{44}\ddot{\psi} + a_{45}\dot{\psi} + a_{46}\psi \left.\right\}$$ (2)
$$+ a_{47}\ddot{\phi} + a_{48}\dot{\phi} + a_{49}\phi = M_\psi$$
$$a_{51}\ddot{y} + a_{52}\dot{y} + a_{53}y + a_{54}\ddot{\psi} + a_{55}\dot{\psi} + a_{56}\psi$$
$$+ a_{57}\ddot{\phi} + a_{58}\dot{\phi} + a_{59}\phi = M_\phi$$

Surge ;

$$a_{61}\ddot{x} + a_{62}\dot{x} + a_{63}x = F_x$$ (3)

Normaly, the optimal breadth of
FOWAD is about 15% of a wave length,
and the optimal length of FOWAD is
almost same as the length of a wave
length [7]. Consequently, the optimal
aspect ratio of length devided by the
breadth is about 8. So, the author
supporsed that the strip method is an
available and convenient method to
estimate the motion of FOWAD in waves.
However, FOWAD has several
characteristics which the ordinaly
ocean structre and ship do not have.
These are the oscillating water column
(OWC) in the air chamber, the
projecting walls and the bottom plate.
Consequently, the strip method have to
be modified to apply to FOWAD.

Strictly speaking, the mass of water
in each air chamber changes at every
moment because it is the OWC, and its
surface is waving also. However, since
such changes and effects due to such
phenomena is not so large, it is
available to neglect such items in this
equations.

That means the mass of water (OWC)
in the air chamber can be regarded as
"the rigid body" which oscillates in
the wave with FOWAD. Consequently, the
total mass of FOWAD should be
considered as the mass of hull added
the mass of OWC in each air chambers.
Furthermore, it was considered that the
restoring force caused by the
displacement of FOWAD is occured by the
discharged volume of the hull of FOWAD
and the OWC in each air chambers.

By the way, the damping force caused
by the orifice on each air chamber must
be considered and taken into the
equations of motion. Because, the air
chamber has a characteristics to absorb
the wave energy efficiently and it
generates a large damping force for
vertical motion of the air chamber [8].
In this report, it was estimated as
"added damping force" which is assumed
the linear damping which is in
propotion to the velocity of vertical
motion of the OWC in each air chambers.

Added damping force D is calculated
by the pressure on the OWC as following
equation.

$$D = \Delta p \cdot Aw$$ (4)

where Δp ; differential pressure
Aw ; sectional area of an air
chamber

Since the differential pressure due to
a Wells turbine, which is equiped for
most numbers of this type of wave power
devices, is in propotion to the
velocity of air flow through the
turbine (orifice) "Va", it is easy to
calculate the value of p using the
damping force coefficient "da" as
follows.

$$\Delta p = da \cdot Va$$ (5)

When the waving of the surface of OWC
is not so large, "Va" is calculated as
follows.

$$Va = (Aw/(Sn \cdot Cn))\dot{\zeta}$$ (6)

Sn ; area of an orifice
Cn ; coefficient of contraction
ζ ; elevation of the OWC

Consequently, damping force coeffici-
ents are calculated as follows.

$$da = .5 * \rho a (Aw/(Sn \cdot Cn)) \omega \zeta a$$ (7)

where ρa ; density of water
ω ; angular velocity of wave
ζa ; wave amplitude

The value of "da" is introduced to the
items of damping of the equation (1),
because it is assumed that the value of
"da" effects on the vertical motion of
the air chamber.

3.2 Results of Calculation

As some results of the calculation, the behaviors of heave, sway and roll responses versus the wave period in regular waves are shown in Fig.2, 3 and 4. In these figure, plots are the measured values by the scale model test and the solid line is calculated values by the modified strip method described above. Furthermore, in the figure of heaving, the dotted line is the calculated line without consideration of the effect due to the damping force by the air chamber "da".

These figure shows that the strip method is available to calculate the motion of FOWAD in regular waves. However, it was made clear that it is necessary to consider the effect due to the damping force caused by the air chamber when it is absorbing the wave energy.

By the way, the behaviors of motion in regular oblique waves are shown in Figure 5, 6, 7 and 8. In every figures, the calculated values shows a similar tendency to measured data except the absolute values in the figure of heave and pitch. However, since it is possible to infer that the calculated values will get near to the measured data under the conditions of longer wave period.

4. Wave Power Absorption

Each air chamber of FOWAD has a "harbour" which is surrounded by both side of projecting walls, a front curtain wall and a bottom plate at the bottom of each air chamber. The author tried to apply "the thermodynamics and wave-kinematics method (TWM)" which was proposed by Takahashi et.al [7] for the estimation of efficiency of the wave power absorption, rather than "the equivalent floating method". However, since FOWAD is oscillating in the waves, TWM was modified in order to consider on the effect due to the oscillation.

By the way, TWM is the theory which is available for only a fixed air chamber on the sea bottom, and there are no consideration on the transmitted waves behind the device. But, FOWAD is floating in the waves, and we can find out the transmitted waves behind it. In order to consider this phenomena, the efficiency calculated by TWM was corrected by the depth of bottom plate. In this report, the energy which travels under the bottom plate to the behind of the FOWAD is considered.

Furthermore, the velocity coefficient in TWM was corrected in order to consider the compression of air

exactly. It made easier to find out the correct number of the velocity coefficient.

4.1 Thermodynamics and wave-kinematics method

When an air chamber is fixed in the waves as shown in Fig.9, there is a following relation between amplitude and phase of incident waves and oscillation of OWC in the air chamber.

$$h_a = \frac{1}{2} h_{owc} [\{\alpha_o f(kh, kd_c) \sin\omega\tau \cdot \cos\omega\tau + kb\}^2$$
$$+ \{\alpha_o f(kh, kd_c) \cos^2\omega\tau + kb/\tan kb\}^2]^{1/2} \quad (8)$$

$$\phi_{owc} = -\tan^{-1}\{(-\alpha_o f(kh, kd_c) \sin\omega\tau \cdot \cos\omega\tau + kb)$$
$$/(\alpha_o f(kh, kd_c) \cos^2\omega\tau + kb/\tan kb)\} \quad (9)$$

where, h_{owc}; amplitude of motion of OWC
ϕ_{owc}; phase of motion of OWC
k ; wave number
h ; water depth
b ; breadth of the air chamber
dc ; depth of the curtain wall
$\alpha_o = Kp_o/\rho_w g d_o$
K = Cp/Cv
Cp ; specific heat at steady pressure
Cv ; specific heat at steady volume
p_o ; atomspheric pressure
ρ_w ; water density
g ; gravitational acceleration
d_o ; height of chamber on the water surface

$$f(kh, kd_c) = \frac{2 \cosh kh \sinh k(h-d_c)}{\cosh k(h-d_c) \sinh k(h-d_c) + k(h-d_c)}$$

$$\omega\tau = \cos^{-1}(\sqrt{1+\beta^2} - \beta)$$

$$\beta = (C_n \cdot C_v \cdot \varepsilon_n)^2 (K-1) \frac{C_p \cdot T_o}{(\omega \cdot d_o)^2} \frac{d_o}{h_a}$$

Cn ; coefficient of contraction
Cv ; velocity coefficient
ε_n ; nozzle ratio
T_o ; absolute temperature of air

Using these equations and some equations on the energy of incident waves, we can derive the equation of efficiency of wave power absorption by the air chamber in regular waves as follows.

$$\eta = \frac{K p_o}{\rho_w g d_o} \frac{b\omega}{Cg} \left(\frac{h_{owc}}{h_a}\right)^2 \sin\omega\tau \cdot \cos\omega\tau \quad (10)$$

where Cg ; group velocity of waves
Tw ; wave period

4.2 Relative Incident Wave Height

Since the air chamber (FOWAD) oscillates in waves, it is neccesary to correct the incident wave height in order to be available to TWM. In this report, the relative wave height was calculated by response and phase of

motion of FOWAD at each air chambers.

The relative wave elevation "hri" between incident wave and FOWAD at the point ℓi apart from the center of FOWAD is

$$hri = hgi - Zi \tag{10}$$

In this equation, "Zi" is the vertical displacement of the point "ℓi" and "hgi" is the wave profile at the point "ℓi" in oblique regular waves of χ in incident angle as follows.

$$hgi = ha \cos\{\omega t - (\ell i + x_i)k \cos\chi \\ - y_i k \sin\chi \} \tag{11}$$

4.3 Velocity Coefficient

When the gas of p_1 in pressure and ρ in density flows out to the region of p_2 in pressure through the orifice, the velocity at the outlet v_2 is

$$v_2 = \left[2 \frac{p_1}{\rho} \frac{k}{k-1} \left\{ 1 - \left(\frac{p_2}{p_1}\right)^{\frac{k-1}{k}} \right\} \right]^{1/2} \tag{12}$$

BY the way, the velocity coefficient φ was defined in TWM as follows.

$$\varphi = \left[\frac{Powc}{\Delta P} \frac{k}{k-1} \left\{ 1 - \left(\frac{P_0}{Powc}\right)^{\frac{k-1}{k}} \right\} \right]^{1/2} \tag{13}$$

Consequently, the velocity coefficient will be calculated by following equation.

4.4 Results of Solution

As some results of solution on efficiency of wave power absorption, the behaviors in the regular waves are shown in Fig.10, 11 and 12. The vertical axis in each figures are the efficiency of wave power absorption.

Fig.10 shows the parformance versus the wave period in model scale. As you can see, it was made clear that the calculated values are available to estimate the efficiency of wave power absorption of FOWAD except the effect by the phenomenon due to the "harbour resonance". AS a consequence, it was confirmed that the maximum efficiency of wave energy absorption by FOWAD will be about 40% except "the harbour resonance", and its band width under the condition of more than 10% in efficiency is wider rather than some former floating wave power device.

Fig.11 shows the tendency of efficiency in oblique waves versus the incident angle of waves. In this figure, 90 in θ means under the condition of the beam sea. The calculated values under the condition of oblique waves are differ from the values under the condition of beam sea.

It was guessed that the effect due to the roll motion and three dimensional phenomena occured and effected.

Fig.12 shows calculated values on the longitudinal distribution of the efficiency of wave power absorption at each air chamber in FOWAD. It was made clear that the effect by the position of the air chamber in FOWAD is not so large even in the oblique waves.

5. Performance in the Short Crested Waves

5.1 Wave Energy of the Short Crested Waves

Wave Energy of the short crested (multi directional) waves per unit length "Ei" is calculated by the following equation.

$$Ei = \rho g \int_{\theta_1}^{\theta_2} \int_0^{\infty} S(\omega) \, G(\theta) \, Cg(\omega) \, d\omega \, d\theta \tag{14}$$

where, S ; wave power spectrum
G ; directional distribution function
Cg ; group velocity of waves
θ ; direction of waves
θ_1 , θ_2 ; lower and upper limit angle of direction of incident waves

In this report, since FOWAD will be installed near the coastal zone at the offing, JONSWAP spectrum was used as the wave power spectrum for the calculation and experiment. Consequently, power spectrum of waves is calculated as follows.

$$S(\omega) = \frac{\alpha Hs}{Tp^4(\omega/2\pi)^5} \exp\left[-\frac{5}{4}\left(Tp\frac{\omega}{2\pi}\right)^{-4} \\ \times \gamma \exp\left\{ \frac{-(Tp\cdot\omega/2\pi - 1)^2}{2\sigma^2} \right\} \right] \tag{15}$$

where, Hs ; significant wave height
Tp ; wave period at the peak of power spectrum ficant wave
α = 0.166
γ = 3.3
σ = 0.07 ($\omega < \omega$m),
0.09 ($\omega > \omega$m)
ωm; peak frequency of power spectrum

The directional distribution function is calculated by the following formula.

$$G(\theta) = Cs \cdot \cos^{2S}(\theta) \tag{16}$$

In this formula, "Cs" is a normalization function as follows.

$$\int_{\theta_1}^{\theta_2} G(\theta) \, d\theta = 1$$

5.2 Absorption of Wave Energy in the Short Crested Waves

When the efficiency of wave energy absorption is a linear function in proportion to the wave frequency and the direction, since the energy of the short crested waves depends on only these parameters, it is possible to estimate the absorbed wave energy by FOWAD in the short crested waves as follows.

$$Ea = \int_{\theta_1}^{\theta_2} \int_0^\infty E_i(\omega,\theta)\, \gamma(\omega,\theta)\, d\omega\, d\theta \qquad (17)$$

However, this equation is available, when the damping system of wave energy conversion is the linear damper. Fortunately, the air turbine of OWC type wave power device has a characteristic of the nearly linear damping system. Consequently, we can say that it is available to estimate the energy of absorption by FOWAD in the short crested waves, and it means that it is possible to estimate the performance of FOWAD in the sea.

5.3 Estimation of Performance

In order to estimate the performance of FOWAD in the short crested waves, the wave power spectrum and the directional distribution function were assumed as shown in Fig.13 and Fig.14. In Fig.14, the value of "2S" is the parameter of directional spectrum.

The efficiency of wave energy absorption in regular oblique waves which was used for calculation is shown in Fig.15. It was the data which were calculated by the method described above. This figure shows that the efficiency of wave energy absorption increases with the decrease of the incident wave angle θ in the region of f <1.0Hz.

The behavior of wave energy absorption which corresponds to the parameter of directional spectrum is shown in Fig.16. From this figure, it was made clear that FOWAD can show the higher efficiency even in the short crested waves at the offing, which has wider distribution of direction rather than in the long crested waves near the coast line.

At last, the perfomance of wave energy absorption by FOWAD in the short crested waves and the long crested waves were estimated and compared with some results which were measured by the scale model test, as shown in Fig.17. Though the difference between the results in the short crested waves and the results in the long crested waves is not so large, the results by calculation agree to the results by experiments almostly. Consequently, it was clarified that the method for estimation of the performance of wave energy absorption by FOWAD in the short crested waves described in this paper is effctive, and its accurancy is enough for the practical use.

Furthermore, it means that the method of surperpotion of the wave power spectrum, the directional distribution function, group velocity of waves and the efficiency of wave energy absorption in regular oblique waves is available to estimate the energy absorption in waves at the offing.

6. Conclusion

(1) It was proved that the strip method considering the added damping force and the added restoring force due to the OWC in the air chamber is effective for the estimation of the motion of FOWAD in waves sufficiently.

(2) Furthermore, for the estimation of the efficiency of wave energy absorption by FOWAD, it became clear that the modified thermodynamics and wave-kinematics method considering the relative incident wave height and the transmission of energy below the bottom plate of FOWAD.

(3) It was confirmed that the method of superpotion is available and effective to estimate the performance of the wave energy absorption of FOWAD in the long crested waves and even in the short crested waves.

(4) It was estimated that the maximum efficiency of the wave energy absorption in the sea will be about 40% without the consideration of the effect caused by the multi-resonance phenomenon due to the projecting walls.

References

1. Ishii,S., Miyazaki,T., Mausda,Y., Kai,G., "Reports and future plants for the KAIMEI project", Proceedings of the 2nd International Symposium on Wave Energy Utilization, The Norwegian Institute of Technology (NTH) Norway, p.305-p.322, 1982
2. International Energy Agency , "Open Sea Trials", Implementing Agreement For a Programme of Research and Development on Wave Power, Annex 2, Volume 4, 1987
3. Hotta,H., Miyazaki,T., Washio,Y., Ishii,S., "On the Performance of the Wave Power Device KAIMEI", Proceedings of the seventh international conference on offshore mechanics and arctic engineering (OMAE), volume 1, p.91-p.96, 1988
4. Hotta,H., Washio,Y., Ishii,S., Masuda,Y., Miyazaki,T., Kudo,K., "The operational test on the shore fixed OWC type wave power generator", Proceedings of the fifth international symposium on OMAE, volume 2, p.546-p.552,1986
5. Hotta,H., Washio,Y., Miyazaki,T., "A study on the performance of the floating terminator type wave power device", Proceedings of international symposium of Techno-Ocean '88, volume 1, p.81-p.86, 1988
6. Malmo,O.,"A study of a multiresonant oscillating water column for wave-power absorption", Dr.Thesis of Norwegian Institute of Technology (NTH) , 1984
7. Takahashi,S., Ojima,R., Suzumura,S., "Air Power of Pneumatic-type Wave Power Extractors due to Irregular Wave Actions", Report of the Port and Habour Research Institute, Vol. 24, No.1, 1985
8. Miyajima,S., Masuda,K., "Study on the Characteristics of a Barge Type Offshore Structure with an OWC Type Power Device", Proceedings of 2nd symposium on Wave Energy Utilization in Japan, JAMSTEC, p.329-p.336, 1987
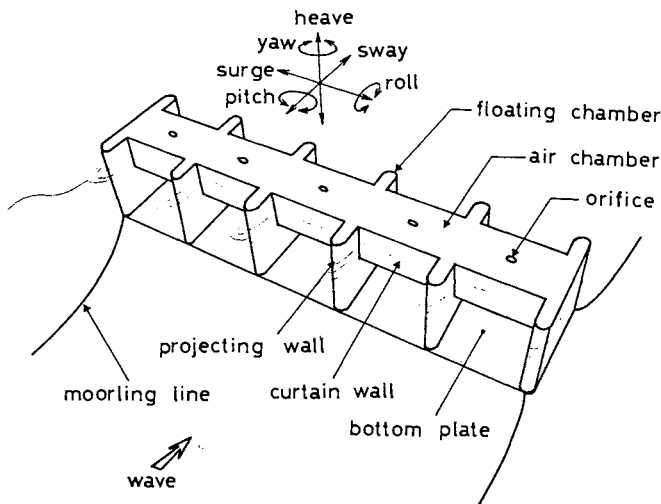
Fig.1 Scheme of the FOWAD and coodinate system

Table 1 Principal particular of FOWAD model

Total Length	;	1,800 mm
Breadth		
Air Chamber (b)	;	200 mm
Floating Chamber	;	400 mm
Bottom·Plate	;	400 mm
Depth	;	350 mm
Draft	;	250 mm
Draft of Curtain Wall (d);		50 mm
Height of inlet (a)	;	200 mm
Number of Air Chamber	;	5
Diameter of Orifice	;	25 mm
Total Weight of hull	;	30 kg
KG	;	87 mm
Natural Period of Roll;		2.1 sec
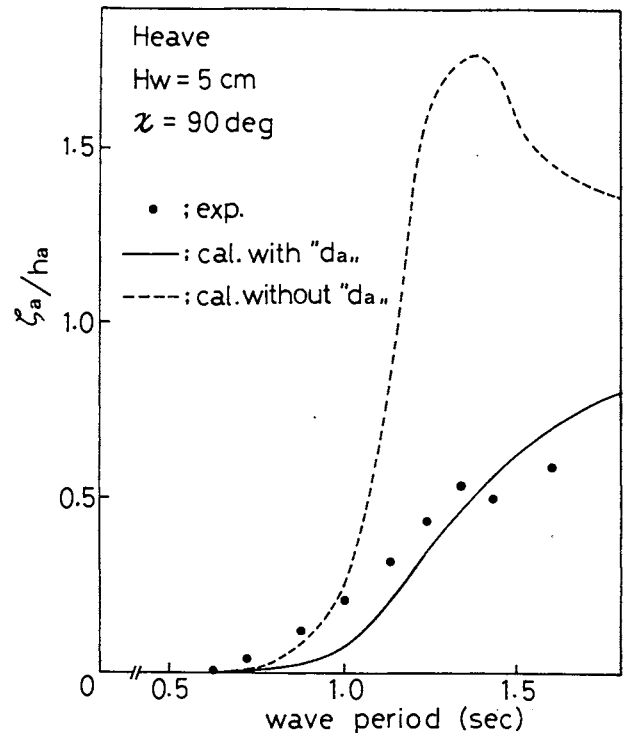
Fig.2 Heave motion in regular waves
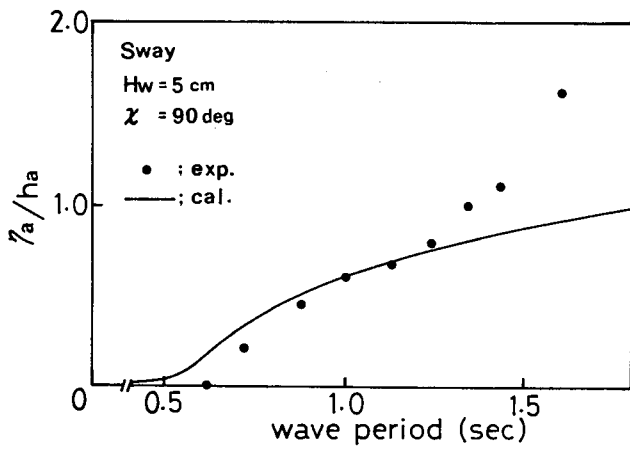
Fig.3 Sway motion in regular waves

Fig.4 Roll motion in regular waves

Fig.5 Heave notion in oblique waves

Fig.6 Pitch motion in oblique waves
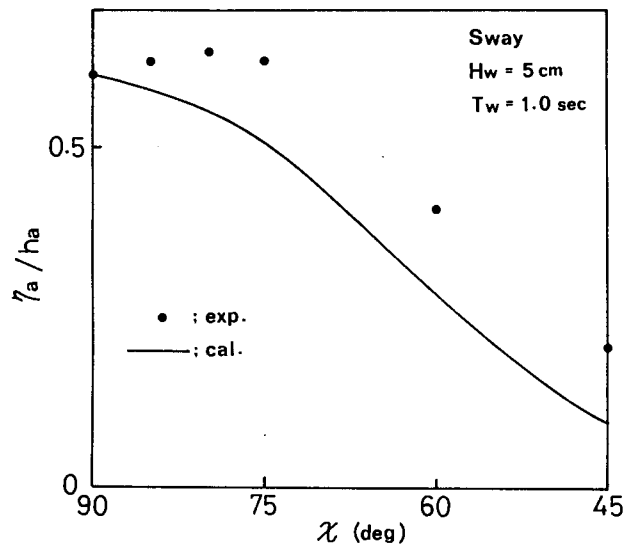
Fig.7 Sway motion in oblique waves
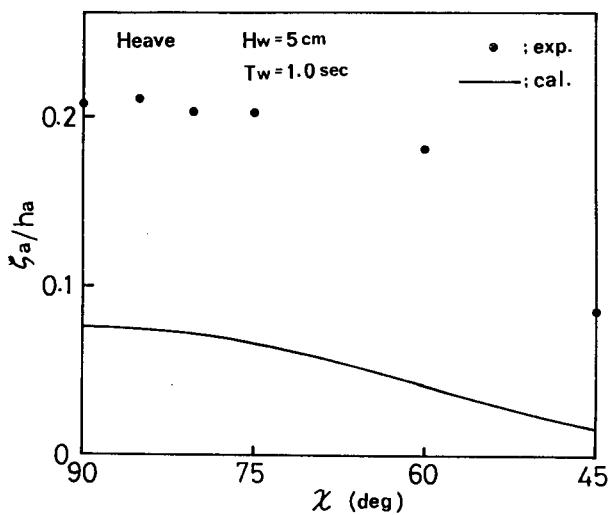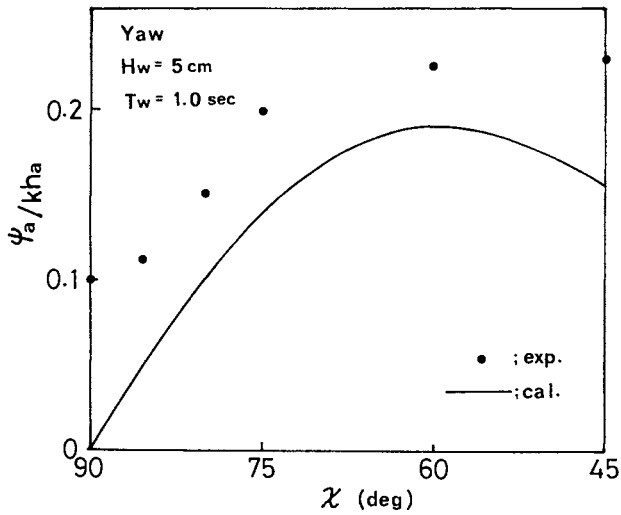
Fig.8 Yaw motion in oblique waves
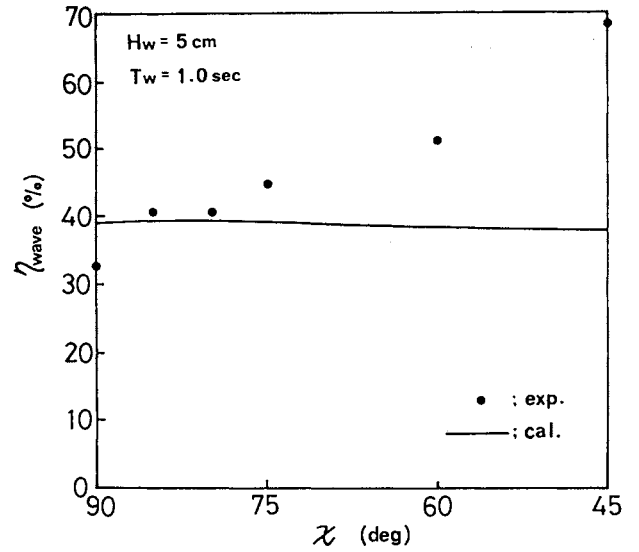
Fig.9 Scheme of sectional plan of the air chamber of FOWAD

Fig.10 Efficiency of wave energy absorption by FOWAD in regular waves

Fig.11 Efficiency of wave energy absorption by FOWAD in oblique waves

Fig.12 Distribution of the efficiency of wave energy absorption
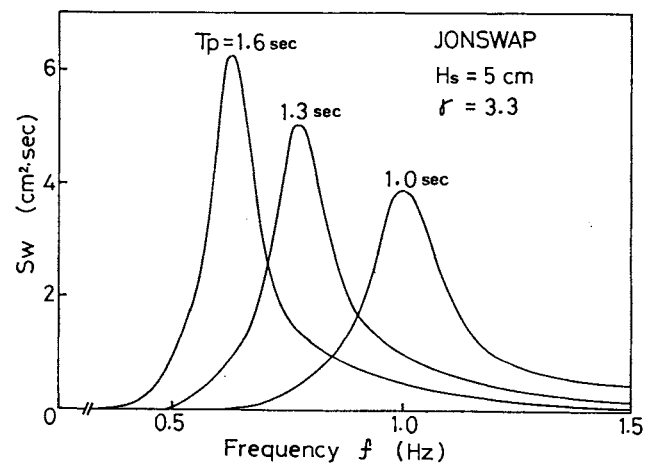
Fig.13 Examples of wave power spectrum for the calculation
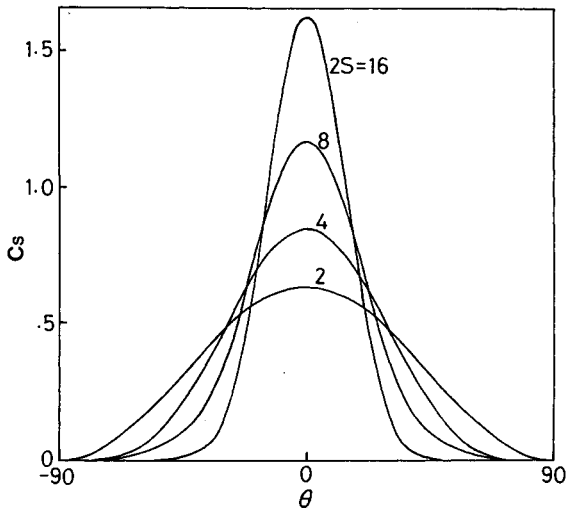
Fig.14 Examples of wave directional distribution parameter for the calculation
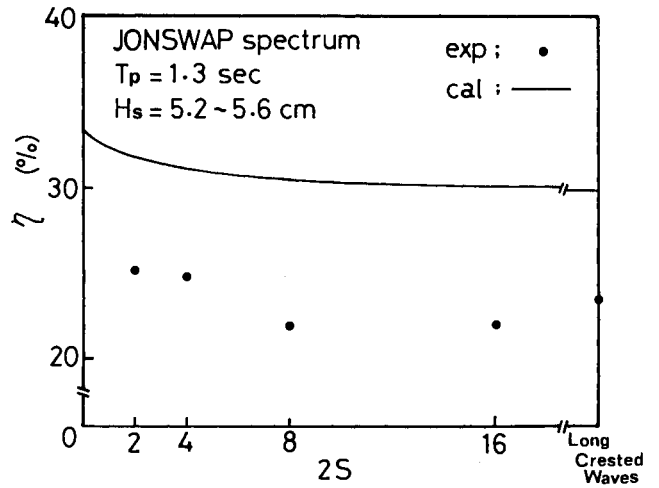
Fig.16 Characteristics of efficiency of wave energy absorption versus the directional distribution parameter of short crested waves
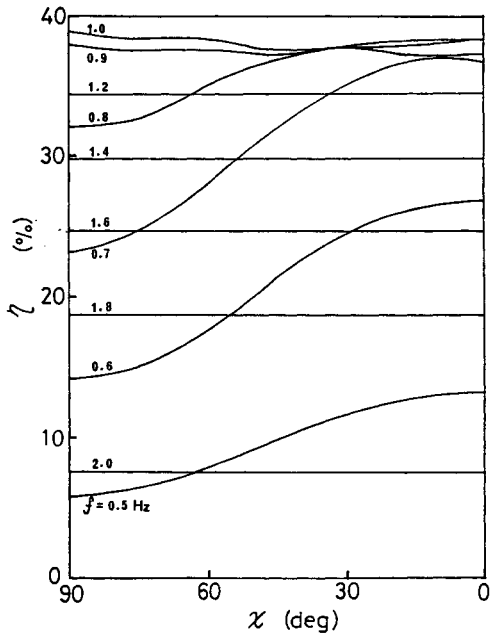
Fig.15 Efficiency of wave energy absorption by FOWAD in oblique waves for the calculation
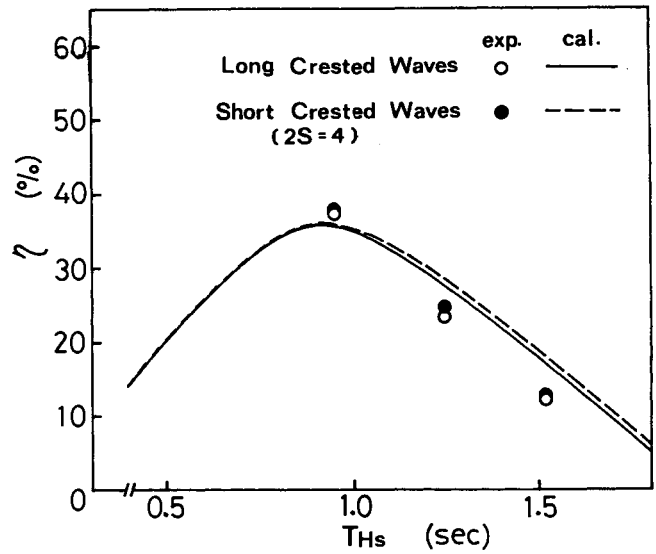
Fig.17 Performance of efficiency of the wave energy absorption by FOWAD in the short crested waves

DEVELOPMENT OF A DOUBLE-OWC FLOATING WAVE POWER EXTRACTOR

Yoshihiro Tanaka*, Yutarou Motora*, Takaaki Nakamura**

* Taisei Corp., Tokyo, Japan
** ING Co., Ltd., Tokyo, Japan

Abstract

A double oscillating water column is proposed as a means to improve the efficiency of wave power conversion over a wide range of wave periods in deep water. A mathematical model of the system based on thermodynamic principles is developed to calculate the efficiency of power-conversion, the hydrodynamic fluid motion, and etc. The physical process by which the proposed concept can significantly improve the efficiency of wave power conversion is clarified through experiments and theoretical treatment.

1. Introduction

The oscillating water column (OWC) in which an entrained column of water acts as a massive piston and pumps large volumes of air, is probably the most well known of the wave energy absorption concepts, and is being worked on in the United Kingdom, Norway, Japan and the U.S.A. Much of the effort expended on OWC energy conversion devices has been devoted to experimentally and theoretically improving the efficiency of power conversion.

Ambli et al. (1982) introduced the idea of adding a harbour, consisting of two parallel projecting sidewalls, to the OWC device so creating an additional resonance within the harbour. A theoretical model developed by Count and Evans (1984) has confirmed the claims of Ambli et al. that the addition of projecting sidewalls increases the wave energy capture.

We propose a Double-Oscillating-Water-Column (DOWC) design as a way to efficiently capture wave power over a wide range of periods in deep water. The DOWC wave power extractor is a terminator device consisting of two air chambers on a semi-submerged floating structure attached by vertical tension legs to gravity foundations on the sea bed as shown in Fig. 1. The air chamber on the sea side efficiently absorbs the incident wave energy with relatively short periods, while the lee-side chamber absorbs radiated wave energy resulting from body motion and having relatively long periods.

A numerical model based on Fredholm integral equations obtained through Green's second identity is described for the two-dimensional taut-moored floating structure containing the DOWC wave power extractor. The theory is based on two non-linear thermodynamic equations and the hydrodynamic equation; the main focus of this theory is therefore a description of the boundary between the compressed/decompressed air in the chamber and the oscillating water surface. Two-dimensional laboratory tests using a 1:40 scale model are used to confirm the validity of the theoretical model.
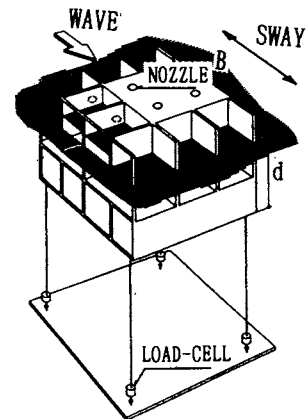
Fig. 1 Conceptual drawing of DOWC Wave Power Extractor
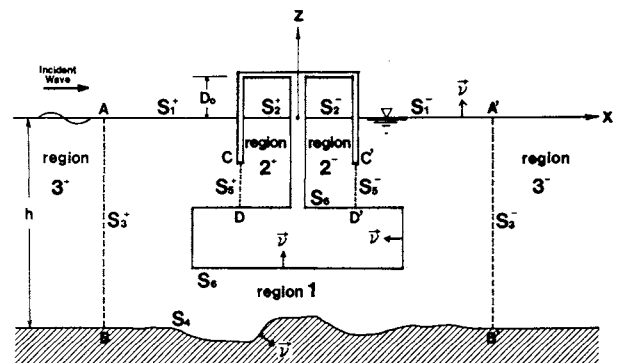
Fig. 2 Definition of coordinates and fluid region

2. Theory

2.1 Division of the Fluid Domain

The definition sketch of the problem is given in Fig. 2. It is assumed that small-amplitude waves with an amplitude ζ_a and angular frequency ω is incident on the floating wave power extractor which is vertically taut moored on the sea bed. Since the air chamber in the floating structure has thin wall members, vertical imaginary boundaries CD and C'D' are employed so as to avoid a singularity when calculating Green's function for the thin wall members. The radiation or matching AB and A'B' are taken sufficiently away from the object for eliminating the effect on local evanescent modes. Thus, we divide the fluid into five sub-regions (1), (2^+), (2^-), (3^+) and (3^-).

Assuming that the fluid is both inviscid and incompressible, while its motion is irrotational, a velocity potential may be expressed as:

$$\Phi(x,z,t) = \phi(x,z) \cdot \exp(i\omega t) \cdots\cdots\cdots\cdots (1)$$

where $i = \sqrt{-1}$. The velocity components may be determined from the following directional derivative of a scalar velocity potential, $\Phi(x,z,t)$ by

$$[u,w] = \vec{\nabla}\Phi \qquad\cdots\cdots\cdots\cdots\cdots (2)$$

where the two-dimensional gradient operator is $\nabla(\cdot) = [\partial/\partial x,\ \partial/\partial z]$.

The potential function $\phi(x,z)$ must satisfy the Laplace equation in each sub-region.

$$\nabla^2 \phi_j = 0 \ ; \ \text{for } j = 1, 2^{\pm}, 3^{\pm} \cdots\cdots\cdots (3)$$

2.2 Equation of Motion of the Floating Structure

Since the floating body is vertically taut moored on the sea bed, we consider only the harmonic swaying motion which can be expressed as $X(t) = X_0 \cdot \exp(i\omega t)$. The equation of motion for the sway mode can be expressed:

$$M\ddot{X} + KX = -i\omega\rho \int_{S_6} \phi_j\, e^{i\omega t}\, n_x ds\ ;$$

$$\text{for } j = 1, 2^{\pm} \qquad\cdots\cdots\cdots\cdots (4)$$

where M = mass of the floating structure, K = spring constant due to the initial tension of the mooring lines and n_x is the directional cosine of the angle θ between the inward normal to the boundary of the floating structure and the x-axis. From Eq. (4), the stationary solution of the sway mode is obtained:

$$X_0 = \frac{-i\omega\rho}{-\omega^2 M + K} \int_{S_6} \phi_j\, n_x ds\ ;$$

$$\text{for } j = 1, 2^{\pm} \qquad\cdots\cdots\cdots\cdots (5)$$

2.3 Potential Function of Sub-Region

In region (3^+) only the incident wave and the reflected waves exist while in region (3^-) there is only transmitted waves. If the reflection coefficient and the transmission coefficient are represented by K_R and K_T respectively, the potential function $\phi_{3\pm}$ in the region $(3^{\pm})$ is given as:

$$\phi_{3+}(x,z) = g\zeta_a\{\exp(ikx)$$
$$+ K_R \cdot \exp(-ikx)\}Z(z)/\omega\cdots\cdots (6)$$

$$\phi_{3-}(x,z) = g\zeta_a K_T \cdot \exp(-ikx)Z(z)/\omega\cdots\cdots (7)$$

where $Z(z) = \cosh k(h+z)/\cosh kh$ and k is the wave number determined by $\omega^2 h/g = (kh)\tanh(kh)$. The potential function $\phi_j(x,z)$ in the region (1), (2^+) can be obtained from the Green's second identity as:

$$\alpha\phi_j(x,z) = \int_{D_j} \left\{ \phi_j(\xi,\eta)\frac{\partial \ln r}{\partial \nu} \right.$$
$$\left. - \ln r\,\frac{\partial \phi_j(\xi,\eta)}{\partial \nu} \right\} ds\ ; \ \text{for } j = 1, 2^{\pm} \cdots (8)$$

where, $r = \sqrt{(\xi-x)^2 + (\eta-z)^2}$, ν = outward normal to the boundary of the fluid region, S = distance along the boundary D_j, and (ξ,η) represents a point on the boundary D_j. When the point (x,z) lies on the boundary D_j, $\alpha = \pi$; while the point (x,z) within the boundary D_j, $\alpha = 2\pi$. The integration of the boundary D_j when $j = 1$: it is calculated counter-clockwise on $D_j = S_{1\pm} + S_{3\pm} + S_4 + S_{5\pm} + S_6$ and when $j = 2^{\pm}$: it is calculated clockwise.

2.4 Boundary Conditions

(1) Imaginary boundaries S_5+ and S_5-

$$\phi_1 = \phi_{2\pm} \qquad (\text{on } S_{5\pm})\cdots\cdots\cdots\cdots (9)$$

$$\partial\phi_1/\partial\nu = \partial\phi_{2\pm}/\partial\nu \qquad (\text{on } S_{5\pm})\cdots\cdots (10)$$

(2) Radiation or matching boundaries S_3+ and S_3-

$$\phi_1 = \phi_{3\pm} \qquad (\text{on } S_{3\pm}) \cdots\cdots\cdots\cdots (11)$$

$$\partial\phi_1/\partial\nu = \partial\phi_{3\pm}/\partial\nu \qquad (\text{on } S_{3\pm})\cdots\cdots (12)$$

(3) Boundary condition in region (1)

$$\partial\phi_1/\partial\nu = \omega^2\phi_1/g \qquad (\text{on } S_{1\pm})\cdots\cdots (13)$$

$$\partial\phi_1/\partial\nu = 0 \qquad (\text{on } S_4) \cdots\cdots\cdots\cdots (14)$$

$$\frac{\partial\phi_1}{\partial\nu} = \frac{\rho\omega^2\, n_x}{-\omega^2 M + K} \int_{S_6} \phi_1\, n_x ds$$

$$(\text{on } S_6) \cdots\cdots\cdots\cdots (15)$$

(4) Boundary condition in region $(2^{\pm})$

$$\frac{\partial\phi_{2\pm}}{\partial\nu} = \frac{\rho^2\omega^2 n_x}{-\omega^2 M + K} \int_{S_6} \phi_{2\pm} n_x ds$$

$$(\text{on } S_6) \cdots\cdots\cdots\cdots (16)$$

The boundary condition for the boundary $S_2^{\pm}$ is given by the dynamic and kinematic conditions of the oscillating water surface in the air chamber. According to the study of Ojima et al. (1985), an approximate solution of the pressure fluctuations was derived on the basis of the conservation energy, the equation of the continuity of mass and the equation of state in a system including the open air and assuming that the air is ideal gas. When the fluctuations of the water surface in the air chamber are defined as $\eta(t) = n_a \cdot \exp(i\omega t)$, the pressure fluctuations in the air chamber $p(t)$ can be expressed as:

$$p(t) = p_0\{1 + \lambda \cdot \sin \omega(t + \tau)\}\cdots\cdots\cdots (17)$$

where

$$\lambda = \gamma |n_a| \cos \omega\tau / D_0 \cdots\cdots\cdots\cdots (18)$$

$$\cos \omega\tau = \pm\sqrt{1+Q^2} - Q \cdots\cdots\cdots\cdots (19)$$

$$Q = \varepsilon_e^2(\gamma-1) \frac{C_p T_0}{(\omega D_0)^2} \cdot \frac{D_0}{|n_a|}\cdots\cdots\cdots (20)$$

and, γ = ratio of specific heat, C_p = specific heat at constant pressure, ε_e = equivalent nozzle opening ratio, T_0 = absolute temperature of open air, p_0 = atmospheric pressure, and D_0 = height of air chamber.

From this approximate solution, it can be seen that the phase difference between the pressure fluctuations $p(t)$ and the water level fluctuations $\eta(t)$ exists and it may be about $\pi/2$. We assumed that the pressure fluctuations $\bar{p}(t)$ may be expressed in terms of the water level fluctuations $\eta(t)$ and the complex variable β which is a function of n_a and τ.

$$\bar{p}(t) = \beta(n_a, \tau) \cdot n(t) \cdots\cdots\cdots\cdots (21)$$

where, $\bar{p}(t)$ is the complex valued function, i.e., $\bar{p}(t) = \bar{p}_a \cdot \exp(i\omega t)$. Therefore, the dynamic boundary condition on the boundary $S_2^{\pm}$ is given as:

$$\partial\phi_{2\pm}/\partial t = -\beta\eta/\rho - g\eta \cdots\cdots\cdots\cdots (22)$$

The linearized kinematic boundary condition on $S_2^{\pm}$ is given as:

$$\partial\phi_{2\pm}/\partial z = \partial\eta/\partial t \cdots\cdots\cdots\cdots (23)$$

From Eqs. (22) and (23), the combined boundary condition can be expressed:

$$\frac{\partial\phi_{2\pm}}{\partial\nu} = -\frac{\omega^2\rho}{\beta+\rho g} \phi_{2\pm} \quad (\text{on } S_2^{\pm}) \cdots\cdots (24)$$

2.5 Method of Convergence

The integral equation (8) can be solved through a numerical process of discretization under the derived boundary conditions. Since the complex variable $\beta(n_a, \tau)$ is a function of η_a and τ, it is necessary to apply the convergence method. The half-interval method is used to calculate the complex variable $\beta(n_a, \tau)$; i.e. first an appropriate initial value of β is taken and $\bar{p}_a$ and n_a are calculated, then a more accurate value of β is modified by:

$$\beta = \bar{p}_a/n_a \cdots\cdots\cdots\cdots\cdots (25)$$

This process is repeated until the value of β satisfies the truncation criterion.

3. Verification of Theory by Model Tests

3.1 Method of Experiment

Two series of experiments were conducted to verify the theory, one in which the model of the structure was fixed, and one with it taut moored on the sea bed. Both experiments were performed by two-dimensional model with scale 1:40 using regular waves. The parameters used in the experiments were, nozzle opening ratio ε = 1/50–1/200, incident wave height Hw = 2 m, 5 m and wave period T = 5–15 seconds by prototype scale. An acrylic model was used, loaded with lead, and 78 cm in width, 100 cm in length and 72.5 cm in height. The fixed tests were carried out to verify the model without including the equation of motion, and to check the total wave force due to the diffraction problem. The wave tank is 47 m in length and 0.8 m in width, and the water depth was kept constant at 1.25 m.

3.2 Comparison of Test Results and Numerical Values

(1) Verification of theory in the fixed condition

Fig. 3 shows the test results and numerical values of horizontal wave force and vertical wave force where a wave of height Hw = 2 m is incident on the fixed floating structure. Measured values of both forces tends to increase with longer periods, matching the numerical values well. Fig. 4 shows the reflection coefficient and the transmission coefficient in the fixed condition. Although the numerical values are somewhat large, they generally correlate well.

(2) Wave absorption and tension fluctuations in the legs

The measured and theoretical values of wave absorption for incident wave heights Hw = 2 m and 5 m are shown in Fig. 5 (a) and (b),

respectively. As the nozzle opening ratio ε is increased, the transmission coefficient K_T tends to go down while the reflection coefficient K_R grows. The non-linear effect of the air compressibility in the air chamber on the wave height demonstrates that the transmission coefficient K_T is smaller when wave height Hw = 2 m than when Hw = 5 m, while the reflection coefficient is opposite. The numerical results agree well with those characteristics of wave absorption.

The values of tension fluctuations in the sea-side legs MF_S and the lee-side legs MF_L, both measured and calculated, are shown in Fig. 6 (a) and (b), respectively. The tension in the lee-side legs is larger than in the sea-side legs independent of the wave height

and nozzle opening ratio. The larger the nozzle ratio ε the greater the tension in the legs. The non-linear characteristics demonstrated, that the larger the wave height the smaller the tension in the legs, are seen in both the measured values and in the theoretical values, and this seems to be advantageous from the view of design point. The tension fluctuations actually measured did not have a harmonic waveform, but included a response component of higher orders at integer multiples of the basic frequency due to the incident wave. According to a study by Yoshida et al. (1979), a remarkable integer multiple harmonic resonance was measured in the tension response of the legs for the tension leg platform, and they concluded that it was caused by higher order components due to the non-linearity of waves.
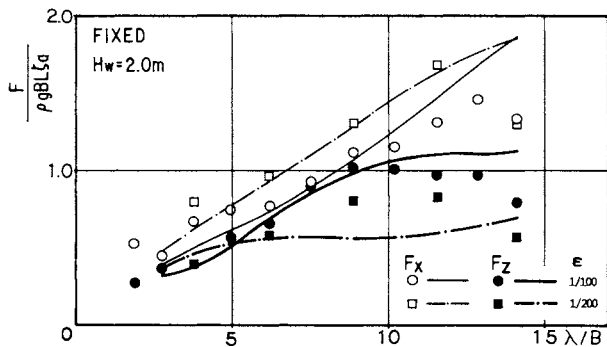
Fig. 3 Horizontal wave force F_H and vertical wave force F_V in the fixed condition
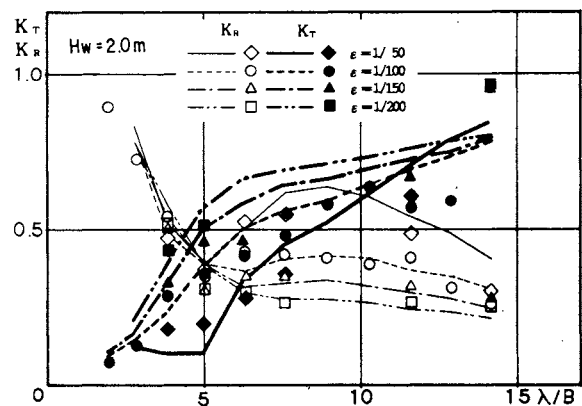
(a) Wave height Hw = 2.0 m
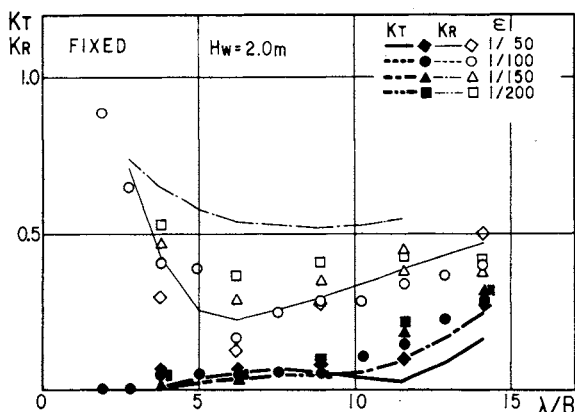
Fig. 4 Reflection coefficient K_R and transmission coefficient K_T in the fixed condition
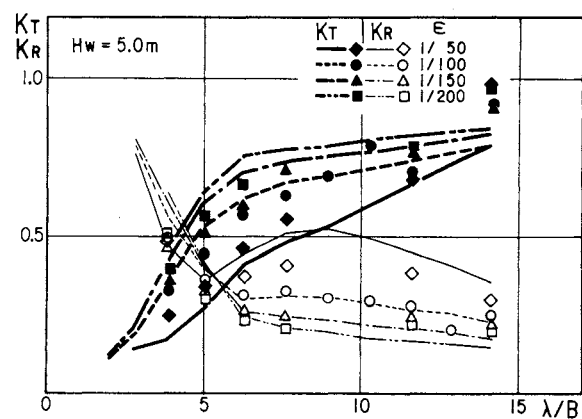
(b) Wage height Hw = 5.0 m

Fig. 5 Reflection coefficient K_R and transmission coefficient K_T
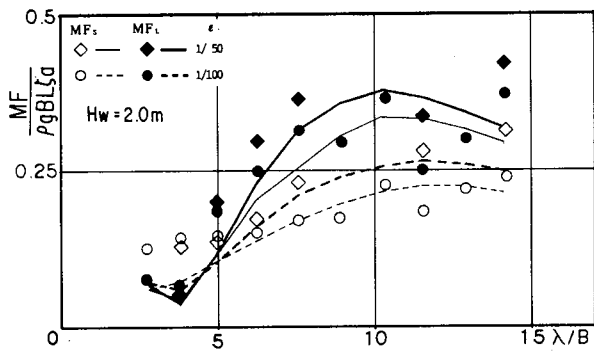
(a) Wage height Hw = 2.0 m
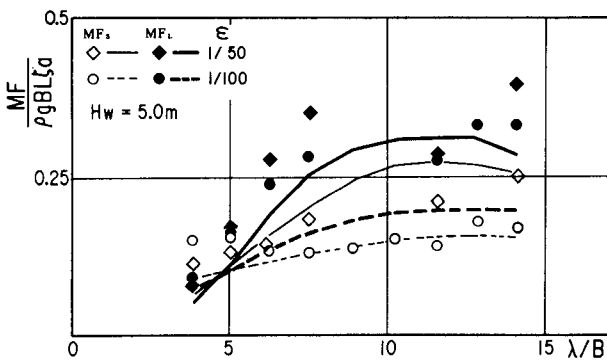
(b) Wage height Hw = 5.0 m

Fig. 6 Tension fluctuations in tension legs
(MF_S: sea-side, MF_L: lee-side)

Fig. 7 Water surface level fluctuations
in air chambers η_a

Fig. 8 Air pressure fluctuations in air
chambers P_a

(3) Conversion efficiency to air power

Fig. 7 shows the test results and the theoretical values of water surface level fluctuations in the sea-side and lee-side air chambers. The water surface level fluctuations have a tendency to increase in both the sea-side and lee-side chambers as the wave periods becomes longer. When waves with short period are incident, the sea-side chamber exhibits larger water surface level fluctuations than the lee-side chamber.

Similarly, Fig. 8 shows the air pressure fluctuations in the air chambers. The dependence of the air pressure fluctuations on the wave period resembles that of the water surface level fluctuations. However, the effects of changing the nozzle opening ratio ε are entirely opposite. Also, the theoretical values are generally larger than the test values.

Fig. 9 (a) shows the conversion efficiency from wave power to air power $\overline{EFF}$. Fig. 9 (b) shows the total $\overline{EFF}$ of the combined air chambers and the measurements of energy loss coefficient K_L^2 (= $1 - K_R^2 - K_T^2$). It can be seen from Fig. 9 (a) that the conversion efficiency of the sea-side air chamber is higher for short wave periods than for long wave periods. On the other hand, the conversion efficiency of the lee-side air chamber is opposite tendency. This fact shown in Fig. 9 (a) can straightforwardly explain the DOWC concept; the sea-side air chamber absorbs well the incident wave power, while the lee-side air chamber absorbs well the radiation wave power. The radiation wave power due to the body motion may increase as the wave period becomes longer. The overall conversion efficiency can be obtained by summing up the both side conversion efficiency; therefore the DOWC device can capture efficiently the wave power over a wide range of wave periods as shown in Fig. 9 (b).
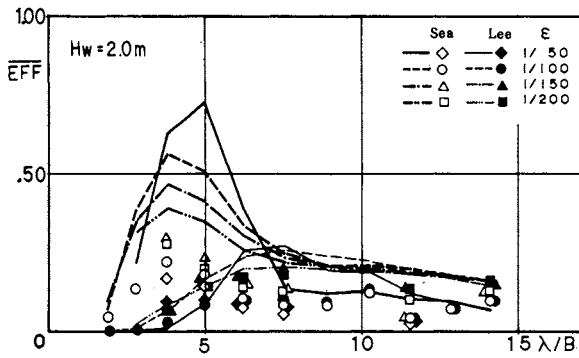
(a) Conversion efficiency of sea-side and lee-side air chambers
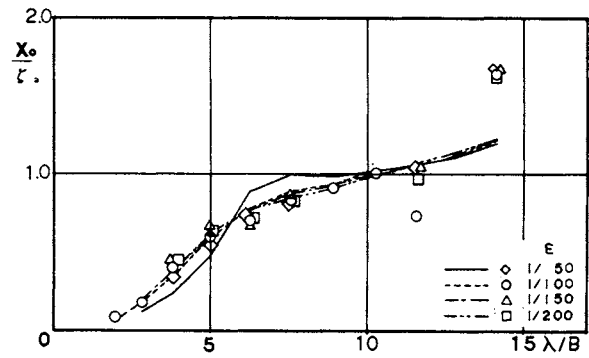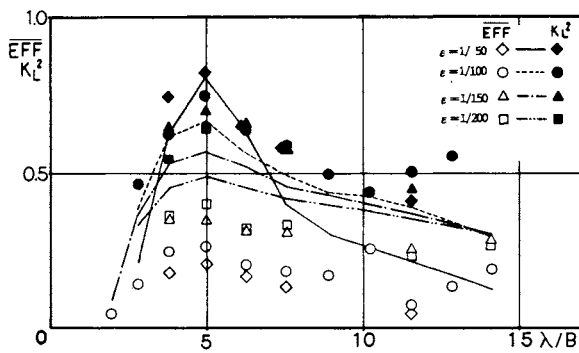
(b) Overall conversion efficiency

Fig. 9 Conversion efficiency from wave power to air power $\overline{EFF}$ and energy loss coefficient K_L^2

Fig. 10 Swaying motion
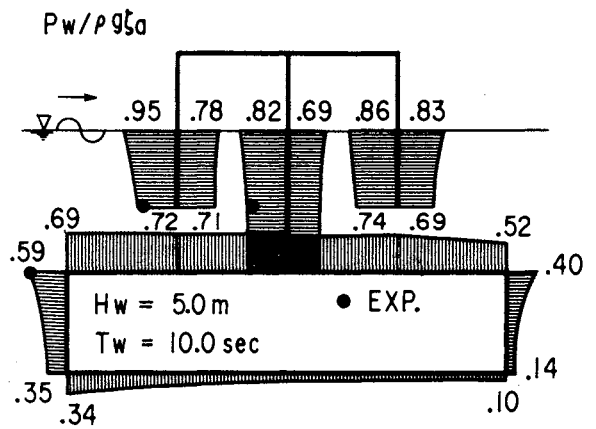
Fig. 11 Hydrodynamic water pressure distribution on floating structure

(4) Motion response and hydrodynamic water pressure distribution

Fig. 10 shows the test results and theoretical values of the swaying motion. The numerical results quite agree with the experimental results. The swaying motion does not depend on the nozzle opening ratio. The trend of the swaying response is similar to that of the characteristics inherent to general TLP. The non-linear effect on the swaying motion is almost negligible. Fig. 11 shows the test results and theoretical values of hydrodynamic water pressure distribution where the wave height Hw = 5 m and the wave period Tw =10 seconds. Both sets of values correlate well, suggesting that this theoretical analysis can be of use in the design of the DOWC floating structure.

4. Conclusions

(1) The proposed DOWC concept device efficiently converts wave power over a wide range of wave periods into an air power. The physical phenomenon of the good efficiency of the DOWC has been clarified by the model tests.

(2) The mathematical model can explain adequately the effects of nozzle opening ratio and the non-linear characteristics due to the thermodynamic behavior. The theoretical values of conversion efficiency EFF, however, are larger than the measured values, and the cause of this error may be over-estimation of the fluctuation pressure in the air chambers

(3) The tension in the lee-side legs is higher than that in the sea-side legs, and the larger the nozzle opening ratio the higher the tension.

(4) The conversion efficiency $\overline{EFF}$ is higher for Hw = 2 m than for Hw = 5 m. The optimum nozzle opening ratio is ε = 1/150-1/200 and EFF = 25-40% can be expected.

References

1. Ambli, N., Bønke, K., Malmo, O. and Reitan, A., "The Kvaerner Multiresonant OWC", In Proc. 2nd Int. Symp. on Wave Energy Utilization, Trondheim, Norway, pp. 275-297 (1982)
2. Count, B.M. and Evans, D.V., "The Influence of Projecting Sidewalls on the Hydrodynamic Performance of Wave-Energy Devices", J. Fluid Mech. Vol. 145, pp. 361-379 (1984)
3. Ojima, R., Suzumura, S. and Goda, Y., "Theory and Experiments on Extractable Wave Power by an Oscillating Water-Column Type Breakwater Caisson", Coastal Engineering in Japan. Vol. 27, pp. 315-326 (1985)
4. Yoshida, K., Yoneya, T., Oka, N., "Dynamic Response Characteristics of Taut Moored Platforms", Journal of the Society of Naval Architects of Japan, pp. 195-205 (1979).

STUDY ON WAVE ENERGY ABSORPTION SYSTEM OF THE IRREGULAR WAVES (-2nd-)

Yoshihiro Suenaga*, Norimasa Takagi**, Masaaki Sakuta*

* Nihon University, Japan
** National Research Institute of Fisheries Engineering, Japan

Abstract

Many wave energy absorption system currently proposed can absorb wave energy with fairly high efficiency, regarding wave energy at a specified frequency band; but they are said to lower their absorption efficiency in irregular waves. This is due to the fact that while waves themselves are composed of wide-range frequencies, the natural frequency of the wave energy absorption system itself is basically a single one, and is so arranged that the wave energy absorption efficiency will become the greatest in the vicinity of its natural frequency. To overcome this discrepancy, ingenuity has been used to estimate the incident waves and functionally change the natural frequency, but this method has not yet been able to enhance the efficiency.

This paper verifies the validity of determing the natural frequency of the water column in the oscillating water-column-type wave energy absorption system, using the same concept as that of the water column in the U-shaped tube, and reports the absorption characteristics when a plural number of water columns, which have different natural frequencies, is used in a single system to absorb wane energy.

1. Introduction

The present study has conceived that the wave energy absorption system is made to correspond to wide frequency bands, which the irregular wave has, by providing a plural number of natural frequencies in a single system, not by changing the natural frequency of the system itself.

An attempt has been made to grasp experimentally the wave energy absorption characteristics. In the present system, it was impossible to provide a plural number of natural frequencies in a single unit, owing to the restriction in scale.

The authors solved this problem by paying attention to the fact that the water column in the U-shaped tube had a natural frequency, and the length of this water column, not its volume, can determine the natural frequency.

Since the existence of a natural frequebcy of a single water column was confirmed, the authors proposed a system which was provided with plural water columns aimed at absorbing the energy of irregular waves, and obtained the oscillation and energy absorption factor of the respective water columns.

Also a comparision was made between the result of the complementary calculation and the result of the test,

and some discussions were given.

On the basis of such discussions, the effectiveness of the system and the principle were examined. And when we think about a real scale of the structure, we examined a planning system to set up the structure and most suitable shape of the structure were suggested.

2. Absorption Length Ratio of a Water Columns

The model which was used in the test had the shape shown in Fig.1. Fig.2 shows the test result of the amplitude of the water column. Solid lines in the figure were obtained by setting up equations of motion with respect to the water column amplitude and by changing damping coefficients at the respective frequencies.

The abscissa of the figures represents a dimensionless wavelength λ /B (B = 0.7m is used), and the ordinate represents a dimensionless quantity of the water column amplitude.

The comparision between the test result and theoretical result indicated that (1) the existence of natural frequencies were observed in the respective water columns, (2) both the results showed good agreement even in frequencies other then the natural one, (3) even when plural water columns were installed in the same system, the existence of natural frequencies were observed as in the case of a single water column, (4) mutual interference between the water columns and effect of the radiation fluid force were minimal and (5) amplitudes of water columns can be accurately calculated with simple formulas.

For the result of absorption length ratio shown in Fig.3, the abscissa in

the figure represents dimensionless λ /B , and the ordinate represents absorption length ratio (η) of the water columns. This value of η is (obtained from the values of the crest voltmeter and damping coefficients accoding to eqs.(1) to (4)),by the energy of incident waves.

From the amplitudes of the respective water columns ($l_1 \sim l_3$), wave energy P absorbed by the respective water columns, will be

$$P = 0.5 \omega^2 l_j^2 N \quad (j = 1 \sim 3) \quad (1)$$

where 1 is the length of the water column and g is gravitational acceleration. N: Damping coefficient
ω : Circular frequency

Further, the energy of incident waves is obtained by the following equation:

$$E_1 = \frac{1}{4} \rho g a l^2 \left(1 + \frac{2kh}{\sinh(2kh)}\right) \sqrt{\frac{g}{k} \tanh kh} \cdot L \quad (2)$$

where h: Water depth (1.2m)
al: Ampitude of incident waves
k: Wave number
ρ : Specific weight of water
L: Width of model (80cm)

The absorption length ratio of each water column and that of the total system (η total) are obtained by following equations:

$$\eta j = P j / E_1 \quad (j = 1 \sim 3) \quad (3)$$

$$\eta total = \sum_{j=1}^{3} \eta j \quad (4)$$

The caluculation result indicated that the absorption length ratio of the single water column was low, but an efficiency of 70% or more was obtained over the total system. This was the same performance as had been obtained by other conventional apparatus.

Therefore, it can be said that the present shape of the system is a proper

one for a wave extinction structure which does not require secondary conversion of wave energy.

3. Planning System

When we think about a real scale, it can be applied to the law of Flued's similarity.

Then, when the real sea were given, we examined a planning system to set up the structure and most suitable shape of the structure were suggested.

An object of maritime meteorology which were given below.

In case of ordinary wheather on the sea, when it is possible to fishery that can be satisfied the working ratio within a 80% .

However, in case of unusual wheather condition, the absorption efficiency is covered by the stability of the structure itself as the same structure of a breakwater which are proposed at present.

For example, we think about TAGONOURA-BAY. When we set up the structure for a extinction, as for the sea condition, we obtain $H_{1/3}$ = 1.43m, $\bar{T}$ = 4.61sec in TAGONOURA-BAY.

$H_{1/3}$: Significant wave height
$\bar{T}$: Average of period

The planning system that determine shape of the structure was shown in Fig.4. As for the width of tube mouth, it is calculated by wave energy spectrum.

Accroding to this planning system indicated that the most suitable wave energy absorption length ratio is given by 9 water columns and each natural frequency of columns at intervals of 1.5sec each. (shown in Fig.5)

This has clarified that when we set

up the structure in TAGONOURA-BAY, the width of the energy absorption band is expanded (ω = 0.5~7.0) and obtain high absorption efficiency.

Therefore, it can be said that the present the planning system is possible to determine shape of the structure for a wave extinction.
(shown in Fig.6)

4. Future Action to be Taken

The above-mentioned result has confirmed that when plural water columns are installed in the same system and are caused to absorb wane energy simultaneously, the absorption length ratio of the single water column is lower than that for the conventional apparatus.

However, the present system as a whole showed high absorption energy.

This has clarified that when the number of water columns is increased, the width of the energy absorption band is expanded. Therefore it will be possible to realize a system which can cope with irregular waves and obtain high absorption efficiency.

Also it is necessary to examine the point at issue when the structure will be constructed on the sea.

$l_1 = 77.5 cm$

$z = 7.5 cm$

$S = 702 cm^2$

$T_{o1} = 1.77 sec$

$l_2 = 107.5 cm$

$z = 17.5 cm$

$S = 702 cm^2$

$T_{o2} = 2.08 sec$

$l_3 = 137.5 cm$

$z = 27.5 cm$

$S = 702 cm^2$

$T_{o3} = 2.35 sec$

natural frequencies

$T_o = 2\pi\sqrt{l/g}$

WAVE HEIGHT METER

WL ▽

No.1
No.2
No.3

l_1
l_2
l_3

400

400

900

750

(mm)
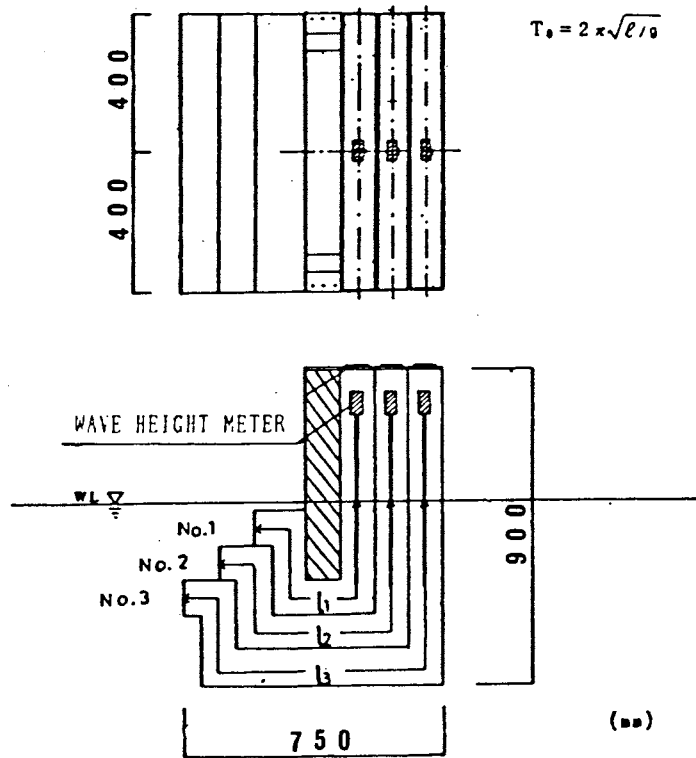
Fig.1 Test Model
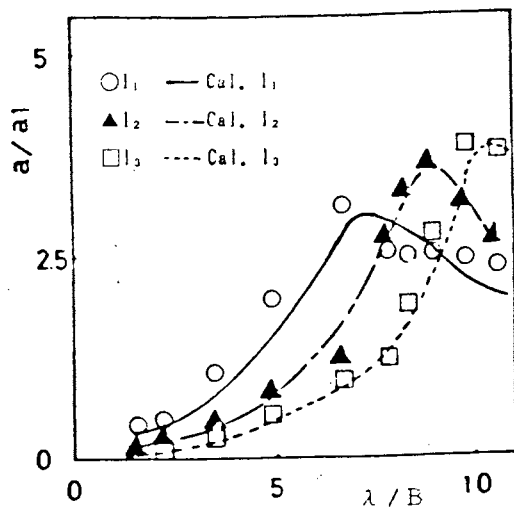
Fig.2 Amplitude of the Water Column
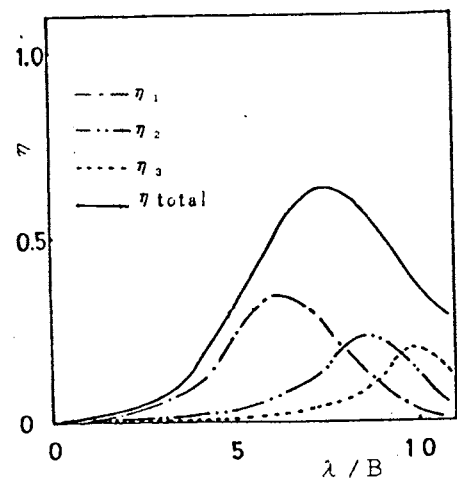
Fig.3 Absorption Length Ratio
of Water Columns

Fig.6 Absorption Length Ratio of Water Columns in TAGONOURA-BAY
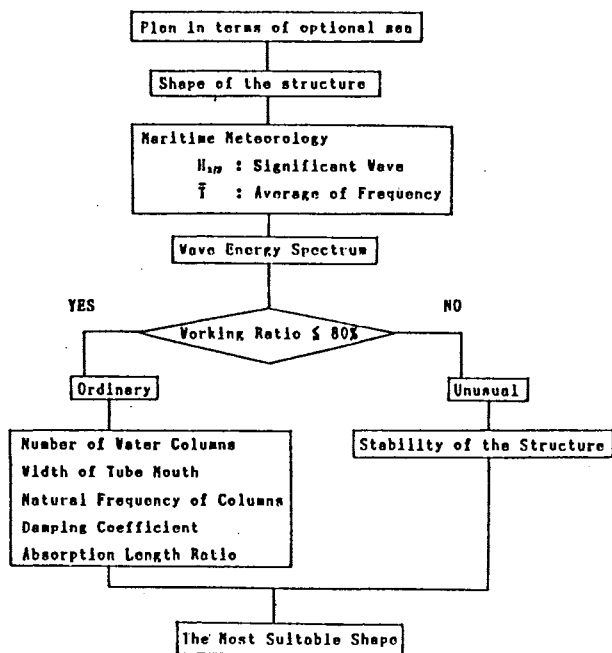
Fig.4 Planning System
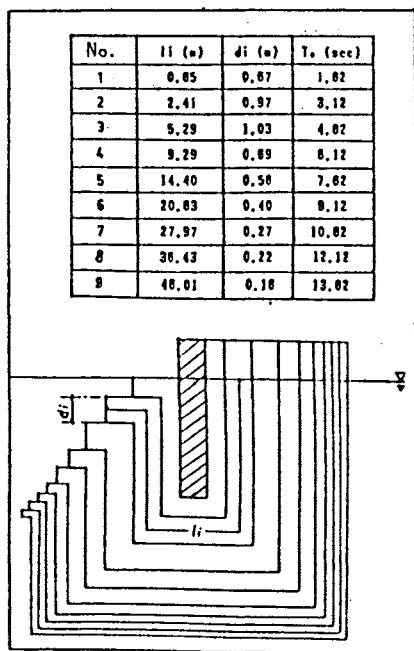
Fig.5 The Most Suitable Shape in TAGONOURA-BAY

References

1) H. Meda, T. Kinoshita and S. Kato : "Fundamental Research on Absorbing Energy from Ocean Waves (2nd report)," The Society of Naval Architects of JAPAN, (1981)

2) H. Maeda, H. Tanaka and T. Kinoshita : Theoretical and experimental study on wave power absorption, "13th Symp. of Narval Hydrodynamics, Tokyo, (1980)

3) A. Iwasaki, K. Kudo and S. Miyajima : "Fundamental Study on the A.R.T. Wave Power Absorber," The Society of Naval Architects of JAPAN, (1983)

4) K. Masuda, H. Maeda and W. Kato : "Fundamental study on the air-turbin type wave power absorber," Work Ship Three Offshore Energy Resources Potential, ECOR, (1981)

5) T. Kinoshita and K. Masuda : "System simulation and optimum dsign method of OWC-Wells turbine wave power generator," Report of the Institude of Industrial Science the University of Tokyo, (1986)

6) Y. Suenaga, N. Takagi and M. Sakuta : "Study on the Wave Energy Absorber with the Plural Oscillating Water Columns (1st, 2nd report)," Summaries of Thechnical Papers of Annual meeting Architectural Institute of Japan, (1987)

WAVE ENERGY CONVERSION SYSTEM INTEGRATED WITH COMPRESSED AIR RESERVOIR

T. Homma, S. Ogata, H. Nakano

The University of Tsukuba, Japan

Abstract

The purpose of this paper is primarily to propose a wave or wind energy conversion system integrated with CAES subsystem which is able to produce 3 isolated heat sources in addioion to electricity. This combined system has a special feature to enable one to control the temperature of the heat sources in order to meet the demand of user by making use of the thermo-electric convertor installed on the compressed air reservoir. This paper also describes the results of feasibility study based on the computing simulation on the system performance.

1. Introduction

In the present state of rapid evolution toward utilizing renewable sources of energy, wave energy is often considered to be low grade energy mainly on the basis of its irregularity and sharp variation in time. In spite of this negative aspect, the concepts and designs of wave energy conversion devices have variously been made aiming at small-scale electric power generation or direct use in the form of mechanical power. However, the irregularity in the energy resources necessitates additional energy regulation appliances and often needs the integration of some kind of energy storage system especially for independent use.

On the other hand, energy storage technologies have recently become more and more important to improve an utility's flexibility in matching its generation to customer demand. Power companies are willing to cut back power generation as usage drops off at night and boost generation as demand rises during the day, combining storage installations into the electric power system to meet the load in the most cost-efficient manner.

Although many types of principle and designs have been suggested for the past hundreds years, the energy storage technologies in widespread use today are only pumped-hydro storage and lead-acid battery. Recently various types of new batteries such as sodium-sulphur, zinc- bromide, redox-flow etc. and superconducting coil are also being developed, these option are not yet practically available at an attractive price and in high reliability. Some power companies are now taking notice of compressed air energy storage system(CAES) as an alternative to those technologies above mentioned. A CAES plant can be described as a simple combustion turbine that has been modified to operate in separate compression and generation cycles. A CAES plant has additional features in the form of the storage chamber and a combination motor-generator that does double duty, powering the compressor during the charging cycle and producing electricity in the generating cycle.

In spite of the situation quite different from the gross power system, the characteristics that both wave energy and CAES are originally the same mechanical energy, coupled with the fact that those are entirely pollution-free, make CAES favorable for the integration with wave energy conversion. A CAES is also capable to produce various heat sources in a wide range of the temperature by taking advantage of the property that the temperature of compressed air rises and drops through the process of compression and expansion respectively. According to the reseach result on the feasibility of mini-CAES by U.S. EPRI, the smaller units retain the attractive features of larger plants while offering additional benefits. Although little information on CAES technology is still available to us, the research results obtained so far over the world indicate that the concept of a wave energy conversion system integrated with CAES appears sufficiently attractive to be the object of a continuous attention.

The purpose of this paper is primarily to propose a wave or wind energy conversion system integrated with CAES subsystem which is able to produce 3 isolated heat sources in addioion to electricity. This combined system has a special feature to enable one to control the temperature of the heat sources in order to meet the demand of user by making use of the thermo-electric convertor installed on the compressed air reservoir. This paper also describes the results of feasibility study based on the computing simulation on the system performance.

2. System and Component

Figure 1 shows the overall system of the wave or wind energy conversion system combined with CAES. The notations of variables are as follows, T; temperature(K), p; pressure(atm), F; compressed air flow rate(mol/s), Q; heat flow(W), and W; power input or output(W), and their suffixes 1, 2, 3, 4, and 5 denote respectively specific positions in Fig.1 to which each variab mle belongs.
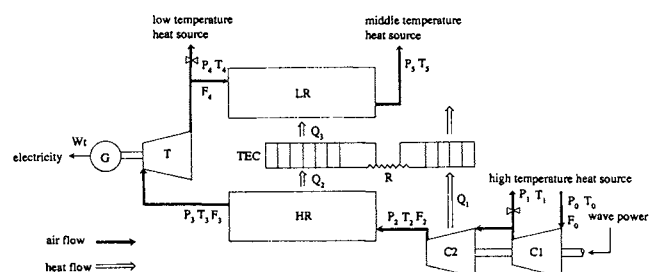
Fig. 1 Wave Energy Conversion System integrated with CAES

The system consists of two types of the air-compressor C1 to run in adiabatic change and C2 to run in isothermal change theoretically, two compressed air reservoir HR for higher temperature and LR for lower temperature, turbine EXP, and the thermo-electric convertor ETC in addition to the wave or wind energy conversion devices. The compressor C1 and C2 are driven with wave or wind power, and if the pressure p_1 of the compressed air is 30 atm at the exit of C1, the air temperature T_1 attains at a highest value of 515°C based on computation. This hot air is available to, for example, a combustion chamber of a gas turbine. The compressed air is led into the reservoir HR once to be stored and there emits a part of its heat flow Q_2 into the eledtro-thermal conversion device ETC. The turbine EXP can be driven to produce electricity Wt, if it is desired, over an adiabatic expansion of the air which is followed by a sharp decline of its temperature. Thus one can obtain a low temperature heat source as low as tens degree below zero centigrade. This cold air is once stored in the reservoir LR to absorbe the heat flow Q_3 from TEC.

TEC consists of N pairs of thermo-couples which are made of p type and n type semiconductor pieces connected in series electrically but in parallel thermally, and two metalic plates which hold N pairs of thermo-couple and also play a role of heat transfer between TEC and the compressed air in HR and LR as shown in Fig. 2. Although DC power output We of TECS is much smaller than that of the turbine-generator Wt.

TEC enable one to control the temperature distribution of the compressed air over the system only by means of regulating the load of it.
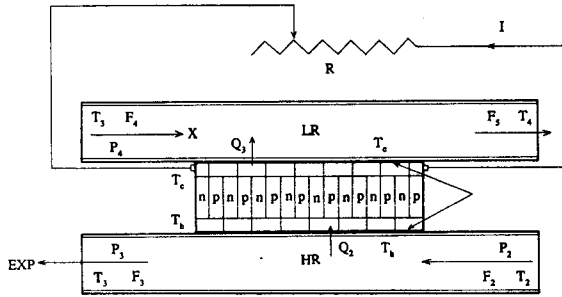
Fig. 2 TEC installed between HR and LR

3. Fundamental Equations

The air temperature T_2 at the exit of C2 and equally at the entrance of HR can be obtained, if p_1 is given, as follows

$$T_2 = T_1 = p_0 (p_1 / p_0) (\gamma - 1)/\gamma \quad \gamma = Cp / Cv = 1.4 \quad (1)$$

and the mechanical power input Wc_1 and Wc_2 for C1 and C2 respectively are written with the air flow rates F_1 and F_2 as

$$Wc_1 = F_1 Cp(T_1 - T_0) \quad (2)$$
$$Wc_2 = F_2 RT_2 \ln (p_2 / p_1) \quad (3)$$

where T_0 and p_0 are the ambient temperature and pressure respectively. Similarly, T_4 and Wt are written with p_4 and F_3 as

$$T_4 = T_3(p_4 / p_3) \quad (4)$$
$$Wt = F_3 Cp(T_3 - T_4) \quad (5)$$

Under the operating condition of a steady state, one can assume the following relations, ignoring the mechanical loss of the air flow due to its viscosity and friction, as

$$F_2 = F_3 = F, \quad p_2 = p_3, \quad F_4 = F_5, \quad p_4 = p_5 \quad (6)$$

and then Q_2 and Q_3 are written as

$$Q_2 = FCp(T_2 - T_3) \quad (7)$$
$$Q_3 = F_4 Cp(T_5 - T_4) \quad (8)$$

These heat flows exactly participate in the output We of TEC.

Assuming that the metalic plates temperatures are Th at the side of HR and Tc at the side of LR, the thermo-electric motive force V due to Seebeck effect and the current I induced in TEC are respectively

$$V = \alpha N(Th - Tc) \quad (9)$$
$$I = V/(R + Nr) \quad (10)$$

where a is Seebeck coefficient of a thermo-couple, R and r are an external and an internal electric resistance respectively.

The following relations hold among Q_2, Q_3, Th, Tc, and I

$$Q_2 = K(Th - Tc) + \alpha ITh - (1/2)rI^2 \quad (11a)$$
$$Q_3 = K(Th - Tc) + \alpha ITc - (1/2)rI^2 \quad (11b)$$

where K is a thermal conductance of a pair of thermo-couple. The 1st, 2nd, and 3rd term in eq.(11) stands for thermal conduction, Peltier effect, and Joule heating respectively. The power output We can also calculated by the equation

$$We = Q_2 - Q_3 = RI \quad (12)$$

4. Steady State Solution

Provided that the compressed air remains in HR and LR for enough time, or the heat transfer between the air in the reservoirs and TEC is large enough, for T_3 and T_5 approximately to coincide with Th and Tc respectively, it becomes relatively easy to caluculate the solution. This assumption can equivalently be formulated in terms of heat transfer performance and air flow rate as

$$Ah/CpF \gg 1$$

where A is the heat transfer area and h is surface coefficient across the boundary layer of the air in the reservoir for both HR and LR.

For simplicity, a parameter "figure of merit" Z(/K) defined to characterize the efficiency of TEC

$$Z = \alpha^2/Kr \quad (13)$$

and two non-dimensional parameters

$$m = R/Nr \quad (14)$$
$$\omega = CpF/KN \quad (15)$$
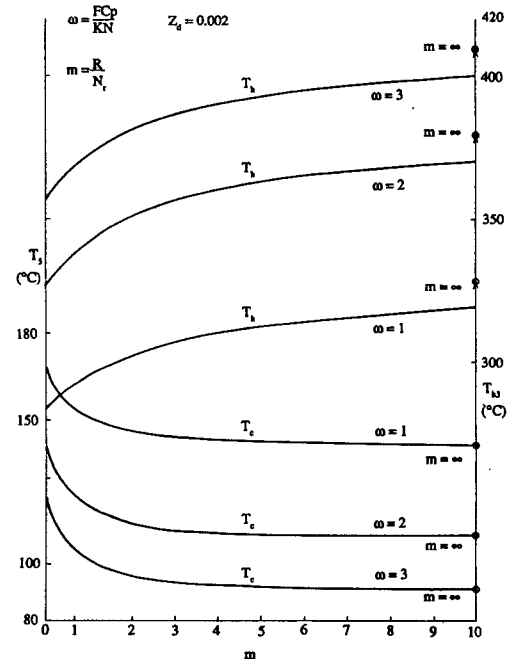
Fig. 3 Temperature Variations of T_3 and T_5 against m
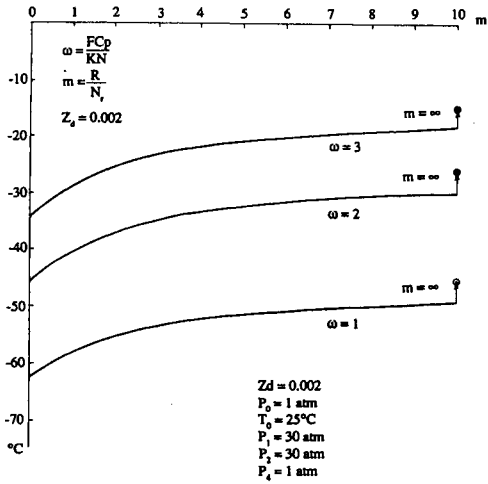
Fig. 4 Temperature Variations of T_4 against m
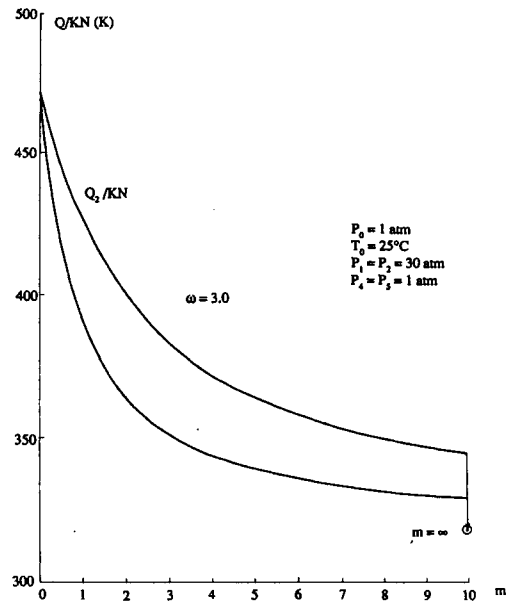
Fig. 6 Variations of Heat flow Q_2 and Q_3 against m for W = 3
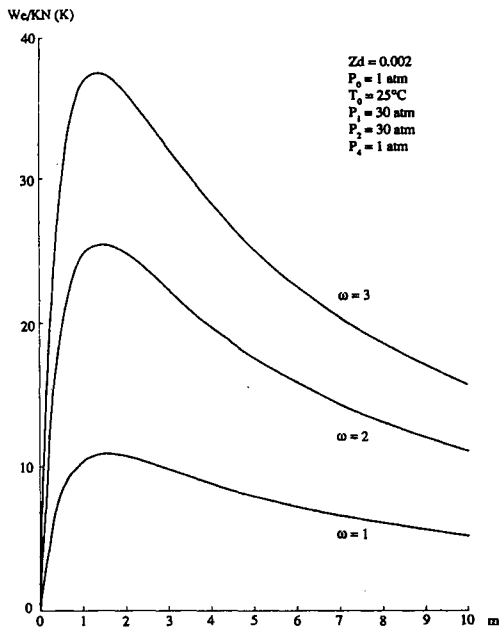
Fig. 5 Variations of We/KV against m
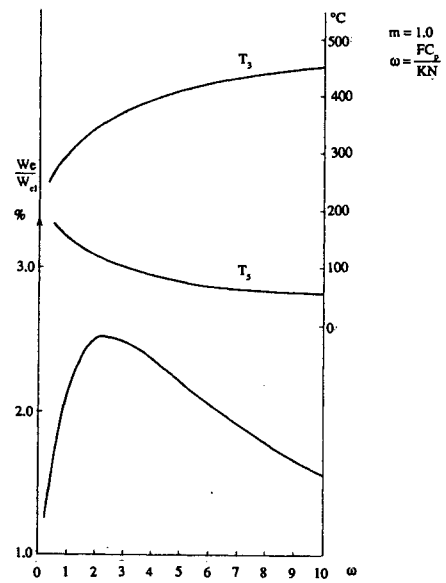
Fig. 7 Variations of T_3, T_5, and We/Wc1 against W for m = 1

are now introduced, taking account of the steady state flow conditions as

$$F = F_2 = F_3 = F_4, \quad T_3 = Th, \quad T_5 = Tc \qquad (16)$$

Substituting eqs.(7),(8), and (10) into (11) and (12) and then applying eqs.(13)-(16) for some arrangement, the following equations can be obtained.

$$\frac{Q_2}{KN} = (T_3 - T_5)\{1 + \frac{2T_3}{m+1} - \frac{2(T_3 - T_5)}{2(m+1)^2}\} = \omega(T_2 - T_3) \qquad (17a)$$

$$\frac{Q_3}{KN} = (T_3 - T_5)\{1 + \frac{2T_5}{m+1} + \frac{2(T_3 - T_5)}{2(m+1)^2}\} = \omega(T_5 - T_4) \qquad (17b)$$

$$\frac{WE}{KN} = \frac{Q_2}{KN} - \frac{Q_3}{KN} = \frac{m2(T_3 - T_5)^2}{(m+1)^2} \qquad (18)$$

In order to know the temperature distribution over the system, one must solve eqs.(17) and (18) in addition to eq.(4) simultaneously under a given condition of p_1, p_2, and p_4. The feature of eqs.(17) and (18) suggests that such varibles as T_3, T_4, T_5, Q_2/KN, Q_3/KN, and We/KN are related only to Z, ω, and m. The authors have completed a computer program to solve these equations simultaneously in any mode of steady state.

Fig.3 illustrates the distribution of $T_3(=Th)$ and $T_5(=Th)$ as a function of m corresponding to each value of ω, under the condition of Z=0.002/K, $p_1=p_2=30$atm, $p_4=p_5=1$atm. Fig.4 shows the temperature variations on T_4 immediately after the expansion of the air, and Fig.5 shows We/KN against m in respect to É+ under the same condition on Z and p. Fig.6 illustrate the variation of heat flows Q_2 and Q_3 against m for ω=3, and Fig.7 is a daiagram of the function on Th, Tc, and We/Wc$_1$ (in this case Wc$_2$=0) against ω for m=1.

5. Equations for Unsteady State

There are various modes in unsteady state. Among them a typical mode where the difference exists in the air flow rate between one and the other side of HR seems to be the most interesting. In the case, for example, as

$$F_3 < F_2 = F + \Delta F \qquad (19)$$

the air quantity stored in HR increases monotonously in time t. This results in not only pressure rise of the air in HR but also its temperature rise under $Q_2 = 0$.

If the air flow rate F_2 has a sudden rise by Δ F at t=0 and continues its value $F_2=F+\Delta$ F for t>0, though F remains unchanged, the quantity of the air x(mol) subjects to the following equation

$$dx/dt = \Delta F = F_2 - F_3 \qquad (20)$$

Applying the first law of thermo-dynamics into HR and using eq.(20), the following differential equation on the air temperature·T in HR can be derived as

$$x(dT/dx) = F_2(\gamma T_2 - T) - F(\gamma - 1)T - Q_2/Cv \qquad (21)$$

Substitution of the steady state condition, mentioned in chaper 3, as

$$dT/dt = 0, \quad F_2 = F_3 = F$$

into eq.(21) results in

$$Q_2 = CpF(T_2 - T)$$

If T is replaced by T_3, the above equation becomes identical with eq.(7).

This means that T can be regarded as the air temperature T_3 at the exit of HR.

On the other hand, substitution of the condition as

$$T = T_3 = \gamma T_2, \quad F_3 = 0, \quad Q_2 = 0$$

into eq.(21) results in dT$_3$/dt=0. This result means that, when the temperature of the air which flow into a ridged reservoir is just $1/\gamma$ times that inside the reservoir, the air temperature T_3 remains unchanged.

One can hold T_3 invariant in time by setting the appropriate value of Q_2 in terms of the regulation on We. Substituting dT/dt=0 into eqx.(21), the following relation is obtained as

$$Q_2/Cv = F_2(\gamma T_2 - T_3) - F_3(\gamma - 1)T_3$$

or after arrangement, using $F_3=F$, and $F_2= F + \Delta$ F

$$Q_2 = FCp(T_2 - T_3) + \Delta FCp(T_2 - T_3/\gamma) \qquad (22)$$

Then eliminating Q2 from eq.(22) together with eq.(17a) yield as

$$\omega(T_2 - T_3) + \Delta \omega(T_2 - T_3/\gamma) =$$

$$(T3 - T5)\{1 + \frac{2T_3}{m+1} - \frac{2(T_3 - T_5)}{2(m+1)^2}\} \qquad (23)$$

where ω is CpF/KN as defined in eq.(15) and

$$\Delta \omega = CpD F/KN \qquad (24)$$

If the output of turbine Wt remains unchanbged as well as F_3 and T_2, T_4 also does not change its value after the sudden rise of F_2, but T_5 probably begins to change up or down based on the change of heat flow Q_3. In order to know both m and T_5, which satisfy with the condition that T_3 and T_4 remains unchanbged in spite of a change of F_2 by Δ F, eq.(17b) should simultaneously be solved together with eq.(23) under a value of $\Delta\omega$. They are both non-linear equations and, therefore should be computed numerically based on the calculated value in the steady state.

6. Conclusion

Fundamental performances have been investigated on the wave energy conversion system integrated with CAES and TEC, based upon the computer simulation about the relation of the temperature distributions against the air flow rate and the external load connected with TEC. The results on simulation describe that T_3 is able to change its value as wide as approximately 50°C between runs of TEC on open and short circuit as shown in Fig.3, and T_4 ideally to decrease to -60°C for ω=1 as shown in Fig.4. Fig.7 illustrates that We/Wc$_1$ has a piak value in the vicinity of ω =2 under m=1 but its peak value is no more than 2.5%. This means that, although both We and Wc$_1$ increases with ω, Wc$_1$ does more rapidly than We. This also implies that only a small fraction of the energy which is to be converted over the major process of the system seems to be extracted into TEC to make possible the temperature control.

An example of unsteady state process has been examined theoretically, but is not yet available numerically.

This work has been carried out aiming at the simulation analysis in an ideal operation condition to make clear the fundamental performances, therefore every losses based on irreversible process such as thermal and mechanical dissipation are not at all treated here. Under such condition as being out of the rated power operation on the compressor and the turbine, these losses appear likely to dominate. Such problems are fully examined in future.

Finally we acknowledge Dr. Y. Osawa, associated professor of the university of Tsukuba, for joining us in the discussion on this matter.

DEVELOPMENT OF WAVE-ACTIVATED PUMP

Y. Mnabe

Taiyo Plant Engineering Co., Ltd, Yokohama, Japan

1. Introduction

Making available such things as Japanese culture, technology, industry, etc. to many countries which lie on the Pacific rim would be helpful for the development of culture and the improvement of public welfare in the region. In islands in the Pacific Ocean, there are some areas where they don't have electricity nor sufficient drinking water. In those areas, they are short of not only electricity and drinking water but also salt, food and a source of power which are indispensable for everyone to live. In many cases, they don't have any sewage disposal facilities or facilities like that and consequently they discharge raw sewage to rivers and the sea. As a result, it causes epidemics. So this is also a big problem for sanitation of those areas.

2. Purpose of the Study

The consideration about the above-mentioned matters reminds us of the fact that the Pacific Ocean is the vast ocean which contains unlimited wave energy and therefore it is possible to make use of existing wave energy by a wave-activated pump to produce water and salt which would improve their living. On the other hand, a source of power and water for dilution are necessary to dispose sewage. And using wave energy, which is clean energy, to drive a wave-activated pump for that purpose would have a great merit because it causes no destruction of natural environment.

Contents and purpose of this study are as follows.

1. Study and development of the wave-activated pump which can desalt seawater with wave energy to make drinking water in islands, especially isolated islands, in the Pacific Ocean.

2. Study and development of the process in which salt is made by supplying concentrated seawater, which is by-product in the process of making the above-mentioned drinking water, to a salt manufacturing plant.

3. Study of electricity generation circuit which can generate electricity by pressurized water which is necessary in the process of desalting seawater.

4. Study and development of a source of power to supply water for dilution which is necessary for sewage disposal.
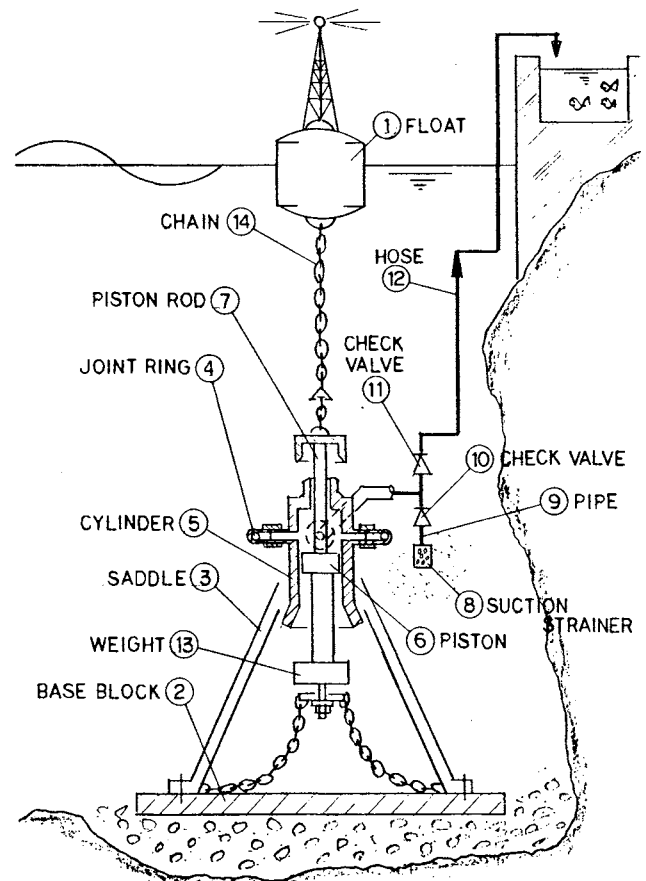
F i g. 1

3. Operating Principles and Wave-Activated Pump Construction

As shown in Fig. 1, a float (1) is allowed to float on the sea surface, and a base block (2) is set on the sea bottom. A saddle (3) and a joint ring (4) that can freely turn are mounted on the base block. In the center of this joint ring is a cylinder (5) containing a piston (6) and a piston rod (7). The piston and piston rod are designed to move freely when set in the joint ring. This joint ring is tubular, and the joint is connected to a suction strainer (8) and pipe (9), as illustrated. The pipes are arranged so that, as the piston in the cylinder moves a check valve (10) is actuated to allow seawater to flow from the suction strainer and the joint ring through another check valve (11) and hose (12) to the fishery pond. A weight (13) attached to the bottom of the piston and rod pulls the piston down. A chain is of appropriate length to permit reciprocation of the piston in the cylinder.

When the float, set up with another parts as described above, is moved laterally by wave action, the joint ring allows the cylinder to tilt in that direction. In this way, the energy of even very large storm waves can be absorbed.
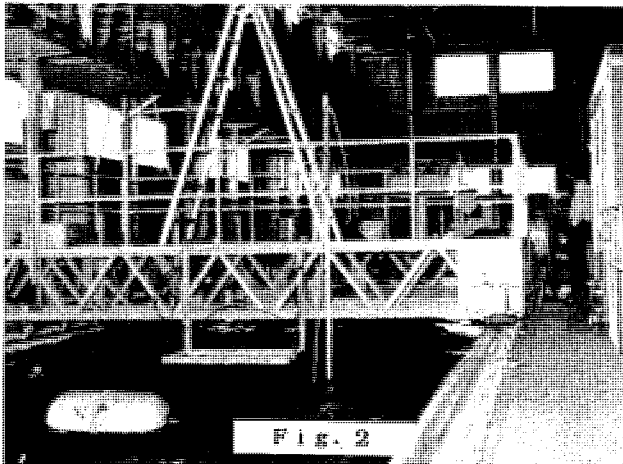
F i g. 2
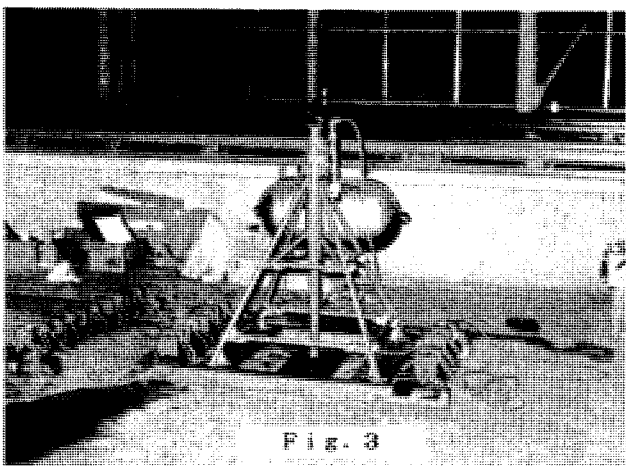
F i g. 3
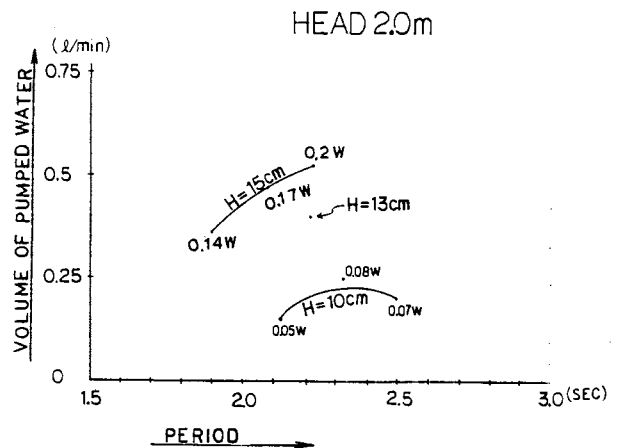
F i g. 4
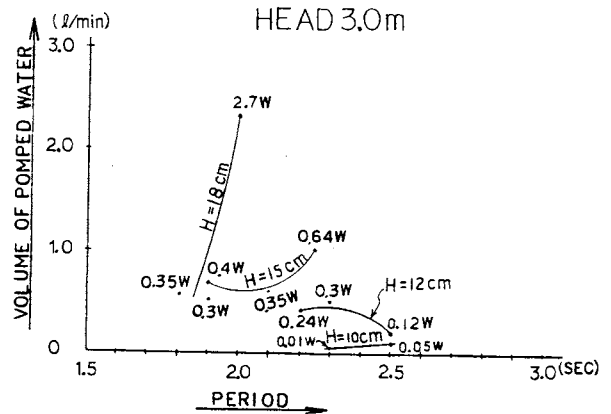
F i g. 5

4. Water Bath Experiments and Output Calculations

The first and second experiments were conducted in April and May 1985 as evaluations by the Oceanographic Development Research Division of the Oceanographic Technological Center, as shown in Figs. 2 and 3. The results of the first experiment in a water bath are shown in Fig. 4, and those of the second experiment in Fig. 5.

The maximum efficiency in the first experiment was approximately 3%, but in the second experiment, after the rubber packing was readjusted, this rose to approximately 30%. One important finding from these experiments is that efficiency increases with reduced friction in moving barts and greater wave period.

F i g. 6

VOLUME OF PUMPED WATER   HEAD
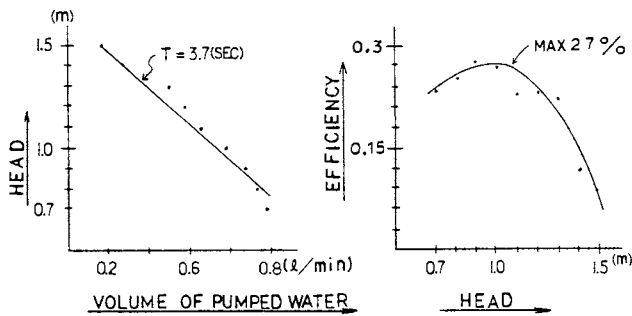
F i g. 7

In November 1986, the Techno-Ocean '86 fair was held in Kobe, where the third experiment was conducted using a miniature model in a water bath. Fig. 6 shows a scene from this experiment, and Fig. 7 presents an example of results. In the miniature experimental setup at the fair, primary consideration was given to wave period rather than wave height to avoid unexpected equipment problems and splashing the spectators during the experiment. Wave period was maintained at 3.7 seconds, approximately that of actual ocean waves. The experiment returned a value of 27%, as shown in Fig. 7, for the efficiency of transduction from wave energy. This value is considered almost satisfactory for a water bath experiment, provided that the grounds for this value are as follows:

ρ (kgf/m^3) = density of seawater,
g (m/sec^2) = acceleration of gravity, and
H (m) = wave height,
the density of wave energy per unit area E (J/m^2), is given by:

$$E = \frac{1}{8} \rho gH^2 \qquad (1)$$

In the design of a wave-activated generator, it is reasonable to consider the flux P (kw/m) of wave energy that passes through a given area of sea surface over a given length of time. This is expressed as the product of the density of wave energy E given by formula (1) and the group velocity of waves V (m/sec).

Where
L (m) = wavelength of waves, and
T (sec) = wave period,
the phase velocity is given by L/T.
Since group velocity V is one-half the phase velocity, we have

$$V = \frac{1}{2} \frac{L}{T} \qquad (2)$$

From formula (1) and (2):

$$P = EV \times 10^{-3} = \frac{1}{8} \rho gH^2 \cdot \times \frac{1}{2} \frac{L}{T} 10^{-3}$$
$$(kw/m) \quad (3)$$

For deep-sea waves, the following equation in either form can apply:

$$L = \frac{1}{2\pi} gT^2 \text{ or } = \frac{L}{T} \frac{g}{2\pi} T = 1.56T \qquad (4)$$

Substituting formula (4) into formula (3), we get:

$$P = \frac{1}{8} \rho gH^2 \frac{1}{2T} \cdot \frac{1}{2\pi} gT^2 \times 10^{-3}$$
$$= \frac{\rho g^2 H^2 T}{32\pi} \times 10^{-3} \text{ (kw/m)} \qquad (5)$$

Substituting ρ = 1030 kgf/m^3 and g = 9.8m/sec^2 into formula (5), we obtain:

$$P = \frac{1030 \times 9.8^2}{32\pi} H^2T \times 10^{-3}$$
$$\fallingdotseq 0.98H^2T \text{ (kw/m)} \qquad (6)$$

Formulas (5) and (6) represent a fundamental equation of energy flux applicable to wave-activated generators.

In applying this equation to the float, the input time was assumed to be the time during which the float is influenced by waves moving forward at any velocity, and formula (7) was obtained by multiplying formula (5) by this input time. This assumption was deemed reasonable, and all calculations of wave energy in the area on the waterline of the float will hereinafter be based on formula (7).

$$P_0 = \frac{\rho g^2 H^2 T}{32\pi} \times 10^{-3} \times \frac{2l}{1.56T}$$
$$\fallingdotseq 1.26H^2 l \text{ (kw/m)} \qquad (7)$$

where P_0 is input wave energy in unit width of the float (kw/m), 1.56T is phase velocity of wave on the deep-sea surface (m/sec), and l is the length of the float (m).

5. A Model (An Example) and Design Concept

Most of salt which is handled in salt manufacturing industry in Japan is imported, including salt for industrial use. This situation is very regrettable for Japan which is surrounded by the sea. And islands in the Pacific Ocean must have the same problem.

Fig. 8 shows the flowsheet of the system to desalt seawater, make salt and generate electricity by the wave-activated pump. This system first pushes up seawater on shore as pressurized seawater and then desalts it by reverse osmosis in the water manufacturing plant. In this case, the pressurized and concentrated seawater, which is the by-product in the water manufacturing process, drives a waterwheel and generates electricity, and then it is supplied to the salt manufacturing plant. And after this concentrated seawater is changed to salt water (20% NaCl) by electrodialysis, salt is made.

The design concept is based on the assumption that this system is installed on a isolated island in the Pacific Ocean.

5.1 Calculation of Required Power of Wave-Activated Pump

Design conditions

1. Design wave height (annual average)is:

    H = 0.8m

2. Population and the number of households to be supplied are:

    400 persons or 100 households

3. The amounts of electric power consumed per month are as follows.

    The amount of electric power consumed by a household per month is:

    250kw·H/month

    The amount of electric power consumed by 100 households per month is:

    Pw_1 = 250 × 100 = 25,000kw·H/month

    The amount of electric power consumed by schools, public offices and something like that per month is:

    Pw_2 = 25,000kw·H/month

4. The amounts of water consumed per month are as follows.

    The amount of water consumed by a household per month is:

    30m³/month

The amount of water consumed by 100 households per month is:

30 × 100 = 3,000m³/month

The amount of water consumed by schools, public offices and something like that per month is:

3,000m³/month

5. The amount of salt manufactured per month is:

    150T/month

The amount of electric power consumed for electrodialysis per month is:

Pw_3 = 45,000kw·H/month

6. The amount of electric power consumed for sewage disposal per month is:

    Pw_4 = 15,000kw·H/month

The amount of electric power consumed in the island per month is:

$$Pw = Pw_1 + Pw_2 + Pw_3 + Pw_4$$
$$= 110,000kw \cdot H/month \qquad (8)$$

The average amount of electric power consumed in the island per hour is:

$$Pwo' = \frac{Pw}{30 \times 24} = 153kw \cdot H \qquad (9)$$

$$Pwo = 153kw \qquad (10)$$

The amount of water consumed in the island per month is:

q = 3,000 + 3,000 = 6,000m³/month

The amount of pumped seawater required to make the above-mentioned water is:

$$Q = \frac{q}{0.4} = 15,000m^3/month \qquad (11)$$

0.4 in formula (11) means the ratio of the amount of osmosis to the total amount of seawater.

If the pressure of seawater which is required to make the above-mentioned water is 60kg·f/cm², then the power of the seawater Q is:

$$PwQ = \frac{15,000 \times 1,030}{30 \times 24 \times 3,600} \times 600 \div 102$$
$$= 35.1kw \qquad (12)$$

If the efficiency of the generator is 80% and that of the waterwheel is 80%, then the required output of the wave-activated pump in the island is:

$$P = \frac{Pwo}{0.8 \times 0.8} + PwQ$$
$$- PwQ \times 0.6 \times 0.8^2 = 261kw \qquad (13)$$

Fig 8

WAVE CONDITION	
AVERAGE WAVE HEIGHT	0.8 m
AVERAGE PERIOD	6 SEC

WAVE

WAVE-ACTIVATED PUMP

WAVE ABSORBING

PUMP HOSE

FISH FARM

SEWAGE DISPOSAL FACILITY

SCHOOL·PUBLIC OFFICE

PRIVATE HOUSE

WATER TANK

GENERATOR

SEAWATER DESALTING EQUIPMENT
(WATER)

SALT MANUFACTURING PLANT

SALT

GENERATOR

8.3 m³/H
1 kg·1/cm²

13.5 KW

.21 m³/H
60 kg·1/cm²

115 m³/H
60 kg·1/c
193 KW

124 KW

12.5 m³/H
1 kg·1/cm²

50 KW

136 m³/H
60 kg·1/cm²

19 m³/H
60 kg·1/cm²
32 KW

20 KW

155 m³/H
60 kg·1/cm²
261 KW

—464—
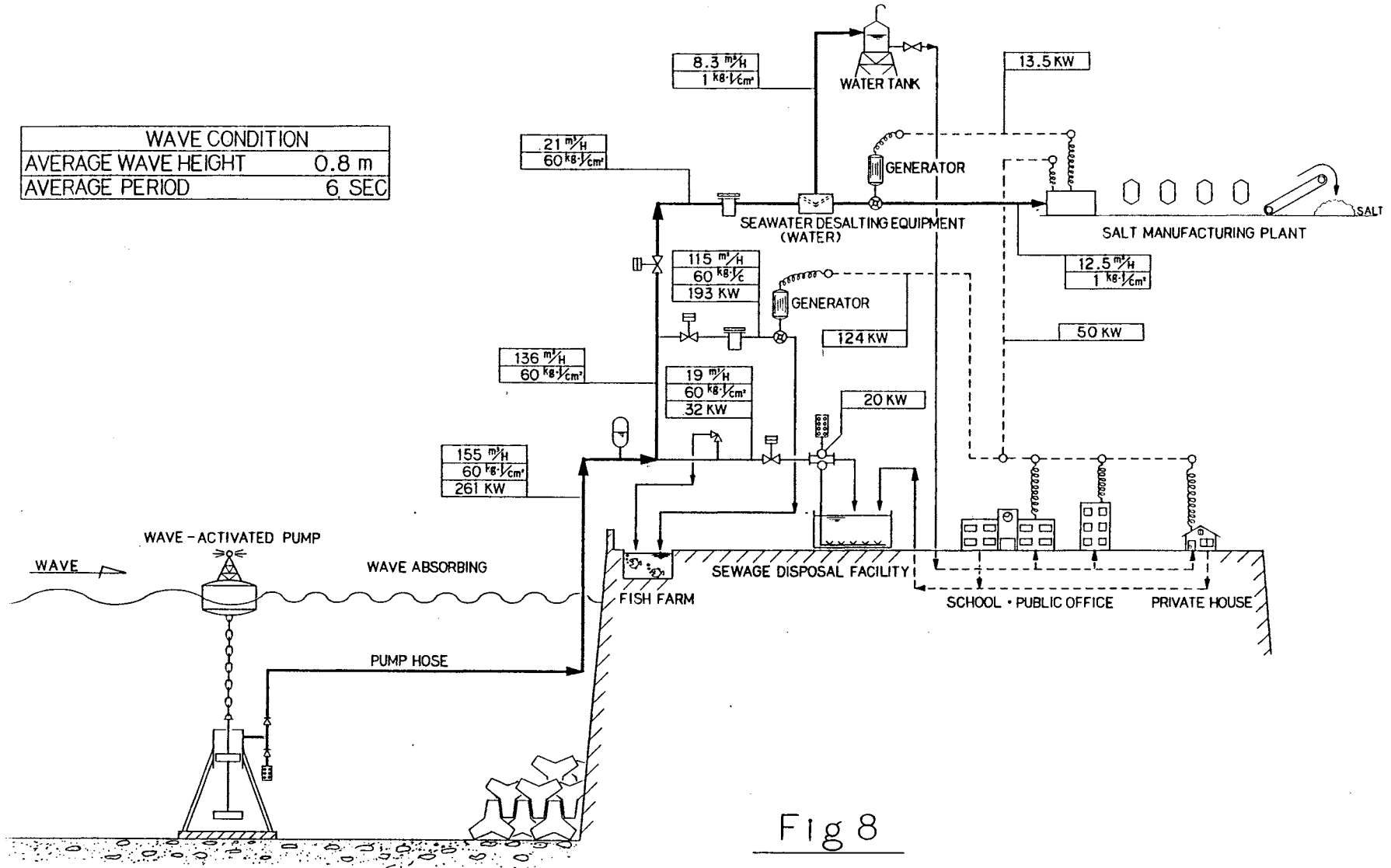
If the efficiency of the wave-activated pump is 70%, then the size of the float is:

$$P = 1.26H^2AF\eta \qquad (14)$$

$$AF = \frac{P}{1.26H^2\eta} = \frac{261}{1.26 \times 0.8^2 \times 0.7}$$
$$= 462m^2 \qquad (15)$$

Assuming that the depth of a float is 15(m), its width is approximately 32(m).

Thus, as is obvious from the above calculations, even if the system is of relatively small scale, it can supply sufficient electricity and drinking water which 400 persons in the island need for living. And as to the salt which is the by-product in that process, it is expected that the sharp reduction in the cost of manufacturing salt can be attained by making use of natural energy such as solar heat, etc. effectively in the process of boiling down salt water.
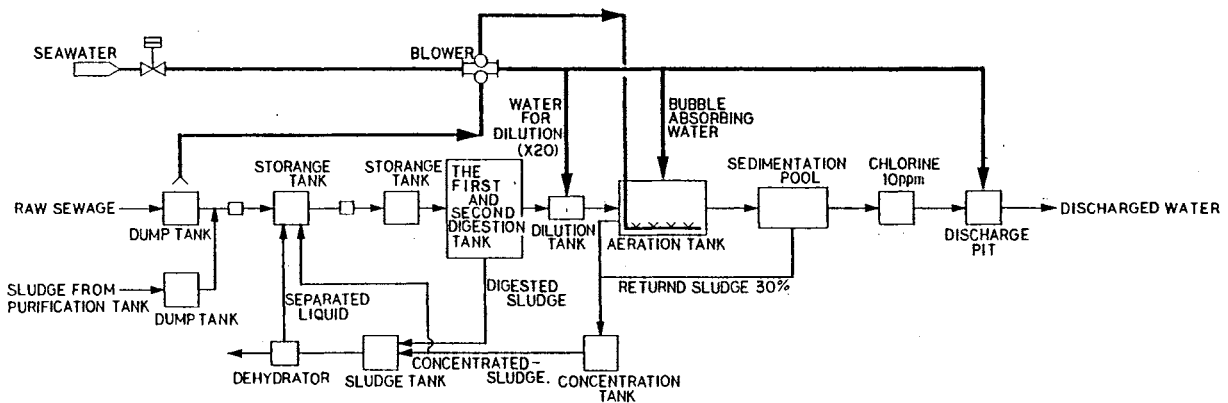
$$\underline{Fig\ 9}$$

5.2 Seawater Supply to Sewage Disposal Facilities and a Source of Power for them

Fig. 9 shows the flowsheet of the sewage disposal facilities where dilution by seawater is applied. A large amount of water is required as water for dilution in sewage disposal facilities. In many sewage works, such fresh water as subterranean water or water of rivers has been used as water for dilution. However, recently subterranean water shows a tendency to dry up, and regulations concerning the amount of water drawn from under the ground have been applied in order to cope with a problem of subsidence of the ground. Moreover, it is inefficient economically to use those kinds of water, and there are problems such as delay of developing new sources of water, etc. For these reasons, it is sometimes impossible to get sufficient water for dilution.

In areas such as coastal cities and isolated islands, where it is difficult to draw rivers' water or subterranean water, even if installing sewage disposal facilities is planed, it can not be carried out until the problem of getting sufficient water for dilution is solved.

In areas in Japan where it is difficult to draw water for dilution from rivers and under the ground, some sewage works which use seawater as water for dilution are operated. For example, there are such sewage works in Miura city, Kanagawa prefecture and in Akita city, Akita prefecture.

Since the amount of seawater is unlimited, probably many coastal cities, towns and villages are interested in using seawater as water for dilution.

By the way, most part of the cost of power required for sewage disposal facilities is the cost of power to draw water for dilution and drive aeration blower in aeration tank. So if both of these powers can be supplied by the pressurized seawater from a wave-activated pump, it is possible to operate sewage works at very low running cost.

T a b l e 1

Item	Specification	Amount
Pump (Main Body)	Structural materials SS41 250t	125,000
″ (″)	Special stainless steel 15t	75,000
″ ″	Concrete block 400 m³	20,000
″ ″	Valves and others	15,000
Piping materials	φ200 mm X 300 m	50,000
Installation and Piping cost	Inclusive of anchoring cost	40,000
	Total	325,000

6. Cost and its Effect

Table 1 is an example of rough estimate of construction cost, including the cost of materials, production cost and installation cost for the wave-activated pump and seabed pipeline which are used in this system. This system consists of a seawater desalting equipment, a salt manufacturing plant, a generator, sewage disposal facilities, a fish farm and other various equipments, and each of them is different from others according to its purpose or use. Since under these conditions, it is difficult to estimate the cost of them, in this section we consider the cost of power of the wave-activated pump including the seabed pipeline, in other words, a unit cost of generation of electricity which is the amount of generation of electricity converted to estimate the cost required for that.

Assuming that durability of this system is 25 years, interest rate of investigation fund is 6% per year and annual cost of maintenance is 4,000,000 yen, then the amount with interest added for 25 years ΣA comes to:

$$\Sigma A = 325,000,000 + \frac{325,000,000 \times 0.06 \times 25}{2}$$
$$+ 4,000,000 \times 25 = 668,750,000 \quad (16)$$

And the total output of wave-activated pump for 25 years ΣP is:

$$\Sigma P = (Pwo+PwQ-PwQ \times 0.6 \times 0.8^2) \times 24 \times 365 \times 25$$
$$= 38,237,400 kw \cdot H \quad (17)$$

$$\therefore \frac{A\Sigma}{P\Sigma} \fallingdotseq 17.5 \ yen/kw \cdot H \quad (18)$$

As shown by the result of the above calculations, this system is relatively inexpensive as a source of power for the various equipments, plant and facilities. And as to drawing seawater for the incidental equipments, plant and facilities, the above calculations are based on the assumption that the wave-activated pump is used to draw seawater to wharf. If any other type of pump is used for this purpose, extra cost is required to draw seawater to wharf. In this point of view, the wave-activated pump is also comparatively advantageous.

Then, as to operating conditions, wave energy changes according to the conditions of the sea and weather. Therefore, it is advisable to operate the incidental equipments, plant and facilities by wave energy suitable for each condition. For example, when the waves are high, it is better to operate the entire system: the seawater desalting equipment, the salt manufacturing plant, the generator and the sewage disposal facilities. On the other hand, when the waves are low, it is preferable to operate some parts of the system such as the sewage disposal facilities and the generator to get the sufficient amount of electric power required for the consumption of households. And if it is late at night, it is wise to operate the sewage desalting equipment and the salt manufacturing plant. The control made by these combined operations will enable us to use the system more economically and effectively. And since in the area of the sea where wave period is long, the efficiency of the wave-activated pump is expected to be raised, the much better result should be obtained there.

Finally, I hope that this system will help people to develop their culture, economy, technology, industries, etc. in areas where they use this system.

References

1. Takuya Honma and two co-autors, "The Ocean Energy Reader", Ohm-sha, Issue No. 2, First Edition, p. 58 (June 30, 1981)
2. Shoji Sato and Yoshizane Goda, "Seashores, Bays and Harbors", Shokoku-sha, Issue No. 4, First Edition, p. 42 (Sept. 20, 1976)
3. Futao Kono, "Hydraulics of Seashores", Morikita Shuppan, p.191
4. Yoshizo Nagao, "Technology of Bays and Harbors", Kyoritsu Shuppan, Issue No. 8, First Edition, p. 73 (Nov. 15, 1978)
5. Shigeru Ohno, Toshio Sakurai and three co-autors, "Function and Control of Sewage Disposal Facilities", The Industrial Water Research Society, First Edition, p. 320 (Jan. 29, 1975)

The application name and number for a patent on this study are as follows.

Wave-Activated Pump
The open gazette of patent,
Showa 61-255277

WAVE PROFILES IN THE CHAMBER OF PENDULOR POWER EXTRACTOR

Satoshi Tamate*, Hideo Kondo* and Tomiji Watabe**

* Muroran Institute of Technology, Japan
** Dept. of Mechanical Eng., ditto., Japan

Abstract

Laboratory investigations have been performed for the wave profiles in chamber to find energy loss charactor of the pendulor power extractor. It is concluded that, the chamber length should be less than a quarter of wave length, and the base mound slope should be gentle to get lower energy loss and hence higher efficiency for power extraction.

1.Introduction

Pendulor system is one of wave power extractors which recieves wave power with an oscillating pendulum plate in a caisson and transmits the power to hydraulic circuit (see Fig.1).
In this study, we have investigated wave profile in the chamber which is formed with a pendulum plate and the caisson walls in order to get information for design of efficient energy conversion as well as stability of caisson against wave force.

2.Wave Profiles due to Mecanical Oscillation of Pendulum Plate

This experiment had been performed by mecanical oscillation of pendulum plate driven with an electric motor (Fig.2).
The distance between back wall and pendulum plate, "B", called chamber length hereafter, and wave length "L" were varied. The wave profiles were measured at the points of B/8, B/4 and B/2 from back wall by capacitance wave gages. The recorded data were analyzed by FFT for each points to get spectra of wave profiles.
The spectrum density for B/L=0.25 concentrated prodominantly to fundamental frequency. When B/L<0.25, the second harmonic component appeared near the back wall. Meanwhile at B/L>0.25, the third harmonic component appeared near the pendulum plate (see Fig.3).

3.Wave Profiles due to Pendulor Movement by Waves (see Fig.4).

The experimental condition was varied for incident wave period and chamber length. Wave period was 1.0∼2.0 with the pitch of 0.05 (sec).
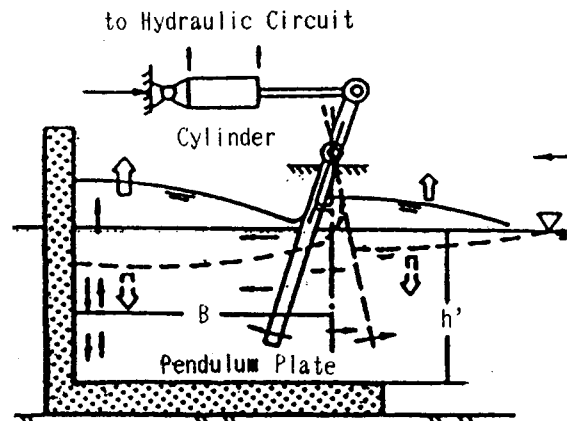
Fig.1. Sketch of Pendulor Power Extractor
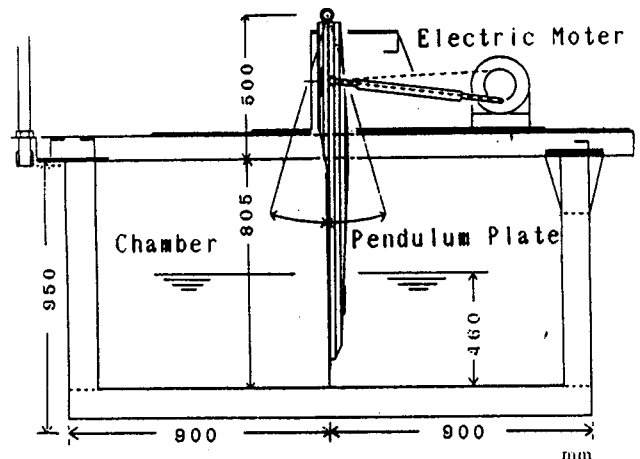
Fig.2. Sketch of Experiment System 1
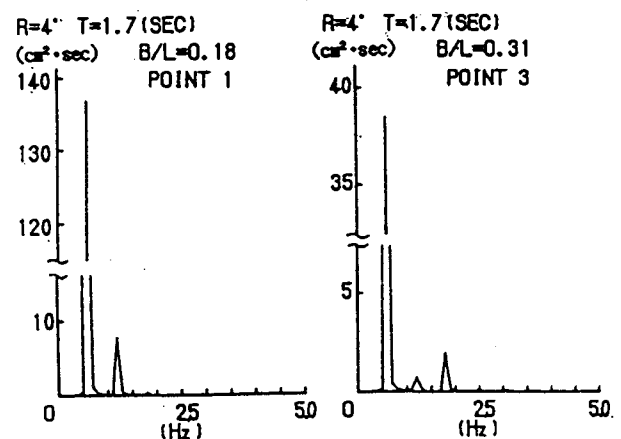
Fig.3. Power Spectrum of Waves in Chamber

The two chamber lengths were set as 62.60 cm and 74.65 cm. The chamber length was chosen to get "B" of a quarter of wave length in chamber for wave periods 1.4 and 1.6 (sec). The recorded data were analyzed by FFT for each points.

Fig.6 shows the power spectrum of fundamental frequency component for each wave period which is essential for driving pendulum plate smoothly. In these cases, we had found approximatly three types of wave profile in chamber depending on B/L (see Fig.5).
(1) B/L<0.18
In this case, the chamber length is too small to fit a quarter wave length. Wave motion in chamber is likely to move up and down and has less horizontal motion.

Waves can not attain a standing wave in chamber. Nevertheless they move like a restoring force to pendulum plate motion and the amplitude of pendulum plate becomes large.
(2) 0.18<B/L<0.35
In this case, the chamber length coincides nearly to a quarter of wave length. But when the chamber length was a little bit smaller than the quarter wave length, the node would appear seaward the pendulum plate. In such a condition, the second harmonic component appeared in chamber.

When chamber length is larger than a quarter of wave length, the node appeared behind the pendulum plate. The third harmonic component appeared in chamber for the case. The components may prevent the pendulor from moving smoothly. These effects can be seen in the Fig.4.

At B/L=0.25 which means "B" fits to a quarter wave length, a standing wave is made in chamber, and waves can attain a resonance in chamber. Little turbulent water motion is expected, but energy loss at pendulum plate is larger because horizontal water particle velocity is much large near the pendulum plate. Therefore the amplitude of pendulum motion is not so large as expected.
(3) B/L>0.35
In this case, the chamber length "B" lies between a quarter wave to one half of wave length. Terefore, total hydrodynamic forces on pendulum plate are deduced.

As conclusions, when a quarter wave length is larger than the chamber length, this system gain a restoring force in chamber.
When the amplitude of motion becomes large, it is expected that the system may bring high efficiency in this condition. But when a quarter of wave length is smaller than the chamber
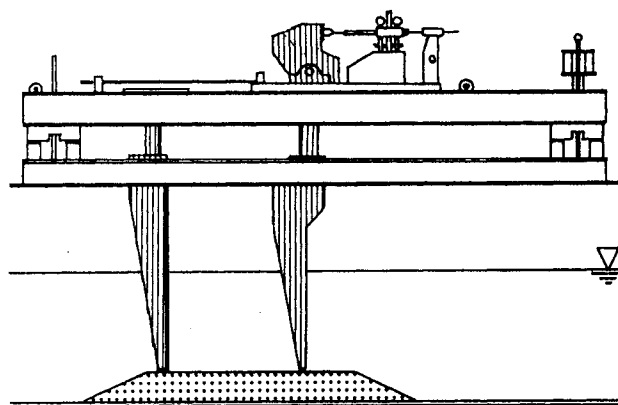
Fig.4. Sketch of Experiment System 2

① B/L<0.18
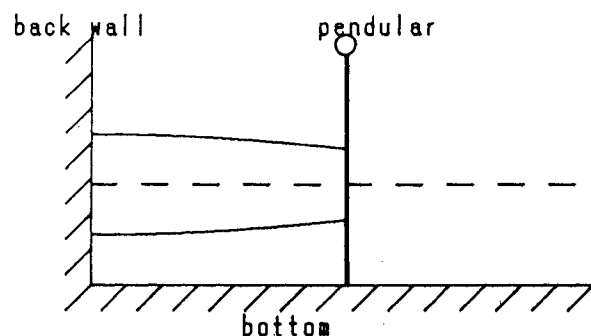
② 0.18<B/L<0.35
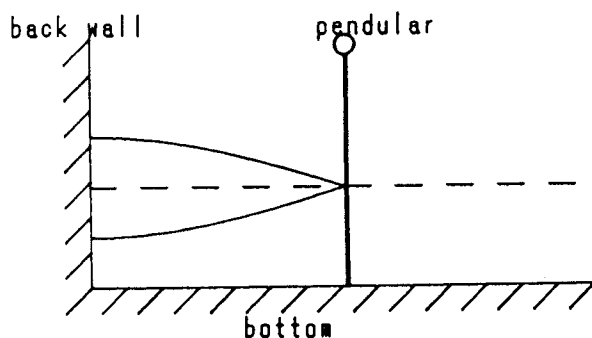
③ B/L>0.35
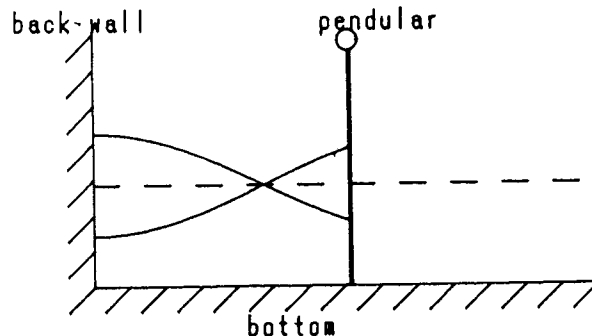
Fig.5. Sketch of Wave Motion in Chamber

—469—

length, water motion becomes turbulent and total hydrodynamic forces on pendulum plate are deduced. Chamber length "B" should be set to get B/L < 0.25.

4.Energy Losses of Pendulor System

It has been already indicated that a standing wave is made in chamber for the case of B/L=0.25. Therefore energy loss at pendulum plate becomes large because horizontal water velocity is so large around the plate.
Principal factors of energy losses are as in the following:
  (1) Energy loss in the mound on which caisson sits.
  (2) Friction loss on the chamber walls.
  (3) Energy loss in the slit between walls and the pendulum plate.
In order to investigate charactor of these energy losses at each point, three kinds of experiment were performed (Fig 7):
Type A is the case of pendulum plate being fixed. Type B is the case of pendulum plate being removed from type A. Type C is the case of a soild wall being set in front of the mound.
Incident wave hight had been kept uniform in the experiment, energy losses at each part were expressed with the difference of wave power two kinds of experiment among the three . They were performed to find of energy loss in the mound and in the chamber.
At first, energy loss in the mound was investigated with an approach shown in Fig.7 (Type A,C)

Incident wave power:

$$Wi = CgE = Cg\frac{1}{8}\rho gH^2$$

Wi : incident wave power

Energy loss ratio in the mound:

$$\Delta W_{mound} = \frac{Wrc - Wra}{Wi}$$

Wrc : reflected wave power in Type C
Wra : reflected wave power in Type A

Energy loss ratio in the chamber:

$$\Delta W_{chamber} = \frac{Wra - Wrb}{Wi}$$

Wrb : reflected wave energy in Type B

In type D, the energy transmitted from the clearance between pendulum plate and caisson walls was measured

FOUNDAMENTAL COMPORNENT OF POWER SPECTRUM
(deg sec) B= 62.6 cm Nb=3
(cm sec) H=8cm

○:PLATE
□:POINT 1
●:POINT 2
▣:POINT 3

2.0 1.8 1.6 1.4 1.2 1.0 (SEC)
0.16 0.18 0.21 0.25 0.31 0.42(B/L)

FOUNDAMENTAL COMPORNENT OF POWER SPECTRUM
(deg sec) B= 74.65cm Nb=3
(cm sec) H=8cm

○:PLATE
□:POINT 1
●:POINT 2
▣:POINT 3

2.0 1.8 1.6 1.4 1.2 1.0 (SEC)
0.19 0.22 0.25 0.30 0.37 0.50(B/L)
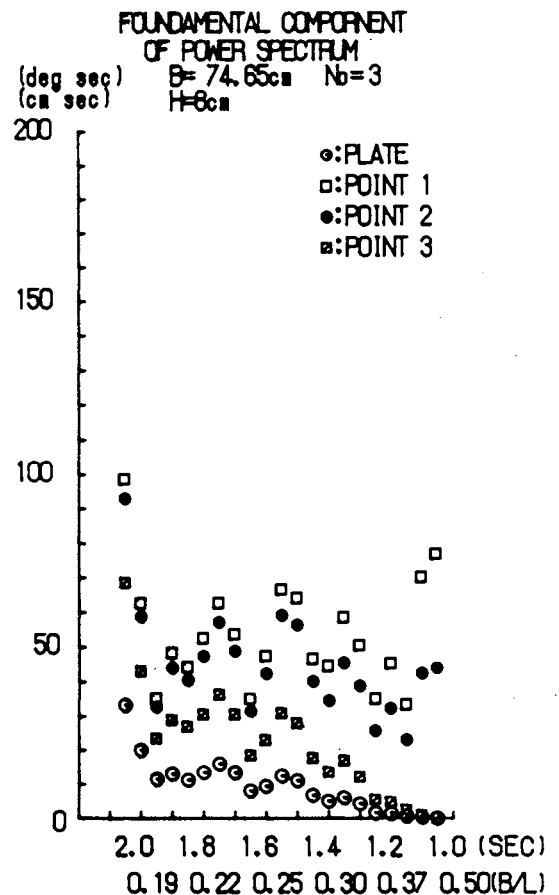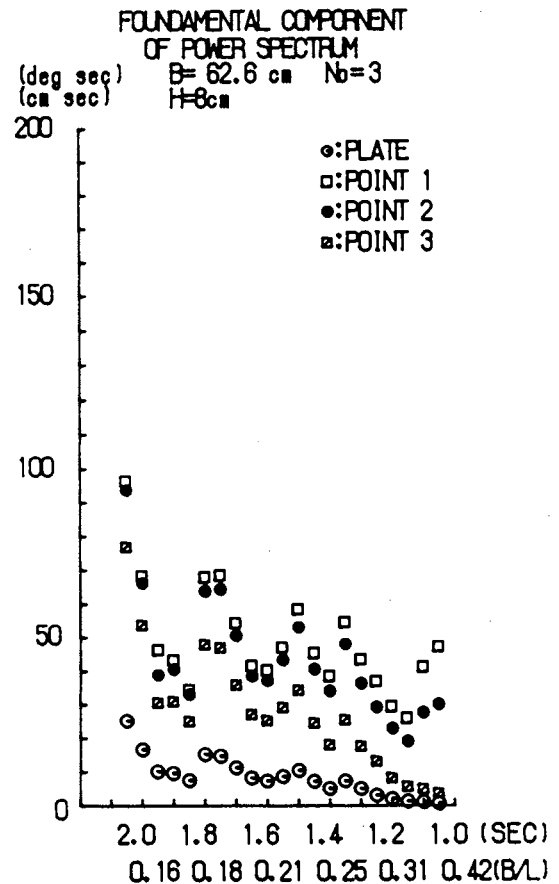
Fig.6. Power Spectrum of Foundermental Component in each point

(Fig.7, Type D).
It is shown in the following descrip-
tion that the transmitted energy ratio
is given by,

transmitted energy ratio to chamber:

$$\Delta W_{transmitted} = \frac{Wc,D}{Wi}$$

Wc,D : transmitted energy to chamber
in type D.

From these results (see Fig 8), when
wave period is small, energy loss
ratio in the base mound becomes large.
This may have been resulted from the
fact that the vortex was made at the
corner of mound and inflow and outflow
water on the surface of mound when
nodes come to near the corner of
mound.
When wave period is large, the phe-
nomenon becomes small because node
departs from the corner.
Energy loss ratio in chamber is al-
most 5∿10% at all period, and it de-
creases from short periods to large
periods. The calculation by the
theory was also performed by taking
account of boundary layer thickness on
all walls (Fig.9).
Energy loss in the slit was obtaind
with the following procedure for the
case of the fixed pendulum plate.

$$W_{slit\ loss} = Wi - Wr - Wt$$

$W_{slit\ loss}$: energy loss at slit

Wi : incident wave energy
Wr : reflect wave energy
Wt : wave energy of transmitted to
chamber

Horizontal water velocity is esti-
mated by the wave potential of inci-
dence (see Fig.9). The energy loss at
slit is the highest for wave period of
1.4 (sec). The reason is that wave
nodes appear near the pendulum plate
since a quarter wave length is made in
chamber and the horizontal velocity
becomes large near the plate. Mean-
while two methods of theoretical cal-
culation were carried out. The first
case employed the horizontal particle
velocity of the incident wave of
potential theory neglecting wave
motion in chamber.
The theoretical result coincides with
the experimental ones for larger and
shorter waves as shown Fig.10.
The broken line in Fig.10 was ob-
tained by the long wave theory by
KONDO[2] proposed for so-called
slotted caisson, which approximates
well for waves of longer period.
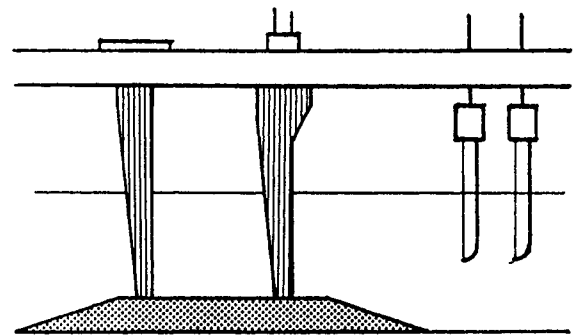
Type A: Pendulum Plate Fixed
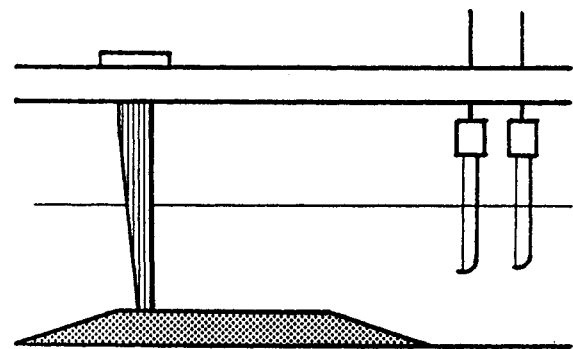
Type B: Pendulum Plate Removed
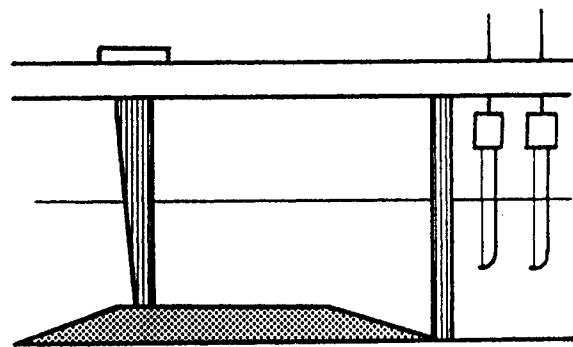
Type C: Partition Wall set in the front
of the Mound
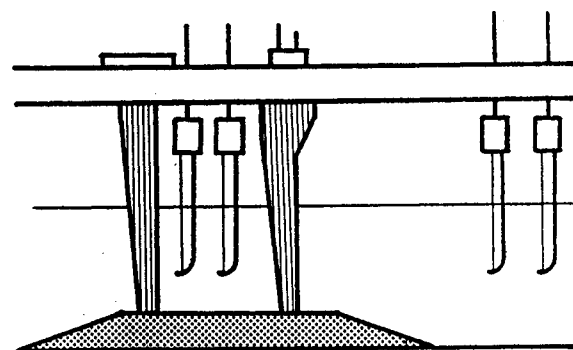
Type D: Pendulum Plate Fixed with Clearances

Fig.7. Experimented Method for Energy Loss
Evaluation

5.Conclusion.

1. Wave motion in chamber

When a quarter of wave length is shorter than the chamber length, node appears behind the pendulum plate and wave in chamber have third harmonics because of tubulant water motion.

When a quarter of wave length is longer than the chamber length, standing wave nodes do not exist behind the pendulum plate in the chamber and hence the amplitude of pendulum motion becomes large.

The chamber length should be set as B/L<0.25 for the period of predominant wave power.

2. Energy loss

Energy loss at slit on fixed pendulum plate becomes large in the period of resonance oscilation, but ratio of energy loss is less than 40%. But when pendulum plate oscillates, 10∿20% of the incident wave energy is dissipated at the slit.

Energy loss ratio at mound becomes large for the waves of smaller periods. When wave period is large, the ratio becomes smaller because node departs from the mound slope.

Energy loss ratio in chamber is almost 5∿10% over the experimental period, and it decrease with increasing the period.

These losses must be decreased at the design stage of practical systems in the light of present study.

References.

1. Kondo, H., T. Watabe and K. Yano: Wave power extraction at coastal structure by means of moving body in the chamber, Proc. of 19th Int. Conf. on Coastal Eng.,ASCE, Vol.III, 2875-2891, 1984.
2. Kondo, H. and H. Takeda (1983). Wave Energy Dissipating Structures, Morikita-Shuppan (in Japanese).
3. Mei, C.C., P.L.F.Liu and A.T.Ippen: Quardratic loss and scattering long wave, Prof.of ASCE, Vol.100, WW3, pp.217-239, 1974.
4 Watabe, T., H. Kondo and M. Kobiyama : Hydroulic technology and utilization of ocean wave power, Proc. of JHPS Int. Symp. on Fluid Power Tokyo, JHPS, 301-308, 1989.
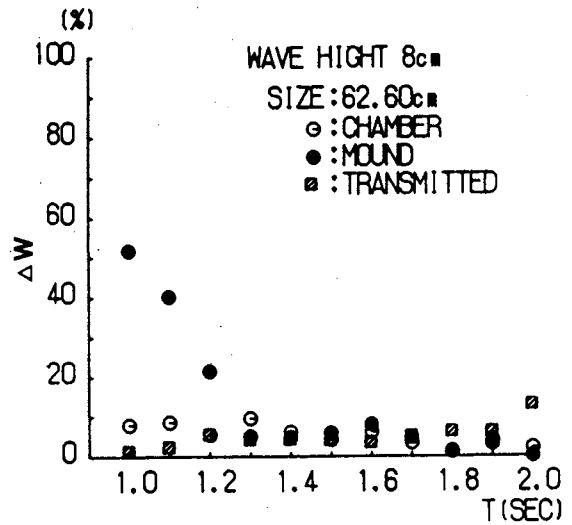
Fig.8. Ratio of Several Energy Losses
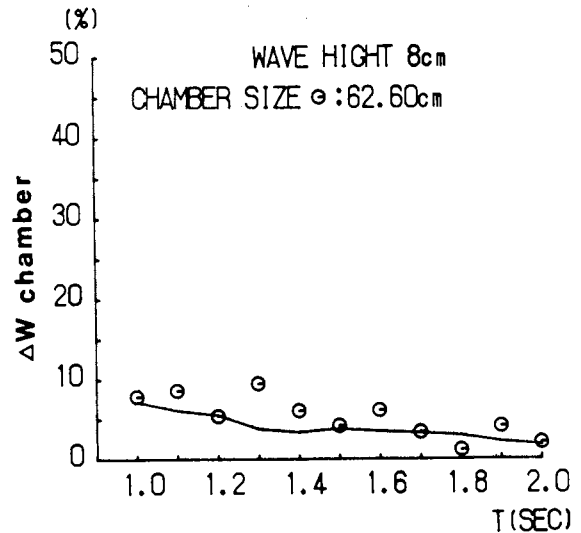
Fig.9. Comparison of the Energy Loss by Experiment and Theory at chamber
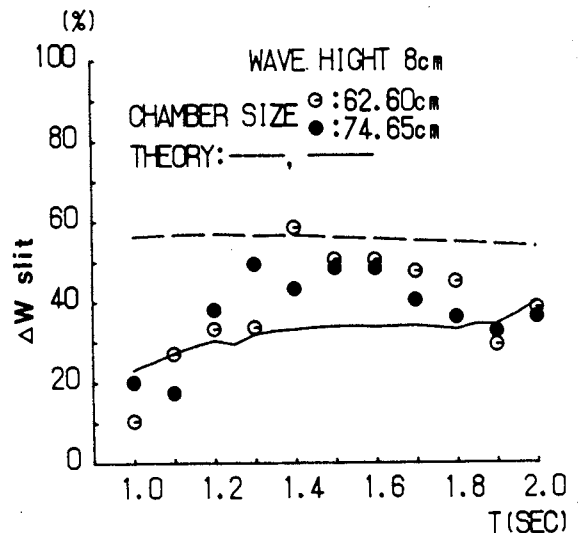
Fig.10. Ratio of Energy loss at slit

STUDIES ON MULTI-PURPOSE UTILIZATION OF THE OCEAN WAVE ENERGY

T. Watabe[*], H. Kondo[*], Y. Kubota[*] & H. Yamagishi[*]

[*] Muroran Institute of Technology, JAPAN

Abstract

The Pendulor system uses oscillating pendulum motion for efficient extraction of ocean wave energy. Since this principle is based on direct conversion of wave force, the system is given an inherently tough nature towards extreme overloads.

One of the major problems with the OTEC system is its poor conversion ratio. In order to solve this condition, it has been proposed that the OTEC system should be combined with the Pendulor.

An OTEC-Pendulor system, in which the Pendulor supplies the OTEC the power for pumping water has been studied to see its feasibility. In this case study, the output of the system was 14% higher than the total output of (each) independent operation by the OTEC and the Pendulor.

When the improvement of the quality and the cost effectiveness are taken into consideration, it will be that the difference between the two is much larger than 14%.

Nomenclature

A_p piston area of the cylinder
B width of pressure plate of the Pendulor
c_n constant
c_p constant
c_Q constant
D_m displacement of the motor
E wave energy entering into the Pendulor during T
g acceleration of gravity
H wave height
h water depth
ΣI equivalent moment of inertia of the Pendulor (including added water)
K restoring coefficient due to water elevation behind the Pendulor
K_o restoring coefficient of the Pendulor
k_o wave number
l height of supporting center (see Fig.1)
M amplitude of exciting moment
M_o reaction moment of the cylinder
N damping coefficient due to radiation waves generated by the Pendulor
n_m motor speed
p_o average pressure
Q_1 heat received from warm water
Q_2 heat transferring to cold water
Q_o average oil flow
Q_w water flow
r arm length (see Fig.1)
T period of wave
t time
T_m output torque of the motor

η_R thermal efficiency
η energy absorption ratio .
ρ density of water
ω circular frequency of wave
θ angular displacement of the Pendulor
θ_a amplitude of the swing
λ wave length

1. Introduction

A wave energy converter named the Pendulor system uses oscillating pendulum motion at resonant for efficient extraction of the ocean wave energy. Since the principle is based on a direct conversion method of the wave force, the system is given an inherently tough nature towards great overloads[1].

From this view point, we have studied the Pendulor which can be used not only as an electric power generator but also as a mechanical power supplier. The system has been proved to have a high extracting ratio. But the Pendulor is liable to have periodic fluctuation in its output, which makes a prospect as a main power source not feasible[2].

However, the OTEC (ocean thermal energy conversion system) has been studied for many years in the world and its poor conversion efficiency is still a major problem. In order to overcome this predicament, an OTEC combined system with the Pendulor has been proposed by the authors, (because the characteristics of the Pendulor are very suitable for driving the water pumps in the OTEC system[3].

In this paper, the optimization problem of the OTEC-Pendulor system has been studied theoretically and its feasibility has been also investigated.

2. Concept of the Multi-Purpose Utilization

Ocean wave energy consists of two kinds of physical energy;- potential and kinetic so that the energy is desirable to be utilized as mechanical energy without any complicated conversion. Fig.1 shows the principles of the Pendulor.
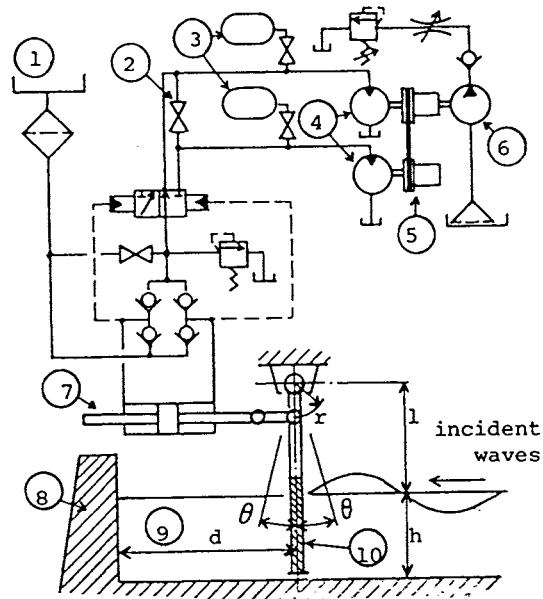
Fig.1 Principles of the Pendulor System

As illustrated in Fig.1, incident waves are changed into standing waves by superposition with reflecting waves on them. At the node of the standing waves, all energies concentrated into horizontal reciprocating water flow. A pendulum with the pressure plate (Pendulor) is driven by the flow and then, the electric generator is supplied with mechanical power from the Pendulor. Since the Pendulor absorbs the wave energy, the wave force towards the caisson becomes weekened by the Pendulor which is set on the caisson. So, Fig.1 is an example of the use of the Pendulor as the energy absorber and as the wave force dampener too, which can improve stability of the caisson[4].

3. Pendulor as an Auxiliary Power Source

The incident wave energy E coming into the Pendulor during T is written in the next form, when the waves are regular ones.

$$E = \frac{1}{4} TB \left(\frac{H}{2}\right)^2 \rho g \frac{\omega}{k_o} \left(1 + \frac{2k_o h}{\sinh 2k_o h}\right) \qquad (1)$$

The Pendulor is driven sinusoidally by the waves, and the motion of the Pendulor can be found by solving the equation of the motion.

$$\Sigma I \ddot{\theta} + N \dot{\theta} + (K_o + K)\theta + M_o = M \sin \omega t \qquad (2)$$

where M is an amplitude of the exciting moment

$$M = \frac{\rho \omega^2 Y_o H}{k_o^3 \sinh k_o h} \qquad (3)$$

$$Y_o = k_o l \sinh k_o h + \cosh k_o h - 1 \qquad (4)$$

The wave number $k_o = 2\pi/\lambda$ must satisfy the dispersion relation $\omega^2/g = k_o \tanh k_o h$. The Pendulor has been studied using a 1/6 scale model driven by regular waves. Fig.2(a) shows characteristics of a fixed type hyd. motor fed oil by the Pendulor. The torque T_m can be expressed approximately the follows.

$$T_m = T_{mo} - (T_{mo}/n_{mo}) n_m \qquad (5)$$

When the hyd. motor is replaced with a variable type one, the efficiency shall be improved through a wide speed range as shown in Fig.2(b). The lower the speed is, the higher the torque T_m becomes. It is an altered form of the wave force. From the torque curves, it is evident that the Pendulor is applicable to even unsteady load. The torque T_m can be controlled by displacement of the motor so that torque constant drive, speed constant drive, and power constant drive are all possible in practical use.

4. OTEC-Pendulor System

Fig.3 shows the basic principle of the OTEC which is expected to become a trustworthy technology in the energy field. The thermal efficiency of the OTEC is shown with the one of Rankin cycle.

$$\eta_R = (Q_1 - Q_2)/Q_1 \qquad (6)$$

Since the actual temperature difference between surface and deep water is about $20^\circ C$, $\eta_R = 3 \sim 4\%$ might be optimal value. As the results, the system consumes 1/3 of the whole generating power for pumping water at least[5].

In a combined system;- the OTEC-Pendulor, the OTEC is supplied the power for pumping from the Pendulor as it is shown schematically in Fig.3.

The output of the OTEC-Pendulor depends on wave energy so that the system has to be set at a place where the temperature difference is large and wave energy is rich as well, (like the sea around Hawaiian Islands). In this system, two water pumps and a line pump are driven by three variable hyd. motors. The Pendulor supplies oil to them. If, the moment which acts onto the Pendulor as supplying oil, is adjusted in an even level of the moment by generating waves, the power flow to the motors achieves maximum value. This is the optimal condition[1].

The average oil flow Q_o and the average pressure p_o are written in the next forms, when the Pendulor is running at the optimal condition[6].

$$Q_o = \frac{1.6\theta_a r A p}{T} = \frac{0.2 r A p k_o Z_o H}{T Y_o \sinh k_o h} \qquad (7)$$

$$p_o \doteq \frac{0.8N\bar{\theta}}{rA_p} = \frac{3.2\pi\rho Y_o H}{rA_p T^2 k_o^3 \sinh k_o h} \qquad (8)$$

$$\theta_a = \frac{k_o Z_o}{4Y_o \sinh k_o h} \cdot \frac{H}{2} \qquad (9)$$

$$Z_o = \sinh 2k_o h + 2k_o h \qquad (10)$$

$$N = \frac{4\omega\rho Y_o^2}{k_o^4 Z_o} \qquad (11)$$

Besides the hyd. motor, its output torque T_m and speed n_m are expressed next.

$$T_m = \frac{D_m p_o}{2\pi} \eta_t \qquad (12)$$

$$n_m = \frac{Q_o}{D_m} \eta_v \qquad (13)$$

and when the motor drives water pump directly, T_m is written by the next equation.

$$T_m = C_n n_m^2 = C_n \eta_v^2 \left(\frac{Q_o}{D_m}\right)^2 = C_p Q_w^2 \qquad (14)$$

Equation(14) shows that the torque T_m varies widely as changing the oil flow Q_o, when D_m is fixed. Since Q_o is proportional to the wave height H, and H never takes a constant value at natural sea condition, the results expressed in equation(14) are unpractical because of the high torque.

In order to improve this state, we consider a case in which fixed motors have been exchanged with variable ones, and the displacement D_m is controlled with Q_o as follows.

$$D_m = c_a \left(Q_o\right)^{1/2} \qquad (15)$$

Substitute equation(15) in equation(14) we get the next relationship.

$$Q_w = \frac{\eta_v}{C_Q} \sqrt{\frac{C_n}{C_p}} Q_o \qquad (16)$$

$$T_m = C_n \left(\frac{\eta_v}{C_Q}\right)^2 Q_o \qquad (17)$$

Fig.4 shows Q_o, p_o, Q_w, E and T_m versus wave height H.

5. Considerations

Since the output of the OTEC-Pendulor system depends on water flow Q_w directly, the results shown in Fig.4 are very preferable for this system, (because the flow Q_w does not decrease rapidly when the wave power E decreases). The OTEC-Pendulor would be hardly influenced by the wave's pulsation in the output. It allows the Pendulor system to become the simpler.

When the OTEC-Pendulor is installed on a floating body of water, the Pendulor can dampen the mooring force of the body[7].

Fig.5 shows a case which an OTEC coupled with a 3000kW generator and a Pendulor driven by a 2000kW wave power are running independently with each other. The net output of the OTEC is 1830kW, because in the case of using the OTEC system independently, the system needs 1170kW for water pumping and besids, in the case of using the Pendulor system independently, the system generates 800 kW, which is not of high quality. Therefore, in the case of using each system independently, we can get only 2630kW.

Comparing with Fig.5, an OTEC-Pendulor generates 3000kW of good electricity in the same condition. The output 1000kW of the Pendulor can utilize water pumping directly. The net output of the system is 370kW (14%) larger than the case of Fig.5. Considering the quality and the cost effectiveness, the difference between the two is more than 14%[3].

In another case, the Pendulor has been proposed for desalting process. The concept includes a high pressure
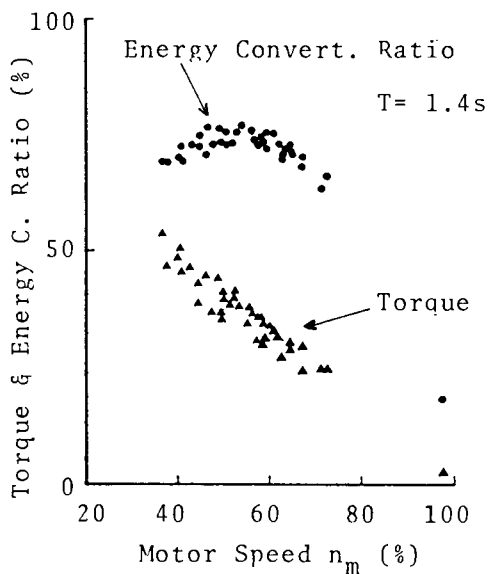
Fig.2(a) Torque Charact. of the Motor
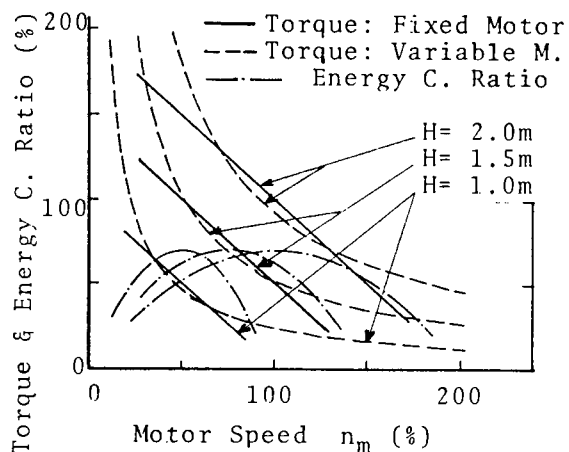
Fig.2(b) Torque Charact. of the Motor
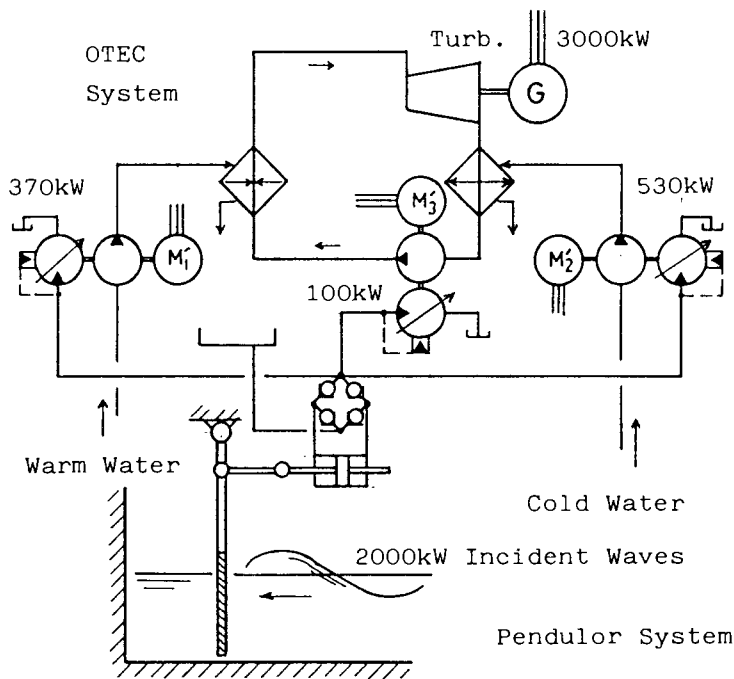
Fig.3 The OTEC-Pendulor System
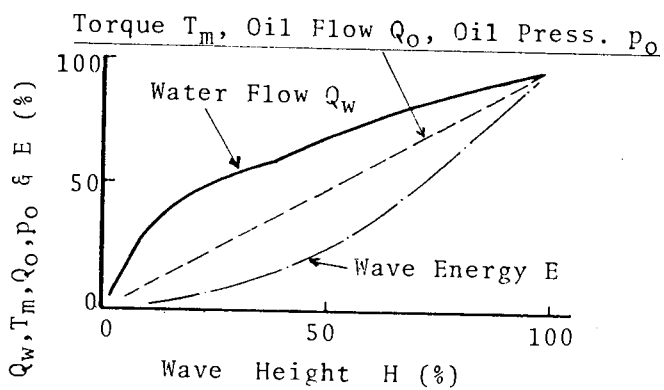
Fig.4 Water Pumping Charact. by the Pendulor

water pump, and displacement type (pro-
bably a piston type pump is most suit-
able for this purpose, but the pump has
a difficulty to be driven because of a
torque variation). The Pendulor can be
applied as the driver of the pump by
reason of its torque characteristics.

6. Conclusions

In order to utilize ocean wave energy
in broad fields, the multi-purpose uti-
lization of it is useful, the Pendulor
system is one of the most appropriate
system, because of its high adaptabil-
ity as a power source.

The OTEC which is supplied pumping
power by the Pendulor, can improve the
efficiency and the Pendulor can be made
the simpler as well.

The total output of independent oper-
ation with a 3000kW OTEC and a 800kW
Pendulor is 370kW less than the total
output combined operation with the same
systems.

7. Acknowledgement

The authors are extremely thankful to
Mr.N.Inoshita who has worked with us
for three years. Major part of the pre-
sent study has been supported by Scien-
ce Research Fund of the Ministry of
Education.

8. References

1. T.Watabe & H.Kondo, Hydraulic tech-
nology & utilization of ocean wave
energy, JHPS Int.Symp. on Fluid Power
Tokyo, Mar. 1989, 301-308

2 T.Watabe et al, Method & apparatus
for generating electric power by
waves, US Pat.4490621, 1984
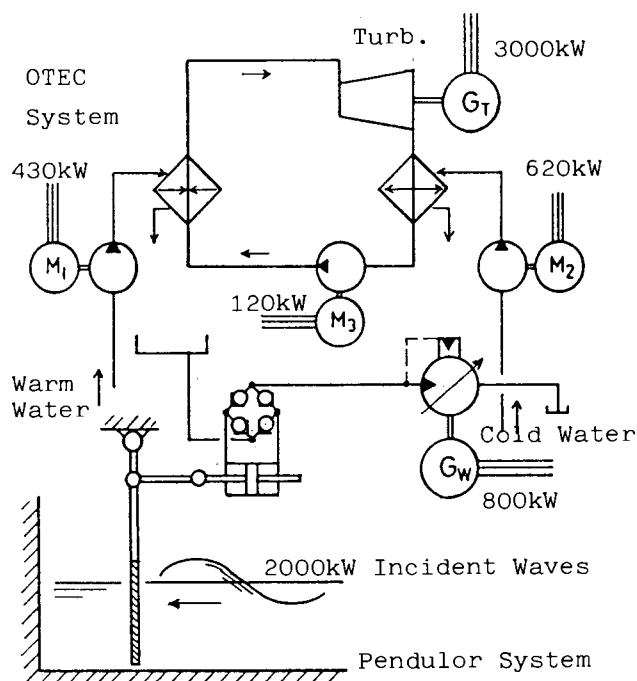
Fig.5 The OTEC System & The Pendulor
System Independent Operation

3 T.Watabe, Ocean thermal energy, Ener-
gy Resources, Vol.11, No.1,1990,45-52
(in Japanese)

4. T.Watabe,H.Kondo & M.Kobiyama, A
case study on the utilization of
ocean wave energy for fish farming in
Hokkaido, 89Int.Symp. on Cold Regions
Heat Transfer, July 1989,159-164

5. H.Uehara et al, The optimal design
of the OTEC for remote islands, Power
Generation by Heat,Atom, Vol.36-7,
July 1985,61-66 (in Japanese)

6. A.Ando et al, On a flap type wave
energy converter, ECOR Int.Conf. Oct.
1984

7. T.Watabe & H.Kondo, Progress on Pen-
dulor type wave energy converter de-
vices, No.PACOM90-122, Int.Symp.
KOREA, June 1990 (in print)

POWER GENERATIONS FROM TIDAL CURRENTS

S. Kihoh*, K. Suzuki*, M. Shiono*

* Nihon University, Tokyo, Japan

Abstract

This paper reports the method of electric power generation from tidal currents and test results of the system which is specially designed for this purpose. The system consists of a vertical axis turbine, a accelerator, an electric generator, and a control unit. The turbine is vertical axis Darrieus rotor, and has three blades. The real test in tidal currents was conducted from 1983 to 1988, at Kurushima straits, and its results are discussed.

Introduction

Attention is gathered on the use of renewable energy as a substitute of fossil fuels. Among others, the tidal energy has been studied for 50 years. Most of such studies, however, were related to optimum location of tidal power stations. It is believed that average tidal range of 5 m of more is required for effective tidal power generation with the efficiency of wheels taken into consideration. It has been also accepted that the energy effectively recovered from the tidal motion is in proportion to the square of tidal range. The tidal range is lower than 5 m at any place in Japan due to the topography. The authors have conducted experiments on tidal power generation from the tidal currents without blocking at bay or strait. This method may be effectively applicable to power generation by the river flow with low head. The tidal currents have a high energy density as compared with winds, solar photovoltaic power, solar heat and temperature difference in ocean [1]. The period of tidal crrents is definitely governed by the relative motion of the sun, the moon and the earth. As it is about 12 hours 25 min. [2], it cannot be synchronized with the daily power demand curve, although it can be used under established schedule. For these reasons, the authors conducted the experiments with the Darrieus type turbines which can take up the energy without regards to the direction of flow. We also conducted power generation experiments three times on-site at the Kurushima Straits. The paper presents description of the power generation systems and data obtained from the test channel experiments.

1. Tidal Currnt Power Generation Unit

Fig.1 shows the configuration of the experimental apparatus employed. The generator and related units are fastened on the bottom (in dotted line) and control and measuring units are installed on the ground and connected to the generator with cables. As the flow speed meter is durable to sea water only for very short time, the flow speed at the location of generator was estimated indirectly. The flow speed near the generator was measured by flow speed meter to establish the relationship between the flow speed and the flow and tidal curves at the channel of Kurushima Straits announced by the Maritime Safety Agency[3]. The flow speed at the location of generator can be estimated by the flow and tidal curves for the date of experiment using the relationship. Side views of the
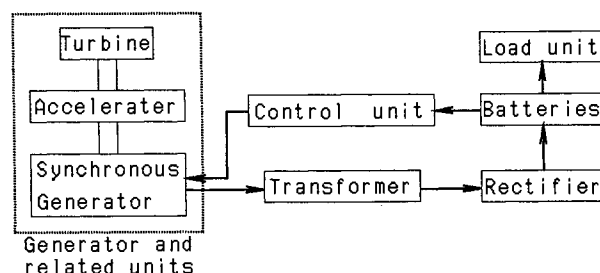
Fig.1 The configuration of the experimental apparatus employed.
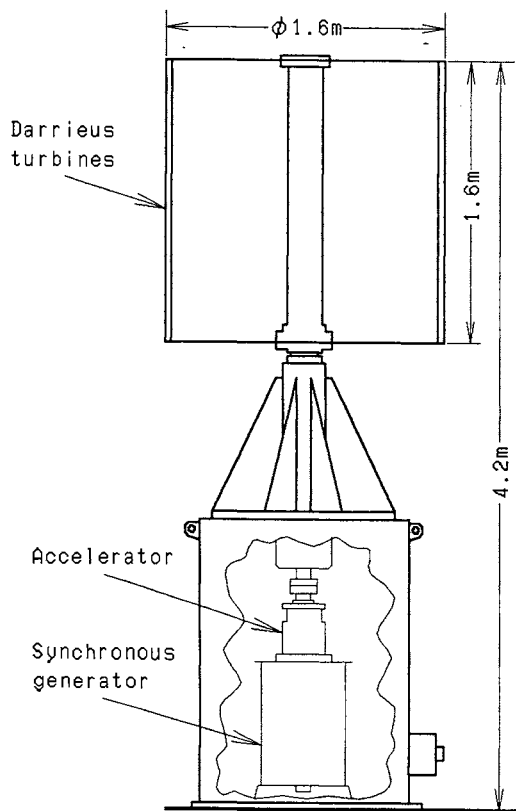
Fig.2 Generator and related units

Table 1. Structure and dimension of generation unit

Hight	4.2m
Total weight	3.9t
Turbine	Darrieus type (3-blades)
Blade type	NACA63$_3$-0018
Blade chord (Solidity)	0.3m (0.179)
Blade quality of the material	CFRP and GFRP
Blade weight	10kg/blade
Generator's rated output	5kVA
Generator's rated rotation	525rpm
Generator's rated voltage	200V
Generator's phase	3

generator and related units used are shown in Fig.2. Dimensions of the experimental unit are listed in Table 1.

1.1 Turbine

The energy of tidal motion varies along time and is reversed at every 6 hours. Sabonius and Darrieus turbines are typical for those which convert the motion energy in alternating directions to revolving energy in a constant direction.

The Sabonius turbine, a reactional type, has a high starting torque, rendering an advantage of automatic
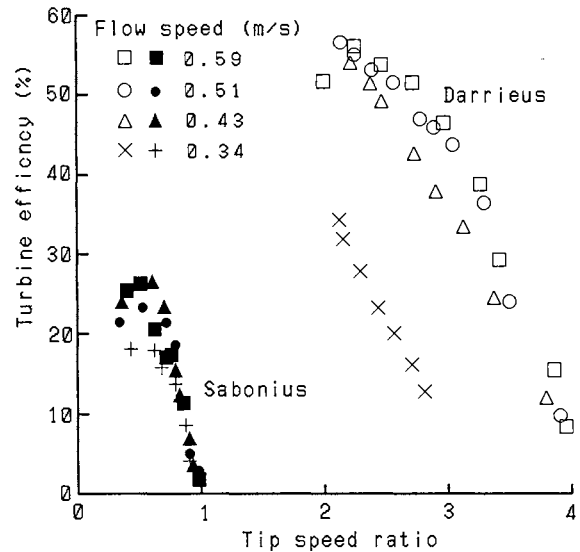
Fig3. Comparison between the Darrieus type characteristic and the Sabonius one.

starting by extremely low speed flow. However, its efficiency and the utilization factor of effective flow speed are low as compared with other types of turbines. Values of efficiency is in a range between 20-30 %. Sabonius type is not suited for the power generation or large scale operation.

The Darrieus turbine is a modification of the Darrieus type wind mill invented by G. J. Darrieus for application to turbine.

Using the Darrieus turbine, the authors conducted experiments to obtain revolving power from the tidal currents, for reasons: the direction of flow changes periodically; the lift type turbine causes the perimetric flow with a speed higher than flow speed, and; it has a high efficiency.

Fig.3 compares the output efficiency of the Sabonius and Darrieus type turbines in a channel experiment. While the efficiency of Darrieus type is obviously higher than the Sabonius type, its efficiency much low at low flow speed. This is the reason for the difficulty in starting the Darrieus type turbines. The tip speed ratio of the Sabonius type does not exceed 1 as it is a reaction type, whereas the ratio of the Darrieus type is 2.1 or higher as it is a lift type, proving it to be high speed of rotation and low starting torque, applicable to the power generation.

The Darrieus type turbine used in the experiment has the vertical axis, around which three blades are mounted at equal interval, as shown in Fig.4.
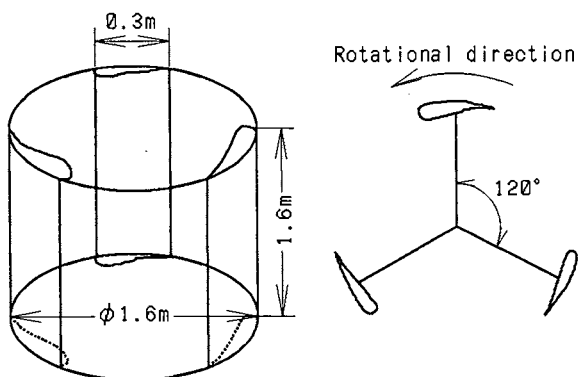
Fig.4 Darrieus type turbine (Three-blade type)
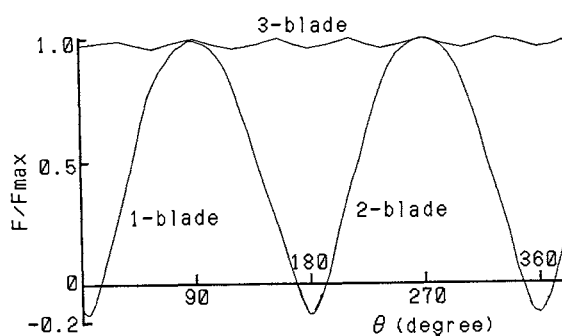
Fig5. Calculation of F/Fmax for θ

Three-blade type was selected for the ease of gaining of sufficient torque at any position of blades as the peak values of the torque would be distributed in 120 degrees. As a result, the variation of revolving force per rotation is significantly improved as compared with single or two-blade turbine. An example of calculation is shown in Fig.5.

Denoting the angular position of a blade as θ, the angle of attack α is given by:

$$\alpha = \tan^{-1}\left(\frac{\sin\theta}{\cos\theta + \lambda}\right) \qquad (1)$$

where, λ : Tip speed ratio

The revolving force applied to the blade F is given by:

$$F = L\sin\alpha - D\cos\alpha \qquad (2)$$

where, L: Lift, D: Drag
Calculation of F/Fmax for θ gives values as shown in Fig.5[4][5].

1.2 Accelerator

The revolving force obtained by the turbine is transmitted to the synchronous generator through an accelerator. The speed of revolution of turbine is increased nine times by the accelerator so that the number of rotations of the generator is maintaining above the rating even with low flow speed.

1.3 Generator And Its Control

A synchronous generator is used, with ratings shown in Table 1. The power generation is initiated when its rotation reaches 200 rpm and the generator is excited. The generator is controlled by either of the maximum output control or the constant exciting current control. In the maximum output control mode, the speed of rotation is detected by rotation meter, although the efficiency of the generator inevitably varies due to the fluctuation in the flow speed, and the exciting current is automatically controlled so that the maximum output is delivered at any number of rotation according to the output characteristics curve. The constant exciting current control mode is applied for the case where the rated speed of rotation cannot be maintained.

1.4 Load Unit

Star-connected variable resistors are used as loads in the characteristics test of the generator. Batteries are used for load of the long term test of generator. Floating charge is employed for the batteries by 24 V DC through a transformer (7:1) and rectifier. DC power is 24 V and is supplied to the lamps for the night, or it was converted to 100 AC by an inverter and similarly supplied for lighting in the night. The power supply cannot be matched to power demand load curve as the tidal current changes at a period of 12 hours 25 min. However, the power can be used according to established schedule using the battery charging. For the purpose, determination of battery capacity is significant.

2. Results

Experiments with test channels were conducted in 1982-83 as a basic study of tidal power generation. Main

subjects included: comparison between the Sabonius and Darrieus types, comparison of straight blade and curved blade of the Darrieus turbine, and; the automatic starting characteristics. Experiments in 1983 and subsequent years were conducted at the Kurushima Straits. The first experiment (August 1983) was conducted with the generator installed at the sea surface[6][7]. The generator was modified for installation on the sea bottom and the second experiment (July - August 1984) was done with it[8]. The third experiment with the sea bottom type generator with reduced weight of blades was carried out for three years (August 1986 - 1988). Results form these experiments are described below.

2.1 Tidal Current And Measurement Of Flow Speed[9]

The tidal current is a periodic horizontal movement of sea water caused by the tidal phenomenon. Therefore, the period of tidal current is 12 hours 25 min. in average with alternating direction four times a day. Similar to the tidal motion, tidal current is weak in the outer sea but very strong in narrow straits, generally accompanied with swirls of various size. The tidal current at the Naruto Straits exceeds 10 knots (1 knot = 0.51 m/s) at the maximum. The currents also exceed 10 knot at Kurushima and Ondo Straits in the Seto Inland Sea and channels in the Ariake Bay. Fig.6 shows a tidal curve with time-dependent changes at the location of the generator for the experiment. The highest speed at the location is about 33 % (north current) of that at in Kurushima Straits. It was found that the south current is far slower than the north current because
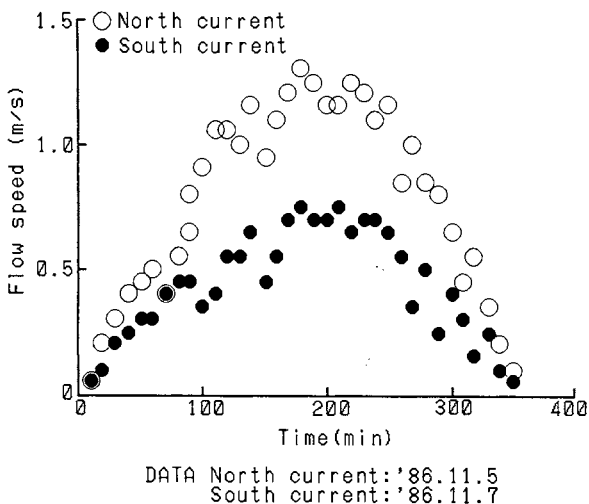
of topography. Speed, curve of flow, difference between directions and swirls significantly affected by the topography as well as the relative motion of the sun, moon and earth. Therefore, data of only the north current is used for characteristics described below.

Propeller type flow speed meter is used for measurement of flow speed. The speed is also indirectly determined for the long term experiment based upon a number of basic experiments.

2.2 Characteristics Of Turbine [9]

Of components of tidal power generation system, the characteristics of turbine for conversion of tidal energy is one of the most significant factors for the system characteristics. Fig.7 shows the characteristics of a Darrieus type turbine. The vertical axis represents the turbine efficiency, equal to the axial output or the total of the generator output, mechanical loss and loss by the resistance of windings including cables divided by energy of the flow. The turbine efficiency is closely related to tip speed ratio, which gives a curve shown in Fig.7. With high tip speed ratio, the turbine efficiency is reduced as the angle of attack is small and the rotation force is small. Is is found that the highest efficiency 56 % of the Darrieus turbine is attained at the tip speed ratio equal to 2.1 for each tidal flow speed.

Comparison with data from channel experiments indicates similar trends

DATA North current:'86.11.5
     South current:'86.11.7

Fig.6 Tidal curve
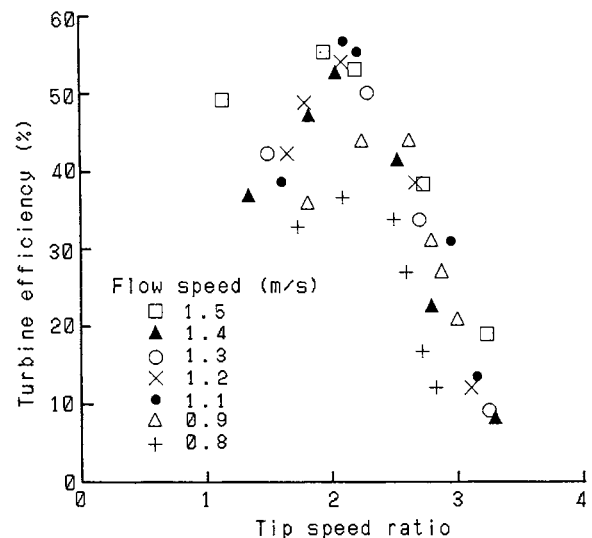
Fig.7 Characteristics of the Darrieus type turbine.
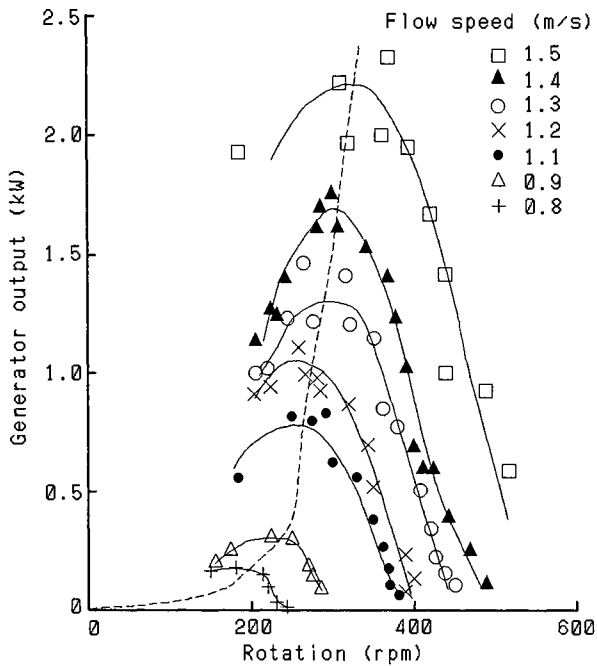
Fig.8 Output characteristics of the generator

with the ocean experiment, showing the maximum efficiency 54 % at the tip speed ratio of 2.1. The efficiency of ideal turbine in free flow is 59.3 %.

2.3 Power Generation Characteristics[9]

The number of rotation and output characteristics of generator is shown with the flow speed as the parameter in Fig.8. With the fact that the energy of flowing fluid is in proportion to the cube of the flow speed taken in consideration, the ideal operation with the maximum power is possible by excitation of the generator with exciting current corresponding to the dotted line connecting the maximum value of each curve. When the excitation current is controlled to maintain the number of rotation at constant, the output frequency is kept constant.

2.4 Operation Characteristics (Long Term)[10]

Fig.9 records total daily power outputs and daily averages of maximum flow speed for a month (March 1987). The flow speed varies at a period of about 13 - 14 days under the influence of the lunar age, accompanied by changes in total power output.
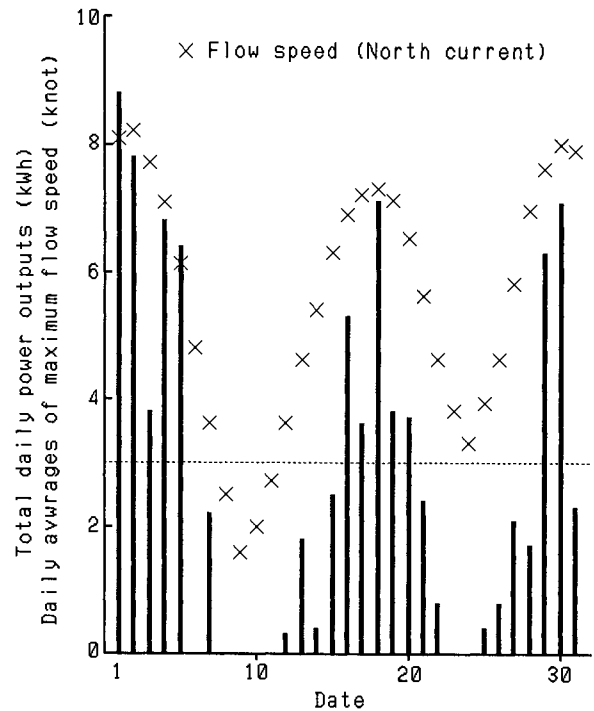
Fig.9 Total daily power output and daily averages of maximum flow speed for a month (March 1987).
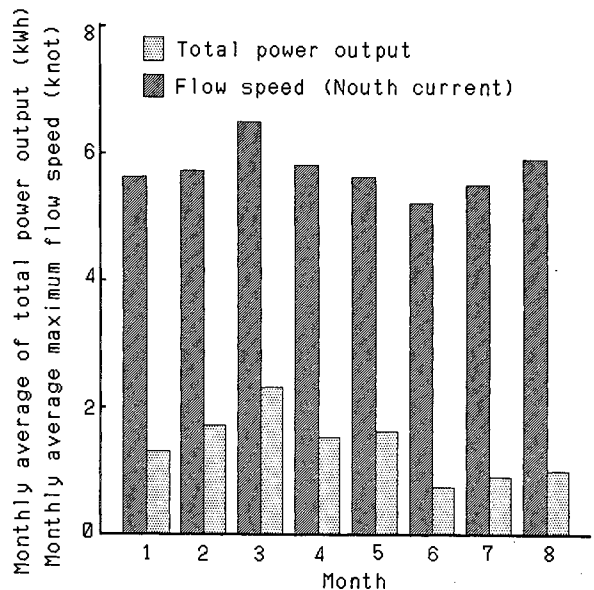
Fig.10 Comparison between the monthly average of total power output in half period and the monthly average maximum flow speed for a long period from the installation of the generator.

Fig.10 compares the monthly average of total power output in half period and monthly average maximum flow speed for a long term from the installation of the generator. It is shown that the average power output is larger with the larger average maximum speed of flow. The total power output decreases slightly after certain time elapsed.

-483-

2.5 Decrease Of Operation Period[10]

Following comparisons were made in order to determine the cause of decrease of power output. Fig.11 compares between data of January and August of the changes in maximum number of rotation of generator for the maximum flow speed with assumption of the constant load. As a good agreement is shown between distribution of measured data for these two months, the rotation characteristics of turbine apparently did not change for a long term of time.

Fig.12 compares changes in power generation period for the maximum flow speed in January with that in August. The duration of power generation in January is longer than that in August, suggesting that the difference of average power output between these two months is caused by the difference between the duration of power generation (period from start to stop of operation).

The reduction of power output is caused by the decreased duration of power generation despite of little changes in the rotation characteristics of turbine. The cause of reduced power output is estimated to be the deterioration of the starting characteristics due to the difficulty of starting the turbine. This is likely to have been caused by the increased drag to the rotation of turbine blades due to deposition of suspended materials and living organisms in the water. The stable power output is expected throughout a year by improving the starting characteristics (rotation power for start) so that it can be started at low flow speed.

3. Conclusion

A number of characteristics of tidal power generator were measured using Darrieus type turbine. Following findings were obtained by the long term experiment of the power generation in hard marine environments.

1) The power generation is possible when the flow speed is 1.0 m/s (2 knots) or higher.

2) High performance was affirmed by the experiments in channel and in ocean. It is sufficiently practical.

3) Continuous operation for a long term is possible by preventing the increase of drag to the rotation due to deposition of marine organism and
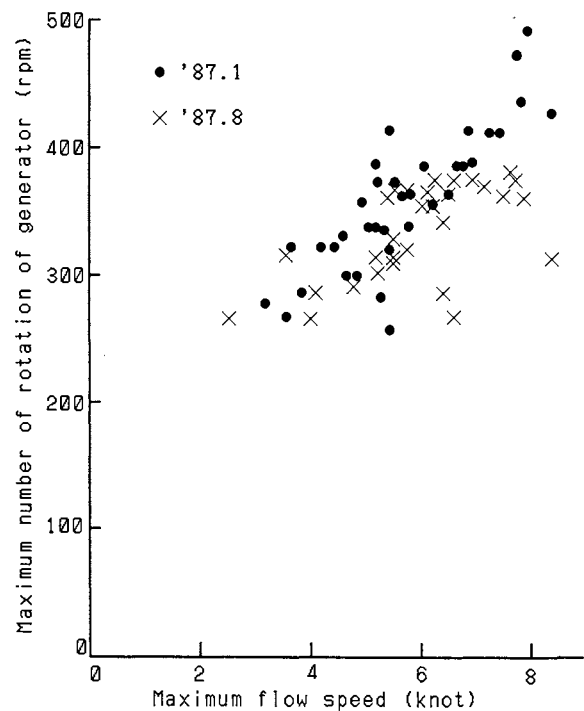
Fig.11 Comparison between data of January and August of the changes in maximm number of rotation of generator for the maximum flow speed with assumption of the constant load.
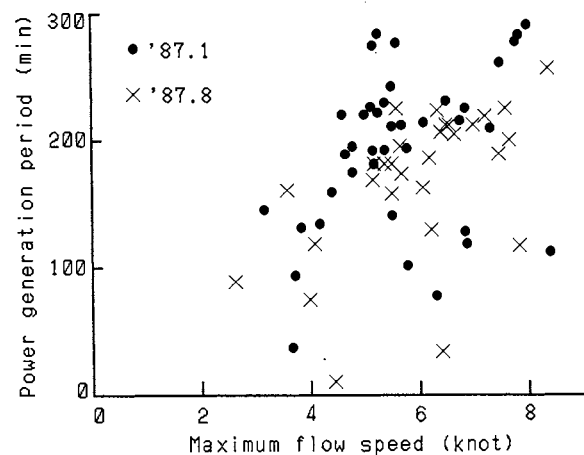
Fig.12 Comparison between data of January and August of the changes in the power generation period for the maximum flow speed.

suspended substances to solve the deterioration of starting characteristics of turbine. For location and system of power generation:

4) The present system was selected to meet the requirements for conservation of ship navigation, fishery, environment and the status of straits as possible. The power output is significantly affected by the topography.

5) The problem of installation of many generators on the bottom is solved.

References

1. Miyagi, Kihoh, Kotajima : "Present and future of the tidal power generation" Journal of Electrical Facility Engineering Vol.4, No.2 (April 1984)

2. Nagata, Hikosaka, Miyazaki : Ocean physics III, p.152 Tokai University Press

3. Tidal chart for Kurushima Straits Maritime Safety Agency (1964)

4. Kihoh, Kotajima, Miyagi, Komatsu, Kojima, Ajiki: "Tidal power generation at Kurushima Straits" 1983 National Meeting of the Electric Society of Japan. No.1105

5. Kihoh, Kotajima, Miyagi, Komatsu, Kojima, Ajiki: "Tidal power generation with Darrieus turbine" 1983 National Meeting of the Electric Society of Japan. No.1106

6. Tabinoki, Kotajima, Kikata, Miyagi, Kojima: "Tidal power generation with Darrieus turbine" 1984 National Meeting of the Electric Society of Japan. No.1183

7. Tabinoki, Kotajima, Kihoh, Miyagi: "Study of the Darrieus turbines for tidal power generation, Parts 1 and 2" 1985 National Meeting of the Electric Society of Japan. No.1143-4

8. Tabinoki, Kotajima, Kihoh, Miyagi: "Tidal power generation at Kurushima Straits" 1985 National Meeting of the Electric Society of Japan. No.1145

9. Shiono, Kihoh, Mutoh, Miyagi: "Tidal power generation at Kurushima Straits, parts 3 and 4" 1987 National Meeting of the Electric Society of Japan. No.1177-8

10. Shiono, Kihoh, Mutoh, Miyagi:"Tidal power generation by Darrieus turbines, part 5" 1988 National Meeting of the Electric Society of Japan. No.1349

AN ANALYTICAL ESTIMATION OF THE POOL LEVEL IN OPEN-CYCLE OTEC EVAPORATORS

Gerard Claude Nihous

Pacific International Center for High Technology Research Honolulu, Hawaii, U.S.A.

Abstract

The minimum water level above the evaporator baffle plate required to drain warm seawater from Open-Cycle Open Thermal Energy Conversion flash evaporators is analytically estimated. A potential-flow solution is first sought, with the spray of droplets originating from the spouts modelled as a uniform vertical two-dimensional source. The resulting fluid kinematics is used as an input to assess the effect of spout geometry upon the flow.

1. Introduction

One of the heat exchangers needed in the Open-Cycle Ocean Thermal Energy Conversion (OC-OTEC) is an evaporator consisting of a vacuum chamber, where warm surface seawater, at about 25°C, is partially flashed into steam. This steam is the thermodynamic working fluid for OC-OTEC as it flows through a low-pressure turbine. The preferred design for such evaporators consists of a baffle plate fitted with many inverted vertical spouts through which the warm seawater is fed into the vacuum chamber. Plants corresponding to net electrical outputs of 1 MWe and above would typically require hundreds of spouts. It is desirable to keep the spout length at a minimum to avoid a large water-side pressure drop; in addition, shorter spouts would allow a better predeaeration of the warm seawater (removal of evolved non-condensable gases prior to flashing) below the baffle plate because of a lower possible predeaereation pressure.

Spout length should be selected to prevent flooding, and, to a lesser extent, to ensure a sufficient evaporator thermodynamic effectiveness. The actual level above the baffle plate should provide enough head to overcome all hydraulic losses through the warm water discharge loop, from the evaporator to the discharge sump. Calculations of water levels are given, for example, in Wassel and Ghiaasiaan (1983). The present study shows how the minimum water level may be estimated in OC-OTEC evaporators as a function of water flow rate, baffle plate radius, spout diameter and density. First, a potential flow solution for the drainage of the axysymmetric baffle plate is determined in terms of modified Bessel funtions; the geometric presence of the spouts is not included, but the flow from the shattered jets originating from the spouts is represented by a uniform two-dimensional vertical source at the pool free surface. Under some realistic assumptions, a universal water profile is obtained in terms of a properly-chosen set of non-dimensional variables. Next, the potential radial velocity field is used in combination with a simplified form of Morison's equation to evaluate the additional pressure drop (head loss) caused by the cylindrical spouts. Frictional loss on the plate itself is negligible. Then, the overall water level may be determined as a function of radial coordinate, and, thereby, the minimum spout length required to prevent spout flooding can be assessed.

2. Potential Flow Solution

For this initial step of the solution procedure, the spouts are ignored altogether. Moreover, water is assumed to be inviscid and the flow irrotational. Because of a symmetry about the baffle plate axis, the fluid domain to be considered is bounded between $r=0$ and $r=R$ radially, and between $z=0$ and $z=Z(r)$ vertically. Laplace's equation for the velocity potential $\varphi(r,z)$ may be written as:

$$\partial^2\varphi/\partial r^2 + \partial\varphi/r\partial r + \partial^2\varphi/\partial z^2 = 0 \qquad (1)$$

Fluid velocity radial and vertical components u_r and u_z are defined as $\partial\varphi/\partial r$ and $\partial\varphi/\partial z$, respectively.

Two of the boundary conditions for this problem are:

$$\partial\varphi/\partial z = 0 \text{ at } z=0 \qquad (2)$$
(impervious baffle plate bottom)

$$\varphi \text{ is bounded at } r=0 \qquad (3)$$

Separation of variables in (1) yields, with $\varphi(r,z)=A(r)B(z)$ and each prime superscript referring to derivation:

$$A''/A + A'/(Ar) = -B''/B = \pm k^2, \ k\geq 0$$

Applying (2), and discarding solutions with a logaritmic behavior at $r=0$ such as $Log(r)$, $Y_0(kr)$ and $K_0(kr)$ by virtue of (3), one is left with $\varphi(r,z)$ a linear combination of functions such as $\cosh(kz)J_0(kr)$ and $\cos(kz)I_0(kr)$. The former type is typical of radially symmetrical wave potentials because of the oscillatory nature of J_0; on the other hand, I_0, like all modified Bessel functions of the first kind, monotonically increases from a finite value. Since u_r is expected to monotonically increase between baffle plate axis and edge, the solution of equations (1), (2) and (3) is chosen to be, by a heuristic argument:

$$\varphi(r,z) = C\cos(kz)I_0(kr)$$

Then, we obtain $u_r = Ck\cos(kz)I_1(kr)$ and $u_z = -Ck\sin(kz)I_0(kr)$. The two constants k and C must be determined by applying additional boundary conditions at $r=R$ and $z=Z(r)$. As water is discharged over the baffle plate edge, we assume that $Z(R)$ is the critical depth Z_c, defined as the cubic root of Q^2/g; this corresponds to a flow over a fall, as discussed in Binder (1973), and should yield a "minimum" pool level. Then, we have the following discharge condition at $r=R$:

$$Q = \int_0^{Z_c} u_r \ dz = C\sin(kZ_c)I_1(kR) \qquad (4)$$

The flow is fed from above by the spray of falling droplets which originate at the spout exits; these droplets carry momentum and energy as they hit the pool surface, generating chaotic wavelets and ripples; this aspect of the problem is neglected, however, and the spray contribution is modelled by a uniform two-dimensional vertical source q equal to $V/(\pi R^2)$. A vector normal to $Z(r)$ (pointing outward) is $n\{-dZ/dr,1\}$, and the outflow across $Z(r)$, i.e. the scalar product $u.n$, must be equal to $-q$, yielding:

$$\cos(kZ)I_1(kr) \ dZ/dr -\sin(kZ)I_0(kr) =-q/(kC) \ (5)$$

Before proceeding further, we can express the conservation of momentum anywhere in the fluid by means of Bernoulli's equation, Laplace's equation being only kinematic in nature:

$$\{ u_r^2 + u_z^2 \}/2 + gz + p/\rho = \text{constant}$$

Differentiating the above equation with respect to r along $z=Z(r)$, where p is the constant evaporator ambient pressure, yields:

$$dZ/dr = - (u_r du_r/dr + u_z du_z/dr)/g \qquad (6)$$

Since $I_1(0)=0$, and I_1 is the derivative of I_0, du_z/dr, u_r, and thus, dZ/dr vanish at the origin, which is physically expected; applying this result to (5), for $r=0$, and calling Z_m the water level there, we obtain:

$$\sin(kZ_m) = q/(kC)$$

i.e., using (4) and the definition $Q = qR/2$:

$$\sin(kZ_m) = 2\sin(kZ_c)I_1(kR)/kR \qquad (7a)$$

Integrating (6) between $r=0$ and $r=R$, and noting that $u_z(0)=-q$, yields:

$$Z_m - Z_c = \{ u_r(R)^2 + u_z(R)^2 - q^2 \} /(2g) \quad (7b)$$

or, after substituting the values of $u_r(R)$ and $u_z(R)$:

$$(Z_m - Z_c)/Z_c = (1/2) kZ_c)^2 \{ 1/\tan^2(kZ_c) + I_0(kR)^2 I_1(kR)^2 \} - q^2/(2gZ_c)$$

(7a) and (7b) are two equations in the two unknowns Z_m and k. At this point, we assume that kZ(r) << 1. In addition, we define the non-dimensional free-surface elevation $Z^* = Z/Z_c$, and the problem characteristic number $\eta = kR$. Thus, (7a) and (7b) become:

$$Z_m^* = 2I_1(\eta)/\eta$$

$$Z_m^* = 3/2 + \{kZ_c I_0(\eta)/I_1(\eta)\}^2/2 - q^2/(2gZ_c)$$

The numerical solution of these equations in Z_m and η was performed for the warm seawater flowrate (6.0 m^3/s) and baffle plate diameters (6.35 and 4.1 m) corresponding to the two evaporators of the OC-OTEC plant design described in Nihous, Syed and Vega (1989). For these cases and for all practical conditions, $Z_m^* \approx 3/2$ so that η is the solution of $I_1(\eta) = 3\eta/4$, i.e. $\eta \approx 1.86$. This leads to a "universal" potential-flow pool elevation $Z^*(r^*)$, with $r^* = r/R$, shown on Figure 1: retaining only the leading term $u_r^2/(2g)$ when integrating (6), with kZ(r) << 1, yields:

$$Z^*(r^*) = 3/2 - \{I_1(r^*\eta)/I_1(\eta)\}^2/2 \quad (8a)$$

Additional quantities are utilized in the following section. Non-dimensional radial velocity and acceleration, u_r^* and $u_r'^*$, and integrals D and E are defined below:

$$u_r^* = u_r/\sqrt{gZ_c} = I_1(r^*\eta)/I_1(\eta) \quad (8b)$$

$$u_r'^* = (R/gZ_c) u_r du_r/dr = \eta I_1(r^*\eta)\{I_0(r^*\eta) - I_1(r^*\eta)/(r^*\eta)\}/I_1^2(\eta) \quad (8c)$$

$$E = \int_0^1 u_r^* dr^* = 1/2 \quad (8d)$$

$$F = \int_0^1 u_r^{*2} dr^* \approx 0.25 \quad (8e)$$

3. Spout Head Loss

As seawater is drained across the baffle plate, we assume that the force F exerted by the fluid upon each vertical cylindrical spout can be simply represented by Morison's equation, with "far-field" fluid kinematics corresponding to the potential flow solution:

$$F(r) = 0.5\rho C_d DZ u_r^2 + 0.25\rho C_m \pi D^2 Z u_r du_r/dr \quad (9)$$

Because of the great number of spouts (N_s >>1), these are considered to be uniformly distributed with the density ($N_s/\pi R^2$). While the fluid moves from r to r+dr, it is exposed to $2\pi r(N_s/\pi R^2)dr$ spouts and the force required is $2\pi r(N_s/\pi R^2)dr$ times $F(r)$, through the vertical surface $2\pi rZ$: the pressure drop incurred by the fluid between r and r+dr is then $(N_s/\pi R^2)F(r)dr/Z$. The additional pool elevation $H_s(r)$ due to the presence of spouts, at a given radial coordinate r, is equal to the cumulative head loss (pressure drop divided by ρg) between r and R:

$$H_s(r) = N_s D/(\pi g R^2)\int_r^R (0.5 C_d u_r^2 + 0.25 C_m \pi D u_r du_r/dr)dr$$

Using definitions (8b) and (8c) yields:

$$H_s^*(r^*) = N_s D\{\int_{r^*}^1 (0.5 R C_d u_r^{*2} + 0.25 C_m \pi D u_r'^*)dr^*\}/(\pi R^2)$$

By virtue of (8e) and (8f), it can be seen that $H_s^*(0) \approx N_s D \{ R C_d + C_m \pi D \} /(8\pi R^2)$.

Figure 1 shows $H_s^*(r)$ for $N_s = 122$, D = 0.25 m, $C_d = 1$, $C_m = 2$, V = 6.0 m^3/s, R = 6.35 and 4.1 m. Overall dimensional pool levels $Z(r) + H_s(r)$ are plotted on Figure 2.

4. Conclusion

The present model permits the assessment of minimum OC-OTEC evaporator spout length and pool level as a function of warm seawater flow rate and baffle plate radius. It is applied to the case of a 1 MWe plant design to evaluate the effect of reducing the baffle plate radius from 6.35 m

to 4.1 m, for a volume flow rate of 6 m³/s; the minimum pool level is shown to rise from less than 0.25 m to about 0.35 m.

Nomenclature

A : r-dependent term in φ

B : z-dependent term in φ

C : proportionality constant in φ (m²/s)

C_d : spout drag coefficient

C_m : spout added-mass coefficient

D : spout diameter (m)

F : force exerted by the fluid upon one vertical spout (N)

g : acceleration of gravity (m/s²)

H_s : head loss due to the presence of the spouts (m)

H_s^* : non-dimensional head loss, H_s/Z_c

k : characteristic inverse-length (m⁻¹)

n : a vector normal to Z(r), {-dZ/dr,1}

N_s : total number of spouts

p : pressure (Pa)

q : two-dimensional source strength, $V/(\pi R^2)$ (m/s)

Q : discharge, $V/(2\pi R)$ (m²/s)

r : radial coordinate measured from baffle plate axis (m)

r^* : non-dimensional radial coordinate, r/R

R : baffle plate radius (m)

u : fluid velocity vector, {u_r, u_z}

u_r : radial velocity (m/s)

u_r^* : non-dimensional radial velocity, $u_r/\sqrt{gZ_c}$

$u_r'^*$: non-dimensional radial acceleration, $(R/gZ_c)u_r du_r/dr$

u_z : vertical velocity (m/s)

V : evaporator volumetric flow rate (m³/s)

z : vertical coordinate measured upward from pool bottom (m)

Z^* : non-dimensional pool free-surface elevation, Z/Z_c

Z : pool free-surface elevation (m)

Z_c : critical depth at baffle plate edge (m)

Z_m : (maximum) water level at baffle plate axis (r=0) (m)

η : charateristic number, kR

φ : velocity potential for the radially symmetric problem (m²/s)

ρ : fluid density (kg/m³)

References

Binder, R. C., Fluid Mechanics, pp. 338-339, Prentice-Hall, 5th Edition, 1973.

Nihous, G. C., M. A. Syed, and L. A. Vega, "Conceptual Design of an Open-Cycle OTEC Plant for the Production of Electricity and Fresh Water in a Pacific Island", Proceedings of the International Conference on Ocean Energy Recovery, Honolulu, November 1989.

Wassel, A. T., and S. M. Ghiaasiaan, "Thermal-Hydraulic Analysis of the 1 MWe OC-OTEC Test Facility", prepared for the Solar Energy Research Institute, Contract#SAI-083-084R-017-LA, October 1983.
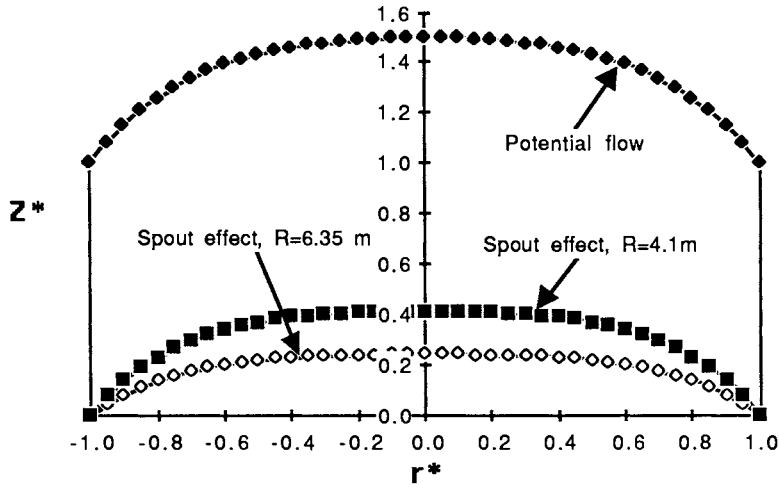
Figure 1 - Non-dimensional potential-flow pool-level profile and spout-induced head losses (V = 6 m³/s, R = 6.35 m and 4.1 m).
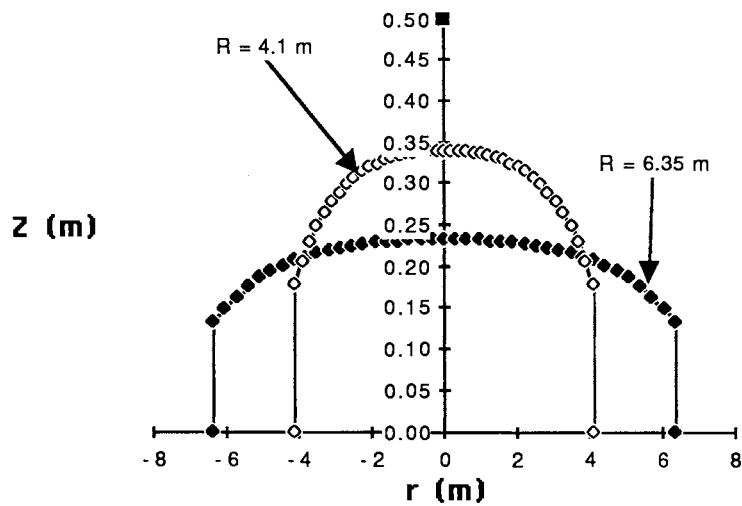
Figure 2 - Pool-level profiles (V = 6 m³/s, R = 6.35 m and 4.1 m).

NEAR TERM MARKET POTENTIAL FOR OTEC IN THE PACIFIC BASIN

L. A. Vega, A. R. Trenka

Pacific International Center for High Technology Research Honolulu, Hawaii, U.S.A.

Abstract

A straightforward analytical model is developed to compare the cost of electricity produced either with OTEC or with petroleum or coal-fired plants. Two generalized markets are considered: industrialized islands (e.g., Oahu, Taiwan); and, smaller less-developed islands with modest needs (e.g., Molokai, Western Samoa). The model is used to establish scenarios under which OTEC could be competitive.

Given the stage of development, it is postulated that the first OTEC commercial plants will be 1 to 10 MWe land-based plants designed for the less-developed islands. The analysis shows that these plants will have to be based on the open-cycle principle wherein desalinated water must be produced to offset the, relatively, higher cost of electricity; and, that their commercialization must be preceded by the installation of a demonstration plant of at least 1 MWe and 3,500 m3, of desalinated water, per day production capacity. This plant would be used to obtain operational information and optimize the design of the first generation of commercial plants.

It is determined that plants of at least 40 MWe capacity would be required for the industrialized islands; and, that if land-based, they should also produce desalinated water to reach wider scenarios. For this purpose, it is proposed to use a hybrid plant, based on the closed-cycle for the electricity production and a second-stage, for desalinated water production, consisting of a flash (vacuum) evaporator and surface condenser. A land-based hybrid demonstration plant of at least 5 MWe and 7,500 m3/day production capacity would have to be designed, installed and operated to optimize the design of the commercial plants.

Closed-cycle plants, without second-stage desalinated water production, are found to be cost effective if housed in self-propelled floating vessels supporting energy intensive factories (e.g., hydrogen factoryship); or a vessel moored, or dynamically positioned, a few kilometers from land, transmitting the electricity to shore via submarine power cables. It is recommended that a floating 5 MWe demonstration plant be designed, installed and operated prior to the commercialization of plants of at least 40 MWe capacity.

The scenarios, under which OTEC is compared with conventional techniques to assess its cost effectiveness, are defined by two parameters: fuel cost; and cost of fresh water production. In the absence of natural sources of fresh water, it is postulated that the cost of producing desalinated water from seawater via reverse osmosis (RO) be considered as a conventional alternative. This technique yields a direct relationship between desalinated water production and fuel cost; and, therefore a scenario defined with one parameter.

Background

The search for renewable sources of energy has resulted in the revival of a concept based on the utilization of the differences in temperature between the warm (22°C to 29°C) tropical surface waters, and the cold (4°C to 5°C) deep ocean waters available at depths of about 1,000 m, as the source of the thermal energy required to vaporize and condense the working fluid of a turbine-generator system. This concept is referred to as Ocean Thermal Energy Conversion (OTEC).

There are two approaches to the extraction of thermal energy from the oceans, one referred to as "closed-cycle" and the other as "open-cycle." In the closed-cycle, seawater is used to vaporize and condense a working fluid, like ammonia, which drives a turbine-generator in a closed loop, producing electricity. In the open-cycle, surface water is flash-evaporated in a vacuum chamber. The resulting low-pressure steam is used to drive a turbine-generator. Cold seawater is used to condense the steam after it has passed through the turbine. The open-cycle can, therefore, be configured to produce fresh water as well as electricity.

The closed-cycle was first proposed in 1881, by D'Arsonval in France, and was demonstrated in 1979, when a small plant mounted on a barge off Hawaii (Mini-OTEC) produced 50 kW of gross power, for several months, with a net output of 18 kW. This closed-cycle plant was sponsored by private industry and the State of Hawaii. Subsequently, a 100 kW gross power land-based plant was operated in the island nation of Nauru by a consortium of companies sponsored by the Japanese government. These plants were designed with public relations as the main objective and minimal operational data was obtained.

The open-cycle concept was first proposed in the 1920's and demonstrated in 1930, off Cuba by its inventor, a Frenchman by the name of Georges Claude. His land-based demonstration plant was designed to resolve some of the ocean engineering issues common to all OTEC plants and, hopefully, to produce net electricity. This plant made use of a direct contact condenser; therefore, fresh water was not a by-product. The plant failed to achieve net power production because of a poor site selection (e.g., thermal resource) and a mismatch of the power and seawater systems; however, the plant did operate for several weeks.

An OTEC hybrid cycle, wherein electricity is produced in a first-stage (closed-cycle) followed by water production in a second-stage, has been proposed as a means to maximize the use of the thermal resource available and produce water and electricity [1]. In the second-stage, the temperature difference available in the seawater effluents from an OTEC plant (e.g.: 12°C) is used to produce desalinated water through a system consisting of a flash evaporator and a surface condenser (basically, an open-cycle without a turbine-generator). In the case of an open-cycle plant, the addition of a second-stage results in doubling water production. Fresh water production with a flash-evaporator and surface condenser system was demonstrated in 1988 in a facility built by the U.S. Department of Energy at the Natural Energy Laboratory of Hawaii (NELH).

Floating vessels, approaching the dimensions of supertankers, housing factories operated with OTEC-generated electricity or transmitting the electricity to shore via submarine power cables have been conceptualized. Large diameter pipes suspended from these plantships extending to depths of 1,000 m are required to transport the deep ocean water to the heat exchangers onboard. The design and operation of these cold-water-pipes as well as the required extended use of the heat exchangers, exposed to biologically and chemically active ocean waters, are major issues that have been resolved [5].

The proof-of-concept projects (i.e., Mini-OTEC, Nauru, Claude, Reference 5) demonstrated that both cycles are technically feasible and only limited, by the large diameters required for the cold water pipe, to sizes of no more than about 85 MW gross [4]. In the case of the open-cycle, due to the low-pressure steam, the turbine, is presently, limited to sizes of no more than 3 MW gross.

Industry has not taken advantage of this information because, at present, the price of oil fuels and coal are such that conventional power plants produce cost-effective electricity. Moreover, the power industry can only invest in power plants whose design is based on similar plants with an operational record. Before OTEC can be commercialized, a prototypical plant must be built and operated to obtain the information required to design commercial systems and to gain the confidence of the financial community and industry. Conventional power plants pollute the environment more than an OTEC plant should and the fuel for OTEC is unlimited and free, as long as the sun heats the oceans; however, it is futile to use these

arguments to convince the financial community to invest in OTEC plants without an operational record.

The trust of the U.S. OTEC programs, at present, is to design and build an experimental open-cycle plant that will produce net power and fresh water; and, to operate the experimental plant for at lease two years as a showcase for financial institutions and to obtain the data base required as input to the design of commercial-size plants. Given the seawater resource already available at the Natural Energy Laboratory of Hawaii (NELH) and the limited funding available, a relatively small 200 kW gross power version has been selected. This experimental apparatus is referred to as the Net Power Producing Experiment (NPPE).

Once the NPPE apparatus is operational, the transition to full commercialization will be accomplished through fabrication of a few small plants producing electricity and water in island communities where open-cycle OTEC systems are now cost effective.

OTEC Potential Market

The following global indicators are useful in relating the size of the plants under discussion with the needs of a community: (1) domestic water needs in developed nations are met with 50 gallons (200 l) per person per day; in agricultural regions the use is 7 to 10 times larger; (2) the electrical power needs (domestic and industrial) of each 1,000 people are met with 1 MW in industrialized nations, while in less developed countries the needs of 5 to 15 times more people can be met with 1 MW.

There are at least two distinct markets for OTEC in the Pacific Basin: (i) industrialized islands; and (ii) smaller or less industrialized islands. Islands with modest needs for power and fresh water like Molokai and Western Samoa, could use small open-cycle plants. These plants could be sized to produce from 1 to 10 MW electricity, and at least 450 thousand to 8 million gallons of fresh water per day (1,700 to 30,000 m³/day).

Hybrid cycle plants can be used in either market by producing electricity and water. For example, a 40 MW hybrid cycle plant could also produce as much as 16 million gallons of water per day (60,600 m³/day). One can envision two plants tailored to the Island of Hawaii (i.e., Big Island) market, as well as smaller plants satisfying all the electricity and power needs of Molokai. In the case of Oahu (population of approximately 750,000 people) all the water needs, and 20% to 30% of the power needs could be met with two to three large plants. Taiwan could use several 40 to 85 MW hybrid cycle plants.

In a study sponsored by the U.S. State Department, it was concluded that the majority of the island nations in the tropics and subtropics had the required ocean water resources, within their territorial waters, to supply all their power needs with floating OTEC [7]. Most of these islands are lacking adequate fresh water supplies and do not have extensive electricity and water distribution systems. Therefore, it would be ideal to utilize open-cycle or hybrid

OTEC plants of the appropriate size to provide the water and electricity needs of specific communities within these islands.

To assess scenarios under which OTEC might be competitive with conventional technologies, in the production of electricity and water, a straightforward analytical model is developed.

The capital cost for OTEC plants, expressed in 1989 $/kWe, is established assuming modest engineering development. The relative capital cost of producing electricity ($/kWh) with OTEC, offset by the desalinated water production, is then equated to the fuel cost of electricity produced with conventional techniques to determine the scenarios (i.e., fuel cost and cost of fresh water production) under which OTEC could be competitive. Inherent to this approach is the assumption that operation and maintenance costs are the same for OTEC and conventional plants of the same power capacity.

No attempt is made at speculating about the future cost of fuel. It is simply stated that if a situation is represented by one of our scenarios, OTEC would be competitive.

For each scenario obtained, the cost of desalinated water produced from seawater by reverse osmosis (RO) is also given because this cost must be greater than the water production credit that OTEC requires to be cost effective. Once the cost effective scenarios are established, under our straightforward approach, a more rigorous economic analysis can be performed to model expected inflation and levelized costs.

OTEC Capital Cost Estimates and Production Rates

The capital costs required to build OTEC plants have been previously estimated (e.g., References 1, 3, 4 and 6). These estimates are summarized herein for land-based plants rated at 1, 10 and 40 MW-net as well as for a 40 MW-net plantship. Production rates are for 0.8 capacity factors (i.e., 7,000 hours of operation per year).

Table 1 gives the estimates for 1 MW-net (nominal) open-cycle plants with and without second-stage desalinated water production as well as a plant with a system including the use of 90 kg/s of 6°C cold seawater as the chiller fluid for a standard air-conditioning unit supporting a 300 ton load. For the purpose of this discussion the 240 kWe of electricity displaced, in this fashion, are considered as additional production, resulting in a total production of 8.6 x 10^6 kWh and an adjusted equivalent capital cost of 20,000 $/kW-net. The cost figures are expressed in 1989 dollars. These plants would be designed utilizing the state-of-the-art bottom-mounted cold water pipe technology (i.e., 1.6 m diameter high-density polyethylene pipe) [1]. It is assumed that the 1 MW plants could be deployed some time after 1995. Their commercialization must be preceded by the installation of a demonstration plant of 1 MWe and 3,500 m^3, of desalinated water, per day production capacity.

Capital costs and production rates for land-based plants are summarized in Tables 2 and 3 for 10 MW open-cycle plants, considered, at present, to be the maximum size for this cycle, and 40 MW closed-cycle or, if water production is marketable, hybrid cycle plants. The design of the 10 MW open-cycle plant would be scaled from the 1 MW demonstration plant with a new design for bottom-mounted cold water pipes [4]. The commercialization of the 40 MW plants must be preceded by the design and operation of a 5 MWe closed-cycle demonstration plant. These plants also require the development of cold water pipes [4].

To consider the moored or slowly drifting OTEC plantship, in the discussions that follow, a capital cost of 4,500 $/kW-net is estimated for an electrical production of 380 x 10^6 kWh (slightly higher than for the land-based plants because of lower pumping power requirements). The cost differential between the moored and the drifting vessels are insignificant at this level of discussion because the savings in mooring system and power cable are offset by the propulsion and positioning requirements, as well as by the product transport, for the factory ship. This cost is also given in 1989 dollars for a system to be deployed by the Years 2000 to 2005 assuming modest engineering development. These plants would be designed utilizing the methodology already available for cold water pipes suspended from a vessel [5].

Conventional Production of Electricity

The thermal efficiency (η) of conventional steam power plants, fired with oil or coal, ranges from 32% to 34% and has been reported to be as high as 36%. The higher value will be assumed in this report. This implies that 36% of the heat added is converted to net work. Net work is defined as the difference between the output from the turbine-generator and the work required to run the plant.

The cycle efficiency for diesel fuel power plants used in Pacific Islands probably ranges from 25% up to 35%. A properly maintained and operated plant can reach efficiencies of up to 36%. This value will be assumed here to determine the work available from the heat added by the diesel fuel. This value is higher than realized in small steam power plants used for generation of electric power only. However, the cost of fuel suitable for the diesel generator is higher than the fuel suitable for the steam plant. Due to fuel availability, most island nations with small electricity requirements (a few MW) utilize diesel generators.

The convention followed in power plant technology, to express plant performance is to consider the heat added to produce a unit amount of work. This parameter is called the heat rate (HR) of the plant and is usually given in Btu/kWh. Therefore, the heat rate is inversely proportional to the thermal efficiency, $\eta = 3413/HR$ (i.e., 1 kWh =

PLANT NOMINAL SIZE:	1 MW; OC-OTEC	1 MW; OC-OTEC with 2nd-Stage	1 MW; OC-OTEC with 2nd-Stage and 300 ton A-C
PRODUCTION:			
Electricity	8.1×10^6 kWh	7.3×10^6 kWh	6.9×10^6 kWh plus the A-C equivalent
Water	0.45 MGD (1,700 m³/day)	0.94 MGD (3,560 m³/day)	0.94 MGD (3,600 m³/day)
A-C Electricity Equivalent	---	---	300 ton A-C @ 0.8 kW/ton Equivalent to 1.7×10^6 kWh
CAPITAL COST:	18,000 $/kW-net	23,000 $/kW	20,000 $/kW (adjusted)
YEAR DEPLOYED:	1995	1995	1995

NOTE: Estimates are from Reference 1 for the Capital Cost expected after engineering development in compressors and turbine efficiency as well as for cost reductions in surface condensers from $215/m² to $100/m². State-of-the-art seawater piping systems are used.. The estimate for the plant with a 300 ton A-C is for electricity production savings due to the use of 90 kg/sec of cold seawater (3% of the total cold water required for power cycle) as a chiller fluid for a standard A-C unit.

Table 1. Capital Cost Estimates ($/kW-net) for 1 MW Land-Based Plants in 1989 Dollars

PLANT NOMINAL SIZE:	10 MW; OC-OTEC	10 MW; OC-OTEC with 2nd-Stage
PRODUCTION:		
Electricity	70×10^6 kWh	63×10^6 kWh
Water	4 MGD (15,000 m³/day)	8 MGD (30,000 m³/day)
CAPITAL COST:	11,000 $/kW-net	15,000 $/kW
YEAR DEPLOYED:	2000	2000

NOTE: Estimates are from Reference 3 for the Capital Cost expected after cost reductions in surface condensers from $215/m² to $100/m²; engineering development resulting in improved turbines and vacuum compressors and new cold-water-pipe technology.

Table 2. Capital Cost Estimates ($/kW-net) for 10 MW Land-Based Plants in 1989 Dollars

PLANT NOMINAL SIZE:	40 MW; CC-OTEC	40 MW; Hybrid Ammonia Power Cycle with 2nd-Stage Water Production
PRODUCTION:		
Electricity	336×10^6 kWh	280×10^6 kWh
Water	n/a	16 MGD (60,600 m³/day)
CAPITAL COST:	6,000 $/kW	9,200 $/kW
YEAR DEPLOYED:	2000 to 2005	2000 to 2005

NOTE: Estimates are rom Reference 3 adjusted as described in Table 2.

Table 3. Capital Cost Estimates ($/kW-net) for 40 MW Land-Based Plants in 1989 Dollars

3413 Btu at 60°F), such that a thermal efficiency of 36% corresponds to a HR of 9500 Btu/kWh.

The heating values of standard coal and fuel oil are 12,000 x (1 ± 0.17) Btu/lbm and 144,000 x (1 ± 0.04) Btu/U.S. gallon, respectively. Therefore, the fuel cost incurred in producing electricity, expressed in $/kWh, with an oil-fired plant is 1.57 x 10^{-3} times CB, the cost of a barrel (42 U.S. gallons) of fuel [9500 Btu/kWh/ 42 gallons/barrel x 144,000 Btu/gallon = 0.00157 barrel/ kWh]. The same expression will be used for diesel generators. For example, at $18 per barrel, the fuel cost is 0.0283 $/kWh.

A 180 MW coal-fired plant under design for Oahu will use Indonesian coal, with a baseline heat value of 12,500 Btu/lbm, to be delivered to the plant for $2.25 per million Btu ($62 per metric ton) such that the fuel cost incurred in producing electricity with a thermal efficiency of 36% would be 0.021 $/kWh [9500 Btu/kWh x $2.25 / 10^6 Btu]. This is equivalent to oil fuel cost of $13/barrel.

The electric output will be sold to Hawaiian Electric Company under a 30-year contract. The total capital cost of the project has been estimated to be $383.5 million; or $2,100/kW [8].

Conventional Production of Desalinated Water

The cost of producing fresh water from conventional desalination plants (i.e., Reverse Osmosis and Multistage Flash) ranges from about 1.3 to 2 $/m³ for a plant capacity of 4,000 m³/day to approximately 1 $/m³ for a 40,000 m³/day plant.

The energy (cost) used in multistage flash (MSF) distillation is in the form of heat, usually as low pressure steam, and the shaft power to drive pumps and other auxiliaries. Reverse osmosis (RO) plants require energy solely as shaft power from, for example, an electric motor. At present, RO is considered the technique of choice. It can be shown that, RO, fresh water production from seawater costs 0.049.CB, in $/m³, where CB is the cost of a barrel (42 gallons) of fuel. This expression is used here to establish the desalinated water cost corresponding to a given fuel cost scenario.

OTEC Production of Electricity

The following formula is used to calculate the production cost of electricity p levelized over the assumed life for the OTEC plant (nominal value: 30 years):

p ($/kWh) = (FC.CC + OM.G.CR) / (NP.CF.8760)

FC : annual fixed charge, taken as 0.10

CC : plant overall investment capital cost, in

OM : operation and maintenance yearly $ expenditures

G : present worth factor, in years, estimated value 20

CR : capital recovery factor, taken as 0.09

NP : net power production, in kW

CF : production capacity factor, chosen as 0.80

8760 : number of hours in one year (CF.8760 = 7,000)

The first term simply represents the payment for a fixed interest loan valued at CC, $, over a prescribed term expressed in hourly payments, where, the loan is for a plant rated at a power of NP, kW. The second term models the levelized cost of operating and maintaining the plant over the term.

For closed-cycle plants, p is estimated with no credit taken for the sale of the fresh water by-product.

Fresh water credit is obtained by multiplying the unit price by the yearly production and subtracting the result from the numerator of the expression given above. For example, a production of 160,000 kilogallons per year at a unit price of $6/kgal for a net power production (NP) of 1,000 kWe and a capacity factor of 0.80 would yield a credit of $0.14/kWh. Under a rigorous approach, the unit price would be levelized (i.e., multiplied by G.CR or 1.8).

The capital cost estimates given above (e.g., Tables 1, 2 and 3) indicate that OTEC is a capital-intensive technology. For example, the capital costs for oil-fired plants and coal-fired plants are less than $2,100/kW, as compared with the $11,000/kW and $6,000/kW given for the 10 MW and 40 MW plants in Tables 2 and 3. The 1 MW plant should be compared with diesel generators whose capital cost is less than 3% the cost of OTEC. However, OTEC incurs no fuel costs while conventional steam plants and diesel generators incur fuel costs. The levelized cost of OTEC electricity can be estimated from the equation given above (e.g., References 1 and 3); however, for the purpose of this report the capital cost of OTEC electricity, adjusted for the capital cost of the conventional technology (taken as $2,000/kW for oil or coal-fired plants and neglected for diesel generators) and the desalinated water by-product, will be compared with the fuel cost for conventional power plants to determine scenarios, given by the costs of electricity and water in a particular location, under which an OTEC plant of a given size could be cost competitive. Implicit in this approach is the assumption that O&M costs are similar for OTEC and conventional plants of the same power rating.

This approach can be formalized as follows for oil-fired plants:

(FC.CC - WC.PW) / (CF.8760.NP) < 1.57 x 10^{-3} .CB

Where, FC, CC, CF and NP are defined above, and

WC : unit price of water, in $/m³

PW : yearly production of water, in m³/year

CB : cost of a barrel of fuel (42 gallons), in $/barrel.

The production capacity factor (CF) is taken as 0.8 (80%) and the fixed charge for the capital (FC) as 0.1 (10%) and all values are expressed in present day costs. The water

NOMINAL NET POWER (MWe)	TYPE	SCENARIO REQUIREMENTS	SCENARIO AVAILABILITY
1 (Table 1)	Land-Based OC-OTEC with 2nd-Stage additional Water Production	• $45/barrel of diesel • $1.6/m³ water	South Pacific Island Nations by Year 1995
10 (Table 2)	Land-Based (as above)	• $25/barrel of fuel oil • $0.85/m³ water —or— • $30/barrel with • $0.8/m³ water	American Island Territories and other Pacific Islands by Year 2000
40 (Table 3)	Land-Based Hybrid (ammonia power cycle with Flash Evaporator downstream)	• $44/barrel of fuel oil • $0.4/m³ water —or— • $22/barrel • $0.8/m³ water	Hawaii, if fuel or water cost doubles by Year 2000
40	• Closed-Cycle Land-Based • Closed-Cycle Plantship	• $36/barrel • $23/barrel	by Year 2005

• OC-OTEC limited by turbine technology to 2.5 MW modules or 10 MW plant (with four modules)
• CC-OTEC or Hybrid (water production downstream of closed-cycle with flash evaporator)

Table 4. OTEC Market Penetration Scenarios

production of an open-cycle plant is related to the amount of warm seawater utilized in the power cycle (i.e., between 0.4% and 0.5% of the warm seawater is flash evaporated in the process). As given in Tables 1, 2 and 3, this can be expressed as, PW = 160 x 10⁶ gal/year/MW (or 60 x 10⁴ m³/year / MW-net). The second-stage described above would, therefore, double the water production in the case of an open-cycle with second-stage or yield water production (PW) in the case of the hybrid plant (i.e., flash evaporator/surface condenser downstream of closed-cycle plant). Therefore, to determine the scenarios under which OTEC is competitive with oil-fired plants, the following expressions are used:

$$\frac{CC^*}{NP} = 110.CB + 6{,}000\ WC,$$ for open-cycle and hybrid cycle;

and

$$\frac{CC^*}{NP} = 110.CB + 12{,}000\ WC,$$ for open-cycle with second-stage.

* For the 10 MW and 40 MW cases, $2,000/kW are subtracted from the capital cost of OTEC to account for the capital cost of the conventional steam power plant. For diesel generators the capital cost can be neglected.

The scenarios identified following this procedure are summarized in Table 4 for the capital cost and net power given in Tables 1, 2 and 3 for 1, 10 and 40 MW plants. Diesel fuel is considered at the 1 MW level, while less expensive oil fuel is used for the 10 MW and 40 MW cases.

1 MW Plants

This approach indicates that the 1 MW open-cycle with second-stage water production (i.e., Table 1) will be competitive in a scenario given by a location where a high unit price of water, 1.6 $/m³ (6 $/kilogallon), and diesel fuel costs at $45/barrel. The cost of producing desalinated water via RO would be 2.2 $/m³ at this fuel cost. This scenario corresponds to conditions existing in certain less-developed Pacific Island Nations with small populations (e.g., Western Samoa). For example, in 1989 the cost of imported diesel fuel paid by the power companies was $47/barrel in Western Samoa [10]; $50/barrel in the Kingdom of Tonga [9]; and, $25/barrel in Molokai.

The analysis indicates that small open-cycle OTEC plants (Table 1) without second-stage water production could only be competitive under a scenario of diesel at $76/barrel and the high unit price for the water, 1.6 $/m³. This scenario does not appear likely. A 1 MW closed-cycle plant would require a scenario where the diesel cost is $164/barrel.

It is interesting to note that the plant including a 300 ton A-C system, described in Reference 1 and summarized in the last column of Table 1, would be competitive under a scenario given by $45/barrel and 1.25 $/m³ of water. This plant could be deployed by the year 1995.

10 MW Plants

For the 10 MW open-cycle plant with second-stage water production, with a capital cost estimate of $15,000/kW (i.e., Table 2), a scenario given by $25/barrel of oil fuel and 0.85 $/m³ of water; or, $30/barrel and 0.8 $/m³ of water is plausible in American Island Territories and other Pacific Islands (e.g., Molokai) by the Year 2000. As indicated above, the capital cost for OTEC has been adjusted to account for the $2,000/kW capital investment for oil fuel plants. Once more, the additional water production makes the difference for OTEC for these relatively small plants. The cost of producing desalinated water via RO would be 1.2 $/m3 and 1.5 $/m3 for fuel at $25/barrel and $30/barrel respectively; and, therefore greater under both scenarios.

A 10 MW closed-cycle plant, with a capital cost estimate of $11,000/kW-net, would only be attractive under a scenario of $82/barrel and no water requirements. This analysis implies that closed-cycle plants of 1 to 10 MW size are unlikely to be cost effective.

There are at present discussions, in the public sector, regarding taxing the electricity produced by non-renewable resources like oil fuels at a rate of $0.02/kWh. This is equivalent to adding $13 per barrel (42 gallons) of fuel to the cost of electricity production. This tax would not suffice to make small OTEC plants cost effective without water production.

40 MW Plants

The land-based plant without water production summarized in Table 3 can be competitive under a scenario of fuel oil at $36/barrel. This is plausible by the years 2000 to 2005. If water production is considered, in Hawaii, with a hybrid cycle plant, a scenario given by oil fuel at $44/barrel and the present unit price of water at $0.4/m³ per 1,000 gallons; or another scenario wherein the unit price of water doubles and oil fuel is $22/barrel would be required for the 40 MW plant. These scenarios might occur by the first decade of next century. The cost of RO water production is greater under both scenarios.

The plantship, housing a closed-cycle 40 MW plant, discussed in previous sections ($4500/kW for capital cost), could be competitive under a scenario of $23/barrel. This is a likely scenario in the near future.

Development Requirements

The analysis presented above indicates that there is a market for OTEC plants that produce electricity and water. Industrialized islands like Oahu and Taiwan, as well as island nations under development, could make use of hybrid plants like the one summarized in Table 3. Less developed or smaller islands could use open-cycle plants with second-stage additional water production (e.g., Table 2) and plantships could make use of the electricity generated with 40 MW closed-cycle plants.

However, operational data must be made available to, for example, establish production factors and plant reliability. These data can only be obtained by building and operating demonstration plants scaled from the commercial-size plants listed in Tables 1, 2 and 3. A plan aimed at achieving the development of OTEC under the scenarios determined in this report can be summarized as follows:

OTEC Development Program Required

Years	Project	Funds Required
1990–1995	A) • Develop advanced bottom-mounted Cold Water Pipes (CWP), • Reduce the cost of Surface Condensers; and, • Develop Low Pressure Steam Turbines rated at about 3 MWe.	$ 10 M
	B) OC-OTEC / 2nd-stage Demonstration Plant (1 MWe / 3,500 m³/day) using state-of-the-art	$ 30 M
1995–2000	C) Deploy Land-Based Plants Optimized from (B) (Total 5 MWe / 17,500 m³/day)	International Banking / Aid Community
	D) Hybrid Land-Based Demonstration Plant (5 MWe / 7,500 m³/day) using newly developed CWP	$ 75 M
	E) CC-OTEC Plantship Demonstration Plant (5 MWe) using existing technology	$ 60 M
2000–2005	F) Deploy 300 MWe of Land-Based Plants in Pacific and Asia. Optimized from (D)	Private
	G) Deploy several 50 MWe Plantship in Tropical Waters Optimized from (E)	Private
2005–2010	H) Provide Projected Power and Water Increase in small Pacific Islands, and part thereof in Oahu, Taiwan, Philippines, etc., and Plantships. (Cumulative Deployed Power: 2100 MW)	Cumulative Capital Investment $13 Billion

Conclusion

Our analysis shows that the combined production of electricity and fresh water utilizing the principle of Ocean Thermal Energy Conversion (OTEC) is cost effective under certain scenarios defined by the fuel cost of electricity production, with conventional fossil fuel plants, and the production cost of water. At least four scenarios can be envisioned.

One scenario corresponds to small island nations in the Pacific, where the cost of diesel-generated electricity and fresh water is such that a small, 1 MWe, land-based open-cycle OTEC plant, with water production, would be cost effective today. A second scenario corresponds to conditions that are plausible in the near future in American territories like Guam, American Samoa, and Northern Mariana Islands, where land-based open-cycle OTEC plants rated at 10 MWe could be cost effective if credit is given for the fresh water produced. A third scenario corresponds to land-based Hybrid OTEC plants for the industrialized islands market (e.g., Hawaii, Taiwan) producing electricity through an ammonia cycle and fresh water through a flash (vacuum) evaporator. This scenario would be cost effective with a doubling of the cost of oil fuel or doubling of water costs, and for plants rated at 40 MWe or larger. The fourth scenario is for floating OTEC electrical plants, rated at 40 MWe or larger, and housing a factory or transmitting electricity to shore via a submarine power cable. These plants could be deployed in the tropical regions of the Pacific Basin.

To move forward with the development of OTEC, demonstration plants must be built and operated. Demonstration plants should be scaled versions of commercial plants and be operated for at least a couple of years. Conventional power plants pollute the environment more than an OTEC plant should and the fuel for OTEC is unlimited and free, as long as the sun heats the oceans; however, it is futile to use these arguments to convince the financial community to invest in OTEC plants without an operational record.

References

[1]   Nihous, G.C., Syed, M.A., and Vega, L.A., "Conceptual Design of a Small Open-Cycle OTEC Plant for the Production of Electricity and Fresh Water in a Pacific Island", Proceedings, International Conference on Ocean Energy Recovery, Honolulu, Hawaii, November 1989,

[2]   Vega, L.A., "Ocean Thermal Energy Conversion: Development Status and Potential Applicability in the Pacific Basin", Viewgraph Presentation to the 18th Annual Session of CCOP/SOPAC, Canberra, Australia, October 1989,

[3]   Nihous, G.C., Udui, E., and Vega, L.A., "Preliminary Evaluation of Potential OTEC Sites in the Northern Mariana Islands, Guam and American Samoa: Bathymetry and Feasibility", PICHTR Publication, Honolulu, Hawaii, December 1989.

[4]   Vega, L.A., Nihous, G.C., Lewis, L. Resnick, A., and Van Ryzin, J., "OTEC Sea Water Systems Technology Status", Proceedings, International Conference on Ocean Energy Recovery, Honolulu, Hawaii, November 1989.

[5]   Vega, L.A., Nihous, G.C., "At-Sea Test of the Structural Response of a Large Diameter Pipe Attached to a Surface Vessel", Proceedings, Offshore Technology Conference, No. 5708, pp. 473-480, Houston, Texas, May 1988.

[6]   Electric Power Research Institute, "Ocean Energy Technologies: The State of the Art", EPRI AP-4921, November 1986.

[7]   Dunbar, L.E., "Market Potential for OTEC in Developing Nations", Proceedings, 8th Ocean Energy Conference, Washington, D.C., June 1981.

[8]   AES Corporation, "AES Closes $383.5 Million Project Financing for Construction of Power Plant in Hawaii", Press Release, April 3, 1990. Contact: P. Hanrahan, Arlington, Virginia (703) 358-0506.

[9]   Udui, E.S., "Socio-Economic Study of the Kingdom of Tonga", PICHTR Publication, Honolulu, Hawaii, July 1989.

[10] Neill, L., Rath, C., "Assessment of Energy and Water Resources in Western Samoa", PICHTR Publication, Honolulu, Hawaii, April 1990.

DUAL-BEAM ECHO-INTEGRATION FOR PRECISE ESTIMATION OF FISH BIOMASS

Y. Takao, M. Furusawa

National Research Institute of Fisheries Engineering, Japan

Abstract

The echo integration method is indispensable for acoustic surveys of fisheries resources. The dual beam method, which uses a narrow and wide beam pair, is widely used for in situ estimation of fish target strengths. Some quantitative echo sounding systems employ both methods. In those systems the wide beam signal is not ordinarily utilized for echo integration. We have developed the dual beam echo integration method, in which echoes from both narrow and wide beams are integrated. This method can improve the accuracy and precision of acoustic estimates of fish abundance in the following ways. By comparing the integrator outputs for both beams, we can (1) get index of avoidance behaviour of fish to the surveying vessel and (2) measure noise contamination. The variance of the integrator output of the wide beam is smaller than that of the narrow beam for shallow and sparse distributions of fish. Errors caused by transducer motion in bad weather conditions are smaller for the wide beam. By combining both beam echoes we can exactly measure the volume backscattering strength within schools. The method is theoretically and experimentally discussed to confirm its effectiveness.

1. Introduction

The echo integration method has been widely and effectively used for fisheries resources surveys [1]. Recent quantitative echo sounders adopt the dual beam or split beam method in order to improve the accuracy of fish target strength (TS) measurements [2]. The dual beam method utilizes coaxial narrow and wide beams. Pulses are transmitted on narrow beam and echoes are received on both narrow and wide beams or channels. This method corrects for the directivity pattern factor by using both channels' signals from the same fish, and gets an accurate TS value. In ordinary quantitative echo sounders, echo integration is performed only for the narrow beam and not for the wide beam (strictly, composite of narrow and wide beams).

We propose that if we perform echo integration also for the wide channel, we can get more information and improve the accuracy and precision of the estimation. By comparing the integrator outputs obtained for both beams, we can (1) get index of avoidance behaviour of fish to a surveying vessel and (2) measure noise contamination. The variance of the integrator output of the wide channel is smaller than that of the narrow channel for shallow and sparse distributions of fish because the sampling volume is greater for the wide beam. The transducer motion error in bad weather conditions is smaller for the wide beam. By measuring echo level of the wide channel where the echo level of both channels are nearly the same, we can get an accurate measure of volume backscattering strength (SV) within individual fish schools.

At first, we consider the above points theoretically. Next, we examine the theoretical results experimentally using data obtained for walleye pollock (Theragra chalcogramma) in the Aleutian Basin area by our quantitative echo sounding system which provides independent and simultaneous echo integrations for both narrow and wide channels.

2. Theory

2.1 Principle

The sound pressure P_i of a single fish echo is shown by

$$P_i{}^2 = P_0{}^2 D_i{}^4 [r_i \exp(\alpha r_i)]^{-4} Ts_i \qquad (1)$$

where P_0 is the source pressure, $D_i = D(\theta_i, \phi_i)$ is the directivity function in the direction of i-th fish which is located at (r_i, θ_i, ϕ_i), α is the attenuation coefficient, and Ts_i is the value

of TS.

The echo pressure of multiple echoes P_r by N fish is obtained by

$$P_r^2 = \sum_{i=1}^{N} P_i^2$$

$$= P_o^2 [r \exp(\alpha r)]^{-4} \sum_{i=1}^{N} D_i^4 Ts_i \qquad (2)$$

Introducing J infinitesimal volumes with solid angle $\Delta \Omega$ and height of $c\tau/2$ where c is sound speed and τ is pulse duration, we can rewrite Eq.(2)

$$P_r^2 = P_o^2 [r \exp(\alpha r)]^{-4}$$

$$\times \sum_{j=1}^{J} r^2 \Delta \Omega \frac{c\tau}{2} n_J D_J^4 Ts \qquad (3)$$

where n_J is distribution density. This can be reduced to integral of continuous functions as

$$P_r^2 = P_o^2 \frac{\exp(-4\alpha r)}{r^2} \frac{c\tau}{2}$$

$$\times \int_\Omega n D^4(\theta, \phi) Ts d\Omega \qquad (4)$$

where Ω is distribution range of fish.

If the density n is homogeneous in space (Assumption 1), we have

$$P_r^2 = P_o^2 \frac{\exp(-4\alpha r)}{r^2} \frac{c\tau}{2} n \Psi <Ts> \qquad (5)$$

where

$$\Psi = \int_{2\pi} D^4(\theta, \phi) d\Omega , \qquad (6)$$

$$<Ts> = \frac{1}{\Psi} \int_\Omega D^4(\theta, \phi) Ts d\Omega \qquad (7)$$

where Ψ is called the equivalent beam angle and $<Ts>$ is averaged TS [3][4]. In general, Ts in Eq.(7) is a function of θ and ϕ and is an averaged value with respect to orientation distribution. If the distribution is not dependent on fish position with respect to beam axis (Assumption 2) and beam width is small then we have

$$<Ts> = \eta Ts , \qquad (8)$$

$$\eta = \int_\Omega D^4 d\Omega / \Psi \qquad (9)$$

where η is the contribution factor [4]. If the size of fish school is large compared with the beam width (Assumption 3) or the integration is done sufficiently, Ω will be equal to 2π and we get

$$\eta = 1 , \quad <Ts> = Ts . \qquad (10)$$

In the echo integration method, our subjects are not only multiple echoes but also single echoes. However, the integration procedure applied to the so called "20 log r TVG" outputs of any echo apparently realizes Eqs.(2) - (10).

2.2 Avoidance Effect

In the general situation where Assumptions 1 and 2 are not valid, measured SV is from Eqs.(4) and (5)

$$S_V = n <Ts>$$

$$= \int_\Omega n D^4 Ts d\Omega / \int_{2\pi} D^4 d\Omega \qquad (11)$$

In the dual beam echo integration method, D^4 of Eq.(11) is replaced by D_N^4 for narrow channel and by $D_N^2 D_W^2$ for wide channel where suffixes N and W mean narrow and wide, respectively.

It is difficult to make an accurate model of avoidance behaviour of fish and the resultant effect [5], but the avoidance may cause a reduction of density and an extreme orientation distribution near the beam axis. From Eq.(11) we can see that SV for the narrow channel will be smaller because the weight of near-beam-axis portion is larger for the narrow channel. Thus, the ratio of measured SV values by narrow and wide channels can be a measure of the magnitude of the avoidance effect. The smaller the ratio, the larger the avoidance.

2.3 Noise

The noise pressure P_n equivalently transformed at the transducer surface is shown by

$$P_n^2 = N_P^2 \Delta f / D_I \qquad (12)$$

where N_P is noise spectrum level, Δf is band width of the receiver, and D_I is directivity index of receiving transducer. This signal is amplified and integrated to give so called "noise SV" shown by

$$S_{Vn} = \frac{P_n^2}{P_o^2} \frac{1}{c\tau} \frac{1}{\Psi} \frac{1}{r_w}$$

$$\times \int_r^{r+r_w} [r \exp(2\alpha r)]^2 dr \qquad (13)$$

where r_w is the width of the integration layer. From Eqs.(12) and (13) the ratio of the noise SV of narrow to wide channels is

$$\frac{S_{VnN}}{S_{Vnw}} = \frac{\Delta f_N}{\Delta f_w} \frac{D_{Iw}}{D_{IN}} \frac{\Psi_c}{\Psi_N} \qquad (14)$$

where Ψ_c is the equivalent beam angle for composite beam.

The directivity index and equivalent beam angle of a circular piston transducer [6] are

$$D_I = (ka)^2 \qquad (15)$$

and

$$\Psi = 5.78 / (ka)^2 \qquad (16)$$

where k is the wave number and a is the transducer radius. If we assume

$$\Psi_c = 5.78 / (k^2 a_N a_w) , \qquad (17)$$

then we have

$$\frac{S_{VnN}}{S_{Vnw}} = \frac{\Delta f_N}{\Delta f_w} \frac{a_w}{a_N} \qquad (18)$$

This can be used as an index of noise magnitude. We may see the noise level from echo integrator outputs of each channel, but it is difficult when fish echoes appeared.

2.4 Sampling Volume

Bodholt [7] showed the following expression for the variance of the normalized integrator outputs:

$$\sigma^2 = \frac{1}{m} \left[\frac{1}{2} \frac{c\tau}{2r_w} + \frac{2}{3} \frac{1}{n \Psi r (r + r_w)} \frac{\langle Ts^2 \rangle}{\langle Ts \rangle^2} \frac{\Psi_4}{\Psi} \right] \qquad (19)$$

where m is the averaging number for pings, and $\langle Ts^2 \rangle / \langle Ts \rangle^2$ is the moment ratio of TS and generally about 2.7. The moment ratio of directivity of transducer Ψ_4/Ψ is about 0.5 where $\Psi_4 = \int D^B d\Omega$.

The second term in the bracket is larger for the narrow channel than for the wide channel by a factor of Ψ_c/Ψ_N. If the depth r is shallow and the weight of the second term becomes large and if a large integration period is not applied (m is small), then the wide channel gives more precise results.

2.5 Transducer Motion Error

Stanton [8] analyzed the transducer motion error in the echo integration method. The transducer motion gives a negative error as the result of reduction of the apparent equivalent beam angle. Here we cite from Stanton an example in the estimation of fish at 400 m depth under the transducer motion with amplitude 5° and period 4 sec. When a pulse is transmitted at motion angle of - 2° and echo is received at 2° , the motion error amount to as much as 64% for 5° beam-width transducer and to only 4 % for 40° beam.

In general, the dual beam method needs a narrow beam in order to resolve single echoes. This will produce large errors in echo integration unless the transducer is stabilized or towed. In this connection, the wide beam echo integration is preferable in bad weather conditions.

2.6 Observation of Volume Backscattering Strength within School

For fisheries and identification purposes, the volume backscattering strength within a school is more important than SV averaged over a large area. It is not easy to accurately measure SV in schools, because (1) the beam must be sharp compared with school size (Assumption 3) and (2) echo formation must be sufficient to get precise SV.

The first point is shown clearly in Eq.(9). We cannot know the distribution range Ω of fish beforehand and we must assume $\eta = 1$. We can use as a criteria the angle where $\eta = 0.9$ and we call the angle "90 % beam angle" or θ_{90} [4]. In other words, if a distribution is larger than θ_{90}, we can measure SV with error less than -10 %. Thus the narrow beam is preferable to lessen the bias. The second point shown above was explained in Section 2.4. The wide beam is better in order to lessen variance.

One of the ways to alleviate the above contradiction is to measure wide channel SV where the narrow channel SV is high. A more accurate and practical method is to measure wide channel SV where the difference of the two channels' SV is small.

3. Experiment

3.1 Method

We examine the theoretical results using data from a walleye pollock survey in the Aleutian Basin and the eastern Bering Sea shelf using our quantitative echo sounding system [9] which has the dual-beam echo-integration function.

Figure 1 shows the system block diagram. Table 1 lists its specifications. The transducer

is mounted on a V-fin type towed body to reduce the error caused by transducer motion, by bubbles, and by noise. We can monitor the towing depth and roll and pitch angles of the towed body. The receiver has four independent TVG channels for two kinds of beam and for "20log r" and "40log r" TVG characteristics. The TVG outputs are indicated on the CRT of a color echo image processor (CEIP) and on a paper recorder. The outputs of "20 log r" TVG are transferred to an echo integrator and "40 log r" TVG outputs to a dual beam processer. All of the TVG outputs are recorded on a video tape as PCM signals with all sounder parameters and navigational information needed for post processings.

The CEIP has all the functions of usual color echo sounders. In addition, it can display absolute echo levels and the special results obtained by combining two of four kinds of TVG outputs. For the present purpose, we only explain its functions using "20 log r " TVG signals and describe two modes of operation. SVR mode shows the wide signal level when the narrow signal level is higher than a predifined threshold level. We can change the threshold level by 0.1 dB step. SVB mode shows the differences between the narrow and wide signal levels. Using these modes, we can accurately measure SV in fish school as shown in Section 2.6.

The echo integration system consists of an echo integrator, a personal computer which stores and monitors data, a color plotter for abundance mapping and a digitizer to input sea chart data. The echo integrator has two independent simultaneous channels to perform integration. The number of integration layers is 60 for each channel. The integration layer width of 50 layers is set automatically and the width is (maximum range)/50 m. We are able to set the widths of the remaining 10 layers at will. All of integrator outputs with navigational information are stored on 3.5" floppy disks. A threshold is set by a SV level at 100 m range and by selecting one of three range functions- "±10 log r," "±20 log r," or "flat." The echo integrator also calculates area backscattering strength (SA), according to the formula:

$$S_A = \Sigma \ r_w \ S_v \qquad (20)$$

where S_A is the value of SA and r_w is integration width.

We conducted three acoustic surveys for walleye pollock. In 1988 and 1989, we chartered a fishing vessel Seiju-maru #28, a 51m stern trawler. As her propeller pitch is fixed, the ship speed is changed by engine speed. In 1988-89 winter survey, we used a research vessel Kaiyo-maru, 92m.

We calibrated our echo sounding system by using a copper sphere (ϕ 60.0 mm, TS=-33.7 [dB])

[10] several times during each survey. We measured noise level received by our system several times to know characteristics of the noise and to set threshold parameters of the echo integrator. The engine speed or ship speed dependence of noise were measured before and after each survey. To measure noise, we stopped transmitting and received only noise. As the TVG outputs of noise were low at shallow depth and increased with range (see Eq.(13)), we chose to integrate noise at depth greater than 200m where the noise contributions is well above our system's minimum detectable SV of -99.9 dB.
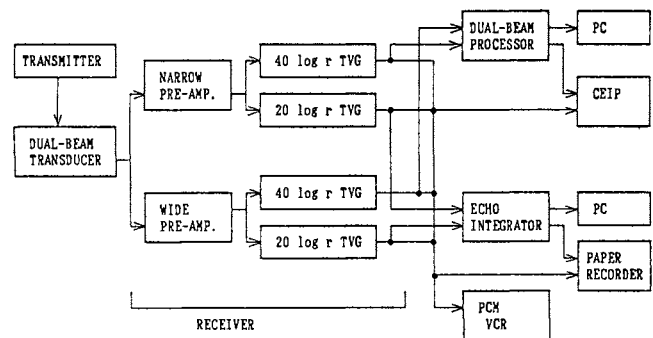
Fig.1　System block diagram

Table 1　Specifications of the echo sounding system

	NARROW	COMMON	WIDE
Frequency		38kHz	
Transducer		79 PZT elements	
Effective transducer radius	19 cm		7 cm
Beam width	6.4°		15.6°
Equivalent beam angle	0.0072 sr		0.012 sr *
Towed body		1.3 m V-fin	
Transmitting Power	2.8kW		
Pulse duration		0.6, 1.2, 2.4 ms	
Maximum range		50, 100, 200, 400, 800 m	
TVG	20 log r +2αr		20 log r +2αr
	40 log r +2αr		40 log r +2αr
α		10.0 dB/km	

* Composite beam

3.2　Results

Figure 2 is an example of color echograms observed on the eastern Bering Sea shelf from 22:21 to 22:45 on 16 September 1989. The water depth was about 105 m and the noise level was low.　We see a patchy distribution of fish between the surface and 60 m depth, and a layer-like distribution between 80 m and the bottom.

We often observed fish distributions similar to Fig.2 on the same day. Narrow and wide SA values summed up over the depth range of 14 m

to the bottom are compared in Fig.3 by black
dots. The maximum range of the echo sounder
was 200m and the integration period was 4 min
(the ping rate is about 100/min). The total
number of SA measurements is 37.

Figure 4(a) shows average SV of each layer
and their coefficients of variation against the
range from transducer obtained for the same
data set as black dots of Fig.3. Coefficients of
variation were calculated assuming data set is
random sample of SV outputs. The width of each
echo integration layer is 4 m. The average SV
curves show that the fish distribution near the
sea bed was dense. There are four peaks of the
coefficient of variation at 10, 32, 58, and 78 m.
It seems that the peaks at 10 and 32 m were
caused by the patchy distribution of fish.
Figure 4(b) shows the differences between
narrow and wide SV plotted against the range
from transducer.

Figure 5 is an echogram observed on the
eastern Bering Sea shelf from 0:38 to 0:52 on 17
September 1989. We made a midwater trawl
sampling between the observations of Figs.2 and
5 and caught juvenile walleye pollock. The fish
sign near the bottom is weaker than that in
Fig.2 and distribution density is less. On the
other hand, the patchy sign near the surface is
stronger than in Fig.2.

White dots in Fig.3 are both channels SA
summed up over the depth range of 12 m to the
bottom from 0:36 to 4:41 on the same day. The
maximum range of the echo sounder was 100 m and
the integration period is 4 min (the ping rate is
170/min). The total number of SA data is 62.

Figure 6(a) shows the average SV of each
layer and their coefficient of variation against
range. We see that SV levels decrease and the
coefficients of variation increases with range.
Figure 6(b) shows the differences between
narrow and wide SV against range.

Figure 7 is a result of noise measurements by
the echo integrator on R/V Kaiyo-maru off
Tateyama. The Y-axis is "noise SV" between 250
and 300m, and the X-axis is ship speed. The
black dots are narrow SV data and white squares
are wide SV. The solid and dotted lines are
obtained from the wide and narrow channel data,
respectively, using a least squares method. The
towing depth was about 10 m.

Figure 8 is a result of a noise measurement
on F/V Seiju-maru #28 in the international zone
of the Aleutian Basin. The "noise SV" between
350 and 400 m are plotted against the engine
speed. The ship speed was 5 kt at 310 rpm and 7.5
kt at 430 rpm. The water depth was greater than
1000 m.

Figure 9 is an example of echograms to which
SVR and SVB modes are applied. This echogram
was obtained near the Aleutian Islands on 27
February 1989. The upper window (SVR mode)
shows SV for wide channel when narrow SV is
higher than -50 dB, and the lower window (SVB

mode) shows the difference between narrow and
wide SV. In this display the color pattern is
set white where the difference is smaller than
± 3 dB. We can read SV within a school at the
middle of the upper window as -33.1 dB.
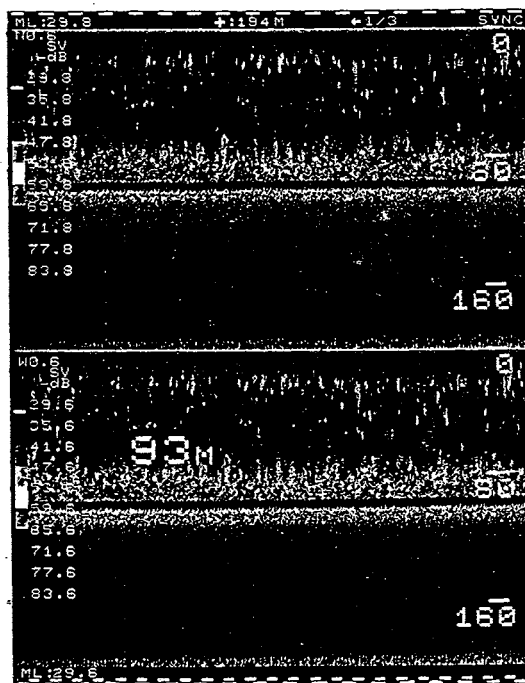
Fig.2 An example of color display on 16
September 1989. The upper window shows
"narrow 20 log r TVG" outputs and the
lower "wide 20 log r TVG" outputs.

9/16/89 20:28-9/17/89 4:41
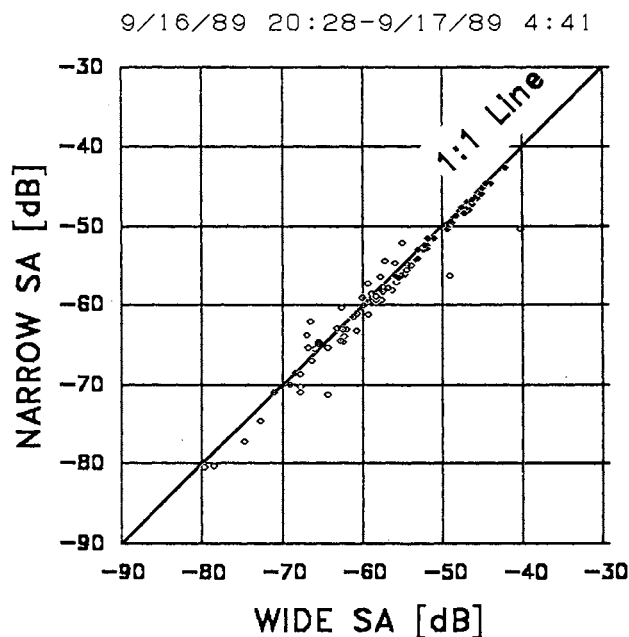
WIDE SA [dB]

Fig.3 Comparison of narrow and wide SA
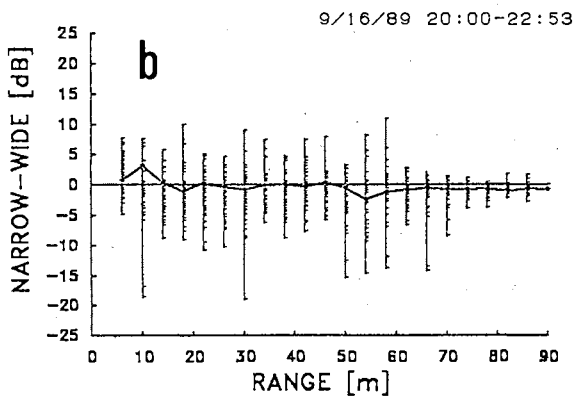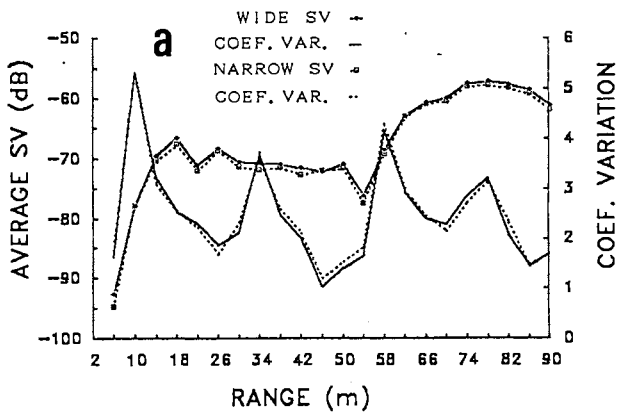
Fig.4 An example of dual beam echo integration on the eastern Bering Sea shelf.
(a) Average SV and its coefficient of variation as a function of depth.
(b) Differences between narrow and wide SV for each integration layer. Black dots connected by a line represent average difference.
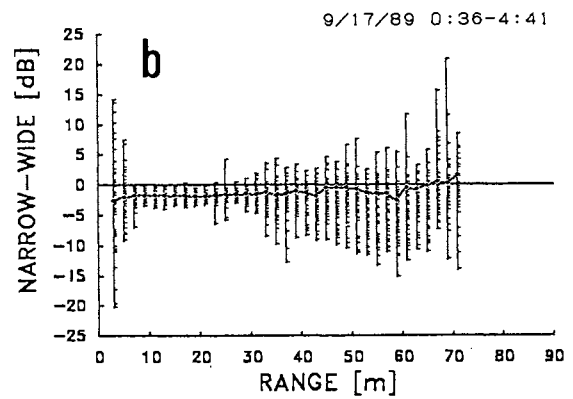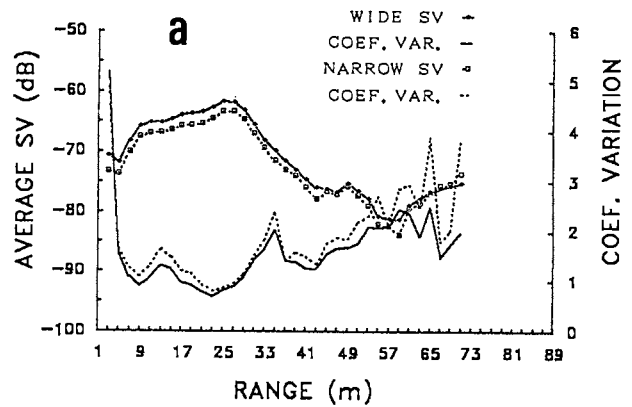
Fig.6 An example of dual beam echo integration applied to patchy fish distribution.
(a) Average SV and its coefficient of variation as a function of depth.
(b) Differences between narrow and wide SV for each integration layer. Black dots connected by a line represent average differences.
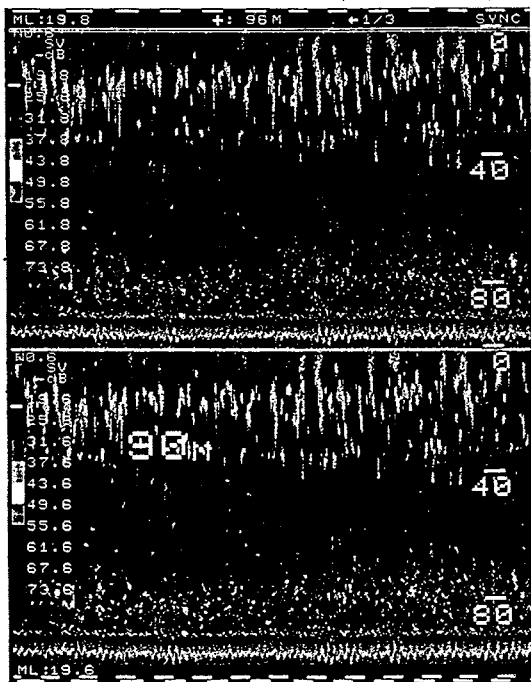
Fig.5 An example of color display on 17 September 1989.
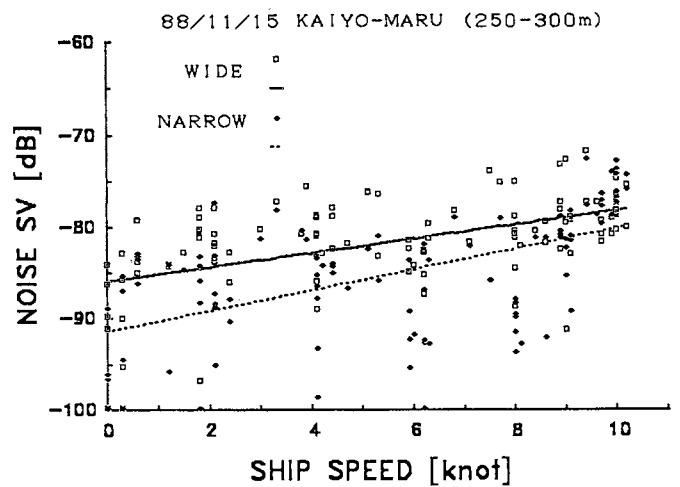
Fig.7 The results of "noise integration " on R/V Kaiyo-maru. Black dots are narrow SV, and white squares are wide SV.

89/10/7 SEIJU-MARU#28 (350-400m)
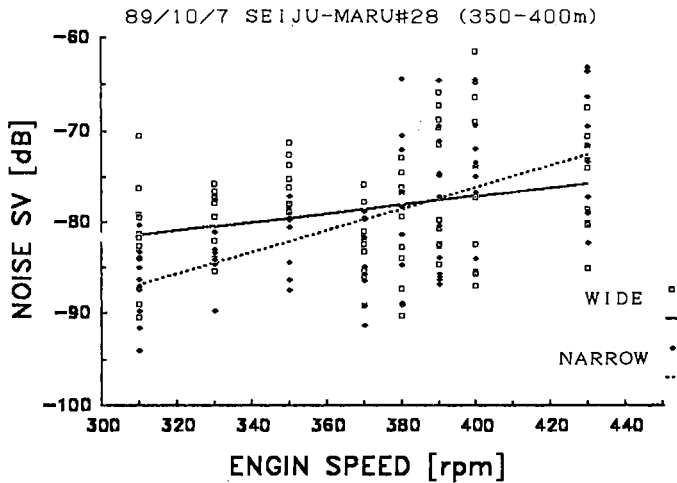
Fig.8 The results of "noise integration " on F/V Seiju-maru #28.
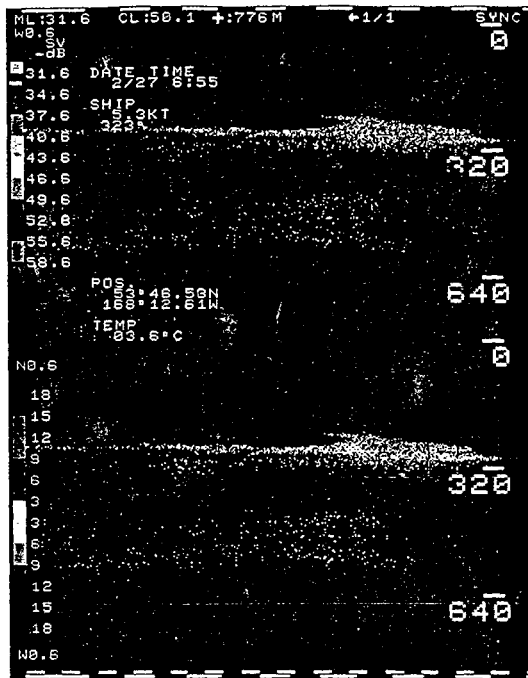
Fig.9 An example of an echogram showing SVR (upper) and SVB (lower) modes.

3.3 Discussion

We observe the following for the results of 16 September. The fish distribution was denser near the bottom than in midwater (Figs.2 and 4(a)). The ratio of narrow to wide SA was almost unity (Fig.3). Near the bottom, the variability in the differences of SV decreases as the average SV value increases (Fig.4(b)).

The integrator outputs of narrow and wide channels will be almost the same when the echo integration period is large enough and the fish distribution is dense and homogeneous (see Eq.(19)). The above results suggests that our system operated well and its calibration was suitable.

We observe the following for the results of 17 September. The fish distribution was denser in shallow depth than near the bottom (Figs.5 and 6(a)). The patchy fish sign in Fig.5 was bigger and stronger than in Fig.2. The wide SV was larger than narrow SV at shallow depth (Fig.6(b)).

We may assume that the smaller the fish depth, the larger the fish avoidance behaviour against the researching vessel [5]. Therefore, we chose the above results for the analysis of avoidance effect. We consider that the difference of wide and narrow SV observed was caused by the fish avoidance, because fish distribution was shallow and patchy. Since the contribution of high frequency noise in echo integrator outputs was low in this case because of the small range, we can ignore the influence of noise on the difference between narrow and wide SV.

Here, we discuss about the noise measurements. Since the band widths of our receivers are equal, the substitution of each effective radius into Eq.(18) yields

$$7/19 = 0.37 = -4.3 \text{ (dB)}$$

and this shows that the noise SV of the wide channel is theoretically 4.3 dB higher than the narrow one.

The difference of the least square curves is about 5dB when Kaiyo-maru was not moving (see Fig.7), and this value agrees well with the above theoretical value. The noise SV of both narrow and wide channels increase as the ship speed increases; however we see some different tendency in the two channels. The narrow noise SV increases more rapidly with ship speed and shows a larger variability.

The differences of the SV's least square curves of Seiju-maru #28 are about 7dB at her engine speed of 310 rpm (see Fig.8). The noise SV of both channels increase as the ship speed increases. However, the narrow SV increases more rapidly than Kaiyo-maru and the narrow SV is larger than the wide SV for engine speeds greater than 390 rpm .

The reason for this may be that environmental noise which has no directivity is superior at low ship speed. The propeller noise increases as the engine speed increases. The propeller noise has directivity and its pattern and noise spectrum level change with speed [11]. As shown by the results, the relationship between noise SV and ship speed becomes complex.

The towed body we used was stable during these surveys, so that we did not collect information on transducer motion errors. However, wide signal echo integration will be effective for vessel mounted transducers.

4. Conclusion

We have discussed the dual beam echo integration method theoretically and experimentally. It is shown that the ratio of narrow to wide SV is unity under the suitable condition. Therefore, we can detect qualitatively the effect of the avoidance, noise, or beam motion by comparing the narrow and wide channel outputs of the echo integrator. Further, we can get a quantitative index of avoidance behaviour of fish to survey vessel. A small ratio of narrow to wide SV implies significant fish avoidance.

The theoretical ratio of narrow to wide "noise SV" shown by Eq.(18) agreed well with the experimental value, when Kaiyo-maru was stopped or sailed at low ship speed.

When fish are at shallow depth, the error caused by fish avoidance is large and, in general, the error by noise is not serious. On the other hand, when fish are deep, the error by noise becomes more serious because "noise SV" increases with the range (see Eq.(13)). We can use this SV ratio effectively during survey operations. When we notice the large differences between narrow and wide SV, we compare and examine echograms. If it is caused only from noise, we measure noise levels, and set suitable threshold parameters. When the causes are not only noise, we must sail more slowly. This is an effective way to reduce the fish avoidance, the noise, and the transducer motion.

The dual beam echo integration method should be used widely for sounders with dual beams, considering the above mentioned superiority. The most useful is the ability to monitor the avoidance effect which can not be realized by only one sounder.

Acknowledgment

References

1. Johannesson, K.A. and Mitson, R.B. "Fisheries acoustics -- A practical manual for aquatic biomass estimation," FAO Fish.Tech.Pep. 240 (FAO, Rome, 1983).
2. Ehrenberg, J.E. "A review of in situ target strength estimation techniques," FAO Fish. Rep. 300, 85-90 (1983).
3. Foote, K.G. "Averaging of fish target strength functions," J.Acoust.Soc.Am. 67, 504-515 (1980).
4. Furusawa, M., Ishii, K. and Maniwa, Y. "A theoretical investigation on ultrasonic echo method to estimate distribution density of fish," J.Acoust.Soc.Jpn. 42, 2-8 (1986) (in Japanese).
5. Olsen, K., Angell, J. and Løvik, A. "Quantitative estimations of the influence of fish behaviour on acoustically determined fish abundance," FAO Fish.Rep. No.300, 139-149 (1983).
6. Clay, C.S. and Medwin, H. Acoustical Oceanography (Wiley, New York, 1977).
7. Bodholt, H. "Variance error in echo integrator output, " Rapp.P.-v.Reun.Cons. int. Explor. Mer 170, 196-204 (1977).
8. Stanton, T.K. "Effects of transducer motion on echo-integration techniques," J.Acoust.Soc.Am. 72, 947-949 (1982).
9. Furusawa, M. and Takao, Y. "Outline of a versatile echo sounding system (VESS)," Document for the working group on U.S.-Japan joint surveys, 1-38 (1988).
10. Foote, K.G. "Optimizing copper spheres for precision calibration of hydroacoustic equipment," J.Acoust.Soc.Am. 71, 742-747 (1982).
11. Mitson, R.B. "Ship noise related to fisheries research," Proc.Inst.Acoust. Vol 11, Part 3, 61-67 (1989).

OPTIMAL CONTROL OF A MIDWATER TRAWL SYSTEM

N. Umeda*

* National Research Institute of Fisheries Engineering, Hasaki, Japan

Abstract

This study presents an optimal control method for a midwater trawl system that consists of a trawler, a trawl winch, warps, otter boards, hand ropes, a net and so on. The system is somewhat simplified and described by using equations of motion. A multi-variable feedback system is designed as an optimal regulator problem. Here manipulated variables are both length of warps and angle of propeller blades. Controlled variables are depth and forward velocity of the net. The optimal control system minimizes a criterion function that the error of depth and forward velocity of the net is small and control actuation is small. Moreover, computer simulation for a realistic set point control problem shows effects of the optimal control of the midwater trawl.

1. Introduction

As a result of fishermen's effort, a bottom trawl method becomes one of the most effective fishing methods.[1] Recently, this bottom trawl method in Russian water area is almost prohibited. Because, this method may threaten reproduction of fisheries resources at seabed. Thus we should replace the bottom trawl method by a midwater trawl method. However, since the midwater trawl method is still young, we should improve it much more to obtain profit without waste of time and energy.[3] A scientific procedure is needed to optimize the midwater trawl method because empirical procedures will take us quite a number of years. An answer of the problem may be an optimal control theory that immediately indicates an optimal control law to minimize a criterion function.[4] This theory may indicate an optimal fishing method without years and months.

In trawl methods one tows a net with constant velocity that is slightly faster than swimming velocity of fish schools and almost constant depth. Then fish schools are gradually forced to enter a cod end. Thus depth and forward velocity of the net are determined if a fish school is detected by a sonar. A practical problem for a fishing gear control arises as follows. After paying out the net, the net becomes steady and a fish school is selected as a target. Thus depth and forward velocity of the net are determined for the fish school. Then one should adjust depth and forward velocity of the net to the determined values and keep this condition for one or two hours until fish gather in the cod end. Here it is a problem how one should change manipulated variables, that is, a blade angle of a controllable pitch propeller (CPP) and warp length. Thus we can regard this problem as a set point control problem where changing manipulated variables turns steady equilibrium to other steady equilibrium.

We have very few examples those introduce concept of control engineering into the field of fishing gears and methods. Muriaas[5] and Hamuro[2,3] reported studies about control of bottom or midwater trawl. However, they mainly concerned with supporting technology, namely, control devices and did not refer to any control laws. Nishiyama et al. dealt with an open loop transfer function of a midwater trawl system, whose input is a propeller thrust or warp length and output is net depth, as a first order lag system. Since practical operation uses both the propeller thrust and the warp length, this kind of classic control theory, that is formulated for a single feedback system, is insufficient. Thus a multi-variable feedback theory, namely, a modern optimal control theory is required and had not yet been applied into the fishing gears and methods.

To solve this problem, this fundamental study applies the optimal control theory to the simplified midwater trawl system and examined the theory by numerical simulations.

2. Nomenclature

x_s	Longitudinal position of trawler
m_{sx}	Virtual mass of trawler
k_s	Resistance coefficient of trawler
K	Form factor of trawler
S	Wetted surface area of trawler
L	Length of trawler
t_p	Thrust deduction fraction of trawler
w	Wake fraction of trawler

n   Revolution number of propeller

D_p Diameter of propeller

P   Propeller thrust

K_{TA} Thrust coefficient under standard pitch ratio

J_p Advance coefficient

T_p Time constant of CPP controller

p   Propeller pitch ratio

p^* Ordered propeller pitch ratio

a,b,c   Coefficients of J_p for K_{TA}

C_{p1} Coefficient of p for K_{TA}

C_{p2} Ditto.

X_w Longitudinal position of winch from midship

Z_w Vertical position of winch from water surface

T_L Time constant of winch

l_1 length of unloaded warp

l_1^* Ordered length of unloaded warp

A_1 Sectional area of warp

E_1 Elastic modulus of warp

T_1 Warp Tension

θ_1 Angle between warp and water surface

m_{1x} Virtual mass of otter boards in x direction

m_{1z} Virtual mass of otter boards in z direction

k_1 drag coefficient of otter boards

$m'_1 g$ Gravity of otter boards in water

l_2 length of unloaded hand rope

A_2 Sectional area of hand rope

E_2 Elastic modulus of hand rope

T_2 Tension of hand rope

θ_2 Angle between hand rope and water surface

m_{2x} Virtual mass of net in x direction

m_{2z} Virtual mass of net in z direction

k_2 Drag coefficient of net

$m'_2 g$ Gravity of net in water

ρ water density

g   gravitational acceleration

ν coefficient of kinematic viscosity

3. Mathematical model of a midwater trawl

A midwater trawl tracks fish schools with three dimensional movements. In this paper, as a first attempt, we only consider movements within a vertical plane for simplicity sake. This assumption means that the trawler and its net go straight in a horizontal plane under perfect control of a rudder and two winches. And heaving and pitching motion of the trawler are assumed to be ignored because the net

motion does not depend on them very much. Further, the otter boards and the net are regarded as material points on which hydrodynamic forces act. In addition, mass and hydrodynamic forces of the warps and the hand ropes are added to the material point for otter boards. Thus, from dynamic view point, the midwater trawl system is simplified as three material points connected with two elastic cables and shown in Fig.1.
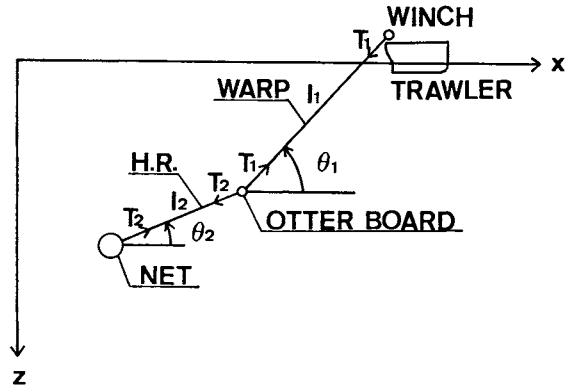
Fig.1 Midwater trawl system

We can obtain an angle and tension of the warps between the ship and the otter boards and those of the hand ropes between the otter boards and the net as follows:

$$\cos\theta_1 = \frac{x_3 + x_w - x_1}{\{(x_3 + x_w - x_1)^2 + (z_1 - z_w)^2\}^{1/2}} \tag{1}$$

$$\sin\theta_1 = \frac{z_1 - z_w}{\{(x_3 + x_w - x_1)^2 + (z_1 - z_w)^2\}^{1/2}} \tag{2}$$

$$\cos\theta_2 = \frac{x_1 - x_2}{\{(x_1 - x_2)^2 + (z_2 - z_1)^2\}^{1/2}} \tag{3}$$

$$\sin\theta_2 = \frac{z_2 - z_1}{\{(x_1 - x_2)^2 + (z_2 - z_1)^2\}^{1/2}} \tag{4}$$

$$T_1 = (A_1 E_1 / l_1)[\{(x_3 + x_w - x_1)^2 + (z_w - z_1)^2\}^{1/2} - l_1] \tag{5}$$

$$T_2 = (A_2 E_2 / l_2)[\{(x_1 - x_2)^2 + (z_1 - z_2)^2\}^{1/2} - l_2] \tag{6}$$

An equation of the ship motion should take its surging motion, tension and effects of CPP into account.

$$m_{3x}\ddot{x}_3 = P - k_3\dot{x}_3|\dot{x}_3| - T_1\cos\theta_1 \tag{7}$$

where

$$P = (1 - t_p)\rho n^2 D_p[K_{TA}\{\dot{x}_0(1 - w)/(nD_p)\} + C_{p1}p + C_{p2}] \tag{8}$$

$$K_{TA}(J_p) = aJ_p^2 + bJ_p + c \tag{9}$$

$$J_p = \dot{x}_0(1 - w)/(nD_p) \tag{10}$$

$$k_3 = 1/2(1 + K)\rho S \cdot 0.483(\log_{10}(\dot{x}_0 L/\nu))^{-2.6} \tag{11}$$

Equations of the otter boards and the net are given by,

$$m_{1x}\ddot{x}_1 = T_1 \cos\theta_1 - k_1\dot{x}_1|\dot{x}_1| \{1 + (\dot{z}_1/\dot{x}_1)^2\}^{1/2} - T_2\cos\theta_2 \qquad (12)$$

$$m_{1z}\ddot{z}_1 = -T_1\sin\theta_1 - k_1\dot{z}_1|\dot{x}_1| \{1 + (\dot{z}_1/\dot{x}_1)^2\}^{1/2} + T_2\sin\theta_2 + m_1' g \qquad (13)$$

$$m_{2x}\ddot{x}_2 = T_2\cos\theta_2 - k_2\dot{x}_2|\dot{x}_2| \{1 + (\dot{z}_2/\dot{x}_2)^2\}^{1/2} \qquad (14)$$

$$m_{2z}\ddot{z}_2 = -T_2\sin\theta_2 - k_2\dot{z}_2|\dot{x}_2| \{1 + (\dot{z}_2/\dot{x}_2)^2\}^{1/2} + m_2' g \qquad (15)$$

The trawl winch and CPP controller can be regarded as a first order lag system.

$$T_L \dot{l}_1 + l_1 = l_1^* \qquad (16)$$

$$T_p \dot{p} + p = p^* \qquad (17)$$

4. Optimal regulator theory

Since the system described by the equations (1)-(17) is non-linear, it is difficult to use a control theory. Thus, we linearlize them near their steady solutions.

First, we substitute the following relations

$$\dddot{x}_s = \ddot{x}_1 = \ddot{x}_2 = \ddot{z}_1 = \ddot{z}_2 = \dot{z}_1 = \dot{z}_2 = \dot{l}_1 = \dot{p} = 0 \qquad (18)$$

$$\dot{x}_s = \dot{x}_1 = \dot{x}_2 = \dot{x}_0 \qquad (19)$$

for the equations (1)-(17). If a steady velocity $\dot{x}_0$ and steady warp length l_{10} are given, the steady solutions of the system are successively determined as follows:

$$\theta_{20} = \tan^{-1}\{m_2' g / (k_2\dot{x}_0|\dot{x}_0|)\} \qquad (20)$$

$$T_{20} = m_2' g / \sin\theta_{20} \qquad (21)$$

$$\theta_{10} = \tan^{-1}\left(\frac{T_{20}\sin\theta_{20} + m_1' g}{T_{20}\cos\theta_{20} + k_1\dot{x}_0|\dot{x}_0|}\right) \qquad (22)$$

$$T_{10} = (T_{20}\sin\theta_{20} + m_1' g) / \sin\theta_{10} \qquad (23)$$

$$p_0^* = p_0 = \frac{1}{C_{P1}}\left[\frac{T_{10}\cos\theta_{10} + k_s\dot{x}_0|\dot{x}_0|}{(1 - t_P)\rho n^2 D_P^4} - K_{TA}\{\dot{x}_0(1-w)/nD_P\} - C_{P2}\right] \qquad (24)$$

$$x_{10} = x_{s0} + x_w - l_{10}\cos\theta_{10} \{T_{10}/(A_1E_1) + 1\} \qquad (25)$$

$$z_{10} = z_{s0} + z_w - l_{10}\sin\theta_{10} \{T_{10}/(A_1E_1) + 1\} \qquad (26)$$

$$x_{20} = x_{10} - l_2\cos\theta_{20} \{T_{20}/(A_2E_2) + 1\} \qquad (27)$$

$$z_{20} = z_{10} - l_2\sin\theta_{20} \{T_{20}/(A_2E_2) + 1\} \qquad (28)$$

Next, one can expand variables near the steady solutions in the Taylor series.

$$\dot{x}_s = \dot{x}_s + \Delta\dot{x}_s \qquad \ddot{x}_s = \ddot{x}_s + \Delta\ddot{x}_s$$

$$\dot{x}_1 = \dot{x}_{10} + \Delta\dot{x}_1 \qquad \ddot{x}_1 = \ddot{x}_1 + \Delta\ddot{x}_1$$

$$\dot{x}_2 = \dot{x}_{20} + \Delta\dot{x}_2 \qquad \ddot{x}_2 = \ddot{x}_2 + \Delta\ddot{x}_2$$

$$z_1 = z_{10} + \Delta z_1 \qquad \dot{z}_1 = \Delta\dot{z}_1 \qquad (29)$$

$$z_2 = z_{20} + \Delta z_2 \qquad \dot{z}_2 = \Delta\dot{z}_2$$

$$l_1 = l_{10} + \Delta l_1 \qquad \dot{l}_1 = \Delta\dot{l}_1$$

$$p = p_0 + \Delta p \qquad \dot{p} = \Delta\dot{p}$$

$$p^* = p_0^* + \Delta p^* \qquad l_1^* = l_{10}^* + \Delta l_1^*$$

After putting

$$\Delta\dot{x}_s = U_s, \qquad \Delta\dot{x}_1 = U_1, \qquad \Delta\dot{x}_2 = U_2,$$
$$\Delta\dot{z}_1 = W_1, \qquad \Delta\dot{z}_2 = W_2 \qquad (30)$$

we define state variables **x** and control variables **u** as follows:

$$\mathbf{x} = (U_s, U_1, W_1, U_2, W_2, \Delta x_1, \Delta z_1, \Delta x_2, \Delta z_2, \Delta l_1, \Delta p_1)^T \qquad (31)$$

$$\mathbf{u} = (\Delta l_1^*, \Delta p^*)^T \qquad (32)$$

Substituting (29) for (1)-(17) and omitting terms higher than the second order, we can obtain the state equation as follows:

$$\dot{\mathbf{x}} = A\mathbf{x} + B\mathbf{u} \qquad (33)$$

Here A is a 12 x 12 matrix and B is a 12 x 2 matrix.

A criterion function J for the optimal control is tentatively defined as follows:

$$J = \int_0^\infty (\mathbf{x}^T R_1 \mathbf{x} + \mathbf{u}^T R_2 \mathbf{u}) \, dt \qquad (34)$$

where R_1 and R_2 are symmetric matrices and nonnegative definite.

$$R_1 = \begin{pmatrix} \lambda_{11} & & 0 \\ & \ddots & \\ 0 & & \lambda_{1212} \end{pmatrix} \qquad (35)$$

$$R_2 = \begin{pmatrix} \rho_1 & 0 \\ 0 & \rho_p \end{pmatrix} \qquad (36)$$

$$\lambda_{11} = 0 \qquad (i \neq 4, i \neq 10)$$

This criterion function penalizes the system error and energy required for the controllers.

An optimal control of the state equation (33) to minimize the criterion function (34) is an optimal linear quadratic regulator. Thus, the optimal feedback law is given by,

$$u = - R_2^{-1} B^T H \; \mathbf{x} \qquad (37)$$

Here the matrix H is efficiently determined.[7] Put matrix Z

$$Z = \begin{pmatrix} A & -BR_2^{-1}B^T \\ -R_1 & -A^T \end{pmatrix} \qquad (38)$$

and diagonalize it as follows:

$$Z = W \begin{pmatrix} \Lambda & 0 \\ 0 & -\Lambda \end{pmatrix} W^{-1} \qquad (39)$$

where Λ is a diagonal matrix composed by eigenvalues of Z whose real part is positive and $-\Lambda$ is that composed by eigenvalues of Z whose real part is negative. W is a square matrix composed by eigenvectors and the i-th row of W is the eigenvector for the eigenvalue in the i-th row of the diagonal matrix composed of Λ and $-\Lambda$. When W is given by,

$$W = \begin{pmatrix} W_{11} & W_{12} \\ W_{21} & W_{22} \end{pmatrix} \qquad (40)$$

we can find the matrix H as follows:

$$H = W_{22} \, W_{12}^{-1} \qquad (41)$$

5. Numerical results and discussion

In this chapter, we discuss whether the optimal regulator shown in chapter 4 is effective for a midwater trawl system.

The system discussed in this paper is a Japanese offshore trawler (124GT) with a midwater trawl net.[8] The lines of the trawler are shown in Fig.2 and its principal particulars are shown in Table 1. The performance of the trawler is evaluated by ordinary experiments in naval architecture. The trawler is equipped with a controllable pitch propeller, whose performance is approximately estimated by a design chart for fixed pitch propellers. The diagram of the midwater net is shown in Fig.3. The drag of the net is estimated from model experiments[8] based on Tauchi's Law.[9] The drag of the otter boards, the warp and the hand ropes is roughly estimated by Koyama's experimental results.[10] The added mass of the otter board is given by that of a rectangular plate because the otter board is almost rectangular. We cannot accurately estimate the added mass of the net because Tauchi's law is not effective for dynamic movement of nets and we have no results of dynamic full scale measurements. Thus tentatively the added mass of sphere whose diameter is equal to the net height is used for that of the net. The wires used for the warps

are JIS (Japanese Industrial Standard) No.1 and 24mm in diameter. The wires used for the hand ropes are JIS No.1 and 20mm in diameter. All numerical values for simulations are given in Table 2.

As an example, computer simulation is carried out for the following set point control problem. At first, the net is towed steady; the velocity is 1.8 m/sec and the depth is 271.8m and the warp length is 310m. Then the set point for control is given; the velocity is 2.0m/sec and the depth is 248.7m and the warp length is 300m. Thus the net should rise and increase its forward velocity. The optimal regulator is designed by the linearlization near the latter steady towing condition and demands that all state variables converge to the latter condition. Though the optimal regulator is a kind of linear approximation for the optimal control, the control input is limited in an actual system that is usually non-linear. The limited values of the control input for the midwater trawl system are assumed to be as follows:

$$| \dot{l}_1 | < 2.0 \text{ [m/sec]} \qquad -300 \text{ [m]} < \Delta l_1 < 400 \text{ [m]} \qquad (42)$$

$$| \dot{p} | < 0.073 \text{ [/sec]} \qquad -1.94 < p < 1.94 \qquad (43)$$

$$WW = T_1 \dot{l}_1 < 220 \text{ [ps]} \qquad (44)$$

$$WP = P \dot{x}_3 < 500 \text{ [ps]} \qquad (45)$$

The weighting coefficients for the input ρ_1, ρ_p reflect these limited values of the input by trial-and-error-procedure of the simulations. As a result, it takes some time to converge the control output. Among the weight for the system error, the author thinks that the error of the net depth is more important. Finally, this paper used the following ratio of the weighting coefficients:

$$\lambda_{44} : \lambda_{1010} : \rho_1 : \rho_p = 0.25 : 1.0 : 5 \times 10^{-2} : 10^6 \qquad (46)$$

As the criterion function is given, the matrix H is calculated by the diagonal method using equations (38)-(41). The backward in time integration of the algebraic Riccati equation is also a well known method to obtain the matrix H.[11] Thus this study tried both methods and confirmed that discrepancies between two methods are less than 10^{-5}. The diagonal method is much more effective to reduce computing time.

The feedback matrix from all state variables is determined by equation (37) with the matrix H. This requires that all the state variables can be detected by some sensors.

The results of the simulation by the optimal feedback input are shown in Figs. 4-17. Fig.17 shows relative positions every thirty seconds after the beginning of the control. First, the trawl winch winds up the warp and the pitch angle of CPP increases. These result that the net begins to rise. While the pitch angle turns to decrease after about thirty seconds, the net continues to rise. As a result, the controlled

Table 1 Principal particulars of the trawler

Length	30.58[m]	Fore draft	1.82[m]
Breadth	7.38[m]	Mean draft	2.62[m]
Depth	4.53[m]	Aft draft	3.82[m]
lcb	2.71[m]	C_B	0.779
Rudder area ratio (A_R/Ld)		1/27.3	
Propeller diameter		2.30[m]	
Gross tonnage		124.77[ton]	
Power of main engine		1800[ps]	

Fig.4 Forward velocity of the trawler

Fig.2 Lines of the trawler
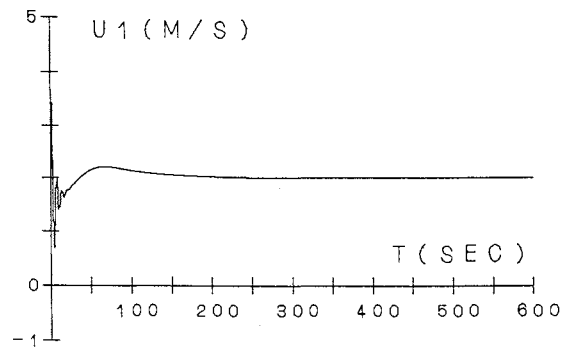
Fig.5 Forward velocity of the otter board
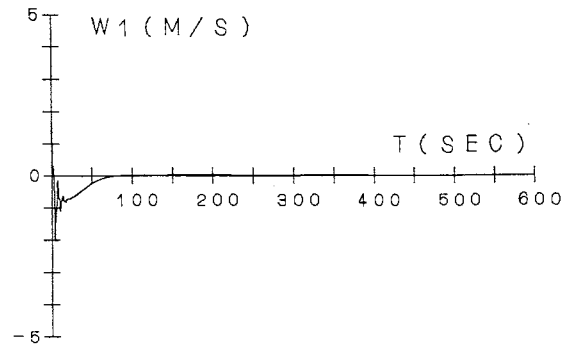
Fig.6 Vertical velocity of the otter board

Fig.3 Diagram of the midwater trawl net
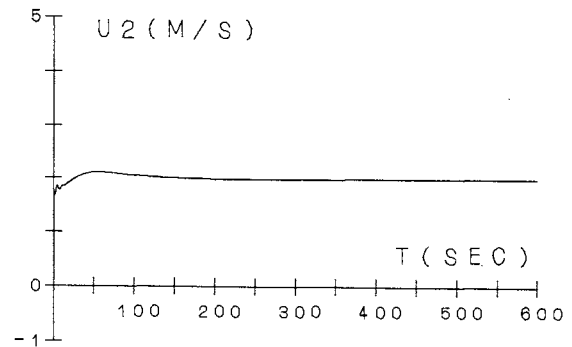
Fig.7 Forward velocity of the net

W2(M/S)

T(SEC)
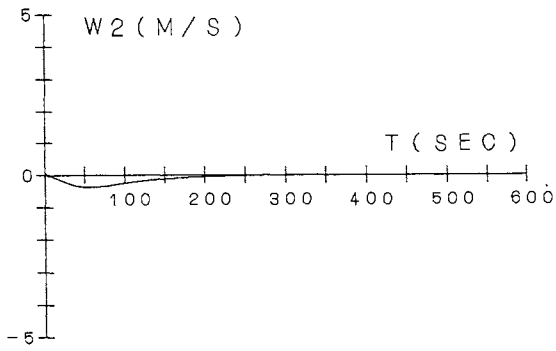
Fig.8 Vertical velocity of the net

DZ1(M)

T(SEC)

Fig.9 Change of the otter board depth

DZ2(M)

T(SEC)

Fig.10 Change of the net depth

DL1(M)

T(SEC)

Fig.11 Change of the warp length

DP

T(SEC)

Fig.12 Change of the pitch ratio of propeller

T1(TON)

T(SEC)

Fig.13 Tension of the warp

T2(TON)

T(SEC)

Fig.14 Tension of the hand rope

WP(PS)

T(SEC)
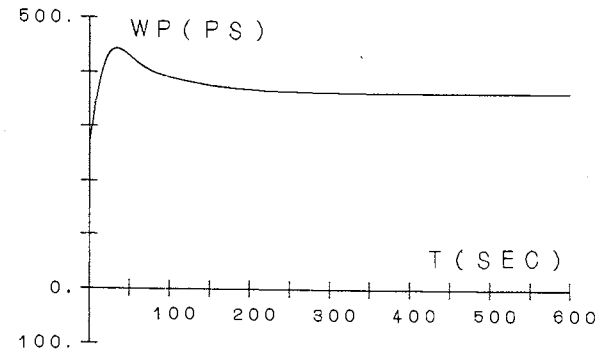
Fig.15 Power of the propeller
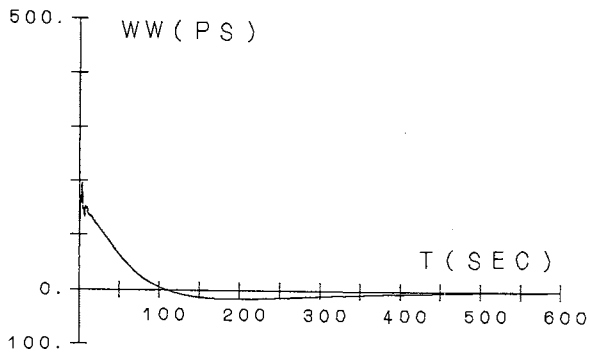
Fig.16 Power of the trawl winch
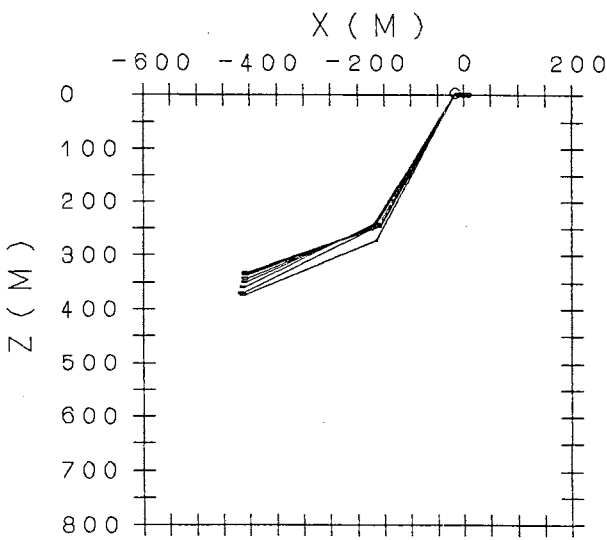
Fig.17 Relative position of the controlled system

Fig.18 Effect of the weighting coefficient of the warp ($\rho_p = 10^6$)
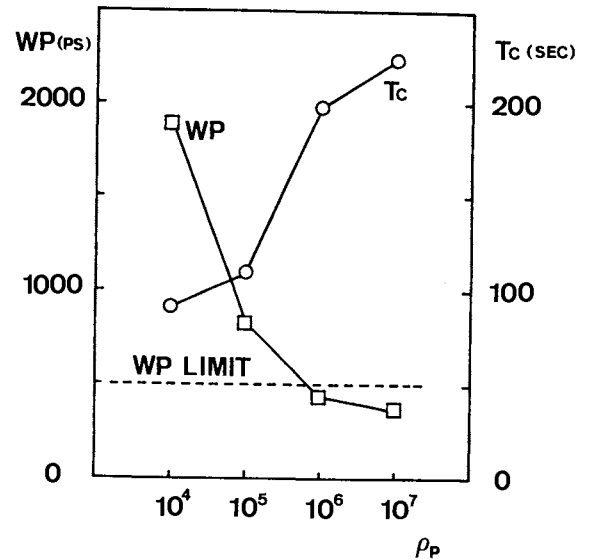
Fig.19 Effect of the weighting coefficient of the pitch ratio ($\rho_1 = 5 \times 10^{-2}$)

Table 2   System parameters for simulation

Trawler	Otter boards
W = 459600[kg]	m_{1x} = 2575 [kgsec^2/m]
m_{ax}= 51916 [kgsec^2/m]	m_{1z} = 1633 [kgsec^2/m]
S = 334.1 [m^2]	k_1 = 331 [kgsec^2/m^2]
K = 1.29	$m_1'g$= 16000[kg]
t_P = 0.131	
w = 0.163	Net
	m_{2x} = 60500[kgsec^2/m]
Propeller	m_{2z} = 60500[kgsec^2/m]
n = 11.67 [rps]	k_2 = 2980 [kgsec^2/m^2]
D_P= 2.30 [m]	$m_2'g$= 4000 [kg]
C_a= -0.147	
C_b= -0.286	Warps
C_c= 0.496	A_1 = 2.33 × 10^{-4}[m^2]
P_A= 0.571	E_1 = 1.30 × 10^{10}[kg/m^2]
P_b= -0.571	
T_P = 15.0 [sec]	Hand ropes
	A_2 = 1.60 × 10^{-4}[m^2]
Trawl Winch	E_2 = 1.30 × 10^{10}[kg/m^2]
x_w= -16.49 [m]	l_2 = 262 [m]
z_w= - 3.45 [m]	
T_L= 200.0 [sec]	

variables, that is, the net depth and forward velocity of the net converge to the set point while they slightly overshoot. The other state variables also converge to the steady condition with their rather large over shoot. The tension of the warps and hand ropes is always smaller than the breaking load during this control. And the control input stays within the limiting values. Thus the result of the control is sufficient under the limitation of the control input.

Since the control results depend on the weighting coefficients, it is important to demonstrate sensitivity of the weighting coefficients. Fig.18 shows how the weighting coefficient of the warp length, ρ_1, changes the maxima of required power of the trawl winch, WW, and the settling time ,T_c, for the net depth with an error that is less than 5 percent of the changing value. When the weighting coefficient for the warp length decreases, the settling time decreases and the required power of the winch violently increases. Fig.19 shows how the weighting coefficient of the pitch ratio, ρ_p, changes the maxima of required power of the propeller, WP, and the settling time, T_c, for the net depth. When the weighting coefficient for the pitch ratio decreases, the settling time decreases and the required power of the propeller increases. In two examples the limiting values in power is dominant and other limiting values count for little.

This paper presents an example of the optimal control for the actual midwater trawl system. Whether this control result is sufficient to catch fish schools should be finally evaluated by considering the fish behavior against the net controlled. If one needs the control with less seconds, a net with smaller drag may be selected because power of a main engine is restricted by our legislation. In other words, one can efficiently and economically control the smallest net required for fish schools. However, to discuss midwater trawl methods in further detail, the study of dynamics of nets including added mass and dynamic deformation should be developed and the optimal control theory should utilize its fruits.

6. Concluding remarks

This study presented an optimal regulator for a set point control to handle a midwater trawl system. To design the controller, a mathematical model of a midwater trawl system was presented. The computer simulation showed effects of this optimal regulator; this can be used to discuss and improve midwater trawl methods.

References

1. Wada,K., "Practical trawl method," Seizando Press, (1976)
2. "Report of development of midwater trawl technique," Trawl fisheries Union of Japan & Fishing Boat Association of Japan, (1988)
3. "Report of development of midwater trawl technique," Trawl fisheries Union of Japan & Fishing Boat Association of Japan, (1989)
4. Kato, K., "Optimal control for engineering use," University of Tokyo Press, (1988)
5. Muriaas, R., "Automatic trawl control system," Proceedings of World Symposium on Fishing Gear and Fishing Vessel Design, New foundland, p396, (1988)
6. Nishiyama, S. et.al., "Dynamic Characteristic of Midwater Trawl Nets," Bulletin of the Japanese Society of Scientific Fisheries, 48(8), p1101, (1982)
7. Kato, K., "Introduction to optimal control," University of Tokyo Press, (1987)
8. "Research report on Safety Measures for Fishing Boats," Society of Ship Research of Japan, No.168R, p46, (1988)
9. Kawakami, T., "The Theory of Designing and Testing Fishing Nets in Model," Fishing Gear of the World, 2, Fishing News Ltd, (1963)
10. Koyama, T., "Study on the Stern Trawl," Bulletin of Tokai Regional Fisheries Research Laboratory, No.77, p171,(1974)
11. Minami, M. & Koyama, T., "Application of Linear Regulator to Dynamic Positioning System," Journal of the Kansai Society of Naval Architects, Japan, No.188, p41,(1983)

MEASUREMENT OF VOLUME BACK SCATTERING STRENGTH WITH SIMRAD ES 400 SPLIT BEAM ECHO SOUNDER

C. Nainggolan*, E. Hamada*, S. Kawahara**

* Tokyo University of Fisheries, Japan
** National Research Institute of Far Seas Fisheries, Japan

Abstract

To estimate the fish abundance using echo sounder, the volume back scattering strength (SV) of fish schools and the target strength (TS) of a single fish have to be known. Some echo sounder aimed for estimating fish density measure SV, but can not measure TS, therefore, the fish density can not directly be estimated.

The Simrad ES 400 split beam echo sounder can measure the TS, which is displayed on the screen. This echo sounder does not measure the SV. In this experiment, we calculated the SV by utilizing the amplitude information collected from the parallel output of the echo sounder, which was connected to a personal computer for collecting data.

This paper describes the calculating method of SV based on the amplitude data collected from the ES 400 split beam echo sounder. The results of the calculated SV were compared with the SV obtained by the Furuno FQ 50 echo sounder, operated simultaneously during experiment which showed similar results.

List of Symbols and Units

SL   source level (dB)
TL   transmission loss (dB)
TVGc echo sounder time varied gain (TVG) constant (dB)
Uout output level at receiver (dB)
VRc receiving voltage response at maximum TVG range (dB)
a   length of transducer in the longitudinal plane (m)
b   length of transducer in the transversal plane (m)
c   sound velocity in sea water (m/s)
r   depth (m)
u   voltage output at receiver (V)
B   two-way beam pattern compensation (dB)
α sound absorption coefficient in sea water (dB/m)
β alongship angle of target (degree)
γ athwartship angle of target (degree)
λ wave length (m)
τ pulse duration (s)
ψ equivalent beam width (steradian)

1. Introduction

The most common acoustic assessment technique used today is echo integration. The integration is aimed to measure the volume back scattering strength (SV) of fish schools. It has shown both experimentally and theoretically that the integrated acoustic

intensity from a fish school is proportional to the density of the fish in the school.

The ES 400 split beam echo sounder is the equipment for measuring the target strength of a single fish and the sizes of the fish. The echo sounder is also equipped with a parallel output which can be used for collecting data. The data contains information such as control byte, amplitude, alongship and athwartship angles, estimated target strength and depth. In this experiment data from fish schools were collected and based on the amplitude information the SV was calculated with the aid of personal computer.

The ES 400 split beam echo sounder in its system applied a Time Varied Gain (TVG) circuit to compensate the echo signal from a single fish, which produces equal signal amplitude to fish of the same size regardless the depth the fish is located. On the other hand, when the echo signals come from fish schools, another TVG circuit is needed, which functions to produce equal signal amplitude to fish school of the same size regardless of its depth. This TVG function is absent in the ES 400 split beam echo sounder. Therefore, in calculating the SV of fish schools, a mathematical correction was used converting the applied TVG function of the echo sounder for a single fish to the TVG function for a fish school.

2. Instruments and Data Processing

The experiment was carried out in Suruga bay using research vessel Shunyo Maru. The vessel has a Furuno 50 scientific echo sounder (50 kHz) and a Simrad ES 400 split beam echo sounder (38 kHz). During the experiment both echo sounders were operated simultaneously. The FQ 50 was used to measure the SV of the fish schools and the ES 400 was used to collect data of the fish schools.

The parallel output of the ES 400 was connected to the personal computer (EPSON PC-286LE) for taking data from the echo sounder. The parallel output forms a high speed, real time data, for every 10 cm column of water throughout the echo sounder range. In order to avail all the necessary information, a program was written for transferring data from the echo sounder to the computer and then saved continuously into floppy disks.

The information received from the parallel output of ES 400 were in binary form and these were further processed into each proper form. The amplitudes are logged in numbers from 0 to 4095, the maximum value corresponds to 2 V calibrated output signal. The angles are logged in numbers from -36 to +36 with an angular resolution of 0.14 degrees from the center of the beam axis. The estimated target strengths are logged in numbers from 0 to 80 with each step corresponding to 0.375 dB, where the maximum number corresponds to the target strength of -26 dB and the minimum number corresponds to target strength of -56 dB. The control byte contains information about the echo sounder condition during operation and also the status of the received data (i.e. whether the data received from bottom or not). Table 1 shows the list of the processed information received from the ES 400 split beam echo sounder.

Before using the amplitude information to calculate the SV of the fish schools, the accuracy of this information should be checked. Checking is done by calculating the target strength based on the amplitude information. The result of the calculated target strength is then compared with the target strength value estimated by the echo sounder which is also received from the parallel output.

In the split beam echo sounder, the calculation of target strength is based upon a combined calculation of signal amplitude and beam compensation value. The beam compensation value is determined from the angles information and it is calculated as follows:

Table 1. Print-out of the processed data of
the ES 400.

Range: 25 m   1989/ 5/22   18:12:02   Ping : 1

Control PRDBAT	Ampli- tude (Volt)	Along- ship (°)	Athwart- ship (°)	TS (dB)	Depth (m)
010011	0.781	0.00	0.00	-34.25	0.1
010011	0.721	0.00	0.00	-35.38	0.2
010011	0.573	0.00	0.00	-37.25	0.3
010010	0.490	0.00	0.00	-38.75	0.4
·	·	·	·	·	·
·	·	·	·	·	·
010000	0.017	-0.28	-0.14		9.9
010010	0.031	-1.12	-1.12	-56.00	10.0
010010	0.037	-1.26	2.94	-56.00	10.1
010010	0.030	-1.40	2.80	-56.00	10.2
010010	0.020	-0.70	-0.14	-56.00	10.3
010010	0.021	0.14	0.28	-56.00	10.4
010010	0.038	1.12	-0.70	-56.00	10.5
010010	0.043	2.38	0.00	-56.00	10.6
010010	0.052	2.52	1.96	-54.50	10.7
010010	0.048	5.46	3.64	-56.00	10.8
010010	0.031	-5.74	-5.04	-56.00	10.9
010010	0.021	0.98	-0.84	-56.00	11.0
010010	0.028	0.56	-1.12	-56.00	11.1
010010	0.040	0.00	-0.84	-56.00	11.2
010010	0.046	0.98	-1.54	-56.00	11.3
010010	0.048	1.82	2.38	-55.63	11.4
010010	0.037	4.90	-2.66	-56.00	11.5
010010	0.025	6.44	-3.64	-56.00	11.6
010010	0.021	3.64	0.42	-56.00	11.7
010010	0.025	6.30	-0.56	-56.00	11.8
010000	0.019	-5.18	2.94		11.9
·	·	·	·	·	·
·	·	·	·	·	·
010010	0.049	-8.68	-7.84	-56.00	23.3
010010	0.032	-2.52	-3.36	-54.50	23.4
011110	0.218	0.00	0.00	-40.63	23.5
011110	1.812	0.00	0.00	-26.00	23.6
011110	1.500	0.00	0.00	-27.50	23.7
000000	0.000	0.00	0.00		0.0
000000	0.000	0.00	0.00		0.0

$$B = 10 \log \{((\sin X)/X) \times ((\sin Y)/Y)\}^4 \qquad (1)$$

$$X = (\pi \times a/\lambda) \sin \beta \qquad (2)$$

$$Y = (\pi \times b/\lambda) \sin \gamma \qquad (3)$$

Combining with the system parameters, the calculated target strength, therefore, is given as

$$TSc = Uout - B - SL - VRc + TVGc \qquad (4)$$

Comparison between the calculated target strength (denoted as TSc) with the estimated target strength received from the parallel output of the echo sounder (denoted as TS) is presented in figure 1. The difference between TS and TSc is very small ($\pm$ 1dB) which means that the received amplitude gives a reliable information about the target detected by the echo sounder
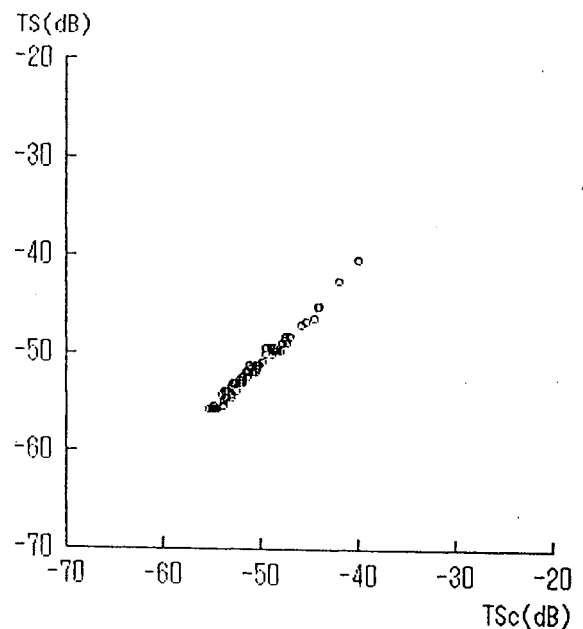
Figure 1. Comparison between TS and TSc.

3. Calculation of Volume Back Scattering Strength

The calculation of SV based on data received from the parallel output of ES 400 split beam echo sounder, combining with the system parameter in use, including correction for the applied 40 log TVG function in the echo sounder into the 20 log TVG function which is needed for calculating the SV, is as follows:

$$Uout = SL - 2TL + TS + VR \qquad (5)$$

$$2TL = 40 \log r + 2 \alpha \times r \qquad (6)$$

$$VR = VRc - TVGc + 40 \log r + 2 \alpha \times r \qquad (7)$$

The target strength (TS) in the equation (5) for a reflecting volume (v) is related to SV as follow:

$$TS = SV + 10 \log v \qquad (8)$$

The volume is determined by the equivalent beam width (ψ), the depth (r), the pulse duration (τ), the sound velocity in sea water (c) and can be expressed as:

$$10 \log v = 10 \log ((c \times \tau /2) \times \psi \times r^2) \qquad (9)$$

Substituting the equations (6), (7), (8) and (9) into equation (5), the Uout becomes,

$$Uout = SL + SV + 10 \log (c \times \tau /2) + 10 \log \psi$$
$$+ 20 \log r + VRc - TVGc \qquad (10)$$

To simplify the equation, the echo sounder constant values are gathered into one constant denoted as CN :

$$CN = TVGc - SL - 10 \log (c \times \tau /2)$$
$$- 10 \log \psi - VRc \qquad (11)$$

and the volume back scattering strength (SV) is expressed as:

$$SV = Uout - 20 \log r + CN \qquad (12)$$

The equation (12) has a term of -20 log r, which usually does not appear in the equation for calculating SV if the echo sounder in its system applied the 20 log TVG function. But the ES 400 split beam echo sounder used the 40 log TVG function, so the term of -20 log r in the equation is a correction factor for the applied TVG function in the echo sounder, thus, total compensation by the TVG function is only 20 log r, as needed for calculating SV.

To calculate the mean SV, it is desirable to leave the decibels notation and derive relations between the absolute values as:

$$10 \log sv = 10 \log u^2 - 10 \log r^2 + 10 \log cn \qquad (13)$$

$$sv = (u^2 / r^2) \times cn \qquad (14)$$

The mean sv was calculated up to ten main layers vertically, from surface over the preset range. The mean sv calculation diagram is shown in figure 2. In order to obtain the mean sv of every layer, calculation by squaring and integrating are necessary. The mean sv for every layer is found by taking the weighted sums of all sv over the out sailed distance sampling interval horizontally (Δl) and the average depth layer (Δd) vertically. The mean sv for each layer is given as:
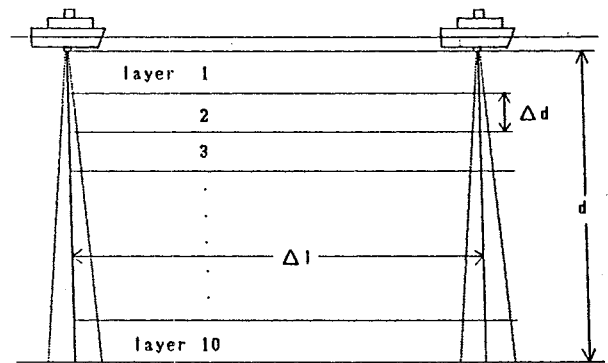
Figure 2. Diagram of SV integration.

$$sv_i = cn \frac{\sum\limits^{P} \sum\limits^{K} (u/r_{(i)})^2}{P \times K} \qquad (15)$$

where,

K : average number of sample in layer i,

P : number of pings for the interval
   sampling distance.

The mean SV for every layer expressed in decibel is :

$$SV_i = 10 \log sv_i \qquad (16)$$

4. Result and Discussion

The results of the calculated mean SV based on data collected by ES 400 split beam echo sounder and related echogram is presented in figure 3. This echogram was made with the aid of personal computer based on the data received from the parallel output of the echo sounder. On the top of the echogram, the time when the data were collected is shown. In the echogram the echo traces of fish schools can be seen, of which the mean SV were calculated. The results of the calculated mean SV from the data collected by ES 400 were then compared to the values of the mean SV obtained by FQ 50 scientific echo sounder.

During the experiment the FQ 50 was operated to integrate the mean SV for every 0.5 nautical miles. To make both mean SV comparable, the calculated mean SV from the ES 400 data was also integrated in every 0.5 nautical miles. On the lower part of the echogram, marks were indicated to distinguish between one integration interval to another. The graphs below the echogram showed the mean SV calculated from the ES 400 data and the mean SV obtained by FQ 50 for every integration interval. The left side graph shows the mean SV values for the first integration, the graph in the middle shows the mean SV values for the second integration and

the right side graph shows the mean SV values for the third integration.

A comparison between the SV values in each graph shows that both SV values are similar especially when fish schools are present. The trends of the curves of the calculated SV from ES 400 were observed to be almost on the same trends with that of the SV curves obtained from FQ 50.

5. Conclusion

In this experiment, by utilizing the amplitude information received from the parallel output of the ES 400 split beam echo sounder, it is possible to measure the volume back scattering strength of fish schools. In addition to the target strength information, future development of programs will surely predict the number of fish. This will lead to a more accurate fish stock estimates by means of the acoustic method.

References

1. Brede, R., Kristensen, F.H. and Solli, H. "Target tracking with a split beam echo sounder", International Symposium on Fisheries Acoustics. June 22 - 26, 1987. Seatle, Washington, USA (1987)

2. Saetersdal, G., Strome, T., Bakken, B. and Piekutowski, L. "Some Observation on Frequency Dependent Back scattering Strength", Symposium on Fisheries Acoustics. Bergen, Norway, 21 - 24 June 1982. FAO report No. 300. (1982)

3. Sasakura, T., Shiraishi, H., Lino, H., Minohara, K. and Aoki, H. "The Furuno FQ 50 an Echo Sounder for Fish Stock Assessment", FAO Fisheries circular No. 778, Rome. (1984)

4. Urick, P, J. "Principles of Underwater Sound", 3rd edition. McGraw-Hill Book Company. New York, USA, p. 237-247 (1983)
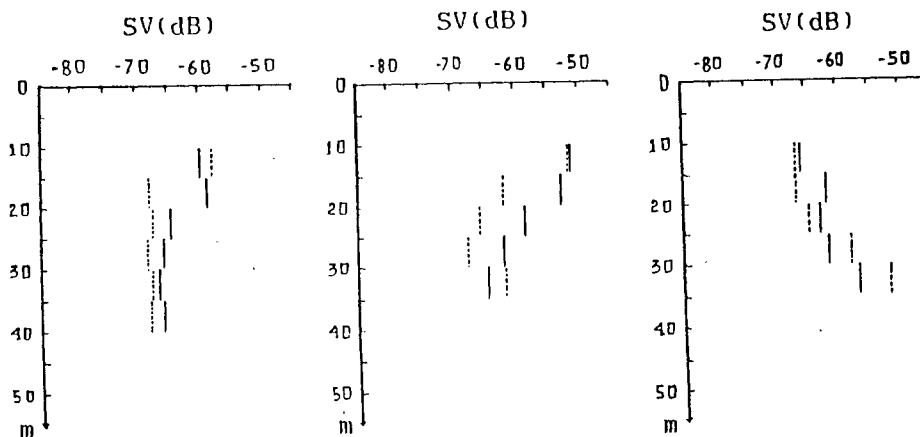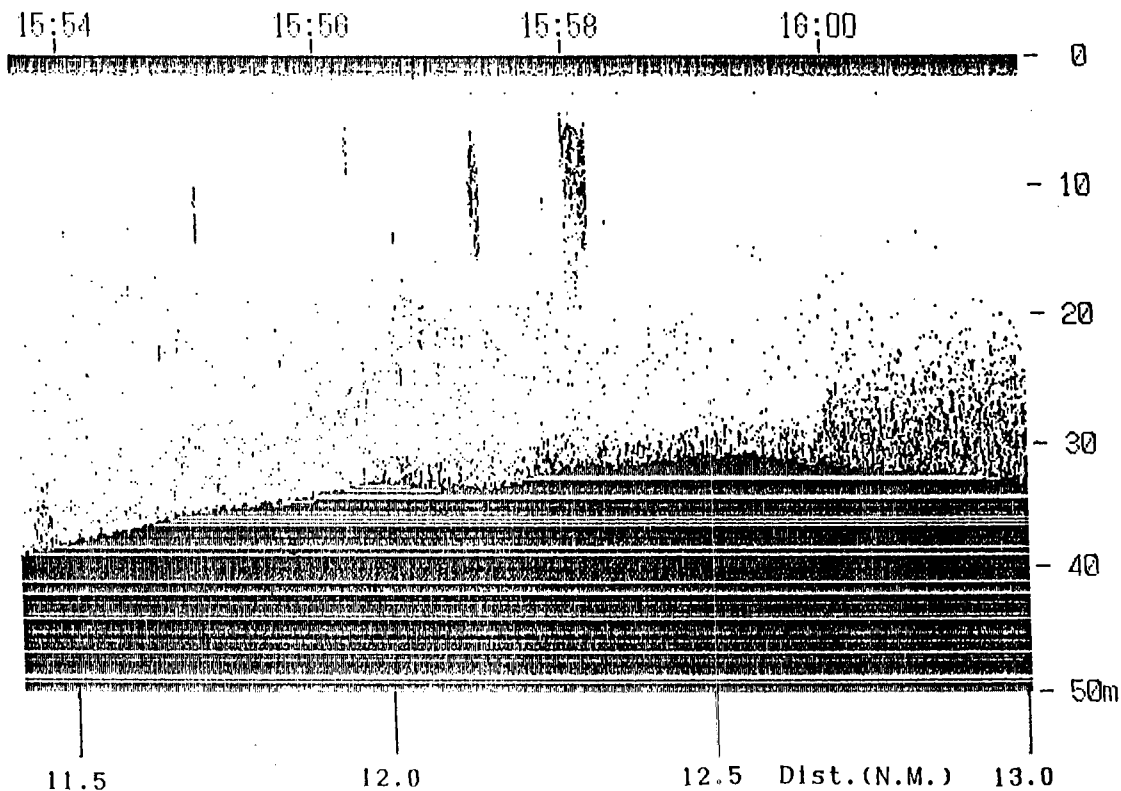
Figure 3. Comparison between the calculated SV from the data collected by ES 400 with the SV obtained by FQ 50 and their related echogram (Suruga bay, May 10, 1989).

ES :---- FQ : ——

JAPAN'S OVERSEAS COOPERATION ON FISHING PORT PROJECTS

M. Noda*, K. Shinoda*, Y. Ugajin**, R. Yamamoto*

* Construction Div., Fishing Port Dept., Fisheries Agency, Min. of Agriculture Forestry and Fisheries, Japan
** Investigation and Research Dept., The Japanese Institute of Technology on Fishing Ports and Communities

Abstract

This paper deals with Overseas Cooperation on Fishing Port Projects by the Government of Japan.

In recent years, refrecting increasing mutual cooperation of many countries in the world, a number of fishing port construction projects have been increased in abroad by Japan's economic cooperation (Official Development Assistance:ODA). Many requests and consultations related to construction of fishing ports have come to the Government of Japan from the governments of developing countries.

Japan's Overseas Cooperation for the fishing port projects in abroad consists of three types, Grant Aid, Loan and Technical Assistance.

When we think of the better way of overseas cooperation on fishing port project by Japan, we feel a little regret of a hasty proceeding schedule of Japan's grant aid.

We feel the necessity of various surveys and studies.

In addition to these necessity, some developing countries carrying out Yen Loan projects may occasionally fall into serious debtors if the exchange rate of foreign currency gets changed

It would be necessary for us to make the overall better way of overseas cooperation.

1. Introduction

In recent years, refrecting incresing mutual cooperation of many countries in the world, a number of fishing port construction projects have been increased in abroad by Japan's economic cooperation (Official Development Assistance:ODA). Many requests and consultations related to construction of fishing ports have come to the Government of Japan from the governments of developing countries.

This paper has been presented to be of help to those who make such requests of consultation.

2. Economic Cooperation
2.1 Outline of Economic Cooperation

Economic Cooperation means Flow of Financial Resources which constribute to economic and social development and welfare of developing countries. This cosists of three types of cooperation as follows,
    (1) Official Development Assistance (ODA)
    (2) Other Official Flows (OOF)
    (3) Private Flows (PF)

Development Assistance Commitee (DAC) which belongs in Organization for Economic Cooperacion and Development (OECD) of the United Nations, manages the classification and taking statistics of the Economic Cooperation.

DAC dosen't give a definition on Least Developed Countries (LDC). Generally speaking, LDC is understood the nation or area which accepts Financial Resources for the development.

DAC says that there are 163 least developed countries and/or area in the world as of 1987.

2.2 Outline of ODA

ODA has been defined as provision of Financial Resources with the following conditions in DAC since 1972.
(1) To be provided by goverments or govermental agencies.
(2) To be principally intended to promote the economic development and welfare of developing countries
(3) To be inclued Grant Element(GE) of at least 25% in order to lighten the burden imposed on developing countries.

Remark:
GE of ODA

$$= \frac{Grant\ Aid\ +\ Loan\ \times\ GE\ of\ Loan}{Total\ amount\ of\ ODA(Grant\ Aid+Loan)}$$

GE of Loan

$$= \frac{T.L.-Present\ Value\ of\ (Reimbursed\ Principal\ +\ Interest)}{Total\ amour\ of\ Loan\ (T.L.)}$$

Discount rate is usually applied 10%/year when Present Value is estimated. Therefore Grant Aid is regarded as GE 100%, and Loan carrying 10%/year interest is regarded as GE 0%.

3. Japan's Overseas Cooperation on Fishing Port Projects

Japan's Overseas Cooperation for the fishing port projects in abroad consists of three types, Grant Aid, Loan and Technical Assistance as follows.

3.1 Grant Aid

The first type of cooperation is Grant Aid. It is one of the forms of Japan's ODA to provide developing countries, at their reqest, with non-reimbursable funds needed to procure eqipment machinery and materials and/or to construct infrastructures for the project of contributing the economic and social development and welfare of developing countries.
Grant Aid for fisheries has reached 10 billion Yen in 1989 (about 70 million US$ as 145 Yen/US$). And the Budget for fishing port construction project has been included

about 4 billion Yen in it.
Enforcement of every project of Grant Aid is dicided by the Government of Japan (the Ministry of Foreign Affairs:MFA) and implemented by Japan International Cooperation Agency (JICA).
The magnitude of previous Grant Aid of each fishing port construction projects has ranged from about 600 million to 2,400 million Yen (about 3 million to 12 million US$ as 200Yen/US$) during the one or two fiscal years.
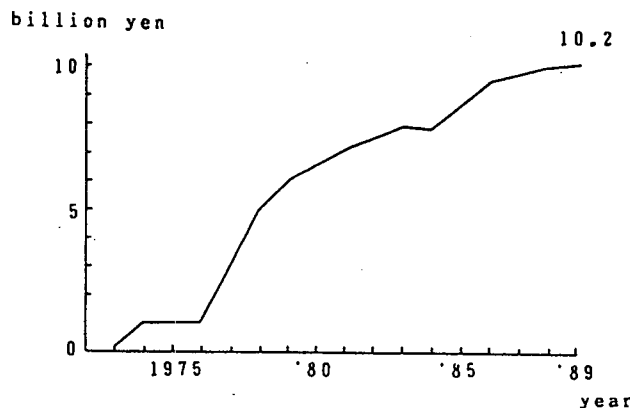
Fig.1   Variation of Grant Aid for Fisheries

3.2 Loan

The second type of cooperation is Loan. In the case of large scale fishshg port development projects have been expected to make a nationwide contribution to the economy, ODA Loan to the goverments (or govermental agencies) of developing countries are provided by the Overseas Economic Cooperation Fund (OECF) of Japan. The Loan are usually referred to as "Yen Loan". The terms of Loan are as of April, 1989 as follows :

interest :1.0~4.0%/year
  (according to the conditions of countries accepted Loan)
imbursement period :30 years
  (included grace period :10 years)

The magnitude of previous Yen Loan of each fishing port construction projects has ranged from about 5 billion to 10 billion Yen (about 25 million to 50 million US$ as 200 Yen/US$).

3.3 Technical Assistance

The third type of cooperation is Technical Assistance. It is also decided to excute by the Goverment of Japan(MFA) and implemented by JICA and intended to contribute to developing countries. Relating to fishing port projects, many technical assistances have been implemented such as dispatch of experts for fishing port planning and/or design,acceptance of trainees for fishing port projects and sending of survey teams for fishing port development projects.

(1) Implementation of Development Study on Fishing Ports

Development study on a project in a developing country involves on-the-site research including the social background, the economic impact, etc. of the project. A report on the feasibility of the plan is drafted by the dispatched members of Japanese Government. In the field of fishing ports, the research team consists of experts on fishing port planning, construction, management, etc.

(2) Dispatch of Expert

Experts are dispached in accordance with the requirements of developing countries. The dispatched experts will work with their counterparts in the countries on the requested projects.

(3) Acceptance of Trainees

Trainees from abroad have been accepted since 1952 in the field of fishing port as a form of technical cooperation.

Usually, trainees can learn basic knowledge and techniques, and also study fishery development in Japan through excursions to see the present condition of fishing ports.

4. The way of ODA Fishing Port Projects by the Governments of Japan

The government of Japan executes ODA in the way of as shown in Fig.3.

Studies on Fishing Port Constructions have been implemented as shown in Table 1.

5. Examples of the Fishing Port Construction Projects
5.1 Apia Fishing Port (Western Samoa)

(1) Outline of the Project
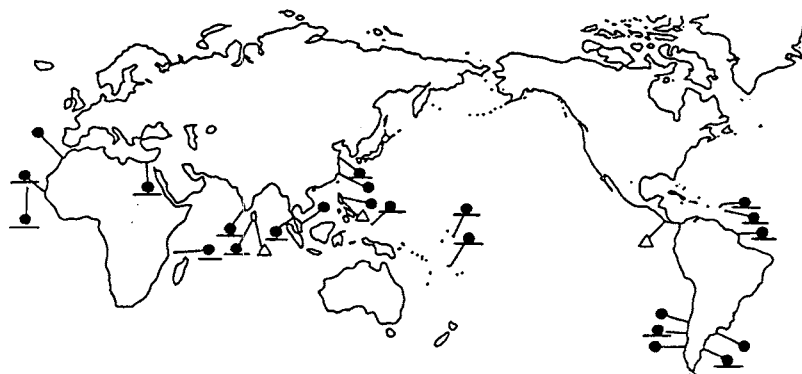
	No. of cases	Contents
●Fisheries Grant Aids	16	Construction of fishing ports, training ships, fish culture, lab equipment, etc.
●Project-based Technical Assistant	7	Fish farming, fisheries training, processing. etc.
△Research/Investigation	3	Fisheries, resource research and investigation system

Fig.2 Major Government-based International Fisheries Cooperation (1987)

the Government of Japan

Ministry of Agriculture, Forestry and Fisheries (MAFF)

Fisheries Agency (FA)

Ministry of Foreign Affairs (MFA)

Japan International Cooperation Agency (JICA)

The Overseas Economic Cooperation Fund (OECF)

⑤

MAFF ⟷ MFA	⟷	Embassy of Japan
↑ ④ ↑ ②		
↓④ ↓④		
FA ⟷ JICA· ──		Overseas office of JICA
④ OECF ──		Overseas office of OECF

③ ↓   ① ⑥ ⑦ ⑧ ⑨ ↑↓

Government of the recipient country
or
its designated authority
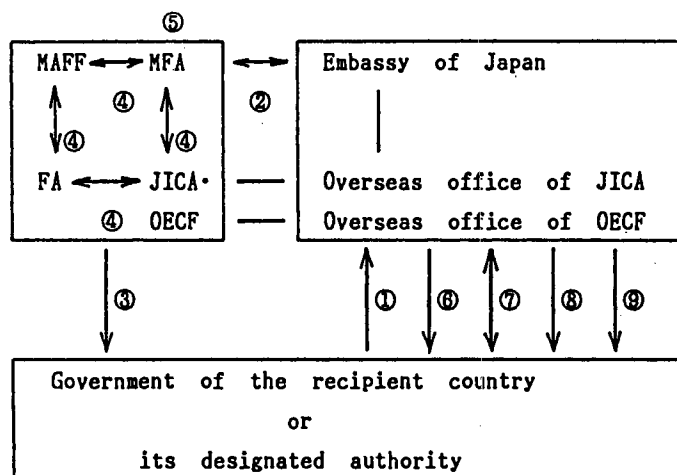
① Request for cooperation

② Screening of the requested projects

③ Dispatch of a survey team

④ Inter-ministerial consultation

⑤ Budget appropriation by the Diet

⑥ Presentation of draft Exchange of Notes

⑦ Singnature on the Exchange of Notes (E/N)

If funds for the completion of the project are provided by
OECF's Loans, the follwiog procedure shall be followed.

⑧ Dispatch of a surver team by OECF

⑨ Conclusion of Loan Agreement (L/A)

Fig.3 Mechanism of the Japans Economic Cooperation on Fishing Port Projects
(up to the Exchange of Notes or Loan Agreement)

The Government of Japan executed the first Grant Aid for Demerara Fishing Port of the mouth of Demerara river, Guyana. After that, the project of Apia Fishing Port would be the first Grant Aid for sea fishing port project.

The fishing port was completed in February 1982, with the details as shown in Fig. 4.

(2) Background of the Project

The Government of Western Samoa carried out its Fourth 5 Years Development Plan between 1980 and 1984. The plan proposed promoting the welfare of the people by making use of resources.

Fisheries in Western Samoa is classifild into three main categories, inner - reef fisheries aimed at self-consumption of the catch, outer-reef operations for earning cash incomes, and experimental fisheries conducted by the Samoan government. Due to the different nature of these fishery types, the government implements different policies for their promotion.

The wharf, a new fishing market and the other fishing port facilities are needed to increase the supply.

(3) Plan of the Fishing Port Construction

a) Target of the Project
This project implemented with the

Table 1. Implementation of Study Team on Fishing Port Construction

No.	Country/Area	Year			Place	Content of Cooperation
1	Argentine	'78.			San Antonio-Oeste,	Study
		'86	'87		Puerto Deseado	Grant Aid
2	Brazil	'90			Recife	Expert
3	Chile	'81	'82		Concepcion	Study
		'84			do.	Expert
		'86			Puerto Monte	Grant Aid
4	Egypt	'89	'90		Ataqua	do.
5	Fiji	'86			Lautoka	do.
6	Ghana	'88			Tema	do.
7	Guatemala	'74			Sipacate	Study
8	Guyana	'75	'78	'80	George Town	Grant Aid
9	Indonesia	'73	'74		Jakarta	Loan
		'77	'78		do.	do.
		'80			Pelabuhan Ratu	Study
10	Kiribati	'80	'85		Tarawa	Grant Aid
11	Malaysia	'69	'70		Kuantan	Study
12	Marshall	'81	'88		Majuro	Grant Aid
		'89			Arno	do.
13	Mauritius	'82	'88		Port Louis	do.
14	Mexico	'72			Mazatlan	Study
		'83			Mexico City	Expert
15	Micronesia	'85			Yap	Grant Aid
16	Mozambique	'86			Quelimane	do.
17	Nigeria	'66			Lagos	Study
18	Palau	'87			Angaur, Ngerchelong, Ngatpang, Melekeok	Grant Aid
19	Papua New Guinea	'76	'77	'78	Kavien, Rabaul	Study
20	Peru	'72			Oquendo	Expert
		'74			Lima, Paita, Samanco, La Puntilla, Oquendo	Study
		'76	'77		Ventanilla	Study
		'79	'81	'82	do.	Expert
		'88	'89	'90	do.	Study
21	Philippines	'63			Navotas	do.
		'78	'80		Iloilo, Lucena, Sual, Camaligan, Zamboanga	Loan
		'81			Cebu, Davao, Tacloban, Cagayan de Oro, Cadiz	Loan
22	Seychelles	'90			Mahe	Grant Aid
23	Sri Lanka	'60			Columbo	Study
		'64			Galle	do.
		'82			Kirinda	Grant Aid
		'86	'87	'88	do.	Study
		'89				
24	Sriname	'89			Paramaribo, New Amsterdam	Grant Aid
25	Taiwan	'65			Anping	Study
26	Tailand	'57			Tertau,	do.
		'69			Bangkok	do.
		'87			Nakhon Si Thammarat	Grant Aid
		'89			Bangkok	Expert
27	Tuvalu	'87			Funafuti	Grant Aid
28	Soviet Union	'75			Pioner	Study
29	Western Samoa	'80			Apia	Grant Aid

target as follows,
(I) To construct market in order to deal with the increasing fishing production.
(II) To increase the income of the fishermen by developing the Fishery
(III) To improve nutritive conditions of the people by the fishing production

b) Plan of the Fishing Port Facilities
The basic facilities and the functional facilities, as shown in Table 3, were constructed.
The quay and wharf is planned for the major type ships, mainly.
The functional facilites are planned in consideration of flows of the fishing production during
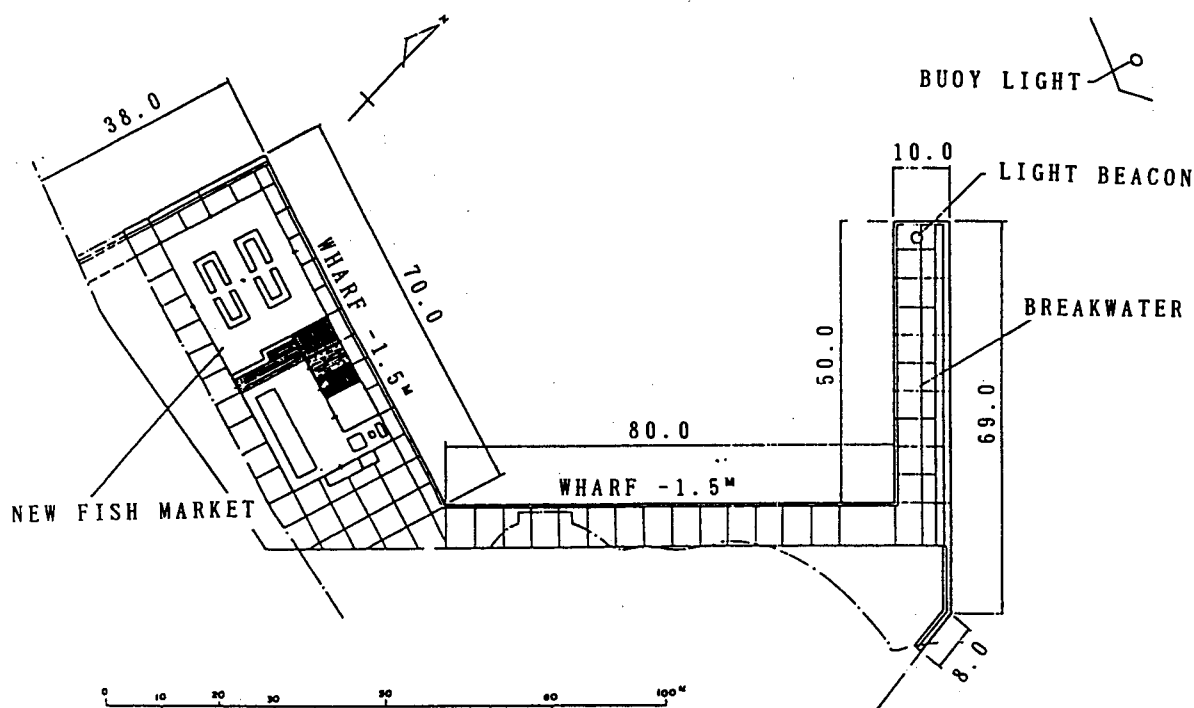
Fig.4   General Plan of Apia Fishing Port

Table 2   Fisheries in Western Samoa (in 1979)

	Fishing Method	Fishing Vessel	No., of Fishermen Per Boat	Est. Catch	Estimated Fishermen Population	Governmental Policy
Inner Reef Fisheries	Harpoons, trapping, using bare hands	Baobao (canoe)	—	500	10.000 side work	Protection
Outer Reef Fisheries	Hual net and bottom fishing	28 ft. Area	4	1300	1000	Cautious promotion Policy
Large-scale Fisheries	Role-and-line (with live bait)	60 ft. Bonito boat	20	7	20	Fish farming with artificial feeding. Experimental fisheries

Table 3. Major Facilities of the Apia Fishing Port

① Basic Facilities	② Functional Facilities
Breakwater 77m, Quay Wall 188m Annex Facilities (Fenders, Mooring Post, Light Buoy, Light Beacon, Illuminations, Water Pipes, Intake Pipes etc.)	Fish Market 1,000 ㎡ (Market for selling 500 ㎡, Management/ Administration Facilities 500 ㎡) Freezer (50 tons) 1 unit Ice maker (1 ton/day) 1 unit

unloading, freezing and sale.

5.2 Jakarta Fishing Port (Indonesia)

(1) Outline of the Project
    The Government of Japan executed the first ODA Loan of fishing port project for Jakarta Fishing Port. Jakarta Fishing Port was completed in July 1984, with the details as shown in Fig.5.

(2) Background of the Project
    The Government of Indonesia carried out its second 5 years Economic Development Plan between 1974 and 1978. Under the Second Plan, further expansion of the fishing industry is proposed to meet the domestic comsumption and export demands.
    Pasar Ikan is Playing a pivotal role in the capacity of a fishing base in Jakarta. However, facilities

required as a fishing port/market, are so narrow, obsolete and insufficient that Pasar Ikan does not fulfill its function as a fishing base, or to the contrany, such a situation results in the prevention of its development in terms of modernization and rationalization of fishing activity and fish distribution.

(3) Plan of the Fishing Port
   Construction
a) Economic Analysis
   An analysis on National Economy was conducted as follows:
   I)Shortening of the time required from arrival to departure of fishing boats through relieving traffic congestion.
   Ⅱ)Increase of fish catch through enlargement of fishing activities
   Ⅲ)Maintain fresh condition with the use of ice
   Ⅳ)Increase of income by switching over from salted and dried fish to fresh fish

b) Plan of the Fishing Port
   Facilities The development of the main facilities is shown in Table 4.
   Construction works for the Breakwater and Revetment include Bamboo Pile and Bamboo Mat,which are made of the native material (bamboo) in Indonesia as shown in Fig. 6~8.

6. Problems to be considered about Overseas Cooperation related to Fishing Port Projects.

Based on some information about overseas fishing ports in developing countries which we have gotten through many opportunities, We would refer to some problems about overseas cooperation related to fishing port projects.
Generally speaking, the administrative organization related to fishery/ fishing port is small and insufficient, and it only manages license and registration of fishermen/ fishing vessels, management
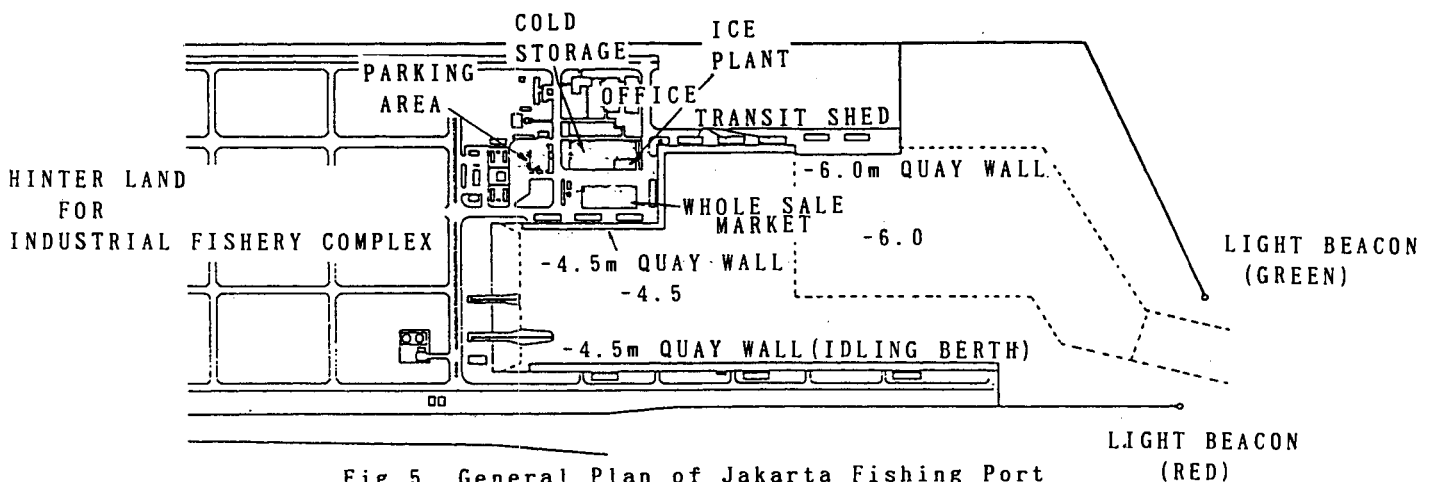
Fig.5   General Plan of Jakarta Fishing Port

Table 4   Major Facilities of the Fishing Port

Phase I

① Basic Facilities
Breakwater 1,040m , Quay Wall 1,504m , Revetment 3,040m
Navigation Aids 2units   , Reclamation Area   601,000m²

Phase Ⅱ

② Utilities Works
Pavement, Landscaping, Fence and Gate, Drainage System, Water Supply System, Fire Fighting System, Fuel Oil Supply System, Sewerage System, Ship Repairing Facilities, Additional Civil Works

③ Building Works
Refrigerator Facilities/Building 4,590m², Transit Shed 324m²× 12units, Whole Sale Market 2,187m², Machinery House 1,166m², Rest House 460m², Administration Building 2,028m², Dormitory 296m², Water Pumping House 60m², Garage 240m², Oil Pumping House 56m², Gas Fuel Storage 34m²,Gate House 27m², Toll Gate 3m², Public Toilet 67m²× 2units

④ Refrigerator Facilities
Ice Making Plant 150tons/day, Ice Storage 200tons, Cold Storage 850tons, Contact Freezer 1.5tons/shift, Emergency Generator 1,000KVA× 2units
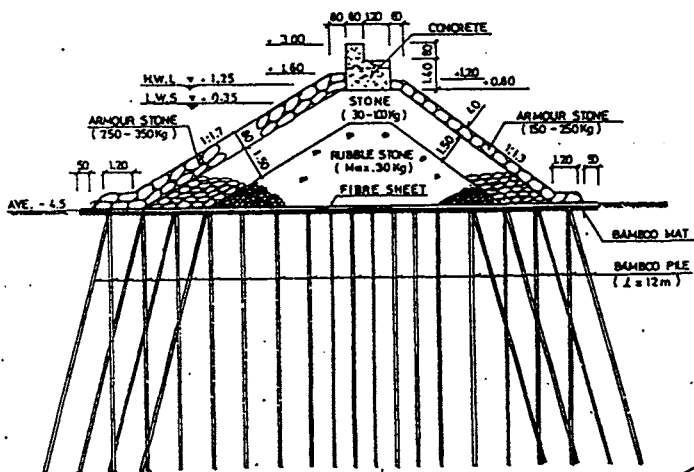
Fig.6   Typical Section of Breakwater
         (Jakarta Fishing Port)
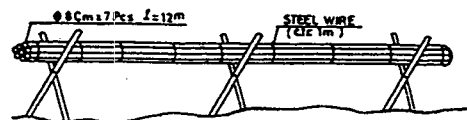
Fig.7 Fabrication of Bamboo Pile
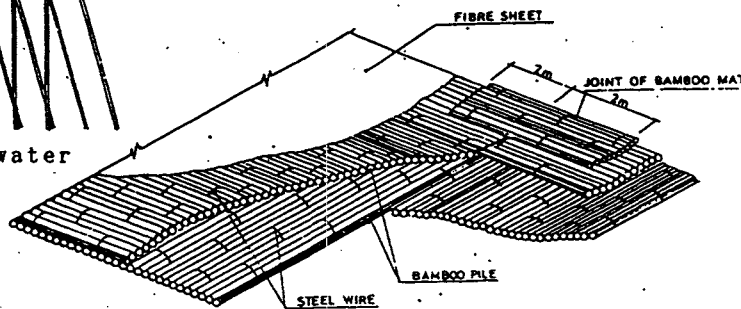
Fig.8   Detail of Bamboo Mat

of ice plants/ cold storages, sale of ice, diffusion of effective new fishing methods and fishing gears, collection/ arrangement of fishery statistic data etc..

The problem of the aspect of staffing is, generally speaking, the technical personnel in the field of fishery, electricity and machinery etc. are assigned only a few in the authorities concerned of fishery/ fishing port, however the civil engineering staff is not assinged.

Therefore, as the administrative organization of fishing port is insufficient about maintenance of the fishing port facilities of breakwaters, wharfs, piers, revetments, roads ,and the depth of routes, anchorages and basins etc., the authorities concerned of fishery/ fishing port are driven by necessity to depend on other departments, for example, port authority or ministry of public works etc..

This causes inconvenient circumstances for them to make development of fishing port and promotion of fisheries actively by themselves.

The problem of the aspect of material and financial matters is, generally speaking, the budget for administration and maintenance is insufficient, and consequently, it causes difficulty of maintenance of fishing port facilities, machinery and equipment etc., and a shortage of repair parts.

When we think of the better way of

overseas cooperation on fishing port project by Japan, we feel a little regret of a hasty proceeding schedule of Japan's grant aid because Japanese budgetary system makes it a principle to execute the budget in one or occasionally two fiscal years if it is necessary and reasonable after the Exchange of Notes between the Government of the recipient country and the Government of Japan.

We feel the necessity of various surveys and studies of weather conditions, marine phenomena and coastal topography etc. around the project site for many years, and also trial small scale work and assessment studies after the completion of fullscale work of the project.

And in addition to these necessity, some developing countries carrying out Yen Loan projects may occasionally fall into serious debtors if the exchange rate of foreign currency gets changed and Yen becomes stronger than the currency of the country when the government of the country would pay back to Japan.

In such case, the self-efforts of the country carrying out the project become offset by other factors.

It would be necessary for us to make the overall better way of overseas cooperation.

CONSTRUCTION OF LARGE SCALE FISHING PORT
<NEW NAGASAKI FISHING PORT>

M. Kishino*, A. Nagano**, M. Kurose*, Y. Ugazin***

* Fishery Department of Nagasaki prefecture Government, Japan
** Fishing Port Department, Fishery Agency, Government of Japan, Japan
*** The Japanese Institute of Technology on Fishing Ports and Communities, Japan

Abstract

New Nagasaki fishing port which has landing capacity of 290,000 tonnage per year ,and New fishery town which has population of 20,000 has been constructed at Mie inlet. Mie inlet is 16km away from Nagasaki city to the north west, NAGASAKI prefecture.

New Nagasaki fishing port construction started at 1973. Amount of investment is ¥130billion from 1973 to 1989. At 2nd october 1989, New Nagasaki fishing port and new Nagasaki fish market have been opened.

Until then, the fish port had located at center of Nagasaki city, where landing fish were treated and auction was taken place from 1914. At this old Nagasaki fishing port, quantity of landing fish was 200,000 tonnage and amount cost of landing fish was ¥80billionat 1982. The old Nagasaki fishing port was one of the biggest fishing ports of Japan.Since Nagasaki city has grown up, the old fishing port which located at center of the city couldn't have the spare of land and basin for fishery factory and boat.The scheme which is the moving out to the place away from the center of the city of such large scale fishing port is the first work in Japan.

New Nagasaki fishing port are consisted of market area 221,482 square meter,fish process factory 26 company in 135,051 square meter, sewage, quay 3,390m and basin area 1,500,000 square meter. There are two fish landing houses, fish live stock pond, middleman house, selling hall related to worker in market,parking area 38,643 square meter, fish box yard, container yard, sea fresh water well facility and garbage collection yard in the market area. And there are ice making facility 480 tonnage per day capacity, ice stock capacity 6,300 tonnage, freezer capacity 476 tonnage per day, cold storage capacity 52,845 tonnage. Behind New fishing port, new fishing town has been constructed with primary and high schools, two banks, many shopping stores referred to fishing gear and food, houses544 and condominium 830.

Now New Nagasaki fishing port has been constructed to become more safety port with making breakwater and improve facility mooring with quay. New scheme which is called International fishery port provided with fishery research and education and laboratory has been planned and has been undergoing.

1. Project Outline

1.1 Problems with the Older Fishing Port

The older Nagasaki fishing port had located at the most interior of Nagasaki inlet, where adjoin to Nagasaki station and the downtown of Nagasaki city. At this site, Port construction and development had continued from 1951 to 1972 under the

Fishing Port Development Plan by the state government. The major structures built during these periods were landing facilities, roads, and parking areas, freezers and refrigerators, ice factories and other industry related necessities. At once, there was a prominent increase in the number of larger vessels and consequently a greater numbers of landings.

The main fishing grounds around the Nagasaki fishing port are the Isei bottom trawling area around the East China Sea and the Yellow Sea, the area ground the Tsusima Strait, the Goto Islands and the seas in and around East China Sea dedicated to large and medium-scale roundhaul netters. Nagasaki is surrounded by rich fishing grounds and is also ideal for the landing of catches and preparing ships for departure.

The total annual landing reached 253,000 tons at 1965, which is the record of landing. But after 1970, the catch landing at older Nagasaki fishing port had been decreasing a little by little. There are 5 main reasons adding up to the gradual decline as following.

1) Decreasing the resources of Isei bottom trawling area and the landing of roundhaul netters.

2) Insufficient depth at quays and ship basins especially for roundhaul netters ship, which has gotten large.

3) Difficulty in developing areas into a fisheries processing complex equipped with cold storage, processing and transportation terminals directly connected with landing area behind the older port.

4) Water pollution in the older port.

5) Insufficient width in the older port's waterways. There are commercial port functionand ship building industry in Nagasaki inlet together.

1.2 Planning a New Fishing Port

The three main functions of Nagasaki inlet, an industrial port as well as commercial

and fishing ports, have delimitting effects mutually. While it is desirable to promote well-balanced development of the port area, physical limitations and a disproportionately developed industrial sector have tipped the balanced development of the port and the older fishing port's transformation into modern fishing port. This being the general state of affairs, there is an increasing need for construction of mooring facilities and areas suited for larger fishing boats, development of both water and shore facilities to accommodate greater landings, and maintaining sufficient hygiene for fresh food products. Construction of a new port was also necessary in terms of securing safe navigation and transportation routes in the shore area.

1) Landed catches and entering fishing boats into The New Fishing Port

In planning the new fishing port, the main purposes included securing required length of the landing quay, water depth, sufficient resting facilities, effective layout of port facilities for ship preparations, and sufficiently large ship basins. Safe and convenient port layout would enable larger vessels (in the 300-1000 DWT range) to moor. Total landings are expected to increase to 249,000 tons in 1994.

2) Distribution and processing

Although the Older Nagasaki Fishing Port as a base for landing and distributing fishery products, the relatively small number of processing companies in the area had been one of its major weaknesses. In order to overcome this difficulty, it was necessary to develop sites for distribution and processing by building a processing complex, in an attempt to bring together catch landing, distribution, and consumption.

The 135,000 square meter-wide fisheries processing complex has already been developed and of this area, 92% has been sold to 20 companies. Eight companies are currently in operation at 1989 present.

3) Developing transportation

Recently transportation by trucks is increasingly more important than railroads and this trend is expected to continue in the future. In order to facilitate truck transportation, access roads to highways need to be developed or built.

4) Developing drinking water supply and water treatment

Estimated water consumption by fisheries-related facilities of the new port and general residential areas is 5,800 tons/day. Also, work has been finished to treat 11,000 tons/day of waste water from the fishing market, processing plants and general sewage.

5) Development of a fisheries- oriented city

The new project calls for the development of area behind the fisheies related facilities into residential housing, parks, and other urban facilities to turn the area into a fisheries oriented town adequate for a population of 20,000 inhabitants.

Table-1 Comparing the Facilities at the Older and New Nagasaki Fishing Port

CATEGORY		SIZE OF THE EXISTING PORT	SIZE OF THE NEW NASAGAKI PORT	
			SIZE	INCREASE OVER PRESENT FACILITIES
TOTAL WHARF LENGTH		2,047m	4,940m	2.4
BREAK-DOWN	LANDING	620m	1,410m	2.3
	RESTING	1,064m	2,250m	2.1
	PREPARATIONS	225m	580m	2.6
	SPECIAL USE	165m	700m	4.2
SHIP BASIN TOTAL AREA		180,000m²	1,500,000m²	8.3
JETTY TOTAL AREA		42,508m²	227,000m²	5.3
PARKING LOTS		3,855m²	32,800m²	8.5
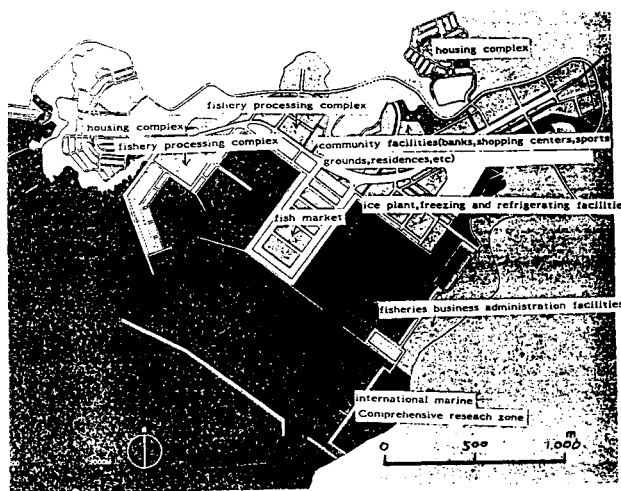
Fig.1 New Nagasaki Fishing Port

2. Fish Market Development

2.1 Market size and capacity

In connection with the New port Development Project, port facilities improvement plans were completed steadily, one after another. The New Nagasaki Fishing Port Wholesale Fish Market was planned at 1981 and started to construct at 1984.

The planned market out of the 350m-wide, 600m-long Central Jetty was decided to be 221,482m², including the sites required for port facilities and public access roads. The target handling volume was set at 235,000 tons for 1990. The capacity of the market facilities was determined based on this figure. The new fish market is expected to create 3,306 jobs.

2.2 Fish Market Facilities - General

The major facilities to be newly built or improved in the 5-years Market Development Project are listed in Table-2. Detailed descriptions of each of these facilities is given below.

1) Wholesaler Building

One building is located to the east and another to the west of the Central Jetty. The East Wing handles the catch from Isei

bottom trawlers and coastal fishing vessels while the West Wing handles mostly the roundhaul netter products.The buildings are made of prefabricated concrete and are specially designed with widely-spaced pillars, which are 20 meters apart.

2) Shipping facilities

The new shipping facilities have been built to match the variety of fish species handled at the market. Of particular importance are the 3 pontoons used for landing and catch classification of Isei bottom trawlers products and another intended to handle the offshore catches. Pontoons are advantageous because they accommodate changing tidal levels. The auctioning area for offshore catches is provided with specially- designed fork lifts which allow catch landing to be made directly from on board the vessel.

3) Auction Area of live fish

In order to accommodate the recent increases in auctioned live fish and shellfish, 13 sea-water tanks of various sizes, with total water capacity of 80 tons, were built outside the auction hall. These tanks are expected to boost trade volume and more species of live fish.

4) Broker's building

The floor of this building contains 65 shops with 7m*6m, or 42 square meter area each. These broker's shops are an outstanding feature of the new port, as they expedite rapidly trading of the various types of fish and fishery products.

5) Shops related to workers in the market and fish products retail dealers.

The shop Building has enough space for 22 small shops selling goods of daily use and 5 restaurants. The well-provided facilities in this building help to promote the use of the market by fishermen, broker and shoppers.

6) Automatic Measuring Instruments

Power and water meters located in the Broker's Building, Shop Building, and Wholesale Building are periodically

monitored by means of telemetry. The date thus obtained is processed by a computer, which can automatically calculate consumption and utility charge. The telemetry and fully automatic system streamline port administration and facilities management.

Table-2 Major Fish Market Facilities

FACILITIES	STRUCTURE/SIZE
Wholesale Buidling West Wing	Single-story FC 17,094m²
Wholesale Building east Wing	Length 520m with storm shutters Single-story FC 15,549
Fresh Fish Facilities (2 wings)	Length 520m with storm shutters, sale floor Ferrobar enforced slated single-story 460 Water capacity 80 tons
Broker's Building	2-story FC 11,707
Shop Building	(1F) 65 shops (2F) offices and other facilities Single-story FC 3,730
Shipping Terminal	22 shops, 5 restaurants, offices and others Ferrobar enforced slated single-story 760
Thermostat Refrigerator	Aluminum panel building 200
Site Offices (6)	2-story prefabricated 2,611
Guardmen's Offices (2)	Single-story FC 14
Seawater Treatment	Single-story FC 608
Waste Dump	Ferrobar enforced slated single-story 106
Outdoor Lavatories (6)	216
Cason Deposit Area	5,864
Container Yard	2,500
Parking Lots	38,643
	(For business use) 909 passenger cars, 74 larger vehicles (For commuting) 814 car spaces
Transport Facilities	Isei Traiwer Landing System, Automatic Sorting Machine

3. Development of Distribution and Processing Facilities

The concept for the New Nagasaki Fishing Port stems from the dire necessity to accommodate the recent increases in volume handled by the older port, which the conventional distribution and processing facilities were unable to do because of physical limitations. In designing the new port, therefore, the "catch phrase" has been a "streamlined flow of operations from catch landing to product distribution."

Regarding new facilities, plans have been made to build an ice factory (with a daily production capacity of 500 ton/day), a 6000-ton ice storage unit, cold storage with the freezing capacity of 355 tons/day and 35,100-ton refrigerators.

The Prefecture Association of Fisheries cooperative built 51 ton-day capacity freezers and 5000-ton refrigerators in 1978 with funding from the national government. However, due to the difficulties involved in Fish Market relocation, it was not until 1984 that full-fledged efforts were made to improve the facilities. Also, it was this year that the new port area was determined

eligible for a comprehensive distribution of fish products development plan by the state government.

In the near future and before the new port becomes fully functional, the total ice production by 3 plants is expected to reach 380 tons/day with a storage capacity of 4,300 tons. When similar projects of the Japan Deep-Sea Roundhaul Netters Association are completed (they plan to build 100 tons/day ice makers and a 2000-ton ice storage unit), it will be possible to meet the initial targets figures.

In terms of cold stores, 216 tons/day freezers and 22,495 ton refrigerators have already been built by 6 companies. An additional 50 ton/day capacity freezers and a 5000-ton storage units are expected to be completed by the end of 1989. Additionally, the fish processing complex has the 210 ton/day freezing and 25,350 ton storage capacity. Compared with the existing facilities, the new port will have 3.3 times more freezing capacity and 2.6 times more refrigeration capacity.

As for processing facilities, the original 73,000m² sites developed for building an industrial complex were quickly sold out. Further development made available a total of 135,051m², but at present, the prepared lots have also completely been sold out.

The Nagasaki Association of Fisheries Processors was the first organization to build a "surimi" (ground fish meat used to make fish cakes) factory in the complex accomplished in 1973. Because of the uncertainty involved in the fish market relocating to the new port site, only 9 companies are currently in operation, but in the next three years, all 26 companies which purchased the lots are expected to finish construction of their processing facilities in the newly developed fish processing complex.

The processing plants already constructed or scheduled for completion in the near future deal in a variety of processed foods (e.g. frozen processed food, surimi, specially prepared delicacies, fish meal and so on). The area is expected to develop into a fisheries operations center in Nagasaki Prefecture within the not too distant future.

The firms that opened plants in the fish processing industrial complex quickly formed a cooperative to discuss the issue of water supply. However, inadequate facilities and the relatively small number of firms that initially moved into the area hindered the ability of the cooperative to function satisfactorily. It was later decided that the prefectural government would finance the water supply project, which would to sold to private corporations at a later time.

At present, the cooperative is managing the water supply project and paying back the government for the plant and equipment.

A notable feature at this industrial complex is the Fisheries Processing Laboratory, built with the state government's assistance. A full-fledged meal processing plant is scheduled for completion by the end of 1989, which is the first attempt of its kind in Nagasaki.The role of the fisheries industrial complex is likely to expand along with the development of the Nagasaki Fishing Port Fisheries Complex Cooperatives. When these firms come into full operation, they are certain to supply a variety of fishery products to meet consumer needs, transforming New Nagasaki Fishing Port into an important base for fisheries production, processing and distribution.

For the firms that joined the consortium for land development, the capital outlay was huge, most of which was spent on the exorbitantly priced land. The prefectural government has backed up the new processing complex development processing complex by undertaking highways connecting the production areas with consumption areas need to be improved, as truck transportation becomes increasingly more important. The completion of the Trans-Kyushu Motorway in

the near future will likely contribute to this trend.
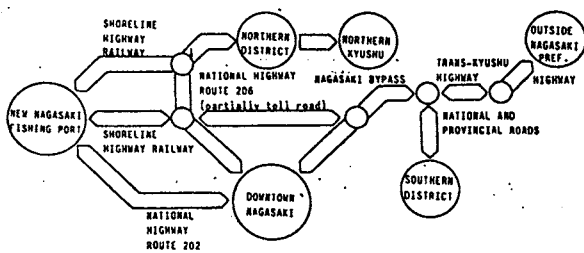
Fig.2 Network of Main Roads and Highways

New processing and distribution facilities are indispensable to the new port and new fish market, whose activities are expected to exceed well over those conducted at the older port. The opening of the new port and fish market, together with such fringe benefits as a strong brokers corps, middlemen, and wholesalers, is certain to revitalize the local economy and further contribute to the economic advancement of southern Nagasaki.

4. City Planning

4.1 Residential Areas - Objectives

People from all walks of life are expected to live and work in the new port area. Some are fishing vessels crew who return home after many months of overseas duties, while others are people working at the fish market, whose day begins at pre-down hours. To satisfy the varied needs and life styles of the areas new residents, it is necessary to carefully plan the habitable areas, requiring the construction of housing, retail shops, parks, medical and welfare facilities and others. The port development authority and all the people concerned are particularly keen on developing a clean and functional environment.

4.2 Residential Area Planning

In accordance with the initial port city development concept, the housing area was scheduled to lie directly behind the port

area.

About 128 lots, or 3.2 hectares, has been alloted to the fisheries related population, while another 4.1 hectares, about 164 housing lots, is reserved for general housing. These areas have been developed by public housing corporation, which is funded by the prefectural government. Of the total available lots, 284 have already been completed and sold.

Nagasaki City planned construction of housing complex for 220 families. At present, 150houses have been built, with the remaining 70 scheduled for completion during the next few months. The prefectural government developed a similar project to built 610 house. About a third (219 homes) have been completed and are already occupied, while constructions presently underway (124 homes) or being scheduled for the future (340 homes).

5. Fish Market Relocation Policies

5.1 Measures Taken against Opposition Relocation

Fishing port relocation had met several difficulties since its inception. The Port relocation plan seemed innocent enough to progress smoothly. However, the project encountered a major set back at 1981 when it was learned that building of new railroad tracks to the new port would be aborted. The trawler's association was quick to react.

They opposed relocation because a direct railway connection was of vital importance. Amid the mounting opposition from these primary producers, distributors and other groups began to side with them and become less enthusiastic in undertaking the project.

In April 1983, after repeated negotiations with the various interest groups, prefectural government authorities recognized themselves and intensified efforts to materialize the project. In view of this.

even the staunch opponents softened and conceded to discuss the relocation project, but not major obstacles were cleared. This was followed by almost spontaneous activities by 13 fsheries and related associations to seek a feasible solution to the problem of the On March 14, 1985, a petition was finally submitted to the governor, containing detailed discussions on regarding relocation costs and other related expenses.

Upon receipt of the petition, the prefectural government conducted wide-range public hearings and announced its response a half year later. The government was willing to give political support, and financial aid in the form of subsidization and loans. More concrete measures proposed by the government are summarized below.

The government promised support fishery private companies and fishery related associations for the construction of port facilities through subsidies and loans. More specifically, support was focused on the construction of ice makers, freezer and refrigeration facilities, and transportation. Long-term, low interest public funding was arranged to facilitate the development of site for transport facilities.

In addition, the government decided to subsidize 75% of the direct expenditure incurred by relocation of offices and shops. A special loan was arranged to help with incidental expenses. Furthermore, a special fund was established to help with the purchase of equipment that such a major relocation would necessitate.

Three years later on December 28, 1988, an agreement was reached in favor of relocation. However, the prefectural government had to increase the funds it previously prepared for the port relocation.

5.2 Measures for The bottom trawl fishing Owner.

Of those opposing relocation, the bottom trawlers group staged the largest and most adamant opposition campaigns. However, October, 1986 saw a new movement. The trawlers group decided to discuss the condition of relocation without the opposition resolution of the group. Gradually, the basic attitude of these people shifted because more positive and they began to talk about the advantages of relocation. In April 1987, a research group in the bottom trawlers group was created to discuss the major issues, of which the development of an effective catch landing system was most important. The activities of this group came to a sudden halt when Typhoon 8712 hit the new port site in August of that year. Amid the brisk restoration of the typhoon damage, heated discussions of development and method to incorporate a new catch landing and handling system resumed. This eventually led to the installation of new machinery which saved tremendous manpower and later became the main attraction of the new fish market.

5.3 Opposition to Relocation due to Typhoon Disasters

The tremendous damage to the new port was brought about by Typhoon 8712. The typhoon moved northward along the Goto Islands of Nagasaki Prefecture and almost totally destroyed the breakwaters the new port. The destruction of "lifeline" structures was truly a nightmare to all the people concerned.

On September 5, 1987, the bottom trawlers group again decided to oppose the relocation movement, arguing that the planned port site was not safe. This action was supported by other fishing groups. The Fishery Agency, However, acted swiftly and wisely. In Tokyo, Nagasaki's Governor received a promise from the Agency that the southern breakwater would be reconstructed with exceeding strength and scope of the ones

demolished by the typhoon. The reconstruction work had finished on March 6, 1989.

In response to the significant assistance promised by the Fishery Agency, the 13 local associations and cooperatives began to soften their opposition. Within a month, they congregated to hear the government's description

of the reconstruction plan and its schedule. In a September 25 1987, interview with the Newspaper, the governor was quoted to have said, "The typhoon attack was most unfortunate, but thank God, this disaster did not occur after the putting to use the new port". Thereafter, restoration was the top priority and in the long run, the wise steps taken at this time contributed greatly to the success of the relocation plan.

In November 1987, all concerned parties were prepared to meet with government representatives and a final agreement was reached on the relocation conditions on December 28, 1988.

16 years have passed since the original inception of the Nagasaki Fishing Port Relocation Plan, and another 10 years since the establishment official of bodies to discuss concrete measures of the relocation. At September 29, 1989, The new Nagasaki Fishing Port and Fishing Market have Relocated.

6. Planning for an International Marine City

6.1 Background of the plan

After the New Nagasaki Fishing Port has been used, Nagasaki prefecture government plan to improve the new port for international marine city.
Nagasaki Prefecture is located close to the East China and Yellow Seas, two of the richest fishing grounds in the world. Various fisherman's associations (E.g. bottom trawlers, large and medium-size roundhaul netters) are active and numerous.

In Western Japan, Nagasaki ranks number one in terms of fisheries production. Also, due to brisk activities in the high seas, it is directly linked to other international operations, it is directly linked to other international operations. The establishment of the 200-mile fishing zone (DFZ) increased difficulty in high sea operations. Another difficulty was the sudden increases in fisheries product imports during recent years. In an effort to overcome these obstacles, the Fishery Agency established the so-called 'Marine innovation concept', for seeking new uses of water resources in the seas surrounding Japan. Based on this national guideline, Nagasaki Prefecture formed the Nagasaki International Marine City Concept. At core of the concept is the promotion of socio-economic activities, while creating comfortable living environment in the coastal areas and transforming the area into a truly international community. These goals are best achieved by promoting the fishery and processing industries, development of the New Nagasaki Fishing Port and realization of other projects such as those directed at the construction of International Maritime ResearchZone and International Resource Management Information Center.

6.2 Organizations and Their Roles in Promoting International Marine Studies

1) Nagaski International Fishing Training center
This research center will provide fisheries-related training to trainees from neighboring countries, especially those located around the East China Sea and the Yellow Sea. Cooperation will be sought from other research organizations in Japan. Special training will also be given to fisheries specialists and to the members of Youth Overseas Corps assigned to overseas duties.

2) Fishery Agency's Western Japan Research Center

This research institute will be dedicated to the study of the the East China Seas and the Yellow seas resources and resource management techniques while conducting basic research for replenishing fishery resources in locally waters. Also included in their research efforts will be the study of the marine environment.

3) University of Nagasaki Research Center for the East China Sea and Yellow Sea

Corroborating with the center's motto, "Preservation and Planned Use of the Ocean", the main activities at this center will include Western Japan Promotion of intramural, comprehensive and international oceanographic research.

4) Nagaski Prefecture Fishery Laboratory

While promoting the introduction of the latest technology and technical research and development, this laboratory will endeavor to develop new industry- application technology. Through cooperation with the Nagasaki University and the Western Japan Marine Research Center, research will be conducted on international resource management in the East China and Yellow Seas.

6.3 Advantages of locating related organizations in one area

Plans have been made to congregate the university and national and local marine and oceanographic research institutes scattered in Nagasaki City to promote mutual assistance. This new system is expected to facilitate up-to-date research, of which the results can be put to immediate use. Greater interaction among researchers visiting Nagaski from many countries will contribute to ensure an international understanding in marine resource conservation and management.
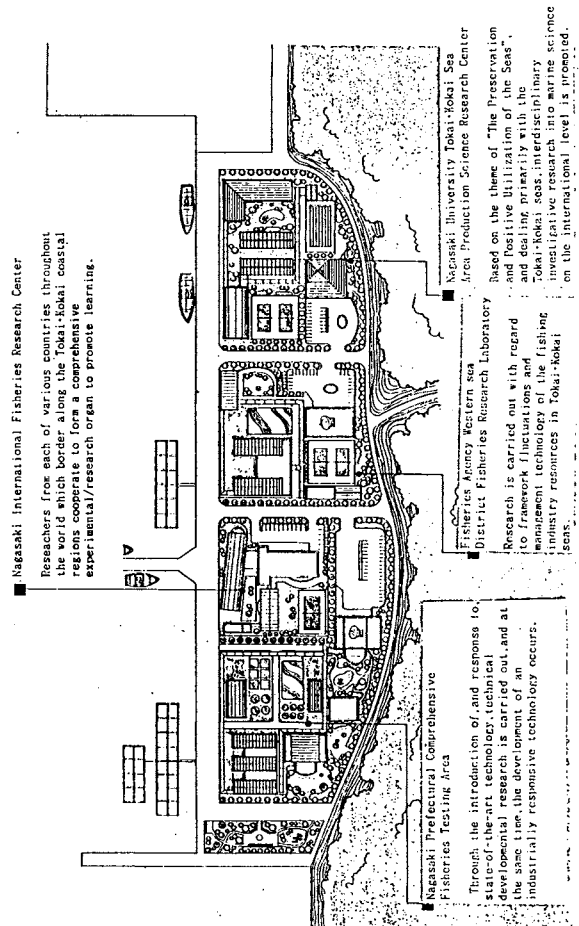
Fig.3 International Marine comprehensive Research Zone

THE LATEST TECHNOLOGY IN CONSTRUCTION OF FISHING PORTS

Masatsugu Fukuya*. Satoshi Kamise** and Masaaki Yamamoto***

* Director-General, Fishing Port Department, Fisheries Agency.
** Deputy-Director, Planning Division, Fishing Port Department, Fisheries Agency.
*** Charman of Hydraulics Fishing Port Section, National Research Institute of Fishing Engineering.

The intricate coastline of Japan totals about 35,000 km in length. The government enacted the Fishing Port Act in 1950 as a legal framework for the nearly 3,000 fishing ports in Japan. The Long-Term National Fishing Port Development Projects have been enacted based on this law to improve fishing port facilities. These projects will be effective for 4 - 8 years. See the table for the first seven projects completed. The eighth project is being promoted with ¥2.41 billion in funds to deal with the social and economic changes surrounding the fishing industry and fishing communities with importance being attached to the following basic targets:

(1) To effectively utilize the water area surrounding Japan;
(2) To establish a distribution and industrial processing system that is functional in the information society; and,
(3) To revitalize fishing communities.

1. Introduction

The concerns for improving fishing ports have changed ith the times; the construction of fundamental facilities, such as break-waters, revetments, quays etc., were important in the early days when the improvement started. However, serious improvements are required these days including repairing access roads to fishing ports; maintaining the sewage systems, parks, etc. and creating quieter fishing ports. Therefore, new technology concerning fishing ports has been developed to cope with these requirements.

This report introduces the current status of the study and development of the latest technology available for practical use concerning fishing ports.

2. The Trend of the Study and Development of the Latest Technology for the Construction of Fishing Ports

Although quite a number of planning and designing methods for fishing ports have been presented since the construction of modern ones started, many peripheral themes have appeared because of the circumstances surrounding fishing, such as the development of resource controlled-fishing. Actions to keep the inner areas of ports calm, to prevent shoaling of these areas by the littoral drift, and to improve the water quality there have been developed to enhance the safety, usefulness and convenience of the ports.

2.1 Development of Breakwaters with Idle Water Parts Which Reduce Water Overtopping

The revetment, which protects the land from sea water, and the breakwater, which maintains calm water within the port, cause problems if they are too high or too low. Therefore, the construction method in Japan of stacking concrete blocks to form a slant face to reduce the wave overtopping and lower the height of the levee crown has been employed. A method has been developed to make more effective breakwaters.

As shown in Fig. 2-1, this new method, called wave-breaking with idle water parts adopts a system which provides an adequate distance between the upright part and the wave-breaking works. In this study, the regular wave experiment was performed first. Then, a variation in water volume, caused by various wave conditions, and the condition resulting from the bank of wave-breaking works were investigated. Which bank shapes were effective was clarified according to the change in wave force as well as the influence of the increased water volume due to the raised water level in the idle water part.

Characteristics of irregular wave forces were researched using the irregular wave experiment. In addition, secondary waves caused by wave overtopping were studied by looking at irregular waves. Fig. 2-2 shows the relationship between water pressure resultant forces (hereafter simply called a wave force) of armoring and idle water part is 0.01 or more. As seen from the influence of the length of idle water part types, as

well as between the height of passing waves
and deepwater waves, Ho. The idle water
part type is expected to cause a greater
reduction in wave pressure than the armoring
type when the height of the levee crowns are
0.55H or more, and the length of the idle
water parts on the wave force, a reduction
appears in wave force when the length is
extended from 0.05L to 0.1L. To achieve the
non-dimensional mean wave pressure strength
of Pmax/wH1/3 to be 1.0wH1/3 or below, at
1 = 0.1L3/3, the required height of levee
crowns of wave-breaking works is 0.7H1/3.

The wave pressure distribution becomes
double the wave pressure type if the levee
crown hc is high. The calming effect of the
idle water part type is larger than the
conventional armoring type that has the same
levee crown height, so its transmission
coefficient is 10 - 16% smaller.

As to the soundness of the breakwaters,
the wave-breaking works were found to be
superior in reducing wave pressure than the
conventional armoring type, when the height of
the levee crowns of the wave-breaking works
were sufficiently high. Also, different from
the conventional type, a load from the block
itself, together with a load transmitted from
the wave force through the block, is not
generated on the upright part. However, the
simple body weight of the block had to be
slightly heavier, by about 1.5 times, than
the Hudson type of wave-breaking works.
Moreover, sufficient scour-protection
measures must be applied to sandy ground.

FIG. 2-1 Model Structure of Submerged Embankment   unit : mm

Although port reformation has improved the
calmness of the water for anchorage, it has
deteriorated circulation of water in the port.
Now clean and fresh sea water is being
demanded, not only for the beauty of nature
and for public health, but also for temporary
storage of fish feed. Overall, the improve-
ment of water quality in the anchorage areas of
fishing ports is considered to be an increas-
ingly important factor of the future. Hence,
the construction method using a breakwater
with a submerged dike has been developed to
exchange sea water at higher rates using the
small waves that always exist. The idle
water part is provided in this system between
the main body of the breakwater and the
impermeable submerged dike. As waves are
forcibly broken above the submerged dike,

raising the mean water level of the idle
water part, sea water will be introduced to
the anchorage through the lead-in hole
provided in the bank.

When the energy of swells and waves existing
in the outer sea is used, sea water is not
exchanged efficiently by merely providing
holes or openings in the breakwater.
Therefore, this system is designed to cause
a rise in the water level by breaking the

2.2 Development of a Construction Method Using a Holed Breakwater with a Submerged Dike by Introducing Sea Water
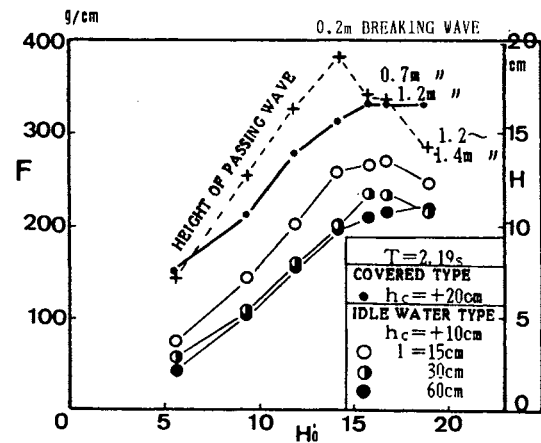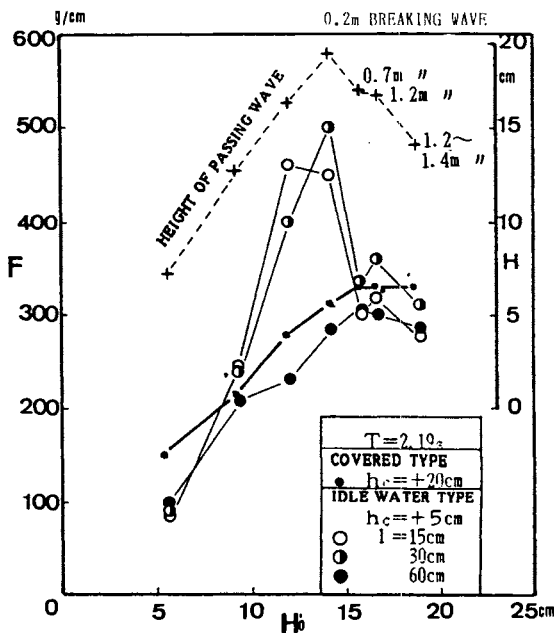
FIG. 2-4-2 Wave Force and Height of Deepwater Wave

water above the impermeable submerged dike. This dike is constructed in front of the main bank, providing water interchange holes (openings or submerged holes) on its back side and introducing sea water into the port by the differing water levels. The amount of sea water interchanged, the height of the transferred water, the wave force, etc., were measured by the hydraulic model experiment to confirm the effectiveness of the sea water exchange method. Also, an optimum design of a breakwater with the submerged dike was studied.

The test results proved that the amount of water exchanged was not affected by the distance between the upright part of the breakwater and the submerged dike, and showed the maximum exchange when the height of the crown of the submerged dike coincided with the water level. The amount of the introduced water that can be calculated is shown in Fig. 2-4. Here, Hc' is the deepwater wave height, h is the water depth where dike is installed, B is the length of the submerged dike, and A is the cross-section area of opening. (See Fig. 2-4)

The submerged dike has an impermeable structure, so singular block concrete bank is most efficient. However, in terms of construction, the block mounted rubblestone would be more effective. It was also found that the height of the wave passing through the breakwater's opening was small enough and did not affect the calm area inside the port.

The water depth (hc) above the submerged dike and the distance (1') to the submerged dike influenced the force of water acting on the breakwater with a submerged dike. The mean wave pressure was 1.0 WH or below when [hc] was 0 - 0.25h (h is water depth) and [1'] was 0.2 - 0.25L (L is length of incident wave) or more. If a submerged dike is provided, the amount of introduced water reaches its maximum level when the depth of water above the submerged dike is 0. The amount of water does not change in the 0.5 Ho' - 0.5 Hc' range.

A flat design with a rectangular dike was especially effective in introducing water from the outer sea with minimal wave force. (See Fig. 2-5)

The construction of breakwater with openings and a submerged dike allows efficient introduction of sea water even when the wave height is small. It also accelerates the exchange of sea water in port areas with a small differnce in tidal level.

3. Activities and Achievements of the Research Society for Development of Fishing Port Technology

3.1 Outline

The Research Society for Development of Fishing Port Technology was founded in August, 1985 to seek ways to meet the diversified needs of fishing ports and fishing communities, while developing technology necessary for improving port facilities. The members of this Society are private corporations, who have exerted great effort in the study and development of new technology for the planning and construction of fishing port facilities.

After selecting a common theme out of the themes currently discussed independently by the member companies, study teams were organized to discuss specific study and development projects. It is necessary that the themes should reflect the actual needs of fishing port management.

Each Study Team applied the results of their discussions to studies at the site. The activities of the Study Teams are outlined below:

The results of the various studies undertaken since August, 1985 have been reported. Some of the findings have been used to improve several fishing ports.

Study Team 1 discussed "Fenders"
Study Team 2 discussed "Floating Wharves"

3.2 New Fender Material for Fishing Ports

3.2.1 Fenders - Original Concept and Development

New fender materials have been developed and put to use in order to reduce the defects
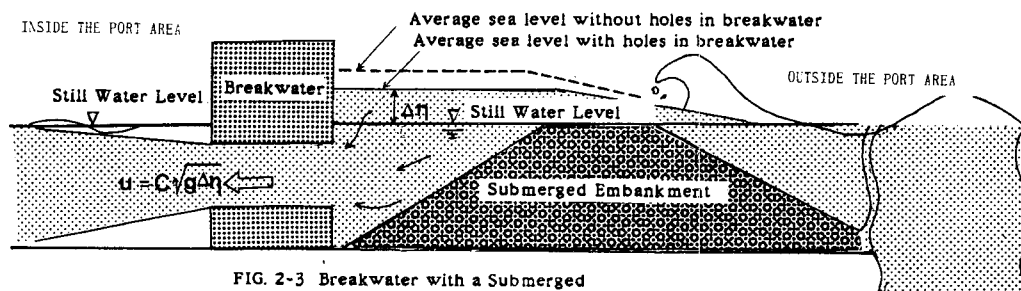
FIG. 2-3 Breakwater with a Submerged Embankment-Conceptual Drawing

encountered with conventional materials. In Europe and the United States, rubber fenders have been in use for the past fifty-five years.

The use of rubber fenders in Japan first began in 1953, when this material was imported from the United States. The following year, Japan successfully developed round fender materials on her own.

The main function of the fender is to absorb the impact when a ship collides with it to protect both the ship and the wharf from friction and damage. A good fender material must meet the following quality requirements:

1. Flexibility
2. Large freedom in deformation
3. Small modulus of elasticity
4. Excellent resistance to friction, cutting and aging; good durability

3.2.2 Background to the Development of New Technology

Based on our studies on the use of fishing ports and fenders, we have concluded that a good fender material must satisfy the following needs:

(1) Resistance to external force: The generally required quality of the fender material includes low reactive force, high absorption of impact energy and good resistance to shearing force as well as partial compression, in other words, good durability.

(2) Sufficient width for easy mooring operation and protection of the ship's body: By providing a wide fender, it is possible to increase the area where the ship's body directly contacts the fender, thus reducing the unit impact.

(3) Convenience and safety in catch landing operations: A good fender must also be useful for landing of the catch.

(4) Protection of the ship and the mooring quay: Sometimes a part of the ship may rest directly on the mooring quay. In order to minimize damage, protrusions and sharp edges must be covered by fending materials to protect the ship.

3.2.3 Development of New Fender for Fishing Port

As described earlier, in order to meet the increasingly diversified needs of fishing ports, fender design has been improved. The V-shape fender, abbreviated as the V-type herein, is described below.

(1) Resistance to Impact: The conventional V-type fender was often damaged in its foundation. By thickening the rubber or providing double rubber faces, it is possible to increase the fender's resistance to shearing forces and particle compression.

(2) Wide-bodied Design: The conventional V-type fender has a small impact receiving area, so ships are subjected to a concentrated load when they collide with the quay. By making the fender area as large as possible, it is possible to reduce the unit impact applied to the ship.

(3) Convenience/Safety: In order to use the fender's top surface for landing or walking, we have designed a stepped structure. In order to contribute to port safety, we have attached ropes that can be used as lifelines.

FIG. 2-4 Average Flow Rate in Water Pipe
(Submerged Embankment Is 30m in Length)
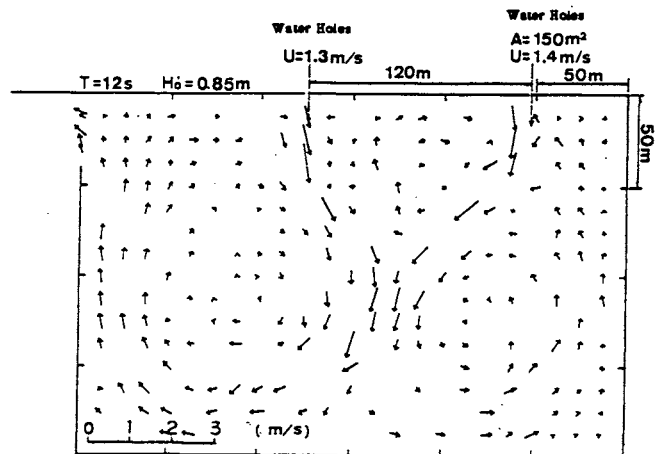
FIG. 2-5 Distribution of Flow Vectors in a Model Moving Basin

3.2.4 Topics for Further Study

Based on the findings of the past study on the development and application of new fender materials, we wish to continue the study to achieve yet greater improvements. Site investigations have identified a new need for specifying replacement timing of the fender materials, based on its damage and deterioration or rubber.

1. Difficulties with Conventional Technology and Special Features of the Controlled Motion Floating Pier

Conventionally, floating piers have been used in areas with a large difference in the tidal level. These piers, however, are attached to the wharf by chains, so they are susceptible to the motions of the waves and winds, which often result in large lateral motion. Also, the need to make such piers wide enough to increase stability often narrows the mooring basin and the landing area.

In order to address these problems, a controlled motion floating pier is secured in position by means of posts. This improves the floating pier in the following ways:

i) The movement of the floating pier is minimized in bad weather, thus increasing work safety and ease of operation.

ii) The pier's width can be made small, making it suitable for small ports.

iii) Reduced lateral movement allows installation of the floating pier close to the wharf. The greatly reduces the water surface area occupied by the pier.

iv) Since it is now possible to stabilize the floating pier, a passage of the same width as the pier can be constructed to which fishing

2. Tying the Floating Pier to Stationary Ports

The number of posts per floating pier is usually four, but two posts will suffice for smaller floating piers. Although the former type offers greater motion control, the latter one has been improved, for example, by tying the pier at two (upper and lower) positions on each post.

The floating pier and the post are connected by a support, which is made up of a 4-point contact, two-way support device. The structure and the features of the more flexible support, known as the cushion roller, is described below.

Table   1
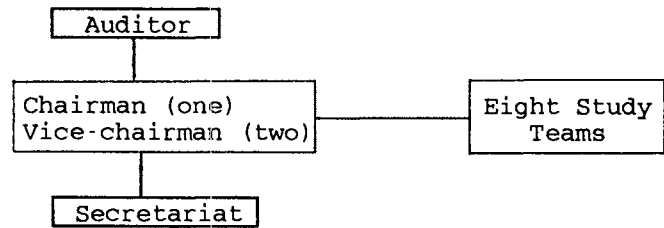
Table 2: Research Theme for Eight Study Teams

Study Meeting	Theme
Study Team 1	"Floating Breakwaters" Discussed the development and application of floating break-waters, design guidelines, and the preparation of standards for executing work.
Study Team 2	"Fenders" Discussed how to develop installation standards for the conventional V-type fenders, fenders for small ships as cushioning materials, and alternative fender materials.
Study Team 3	"Floating Wharves" Discussed how to develop an oscillation control in a floating wharf to be built in areas with great changes in the tide level.
Study Team 4	"Large, deep-water breakwaters" To develop new structure and work execution guidelines for breakwater to be installed in deep water areas.
Study Team 5	"New Wavebreaker Structures" To develop complex constructions utilizing aggregative blocks.
Study Team 6	"Measures against Strong Winds" To study and prepare the planning standard for measures against wind necessary for prevention of damage to the moored fishing boats in the sea areas inside ports.
Study Team 7	"Iron Steel Structures" To study how to utilize PC structures for fishing port facilities.
Study Team 8	"PC Structures" To study how to utilize PC structures for fishing port facilities.

A cushion roller consists of the roller section which conforms to be vertical movement of the pier, and the cushion section, which is designed to absorb the energy of other movements. The roller section has laminated rubber and enforced fiber layers, which result in small deformation under foreign forces. Furthermore, it is durable and can be made into a compact design.

The cushion section undergoes compressive deformation, or shearing deformation, thanks to rubber's elasticity and deformation of the hollow section. An initial displacement in the cushion material makes it possible to make fine adjustments at the installation site. The resilient force of rubber also contributes to reducing the motion of the floating pier when external forces are not too large.

Table 3: Targets for Developing New Fender Material

Purpose	Special Features
Resistance to impact	Good resistance to shearing force and particle compression.
Wide-bodied design	Effective in enlarging the contact area, minimizing impact on ship with ease in mooring operation.
Convenience/Safety	Fender should serve various purposes, e.g., landing operations, life-saving purposes and protecting both the quay and the ship.
Covering sharp edges	Protection of the quay's angular parts, while preventing damage to the ship.
Other	Adoption of colored rubber not to discolor or mar the ship's paint color.

3. Passage

The passage can be made the same width as the loading pier, thus allow mooring of fishing vessels. The external forces acting on the passage are wind pressures and impact forces when the vessel is pressed against it. Both the shore-side and vessel-side supports must be able to withstand lateral forces, while enabling the passage to closely follow the movement of the floating pier. To achieve this, the supports must have flexibility in the following directions:

i)   Shore-side support: Flexibility in rotation around its shorter axis and horizontal rotation.

ii)   Pier-side support: Flexibility in rotation around its shorter axis, horizontal rotation, and longitudinal slides.

Any inclination around the longer axis will be balanced out by the reactive force of the passage. When the above flexibility requirements are satisfied, it is possible to control the motion of the floating pier. To date, various support structures have been experimented with and applied to actual facilities.

4. Conclusion

We feel it is always necessary to develop new technology to meet the changing technological demands of fishing ports. There is an increasing demand for a safe, easy-to-use and enjoyable port. At the same time, in addition to fulfilling the basic economic needs of a fishing port, it is important to also address the newer roles they play, for example, in marine leisure activities and sports fishing.

THE INTESTINAL MICROFLORA OF FRESHWATER FISH, WITH SPECIAL REFERENCES TO VITAMIN B_{12}-PRODUCTION

H. Sugita*, C. Miyajima*, J. Takahashi*, Y. Deguchi*

* Nihon University, Tokyo, Japan

Abstract

The present study was undertaken to investigate the vitamin B_{12}-producing ability of the intestinal microflora in six freshwater fishes including Japanese eel, carp, goldfish, ayu, tilapia and channel catfish. *Aeromonas* spp., Enterobacteriaceae and *Pseudomonas* distributed widely in the intestinal tract of freshwater fish. An obligate anaerobes, *Bacteroides* type A predominated in the carp and tilapia which do not require the vitamin B_{12}, along with the goldfish and ayu. Contrary, this bacterium was not detected in the vitamin B_{12}-requiring fish (the eel and channel catfish). In general, the vitamin B_{12}-producing ability of obligate anaerobes including *Bacteroides* type A, other Bacteroidaceae and *Clostridium* was much higher than aerobes and facultative anaerobes. It was clarified, furthermore, that there is a close relationship between the amount of vitamin B_{12} and the viable count of *Bacteroides* type A in the intestinal contents of carp. These results strongly suggested that the *Bacteroides* type A closely involves the vitamin B_{12} production in intestinal tracts of warmwater fish.

1. Introduction

Japanese eel *Anguilla japonica* and channel catfish *Ictalurus punctatus* fed vitamin B_{12}-deficient diets show deficiency syndrome of the vitamin B_{12} such as poor growth and poor appetite while tilapia *Tilapia nilotica* (=*Oreochromis niloticus*) and carp *Cyprinus carpio*, even fed the similar diet, show no deficiency syndrome [1, 2]. Lovell and his co-worker [3, 4] reported that the apparent rate of intestinal bacterial synthesis of the vitamin B_{12} in the tilapia fed a vitamin B_{12}-deficient diet (at least 11.2 ng per g of body weight per day) was eight times that found in the channel catfish (ca. 1.4 ng/g/day) fed the similar diet. Although much is known about how intestinal microflora contributes the synthesis of vitamin B_{12} in mammals [5, 6], little is known about the vitamin B_{12}-producing ability of fish intestinal bacteria, except for the report of Teshima and Kashiwada [7], who showed the evidence of vitamin B_{12} production of the aerobic bacteria from carp *Cyprinus carpio*.

On the other hand, Sugita et al. [8, 9] reported that an obligate anaerobes, *Bacteroides* type A, occurred predominantly in the intestinal tract of many freshwater fishes. However, there is little information on the vitamin B_{12}-producing ability of this bacterium. The present study was undertaken to investigate the vitamin B_{12}-producing ability of intestinal microflora including aerobes and anaerobes from six freshwater fishes.

2. Materials and Methods

2.1 Bacteriological Sampling

Five specimens of Japanese eel (20-45 g body weight), carp (21-56 g), goldfish *Carassius auratus* (25-38 g), ayu *Plecoglossus altivelis* (25-38 g) and tilapia (19-46 g), and four of channel catfish (3.7-4.7 g), which were reared in glass aquaria or fish culture ponds.

The fecal pellets or intestinal content was aseptically removed from each specimen according to Sugita et al. [10], and liquefied in a nine-fold volume of a diluent of phosphate buffer (pH 7.6) containing 0.05% L-cysteine hydrochloride and 0.1% Bacto-agar (Difco, Detroit, MI). Each sample thus prepared was serially diluted and plated onto seven different media: Trypticase soy blood agar (TS) (BBL, Cockeysville, MD), phenylethyl alcohol blood agar (PEA) (BBL), MacConkey agar (Eiken Chemical Co., Tokyo), Eggerth-Gagnon blood agar (EG) (Nissui Seiyaku, Tokyo), Fradiomycin-*Clostridium welchii* blood agar (FM-CW) (Eiken Chemical Co.), *Bacteroides* type A-selective blood agar (AS) and *Bacteroides* type B-selective blood agar (BS) [11]. The inoculated TS, PEA and MacConkey agar plates were incubated aerobically, and the EG, FM-CW, AS and BS agar plates were incubated anaerobically, both at 25°C for 7 days. Anaerobiosis was established by evacuating the atmosphere of an anaerobic jar containing steel wool, which was activated by acidic cupric sulfate, and replacing it with a 20% CO_2-80% N_2 gas mixture [12].

After incubation, the bacterial colonies were counted and ca. 20 colonies were isolated at random from each plate for further characterization. Gram-negative aerobes and facultative anaerobes isolated aerobically were identified to the genus level using a modified scheme [13] of Shewan et al. [14]. Vibrionaceae

strains were further classified into three types: *Aeromonas hydrophila, Plesiomonas shigelloides* and other *Aeromonas* as reported in the previous paper [9]. Gram-positive bacteria were identified according to the procedure of Cowan [15].

The obligate and facultative anaerobes isolated anaerobically were classified on the basis of Gram reaction, cellular morphology and arrangement, spore formation, and the ability to grow aerobically. Bacteroidaceae strains were further classified into three types: *Bacteroides* type A, *Bacteroides* type B, and other Bacteroidaceae since the first two types can be identified according to their specific morphology [16] and ability to grow on the AS or BS medium [11].

After identification of bacteria, suitable dilutions of colonies of each bacterial group on the original plates were counted and expressed in number per g wet or dry weight of material. For each bacterial group, the highest count obtained on the different agar media was regarded as the estimated viable count for that group. The total viable count was obtained by summation of viable counts of all bacteria genera.

2.2 Determination of Vitamin B_{12}

About three strains for each genus of intestinal bacteria which showed the highest count through the seven agar media used, were selected from each specimen and incubated in GAM broth (Nissui Seiyaku) at 25°C for 5 days under aerobic or anaerobic conditions. The culture and uninoculated medium were then assayed microbiologically for vitamin B_{12} (as cyanocobalamin) using *Lactobacillus leichmannii* IAM 12066 (=ATCC 7830), according to the procedure of Sato [17].

2.3 Determination of the Viable Count of Bacteroides type A and Amounts of Vitamin B_{12} in the Carp's Intestine

Intestinal tracts (485-680 mm length) were aseptically removed from five specimens of carp (984-1288 g), and were evenly divided into four parts. Content samples from each intestine segment were examined for the viable count of *Bacteroides* type A and the amount of vitamin B_{12} as described above.

3. Results

3.1 Intestinal Microflora of Freshwater Fishes

The intestinal microflora of six warmwater fishes is shown in Figs. 1-6. A total of ten aerobic and facultative anaerobic components and four obligately anaerobic components were detected, and the total viable count ranged from 2.2×10^5 (channel catfish) to 7.6×10^9 CFU/g wet wt. (goldfish). Of aerobes and facultative anaerobes, *Aeromonas* sp., Enterobacteriaceae and *Pseudomonas* distributed predominantly in the intestinal tract of almost all fish specimens with occurrence from 25 to 100 %. An obligate anaerobe, *Bacteroides* type A, occurred predominantly in the carp, goldfish, ayu and tilapia with a bacterial density from 2.7×10^5 (carp) to 1.4×10^9 CFU/g dry wt. (tilapia), but was not detected in the eel and channel catfish.

Bacteroides type B was detected in only the tilapia. Other obligate anaerobes including Bacteroidaceae (except *Bacteroides* types A and B) and *Clostridium* sometimes occurred in the intestinal tract of all fish species, except for ayu, at densities up to 1.5×10^8 CFU/g. These results generally agreed with the previous papers [8,9].

3.2 Vitamin B_{12}-producing Ability of the Intestinal Bacteria

A total of 235 strains of bacteria including aerobes and anaerobes, from six freshwater fishes were examined for the vitamin B_{12}-producing ability and the result was summarized in Figs. 1-6 . The GAM broth contained about 1.25 ng vitamin B_{12}/ml. Generally, the aerobes and facultative anaerobes poorly produced the vitamin B_{12}, except for six strains of Enterobacteriaceae (18%), three of *Pseudomonas* (13%) and one of *Plesiomonas shigelloides* (7%), respectively, which produced the vitamin of ≥ 5 ng per ml culture per optical density at 630 nm (OD_{630}). Contrary to this, obligate anaerobes, that is, the *Bacteroides* type A (97%), *Clostridium* (75%) and Bacteroidaceae (67%) produced the vitamin B_{12} abundantly (≥ 5 ng/ml/OD_{630}) although the *Bacteroides* type B could not produce the vitamin efficiently.

3.3 Relationship between the Viable Count of Bacteroides Type A and the Amount of Vitamin B_{12} in Carp's Intestine

The above results indicate that the *Bacteroides* type A is a predominant component and seems to be the major producer of the vitamin B_{12} in the intestine of freshwater fishes except the Japanese eel and channel catfish. Therefore, the viable count of *Bacteroides* type A and the amount of the vitamin B_{12} in the content of four intestine segments of carp was determined, and the result obtained was summarized in Fig. 7. The *Bacteroides* type A ranged from 3.5×10^5 to 4.4×10^{10} CFU/g dry wt. and the vitamin B_{12} was from 31.4 to 902 ng/g dry wt. It was found, furthermore, that there is a close relationship between these two parameters ($r = 0.91$). The present data, along with the above results, strongly suggests that the *Bacteroides* type A closely involves the vitamin B_{12}-production in the intestinal tract of carp.

Discussion

Aoe [1] reviewed that the poor growth and/or poor appetite were observed in the Japanese eel and channel catfish fed a vitamin B_{12}-deficient diet while any deficiency syndrome was not found in the carp, fed the similar diet. Lovell and his co-worker [3,4] reported that the intestinal microorganisms in the tilapia which fed a vitamin B_{12}-deficient diet synthesized at least 11.2 ng per g of body weight per day, which will satisfy the requirement of the host fish, whereas those in channel catfish synthesized approximately 1.4 ng/g/day. It remained unclarified, however, how the intestinal microflora is attributed to the difference of those fish species in vitamin B_{12}

synthesizing rate. Teshima and Kashiwada [7] reported that about half the aerobic bacterial strains (including facultative anaerobes) produced the vitamin B_{12}. Recently, it was found that many freshwater fishes predominantly harbour obligate anaerobes as well as aerobes and facultative anaerobes [8,9]. Therefore, the intestinal bacteria including aerobes and anaerobes were determined for the vitamin B_{12}-producing ability in the present study. As a result, it was known that the ability of obligate anaerobes including the Bacteroides type A, Bacteroidaceae and Clostridium, was much higher than the aerobes and facultative anaeorbes, except a few strains of Enterobacteriaceae, Pseudomonas and Plesiomonas shigelloides (Figs. 1-6). Especially, almost all the Bacteroides type A strains (97%) produced the vitamin B_{12} abundantly (≥ 5 ng/ml/OD$_{630}$). The Bacteroides type A occurred predominantly in the intestinal tract of the carp and tilapia which do not require the vitamin B_{12}. In contrast, this bacterium was not detected in the Japanese eel and channel catfish which require the vitamin B_{12} (Figs. 1 and 6). Moreover, the viable count of the Bacteroides type A closely related with the amount of vitamin B_{12} in the carp's intestine (Fig. 7), although it is easily suspected that a part of the vitamin produced was absorbed and utilized by the host animal. These results strongly suggest that mainly the Bacteroides type A contributes to the vitamin B_{12} production in the freshwater fish although other bacteria may be partly attributed to the production of the vitamin. Since it is

much laborious and time-consuming to determine the vitamin requirement of fish, the viable count of Bacteroides type A may become an excellent indicator for the criteria of the vitamin B_{12} requirement of warmwater fish. In addition, these results indicate the possibility to change the vitamin B_{12} requirement of warmwater fish if the Bacteroides type A could be made to establish in the intestinal tract of the vitamin B_{12}-requirng fish species. Further studies along those lines are now in progress.

On the other hand, the intestinal tract of freshwater fish is generally colonized by Aeromonas hydrophila, and Bacteroides type A, with some exceptions, while other bacteria such as Plesiomonas shigelloides, Pseudomonas, Enterobacteriaceae, Micrococcus and Bacteroides type B vary with fish species as indicated by the present study (Figs. 1-6), along with the previous works [8, 9]. However, the intestinal microflora of fish is found to be influenced by endogenous exogenous factors including the developmental stage [11, 18, 19] and structure [20, 21], rearing conditions [22-25], salinity [24, 26, 27] and temperature [28,29] of ambient water, handling stress [30] and oral administration of antibiotics [31,32]. Additionally, it was recently shown that there is the daily fluctuation and inter-individual variation in the intestinal tract of goldfish, tilapia and carp [33-35]. These facts strongly suggest that the synthesis rate of vitamin B_{12} is influenced by the above factors. Further studies along those lines are desired in near future.

Fig. 1 The intestinal microflora of five specimens of Japanese eel (a); and the vitamin B_{12}-producing ability of each bacterial component isolated (b): □ , <0.1 ng/ml/OD$_{630}$; ▨ , 0.1-1.0; ▣ , 1.1-5.0; ▥ 5.1-10.0; ■ , >10.1.

Fig. 2 The intestinal microflora of five specimens of carp (a); and the vitamin B_{12}-producing ability of each bacterial component isolated (b): Refer to the symbol in Fig. 1.

Fig. 3 The intestinal microflora of five specimens of goldfish (a); and the vitamin B_{12}-producing ability of each bacterial component isolated (b): Refer to the symbol in Fig. 1.

Fig. 4 The intestinal microflora of five specimens of ayu (a); and the vitamin B_{12}-producing ability of each bacterial component isolated (b): Refer to the symbol in Fig. 1.

Fig. 5 The intestinal microflora of five specimens of tilapia (a); and the vitamin B_{12}-producing ability of each bacterial component isolated (b): Refer to the symbol in Fig. 1.
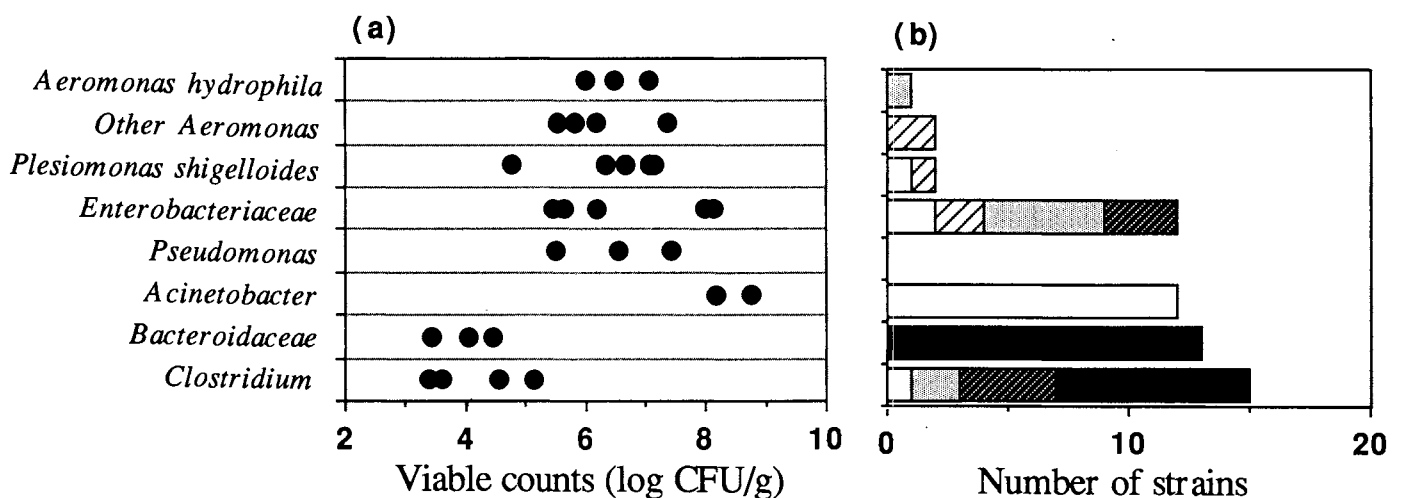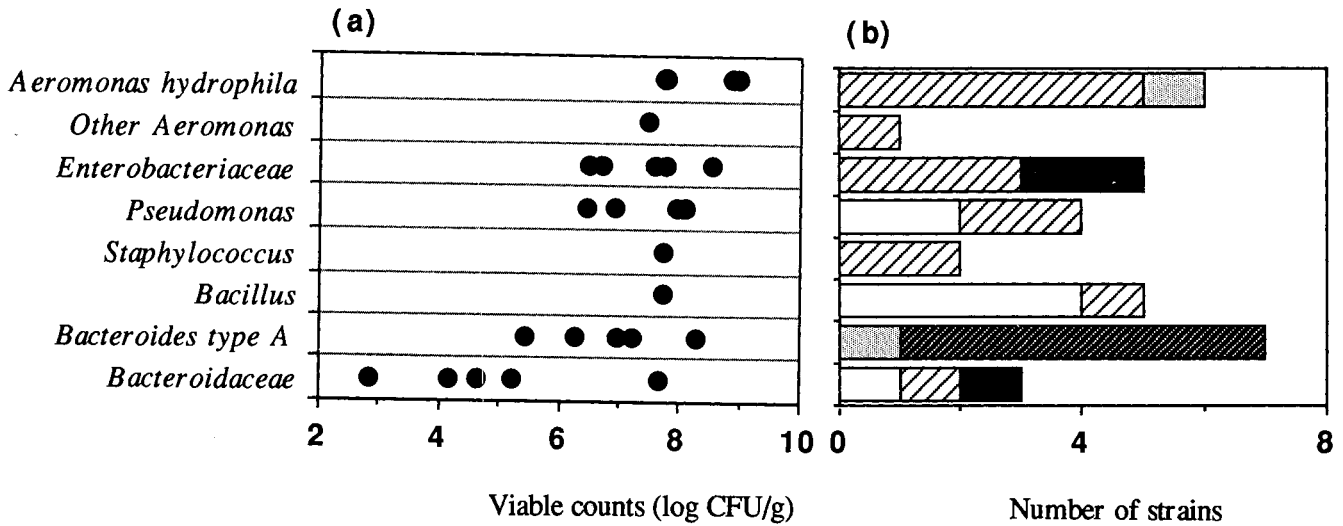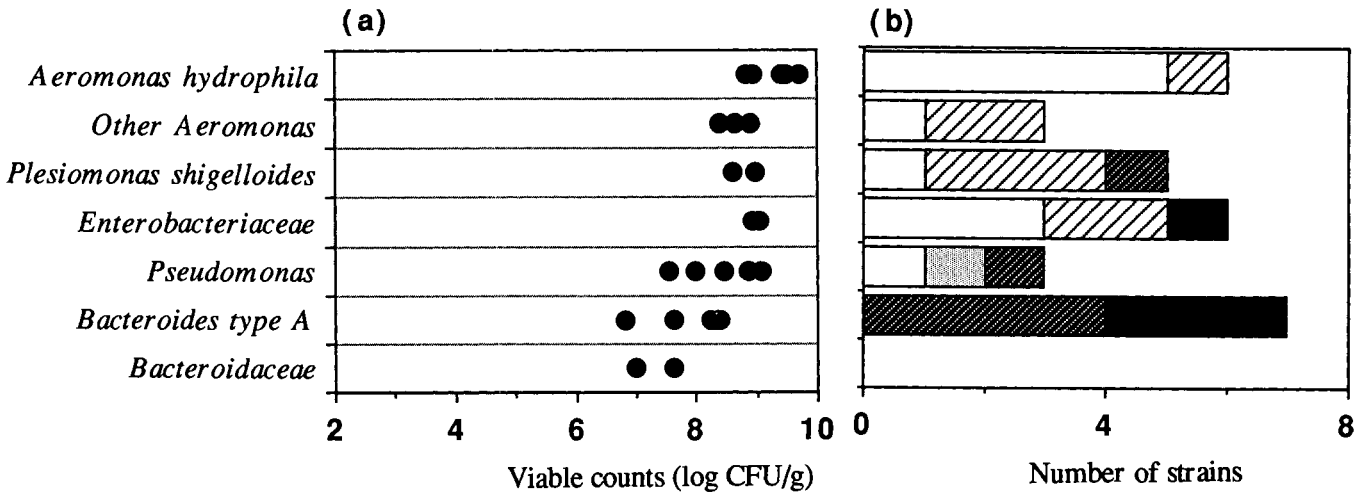

Fig. 6 The intestinal microflora of five specimens of channel catfish (a); and the vitamin B_{12}-producing ability of each bacterial component isolated (b): Refer to the symbol in Fig. 1.
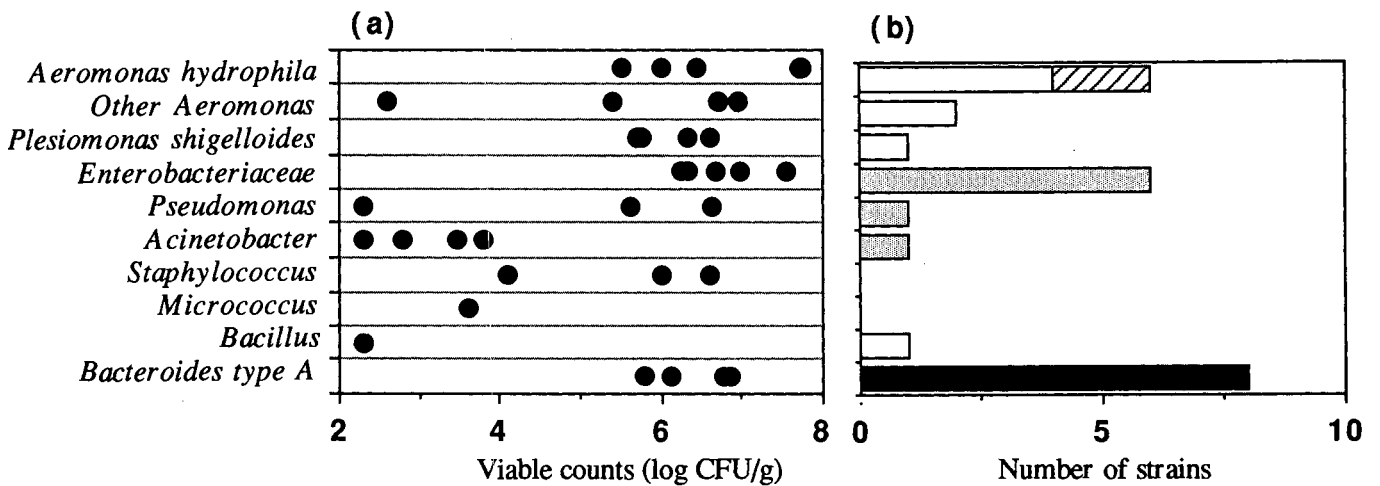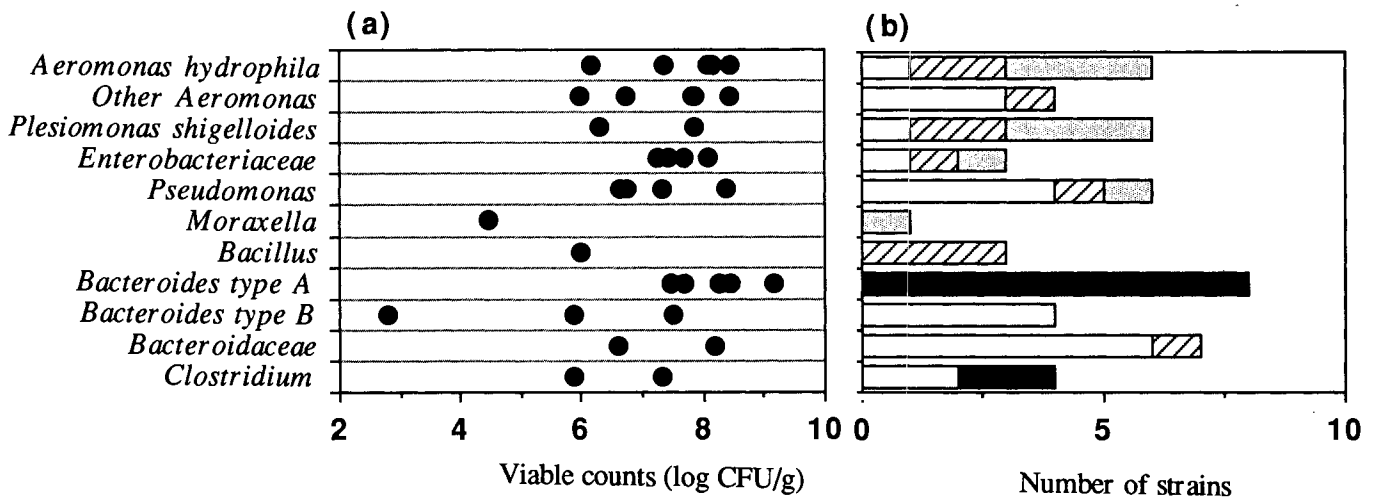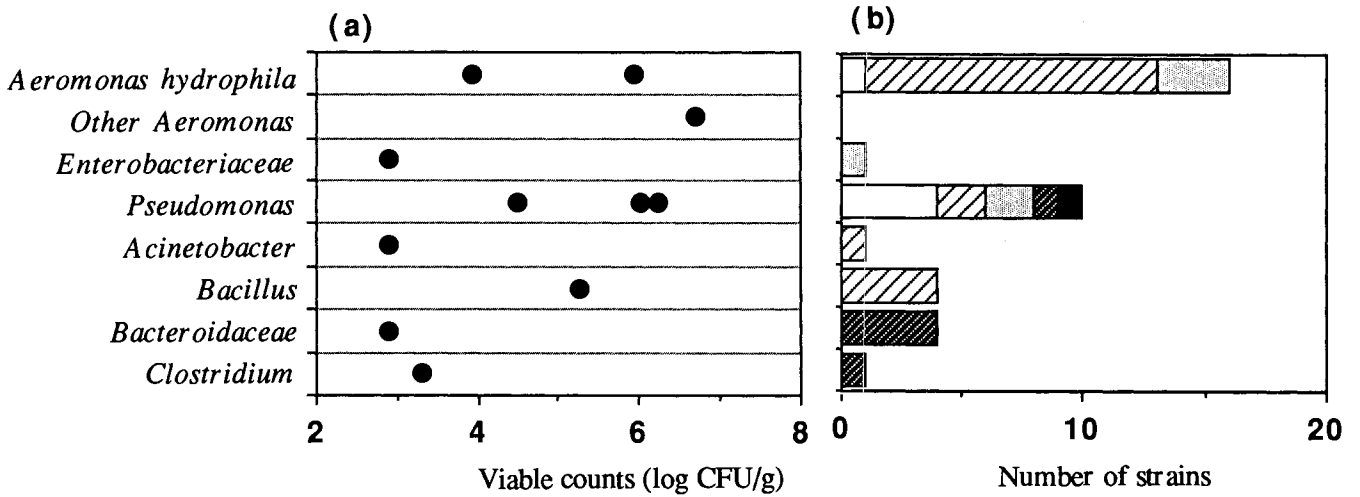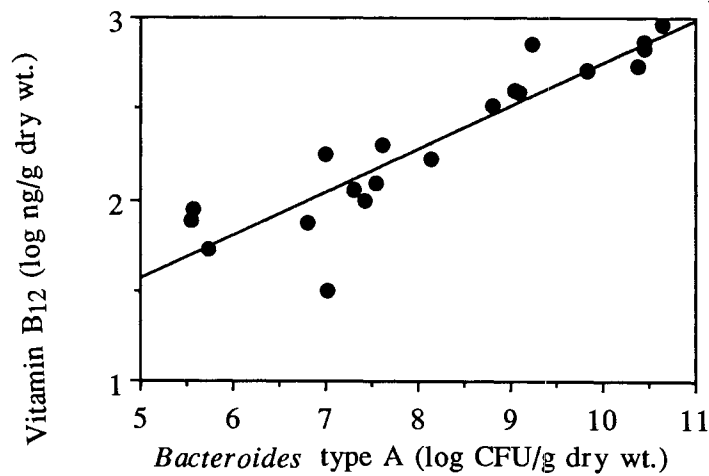

Fig. 7 Relationship between the viable count (CFU/g dry wt.) of *Bacteroides* type A and the amount of vitamin B_{12} (ng/g dry wt.) in the intestinal content of carp.

References

1. Aoe, H., "Vitamins". In "Nutrient and Feed of Fish"(ed. by C. Ogino), Koseisha-Koseikaku, Tokyo, p. 186 (1980)
2. Halver, J.E., "Fish Nutrition, 2nd edition", Academic Press, San Diego, p. 31 (1989)
3. Limsuwan, T., and Lovell, R.T., "Intestinal synthesis and absorption of vitamin B_{12} in channel catfish", J. Nutr. Vol. 111, p. 2125 (1981)
4. Lovell, R.T., and Limsuwan, T., "Intestinal synthesis and dietary nonessentiality of vitamin B_{12} for Tilapia nilotica", Trans. Am. Fish. Soc. Vol. 111, p. 485 (1982)
5. Uphill, P.F., Jacob, F., and Lall, P., "Vitamin B_{12} production by the gastrointestinal microflora of baboons fed either a vitamin B_{12} deficient diet or a diet supplemented with vitamin B_{12}", J. Appl. Bacteriol. Vol. 43, p. 333 (1977)
6. Drasar, B.S., and Barrow, P.A., "Intestinal Microbiology", Van Nonstrand Reinhold (UK) Co., Workingham, p. 59 (1985)
7. Teshima, S., and Kashiwada, K., "Studies on the production of B vitamins by intestinal bacteria of fish-III. Isolation of vitamin B_{12} synthesizing bacteria and their bacteriological properties", Bull. Jpn. Soc. Sci. Fish. Vol. 33, p. 979 (1967)
8. Sugita, H., Sakata, T., Ishida, Y., Deguchi, Y., and Kadota, H., "Aerobic and anaerobic bacteria in the intestine of ayu, Plecoglossus altivelis", Bull. Coll. Agric. Vet. Med., Nihon Univ. Vol. 38, p. 302 (1981)
9. Sugita, H., Tokuyama, K., and Deguchi, Y., "The intestinal microflora of carp Cyprinus carpio, grass carp Ctenophryngodon idella and tilapia Sarotherodon niloticus", Bull. Jpn. Soc. Sci. Fish. Vol. 51, p. 1325 (1985)
10. Sugita, H., Tsunohara, M., Fukumoto, M., and Deguchi, Y., "Comparison of microflora between intestinal contents and fecal pellets of freshwater fishes", Nippon Suisan Gakkaishi. Vol. 53, p. 287 (1987)
11. Sugita, H., Tsunohara, M., Ohkoshi, T., and Deguchi, Y., "The establishment of an intestinal microflora in developing goldfish (Carassius auratus) of culture ponds", Microbial Ecol. Vol. 15, p. 333 (1988)
12. Azuma, R., Ogimoto, K., and Suto, K., "Anaerobic culture method with steel wool", Jpn. J. Bacteroiol. Vol. 17, p.802 (1962)
13. Sugita, H., Tanaami, H., Kobashi, T., and Deguchi, Y., "Bacterial flora of coastal bivalves", Bull. Jpn. Soc. Sci. Fish. Vol. 47, p. 655 (1981)
14. Shewan, J.M., Hobbs, G., and Hodgkiss, W., "A determinative scheme for the identification of certain genera of gram-negative bacteria, with special references in Pseudomonadaceae", J. Appl. Bacteriol. Vol. 23, p. 379 (1960)
15. Cowan, S.T., "Cowan and Steel's Manual for the Identification of Medical Bacteria", University Press, Cambridge, 238 p. (1974)
16. Sakata, T., Sugita, H., Mitsuoka, T., Kakimoto, D., and Kadota, H., "Characteristics of obligate anaerobic bacteria in the intestines of freshwater fish", Bull. Jpn. Soc. Sci. Fish. Vol. 47, p. 421 (1981).
17. Sato, K., "Assay methods of vitamin B_{12}", Vitamins (Japan), Vol. 57, p. 609 (1983)
18. Bell, G.R., Hoskins, G.W., and Hodgkiss, W., "Aspects of the characterization, identification and ecology of the bacterial flora associated with the surface of stream-incubating Pacific salmon (Onchorhynchus) eggs", J. Fish. Res. Board Can. Vol. 28, p. 1511 (1971)
19. Sugita, H., Enomoto, A., and Deguchi, Y., "Intestinal microflora in the fry of Tilapia mossambica", Bull. Jpn. Soc. Sci. Fish. Vol. 48, p. 875 (1982)
20. Sugita, H., Ishida, Y., Deguchi, Y., and Kadota, H., "Aerobic microflora attached to wall surface in the gastrointestine of Tilapia nilotica", Bull, Coll. Agric. Vet. Med., Nihon Univ. Vol. 39, p. 212 (1982)
21. Sera, H., Ishida, Y., and Kadota, H., In "Effect of the Ocean Environment on Microbial Activities" (ed. by R.R. Colwell and R. Y. Morita), University Park Press, Baltimore, MD, p. 467 (1974)
22. Trust, T.J., and Sparrow, R.A., "The bacterial flora in the alimentary tract of freshwater salmonid fishes", Can. J. Microbiol. Vol. 20, p. 1219, (1974)
23. Trust, T.J., "Facultative anaerobic bacteria in the digestive tract of chum salmon (Onchorhynchus keta) maintained in freshwater under defined culture conditions", Appl. Microbiol. Vol. 29, p. 663 (1975)
24. Horsley, R.W., " A review of the bacterial flora of teleosts and elasmobranchs, including methods for its analysis", J. Fish Biol. Vol. 10, p. 529 (1977)
25. Sugita, H., Oshima, K., Tamura, M., and Deguchi, Y., "Bacterial flora in the gastrointestine of freshwater fishes in the river", Bull. Jpn. Soc. Sci. Fish. Vol. 49, p. 987 (1983)
26. Yoshimizu, M., and Kimura, T., "Study on the intestinal microflora of salmonids", Fish Pathol. Vol. 10, p. 243 (1976)
27. Sugita, H., Ishida, Y., Deguchi, Y., and Kadota, H., "Bacterial flora in gastrointestine of Tilapia nilotica adapted in seawater", Bull. Jpn. Soc. Sci. Fish. Vol. 48, p. 987 (1982)
28. Lesel, R., and Peringer, P., "Influence of temperature on the bacterial microflora in Salmo gairdneri Richardson", Arch. Hydrobiol. Vol. 93, Vol. 109 (1981)
29. Sugita, H., Iwata, J., Miyajima, C., Kubo, T., Noguchi, T., Hashimoto, K., and Deguchi, Y., "Changes in microflora of a puffer Fugu niphobles, with different water temperature", Marine Biol. Vol. 101, p. 299 (1989)
30. Lesel, R., and Sechet, J., "Influence d'un stress de manipulation sur le transit de la microflore bacterienne digestive chez la truite arc-en-ciel Salmo gairdneri Richardson", Acta Ecol. Applic. 22. Vol. 3, p. 23 (1982)
31. Sugita, H., Fukumoto, M., Koyama, H., and Deguchi, Y., "Changes in the fecal microflora of goldfish Carassius auratus with the oral administration of oxytetracycline", Nippon Suisan Gakkaishi (formerly, Bull. Jpn. Soc. Sci. Fish.). Vol. 54, p. 2181 (1988)
32. Sugita, H., Miyajima, C., Fukumoto, M., Koyama,

H., and Deguchi, Y., "Effect of oxolinic acid on fecal microflora of goldfish (*Carassius auratus*)", Aquacult. Vol. 80, p. 163 (1989)

33. Sugita, H., Fukumoto, M., Tsunohara, M., and Deguchi, Y., "The fluctuation of the fecal flora of goldfish, *Carassius auratus*), Nippon Suisan Gakkaishi. Vol. 53, p. 1443 (1987)

34. Sugita, H., Miyajima, C., Kobiki, Y., and Deguchi,

Y., "Daily changes of the fecal flora of tilapia *Sarotherodon niloticus*", Nippon Suisan Gakkaishi. Vol. 55, p. 1865 (1989)

35. Sugita, H., Miyajima, C., Kobiki, Y., and Deguchi, Y., "The daily fluctuation and inter-individual variation of the faecal flora of carp, *Cyprinus carpio* L.", J. Fish. Biol. Vol. 36, p. 103 (1990)

COMPOUNDS FROM SOFT CORALS THAT INHIBIT BARNACLE SETTLEMENT: ISOLATION AND BIOLOGICAL POTENCY

R. Nagabhushanam, R. Sarojini, Sr. Uvann Mary

Marathwada University, Aurangabad, India

ABSTRACT

The overall objective of this investigation was to understand larval barnacle settlement, with the practical goal of developing non-toxic antifouling agents by the isolation and partial purification of new antibarnacle settlement compounds from soft corals. Bioactive compounds from five soft corals : Solenocaulon tortuosum Suberogorgia suberosa, Echinogorgia complexa, Juncella juncia and Spongodes sp. inhibited barnacle settlement at levels from several parts per million to several parts per trillion. Inhibitors from Juncella juncea were the most potent. Two active fractions obtained by TLC band 3 and 4 have L EC50 values of 5.7 ng/ml and 3 ng/ml based onthe weight of the unfractionated methylene chloride extract. The experiments showed that all the five soft corals are not toxic to cyprids and hence contain non-toxic antifouling compounds.

INTRODUCTION

Soft corals are often supported by horny proteinaceous substance, gorgonin. The gorgonians are all colonial octocorals with skeletons composed at least partially of more or less conso-lidated bits of calcium carbonate called spicules. Being attached to the bottom they have the problem of protection against predators in a medium in which animals are always hungry. Inspite of their stationary nature, soft corals remain remarkably free from predation, fouling or overgrowth. The success of vigorous growth against predation and severe competition for space on solid substrate in coral reef may be due to the production of organic compounds by the gorgonians used as chemical defence against assilant (10, 3).

Gorgonians have proved to be a rich source of a great variety of chemi-cally interesting organic compounds. Many gorgonians have an odor which one would call aromatic, readily noticed shortly after the animals are taken out of the sea. The lack of fouling is characteristic of living gorgonian colonies only. Chemical extraction of gorgonians or horny corals yields large amounts as much as 1 to 2 % of dry wt. of disterpenoid compounds related to cembrane a diterpene with a 14-membered ring (4). Possible ecological signi-ficance of this high concentration has been suggested (5,7), as a defence against predation and overgrowth.

Until now, chemical investigations of the extracts of various gorgonians, have led to the discovery of many novel and interesting molecules including oxabridged cambranolides (15), prostagla-ndins (16), sesquiterpene hydrocarbons (15), unusual antibacterial dodecane bisbutanolide (13) and also some ammonium compounds which appear to account for the skin and eye irritation produced by handling of the animals. Rittschof et al (12) showed that the compounds from Leptogorgia virgulata that inhibit settlement of larval barnacles are discrete low molecular weight substances. Extracts of the Atlantic sea pansy Renilla reniformis, which inhibits the settlement of barnacle larvae, have been found to contain three new diterpenes : renilafouling A(1), B(2) and C(3),(8) These three and three forms of pukalide from Leptogorgia virgulata are used as examples in a U S Patent on nontoxic antifoulants.

Larval settling behaviour is dependent on substratum type,substratum rugosity, light intensity, existing surface films, host inductance, larval chemoreception and other factors.

Since barnacles are dominant members of the fouling community, they are important organisms to study the effects of bioactive substances from soft corals. They also have major economic impact and contain biochemical secret (for example a biochemical glue that sets underwater) with future application. There is worldwide interest in the potential of biochemical natural products as antifoulants in antitumor and in antiviral activity. The South East Indian Ocean is a potentially rich source of such compounds.

The overall objective of this investigation was to understand larval barnacle settlement, with the practical goal of developing non-toxic antifouling agents by the isolation and partial purification of new antibarnacle settlement compounds from soft corals. The functioning programme in the present study would serve as a nucleus for additional development in this fast growing areas.

MATERIAL AND METHODS

Collection and Extraction of Octocorals

Colonies of <u>Solenocaulon tortuosum</u>, <u>Suberogorgia suberosa</u>, <u>Echinogorgia complexa</u>, <u>Juncella juncea</u> and <u>Spongodes</u> sp. were collected in 10 to 20 meters of water in the Indian Ocean along the Gulf of Mannar off the southeast coast of India. Living colonies were transported to the laboratory in sea water. Colonies were blotted dry, weighed, cut into pieces and frozen at -20°C. Frozen samples were freezed dried and weighed. Dry material was extracted (1:3 weight to volume) with methanol.

Analysis by Thin Layer Chromatography

Material extracted into methylene chloride was fractionated using preparative thin layer chromatography. Prior to the preparative step, solvent systems for separation were established on microscope slide analytical TLC plates (Whatman PK 6F). For preparative TLC, Methylene chloride extracts (extract equivalent to approximately 200 grams of original wet weight of coral) was applied to Whatman Pk6F 20 x 20 cm plates in a 0.5 X 20 cm band 2.5 cm from the bottom of the plate. The plates were developed to within 2.5 cm of the top. The solvent system used was that solvent system that gave intermediate mobilities (between 0.3 and 0.7 rf) of compounds that inhibited barnacle settlement. Solvent systems used were : methylene chloride : acetonitrile (9:1), hexane : ethyl acetate (1:1); and ether (100%). Decisions of zones of separation were based upon fluorescence and quenching

under 250 to 270 and 230 to 240 nm light. Separated material was recovered from the plates by scraping and elution with HPLC grade methanol. Methanol was removed by rotary evaporation.

Biological Assays

Settlement Assays

The settlement assay was the 22 h assay (Branscomb and Rittschof, 1984; Rittschof <u>et al.</u>, 1984). Approximately 50 to 100 cyprids were placed into Falcon 1006 (Falcon plastics, Cockeysville, Maryland) polystyrene containers, containg 5 ml sea water as control or 5 ml desired concentration of vacuum dried test material. From two to six concentrations of test solutions, each with replicates were tested to compare the frequency of attachment in experimental solutions with attachment in the controls. Test petridisches were incubated for 22 hr at 28°c and 15 : 9 light : dark regime. Attached and unattached cyprids were counted.

Statistical Analysis

The effective concentrations giving 50 % inhibition of settlement (EC 50 %) (with 95 % confidence limits) were calculated by the probit technique of Finney with a Basic program for microprocessors written by Lieberman (1983). Calculations were confirmed by repeating the entire experiment at least twice using larvae from different mass culture.

RESULTS

Effect of Methylene Chloride Extract from Solenocaulon tortuosum on Barnacle Settlement.

The methanol soluble fraction of the aqueous extract of <u>Solenocaulon tortuosum</u> was partitioned between methylene chloride and water. The methylene chloride soluble material extract of <u>Solenocaulon tortuosum</u> contained inhibitory activity. The percentage of barnacle larval settlement response to different concentrations of methylene chloride extract is shown in Figure 1. Near complete settlement xxxxxx inhibition was observed at 10 mg original animal wet weight/ml. EC 50 value was 0.02 mg original/ml. and 50 ug/ml. based upon dry weight of the extract. The methylene chloride soluble compounds were separated by preparative gel TLC.

MG Original /ml

MG Original /ml

Fig.1. Barnacle settlement assays of methylene chloride extract of Solenocaulon tortuosum. Near complete settlement inhibition was observed at 10 mg original/ml.

Thin Layer Chromatographic Fractions

The methylene chloride extract was fractionated by preparative thin layer chromatography on silica. The plates were developed with methylene chloride acetonitrile 9:1. This solvent system yielded 7 uv quenching bands with relative mobilities 0.1 to 0.9.

Effect of Suberogoria suberosa Methylene Chloride Extract on Barnacle Settlement

The methanol - soluble fraction of the aqueous extract of Suberogorgia suberosa was partitioned between methylene chloride and water. The methylene chloride soluble material contained inhibitory activity.Settlement inhibition of barnacle larvae was observed at concentrations from0.004 to 9 mg original/ml. Suberogorgia suberosa methylene chloride extract had an EC 50 value 0.914 mg original animal wet weight/ml and 4.43 ug/ml based upon the dry weight of the extract (Fig. 2)

Thin Layer Chromatographic Fractions

The methylene chloride extract was fractionated by preparative thin layer chromatography on silica. The plates were developed with methylene chloride : acetonitrile 9:1. This solvent system yielded 6 uv quenching bands with relative mobilities 0.32 to 0.9. Of the 6 uv quenching bands, bands 1 and 5 with Rf 0.32 and 0.82 inhibited barnacle cyprid settlement. Further bioassay of band 1 gave the EC 50 170 ng/ml and band 5 gave the EC 50 965 ng/ml based on the dry weight of the extract.
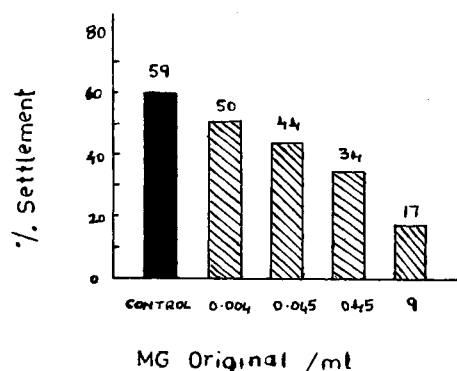
Fig. 2 : Barnacle settlement assays of methylene chloride extract of Suberogorgia suberosa. Settlement inhibition of barnacle larvae was observed at concentrations from0.004 to 9 mg original/ml.

Effect of Methylene Chloride Extract from Echinogorgia complexa on Barnacle Settlement

The methanol -soluble fraction of the aqueous extract of Echinogorgia complexa was partitioned betweeen methylene chloride and water. The methylene chloride soluble material contained potent inhibitory activity when tested in the barnacle settlement assay. The EC 50 value for the extract was 0.3 ug original animal wet weight/ml and 0.0013 ug/ml based upon the dry weight of the animal. The methylene chloride soluble compounds were separated by preparative silica gel TLC (Fig.3).
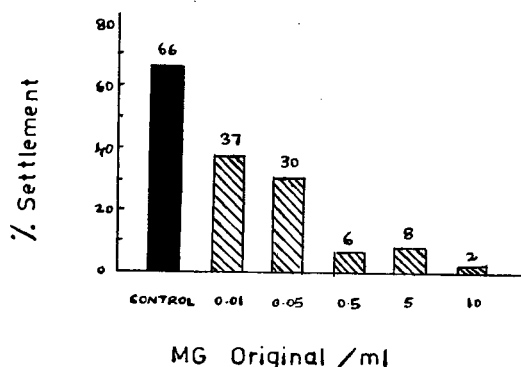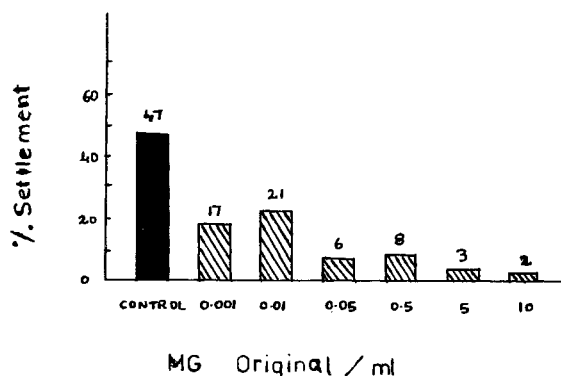

MG Original / ml

Fig.3: Barnacle settlement assays of methylene chloride extract of Echinogorgia complexa. Near complete settlement inhibition was observed at 10 mg original/ml.

Thin Layer Chromatographic Fractions

Preparative silica thin layer chromatography was used to fractionate the methylene chloride extract of E. complexa. Development with 9 : 1 methylene chloride : acetonitrile yielded 7 quenching bands with mobilities 0.0 to 0.9. There was only one band with Rf value of 0.208 with potent antibarnacle settlement activity. The EC 50 was 350 mg/ml based upon the dry weight of the extract. This band was split into 3 bands when return on silica with hexane : ethylacetate 1:1. Among these three bands, the bands denoted as DBR 1 and OBR 2 were active. The EC 50 for DBR 1 was 375 ng/ml and EC 50 for DBR 2 was 426 ng/ml baed upon dry weight of the extract.

Effect of Juncella juncea Methylene Chloride Extract on Barnacle Settlement :

The methanol - extract of freeze-dried Juncella juncea was diluted with water and extracted with methylene chloride giving an extract containing potent inhibitors of barnacle settlement. No settlement was observed at 1 mg original animal wet weight/ml. Strong antisettlement activity was observed at 0.01 mg original animal/ml. Juncella juncea methylene chloride extract had an EC 50 value of 0.04 ng original animal/ml on wet weight basis. The methylene chloride soluble compounds were separated by preparative silica gel TLC (Fig.4).
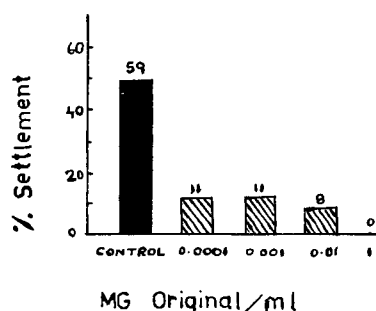
potent inhibitory activity when tested with barnacle settlement assay. The methylene chloride extract was fractionated by preparative thin layer chromatography on silica. The plates were developed with hexane : ethylacetate 1:1. This solvent system yielded 10 quenching bands with relative mobilities 0.2 to 0.9. Of the 10 uv quenching bands, bands 2,3 and 4 with Rf value respectively of 0.33, 0.47 and 0.57 inhibitedbarnacle cyprid settlement. The origin, is the region of the TLC plate where the extract is loaded.Band 6 (Rf 0.757) and band 10 (Rf 0.92) enhance barnacle cyprid settlement. Further purification with hexane : ethylacetate 1:1 showed that bands 3 and 4 (Rf 0.48 and 0.6) contained potent inhibitor activity. The band 3 gave the EC 50 5.7 ng/ml and the band 4 gave the EC 50 value 3 ng/ml based on the dry weight of the extract.

Effect of Spongodes sp. Methyelene Chloride Extract on Barnacle Settlement

The methanol - soluble fraction of the aqueous extract of Spongodes sp was partitioned between methylene chloride and water. The methylene chloride extract of Spongodes sp. contained potent inhibitors of barnacle settlement. Spongodes sp methylene chloride extract had an EC 50 value of 2.076 mg original animal/ml on wet weight basis and 3.342 mg/ml basedupon the dry weight of the extract. The methylene chloride soluble compounds were separated by preparative silica gel TLC (Fig. 5).

MG Original/ml

Fig.4: Barnacle settlement assays of methylene chloride extract of Juncella juncea. No settlement was observed at 1 mg and strong antisettlement activity was observed at 0.01 mg original animal wet weight/ml.

Thin LayerChromatographic Fractions:

Thin layer chromatographic fractions of methylene chloride soluble material from Juncella juncea showed

MG Original /ml

Fig.5: Barnacle settlement assays of methylene chloride extract of Spongodes sp.

Thin Layer Chromatographic Fractions

Thin layer chromatographic fractions of methyelene chloride soluble material from Spongodes sp. showed pote-nt inhibitory activity when tested with barnacle settlement assay. The solvent system used for development was methylene banalx chloride : acetonitrile 9:1 For six bands with relative mobilities of 0.14, 0.24, 0.39, 0.59, 0.73, 0.85 probit analysis gave ED 50 values respectively of 13.312, 13.836, 11.298, 0.989, 16.218 and 0.911 original mg/ml. Bands 4 and 6 gave EC 50 values 0.989 and 0.911ng/ml. Further bioassay of band 4 gave the EC 50 480 ng/ml on dry weight basis.

TLC band 6 of the methylene chloride extract had antisettlement activity. The EC 50 value for band 6 was 0.091 mg/ml on wet weight basis.

TLC band 4 was retun on silica PK 6 F with hexane : ethyle acetate 1:1 and separated into 5 bands. These 5 bands are marked as MPR 1 to 5. Band 1 (Rf 0.63) which is marked as MPR 1 had an EC 50 value of 3.474 ug/ml.

The methylene chloride soluble materials from soft corals showed potent inhibitory activity. EC 50 values based on original animal/ml on wet weight basis, 95% confidence interval, and EC 50 values based upon the dry weight of the methylene chloride extract are shown in Table 1. EC 50 values of thin layer chromatographic fractions of methylene chloride soluble material are summarized in Table 2.

Table - 1 The methylene chloride soluble materials from soft corals showed potent inhibitory activity.

Soft corals	EC 50 original m$_0$/ml	95% confi-dence interval	EC 50 CH_2CL_2 dry wt micro/ml
S.tortuosum	0.02	0.05-0.004	50.4
S. suberosa	0.91	2.5 - 0.3	4.04
E. complexa	0.000 3	1.9-0.005	0.0013
J. juncea	No settlement even at 0.04 ng/ml		
Spongodes sp	2.07	3.6 - 0.9	3.34

Table 2 EC_{50} of Thin layer chromatographic fractions of methylene chloride soluble material from softcorals.

Soft coral	Fraction	EC_{50}(ng/ml) dry wt basis
S. tortuosum	2. RF 0.42	15 ng/ml
	AP_2Rf 0.416	71 ng/ml
	Ether Rf 0.82	0.2 ng/ml
S. suberosa	1. Rf 0.323	170 ng/ml
	5. Rf 0.892	965 ng/ml
E. complexa	1. Rf 0.20	350 ng/ml
	OBR 1 Rf 0.36	375 ng/ml
	DBR 2 Rf 0.68	426 ng/ml
J. juncea	3. Rf 0.48	5.7 ng/ml
	4. Rf 0.6	3 ng/ml
Spongodes sp.	4. Rf 0.59	480 ng/ml
	MPR 1 Rf 0.64	0.990 ng/ml

DISCUSSION

Preliminary evidence supports the suggestion that tropical marine orga-nisms may show greater potential as toxic antifoulers than do temperate latitude species (Bakus and Kawaguchi, 1984). However, there is also evidence that many temperate organisms contain compounds with antifoulant properties (14,12). Experiments conducted (1) indicate that extracts from tropical gorgonians and sponges can inhibit, enhance, or not affect the settling of dominant marine fouling organisms. Although Leptogorgia colonies are generally free of fouling organisms, they do harbour several symbiotic animals (11). One of these is the barnacle Conopea galeata, which occurs exclusively on gorgonians.

Octocoral defences against larval settlement was first proposed by Ciereszko (3). Standing et al. (14) tested a common subtropical gorgonian, Leptogorgia virgulata (Lamark), for substances that inhibited settlement of the barnacle, Balanus amphitrite Darwin. The dialyzable low molecular weight fraction of an aqueous homo-genate of L. virgulata soft tissue

contains at least two types of inhibitory substances. One type affects larval behaviour, the other including at least two substances,(12) inhibits settlement (12). They further showed that settlement inhibitor does not directly effect the behaviour of cyprids. The authors suspected that larval settlement is inhibited by an interaction of the substances with the settlement substrate. They supported their argument with observations of lower EC 50 values or substances with higher affinity for the compounds. They proposed that inhibitors manifested themselves at surfaces as do chemical facilitators of settlement function (6,9).

Working hypothesis as to the mechanism of action of the compounds from soft corals will be modified as additional compounds are identified and structures determined, as many of the affective compounds are not toxic even in very high concentrations. Understanding of the mechanism of action of these has great potential commercial application. The first step in the process of identification is, the identification of biological activity and purification of the compounds responsible.

Our experiments showed that soft corals Solenocaulon tortuosum, Suberogorgia suberosa, Echinogorgia complexa, Juncella juncea and Spongodes sp. are not toxic to cyprids. Thus the soft corals studied contain nontoxic antifoulant compounds. Elucidation of the structures of these compounds will provide additional information to the mechanism of action.

REFERENCES

1. Bakus, G.J. Evans T., Mading B., and Kouros, P. The use of natural synthetic toxins as shark repellents and antifouling agents. Toxicon (suppl) p. 25 (1983).

2. Bakus, G.J. and Kagaguchi, M. Toxins from marine organisms : Studies on antifouling. In: L. Bolis J. Zedunaisky and R. Gilles (eds). Toxins, Drugs and Pollutants in Marine animals Springer - Verlag, New York, p. 43.

3. Ciereszko, L.S. Chemistry of coelenterates. III Occurrence of antimicrobial terpenoid compounds in the Zooxanthellae of alcyonarians. Trans. N.Y. Acad. Sci. vol. 24, p. 502 (1962).

4. Ciereszko, L.S., Sifford,D.H. and Weinheimer A.J. Chemistry of terpenoid compounds in gorgonians. Ann. N.Y. Acad. Sci. vol. 90, p.917 (1960).

5. Cierreszko, L.S. and T.L.B. Karns. Comparative biochemistry of coral reef coelenterates.In: Biology and geology of coral reefs. Vol.II Biology I, Ed. by D.A. Jones and R. Endean, Academic Press, INC New York p. 183 (1973).

6. Crisp, D.J. Overview of research on marine invertebrate larvae. In J.D. Costlow andR.C. Tipper (eds) Marine Biodeterioration : An interdisciplinary approach Naval Institute Press, Annapolis, Maryland, p. 103, (1984).

7. Hadfield, M. and L.S.Ciereszko: Action of Cembranolides derived from octocorals on larvae of the Nudibranch Phestilla sibogae P.K. Kaul and J.Sinderman (eds) Drugs and Food from the sea. University of Oklahoma Press, Norman, Oklahoma, p. 145 (1978).

8. Keifer Paul A. and Kenneth L. Rinehart Jr. and Irving R. Hopper : Reniliafouline, Antifouling diterpenes from the Sea Pansy Renilla reniformis (Octocorallia) The Journal of organic chemistry vol. 41, p. 4450 (1986).

9. Morse, A.N.C. and Morse, D.: Recruitment and metamorphosis of Haliotis larvae induced by molecules uniquely available at the surface of crustace red algae, J. Exp. Mar. Biol. Ecol. vol.75, p. 191. (1984).

10. Nigrelli R.F. Antim Antimicrobial substances from marine organisms. Introduction : The role of antibiosis in the sea., Trans. N.Y. Acad. Sci. vol.24, p. 496 (1962).

11. Patton W.K. Studies on the animal symbionts of the gorgonian coral, Leptogorgia virgulata (Lamark). Bull. Mar. Sci. vol.22, pp 419 (1972).

12. Rittschof, D., Hopper,I.R.,Branscomb E.S., andCostlow J.D.: Inhibition of barnacle settlement and behaviour by natural products from whip corals Leptogorgia virgulata (Lamarck,1815). J. Chem. Ecol. vol.11,p. 551 (1985).

13. Schmitz, F.J., Karaus, K.W.,
Ciereszko, L.S., Sifford, D.H.
and Winheimer, A.J. Chemistry
of coelenterates - V. Ancepsolide:
A novel bisbutenolide of marine
origin Tet. Lett. vol.1, p. 97
(1966).

14. Standing, J.,Hopper, I.R., and
Costlow, J.D. Inhibition and
induction of barnacle settlement
by natural products present in
Octocorals., J. Chem. Ecol.
vol. 10, p. 823.

15. Weinheimer A.J., Middlebrook R.E.
Bledsoe,J.D. Jr. Marsico W.E. and
Karns T.K.B. Eunicin, an oxa-
bridged cembranolide of marine
origin., Chem. Comm. 384 (1968).

16. Weinheimer A.J. and Soraggings,R.
L. The occurrence of two new
prostaglan din derivatives 915-
epi - PGA2 and its acetate methyl
ester) in the gorgonians Plexaura
homomalia : Chemistry of Coelen-
terates XV Tett, vol. 59,
p. 5185 (1969).

PAPERMAKING OF ALGAL POLYSACCHARIDES FOR A POTENTIAL INDUSTRIAL UTILIZATION OF ALGAE

Y. Kobayashi, H. Kamishima, S. Fukuoka and H. Obika

Government Industrial Research Institute, Japan

Abstract

Paper is generally made from cellulose produced by land plants. Its production amount annually to 210 million tons, which attractive to the target of potential industrial applications of algal polysaccharides as development of marine resources. Algal polysaccharides, however, are not naturally in the form of fibers like cellulose but in gel form. To substitute for cellulosic pulp by algal polysaccharides, therefore, the polysaccharides are required to be spun to give fibers. Among various algal polysaccharides, algin was the most suitable polymer because of its high spinnability. Water insoluble alginate fibers were made by spinning of the dope consisting of Na alginate using higher valent of metallic chloride solution as coagulants. The fibers were cut to several mm in length. The alginate fiber paper was made by usual papermaking method using these cut fibers without interfiber adhesive agents. This process was almost same as that of rayon paper. This paper was applicable to a speaker cone material because it was not so much rigid as cellulosic paper. As the algal paper was made in all aqueous system, the enzymes were immobilized no only in the fiber but also in the form of paper, which was expected to have potential applications of bioreactors and biosensors.

Paper is mass-produced from cellulose, land plant polysaccharide, amounting annually to 210 million tons, but very few reports have been published to produce paper from algal polysaccharides before the authors' investigation[1]. Brown algae in sea, corresponding to forest woods on land, are mainly constituted from alginic acid in cell wall and intercellular cementing matrix. Quite different from cellulose, alginic acid does not exist in fiber form in the algae. For the production of paper, alginic acid must be span. Fortunately this acid is a linear block polymer consisting of D-mannuronic acid and L-guluronic acid and has spinnability. Papermaking of the cut fiber was successfully carried out without inter-fiber binder. In this presentation are given the preparation and properties of alginate fiber paper and its applications as speaker cone paper and enzyme entrapping paper.

1. Papermaking of alginate fibers

Sodium alginate has well been known to have spinnability. Two patents[2,3] suggesting the application possibilities of Ca alginate fiber to papermaking have been published to date but did not provide methods for producing paper with good formation because of the application of Na alginate binder and crushing the gel fiber by beating.

Based on the authors' finding that the wet web had interfiber selfbonding properties in water without beating, papermaking with the fiber has succeeded in yielding paper with good formation very similar to that of cellulosic paper.

Production method of staple fibers
Aqueous dopes(3-5wt.%) of Na alginate were filtered through ceramic filter having fine holes of 50 micron under pressure. The filtered dopes were extruded through a nozzle with 1000 holes of 0.1-0.55 mm in diameter using a wet spinneret into a coagulating solution of 5.0 wt.% metallic chloride (Ca^{2+}, Ba^{2+}, Al^{3+}, Cu^{2+} etc.) at a spinning rate of 13.8 ml/min followed

by stretching 1.2-1.3 times. The wound continuous yarns were cut using a guillotine cutter in fiber length of 1.5-5.0 mm. The fibers having fiber length greater than 5.0 mm were not well dispersed in water. Fiber composed of alginic acid(free acid form) was prepared by soaking the corresponding Ca salt fibers in HCl for 20 min, followed by water washing. finding that the wet

Papermaking method After defibration of the short-cut fibers in a disintegrator with a capacity of 10 liter at a consistency of approximately 2.5-6.0 wt.% for 30 min, the fibers were filtered through a 6-cut flat screen to remove clots and bundles. Hand sheets were made according to JIS P 8209. As the webs had high shrinkage, they were air-dried by fixing them together with filter paper upon dry rings under tension with a cover of filter paper.

Spinability and aqueous dispersability of insoluble alginate cut fibers The spinnability of Na alginate dope was not affected by MW within the range of $1.8-7.8 \times 10^5$ dalton but was dependent upon coagulating metallic salts. $CaCl_2$, $BaCl_2$, $CuCl_2$ gave smoothly continuous yarns. These insoluble fibers had good dispersing ability for papermaking.

Interfiber self-bonding Regenerated cellulosic fibers, e.g., viscose rayon, have usually far less interfiber self-bonding than natural cellulosic pulps and require generally binders to make rayon paper. Alginate fibers are a kind of regenerated one, but were found to have paper-formability by interfiber self-bonding provided that the aspect ratio is within suitable ranges.

Effect of molecular weight Fixing at fiber length of 3.0 mm, four types of the paper were prepared: Ca alginate and free alginic acid fibers spun through 0.1 and 0.055 mm in hole diameter. Representative physical properties of the paper were measured as a function of MW. As a typical example, dependence of breaking length on MW is shown in Fig. 1. This tensile strength was relatively small in the smaller MW ranges but rapidly increased over a MW of 5.0×10^5 dalton. This indicated the fact that higher tensile strength required higher MW fibers. The strength was almost equivalent to that of news print.

Effects of fiber length and metallic ions The fiber length was limited within the range from 1.0 to 5.0 mm because fibers having fiber length longer than 5.0 mm were easily to aggregate. As shown in Fig. 2, the
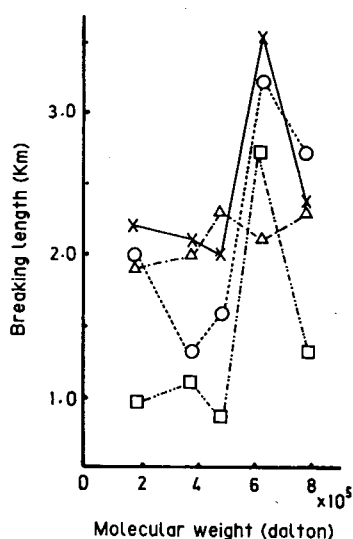
Fig. 1 Dependence of breaking length on molecular weight of alginate composing paper
x-x Ca alginate fiber prepared through
O—O 0.1 mm nozzle hole
   Alginic acid fiber through 0.1 mm
△··△ Ca alginate fiber through 0.055 mm
□—□ Alginic acid fiber through 0.055mm
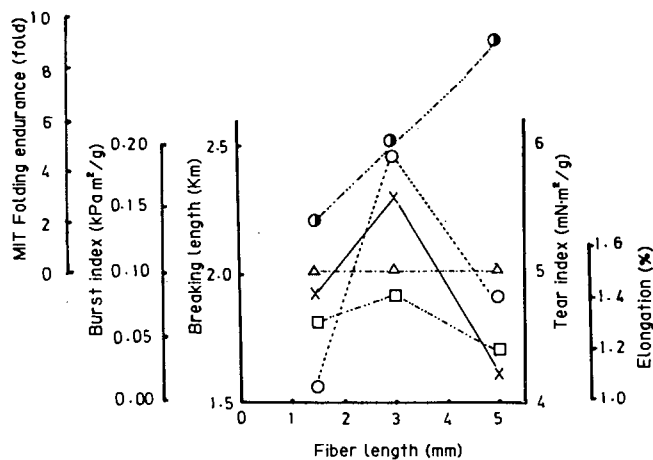
Fig.2 Dependence of strength properties on fiber length in papers made from Ca alginate and alginic acid having MW of 1.8×10^5 dalton.
(x—x) breaking length; (△——△) burst index; (O· ·O) tear index;
(□– — · □) elongation; (●- ··· -●) MIT folding endurance.

dependence of fiber length on strength properties was determined using sheets composed of Ca alginate fibers with nozzle hole diameter of 0.055 mm and MW of 6.3×10^5 dalton.

Sheets were hand-made from Al^{3+}, Ba^{2+}, and Fe^{3+} alginate fibers in addition to Ca^{2+} alginate fibers. These fibers were 3.0 mm in length. Physical properties are summarized in Table 1. From view points of papermaking, the order of metallic ions as coagulants was as follows: $Ca^{2+} > Ba^{2+} > Al^{3+} >> Fe^{3+}$. Trivalent metals gave paper with poor physical properties.

Table 1
Physical Properties of Papers Made From Fibers of Various Metallic Salts of Alginic Acid

| Fiber diameter (mm) (spinning base) | 0.10 | | | | 0.055 | |
| Molecular weight (dalton) | 6.3×10^5 | | | | 3.8×10^5 | |
Alginate salt	Ca^{2+}	Ba^{2+}	Al^{3+}	Fe^{3+}	Ca^{2+}	Ba^{2+}
Bulk density (g/cm^3)	0.54	0.59	0.51	0.32	0.65	0.78
Breaking length[a] (km)	3.6	1.7	1.5	1.6	2.0	1.4
Zero span breaking length (km)	5.4	4.2	2.6	UM[b]	5.5	3.6
Tear index (mN·m^2/g)	5.9	4.2	2.6	UM	7.0	5.4
Burst index (kPa·m^2/g)	0.27	0.03	0.13	UM	0.14	0.08
MIT folding endurance (folds)	53	UM	UM	UM	9	8
Elongation (%)	2.7	0.8	1.6	1.3	1.5	1.0

[a] Fibers were 3.0 mm long.
[b] Unmeasurable.

Table 2
Entrapment of various kinds of enzymes in alginate fibers and their papers.[a]

| Enzyme | Spinning conditions | | | Fiber[b] | | Paper[b] | | Beads[c] | |
	Diameter of nozzle hole (mm)	Stretching (times)	Discharge rate (mL/min)	Enzyme activity[d] (U/g)	Specific activity[e] (U/mg)	Enzyme activity[d] (U/g)	Specific activity[e] (U/mg)	Enzyme activity[d] (U/g)	Specific activity[e] (U/mg)
Glucoamylase	0.10	1.23	13.7	3360 (100.0)	27.1 (100.0)	1135 (33.8)	23.0 (84.8)		
	0.055	1.23	13.7	2370 (100.0)	27.5 (100.0)	971 (41.0)	20.1 (73.1)	596 (17.7)	15.1 (54.9)
CGTase	0.10	1.21	13.7	655 (100.0)	31.7 (100.0)	101 (15.4)	37.5 (118)	ND	ND
	0.10	1.48	17.2	645 (100.0)	30.2 (100.0)	90 (14.0)	31.8 (105)		
endo-Polygalacturonase	0.10	ND	13.7	120 (100.0)	3.82 (100.0)	121 (101)	9.24 (242)		
	0.10	ND	17.2	102 (100.0)	5.16 (100.0)	126 (124)	5.54 (107)	21.5 (17.9)	2.49 (30.9)
	0.055	ND	13.7	39 (100.0)	8.06 (100.0)	51 (131)	4.90 (60.8)		
Protease	0.10	1.11	13.7	4520 (100.0)	69.9 (100.0)	2310 (51.1)	79.7 (114)	804 (17.8)	112 (160)
Glucose oxidase	0.10	1.24	13.7	12400	66.4	ND	ND	ND	ND
	0.055	1.24	13.7	9640	51.1	ND	ND	ND	ND
Peroxidase	0.10	1.24	13.7	330	ND	ND	ND	ND	ND
	0.055	1.24	13.7	175	ND	ND	ND	ND	ND

[a] ND, not determined.
[b] Numbers in parentheses are percentage of activity or specific activity entrapped in fibers.
[c] Numbers in parentheses are percentage of maximum activity or specific activity entrapped in fibers.
[d] Oven-dried base of alginate.　　[e] Based on weight on enzyme protein entrapped.

2. Enzyme-entrapped alginate fibers and their paper

Fiber forms have in general high specific surface area and are suitable for enzyme immobilization. Researches on immobilized enzymes in the form of fibers are so far scarce; entrapment by cellulose triacetate[4,5], bonding by functional groups on fiber surfaces of polyvinyl alcohol[6], polyamide[7] and cellulose[8].

Applying the fact that Ca alginate gel in the form of small beads has been widely used as a biomaterial support, enzymes were found to be entrapped by alginate fibers and their paper[9]. These methods were superior in the characteristics that alginate fibers and their papers were made under very mild conditions using aqueous systems.

Preparation of entrapped enzymes in alginate fibers

In saline was dissolved an enzyme preparation. Sodium alginate was gradually added to the enzyme solution and well mixed in a kneader. the dope thus obtained was filtered through a sintered ceramic filter(pore size was 50 m or less). The filtrate was spun by a wet spinneret through a nozzle.

Using $CaCl_2$ as a coagulating reagent, various kinds of enzymes were entrapped in Ca alginate fibers and their paper. The results are summarized in Table 2 by comparison with the entrapped enzyme activities in the corresponding beads, approximately 2-3 mm in diameter. These beads were in parallel prepared by dropping the dope through small holes, about 1.0 mm diameter, into 5.0 wt.% $CaCl_2$ solution.
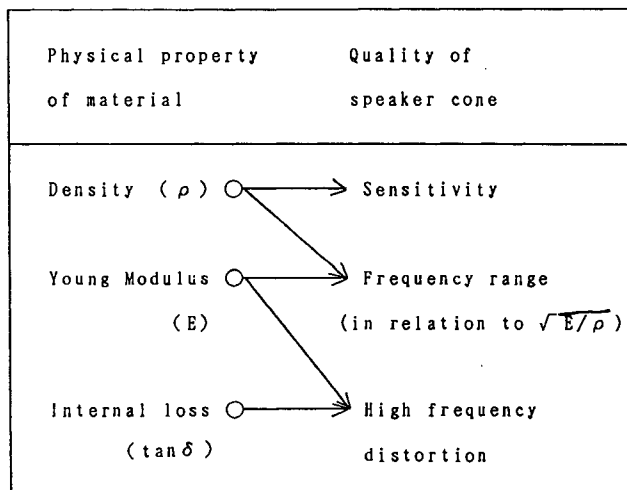
Table 3   Effect of divalent cations as coagulating agents on entrapment of glucoamylase in alginate fibers and their papers.

Spinning Conditions			Fiber		Paper		Beads	
Group	Divalent cation	Diameter of nozzle hole (mm)	Enzyme activity[a] (U/g)	Specific activity[b] (U/mg)	Enzyme activity[a] (U/g)	Specific activity[b] (U/mg)	Enzyme activity[a] (U/g)	Specific activity[b] (U/mg)
I	Cu^{2+}	0.10	1840	17.5	540	8.8	136	4.9
		0.055	1220	15.8	752	10.7		
IIa	Sr^{2+}	0.10	2380	29.3	219	25.9	81.0	24.8
	Ba^{2+}	0.10	354	19.5	53	11.5	61.3	4.8
		0.055	488	21.3	128	14.5		
IIb	Zn^{2+}	0.10	2240	25.9	2140	38.3	4.0[c]	0.8[c]
	Sn^{2+}	0.10	12.4	0.37	39.1	6.4	18.9	3.8
IVa	Pb^{2+}	0.10	220	10.6	167	8.9	132	21.1
VII	Mn^{2+}	0.10	425	3.1	12.0	1.0	125	1.4
		0.055	671	4.0	27.6	3.0	125	1.4
VIII	Co^{2+}	0.10	2280	13.5	975	18.3	430	9.6
		0.055	1500	7.9	954	22.3	430	9.6
	Ni^{2+}	0.10	1720	23.9	1930	36.9	569	22.3
		0.055	2010	25.2	1520	36.2	569	22.3

[a] Based on oven-dried alginate.
[b] Based on weight of entrapped enzyme.
[c] Degradation by hydrolysis was estimated.

Although the enzyme activities and specific activities were more or less scattered because of the complicated procedures, the following results could be obtained: (1) the thicker fiber could immobilize the higher amounts of enzymes (diameter of extruding holes 0.10 mm > 0.055 mm); (2) the entrapping yields of beads were always lower than those in the corresponding fibers and papers; (3) in the process of papermaking, the leakage was observed in most of the enzymes but some enzymes such as endo-polygalacturonase were almost completely fixed; and (4) the specific actvities did not decrease so greatly as the corresponding activities.

Effect of divalent ions on entrappment of enzymes   The entrapment of glucoamylase in alginate fibers and their papers were made using chlorides of various divalent metallic ions as coagulating agents. The results are summarized in Table 3. The order of immobilization rate of glucoamylase in the fiber was roughly as follows: Ca^{2+} > Sr^{2+}, Zn^{2+}, Co^{2+} > Ni^{2+}, Cu^{2+} > Mn^{2+}, Ba^{2+} > Pb^{2+} > Sn^{2+}. In process of papermaking, the entrapped enzyme leaked through metal chelate linkages; their order of entrapment in the paper was slightly altered: Zn^{2+} > Ni^{2+} > Ca^{2+} > Co^{2+} > Cu^{2+} > Sr^{2+} > Pb^{2+}, Ba^{2+}, Sn^{2+} > Mn^{2+}. Roughly speaking, transition-metal and alkali-earth ions gave higher immobilization rates and the entrapment was more stable in the former as observed in paper entrapment. These orders could be related neither with affinity of metal ions nor with gel strengths but were approximately equal to ionotropic series of Thiele.

Physical property of material	Quality of speaker cone
Density (ρ)	Sensitivity
Young Modulus (E)	Frequency range (in relation to $\sqrt{E/\rho}$)
Internal loss ($\tan\delta$)	High frequency distortion

3 Relationship between performance speaker cone and fundamental erties of diaphragm

3. Application of alginate fiber paper to speaker cone

Recently such new fiber materials as synthetic fibers, carbon fibers, and metallic fibers have been applied to diaphragms for speaker, generally so-called speaker cone[10]. The relationship between performance as diaphragm and material properties is shown in Fig. 3.

The required physical properties for the diaphragm materials are summarized as follows: (1)smaller density for high efficiency and sensitivity, (2)higher modulus of elasticity for broader regenerative band width, and (3)moderate internal loss for damping resonance. To fill these requirements,

Table 4 fundamental properties of Ca alginate fiber paper for speaker cone

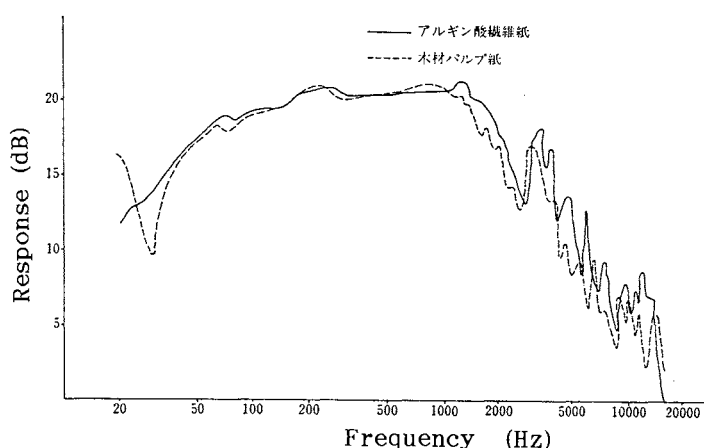| Density	Specific volume	Young Modulus	Internal loss	Propagation speed	Coefficient of elasticity loss
ρ		E	$\tan\delta$	$\sqrt{E/\rho}$	E''
g/cm^2	cm^3/g	$dyne/cm^2$ $\times 10^{10}$	$\times 10^{-2}$	cm/sec $\times 10^5$	$dyne/cm^2$ $\times 10$
0.422	2.37	4.02	5.52	3.08	22.2

Fig. 4 Acoustic properties of speaker cone composing of Ca alginate fiber paper

many kinds of fibers have been tried as materials for speaker cones. When physical properties of alginate fiber paper were analyzed from viewpoints of speaker cone materials, it was found that the paper had merits for this application as given in Table 4. The Table shows that the paper had following superior properties: (1)smaller bulk than that of wood pulp sheets depending upon selection of papermaking methods, (2)higher propagation rate for improved timbre and (3)moderate internal loss ranging 5.5 x 10^{-2}. This paper had other merits such as applicability of existing papermaking equipments and expectation of special tone color.

Based on these basic investigation, several kinds of speaker cone were made on experimental base using various kinds of alginate fibers. Though the measured relationship between frequency and response was very similar to that of wood pulp sheets as given in Fig. 4, the response was quite specific especially in bass bands and the tone color was found to be clear in being suitable to classical music.

4. Conclusions

Quite similar process of rayon papermaking process, it was found to produce alginate fiber paper from agal polysaccharides. This was so-called paper from marine plant, corresponding to usual paper from cellulose originating from land plants. As the cellulosic paper has extraordinarily wide applications, the newly born paper from seaweeds can expected to make full use in the fields of medical applications and electronics. In this presentation, two applications, i. e., immobilization of enzymes and a materials for speaker cone, were exemplified.

References

1. Kobayashi, Y., Matsuo, R., and Kawakatsu, H., "Manufacture and Physical Properties of Alginate Fiber Paper as an Analysis Model of Cellulosic Fiber Paper", J. Appl. Polymer Sci., **31**, 1735 (1986).
2. Gohda, T., "Method of Production of New Artificial Silk from Seaweed", Brit. Patent 417,222 (1934).
3. Gohda, T., "Method of Production of New Artificial Wool from Seaweed", Brit. Patent 420,857 (1934).
4. Dinelli,D., Marconi, W., and Morisi, F., "Fiber-Entrapped Enzymes", Methods. Enzymol., **44**, 227 (1976).
5. Marconi, W., Bartoli, F., Gulinellin, S., and Morisi, F., "Fiber-entrapped Enzymes in Analytical Chemistry", Process Biochem., 9 (4), 22 (1974).
6. Ichijo, H., Suehiro, T., Yamauchi, A., Ogawa, S., Sakurai, M., and Fujii,N., "Fibrous Support for Immobilization of Enzymes", J. Appl. Polymer Sci., **27**, 1665 (1982).
7. Shemer,L., Granot, R., Freeman, A., Sokolvsky, M., and Goldstein, L., "Multilayer Immobilized Enzyme Filter Reactors; Urease Bound to Nylon Fabric Filters", Biotechnol. Bioeng., **21**, 1007 (1979).
8. Miyamoto, T., "Functional Cellulose", Kami to Shuhengijutsu, **1**, 33 (1988).
9. Kobayashi, Y., Matsuo, R., Ohya, T., and Yokoi, N., "Enzyme-Entrapping Behaviors in Alginate Fibers and Their Papers", Biotechnol. Bioeng., **30**, 451 (1987).
10. Kobyashi, Y., and Kawahara, F., "Agal Paper as a Speaker Cone Material", Kogyo Zairyo, **35**, (3), 19 (1987).

BIOTECHNOLOGICAL APPROACHES REVEAL MOLECULAR CUES FOR CRASSOSTREA SET: ROLE OF MOLECULAR BIOLOGY IN OYSTER FARMING

R. Weiner, M. Walch, C. Fuqua, D. Sledjeski, L. Dagasan, S. Coon, D. Bonar, R. Colwell

University of Maryland, College Park, Maryland and Center of Mrine Biotechnology, Baltimore, Maryland, U.S.A.

Abstract

Alteromonas colwelliana is a periphytic marine bacterium that has been shown to enhance oyster set 3-8 fold. Enhancement is most pronounced on 72 hours or older biofilms that form on set surfaces. Many of the factors by which this bacterium promotes oyster development have been determined. Briefly, it released ammonia which is a swim search cue, L-dihydroxyphenylalanine (L-dopa) which promotes crawl search behavior, and exopolysaccharide (EPS) on which larvae preferentially cement down and metamorphose. Periphytic A. colwelliana also release quinones and other aromatic compounds that have been shown to inhibit the growth of microorganisms that parasitize oysters. Lastly, periphytic cells of A. colwelliana are in the size range where they can be filter fed by bivalves.

Using recombinant DNA technology, we have cloned the tyrosinase gene and enhanced its expression leading to increased production of L-dopa quinones and other benefical products. We made mutants with increased surface adhesion and EPS production. None of these modifications introduced qualitive alterations; only quantative enhancement.

Cultch has long been used as the Crassostrea virginica set surface in Chesapeake Bay. It is now in short supply. In any case, large hatcheries have discovered surfaces which are easier to manipulate, and which, when coated with certain microbial biofilms, yield better grow out than does cultch. In laboratory microcosms and in small scale hatchery trials, biofilms of A. colwelliana have enhanced C. virginica and C. gigas set on glass, cultch and mylar.

Additionally, A. colwelliana that has been genetically enhanced for EPS production and adhesion and/or engineered for increased tyrosinase/DOPA synthesis will be tested for the first time in microcosm regimes as we have previously tested wild type A. colwelliana. Should these "enhanced" strains cue more set than the wild type, they will also be tested

in scaled-up biofilm surfaces. Such surfaces will include French Tubes, corrugated acrylic panels and mylar sheets, each of which is now being used as artifical set surfaces at one or more hatcheries.

1. Introduction

In the natural environment, oyster larvae undergo a sterotypical sequence of actions before they become sessile and metamorphose. Each of these actions is cued by environmental stimuli that direct the motile larvae to fertile surface targets that are conducive for their development. It has long been known that certain bacterial biofilms are beneficial to oyster set (Cole and Knight-Jones, 1939). Recently, it has been recognized that these biofilms sequester nutrients, thus providing fertile surfaces. There may be multiple signals that attract invertebrate larvae to such surfaces (Chia and Bickell, 1978).

2. Results and Discussion

We have isolated and characterized specific chemical cues from bacteria that are important and perhaps essential, for oyster set. We have demonstrated that ammonia, the widely encountered product of protease and deaminase activities, inititates swim search behavior above the biofilm (Coon, et al. 1988). We propose that products of tyrosinase activity cue swim and crawl search behavior just above and on the biofilm (Coon, et al. 1985). Using a cosmid system in Escherichia coli we have cloned (Fig. 1) and expressed the tyrosinase gene (Tyr) of A. colwelliana (Fig. 2), a bacterium which was most beneficial to oyster set among 100 species that were tested (Weiner et al. 1985 Table 1). The DNA fragment encoding tyrosinase was subcloned in a pUC19 vector, sequenced (manuscript in preparation) and reduced to 1.3 KB. The gene was expressed, in vitro, using an S_{30} system and found to encode a 40,000 MW protein, which correlated with the size of its DNA open reading frame (manuscript in preparation).

The gene has been placed downstream of a Lac promoter providing amplified tyrosinase production. This construct can be moved back
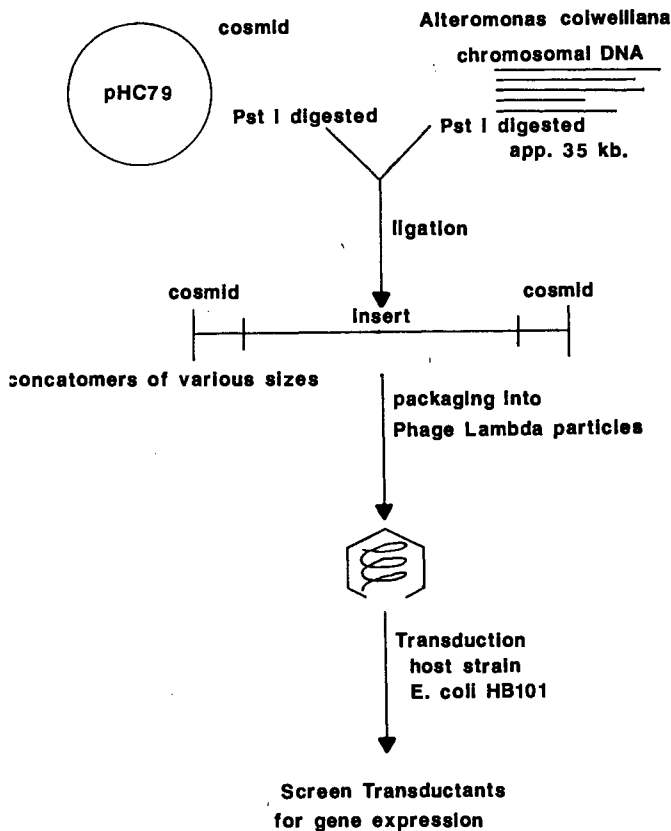
CLONING STRATEGY

Fig. 1 Alteromonas colwelliana cloning
strategy. The cosmid system was used
to maximize chance of inserting the
entire code necessary to express
tyrosinase. Screening was on Marine
agar with copper and tyrosine addi-
tions. Expression was detected by
melanin production (black colonies).

into A. colwelliana on a broad host range
plasmid (RP$_4$) for enhanced synthesis of the
search cue. The products of the tyrosinase
were identified (Dagasan and Weiner, 1988)
after fractionation in a C-18 reverse phase
HPLC column, by electrochemical detection of
di- and trihydroxy phenyl products (Morrison
and Cohen, 1983). An atypical reaction
product was isolated, 5-hydroxy dihydroxy
phenylalanine (5-TOPA), which was one of the
strongest inducers of swim-search behavior
that we have ever observed. In the relatively
anoxic and acetic biofilm niche, this compound
would, theoretically, be stable and active.

During swim/crawl-search, Crassostrea lar-
vae cement down. If not, they resume search
behavior and may die in the process. We have
examined the biofilms of marine bacteria,
particularly A. colwelliana, to test the
hypothesis that a specific bacterial product
cues the ultimate decision to become sessile.
One strategy was to present purified exopoly-
saccharide (EPS) and other surface bacterial

Fig. 2 Transmission electron micrograph of
Alteromonas colwelliana. Dark granules
are postulated to be melanin. Cells
were harvested in stationary phase of
growth. Bar represents one micrometer.

Table 1 Percent of oyster larvae that set and
metamorphosed on various surface films
in estuarine water at 20°C. The
Alteromonas and autochthonous films
promoted statistically significant
more set than other sample surfaces.
Results of 3 experiments using
competent, eyed Crassostrea gigas.

Substratum	% Set and Metamorphosed
Glass Control	8
Cultch (Shell Control)	23
Hyphomonas neptunium film	12
Pseudomonas fluorescens film	5
Vibrio fischeri film	9
Aeromonas hydrophila film	15
Shewanella colwelliana film	47
(nee Alteromonas, nee LST)	
Autochthonous film	45

Table 2 Lectin Binding to A. colwelliana

Lectin binding to whole cells of
S. colwelliana

Reaction	Lectin and Specificity	
+/-	GS-I	alpha-D-Galactose
++	WGA	Sialic Acid/N-acetylglucosamine
-	PNA	Methyl alpha-D-galactose>>>D-galactose
-	MPA	alpha-D-galactopyranoside
-	GS-II	alpha and ß-D-2 acetoamido-2-deoxy-D-glucose
-	SBA	alpha and ß-D-N-acetyl galactosamine>alpha-D-galactose
-	BPA	N-acetyl galactosamine
-	UEA I	alpha-L-fucose
-	DBA	Methyl 2-acetamido-2-deoxy-D-galactose
-	ConA	alpha-D-glucose, alpha-D-mannose

++ very strong reaction; +/- weak reaction; - no reaction

WGA binds very strongly to S. colwelliana indicating the presence of sialic acid or N-acetylglucosamine residues on its surface. Weak binding of GS-I indicates a small number of galactose residues on its surface.
Whole cells were heat fixed to slides and incubated for 30 minutes with an appropriate dilution of FITC conjugated lectin, washed and examined under flourescent microscope for binding.

components, such as lipopolysaccharide (LPS), to competent larvae. The other was to block determinants, of these molecules so they would not be available to cue set. Lectins (Table 2) and monoclonal antibodies (manuscript in preparation) to formalinized whole cells, purified EPS and outer membrane components were used for this purpose (Sledjeski and Weiner, 1988). Wheat germ agglutinin (WGA), known to bind sialic acid residues, had the strongest affinity and GS-I, known to bind to alpha-D-galactose, had a weaker affinity which appeared to be localized on specific sites of the A. colwelliana cell envelope.

Neither the lectins nor monoclonal antibodies to EPS blocked the ability of A. colwelliana films to cue set. From this and other evidence we theorize that an integral biofilm determinant does not cue set but rather that the chemical cue is likely to be some molecule (e.g. 5-TOPA) that is bound by EPS (Weiner, et al. 1989). We have recently made strains that hyper-produce EPS.

These results are being applied to increase oyster production in the Chesapeake Bay. Larvae are being treated with catecholamine precursors prior to their release over natural oyster beds. Cultch and several synthetic surfaces, coated with A. colwelliana biofilms, are being tested for potential use in hatcheries and in remote setting.

References

1. Chia, F.S. & L. Bickell., "Mechanisms of larval attachment and the induction of settlement and metamorphosis in coelenterates: A review. In Chia, F.S. & M. E. Rice (eds.) Settlement and Metamorphosis of marine Invertebrate Larvae, Elsevier, NY, pp. 1-12.

2. Cole, H.A. & E. W. Knight-Jones. 1939. Some observations and experiments on the setting behavior of Ostrea edulis. J. Cons.

Perm. Int. Explor. Mer. 14:86-105.

3. Coon, S.L., M. Walch, W.K. Fitt, D.B. Bonar & R.M. Weiner. 1988. Induction of settlement behavior in oyster larvae by ammonia. Amer. Zool. 28:70A.

4. Coon, S.L., D.B. Bonar & R.M. Weiner. 1985 Induction of settlement and metamorphosis of the Pacific oyster Crassostrea gigas (Thunberg) by L-DOPA and catecholamines. J. Exp. Mar. Biol. Ecol. 94:211-221.

5. Dagasan, L. & R.M. Weiner. 1988. Characterization and in vitro translation of an atypical tyrosinase from peripytic marine bacterium. Abstracts of 3rd Annu. Amer. Soc. Microbiol. Conf. Biotechnol. p. 43.

6. Morrison, M.E. and G. Cohen. 1983. Novel substrates for tyrosinase serve as precursors of 6-hydroxydopamine and 6-hydroxydopa. Bochem. 22:2134-2147.

7. Sledjeski, D.D. & R.M. Weiner. 1988. Characterization of Alteromonas sp. surface antigens. Abst. 88th Annu. Meet. Amer. Soc. Microbiol. p. 224.

8. Weiner, R.M., M. Walch, M. Labare, D. Bonar, and R. Colwell. 1989. Effect of Biofilms on the marine bacterium A. colwelliana (LST) on set of the oysters C. gigas and C. virginica. J. Shellfish Res. 8:117-123.

9. Weiner, R.M., V. Coyne, S.F. Raiken & P. Brayton. 1988. Alteromonas colwelliana, a new species from oyster water. Int. J. Syst. Bacteriol. 38:240-244.

10. Weiner, R.M., A.M. Segall & R.R. Colwell. 1985. Characterization of marine bacterium associated with Crassostrea virginica (the Eastern Oyster). Appl. Environ. Microbiol. 49:83-90.

Acknowledgement

GENE TRANSFER AND TRANSGENIC FISH: A NEW APPROACH TO AQUACULTURE

Thomas T. Chen[1], Rex A. Dunham[2], Deniis A. Powers[3]

1 Center of Marine Biotechnology, University of Maryland and Department of Biological Sciences, University of Maryland Baltimore County, Baltimore, MD.
2 Depertment of Fisheries and Allied Aquaculture, Auburn University, Auburn, Ala.
3 Hopkins Marine Station, Stanford University, Pacific Grove, CA.

ABSTRACT

As the world population increase rapidly, there is an urgent need to increase production of animal protein food sources. Aquaculture and mariculture possess a great potential to meet this demand. Studies conducted by us and others showed that application of biosynthetic trout GH to juvenile rainbow trout resulted in significant increases in growth rates. These results indicate that growth hormone, growth factor and their genes can be used to promote rapid growth of cultured fish. In this paper we will discuss application of molecular biology and biotechnology methods to promote rapid growth of cultured fish via manipulation of growth hormone and/or growth factor genes.

INTRODUCTION

As the world population increases rapidly, there is an urgent need to increase production of protein food sources. Since fish products are an excellent source of protein, they possess a great potential to meet this world demand. Traditionally, success in fisheries has been largely dependent upon the natural population of freshwater and marine finfish, shellfish and macroalgae. In 1986, the world-wide harvest of fish products reached 92 million metric tons. However, due to increasing world consumption of fish products, an increase release of chemical pollutants into the aquatic environments, and poor restocking and management efforts, the total world-wide annual harvest level of fish products is rapidly approaching the maximal potential harvest level of between 100 to 150 million metric tons, recently reported by the U.S. Department of Commerce and NOAA. Recently a number of regions have shown significant decline in the catches of important fish species such as salmon, striped bass, sturgeons, eels, jacks, mullets, mackerel, krill, abalone, oysters and crabs (FAO 1988). As a result, fisheries have traveled farther to exploit more productive areas, switched to alternative species, and begun to employ sophisticated technology. These developments have resulted in a significant increase of international fish prices. In recent years U.S. has imported twice as much fish products as they have exported, and thus contributed significantly to the trade deficient. This trade deficit in fish products has escalated to 6.6 billion U.S. dollars per year in 1989. In order to cope with these problems, drastic measures to increase fish production are required.

As a means of increasing the production of fish products, many countries have turned to aquaculture and mariculture. In 1985, the production of finfish, shellfish and macroalgae by aquaculture/mariculture reached 10.6 million metric tons, which was 12.3% of the world-wide catch tonnage generated. Clearly aquaculture/mariculture has the potential to significantly increase the world production of fish products, and thus affect the trade balance of fish products.

Success in aquaculture/mariculture revolves around four key requirements: breeding, feeding, disease protection, and management. Molecular biology and biotechnology can help to improve breeding, feeding and disease protection. These applications include enhancing growth rates, controlling reproductive cycle, improving feeds, developing vaccines, developing disease resistance and hardier genetic stocks, and many other possibilities. Using economically important fish species as models, our laboratories are investigating strategies to increase growth rates of finfish and shellfish in intensive culture operations via manipulation of growth hormone (GH) and growth factor genes. In this paper we shall discuss some of our recent findings to illustrate our approach.

GROWTH ENHANCEMENT OF THE GROWTH HORMONE:

Through molecular cloning, two genes encoding growth hormone polypeptides (GH1 and GH2) were identified in rainbow trout, Oncorhynchus mykiss (Agellon and Chen, 1986; Agellon et al., 1988a, 1988b). A large

amount of biologically active rainbow trout biosynthetic GH polypeptide was prepared by expressing rainbow trout GH1 cDNA sequence in E. coli cells (Agellon et al., 1988c). This biosynthetic hormone is a fusion protein, containing 9 amino acid residues derived from the N-terminus of E. coli beta-galactosidase and the entire sequence of the mature GH polypeptide. Agellon et al. (1988c) demonstrated in a series of experiments that application of this hormone to yearling rainbow trout resulted in a significant growth enchancement. After treatment of yearling rainbow trout with the biosynthetic GH for four weeks at a dose of 1 ug/g body weight/week, the weight gain in the individuals of the hormone-treated group was two times greater than that of their controls. Significant length gain was also evident in hormone-treated animals. When the same biosynthetic hormone preparation was administered to rainbow trout fry by immersing the fish in a GH containing solution, the same growth-promoting effect was also observed (Agellon et al., 1988c; Leong and Chen, unpublished results). These results are in agreement with those reported by Sekine et al. (1985) and Gill et al. (1985) that application of biosynthetic GH from other sources to rainbow trout, chum salmon or coho salmon also resulted in growth-enhancement. Several years ago, Morse (1984) reported that bovine insulin and GH enhanced the growth of California red abalone. Recently Paynter and Chen (unpublished results) have observed that administration of biosynthetic rainbow trout GH polypeptide to spats of juvenile oysters by the "dipping method" referred to above also resulted in significant increases in shell height, shell length, shell weight, as well as oyster wet weight and dry weight. Although the above discussed data clearly point to the possibility of enchancing the growth rates of cultured finfish and shellfish by supplying optimal levels of biosynthetic GH, many studies are still required to delinate a number of basic and practical scientific issues. These issues include: (i) efficient methods for large scale production, purification and renaturation of biosynthetic GH polypeptide; (ii) effective means of hormone delivery; (iii) detailed dose regimens for each target fish species; (iv) effects of both chronic and acute GH treatment; (v) nutrient requirements of GH-treated organisms; and (vi) genetic and physiological regulation of GH action.

GENERATION OF TRANSGENIC FISH

Although exogenous application of biosynthetic GH enchances growth rates of cultured fish, it may or may not be cost effective. The use of gene transfer technology to generate new strains of fish that express higher levels of GH, as an alternative, would bypass many of the problems associated with exogenous GH treatment. Moreover, once transgenic fish strains have been generated, they would be far more cost effective than their non-transgenic counterparts because these fish would have their own means of producing and delivering the hormone, and could transmit their enhanced growth characteristics of their offspring.

Zhu et al. (1985), in China, reported the first successful transfer of human GH gene fused to a mouse metallothionein gene promoter into goldfish. According to Zhu (personal communication), the F_1 offspring of these transgenic fish grew twice as large as their non-transgenic sibilings. Although Zhu and his colleagues did not present compelling evidence for integration and expression of the foreign genes in transgenic fish, many laboratories (including our groups) have successfully confirmed their work by demonstrating that GH gene and other gene constructs can be transferred into embryos of a number of fish species and integrated into the genomic DNA of the host fish (for review, see Chen and Powers, 1990). While a few groups have demonstrated expression of foreign genes in transgenic fish, at present, we are the only group to document that foreign fish GH genes are: (a) transferred to the target fish species; (b) integrated into the fish genome; (c) genetically transmitted to the next (F_1) generation; and (d) able to increase growth rates of both P_1 and F_1 generations of transgenic fish (Zhang et al., 1990; Chen et al., 1990).

In studies conducted in our laboratories (Zhang et al., 1990; Chen, et al., 1990), about 10^6 molecules of linearized recombinant plasmid containing the long terminal repeat (LTR) sequence of avian Rouse sarcoma virus (RSV) fused to the rainbow trout GH1 cDNA were injected into the cytoplasm of one-cell, two-cell and four-cell common carp embryos. Genomic DNA samples extracted from the pectoral fin of individuals derived from these embryos were analyzed for the presence of RSVLTR-rtGH1-cDNA by dot blot and Southern blot hybridization, using radio-labelled LTR of RSV and trout GH1 cDNA as probes. Results of this study showed that about 35% of the injected embryos survived at hatching, of which about 10% of the survivors have stably integrated the pRSVLTR-rtGH1-cDNA sequence. Southern blot analysis of the genomic DNA of several transgenic fish revealed that a single copy of the RSVLTR-rt-GH1-cDNA sequence was integrated at multiple chromosomal sites. In some cases, the Hind III site residing between RSVLTR and rtGH1-cDNA was modified. While foreign gene sequences introduced into embryos by micro-injection are usually integrated as a head-to-tail concatamer at a single chromosomal site and modified (Palmiter et al., 1982; Dunham et al., 1987), examples of single or low copy integrations of foreign gene sequences exhibiting deletions, modifications or rearrangements have also been observed (Gordon and Ruddle, 1985). Hence our results of pRSVLTR-rtGH1-cDNA integration in transgenic carp agree with those reported in other system.

EXPRESSION AND INHERITANCE OF FOREIGN GENES IN TRANSGENIC FISH:

As reported by Agellon et al. (1986) that polyclonal antibodies to chum salmon GH reacted specifically with GH of rainbow trout, hence these antibodies had been used as probes for detecting the production of trout GH in transgenic carp by a quantitive dot blot immunochemical method. Since these polyclonal antibodies shoed a partial cross-reactivity with common carp GH, they were rendered specific to rtGH by extensive re-absorption with pituitary extracts of common carp. We did not detect rtGH in the circula-tion of transgenic individuals, since the rtGH1-cDNA used in the gene transfer studies did not contain a signal peptide sequence. Instead, various levels of rtGH were detected in the red blood cell (RBC) extracts of transgenic individuals: ranged from 8.0 to 89.1 ng/mg RBC proteins (Zhang et al., 1990; Chen et al., 1990). As expected, there was no correlation between the number of pRSVLTR-rtGH1-cDNA integrated levels of rtGH expressed in RBC. These results are consistant with those in transgenic mice reported by Palmiter et al. (1982). Although there was considerable variation in sizes among the P_1 transgenic fish, they were 22% larger (p<0.05), on the average, than their sibling controls.

To study patterns of inheritance of RSVLTR-rtGH1-cDNA sequence in transgenic carp, sexually matured P_1 male transgenic fish (4R, 36L, 131L and 94R) were crossed to one non-transgenic female, and DNA samples extracted from resulting F_1 progeny were assayed for the presence of RSVLTR-rtGH1-cDNA sequence by dot blot hybridization. None of the F_1 progeny derived from transgenic male 04R received the RSVLTR-rtGH1-cDNA sequence from their father, suggesting that the RSVLTR-rtGH1-cDNA sequence was not inte-grated into the germ line of fish 04R. Although most of the F_1 progeny derived from fish 36L died, the four survivors in-herited the foreign gene sequence. Results obtained from F_1 progeny of fish 131L and 94R are most informative. About 31.3% and 42.3% of F_1 progeny derived from fish 131L and 94R respecively carried RSVLTR-rtGH1-cDNA sequence. Since transgenic fish are indepen-dently derived by injecting the foreign gene at different stages of development, one would expect transgenic animals mosaic for RSVLTR-rtGH1-cDNA. The degree of mosaicism in transgenic animals determines whether a foreing gene will be present in the germ line and whether it will be transmitted to subsequent generations. Since nearly 50% of the progeny derived from fish 94R carry RSVLTR-rtGH1-cDNA, the transformed progenitor cells must be primoridal to the entire germ-line. Conseversely, the progeny ratios of 1 transgenic: 3 non-transgenic from fish 131L suggests that his germ-line is mosaic.

The body weights of F_1 progeny derived from 131L and 94R were measured at the age of three months. The positive F_1 progeny of fish 131L and 94R were about 20.8% (p<0.05) and 40.1% (p<0.0001) larger than their non-transgenic sibilings, respectively. Further-more, these progeny were 32% and 46% larger than their largest non-transgenic sibilings respectively. These results clearly demon-strated that the growth enhancement phenotype resulting from the presence of RSVLTR-rtGH1-cDNA sequence in transgenic fish 131L and 94R have been passed down to their respective F_1 progeny through germ-line inheritance.

FUTURE PROSPECT

Although results from our studies and others showed that transfer, expression and inheritance of a foreign gene in finfish have been achieved, considerable amount of research is still required in order to develop strains of transgenic fish for commercial aquaculture/mariculture purposes. To achieve this ultimate goal of applying gene transfer technology in aquaculture/mariculture, several major breakthroughs are required. These include: (a) developing efficient mass gene transfer technologies; (b) developing rapid procedures for identifying presumptive trans-genic individuals; (c) developing methods for targeting foreign gene integration into specific areas of the fish genome; (d) identi-fying suitable promoters to drive the express-ion of the foreign gene; (3) determining physiological, nutritional, immunological, and environmental factors that will maximize the performance of transgenic individuals; (f) assessing safety and environmental impacts of transgenic fish.

REFERENCES

Agellon, L.D., Chen, T.T., van Beneden, R., Sonstegard, R.A., Wagner, G.F. and McKeown, B.A. (1986) Cand. J. Fish. Aqua. Sic. 43:1327-1331.

Agellon, L.B. and Chen, T.T. (1986) DNA 5:463-471.

Agellon, L.B., Davies, S.L., Chen, T.T. and Powers, D.A. (1988a) Proc. Natl. Acad. Sci. USA 85:5136-5140.

Agellon, L.B., Davies, S.L., Lin, C.M., Chen, T.T, and Powers, D.A. (1988b) Molec. Reproduc. Develop. 1:11-17.

Agellon, L.B., Emery C.J., Jones, J.M., Davies, S.L., DIngle, A.D., and Chen, T.T. (1988c) 45:146-151.

Chen, T.T., Lin, C.M., Zhu, Z., Gonzalez-Villa-senor, L.I., Dunham, R.A., and Powers, D.A. (1990) in "Transgenic Models in Medicine and Agirculture" (ed. by R. Church), pp. 127-139, Wiley-Liss, Inc., N.Y.

Chen, T.T., and Powers, D.A. (1990) Trends in Biotechnology (in press).

Dunham, R.A., Eash, J., Askins, J., Townes, T.M. (1987) Trens. Am. Fish. Soc. 116:87-91.

Fisheries Department (1988) FAO Yearbook, Food and Agriculture Organization of the United Nations 1986. Vol. 62,63.

Gill, J.A., Stumper, J.P., Donaldson, E.M. and Dye, H.M., (1985) Biotechnology 3:4306-4310.

Gordon, J.W., and Ruddle, F.H. (1985) Gene 33:121-136.

Morse, D.E. (1984) Aquaculture 39:263-282.

Palmiter, R.D., Brinster, R.L., Manner, R.E., Trumbauer, M.E., Rosenfeld, M.G., Birnberg, N.C., and Evans, R.M. (1982) Nature 300: 611-615.

Sekine, S., Miizukzmi, R., Nishi, T., Kuwana, Y., Saito, A., Sato, M., Itoh, H. and Kawauchi, H. (1985) Proc. Natl. Acad. Sci. USA 82:4306-4310.

Zhang, P., Hayat, M., Joyce, C. Gonzalez-Villasenor, L.I., Lin, C.M. Dunham, R.A., Chen, T.T., and Powers, D.A., (1990) Molec. Reproduc. Develop. 25: 13-25.

Zhu, Z., Li, G., He, L., and Chen, S. (1985) Z. Agnew Ichthyol. 1:31-34.